

International Series on
MATERIALS SCIENCE AND TECHNOLOGY
Volume 33—*Editor*: D. W. HOPKINS, M.Sc.

PERGAMON MATERIALS ADVISORY COMMITTEE

Sir Montague Finniston, Ph.D., D.Sc., F.R.S., Chairman

Dr. George Arthur

Professor J. W. Christian, M.A., D.Phil., F.R.S.

Professor R. W. Douglas, D.Sc.

Professor Mats Hillert, Sc.D.

D. W. Hopkins, M.Sc.

Professor H. G. Hopkins, D.Sc.

Professor W. S. Owen, D.Eng., Ph.D.

Mr. A. Post, Secretary

Professor G. V. Raynor, M.A., D.Phil., D.Sc., F.R.S.

Professor D. M. R. Taplin, D.Sc., D.Phil., F.I.M.

NOTICE TO READERS

Dear Reader

If your library is not already a standing order customer or subscriber to this series, may we recommend that you place a standing or subscription order to receive immediately upon publication all new issues and volumes published in this valuable series. Should you find that these volumes no longer serve your needs your order can be cancelled at any time without notice.

The Editors and the Publisher will be glad to receive suggestions or outlines of suitable titles, reviews or symposia for consideration for rapid publication in this series.

ROBERT MAXWELL

Publisher at Pergamon Press

Analysis of Welded Structures

*Residual Stresses, Distortion, and their
Consequences*

by

KOICHI MASUBUCHI

*Professor of Ocean Engineering and Materials Science
Massachusetts Institute of Technology, U.S.A.*



PERGAMON PRESS

OXFORD · NEW YORK · TORONTO · SYDNEY · PARIS · FRANKFURT

U.K.	Pergamon Press Ltd., Headington Hill Hall, Oxford OX3 0BW, England
U.S.A.	Pergamon Press Inc., Maxwell House, Fairview Park, Elmsford, New York 10523, U.S.A.
CANADA	Pergamon of Canada, Suite 104, 150 Consumers Road, Willowdale, Ontario M2J 1P9, Canada
AUSTRALIA	Pergamon Press (Aust.) Pty. Ltd., P.O. Box 544, Potts Point, N.S.W. 2011, Australia
FRANCE	Pergamon Press SARL, 24 rue des Ecoles, 75240 Paris, Cedex 05, France
FEDERAL REPUBLIC OF GERMANY	Pergamon Press GmbH, 6242 Kronberg-Taunus, Hammerweg 6, Federal Republic of Germany

Copyright © 1980 Pergamon Press Ltd.

All Rights Reserved. No part of this publication may be reproduced, stored in a retrieval system or transmitted in any form or by any means; electronic, electrostatic, magnetic tape, mechanical, photocopying, recording or otherwise, without permission in writing from the publishers.

First edition 1980

British Library Cataloguing in Publication Data

Masubuchi, Koichi

Analysis of Welded Structures.

(Pergamon international library: international series on materials science and technology; 33).

1. Deformations (Mechanics)

2. Strains and stresses

3. Welded joints

I. Title

671.5'20422 TA646 79-40880

ISBN 0-08-022714-7 (Hard cover)

ISBN 0-08-0261299 (Flexi cover)

*Printed and bound in Great Britain by
William Clowes (Beccles) Limited,
Beccles and London*

Preface

FROM December 1974 through November 1977, a research program entitled "Development of Analytical and Empirical Systems of Design and Fabrication of Welded Structures" was conducted at the Department of Ocean Engineering of the Massachusetts Institute of Technology for the Office of Naval Research, U.S. Navy under Contract No. N000 14-75-C-0469 NR031-773 (MIT OSP # 82558). The objective of the research program was to develop analytical and empirical systems to assist designers, metallurgists and welding engineers in selecting optimum parameters in the design and fabrication of welded structures. The program included the following tasks:

- Task 1: The development of a monograph about the prediction of stress, strain and other effects produced by welding.
- Task 2: The development of methods of predicting and controlling distortion in welded aluminum structures.

Efforts under Task 1 have resulted in a monograph entitled "Analysis of Design and Fabrication of Welded Structures". This book has been prepared from the monograph. This book covers various subjects related to design and fabrication of welded structures, especially residual stresses and distortion, and their consequences. How and whom this book is intended to help is written in Chapter 1 (Section 1.1.3).

Results of Task 2 are incorporated in Chapter 7. The final report of this research project is included as Reference (720).

Financial assistance also was given, especially in preparing the final draft of this book from the original monograph prepared under Task 1, by a group of Japanese companies including:

- Hitachi Shipbuilding and Engineering Co.
- Ishikawajima Harima Heavy Industries
- Kawasaki Heavy Industries
- Kobe Steel
- Mitsubishi Heavy Industries
- Mitsui Engineering and Shipbuilding Co.
- Nippon Kokan Kaisha
- Nippon Steel Corporation
- Sasebo Heavy Industries
- Sumitomo Heavy Industries

The author wishes to acknowledge financial assistance provided by the Office of Naval Research and the above Japanese companies.

The author also acknowledges a group of individuals who provided guidance, encouragement, and assistance. A number of people in the U.S. Navy, especially Dr. B. A. MacDonald and Dr. F. S. Gardner of the Office of Naval Research, reviewed

the monograph and provided numerous valuable comments. Professor W. S. Owen, Head of the Department of Materials Science and Engineering of M.I.T., provided various suggestions. Dr. K. Itoga of Kawasaki Heavy Industries, Ltd., Kobe, Japan, who was a research associate at M.I.T. from April 1975 through April 1978, assisted the author in preparing Chapters 9 to 10. Mr. V. J. Papazoglou assisted the author in preparing Chapter 13. Mrs. J. E. McLean, Mrs. M. B. Morey, and Miss M. M. Alfieri helped the author in typing.

In order to write this book, while working as professor at M.I.T., the author spent numerous hours during nights and weekends. The author sincerely thanks his wife Fumiko for her encouragement and understanding during these days.

KOICHI MASUBUCHI

Units

CURRENTLY changes are being made, slowly but steadily, in the United States in the use of units from the English system to the metric system, or more precisely the SI system (le Système international d'Unités). However, many articles referred to in this book use the English system and many readers of this book are still accustomed to the English system. To cope with this changing situation, the book has been prepared in the following manner.

- (a) All values given in the text are shown in both English and the SI units—the unit used in the original document first followed by a conversion. For example, when the plate thickness used was 1 inch it is shown as 1 in. (25.4 mm or 25 mm). On the other hand, when the original experiment was done with a 20-mm-thick plate, it is shown as 20 mm (0.8 in.). In the case of stresses, values are written in psi (or ksi), kg/mm², and newton/m² (or meganewton/m²).
- (b) Most figures and tables are shown as they appear in the original document, although in some cases both the English and the SI units are used.

The author hopes that the way in which this book is written provides a compromise rather than a confusion, thus making the book easy to read by people in various countries.

Below is a conversion table for units frequently used in this book.

<i>To convert from</i>	<i>to</i>	<i>multiply by</i>
inch (in.)	meter (m)	2.54×10^{-2}
inch	mm	2.54
foot (ft)	meter	3.048×10^{-1}
lbm/foot ³	kilogram/meter ³	1.601×10
Btu	joule (J)	1.055×10^3
calorie	joule	4.19
lbf (pound force)	newton (N)	4.448
kilogram force (kgf)	newton	9.806
pound mass (lbm)	kilogram (kg)	4.535×10^{-1}
lbf/inch ² (psi)	newton/meter ² (N/m ²)	6.894×10^3
ksi	MN/m ² *(a)	6.894
kgf/meter ²	newton/meter ²	9.806
Fahrenheit (t _F)	Celcius (t _C)	$t_C = (5/9)(t_F - 32)$

(a) MN (meganewton) = 10⁶ N (newton).

Notations

EFFORTS were made to use the same notation symbols, as much as possible, to express various quantities throughout the entire book. For example, I and V are used to express welding current and arc voltage, respectively. However, the author has found that it is almost impossible to use a single, unified system of notation throughout the entire book because:

1. the book covers many different subjects,
2. the book refers to works done by many investigators who used different notations.

Efforts were made to provide sufficient explanations whenever symbols are used.

References

REFERENCES are numbered by the number of the chapter in which the document is referred to first and the sequence in that chapter. For example, (103) is the third reference in Chapter 1, and (809) is the 9th reference in Chapter 8. At the end of each chapter, references which are used in that chapter for the first time are listed. For example, references (901), (902), ..., are listed at the end of Chapter 9.

When a reference is used repeatedly in later chapters, the original reference number is used throughout this book. For example, if reference (101) is used in a later chapter, it is still referred to as (101).

CHAPTER 1

Introduction

THIS chapter provides the necessary background information on structural materials and welding processes to enable those readers whose knowledge in these areas is limited to understand the remainder of this book.

1.1 Advantages and Disadvantages of Welded Structures and Major Objective of this Textbook

Since this book discusses at length the problems associated with the design and fabrication of welded structures, it risks creating the impression that welded structures are impractical due to their many special problems and their tendency to fracture. On the contrary, welded structures are superior in many respects to riveted structures, castings, and forgings. It is for this reason that welding is widely used in the fabrication of buildings, bridges, ships, oil-drilling rigs, pipelines, spaceships, nuclear reactors, and pressure vessels.

Before World War II, most ships and other structures were riveted; today, almost all of them are fabricated by welding. In fact, many of the structures presently being built—space rockets, deep-diving submersibles, and very heavy containment vessels for nuclear reactors—could not have been constructed without the proper application of welding technology.

1.1.1 *Advantages of Welded structures over riveted structures*

(A) *High joint efficiency.* The joint efficiency is defined as:

$$\frac{\text{Fracture strength of a joint}}{\text{Fracture strength of the base plate}} \times 100(\%)$$

Values of joint efficiency of welded joints are higher than those of most riveted joints. For example, the joint efficiency of a normal, sound butt weld can be as high as 100%. The joint efficiency of riveted joints vary, depending on the rivet diameter, the spacing, etc., and it is never possible to obtain 100% joint efficiency.

(B) *Water and air tightness.* It is very difficult to maintain complete water and air tightness in a riveted structure during service, but a welded structure is ideal for structures which require water and air tightness such as submarine hulls and storage tanks.

(C) *Weight saving.* The weight of a hull structure can be reduced as much as 10 and 20% if welding is used.

(D) *No limit on thickness.* It is very difficult to rivet plates that are more than 2 inches

2 *Analysis of Welded Structures*

thick. In welded structures there is virtually no limit to the thickness that may be employed.

(E) *Simple structural design.* Joint designs in welded structures can be much simpler than those in riveted structures. In welded structures, members can be simply butted together or fillet welded. In riveted structures, complex joints are required.

(F) *Reduction in fabrication time and cost.* By utilizing module construction techniques in which many subassemblies are prefabricated in a plant and are assembled later on site, a welded structure can be fabricated in a short period of time. In a modern shipyard, a 200,000-ton (dead weight) welded tanker can be launched in less than 3 months. If the same ship were fabricated with rivets, more than a year would be needed.

1.1.2 *Problems with welded structures*

Welded structures are by no means free from problems. Some of the major difficulties with welded structures are as follows:

(A) *Difficult-to-arrest fracture.* Once a crack starts to propagate in a welded structure, it is very difficult to arrest it, therefore, the study of fracture in welded structures is very important. If a crack occurs in a riveted structure, the crack will propagate to the end of the plate and stop; and, though a new crack may be initiated in the second plate, the fracture has been at least temporarily arrested. It is for this reason that riveted joints are often used as crack arresters in welded structures.

(B) *Possibility of defects.* Welds are often plagued with various types of defects including porosity, cracks, slag inclusion, etc.

(C) *Sensitive to materials.* Some materials are more difficult to weld than others. For example, steels with higher strength are generally more difficult to weld without cracking and are more sensitive to even small defects. Aluminum alloys are prone to porosity in the weld metal.

(D) *Lack of reliable NDT techniques.* Although many non-destructive testing methods have been developed and are in use today, none are completely satisfactory in terms of cost and reliability.

(E) *Residual stress and distortion.* Due to local heating during welding, complex thermal stresses occur during welding; and residual stress and distortion result after welding. Thermal stress, residual stress, and distortion cause cracking and mismatching; high tensile residual stresses in areas near the weld may cause fractures under certain conditions; distortion and compressive residual stress in the base plate may reduce buckling strength of structural members.

Consequently, in order to design and fabricate a soundly welded structure, it is essential to have: (1) adequate design; (2) proper selection of materials; (3) adequate equipment and proper welding procedures; (4) good workmanship; and (5) strict quality control.

1.1.3 *Major objective of this book*

Figure 1.1 shows the importance of residual stresses and distortion in the design and fabrication of welded structures.

When a practicing engineer is concerned with residual stresses and distortion, he is

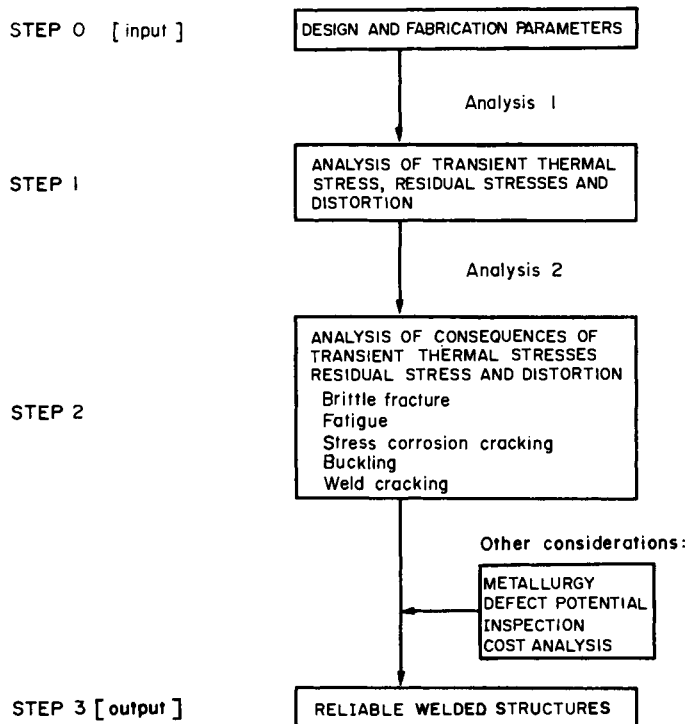


FIG. 1.1. Importance of residual stresses and distortion in the design and fabrication of welded structures.

also likely to be concerned with their adverse effects on the service performance of the structure which he is designing or fabricating. High tensile residual stresses in regions near the weld may promote brittle fracture, fatigue, or stress corrosion cracking. Compressive residual stresses and initial distortion may reduce buckling strength. What complicates the matter is that the extent of the effects of residual stresses is not only governed by residual stresses but also brittleness of the material. When the material is brittle, residual stresses may reduce the fracture strength of the weldment significantly. When the material is ductile, on the other hand, the effects of residual stresses are practically zero.

In fact what the practicing engineer wishes to do is to change design and fabrication parameters, such as plate thickness, joint design, welding conditions, welding sequence, etc., so that the adverse effects of residual stresses and distortion can be reduced to acceptable levels. It is much better to achieve this goal during an early stage of design and fabrication rather than confronting the problem at later stages of fabrication.

In order to accomplish this task, the engineer needs at least two kinds of analysis:

1. An analysis of transient thermal stresses, residual stresses, and distortion (Analysis 1 between Steps 0 and 1 in Fig. 1.1).
2. An analysis of the effects of thermal stresses, residual stresses and distortion on the service behavior of welded structures (Analysis 2 between Steps 1 and 2).

The major objective of this book is to cover the present knowledge of these two analyses.

Chapters 2 through 7 cover Analysis 1, while Chapters 8 through 14 cover Analysis 2.

The engineer also must consider many subjects other than residual stresses and distortion, and their consequences. These subjects include metallurgy, weld defect potential, inspection, fabrication cost, etc. The welding conditions that would give the minimum amount of distortion may not be usable because of the poor metallurgical properties or excessively high fabrication cost, for example. Therefore, what the engineer really needs is an integrated system which can analyze all the relevant subjects required. However, such an integrated system, yet to be developed, would be too extensive to be covered in a single book.

This book primarily covers subjects related to residual stresses and distortion, and their consequences. Attempts have been made to minimize duplications with other existing books. For example, a number of books have been written on brittle fracture, fatigue, stress corrosion cracking, buckling etc. Discussions in this textbook emphasize those subjects characteristic of welded structures, especially those related to residual stresses and distortion.

In preparing this book, discussions on welding processes, materials, and welding metallurgy have been kept to a minimum. The author plans to cover these subjects in subsequent books with the desire that the entire system will one day be fully integrated.[†]

1.2 Historical Overview and Future Trends⁽¹⁰¹⁾

When one thinks about what may happen in the future, it is often worthwhile to first examine what has happened in the past and what is happening now, because the future can be regarded as an extension of the past and present (although abrupt changes often take place). Figure 1.2 illustrates some major events in recent world history, the use of materials for ships and other large structures, and the development of joining methods and their applications.

1.2.1 *Materials for large structures*

From wood to steel. Until around 1850 wood was the principal material for building ships, bridges, and other structures. Around the middle of the nineteenth century, iron was introduced as a construction material. By the early 1900s, however, iron also became obsolete; since then steels, alloys of iron and carbon, and other elements have become the principal materials for ships and various other structures. Although other construction materials have been developed, steel still remains the most widely used material for the construction of ships and other large structures. Low carbon steels are used for most applications. However, high-strength steels are experiencing an increased use.

Figure 1.3 shows how the yield strength of materials used for U.S. Navy submarines and submersibles has increased.^(101,102) Prior to the early 1940s, combat submarines were fabricated largely from low-carbon steel, a material with a tensile yield strength of about 32,000 psi (22.4 kg/mm² or 220 MN/m²). Between 1940 and 1958 high-tensile-strength steel (HTS) with a 50,000 psi (35.2 kg/mm² or 344.7 MN/m²) yield strength was used in most submarine structures. In 1958 HY-80 steel, a quenched-and-tempered

[†] The following three books are under preparation: (1) *Welding Engineering*, (2) *Fractures of Welded Structures*, (3) *Materials for Ocean Engineering* [revision of Reference (102)].

Year	General Events	Materials for Marine Structures	Joining Methods
1776	Independence of U.S.A.	Wooden Structures	
1800			Brazing, Forging
1850	Civil War	Iron Structures Iron	
1900		Steel Structures	Inventions of Modern Joining Processes
	World War I Washington Conf.	Steel	Covered Electrode
	World War II	Light Metal Aircraft	Invention of Inert Gas Welding Submerged Arc Liberty Ships
1950	Suez Crisis	Aluminum	EB Welding Laser Welding
	Apollo Lunar Landing	Ti	
1976	Oil Embargo		
2000			

FIG. 1.2. Some major events.

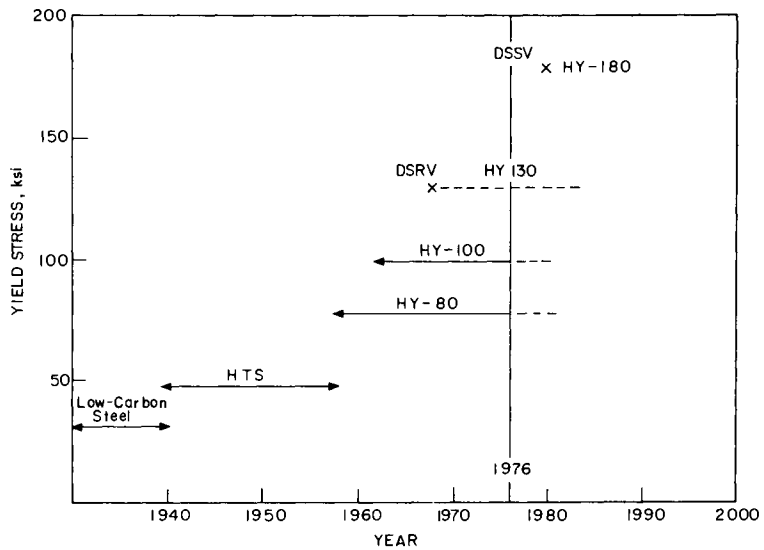


FIG. 1.3. Use of high-strength steels for U.S. Navy submarines and submersibles.

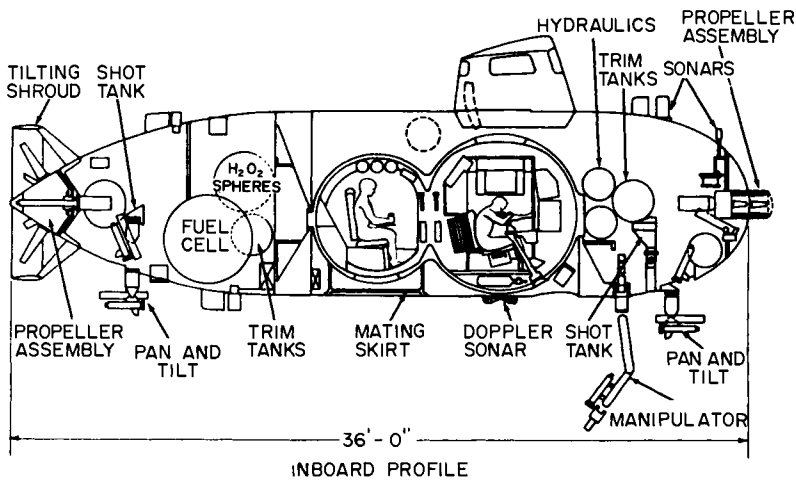


FIG. 1.4. General schematic of 20,000 ft (6100 m) DSSV. This figure is taken from Reference (103). Some design changes may have been made.

steel with a minimum yield strength of 80,000 psi (56.2 kg/mm^2 or 552 MN/m^2) was first introduced to submarine hulls. Some years later HY-100, a steel with 100,000 psi (70.3 kg/mm^2 or 689 MN/m^2) minimum yield strength and very similar to HY-80, was introduced. Today, HY-80 and HY-100 are the basic fabrication steels for submarine hulls.

The next steel in line is HY-130. This steel was first called HY-140; however, it was discovered later that only 130,000 psi (91.4 kg/mm^2 or 896 MN/m^2) yield strength can be guaranteed in the welds. In 1969 the first Deep Submergence Rescue Vehicle (DSRV) was fabricated by Lockheed Missile and Space Company using HY-130. DSRV is capable of diving to a depth of 6000 ft (1830 m). The U.S. Navy plans to use HY-130 for submarines in the next decade. The U.S. Navy also has a plan to build Deep Submergence Search Vehicle (DSSV) with a depth capability of 20,000 ft (6100 m). The material being considered is HY-180.

Figure 1.4 is a general scheme of the DSSV which is designed to operate at the maximum depth of 20,000 ft (6100 m).⁽¹⁰³⁾

Applications of high-strength steels to commercial structures, including ships, bridges, and pressure vessels, occurred several years later; and most applications have been limited to steels up to 120,000 psi (84.4 kg/mm^2 or 827 MN/m^2) yield strength. Besides the Navy's HY-80 and HY-100, there are a number of commercial quenched and tempered steels such as ASTM A514/517. These steels have excellent fracture toughness at low temperatures and they have been extensively used for various structures.

So far, attention has been placed on development of high-strength steels. Another important development involves materials with excellent fracture toughness at cryogenic temperatures primarily for tanks for liquefied natural gas (LNG) carriers. Table 1.1 list several tank systems developed to date.⁽¹⁰¹⁾ The most important feature from the viewpoint of materials and welding technology is the cryogenic tank. Ferrous alloys which have been used include:

- 9% and 5½% nickel steel,
- Austenitic stainless steel,
- 36% nickel steel (Invar).

TABLE 1.1. Tank systems for LNG Carrier.

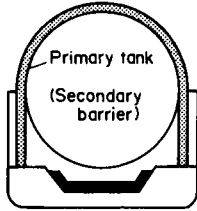
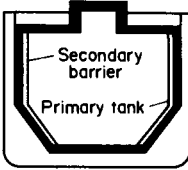
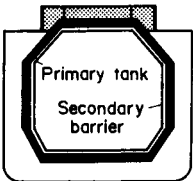
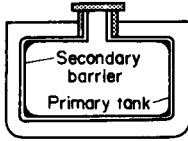
Tank system	Independent tank					
	Spherical type			Square type		
Midship section						
Licensee	Moss-Kvaener	Techni-Gaz	Gaz-Transport	Conch	ESSO (single tank)	ESSO Conch (double tank)
Tank material	9% Ni steel and aluminum	9% Ni steel	9% Ni steel	Aluminum	9% Ni steel	Aluminum
Midship section						
Licensee	Techni-Gaz		Gaz-Transport	Bridgestone Liq. Gas	Ishikawajima-Harima	
Tank material	Stainless steel		36% Ni steel (invar)	9% Ni steel and aluminum	Aluminum	



FIG. 1.5. Surface effect ship-SES 100.⁽¹⁰¹⁾ This photograph shows SES 100, a 100-ton surface effect ship completed in 1975 by the Bell Aerospace for the U.S. Navy. This ship cruises at a speed of over 80 knots. The U.S. Navy plans to build surface effect ships as large as 2000 tons with a cruising speed of 100 knots.

Aluminum. The first use of aluminum in ships occurred in the 1890s, very shortly after steel was introduced. In 1889 aluminum was used in U.S. Navy torpedo boats.

Since the 1930s aluminum alloys have been used extensively in aircraft, primarily due to its light weight. Aluminum alloys also have been used for other structures. In ships, for example, aluminum alloys are used primarily for superstructures. Aluminum alloys are extensively used for hull structures of advanced high-performance ships (AHPS), including surface effect ships (SES), as shown in Fig. 1.5.

Besides light weight, aluminum alloys have good toughness at extremely low temperatures. Aluminum alloys have been extensively used for tanks containing cryogenic cargos. For example, the huge tanks containing the fuel (kerosene and liquid hydrogen) and the oxidizer (liquid oxygen) of the Saturn V space rocket used in the Apollo program were built with aluminum alloys (see Fig. 1.6). These tanks were welded.

Aluminum alloys also have been considered as important structural materials for the cryogenic tanks of LNG carriers, as shown in Table 1.1.

Titanium alloys. Titanium alloys were first used for aerospace applications in the late 1950s. Today titanium alloys are used for various parts of aircraft structures (especially supersonic aircraft) and jet engines. However, it was not until 1963 that the submarine hull program of the U.S. Navy was actually started. Uses of titanium alloys for structures other than aerospace and chemical applications so far have been very limited.

The major advantages of titanium alloys are high strength-to-weight ratio and excellent corrosion resistance. Extremely high material and fabrication costs are the principal drawbacks.

1.2.2 *Joining technology*

Historians can trace welding techniques back to prehistoric days. Men were soldering with copper-gold and lead-tin alloys before 3000 B.C. However, the only sources of heat available until around 1850 were wood and coal. Because of the relatively low temperature available, the joining processes used were limited to soldering, brazing, and forging.

Development of modern welding technology began in the latter half of the nineteenth century when electrical energy became commercially available. Most of the important discoveries leading to modern welding processes were made between 1880 and 1900. Processes invented during this period include: carbon arc, arc welding, oxyacetylene, and electric resistance processes. Covered electrodes were introduced around 1910.

During World War I, metal-arc welding was used for the first time in ship construction, primarily for repairs. In 1921 the first all-welded, ocean-going ship was built. From these beginnings, applications of welding increased steadily in the 1930s. Demand for reliable methods for welding light-metal alloys for aircraft accelerated the development of inert-gas arc welding processes. The submerged arc process was also introduced in the 1930s.

A drastic change in ship construction occurred during World War II from riveting to welding. To meet the urgent demand for a large number of ships needed for the war, the United States entered into the large-scale production of welded ships for the first time in history. By that time the technique of welding steel plates had been well established. However, there had not been enough knowledge and experience regarding design and fabrication of large welded structures and their fracture characteristics.

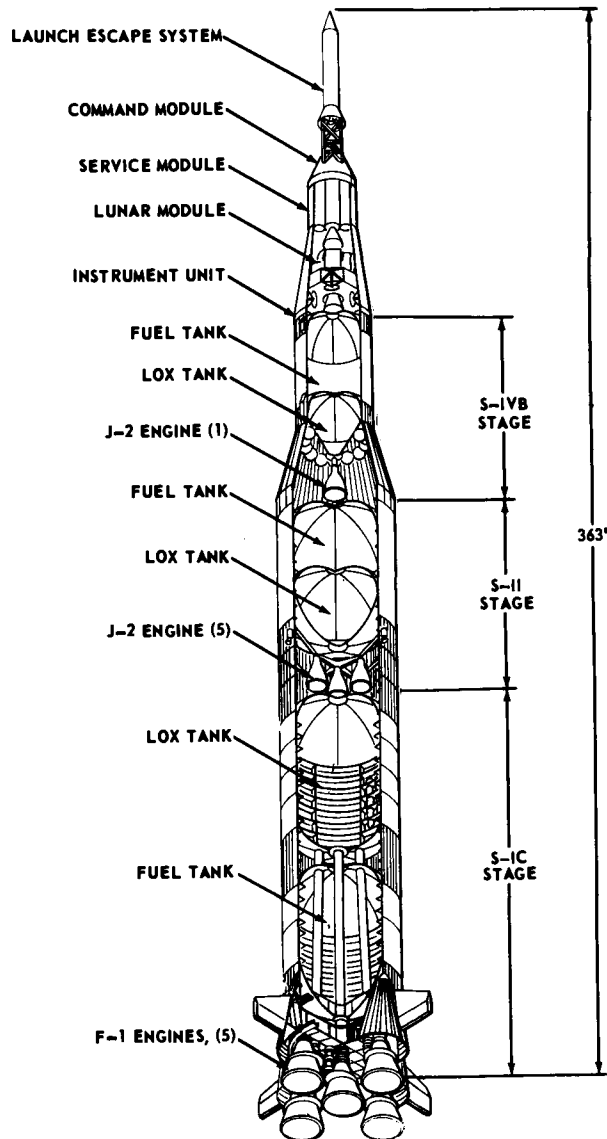


FIG. 1.6. Saturn V Space Vehicle⁽¹⁰⁴⁾. The Saturn V space vehicle stands 363 ft (110.6 m) high with its Apollo spacecraft in place. Its maximum diameter is 33 ft (10 m). The first stage, which is called S-IC, is powered by five F-1 engines, which burn kerosene and liquid oxygen. The second stage, S-II, and the third stage, S-IVB, are powered by J-2 engines, which burn liquid hydrogen and liquid oxygen.

As far as the weight is concerned, the Saturn V may be considered as an assembly of huge fuel and oxidizer tanks. The Saturn V filled with fuel and liquid oxygen weighs about 2700 tons, while its emptied weight is only 170 tons.

Aluminum alloys 2014 and 2219 were used for structural alloys for fuel and oxidizer tanks because of their attractive strength-to-weight ratio in the range of temperatures to be encountered. Joint thickness ranged from $\frac{1}{8}$ to 1 in (3.2 to 25.4 mm). The tanks were welded with gas tungsten arc and gas metal arc processes.

Among approximately 5000 merchant ships built in the United States during World War II, about 1000 ships experienced structural failures. About twenty ships broke in two or were abandoned due to structural failures. These failures led to an enormous research effort on brittle fracture and welding, and the technology for fabricating welded ships and other structures was established between 1954 and 1955. By 1960 most ships built in the world were fabricated by welding.

A number of new welding processes have been developed during the last 30 years. They include: CO₂-gas shielded arc, electroslog, electrogas, ultrasonic, friction, electron-beam, plasma arc, and laser welding processes. As a result, most metals used in present-day applications can be welded.

1.3 Requirements for the Selection of Materials⁽¹⁰²⁾

1.3.1 Required properties

The following pages discuss some of the important properties materials must possess to be used successfully for strength members of structures.

Strength-to-weight ratio. The weight density of a material is frequently a critical characteristic, since structural weight is so often a major design consideration. In many cases it is not the absolute density itself which is important but a strength-to-weight ratio, usually represented by the ratio of either yield stress or ultimate stress to the weight density. Such a parameter is usually employed in cases where maintaining a certain level of strength to the minimum structural weight is desirable.

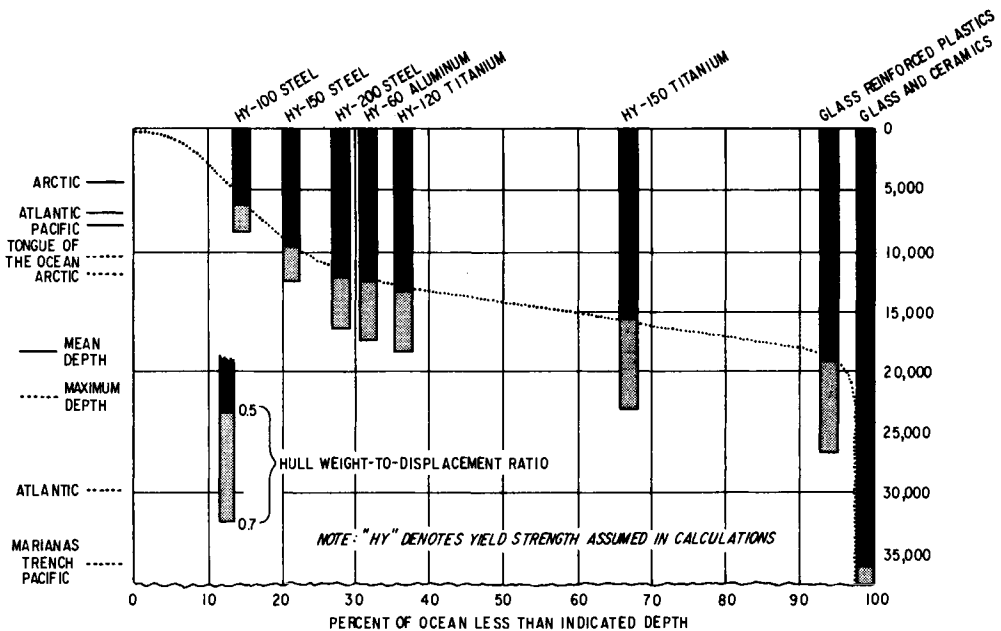


FIG. 1.7. Operating depth potential of submersibles made in different materials⁽¹⁰⁵⁾

Among various ocean engineering structures, submarine hulls present the most crucial problems. Figure 1.7 shows curves representing the calculated performance of near-perfect spherical pressure hulls in various materials.⁽¹⁰⁵⁾ Shown here are relationships between the collapse depth and the ratio of collapse or buckling stress (which is dependent on geometry) to density. The advantage of materials with high strength-to-weight ratio is obvious especially at a greater depth.

It is important to mention that techniques for fabricating submarine hulls with various materials are not necessarily available at the present. The Navy classifies materials according to background and experience.

Category 1 materials include those alloys such as HY-80 and HY-100 for which there is an abundance of technical data and operational experience. Category 2 materials include those alloys such as HY-130, Marming (190) steel, HP 9-4-25, and annealed Ti-Al-4V. There is also an abundance of data, but experience in the operations environment is limited. Category 3 contains those materials for which there is little technical data and experience. Several Category 3 materials have high collapse-stress-to-density ratios. They include heat-treated titanium alloys, ultrahigh-strength steels, glass, ceramics such as aluminum oxide, advanced metal-matrix and resin-matrix composites, and dualalloy, diffusion-bonded plates.

Fracture toughness. Fracture toughness is a measure of a material's ability to absorb energy through plastic deformation before fracturing. Several technical terms including "ductility", "notch toughness", and "fracture toughness" are used to describe the resistance of a material to fracture. Notch toughness, for example, refers to the ability of a material to resist brittle fracture in the presence of a metallurgical or mechanical crack or notch. In general, the more energy absorbed, the more ductile or tough the material is said to be. Chapter 9 discusses fracture toughness in detail.

Fracture toughness often becomes a critical problem when a material with high strength is considered, because there is a general tendency for fracture toughness to decrease with increasing strength. Notch toughness also becomes a critical problem when a structure is subjected to low temperatures.

Fatigue strength. Loads which do not cause fracture in a single application can result in fracture when applied repeatedly. The mechanism of fatigue failure is complex, but it basically involves the initiation of small cracks, usually from the surface, and the subsequent growth under repeated loading. Chapter 11 covers subjects related to fatigue failures.

Resistance against corrosion and stress corrosion cracking. Materials used for structural components exposed to seawater and other environments must have adequate resistance against corrosion and stress corrosion cracking.

Corrosion is the destructive attack of a metal by chemical or electrochemical reaction with the environment. Stress corrosion cracking, on the other hand, is the fracture of a material under the existence of both stress and certain environments. Chapter 12 covers stress corrosion cracking and hydrogen embrittlement.

Other properties. Other material characteristics which merit consideration include ease of fabrication, weldability, durability, maintenance, general availability, and finally (but not least important), cost. With several possible modes of failure to be anticipated in each element of a structure and weight and/or cost to be minimized (or perhaps

other performance characteristics to be maximized) trade-off studies must be resorted to before a final optimum choice of material can be made for any specific application.

1.3.2 *Commonly used or promising structural materials*

Structural materials which are commonly used at present and which are promising in the future fall into four main categories: ferrous metals, non-ferrous metals, non-metals, and composites.

Steel. Steels show promise mainly because of the extremely high strengths which new heat-treatment techniques are making possible. These new steels include such types as HY-80, HY-100, HY-130, HY-180, and the maraging steels. Yield stresses range from 80,000 psi (56.2 kg/mm² or 552 MN/m²) for HY-80 to approximately 300,000 psi (211 kg/mm² or 2068 MN/m²) for some maraging steels. A tendency toward brittle behavior and low notch toughness, in addition to only moderate increase of fatigue life are the major drawbacks of these high-strength steels.

As the strength level increases, steels tend to become more difficult to weld without cracks and other defects. Some high-strength steels also are sensitive to stress corrosion cracking. Section 1.4 discusses more about structural steels.

Aluminum. Aluminum is of interest mainly because of its low density. Aluminum alloys also have good fracture toughness at low temperatures, and they are antimagnetic. Some of the new aluminum alloys are competitive with some steels in yield and ultimate strength. As with steel, as strengths increase, aluminum alloys show a tendency toward lower notch toughness, and questionable fatigue life.

Some high-strength aluminum alloys, especially those which are heat treated, also are difficult to weld, and are sensitive to stress corrosion cracking. Section 1.5 discusses aluminum alloys for structural uses.

Titanium. Titanium combines a relatively low density with very high strength, excellent fatigue properties and corrosion resistance, and antimagnetic properties. Titanium alloys are considered to be promising materials for high-performance aerospace and hydrospace structures despite the high costs of materials and fabrication. Section 1.6 discusses titanium alloys for structural uses.

Other metals. Various metals other than steels, aluminum alloys, and titanium alloys are used or can be used for various components of engineering structures. They include nickel alloys, bronze, and other copper alloys, etc.

Composite materials. Composite materials are made of filaments of some material specifically oriented in a matrix material. The filaments may be of either a metallic or non-metallic material. Glass and boron are commonly considered. Such fiber composites are being developed with very high strength-to-weight ratios. Current major problems of composite materials involve joining and delamination under pressure in long-term use.

Glass and ceramics. Glass and ceramics are of interest because of their extremely high strengths in compression. They also demonstrate excellent corrosion resistance. Glass, in addition, offers the advantage of transparency. The chief drawback of glass and ceramics is their brittle behavior.

Other materials. Plywood and concrete have been used for various structures. The main advantage of both is their relatively low cost. In addition, concrete possesses good compressive strength, good availability, resistance to corrosion, and excellent formability. Its chief disadvantage is its limit tensile strength.

Since this book is concerned primarily with welding of structural materials, the following pages discuss steel, aluminum alloys, and titanium alloys.

1.4 Structural Steels⁽¹⁰²⁾

The following pages cover various steels which have been or may be used for structures. These steels include: carbon steels, low-alloy high-strength steels, quenched-and-tempered steels, and maraging steels.

1.4.1 Low carbon steels and high-strength steels with less than 80,000 psi yield strength

Low carbon steels and high-strength steels with less than 80,000 psi (56.2 kg/mm² or 522 MN/m²) yield strength are among the most widely used structural materials.

For many years ASTM A7 steel was the basic structural carbon steel and was produced to a minimum yield strength of 33 ksi (23.3 kg/mm² or 228 MN/m²)⁽¹⁰⁶⁾ for welded structures, ASTM A 373 steel with a minimum yield strength of 32 ksi (22.5 kg/mm² or 220 MN/m²) was frequently used. In 1960 ASTM A 36 steel was introduced with a yield strength of 36 ksi (25.3 kg/mm² or 248 MN/m²) and improved weldability over A7 steel.

With regard to ship-hull steels, United States merchant vessels are constructed in accordance with requirements established by the U.S. Coast Guard and the American Bureau of Shipping. Naval combatant vessels and many merchant-type naval vessels are constructed in accordance with U.S. Navy specifications.

The American Bureau of Shipping requirements can be found in its *Rules for Building*

TABLE 1.2 *ABS requirements for ordinary-strength hull structural Grades, A, B, D, E, DS, and CS
Process of manufacture: Open-hearth, Basic-oxygen, or Electric furnace*

Grades	A	B	D	E	DS	CS
<i>Deoxidation</i>	Any method except rimmed steel ¹	Any method except rimmed steel	Fully killed, fine-grain practice ^{2, 10}	Fully killed, fine-grain practice ¹⁰	Fully killed, fine-grain practice ¹⁰	Fully killed, fine-grain practice ¹⁰
<i>Chemical composition³</i> (Ladle analysis)						
Carbon, %	0.23 max. ⁴	0.21 max.	0.21 max.	0.18 max.	0.16 max.	0.16 max.
Manganese, %	⁵	0.80–1.10 ^{7, 8}	0.70–1.50 ^{7, 9}	0.70–1.40 ⁷	1.00–1.35 ⁷	1.00–1.35 ⁷
Phosphorus, %	0.04 max.	0.04 max.	0.04 max.	0.04 max.	0.04 max.	0.04 max.
Sulphur, %	0.04 max.	0.04 max.	0.04 max.	0.04 max.	0.04 max.	0.04 max.
Silicon, %		0.35 max.	0.10–0.35	0.10–0.35	0.10–0.35	0.10–0.35

Tensile test

Tensile strength For all Grades: 41–50 kg/mm² or 58,000–71,000 psi^{11, 12}
 Yield point, min. For all grades: 24 kg/mm² or 34,000 psi¹³
 Elongation, min. For all grades: 21% in 200 mm (8 in.) or 24% in 50 mm (2 in.) or 22% in 5.65√A (A equals area of test specimen)¹¹

(Contd.)

TABLE 1.2 (Contd.)

<i>Impact test</i>						
<i>Charpy V-notch</i>						
Temperature	- 20°C (- 4°F)		- 40°C (- 40°F)			
Energy, avg. min.						
Longitudinal specimens	2.8 kg-m		2.8 kg-m			
or	(20 ft-lb)		(20 ft-lb)			
Transverse specimens	2.0 kg-m		2.0 kg-m			
	(14 ft-lb)		(14 ft-lb)			
No. of specimens	3 from each 40 tons ¹⁴		3 from each plate			
<i>Heat treatment</i>						
			Normalized over 35 mm (1 $\frac{3}{8}$ in.) thick. ¹⁵	Normalized	Normalized over 35 mm (1 $\frac{3}{8}$ in.) thick	Normalized
<i>Stamping</i>	$\frac{AB}{A}$	$\frac{AB}{B}$	$\frac{AB^{16}}{D}$	$\frac{AB}{B}$	$\frac{AB^{16}}{DS}$	$\frac{AB}{CS}$

Notes

- 1 Grade A steel equal to or less than 12.5 mm (0.50 in.) in thickness may be rimmed.
- 2 Grade D may be furnished semi-killed in thicknesses up to 35 mm (1.375 in.) provided that the steel over 25.5 mm (1.00 in.) in thickness is normalized. In this case the requirements relative to minimum Si and Al contents and the fine-grain practice of Note 10 do not apply.
- 3 For all grades exclusive of Grade A shapes and bars the carbon content plus $\frac{1}{6}$ of the Mn content is not to exceed 0.40%.
- 4 A maximum carbon content of 0.26% is acceptable for Grade A plates equal to or less than 12.5 mm (0.50 in.) and all thicknesses of Grade A shapes and bars.
- 5 Grade A plates over 12.5 mm (0.50 in.) in thickness are to have a minimum manganese content not less than 2.5 times the carbon content, Grade A shapes and bars are not subject to the manganese/carbon ratio of 2.5.
- 7 For all grades the specified upper limit of the manganese may be exceeded up to a maximum of 1.65% provided carbon content plus $\frac{1}{6}$ Mn content does not exceed 0.40%. For Grade B, the lower limit of the manganese may be reduced to 0.60% when the Si content is 0.10% or more (killed steel).
- 8 For Grade B where the use of cold-flaging

quality has been specially approved the manganese range may be reduced to 0.60–0.90%.

- 9 For Grade D steel equal to or less than 25.5 mm (1.00 in.) in thickness 0.60% minimum Mn content is acceptable.
- 10 See above.
- 11 The tensile strength of cold-flaging steel is to be 39–46 kg/mm² (55,000–65,000 psi), the yield point 21 kg/mm² (30,000 psi) minimum, and the elongation 23% minimum in 200 mm (8.00 in.).
- 12 A tensile strength range of 41–56 kg/mm² (58,000–80,000 psi) may be applied to Grade A shapes and bars.
- 13 For Grade A over 25.5 mm (1.00 in.) in thickness, the minimum yield point may be reduced to 23 kg/mm² (32,000 psi).
- 14 Impact tests are not required for normalized Grade D when furnished fully-killed fine-grain practice.
- 15 Control rolling of Grade D steel may be specially considered as a substitute for normalizing in which case impact tests are required for each 20 tons of material in the heat.
- 16 Grade D or DS hull steel which is normalized for special applications as specified in 43.3.8b is to be stamped $\frac{AB}{DN}$ or $\frac{AB}{DSN}$ respectively.

TABLE 1.3 *ABS requirements for higher strength hull structural steel, Grades AH32, EH32, AH36, DH36, and EH36 Process of manufacture: Open hearth, Basic oxygen or Electric furnace*

Grades ¹	AH32	DH32	EH32	AH36	DH36	EH36
<i>Deoxidation</i>	Semi-killed or killed ³	Killed, fine grain practice ⁵	Killed, fine grain practice ⁵	Semi-killed or killed ³	Killed, fine grain practice ⁵	Killed, fine grain practice ⁵
<i>Chemical compositions for all grades (Ladle analysis)</i>						
Carbon, %	0.18 max.					
Manganese, % ²	0.90–1.60					
Phosphorus, %	0.04 max.					
Sulfur, %	0.04 max.					
Silicon, % ³	0.10–0.50					
Nickel, %	0.40 max.					
Chromium, %	0.25 max.					
Molybdenum, %	0.08 max.					
Copper, %	0.35 max.					
Columbium, % (Niobium)	0.05 max.					
Vanadium, %	0.10 max.					
<i>Tensile Test</i>						
Tensile strength	48–60 kg/mm ² ; 68,000–85,000 psi			50–63 kg/mm ² ; 71,000–90,000 psi		
Yield point, min.	32 kg/mm ² ; 45,500 psi			36 kg/mm ² ; 51,000 psi		
Elongation, min.	For all grades: 19% in 200 mm (8 in.) or 22% in 50 mm (2 in.)					or 20% in 5.65√A (A equals area of test specimen).
<i>Heat treatment: see Table 43.4</i>						
<i>Impact test</i>						
<i>Charpy V-notch</i>						
Temperature	None required	– 20°C (– 4°F)	– 40°C (– 40°F)	None required	– 20°C (– 40°F)	– 40°C (– 40°F)
Energy, avg. min.						
Longitudinal specimens or Transverse specimens		3.5 kg-m (25 ft-lb) ⁶	3.5 kg-m (25 ft-lb)		3.5 kg-m (25 ft-lb) ⁶	3.5 kg-m (25 ft-lb)
No. of specimens		3 from each 40 tons plate	3 from each plate		3 from each 40 tons plate	3 from each plate
<i>Stamping</i>	AB/AH32	AB/DH32 ⁷	AB/EH32	AB/AH36	AB/DH36 ⁷	AB/EH36

Notes

- The numbers following the Grade designation indicate the yield point to which the steel is ordered and produced in kg/mm². A yield point of 32 kg/mm² is equivalent to 45,500 psi and a yield point of 36 kg/mm² is equivalent to 51,000 psi.
- Grade AH 12.5 mm (0.50 in.) and under in thickness may have a minimum manganese content of 0.70%.
- Grade AH to 12.5 mm (0.50 in.) inclusive may be semi-killed in which case the 0.10% minimum

silicon does not apply. Unless otherwise specially approved, Grade AH over 12.5 mm (0.50 in.) is to be killed with 0.10 to 0.50% silicon.

- Grades DH and EH are to contain at least one of the grain refining elements in sufficient amount to meet the fine grain practice requirement.
- Impact tests are not required for normalized Grade DH.
- The marking AB/DHN is to be used to denote Grade DH plates which have either been normalized or control rolled in accordance with an approved procedure.

TABLE 1.4 *Heat treatment requirements for ABS higher-strength hull structural steels*

<i>Aluminum-treated steels</i>	
AH	— Normalizing not required
DH ^{1,2}	— Normalizing required over 25.5 mm (1.0 in.)
EH	— Normalized
<i>Columbium (niobium)- treated steels</i>	
AH ¹	— Normalizing required over 12.5 mm (0.50 in.)
DH ¹	— Normalizing required over 12.5 mm (0.50 in.)
EH	— Normalized
<i>Vanadium-treated steels</i>	
AH	— Normalizing not required
DH ¹	— Normalizing required over 19.0 mm (0.75 in.)
EH	— Normalized

Notes

- Control rolling of Grades AH and DH may be specially considered as a substitute for normalizing in which case impact tests are required on each plate.
- Aluminum-treated DH steel over 19.0 mm (0.75 in.), intended for the special applications is to be ordered and produced in the normalized condition.
- When columbium or vanadium are used in combination with aluminum, the heat-treatment requirements for columbium or vanadium apply.

and *Classing Steel Vessels*, which is revised annually. Tables 1.2 and 1.3 show ABS requirements in 1977 for ordinary and high-strength hull structural steel. The present rules include high-strength steels of about 46,000 to 51,000 psi (32.3 to 35.9 kg/mm² or 317 to 352 MN/m²) yield strength. Table 1.4 shows heat-treatment requirements for high-strength steels. The ABS specifications for hull steels since 1948 recognize variations in notch toughness due to thickness of plates by specifying grades. Requirements for notch toughness are specified for steels under Grades D, E, DH32, EH32, DH36, and EH36. Tables 1.5 and 1.6 show applications of these steels.

The U.S. Navy Specification MIL-S2269A, Steel Plate, Carbon, Structural for Ships, is in substantial agreement with the American Bureau of Shipping specifications for ordinary-strength hull steels as follows:

- Grade HT, a carbon steel with minimum yield strength 42,000 to 50,000 psi (29.5 to 35.2 kg/mm² or 290 to 345 MN/m²) depending upon thickness.
- QT 50, a carbon manganese steel heat-treated by quenching with minimum yield strength 50,000 to 70,000 psi (35.2 to 49.2 kg/mm² or 345 to 483 MN/m²).

In regard to the last steel mentioned, QT 50, quenching is required to prevent a transformation of the high temperature austenite phase to undesirable microstructure constituents which are a normal result of transformations on “slow” cooling in temperatures 400–1250° F (204–677°C) for one to several hours. The highest tempering temperature results in the lowest strength and maximum fracture toughness, and the converse is true.

In addition to the above steels which have been developed for ship-hull applications, there are many other steels which can be used or have been used for various applications. Tables 1.7(a) and (b) provide lists of various steels used for structures.⁽¹⁰⁷⁾ These tables are prepared from Technical and Research Bulletin No. 2-11a, *Guide for the Selection of High-strength and Alloy Steels*, published by the Society of Naval Architects and Marine Engineers.⁽¹⁰⁸⁾

TABLE 1.5 Applications of ABS ordinary-strength hull structural steels

-
- (a) *Plates 51.0 mm (2.00 in.) in thickness and under—ordinary applications.* Plates 51.0 mm (2.00 in.) in thickness and under, where intended for ordinary applications, are to be of the following grades.
- Grade A. Acceptable up to and including 19.0 mm (0.75 in.) in thickness. Acceptable over 19.0 mm (0.75 in.) up to and including 51.0 mm (2.00 in.) in thickness except for the bottom, sheerstrake, strength-deck plating within the midship portion and other members which may be subject to comparatively high stresses.
- Grade B. Acceptable up to and including 25.5 mm (1.00 in.) in thickness and up to and including 51.0 mm (2.00 in.) where Grade A is acceptable.
- Grades D and DS. Acceptable up to and including 51.0 mm (2.00 in.) in thickness.
- Grades CS and E. Acceptable up to and including 51.0 mm (2.00 in.) in thickness.
- (b) *Plates 51.0 mm (2.00 in.) in thickness and under—special applications.* Plates 51.0 mm (2.00 in.) in thickness and under, where required elsewhere in these Rules to be of special material owing to their application in the deck and shell plating, are to be of the following grades.
- Grade A. Acceptable up to and including 19.0 mm (0.75 in.) in thickness for the bilge strake, where a Rule double bottom is fitted.
- Grade B. Acceptable up to and including 16.0 mm (0.63 in.) in thickness and up to and including 19.0 mm (0.75 in.) where Grade A is acceptable.
- Grade D. Acceptable up to and including 22.5 mm (0.89 in.) in thickness when furnished as rolled and acceptable up to and including 27.5 mm (1.08 in.) in thickness when fully killed, fine grain normalized. (See Note 16 of Table 1.2.)
- Grade DS. Acceptable up to and including 22.5 mm (0.89 in.) in thickness when furnished as rolled and acceptable up to and including 51.0 mm (2.00 in.) in thickness when normalized (see Note 16, Table 1.2).
- Grades CS and E. Acceptable up to and including 51.0 mm (2.00 in.) in thickness.
- (c) *Plates Over 51.0 mm (2.00 in.) in thickness* Plates over 51.0 mm (2.00 in.) in thickness are to be produced to specially approved specifications.
- (d) *Shapes and bars.* Unless otherwise specified, steel meeting the requirements of Grade A is acceptable.
-

TABLE 1.6 Applications of ABS higher-strength hull structural steels

-
- (a) *Plates 51.0 mm (2.00 in.) in thickness and under—ordinary applications.* Plates 51.0 mm (2.00 in.) in thickness and under, where intended for ordinary applications, are to be of the following grades:
- Grade AH. Acceptable up to and including 19.0 mm (0.75 in.) in thickness. Acceptable over 19.0 mm (0.75 in.) up to and including 51.0 mm (2.00 in.) in thickness except for the bottom, sheerstrake, strength-deck plating within the midship portion, and other members which may be subject to comparatively high stresses.
- Grade DH. Acceptable up to and including 51.0 mm (2.00 in.) in thickness.
- Grade EH. Acceptable up to and including 51.0 mm (2.00 in.) in thickness.
- (b) *Plates 51.0 mm (2.00 in.) in thickness and under—special applications.* Plates 51.0 mm (2.00 in.) in thickness and under, where required elsewhere in these Rules to be of special material owing to their application in the deck and shell plating, are to be of the following grades:
- Grades AH and DH. Acceptable up to and including 19.0 mm (0.75 in.) in thickness.
- Grade DH. Acceptable up to and including 27.5 mm (1.08 in.) in thickness, provided the material is normalized. However, normalizing is not required for thicknesses up to and including 19 mm (0.75 in.) unless required by Table 1.4.
- Grade EH. Acceptable up to and including 51.0 mm (2.00 in.) in thickness.
- (c) *Plates over 51.0 mm (2.00 in.) in thickness.* Plates over 51.0 mm (2.00 in.) in thickness are to be produced to specially approved specifications.
- (d) *Application of shapes and bars.* Unless otherwise specified, steel meeting the requirements of Grade AH semi-killed is acceptable.
-

TABLE 1.7 Chemical compositions and properties of some structural steels^(a)(107, 108)
 (a) Steels with less than 80,000 psi minimum yield strength

Type →	30,000–49,000 psi min yield strength				50,000–79,000 psi min yield strength				MIL-S-13326 70,000 class
	ASTM A-255 Grade A fl. qual.	ASTM A-242	ASTM A-441	MIL-S-16113C Grade HT	CA C-Mn	ASTM A-302 Grade B	C.M.V. (or Cb)	C-Mn-V (or Cb)	
Composition ^(b)									
Carbon, %	0.21	0.18	0.22	0.18	0.22	0.23	0.24	0.24	0.20
Manganese, %	0.80–1.10	1.45	1.25	1.30	1.35	1.15–1.50	1.40	1.40	1.40
Phosphorus, %	0.05	0.035	—	0.04	0.040	0.035	0.040	0.040	0.040
Sulfur, %	0.05	0.04	0.05	0.05	0.040	0.040	0.050	0.050	0.040
Silicon, %	—	0.15–0.30	0.030	0.15–0.35	0.15–0.30	0.15–0.30	0.15–0.30	0.15–0.30	0.15–0.30
Chromium, %	—	—	—	0.15	—	—	—	—	—
Nickel, %	—	—	—	0.25	—	—	—	—	—
Molybdenum, %	—	—	—	0.06	—	0.45–0.60	—	—	—
Vanadium, %	—	0.09–0.14	0.02 ^(d)	0.02 ^(d)	—	—	0.02 ^(d, b)	—	—
Copper, %	—	—	0.02 ^(d)	0.35	—	—	—	—	—
Titanium, %	—	—	—	0.005	—	—	—	—	—
Heat treatment	As-rolled	As-rolled	As-rolled	Norm.	As-rolled	As-rolled	As-rolled	As-rolled	Q & T
Min tensile strength, psi	58,000	70,000	67,000	88,000 ^(f)	70,000	80,000	65,000	70,000	90,000
Min yield strength, psi	32,000 ⁽ⁱ⁾	40,000	46,000	47,000	50,000	50,000	50,000	55,000	70,000
Elongation (in 8 in.), %	28	17	19	20	19	15	18	15	17
Approx. NTD range, °F	–20° to +40°	+20° to +90°	–20° to +40°	–60° to +20°	–10° to +40°	–20° to +50°	–60° to +30°	–40° to +40°	–75° to –30°
Weldability	Good	Good	Good	Good	Good	Special	Special	Special	Good
Available thickness, in.	½–1	¾–4	¾–4	No limit	¾–1¼	¼–min.	¾–1½	¾–1¼	¾–2
Relative cost ^(c)	1	1.77	1.20	1.67	1.12	1.77	1.12	1.15	1.43

(b) Steels with 80,000 to 120,000 psi minimum yield strength

Type →	80,000–120,000 psi min yield strength							
	Proprietary Grades ^(a)	MIL-S-16216 HY-80	ASTM A-543 Class 1	ASTM A-543 Class 2	ASTM A-517-67 ^t	MIL-S-13326 Class 90	MIL-S-16216 HY-100	MIL-S-13326 Class 120
Composition ^(b)								
Carbon, %	0.21	0.18	0.23	0.23	0.21		0.20	
Manganese, %	—	0.10–0.40	0.40	0.40	—		0.10–0.40	
Phosphorous, %	0.040	0.025	0.035	0.035	0.035		0.025	
Sulfur, %	0.040	0.025	0.040	0.040	0.040	Chemistry	0.025	Chemistry
Silicon, %	—	0.15–0.35	0.20–0.35	0.20–0.35	—	not specified	0.15–0.35	not specified
Chromium, %	—	1.00–1.80	1.50–2.00	1.50–2.00	—		1.00–1.80	
Nickel, %	—	2.00–3.25	2.60–3.25	3.00–4.00	—		2.25–3.50	
Molybdenum, %	—	0.20–0.60	0.45–0.60	0.45–0.60	—		0.20–0.60	
Vanadium, %	—	—	0.03	0.03	—		—	
Heat treatment	Q & T	Q & T	Q & T	Q & T	Q & T	Q & T	Q & T	Q & T
Min. tensile strength, psi	(1)	1	105,000	115,000	115,000	(1)	(1)	(1)
Min yield strength, psi	80,000	80,000	85,000	100,000	100,000	90,000	100,000	120,000
Elongation (in 2 in.) %	18	20	16	16	16	(1)	18	(1)
Approx NDT range, °F	– 40° or lower	– 130° or lower	– 120° or lower	– 90° or lower	– 50° or lower	– 40° or lower	– 100° or lower	– 20° or lower
Weldability	Special	Special	Special ^(m)	Special ^(m)	Special	Special	Special	Special ^(m)
Available thickness, in.	$\frac{3}{16}$ –2 $\frac{1}{2}$ ^(m)	$\frac{3}{16}$ –8	$\frac{3}{16}$ –4	4	$\frac{3}{16}$ –2 $\frac{1}{2}$	(1)	$\frac{3}{16}$ –3	(1)
Relative cost ^(c)	2.0	3.5	3.0	3.0	2.0	2.0	3.5	3.5

^(a) From: *Guide to Selection of High Strength and Alloy Steels*, Soc. Naval Architects and Marine Engineers. ^(b) Ladle analysis. Percentages shown are maximum values unless given as range or otherwise noted. ^(c) Relative to ABS Class B, Dec '63. ^(d) Minimum. ^(e) Can vary depending on supplier. ^(f) Maximum. ^(g) Plate over $\frac{3}{4}$ in. thick should be normalized for structural ship applications. ^(h) Or columbium. ⁽ⁱ⁾ Aluminum deoxidized, fine-grain practice. ^(j) Approximate; yield strength not specified. ^(k) Includes proprietary grades individually identified by composition, mechanical properties, and thickness range. ^(l) About 10,000 to 15,000 psi above yield strength. ^(m) Below 21°C. ⁽ⁿ⁾ Normal range available; plate up to 8 in. available in some grades. ^(o) No limit specified.

Steel plates and shapes listed in these tables are for ship structures requiring an increase of strength not originally available with standard ship steels. The values tabulated are for steels of 1-in. thickness and may vary with steel mill practice. Further details of these steels are available in ASTM or manufacturers' specifications.

Steels with less than 60,000 psi (42.2 kg/mm² or 414 MN/m²) minimum yield strength are usually available in the as-rolled or normalized condition, while steels with minimum yield strength over 60,000 psi (42.2 kg/mm² or 414 MN/m²) are usually available in the quenched-and-tempered condition.[†]

Notch-toughness requirements. Structural steels must have a suitable degree of notch toughness and weldability in addition to conventional mechanical properties such as ultimate tensile strength, yield strength, and elongation. Notch toughness is important in avoiding brittle fracture of welded structures. Notch toughness of steel is discussed in detail in Chapter 9. Table 1.7 provides notch toughness data given in Nil Ductility Transition (NDT) temperatures of various steels.

Welding of low-carbon steels. Shielded metal-arc welding continues to be the major welding process for fabricating structures in low carbon steels. Electrodes for use in welding ship hulls should meet the requirements of the AWS-ASTM Tentative Specifications for Mild-steel-covered-arc Welding Electrodes or the American Bureau of Shipping rules for the approval of Electrodes for Manual Arc Welding. The E60xx series is used for all hull construction except for E6012 and E6013, which are not approved for any joints in shell plating, strength decks, tank tops, bulkheads and longitudinal members of large vessels or in galvanized material because of their slightly lower ductility. (See Table 9.8)

Electrodes of the E7015, E6016, and E7018 classes are often used where improved mechanical properties in the weld are desirable. The trend is toward the use of electrodes having iron-powder coatings, because they offer high deposition rates.

Various automatic and semi-automatic processes are often used in the fabrication of ships and ocean engineering structures. Such processes include submerged arc, gas metal-arc, electroslag, and electrogas processes. Welding processes with high deposition rate, such as submerged arc, electroslag, and electrogas processes, often provide weld metals with rather low notch toughness. This problem is discussed in detail in Section 9.8.

Welding of high-strength steels.⁽¹⁰²⁾ The U.S. Navy provides an electrode specification, MIL-E-2220011, with the following classifications and intended uses:

Type MIL-7018: For welding of medium carbon steels such as Classes A, B, C and Grade HT (under $\frac{5}{8}$ -in. (10 mm) thickness).

Type MIL-8018: For welding Grade HT ($\frac{5}{8}$ -in. (16 mm) and thicker).

In welding high-strength steels there are two factors to be emphasized.⁽¹⁰⁹⁾ First, select the proper electrode to meet the strength requirements for the welded joint. Second, select an adequate preheat to assure that a sound weld will be produced. In cases of high restraint it is recommended that higher preheats be used. Better results are obtained when low-hydrogen electrodes are used with the higher strength grades.

[†]This trend is true for steels with minimum yield strength over 80,000 psi (56.2 kg/mm² or 552 MN/m²) (see Table 1.7).

Satisfactory welds can be obtained using these electrodes at much lower preheats than are necessary for conventional electrodes. Further discussions on prevention of cracking in welding high-strength steels are given in Chapter 14.

High-strength steels can also be welded with various other processes. However, further discussions of welding high-strength steels are not included here, because the subject is considered to be outside the scope of this book. For those who are interested in this subject, a book from the American Society for Metals (ASM) entitled *Welding High-strength Steels* is recommended.⁽¹¹⁰⁾

1.4.2 Quenched and tempered steels⁽¹⁰²⁾ up to 120,000 psi yield strength

Table 1.7(b) lists several steels with 80,000 to 120,000 psi (56.2 to 84.4 kg/mm² or 552 to 827 MN/m²) specified yield strength. To obtain high strength, good notch toughness and good weldability, all steels listed here are quenched and tempered. Quenching is conducted to prevent the transformation of high-temperature austenite phase into undesirable microstructure constituents which are a normal result of “slow” cooling in the 800–1100°F (427–593°C) range. Tempering involves reheating for one to several hours to temperatures 400° to 1250°F (204 to 677°C). HY-80 and HY-100, made to MIL-S-16216, are used principally for naval ships. Specification MIL-S-13326 covers four strength levels, including 90,000 and 120,000 psi (63.3 and 84.4 kg/mm² or 620 and 827 MN/m²).

Among the steels listed, HY-80 is the most commonly used for submarines. ASTM A517-67 is also commonly used for commercial applications including pressure vessels, storage tanks, and merchant ships. Compared with HY-80, ASTM A517-67 contains less nickel and is less costly; about twice as expensive as ABS B steel while HY-80 is about 3.5 times as expensive as ABS B steel. Since HY-80 is the most well known among the steels listed in Table 1.7(b), the following discussions primarily concern HY-80 steel.

Chemical composition of HY-80 steel. The specification limits of chemical compositions of HY-80 steel are (see Table 1.7(b)).^{(111)†}

1. 0.18% for carbon, which is the same requirement for HTS.
2. 0.15–0.35% for silicon, which is used for deoxidation.
3. 0.025% each for sulfur and phosphorus, not to exceed 0.045 altogether. This strict control of sulfur and phosphorus requires that more care than usual be taken during the steel-making process.
4. 0.10–0.40% for manganese which is again used for sulfur control, rather than strength. An amount over 1.0% of Mn would cause embrittled steel during heat treatments.
5. Molybdenum, slight quantities for lowering the temper embrittlement.
6. Nickel, slight quantities for toughness.

Mechanical properties of HY-80 steel. Table 1.8 shows specification limits for mechanical properties of HY-80 steel. Values of specified yield strengths are 80,000 to 100,000 psi (56.2 to 70.3 kg/mm² or 552 to 689 MN/m²) for plates less than $\frac{5}{8}$ in. (16 mm) thick and 80,000 to 95,000 psi (56.2 to 66.8 kg/mm² or 552 to 655 MN/m²) for plates ($\frac{5}{8}$ in. (16 mm) and over. Minimum specified Charpy V-notch impact energy values at – 120°F (– 84°C)

† Chapter 9 covers effects of chemical composition on notch toughness of steel.

TABLE 1.8 Specification limits of HY-80 mechanical properties⁽¹¹¹⁾

Property	Plate thickness	
	Less than $\frac{5}{8}$ in.	$\frac{5}{8}$ in. and over
Ultimate strength (psi)	For information	For information
Yield strength at 0.2% offset (psi)	80,000 to 100,000	80,000 to 95,000
Min. elongation in 2 in. (%)	19	20
Reduction in area (%)		
Longitudinal	—	55
Transverse	—	50

Charpy V-notch energy requirements			
Plate thickness	Specimen size (mm)	Foot pounds (min)	Test temperature (Degrees F)
$\frac{1}{4}$ in. to $\frac{1}{2}$ in. excl.	10 × 5	For information	-120
$\frac{1}{2}$ in. to 2 in. incl.	10 × 10	50	-120
Over 2 in.	10 × 10	30	-120

are 50-lb (6.9 k2/m) for plates $\frac{1}{2}$ in. (12.5 mm) to 2 in. (51 mm) inclusive and 30 ft-lb (4.1 kg/m) for plates over 2 in. (51 mm).

Figure 1.8 shows typical Charpy V-notch energy bands for production of HTS and HY-80.⁽¹¹¹⁾ The figure shows that notch toughness of HY-80 is much superior to that of HTS.

Welding of HY-80 steel. In welding any material, the goal is to produce weld metals with properties the same as those of the base metal. It is not easy with even common materials, but with a high-strength notch-tough steel such as HY-80 it is extremely difficult. So far it has not been possible to develop electrodes which produce weld

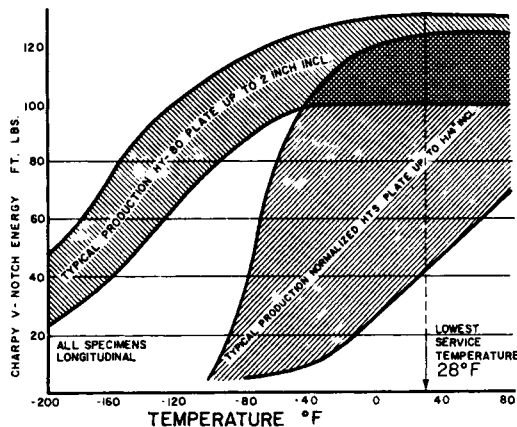


FIG. 1.8. Typical Charpy V-notch energy bands for production HTS and HY-80.⁽¹¹¹⁾

TABLE 1.9 HY-80 welding electrodes and application⁽¹¹¹⁾

Elec. type	Specification	Process	Position	Application
MIL-11018	MIL-E-22200/1	Shielded metal arc	All	All
MIL-10018	MIL-E-22200/1	Shielded metal arc	All	Fillet, fillet groove or groove joints
MIL-9018	MIL-E-22200/1	Shielded metal arc	All	Limited use
MIL-B88	MIL-E-19822	Semi-automatic or automatic metal inert-gas arc	Flat or horizontal	All
MIL-EB82 ^(a)	MIL-E-22749	Submerged arc	Flat	All
MIL-MI88 ^(a)	MIL-E-22749n	Submerged arc	Flat	All
MIL-8218Y QT	MIL-E-22200/5	Shielded metal arc	All	Limited to procedure approval

^(a) Granular flux particle size 10 × 50.

^(b) Granular flux particle size 12 × 150.

metals as notch tough as HY-80 base plate. This problem is discussed in detail in Section 9.8.

Table 1.9 lists electrodes currently used for welding HY-80 and their application in submarine construction.⁽¹¹¹⁾ In addition to the electrode type designation, the appropriate Military Specifications, welding processes, welding positions, and applications are included in the table. Regarding electrodes for shielded metal arc process, the low-hydrogen iron powder/Exx18-types are used most widely. Table 1.9 also includes electrodes for inert-gas metal arc (semi-automatic and automatic) and submerged arc processes.

Table 1.10 shows specification limits of mechanical properties of as-deposited weld metals. A family of Exx18-type electrodes has been developed which can provide a range of yield strength from 60,000 to 100,000 psi (42.2 to 70.3 kg/mm² or 414 to 689 MN/m²), therefore, to select from Table 1.10 an electrode which will undermatch, match, or overmatch the strength of HY-80 base metal as desired or required by the design.

1.4.3 Steels over 120,000 psi yield strength

Table 1.7 lists mechanical properties and chemical compositions of some quenched-and-tempered steels with minimum yield strength of up to 120,000 psi (84.4 kg/mm² or 827 MN/m²). Rigorous efforts have been and are being made to develop steels with higher and higher strength. Table 1.11 presents a highly simplified summary of compositional aspects of weldable, high-strength steels. The first four are quenched and tempered steels, while the last two are maraging steels. As the strength level increases it becomes increasingly difficult to maintain sufficient fracture toughness.

Trends in fracture toughness. According to Pellini,^(112,113) the general effects of increasing strength level on the temperature and strength transitions are shown schematically in the three-dimensional plot of Fig. 1.9. The vertical scale references the dynamic tear (DT) test energy. One of the horizontal axes defines the transition

TABLE 1.10. Specification limits of deposited weld metal mechanical properties⁽¹⁰²⁾

Property	for HTS									
	MIL-7018	MIL-8018	MIL-9018	MIL-10018	MIL-11018	MIL-B88	MIL-EB82	MIL-MI88	MIL-8218YQT	
Ultimate strength (psi)	70,000	80,000	90,000	100,000	110,000	—	—	110,000	—	
Yield strength at 0.2% offset (psi)	60,000–75,000	70,000–82,000	78,000–90,000	90,000–102,000	95,000–107,000	88,000	82,000	88,000	82,000	
Elongation in 2 in. (%)	24	24	24	20	20	14	16	20	18	
Charpy V-notch impact Energy (ft/lb) at -10°F	20	20								
At -60°F			20	20	20	20	20	30	20	
At -80°F							20			

Note: Single values are minimum.

TABLE 1.11 Weldable high-strength steels⁽¹⁰²⁾

Type	Yield strength range (ksi)	Section size limit ^(a) (in.)	Heat treatment and melting practice	Primary alloying elements (%)							Impurity level (%)		
				C	Mn	Ni	Cr	Mo	Co	V		B	P & S
Commercial low alloy	90-125	2	Q & T (Air)	0.15	1.0	1.0	0.50	0.50	—	—	0.05	0.005	0.03
Ni-Cr-Mo	80-100	6	Q & T (Air)	0.15	1.5	—	—	0.50	—	—	—	0.005	0.03
	130-140	6	Q & T (Air)	0.15	0.30	3.0	1.5	0.50	—	—	—	—	0.02
High Ni + Co	160-200	6	Q & T (Air) (VAR to VIM + VAR)	0.10	0.80	5.0	0.50	0.50	—	—	0.10	—	0.008
				0.20	0.30	9.0	0.80	1.0	4.0	0.10	0.10	—	0.005
12-5-3 marage	160-200	6+	Q & A (VAR to VIM + VAR)	0.02	—	12.0	5.0	3.0	—	—	—	0.10 to 0.30	0.005
18-8-4 marage	200-240	6+	Q & A (VAR to VIM + VAR)	0.02	—	18.0	—	4.0	8.0	—	—	0.10 to 0.30	0.005

Codes: Q & T Quench and temper.
Q & T Quench and age.

Air Air melting under slags
VAR Vacuum arc remelt
VIM Vacuum induction melting
+ For best properties

^(a) For optimized properties.

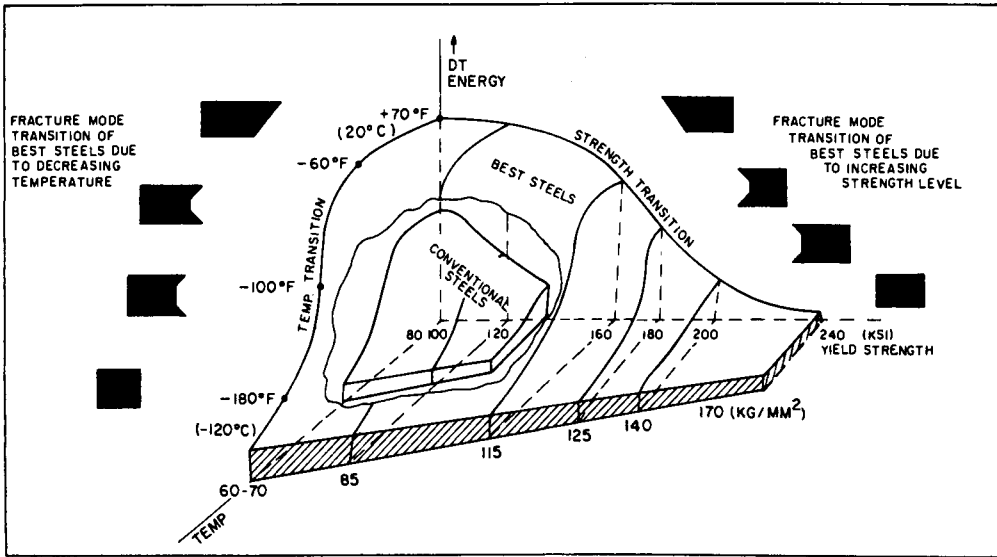


FIG. 1.9. Schematic illustrations of three-dimensional DT test energy surface evolved by combined effects of temperature- and strength-induced transitions. The nature of changes in fracture appearance for the 1-in. DT specimens are illustrated by the drawings. Transitions from ductile to brittle fracture are developed as a consequence of decreasing temperature or increasing strength level.^(111, 112)

temperature range features, and the other the strength transition features. Two surfaces are indicated in this plot. The outer surface relates to the best (premium) quality steels that have been produced to date for the respective yield strength levels. The inner surface, which lies at generally lower DT test energy values, pertains to commercial products of lowest practical cost. The latter steels are produced with minimum alloy content for the section size involved and are melted by conventional practices which result in relatively large amounts of non-metallic inclusions. Both aspects are a result of the desire to minimize costs.

A simple, yet highly significant, zoning of metallurgical type is developed in Fig. 1.10 by tracing the effects of increasing strength level on the shelf transition features of various generic classes of steels. Further discussions on the Ratio Analysis Diagram (RAD) are given in Section 10.4. A series of metallurgical quality corridor zones, which are related to the melting and processing practices used to produce the steels, become evident. The lowest corridor zone involves relatively low-alloy commercial Q&T steels produced by conventional low-cost melting practices. The corridor is defined by the strength transition of these steels to the 0.5 ratio level, as the result of heat treatment to yield strength levels in the order of 130 to 150 ksi (91.4 to 105.5 kg/mm² or 896 to 1034 MN/m²). Optimum levels of alloy content, coupled with improved melting and processing practices, elevate the corridors to higher levels. The strength transition to the 0.5 ratio is shifted accordingly to higher levels of yield strengths. Recent metallurgical investigations of high-strength steels have emphasized processing and metal purity aspects rather than purely physical metallurgical considerations of transformations.

Welding of high-strength steels. With increasing strength levels, welding of higher strength steels presents various problems. One of the most difficult problems is how to

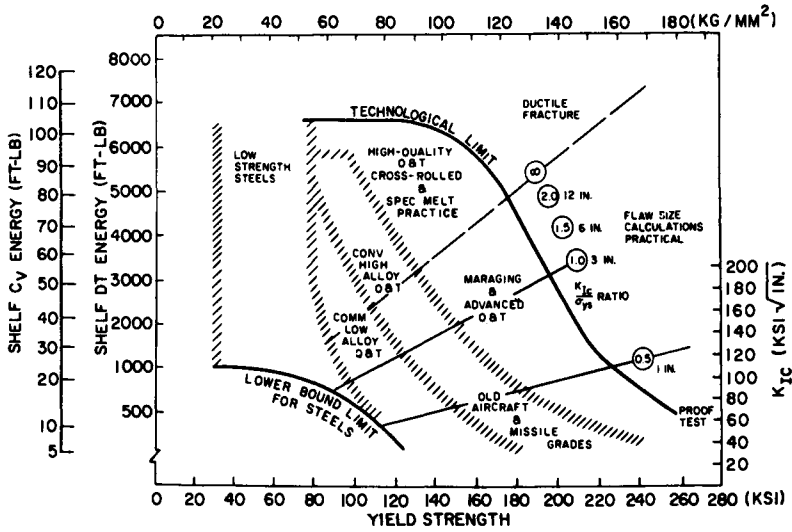


FIG. 1.10. Metallurgical zoning of the ratio analysis diagram which defines the general effects of melting and processing factors on the strength transition.^(111,112) The three corridors of strength transition relate to metallurgical quality (void site density) which controls microfracture processes and, thereby, the macroscopic fracture toughness of the metal. The location of generic alloy steel types are indicated by the notations.

obtain weld metals which have both strength and toughness comparable to those of the base plate. For steels in the yield strength range of 130 to 180 ksi (91.4 to 126.6 kg/mm^2 or 896 to 1241 MN/m^2) the research effort expended for the weld metal development ordinarily exceeds that for the base material by several fold.

Pellini^(112,113) has prepared Fig. 1.11 which provides the weld metal zoning of the

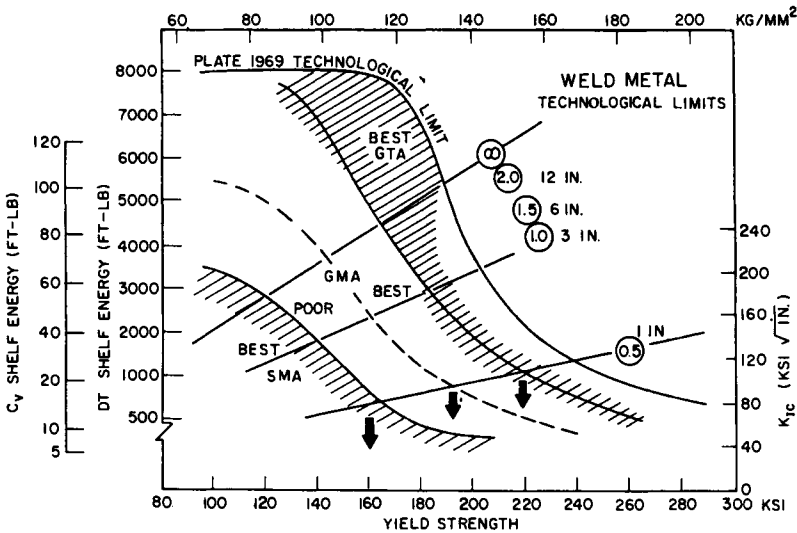


FIG. 1.11. Zoning of the ratio analysis diagram which defines weld metal factors of first-order importance to strength transition features. The strength transition corridors relate to weld metal deposited by metal arc (SMA), inert gas shielded metal arc (GMA), and inert gas shielded tungsten arc (GTA). The bold arrows indicate the strength level of transition to the 0.5 ratio value.

ratio analysis diagram (RAD). This presentation highlights the strong effects of metal-quality factors as related to the welding procedure. For attainment of high corridor features it is essential to use weld wire of high metallurgical quality (equal to the low-void-site-density of high corridor base metals) and then to protect the weld metal pool by the use of inert gas shielding. The gas tungsten arc (GTA) method is superior to the gas metal arc (GMA) method in these respects. Because of poor protection from atmospheric gases, shielded metal arc (SMA) welds are limited to the low corridor irrespective of improvements in wire quality. Adjusting weld alloy compositions to control microstructures is not sufficient—the metal quality aspects related to void coalescence processes must also be controlled if the highest corridor relationships are to be utilized in practice.

The heat-affected zone (HAZ) of high-strength metals also poses difficult metallurgical problems because of the off-standard nature of the heat treatments developed in the welding cycles. In this case there is no recourse to changing compositions as for the weld metal. For the high-alloy base materials which follow high RAD corridors, the HAZ problem is minimized, and excellent properties are obtained with latitude in the control of welding parameters. The high-alloy contents promote the development of optimum metallurgical structures over fairly wide ranges of weld heat-treatment variables, as compared to the low-alloy steels.

For the low-alloy commercial steels which follow the low-corridor relationships, the HAZ problem becomes more difficult to resolve. This results from the marginal alloy contents which are barely adequate for developing desirable microstructures under controlled mill heat-treatment conditions. Thus, weld HAZ for such metals may be seriously degraded by non-optimum welding procedures. The shelf characteristics for the HAZ of steels featuring only 90 to 120 ksi (63.3 to 84.4 kg/mm² or 620 to 827 MN/m²) yield strength may then drop to the very low levels described previously for the ultrahigh-strength steels. The shelf level differential between the base metal and the HAZ for such cases is so large that fracture along the HAZ becomes the expected fracture mode in structures.

1.5 Aluminum Alloys

1.5.1 *Metallurgy and properties of aluminum alloys*^(102, 114–116)

Pure aluminum can be alloyed readily with many other metals to produce a wide range of physical and mechanical properties. Table 1.12 describes the major alloying elements in the wrought aluminum alloys.^(102, 114) The four-digit system of classifying aluminum alloys is used by the Aluminum Association:

- 1st digit = major constituents
- 2nd digit = the modification
- 3rd and 4th digits = alloy

In the 2xxx-8xxx alloy classification group, the last two digits have no special significance, but are used to identify different aluminum alloys in the group.

1xxx series. This series is demonstrated by alloy 1100, which is 99% pure aluminum, non-heat treatable, soft and ductile, highly corrosion resistant, formable and weldable.

2xxx series. The “aircraft alloys”, as this group is called, has high strength, and is heat treatable, but lower ductility than 1xxx. Furthermore, it requires spot or seam

TABLE 1.12 Designations for alloy groups^a

Major alloying element	Designation
99.0% minimum aluminum and over	1xxx
Copper	2xxx
Manganese	3xxx
Silicon	4xxx
Magnesium	5xxx
Magnesium and silicon	6xxx
Zinc	7xxx
Other elements	8xxx
Unused series	9xxx

^a Aluminum Association designations.

welding as opposed to fusion welding. It is less corrosion resistant than 1xxx, but may be good if mechanical fastening for parts can be used.

3xxx series. This class is non-heat treatable. 3003, used extensively for military structures, has Mn added and is 20% stronger than 1100.

4xxx series. The addition of silicon in amounts up to 12% will yield aluminum alloys particularly suitable as a filler material for welding and brazing, because they have low melting points. Aluminum alloys containing silicon also are used for casting and forging; however, casting alloys have different numerical designations.

5xxx series. This is the most important material for structural applications. It is a weldable Mg–Mn alloy formable, highly corrosion resistant, has a high weld zone ductility and high strength. Advances in 5052, 5083, 5086, and 5456 welding make realistic the welding of aluminum in applications where welds are subject to heavy dynamic loading.

6xxx series. A heat-treatable material, this alloy has sheets, plate and extrusions two-thirds to three-quarters less in strength than the 2xxx series. However, it is easily available, weldable and cheap, which makes it practical for structures with low dynamic loading factors. Alloys 6063 and 6061 are two of the most versatile of aluminum alloys of intermediate strength. They have outstanding corrosion resistance.

7xxx series. This group contains the highest strength. It is used in aircraft, although it involves some forming difficulties. 7079 in particular hardens to a great depth.

Alloys and heat treatments.^(102,117) Alloys are classified further into two broad categories: heat treatable and non-heat treatable. The first is stronger and more expensive because of the heat treatment involved.

A letter following the alloy designation and separated from it by a hyphen indicates the basic-temper designation. The addition of a subsequent digit, where applicable, indicates the specific treatment employed to produce the basic temper. Those compositions that are hardenable only by strain hardening are given “–H” designations; whereas those hardenable by heat treatment through precipitation or a combination of cold work and precipitation are given the letter “–T” in accordance with the following classification:

- F As fabricated
- O Annealed, recrystallized (wrought only)
- H Strain-hardened

- H1 strain-hardened only
- H2 Strain-hardened and then partially annealed
- H3 Strain-hardened and then stabilized
- W Solution heat-treated—unstable temper
- T Heat-treated to stable tempers
 - T2 Annealed (cast only)
 - T3 Solution treated and cold-worked
 - T4 Solution treated followed by natural aging at room temperature
 - T5 Artificially aged only after an elevated-temperature, rapid cool fabrication process such as casting or extrusion
 - T6 Solution treated and artificially aged
 - T7 Solution treated and stabilized to control growth and distortion
 - T8 Solution treated, cold-worked, and artificially aged
 - T9 Solution treated, artificially aged, and cold-worked

A second numeral following the basic temper letter indicates the degree of hardness produced by the specific processing operation. The numeral “8” designates the full hard commercial temper, whereas the numeral “4” indicates a hardness midway between the fully annealed (0) and 8 temper. The extra hard temper is designated by the numeral “9”. As an illustration, the designation 1100-H14 refers to commercially pure wrought aluminum, indicated by 1100, which has been strain-hardened, indicated by -H1, to a tensile strength midway between the hardest and softest commercial tempers, indicated by 4.

1.5.2 *Aluminum alloys for marine applications*^(102, 116)

Aluminum alloys in the 5xxx series and the 7xxx series are used extensively in marine applications; therefore, these groups are discussed in more detail.

The 5xxx group involves magnesium as a major additive. The 7xxx group, on the other hand, is composed of magnesium, zinc, magnesium and zinc, or copper.⁽¹⁶⁾

The mechanical properties of these alloys, beyond that obtained by solid solutions, include:

1. strain hardening,
2. artificial aging.

Table 1.13 shows mechanical properties of aluminum alloys for marine applications.

The 5xxx series has been used for more than 10 years in marine structures. It is valuable for its high resistance to corrosion in the water. These materials are non-heat treatable and derive their mechanical properties from combinations of chemistry and work hardening. In the 5xxx series in general, annealing takes place between 650–800°F (343–427°C) with cooling in still air. Usually it is then strained to get various strength levels and, finally, it is thermally stabilized. Stability treatments vary, but usually involve hot forming at 425°F (218°C). Such treatment attains stability but lowers the strength.

The 7xxx series, also used for ocean engineering structures, is solution heat treated at 850°F (454°C) with a soaking time depending upon the thickness of the material.

TABLE 1.13 *Mechanical properties of aluminum alloys for marine applications (1-in. plate)^(1,16)*

Alloy Designation and temper	Tensile ultimate strength (ksi)	Tensile yield strength (ksi)	Percent elongation in 2 in.	Compressive yield strength (ksi)
5083-0	40	18	16	18
5083-H112	40	18	12	19
5083-H113	44	31	12	26
5086-H34	44	34	10	32
5086-H112	35	16	10	16
5454-H32	36	26	12	24
5454-H34	39	29	10	27
5454-H112	31	12	11	12
5456-H321	46	33	12	27
X7002-T6	61	50	9	53
X7005-T6	45	36	7	36
X7106-T6	55	50	—	50
X7106-T63	56	50	9	50
X7039-T6	65	55	13	58
X7039-T61	62	51	14	—
X7139-T63	63	55	13	—
X7005-T63	47	38	7	38

Note: "X" refers to experimental.

After soaking, it is immediately cold-water quenched. This treatment gives the exceptional strength properties inherent in the 7xxx series alloys.

1.5.3 Mechanical characteristics of aluminum alloys^(1,02)

Figure 1.12 shows a typical stress-strain diagram for various structural materials as follows:^(1,16)

- Aluminum alloy 5083-H113 base metal.
- Weldment of 5083-H113 welded with 5183 filler wire.
- Ship steel plate, ASTM-131.
- Reinforced polyester laminates with grain.

Table 1.14 presents a comparison of weight and strength in these materials.

Strength. Maximum tensile strength and yield strength of aluminum are comparable to those of low-carbon steel. Or, to cite another comparison, most 5000 series aluminum alloys have a strength of 31,000–63,000 psi (21.8–44.3 kg/mm² or 214–434 MN/m²). Most steels used in ocean structures have 58,000–71,000 psi (40.8–49.9 kb/mm² or 400–498 Mn/m²). However, on the weight basis, aluminum is stronger.

Weight. Aluminum weighs about half as much as steel with the same strength. Therefore, a smaller amount or weight of aluminum can be used in a structure in order to achieve the same strength as steel.

Modulus of elasticity. The modulus of elasticity of aluminum is about one-third that of steel. If section deflection, as opposed to strength, is the most important consideration, a low modulus of elasticity is a limiting factor.

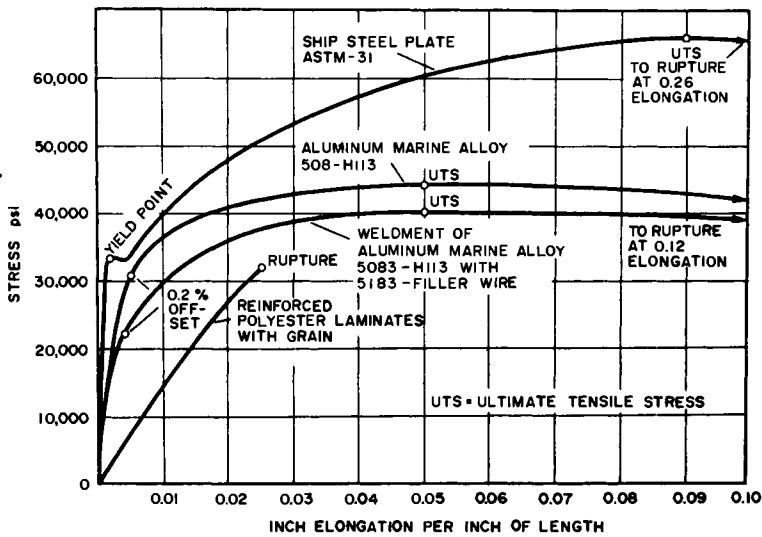


FIG. 1.12. Typical stress-strain diagrams for various marine applications.^(102,116)

TABLE 1.14 Comparison of weight and strength of various structural materials⁽¹¹⁶⁾

Column 1	Column 2	Column 3	Column 4	Column 5	Column 6	Column 7
Material	Weight (lb/in ³)	Typical strength (psi)			Tensile modulus of elasticity (x10 ⁶)	Strength to-weight col. 3/col. 2 (x1000)
		Ultimate tensile	Yield tensile	Ultimate shear		
(1) Aluminum alloy:						
5083-H113	0.096	46,000	33,000	27,000	10.3	480
5086-H34	0.096	47,000	37,000	27,000	10.3	490
6061-T6	0.098	45,000	40,000	30,000	10.0	460
Ship steel ASTM-A131	0.29	66,000	33,000		29.0	230
Mild steel ASTM-A100	0.28	56,000	30,000	42,000	29.0	200
Copper, hard sheet	0.32	46,000	40,000		17.0	140
(2) Reinforced polyester laminates:						
With grain	0.062	32,000		13,000	1.4	520
Across grain	0.062	21,000		14,000	1.1	340

Fracture toughness. Aluminum which has a face-centered cubic atomic arrangement is ductile even at low temperatures. Aluminum alloys generally are less notch sensitive than many steels. However, there has been concern recently about fracture toughness of aluminum alloys in the presence of a sharp notch.

Figure 1.13 shows a summary of V-notch Charpy impact energy of aluminum alloys as a function of strength level.⁽¹¹⁸⁾ The figure shows the following:

- (1) For aluminum alloys, the impact energy does not change drastically with temperature as observed for steel.
- (2) As the strength level of an aluminum alloy increases, the impact energy generally decreases.

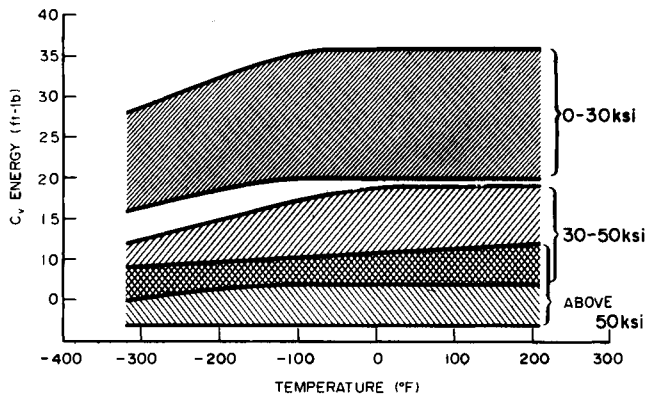


FIG. 1.13. Summary of V-notch Charpy impact energies of aluminum alloys as a function of strength level.⁽¹¹⁸⁾

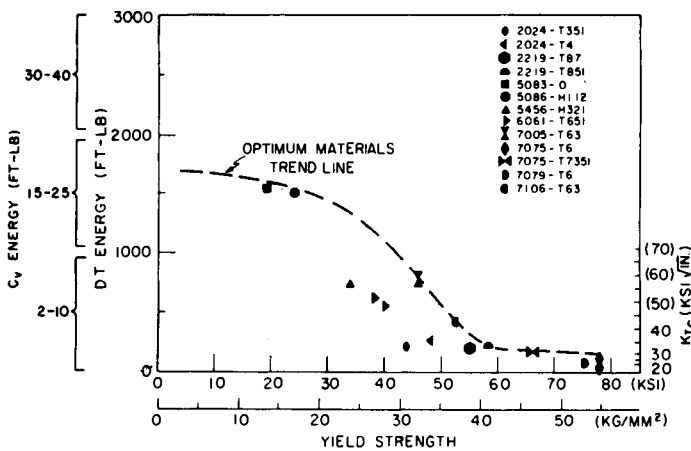


FIG. 1.14. OMTL diagram for aluminum alloys. The diagram presents relationships to C_v , DT, and K_{1C} scales.⁽¹¹⁸⁾

(3) Compared with steel and titanium, impact energy for an aluminum alloy is considerably low.

Figure 1.14 shows the optimum material trend line (OMTL) for aluminum alloys.⁽¹¹⁸⁾ The figure shows the following values:

- V-notch Charpy impact energy, C_v ft-lb,
- drop-weight tear test energy, DT, ft-lb,
- plane strain fracture toughness, K_{1C} , ksi $\sqrt{\text{in}}$.

Fracture toughness decreases as the yield strength increases. Generally speaking, 5000 series alloys have the highest fracture toughness followed by 6000 series, 2000 series, and 7000 series.

1.5.4 Cutting and welding of aluminum alloys⁽¹⁰²⁾

Aluminum can be cut relatively easily by saw. However, it cannot be cut with an oxyacetylene torch because it forms oxides which have melting points much higher

than that of aluminum plate. Aluminum can be cut by a tungsten arc and a plasma arc.

The advances in welding aluminum greatly affected its use as a construction material. Until suitable welding techniques were developed for aluminum, use of the material was greatly restricted. New processes allow high-speed welding with manual or automatic equipment which is standardized and readily available. Many times the power source for steel welding can be applied to aluminum welding. Two welding processes are most used with aluminum—gas tungsten arc welding (GTA) and gas metal arc welding (GMA).

GTA. The process involves no flux, but is slow and not commonly used for joining heavy plates. It is used on thickness down to 0.04 in. (1 mm). The usual commercial thickness is 0.062 to 0.25 in. (1.6 to 6.4 mm).

GMA. The process is faster and cheaper and requires less manual dexterity than GTA. It is used for thicknesses of 0.081 in. (2mm) and higher. No preheating is required. This is the most common type of welding used for aluminum fabrication. Table 1.15 presents recommended practices for welding of aluminum alloys.⁽¹¹⁶⁾ Table 1.16 shows

TABLE 1.15 *Recommended practices for GMA welding of aluminum alloys*^(102, 116)

Material thickness (in.)	Welding position	Joint design	Current amps-dc	Arc voltage	Filler wire dia.	Argon ^(a) gas flow CFH	No. of passes
$\frac{3}{32}$	Flat	None	70–110	18–22	0.030	30	1
			100–120	18–22	$\frac{3}{64}$	30	1
$\frac{1}{8}$	Flat	None	110–130	20	$\frac{3}{64}$	30	1
	Horiz. & vert.	None	100–120	20	$\frac{3}{64}$	30	1
	Overhead	None	100–120	20	$\frac{3}{64}$	40	1
$\frac{1}{4}$	Flat	None or single bevel	200–225	26–28	$\frac{1}{16}$	40	1
	Horiz. & vert.	Single bevel	170–190	26–28	$\frac{1}{16}$	45	2 or 3
	Overhead	Single bevel	180–200	26–28	$\frac{1}{16}$	50	2 or 3
	Flat	None	220–250	28–30	$\frac{1}{16}$	80	2
$\frac{3}{8}$	Flat	Single or double bevel	230–320	26–28	$\frac{1}{16}$	50	1 or 2
	Horiz. & vert.	Single or double bevel	180–235	26–28	$\frac{1}{16}$	50	3
	Overhead	Single or double bevel	200–240	26–28	$\frac{1}{16}$	50	5
	Flat	None	260–280	28–30	$\frac{1}{16}$	80	2
$\frac{1}{2}$	Flat	Single or double bevel	280–340	26–30	$\frac{3}{32}$	50	2 or 3
	Horiz. & vert.	Single or double bevel	210–250	26–30	$\frac{1}{16}$	50	3 or 4
	Overhead	Single or double bevel	225–275	26–30	$\frac{1}{16}$	80	8 to 10
	Flat	None	280–320	30–32	$\frac{1}{16}$	80	2
1	Flat	Single or double bevel	320–420	26–30	$\frac{3}{32}$	60	4 to 5
	Horiz. & vert.	Single or double bevel	225–285	26–30	$\frac{1}{16}$	60	4 to 6
	Overhead	Single or double bevel	225–285	26–30	$\frac{1}{16}$	80	15 or more
	Flat	None	390–400	35–37	$\frac{1}{16}$	80	2
2	Flat	Single or double bevel	350–450	26–30	$\frac{3}{32}$	60	12 or more
3		Single or double bevel	350–450	26–30	$\frac{3}{32}$	60	20 or more

^aGas flows for helium are slightly higher than for argon.

TABLE 1.16 Typical mechanical properties of inert-gas metal-arc welded joints in aluminum alloys 5086 and 5083^(102, 116)

Alloys, temper and gage	Tensile strength (psi)	Yield strength ^(a) (psi)	Elongation (% in 2 in.)	Joint efficiency (%)* ^(b)	Location of fracture
Tested with beads in place					
5086, 0, $\frac{1}{4}$ in.	38,000	18,000	15.4	100	Parent plate, fusion line
5086, H112, $\frac{1}{4}$ in.	38,000	19,000	14.0	100	Parent plate, fusion line
5086, H34, $\frac{1}{4}$ in.	38,000	21,000	8.3	80	Parent plate, fusion line, weld metal
5086, H112, $\frac{1}{2}$ in.	39,000	21,000	11.4	100	Fusion line
5086, H34, $\frac{1}{2}$ in.	39,000	21,000	12.0	84	Fusion line
5886, H112, $\frac{3}{4}$ in.	41,000	21,000	16.7	100	Fusion line, parent plate
Tested with beads machined off					
5086, 0, $\frac{1}{4}$ in.	35,000	17,000	12.5	100	Fusion line
5086, H112, $\frac{1}{4}$ in.	37,000	17,000	14.3	94	Fusion line, weld metal
5085, H34, $\frac{1}{4}$ in.	37,000	18,000	12.9	78	Fusion line, weld metal
5086, H112, $\frac{1}{2}$ in.	39,000	20,000	16.5	100	Fusion line
5086, H112, $\frac{3}{4}$ in.	39,000	20,000	16.8	100	Fusion line, weld metal
Tested with beads in place					
5083, 0, $\frac{1}{4}$ in.	43,000	20,000	16.2	100	Fusion line, parent plate
5086, H113, $\frac{1}{4}$ in.	46,000	24,000	16.6	100	Fusion line
5083, H113, $\frac{1}{2}$ in.	45,000	22,000	12.5	88	Fusion line
5083, H113, $\frac{3}{4}$ in.	45,000	23,000	16.0	97	
Tested with beads machined off					
5083, 0, $\frac{1}{4}$ in.	40,000	20,000	15.3	97	Weld metal
5083, H113, $\frac{1}{4}$ in.	42,000	22,000	14.0	91	Weld metal
5083, H113, $\frac{1}{2}$ in.	42,000	21,000	16.3	93	Weld metal
5083, H113, $\frac{3}{4}$ in.	42,000	21,000	18.3	90	

^(a) At 0.2% offset.

^(b) Based on the typical tensile strength shown in the *Kaiser Aluminum Sheet and Plate Book*, Second Edition, 1958.

typical mechanical properties of GMA welded joints in aluminum alloys 5086 and 5083.⁽¹¹⁶⁾

Problems in welding aluminum. As described above, aluminum alloys are definitely weldable. However, this does not mean aluminum welding is problem free. Major problems in welding aluminum include:

1. Porosity in welds. Compared with steel, aluminum alloys are more active and thus are prone to weld porosity.

2. Shrinkage and distortion. Aluminum alloys, compared with steel, have higher heat conductivity, larger thermal expansion coefficients, and a lower modulus of elasticity. Therefore, welds in aluminum alloys have more shrinkage and distortion.
3. Loss of strength in the heat-affected zone. A reduction in the strength of the heat-affected zone has been experienced in weldments in aluminum alloys, especially heat-treated alloys.

A report by Masubuchi⁽¹⁰⁴⁾ describes the results of extensive studies on welding aluminum supported by the National Aeronautics and Space Administration. The studies are primarily on alloys 2014 and 2219 which are used extensively in the fabrication of fuel and oxidizer tanks of the Saturn V space vehicle. Results of these studies should be useful for welding of aluminum alloys for other structures.

1.6 Titanium Alloys⁽¹⁰²⁾

1.6.1 *Titanium and its alloys*

Pure titanium at room temperature is in a hexagonal, close-packed form. At about 1620°F (882°C) allotropic transformation occurs and titanium takes on a body-centered cubic lattice. Only a 0.1% volume change takes place during this transformation. The low-temperature phase of this process is designated alpha titanium. The high-temperature phase is beta titanium.⁽¹¹⁹⁾

The addition of alloying elements to titanium either raises or lowers the transformation temperature and slows down or speeds up the transformation from the high-temperature beta phase to the room-temperature alpha phase. Titanium alloys are classified into alpha, alpha-beta, and beta types, depending upon the predominant phases in microstructure. Furthermore, the type of structure that exists at room temperature determines if the titanium alloy can be heat treated and if it is sensitive to thermal embrittlement, which hinders weldability.⁽¹²⁰⁾

An addition to titanium of an element such as aluminum, tin, or oxygen raises the transformation temperature. These elements are called "alpha stabilizers". On cooling from a high temperature, the alloy with the above additions reaches the transformation stage sooner than pure titanium; therefore the alpha phase is formed faster.⁽¹²¹⁾ An alloy with alpha stabilizers is referred to as a "non-heat treatable" alloy, since no further basic change takes place by subsequent heating in the low-temperature-phase region.

Elements such as iron, chromium, and vanadium, which lower the transition temperature, are called "beta stabilizers". Thus, at a given cooling rate the transformation is retarded in time and takes place at a lower temperature than that of pure titanium. As a result, it is possible for the transformation at lower temperature to become much slower, permitting intermediate microstructures of alpha to be produced. These forms of alpha have different properties from the alpha formed at high temperatures. When added in sufficient amounts, certain beta-stabilizing elements will cause retention of the beta-phase indefinitely at room temperature. These alloys are metastable beta alloys at room temperature.

The relative amounts of alpha and beta stabilizers in an alloy (and the heat treatment) determine whether its microstructure is predominantly one-phase alpha, a mixture of alpha and beta, or the single-phase beta, over its useful temperature range.

TABLE 1.17(a) *Titanium alloys in commercial production*^(1,19)

Nominal composition (%)	Other designations		Recommended heat treatments ^(d)			
	AMS no.	Military no. ^(a)	Forms available ^(c)	Stress-relief annealing	Annealing treatment	Solution treatments (aging treatment)
99.5			B, b, P, S, s, T, W, E	1000 to 1100 °F, $\frac{1}{2}$ hr, AC	1250 to 1300 °F, 2 hr, AC	Not heat treatable
99.2		T-9047B-1	B, b, P, S, s, T, W, E	1000 to 1100 °F, $\frac{1}{2}$ hr, AC	1250 to 1300 °F, 2 hr, AC	Not heat treatable
99.0	4900A	T-7993B	B, b, P, S, s, T, W, E	1000 to 1100 °F, $\frac{1}{2}$ hr, AC	1250 to 1300 °F, 2 hr, AC	Not heat treatable
99.0	4901B		B, b, P, S, s, T, W, E	1000 to 1100 °F, $\frac{1}{2}$ hr, AC	1250 to 1300 °F, 2 hr, AC	Not heat treatable
98.9	4921		B, b, P, S, s, T, W, E	1000 to 1100 °F, $\frac{1}{2}$ hr, AC	1250 to 1300 °F, 2 hr, AC	Not heat treatable
0.15 to 0.20 Pd (balance Ti)			B, b, P, S, s, T, W, E	1000 to 1100 °F, $\frac{1}{2}$ hr, AC	1250 to 1300 °F, 2 hr, AC	Not heat treatable
ALPHA ALLOY GRADES						
5A1-2.5Sn	4910 4926 4953 4966		B, b, P, S, s, W, E	1000 to 1200 °F, $\frac{1}{4}$ to 2 hr, AC	1325 to 1550 °F, 10 min to 4 hr, AC	Not heat treatable
5A1-2.5Sn (low O)			B, b, P, S, s, W, E	1000 to 1200 °F, $\frac{1}{4}$ to 2 hr, AC	Same	Not heat treatable
5A1-5Sn-5Zr		In preparation	B, b, P, S, s, W, E	1100 °F, $\frac{1}{2}$ hr, AC	1650 °F, 4 hr, AC	Not heat treatable
7A1-12Zr		In preparation	B, b, P, S, s, W, E	1000 °F, $\frac{1}{2}$ hr, AC	(1) ^(b) 1600-1650 °F, $\frac{1}{2}$ to 4 hr, AC (2) 1300 °F, 1 hr, AC	Not heat treatable
7A1-2Cb-1Ta ^(b)		In preparation	B, b, P, S, W, E	1100 to 1200 °F, $\frac{1}{2}$ hr, AC	1650 °F, 1 hr, AC	Not heat treatable
8A1-1Mo-IV	In preparation	In preparation	B, b, P, S, s, W, E	1100 to 1200 °F, 1 hr, AC For sheet and plate	(1) 1450 °F, 8 hr, FC (consult producers for other treatments) (2) 1450 °F, 8 hr, FC + 1450 °F, $\frac{1}{4}$ hr, AC (Duplex) (3) 1450 °F, 8 hr, FC + 1850 °F, 5 min; AC + 1375 °F, $\frac{1}{4}$ hr, AC (Triplex) (4) 1850 °F, 1 hr, AC + 1100 °F, 8 hr, AC	Not heat treatable

TABLE 1.17(b) Titanium alloys in commercial production⁽¹¹⁹⁾

Alpha-Beta Alloy Grades															
8Mn	W not recommended	S	Ann	16.4	137	125	15	14.4	98	75	13	800	80	59	15
2Fe-2Cr-2Mo	W not recommended	b	Ann	16.7	137	125	18	14.7	95	65	19	800	75	55	30
		b	Aged	—	179	171	13	—	136	112	16				12-15 8-10
2.5Al-16V	W not recommended	S	SHT	—	105	45	16								
		S	Aged	15.0	180	165	6	13.5	155	140	8	800	140	125	10
3Al-2.5V		S	Ann	15.5	100	85	20	13.0	70	50	25				
4Al-4Mn	W not recommended	b	Ann	16.4	148	135	15	13.9	110	90	17	800	100	85	21
		b	Aged	—	162	143	10	—	125	100	11				10-15
4Al-3Mo-IV	Special conditions permit some W	S	Ann	16.5	140	120	15	14.0							
		S	Aged	—	195	167	6	—	152	120	7	800	145	115	8
5Al-1.25Fe-2.75Cr	Special conditions permit some W	b	Ann	16.8	155	145	15	15.5	122	102	20				10-15
		b	Aged	17.6	190	175	6	16.2	144	117	10				
5Al-1.5Fe-1.4Cr-1.2Mo	W not recommended	b	Ann	16.5	154	145	16	15.0	115	100	16	800	118	100	20
		b	Aged	17.0	195	184	9	14.6	150	125	14				
6Al-4V	Weldable	S, b	Ann	16.5	138	128	12	13.5	105	95	11	800	90	78	18
		S	Aged	—	170	155	8	—	130	105	7	800	130	100	8
6Al-4V (low O)	Weldable	S	Ann	16.5	135	127	15	13.5	105	95	12	320	220	205	13
6Al-6V-2Sn-1(Fe, Cu)	Special conditions permit some W	b	Ann	15.0	165	150	15	13.4	132	117	20	800	90	80	15
		b	Aged	16.5	190	180	10	14.5	150	132	15				
7Al-4Mo	Special conditions permit some W	b	Ann	16.2	160	150	16	14.2	127	108	18	800	117	94	18
		b	Aged	16.9	185	175	10	15.0	150	123	12				10

Beta Alloy Grades															
1Al-8V-5Fe	W not recommended	b	Ann	16.5	177	170	8	14.7	128	115	19	800	108	85	32
		b	Aged	16.5	221	215	10	14.5	140	123	12	800	120	100	30
3Al-13V-11Cr	Weldable	S	Ann	14.2	135	130	16	13.2				800	115	110	18
		S	Aged	14.8	185	175	8	13.8	175	145	8	800	160	120	12
		S	CR + Aged	—	260	245	4								8

^(a) Other numbers T-12117 and WA-PD-76C (1) apply to all grades and all products; T-14557, T-14558, T-9046C, and T-9047C apply to all grades; and T-8884(ASG) applies to various grades.

^(b) Formerly Al-2Cb-1TA. All data given are for the 8-2-1 composition.

^(c) B—billet, b—bar, P—plate, S—sheet, s—strip, T—tubing, W—wire, E—extrusions.

^(d) AC—air cool, SC—show cool, FC—furnace cool, WQ—water quench, CR—cold rolled.

TABLE 1.17(c) Titanium alloys in commercial production^(1,19)

Nominal composition (%)	Weldability remarks	Form	Condition	Typical tensile properties										RT Charpy V impact (ft-lb)			
				Room temperature			600 °F			Extreme temperatures			YS (ksi)		YS (ksi)	EL (%)	
				E (10 ⁶ psi)	US (ksi)	YS (ksi)	E (10 ⁶ psi)	US (ksi)	YS (ksi)	Test temp (°F)	US (ksi)	YS (ksi)					EL (%)
99.5	All unalloyed grades are completely weldable (W)	S	Ann	14.9	38	27	30	12.1	20	10	50						
99.2		S	Ann	14.9	60	45	28	12.3	28	13	45	-423	175				25-40
99.0		S	Ann	15.0	75	60	25	12.5	33	19	33	-321	165				20-35
99.0		S	Ann	15.1	90	75	20	12.5	43	27	28	-321	175				11-15
98.9		S	Ann	15.5	100	85	17	12.6	47	30	25						
0.15 to 0.20 Pd (Balance Ti)	Completely W	S	Ann	14.9	62	46	27	12.3	28	13	30						
Alpha Alloy Grades																	
5Al-2.5Sn	Weldable	S b	Ann Ann	16.0 16.0	125 115	117 110	18 20	13.4 13.4	82 82	65 65	19 19	1000 1000	75 75	56 56	18 18		19
5Al-2.5Sn (low O)	Weldable	S	Ann	16.0	110	95	20	13.4	78	60	20	-423	229	206	15		19
5Al-5Sn-5Zr	Weldable	S	Ann	16.0	125	120	18	14.2	94	74	20	1000	84	67	21		
7Al-12Zr	Weldable	S b	(1) Ann (2) Ann	16.0	135	130	15	14.3	109	86	21	1000	93	75	23		
7Al-2Cb-1Ta ^(b)	Weldable	b	Ann	17.7	126	120	17	15.1	100	81	25						
8Al-1Mo-IV	Weldable	S S S b	(1) Ann (2) Ann (3) Ann (4) Ann	18.5 18.0	160 145	150 138	18 15					1000	85	70	20		
				15.0	142	142	13										
				141	130	18			107	85	19	1000	88	71	20		

TABLE 1.17(d) Titanium alloys in commercial production^(1,19)

		ALPHA - BETA ALLOY GRADES			
8Mn	4908 A	P, S	900 to 1100° F, ½ to 2 hr, AC	1250 to 1300° F, 1 hr, FC to 1000° F	Solution treatment not recommended
2Fe-2Cr-2Mo	4923	B, b, S, s	900 to 1000° F, ½ to 1 hr, AC	1200° F, ½ hr, AC	1400 to 1480° F, 1 hr, WO or AC (900 to 950° F, 2 to 8 hr, AC) 1360 to 1400° F, 10 to 30 min, WQ (960 to 990° F, 4 hr, AC)
2.5Al-16V	T-8884(1)	B, b, P, S, s W			Solution treatment not recommended
3Al-2.5V	4925 A	s, T	1300° F, 1 hr, AC		1400 to 1500° F, ½ to 2 hr, WQ (800 to 1000° F, 8 to 24 hr, AC) 1625 to 1650° F, ¼ hr, WQ (925° F, 8 to 12 hr, AC)
4Al-4Mn	4912	B, b, P, W	1300° F, 2 hr, FC	1300° F, 2 to 4 hr, FC	1350 to 1500° F, 2 hr, WQ (900 to 950° F, 5 to 6 hr, AC)
4Al-3Mo-1V	4913	P, S, s	1000 to 1100° F, 1 hr, AC	1225° F, 4 hr, SC to 1050 F, AC	1600 to 1625° F, 1 hr, WQ (1000° F, 24 hr, AC)
5Al-1.25Fe-2.75Cr	4929	B, b, P, S, S	1100° F, 1 hr, AC	1450° F, 1 hr, SC to 1050 F, AC	1550 to 1750° F, 5 min to 1 hr, WQ (900 to 1000° F, 4 to 8 hr, AC)
5Al-1.5Fe-1.4Cr-1.2Mo	4969	B, b, P	1200° F, 2 hr, AC	1200° F, 4 to 24 hr, AC	1600 to 1625° F, 1 hr, WQ (1000° F, 24 hr, AC)
6Al-4V	4911				
6Al-4V	4928 A	B, b, P, S, s W, E	900 to 1200° F, 1 to 4 hr, AC	1300 to 1550° F, 1 to 8 hr, SC	1550 to 1750° F, 5 min to 1 hr, WQ (900 to 1000° F, 4 to 8 hr, AC)
6Al-4V	4935	OS-10737 OS-10740	(Usual: 1 hr, 1100° F, AC)	1300 to 1550° F, 1 to 8 hr, SC to 1050° F, AC	1600 to 1675° F, 1 hr, WQ (900 to 1100° F, 4 to 8 hr, AC)
6Al-4V (low O)		B, b, P, S, s, T, W, E	Same	same	Solution treatment not recommended
6Al-6V-2Sn-1(Fe, Cu)	T-46036 T-46038	B, b, P, W, E	1100° F, 2 hr, AC	1300 to 1400° F, 1 to 2 hr, AC	1600 to 1675° F, 1 hr, WQ (900 to 1100° F, 4 to 8 hr, AC)
7Al-4Mo		B, b, P, W, E	900 to 1300° F, 1 to 8 hr, AC	1450° F, 1 to 8 hr, AC 1050° F, AC	1650 to 1750° F, ½ to 1½ hr, WQ (900 to 1200° F, 4 to 16 hr, AC)
BETA ALLOY GRADES					
1Al-8V-5Fe		B, b, P	1000 to 1100° F, 1 hr, AC	1250° F, 1 hr, FC to 900° F, AC	1375 to 1425° F, 1 hr, WQ (925 to 1000° F, 2 hr, AC)
3Al-13V-11 Cr	4917	B, b, P, S, s W			1400 to 1500° F, ½ to 1 hr, WQ or AC (900° F, 2 to 96 hr, AC) 1450° F, ½ hr, AC + CR + 800° F, 24 hr, AC

^(a) Other number T-12117 and WA-PD-76C (1) apply to all grades and all products; T-14557, T-14558, T-9046C, and T-9047C apply to all grades; and T-8884 (ASG) applies to various grades.

^(b) Formerly Al-2Cb-1Ta. All data given are for the 8-2-1 composition.

^(c) B—billet, b—bar, P—plate, S—sheet, s—strip, T—tubing, W—wire, E—extrusions.

^(d) AC—air cool, SC—slow cool, FC—furnace cool, WQ—water quench, CR—cold rolled.

Properties are directly related to microstructure. Single-phase alloys are usually weldable with good ductility. Some two-phase alloys are also weldable, but their welds are less ductile. Two-phase alpha-beta alloys are stronger than the one-phase alpha alloys, primarily because body-centered cubic beta is stronger than the close-packed hexagonal alpha. More important, two-phase alloys can be strengthened by heat treatments, because of the microstructure, which can be manipulated by controlling heating, quenching, and aging cycles.

At present there are about twenty-five different titanium alloys in commercial production. Table 1.17 contains a list of these alloys with the appropriate specifications and mechanical properties.⁽¹¹⁹⁾ In some instances, cryogenic properties and elevated temperature properties are given. Alloys for which these properties are given are those which can be used advantageously at the respective temperatures. The table also notes the welding capabilities of particular alloys.

Titanium alloys which have been used and which may be used for structural applications include:^(121, 122)

1. Commercially pure titanium of different grades depending upon differences in interstitial elements. For example, a 99.5% pure titanium contains the following elements:

0.1%	maximum oxygen
0.1%	maximum nitrogen
0.07%	maximum carbon
0.2%	maximum iron

The ultimate tensile strength ranges from 38,000 psi (26.7 kg/mm² or 262 MN/m²) for 99.5% pure titanium to 100,000 psi (70.3 kg/mm² or 689 MN/m²) for 98.9%.

2. The Ti-7Al-2Cb-1Ta alpha alloy of about 125,000 psi (87.9 kg/mm² or 862 MN/m²) ultimate tensile strength. The designation indicates that the principal alloying elements are 7% aluminum, 2% columbium, and 1% tantalum.
3. The Ti-5Al-2.5Sn alpha alloy of about 120,000 psi (84.4 kg/mm² or 827 MN/m²) ultimate tensile strength. The designation indicates that the principal alloying elements are 5% aluminum and 2.5% tin.
4. The Ti-6Al-4V heat-treatable alpha-beta alloy. This has an ultimate tensile strength of 130,000 psi (91.4 kg/mm² or 896 MN/m²) in the annealed condition and up to 160,000 psi (112.5 kg/mm² or 1103 MN/m²) in the heat-treated condition. The designation indicates that the principal alloying elements are 6% aluminum and 4% vanadium.
5. The Ti-6Al-6V-2Sn heat-treatable alpha-beta alloy with a tensile strength of 165,000 psi (116 kg/mm² or 1138 MN/m²) under the annealed condition and up to 190,000 psi (133.6 kg/mm² or 1310 MN/m²) under the aged condition. The designation indicates that the principal alloying elements are 6% aluminum, 6% vanadium, and 2% tin. Among these alloys, pure titanium and the Ti-6Al-4V alloy have been most commonly used for marine applications.

1.6.2. *Effects of impurities and alloying elements on mechanical properties*

Pure titanium is very ductile and relatively low in strength. A small addition of

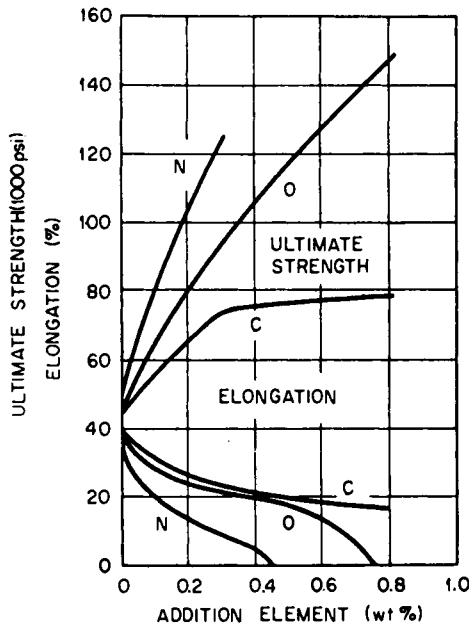


FIG. 1.15. Effects of impurities on mechanical properties of titanium.^(102, 114)

impurities such as oxygen, nitrogen, and carbon causes increase in strength and a decrease in ductility. Other elements also can strengthen the metal with some reduction in ductility.

Impurities. The elements carbon, hydrogen, nitrogen and oxygen form interstitial solid solutions with titanium. Figure 1.15 shows the individual effect of carbon, nitrogen, and oxygen on ultimate tensile strength and elongation of titanium. Hydrogen also causes an increase in strength and a reduction in ductility.

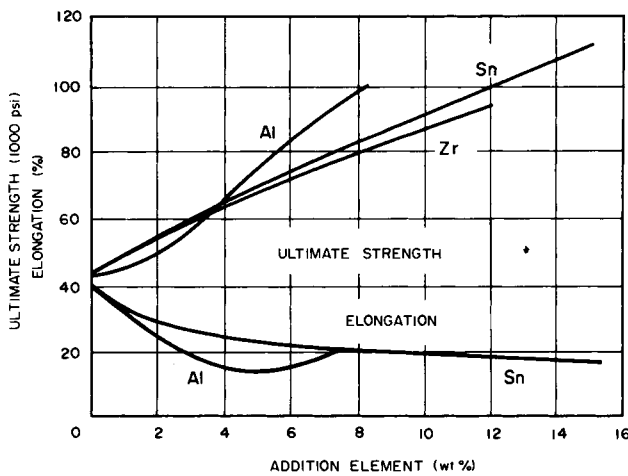


FIG. 1.16. Effect of alloy additions on mechanical properties of alpha titanium alloys.^(102, 114)

Alloying elements. Figure 1.16 shows the individual effect of aluminum, tin, and zirconium, which are added to many titanium alloys, on the ultimate strength and elongation of titanium. These alpha alloys cannot be strengthened by heat treatment. Therefore, strengthening can be achieved either by increasing the alloy content or by cold working.

1.6.3 Fracture toughness of titanium alloys

Titanium and titanium alloys, like steel, are sensitive to a notch. Figure 1.17 presents a summary of V-notch Charpy impact data for titanium alloys with different levels of yield strength. As the strength level increases, notch toughness decreases.⁽¹¹⁸⁾ Compared to steels, titanium alloys do not show a sharp transition in fracture toughness with temperature changes and only a gradual change is noted over a relatively broad range of temperatures.

Optimum material trend line (OMTL). Figure 1.18 shows the fracture toughness for all different generic families of titanium alloys. Here, fracture toughness is given in three different scales:

1. V-notch Charpy impact energy, Cv, ft-lb.
2. Drop weight tear test energy, DT, ft-lb.
3. Critical plane strain fracture toughness, K_{IC} , $ksi\sqrt{in}$.

The data shown in Fig. 1.18 represents as-rolled material and a variety of processing

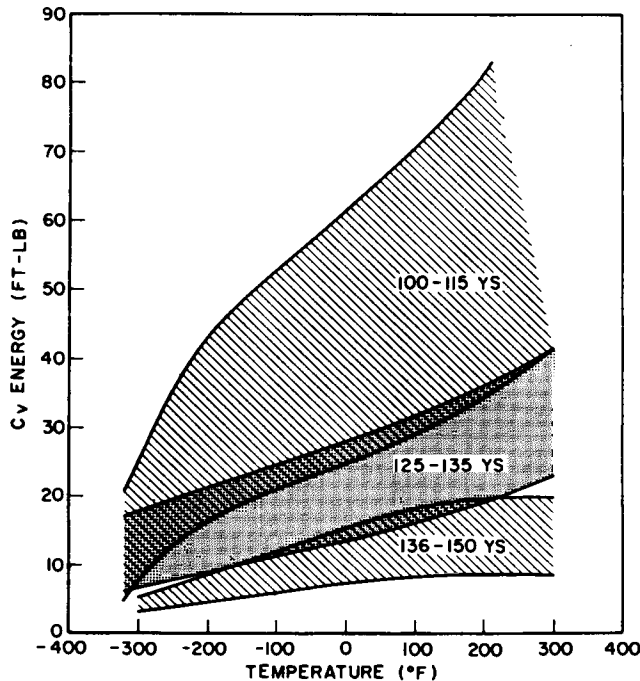


FIG. 1.17. Summary of relationship between V-notch Charpy curves for titanium alloys and different level of yield strength.⁽¹¹⁸⁾

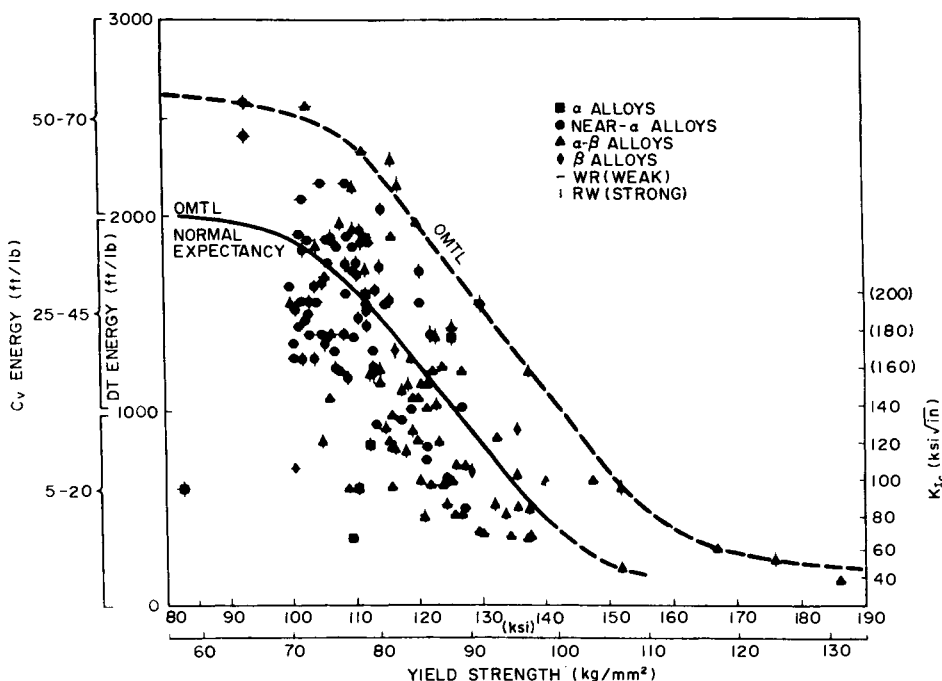


FIG. 1.18. OMTL diagram for titanium alloys. Data points relate to 1-inch thick DT test values. The other fracture toughness scales are indexed to DT energy by correlation.⁽¹¹⁸⁾

and heat-treatment conditions for alloys in each family. The upper OMTL curve relates to the highest “weak” direction fracture toughness values determined for the related level of yield strength. The normal expectancy OMTL curve relates to the level of fracture toughness that can be expected with reasonable confidence if the chemistry, processing, and heat treatment are specified in the best way. The range of fracture toughness indicated for any given level of yield strength results from chemical composition, impurities, processing, and heat-treatment variables. Fracture toughness generally decreases as the yield strength increases.

1.6.4 Welding of titanium and its alloys

Shielding during the welding process is vital in preventing absorption of impurities at welding temperatures. For this purpose, inert gas-shielded arc welding processes are used most commonly.⁽¹¹⁹⁾ The weld zones should be protected at 1200°F (649°C) or higher. The molten weld metal area is the most critical point for this protection. In this region, impurities diffuse into the titanium quickly and may result in severe weld embrittlement. Weld zones that are not molten but at temperatures of 1200°F (649°C) are subject to surface contamination from the air which may lead to early failures in service.⁽¹²³⁾

Vacuum purging offers the best inert-gas atmosphere possible for welding titanium. Pre-weld cleaning with alkaline washes of dilute solutions of sodium hydroxide may also be required as well as an acid pickling treatment to remove the light oxide scale.

This again stresses the need for purity of the material during welding and purity of the gas used during the process.

Commercially pure titanium. A weld in titanium that is commercially pure is essentially a casting. The grain size is very large and the structure consists of beta dendrites. Oxygen and hydrogen in normal quantities have little effect on the microstructure, but extra carbon (over 0.2%) make TiC precipitate out of the melt into a network pattern which tends to lower ductility.⁽¹²⁴⁾

Titanium alloys. The structure of titanium alloy welds varies according to the alloy content. The weld is still a large grained casting which also has some transformation structures. A segregation effect during solidification occurs due to differences in composition between liquids and solids of the alloy. Dendritic structures, precipitated particles and some retained beta are present in certain microstructures.⁽¹¹⁹⁾

“Two important factors in welding titanium and titanium alloys are:

1. At temperatures present in the weldment and heat-affected zone, the material readily reacts with air and most elements and compounds (excluding the inert gases).
2. The mechanical properties of these materials are affected in an extreme manner by relatively minute amounts of impurities, especially nitrogen, oxygen, carbon, and hydrogen.”⁽¹¹⁹⁾

Contamination. When hot, titanium will easily absorb or combine with almost every other element. Most such combinations result in greater strength and ductility and toughness. Consequently, when titanium is welded, it must be completely protected from external elements, including not only the molten weld puddle, but all metal that is hot. As a general rule, a temperature above 1200°F (649°C) is regarded “hot” for the periods of time at temperature associated with welding.

Normal fluxes provide inadequate protection for titanium. In fact, they may actually contribute to a loss of weld ductility by alloying with the metal. Developmental work in the U.S. shows the feasibility of fluxes; and they are reportedly used in U.S.S.R. for joining titanium. A flux for titanium must be relatively non-reactive and produce no harmful compounds in the metal. Furthermore, it must have a greater free energy of formation with oxygen than does titanium, and be oxygen free itself. Only the halogen salts of the alkaline metals (specifically calcium fluoride) come close to meeting these requirements. The toxicity of this and similar compounds always will restrict their use.⁽¹²²⁾

Oxygen effects. Oxygen has the greatest effect on titanium welds; it is ever present, readily absorbed by hot titanium and small amounts have a tremendous influence on mechanical properties. Titanium normally contains a thin, self-healing surface oxide film. This provides the corrosion resistance noted earlier and, in itself, does not cause any welding problems. This film thickens as titanium is treated in air, and the titanium dissolves its own oxide. Oxygen atoms diffuse from the surface oxide film into the metal, causing an increased oxygen content and reduced ductility toughness. Both processes are continuous; the surface oxidizes and the metal underneath dissolves the oxides. The surface oxidation proceeds generally at a faster rate than its solution, so that after a heating cycle the metal will have a heavier than normal surface oxide. If the surface

oxide is not too heavy, it acts as a refractor of light and appears to the eye as colors. Different colors represent different thicknesses. They show the thermal cycle the metal has seen experienced. However, they do not directly indicate the amount of oxygen in solution or weld contamination. Their only source of contamination is the diffusion of oxygen into the metal which is also dependent upon the thermal cycle, so the colors are an indirect measure of weld contamination. These colors on a weld always can indicate if a weld is bad, but they cannot prove that a weld is not contaminated.⁽¹²²⁾

Porosity. Titanium welders are constantly confronted with the problem of porosity. It is believed that porosity is caused by hydrogen; however, the origin of this hydrogen is not certain. All titanium contains some hydrogen, usually less than 100 ppm, as an impurity. However, it is unlikely that porosity is caused by this “dissolved” hydrogen. Other possible causes of porosity include dirt, microscopic particles, and water vapor. Whatever the cause, it has been demonstrated that a fresh, clean joint edge is required to produce minimum porosity.⁽¹²²⁾

Mechanical properties of welds. Figure 1.19 shows comparisons between tensile yield strength and drop-weight tear energy of welds in various titanium alloys.⁽¹²²⁾ Alloys types of the base metal and filler wire used are shown also.

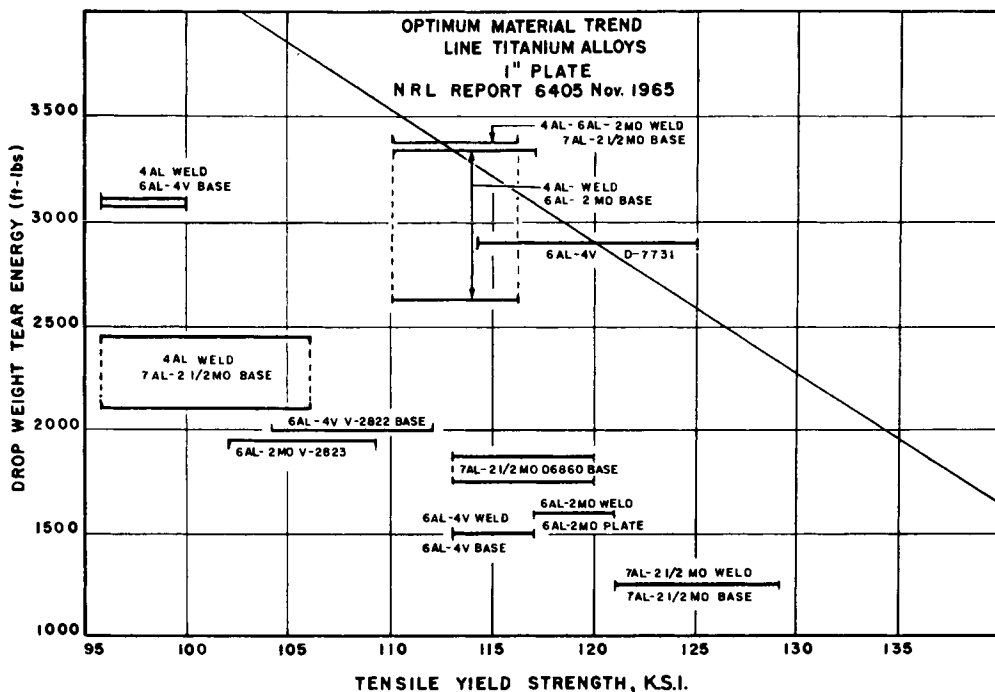


FIG. 1.19. Comparison of drop weight tear test and tensile yield strengths in base plates and weldments.⁽¹²²⁾

1.7 Welding Processes

1.7.1 Classification of welding processes

Today, more than fifty different processes, used in various applications, are available commercially to join metals. These joining processes, as presently practiced, can be classified into the five basic categories:

1. Fusion welding, in which the parts to be joined are heated until they melt together. Pressure is not a requisite. Examples are arc welding, gas welding, electron-beam welding, and laser welding.
2. Electrical-resistance welding, which involves first heating by passage of an electric current through the parts to be welded, and second, the application of pressure. Examples are spot welding, upset welding, and percussion welding.
3. Solid-phase welding, in which pressure is applied but the metals to be joined do not melt, except for very thin layers near the surfaces to be joined. Examples are forge welding, friction welding, and pressure welding.
4. Liquid-solid phase joining, in which the parts to be joined are heated to a temperature lower than their melting points and a dissimilar molten metal is added to form a solid joining upon cooling. Examples are brazing and soldering.
5. Adhesive bonding, in which joints are formed as a result of the molecular attraction exerted between the surface to be bonded and the adhesive. Examples of adhesives are animal and vegetable glues, cements, asphaltums, and various plastics such as epoxy. The term "welding" is used for those processes included in categories 1 through 3.

As far as the fabrication of large structures are concerned, the following welding processes are commonly used:

- (1) Shielded metal-arc welding.
- (2) Submerged arc welding.
- (3) Gas-shielded-arc welding.
- (4) Vertical automatic welding (electroslag and electrogas processes).

1.7.2 Shielded metal-arc welding^(102, 125)

Shielded metal-arc welding is an arc-welding process wherein coalescence is produced by heating with an electric arc between a covered electrode and the work. Shielding is obtained from decomposition of the electrode covering. Pressure is not used and filler metal is obtained from the electrode.

In practice, the process is limited primarily to manual covered electrodes in which the welding operator manipulates the electrode.

Figure 1.20 is a schematic representation of the shielded metal-arc process. Equipment to operate the electrode usually consists of an electric power supply specifically designed for the process, insulated electrode holders of adequate electric and thermal capacity, cable, and grounding clamps. The process may use either alternating current or direct current with the electrode either positive or negative. Currents between 15 and 500 amperes with arc voltages between 14 and 40 volts, depending upon the covering characteristics, are normal.

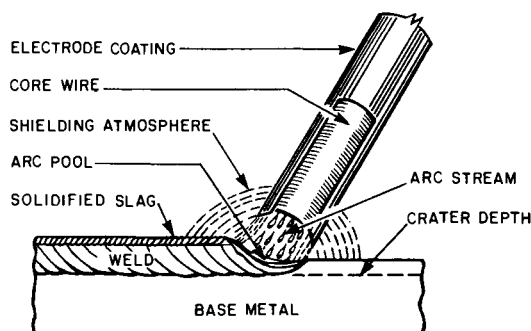


FIG. 1.20. Schematic representation of shielded metal-arc process.

Coated electrodes for manual arc welding are classified by the American Welding Society (AWS) and the American Society for Testing Materials (ASTM).^(126,127) Table 1.18 shows electrodes commonly used for welding low carbon steel. The electrodes are classified according to the operating characteristics, the type of coating, and the strength level of the weld metal. For example, E-60XX electrodes produce deposited metal having a minimum specified ultimate tensile strength of 60,000 psi (42.2 kg/mm² or 414 MN/m²). The last two digits in the electrode designation refer to the type of coating and operating characteristics as shown.

Electrodes used for military applications are specified by MIL-E-22200/1. Electrodes MIL-9018, MIL-10018, MIL-11018, and MIL-12018 are similar to those of AWS specifications E-9018-M, E10018-M, E11018-M, and E12018-M. The U.S. Navy specification NAVSHIP 250-637-3 specifies among other processes the use of covered electrodes in the fabrication of HY-80 submarine hulls. MIL-11018 and 9018 electrodes are used most commonly.

Electrodes as large as $\frac{5}{16}$ in. (8 mm) diameter may be employed, depending upon the plate thickness and type of joint. The welds are built up in relatively thin layers, approximately ten layers per inch of thickness. This will permit a partial progressive

TABLE 1.18 *Electrodes commonly used for welding low-carbon steel*

AWS-ASTM electrode class	Coating	Current, polarity ^(a)	Welding position ^(b)
E6010	High cellulose, sodium	dcrp	F, V, OH, H
E6011	High cellulose, potassium	dcrp, ac	F, V, OH, H
E6012	High titania, sodium	dcsp, ac	F, V, OH, H
E6013	High titania, potassium	dcsp, ac	F, V, OH, H
E6014	Iron powder, titania	dcsp, ac	F, V, OH, H
E7016	Low-hydrogen, potassium	dcrp, ac	F, V, OH, H
E7018	Low-hydrogen, iron powder	dcrp, ac	F, H
E6020	High iron oxide	dcrp, dcsp, ac	F, H
E7024	Iron powder, titania	dcrp, dcsp, ac	F, H
E6027	Iron powder, iron oxide	dcrp, dcsp, ac	F, H

^(a) dcrp—direct current reverse polarity, electrode positive; dcsp—direct current straight polarity, electrode negative; ac—alternating current.

^(b) F—flat; V—vertical; OH—overhead; H—horizontal.

grain refinement of proceeding layers resulting in an improvement in ductility and impact resistance of the weld metal.

Semi-automatic processes. Some attempts have been made at mechanizing the shielded metal-arc process. The idea of making shielded metal-arc welding semi-automatic by laying an electrode along the joint has existed for more than 30 years. However, the electrodes were not advanced enough to be used for actual production in large scale. The development of contact electrodes using high iron oxide and iron-powder coating has shown that a weld metal with sound quality can be obtained without manipulating electrodes.^(128, 129)

A group of Japanese electrode manufacturers and shipbuilders has developed electrodes and welding devices which can be used for production in a semi-automatic operation. Electrodes are 25 to 40 in. (635 to 1000 mm) long and one operator can handle four to six electrodes simultaneously.

1.7.3 Submerged-arc welding^(102, 125)

Submerged-arc welding is an arc-welding process wherein coalescence is produced by heating with an electric arc or arcs between a bare metal electrode or electrodes and the work. The welding is shielded by a blanket of granular, fusible material on the work. Pressure is not used, and filler metal is obtained from the electrode and sometimes from a supplementary welding rod. Figure 1.21 shows how a submerged-arc groove weld is made.

The fusible shielding material is known as “flux”, “welding composition”, or “melt”. This is a finely crushed mineral composition and will be referred to as flux in this book. Flux, when cold, is a non-conductor of electricity, but in the molten state it becomes highly conductive.

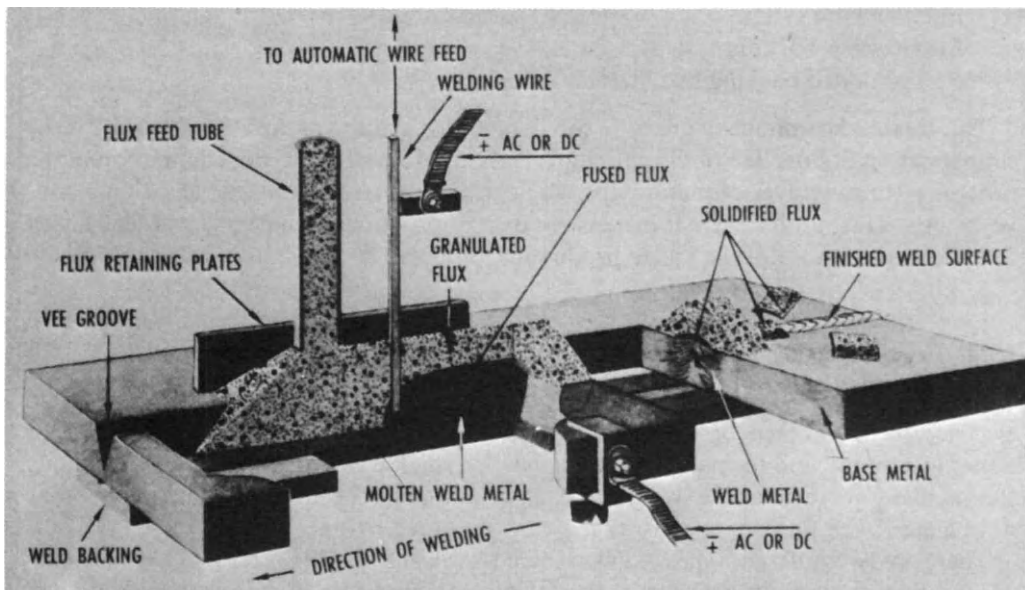


FIG. 1.21. The processes of a submerged arc groove weld.^(102, 125)

The wide use of submerged arc welding stems from its ability to produce satisfactory welds at high rates of deposition. Currents used in submerged arc welding are much higher than those employed in manual shielded metal-arc welding. The maximum electrode usually employed is $\frac{5}{16}$ in. (8 mm) diameter and the maximum current (for single electrode) is approximately 2000 amperes.

It should be pointed out that high amperage results in a very coarse columnar structure in the weld metal with an enlarged heat-affected zone in the base metal as compared to multipass welding wherein the energy input is relatively small. This is important in connection with vessels which will operate at low temperature. The coarse columnar structure of the high amperage weld usually results in lower impact resistance as compared to multipass welds. Therefore, particular consideration should be given to the welding procedure in terms of the service requirements involved.

One-side submerged-arc welding. As the structure under construction keeps getting bigger, the need for one-side submerged-arc welding becomes more critical. In some shipyards, where tankers as large as 300,000 DWT or even bigger are being fabricated, plate assemblies which measure 60 ft (18 m) by 60 ft (18 m) or even larger are commonly handled.

When the size of an assembly was not so large, automatic welding was done by one pass from each side of the plate. However, the job of turning the plate over can be dangerous. And it can be economically impractical. A fabrication shop with a very high ceiling is required. To further increase the size of an assembly, the ceiling has to be raised. Of course, that can be an extremely costly operation.

Several types of one-side submerged-arc welding systems have been developed and installed in a number of shipyards.⁽¹³⁰⁻¹³³⁾ The welding systems can be classified into four groups depending upon the backing system employed as follows:

- Copper backing system.
- Flux backing system.
- Flux-copper backing system.
- Resin-bonded backing flux system.

The greatest advantage of one-side submerged-arc welding at the assembly state is the simplification of flow line of the entire fabrication system. Due to the elimination of the process of turning over of plating, the whole assembly system can be placed on a conveyor line. This results in great increase in overall production efficiency and lends itself to systematic control of the entire production process.

1.7.4 *Gas-shielded-arc welding*

In the gas-shielded-arc welding process, coalescence is produced by fusion from an electric arc maintained between the end of a metal electrode, either consumable or non-consumable, and the part to be welded with a shielded of protective gas surrounding the arc and weld region. The shielding gas may or may not be inert; pressure may or may not be used; and filler metal may or may not be added.

There are two different types of gas-shielded-arc welding. One is termed gas tungsten-arc welding. It employs a tungsten electrode or an electrode of some other refractory, high-melting-point material, such as graphite, which will not melt or be vaporized too

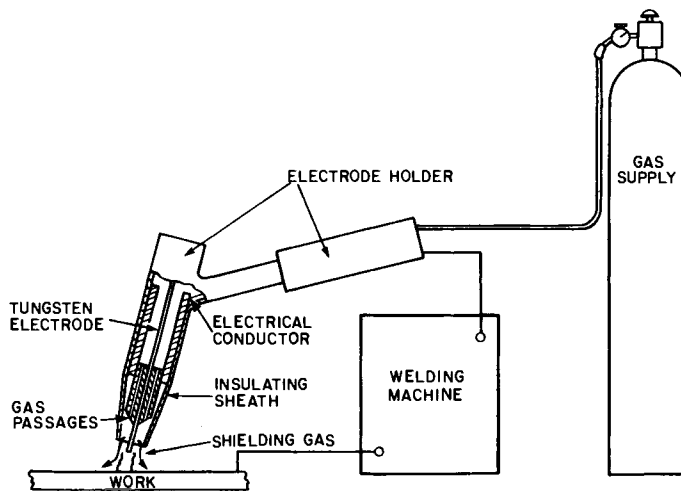


FIG. 1.22. Schematic diagram of gas tungsten-arc welding.⁽¹²⁵⁾

rapidly in the intense heat of the arc. The other type is termed gas metal-arc welding. It employs a continuously fed electrode which melts in the intense arc heat and is deposited as weld metal.

Gas tungsten-arc welding. Gas tungsten-arc welding is also known as GTA welding, while gas metal-arc welding is called GMA welding.[†]

Figure 1.22 shows basic features of gas tungsten-arc welding. The shielding gas is fed through the electrode holder which is generally referred to in this process as a torch. Argon, which is an inert gas, is commonly used for the shielding gas. The use of helium as the shielding gas is rather rare. A small percentage of oxygen is often added to the inert shielding gas. Carbon dioxide and a mixture of CO_2 and O_2 have been found to be effective as the shielding gas for use in welding carbon and low-alloy steels. More recently, fluxes have been added as a core within a tubular sheath or as a granular magnetic material which adhere to the filler wire surface.

Gas metal-arc welding. Figure 1.23 shows basic features of gas metal-arc welding. The filler wire, which is manufactured in a coil form, is fed mechanically into the welding arc. The arc travel is controlled manually in the semi-automatic process and mechanically in the automatic process.

A bare wire is commonly used for the electrode, but flux-covered wires are used also.

Various gases are used for shielding, including:

- (1) Pure inert gases, such as argon and helium.
- (2) Mixtures of argon, CO_2 , O_2 , and other gases.
- (3) CO_2 .

Because of the high cost of inert gas, CO_2 and a mixture of CO_2 and O_2 are widely used for welding carbon steel and low-alloy high-strength steels. Argon and a mixture of argon and CO_2 are often used for welding quenched-and-tempered steels and ultra-

[†] In the past gas tungsten-arc welding was known as TIG (tungsten inert-gas) welding, and gas metal-arc welding was known as MIG (metal inert-gas) welding.

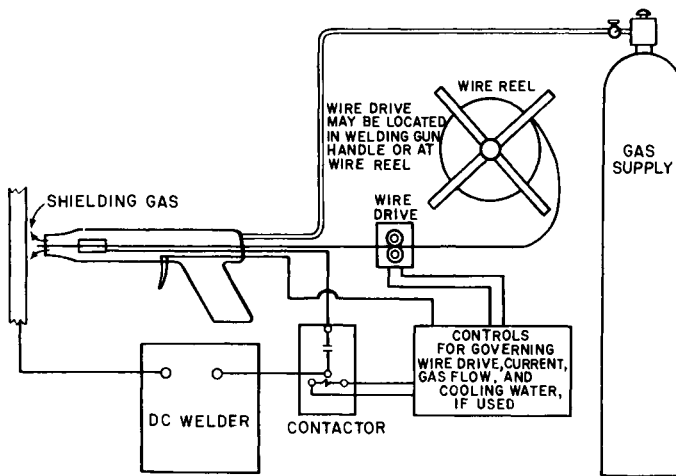


FIG. 1.23. Schematic diagram of gas metal-arc welding.^(1,25)

high-strength steels. Inert gases, which may contain small portions of other gases, are used almost exclusively for welding stainless steels, aluminum, titanium, and other non-ferrous metals.

Compared to the gas tungsten-arc welding, the gas metal-arc welding is characterized by a high deposition rate. Therefore, the GMA process is chiefly used in welding heavy plates, while the GTA process is used mainly in welding thin sheets.

Narrow-gap welding process. A new gas metal-arc welding process, which is called the narrow-gap process, has been developed at several laboratories including Battelle Memorial Institute.^(1,34) The narrow-gas process is especially suited for joining heavy plates in high-strength quenched-and-tempered steel.

As the name implies, the narrow-gap process differs from conventional welding processes in the type of joint design used. The new procedure uses a square-butt joint with a narrow root opening (approximately $\frac{1}{4}$ in. (6.4 mm)). The use of this type of joint results in a weld deposit with a small fusion zone. A typical weld deposited by this process in 2-in. (50 mm) thick HY-80 steel is shown in Fig. 1.24. The very high depth-to-width ratio and the very narrow, uniform heat-affected zone are apparent. A mixture of argon and CO_2 is used as the shielding gas. Welds are deposited from one side of the plate using a specifically designed guide tube that extends into the joint. Welds can be made in all positions—the weld shown in Fig. 1.24 was made in the vertical position.

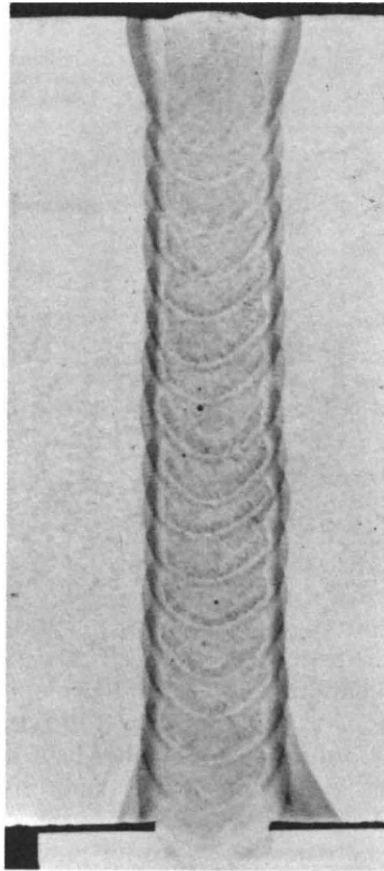
1.7.5 Vertical automatic welding processes

Vertical automatic welding processes used in fabrication include:

Electroslag process, as shown in Fig. 1.25.

Electrogas process, as shown in Fig. 1.26.

Electroslag welding.^(102,125) The process is based on the generation of heat production by passing an electrical current through molten slag. In electroslag welding, the electrode is immersed in the molten slag pool between the components to be welded and the copper molding devices. The melt is heated to a high temperature by a current passing



2X

FIG. 1.24. A weld deposited by the narrow-gap process (2 inches thick).

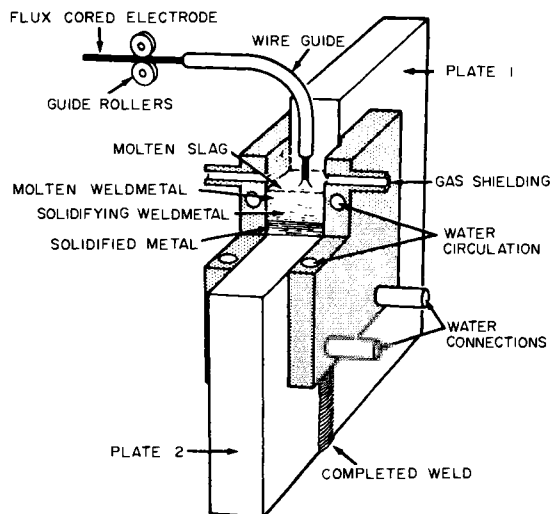


FIG. 1.25. The electrogas welding process.⁽¹²⁵⁾

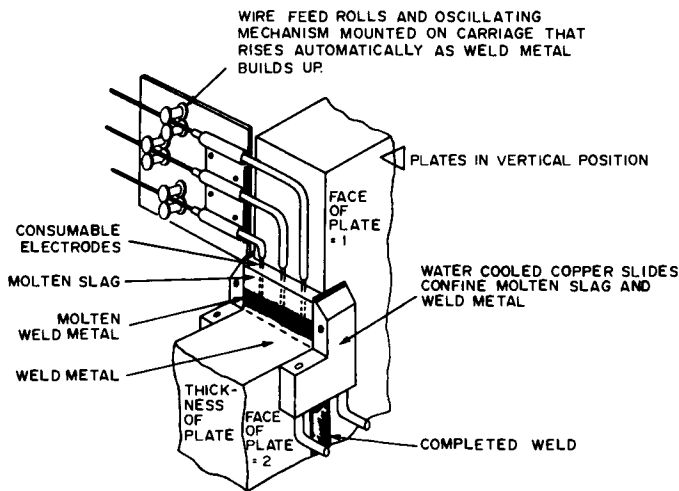


FIG. 1.26. The process of electroslag welding.⁽¹²⁵⁾

between the electrode and the base metal and electrical conductivity is increased. The temperature of the slag pool must exceed the melting point of the base and filler metal. Therefore, the slag melts the faces of the work and the electrode is immersed in the molten slag. The weld pool is formed when the molten base and filler metal collect at the bottom of the slag pool. This weld pool solidifies and forms the weld and joints the faces of the components. The electrode is lowered as it melts.

Electroslag welding originally was developed for joining thick sections positioned vertically. Theoretically, any thickness can be welded in a single pass, but the maximum reported thickness is 1000 mm (40 in.). Single-pass welds are made in any practical thickness of steel or alloy steel. Welding starts at the bottom of the joint and progresses upward, usually by moving the welding head and auxiliary equipment.

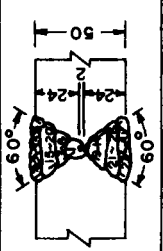
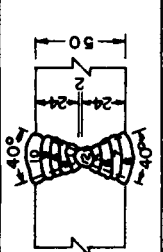
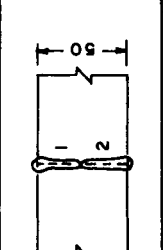
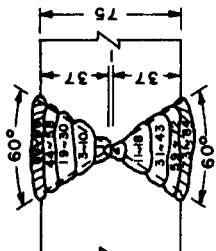
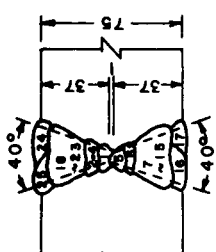
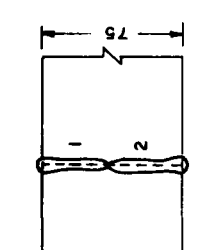
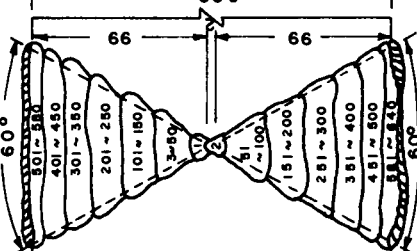
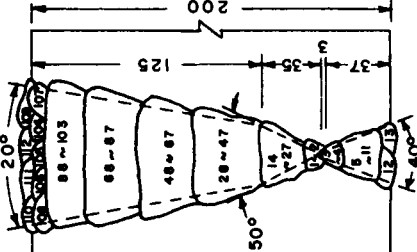
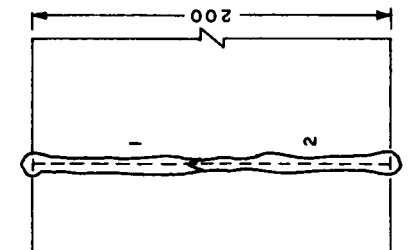
Although the electroslag process offers economic savings through reduced welding costs and lower capital-equipment inventories in heavy-machine-building factories, application of the process in the United States has been limited.

Electrogas welding.^(102,125) A fully automatic process, electrogas welding provides a method of fusion welding of butt, corner, and tee joints in the vertical position. Metal sections ranging from $\frac{1}{2}$ in. (12.7 mm) to several inches in thickness can be joined in a single pass by adapting the operational concepts of electrogas welding equipment to spray-type arc welding.

In electrogas welding, water-cooled copper shoes bridge the gap between the components being welded and form a rectangular pocket or cavity containing the welding operation. A wire guide feeds a flux-cored wire or solid wire into the pocket. An electric arc is established and maintained continuously between the electrode and the weld puddle. To provide a suitable atmosphere for shielding the arc and weld puddle, helium, argon, carbon dioxide or mixtures of these gases are continuously fed into the pocket. The weld metal is cleaned by deoxidizers and slagging materials provided by the flux core of the electrode.

As the weld metal is deposited, the wire feed, carrying the wire guide and copper shoes,

TABLE 1.19. Development of welding process for heavy aluminium plate of LNG carriers⁽¹³⁶⁾

plate thickness (mm)	weld sequence	welding process		
		conventional GMA welding	narrow groove GMA welding	electron beam welding
50	deposit sequence			
	pass number	36 passes	10 passes	2 passes
75	deposit sequence			
	pass number	96 passes	25 passes	2 passes
200	deposit sequence			
	pass number	640 passes	112 passes	2 passes

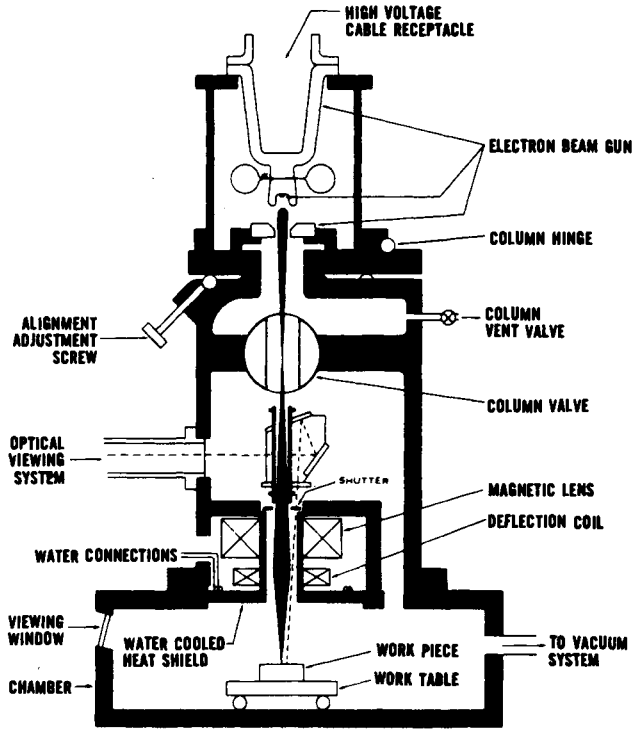


FIG. 1.27. Schematic of high-voltage electron beam welding equipment.⁽¹³⁵⁾

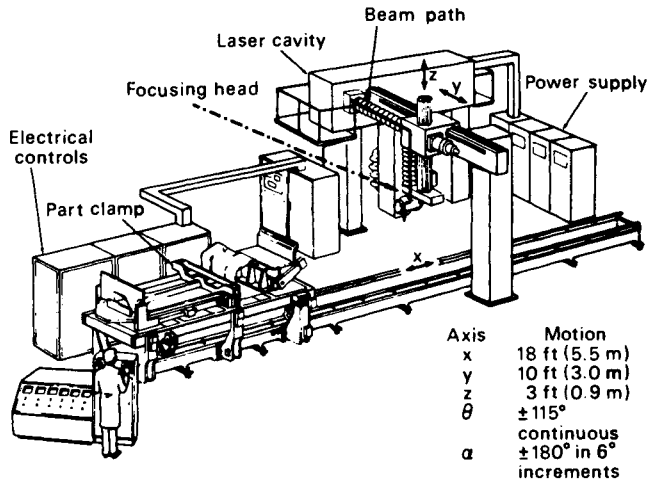


FIG. 1.28. Schematic of laser underbody welding system. (Supplied by Hamilton-Standard for Ford Motor Co.)⁽¹⁴⁰⁾

moves steadily upward to provide a weld pocket of uniform depth in which the weld is deposited.

1.7.6 Electron beam welding

The electron beam (EB) welding is a fusion joining process in which the workpiece is bombarded with a dense stream of high-velocity electrons, as shown in Fig. 1.27.⁽¹³⁵⁾ Welding usually takes place in an evacuated chamber.

The major advantage of EB welding is the very deep penetration that can be achieved. The major problem, however, is how to deal with the vacuum needed for the process. Attempts have been made to join large structural components by use of a partial vacuum system and a movable chamber which can slide on the surface of the structure to be welded. Efforts have been made to develop an EB welding system suitable for fabricating critical structures for aerospace, marine, and nuclear applications.⁽¹³⁶⁾ One example is welding of heavy aluminum sections to be used for equator rings of the cryogenic tanks of LNG carriers.

Table 1.19 shows cross-sections of typical butt welds in aluminum plates in different thicknesses: 2 in. (50 mm), 3 in. (75 mm), and 8 in. (200 mm). For example, joining of plates 8 in. (200 mm) thick requires over 600 passes when conventional gas metal arc processes are used. Over 100 passes are needed even using a specially developed narrow-groove process. By using the EB process, the plate can be welded in only two passes.

1.7.7 Laser welding

Lasers can be used for various metal working operations including drilling and cutting, as well as welding. Several recent publications discuss the present state-of-the-art and future possibilities.⁽¹³⁷⁻¹⁴⁰⁾ For example, Fig. 1.28 shows schematically a 6-kw welding system for fabricating an automobile underbody.⁽¹⁴⁰⁾ In this system, stamped panels are loaded in an assembly fixture which is part of a transfer table. The table provides one axis of weld motion (the *x*-axis is Fig. 1.18). The platform-mounted laser has its beam directed through a transport system which provides four axes of motion. Two are translation, *y*- and *z*-motions; and two are rotations, one in the horizontal and one in the vertical plane.

Another possible application is the fabrication of stiffened panel structures commonly used for ships, aircraft, and other structures.⁽¹³⁸⁾ Stiffeners can be laser-welded onto panels with no filler materials. There is no doubt that lasers will be used in various ways in metal fabrication industries. However, it is rather difficult to predict how extensively they will be used and how soon.

References

- (101) MASUBUCHI, K. and TERAI, K., "Future trends of materials and welding technology for marine structures", paper presented at the 1976 spring meeting of the Society of Naval Architects and Marine Engineers, Philadelphia, PA, 2-5 June 1976.
- (102) MASUBUCHI, K., *Materials for Ocean Engineering*, M.I.T. Press, 1970.
- (103) EVANS, J. HARVEY and ADAMCHAK, JOHN C., *Ocean Engineering Structures*, M.I.T. Press, 1969.
- (104) MASUBUCHI, K., *Integration of NASA Sponsored Studies on Aluminum Welding*, NASA Contractor Report NASA CR-2064, National Aeronautics and Space Administration, Washington, D.C., June 1972, for sale by the National Technical Information Service, Springfield, Virginia 22151.

- (105) SHEN-D'GE, N. J., "Structures/materials synthesis for safety of oceanic deep-submergence bottom-fixed manned habitat", *Journal of Hydronautics*, 2 (3) 120-130 (July 1968).
- (106) "Classification of steels for structures" by Task Group 5, Column Research Council, *AISC Engineering Journal*, pp. 99-109 (July 1971).
- (107) "Materials to Fight Marine Environments", Special Report, *Materials Engineering*, pp. 27-38 (Jan. 1971).
- (108) Technical and Research Bulletin No. 2-11a, *Guide for the Selection of High Strength and Alloy Steels*, The Society of Naval Architects and Marine Engineers, Sept. 1968.
- (109) MARTIN, D. C. "Welding of High-strength Steels", Lecture presented at a Special Summer Session on "Welding Fabrication in Ship-building and Ocean Engineering", M.I.T. 19 Aug. 1969.
- (110) *Welding High Strength Steels*, American Society for Metals, 1969.
- (111) HELLER, CAPT. S. R., JR., FIORITI, I and VASTA, J., "An evaluation of HY-80 steel as a structural material for submarines, Part I", *Naval Engineers Journal*, pp. 29-44 (Feb. 1965).
- (112) PELLINI, W. S., *Evolution of Engineering Principles for Fracture-safe Design of Steel Structures*, NRL Report 6957, U.S. Naval Research Laboratory, Sept. 1969.
- (113) PELLINI, W. S., "High-strength steels", NRL Report 6167, *Status and Projections of Developments in Hull Structural Materials for Deep Ocean Vehicles and Fixed Bottom Installations*, U.S. Naval Research Laboratory, pp. 16-30 (Nov. 1964).
- (114) *Metals Handbook*, American Society for Metals, 1961.
- (115) WILLNER, A. R., "Aluminum alloys", NRL Report 6167, *Status and Projections of Developments in Hull Structural Materials for Deep Ocean Vehicles and Fixed Bottom Installations*, U.S. Naval Research Laboratory, pp. 42-43 (Nov. 1964).
- (116) LEVEAU, C. W., "Aluminum and its use in naval craft, Parts I and II", *Naval Engineers Journal*, pp. 13-27 (Feb. 1965), and pp. 205-219 (April 1965).
- (117) CLARK, D. S. and VERNY, W. R., *Physical Metallurgy for Engineers*, American Book, Van Nostrand, Reinhold, New York, 1952.
- (118) JUDY, R. W., JR., GOODE, R. J., and FREED, C. N., *Fracture Toughness Characterization Procedures and Interpretations to Fracture-safe Design for Structural Aluminum Alloys*, NRL Report 6871, Naval Research Laboratory (Mar. 1968).
- (119) *Welding Handbook*, Section IV, American Welding Society, 1960 (Fourth Edition) and 1966 (Fifth Edition).
- (120) WILLIAMS, W. L. and LANE, I. R., "Titanium alloys", NRL Report 6167, *Status and Projections of Developments in Hull Structural materials for Deep Ocean Vehicles and Fixed Bottom Installations*, U.S. Navy Research Laboratory, pp. 31-41 (Nov. 1964).
- (121) WILLIAMS, W. L., "Metals for hydrospace", Gillett Memorial Lecture, reprinted in *Journal of Materials*, 2 (4) (Dec. 1967).
- (122) FEIGE, N. G., "Welding titanium alloys for marine applications", Lecture presented at a special summer session on "Welding Fabrication in Ship-building and Ocean Engineering" at M.I.T., 20 Aug. 1969. Reprinted by Titanium Metals Corporation of America, 1969.
- (123) FAULKNER, G. C. and COLDRICH, C. G., "Interpretive report on welding titanium and titanium alloys", *Welding Research Council Bulletin Series*, no. 56, pp. 1-20 (Dec. 1959).
- (124) MINKLER, W. W. and FEIGE, N. G., "Titanium for deep submergence vehicles", *Undersea Technology*, pp. 26-29 (Jan. 1965).
- (125) *Current Welding Process*, American Welding Society, 1964.
- (126) *Specification for Mild Steel Covered Arc-welding Electrodes*, AWS A5.1-69, American Welding Society, 1969.
- (127) *Specification for Low-alloy Steel Covered Arc-welding Electrodes*, AWS A5. 5-69, American Welding Society, 1969.
- (128) MASUBUCHI, K., "Welding in modern industry", *Technology Review*, pp. 23-29 (Dec. 1969).
- (129) *Mitsubishi New Welding Practice*, published by Mitsubishi Heavy Industries, Ltd., Tokyo, Japan, 1969.
- (130) MASUBUCHI, K., "One-side welding: it's big in Japan", *Iron Age*, pp. 71 and 73 (26 Feb 1970).
- (131) TERAI, K., and ARIKAWA, M., *Recent Developments in One-Side Automatic Welding*, published in English by the Sampo, Inc., Kanda Sakuma-cho, Chiyoda-Ku, Tokyo, 1968.
- (132) HASEGAWA, M., *Automatic Welding as Applied to Japanese Shipbuilding*, Osaka Transformer Company, Ltd., April 1968.
- (133) TERAI, K., *One Side Automatic Welding in Japan*, August 1970, a publication from Kawasaki Heavy Industries, Ltd., Kobe, Japan.
- (134) MEISTER, R. P., and MARTIN, D. C., "Narrow-gap welding process", *British Welding Journal*, 13, (5), 252-257 (1966)
- (135) *Modern Joining Processes*, American Welding Society, 1966.
- (136) MASUBUCHI, K., and TERAI, K. "EB welding sets sights on shipbuilding in Japan", *Iron Age*, pp. 41-43 (24 Mar. 1965).

- (137) SEASMAN, F. D. and LOCKE, V., "Metal-working capability of a high power laser", Paper 740864 presented before the National Aerospace Engineering and Manufacturing Meeting, San Diego, California, October 1974.
- (138) "Metalworking lasers: their time has come", *Iron Age*, (9 Sept. 1974).
- (139) *A New Manufacturing Process for the Metalworking Industry*, Bulletin No. 369R 3M 175, Sciaky Bros., Inc., Chicago, Illinois, 1975.
- (140) YESSIK, M. and SCHMATZ, D. J., "Laser processing at Ford", *Metal Progress*, pp. 61-66 (May 1975).

CHAPTER 2

Heat Flow in Weldments

THE heat supplied by a welding arc produces complex thermal cycles in the weldment and these in turn cause changes in the microstructure of the heat-affected zone, cause transient thermal stress and metal movement, and result in the creation of residual stress and distortion in the finished product. In order to analyze these problems, we must first analyze heat flow during welding.

Many investigators have studied heat flow during arc welding both analytically and experimentally.^(201 - 206) Analytic methods already developed are capable of computing with reasonable accuracy temperature distributions in simple weldments, such as bead-on-plate welding. The accuracy of the analysis is reasonably high in dealing with temperature changes in areas not too close to the welding arc. The accuracy generally drops considerably when one tries to analyze temperature changes in the heat-affected zone and the weld metal. However, with the advancement of computer technology and such techniques as the finite element method it is quite possible to significantly advance the technology of analyzing heat flow in weldments.

This chapter presents a rather elementary discussion of heat flow in weldments as an introduction to the analysis of thermal stresses during welding which is discussed in Chapter 5. This chapter also includes some discussions on cooling rates and the metallurgy of the heat-affected zone.

2.1 Generation and Dissipation of Welding Heat

2.1.1 Heat generated by the welding arc

The sources of heat generated during metal-arc welding are as follows:

- (1) Heat generated by the electric power of the welding arc, H ,

$$H = VI \text{ watts (joules per second)} \quad (2.1)$$

where V = arc voltage, volts,

I = arc current, amperes.

The thermal equivalent of the electric power is 0.24 calories per second.

- (2) Heat caused by chemical reactions which take place in the electrode coatings, arc atmosphere, and the molten pool (reaction between slag and molten metal, etc.)
- (3) Heat caused by transformation of metal.

By far the largest contributor of heat is the electric power of the welding arc.

The energy input (or heat input of the welding arc, h , given in terms of joules per inch

(or joules per cm) of weld, is commonly used to express the intensity of the welding heat source:

$$h = 60 \times \frac{VI}{v}, \text{ joules per inch} \tag{2.2}$$

where v = travel speed of the welding arc in inches per minute.

Dissipation of welding heat. The heat generated by the welding arc dissipates into:

- (1) The workpiece by thermal conduction.
- (2) The electrode by thermal conduction (most of the heat is used for melting the electrode).
- (3) The surrounding atmosphere by radiation directly from the arc and from the workpiece.

The welding arc transfers most of its heat into the portion of the workpiece immediately under the arc. The heat then spreads into farther portions of the workpiece. Customarily we express the amount of heat supplied to the workpiece, Q , cal/sec, as a portion of the thermal equivalent of the electric power of the welding arc (or arc energy), $0.24VI$, as

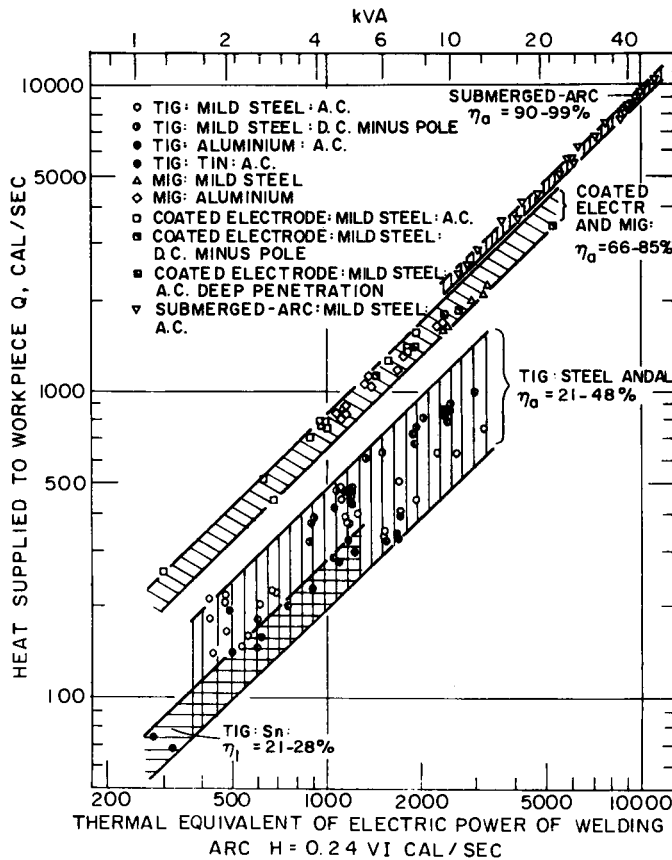


FIG. 2.1. Measured values of arc efficiency for various welding processes and materials (Christensen *et al.*⁽²⁰⁷⁾).

follows:

$$Q = \eta_a \times 0.24VI \quad (2.3)$$

where η_a is called arc efficiency and Q may be called the net heat or effective thermal power of the welding arc.

Figure 2.1, presented by Christensen *et al.*,⁽²⁰⁷⁾ shows measured values of arc efficiency for various welding processes and materials. This logarithmic presentation covers the range of energies from 300 to 12,000 cal (1 to 50 kVA). The position of the curves or bands representing each process gives the arc efficiency, η_a . The slope of these bands, by definition, remains constant at 45 degrees.

Submerged-arc welding is represented in Fig. 2.1 by a narrow band, corresponding to arc efficiencies between 90 and 99%. The heat loss of 1 to 10% may be accounted for by that part of the flux which is heated but not fused.

In ac, shielded metal-arc welding of mild steel, arc efficiency ranges from 66 to 85%. According to Rykalin,⁽²⁰²⁾ the range for coated electrode welding is 75 to 85%.

For GMA welding, arc efficiencies range from 66 to 70% in deposition on mild steel and from 70 to 85% on aluminum.

In contrast to the consumable-electrode processes, GTA welding exhibits a wide range of arc efficiencies as well as lower absolute values. In GTA welding, a substantial part of the heat generated at the electrode tip dissipates into the electrode holder. The data plotted in Fig. 2.1 yields the following ranges:

Mild steel, ac:	22 to 48%
Mild steel, dc:	36 to 46%
Aluminum, ac:	21 to 43%
Tin, ac:	21 to 28%

According to Rykalin,⁽²⁰²⁾ the arc efficiency for carbon-arc welding ranges from 50 to 75%.

2.2 Mathematical Analysis of Heat Flow in Weldments—Basic Considerations and Present State-of-the-art

2.2.1 Basic considerations

Figure 2.2 shows schematically the temperature distribution in a plate when a surface weld bead is being laid at a speed v . Curves 1 to 6 represent isothermal curves on the surface while the dotted curves represent isothermal curves on the transverse section, $ABCD$. O - xyz is the coordinate axis; the origin, O , is on the surface underneath the welding arc, the x -axis lies in the direction of welding, and the z -axis is placed in the thickness of the plate, downward.

The fundamental equation of heat conduction in a solid is^(204, 208)

$$\rho c \frac{\partial \theta}{\partial t} = \dot{Q}_G + \frac{\partial}{\partial x} \left(\lambda \frac{\partial \theta}{\partial x} \right) + \frac{\partial}{\partial y} \left(\lambda \frac{\partial \theta}{\partial y} \right) + \frac{\partial}{\partial z} \left(\lambda \frac{\partial \theta}{\partial z} \right) \quad (2.4)$$

where ρ = density, g cm^{-3} ,

c = specific heat, cal g^{-1} ,

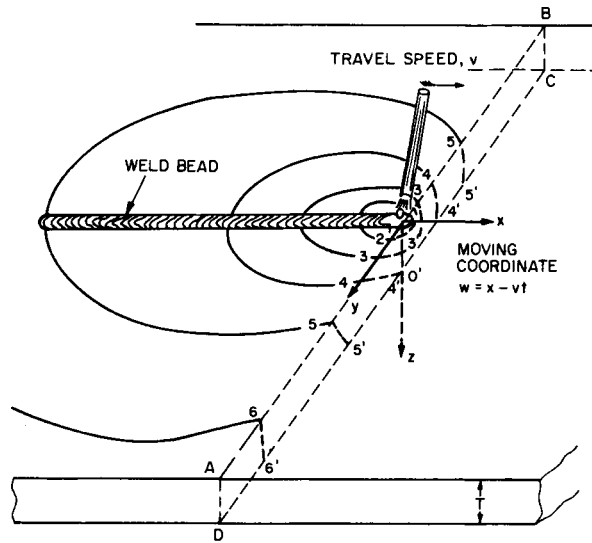


FIG. 2.2. Schematic figure showing the temperature distribution in a plate when a weld bead is laid on the surface.

λ = thermal conductivity cal cm⁻¹ sec⁻¹ °C⁻¹,

\dot{Q}_G = rate of temperature change due to heat generated per volume,
°C sec⁻¹ cal cm⁻³

Table 2.1 shows how eqn. (2.4) is obtained. Table 2.2 lists symbols used throughout this chapter.

Equation (2.4) can be written:

$$\rho c \frac{\partial \theta}{\partial t} = \dot{Q}_G + \lambda \left[\frac{\partial^2 \theta}{\partial x^2} + \frac{\partial^2 \theta}{\partial y^2} + \frac{\partial^2 \theta}{\partial z^2} \right] + \frac{\partial \lambda}{\partial \theta} \left[\left(\frac{\partial \theta}{\partial x} \right)^2 + \left(\frac{\partial \theta}{\partial y} \right)^2 + \left(\frac{\partial \theta}{\partial z} \right)^2 \right]. \quad (2.5)$$

The mathematical analysis of heat flow in a weldment is essentially a solution of eqn. (2.5) for a given initial condition (initial temperature distribution) and a boundary condition (shape and intensity of the heat source, geometry of the weldment, etc.).

If the value of thermal conductivity does not change with temperature, or $\partial \lambda / \partial \theta = 0$, eqn (2.5) can be reduced to a linear differential equation:

$$\rho c \frac{\partial \theta}{\partial t} = \dot{Q}_G + \lambda \left[\frac{\partial^2 \theta}{\partial x^2} + \frac{\partial^2 \theta}{\partial y^2} + \frac{\partial^2 \theta}{\partial z^2} \right]. \quad (2.6)$$

If there is no heat sink or heat source in the element concerned or $\dot{Q}_G = 0$, eqn. (2.6) can be further reduced to:

$$\frac{\partial \theta}{\partial t} = \kappa \left[\frac{\partial^2 \theta}{\partial x^2} + \frac{\partial^2 \theta}{\partial y^2} + \frac{\partial^2 \theta}{\partial z^2} \right] \quad (2.7)$$

where $\kappa = \lambda / \rho c =$ thermal diffusivity, cm² sec⁻¹.

In order to avoid mathematical complexity in solving a non-linear equation, eqn. (2.5),

TABLE 2.1 Fundamental equation of heat flow^(a)

The rate of heat flow, $\frac{dQ}{dt}$ or \dot{Q} , across a surface A is:

$$\dot{Q} = -\lambda A \frac{d\theta}{dx}$$

where t = time

λ = thermal conductivity,

A = cross-sectional area,

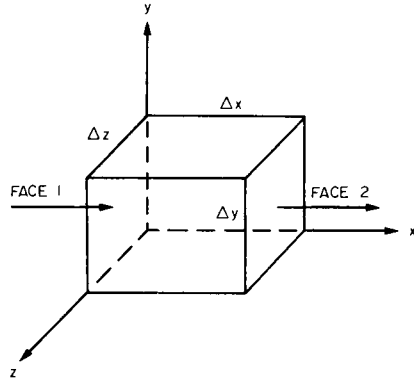
θ = temperature.

The rate of the heat transfer across Face 1 is:

$$\dot{Q}_1 = -\left(\lambda \frac{\partial \theta}{\partial x}\right)_{|x} \Delta y \Delta z$$

and across Face 2 is:

$$\dot{Q}_2 = -\left(\lambda \frac{\partial \theta}{\partial x}\right)_{|x+\Delta x} \Delta y \Delta z.$$



Net rate of heat transfer per unit volume flowing to the cube in the x-direction:

$$\frac{\dot{Q}_1 - \dot{Q}_2}{\Delta x \Delta y \Delta z} = \frac{\left|\lambda \left(\frac{\partial \theta}{\partial x}\right)\right|_{|x+\Delta x} - \left|\lambda \left(\frac{\partial \theta}{\partial x}\right)\right|_{|x}}{\Delta x}$$

We assume that in the limit as Δx approaches zero

$$\lim_{\Delta x \rightarrow 0} \frac{\dot{Q}_1 - \dot{Q}_2}{\Delta x \Delta y \Delta z} = \frac{\partial}{\partial x} \left(\lambda \frac{\partial \theta}{\partial x} \right).$$

The rate of heat transfer in the three directions is:

$$\frac{\partial}{\partial x} \left(\lambda \frac{\partial \theta}{\partial x} \right) + \frac{\partial}{\partial y} \left(\lambda \frac{\partial \theta}{\partial y} \right) + \frac{\partial}{\partial z} \left(\lambda \frac{\partial \theta}{\partial z} \right).$$

The time rate of change of internal energy per unit volume is:

$$Q_v = \rho c \frac{\partial \theta}{\partial t}.$$

We will define \dot{Q}_G as the net heat generated per unit volume per unit of time by heat sources or sinks which exist in the small unit. Thus, from conservation of energy, the final balance becomes:

$$\rho c \frac{\partial \theta}{\partial t} = \dot{Q}_G + \frac{\partial}{\partial x} \left(\lambda \frac{\partial \theta}{\partial x} \right) + \frac{\partial}{\partial y} \left(\lambda \frac{\partial \theta}{\partial y} \right) + \frac{\partial}{\partial z} \left(\lambda \frac{\partial \theta}{\partial z} \right).$$

^(a) For further details read Reference (204).

almost all analyses on heat flow during welding have assumed that thermal properties do not change with changes in temperature, i.e. $\partial \lambda / \partial \theta = 0$.

The characteristics of heat flow during metal-arc welding are affected by the following:

- (1) The heat source moves, usually at a constant speed, on or near the surface of the workpiece.
- (2) The size of the heat source (welding arc) is small compared to the size of the workpiece.

Quasi-stationary state and non-stationary state. Heat flow in arc welding involves three stages:

Stage 1: Heat saturation process during which the temperature around the heat source is rising.

TABLE 2.2 Symbols used for heat-flow analysis

Symbols	Designation	C.G.S. or physical units	Practical units
θ	Temperature	$^{\circ}\text{C}$	$= \frac{5}{9} (^{\circ}\text{F} - 32)$
θ_0	Initial temperature	$^{\circ}\text{C}$	$= \frac{5}{9} (^{\circ}\text{F} - 32)$
λ	Thermal conductivity	$\text{cal cm}^{-1} \text{sec}^{-1} \text{ } ^{\circ}\text{C}^{-1}$	$= 0.56 \times 10^{-2} \text{Btu. in.}^{-1} \text{sec}^{-1} \text{ } ^{\circ}\text{F}^{-1}$
κ	Thermal diffusivity $\kappa = \frac{\lambda}{c\rho}$	$\text{cm}^2 \text{sec}^{-1}$	$= 0.155 \text{in.}^2 \text{sec}^{-1}$
c	Specific heat	$\text{cal g}^{-1} \text{ } ^{\circ}\text{C}^{-1}$	$= 0.999 \text{Btu. lb}^{-1} \text{ } ^{\circ}\text{F}^{-1}$
ρ	Density	g cm^{-3}	$= 0.03613 \text{lb in.}^{-3}$
t	Time	sec	
t_0	Time interval of welding	sec	
t_1	Time after arc extinguishment	sec	
x, y, z	Coordinates of a point	cm	$= 0.3937 \text{in.}$
x_0	Coordinate fixed at the starting point of welding	cm	$= 0.3937 \text{in.}$
x_1	Coordinate fixed at the finishing point of welding $x_1 = x_0 - vt_0$	cm	$= 0.3937 \text{in.}$
w	Moving coordinate, $w = x - vt$	cm	$= 0.3937 \text{in.}$
v	Traveling speed of welding arc	cm sec^{-1}	$= 23.6 \text{in. min}^{-1}$
Q	Effective thermal power of welding arc	cal sec^{-1}	$= 0.238 \text{Btu. min}^{-1}$
q	Intensity of line heat source, $q = Q/T$	$\text{cal cm}^{-1} \text{sec}^{-1}$	$= 0.605 \text{Btu. in}^{-1} \text{min}^{-1}$
T	Plate thickness	cm	$= 0.3937 \text{in.}$
V	Arc volatage	volt	
I	Welding current	ampere	
η_a	Arc efficiency		

Stage 2: Quasi-stationary state in which the temperature distribution is stationary in a coordinate system which moves with the heat source.

Stage 3: Levelling off stage in which the temperature evens out after the welding arc is extinguished.

In the quasi-stationary state, the mathematical analysis is simple, since the problem can be treated as a steady-heat-flow problem for a moving coordinate. The quasi-stationary state occurs in a small area close to the weld during long welding cycles. Most of the mathematical analyses conducted so far on heat flow in weldments have been on the temperature distribution in the quasi-stationary state.

In areas near the start (Stage 1) and the end (Stage 3) of a weld, heat flow is in the non-stationary state, even when the weld is made over a considerable length. When welding is performed over a short length, the quasi-stationary state is never reached, and metal areas adjacent to a short bead or an arc strike cool much faster than those adjacent to a long weld bead. Mathematical analysis of heat flow in the non-stationary state is much more complex than that in the quasi-stationary state.

Effect of the heat-source shape. The local effect principle of the heat-conduction theory shows that the heat distribution pattern of a local source affects temperature distribution substantially only in the region adjacent to the source. Therefore, temperature distribution in outlying areas of the workpiece can be calculated with sufficient accuracy by schematizing the pattern of heat distribution. In Fig. 2.2 the temperature distribution in areas outside curve 4 can be calculated with sufficient accuracy by assuming that the heat source is at point O . The difference in temperature at a

corresponding point on the top and the bottom surface is less pronounced the further the point is from the welding arc, as indicated by curves 5 and 6. If it is assumed that the heat source is concentrated along line OO' (line source), the calculation of the temperature distribution can be reduced to a two-dimensional plane problem.

In computing heat flow in a actual weldment, however, especially a heavy weldment, one must often take into consideration the effect of the size and shape of the heat source. This can be done by treating the heat source to be distributed over a volume or an area.

Physical constants (linear and non-linear theories). Figure 2.3 shows the thermal conductivity (λ) of plain carbon steel (AISI 1010), stainless steel (Type 316), and aluminum.⁽²⁰⁹⁾ Figure 2.4 shows thermal diffusivity (κ) for the same materials. Thermal properties, which are expressed as coefficients in eqn. (2.4), are not really constants but change with the temperature, the extent of the change varying according to the kind of metal.

When the values of thermal properties are treated as variables that change with the temperature, eqn. (1.7) becomes non-linear and the mathematical analysis becomes extremely complex. Grosh *et al.*⁽²¹⁰⁾ analyzed heat flow in weldments but assumed that thermal properties change linearly with the temperature. Only limited work has been done on the non-linear analysis of heat flow in weldments.

To date, almost all of the mathematical analyses of heat flow in weldments, even those utilizing computers, have used the linear theory in which thermal properties are assumed to be constants. Through experience over a number of years, M.I.T. researchers

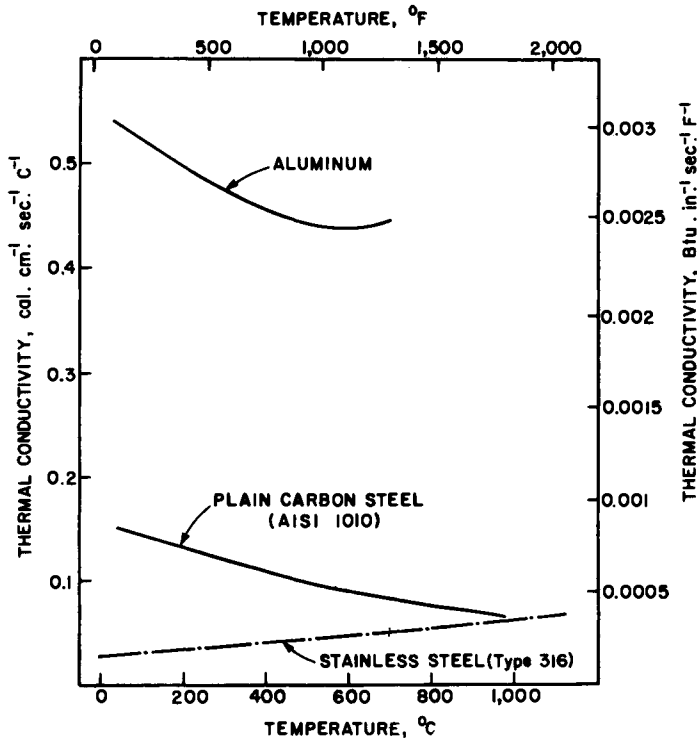


FIG. 2.3. Thermal conductivity of plain carbon steel, and aluminum⁽²⁰⁹⁾

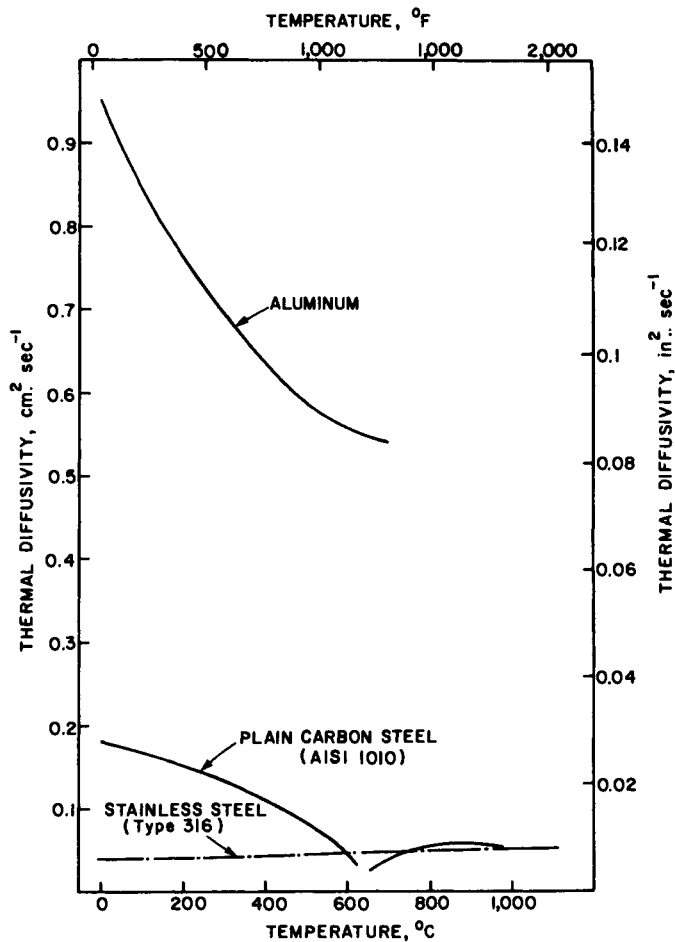


FIG. 2.4. Thermal diffusivity of plain carbon steel, stainless steel, and aluminum.⁽²⁰⁹⁾

have found that reasonably accurate results can be obtained by using modified linear solutions; different thermal properties are used depending upon the temperature of the locations being studied.⁽²¹¹⁾ This is done by means of an iteration technique. This will be discussed further in Chapter 5.

2.2.2 Development of mathematical analyses of heat flow in weldments

The most significant early work was done by Rosenthal^(201, 212) in the late 1930s and the early 1940s. His study is essentially an analysis of the pattern of heat conduction in a solid when a moving heat source is in use. Even today some of the solutions obtained by Rosenthal are widely used.

Analyses prior to 1960. In the study by Rosenthal, assumptions were made to simplify the analysis as follows (see Table 2.3):

1. The analysis was limited to the quasi-stationary state.

TABLE 2.3 *Summary of past studies on heat flow in weldments*

	U.S.A.	Europe	Japan
1935-40	Basic study by Rosenthal (quasi-stationary)		Tanaka, 1940 (non-stationary)
1945-55	Nippes and Savage · Tried to use Rosenthal equation · Then used graphical approach		Naka Masubuchi, 1950
1950-55	Adams	Rykalin (Russia) Wells (England) Christensen (Norway)	Suzuki (1955-60) (analytical-empirical)
1965	Univ. of Wisconsin McDonnell-Douglas	Battelle-Geneva	
1970	M.I.T. (underwater)		
1972-73	M.I.T. (Skylab) Finite element programs		

1975-present. Computer-aided analyses of heat flow in weldments.

- It was assumed that the welding heat would be concentrated at a point (in the three-dimensional analysis) or along a line (in the two-dimensional).

Although the studies on heat flow were expanded by a number of investigators, including Adams^(213,214) and Rykalin,⁽²⁰²⁾ all the studies conducted in U.S.A. and U.S.S.R. were of heat flow in the quasi-stationary state.

More recently, heat flow in the non-stationary state has been studied by several Japanese investigators, including Tanaka,⁽²¹⁵⁾ Naka,⁽²¹⁶⁾ and Masubuchi^(206,217,218) and efforts have been made to apply mathematical analyses to the practical problems caused by non-stationary heat flow. Whenever an arc strike or short weld is used, the cooling rates are high and the heat flow is non-stationary in the surrounding metal areas.

In the late 1940s and the early 1950s, Nippes and Savage^(219,220) studied the cooling rates of heat-affected zones. They used the Rosenthal equations in analyzing experimental data and found large discrepancies between analytical and experimental results. Because of this, they simply graphed their experimental data.

In the late 1950s Suzuki conducted a comprehensive study of the metallurgical structure of the heat-affected zone of weldments in high-strength steels.^(222,223) He developed an analytical-empirical method of studying the effects of welding parameters on metallurgical structures. Some of his results are presented in Section 2.4. Further details are given in a book written by Kihara *et al.*⁽²²²⁾

Analytical-empirical approaches also were taken by other investigators including Christensen⁽²²⁴⁾ and Wells.⁽²²⁵⁾

Recent computer-aided analyses. Recently, there has been a renewed interest in the use of computers in the mathematical analyses of heat flow in weldments.*

In the late 1960s the Battelle Institute Geneva Laboratory in Switzerland conducted a comprehensive study on the metallurgical structure of the heat-affected zone of weld-

* In a recent survey made at M.I.T., it was found that the use of computers in welding fabrication started around 1965.⁽²²⁶⁾

ments in high-strength steels. Attempts were made to use a computer-aided mathematical analysis of heat flow in order to predict the metallurgical structure of the heat-affected zone.⁽²²⁷⁾

Since 1965, computer-aided analyses of heat flow in weldments have been conducted in a number of laboratories, including those at the University of Wisconsin,^(204,228) McDonnell Douglas Aircraft Company,⁽²²⁹⁾ and M.I.T. researchers at M.I.T. have developed computer programs for analyzing heat flow during underwater welding.⁽²³⁰⁾ Paley and Hibbert of the Department of Energy, Mines and Resources, Ottawa, Canada, have developed computer programs capable of computing temperatures in actual weld designs.⁽²³¹⁾

Researchers at M.I.T. recently completed a study on heat flow for the G. C. Marshall Space Flight Center, NASA, during two joint experiments conducted in space as a part of the Skylab program.^(232,233) In this study, finite element programs on heat flow during welding have been developed.⁽²³⁴⁾ Based upon this study a manual entitled "Computer Programs Useful for the Analysis of Heat Flow in Weldments" has been developed. A number of investigations in various countries are currently engaged in computer-aided analyses of heat flow in weldments.⁽²³⁵⁾

2.3 Some Simple Solutions Useful for Analyzing Heat Flow in Weldments

On the following pages are some simple solutions useful for the analysis of heat flow in weldments.

2.3.1 Temperature distributions in the quasi-stationary state

Mathematical analyses of heat flow in welding in the quasi-stationary state have been made by Boulton and Lance-Martin,⁽²³⁶⁾ Rosenthal and Schmerbes,⁽²¹²⁾ Rykalin,⁽²⁰²⁾ and many other investigators.

Using a coordinate (w, y, z), which moves at the same speed as the welding arc, as shown in Fig. 2.2:

$$w = x - vt \quad (2.8)$$

The temperature undergoes no change in the new system of a moving coordinate, thus eqn. (2.7) is expressed as follows:[†]

[†] Since $w = x - vt$,

$$\begin{aligned} \frac{\partial w}{\partial x} &= 1, & \frac{\partial w}{\partial t} &= -v, \\ \frac{\partial \theta}{\partial x} &= \frac{\partial \theta}{\partial w} \frac{\partial w}{\partial x} = \frac{\partial \theta}{\partial w}, & \frac{\partial^2 \theta}{\partial x^2} &= \frac{\partial^2 \theta}{\partial w^2}. \end{aligned}$$

The relationship between $(\partial\theta/\partial t)$ for the fixed coordinate $(\partial\theta/\partial t)_{FC}$ and that of the moving coordinate $(\partial\theta/\partial t)_{MC}$ is:

$$\left(\frac{\partial\theta}{\partial t}\right)_{FC} = \left(\frac{\partial\theta}{\partial t}\right)_{MC} + \frac{\partial\theta}{\partial w} \frac{\partial w}{\partial t} = \left(\frac{\partial\theta}{\partial t}\right)_{MC} - v \left(\frac{\partial\theta}{\partial w}\right).$$

In the quasi-stationary state, $(\partial\theta/\partial t)_{MC} = 0$.

Then eqn. (2.7) can be expressed by eqn. (2.9). Further details of mathematical derivations are given in References (201) and (202).

$$\frac{\partial^2 \theta}{\partial w^2} + \frac{\partial^2 \theta}{\partial y^2} + \frac{\partial^2 \theta}{\partial z^2} = -\frac{v}{\kappa} \left(\frac{\partial \theta}{\partial w} \right). \quad (2.9)$$

Now, θ is a function of position (w, y, z) only.

Equation (2.9) is more easily handled by replacing it with the following expression:

$$\theta = \theta_0 + e^{-(v/2\kappa)w} \phi(w, y, z) \quad (2.10)$$

where θ_0 = initial temperature,

$\phi(w, y, z)$ = function to be found.

Putting the expression (2.10) in (2.9) and performing the calculations, we find

$$\frac{\partial^2 \phi}{\partial w^2} + \frac{\partial^2 \phi}{\partial y^2} + \frac{\partial^2 \phi}{\partial z^2} - \left(\frac{v}{2\kappa} \right)^2 \phi = 0. \quad (2.11)$$

A similar differential equation is encountered in problems of electric waves.

Some examples of solutions for special cases follow:

1. *Three-dimensional case, semi-infinite plate.* This solution applies when a single bead is deposited on the surface of a very large, thick plate ($T \rightarrow \infty$ in Fig. 2.2). The solution of eqn. (2.9) must satisfy the following conditions:

(a) Since the source is a point source, the heat flux through the surface of the hemisphere drawn around the source must tend to the value of the total heat, Q , delivered to the plate, as the radius of the sphere tends to zero. Mathematically speaking, if R is the radius of the sphere,

$$\lim_{R \rightarrow 0} -2\pi R^2 \lambda \frac{\partial \theta}{\partial R} = Q_p \quad (2.12)$$

where $R = \sqrt{w^2 + y^2 + z^2}$.

(b) Heat loss through the surface being negligible, there is no heat transmission from the plate to the surrounding atmosphere:

$$\frac{\partial \theta}{\partial z} = 0 \quad \text{for } z = 0 \text{ and } R \neq 0. \quad (2.12')$$

(c) The temperature of the plate remains unchanged at a very great (infinite) distance from the source, i.e.,

$$\theta = \theta_0 \quad \text{for } R = \infty. \quad (2.12)''$$

The following solution of eqn. (2.9) satisfies the above conditions:

$$\theta - \theta_0 = \frac{Q_p}{2\pi\lambda} e^{-(v/2\kappa)w} \frac{e^{-(v/2\kappa)R}}{R}. \quad (2.13)$$

2. *Three-dimensional case, finite thickness.* We can obtain the temperature distribution in a plate of finite thickness, T , from the former solution by neglecting the radiation from the surface. The condition on the surface is

$$\frac{\partial \theta}{\partial z} = 0, \quad \text{for } z = 0 \text{ and } z = T. \quad (2.14)$$

The solution is obtained by adding an infinite series to eqn. (2.13) as follows:

$$\theta - \theta_0 = \frac{Q}{2\pi\lambda} e^{-(v/2\kappa)w} \left[\frac{e^{-(v/2\kappa)R}}{R} + \sum_{n=1}^{\infty} \left(\frac{e^{-(v/2\kappa)R_n}}{R_n} + \frac{e^{-(v/2)R'_n}}{R'_n} \right) \right] \quad (2.15)$$

where

$$R_n = \sqrt{w^2 + y^2 + (2nT - z)^2},$$

$$R'_n = \sqrt{w^2 + y^2 + (2nT + z)^2}.$$

3. *Two-dimensional case, infinite plate.* Equation (2.16) gives the temperature change caused by a line source (intensity: $q = Q/T$) which moves along the x -axis of an infinite plate:

$$\theta - \theta_0 = \frac{q}{2\pi\lambda} e^{(v/2k)w} K_0\left(\frac{v}{2k}r\right) \quad (2.16)$$

where

$$r = \sqrt{w^2 + y^2}.$$

$K_0(z)$ is the modified Bessel function of the second kind and zero order.[†]

This solution applies to butt welds in large, thin plates.

4. *Two-dimensional case, finite breadth.* If the breadth of the plate is $2B$, the condition at the plate edge is:

$$\frac{\partial\theta}{\partial y} = 0 \quad \text{for } y = \pm B. \quad (2.17)$$

The solution can be obtained by adding an infinite series to eqn. (2.17).

2.3.2 Dimensionless expressions of the heat-flow solution

As shown in eqns. (2.13), (2.15), and (2.16), the temperature change at a certain point during welding is determined by (1) the location of the point, (2) time, (3) heat supplied by the welding arc, (4) travel speed of the arc, (5) size and thickness of the plate, and (6) thermal properties of the material, etc. Investigators, including Jhaveri, *et al.*,⁽²¹⁴⁾ Naka and Masubuchi,⁽²¹⁷⁾ and Christensen *et al.*,⁽²⁰⁷⁾ have used dimensional expressions to simplify numerical calculations of heat-flow solutions. For example, eqn. (2.13)

[†] Detailed descriptions of the modified Bessel functions are given in References (237) and (238). Values of $K_0(z)$ are given in many books including References (237) and (238).

$$K_0(z) = \int_{-1}^{\infty} \frac{e^{-zt}}{\sqrt{t^2 - 1}} dt$$

when (z) is large enough, $K_0(z)$ can be expressed as follows:

$$K_0(z) \simeq \sqrt{\frac{\pi}{2z}} e^{-z}.$$

for a semi-infinite solid is expressed as follows:

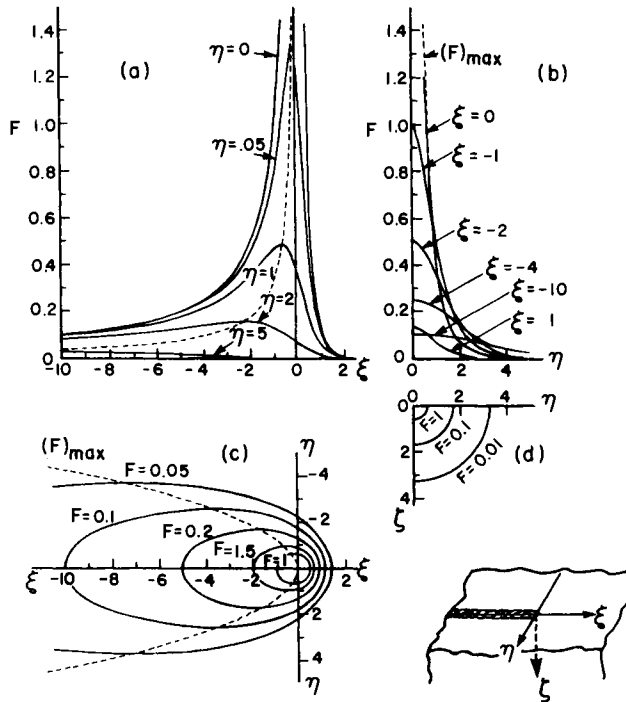
$$\theta - \theta_0 = MF, \tag{2.18}$$

$$M = \frac{Qv}{4\pi\lambda\kappa}, \tag{2.18Y}$$

$$F = \frac{1}{\rho} e^{-(\rho + \xi)}, \tag{2.18''}$$

$$\xi = \frac{v}{2\kappa} w, \quad \rho = \frac{v}{2\kappa} r. \tag{2.18'''}$$

The temperature change $\theta - \theta_0$ is expressed as a product of M and F . The parameter, M , governs the amount of heat. This parameter is determined by the intensity of the heat source, Q , the travel speed of the welding arc, and the thermal properties of the material, λ and κ . A dimensionless function, F , determines the temperature distribution in the welded joint. F is a function of dimensionless variables, ξ and ρ , which are determined by x , r , v , and κ .



$$F = \frac{1}{\rho} e^{-(\rho + \xi)}$$

$$\xi = \frac{v}{2\kappa} w, \quad \eta = \frac{v}{2\kappa} y, \quad \zeta = \frac{v}{2\kappa} z, \quad \rho = \frac{v}{2\kappa} r = \sqrt{\xi^2 + \eta^2 + \zeta^2}$$

FIG. 2.5. Dimensionless function F for heat flow in a semi-infinite solid due to a moving heat source.⁽²⁰²⁾

Figure 2.5 shows values of F given in eqn. (2.20)' as follows:

- Figure 2.5a. Values of F on the surface ($\zeta = 0$) along lines parallel to the ξ -axis with various lateral distances $\eta = 0, 0.1, 0.5, 1, 2$, and 5 .
- Figure 2.5b. Values of F on the surface ($\zeta = 0$) along lines parallel to the η -axis with various longitudinal distances $\xi = 1, 0, -1, -2, -4$, and -10 .
- Figure 2.5c. Equi- F curves (or isothermal curves) on the plate surface ($\zeta = 0$).
- Figure 2.5d. Equi- F curves (or isothermal curves) on the transverse section passing the heat source, $\xi = 0$.

The type of chart shown in Fig. 2.5, when extended over a wide range of F contours, is generally applicable to all combinations of materials and welding conditions. We can easily calculate the temperature change at any point, as shown in the following example.

Suppose that a weld bead is laid on a heavy, mild-steel plate using a covered electrode and conditions of $I = 180$ amperes, $V = 25$ volts, and $v = 0.2$ cm/sec (4.7 in./min). According to Fig. 2.1, Q is estimated to be 800 cal/sec. When the initial temperature of the plate, θ_0 , is 15°C (59°F), the temperature, θ , of a point under the weld bead 3 cm away from the arc ($x = -3$ cm, $y = z = 0$) is calculated as follows:

$$\xi = \frac{v}{2\kappa}x = -\frac{0.2}{0.26} \times 3 = -2.31$$

where it is assumed that $\kappa = 0.13$ cm² sec⁻¹ (see Fig. 2.4). From Fig. 2.5a, $F = 0.433$ for $\xi = -2.31$, $\eta = \zeta = 0$.

$$M = \frac{800 \times 0.2}{4\pi \times 0.12 \times 0.13} = 816,$$

$$\theta - \theta_0 = 816 \times 0.433 = 353,$$

$$\theta = 368^\circ\text{C}.$$

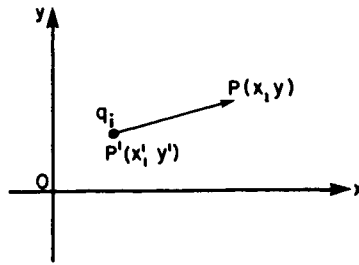
2.3.4 Temperature distribution in the non-stationary state

Solutions for a non-stationary heat flow. Naka⁽²¹⁶⁾ obtained analytical solutions for non-stationary heat flow in a plate during welding. Masubuchi and Kusuda⁽²¹⁸⁾ later obtained solutions for the three-dimensional non-stationary heat flow. Solutions for the two-dimensional case follow.

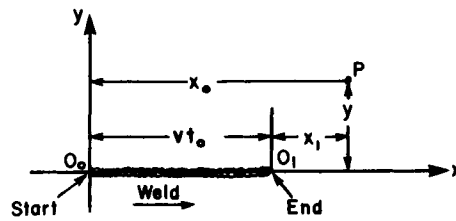
Suppose that an instantaneous line source, q_i , cal/cm, occurs at $P'(x', y')$ at an infinite plate, as shown in Fig. 2.6a, at a time t' and is then extinguished. Equation (2.19) gives the temperature change at $P(x, y)$ at time T ⁽²⁰⁸⁾

$$\theta - \theta_0 = \frac{e^{-[(x-x')^2 + (y-y')^2]/4\kappa(t-t')}}{4\pi\kappa(t-t')} \frac{q_i}{c\rho}. \quad (2.19)$$

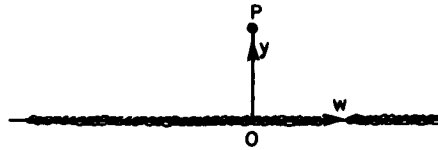
Temperature change due to a moving point source can be obtained by using eqn. (2.19). A line source of intensity q initiates at point O_0 and moves along the x -axis at a constant velocity, v , for a period t_0 . It is then extinguished at point O_1 as shown in Fig. 2.6b. The temperature change, θ , at point P at time t_1 , after the extinguishment of



a. Instantaneous Heat Source at $P'(x', y')$



b. Welding Along the X-axis from O_0 to O_1 for a Distance vt_0



c. Quasi-stationary State

FIG. 2.6. Coordinates in the two-dimensional heat flow due to welding.

the heat source is:

$$\theta - \theta_0 = \int_0^{t_0} \frac{e^{-[(x-vt)^2 + y^2]/4\kappa(t_0 + t_1 - t)}}{4\kappa\pi(t_0 + t_1 - t)} \frac{q}{c\rho} dt. \quad (2.20)$$

Equation (2.20) can be expressed as follows:

$$\theta - \theta_0 = \frac{q}{4\pi\lambda} e^{-(v/2\kappa)w} \int_{(v^2/4\kappa)t_1}^{(v^2/4\kappa)(t_0 + t_1)} \frac{e^{-\zeta - (y^2/\zeta)}}{\zeta} d\zeta \quad (2.21)$$

where

$$w = x - v(t_0 + t_1),$$

$$r^2 = \left(\frac{v}{4\kappa}\right)^2 (w^2 + y^2).$$

Equation (2.21) represents a general solution for two-dimensional heat flow when

laying a straight weld bead. For example, by assuming that welding continued from $t_0 = -\infty$ to $+\infty$, we obtain the temperature distribution in the quasi-stationary state from eqn. (2.21) as follows:

$$\theta - \theta_0 = \frac{q}{4\pi\lambda} e^{-(v/2\kappa)w} \int_{-\infty}^{\infty} \frac{e^{-\zeta - (v^2/\zeta)}}{\zeta} d\zeta = \frac{q}{2\pi\lambda} e^{-(v/2\kappa)w} K_0\left(\frac{v}{2\kappa}r\right). \quad (2.22)$$

In the above equation, the origin of the moving coordinate (w, y) is taken as shown in Fig. 2.6c; i.e. $t = 0$ when the heat source passes point O . Equation (2.12) is the same as eqn. (2.16)

Temperature changes at the start and end of weld. We can determine temperature changes at the starting point or the end (crater) of a weld bead (points O_0 and O_1 in Fig. 2.6) from eqn. (2.21) as follows:

Starting point:

$$\theta - \theta_0 = \frac{q}{4\pi\kappa} e^{(v^2/2\kappa)t_0} K_0\left(\frac{v^2}{2\kappa}t_0\right). \quad (2.23)$$

End point:

$$\theta - \theta_0 = \frac{q}{4\pi\lambda} e^{(v^2/2\kappa)t_1} K_0\left(\frac{v^2}{2\kappa}t_1\right). \quad (2.23')$$

To simplify the analysis, we assume that welding is continued for a long time; that the weld initiated at $t_0 = 0$ and continued to $t_0 \rightarrow \infty$. For the end point, we assume that the weld stopped at $t_1 = 0$ after being continued for a long time to $t_0 \rightarrow \infty$.

A comparison of Eqns. (2.22), (2.23), and (2.23)' shows that the temperature at the weld starting point changes in the same way as the temperature at the end of the weld (or the crater). It also shows that the temperatures at these two points at any given time are equal to one-half the temperature at a point on the weld line under the quasi-stationary state.

2.4 Thermal history of the heat-affected zone

2.4.1 Determinations of thermal history of the heat-affected zone

The metal adjacent to a weld is exposed to rapid thermal cycles, and often undergoes complex metallurgical changes. Several investigators, including Nippes and associates⁽²¹⁹⁻²²¹⁾ and Kihara *et al.*,^(222, 223) have studied the thermal history of the heat-affected zone and have found it difficult to make experimental data fit analytical results based on linear theory. It is apparent that the assumptions used in the mathematical analyses given in eqns. (2.13), (2.15), and (2.16) do not really apply to the thermal history of a heat-affected zone, the reasons being:

- (1) The heat-affected zone is so close to the heat source that we cannot assume that the heat source is a point source located at the plate surface.
- (2) The temperature change encountered in the heat-affected zone is so great that we cannot neglect the change of thermal properties.

Consequently, investigators have commonly used experimental investigation to deter-

mine the thermal cycles in a heat-affected zone. The most popular technique is temperature measurement using thermocouples mounted at precise locations on the workpiece. Careful experimental techniques are essential for accurate results. Of special importance is the secure mounting of the thermocouples to the workpiece and the preciseness of their location.

Figure 2.7 shows thermal cycles measured by Kihara *et al.*⁽²²²⁾ of the heat-affected zone of a bead-welded specimen. A weld bead was laid on a low-carbon, high-strength steel plate 0.7 in. (18 mm) thick, 6 in. (152 mm) wide, and 14 in. (356 mm) long. Low-hydrogen type electrodes (AWS E7016) $\frac{5}{32}$ in. (4 mm) in diameter were used. The weld was made with a heat input of 47,600 joules per inch (arc current: 170 amperes; arc voltage; 28 volts; and arc travel speed: 6 in. (152 mm) per minute). Small holes, 0.06 in. (1.5 mm) in diameter, were drilled normal to the surface from the back side to a predetermined depth. An alumel–chromel thermocouple, 0.012 in. (0.3 mm) in diameter, was welded to the specimen at the bottom of a hole. The hot junction of the thermocouple was melted into the weld metal, so that the thermocouple would indicate the temperature at the weld fusion zone. A coated electrode was fed by a specially designed automatic welding machine so that the weld bead was laid at a predetermined position on the specimen.

Figure 2.7 shows the thermal cycles for two locations: (a) at the bottom of the weld and (b) at the toe of the weld bead. The metal at the toe of the weld bead cooled at a faster rate than did the metal at the bottom of the weld bead. Also shown in the figure are values of cooling rates at three temperature levels, 700, 540, and 300°C (1292, 1004, and 572°F), measured on three specimens, 18 mm (0.71 in.), 24 mm (0.94 in.), and 30 mm (1.2 in.) thick. The cooling rate at 300°C, (572°F) was about 11 % greater at the toe than at the bottom of the weld metal, but the difference was negligible at temperatures below 350°F (177°C).

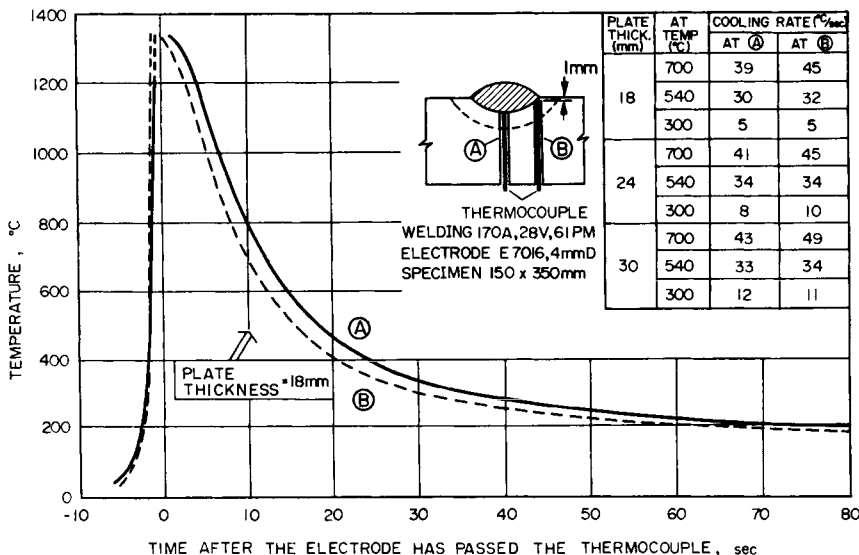


FIG. 2.7. Thermal cycles at two locations of the heat-affected zone of a bead-welded specimen (Kihara *et al.*⁽²²²⁾).

2.4.2 Factors influencing the cooling rate of the heat-affected zone

The microstructure and hardness of the heat-affected zone depend upon the cooling rate. This rate is influenced by various factors including plate thickness, welding conditions, preheat, the length of weld, joint geometry, etc. Many research programs have been carried out to study the effects of welding variables on the cooling rate of the heat-affected zone.

Plate thickness and preheating temperature. Figure 2.8 shows the effect of plate thickness and preheating temperature on the cooling rate of the fusion zone in bead-welded specimens. Weld beads were laid on low-alloy, high-strength steel plates 3 in. (76 mm) wide and 8 in. (203 mm) long. Welds were made with a heat input of 47,600 joules/in. (18,740 joules/cm). The thermal cycles of the heat-affected zones were measured with thermocouples. Shown in the figure are cooling rates at three temperature levels: 700°, 540°, and 300°C (1292°, 1004°, and 572°F). The cooling rates increased with increasing plate thickness. For the cooling rate at 540°C (1004°F) no further increase in the cooling rate was observed when the plate thickness exceeded 25 mm (1 in.).

Welding conditions (heat input). Figure 2.9 shows the effect of welding conditions or heat input on the cooling rate of the heat-affected zone in a bead-welded specimen.

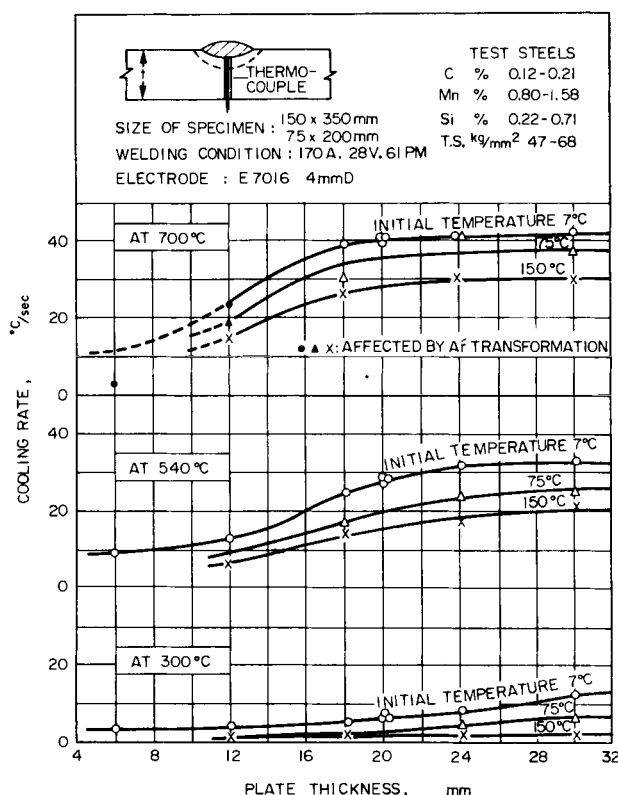


FIG. 2.8. Cooling rates of the fusion zone at 700, 500, and 300°C, as affected by plate thickness and initial plate temperature (Kihara *et al.*⁽²²²⁾).

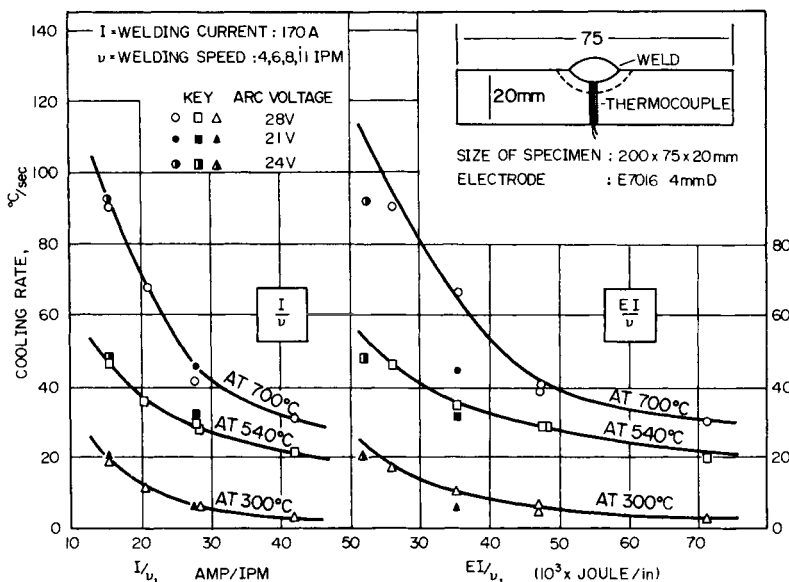


FIG. 2.9. Effects of welding conditions on cooling rates at 700, 540, and 300°C of the fusion zone (Kihara *et al.*⁽²²²⁾).

Weld beads were laid on steel specimens 20 mm (0.79 in.) thick with E7016 electrodes 4 mm ($\frac{5}{32}$ in.) in diameter under the following conditions:

- arc current $I = 170$ amperes,
- arc volts $V = 21, 24,$ and 28 volts,
- arc travel speed $v = 4, 6, 8,$ and 11 in./min.

Figure 2.9 shows values of the cooling rate determined experimentally at three temperature levels: 700°, 540°, and 300°C (1292°, 1004°, and 572° F). The experimental results are plotted against two values: I/v and VI/v which is proportional to the heat input, see eqn. (2.2). The values of cooling rate had a better correlation with I/v than VI/v . The results indicate that the amount of heat supplied to the plate Q is proportional to the arc current rather than the electric power of the arc VI .

Types of electrode coating. Variations in the type of electrode coating introduce corresponding differences in the heat of the chemical reaction and in the melting point of the coating or slag and thus differences in the thermal cycle. According to the information presently available, differences in the cooling rate due to variations in the type of electrode coating are moderate, as long as welds are made under the same conditions.

Weld length and joint geometry. Figure 2.10 shows the effects of weld length on the cooling rates of the heat-affected zones in bead-welded and fillet-welded specimens. Measurements were made at two locations: the center of the weld and the crater (or at the end of the weld). The cooling at the center of the weld increased when the weld length was less than about 5 in. (127 mm). At the end of the weld, the cooling rate increased when the weld length was less than about $2\frac{1}{2}$ in. (64 mm). The cooling rate at the end of the short weld was about twice the cooling rate at the center of a long weld; this can be illustrated by comparing eqns. (2.22) to (2.23)'.

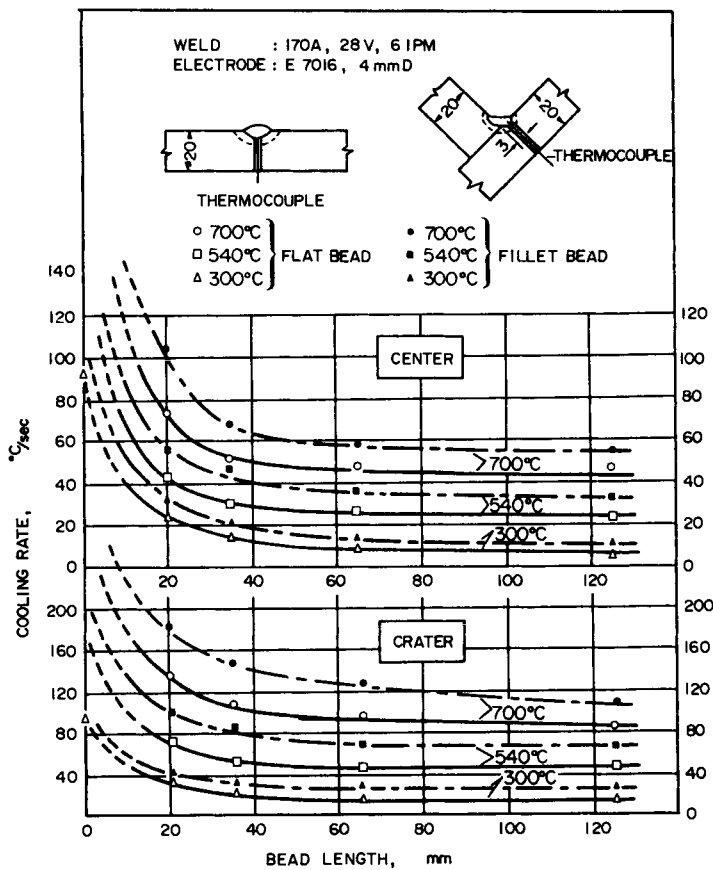


FIG. 2.10. Effects of weld length on the cooling rates of the heat-affected zones in bead-welded specimens and filler-welded specimens (Kihara *et al.*⁽²²²⁾).

Figure 2.10 also shows that the cooling rate of the heat-affected zone in a fillet-welded specimen is about 40% greater than that in a bead-welded specimen made under the same welding conditions. In a fillet weld, the welding heat dissipates in three directions; in a bead-weld it dissipates in two directions. Kihara *et al.*⁽²²²⁾ also found that the cooling rate of the first pass of a double-vee joint is about equal to that of a bead-on-plate weld.

Combined effect of factors. Kihara *et al.*⁽²²²⁾ have proposed, on the basis of data obtained in an extensive investigation, that the combined effect of the plate thickness, preheating temperature, and welding conditions on the cooling rate of the heat-affected zone can be analyzed by a parameter, P , as follows:

$$P \equiv \left[\frac{T - T_0}{I/v} \right]^{1.7} \times \left[1 + \frac{2}{\pi} \arctan \frac{t - t_0}{\alpha} \right] \quad (2.24)$$

where

- T = temperature at which the cooling rate is considered, °C,
- T_0 = initial temperature or preheating temperature of the plate, °C,
- I = arc current, amperes,
- v = arc travel speed, inches per minute,

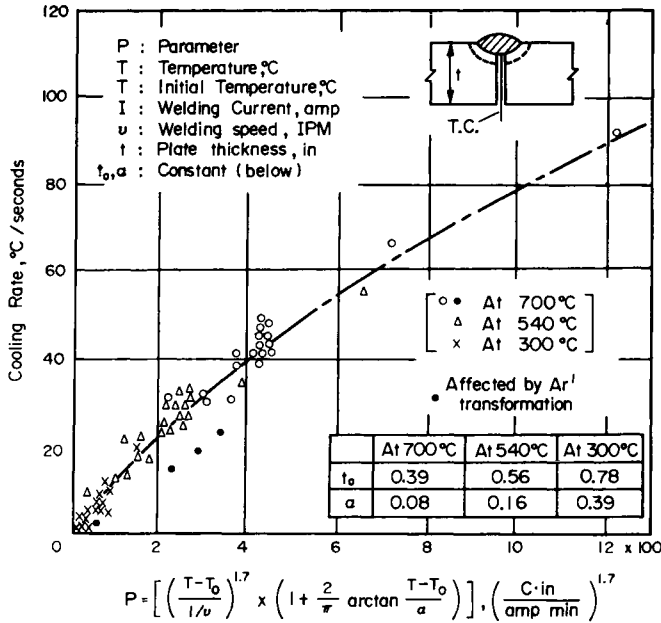


FIG. 2.11. Combined effects of welding parameters on the cooling rate of the heat-affected zone.^(2,22,2,2,2,3)

t = plate thickness, inches,
 t₀, α = constants.

Figure 2.11 shows the relationship between the p-value determined by welding conditions and cooling rates of the heat-affected zone. The following relationship exists:

$$\text{Cooling rate (°C/sec)} = 0.35p^{0.8} \tag{2.25}$$

Suzuki⁽²²³⁾ further developed a monograph determining the cooling rate from welding conditions.

2.4.3 Control of welding heat input

In the fabrication of welded structures, especially in high-strength steels, one must always consider the effects of welding conditions on the metallurgical characteristics of a weldment. How to control welding heat input to obtain optimum heat-affected-zone structures for various materials is an important subject in welding metallurgy. Many publications are available on this subject.^(239 - 245)

The following pages describe very briefly the effects of welding conditions on properties of HAZ structures in weldments in steels, especially high-strength steels.

Current practice. For welding ferritic steels, especially low-alloy high-strength steels, control of welding heat input is exercised basically to achieve the following:

- (1) To avoid rapid cooling to prevent the occurrence of hard, brittle martensite and possible cracking.
- (2) To avoid too slow cooling to prevent the occurrence of less ductile heat-affected structures.

The first subject is important to all steels, while the second subject is especially important to heat-treated steels of which excellent fracture toughness is achieved by quench-and-temper and other heat treatments. Limitations on maximum welding heat input are commonly set for quenched and tempered steels such as HY-80 and HY-100 steels. NAVSHIPS 0900-000-1000⁽²⁴⁶⁾ specifies the maximum welding heat input for welding HY-80/100 and other Q & T steels, as follows:

Plate thickness	Maximum joules/in.
Less than $\frac{1}{2}$ in.	45,000
$\frac{1}{2}$ in. and greater	55,000

Note: The word "maximum" shall not be interpreted as either nominal or average.

Discussions. The information given here comes primarily from *Welding Metallurgy* by Linnert.⁽²³⁹⁾ Those who need more information are advised to refer to this book or other references.⁽²⁴⁰⁻²⁴⁵⁾

It has been found that continuous cooling transformation (CCT) diagrams are useful for studying the effects of welding heat input on metallurgical structures of the heat-affected zone. A number of investigators have developed CCT diagrams for various steels.* Figure 2.12 is an example of a CCT diagram for a steel containing 0.17% carbon. Note that time is expressed in a logarithmic scale.

A CCT diagram shows relationships between time and temperature indicating the beginning and end of transformation under continuous cooling conditions. To develop a CCT diagram for a certain steel, a group of specimens are heated to temperature above the A_3 temperature and then cooled at various rates representing welds made by the shielded metal-arc process for given heat inputs (see Fig. 2.13).

Fig. 2.14 shows the relationship between cooling time (for 800–500°C temperature range) and maximum hardness in the base metal heat-affected zone.[†] Hardness decreased as cooling time increased.

Figure 2.15 shows relationships between cooling time and mechanical properties of specimens cooled at various rates from 1300°C (2372°F). Shown here are:

- (1) bent angle by impact and slow bending, degrees,
- (2) Charpy V-notch impact value at 0°C, kg-m, and
- (3) Vickers hardness (10-kg load).

As the cooling rate increased, hardness decreased monotonously. However, the change of the impact value is rather complex. When the cooling time was less than about 10 seconds, the absorbed energy was very low, indicating that the material was very brittle. The absorbed energy increased suddenly when cooling time was longer than 10 seconds.

* A CCT diagram is similar to a time-temperature-transformation (TTT) diagram, which shows the beginning and end of transformation under isothermal conditions. Specimens are cooled from temperatures above A_3 to a predetermined temperature and kept at the temperature. For the same steel, these diagrams have similar shapes. Compared to the TTT diagram, the CCT diagram represents lower temperatures and longer times.^(245, 246)

[†] In a recent book by Sekiguchi, he uses an A_3 temperature of 796°C (1466°F), while Linnert uses the rounded number of 800°C (1472°F).

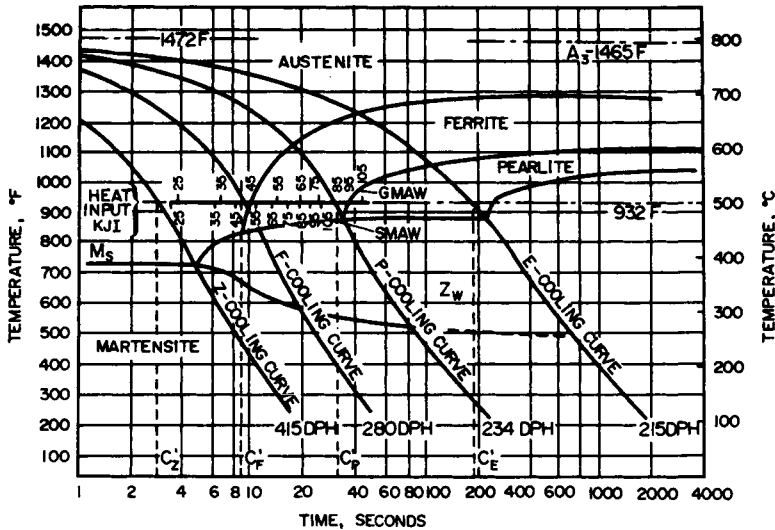


FIG. 2.12. CCT diagram for continuous-cooling transformation showing critical points, critical cooling curves and critical cooling times. (After Inagaki and Sekiguchi).⁽²⁴³⁾

The diagram depicts the transformation behavior of the 0.17% carbon steel described in Fig. 2.13. The scale correlating heat input and cooling rate placed along the 932°F temperature level applies to the heat-affected zones produced in a $\frac{5}{8}$ -in-thick (16 mm) plate welded under bead-on-plate conditions. The maximum hardness values shown usually were found in the coarse-green region immediately adjacent to the fusion line.

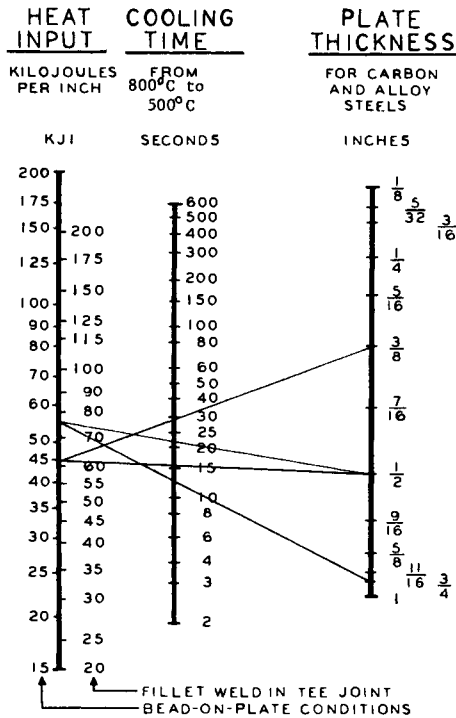


FIG. 2.13. Nomograph for calculating cooling time which elapses between 800 and 500°C (1472 and 932°F) when the base metal heat-affected zone cools from an arc-welding operation. (After Inagaki and Sekiguchi).⁽²⁴³⁾

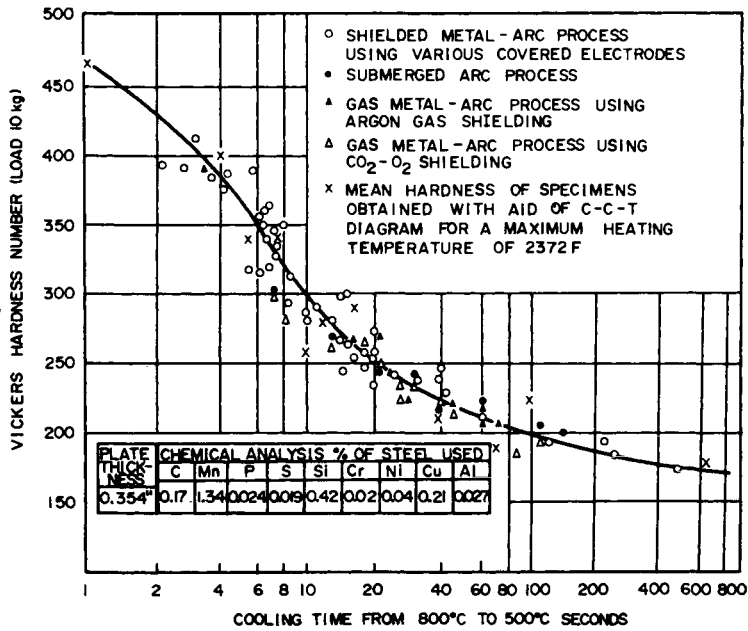


FIG. 2.14. Relationship between cooling time (for 800–500°C temperature range) and maximum hardness in base metal heat-affected zone as determined for various welding processes. (After Inagaki and Sekiguch.⁽²⁴³⁾)

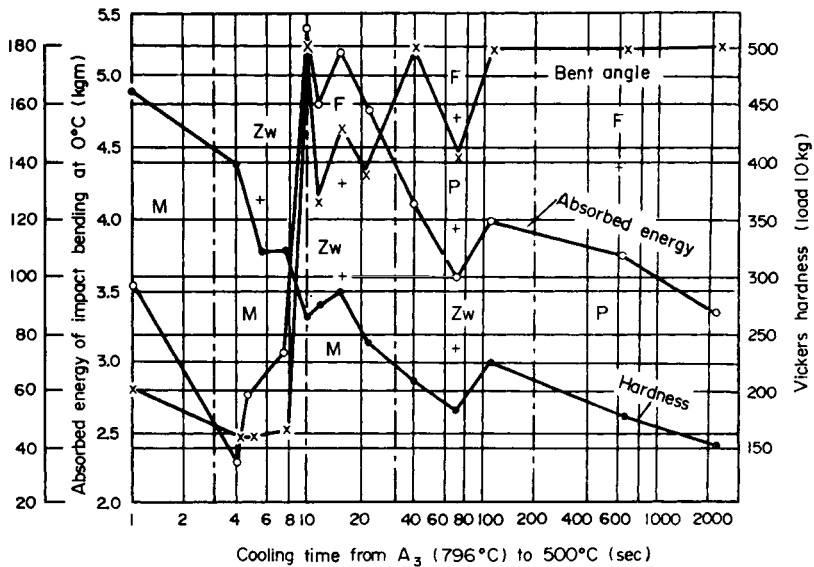


FIG. 2.15. Relations between mechanical properties and cooling times of specimens for rapid heating maximum temperature 1300°C.⁽²⁴²⁾

However, as the cooling time increased further, the impact value decreased steadily, indicating that too slow cooling is detrimental to notch toughness.

Inagaki and Sekiguchi explained the above-mentioned phenomena by use of the CCT diagram shown in Fig. 2.12. If the heat input during welding is very low and cooling takes place at a rate more rapid than the "Z"-cooling curve, then the heat-affected zone structure will be entirely martensitic and its hardness will exceed 415 DPH. If cooling should occur at a rate that falls between the "Z"-cooling curve and the "F"-cooling curve, some transformation to an intermediate structure (Widmanstatten structure), which the investigators have identified by the symbol "Z", will develop and the final heat-affected zone structure will be a blending of martensite and intermediate structures. The hardness of this zone will be lower than 415 DPH. Slower cooling along a curve passing to the right of the "F"-cooling curve will see the formation of some proeutectoid ferrite, and the final structure will consist of ferrite, intermediate structure, and martensite. If cooling is carried out at a slower rate than marked by the "P"-cooling curve, some pearlitic structure also develops and the final structure consists of pearlite, ferrite, intermediate structure, and martensite. A further decrease in cooling rate beyond the "E"-cooling curve usually enables transformation in the heat-affected zone to proceed entirely to ferrite and pearlite. The investigators found that heat-affected zones which cooled at a rate sufficiently slow to produce at least some transformation to proeutectoid ferrite ordinarily did not crack spontaneously and exhibited a reasonable degree of ductility and toughness. They concluded, therefore, that the cooling rate which marked the appearance of proeutectoid ferrite could be identified by the symbol " C_F " and that this rate represented a limiting weldability index. Accordingly, a given steel always should be welded by a procedure (heat input, or possibly through preheat) which produces a heat-affected zone cooling rate slower than C_F ; or when the welding procedure is fixed, the steel employed should have the smallest practicable value of C_F and yet provide the desired strength. In any event, the welding should be carried out in a manner that heat-affected zones cool over a longer period than C_F (or C'_F as shown on Fig. 2.12).

However, too slow cooling is deleterious to notch toughness, as shown in Figure 2.14.

Considering the above two factors, optimum welding conditions are those which produce cooling curves between the F and P curves. The cooling is slow enough to avoid the formation of brittle martensite, but it is rapid enough not to lose good toughness.

Discussions so far have been based upon the results obtained by Inagaki and Sekiguchi on a low-alloy steel. Many investigators have developed CCT diagrams and other data on various steels. Although details are different for various steels, the general trend is similar to most structural steels.

As a matter of exercise, let us estimate the cooling time when a weld is made following the maximum heat-input limitations specified by the Navy for welding HY-80 steel. Suppose that bead-on-plate welds are made with the heat input of 45,000 joules/in. on HY-80 steel plates $\frac{1}{2}$ and $\frac{3}{8}$ in. thick. Cooling times from 800 to 500°C are estimated to be 15 and 30 sec. When similar welds are made on $\frac{1}{2}$ - and $\frac{3}{4}$ -in. plates using a heat input of 55,000 joules/in., values for the cooling times are 20 and 10 sec., respectively. In a study on weldability of HY-80 steel, Ivens⁽²⁴⁴⁾ concluded that to prevent cold cracking in the heat-affected zone of recharged welds of HY-80 steel, welding with low-hydrogen electrodes and a minimum cooling time at Δt (800–500°C) = 15 sec. is advised.

2.5 Heat Flow Problems of Electrode and Weld Metal

The temperatures in the liquid weld metal have not been studied as extensively as those in the base metal. Christensen and Chipman⁽²⁴⁸⁾ attempted direct measurements by means of W–Mo thermocouples. Rabkin⁽²⁴⁹⁾ measured the temperature distribution in the weld pool of automatically weld aluminum. Pokhodnya and Frumin⁽²⁵⁰⁾ made a corresponding investigation on steel. Recently Paley and Hibbert conducted a computer-aided analysis of the heat flow in weld metals of actual designs.⁽²³¹⁾ Dilawari *et al.*⁽²⁵¹⁾ analyzed heat and fluid-flow phenomena in electroslag welding.

An interesting engineering problem related to the thermal history of weld metal is to study the size and form of the weld nugget and the depth of penetration. Christensen and Davis⁽²²⁴⁾ used dimensionless parameters to study the effect of welding variables on the size of the weld nugget. Figure 2.16 is a dimensionless presentation of fused metal and recrystallized metal cross-sections. The dimensionless parameter on the ordinate axis represents the cross-sectional area, and the dimensionless parameter n is determined by the intensity of the heat source and other factors. The theoretical relationship between the area parameter and the parameter n were derived from a point-source model. The

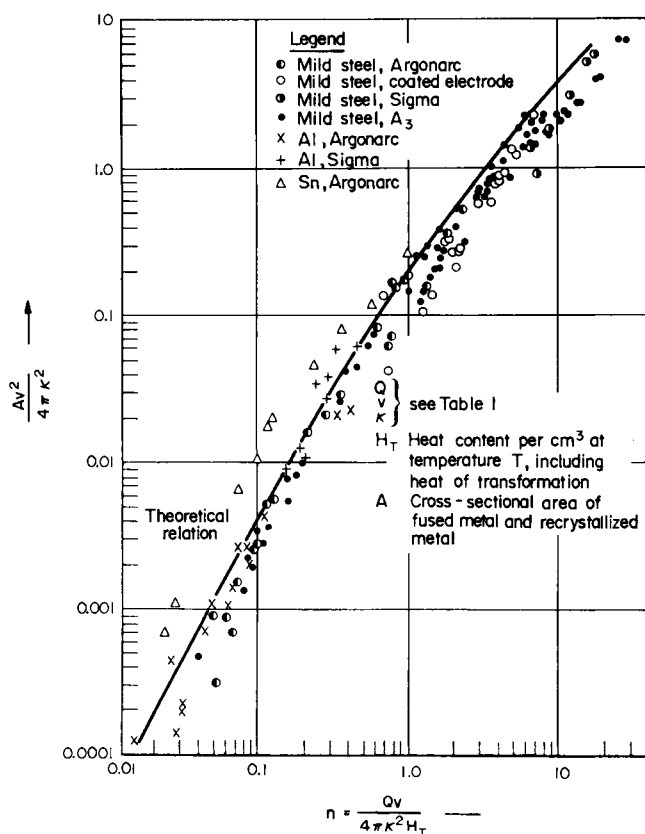


FIG. 2.16. Dimensionless presentation of fused-metal and recrystallized-metal cross-sections (Christensen and Davies⁽²²⁴⁾).

curve in Fig. 2.16 shows this relationship. An excellent correlation was obtained between the calculated curve and experimental data.

References

- (201) ROSENTHAL, D., "Mathematical theory of heat distribution during welding and cutting", *Welding Journal*, **20** (5), Supplement 220-s to 234-s (1941).
- (202) RYKALIN, N. N., "Calculation of heat process in welding", printed in 1960 in Moscow, U.S.S.R.
- (203) *Background for the Development of Materials to be Used in High-strength Steel Structural Weldments*, DMIC Report 172, Defense Metals Information Center, Battelle Memorial Institute (July 1962).
- (204) MYERS, P. S., UYEHARA, O. A., and BORMAN, G. L., "Fundamentals of heat flow in welding", *Welding Research Council Bulletin*, **123** (July 1967).
- (205) MASUBUCHI, K., Chapter 4 of "Heat flow in weldments" of a textbook under preparation.
- (206) MASUBUCHI, K., "Temperature distribution of welded plates", Part I, Plane problem, *Monthly Report of Transportation Technical Research Institute*, Tokyo, **2** (2), 47-56 (1953).
- (207) CHRISTENSEN, N., DAVIS, V. de L., and GJERMUNDSEN, K., "Distribution of temperatures in arc welding", *British Welding Journal*, **12** (2), 54-75 (1965).
- (208) CARSLAW, H. S. and JAEGER, J. C., *Conduction of Heat in Solids*, Oxford University Press, 1959.
- (209) GOLDSMITH, A., HIRSHHORN, H. J., and WATERMAN, T. E., *Thermal properties of solid materials*, Vol. 2 Alloys, Wadco Technical Report 58-476, Wright Air Development Division (Nov. 1960).
- (210) GROSH, R. J., TRABANT, E. A., and HAWKINS, G. A., "Temperature distribution in solids of variable thermal properties heated by moving heat sources", *Quarterly of Applied Mechanics*, **13** (2), 161-167 (July 1965).
- (211) MASUBUCHI, K., NISHIDA, M., YAMAMOTO, G., KITAMURA, K., and Taniguchi, C., "Analysis of thermal stresses and metal movements of weldments: a basic study toward computer-aided analysis and control of welded structures", a paper presented at the Annual Meeting of the Society of Naval Architects and Marine Engineers, New York, N.Y., 13-15 Nov. 1975.
- (212) ROSENTHAL, D. and SCHMERBER, R., "Thermal study of arc welding", *Welding Journal*, **17** (4), Supplement 208 (1938).
- (213) ADAMS, C. M., JR., "Cooling rates and peak temperatures in fusion welding", *Welding Journal*, **37** (5), Research Supplement, 97s to 104s (1963).
- (214) JHAVERI, P., MOFFAT, W. G., and ADAMS, C. M., JR., "The effects of plate thickness and radiation on heat flow in welding and cutting", *Welding Journal*, **41** (1), Research Supplement, 12s to 16s (1962).
- (215) TANAKA, S., "Temperature distribution during welding", *Journal of the Japan Welding Society*, **13** (9), 347-359 (1933).
- (216) NAKA, T., "Temperature distribution during welding", *Journal of the Japan Welding Society*, **11** (1), 4-16 (1941).
- (217) NAKA, T. and MASUBUCHI, K., "Temperature distribution of welded plates", *Journal of the Japan Welding Society*, **16** (7), 281-290 and **16** (12), 374-378 (1947).
- (218) MASUBUCHI, K. and KUSUDA, T., "Temperature distribution of welded plates", *Journal of the Japan Welding Society*, **22** (5), 14-17 (1953).
- (219) NIPPES, E. F., MERRILL, L. L., and SAVAGE, W. F., "Cooling rates in arc welds in 1/2 plates", *Welding Journal*, **28** (11), Research Supplement, 556s to 564s (1949).
- (220) NIPPES, E. F., SAVAGE, W. F., and ALLIS, R. J., "Studies of the weld heat affected zone of T-1 steel", *Welding Journal*, **36** (12), Research Supplement, 531s to 540s (1957).
- (221) NIPPES, E. F. and NELSON, E. C., "Prediction of weld heat-affected zone microstructures from continuous cooling transformation data", *Welding Journal*, **37** (7), Research Supplement, 289s to 294s (1958).
- (222) KIHARA, H., SUZUKI, H., and TAMURA, H., *Researches on Weldable High-strength Steels*, 60th Anniversary Series, Vol. 1, The Society of Naval Architects of Japan, Tokyo, 1957.
- (223) SUZUKI, H., *Modern Welding Handbook*, published by Sankaido Publishing Co., Tokyo, 1962.
- (224) CHRISTENSEN, N. and DAVIS, VDE L., *Distribution of Heat Around Finite Moving Sources*, Report from the Engineering Research Foundation at the Technical University of Norway to U.S. Department of the Army, European Research Office (Contract DA-91-508-EUC-378), Sept., (1959).
- (225) WELLS, A. A., "Heat flow in welding", *Welding Journal*, **31** (5), Research Supplement, 263s to 267s (1952).
- (226) MASUBUCHI, K. and YADA, T., "Use of computers in welding fabrication", paper presented at the *International Conference on Computer Application in the Automation of Shipyard Operation and Ship Design*, 28-30 Aug. 1973, Tokyo, Japan
- (227) Private communication.
- (228) PAVELEC, V., "Temperature histories in thin steel plate welded with TIG", Ph.D. Thesis, University of Wisconsin. 1968.

- (229) STOECKINGER, G. R., CALABRESE, R. A., and MENAUL, R. F., "Computerized prediction of heat distribution in weld tooling", *Welding Journal*, **49** (1 and 6), Research Supplement, 14s to 26s and 272s to 277s (1970).
- (230) BROWN, A. J., BROWN, R. T., TSAI, C. L., and MASUBUCHI, K., Report on *Fundamental Research on Underwater Welding*", Report No. MITSG 74-29, M.I.T. Sea Grant Program, Sept. 1974.
- (231) PALEY, Z. and HIBBERT, P. D., "Computation of temperatures in actual weld designs", *Welding Journal*, **54** (11), Research Supplement, 385s to 392s (1975).
- (232) MURAKI, T. and MASUBUCHI, K., *Thermal Analysis of M551 Experiment for Materials Processing in Space*, Final Report under Contract NAS8-28732 for the G. C. Marshall Space flight Center, NASA, from M.I.T., Dec., 1973.
- (233) MURAKI, T. and MASUBUCHI, K., *Thermal Analysis of M552 Experiment for Materials Processing in Space*, Final Report under contract NAS8-28732 for the G. C. Marshall Space flight Center, NASA, from M.I.T., Dec. 1973.
- (234) MURAKI, T. and MASUBUCHI, K., *Numerical Analysis of Heat Conduction in Solids—With Special Applications to Welding*, Special Report under contract NAS8-28732 for the G. C. Marshall Space Flight Center, NASA, from M.I.T., Mar. 1974.
- (235) Colloquium on "Applications of Numerical Techniques in Welding", 1978, Annual Assembly of the International Institute of Welding, Dublin, Ireland, 2-8 July 1978.
- (236) BOULTON, N. S. and LANCE-MARTIN, H. E., "Residual stresses in arc welded plates", *Proceedings of the Institution of Mechanical Engineers*, **133**, 295-339 (1936).
- (237) WATSON, G. N., *Theory of Bessel Functions*, Cambridge, New York, and London, 1922.
- (238) MCLOCHLAN, N. W., *Bessel Functions for Engineers*, Oxford University Press, 1955.
- (239) LINNERT, G. E., *Welding Metallurgy*, American Welding Society, 1965.
- (240) STOUT, R. D., and Doty, W. D., *Weldability of Steel*, Welding Research Council, Second Edition (1971).
- (241) *The Metallurgy and Weldability of QT 35 and HY-80 Steels*, The Welding Institute, Abington, Cambridge, England, 1974.
- (242) SEKIGUCHI, H., *Fundamental Research on the Welding Heat-affected Zone of Steel*, The Nikkan Kogyo Shimbun, Ltd., Tokyo, Japan, 1976.
- (243) INAGAKI, M. and SEKIGUCHI, H., "Continuous cooling transformation diagrams of steels for welding and their applications", *Transactions of the National Research Institute for Metals*, Tokyo, Japan, vol. 2, no. 2, pp. 102-125, 1960.
- (244) IVENS, P. F., "Weldability of HY-80 steel", I.I.W. Document IX-702-70, Technical University of Delft, Delft, The Netherlands (1970).
- (245) PHILLIPS, A. L. (editor), *Introductory Welding Metallurgy*, American Welding Society, 1967.
- (246) NAVSHIPS 0900-000-1000, "Fabrication, Welding, and Inspection of Ship Hulls", Naval Ship Systems Command, Department of the Navy, Washington, D.C. 20360 (Oct. 1968).
- (247) CLARK, D. S. and VARNEY, W. R., *Physical Metallurgy for Engineers*, American Book-Van Nostrand-Reinhold, New York, Second Edition, 1962.
- (248) CHRISTENSEN, N. and CHIPMAN, J., "Slag-metal interaction on arc welding", *Welding Research Bulletin*, no. 15 (Jan. 1953).
- (249) RABKIN, D. M., "Temperature distribution through the weld pool in the automatic welding of aluminum", *British Welding Journal*, **6** (8), 132-137 (1959).
- (250) POKHODNYA, I. K. and FRUMIN, I. I., "The temperature in the weld pool", *Avtomaticheskaya Svarka*, no. 5 (1955).
- (251) DILAWARI, A. H., EAGAR, T. W., and SZEKELY, I., "An analysis of heat and fluid flow phenomena in electroslag welding", *Welding Journal*, **57** (1), Research Supplement, 24s to 30s (1978).

CHAPTER 3

Fundamental Information on Residual Stresses

THIS chapter presents fundamental information on residual stresses. First elementary information on stresses, strains, and mechanical properties of metals is presented. Then discussions on fundamentals of residual stresses are given. Presented here are basic concepts, and mathematic derivations are kept to a minimum. Residual stresses in metal structures occur not only during welding but also in many manufacturing processes.

From the mathematical viewpoint, residual stresses are caused by some singularities in a continuous body, which may be called “dislocations”. A dislocation can be on a macroscopic scale, or it can be on a microscopic scale. When one considers in a broader sense effects of singularities in the continuum mechanics he finds a number of examples such as vorticity in the fluid mechanics and fracture of a solid. Although this book discusses in depth residual stresses in weldments, it is important to recognize that similar mathematical analyses are used in seemingly different engineering theories including residual welding stresses, fracture mechanics, dislocation theory, and the theory of vorticity.

3.1 Stresses, Strains, and Mechanical Properties of Metals

3.1.1 Stress and strain

When a body is in equilibrium under the action forces, it is said to be in a condition of stress or in a stressed state.⁽³⁰¹⁾ Such stresses cause deformations or strains in the body.

Stress. Stress intensity is usually expressed in load or force per area, such as pounds per square inch (psi), kilograms per square millimeter (kg/mm^2) or Newton per square meter (N/m^2).^{*} In the simple case of a prismatical bar subjected to tension, the stress, σ , is (see Figure 3.1)

$$\sigma = \frac{P}{A} \quad (3.1)$$

where P = total tensile force, or tensile load,
 A = cross-sectional area.

In a general stress field, stresses are not distributed uniformly and are not uniaxial. Figure 3.2 shows how stress components act on the three perpendicular planes passing

^{*} 1 psi = 0.000 703 kg/mm^2 = 6.894 N/m^2 .

TABLE 3.1 Stresses acting on an inclined plane

To simplify the discussion, an analysis for the two-dimensional plane stress ($\sigma_z = \tau_{xz} = \tau_{yz} = 0$) is given here. Stress components on plane BC are:

$$\begin{aligned} \sigma_n &= \sigma_x \cos^2 \phi + \sigma_y \sin^2 \phi + 2 \tau_{xy} \sin \phi \cdot \cos \phi, \\ \tau &= \tau_{xy}(\cos^2 \phi - \sin^2 \phi) + (\sigma_y - \sigma_x) \sin \phi \cos \phi, \end{aligned}$$

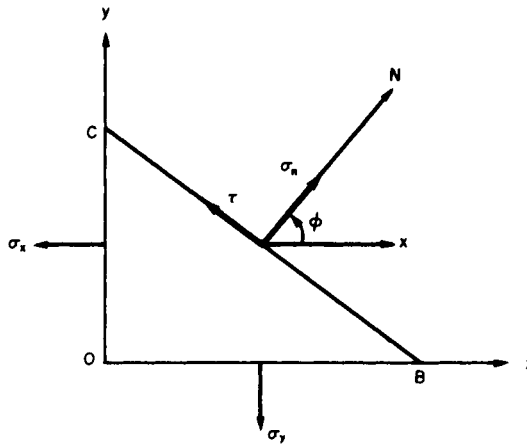
where

- σ_n is the normal stress on plane BC ,
- τ is the shearing stress on plane BC ,
- ϕ is the angle between the normal to the plane, N , and the x -axis

$\tau = 0$ at the following angles ϕ and $\phi + \frac{\pi}{2}$:

$$\frac{1}{2} \tan 2\phi = \frac{\sin \phi \cdot \cos \phi}{\cos^2 \phi - \sin^2 \phi} = \frac{\tau_{xy}}{\sigma_x - \sigma_y}.$$

These two directions are called the principal directions.



through any point, O , of a body. On each pair of parallel planes there are three components: a normal stress perpendicular to the plane and two components of shearing stress acting in the plane. Acting on the plane perpendicular to the x -axis, for example, are the normal stress σ_x , and the shearing stresses, τ_{xy} and τ_{yx} , acting in the directions parallel to the y - and z -axes, respectively. Because of the equilibrium of the element, only six components are independent, as follows:

$$\sigma_x, \sigma_y, \sigma_z; \quad \tau_{xy} = \tau_{yx}; \quad \tau_{yz} = \tau_{zy}; \quad \tau_{zx} = \tau_{xz}.$$

These six quantities are designated the components of stress for that point.

If the six components of stress are known, the stress on any inclined plane through the same point can be calculated (refer to Table 3.1). There are always three perpendicular planes in which there are no shearing stresses. These planes are called the principal planes (coordinate axes perpendicular to these planes are called the principal axes) and stresses acting on these planes are called principal stresses.

Strain. When forces are applied to a body, the body deforms slightly. In the simple case, as shown in Fig. 3.1, the length of the bar increases from its original value L to

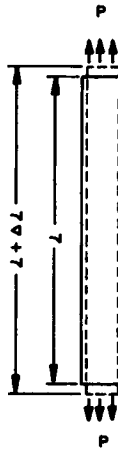


FIG. 3.1 Prismatical bar subjected to tension load, P .

$L + \Delta L$. The strain, ϵ , is expressed as follows:

$$\epsilon = \frac{\Delta L}{L}. \tag{3.2}$$

In a general strain field there are six independent strain components: normal strains, ϵ_x , ϵ_y , and ϵ_z , and shearing strains, γ_{xy} , γ_{yz} , and γ_{zx} .

Stress–strain relationship, Hooke’s law. In most engineering stress analyses it is customary to assume that structural materials are purely elastic, homogeneous, and isotropic (material properties are the same in all directions). According to Hooke’s law, the magnitudes of strains and stresses are proportional as follows:

$$\begin{aligned} \epsilon_x &= \frac{1}{E} \{ \sigma_x - \nu(\sigma_y + \sigma_z) \}, \\ \epsilon_y &= \frac{1}{E} \{ \sigma_y - \nu(\sigma_z + \sigma_x) \}, \\ \epsilon_z &= \frac{1}{E} \{ \sigma_z - \nu(\sigma_x + \sigma_y) \}, \\ \gamma_{xy} &= \frac{1}{G} \tau_{xy}, \quad \gamma_{yz} = \frac{1}{G} \tau_{yz}, \quad \gamma_{zx} = \frac{1}{G} \tau_{zx}, \end{aligned} \tag{3.3}$$

where E = modulus of elasticity (in tension), or Young’s modulus,
 ν = Poisson’s ratio,

$$G = \frac{E}{2(1 + \nu)} = \text{modulus of rigidity, or shear modulus}$$

Stress–strain relationships in the plastic condition are much more complex.

3.1.2 Mechanical properties of metals

Figure 3.3 shows schematically the stress–strain curve of a metal such as an aluminum

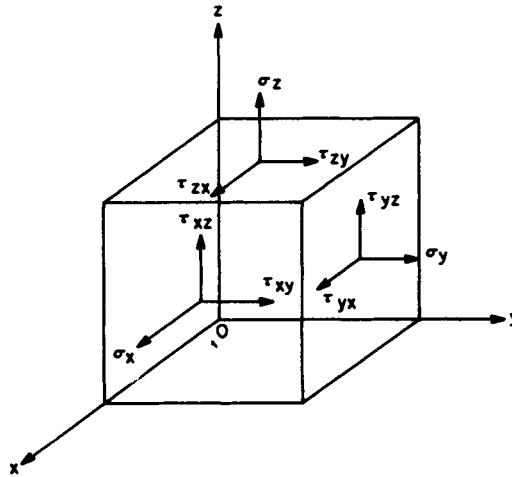


FIG. 3.2. Stress components.

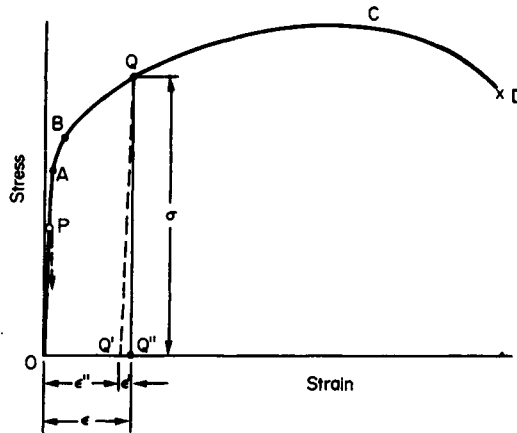


FIG. 3.3 Stress-Strain curve of a metal.

alloy. As the load or stress increases the strain changes as shown by the curve *OABCD*. The region *OA* is the elastic region and its slope corresponds to Young's modulus. The stress at point *B* is the yield stress, and when the load is increased, the metal deforms plastically. Some metals, including carbon steel, clearly exhibit yielding, while others, including aluminum alloys, do not. In metals such as aluminum alloys, the stress at which 0.2% permanent extension has taken place is commonly designated the yield stress.

Point *C* represents the ultimate tensile strength, and point *D* indicates when the piece fractures.

The strain changes when the load is decreased or when the metal is unloaded. When stress is decreased from an arbitrary point, *P*, on the line *OA*, strain decreases as shown by the dotted arrow and no permanent set remains after the load is removed (returns to

the origin, O). When stress is decreased from an arbitrary point, Q , on the curve BC , strain changes as shown by the line QQ' . QQ' ($= \epsilon''$) represents the permanent set or the plastic strain. The line QQ' is parallel to the line AO . If the metal is loaded again, strain changes as shown by $Q'QCD$, indicating an increase in the elastic limit from the stress which corresponds to A to that which corresponds to Q . The magnitude of stress σ at point Q can be determined by measuring the amount of elastic strain, $Q'Q'' = \epsilon'$, which takes place during unloading, as follows:

$$\sigma = E\epsilon' \quad (3.4)$$

During unloading, metals behave in a purely elastic manner, even if they have undergone plastic deformation. This characteristic is the basis for the strain-relaxation techniques that have been developed for measuring residual stresses in metals.

In most cases involving measurement of residual stress, the history of the metal being investigated is not known. In many cases at least some portions of the specimen have undergone plastic deformation, a condition which, when non-uniform, is a major source of residual stresses. Even so, it is possible to determine the magnitude of residual stress by measuring the amount of elastic strain that takes place during unloading.

3.2 Residual Stresses

3.2.1 Residual stresses

Residual stresses are those stresses that would exist in a body if all external loads were removed. Various technical terms have been used to refer to residual stresses, such as⁽³⁰²⁾

- Internal stresses
- Initial stresses
- Inherent stresses
- Reaction stresses
- Locked-in stresses

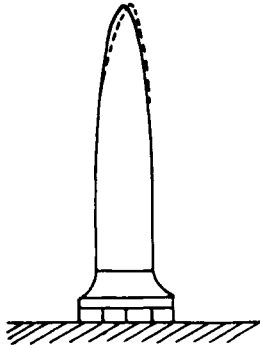
Residual stresses also occur when a body is subjected to a non-uniform temperature change; these stresses are usually called thermal stresses.

Macroscopic and microscopic residual stresses. Areas in which residual stresses can exist vary greatly in scale from a large portion of a metal structure down to areas measurable only on the atomic scale. Figure 3.4 shows macroscopic residual stresses on several different scales.⁽³⁰¹⁾ When a structure is heated by solar radiation from one side, thermal distortions and thermal stresses are produced in the entire structure, as shown in Fig. 3.5(a). Figure 3.5(c) shows how the residual stresses produced by grinding are highly localized in a thin layer near the surface.

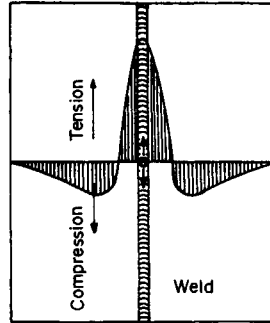
Residual stresses also occur on a microscopic scale. For example, residual stresses are produced in areas near martensitic structures in steel since the martensite transformation that takes place at relatively low temperatures results in the expansion of the metal. Residual stresses on the atomic scale exist in areas near dislocations.

This chapter is concerned with macroscopic residual stresses.

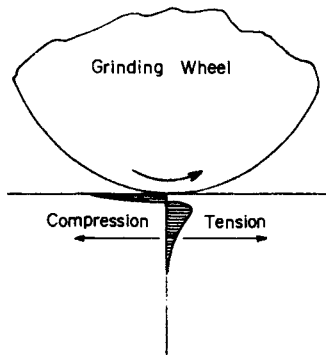
Equilibrium condition of residual stresses. Since residual stresses exist without external forces, the resultant force and the resultant moment produced by the residual stresses



(a) Thermal Distortion in a Structure Due to Heating by Solar Radiation

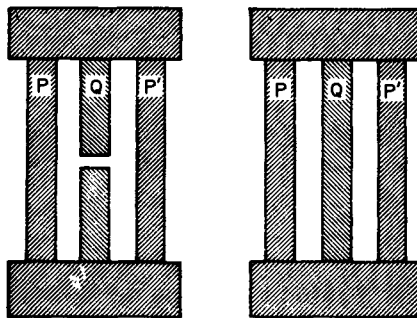


(b) Residual Stresses Due to Welding



(c) Residual Stresses Due to Grinding

FIG. 3.4. Macroscopic residual stresses on various scales.⁽³⁰¹⁾



(a) Free State (b) Stressed State

FIG. 3.5. Residual stresses produced when bars with different lengths are forcibly connected.

must vanish:

$$\int \sigma \cdot dA = 0 \text{ on any plane section} \quad (3.5)$$

and

$$\int dM = 0. \quad (3.6)$$

It is very important to check whether the residual-stress data recorded in any experiment satisfies the above conditions.

3.2.2 Occurrence of residual stresses

Residual stresses in metal structures occur for many reasons during manufacturing. Residual stresses may be produced:

- (1) In many materials including plates, bars, and sections during rolling, casting, forging, etc.
- (2) During forming and shaping of metal parts by such processes as shearing, bending, machining, and grinding.
- (3) During fabrication processes, such as welding.

Heat treatments during manufacturing can also influence residual stresses. For example, quenching produces residual stresses while stress-relieving heat treatments reduce residual stresses.

Residual stresses are classified according to the mechanisms which produce them:

- (1) Those produced by structural mismatching.
- (2) Those produced by uneven distribution of non-elastic strains, including plastic and thermal strains.

3.2.3 Residual stresses produced by mismatching^(302,303)

Figure 3.5 shows a simple case in which residual stresses are produced when bars of different lengths are forcibly connected. Tensile stresses are produced in the shorter bar, Q , and compressive stresses are produced in the longer bars P and P' .

Figure 3.6 shows how a heating-and-cooling cycle causes mismatching resulting in residual stress.⁽³⁰⁴⁾ Illustrated are three carbon-steel bars of equal length and sectional area connected by two rigid blocks at the ends; the middle bar is heated to 1100°F (593°C) and then cooled to room temperature while the side bars are kept at room temperature. Figure 3.6 plots the stress in the middle bar against the temperature and shows the amount of residual stress produced. Since the two side bars are resisting the deformation of the one middle bar, the stress in each side bar, σ_s , is always equal to half the stress in the middle bar, σ_m , and opposite in sign from the equilibrium condition:

$$\sigma_s = \frac{1}{2} \sigma_m. \quad (3.7)$$

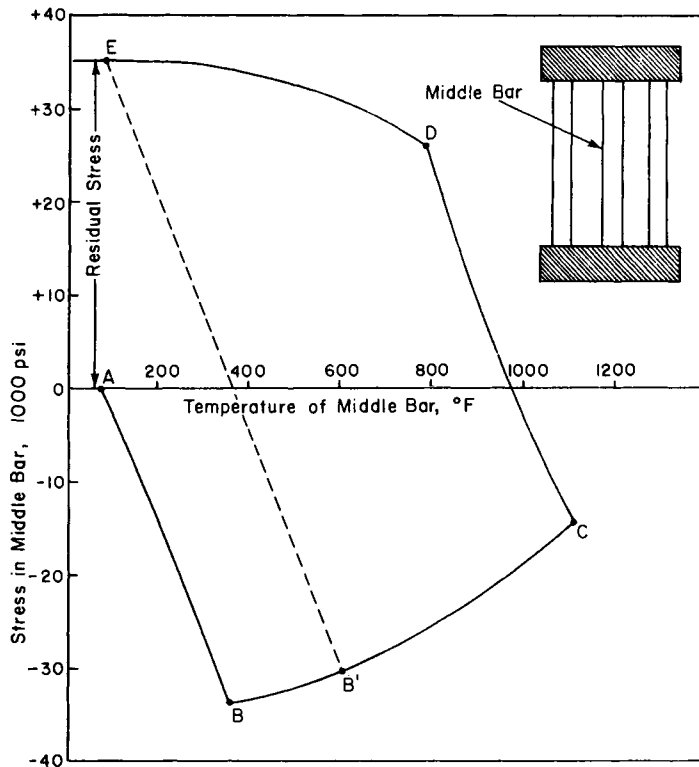


FIG. 3.6. Stress-temperature curve for middle bar of a three-bar frame

Since the lengths of the middle and side bars must be the same, the following equation must be satisfied:

$$\frac{\sigma_m}{E_t} + \alpha \Delta T + \frac{\sigma_s}{E} = 0 \tag{3.8}$$

where E = modulus of elasticity at room temperature, T_0 ,
 E_t = modulus of elasticity at temperature, T ,
 $\Delta T = T - T_0$ = increment of temperature,
 α = coefficient of linear thermal coefficient,

then

$$\sigma_m = -\alpha \Delta T \frac{2E}{1 + 2E/E_t} \tag{3.9}$$

The stress in the middle bar σ_m , at various stages of the thermal cycle can be calculated from eqns. (3.7) and (3.8).

As the temperature of the middle bar increases, the stress in it changes when the

change, while a neighboring point Q moves to Q' . When there is no dislocation, the vector $\vec{P'Q'}$ becomes infinitesimally small when Q approaches P , or:

$$\lim \vec{P'Q'} = 0, \text{ if } \vec{PQ} \rightarrow 0. \tag{3.10}$$

The situation is different when stress changes involve dislocation. Suppose a crack occurs along the line AB , as shown in Fig. 3.7(b). When the neighboring point Q is located on the same side of the line AB , eqn. (3.10) still holds. However, when the point is located on the opposite side of the line AB , as shown by the point R , the vector $\vec{P'R'}$ does not approach zero, but approaches a definite value, which is designated the “crack opening”. This vector $\vec{P'R'}$ is generally called the “dislocation”.

Volterra⁽³⁰⁵⁾ called this mismatched deformation “distorsioni” and Love⁽³⁰⁶⁾ named it “dislocation”. Taylor⁽³⁰⁷⁾ and Orowan⁽³⁰⁸⁾ used the concept of dislocation to explain atomic mechanisms of plastic deformation, and this concept has been widely used to explain many phenomena in physical metallurgy. The important fact about dislocation is that displacement is multi-valued when dislocation occurs.^(309–313) A dislocation can be on a macroscopic scale, or it can be on a microscopic scale. This chapter discusses macroscopic dislocations.

Figure 3.7(b) shows how the stress changes that occur from state I to state II are those of cracking or fracturing while the stress changes that occur from state II to state I are reaction stresses caused by closing a mismatch. Consequently, the basic equations used in the fracture mechanics theory are similar to those used in the analysis of residual stresses in weldments. Some examples will be discussed later in this chapter.

Figure 3.7(b) also shows that dislocation is related to a topological change of the body. In state I, the body occupies a singly connected region, while the body in state II occupies

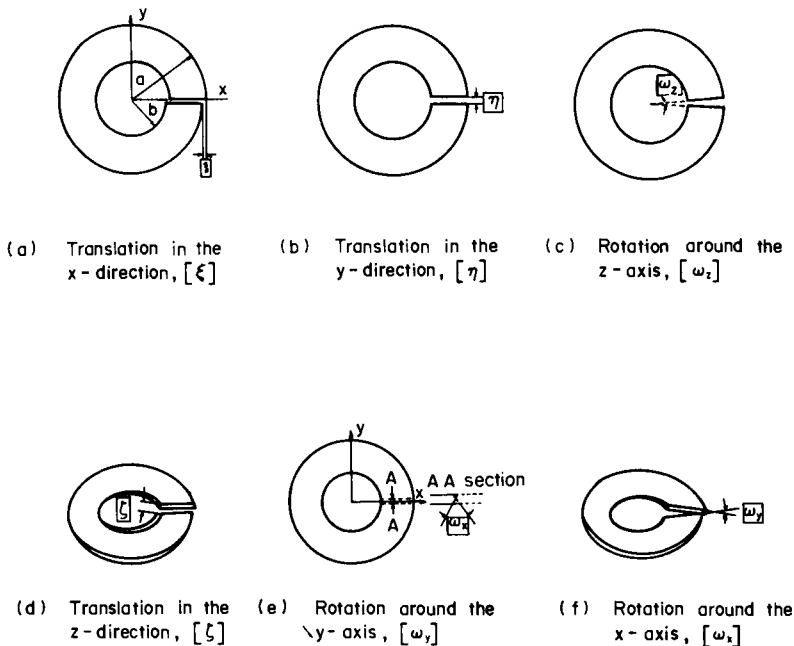


FIG. 3.8. Dislocations in a ring

a multiply connected region. It has been found that when a body occupies a multiply connected region displacement can be multi-valued.

Dislocation in a circular ring. A circular ring is a simple example of a multiply connected region. Figure 3.8 shows the six basic types of dislocations that can occur in a ring-shaped plate, as follows:

- (1) Translation in the x -direction, $[\xi]$, as shown in Fig. 3.8(a).
- (2) Translation in the y -direction, $[\eta]$, as shown in Fig. 3.8(b).
- (3) Rotation around the z -axis or rotation in the xy -plane, $[\omega_z]$, as shown in Fig. 3.8(c).
- (4) Translation in the z -direction, $[\zeta]$, as shown in Fig. 3.8(d).
- (5) Rotation around the y -axis, $[\omega_y]$, as shown in Fig. 3.8(e).
- (6) Rotation around the x -axis, $[\omega_x]$, as shown in Fig. 3.8(f).

The dislocations shown in Figs. 3.8(a), (b) and (c) cause residual stresses uniform in the z -direction of the flat plate which will remain after the rings are joined. Dislocations shown in Figs. 3.8(d), (e), and (f) cause residual stresses not uniform in the z -direction and the flat plate will be bent after the rings are joined.

Table 3.2 shows Goursat's stress functions for dislocations $[\xi]$, $[\eta]$, and $[\omega_z]$.⁽³¹⁴⁾ Solutions for $[\zeta]$, $[\omega_y]$, and $[\omega_x]$ are shown in Table 3.3 Table 3.4 provides the basic characteristics of Goursat's stress functions. The relationship between Goursat's stress functions $\phi(z)$, $\psi(z)$ and Airy's stress function $F(x, y)$ is:⁽³¹⁵⁾

$$F(x, y) = \text{Re} \{ \bar{z} \phi(z) + \psi(z) \} \tag{3.11}$$

where

$$z = x + iy, \bar{z} = x - iy.$$

Stress components are expressed as follows:

$$\left. \begin{aligned} \sigma_x &= \frac{\partial^2 F}{\partial y^2}, \\ \sigma_y &= \frac{\partial^2 F}{\partial x^2}, \\ \tau_{xy} &= -\frac{\partial^2 F}{\partial x \partial y}. \end{aligned} \right\} \tag{3.12}$$

By examining stress functions in Table 3.2 one will notice that expressions for $\phi(z)$ and $\psi(z)$ are composed of two parts, the first part which contains $\log z$ or $z \log z$ and the second part which does not contain logarithmic expressions. The first part causes dislocation, while the second part is included to satisfy the boundary conditions that no external force exists, or

$$\sigma_r + i\tau_{r\theta} = 0 \quad \text{along } r = a, \quad r = b. \tag{3.13}$$

Table 3.5 shows detailed calculations for dislocations $[\xi]$ and $[\eta]$. Equations in Tables 3.2 and 3.3 show that dislocations are caused by logarithmic terms as described in Goursat's stress functions. When these terms exist, stresses can be continuous and single-valued while displacement is multi-valued.

TABLE 3.2 Goursat's stress functions for $[\xi]$, $[\eta]$, $[\omega_z]$

(1) Displacement Type Dislocations $[\xi]$, $[\eta]$	
<i>Stress functions</i>	
$\phi(z) = \frac{E}{8\pi} \left\{ ([\eta] - i[\xi]) \log z - ([\eta] + i[\xi]) \frac{z^2}{a^2 + b^2} \right\}$	
$\psi(z) = \frac{E}{8\pi} \left\{ ([\eta] + i[\xi]) z \log z + ([\eta] - i[\xi]) \frac{a^2 b^2}{a^2 + b^2} \frac{1}{z} \right\}$	(1)
<i>Stress components</i>	
$\sigma_r = \frac{E}{4\pi} \frac{1}{a} ([\eta] \cos \theta - [\xi] \sin \theta) \frac{(\rho^2 - \lambda^2)(1 - \rho^2)}{(1 + \lambda^2)\rho^3}$	
$\sigma_\theta = \frac{E}{4\pi} \frac{1}{a} ([\eta] \cos \theta - [\xi] \sin \theta) \frac{\rho^2(1 - 3\rho^2) + \lambda^2(1 + \rho^2)}{(1 + \lambda^2)\rho^3}$	(2)
$\tau_r\theta = \frac{E}{4\pi} \frac{1}{a} ([\eta] \sin \theta + [\xi] \cos \theta) \frac{(\rho^2 - \lambda^2)(1 - \rho^2)}{(1 + \lambda^2)\rho^2}$	
(2) Rotation Type Dislocation $[\omega_z]$	
<i>Stress functions</i>	
$\phi(z) = \frac{E}{8\pi} [\omega_z] \left\{ z \log z - \frac{a^2 - b^2 + 2a^2 \log a - 2b^2 \log b}{2(a^2 - b^2)} z \right\}$	(3)
$\psi(z) = \frac{E}{8\pi} [\omega_z] \frac{a^2 b^2}{a^2 - b^2} \log \frac{a}{b} \log z$	
<i>Stress components</i>	
$\sigma_r = \frac{E}{4\pi} [\omega_z] \left\{ \log \rho - \frac{\lambda^2 \log \lambda (1 - \rho^2)}{(1 - \lambda^2)\rho^2} \right\}$	
$\sigma_\theta = \frac{E}{4\pi} [\omega_z] \left\{ 1 + \log \rho + \frac{\lambda^2 \log \lambda (1 + \rho^2)}{(1 - \lambda^2)\rho^2} \right\}$	(4)
$\tau_r\theta = 0$	

Note: $\lambda = \frac{b}{a}$, $\rho = \frac{r}{a}$, $z = x + iy$.

TABLE 3.3 Displacement functions for dislocations involving bending - plates

	$\psi b(z)$	$\psi c(z)$
$[\xi]$	0	$-i \frac{D}{2\pi} [\xi] \log z$
$[\omega_z]$	$\frac{1 - \nu}{8\pi} D [\omega_z] \log z$	$-\frac{3 + \nu}{8\pi} [\omega_z] z \log z$
$[\omega_y]$	$i \frac{1 - \nu}{8\pi} D [\omega_y] \log z$	$i \frac{3 + \nu}{8\pi} [\omega_y] z \log z$

Note: Shown here are only the principal parts of the displacement functions pertinent to dislocation—similar to the first terms of $\phi(z)$ and $\psi(z)$ shown in Table 3.2.

3.2.4 Residual stresses produced by uneven distribution of non-elastic strains

When a material is heated uniformly, it expands uniformly and no thermal stress is produced. But when the material is heated unevenly, thermal stress is produced. Residual

TABLE 3.4 *Basic characteristics of Goursat's stress function*

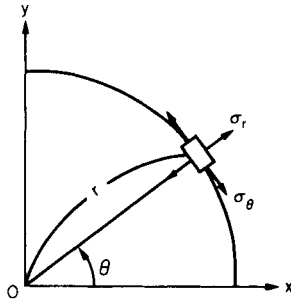
Stress components

$$\begin{aligned} \sigma_x + \sigma_y &= \frac{1}{4} R_e[\phi'(z)] \\ \frac{1}{2} [\sigma_y - \sigma_x] + i \tau_{xy} &= \bar{z} \phi''(z) + \psi''(z) \end{aligned} \quad (1)$$

Displacement

$$E(u - iv) = (3 - \nu) \bar{\phi}(\bar{z}) - (1 + \nu) [\bar{z} \phi'(z) + \psi'(z)] \quad (2)$$

Stress components expressed in the polar coordinates



$$\begin{aligned} x &= r \cos \theta, & y &= r \sin \theta \\ \text{or } x + iy &= r e^{i\theta} & i &= \sqrt{-1} \end{aligned}$$

$$\begin{aligned} \frac{1}{2} (\sigma_\theta + \sigma_r) &= \frac{1}{2} (\sigma_y + \sigma_x) \\ \frac{1}{2} (\sigma_\theta - \sigma_r) + i \tau_{r\theta} &= \left[\frac{1}{2} (\sigma_y - \sigma_x) + i \tau_{xy} \right] e^{2i\theta}. \end{aligned}$$

TABLE 3.5 *Dislocations produced by stress functions shown in Table 3.2*

Displacement

$$\begin{aligned} E(u - iv) &= (3 - \nu) \bar{\phi}(\bar{z}) - (1 + \nu) [\bar{z} \phi'(z) + \psi'(z)] \\ &= (3 - \nu) \frac{E}{8\pi} \left[([\eta] + i[\xi]) \log \bar{Z} - ([\eta] - i[\xi]) \frac{\bar{Z}^2}{a^2 + b^2} \right] \\ &\quad - (1 + \nu) \frac{E}{8\pi} \left[z([\eta] + i[\xi]) \frac{1}{Z} - \bar{Z}([\eta] + i[\xi]) \frac{2Z}{a^2 + b^2} \right] \\ &\quad + ([\eta] + i[\xi]) (\log Z + 1) - ([\eta] - i[\xi]) \frac{a^2 b^2}{a^2 + b^2} \frac{1}{Z^2} \end{aligned}$$

Dislocation

$$\begin{aligned} [u] - i[v] &= |u - iv|_{\theta=2\pi} - |u - iv|_{\theta=0} \\ &= (3 - \nu) \frac{1}{8\pi} [([\eta] + i[\xi]) (-2\pi i)] \\ &\quad - (1 + \nu) \frac{1}{8\pi} [([\eta] + i[\xi]) (2\pi i)] \\ &= \frac{1}{8\pi} ([\eta] + i[\xi]) (-2\pi i) [(3 - \nu) + (1 + \nu)] \\ &= \{ [\eta] + i[\xi] \} (-i) \\ &= [\eta] - i[\xi] \end{aligned}$$

Note: $\log Z = \log r e^{i\theta} = \log r + i\theta$
 $|\log Z|_{\theta=2\pi} - |\log Z|_{\theta=0} = 2\pi i.$

stresses are also produced when unevenly distributed non-elastic strains such as plastic strains exist. The following are the fundamental relationships in a two-dimensional plane stress ($\sigma_z = 0$) residual stress field^(302, 303) (see Fig. 3.3):

- (1) Strains are composed of elastic strain and non-elastic strain:

$$\begin{aligned} \varepsilon_x &= \varepsilon'_x + \varepsilon''_x, \\ \varepsilon_y &= \varepsilon'_y + \varepsilon''_y, \\ \gamma_{xy} &= \gamma'_{xy} + \gamma''_{xy} \end{aligned} \tag{3.14}$$

where

$\varepsilon_x, \varepsilon_y, \gamma_{xy}$ are components of the total strain,
 $\varepsilon'_x, \varepsilon'_y, \gamma'_{xy}$ are components of the elastic strain,
 $\varepsilon''_x, \varepsilon''_y, \gamma''_{xy}$ are components of the non-elastic strain. The non-elastic strain can be plastic strain, thermal strain, etc.[†]

- (2) A Hooke's law relationship exists between stress and elastic strain—refer to eqn. (3.3):

$$\begin{aligned} \varepsilon'_x &= \frac{1}{E}(\sigma_x - \nu\sigma_y), \\ \varepsilon'_y &= \frac{1}{E}(\sigma_y - \nu\sigma_x), \\ \gamma'_{xy} &= \frac{1}{G}\tau_{xy}. \end{aligned} \tag{3.15}$$

- (3) The stress must satisfy the equilibrium conditions:

$$\begin{aligned} \frac{\partial \sigma_x}{\partial x} + \frac{\partial \tau_{xy}}{\partial y} &= 0, \\ \frac{\partial \tau_{xy}}{\partial x} + \frac{\partial \sigma_y}{\partial y} &= 0. \end{aligned} \tag{3.16}$$

- (4) The total strain must satisfy the condition of compatibility:

$$\left(\frac{\partial^2 \varepsilon'_x}{\partial y^2} + \frac{\partial^2 \varepsilon'_y}{\partial x^2} - \frac{\partial^2 \gamma'_{xy}}{\partial x \cdot \partial y} \right) + \left(\frac{\partial^2 \varepsilon''_x}{\partial y^2} + \frac{\partial^2 \varepsilon''_y}{\partial x^2} - \frac{\partial^2 \gamma''_{xy}}{\partial x \cdot \partial y} \right) = 0. \tag{3.17}$$

The above equations indicate that residual stresses exist when the value of R , which is determined by the non-elastic strain as follows, is not zero:*

$$R = - \left(\frac{\partial^2 \varepsilon''_x}{\partial y^2} + \frac{\partial^2 \varepsilon''_y}{\partial x^2} - \frac{\partial^2 \gamma''_{xy}}{\partial x \cdot \partial y} \right), \tag{3.18}$$

R is the cause of residual stress.^(302, 303) Moriguchi^(315, 316) called R “incompatibility”.

Important findings obtained from these mathematical analyses include:

[†] In the case of thermal stress:

$$\varepsilon''_x = \varepsilon''_y = \alpha \Delta T, \quad \gamma''_{xy} = 0$$

where α is the coefficient of linear thermal expansion,

ΔT is the change of temperature from the initial temperature.

$R = 0$, consequently, residual stress will not occur when the non-elastic strain components are linear functions of the position:

$$\epsilon''_x = a + bx + dy, \quad \epsilon''_y = e + fx + gy, \quad \gamma''_{xy} = k + lx + my.$$

- (1) Residual stresses in a body cannot be determined by measuring the stress change that takes place when an external load is applied to the body. (Because of this, the body is cut to determine residual stresses.)
- (2) Residual stresses σ_x , σ_y , and τ_{xy} can be calculated from eqn. (3.15) when elastic-strain components ϵ'_x , ϵ'_y , and γ'_{xy} are determined. However, components of non-elastic strain ϵ''_x , ϵ''_y , and γ''_{xy} , which have caused residual stress, cannot be determined without knowing the history of the formation of the residual stress.

Mathematical analysis. Several studies have been made to calculate stress components σ_x , σ_y , and τ_{xy} from knowing the distribution of non-elastic strains, ϵ''_x , ϵ''_y , and τ''_{xy} under various boundary conditions. Moriguchi has developed a particular solution for calculating stresses due to incompatibility distributed in a solid body. Masubuchi⁽³¹⁷⁾ has developed a particular solution for calculating stresses due to incompatibility distributed in a plate.

By introducing Airy's stress function $F(x, y)$ as defined by eqn. (3.12), the equilibrium condition (3.16) can be satisfied. Then strain components can be expressed from eqn. (3.15) as follows:

$$\left. \begin{aligned} \epsilon'_x &= \frac{1}{E} \left(\frac{\partial^2 F}{\partial y^2} - \nu \frac{\partial^2 F}{\partial x^2} \right), \\ \epsilon'_y &= \frac{1}{E} \left(\frac{\partial^2 F}{\partial x^2} - \nu \frac{\partial^2 F}{\partial y^2} \right), \\ \gamma'_{xy} &= -\frac{2(1 + \nu)}{E} \frac{\partial^2 F}{\partial x \cdot \partial y} \end{aligned} \right\} \quad (3.19)$$

Then from eqn. (3.17);

$$\frac{1}{E} \left(\frac{\partial^4 F}{\partial x^4} + 2 \frac{\partial^4 F}{\partial x^2 \cdot \partial y^2} + \frac{\partial^4 F}{\partial y^4} \right) = R(x, y) \quad (3.20)$$

or

$$\left(\frac{\partial^2}{\partial x^2} + \frac{\partial^2}{\partial y^2} \right)^2 F(x, y) = ER(x, y). \quad (3.21)$$

$F(x, y)$ is generally expressed as follows:

$$F(x, y) = F_1(x, y) + F_2(x, y) \quad (3.22)$$

where $F_1(x, y)$ is a solution of the following equation:

$$\left(\frac{\partial^2}{\partial x^2} + \frac{\partial^2}{\partial y^2} \right)^2 F_1(x, y) = 0. \quad (3.23)$$

$F_2(x, y)$ is a particular solution of eqn. (3.21).

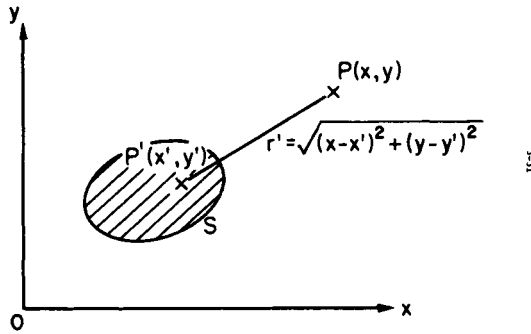


FIG. 3.9. Incompatible strains distributed in an area S.

Equation (3.23) is a familiar equation for an ordinary electricity analysis. The solution for eqn. (3.23) is generally called a biharmonic function which can be expressed as a combination of two harmonic functions:

$$F_1(x, y) = \text{Re} [\bar{z} \phi(z) + \psi(z)]. \tag{3.24}$$

According to Masubuchi,⁽²⁶⁾ a particular solution, $F_2(x, y)$ for stresses caused by incompatibility distributed in an area S of an infinite plate is (see Fig. 3.9):

$$F_2(x, y) = \iint_S R(x', y) r'^2 \ln r' dx' dy' \tag{3.25}$$

where, $R(x', y)$ = incompatibility at a point (x', y') .

$$r' = \sqrt{(x - x')^2 + (y - y')^2}.$$

Later, Kawai and associates^(318, 319) developed solutions for a strip with a finite width and for a rectangular plate. They also have analyzed lateral distortion of plates and shells containing incompatible strains and have proposed the use of an energy method for determining residual stress. Here, the stress distribution that provides a minimum strain energy under a given boundary condition can be determined. The energy method appears to be useful for obtaining solutions under complicated boundary conditions where accurate solutions are difficult to obtain.

From a mathematical point of view, incompatibility is a form of singularity in a stress field. Investigators have used different types of singular points, such as a concentrated load or a center of dilatation, for solving various stress problems. Muskhelishvili's work in this area is well known.⁽³¹³⁾ Solutions using singular points for solving stress problems under various boundary conditions are useful for analyzing residual stress and distortion under similar boundary conditions.

3.2.5 Similarities among the analysis of residual stress, the vortex theory in hydrodynamics and the fracture mechanics theory

The analysis of residual stress, the vortex theory in hydrodynamics and the fracture mechanics theory all deal with effects (stress and flow) due to singularities. Recognizing common ground such as this often helps in developing new concepts: ideas already developed in one field can be borrowed and modified for use in another.⁽³²⁰⁾

Analysis of residual stress vs. vortex theory. Moriguchi⁽³¹⁶⁾ developed the fundamental

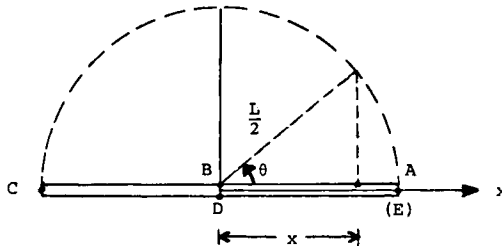


FIG. 3.10. Coordinate systems used for the analysis of stresses near a slit of length $L = 2C$.

Point A	$\theta = 0$	Point C	$\theta = \pi$
Point B	$\theta = \pi/2$	Point D (A)	$\theta = \frac{3}{2}\pi$
			$\theta = 2\pi$

theory of incompatible strains through his observation of the similarities between the theory of residual stress and the vortex theory of hydrodynamics. He visualized that the analysis of residual stress due to welding could be handled in a way similar to Prandtl's three-dimensional wing theory.⁽³²¹⁾

Table 3.6 compares values related to the stress problems caused by dislocation in an infinite plate and values related to the air flow around the wings of an airplane.^(303, 322) Equation (1) in the left column of the table shows the relationship between the dislocation $[v]$, which occurs along the part of the x-axis between $(-L/2, 0)$, and the transverse stress produced at that part of the x-axis designated σ_{y0} . The physical meaning of this stress problem can be interpreted as follows. When transverse stress, σ_{y0} , as given by eqn. (3), is applied along both sides of a slit of length L located on the x-axis, the relative displacement of the sides of the slit can be determined using eqn. (2).

To express the arbitrary distribution of $[v]$, eqn. (2) is used. In eqns. (2) and (3), a parameter θ is used to express various locations along the slit (see Fig. 3.10):

$$x = \frac{L}{2} \cos \theta. \tag{3.26}$$

Then locations along the upper side of the slit are expressed by changing θ from π to 2π .

Equation (2) is an adequate way of expressing an arbitrary dislocation, because the value of dislocation (v) must be zero at the both ends of the slit $\theta = 0$ and π .

Equation (4) shows the average value of dislocation along the slit, (v).

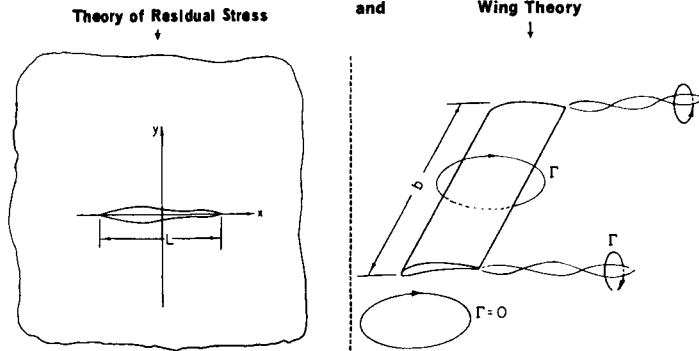
Equation (5) shows the elastic energy stored in the plate (per unit plate thickness) when the transverse stress σ_{y0} is applied along the slit.

Shown on the right column are equations for calculating down-wash, circulation, lift, and induced resistance when a wing of width b is traveling at a speed V .⁽³²²⁻³²⁴⁾

Equations shown in Table 3.6 indicate that the following semi-exist between physical values in the stress problem caused by dislocation and the wing theory:

<i>Stress problem caused by dislocation</i>	<i>Wing theory</i>
Stress	Down wash
Dislocation	Circulation
Mean dislocation	Lift
Strain energy	Induced resistance

TABLE 3.6 Comparison Between Theory of Residual Stress and Wing Theory



Theory of Residual Stress
 Stress: $\sigma_x, \sigma_y, \tau_{xy}$
 Slit length (weld length): L
 Transverse Stress on Slit: σ_{y0}

$$\sigma_{y0} = \frac{E}{4\pi} \int_{-L/2}^{L/2} \frac{1}{x-x'} \left(\frac{d[v]}{dx} \right)_x dx' \quad (1)$$

where:
 E = Young's modulus.
 $[v]$ = dislocation.

$$[v] = \sum_{n=1}^{\infty} A_n \sin n\theta \quad (2)$$

$$\sigma_{y0} = \frac{E}{2L} \sum_{n=1}^{\infty} n A_n \frac{\sin n\theta}{\sin \theta} \quad (3)$$

 $x = \frac{L}{2} \cos \theta$

Mean Dislocation: $[\bar{v}]$

$$[\bar{v}] = \frac{1}{L} \int_{-L/2}^{L/2} [v] dx$$

$$= \frac{1}{L} \int_0^\pi \frac{L}{2} \left(\sum_{n=1}^{\infty} A_n \sin n\theta \right) \sin \theta d\theta$$

$$= \frac{\pi}{4} A_1 \quad (4)$$

The magnitude of mean dislocation is determined only by the value A_1 .

Strain Energy: U

$$U = \int_{-L/2}^{L/2} \frac{1}{2} \sigma_{y0} [v] dx$$

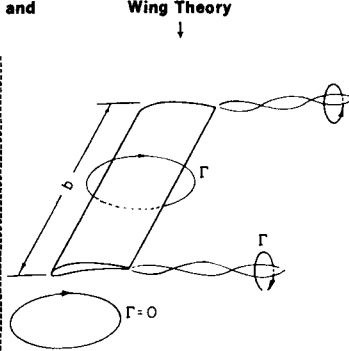
$$= \frac{\pi}{16} E \left(\sum_{n=1}^{\infty} n A_n^2 \right)$$

$$= \frac{\pi}{16} E (1 + \delta) A_1^2 \quad (5)$$

where:

$$\delta = \frac{1}{A_1^2} \left(\sum_{n=2}^{\infty} n A_n^2 \right) \quad (5')$$

The magnitude of strain energy becomes minimum when $\delta = 0$ provided that the length of L and mean dislocation $[v]$ remain constant. When $\delta = 0$, the form of dislocation $[v]$ is elliptical and the distribution of transverse stress σ_{y0} is uniform along the slit.



Wing Theory
 Velocity: u, v
 Wing breadth: b
 Down Wash: w

$$w = \frac{1}{4\pi} \int_{-b/2}^{b/2} \frac{1}{x-x'} \left(\frac{d\Gamma}{dx} \right)_x dx'$$

where:
 Γ = circulation.

$$\Gamma = 2\delta V \sum_{n=1}^{\infty} A_n \sin n\theta$$

$$w = V \sum_{n=1}^{\infty} n A_n \frac{\sin n\theta}{\sin \theta}$$

 V = velocity at infinity
 $x = \frac{b}{2} \cos \theta$

Lift: L

$$L = \rho V \int_{-b/2}^{b/2} \Gamma(x) dx$$

$$= \frac{\pi}{2} \rho b^2 V^2 A_1$$

where: ρ = density.
 The magnitude of lift is determined only by the value A_1 .

Induced Resistance: D_i

$$D_i = \rho \int_{-b/2}^{b/2} \Gamma(x) w(x) dx$$

$$= \frac{\pi}{2} \rho b^2 V^2 \left(\sum_{n=1}^{\infty} n A_n^2 n \right)$$

$$= \frac{\pi}{2} \rho b^2 V^2 (1 + \delta) A_1^2$$

where:

$$\delta = \frac{1}{A_1^2} \left(\sum_{n=2}^{\infty} n A_n^2 \right)$$

The magnitude of induced resistance becomes minimum when $\delta = 0$, provided that the wing breadth and lift L remain constant. When $\delta = 0$, the distribution of circulation Γ is elliptical and the distribution of down wash is uniform along the wing.

The above discussion provides an insight into ways of conducting analytic studies of residual stresses and distortion in weldments. In aerodynamic theory, analytical studies usually separate the problem into:

- (1) Determination of the distribution of vorticity around the wing.
- (2) Determination of the effects on the flow of air around the wing induced by the vorticity.

The analysis of the first step is very complex, because the air must be treated as a viscous fluid. In the analysis of the second step, however, the air can be treated as a perfect fluid containing vorticity.

Masubuchi has conducted analytic studies of several practical problems related to residual stress and distortion utilizing the similarities between the analysis of residual stresses and the vortex theory.^(314, 322) The analysis of residual stresses and distortions of weldments can be separated into:

- (1) Determination of the distribution of plastic strains in regions near the weld.
- (2) Determination of the effects of the plastic strains produced in the vicinity of the weld on stresses and deformations of the weldment.

The analysis in the first step is very complex, because the material must be treated as elasto-plastic and transient changes during welding must be considered. In the analysis of the second step, however, the material can be treated as perfectly elastic containing plastic strains in regions near the weld.

Analysis of residual stress vs. fracture mechanics theory. The stress problem referred to in the left column of Table 3.6 is the reversed for the case of cracking in a wide plate.

When a straight crack of length L occurs in an infinitely wide plate, the relationship between the stresses that existed before cracking, σ_{y0} , and the crack opening $[v]$ can be expressed by eqn. (1) of Table 3.6. Equations (2) and (3) show the arbitrary distribution of $[v]$ and σ_{y0} , respectively.

If we take the simplest case that:

A_1 only exists and $A_2 = A_3 = \dots = 0$
then,

$$\left. \begin{aligned} [v] &= A_1 \sin \theta, \\ \sigma_{y0} &= \frac{E}{2L} A_1 \end{aligned} \right\} \quad (3.27)$$

This means that a crack occurs in a uniform stress field, as shown in Fig. 3.11(b) the crack opening can be expressed as:

$$\begin{aligned} [v] &= \frac{2L}{E} \sigma_{y0} \sin \theta \\ &= \frac{2L}{E} \sigma_{y0} \sqrt{1 - \left(\frac{2x}{L}\right)^2}. \end{aligned} \quad (3.28)$$

Then the strain energy released by cracking, U , is from eqn. (5):

$$U = \frac{\pi}{16} E A_1^2 = \pi \frac{L^2 \sigma_{y0}^2}{4 E} \quad (3.29)$$

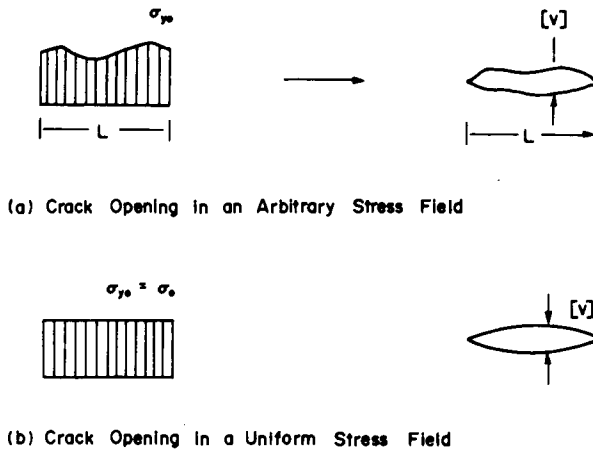


FIG. 3.11. Stress changes due to cracking.

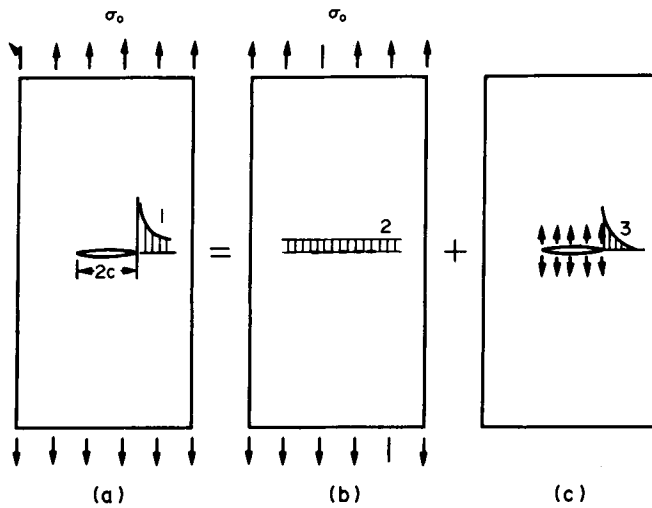


FIG. 3.12. Stress concentration around a sharp notch of a specimen under tensile load.

The last example is very useful for studying stress concentrations around a sharp notch, as shown in Fig. 3.12. Suppose that a specimen containing a sharp straight notch of length L is subjected to a tensile loading of σ_0 , as shown in Fig. 3.13(a). Based upon the principle of superposition, the stress distribution near the crack, curve 1, is:

$$\text{curve 1} = \sigma_0 + \text{curve 3.}$$

Consequently, eqns. (3.33) and (3.34) can be used to study the stresses around the notch. For example, when a uniform stress σ_0 is applied to a plate containing a straight notch of length L , the opening of the notch $[v]$ is expressed as:

$$[v] = \frac{2L}{E} \sigma_0 \sqrt{1 - \left(\frac{2x}{L}\right)^2}. \quad (3.30)$$

Extensive research has been conducted during the last two decades on fracture. The fracture mechanics theory has been developed by Irwin and other investigators (refer to Chapter 10). Many similarities exist between the fracture mechanics theory and the analysis of residual stresses. Some examples are shown below.

In the fracture mechanics theory, stress intensity factor, K , is widely used. For example, when uniform tensile stress σ_0 is applied to a wide plate containing a crack of length $L = 2c$:

$$K = \sigma_0 \sqrt{\pi c}. \quad (3.31)$$

The strain energy released due to the occurrence of the crack, U , is:

$$U = \frac{\pi \sigma_0^2}{E} \left(\frac{L}{2} \right)^2 \quad (3.32)$$

Then the strain energy release rate, G , is:

$$G = \frac{\partial U}{\partial L} = \frac{\pi \sigma_0^2}{E} \frac{L}{2} = \frac{K^2}{E}. \quad (3.33)$$

By comparing eqns. (3.32) and (3.33) to eqns. (3.29) one finds that eqns. (1) through (5) shown in Table 3.6 can be readily used for the analysis of crack growth in an arbitrary stress field. Further discussions are given in Chapter 10.

3.3 Analysis of Residual Stress and Distortion in Weldments and Their Effects on Service Performance

Through the discussion in the preceding pages we have introduced an approach to the development of methodologies for analyzing residual stress and distortion of weldments and for determining their effects on service performance.

There are many factors that contribute to the total distortion in a weldment. These factors, their interaction, and their effect on the total distortion are shown in Fig. 3.13. This figure indicates that distortion in a welded structure is a function of the structural parameters, the material parameters and the fabrication parameters.

The structural parameters include the geometry of the structure (whether it is a panel stiffened with frames, a cylinder, a spherical structure, etc.), plate thickness and joint type (whether it is a butt joint, fillet joint, etc.).

The material parameters include types and condition of baseplate and filler-metal materials.

Among the fabrication parameters are the welding processes, including shielding metal-arc, submerged arc, GMA, GTA, and others; the procedure parameters: welding current, voltage, arc travel speed, preheat and interpass temperature, etc., and the assembly parameters: welding sequence and degree of constraint, among others.

To determine residual stresses and distortion analytically, it is necessary to establish analytic relationships among these three sets of parameters and distortion. This can be done by:

1. Determining dimensional changes produced in the structure by each weld.
2. Determining distortion induced in the structure by these dimensional changes.
3. Combining all dimensional changes and induced distortions.

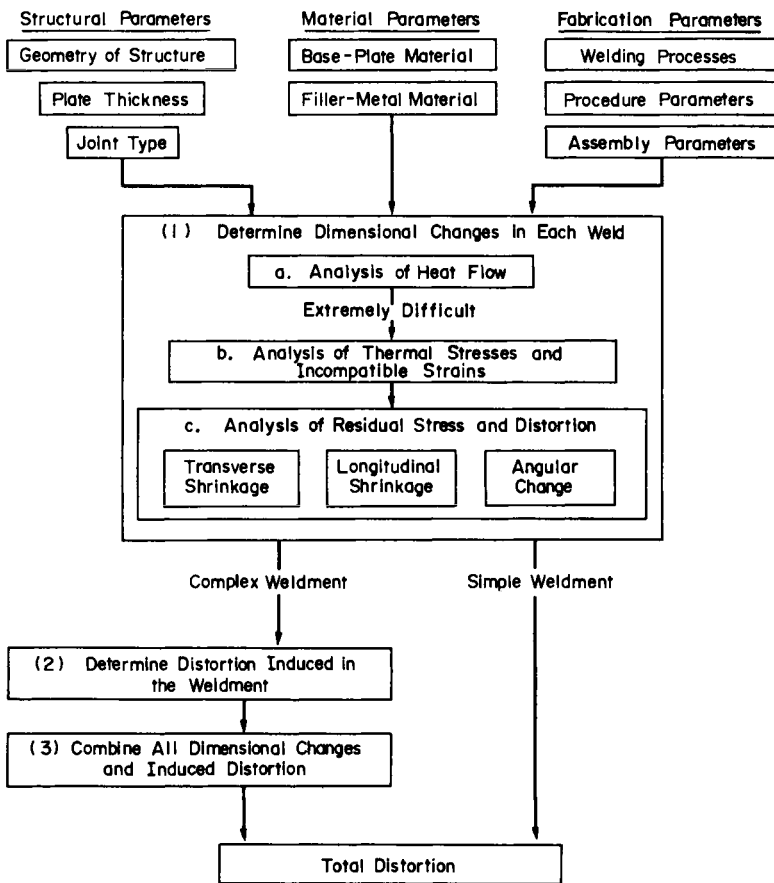


FIG. 3.13. Factors that contribute to weld distortion and their relation to each other and to the total distortion.

For a simple weld, the second and third steps are not necessary.

The first step—determination of dimensional changes in each weld—can be further divided into the following:

- (a) Analysis of heat flow.
- (b) Analysis of thermal stresses during welding to determine incompatible strains that do not satisfy the condition of compatibility of the theory of elasticity.
- (c) Determination of dimensional changes, including transverse shrinkage, longitudinal shrinkage, and angular change, induced by the incompatible strains.

In fusion welding, a weldment is locally heated by the welding heat source. During the thermal cycle, the weldment is subjected to thermal stresses. When the weld is completed, incompatible strains remain in regions near the weld. Incompatible strains, which include dimensional changes associated with solidification of the weld metal, metallurgical transformations, and plastic deformation, are the sources of residual stresses and distortion. When welding processes and parameters are changed, the heat-flow patterns are also changed. The change in heat-flow pattern causes a change in the

distribution of incompatible strains, and this causes changes in shrinkage and distortion.

A number of articles have been published on the subject of heat flow, and, although not an easy problem, it can be handled analytically. Chapter 2 discusses heat flow in weldments.

It is difficult to determine the distribution of incompatible strain. When a material undergoes plastic deformation, the stress-strain relationship is not linear and the plastic properties of the material change with the temperature. Some results are described in Chapter 5. Even with the use of the computer, however, no complex geometric analysis has yet been made of practical weldments.

When the incompatible strains are determined, be it analytically or experimentally, the third stage in determining dimensional changes can be handled analytically. Moriguchi has developed a fundamental theory concerning stress caused by incompatible strains, and Masubuchi has applied Moriguchi's theory to the study of residual stress and distortion due to welding. Some of their results are included in later parts of this monograph.

Assuming that the dimensional changes in the welds are found either analytically or experimentally, the second step is to determine the distortion induced in the structure by these dimensional changes. The solution to this problem is rather straightforward. Although plastic deformation is produced in small areas near the weld, most of the remaining material in the structure is elastic. Consequently, the induced distortion can be analyzed by elastic theory. Solutions for a large number of boundary conditions are already available. The elastic theory equations used to determine the induced distortion are independent of fabrication parameters and involve only well-established material parameters. Consequently, after the first experiments, the induced distortions can be readily calculated for all types of materials.

References

- (301) MASUBUCHI, K., *Nondestructive Measurement of Residual Stresses in Metals and Metal Structures*, RSIC-410, Redstone Scientific Information Center (April 1965).
- (302) KIHARA, H. and MASUBUCHI, K., *Theoretical Studies on the Residual Welding Stress*, Report No. 6 of Transportation Technical Research Institute, pp. 1-40 (June, 1953).
- (303) MASUBUCHI, K., "Control of distortion and shrinkage in welding", *Welding Research Council Bulletin*, **149** (April 1970).
- (304) WILSON, W. M., and HAO, C. C., "Residual stresses in welded structures", *The Welding Journal*, **26** (5), Research Supplement, 295s to 320s (1974).
- (305) VOLTERRA, V., "Sur l'equilibre des corps elastiques multiplement connexes", *Journal title?* **25**, **24** 401-517 (1907).
- (306) LOVE, A.E.H., *Mathematical Theory of Elasticity*, Fourth Edition, Cambridge University Press, 1934.
- (307) TAYLOR, G. I., "The mechanism of plastic deformation of crystals—Part I. Theoretical", *Proceedings of the Royal Society London A*, **145**, 362-387 (1934).
- (308) OROWAN, E., "Problems of plastic gliding", *Physical Society London*, **52**, 8-22 (1940).
- (309) NEMENYI, P., "Selbstspannungen elastischer Gebilde", *Handbuch der Physikalischen und Technischen Mechanik*, Band IV-1 Halfte, Verlag Von Johann Ambrosius, Leipzig, Germany, pp. 190-212 (1931).
- (310) REISSNER, VON H., "Eigenspannungen und Eigenspannungsquellen", *Zeitschrift für angewandte Mathematik und Mechanik*, **11** (1), 1-8 (Feb. 1931).
- (311) KRONER, E., "Dislocations and continuum mechanics", *Applied Mechanics Reviews*, **15** (8), 599-606 (1962).
- (312) OROWAN, E., "Classification and nomenclature of internal stresses", Symposium on Internal Stresses in Metals and Alloys, The Institute of Metals, pp. 47-59 (1948).
- (313) MUSKHELISHVILI, N. I., *Some Basic Problems of the Mathematical Theory of Elasticity*, Translated from the Russian by J.R.M. Radok, P. Noordhoff Ltd. Groningen, The Netherlands, 1963.

- (314) MASUBUCHI, K., "New approach to the problems on residual stresses and distortions due to welding", *Monthly Reports of Transportation Technical Research Institute, Tokyo*, **8**, no. 12 (Mar. 1959).
- (315) MORIGUCHI, S., *Theory of Two-dimensional Elasticity*, Modern Applied Mechanics Series, B. 7-a, Iwanami Publishing Co., Tokyo, 1956.
- (316) MORIGUCHI, S., "Fundamental theory of dislocation in an elastic body", *Oyo Sugaku Rikigaku*, **1**, 29–36, 87–90 (1948).
- (317) MASUBUCHI, K., "Stresses due to the distributed incompatibility (plane problems)", *Journal of the Society of Naval Architects of Japan*, **88**, 189–200 (1950).
- (318) KAWAI, T., "A study on residual stresses and distortion in welded structures", *Journal of the Japan Welding Society*, **33** (3), 314 (1964).
- (319) KAWAI, T., and YOSHIMURA, N., "A study on residual stresses and distortion of welded structures (Part 2)", *Journal of the Japan Welding Society*, **34** (2), 214 (1965), and Part 3, **34** (12), 215 (1965).
- (320) MASUBUCHI, K., "Simulations among theories of residual stresses, joint restraint and fracture mechanics", International Institute of Welding Document No. IX-1054–77/ X-871–77, May 1977.
- (321) MORIGUCHI, S., "Fundamental theory of elastic dislocation in elastic solids", *Applied Mathematics and Mechanics*, **1**, 29–36, 87–90 (1948).
- (322) MORIGUCHI, S., "On the analogy between wing theory and theory of residual welding stress", presented at the 5th National Congress for Applied Mechanics of Japan (1955).
- (323) MASUBUCHI, K., "Analytical investigation of residual stresses and distortions due to welding", *Welding Journal*, **39** (12), Research Supplement, 525s–537s (1960).
- (324) DURAND, W. F., *Aerodynamic Theory*, vols. 3 and 7, Julius Springer, Berlin, 1934.

Measurement of Residual Stresses in Weldments

4.1 Classification of Techniques for Measuring Residual Stresses

Many techniques have been used for measuring residual stresses in metals. The information on the measurement of residual stresses has been reviewed by investigators including Treuting *et al.*,⁽⁴⁰¹⁾ Heindlhofer,⁽⁴⁰²⁾ Horger,⁽⁴⁰³⁾ Gunnert,⁽⁴⁰⁴⁾ Masubuchi,⁽³⁰¹⁾ and Parlane.⁽⁵⁰⁵⁾ The proceedings of a workshop on "Nondestructive Evaluation of Residual Stress" held in 1975 provides a review of recent developments in methods of determining residual stresses.⁽⁴⁰⁶⁾ The discussions in this chapter emphasize those techniques that are applicable to weldments.

Table 4.1 lists presently available techniques for measuring residual stress and classifies them in the following groups:

- A. Stress-relaxation techniques.
- B. X-ray diffraction techniques.
- C. Techniques by use of stress-sensitive properties.
- D. Cracking techniques.

In the stress-relaxation technique, residual stress is determined by measuring the elastic-strain release that takes place when a specimen is cut into pieces or has a piece removed. In most cases, electric or mechanical strain gages are used for measuring this strain release (Group A-1). A variety of these techniques exist; there are many ways to section a specimen to determine residual stress. Some techniques are used in the study of stress in plates, while others are used in cylinders, tubes, or three-dimensional solids. Strain release during stress relaxation can also be determined by using grid systems, brittle coatings, or photoelastic coatings instead of the electrical or mechanical strain gages (Group A-2). An inherent disadvantage of stress-relaxation techniques is that they are destructive; the specimen must be partially or entirely sectioned. Nevertheless, the stress-relaxation techniques provide reliable quantitative data and are the most widely used for measuring residual stresses in weldments.

In metals that have crystalline structures, elastic strains can be determined by measuring the lattice parameter with X-ray diffraction. Since the lattice parameter of a metal in the unstressed state is known or can be determined separately, elastic strains in the metal can be measured nondestructively without machining or drilling. Two techniques are available at present: the X-ray film technique and the X-ray diffractometer technique. With the X-ray diffraction techniques, surface strains can be determined within a small area, say to a depth of 0.001 in. (0.025 mm) and 0.0001 in. (0.0025 mm) in diameter. X-ray diffraction is the only means presently available for the measurement of residual

TABLE 4.1 Classification of techniques for measuring residual stresses

[A-1] Stress-relaxation using electrical and mechanical strain gages	Techniques applicable primary to plates	1. Sectioning technique using electrical resistance strain gages
	Techniques applicable primarily to solid cylinders and tubes	2. Gunnert technique 3. Mathar-Soete drilling technique 4. Stäblein successive milling technique
	Technique applicable primarily to three-dimensional solids	5. Heyn-Bauer successive machining technique 6. Mesanger-Sachs boring-out technique 7. Gunnert drilling technique 8. Rosenthal-Norton sectioning technique
[A-2] Stress-relaxation techniques using apparatus other than electrical and mechanical strain gages		9. Grid system—dividing technique 10. Brittle coating—drilling technique 11. Photo-electric coating—drilling technique
[B] X-ray diffraction techniques		12. X-ray film technique 13. X-ray diffractometer technique
[C] Techniques based on stress-sensitive properties	Ultrasonic techniques	14. Polarized ultrasonic wave technique 15. Ultrasonic attenuation technique
	Hardness techniques	16. Hardness techniques
[D] Cracking techniques		17. Hydrogen-induced cracking technique 18. Stress-corrosion cracking technique

stress in ball bearings, in gear teeth, and in material surfaces after machining or grinding.

But X-ray diffraction techniques have disadvantages. They are timeconsuming. At each measuring point, measurements requiring a film exposure time of 15 to 30 minutes must be made in two directions. The technique is not very accurate, especially in situations where high temperatures have distorted the atomic structure of the material.

Attempts have been made to determine the residual stresses in metals by measuring their stress-sensitive properties. Stress measuring techniques which have been proposed include:

1. *Ultrasonic techniques.*

(a) The polarized ultrasonic wave technique, which makes use of a stress-induced change in the angle of polarization of polarized ultrasonic waves (similar to the photoelastic technique).⁽⁴⁰⁷⁾

(b) The ultrasonic attenuation technique, which makes use of a stress-induced change in the rate of absorption of ultrasonic waves.⁽⁴⁰⁸⁾

2. *Hardness techniques which make use of stress-induced changes in hardness.*⁽⁴⁰⁹⁾ However, none of these techniques have been developed beyond the laboratory stage and they have not been used successfully for the measurement of residual stresses in weldments. These techniques are therefore not discussed in this chapter.

Another technique developed for the study of residual stresses involves the close observation of cracks induced in the specimen by hydrogen or stress corrosion. Cracking techniques are useful when studying residual stresses in complex structural models in which the residual-stress distribution is complicated, but these techniques provide only qualitative and not quantitative data.

4.2 Measurement of Residual Stresses by Stress-relaxation Techniques

The stress-relaxation techniques are based upon the principle that strains created during unloading are elastic even when the material has undergone plastic deformation. It is therefore possible to determine residual stresses without knowing the history of the material.

Summarized in the following pages are eleven techniques of measuring residual stresses based on stress-relaxation techniques. Techniques 1 through 4 are applicable primarily to plates, 5 and 6 to solid cylinders and tubes, and 7 and 8 to three-dimensional solids. All of the first eight techniques employ electrical or mechanical strain gages. The last three techniques discussed (9 through 11) employ a grid system, a brittle coating, or a photo-elastic coating.

The name of each technique indicates the principle involved, the strain-measuring technique used, or the name of the person who has developed or described it. For each of these techniques the description will include experimental procedures, range of application, and advantages and disadvantages.

4.2.1 Sectioning techniques using electrical-resistance strain gages (plates)

After the mounting of electrical strain gages on the surface of the test plate, structure or specimen, a small piece of metal containing the gages is removed from the structure, as shown in Fig. 4.1. In the resistance-type bonded strain-gage techniques, gages are bonded on the test specimen. As the specimen is strained, the resistance of the gages changes, and the magnitude of strain is determined by measuring the resistance change. Most bonded electrical-resistance strain gages are made from either metallic wire or foil materials. There are also the recently developed semiconductor gages. A variety of sizes, shapes, and configurations are available including single-element gages and

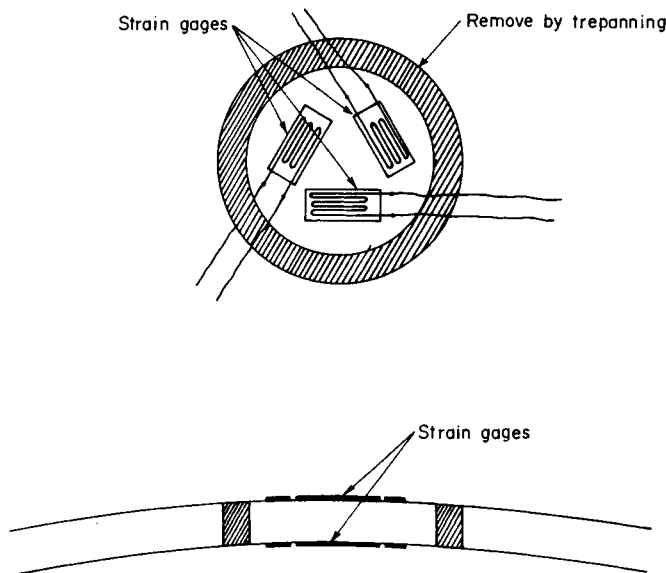


FIG. 4.1. Complete stress-relaxation technique applied to a plate.

rosettes with two, three, or four elements. Information on electrical strain gages is available in numerous sources including the *Handbook of Experimental Analysis*⁽⁴¹⁰⁾ and in reviews by Crites^(411, 412) and Masubuchi.⁽³⁰¹⁾

Changes in temperature tend to cause an apparent strain; therefore, some type of temperature compensation is needed. Frequently, a “dummy gage”, which is not subjected to the strain, is exposed to the same temperature as the actual gage to provide a basis for comparison. A temperature-compensated gage can also be used.

Gages must be bonded securely to the specimen. Various types of cements have been developed. In most residual stress measurements, gages must be protected from metal chips produced during machining as well as from the oil or water necessary to cool the specimen. A number of systems have been devised for protecting gages under various conditions.

A measurement is taken of the strain changes $\bar{\epsilon}_x$, $\bar{\epsilon}_y$, and $\bar{\gamma}_{xy}$ that take place during the removal of the piece. If the piece is small enough, it is assumed that residual stress no longer exists in the piece and that the following holds good:

$$\bar{\epsilon}_x = -\epsilon'_x \quad \bar{\epsilon}_y = -\epsilon'_y \quad \bar{\gamma}_{xy} = -\gamma'_{xy} \quad (4.1)$$

where ϵ'_x , ϵ'_y , and γ'_{xy} are elastic-strain components of the residual stress. The minus signs in eqn. (4.1) indicate that when tensile residual stress exists shrinkage (not elongation) takes place during stress-relaxation. Then residual stresses are

$$\begin{aligned} \sigma_x &= -\frac{E}{1-\nu^2}(\bar{\epsilon}_x + \nu\bar{\epsilon}_y), \\ \sigma_y &= -\frac{E}{1-\nu^2}(\bar{\epsilon}_y + \nu\bar{\epsilon}_x), \\ \sigma_{xy} &= -G\bar{\gamma}_{xy}. \end{aligned} \quad (4.2)$$

Because there may be residual stresses caused by bending, it is advisable to measure the strain on both surfaces of the plate. The mean value of the strains measured on both surfaces represents the plane-stress component, while the difference between the strains measured on both surfaces represents the stress component caused by bending.

Application: For all-round use; the measuring surface can be placed in any position.

Advantages: Is a reliable method. Principle involved is simple; is highly accurate.

Disadvantages: Is a destructive method. Only gives the average stress for the area of the specimen from which the piece was removed, and does not measure locally concentrated stresses. The machining involved is sometimes expensive and time consuming.

4.2.2 The Gannert technique for a plate⁽⁴¹³⁾

Gunnert has proposed a technique for measuring residual stress in weldments using a mechanical extensometer.

Figure 4.2(a) shows the mechanical extensometer developed by Gunnert for the measurement of residual stress. The legs, 1 and 2, support each other at two points, 3. The adjusting screw, 4, is threaded into leg 1 and the nut, 5, is fixed to leg 2. The flat end of the adjusting screw lies against the gage pin, 7, of the special indicator, 6, invented

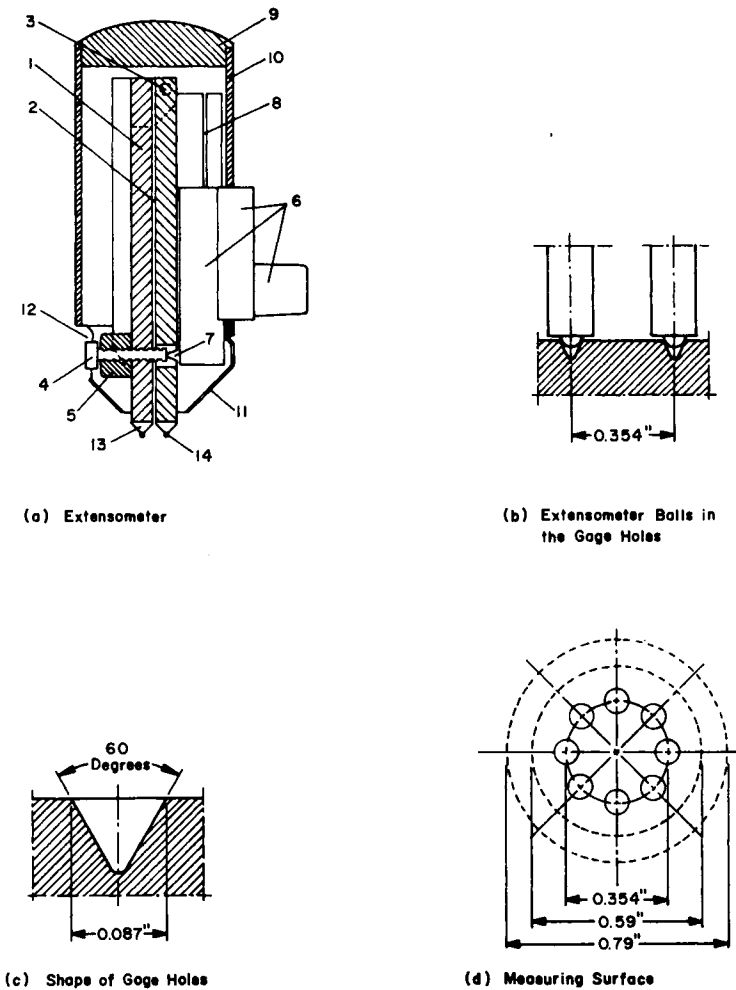


FIG. 4.2. Gunnert's method of measuring residual stress in a plate^(4,13)

by Abramson. The indicator is fixed to leg 2 by holder 8. The parts 9, 10, and 11 form a protective cover. The adjusting screw, 4, is fixed to the lower part of legs 1 and 2. These balls are Brinell balls and are 2 mm (0.079 in.) in diameter.

In measuring strain, the Gunnert extensometer is placed with its balls in conical depressions 9 mm (0.354 in.) apart on the test specimen, as illustrated in Fig. 4.2(b). The shape of the depressions is shown in Fig. 4.2(c). For measuring residual stresses, eight depressions are made along the periphery of a circle 4.5 mm (0.177 in.) in radius. After the distances between four sets of depressions are measured, the measuring area is freed from the surrounding material by means of a core drill which produces a groove around the measuring area, as shown by the broken lines in Fig. 4.2(d). The distance between the four sets of depressions are measured to determine elastic strains released during the stress relaxation.[†]

[†] Theoretically, measurements of distances between three sets of depressions are enough for determining residual stresses. The fourth set is used in insuring the accuracy of the measurement.

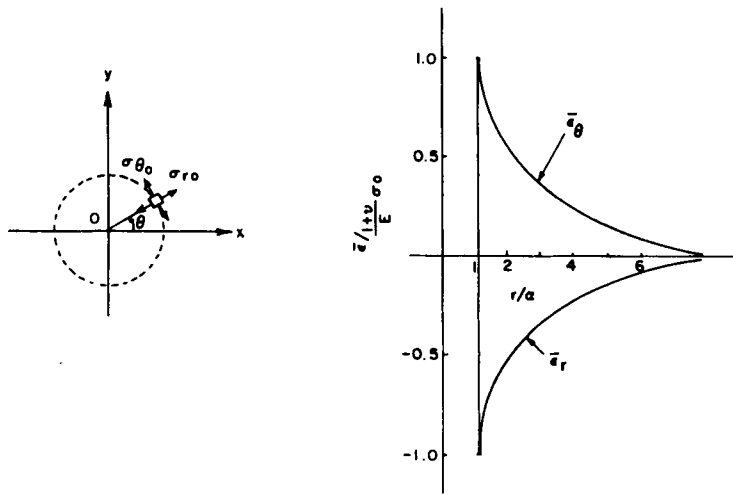
Application: Suitable for laboratory and field work. Can be used on horizontal, inclined, or vertical measuring surfaces.

Advantages: Quick—the main stresses at a measuring point can be determined both as regards direction and magnitude in about 1 hour. Easily repaired damage of the measured object. Permits some measurement of stress peaks owing to the small measuring distances. Sturdy apparatus permits measurements in unfavorable weather.

Disadvantages: The method entails considerable manual training to ensure correct manipulation.

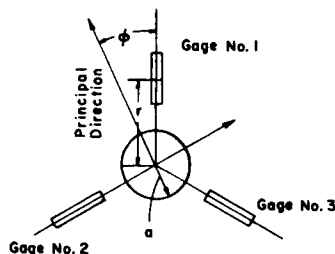
4.2.3 The Mathar–Soete drilling technique^(414–416)

When a small circular hole is drilled in a plate containing residual stresses, residual stress in areas outside the hole are partially relaxed. Residual stresses that existed in the drilled area are determined by measuring the amount of stress relaxation that takes



(a) Radial and Tangential Residual Stress, $\sigma_{r\theta}$ and $\sigma_{\theta r}$, Along the Periphery of a Small Circle Surrounding Point O

(b) Distribution of $\bar{\sigma}_r$ and $\bar{\sigma}_\theta$ for $\sigma_{x0} = \sigma_{y0} = \sigma_0$, $\tau_{xy0} = 0$



(c) 120-Degree Star Arrangement of Strain Gages

FIG. 4.3. The Mathar method of measuring residual stress.

place in the area surrounding the drilled hole. The hole method of measuring stress was first proposed and used by Mathar⁽⁴¹⁴⁾ and was later developed by Soete⁽⁴¹⁵⁾ and Suppiger/*et al.*⁽⁴¹⁶⁾

For an illustration of how the technique is used, suppose that the components of residual stress at point O are σ_{x_o} , σ_{y_o} , and $\sigma_{x_y_o}$. Then the components of residual stress along the periphery of a small circle surrounding point O are given by eqn. (4.3) (see Fig. 4.3(a)).

$$\begin{aligned}\sigma_{r_o} &= \frac{1}{2}(\sigma_{x_o} + \sigma_{y_o}) + \frac{1}{2}(\sigma_{x_o} - \sigma_{y_o}) \cos 2\theta + 2\tau_{x_y_o} \sin 2\theta, \\ \sigma_{\theta_o} &= \frac{1}{2}(\sigma_{x_o} + \sigma_{y_o}) - \frac{1}{2}(\sigma_{x_o} - \sigma_{y_o}) \cos 2\theta - 2\tau_{x_y_o} \sin 2\theta, \\ \tau_{r\theta_o} &= \tau_{x_y_o} \cos 2\theta - \frac{1}{2}(\sigma_{x_o} - \sigma_{y_o}) \sin 2\theta,\end{aligned}\quad (4.3)$$

where

σ_{r_o} = the radial component,

σ_{θ_o} = the tangential component,

$\tau_{r\theta_o}$ = the shearing component of residual stress along the periphery at an angle θ .

In eqn. (4.3) it is assumed that residual stresses are uniform in the area inside the small circle.

The next step is to calculate the strain change that will take place in areas outside the small circle, radius a , when the material inside the circle is removed, e.g. by drilling. The important fact about the strain change is that the circle will become stress free; in other words, σ_{r_o} and $\tau_{r\theta_o}$ will vanish. Therefore, the strain change during the stress-relaxation process is the same as the strain caused in a plate with a hole (but no residual stress) by applying stresses $-\sigma_{r_o}$ and $-\sigma_{\theta_o}$ to the edge of the hole.

To simplify discussion, assume that $\sigma_{x_o} = \sigma_{y_o} = \sigma_o$ and $\sigma_{x_y_o} = 0$; or residual stresses are biaxially tensile. Then, $\sigma_{r_o} = \sigma_o$ and $\tau_{r\theta_o} = 0$. The strain release which takes place at point $P(r, \theta)$ when a hole (radius a) is drilled around point O is given in eqn. (15) and shown in Fig. 4.3(b):

$$\begin{aligned}\bar{\epsilon}_r &= -\bar{\epsilon}_\theta = -\frac{1+\nu}{E} \sigma_o \left(\frac{a}{r}\right)^2 \\ \bar{\gamma}_{r\theta} &= 0,\end{aligned}\quad (4.4)$$

where $\bar{\epsilon}_r$, $\bar{\epsilon}_\theta$, and $\bar{\gamma}_{r\theta}$ are components of the strain release.

When residual tensile stresses exist in areas around point O , the strain change in the radial direction $\bar{\epsilon}_r$ will be shrinking from the stretched state. Equation (4.4) indicates that if values of a and r are known and $\bar{\epsilon}_r$ or $\bar{\epsilon}_\theta$ is measured, it is possible to determine the amount of the residual stress, σ_o .

In the case of a general stress field in which three components, σ_{x_o} , σ_{y_o} , and $\tau_{x_y_o}$ exist, the strain release that takes place around the drilled hole is more complex than that given in eqn. (4.4). A common way to determine stresses is to place strain gages in a star form, at 120 degrees from each other, as shown in Fig. 4.3(c). The magnitudes and directions of the principal stresses are determined as follows:

$$\begin{aligned}\sigma_1 &= -E \{ \mu_1(\lambda) \cdot a + \mu_2(\lambda) \beta \}, \\ \sigma_2 &= -E \{ \mu_1(\lambda) a - \mu_2(\lambda) \beta \}, \\ \tan 2\phi &= \frac{\delta}{\bar{\epsilon}_{r1} - a},\end{aligned}\quad (4.5)$$

where

σ_1 and σ_2 = the magnitudes of principal stresses,
 ϕ = the angle between the No. 1 gage and the direction of the σ_1 -principal stress,

$\lambda = \frac{r}{a}$ = the ratio of the distance of the measuring points from the center of the hole, r , and the radius of hole, a .

$$\begin{aligned} \mu_1(\lambda) &= \frac{\lambda^2}{1 + \nu}, \\ \mu_2(\lambda) &= \frac{\lambda^4}{4\lambda^2 - 3(1 + \nu)}, \\ a &= \frac{1}{3}(\bar{\epsilon}_{r1} + \bar{\epsilon}_{r2} + \bar{\epsilon}_{r3}), \\ \beta &= \sqrt{(\bar{\epsilon}_{r1} - a)^2 + \delta^2}, \\ \delta &= \frac{1}{\sqrt{3}}(\bar{\epsilon}_{r2} - \bar{\epsilon}_{r3}), \end{aligned} \tag{4.6}$$

where $\bar{\epsilon}_{r1}$, $\bar{\epsilon}_{r2}$, and $\bar{\epsilon}_{r3}$ = radial strains measured on No. 1, No. 2, and No. 3 strain gages, respectively.

Application: This method can be used for laboratory and field work and on horizontal, vertical, and overhead surfaces.

Advantages: A simple principle. Causes little damage to the test piece, convenient to use on welds and adjoining material.

Disadvantages: Drilling causes plastic strains at the periphery of the hole, which may displace the measured results. The method must be used with critical care.

4.2.4 The stäblein successive milling technique⁽⁴¹⁷⁾

If material is milled away from one side of a bar-shaped body containing tensile stresses, the bar will bend away from the milled side (see Fig. 4.4) and the dimensions of the side opposite the milling will be changed. If measuring devices such as strain gages are attached to this opposite side, it becomes possible to measure how much the surface changes in length each time a layer of material is removed, and, from the values read off, the residual stresses in the different layers can be calculated.

Application: Measurement of the uniaxial residual stresses along plates, shafts, surface-treated, heat-treated, or surface bar-shaped objects.

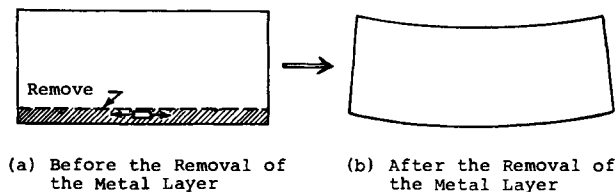


FIG. 4.4. Residual stress measurement by successive removal of metal layers.

Advantages: Reliable method for measuring the mean stresses over a relatively large surface.

Disadvantages: Does not permit measurement of stress. Involves total destruction of the object measured. Only uniaxial stresses are measured. Risk of residual stresses set up mechanically owing to the milling.

4.2.5 *The Heyn–Bauer machining technique*^(418,419)

Thin outside layers of a cylindrical specimen are removed in series, the length of the specimen being measured after each removal. From the data recorded, residual stress is calculated.

Application: Cylindrical bodies with rotationally symmetrical stresses.

Advantages: Simple method.

Disadvantages: Longitudinal stresses only are measured; limited application.

4.2.6 *The Mesnager–Sachs boring-out technique*^(420,421)

Measuring devices such as strain gages are attached to the outside of a cylindrical body in longitudinal and tangential directions. A central hole is drilled in the body and gradually increased through repeated drillings. The changes indicated by the measuring devices are recorded.

Application: Circular cylindrical bodies with rotationally symmetrical distribution stresses.

Advantages: Permits the measurement of the uni- and biaxial residual stress distribution in the whole of the test piece.

Disadvantages: Assumes that the stresses are constant along the cylinder and that the stress distribution is rotationally symmetrical. Involves total destruction. Risk of mechanically caused residual stresses due to boring. Not very suitable for measuring residual stresses in welds.

4.2.7 *The Gunnert drilling technique*^(422,423)

Four 3-mm (0.12 in.) parallel holes located at the periphery of a circle with a 9-mm (0.354 in.) diameter are drilled through the plate at the measuring point, as shown in Fig. 4.5. The diametrical distance between these holes at different levels below the surface

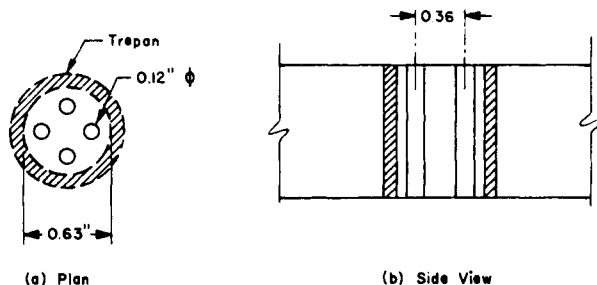


FIG. 4.5. The Gunnert drilling method.

of the plate is measured by means of a specially designed mechanical gage. The perpendicular distance between the plate surface and measuring points at different levels below the surface is also measured. A groove is then drilled around the measuring points in steps of about 2 mm (0.08 in.) in depth. The perpendicular distance is read off for each step. After the groove has been drilled to the desired depth, the four holes are located in a plug with a diameter of 16 mm (0.63 in.). This plug is free from the surroundings and is thus also free from residual stresses. A further measurement of the diametrical distance at all levels previously measured, together with the perpendicular measurements, provide information for calculating the original residual stresses.

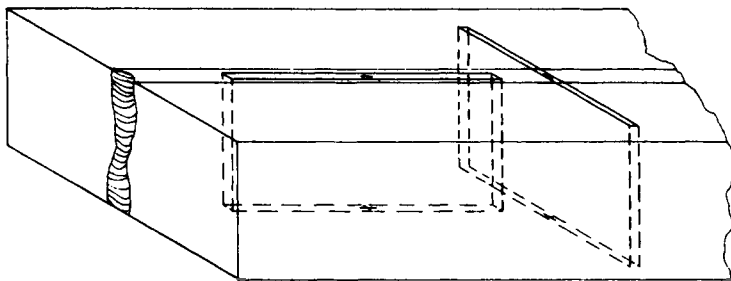
Application: Can be used for laboratory and field work. The surface of the plate must be substantially horizontal.

Advantages: Rugged and simple apparatus. Semi-non-destructive; damage to the object tested can be easily repaired.

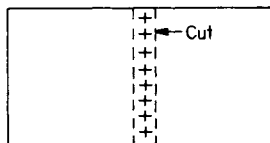
Disadvantages: Relatively large margin of error for the stresses measured in a perpendicular direction. The underside of the plate must be accessible for the attachment of the fixture. Method requires manual training.

4.2.8 The Rosenthal–Norton sectioning technique

This is a technique for determining residual stresses in heavy weldments. Two narrow blocks having the full thickness of the plate are cut with their long axes directed along the axis of weld and transverse to the weld, as shown in Fig. 4.6. The blocks should be made narrow with respect to the thickness; then it may be assumed that the operation



(a) Sectioning the Weldment to prepare Longitudinal and Transverse Blocks



(b) Further Sectioning of Block

FIG. 4.6. Rosenthal–Norton sectioning method.

has relieved practically all of the residual stresses acting in the direction perpendicular to the long axis, while relieving only a part of the stress in the direction parallel to the long axis. At the same time, the blocks should be made long enough with respect to thickness (twice the thickness or more, if possible). Subsequently, the stress that has been relieved in the central portion of the block is very nearly a linear function of the thickness. In other words, if the value of this stress is known on the top and bottom faces of the plate, then values of the stress relieved throughout the thickness can be computed. The next step is to determine residual stresses still left in the blocks. This can be done by mounting strain gages on the walls of the blocks and then measuring strain relaxation that results from slicing them into small pieces.

Two blocks, one longitudinal and one transverse, must be cut in order to determine three-dimensional stress distribution. Since two blocks cannot be cut from the same spot, the layout must be arranged so as to make use of the symmetry of the specimen, or using interpolation.

Application: For laboratory measurements.

Advantages: Accurate data can be obtained when measurements are done carefully.

Disadvantages: A troublesome, time-consuming and completely destructive method.

4.2.9 Grid systems—dividing technique⁽³⁰¹⁾

The surface of the specimen is provided with a system of suitably located measuring points, such as the intersections within a network of squares (a grid). The distance between the points, which may consist of depressions or punched-in balls, is measured, including the diagonals. The entire object is then cut into square elements, each containing four measuring points. The distances previously measured are measured again, and stresses are calculated from the difference between the two measurements.

Application: Laboratory method, since a division of the object tested is not usually permissible.

Advantages: Simple principle and measurement. Allows the determination of closely adjoining areas over large surfaces.

Disadvantages: Involves total destruction of the object.

4.2.10 Brittle coating—drilling technique⁽⁴²⁵⁾

The measuring point and its surrounding areas are coated with a brittle lacquer.

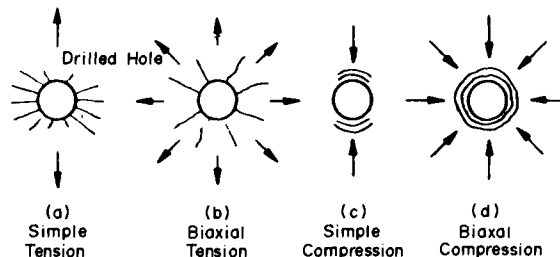


FIG. 4.7. Typical crack pattern obtained under various surface-stress conditions, showing combination of the Mather hole method and brittle coating.

A hole (diameter d , e.g. $\frac{1}{8}$ in. (3.2 mm)) is drilled at the measuring point to a depth of between $\frac{1}{2}d$ and d . Cracks are produced in the lacquer due to relaxation of residual stresses caused by the drilling. As shown in Fig. 4.7, radial cracks occur if residual stresses are tensile, and circular cracks occur if they are compressive. From the direction and distribution of the cracks, it is possible to determine the direction of main stresses since the latter are perpendicular to the direction of the cracks.

Application: Preferably a laboratory method, but it can also be used for field measurements if the atmosphere is dry. The measuring surface can be chosen as desired.

Advantages: Little damage to the test piece. Rapid determination of the directions of the principal stresses and an indication of their magnitude.

Disadvantages: Only qualitative.

4.2.11 Photo-elastic coating—drilling technique^(426, 427)

Under the action of stresses, transparent materials become doubly refracting (birefringent) and if a beam of a polarized light is passed through a model (under stress) made of such a material, a colored picture is obtained from which the stress distribution can be determined. This technique is called the photoelastic technique.^{(410)†}

The actual structure to be stress analyzed is coated with a photoelastic plastic. When strains occur in the specimen, they are transmitted to the plastic coating, which then becomes birefringent. This can be observed and measured using a reflection polariscope (see Fig. 4.8). Figure 4.9 is a typical fringe pattern.⁽³⁰¹⁾ Instructions for analyzing fringe patterns in this application (nearly the same as those obtained in ordinary photoelasticity) are provided by the manufacturer.

The photoelastic coating be applied by brushing a liquid plastic on the surface of the

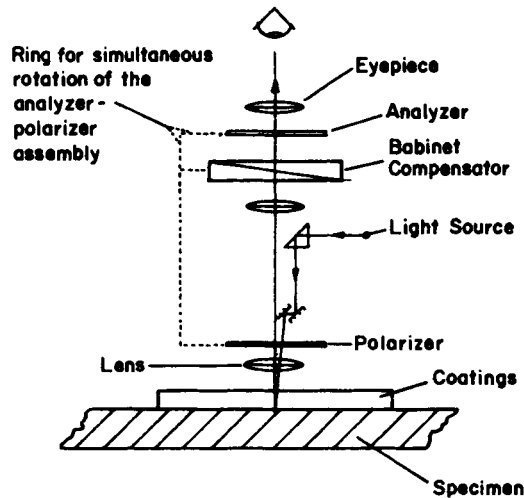


FIG. 4.8. Schematic of optical system of reflection polariscope.

† The usual photoelastic technique which employs models made with special plastic materials are seldom used for studying residual stresses in metals and metal structures primarily because distributions of residual stresses produced in metals are different from those produced in the plastic materials.

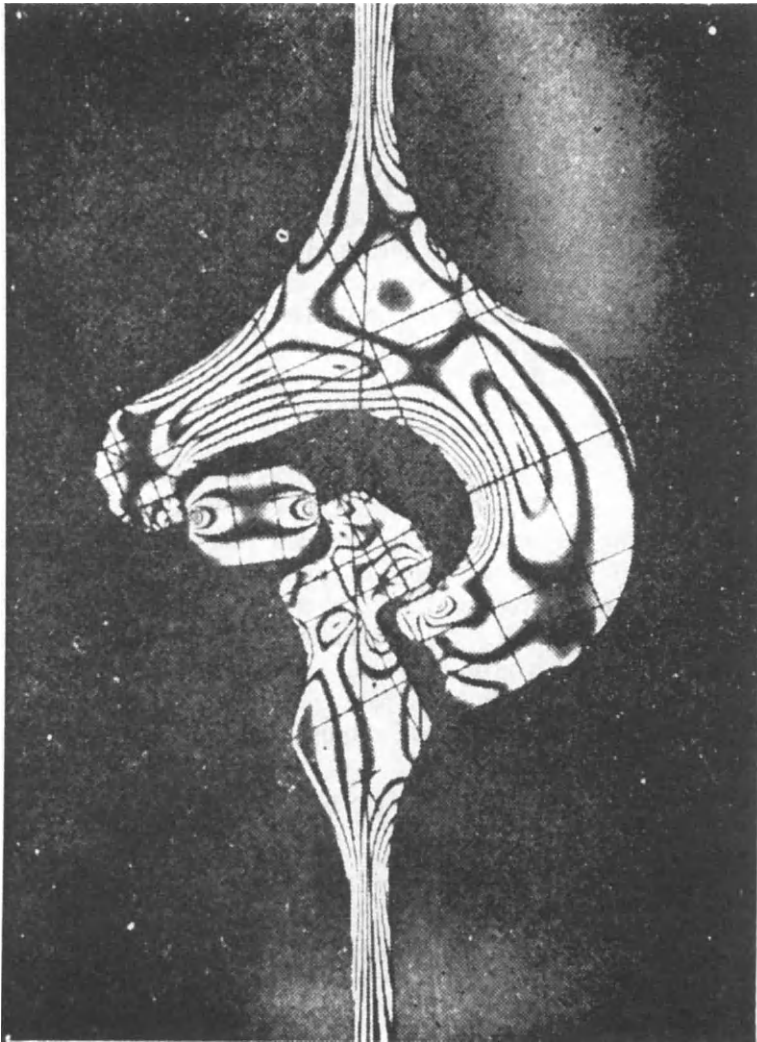


FIG. 4.9. Photostress coating technique for the measurement of stress.

specimen and polymerizing it by applying heat. Alternatively, a prefabricated flat or countered sheet of plastic can be bonded to the part at room temperature. The maximum strain measured ranges between 3 and 50%, depending on the type of plastic used; the strain sensitivity usually decreases with the increase in the maximum measurable strain.

Application: Primarily a laboratory method, but it can also be used for field measurements under certain circumstances.

Advantages: Permits the measurement of local stress peaks. Little damage to the material.

Disadvantages: Sensitive to plastic strains which sometimes occur at the edge of the drilled hole.

4.3 Measurement of residual stresses by X-ray diffraction

Elastic strains in metals that have crystalline structures can be determined by measuring the lattice parameter by X-ray diffraction.⁽⁴²⁸⁻⁴³²⁾ Since the lattice parameter of a metal in the unstressed state is known or can be determined separately, elastic strains in the metal can be determined non-destructively without machining or drilling. X-ray diffraction techniques are applicable only to crystalline materials having randomly oriented small grains. Most metals fall into this category.

Information on this subject is available in many books and reports. Reference (406) contains several papers covering recent developments in X-ray diffraction technique. One of significant achievements is the development of a portable X-ray analyzer at the Northwestern University.⁽⁴³³⁾

4.3.1 Basic principles⁽³⁰¹⁾

When external or internal forces are applied to a structure made up of metallic crystals, the crystalline lattice is distorted, thus changing the interatomic distances. When the deformation exceeds the elastic limit, plastic deformation takes place as a result of slipping between the lattice planes. The change in the interatomic spacing is always directly proportional to the stress.

This technique is made possible by the fact that the wavelengths of X-rays are of the same general order of magnitude as the atomic spacings in metallic crystals (1 angstrom unit or 4×10^{-9} in.). The short wavelength of X-rays makes it possible for the rays to penetrate the crystalline lattice to some extent and be reflected back from the atomic planes which they have penetrated.

Suppose that a monochromatic plane wave is introduced to the atomic planes in the direction *AB*, as shown in Fig. 4.10. The reflected beams from successive parallel planes of atoms are reinforced in one direction *BC*: the diffraction direction. Bragg's law defines the condition for diffraction as follows:[†]

$$n\lambda = 2d \sin \theta, \tag{4.7}$$

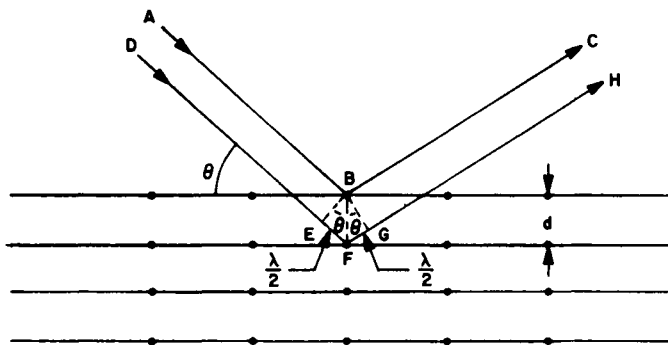


FIG. 4.10. Diffraction resulting from reflections from adjacent atomic planes of a monochromatic plane wave.

[†] *ABC* and *DFH*, in Fig. 4.10, represent paths traveled by points in the wave front which excite atoms at *B* and *F* in adjacent planes. Reinforcement in the direction *BC* (or *FH*) requires that the path difference (*EF* + *FG*) be equal to an integral number of wavelengths, i.e.

$$EF = FG = \frac{1}{2} \lambda = n\lambda, \text{ where } n \text{ is an integer.}$$

where λ = the wavelength of incident beam,
 θ = the angle between incident or reflected beams and surface of reflecting planes,
 d = the interplaner spacing,
 n = the order of reflection ($n = 1, 2, 3, \dots$).

Equation (4.7) shows that, if the wavelength of the X-ray is known, the interplaner spacing, d , can be determined by measuring the angle θ .

Table 4.2 gives the diffraction angle, θ , the diffraction plane (hkl), and the radiation employed for stress analysis of a number of metals.[†] In aluminum, for example, X-rays produced by a copper target can be used (the diffraction angle is 81 degrees). Sometimes, however, these optimum conditions cannot be employed because of adverse X-ray scattering by the sample. When this condition occurs, other diffraction planes must be chosen, at some sacrifice in the precision of the analysis.

Two general methods are employed in the recording of diffraction patterns:

1. The photographic or X-ray film method, as shown in Fig. 4.11.
2. The X-ray diffractometer or counter-tube method, with electrical readout attachments, as shown in Fig. 4.12.

Equipment shown in Fig. 4.11 is portable and can be mounted in place on a large structure for field use. The diffractometer type shown in Fig. 4.12 is a laboratory instrument, and the size of specimen that could be tested is limited by the geometry of the instrument.

4.3.2 X-ray film method

The apparatus consists essentially of a film in a light-tight cassette mounted perpendicularly to the incoming X-ray beam, with a hole through which is inserted the pinhole

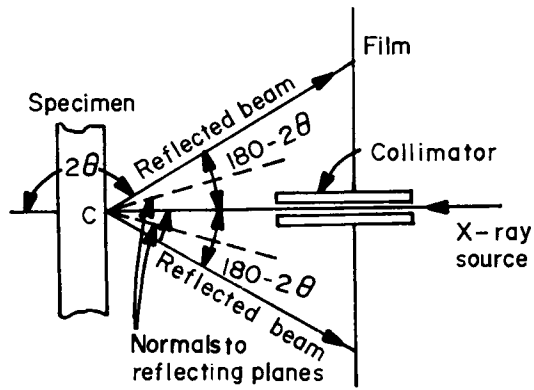
TABLE 4.2 *Properties of metals for X-ray analysis* (Vaughan and Crites)⁽⁴²⁸⁾

Metal of test specimen	Crystallographic plane (hkl)	Target to produce radiation (in X-ray tube)	Wavelength, λ , angstrom units		Diffraction angle ^(a) (degrees)
			K_{α_1}	K_{α_2}	
Ferritic iron	310	Cobalt	1.788 90	1.792 74	80.6
	211	Chromium	2.289 62	2.293 52	78.0
Austenitic steels	311	Manganese	2.101 74	2.105 70	78.0
	420	Copper	1.540 70	1.544 34	76.0
Aluminum	511	Copper	1.540 50	1.544 34	81.0
Copper	400	Cobalt	1.788 90	1.792 79	81.7
Magnesium	105	Iron	1.935 97	1.939 91	83.0

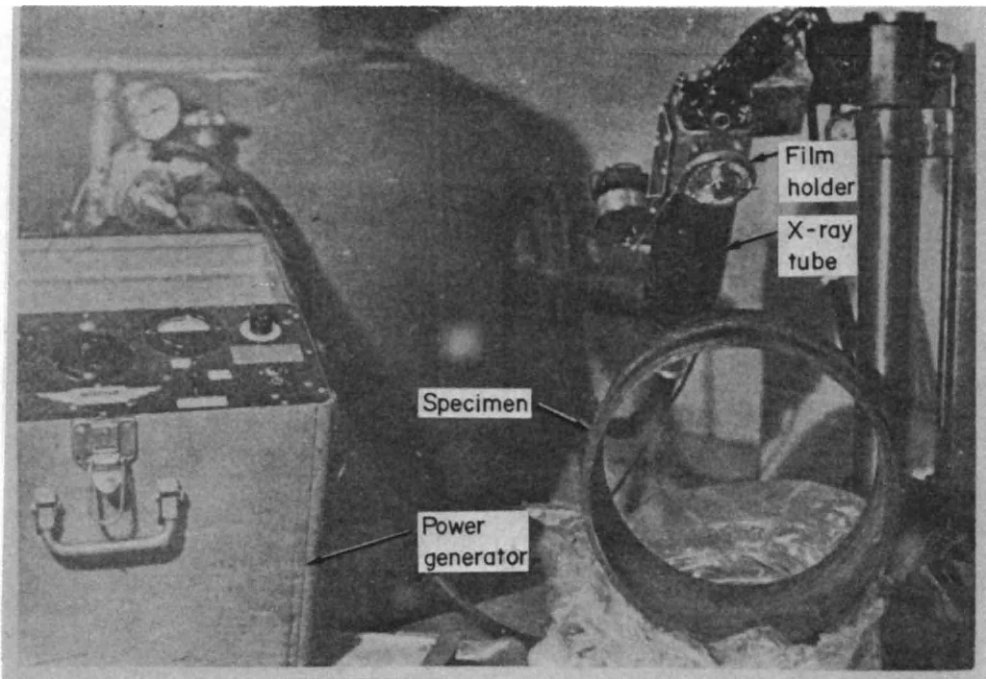
^(a) Nominal values for the metals; the diffraction angles differ somewhat for various alloys and are modified by the magnitude of the strain.

[†] The Miller index, hkl , is the crystallographers' method of defining the various sets of planes in reference to the three coordinate axes of crystals.

It would be possible to build a specially designed diffractometer-type piece of equipment that could be used for the field measurement of residual stresses in large structural components of space rockets, although no such equipment is commercially available at the present time.



(a) Schematic diagram

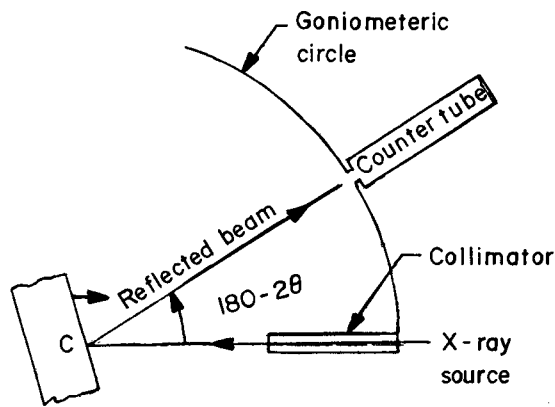


(b) Apparatus

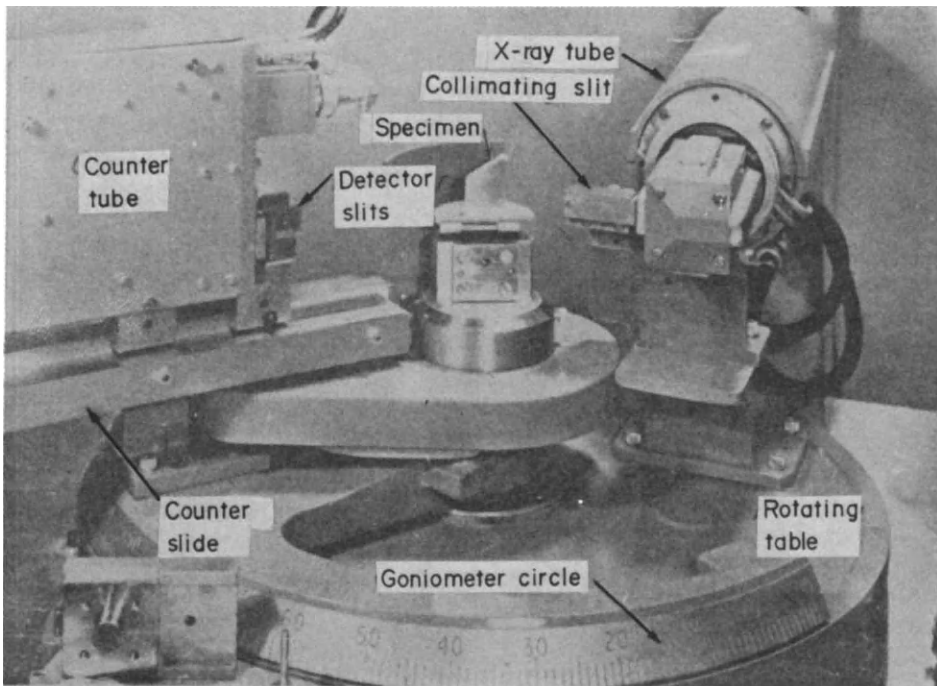
FIG. 4.11. Portable X-ray Diffraction equipment which employs film method (Vaughan and Crites)⁽⁴²⁸⁾

system that collimates the beam, as shown in Fig. 4.11(a). The film records the rays diffracted by the specimen, and shows, on development, almost circular rings. The diameter of a diffraction ring divided by the distance from the film to the specimen gives $2 \tan (180-2\theta)$ from which θ is obtained for insertion in eqn. (4.7).

For best results it is advisable to oscillate the film using the metal tube containing



(a) Schematic diagram



(b) Apparatus

FIG. 4.12. X-ray diffractometer setup (Vaughan and Crites),⁽⁴²⁸⁾

the pinholes as the axis of oscillation. This removes much of the spottiness of the diffraction lines, as shown in Fig. 4.13. If the grain size of the specimen is large, it may also be necessary to oscillate the specimen a few degrees, keeping the distance from the film to the irradiated spot on the specimen strictly constant. This distance can be measured by inside micrometers or can be adjusted a predetermined distance by means of a special

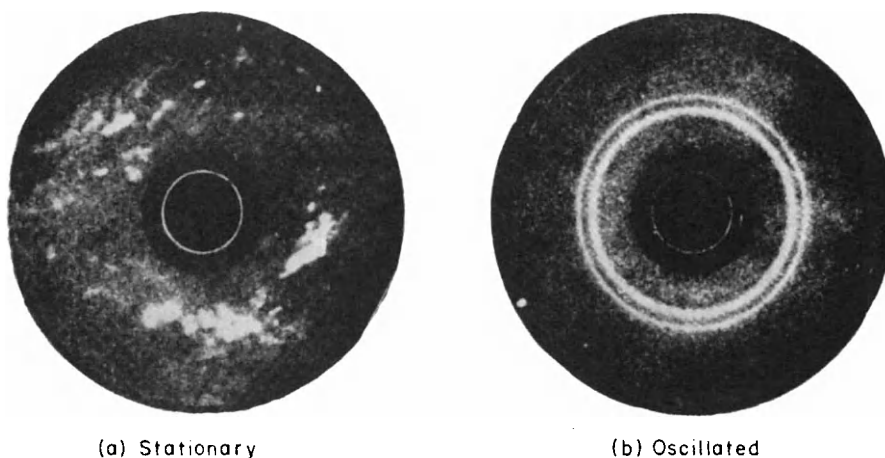


FIG. 4.13. Improvement of diffraction lines by oscillation (Norton and Rosenthal).⁽⁴³⁰⁻⁴³²⁾

gage inserted between the cassette and the specimen. Another method frequently employed is to compute the distance from specimen to film by measuring the diameter of a calibrating ring of known θ on the film. In this method a strain-free powder is placed on the surface of the test object. The powder is chosen to yield a ring near $\theta = 90$ degrees that does not interfere with measurements of the ring produced by the specimen. Silver powder is used for aluminum alloys.

For maximum accuracy, the surface of the test object should be free from cold work introduced by machining. If the surface is not in suitable condition, electropolishing is probably the best way to condition it, but good results are also obtained by etching the surface, provided the etching does not leave etch pits so deep that they relieve the surface stresses.

Visual reading of the films can be made by removing a very fine cross hair or scratch

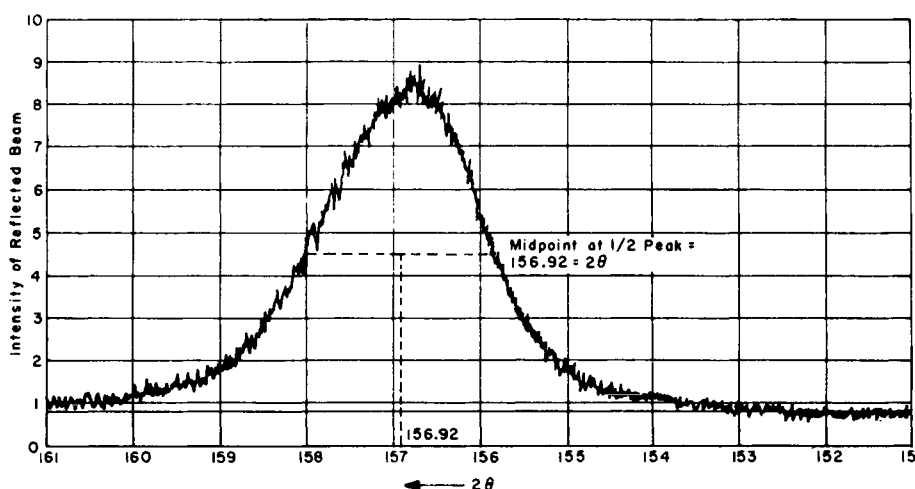


FIG. 4.14. An example of intensity recording by a counter (Vaughan and Crites).⁽⁴²⁸⁾

over the film under good illumination. The reading also may be made using micro-photometers.

4.3.3 X-ray diffractometer method

The X-ray diffraction method and the film method differ, in most cases, only in the detector and the angle made by the specimen with the X-ray beam. The angle between the X-ray beam and the specimen surface is 90 degrees in the film method but is an angle of θ degrees for the diffraction method.

A counter and a receiving slit are moved along a geometric circle to record the intensity of the reflected beam, as shown in Fig. 4.14. The diffraction angle is determined as the angle of the maximum intensity.

4.4 Determination of Residual Stresses by Measuring Stress-sensitive Properties

When stresses exist in metals, some of the physical or mechanical properties, such as the propagation speed of shear waves and hardness, are changed. It is theoretically possible to develop techniques for determining residual stress by measuring such stress-sensitive properties. Stress-measuring techniques that have been developed or proposed include ultrasonic techniques and hardness-measuring techniques. However, none of these techniques have been developed beyond the laboratory stage.

4.4.1 Ultrasonic techniques

It has been recognized for some time that velocity and attenuation of sound waves in a metal specimen often change when stresses are applied to the specimen. Attempts have been made to use this phenomenon for determining stresses in metals. Since shorter waves are able to penetrate more (or are absorbed less) in metals, the ultrasonic waves are more suitable than ordinary sound waves.

Firestone and Frederick⁽⁴³⁴⁾ first reported that the velocity of Rayleigh waves was affected by surface stresses and Frederick⁽⁴³⁵⁾ has more recently reported on the utilization of this phenomenon to measure residual surface stresses. Hikata *et al.*⁽⁴³⁶⁾ measured the stress-induced changes in the velocity and attenuation of compressional waves propagating through aluminum. A number of other investigators have reported experimental results that illustrate the stress dependence of ultrasonic velocity or attenuation.^(407, 408, 437, 438)

The velocity of an elastic wave, V , propagating through a homogeneous elastic medium is given by

$$V = \sqrt{\frac{C}{\zeta}}, \quad (4.8)$$

where C is the elastic modulus and ζ is the density. By taking the differential of the above equation, one finds that

$$\frac{\Delta V}{V} = \frac{1}{2} \left[\frac{\Delta C}{C} - \frac{\Delta \zeta}{\zeta} \right], \quad (4.9)$$

Equation (4.9) shows that a fractional change in the elastic modulus or the density would affect the velocity. The density of a metal changes as a compressive or tensile stress is applied. One would expect that the speed would increase when compressive stresses are applied and the density increases. It has been found that stresses cause changes in $\Delta C/C$ and $\Delta \zeta/\zeta$ (shear stresses will cause no change in $\Delta \zeta/\zeta$). Among various techniques that have been proposed so far for determining residual stresses, the following two appear to be promising:

1. The Polarized Ultrasonic Wave Technique, which makes use of a stress-induced change in the angle of polarization of polarized ultrasonic waves. This technique is based on the stress-acoustic effect similar to the familiar stress-optic effect on which the photoelastic technique is based. In the optical case, a stress inside an optically transparent object will change the index of refraction, thus changing the velocity of the beam of light. When a polarized light beam is passed through that object, the different components of light traveling along the axes of principal stress will have different velocities and will cause a rotation of the angle of polarization of the light beam.

When polarized ultrasonic waves pass through a stressed metal, the angle of polarization changes proportionally to the stress level. Benson and Raelson⁽⁴⁰⁷⁾ mentioned this phenomenon as the acoustoelastic phenomenon. Figure 4.15 shows an example of the acoustoelastic setup. Ultrasonic waves are generated by a radio-frequency pulse generator coupled to a Y-cut quartz crystal. The crystal is mounted against the test sample with wax, and another such crystal is mounted at the output end of the sample. Signals passing through the sample are then amplified and displayed on an oscilloscope.

2. The Ultrasonic Attenuation Technique makes use of stress-induced change in the absorption of ultrasonic waves. It is well known that the absorption of mechanical vibrational energy (megacycle frequencies, for example) depends on the mechanical properties of the metal. A residual stress is therefore indicated when there is a change in the absorption of vibrational energy. By opposing the effect of this stress on the ultrasonic attenuation by suitable means, such as the application of an opposite external stress, a measure of the respective residual stress (tension, compression) component might be obtained. In the case of ferromagnetic material, an external magnetic field might be employed.

The technique proposed by Bratina and Mills⁽⁴⁰⁸⁾ involves the following procedures. By plotting the relative attenuation (db/ μ sec) versus applied elastic stress (or magnetic field strength), a point is reached where the respective components of the residual and the external stresses are equal and opposite. This point corresponds to a maximum in attenuation.

4.4.2 Hardness-measuring techniques

Kokubo⁽⁴³⁹⁾ performed experiments on a number of metals to show the effect of strain

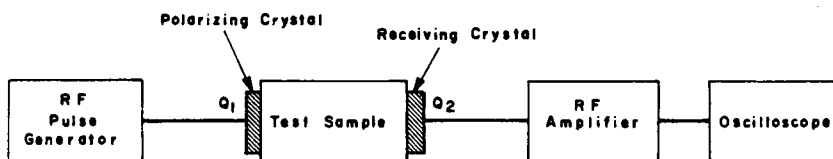


FIG. 4.15. Acoustoelastic setup (Benson and Raelson).⁽⁴⁰⁷⁾

TABLE 4.3 *Effect of strain on hardness measurement (Kokubo)⁽⁴³⁹⁾*

Material	Condition	0.3% applied strain	Change in Vickers hardness	Change in hardness (%)
Armco iron	{ Rolled Annealed	{ + -	- 12.5 2.5	- 8.0 2.5
		{ + -	1.0 4.0	1.0 5.0
0.2% carbon steel	{ Rolled Annealed	{ + -	- 15.0 2.5	- 11.0 2.0
		{ + -	- 8.0 1.0	- 7.0 1.0
0.7% carbon steel	{ Rolled Annealed	{ + -	- 22.0 2.0	- 9.0 1.0
		{ + -	- 14.0 5.0	- 6.5 3.0
Brass	{ Rolled Annealed	{ + -	- 16.0 3.0	- 12.0 2.0
		{ + -	- 2.0 2.0	- 1.5 3.0
Aluminum	{ Rolled Annealed	{ + -	- 2.0 1.0	- 5.0 2.0
		{ + -	0.7 1.2	4.0 6.0
Copper	{ Rolled Annealed	{ + -	- 9.0 0.0	- 10.0 0.0
		{ + -	0.0 4.0	0.0 8.0

on hardness measurements. He applied a bending load sufficient to cause 0.3% strain on the outer fibers of the specimen and took Vickers hardness readings, using a 5-kg (11-lb) load, on the material in the strained state. A summary of his data is presented in Table 4.3. It can be seen that in all cases, except for the brass, aluminum, copper, and Armco iron, all in the annealed condition, the applied tensile stresses made the material appear 5 to 12% softer while the compressive stresses caused only 0 to 3% increase in apparent hardness.

Based on the information obtained by Kokubo, Sines, and Carlson⁽⁴⁰⁹⁾ suggested a non-destructive method for determining residual stresses in machine parts and structures. The method called for external loads of varying degrees to be applied to a part while hardness measurements are taken.⁽⁴⁴⁰⁾ If the residual stress is compressive, an applied compressive stress will have little or no effect on the hardness measurements and a tensile stress also will show no effect as long as the sum of the applied stress and residual stresses is compressive; but, if the tensile stress is great enough so that the sum becomes tensile, the material will appear softer as the applied compressive stress is increased. However, if the metal appears to increase in hardness as the applied compressive stress is increased, it is known that the sum of the applied and residual stress is still tensile; but when a compressive stress is reached that gives no further increase in the hardness measurements, the sum becomes compressive. The residual stress is equal and opposite to the applied stress that causes the transition in hardness measurements.

The state of surface residual stress influences the yield compressive strength obtained

when a small hard ball is gently pressed on the smooth surface of the specimen to be studied. Pomey *et al.*⁽⁴⁴¹⁾ suggested a method of measuring residual stresses based on the above phenomenon. A small hard ball, 0.06 to 0.16 in. (1.5 to 0.4 mm) in diameter, is pressed with increasing load on the specimen surface, and a relationship between the load and the electric resistance of the contact point is obtained. A sudden fall in resistance occurs when portions of the specimen under the ball become plastic. The corresponding load gives surface stresses of the specimen.

4.5 Determination of Residual stresses by Hydrogen-induced and Stress-corrosion Cracking Techniques

Another group of techniques developed to determine stress involves the close observation of cracks caused in the specimen due to the stress. The cracks are induced by hydrogen or stress corrosion.

4.5.1 Hydrogen-induced cracking technique applied to high-strength steel specimens

Masubuchi and Martin⁽⁴⁴²⁾ investigated the use of hydrogen-induced cracking to study residual stresses in welded joints, especially in complex weldments. Welded specimens were made with heat-treated SAE 4340 steel (approximate ultimate tensile strength was 260,000 psi, 183 kg/mm² or 1792 MN/m²). Specimens were then immersed in an electrolyte and charged with hydrogen by applying dc current, using the specimen as the cathode and a set of lead strips as the anode. The electrolyte was 4% sulfuric acid to which was added 5 drops per liter of poison; the poison was 2 grams of phosphorus dissolved in 40 milliliters of CS₂. The current density ranged between 0.35 and 0.8 ampere per square inch of exposed specimen surface.

A number of different crack patterns that could be related to a residual-stress distribution were obtained when tests were conducted using different welding procedures and several kinds of specimen. Figure 4.16 is a typical crack pattern for a simple butt weld. Transverse cracks were produced when residual stresses ran in the longitudinal direction (parallel to the weld). Figure 4.17 shows the crack pattern produced in a complex welded specimen. In the case of specimens welded in SAE 4340 steel oil quenched and tempered at 500°F (260°C) it took 1 to 2 hours to produce a stable crack pattern.

Hydrogen-induced-cracking tests were conducted on weldments in a heat-treated, low-alloy, high-strength steel (ultimate tensile strength was about 120,000 psi) (84.4 kg/mm² or 827 MN/m²) the U.S. Navy Hy-80 steel, a quenched-and-tempered strength steel with yield strength over 80,000 psi (56.2 kg/mm² or 552 MN/m²), and carbon steel. When steels of lower strength were used, longer charging times were required to produce cracks, and crack patterns were less pronounced. The hydrogen-induced-cracking techniques do not seem to work on a carbon-steel weldment.

A mathematical analysis based upon the fracture mechanics theory was also made to determine the relationships between the residual-stress distribution and the crack pattern.⁽⁴⁴²⁾

4.5.2 Stress-corrosion cracking technique applied to steel specimens

Investigators including McKinsey,⁽⁴⁴³⁾ Radeker,⁽⁴⁴⁴⁾ and Masubuchi and Martin⁽⁴⁴²⁾

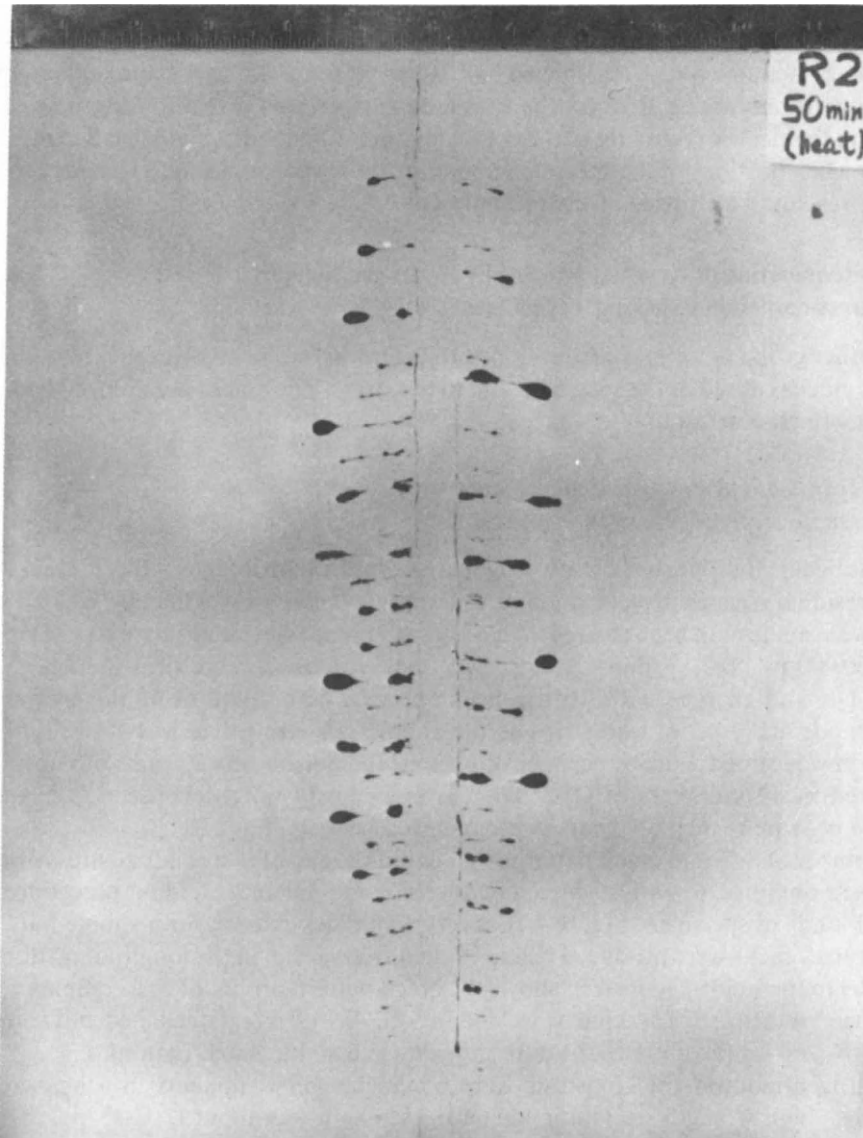


FIG. 4.16. Crack pattern in a simple butt joint made from SAE 4340 steel—oil quenched and tempered at 500°F (Specimen R2)—after hydrogen-induced cracking test for 50 minutes. After the test, the specimen was heated in a furnace at 400°F (204°C) for 2 hours.

have used stress-corrosion cracking to study residual stresses in welded joints in carbon steel and in low-alloy high-strength steels. Figure 4.18 is a radiograph of a butt-welded specimen in a commercial heat-treated, low-alloy, high-strength steel after being immersed for 31 hours in a boiling aqueous solution of 60% $\text{Ca}(\text{NO}_3)_2$ and 4% NH_4NO_3 . The crack pattern is quite similar to those obtained in SAE 4340 steel specimens tested by the hydrogen-induced cracking technique.

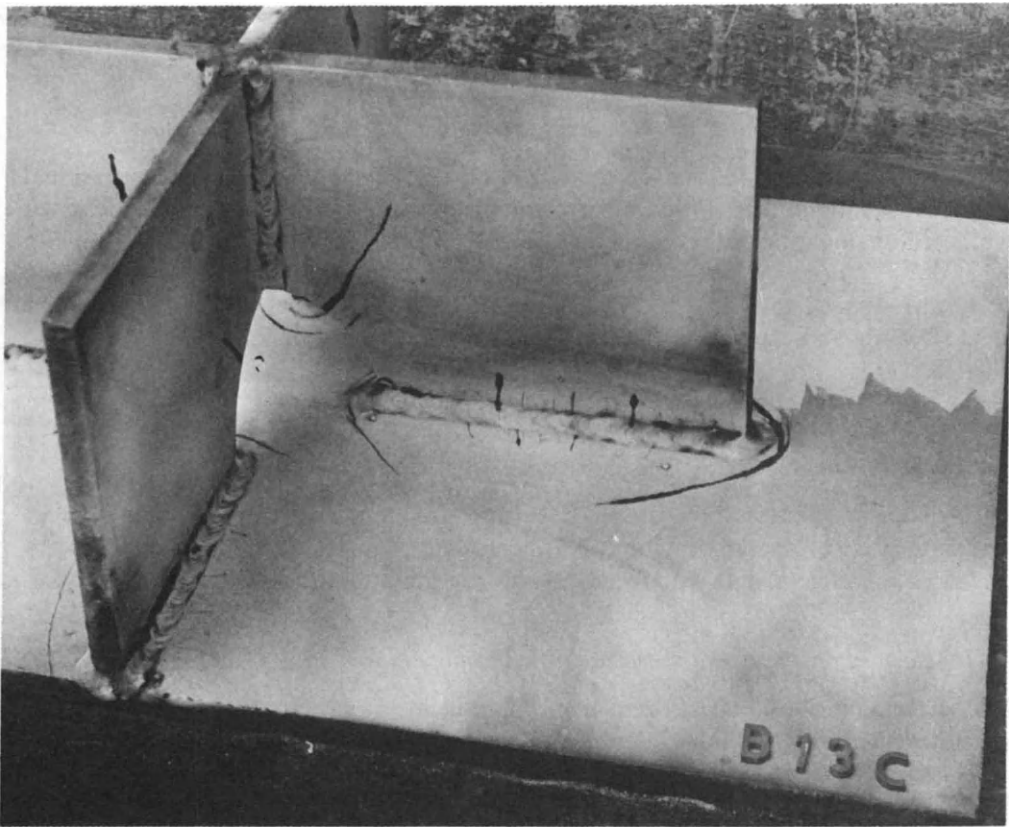


FIG. 4.17. Crack pattern produced by hydrogen-induced cracking technique in a complex-structure specimen made with heat-treated SAE 4340 steel plates (Masubuchi and Martin^(4,42)).

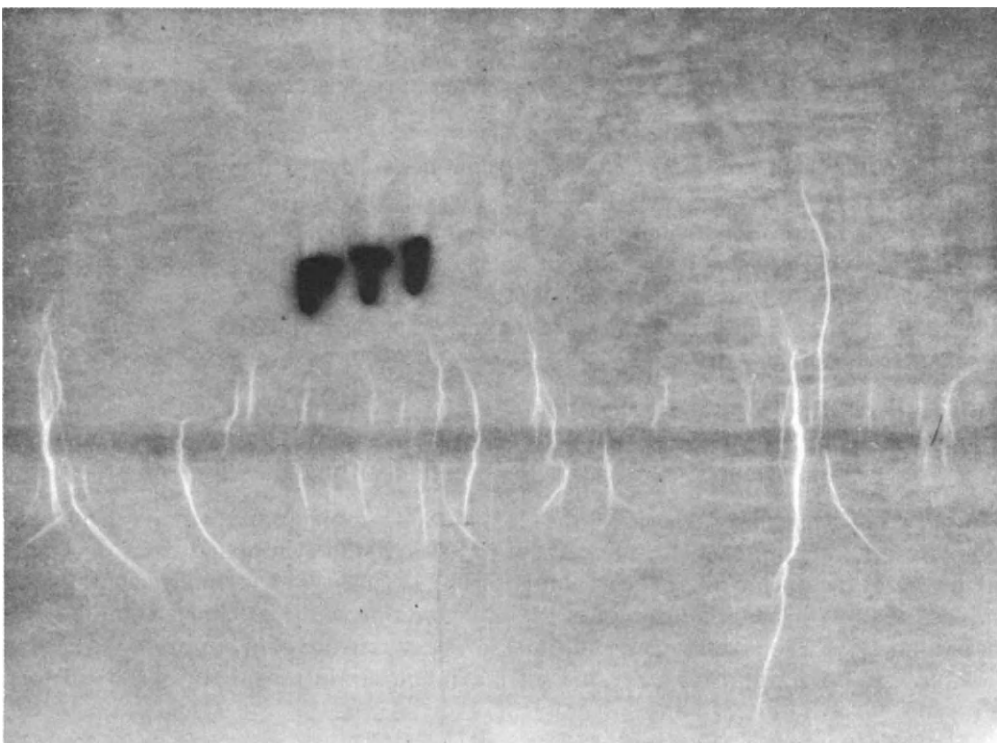


FIG. 4.18. Radiograph of butt-welded specimen made with a commercial low-alloy high-strength steel plate after stress-corrosion cracking test for 31 hours (Masubuchi and Martin).

4.5.3 *Use of cracking technique in studying residual stresses in aluminum alloys*

No work has been reported on the use of cracking techniques in studying residual stress in aluminum alloys. Stress-corrosion cracking, however, has been identified with certain aluminum alloys of the Al–Cu, Al–Mg, Al–Zn–Mg–Cu, and Al–Si–Mg types.^(445,446) For example, failures developed in 2 days when a specimen of 7079–T6 alloy was stressed to 48,000 psi (33.7 kg/mm² or 331 MN/m²) which is 75% of the yield strength, and exposed to the 3.5% NaCl alternative immersion test.

4.6 Selection and Use of Appropriate Measurement Techniques and Evaluation of Results

This section discusses how to select the appropriate measuring technique, how to use mathematical analysis in the experimental study of residual stress, and how to evaluate experimental data with regard to how residual stress affects structural behavior.

4.6.1 *Selection of appropriate measurement techniques*

In determining residual stresses in metals and metal structures it is important to select measurement techniques that are most appropriate for a particular job. Factors to be considered are:

- permissible extent of damage to the structure (destructive or non-destructive testing);
- required quality of measurement (accuracy of data, determination of stress components, etc.);
- effects of variations in metal properties;
- applicability to field tests;
- cost and time.

Table 4.4 shows the characteristics of typical methods for measuring residual stresses.

(a) *Permissible extent of damage to the structure*

This is an important consideration. Some techniques are destructive (stress-relaxation). Of these, certain ones can be classified semi-non-destructive (the Gunnert technique, for example, requires making circular plugs 0.8 in. (20 mm) in diameter).

If absolutely no damage to the structure is permissible, the only presently available technique is the X-ray diffraction technique. The ultrasonic technique is still in the development stage. The hardness technique and cracking techniques are not suitable to be applied to actual structures.

(b) *Requires quality of measurement*

The technique used must provide data that will meet the requirements of quality, accuracy, and completeness according to the situational demands.

Accuracy of strain measurement. Some techniques are more accurate than others and some are only qualitative. The accuracy of measured values in actual cases depends upon various factors including the strain sensitivity of gages used, methods of cutting in the case of stress-relaxation techniques, surface condition of the specimen, condition of measuring devices and equipment, and the skill and experience of operators.

Table 4.4 shows approximate values of maximum strain sensitivity of devices (or

TABLE 4.4 Characteristics of techniques for measuring residual stresses

	Stress-relaxation techniques			X-ray diffraction technique			Cracking techniques				
	Strain gages	Extensometer	Grid system	Photoelastic coating	Brittlecoating	Film technique		Diffractometer techniques			
(1) Extent of damage to the structure	← Destructive (extent varies) →			← Non-destructive →			→ Destructive				
(2) Quality of measurement	← Destructive (extent varies) →			← Non-destructive →			→ Destructive				
Approximate strain sensitivity, min./in.	5	(10 to 100)	50	10	500	400	300	10,000 psi ^(a)	500	Not appropriate	Indirect
Determine stress components	Yes	Yes	Yes	Yes	Not appropriate	Yes	Yes	No	No	Yes	Yes
Usual gage length, in.	$\frac{1}{8}$ to 1	Varies	Varies	Very small	Very small	Yes	← Lattice spacing →	←	←	←	←
Applicability to uneven stress field	Yes	Yes	Yes	Yes	Yes	Yes	Yes	No	No	Yes	Yes
Surface or interior strains	← Surface measurement →			← Surface strain →			← Interior stress →			← Surface stress →	
(3) Effects from variations in materials	← Not affected →			← Not affected →			← Affected →			← Affected →	
(4) Field application	Field, F, or laboratory, L	F, L	Primarily L	L, F	L, F	L, F	L	L, F	L, F	Primarily L	L
Remote indicating	Yes	No	No	No	No	No	No	Yes	Yes	No	—
Operating environment	A, W ^(b)	A	A	A	A, W	A	A	A	A	A	—
(5) Cost and time	← Surface measurement →			← Surface strain →			← Interior stress →			← Surface stress →	
Complexity of equipment ^(c)	1, 2	1, 2	1, 2	3	1	4	4	4	4	2	2
Time required ^(d)	1	1	2	2	1	3	3	1	2	2	4
Required operator experience ^(e)	2	2	2	3	1	4	4	4	4	2	2

^(a) Sensitivity in stress is given.

^(b) A: air; W: water.

^(c) 1-4: less expensive—expensive.

^(d) 1-4: short—long.

^(e) 1-4: less experienced—highly experienced.

the lowest strains that can be detected by the devices) in microinches per inch. For aluminum alloys with Young's modulus of approximately 10×10^6 psi (7000 kg/mm^2), 10 microinch-per-inch strain corresponds to 100 psi (0.07 kg/mm^2) stress. Bonded strain gages provide the best strain sensitivity. However, it must be mentioned that the fluctuation of data in the actual measurement would be considerably greater than the maximum strain sensitivity of the gages unless extreme care is taken during the measurement.

Determination of stress components. Some techniques provide information on stress components so that the directions and the magnitudes of the principal stresses can be determined, while others do not provide enough information on stress components. Techniques that belong to the first group include bonded strain gages, extensometers, grid systems, photoelastic coatings, and the X-ray diffraction technique.

Gage length. Table 4.4 shows usual gage lengths used in various techniques. The gage length must be short enough so that variations in stress can be detected; however, too short a gage length also is not useful. For example, when the X-ray diffraction technique is used to determine residual stresses that are widely distributed in a large structure, such as those shown in Fig. 3.5(a), extreme care must be taken to eliminate the effects of localized residual stresses such as those caused by grinding, as shown in Fig. 3.5(c).

Application to uneven stress field. Most techniques are applicable to specimens that contain unevenly distributed residual stress, although some are not applicable to such cases. At the present stage of development the ultrasonic technique is not applicable to unevenly distributed residual stresses.

Surface strain or strains in the interior determined. Suppose that the curve $ABCD$ in Fig. 4.19 represents the thickness-direction distribution of residual stresses parallel to the plate surface, σ_x , having highly localized tensile stresses in a thin layer near the surface. Stresses determined by different techniques may vary considerably.

When the X-ray diffraction technique is used, only surface strains to a depth of approximately 0.0001 in. (0.0025 mm) are determined; the surface stress OA is measured. In the stress-relaxation techniques using bonded strain gages, extensometers, grid systems, photoelastic coatings, and brittle coatings, strain measurements are made on the surface. However, the measured values do not exactly represent the stress on the very surface, OA . When a plug is cut as shown in Fig. 4.19, for example, the relaxation of the surface stress is restricted by the metal in the central portion and residual stresses

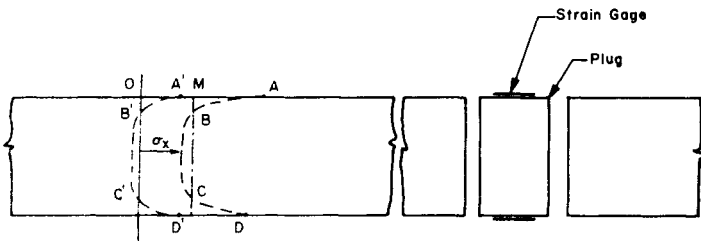


FIG. 4.19. Thickness-direction distribution of residual stress.

as shown by a curve $A'B'C'D'$ may still remain in the plug. Therefore, the stress determined by strain release measured on the surface does not represent OA but AA' which is somewhat between the localized skin stress OA and the means stress OM . OA' depends on various factors including the stress distribution, $ABCD$, or sharpness of the curve near the surface, the plate thickness, and the size of the plug.

In the ultrasonic technique, it is believed that stresses in the interior of the material, e.g. around BC , are determined.

(c) *Effects of variations in material properties*

Large fabricated structures contain variations in metal properties: welded structures have the weld metal, the heat-affected zone, and the base metal, and heat treatments also change material properties. These variations in metal properties can cause serious problems when the X-ray diffraction technique and the ultrasonic technique are used.

It has been recognized that diffraction lines are broadened, resulting in lower accuracy in strain measurements when the X-ray diffraction technique is used on heat-treated materials.

(d) *Field application*

Some techniques are applicable to both laboratory and field tests, while others are applicable to laboratory tests only. Diffractometers commercially available at the present time are for the laboratory use; however, special equipment for a field test may be made.

Whether or not readings can be taken under field conditions is an important factor in selecting techniques for field tests. The use of bonded strain gages is more appropriate than other techniques in this respect.

Some structures may be exposed to environments other than air, i.e. water or oil, and this factor must be taken into consideration. Some techniques may be appropriate to one environment and not another.

(e) *Cost and time*

The amount of cost and time required for the determination of residual stress depends on many factors including the shape and size of the specimen, the number of measuring points, and the accuracy of measurement required. Table 4.4 shows in relative numbers the complexity of equipment, the time, and the amount of operator experience required.

Electric-resistance strain gages are relatively simple to operate and not expensive, but the cost and the time required for such stress-relaxation procedures as drilling or sectioning can be tremendous.

The X-ray diffraction technique is a slow process. At each measuring point, an X-ray diffraction measurement must be taken in two directions, each measurement requiring 15 to 30 minutes of exposure time.

(f) *Use of various techniques in studying residual stresses in metal structures*

As can be seen in Table 4.4, there is no single residual-stress measuring technique that is quick, easy, non-destructive, sensitive to high strain, applicable to field testing and low in cost. However, each technique does present certain advantages over the others and each has its own appropriate area or areas of application.

Bonded strain gages are widely used in residual-stress measurement, since they provide high-quality data at low cost. They are attached directly to the structure so that strain

changes which take place during fabrication can be traced. Whenever portions of the metal are removed during this fabrication process, the drilling or cutting of holes, for example, the stress-relaxation that results will be indicated by the bonded strain gages.

The use of *extensometers, grid systems, photoelastic coatings, and brittle coatings* is limited to several unique areas of application. The Gunnert method, which employs a mechanical extensometer with short gage length, has been used to measure residual stress in welded plates. The Gunnert method also has been used to measure residual stresses in actual structures such as ships.⁽⁴⁴⁷⁾

X-ray diffraction techniques have been widely used and provide the only means of measuring residual stress in ball bearings, gear teeth, and metal surfaces after machining or grinding.⁽⁴⁴⁸⁻⁴⁵²⁾ X-ray diffraction has also been used to measure residual stress in the structural components of airplanes.⁽⁴⁵³⁾

According to recent information, the *ultrasonic technique* is capable of determining the magnitude of stresses in simple stress field, such as a bar under tensile loading. However, it has not been proved that this technique is useful for determining unevenly distributed residual stresses in metal structures.

No actual application of the *hardness techniques* has been reported.

Cracking techniques are useful for studying residual stresses in complex structural models, but they are not suitable for application to actual structures.

4.7 Strain Measurement of Transient Strains During Welding

Studies have been made to measure strain changes during welding by use of electric-resistance strain gages mounted on the surfaces of plates being welded.

The resistance change recorded by an electric-resistance strain gage, ΔR , consists of:

$$\Delta R = \Delta R_1(\varepsilon_e) + \Delta R_2(\varepsilon_p) + \Delta R_3(\alpha \cdot \Delta T) + \Delta R_4(T) \quad (4.10)$$

where

$\Delta R_1(\varepsilon_e) =$ The resistance change corresponding to the elastic strain, ε_e , from which stresses can be computed.

$\Delta R_2(\varepsilon_p) =$ The resistance change corresponding to the plastic strain, ε_p .

$\Delta R_3(\alpha \cdot T) =$ The resistance change corresponding to the thermal strain caused by the temperature change, $\alpha \cdot \Delta T$.

$R_4(T) =$ The resistance change caused by the change in temperature.

By measuring changes of temperature, T , ΔR_3 , and ΔR_4 can be determined, making it possible to determine $(\varepsilon_e + \varepsilon_p)$, usually designated mechanical strain.

Figure 4.20 is a schematic diagram of one means of measuring the transient strains that develop during welding. Some experimental results using this method are given in Chapter 5.

However, it is not possible to experimentally separate ε_e from ε_p using the technique shown in Fig. 4.20. The amount of elastic strain that exists after the welding is complete can be determined experimentally by using the strain-relaxation technique (see Fig. 4.23). A computer-aided analysis is also an effective way of determining ε_e and ε_p , and will be discussed in detail in Chapter 5.

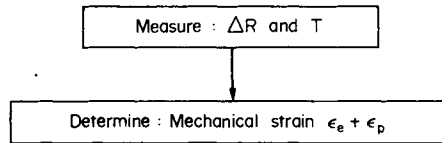
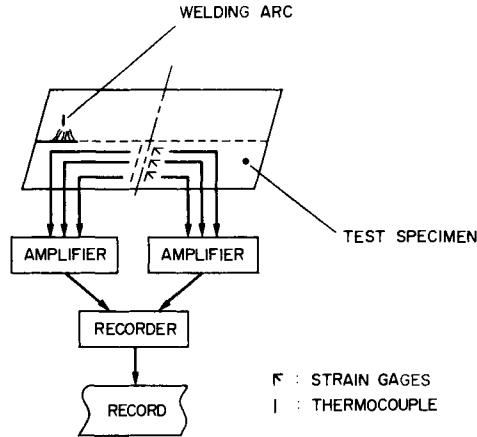


FIG. 4.20. Schematic diagram of measurement of transient strains during welding.

4.7.1 Measurement of transient reaction stresses

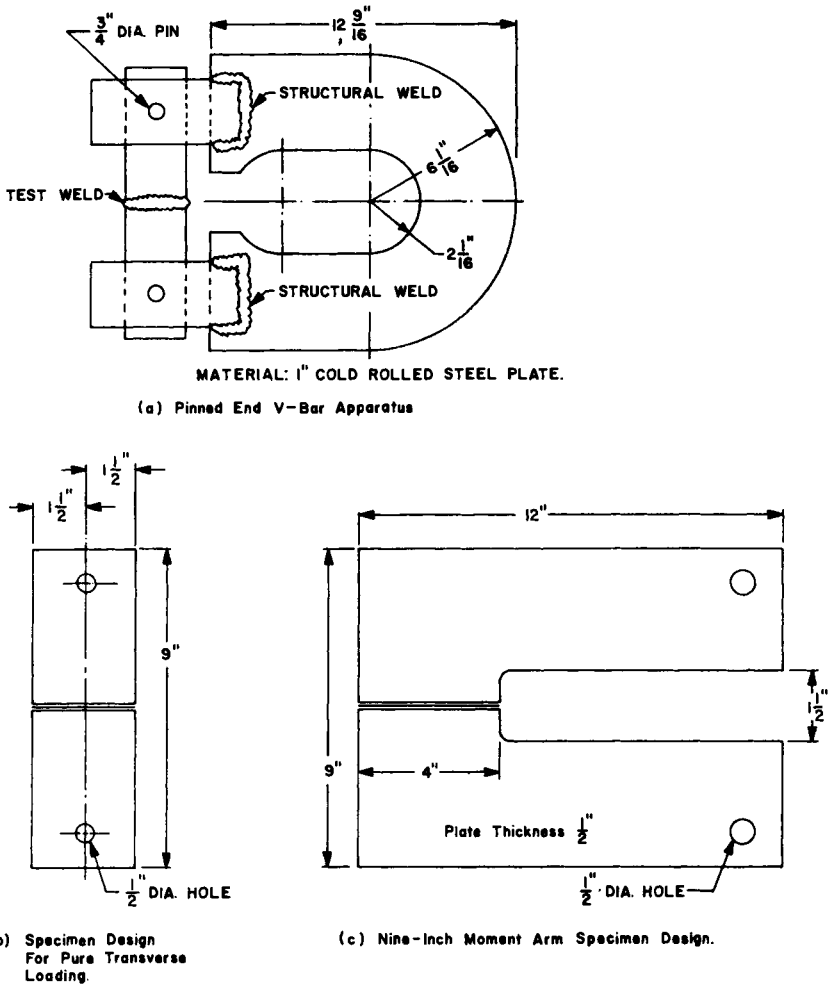
When strain change measurements are taken at locations some distance from the weld where the strain is purely elastic, the stress changes can be determined.

Travis, *et al.*⁽⁴⁵⁴⁾ used constrained joints to study cracking under hindered contraction (see Fig. 4.21). The change of reaction stresses produced in the constraining bar was measured by strain gages mounted on the bar. Two specimens were used (see Fig. 4.21), the latter designed to cause a bending moment as well as a separating force to be imposed upon the test weld. According to the investigators, the 9-in. moment specimen was more suitable than the pure transverse loading-type specimen for studying weld cracking.

Figure 4.22 shows examples of experimental results obtained on the moment-type specimens made from U.S. Navy HY-80 steel. The separating force of the U-bar was calculated from the strain measured on the bar. The figure illustrates the effects of preheating on the magnitude of separating force and on cracking under the restrained condition. The occurrence of weld cracking is indicated by a decrease in the separating force, since cracking reduces residual stress. With a sufficiently high preheating temperature, there was no cracking. With no preheating, cracking took place in 15 minutes after the start of welding. With a 200°F (93°C) preheating temperature, cracking was delayed more than 1½ hours.

4.7.2 Measurement of elastic and plastic strains in areas near the weld

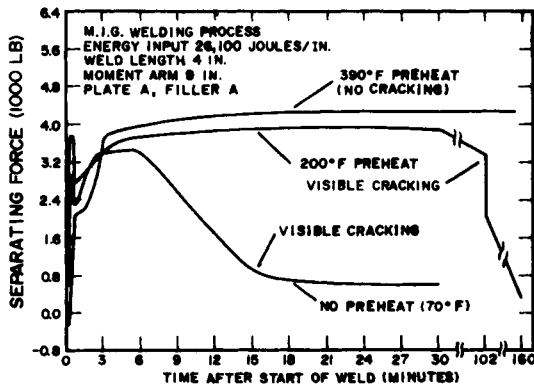
Using a Gunnert strain indicator, Masubuchi^(314,322) investigated the distribution



Note: Other apparatus designs including the horizontal lever arm apparatus and the fixed-end V-bar apparatus also were used.

FIG. 4.21. Constrained joint to study cracking under hindered contraction.⁽⁴⁵⁴⁾ (Travis *et al.*).

of elastic and plastic strains in areas near a weld (see Fig. 4.21). The specimen was a slit-type weldment in carbon steel (see Fig. 4.23); a double-vee slit 10 in. (254 mm) long was made by machining in a plate $\frac{3}{4} \times 31 \times 43$ in. (19 × 787 × 1092 mm) and the slit was welded with covered electrodes. Figure 4.23 also shows locations of strain-measuring depressions that were prepared prior to welding on the specimen surface and the distance between the depressions were measured. After the specimen was welded, the distances between the depressions were measured again to determine strains produced by welding. Since the strain produced by welding may contain both elastic and plastic strains, particularly in areas near the weld, the elastic part of the strain also was measured by relaxation using a Gunnert core drill. Details of experimental results are presented in Chapter 6 (Section 6.3.1).



Chemical Comparison (percent) of the Base and the Filler Metal

	C	Mn	Si	S	P	Mo	Cr	V
Plate A	0.29	1.73	0.22	0.020	0.018	0.48	—	—
Filler Metal A	0.35	1.00	0.45	0.020	0.020	—	1.10	0.18

FIG. 4.22. Change of separating force after welding in 9-inch arm specimen in HY-80 steel (Travis *et al.*)⁽⁴⁵⁴⁾

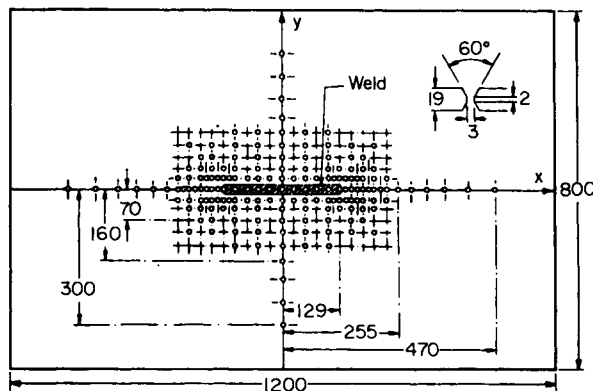


FIG. 4.23. General view of slit-type specimen and location of residual-stress measuring points (values are shown in millimeters) (Masubuchi)^(314, 322)

4.7.3 Measurement of residual stresses of a weldment

Most of the techniques discussed in Sections 4.2 and 4.3 can be used for measuring the residual stress in a weldment. The most widely used among these techniques is the strain-relaxation technique with electric-resistance strain gages. In fact most of the experimental data generated by the author and his associates were obtained using this technique. It usually provides accurate results.

Figure 4.24 shows a typical arrangement of the strain gages for the measurement of a

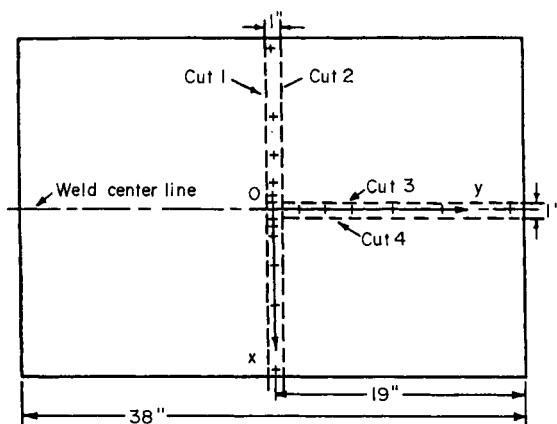


FIG. 4.24. Distribution of I as calculated from strain produced by welding. See Equation (4.11) (Masubuchi)^{314,323}

simple butt weld. Strain gages are mounted on both surfaces of the plate to study the effects of bending stresses. Gages are spaced closer together near the weld where the residual stresses vary drastically. Strips about 1 in. wide are cut from the specimen.

4.8 Use of Mathematical Analysis in the Experimental Study of Residual Stress and Distortion

The use of a mathematical analysis based on the theory of elasticity and plasticity is sometimes useful in the study of residual stress in metal structures. In simple cases, the distribution of residual stress can be calculated analytically, but in most practical cases the geometry of the structure is too complicated. Nevertheless, mathematical analysis is useful in practical situations as an aid to understanding the problem. Different sets of data such as residual stress and distortion can be related quantitatively and the number of experimental conditions necessary to obtain the desired information can be reduced.

With the development of computer technology and such techniques as finite-element analysis, it is quite possible that the computer-aided determination of residual stress in practical weldments will become common in the future. The following pages discuss this new area and give several examples.

4.8.1 Measurement of residual stress in heavy and complex weldments

In all of the stress measurement techniques in use today, including strain gage and X-ray diffraction techniques, the stresses are measured by measuring the strains on the surface of the specimen. There is no method, other than the as-yet undeveloped ultrasonic technique, that is capable of measuring the stress inside a body. When residual stress is measured in a heavy weldment, the surface on which the measurements are to be taken must be exposed through drilling or sectioning. Figure 4.5 shows the Gunnert drilling method and Fig. 4.6 shows the Rosenthal-Norton sectioning method.

These methods are time consuming and costly; they provide stress measurements only at the drilled hole or along the sectioned block. Techniques for the calculation of stress along many sections of a heavy weldment have not yet been developed, though

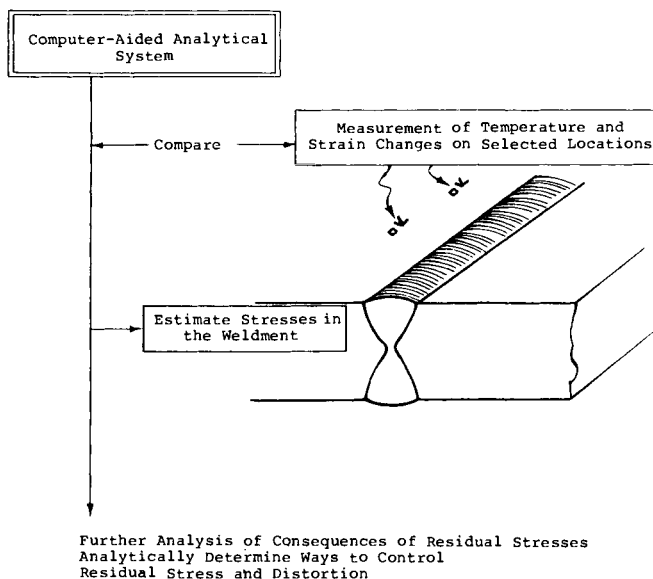


FIG. 4.25. Use of the computer-aided analytical system for studying residual stresses in a heavy weldment and their consequences.

such information would be extremely useful. It is now technically possible to develop computer programs predicting transient thermal strains during welding heavy plates, as discussed in Chapter 5. If these analytical predictions agree with measurements taken at selected locations on the specimen surface, to compute the stress distributions inside the specimen (see Fig. 4.25), these computations could then be verified using spot-check drilling or sectioning.

This would be an integrated approach taking advantage of both analytical and experimental methods. With it, the distribution of residual stress inside a heavy weldment could be determined, data especially useful in predicting the service behavior of a welded structure.

Residual stress can result in brittle fracture, fatigue, stress corrosion, cracking, and buckling; it is therefore necessary to find a welding procedure and sequence that will reduce residual stress and distortion to a minimum. Its measurement is only the first step toward its control. Its distribution and effect on service behavior must be calculated before welding procedures counteracting these problems can be developed.

Because so much information is necessary for the effective control of residual stress, the problem must be approached in an integrated manner, and a computer-aided analysis using experimental data as a check can be the backbone of this approach.

A similar approach can be taken in studying residual stress and distortion in complex welded structures. A computer-aided analytical system can be the backbone of the study, and experimental data obtained at selected locations can be used to verify the accuracy of the analysis.

Analytical systems developed thus far are capable of handling only simple problems such as butt welds. However, analyses capable of handling weldments in the various practical shapes will be developed in the near future.

References

- (401) TREUTING, R. G., LYNCH, J. J., WISHART, H. B., and RICHARDS, D. G., *Residual Stress Measurements*, American Society for Metals, 1952.
- (402) HEINDLHOFFER, K., *Evaluation of Residual Stress*, McGraw-Hill Book Co., Inc., New York, 1948.
- (403) HORGER, O. J., "Residual Stresses", Chapter 11 of *Handbook of Experimental Stress Analysis*, edited by Hetenyi, M., John Wiley & Sons, Inc., New York, pp. 459–578, 1950.
- (404) GUNNERT, R., "Measuring of residual stresses and strains", Document No. X-286–62-OE, Commission X of the International Institute of Welding (1962).
- (405) PARLANE, A.J.A., *Residual Stresses in Thick Weldments-A Review of Contemporary Measurement Techniques*, The Welding Institute, Abington, Cambridge, England, Aug. 1977.
- (406) Proceedings of a Workshop on "Nondestructive Evaluation of Residual Stresses" sponsored by the Air Force Materials Laboratory was held at the Southwest Research Institute, San Antonio, Texas, 13 and 14 August, 1975. Nondestructive Testing Information Analysis Center, Southwest Research Institute, San Antonio, Texas NTIAC-76–2, 1976.
- (407) BENSON, R. W. and RAELSON, V. T., "Acoustoelasticity", *Product Engineering*, **30** (29), 56–59 (20 July, 1959).
- (408) BRATINA, W. J. and MILLS, D., "Investigation of residual stress in ferromagnetics using ultrasonic", *Nondestructive Testing*, **18** (1), 110–112 (1960).
- (409) SINES, G. and CARLSON, R., "Hardness measurements for determination of residual stresses", *ASTM Bulletin*, no. 180, 35–37 (Feb. 1952).
- (410) HETENYI, editor, *Handbook of Experimental Stress Analysis*, John Wiley & Sons, Inc., New York, 1950.
- (411) CRITES, N. A., "Your guide to today's strain gages", *Product Engineering*, **33** (4), 69–81 (19 Feb. 1962).
- (412) CRITES, N. A., "Equipment and application—today's strain gages", *Product Engineering*, **33** (6), 85–93 (19 Mar. 1962).
- (413) GUNNERT, R., *Residual Welding Stresses, Method for Measuring Residual Stress and its Application to a Study of Residual Welding Stresses*, Almquist E. Wicksell, Stockholm, 1955.
- (414) MATHAR, J., "Determination of metal stress by measuring the deformation around drill holes", *Transactions of the American Society of Mechanical Engineers*, **86**, 249–254 (1934).
- (415) SOETE, W., "Measurement and relaxation of residual stresses", *Welding Journal*, **28** (8), Research Supplement, 354s–364s (1949).
- (416) SUPPIGER, E. W., RIPARBELLI, C., and WARD, E. R., "The determination of initial stresses and results of tests on steel plates", *Welding Journal*, **30** (2), Research Supplement, 91s–104s (1951).
- (417) STÄBLEIN, E., "Stress measurements on billets quenched from one side", *Stahl und Eisen*, **52**, 15–17 (1932).
- (418) HEYN, E. and BAUER, O., "On stresses in cold drawn metals", *Internationale Zeitschrift für Metallographic*, **1**, 16–50 (1911).
- (419) HEYN, E., "Internal strains in cold wrought metals, and some troubles caused thereby", *Journal of the Institute of Metals*, **12**, 1–37 (1914).
- (420) MESNAGER, M., "Methods de determination des tensions existant dans un cylindre circulaire", *Comptes Rendus hebdomadaires des Seances de l'Academie des Sciences*, **169**,
- (421) SACHS, G., "Evidence of residual stresses in rods and tubes", *Zeitschrift für Metallkunde*, **19**, 352–357 (1927).
- (422) GUNNERT, R., "Method for measuring tri-axial residual stresses", Document No. X-184–57-OE, Commission X of the International Institute of Welding (1957), and *Welding Research Abroad*, **4** (10), 1725 (1958).
- (423) GUNNERT, R., "Method for measuring residual stresses in the interior of a material", Document No. X-162–57, Commission X of the International Institute of Welding (1957), *Welding Research Abroad*, **6** (6), 10–24 (1960).
- (424) ROSENTHAL, D. and NORTON, T., "A method for measuring triaxial residual stress in plates", *Welding Journal*, **24** (5), Research Supplement, 295s–307s (1945).
- (425) GADD, C. W., "Residual stress indications in brittle lacquer", *Proceedings of the Society for Experimental Stress Analysis*, **4** (1), 74–77 (1946).
- (426) ZANDMAN, F. and WOOD, M. R., "Photo stress", *Product Engineering*, **27** (9), 167–178 (Sept. 1956)
- (427) ZANDMAN, F., "Photoelastic-coating technique for determining stress distribution in welded structures", *Welding Journal*, **39** (5), Research Supplement, 191s–198s (1960).
- (428) VAUGHAN, D. A. and CRITES, N. A., "Measurement of stress by X-ray diffraction", *Product Engineering*, **34** (20) (Sept. 1963).
- (429) BARRETT, C. S., "X-ray analysis", Chapter 18 of *Handbook of Experimental Stress Analysis*, edited by Hetenyi, M., John Wiley & Sons, Inc., New York, pp. 977–1012, 1950.
- (430) NORTON, J. T. and ROSENTHAL, D., "Recent contributions to the X-ray method in the field of stress analysis", *Proceedings of the Society for Experimental Stress Analysis*, **5** (1), 71–77 (1947).

- (431) NORTON, J. H. and ROSENTHAL, D., "Applications of the X-ray diffraction method of stress measurement to problems involving residual stresses in metals", *Proceedings of the Society for Experimental Stress Analysis*, **1** (2), 77-81 (1944).
- (432) NORTON, J. H. and ROSENTHAL, D., "Stress measurement by X-ray diffraction", *Proceedings of the Society for Experimental Stress Analysis*, **1** (2), 73-76 (1944).
- (433) JAMES, M. and COHEN, J. B., "PARS—a portable X-ray analyzer for residual stresses", *Journal of Testing and Evaluation*, **6**, 91-97 (1978).
- (434) FIRESTONE, F. A. and FREDERICK, J. R., "Refinements in supersonic reflectoscopy, polarized sound", *Journal of the Acoustical Society of America*, **18**, 200-211 (1946).
- (435) FREDERICK, J. R., "Use of ultrasonic surface waves in the determination of residual stress in metals", *Journal of the Acoustical Society of America*, **32**, 1499 (Nov. 1960).
- (436) HIKATA, A., TRUPELL, R., GRANATO, A., CHICK, B., and LUCKE, K., "Sensitivity of ultrasonic attenuation and velocity changes to plastic deformation and recovery in aluminum", *Journal of Applied Physics*, **27**, (4), 396-404 (1956).
- (437) BERGMAN, R. H. and SHAHBENDER, R. A., "Effect of a statically applied stress on the velocity of propagation of ultrasonic waves", *Journal of Applied Physics*, **29** (12), 1736-1738 (1958).
- (438) Midwest Research Institute, *Ultrasonic Methods for Nondestructive Measurement of Residual Stress*, F. Rollins WADD Technical Report 61-42, Part 1 (May 1961).
- (439) KOKUBO, S., "Changes in hardness of a plate caused by bending", *Science Reports of the Tohoku Imperial University, Japan*, Series I, **21**, 256-267 (1932).
- (440) Private communication.
- (441) POMEY, J., GOUDEL, F., and ABEL, L., "Determination des contraintes résiduelles dans les pièces cimentées", *Publications scientifiques et Techniques du Ministère de l'air*, 263 (1950).
- (442) MASUBUCHI, K. and MARTIN, D. C., "Investigation of residual stresses by use of hydrogen cracking", *Welding Journal*, **40** (12), Research Supplement, 553s to 563s (1961); and Final Report on *Investigation of Residual Stresses in Steel Weldments*, to Bureau of Ships on Contract No. NObs-92521 from Battelle Memorial Institute (30 Sept. 1965).
- (443) MCKINSEY, C. E., "Effect of low-temperature stress relieving on stress-corrosion cracking", *Welding Journal*, **33** (4), Research Supplement, 161s to 166s (1954).
- (444) RÄDEKER, W., "A new method for proving the existence of internal stress caused by welding", *Schweissen und Schneiden*, **10** (9), 351-358 (1958). See also abstract by Dr. Claussen, *Welding Journal*, **38** (4), 300 (1959).
- (445) Aluminum Company of America, "Avoiding stress corrosion cracking in high strength aluminum alloy structures", E. H. Sphuler and C. L. Burton (1 Aug. 1962).
- (446) RUTEMILLER, H. C. and SPROWLS, D. O., "Stress corrosion of aluminum—Where to look for it, how to prevent it", paper prepared for presentation at the Missile Industry Symposium of the 18th Conference and Corrosion Show of N.A.C.E. (19-23 Mar. 1962).
- (447) Commission X of the International Institute of Welding, "Changes of the residual stresses in the interior of welds and plates in the main decks of ships during service", R. Gunnert, Document No. X-228-59-OE, (1959).
- (448) CHRISTENSON, A. L. and ROWLAND, E. S., "X-ray measurement of residual stress in hardened high carbon steel", *Transactions American Society for Metals*, **45**, 638-676 (1953).
- (449) KINELSKI, E. H. and BERGER, J. A., "X-ray diffraction for residual stress measurements of restrained weldments", *The Welding Journal*, **36** (12), Research Supplement, 513s-517s (1957).
- (450) ROBERTS, J. G., "X-ray find residual stress in hardest steels", *SAE Journal*, **70** (3), 50-51 (1962).
- (451) Battelle Memorial Institute, *Determination of Residual Stress in Bearingized Bolt Holes in 2014-T6 Aluminum*, Vaughan, D. A. and Schwarts, C. M., Final Report to Ogden Air Materials Area, Hill Air Force Base (15 Sept. 1964).
- (452) YOSHIDA, T. and HIRANO, K., "Measurement of residual stress in weldments by X-ray diffraction method", Part 1 and Part 2, *Journal of the Japan Welding Society*, **33** (7), 533-537, 538-543 (1964).
- (453) BOLSTAD, D. A., DAVIS, R. A., QUIST, W. E., and ROBERTS, E. G., "Measuring stress in steel parts by X-ray diffraction", *Metal Progress*, **84** (1), 88-124 (1963).
- (454) TRAVIS, R. E., BARRY, J. M., MOFFATT, W. G., and ADAMS, JR., C. M., "Weld cracking under hindered contraction: comparison of welding process", *Welding Journal*, **43** (11), Research Supplement, 504-513s (1964).

Transient Thermal Stresses and Metal Movement During Welding

BECAUSE a weldment is heated locally by the welding heat source, the temperature distribution in the weldment is not uniform and changes as the welding progresses. During the welding cycle, complex strains occur in the weld metal and the base metal regions near the weld. This chapter discusses transient thermal stresses and metal movement during welding.

5.1 Thermal Stresses During Welding—How They are Produced

Figure 5.1 shows schematically the changes of temperature and resulting stresses that occur during welding. A bead-on-plate weld is being made along the x -axis. The welding arc, which is moving at a speed v , is presently located at the origin, O , as shown in Fig. 5.1(a).

Figure 5.1(b) shows the temperature distribution along several cross sections. Along Section $A-A$, which is ahead of the welding arc, the temperature change due to welding, ΔT , is almost zero. Along Section $B-B$, which crosses the welding arc, the temperature change is extremely rapid and the distribution is very uneven. Along Section $C-C$, which is some distance behind the welding arc, the distribution of temperature change is as shown in Fig. 5.1 (b)-3. Along Section $D-D$, which is very far from the welding arc, the temperature change due to welding again diminishes.

Figure 5.1(c) shows the distribution of stresses along these sections in the x -direction, σ_x . Stress in the y -direction, σ_y , and shearing stress, τ_{xy} , also exists in a two-dimensional stress field.[†]

Along Section $A-A$, thermal stresses due to welding are almost zero. The stress distribution along Section $B-B$ is shown in Fig. 5.1(c)-2. Because molten metal will not support a load, stress underneath the welding arc is close to zero. Stresses in regions a short distance from the arc are compressive, because the expansion of these areas is restrained by the surrounding metal where the temperatures are lower. Since the temperatures of these areas are high and the yield strength of the material low, stresses in these areas are as high as the yield strength of the material at corresponding temperatures. The magnitude of compressive stress passes through a maximum increasing distance from the weld or with decreasing temperature. However, stresses in areas away from the weld are tensile and balance with compressive stresses in areas near the weld. In

[†] In a general three-dimensional stress field, six stress components, σ_x , σ_y , σ_z , τ_{xy} , τ_{zy} , and τ_{zx} , exist (see Section 3.1).

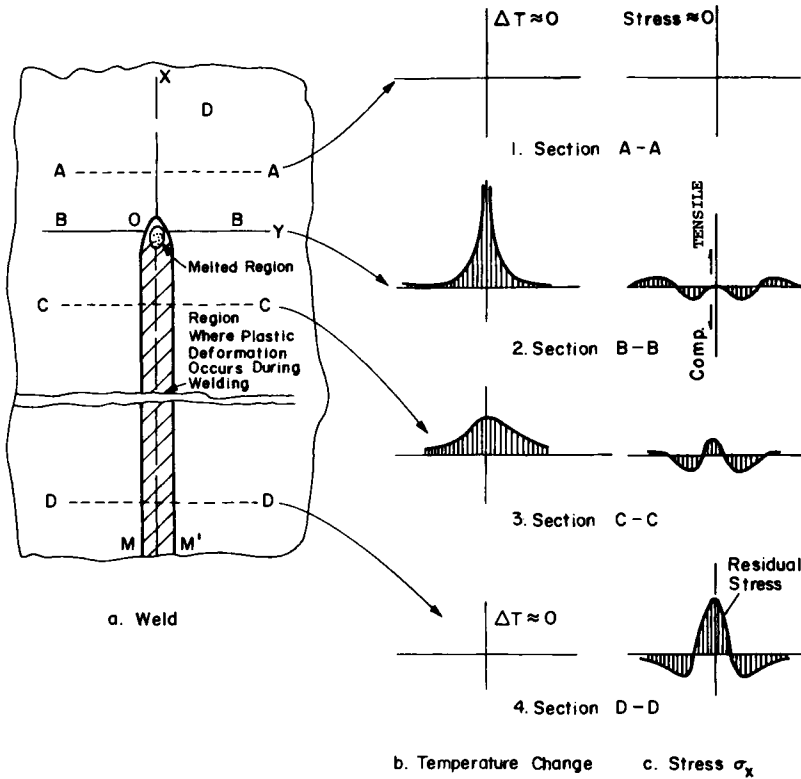


FIG. 5.1. Schematic representation of changes of temperature and stresses during welding

other words,

$$\int \sigma_x dy = 0 \tag{5.1}$$

across Section B-B.[†] Thus, the stress distribution along Section B-B is as shown in Fig. 5.1(c)-2.

Stresses are distributed along Section C-C as shown in Fig. 5.1(c)-3. Since the weld metal and base metal regions near the weld have cooled, they contract and cause tensile stresses in regions close to the weld. As the distance from the weld increases, the stresses first change to compressive and then become tensile.

Figure 5.1(c)-4 shows the stress distribution along Section D-D. High tensile stresses are produced in regions near the weld, while compressive stresses are produced in regions away from the weld. This is the usual distribution of residual stresses that remain after welding is completed.

The cross-hatched area, M-M', in Fig. 5.1(a) shows the region where plastic deformation occurs during the welding thermal cycle. The egg-shaped region near the origin o indicates the region where the metal is melted.

The region outside the cross-hatched area remains elastic during the entire welding thermal cycle.

[†] Equation (5.1) neglects the effect of σ_y and τ_{xy} on the equilibrium condition.

5.2 Historical Development of Studies of Thermal Stresses and Metal Movement During Welding

Studies on transient thermal stresses during welding started in the 1930s. In a paper published in 1936, Boulton and Lance-Martin⁽²³⁶⁾ discussed the transient thermal stresses that occur along the edge of a plate during welding. Because the computation required for analyzing transient phenomena is complex, only limited studies have been done on transient thermal stresses and metal movement. Before the use of modern computers, analyses of transient stresses were limited to such simple cases as:

1. Spot welding in which temperature and stresses changes are axially symmetric.
2. Instantaneous heating along the edge of a strip in which temperature and stress changes are functions of only one axis.

However, these cases are far too simple to represent actual welds. Results of these studies are included several books and reports.^(303, 501-509)

The first significant attempt to use a computer in the analysis of thermal stresses during welding was done by Tall^(510, 511) in a Ph.D. thesis in 1961. He developed a simple program on thermal stresses during bead welding along the center line of a strip. The temperature distribution was treated as two-dimensional; however, in analyzing stresses it was assumed that (1) longitudinal stress, σ_x , is a function of the lateral distance y only and (2) that σ_y and τ_{xy} are zero (see Fig. 5.1). In this textbook, such an analysis is designated one-dimensional.

In 1968 Masubuchi *et al.*⁽⁵¹²⁾ of Battelle Memorial Institute developed, based upon Tall's analysis, a FORTRAN program on the one-dimensional analysis of thermal stresses during welding.

Since 1970 the computer analysis of transient thermal stresses during welding has become more common. At M.I.T. and several other laboratories around the world, investigators are currently developing computer programs related to or specifically

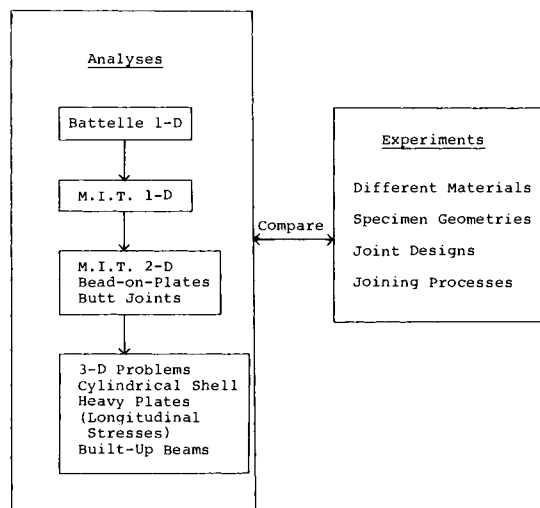


FIG. 5.2. Development of analytical and empirical studies at M.I.T. on thermal stresses and metal movement during welding.

for this kind of analysis. For example, finite-element programs on welding thermal stresses have been developed at Brown University,⁽⁵¹³⁾ Osaka University,^(514, 515) and the University of Tokyo^(516, 517) as well as M.I.T.

Commission X (Residual Stress, Stress Relieving, and Brittle Fracture) of the International Institute of Welding established in 1972 a working group on “Numerical Analyses of Stresses, Strains, and Other Effects Produced by Welding”. The working group has prepared reports covering studies being made in various laboratories in the world.^(518, 519) At the Colloquium on “Application of Numerical Techniques in Welding” held during the 1978 Annual Assembly of the International Institute of Welding several papers on the analyses of thermal stresses during welding were presented⁽²³⁵⁾.

Since details of most computer programs are not published, further discussions of this chapter are based upon results generated at M.I.T. Figure 5.2 shows development of analytical and empirical studies at M.I.T. on thermal stresses and metal movement during welding.

5.3 One-dimensional Analyses

The first to be developed were the one-dimensional programs. The original Battelle program⁽⁵¹²⁾ developed in 1968 has since been improved at M.I.T.

5.3.1. Battelle program

In a study for the G. C. Marshall Space Flight Center, NASA, Masubuchi *et al.*⁽⁵¹²⁾ developed some computer programs for the calculation of thermal stresses in bead-on-plate welding. This Battelle study uses a technique that was originally developed by Tall.^(510, 511)

First, the temperature distribution around the moving arc was calculated using eqn. (2.16). In calculating stresses, it was assumed stress changes in the x -direction are much less than those in the y -direction, in Fig. 5.1. From the equilibrium condition, eqn. (3.16), one could then assume that (1) the longitudinal stress, σ_x , is a function of y only and (2) σ_y and τ_{xy} are zero. The field is divided into a set of transverse strips of width, h_0 , as shown in Fig. 5.3. The time intervals represented by the strip width must

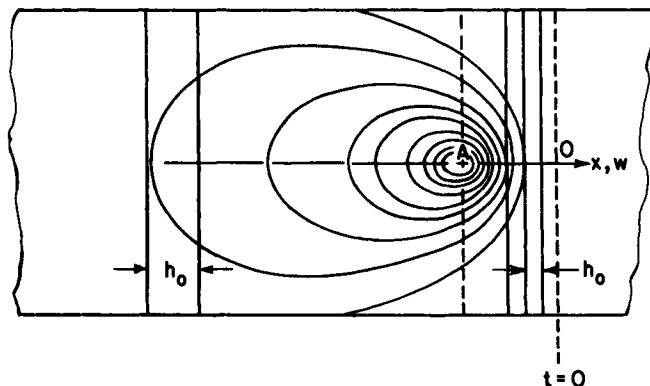


FIG. 5.3. Dividing the stress field into transverse strips for calculating thermal and residual stresses.

be short so that the temperature and thermal stress for each increment can be treated as a constant. Since the greatest changes in temperature occur near the arc, narrow strips are used in areas near the arc. Details of the Battelle analysis are reported in RSIC-820.⁽⁵¹²⁾ The welding Research Council Bulletin 149 describes some of the results of the Battelle study.⁽³⁰³⁾

The calculation starts on a strip some distance ahead of the welding arc where the temperature change is negligible and the stresses purely elastic. Time zero is fixed on the strip. For example, in the calculations shown later (Fig. 5.4 through 5.7), the heat source is located at $t = 9$ seconds. Since the welding speed in this particular case is 0.233 ips, or 14 ipm, the calculation starts at a strip 2.1 in. (0.233×9) ahead of the arc.

First, stresses in the strip crossing the origin, O , are calculated based on elasticity theory. Then stresses in the second strip are calculated by adding stresses caused by the temperature increment. In this case, analysis is made whether or not any plastic deformation has taken place. It is assumed that the stresses at a given point do not exceed the yield stress of the material at the temperature of that point. Similar analyses are conducted step by step on the strips following. In this way the stress distribution in the entire field can be determined.

Figures 5.4 through 5.7 show the results of one example. In this example, calculations were made under the following conditions:

- Aluminum alloy 2014-T6, $\frac{1}{4}$ in. (6.4 mm) thick.
- Plate width: 8 in. (200 mm).
- Welding current: 254 amp.
- Arc voltage: 10 v.
- Arc travel speed: 0.233 ips (14 ipm).
- Arc efficiency: estimated to be 80%.

Except for some lettering such as "Center Line", "1 inch (25 mm) out from Center Line", and "Edge" in Fig. 5.4 and "100°F", "200°F", etc., in Fig. 5.5, most of the lines and lettering in Fig. 5.4 through 5.7 were plotted by a Cal-Comp plotter.

Figure 5.4 shows the temperature changes along the weld center line ($y = 0$), $y = 1$ in. (25 mm), and $y = 4$ in. (100 mm). The abscissa is given in terms of time, and the arc is located at 9 seconds. Each curve shows the thermal cycle at a point some distance away from the weld.

Figure 5.5 shows the isotherm pattern around the arc. The longitudinal coordinate x is again the time scale.

Figure 5.6 shows stress changes along $y = 0$, 1 and 4 in. (0, 25, and 100 mm). Along the weld center line ($y = 0$), stresses are in compression in areas ahead of the arc. As the arc approaches the point and the temperature increases, the absolute value of the compressive stress first increases and then decreases. At the point directly below the arc, the stress is zero. As areas behind the arc cool, the stresses become tensile.

Figure 5.7 shows the isostress pattern around the arc. It is interesting that the high compressive stresses extending ahead of the arc and continuing along both sides form a horseshoe-shaped region.

5.3.2. *M.I.T. one-dimensional programs*

Initial effort. The Battelle program was first improved at M.I.T. in a study completed

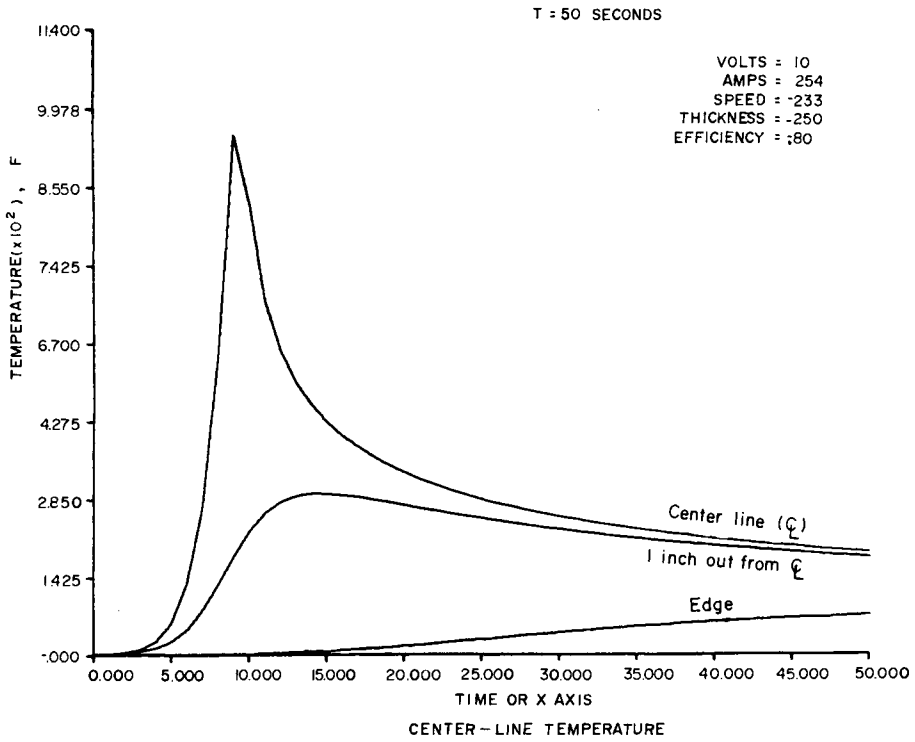


FIG. 5.4. Temperature changes along three longitudinal lines.^(303,512)

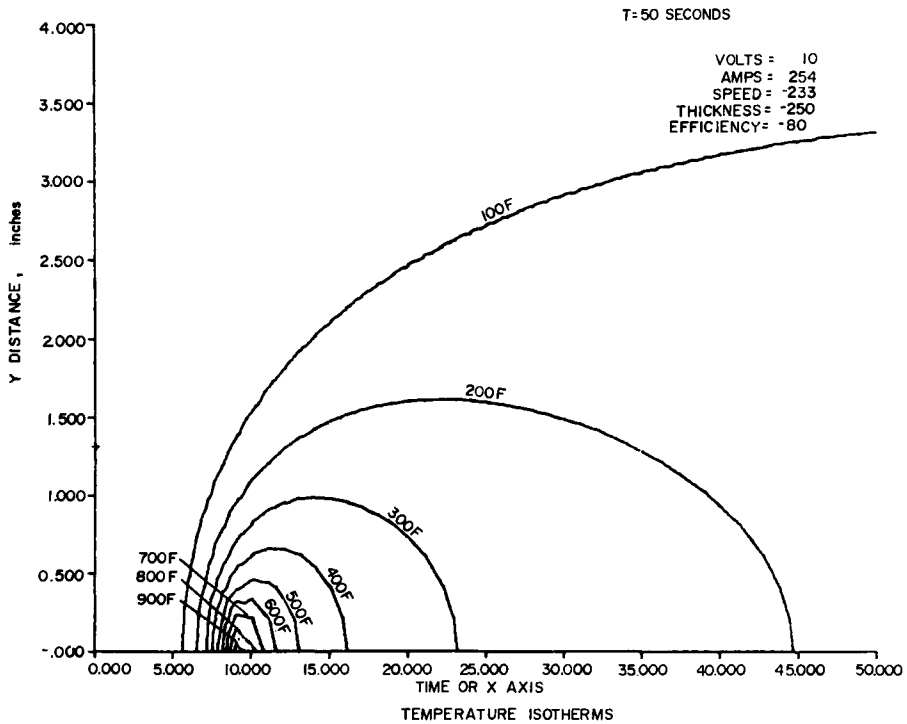


FIG. 5.5. Isotherm pattern around the moving arc.^(303,512)

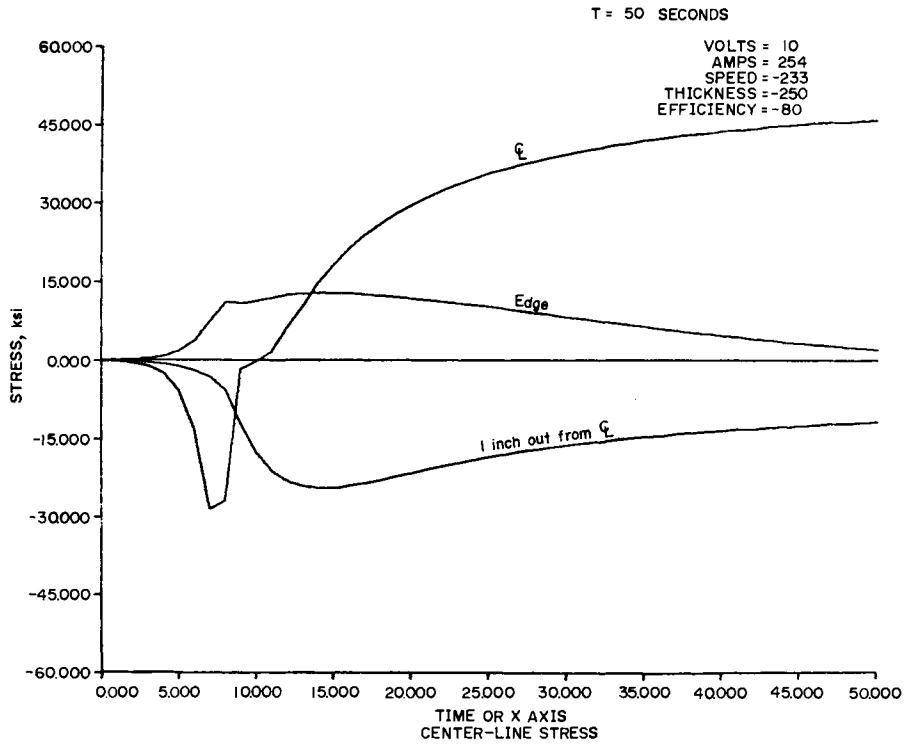


FIG. 5.6. Stress changes along three longitudinal lines.^(303,512)

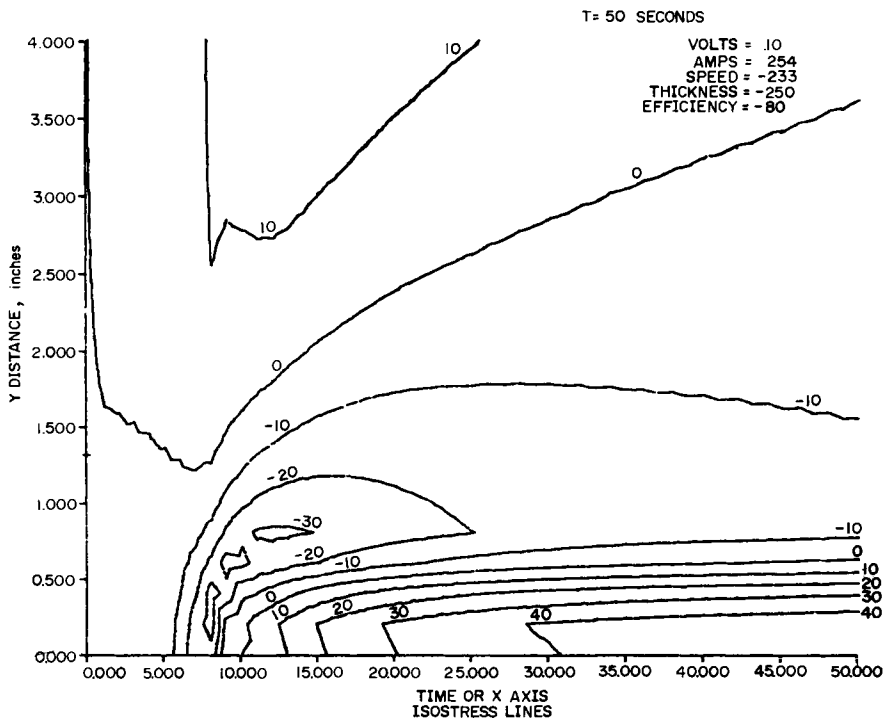
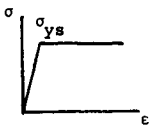
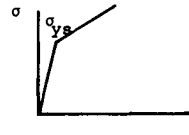


FIG. 5.7. Isostress pattern around the moving arc.^(303,512)

TABLE 5.1 Comparison between the Battelle and M.I.T. program

	Battelle Program	M.I.T. Program
Type of Weld Analyzed	Bead-on-plate	Bead-on-plate, Edge, and Butt weld
Configuration	Flat plate with finite width	Flat plate with finite width
Stress Analysis	Longitudinal stress only $\sigma_x = f(x,y)$ $\sigma_y = \tau_{xy} = 0$	Longitudinal stress only $\sigma_x = f(x,y)$ $\sigma_y = \tau_{xy} = 0$
Material Behavior	Perfectly plastic* 	Strain hardening (linear) included* 
Analysis of Strain	Not included	Includes total strain and plastic strain
Temperature distribution	Calculated by same program	Calculated by separate program. Distributions from other sources may be used for stress calculation

*Yield strength varies with temperature.

in 1970.⁽⁵²⁰⁾ Table 5.1 compares the Battelle program and the M.I.T. program. Although both are one-dimensional analyses, the M.I.T. program is an improved version of the Battelle program. For example, while the material is assumed to be perfectly plastic in the Battelle program, in the M.I.T. program strain hardening of the material is considered. In both programs the yield strength, σ_{ys} , changes with the temperature, but the M.I.T. program also includes the analysis of strain. This is important when comparing theoretical conclusions with experimental data, since strains rather than stresses are the measure in experimental analysis.

The M.I.T. program is written in FORTRAN IV for use on an IBM 360/65 computer. Details of the M.I.T. analysis, including the computer programs, are given in the NASA Contract Report CR-61351.⁽⁵²⁰⁾

Further developments. More recently the program has undergone further development and can now handle certain practical problems such as:

1. *Weld location.* The program can handle problems relating to welds made anywhere in the strip, i.e. center, edge, or a line at an arbitrary distance from the center line.
2. *Distortion analysis.* The program is capable of computing the transient distortion that occurs when the weld is not along the center line of the strip.
3. *Multipass effect.* The weld line often changes location during multipass welding.

The program can analyze the thermal stresses set up during multipass welding, including the effects of temperature changes and strains produced during preceding passes. Results can be printed out after several passes or after each pass.

Reference (211) contains in its appendix a brief description the one-dimensional program developed by Nishida.

5.4 Two-dimensional Analyses

In 1970 Iwaki⁽⁵²¹⁾ developed a two-dimensional finite-element program for the analysis of thermal stresses during bead-on-plate welding. This first effort, continued by Urushihara,⁽⁵²²⁾ was then significantly improved by Muraki who expanded the two-dimensional program so that thermal stresses during butt welding as well as those during bead-on-plate welding could be analyzed.⁽⁵²³⁾ During the first pass of butt welding, the boundary conditions near the welding arc change as the arc advances.

Toshioka^(254, 525) included the effects of metallurgical transformation on the transient thermal stresses during welding in the analysis. First the heat flow was analyzed. Then the material properties were determined using a continuous cooling transformation (CCT) diagram. Dimensional changes due to metallurgical transformation were considered in addition to the thermal strains.

The following pages describe the analyses developed by Muraki.⁽⁵²³⁾

5.4.1. Mathematical formulation⁽⁵²³⁾

Constitutive equations. The temperature dependency of both the material properties and the yield criterion is one of the most important elements in the analysis of thermal stresses. General constitutive equations are therefore provided for the analysis of thermal stresses. Generally speaking, the rate of strain is

$$\dot{\epsilon}_{ij} = \dot{\epsilon}_{ij}^{(e)} + \dot{\epsilon}_{ij}^{(p)} \quad (5.2)$$

where superscripts e and p refer to the elastic and plastic strains, respectively.

The rate of plastic strain is assumed to be

$$\dot{\epsilon}_{ij}^{(p)} = \Lambda \frac{\partial f}{\partial \sigma_{ij}} \quad (5.3)$$

where Λ, f , and σ_{ij} are the proportional constant, the yield function, and the stress component, respectively.

The yield function is assumed to be

$$f(\sigma_{ij}, \epsilon_{ij}^{(p)}, \kappa(\epsilon_{ij}^{(p)}), T) = 0 \quad (5.4)$$

where κ is the parameter related to the strain hardening of the material and T is the temperature.

After differentiating eqn. (5.4) and using the result with eqn. (5.3), the following relationship is obtained:

$$\dot{\epsilon}_{ij}^{(p)} = \hat{G} \left| \frac{\partial f}{\partial \sigma_{ij}} \frac{\partial f}{\partial \sigma_{kl}} \dot{\sigma}_{kl} + \frac{\partial f}{\partial \sigma_{ij}} \frac{\partial f}{\partial T} \dot{T} \right| \quad (5.5)$$

where

$$\hat{G} = - \frac{1}{\left(\frac{\partial f}{\partial \varepsilon_{ij}^{(p)}} + \frac{\partial f}{\partial \kappa} \frac{\partial \kappa}{\partial \varepsilon_{ij}^{(p)}} \right) \frac{\partial f}{\partial \sigma_{ij}}} \quad (5.6)$$

If von Mises' yield criterion is adopted, the temperature dependency can then be expressed

$$f = \bar{\sigma} - c(\varepsilon_{ij}^{(p)}, T) \quad (5.7)$$

where c is the parameter related to the strain hardening of the material and $\bar{\sigma}$ is defined as

$$\bar{\sigma} = \sqrt{\frac{3}{2}} \sqrt{\sigma'_{ij} \sigma'_{ij}} \quad (5.8)$$

where σ'_{ij} is the stress deviation.

Using eqn. (5.7), (5.6) becomes

$$\hat{G} = - \frac{1}{\frac{\partial f}{\partial \varepsilon_{ij}^{(p)}} \frac{\partial f}{\partial \sigma_{ij}}} \quad (5.9)$$

Here, introducing the rate of equivalent strain,

$$\dot{\bar{\varepsilon}}^{(p)} = \sqrt{\frac{2}{3}} \sqrt{\dot{\varepsilon}_{ij}^{(p)} \dot{\varepsilon}_{ij}^{(p)}} \quad (5.10)$$

and then, using eqns. (5.3) and (5.7), we have

$$1 = \frac{\partial f}{\partial \sigma_{ij}} \frac{\partial \bar{\varepsilon}^{(p)}}{\partial \varepsilon_{ij}^{(p)}} \quad (5.11)$$

Hence, eqn. (5.9) becomes

$$\hat{G} = - \frac{1}{\frac{\partial f}{\partial \varepsilon_{ij}^{(p)}} \frac{\partial \varepsilon_{ij}^{(p)}}{\partial \bar{\varepsilon}^{(p)}}} = \frac{1}{H'} \quad (5.12)$$

where

$$H' = - \frac{\partial f}{\partial \bar{\varepsilon}^{(p)}} \quad (5.13)$$

Finally, using eqns. (5.7), (5.8), and (5.12) the rate of plastic strain becomes

$$\dot{\varepsilon}_{ij}^{(p)} = \frac{1}{H'} \left(\frac{3\sigma'_{ij}}{2\bar{\sigma}} \frac{3\sigma'_{kl}}{2\bar{\sigma}} \dot{\sigma}_{kl} + \frac{3\sigma'_{ij}}{2\bar{\sigma}} \frac{\partial f}{\partial T} \dot{T} \right) \quad (5.14)$$

or

$$\dot{\varepsilon}_{ij}^{(p)} = \frac{1}{H'} \left(\frac{3\sigma'_{ij}}{2\bar{\sigma}} \dot{\bar{\sigma}} + \frac{3\sigma'_{ij}}{2\bar{\sigma}} \frac{\partial f}{\partial T} \dot{T} \right) \quad (5.15)$$

Equations (5.14) and (5.15) indicates that if the temperature dependency of the yield function is expressed as in eqn. (5.7), the effect of the temperature is indicated by an additional term in the well-known relationship between strain and stress rates. From the above derivation, it is also obvious that the more general relationship can be obtained if necessary.

For the elastic part, we have:

$$\dot{\varepsilon}_{ij}^{(e)} = \frac{1-2\nu}{E} \dot{\sigma} \delta_{ij} + \frac{\sigma'_{ij}}{2G} - \frac{1-2\nu}{E^2} \dot{E} \sigma \delta_{ij} - \frac{1}{2G^2} \dot{G} \sigma'_{ij} + \varepsilon^\theta \delta_{ij} \quad (5.16)$$

where σ and δ_{ij} are the average hydrostatic stress and Kronecker symbol, respectively. ν , E , and G are Poisson's ratio, Young's Modulus and shear modulus, respectively. ε^θ denotes the thermal strain caused by the temperature distribution.

Substituting eqns. (5.14) and (5.16) into eqn.(5.2), the total strain rate becomes

$$\dot{\varepsilon}_{ij} = \frac{1-2\nu}{E} \dot{\sigma} \delta_{ij} + \frac{\sigma'_{ij}}{2G} + \frac{3\sigma'_{ij}}{2\bar{\sigma}H'} \dot{\sigma} + \varepsilon^\theta \delta_{ij} - \frac{1-2\nu}{E^2} \dot{E} \sigma \delta_{ij} - \frac{1}{2G^2} \dot{G} \sigma'_{ij} + \frac{3\sigma'_{ij}}{2\bar{\sigma}H'} \frac{\partial f}{\partial T} \dot{T}. \quad (5.17)$$

The inverse relation of eqn. (5.19) becomes:

$$\dot{\sigma}_{ij} = \frac{E}{1-2\nu} \dot{\varepsilon} \delta_{ij} + 2G \dot{\varepsilon}_{ij} - \frac{3G\sigma'_{ij}\sigma'_{kl}\dot{\varepsilon}_{kl}}{\bar{\sigma}^2 \left(\frac{H'}{3G} + 1 \right)} + \dot{\sigma}_{ij}^\theta \quad (5.18)$$

where

$$\varepsilon = \frac{1}{3} \varepsilon_{ii}$$

$$\begin{aligned} \dot{\sigma}_{ij}^\theta = & -\frac{E}{1-2\nu} \varepsilon^\theta \delta_{ij} + \frac{\sigma}{E} \dot{E} \delta_{ij} + \frac{\sigma'_{ij}}{G} \left\{ 1 - \frac{1}{\left(\frac{H'}{3G} + 1 \right)} \right\} \dot{G} \\ & - \frac{3G\sigma'_{ij}}{\bar{\sigma}H'} \frac{\partial f}{\partial T} \left\{ 1 - \frac{1}{\left(\frac{H'}{3G} + 1 \right)} \right\} \dot{T} \end{aligned} \quad (5.19)$$

$\dot{\sigma}_{ij}^\theta$ consists of the terms related to the rate of thermal strain and the temperature dependency of the material properties and of the yield criterion.

If an element in question is plastic, the element takes one of the following states during the next time increment:

$$\begin{aligned} f = 0 \quad \dot{f}' < 0 & \quad (\text{unloading}), \\ f = 0 \quad \dot{f}' = 0 & \quad (\text{neutral}), \\ f = 0 \quad \dot{f}' > 0 & \quad (\text{loading}) \end{aligned} \quad (5.20)$$

where

$$\dot{f}' = \frac{\partial f}{\partial \sigma_{ij}} \dot{\sigma}_{ij} + \frac{\partial f}{\partial T} \dot{T}.$$

If the yield function does not move and does not change the size, the loading in the element does not occur. In other words, the unloading or neutral state is possible.

The temperature dependency of the material properties and of the yield criterion makes the above analysis complex.

Finite-element formulation. For the finite-element approach to plate-stretching problems, the principle of virtual work is most helpful, because it is easy to find displacement fields assumed in an element which satisfy the continuity of the fields along interelement boundaries.

The principle of virtual work is, in general,

$$\iiint_V \dot{\sigma}_{ij} \delta \dot{\epsilon}_{ij} dV - \iiint_V \dot{P}_i \delta \dot{u}_i dV - \iint_{S_1} \dot{F}_i \delta \dot{u}_i dS = 0 \quad (5.21)$$

where \dot{P}_i , \dot{F}_i , and \dot{u}_i are components of the body force, the surface force, and the displacement, respectively. The displacement fields in a basic triangular element are assumed to be

$$\begin{aligned} u &= \alpha_0 + \alpha_1 x + \alpha_2 y, \\ v &= \alpha_3 + \alpha_4 x + \alpha_5 y. \end{aligned} \quad (5.22)$$

Once the displacement fields are assumed, the derivation of a stiffness matrix and a load vector for an element is determined by using eqns. (5.18), (5.19), and (5.22). The final form of eqn. (5.21) is

$$\sum_{i=1}^N \delta \{\dot{q}\}^T [K] \{\dot{q}\} - \sum_{i=1}^N \delta \{\dot{q}\}^T \{\dot{F}_P\} - \sum_{i=1}^{N_1} \delta \{\dot{q}\}^T \{\dot{F}_F\} + \sum_{i=1}^N \delta \{\dot{q}\}^T \{\dot{F}_\theta\} = 0 \quad (5.23)$$

where \dot{q} = nodal displacement vector,

$[K]$ = stiffness matrix,

$\{\dot{F}_P\}$ = load vector due to the body forces,

$\{\dot{F}_F\}$ = load vector due to the surface forces,

$\{\dot{F}_\theta\}$ = load vector due to the thermal strain and the effect of temperature dependency on the material properties and the yield criterion,

N = total number of elements,

N_1 = total number of surfaces related to surface forces.

Equation (5.23) finally becomes:

$$[K] \{\dot{q}\} = \{\dot{F}\} \quad (5.24)$$

where subscript \sim refers to a whole body,

Equation (5.24) is valid for each load increment caused by body force, surface force, and other forces related to the thermal stresses and by the effect of the temperature dependency of the material properties and of the yield criterion.

5.4.2. Heat flow, boundary conditions and material properties

A thermal stress problem can be solved if the heat flow is known. Heat flow in a weldment may be expressed using an analytical solution, such as eqn. (2.16). Of course, the finite-element method can also be used for analyzing this heat flow. An important problem in the analysis of thermal stresses during welding is how to set up stress conditions in regions near the welding arc. In the analysis of thermal stresses during bead-on-plate welding, it was assumed that:

1. The molten zone is in a state of zero stress; stresses are zero in regions where temperatures exceed the melting temperature of the material.
2. The solidified material re-acquires its original material properties; the weld metal

temperatures below the melting temperature behaves the same as the original material at the corresponding temperatures. In the analysis of thermal stresses during butt welding, it was further assumed that:

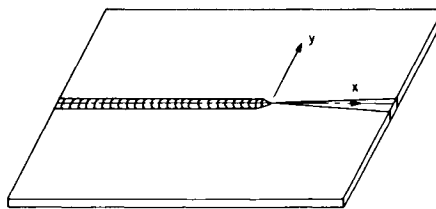
3. Except in regions where tack welds are made, the unwelded portion of the joint is in a stress-free condition. Consequently, as the welding arc advances, the stress state in regions near the welding arc changes from the free stress condition to the molten stage, and then back to the solidified stage.

Though the existing data on material properties at elevated temperatures, especially at temperatures near the melting point, is inadequate, no attempt has as yet been made at M.I.T. to experimentally refine this data. Table 5.2 lists some properties of Type 6061 aluminum alloy used by Bryan⁽⁵³²⁾ for his experimental study.

5.4.3 Plane stress and plane strain analyses

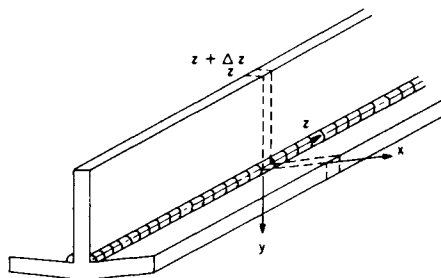
There are basically two types of two-dimensional analyses of thermal stresses during welding. They are plane stress and plane strain analyses.

A typical case of a two-dimensional plane stress condition is the stress field that is set off during the welding of a plate, as shown in Fig. 5.8. One of the above programs can analyze the transient stresses in any location on the plate, including the regions near the edges of the plate. However, it is assumed that the stresses are uniform in the thickness direction. In other words, σ_x , σ_y , and τ_{xy} are functions of x , y ; and $\sigma_z = \tau_{yz} = \tau_{zx} = 0$. This is the most basic of the programs.



Typical 2D Plane Stress Field --
Welding Plates

FIG. 5.8. Typical 2D plane stress field — welding plates.



Typical 2D Plane Strain Field -- Angular
Distortion of a Built-Up Beam

FIG. 5.9. Typical 2D plane strain field — angular distortion of a built-up beam.

Figure 5.9 shows a typical two-dimensional plane strain condition: the stress field in a cross-section of the central portion of long weldment. The weld line is in the z -direction. The stresses in cross-section z at time t are assumed to be the same as the stresses in cross-section $z + \Delta z$ at time $t + \Delta t$, provided that:

$$\Delta z = v \cdot \Delta t \quad (5.25)$$

where v = welding speed.

5.5 Analyses of Stresses in Three-dimensional Cases

Efforts have been made to extend the analysis into three dimensions, making it possible to treat such cases as cylindrical shells and heavy weldments. In fact, efforts are being continued rigorously.

5.5.1. Cylindrical shell

Muraki⁽⁵²⁶⁾ analyzed thermal stresses caused by an arc travelling along the girth of a thin cylindrical shell, as shown in Fig. 5.10. Further efforts are currently made.

5.5.2. Thick plate

Efforts have been made and are being continued to develop computer programs for analyzing thermal stresses during the welding of thick plates. An important problem here is cost. It is not only very expensive to develop a three-dimensional program in a true sense for analyzing thermal stresses during welding but also it is expensive to run it.

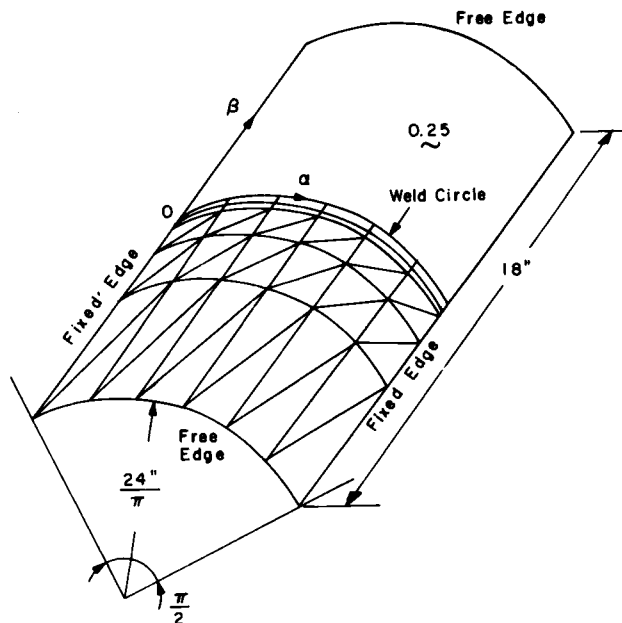


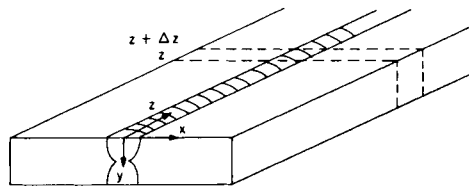
FIG. 5.10. Mesh pattern and main dimensions.

The one-dimensional welding thermal stress programs cost only a few dollars per calculation (computer cost only, not including labour cost). The present two-dimensional programs cost well over 100 dollars per calculation. Costs for running a three-dimensional program, under the present condition, would be thousands of dollars. Consequently major current efforts are being directed at determining how two-dimensional programs can be used for studying thermal stresses during welding heavy plates. When one examines the stress distribution in two cross-sections of a long weldment, z and $z + \Delta z$, the stress distributions prove to be similar, or

$$\frac{\partial \sigma}{\partial z} \ll \frac{\partial \sigma}{\partial x} \quad \text{and} \quad \frac{\partial \sigma}{\partial z} \ll \frac{\partial \sigma}{\partial y}.$$

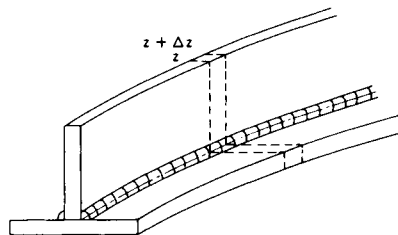
In other words, stress changes in the x -direction are much smaller than those in the y -direction and the z -direction. Under such conditions, the most important stress component σ_z , expressed as a function x and y . This is very similar to the one-dimensional analysis discussed earlier (Section 3.2). In the one-dimensional analysis the stress component parallel to the well line is analyzed as a function of the lateral distance from the weld. In this case, the longitudinal stress only is analyzed as a function lateral and thickness direction.

This type of analysis can be regarded as the first step toward the development of comprehensive analyses of stresses of the heavy weldments. In the first program developed, however, it was assumed that the plate surface does not bend during welding, as shown in Fig. 5.11. In the record program longitudinal distortion is included, as shown in Fig. 5.12.



Typical Case for 1D Analysis in Manual # 4 - Heavy Weldment

FIG. 5.11. Typical case for 1D analysis in manual—4-heavy weldment.



Typical Case for 1D Analysis Including -- Longitudinal Bending Distortion of a Built-Up Beam

FIG. 5.12. Typical case for 1D analysis including—longitudinal bending distortion of a built-up beam.

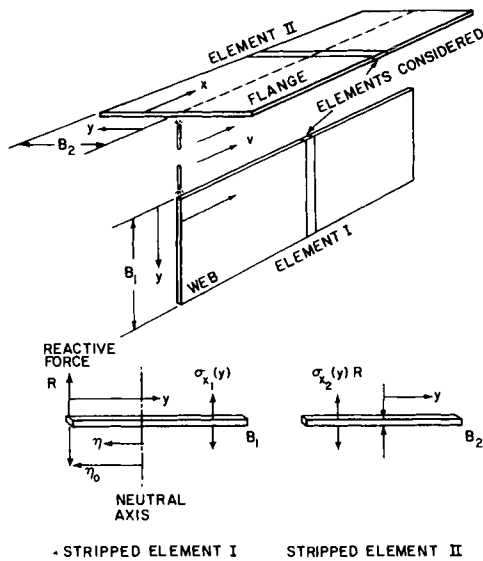


FIG. 5.13. Elements of T-shaped built-up beam.

5.5.3. Built-up beams

It is possible to develop a one-dimensional program to analyze the longitudinal distortion created during the welding of a built-up beam, as shown in Fig. 5.13. Nishida⁽⁵²⁷⁾ developed a one-dimensional program for analyzing the transient distortion of a T-beam, treating each element of the built-up beam separately. Details of the program are given in Nishida's thesis. It should be noted that the vertical reaction force between the members to be joined, R , must be determined. Once the transient thermal strains are calculated, it is then possible to calculate the transient deflections of the welded plates and built-up beams. Curvature, ρ , at a given time is:

$$\rho = \frac{d^2w(x)}{dx^2} \quad (5.26)$$

where w is the deflection in the y -direction at location x . The shape of deflection, w , can then be obtained by integrating the known ρ -curve twice along the x -direction.

The results were found to be greatly affected by the material properties at high temperatures. Nishida therefore suggested that precise values of high-temperature properties should be used in the calculation.

5.6 Experimental Studies on Thermal Stresses and Metal Movement

In studying the thermal stresses that occur during welding, it is important to compare any analytical predictions with experimental results. In a series of experiments conducted at M.I.T. on weldments in various materials and thickness, thermocouples were used to measure temperature changes and electrical resistance strain gages to measure strain changes.

Table 5.3 lists these experimental studies. Included here are (1) the names of the

TABLE 5.3 Past experimental studies on thermal stresses and metal movement during welding

No.	Principal personnel	Sponsor	Material, joint type, etc.
1.	Arita ⁽⁵²⁰⁾	NASA	Bead-on-plate welding of 2219-0 aluminum alloy plates (18 × 30 × ¼ in.) gas metal arc processes
2.	Klein ^(528, 529)	U.S. Navy	Multipass welding of butt welds (up to 1 in. thick and 20 passes) in several types of steel (low-carbon, HY-80, HY-130, and higher-strength steels), GMA
3.	Johnson ⁽⁵³⁰⁾	USCG	Strain changes during flame heating along a straight line of several steel plates
4.	Hirsch ⁽⁵³¹⁾	NASA	Bead on plate welding of columbium and tantalum sheets, 0.012 to 0.015 in. thick, gas tungsten-arc process
5.	Bryan ^(523, 532)	NASA	Bead on plate and butt welds in 6061-T6 aluminum alloy plates ¼ in. thick, GMA
6.	Yamamoto ^(211, 537)	NSF, WRC & a group of Japanese cos.	Welding along the longitudinal edge of rectangular plates, ½ in. thick, GMA and GTA
7.	Serotta ⁽⁵³⁴⁾	NSF, WRC & a group of Japanese cos.	Longitudinal distortion during welding along the longitudinal edge of rectangular plates and welding T-joints, steel, and aluminum
8.	Hwang ⁽⁵³⁵⁾	A group of Japanese cos. & NSRDC	Welding along the longitudinal edge of rectangular plates in low-carbon steel, quenched and tempered steels, stainless steel, and a titanium alloy

principal personnel involved (graduate students), (2) the names of the sponsors, and (3) the materials, joint types, and joining processes used. The experiments were conducted under the following conditions:

1. *Materials*: low-carbon steel, high-strength steels, stainless steel, aluminum alloys, titanium alloys, columbium and tantalum.
2. *Plate thickness*: 0.012 to 1 in (0.3 to 25 mm).
3. *Joint types and processes*: bead-on-plate and butt welds in single and multipasses (up to 20 passes); gas metal-arc and gas tungsten-arc as well as flame heating of plates.

Experimental results are available in various reports, theses, and papers.^(520, 523, 526 – 535)

After the analytical predictions had been compared with the experimental data, the following conclusions were drawn:

1. The one-dimensional program is sufficiently accurate in predicting longitudinal strains during bead-on-plate welding and butt welding. The experimental data and the analytical predictions were in close agreement in most of the materials studied, including low-carbon steel, stainless steel, aluminum, titanium, columbium, and tantalum.

2. During the welding of HY-130 steel, sudden changes in thermal strain were observed immediately following the passage of the welding arc.^(528, 529) It was also found that in HY-80 steel the experimental data did not closely agree with the analytical predictions. It has therefore been speculated that the effects of metallurgical transformation might be significant in the analysis of transient thermal strains. Results of a recent analysis that did take into consideration the effects of metallurgical transformation agreed closely with experimental data.

3. The two-dimensional, finite-element program is, of course, more versatile than the one-dimensional program. In an experiment on butt welds in aluminum, close agreement was obtained between analytical and experimental results on longitudinal strain and transverse strain as well as changes of the root gap.^(211, 537)

4. Insufficient agreement was obtained between experimental data on thermal strains during flame heating along a straight line and results predicted by the one-dimensional analysis. This is probably because even though the flame-heat source affects a large area, the analysis assumes a concentrated heat source. Experimentally determined thermal strains were almost as large as longitudinal strains. Consequently, a two-dimensional program is necessary when analyzing thermal stresses during flame heating, and no two-dimensional analysis has as yet been done on thermal stresses during flame heating.

In order to avoid an excessively lengthy discussion, this chapter simply presents the results of the two studies as follows:

1. Thermal stresses in weldments in high-strength steels.
2. Thermal stresses and metal movement during welding along the longitudinal edge of a strip in aluminum.

5.7 Experiments on Thermal Stresses in Weldments in High-strength Steels^{528, 529}

Experiments were conducted to measure the temperature and strain changes during welding. The experiments, supported by the U.S. Navy, were conducted by K. M. Klein^(528, 529) for his thesis work at M.I.T. The experiments were designed to approximate ship structural weldments in high-strength steels.

5.7.1. Specimens and experimental procedures

Bead-on-plate welds and butt joints were prepared in the following steel plates:

Low-carbon steel, $\frac{1}{4}$ in. (6.4 mm) thick.

HY-80 steel, $\frac{1}{4}$ in. and $\frac{3}{4}$ in. (6.4 and 19 mm) thick.

HY-130 steel, $\frac{3}{4}$ in. (19 mm) thick.

Experimental steel with 180,000 psi (127 kg/mm² or 1241 MN/m²) yield strength, 1 in. (25 mm) thick.

The specimens were 18 in. (460 mm) wide and 30 in. (760 mm) long. Table 5.4 shows the conditions under which these welds were made. The first two specimens (in low carbon steel and HY-80 steel) were bead-on-plate welds and were prepared in one pass. The other three specimens were butt joints welded in multipasses; in the case of one joint in an experimental high-strength steel with 180,000 psi (126.6 kg/mm² or 1.241 MN/n²) yield strength, 20 passes were used.

All the specimens were welded using a semi-automatic, gas metal-arc process with argon shielding.

Temperature changes during welding were measured by chromel/alumel thermocouples adhesive-bonded on the specimen surface. Strain changes were measured by electrical resistance wire strain gages mounted on the specimen surface. Rosette-type

TABLE 5.4 Welding conditions used

Test plate	Mild steel ^(a)	HY-80 ^(a)	HY-80	HY-130	180-ksi
Weld type	Bead-on-plate	Bead-on-plate	Butt joint	Butt joint	Butt joint
Process	GMA	GMA	GMA	GMA	GMA
Arc volts	30	30	28	28	28
Polarity	DCRP	DCRP	DCRP	DCRP	DCRP
Travel speed (ipm) ^b	24	24	15, 20	14	14
Heat input (kjoules/in)	21	21	32, 24	35	35
Filler wire	$\frac{1}{16}$ in. B-88	$\frac{1}{16}$ in. B-88	$\frac{1}{16}$ in. AIRCO 632	$\frac{1}{16}$ in. LINDE-140	$\frac{1}{16}$ in. LINDE-140
Shielding gas	Argon, 2% O	Argon, 2% O	Pure argon	Pure argon	Pure agron
No passes	1	1	18	8	20
Pre-heat and interpass temp.	70° F	70° F	125–150° F	125–150° F	125–150° F

^(a) Experiments were performed at the Portsmouth Naval Shipyard.

^(b) Travel speed was changed to 15 to 20 inches per minute after the third pass to improve weld appearance.

TABLE 5.5 Test geometry and sensor location, steel

TEST PLATE	MILD STEEL	HY - 50	HY - 80	HY-130	180 - ksi
LENGTH (in)	30	30	30	30	15
WIDTH (in)	18	18	18	18	16
THICKNESS (in)	0.25	0.25	0.75	0.75	1.0
BEVEL ANGLE	NONE	NONE	60°	45°	60°
ROOT GAP (in)	NONE	NONE	3/16	3/16	3/16
BACKING PLATE	NONE	NONE	$\frac{1}{4}$ - in. HY-80	$\frac{1}{4}$ - in. HY-80	$\frac{1}{4}$ - in. HY-80
CONSTRAINT	TACKED	TACKED	CLAMPED	CLAMPED	CLAMPED
SENSOR LOCATION AND ORIENTATION					

Note on sensor location and orientation: T = Thermocouple A-B-C= Strain gage rosette elements

The mild steel plate had a thermocouple and a strain gage rosette mounted on the back side of the plates opposite the one-inch-from-the-weld line location.

foil gages were used to determine the three strain components. Table 5.5 shows the test geometry and sensor locations. On the mild steel specimen, for example, the measurements were made on three locations as follows:

1. One inch (25 mm) from the weld line on the top surface.
2. One inch (25 mm) from the weld line on the bottom surface.
3. Two and a half inches (64 mm) from the weld line on the top surface.

On the other four specimens, measurements were made on the top surface only.

The measuring system used is shown in Fig. 4.20. Strain gage and thermocouple circuits were fed into a recorder. In the case of welding thermal strains, the resistance

change observed on a strain gage, ΔR , is composed of four elements, as shown in eqn. (4.10).

Computer programs were developed to process the large amount of data that was generated. For each set of temperature (T) and strain (ΔR) measurements, the mechanical strain ($\Delta R_1 + \Delta R_2$) had to be calculated. A computer program was developed to conduct the apparent strain corrections. Using another computer program, the three readings from the strain rosette were combined into principal strain readings using the Mohr's Circle model.

5.7.2. Experimental results

Figure 5.14 shows the weld cross-section and gage location for Test 1 (mild steel). Figure 5.15 shows the measured temperature and strain changes.

The plots are constructed on semilog scales. The horizontal axis is a log time scale, expressed in seconds. Zero time is an arbitrary point occurring some time after the arc has started. The point at which the arc is closest to the gage location is marked "Arc". The limiting time on the scale (10,000 seconds) is not meant to be taken literally, but represents a time in excess of several hours during which the plate reaches ambient (residual) conditions.

The vertical axis is a linear scale of both temperature and mechanical strain. In order to fit neatly on the same scale, both quantities are expressed in unusual terms. Temperature is plotted in degrees Fahrenheit, divided by 1000 and added to 1.0, as shown in Fig. 5.14. Thus, 1.250 indicates a temperature of 250°F (121°C). Mechanical strain is expressed in microstrain (10^{-6}) divided by 1000. Thus, a value of -1.0 read off the strain scale would indicate a compressive strain of 1000 microstrain or -10^{-3} .

The dotted points in Fig. 5.15 show the temperature and strain changes observed at points 1.0 in. (25 mm) from the weld line on the back surface of the plate. The temperature and strain changes observed on both surfaces coincided, indicating that the temperature and strain fields are two dimensional in regions as close as 1 in. (25 mm) from the weld.

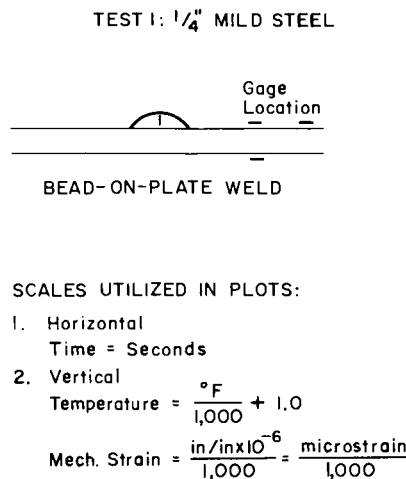


FIG. 5.14. Weld cross-section and gage location for Test 1, mild steel.

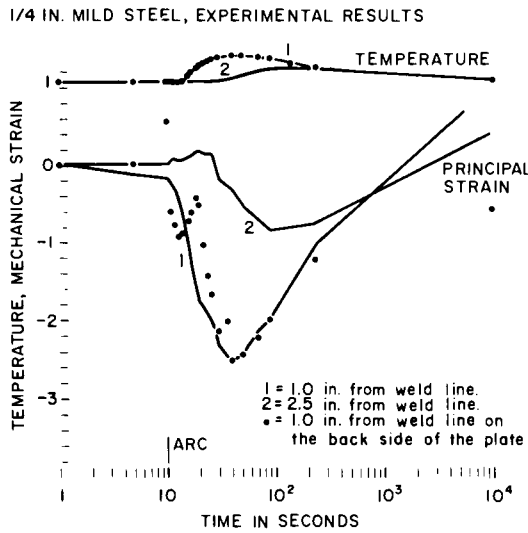


FIG. 5.15. Measured temperature and strain changes for Test 1, mild steel.

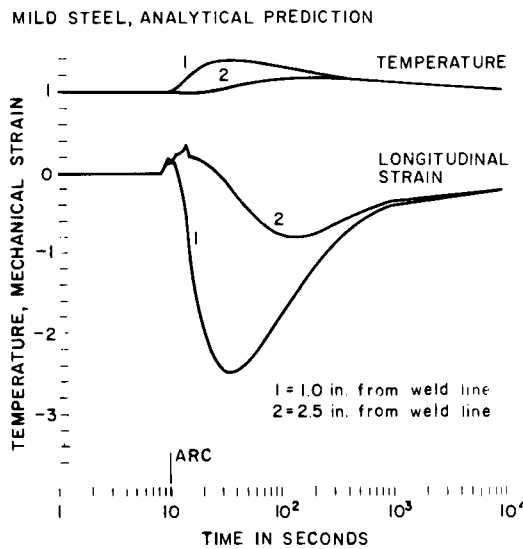


FIG. 5.16. Analytical predictions for Test 1, mild steel.

Figure 5.16 shows some analytical predictions calculated using the M.I.T. one-dimensional program. The analytical and experimental results were in close agreement. It must be noted that Fig. 5.16 shows ϵ_x assuming that $\sigma_y = \tau_{xy} = 0$, while Fig. 5.15 shows values of principal strains determined by the three strain components observed on a rosette gage. The fact that the results shown in Fig. 5.15 and 5.16 are in agreement indicates that the principal axis of thermal stress is approximately parallel to the weld line.

Results obtained on the other four specimens were similar. These 4 (HY-130 steel), Figs. 5.17, 5.18, and 5.19, involved a butt joint welded in 8 passes. Figure 5.18 shows the

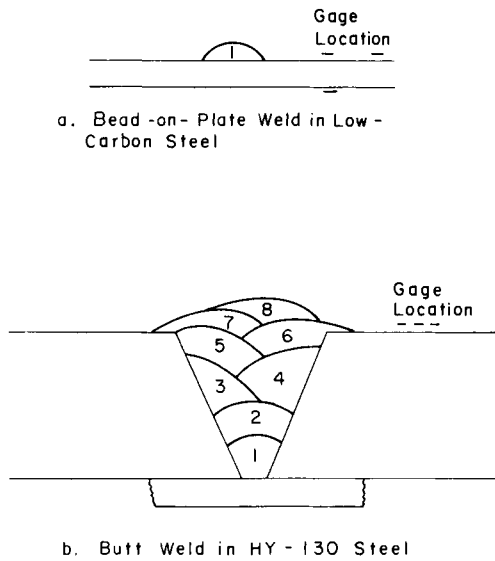


FIG. 5.17. Weld cross-section and gage location for Test 4, HY-130 steel.

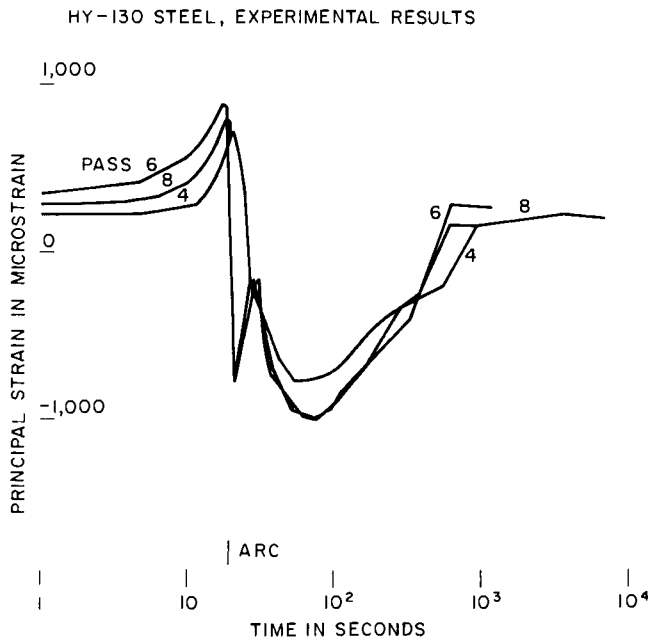


FIG. 5.18. Measured strain changes for Test 4, HY-130 steel.

weld cross-section and the locations of the gages. Figure 5.18 shows the measured strain changes observed 1 in. (25 mm) from the weld center line (plate thickness = $\frac{3}{4}$ in.) during the welding of passes # 4, # 6, and # 8. The largest strain changes were observed during the welding of pass # 6, which was closest to the gage location.

It should be noted that during multipass welding the base line value before each

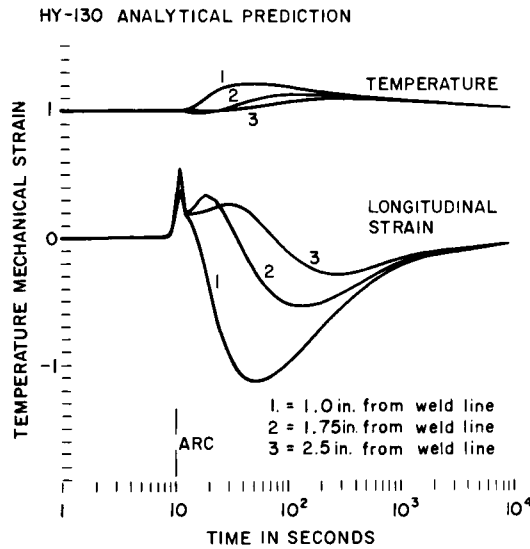


FIG. 5.19. Analytical prediction for Test 4, HY-130 steel.

welding pass changes, indicating the cumulative strain effects. In Fig. 5.18, for example, a considerable increase in the base line value was obtained between pass # 4 and pass # 6, indicating a build-up in residual stress. The reduction in the base-line value between pass # 6 and pass # 8 may reflect the partial stress-relieving effect of the additional pass at the top surface.

Figure 5.19 shows some analytical predictions for Test 4 at three locations: 1.0, 1.75, and 2.5 in. (25, 45, and 65 mm) from the weld center line. The characteristics of curve 1 in Fig. 5.19 are similar to those of the data shown in Fig. 5.18. However, the observed strain values were somewhat smaller than the analytically predicted ones. It was generally observed that the thermal strain response of thick section plates to a single pass weld is slightly less than the response of thin section plates under the same conditions.

Comparisons between experimental and analytical results were conducted for the five tests performed. The experimental and analytical results agreed as far as the general trends in strain changes were concerned. However, a close examination revealed a considerable difference between the experimental and analytical results as far as thermal strains in regions near the welding arc were concerned. Two major reasons for this discrepancy were:

1. The analysis does not produce accurate results near the welding arc where the strain field is not one dimensional.
2. Phenomena other than ordinary plastic deformation need to be considered; the deformation due to solid-state transformation during the welding of quenched-and-tempered steels, for example.

Further studies are needed to clarify these points. It was noticed that strains observed on weldments during the experiments decreased as the strength level of the base metal increased. Figure 5.20 shows how the maximum mechanical strain observed at the location 1 in. (25 mm) from the weld center decreases as the yield strength of the base

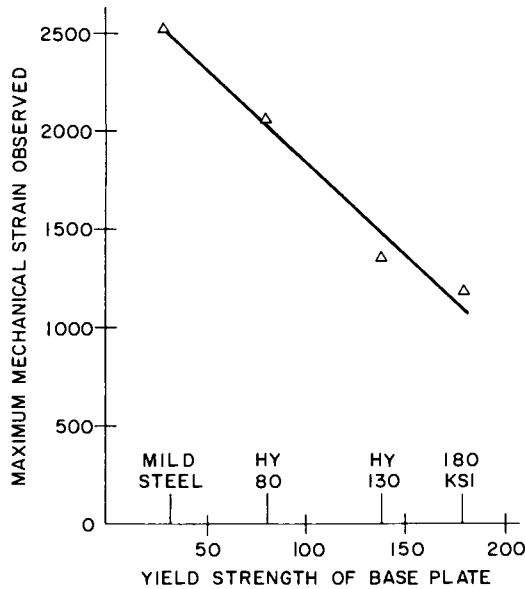


FIG. 5.20. Maximum mechanical strains observed at locations 1 inch from weld line (micro-inches per inch) versus yield strength (ksi) of the base plate.

metal increases. The strain response is roughly proportional to the inverse of the plate strength.

This phenomenon can be explained by noting that of the parameters directly affecting thermal strains, only the yield strength changed significantly in these experiments (the same can also be said of most production welds). Young's modulus, thermal expansion and conductivity coefficients, density, as well as welding heat input varied only slightly while the base metal strength increased 600%. As a result, only a very narrow zone on the high-strength steel specimens yielded plastically and the strains observed outside that zone were proportionally small. Several other investigators have reported that residual stresses in weldments in high-strength steels are not as high as the yield stress of the base metal. This subject will be discussed in detail in Chapter 6.

5.7.3. *Conclusions of the study*

Important conclusions of this study are as follows:

1. The weld analysis computer programs developed at M.I.T. are useful for studying thermal stresses in butt joints in high-strength steels for marine applications. In fact, without the analytical program it is rather difficult to understand what goes on during welding. The programs can also be used to study welding parameter variations on thermal strains during welding and residual stresses.

2. The thermal strain response of thick section plates to a single weld pass is slightly less than the response of thin section plates under the same conditions. Multiple passes, however, produce cumulative strain effects, especially during the first few passes. Little or no accumulation is noted in later passes.

3. At a finite distance from the weld line, maximum mechanical strains caused by the welding arc are roughly proportional to the inverse of base plate yield strength.

4. In certain ultra-high-strength steels, the passage of the welding arc produces an unusually large strain response, possibly linked to phase transformation during cooling.

5. Except in the immediate area of the welding arc itself, the longitudinal strain predominates over the transverse and shear strains. Near the arc, the strain field is complex and rapidly changing.

5.8 Experiments on Thermal Stresses and Metal Movement During Welding Along the Longitudinal Edge of a Strip

The analysis of thermal stresses and metal movement involves several steps:

1. Heat flow.
2. Transient thermal strains (and stresses).
3. Transient metal movement or distortion.
4. Residual stresses and distortion after welding is completed.

Before techniques for the computer simulation of thermal stresses and metal movement can be developed, analytical predictions must agree with experimental data in all four areas and, although a number of studies have been done with this in mind, few of them so far have produced a complete set of data. We felt that, in order to lay a solid foundation, a set of data should be generated on a simple, fundamental weldment: a weld along the edge of a rectangular strip.

It was decided that welds would be made under two conditions: with weld metal and without weld metal (or simple heating by a tungsten arc). The difference between the two sets of data should indicate how the weld metal influences the stress field. So far experiments have been conducted on the following materials:

- Low carbon steel.
- Quenched-and-tempered steel.
- Stainless steel.
- Aluminum alloy.
- Titanium alloy.

Data obtained on these materials should provide information on how different materials behave during welding. In the case of quenched-and-tempered steel, the role of phase transformation in thermal stresses during welding is an especially important consideration. The following pages present the results obtained on the aluminum specimen welded using the gas-metal-arc process.

5.8.1. Specimen and experimental procedure⁽²¹¹⁾

Figure 5.21 shows the specimen geometry and locations of thermocouples and strain gages. The specimen was 6 in. (152 mm) wide, 48 in. (1220 mm) long, and $\frac{1}{2}$ in. (12.5 mm) thick. The material was 5052-H32 aluminum alloy. Six strain gages $\frac{1}{4}$ in. (6.4 mm) gage length) were placed at distances 1.5, 3.0, 4.5, and 5.7 in. (38, 76, 114, and 145 mm) from the plate edge to be welded. Single-direction gages were used, because we were primarily interested in measuring longitudinal strains. Four thermocouples (chromel/alumel) also were mounted at distances of 0.5, 1.5, 3.0, and 5.7 in. (12.5, 38, 76, and 145 mm). To determine the maximum temperatures attained during welding at various locations, a

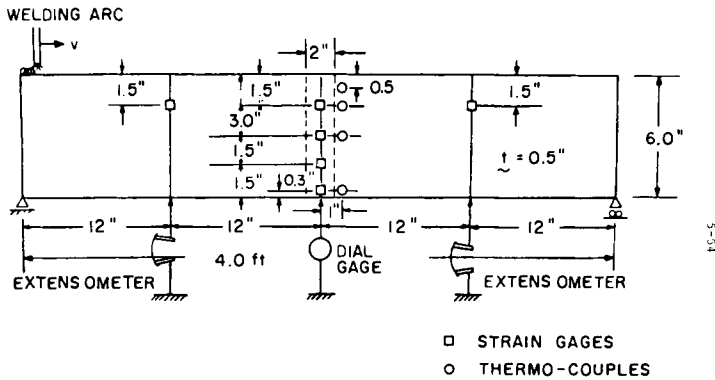


FIG. 5.21. Specimen and locations of strain gages, thermocouples, and devices for measuring distortion.

portion of the specimen surface was painted with a series of temperature-sensitive paints with different index temperatures.

The specimen was positioned vertically and supported at both ends of the lower edge. Welding was done along the upper edge. A dial gage (placed at midlength) and two extensimeters (placed at 12 in. (305 mm) from both ends) were used to measure transient deformation of the specimen during welding. The specimen was made much longer than its width in order to produce large amounts of distortion.

After welding was completed and the specimen cooled to room temperature, five additional strain gages were mounted along the midlength on both surfaces of the specimen to measure residual stresses. This time rosette gages were used to determine longitudinal stresses. A strip 2 in. (50 mm) wide, as shown by the broken lines in Fig. 5.21, was removed from the specimen with a saw. Amounts of strain relaxation were measured and residual stresses were determined.

5.8.2 Experimental results

Table 5.6 lists welding conditions for the gas metal-arc-welded specimen.

Figure 5.22 shows temperature changes observed at the four thermocouples. The arc passed the midlength of the specimen 83 seconds after the welding was begun, and completed the pass in 166 seconds.

Figure 5.23 shows the distribution of the maximum temperatures attained during welding.

TABLE 5.6 Welding conditions for gas metal-arc process

Welding current, I	260 amperes
Arc voltage, V	23 volts
Arc travel speed, v	0.289 in./sec (17.3 in./min)
Total time of welding	166 sec
Heat input, $h = \frac{I \cdot V}{v}$	20,700 joules/in.
Filler wire	4043, $\frac{1}{16}$ in. ϕ
Wire feed speed	400 in./min
Shielding gas	Argon

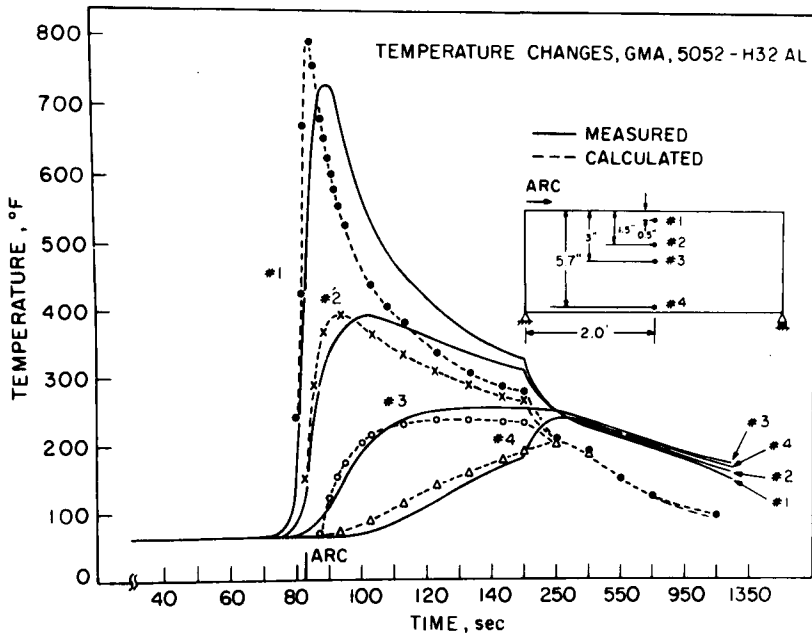


FIG. 5.22. Temperature changes at four locations during welding (note that different time scales are used after 150 seconds).

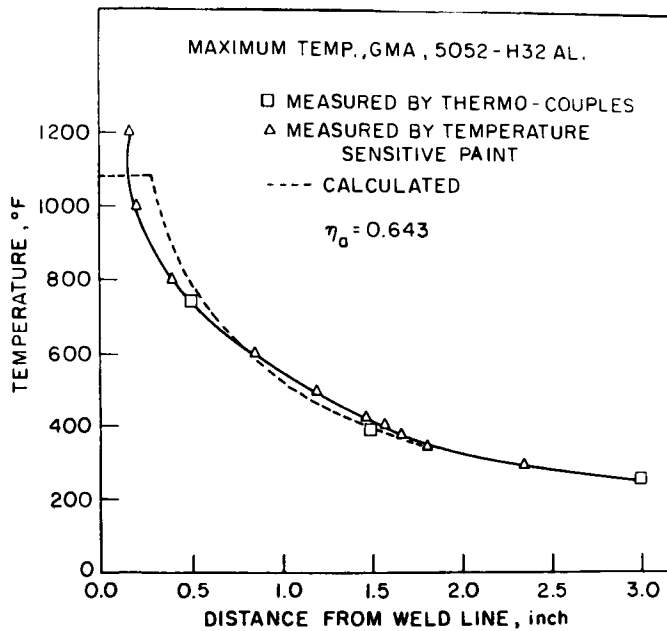


FIG. 5.23. Maximum temperature attained during welding.

Figure 5.24 shows the changes of longitudinal strains observed using four strain gages mounted along the midlength. On gage # 1, located 1.5 in. (38 mm) from the weld line, compressive strains were produced when the welding arc approached the gage, and strains later changed to tensile. Strains observed on gage # 4 underwent rather complex changes during welding and became compressive after the specimen cooled to room temperature.

Figure 5.25 shows the changes of deflection at midlength. During the early stages of

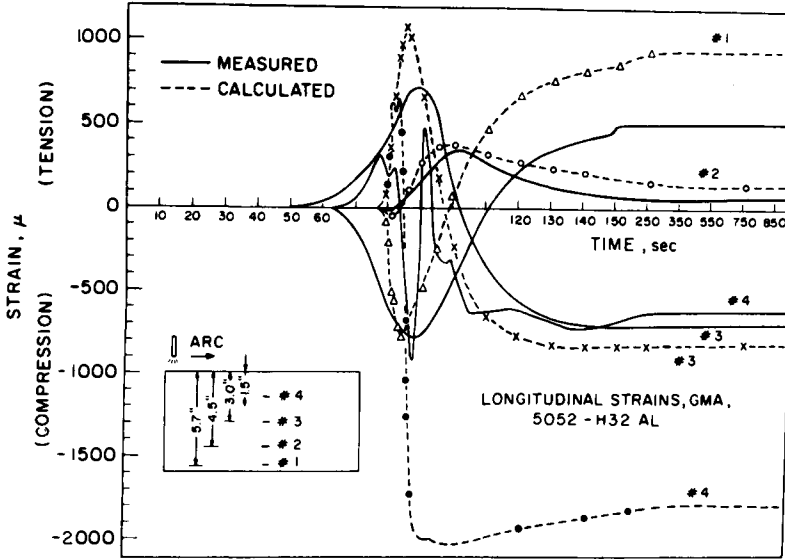


FIG. 5.24. Longitudinal strains observed at different locations during welding.

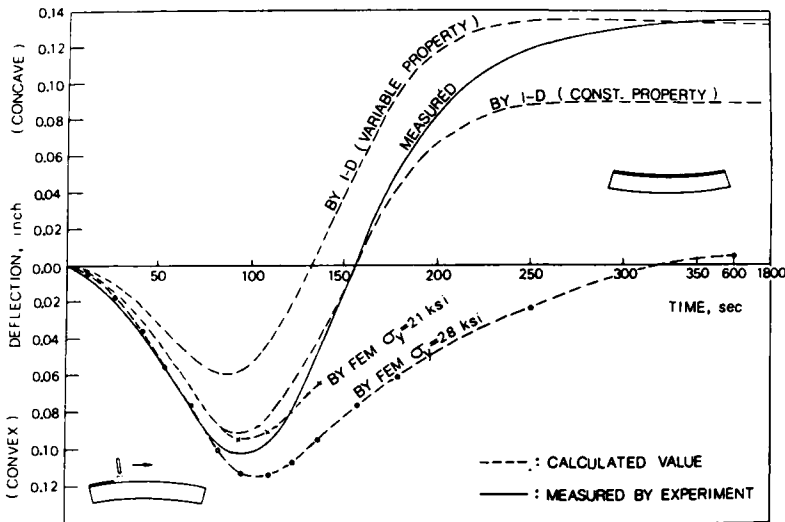


FIG. 5.25. Changes of deflection during welding.

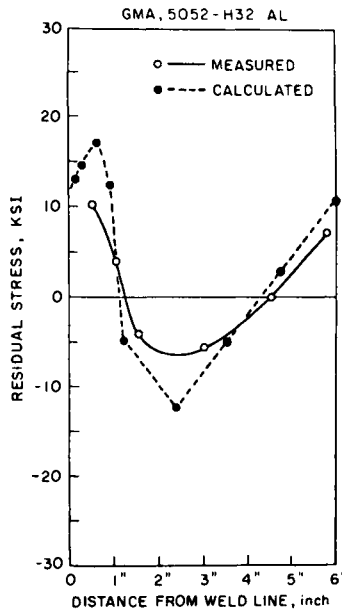


FIG. 5.26. Residual stresses along midlength section.

welding, the upper edge being welded expands and the central portion of the specimen moves upward. This distortion is written as negative in Fig. 5.25. As the specimen cools down and the weld metal shrinks along the entire weld length, the direction of deflection changes. At about the time when welding was completed (166 seconds), the specimen was virtually without distortion. This phenomenon suggests that a method of reducing distortion could be devised.

Figure 5.26 shows the distribution of longitudinal residual stress, σ_x , along the midlength section. The stress distribution can be interpreted as a combination of:

1. The shrinkage of the weld which causes high tensile residual stress in regions near the weld and moderately low compressive stresses in regions away from the weld.
2. The shrinkage of the weld along the edge which causes a bending distortion resulting in compressive stresses in regions between the neutral axis and the weld line and tensile stresses in regions outside the neutral axis.

As a result, tensile stresses are produced in regions near the weld, but their values are considerably lower than the yield stress of the material at room temperature. Compressive stresses are produced in regions near the neutral axis. The tensile stresses in regions near the unwelded edge are caused by bending distortion.

5.8.3 Analysis of heat flow

In order to analyze thermal stresses and metal movement during welding, it is first necessary to analyze heat flow during welding. In fact, it is very important to conduct an accurate analysis of heat flow in order to accurately measure the thermal strains and the resulting distortion.

Chapter 2 discusses heat flow in weldments. As stated in Section 2.2.1, a basic problem

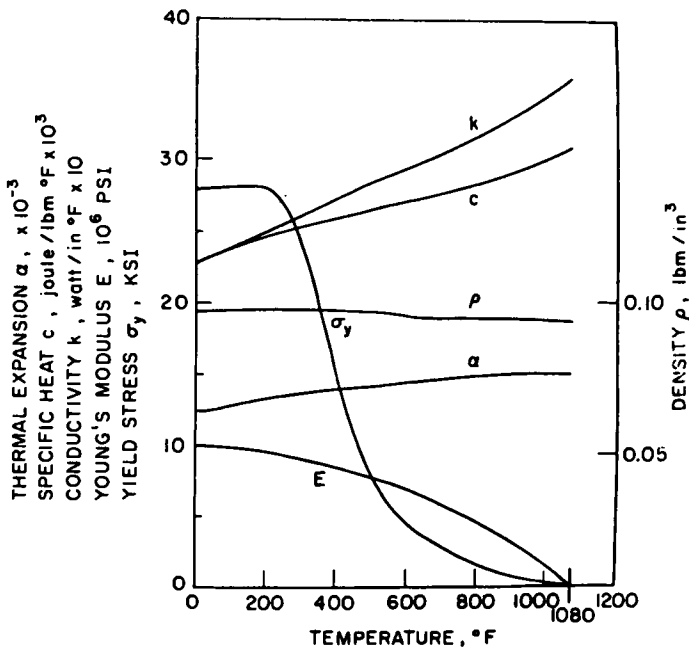


FIG. 5.27. Material properties vs. temperature of 5052-H32 aluminum alloy.⁽³⁹⁾

in the analysis of heat flow during welding is how to take into account those material properties that change as the temperature changes. Figure 5.27 shows how physical and mechanical properties of 5052-H32 aluminum alloy change with the temperature.⁽⁵³⁶⁾

If we treat the thermal properties of the material as temperature dependent, the basic equation of heat flow becomes non-linear. On the other hand, if we treat them as temperature independent, the basic equation of heat flow remains linear. In order to avoid the mathematical complexity involved in solving non-linear equations, almost all of the analyses on heat flow during welding, even those that have employed computers, have used linear equations.

Through experience over a number of years, M.I.T. researchers have found that reasonably accurate results can be obtained by employing the following method:

1. Ordinary linear solutions are used, such as those developed by Rosenthal and others (see Section 2.3).
2. But through the use of an iteration technique, different thermal properties are assigned, depending upon the temperatures of the locations being studied. For example, in the analysis of the experimental data shown in Fig. 5.24 temperatures were first calculated using thermal properties at 500°F (260°C). If the temperature calculated was different from 500°F (260°C), properties of that temperature were used. This iteration was continued until the temperature calculated was within $\pm 0.5^\circ\text{F}$ of the temperature of the properties used.

How to determine the value of arc efficiency, η_a , is an important practical problem in the analysis of heat flow. According to the literature, the thermal efficiency of a gas-

metal-arc ranges from 60 to 70%.[†] By comparing the experimental data with the analytical results, the thermal efficiency of the arc used in this experiment was determined to be 64.3%, or $\eta_a = 0.643$.

Figure 5.22 shows that the calculated temperature changes agreed reasonably well with the experimental data. Figure 5.23 shows that the calculated maximum temperatures attained during welding at various distances from the weld line also agreed with experimental results determined by thermocouples and temperature-sensitive paints.

A simple experiment using temperature-sensitive paint often proves to be very useful in practical applications of computer analysis, because:

1. By comparing experimental and analytical results, one can determine the arc efficiency in a particular experiment.
2. By comparing experimental and analytical results, one can evaluate the accuracy of the heat-flow analysis being employed. If necessary, one can even modify the analysis in order to improve the accuracy.

5.8.4 Analysis of thermal stresses and metal movement

The primary objective of this study is to develop an analytical technique to simulate the deflection that occurs during the welding of a long strip, as shown in Fig. 5.28. The stress field in the specimen can be measured using a one-dimensional analysis. Except in areas near the moving arc, stress changes in the longitudinal direction are always much less than those in the transverse direction, or $\partial\sigma/\partial x \ll \partial\sigma/\partial y$. Consequently, the analysis was conducted mainly by a 1-D program.

One-dimensional analysis. Since the subject of the experiment is a single-pass weld, the program used is basically the same as that described in the NASA Contractor Report CR-61351.⁽⁵²⁰⁾

Figures 5.24, 5.25, and 5.26 show transient thermal strains, transient deflection, and residual stresses in the midlength section, respectively. In the computation, material properties were changed according to the temperature. The analytical predictions were

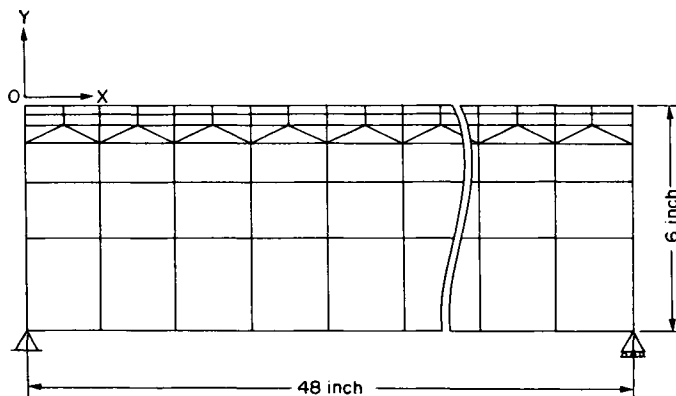


FIG. 5.28. Finite-element mesh pattern and coordinate system.

[†] See Section 2.1.

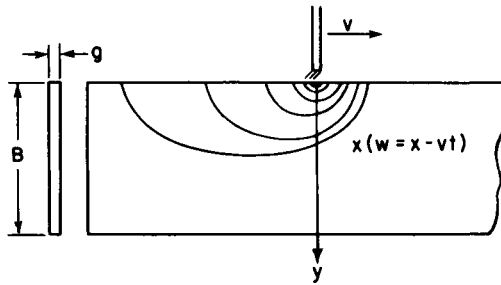


FIG. 5.29. Coordinate system.

in fairly close agreement with the experimental data, except in the case of transient thermal strains on gage # 4 (Fig. 5.24).[†]

Two-dimensional analysis. A limited study was done to develop a means of computing metal movement using the 2-D finite element program. The analysis is described in a paper by Muraki *et al.*⁽⁵²³⁾ presented in the *Journal of Engineering Materials and Technology*. Figure 5.29 shows the finite element mesh pattern and coordinates used.

Figure 5.25 includes two curves of transient deflection calculated by the 2-D, FEM program. In one calculation, it was assumed that all regions in the specimen would retain the yield stress at room temperature, $\sigma_{ys} = 28,000$ psi (19.7 kg/mm² or 193 MN/m²). In welding, however, temperatures in regions near the weld are considerably higher than room temperature. To compensate for this effect in the second calculation $\sigma_{ys} = 21,000$ psi (14.8 kg/mm² or 145 MN/m²) was assumed, and the results were in reasonably close agreement with the experimental data.

The calculations were continued, using 20 minutes of computer time. Although the results shown in Fig. 5.25 indicate that a close agreement could be obtained by using different material property data for each temperature, no further computation was made in this case. We are continuing efforts for developing an analysis which provides an accurate results with a minimum cost.

5.9 Computer Simulation

Once it is proved that the analytical models are reasonably accurate it is possible to simulate thermal stresses and metal movement by computer. Since the one-dimensional program is relatively inexpensive, it can be used in various ways. The following pages present two sets of analyses:

1. The effects of welding parameters on thermal stresses and the resulting residual stresses in aluminum welds.
2. The effects of welding parameters on the longitudinal distortion that takes place due to the edge welding of a strip.

5.9.1 *Effects of welding parameters on thermal stresses and the resulting residual stresses*

This topic was studied by Arita in welds made in 2219-0 aluminum alloy. The study was to supplement the experimental investigation.

[†] The reason for the disagreement with the data on gage # 4 is unknown. On the gas tungsten-arc specimens, all four gages were in close agreement.

TABLE 5.7 Welding parameters used in the analysis

Case number	Arc travel speed, v		Linear net heat input, $h^{(a)}$ joules/in. ²	Linear net heat intensity, $q^{(a)}$ joules/sec/in.
	in./min	in./sec		
1	5	0.0833	10,000	833
2	5	0.0833	32,000	2667
3	5	0.0833	56,000	4666
4	5	0.0833	80,000	6667
5	10	0.1667	10,000	1667
6	10	0.1667	32,000	5333
7	10	0.1667	56,000	9333
8	10	0.1667	80,000	13,333
9	20	0.333	10,000	3333
10	20	0.333	32,000	10,667
11	20	0.333	56,000	18,667
12	20	0.333	80,000	26,667
13	30	0.500	10,000	5000
14	30	0.500	32,000	16,000
15	30	0.500	56,000	28,000
16	30	0.500	80,000	40,000

^(a) Values of h and q are actual values supplied to the plate.

Welding parameters used in the analysis. Table 5.7 shows values of welding parameters used in the sixteen cases studied. The definitions of linear net heat input, h , and linear net heat intensity, q , are:

$$h = H/T \quad q = Q/T \quad H = Q/v \tag{5.27}$$

where $Q = \eta_a V.I$ thermal power of heat source in watts or joules/second,

- η_a = arc efficiency,
- V = arc voltage, volts,
- I = arc current, amperes,
- v = welding speed, in./sec
- T = plate thickness, in.,

From the definitions, q is the intensity of a line heat source, or the average value of the intensity of the heat source in the thickness direction; therefore, q is called the “linear net heat intensity”. The value h is the net heat input supplied to a unit plate thickness; therefore, it is called the “linear net heat input”.

As shown in Table 5.7, welding speed v was set at four levels: 5, 10, 20, and 30 in./min (12.7, 25.4, 50.8, and 76.2 mm/min) or 0.0833, 0.1667, 0.333, and 0.500 in./min (2.12, 4.23, 8.46, and 12.7 mm/sec). Linear net heat input h was also set at four levels: 10,000, 32,000, 56,000, and 80,000 joules/in. (1550, 4960, 8680, and 12,400) joules/cm/cm). When the value of arc efficiency was 0.7, for example, these net heat input values corresponded to 14,300, 45,700, 80,000, and 114,000 joules/in./in. (2220, 7085, 8680, and 17670 joules/cm/cm) respectively.

It must be mentioned that the linear net heat input, h , and the welding speed, v , are not independent, as shown from eqn. (5.31). For example, when v is increased to $2v$, while q is unchanged, h will be reduced to $\frac{1}{2}h$. Figure 5.30 shows the welding parameters used for the sixteen conditions studied. The value of the linear net heat intensity q was

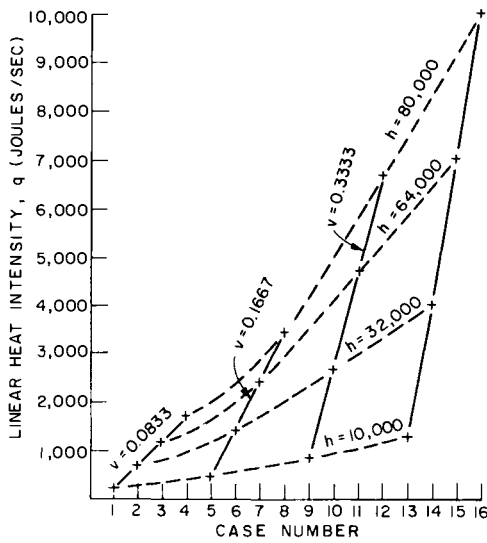


FIG. 5.30. Welding parameters used for the sixteen conditions studied.

lowest in case 1 with a low heat input and welding speed, and the highest in case 16 with a high heat input and welding speed.

All calculations were done on a bead-on-plate weld along the longitudinal center line of a infinitely long strip, 18 in. wide.

Results of the analysis. The analysis included the effects of welding parameters on:

1. High tensile thermal stresses in regions behind the arc.
2. Compressive thermal stresses in regions ahead of the arc.
3. Size of plastic zone.
4. Residual stress distributions.[†]

The following pages discuss how welding parameters affect residual stress distributions.

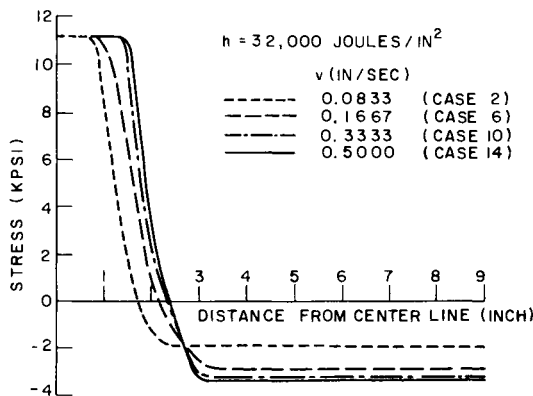


FIG. 5.31. Distributions of longitudinal residual stresses for cases 2, 6, 10, and 14 ($h = 32,000$ joules/in²).

[†] See Hill⁽⁵³⁷⁾ for a study of residual stresses in weldments in aluminum alloys.

Figure 5.31 shows the distributions of longitudinal residual stresses for cases 2, 6, 10, and 14 ($h = 32,000$ joules/in²). High tensile stresses are produced in areas near the weld, and compressive stresses are produced in areas a certain distance from the weld. The maximum residual stress at the weld center line is about 11,000 psi, which is also the yield stress level at room temperature, regardless of welding conditions.[†]

The width of this tensile residual stress zone is affected by the welding parameters. In the case shown in Fig. 5.31, for example, the width of the tensile stress zone increased as the welding speed increased, though the linear heat input, h , was constant.

Figure 5.32 shows the half width of the tensile residual stress zone as affected by the

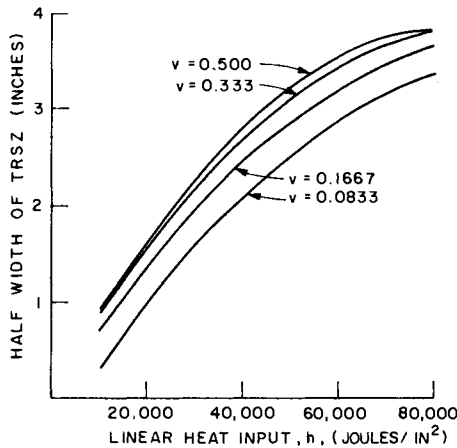


FIG. 5.32. Effects of linear heat input, h , and welding speed, v , on the width of tensile residual stress zone.

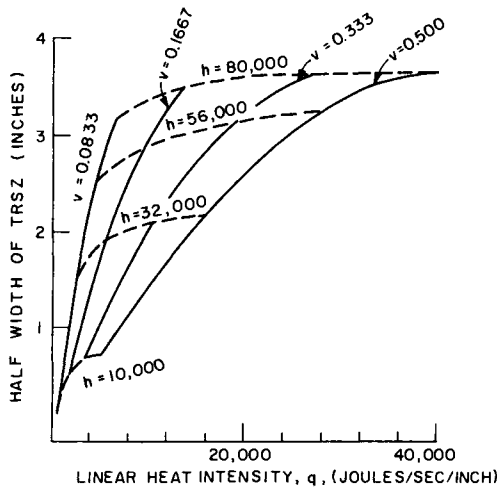


FIG. 5.33. Effects of linear heat intensity, q , and welding speed, v , on the width of tensile residual stress zone.

[†] *Reminder:* The results shown in Fig. 5.31 are analytical. Some experiments have produced residual stresses lower than the room-temperature yield strength.

linear net heat input, h , and the welding speed, v ; while Fig. 5.33 shows the half-width of the tensile residual stress zone as affected by the linear net heat intensity, q , and the welding speed, v .

Figures 5.32 and 5.33 show that the linear net heat input, h , is the most significant factor affecting the width of the tensile residual stress zone, which increases with an increasing heat input. The effect of heat input, however, is not linear. The increase in the width of the tensile residual stress zone per unit increase in the heat input decreases as the heat input increases.

From the practical viewpoint, the results clearly show the advantage of using a low welding heat input to reduce residual stresses and distortion.

5.9.2 *Effects of welding parameters on longitudinal distortion*

Nishida⁽⁵²⁷⁾ studied how welding conditions and specimen geometry affect thermal strains and metal movement.⁽²¹¹⁾ The specimen studied was the rectangular plate shown in Fig. 5.21 welded under the following conditions (see Table 5.6):

Welding current, $I = 260$ amperes

Arc voltage, $V = 23$ volts

Welding speed, $v = 0.289$ in./sec (7.34 mm/sec)

Heat input, $h = \frac{IV}{v} = 20,700$ joules/in. (8150 joules/cm)

A series of computations were made to find out how distortion changed when welding speed, v , and the specimen width, B (see Fig. 5.25), were changed. Computations were made under forty-two different conditions:

$v = 0.072, 0.144, 0.217, 0.289, 0.361, 0.433, 0.506$ in/sec.

$B = 3.0, 4.5, 6.0, 7.5, 9.0, 10.5$ in.

The welding speed, v , was changed each time so that the value of the heat input, h , would remain the same, allowing the amount of weld metal per unit weld length (the cross-section of the weld metal) to remain approximately the same. In other words, when the speed was increased, the welding current was also increased proportionally. In addition, limited calculations were made by changing the welding speed while welding current I and arc voltage V were kept unchanged.

Some of these combinations of welding conditions would make it impossible to produce welds with an acceptable appearance and/or quality, but these practical considerations were not a part of this analysis.

Computations were made of temperature, thermal strain, and transient deflection. The total cost of computation for all forty-two conditions was less than \$50. As an example of the analytical results, Fig. 5.34 shows exactly how the welding speed and the breadth of the specimen affects the residual deflection (deflection after welding is completed and the specimen has cooled to room temperature) at the midlength. Points P and P' indicate the experimental data and the analytical predictions, respectively, for the 6-in. wide specimen (see Fig. 5.34).

In order to determine the validity of the analysis, an additional experiment was made with a specimen 4 in. wide. The new specimen (specimen # 3) was welded using the same welding conditions as those used for the specimen 6 in. wide (specimen # 1). Point Q

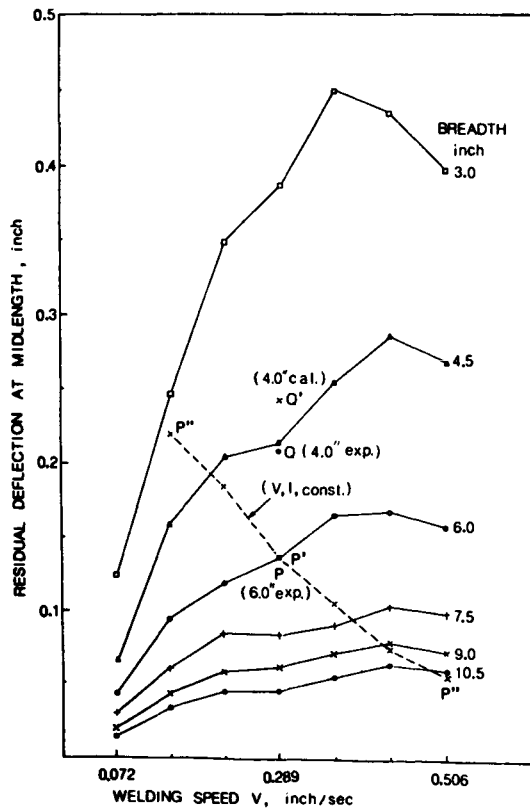


FIG. 5.34. Effect of welding speed and specimen breadth on residual distortion at midlength (aluminum, heat input = 20,700 joules/in.)

shows the experimental data (0.021 in.) obtained with the new specimen (# 3), while point Q' shows the analytical prediction, indicating that the computer analysis is reasonably accurate.

Line $P'' P P''$ shows the calculated residual distortions for 6-in.-wide specimens welded using different welding speeds while the welding current and the arc voltage are kept constant. When welding speed is increased while I and V are kept constant, the amount of distortion sharply decreases. One must recognize, however, that the weld cross-section decreases as the welding speed increases. This means that more passes are required to obtain the same weld cross-section.

On the other hand, when welding speed is increased and the heat input kept unchanged, the residual distortion increases as shown by the solid lines in Fig. 5.34. The results in Fig. 5.34 indicate that there is a welding speed in which the distortion reaches its maximum.

Distortion increases as the specimen breadth decreases, due primarily to a reduction in rigidity.

Concluding remarks. With the advancement of computer technology, it is possible to simulate the thermal stresses and metal movements that occur during welding. Although to date studies have been primarily within laboratories, it will soon be possible to utilize this computer-aided analyses in the solving of practical problems.

For example, among the various automatic welding machines already used in shipyards is a one-side submerged arc welding unit used to join large steel plates and various automatic welding machines used to fabricate large sections. Troubles related to metal movement and distortion often occur when these large welding machines are used. For example, when excessive distortion occurs in the fabrication of a large section, the determination of the optimum welding condition by a purely empirical method is expensive. The 1-D program described in this paper could be used to economically determine these optimum welding conditions. The results shown in Fig. 5.34, for example, could provide some clues as to way of reducing distortion.

When adapting a program for practical use, the most important considerations include: (1) the accuracy of the computation, (2) the complexity involved, and (3) the cost. In many applications, engineers prefer a simple, inexpensive method of calculation; in others they see the need for a more sophisticated approach, provided it yields accurate results. Often the most effective approach is a combination of experimentation and computer analysis. Computer simulation allows us to obtain the maximum amount of information using the smallest number of specimens.

Although this paper has concentrated primarily on the 1-D program and its application in the analysis of bending distortion, there are a number of cases where computer simulation can be effectively used for solving the various practical problems in welding fabrication.[†]

5.10 Assessment of the Current Status and Future Prospects

This paper has described the work done at M.I.T. on analytical and experimental methods of studying thermal stress and metal movement during welding. One result of this work has been a series of computer programs including (see Fig. 5.21):

1. A one-dimensional program.
2. Two-dimensional, finite-element programs (bead-on-plates and butt joints).
3. A program for girth welding along a cylindrical shell.
4. Programs for analyzing longitudinal stresses in heavy plates.
5. A program for analyzing the distortion in built-up beams.

At the same time a large amount of experimental data on thermal stresses and metal movement during welding has been generated. The experiments used different materials, specimen geometries, joint designs, and joining processes. The materials investigated included:

- Low carbon steel
- Several kinds of high-strength steels
- Stainless steel
- Aluminum alloys
- Titanium alloy
- Columbium
- Tantalum

[†] For example, some Japanese companies have experienced cracking problems during the one-side submerged arc welding of large butt joints. Several investigators have used finite-element programs to study metal movement during welding.^(538, 539)

It is hoped that the current efforts will be continued and expanded. By comparing experimental data and analytical predictions, analytical models can be improved to more accurately describe the welding process. Probably the most crucial subject at present is how to model the metal and the effects of metallurgical transformation. An effort has been made at M.I.T. to give due consideration to metallurgical transformation when studying the thermal stresses that occur during welding.

In the future, efforts will be made to extend the analysis to cover more complex, realistic structures, so that the industrial application of computer analysis can begin. We hope to be able to analytically simulate the thermal stresses and the metal movement in weldments. When computer simulations of welding become an accomplished fact, they will greatly affect welding fabrication. Computer simulations can help designers and production engineers, especially those who fabricate critical, expensive structures, to optimize the welding designs and procedures. Hopefully, it will only be a short time before the computer simulation of simple joints such as the fabrication of a built-up beam and the one-pass welding of a butt weld becomes commonplace industrial practice.

References

- (501) MASUBUCHI, K., *Residual Stresses and Distortion in Welded Aluminum Structures and their effects on Service Performance*, Welding Research Council Bulletin 174, July 1972.
- (502) SPRARAGEN, W. and CLAUSSEN, G. E., "Shrinkage distortion in welding, a review of the literature to January 1, 1937", *Welding Journal*, **16**, no. 7, Research Supplement, pp. 29-40 (1937).
- (503) SPRARAGEN, W. and CORDVI, M. A., "Shrinkage distortion in welding", *Welding Journal*, **23**, no. 11, Research Supplement, 545s-559s (1944).
- (504) SPRARAGEN, W. and ETTINGER, W. G., "Shrinkage distortion in welding", *Welding Journal*, **29**, nos. 6 and 7, Research Supplement, 292s-294s and 323s-335s (1950).
- (505) KIHARA, H. and MASUBUCHI, K., *Residual Stresses and Distortion in Weldments*, The Sampo Company, Tokyo, 1957 (in Japanese).
- (506) KIHARA, H., WATANABE, M., MASUBUCHI, K., and SATOH, K., "Researches on welding stress and shrinkage distortion in Japan", *60th Anniversary Series of the Society of Naval Architects of Japan*, Vol. 4, 1959.
- (507) WATANABE, M. and SATOH, K., *Welding Mechanics and Its Applications*, Asakura Publishing Co., Tokyo, 1965 (in Japanese).
- (508) OKERBLOM, N. O., *The Calculation of Deformations of Welded Metal Structures*, Her Majesty's Stationery Office, London, 1958.
- (509) VINOKUROV, V. A., *Welding Distortions and Stresses*, Mashinostroeniye, Moscow, 1968 (in Russian).
- (510) TALI, L., "The strength of welded built-up columns", Ph.D. Dissertation, Lehigh University, 1961.
- (511) TALL, L., "Residual stresses in welded plates—a theoretical study", *Welding Journal*, **43** (1), Research Supplement, 10s-23s (1964).
- (512) MASUBUCHI, K., SIMMONS, F. B., and MONROE, R. E., *Analysis of Thermal Stresses and Metal Movement During Welding*, RSIC-820, Redstone Scientific Information Center, Redstone Arsenal, Alabama, July 1968.
- (513) HIBBIT, H. D. and MARCAL, P. V., *A Numerical Thermo-mechanical Model for the Welding and Subsequent Loading of a Fabricated Structure*, Department of the Navy, NSRDC Contract No. N00014-67-A-019-0006, Technical Report No. 2, March 1972.
- (514) UEDA, Y., and YAMAKAWA, T., "Analysis of thermal elastic-plastic stress and strain during welding", Document X-616-71, The International Institute of Welding, 1971.
- (515) SATOH, K., UEDA, Y., and MATSUI, S., "1972-73 literature survey on welding stresses and strains in Japan", Document X-699-73, presented at the 1973 Annual Assembly of Commission X of the International Institute of Welding.
- (516) NOMOTO, T., "Finite element analysis of thermal stresses during welding", Ph.D. Thesis, University of Tokyo, 1971.
- (517) FUJITA, Y., TERAI, K., MATSUI, S., MATSUMURA, H., NOMOTO, T., and OTSUKA, M., "Studies on prevention of end cracking in one-side automatic welding, Part 3", *Journal of the Society of Naval Architects of Japan*, **136**, 459-465 (Dec 1974).
- (518) MASUBUCHI, K., "Report on current knowledge of numerical analysis of stresses, strains, and other effects produced by welding", *Welding in the World*, **13** (11/12), 271-288 (1975).

- (519) MASUBUCHI, K., "Activities of working group on numerical analysis of stresses, strains and other effects produced by welding", Document X-786-75, Commission X, International Institute of Welding, 1975.
- (520) ANDREWS, J. B., ARITA, M., and MASUBUCHI, K., *Analysis of Thermal Stress and Metal Movement During Welding*, NASA Contractor Report NASA CR-61351, prepared for the G. C. Marshall Space Flight Center, Dec. 1970 (for sale by the National Technical Information Service, Springfield, Virginia 22151).
- (521) MASUBUCHI, K. and IWAKI, T., "Thermo-elastic analysis of orthotropic plastic by the finite method", *Journal of the Society of Naval Architects of Japan*, **130**, 195-204 (1971).
- (522) MASUBUCHI, K., ANDREWS, J. B., and URUSHIHARA, A., "Finite element analysis of thermo-elastic deformations in butt welding", I.I.W. Document X-692-73, 1973.
- (523) MURAKI, T., BRYAN J. J., and MASUBUCHI, K., "Analysis of thermal stresses and metal movement during welding. Part I: Analytical study and Part II: Comparison of experimental data and analytical results", *Journal of Engineering Materials and Technology*, ASME, pp. 81-84 and 85-91 (Jan. 1975).
- (524) TOSHIOKA, Y., "Deformation of quenched steel bar", M.I.T., March 1974 (unpublished).
- (525) TOSHIOKA, Y., "Effects of material properties on residual stresses and deformation of welded part", M.I.T., June 1974 (unpublished).
- (526) MURAKI, T. and MASUBUCHI, K., "Finite element analysis based upon the generalized variational principle of plastic and elastic distortion of plates and shells", paper presented at the International Conference on Computer Applications in the Automation of Shipyard Operation and Ship Design, Tokyo, Aug. 28-30, 1973.
- (527) NISHIDA, M., "Analytical prediction of distortion in welded structures", M.S. Thesis in March 1976.
- (528) KLEIN, K. M., "Investigation of welding thermal strains in marine steels", Thesis for M.S. degree, M.I.T., May 1971.
- (529) KLEIN, K. M. and MASUBUCHI, K., "Investigation of welding thermal strains in high-strength steels for marine application", paper presented at the Second International Ocean Development Conference, Tokyo, 5-7 Oct. 1972.
- (530) JOHNSON, E. K., "Study of flame heating of steel plate", Thesis for M.S. degree, M.I.T., May 1971.
- (531) HIRSCH, A. K., "Investigation of thermal stress and buckling during welding of tantalum and columbium sheets", Thesis for M.S. degree, M.I.T., May 1973.
- (532) BRYAN, J. J., "Analysis of two-dimensional thermal stresses and metal movement during welding", Thesis for ocean engineer's degree, M.I.T., May 1973.
- (533) YAMAMOTO, G., "Study of longitudinal distortion of welded beams", Thesis for M.S. degree, M.I.T., May 1975.
- (534) SEROTTA, M. D., "Reduction of distortion in weldments", Thesis for ocean engineer's degree, M.I.T., Aug. 1975.
- (535) HWANG, J. S., "Residual stresses in weldments in high strength steels", Thesis for M.S. degree, M.I.T., Jan. 1976.
- (536) *Aerospace Structural Metals Handbook*, AFML-TR-68-115, Air Force Materials Laboratory, Air Force Systems Command, Wright-Patterson Air Force Base, Ohio, 1970.
- (537) HILL, H. N., "Residual welding stresses in aluminum alloys", *Metal Progress*, **80** (2), 92-96 (1961).
- (538) UEDA, Y., Takahashi, E., Fukuda, K., and Kanacho, K., "Transient and residual stresses in multipass welds", I.I.W. Document X-698-73, 1973.
- (539) SATOH, K., SEO, K., IWAI, K., and TAKAHASHI, D., "Thermal elasto-plastic analysis on stress and strain in weld metal during multipass welding", I.I.W. Document X-706-73, 1973.

The Magnitude and Distribution of Residual Stresses in Weldments

DURING welding a weldment undergoes complex temperature changes that cause transient thermal stresses, and non-elastic or incompatible strains are produced in regions near the weld. After welding is completed, the residual stresses that remain are the result of these strains. This chapter presents fundamental information on residual stresses: how to understand their mechanisms and how to analyze the effects of various factors on their magnitude and distribution.

6.1 Development of Techniques for Analyzing Residual Stresses in Weldments

6.1.1 Methodologies for analyzing residual stresses in weldments

Figure 6.1 shows several ways to analyze residual stresses in a weldment.

The first method, “analytical simulation”, examines what actually happens during welding. The steps in this approach are as follows:

- Step 1.* Analysis of heat flow.
- Step 2.* Analysis of transient thermal stresses.
- Step 3.* Determination of incompatible strains.
- Step 4.* Analysis of residual stresses.

When analyzing residual stresses, step 3 is the most important. If transient thermal stresses are completely elastic and no incompatible strains are formed, no residual stresses will remain. As was mentioned in Section 3.3, the determination of incompatible strains (plastic strains, strains due to solidification and solid-phase transformation—see Fig. 3.13) is difficult. Once the distribution of incompatible strains is determined, analytically or otherwise, the residual stresses can be treated as an elasticity problem that includes incompatible strains.

Analytical simulation is obviously the most orthodox approach to the problem, but the complexity involved, especially in step 3, often makes it impractical, and it is difficult to use when complex weldments are involved.

Since residual stresses can be determined from the distribution of incompatible strains alone, a second method that by-passes steps 1 and 2 (see Fig. 6.1) and avoids complex plasticity analysis has been developed. Unlike the first method, this one can be used to analyze stresses in complex weldments. On the other hand, there is no sure way to accurately estimate the distribution of incompatible strains.

The third method combines the first two. An analytical simulation is used to refine the

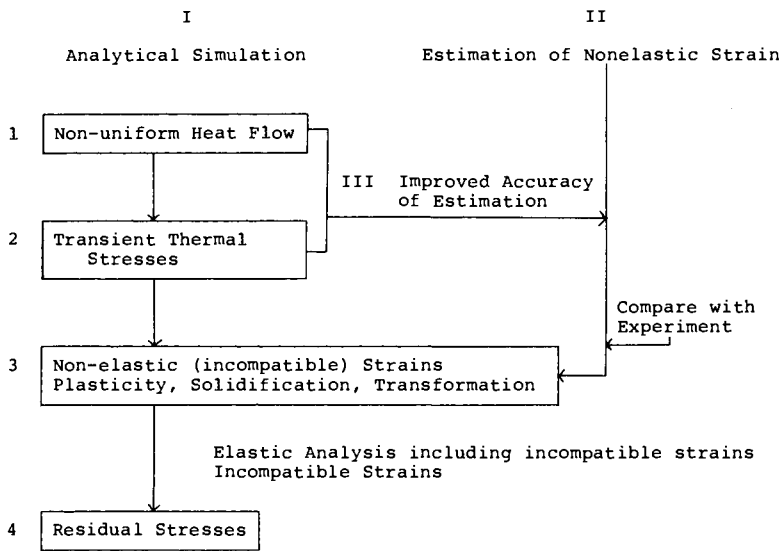


FIG. 6.1. Methodologies for analyzing residual stresses in weldments.

estimation that is made of the distribution of incompatible strains. A basic outline of the third method is given in Section 4.8 (see Fig. 4.25).

6.1.2 Development of analyses of residual stresses in weldments

Analytical simulation was done as early as the 1930s (see Section 5.2). But until very recently, the mathematical complexity involved has limited the analysis of transient thermal stresses to very simple welds.

Most of part studies covered only the residual stresses and distortion that remain after welding is completed. Results of these studies are included in several books and reports.^(303, 501, 506) During the 1950s several Japanese investigators, including Kihara, Watanabe, Masubuchi, and Satoh, studied residual stresses and distortion in practical weldments using the second method described above.⁽⁵⁰⁶⁾ The basic concept involved in this method was developed by Masubuchi.^(314, 323) By using this method, it was possible to analyze residual stresses in certain practical joints without the use of modern computers. One important development during this period was the use of the electrical resistance strain gage, with which it was possible to experimentally determine the distribution of residual stresses in practical joints. Comprehensive studies of residual stresses were also done by several Russian investigators.^(508, 509)

Most of past studies on residual stresses dealt with weldments in low-carbon steels made using covered electrodes. Only a limited amount of information has been generated on weldments in other materials, such as high-strength steels, alloy steels, aluminum and titanium alloys, and other welding processes, such as submerged arc, gas metal-arc, electroslog, and electron beam processes. But generating this kind of information on weldments in different materials with different processes using experimentation only is time consuming and costly.

In the 1970s and since the development of modern computers, there has been a renewed interest in improving the first method (see Chapter 5). A great deal of research currently

in progress in welding mechanics is aimed toward the development of computer programs simulating transient thermal stresses and metal movement. As mentioned in Section 5.10, it is probable that within a few years the computer simulation of certain simple joints (such as the fabrication of built-up beams or the one-pass welding of butt welds) will be an accomplished fact.

However, the simulation method may not be the best way to analyze residual stresses when the weldments are complex. Computer simulation is wasteful in this situation, because huge amounts of computer time are required to accomplish step 3. In order to extend the analysis to complex (practical) joints, we must find some way of reducing the cost of step 3.

The third method (see Fig. 6.1) should be helpful in accomplishing this. The computer simulation technique can be used to improve accuracy when incompatible strains in practical joints are estimated. Figure 4.26 illustrates how this technique can be used when heavy weldments are involved. Recently developed experimental techniques including the Moiré technique and laser holography can also be used to verify the accuracy of the analysis.

Although the most recent studies have in large part involved the computer simulation of transient thermal stresses in welds that are relatively simple, in the near future it is certain that the studies will involve the computer simulation of residual stresses in weldments that are complex.

6.2 Residual Welding Stresses and Reaction Stresses

Residual stresses produced during the fabrication of welded structures are of two types:

1. Residual welding stresses that are produced in the welding of unrestrained members.
2. Reaction stresses that are caused by external restraint.

Figure 6.2 shows a typical distribution of residual stresses in a butt weld. The important stresses are those parallel to the weld direction, designated σ_x , and those transverse to it, designated σ_y .

Figure 6.2(b) shows the distribution of the longitudinal residual stress, σ_x . Tensile stresses of high magnitude are produced in the region near the weld; these taper off rapidly and become compressive after a distance several times the width of the weld metal. The stress distribution is characterized by two parameters: (1) the maximum stress at weld region σ_m , and (2) the width of the tension zone of residual stress b . In weldments made in low-carbon steel, the maximum residual stress, σ_m , is usually as high as the yield stress of the weld metal.

According to Masubuchi and Martin,⁽⁴⁴²⁾ the distribution of longitudinal residual stress σ_x can be approximated by the following equation.[†]

$$\sigma_x(y) = \sigma_m \left\{ 1 - \left(\frac{y}{b} \right)^2 \right\} e^{-\frac{1}{2}(y/b)^2}. \quad (6.1)$$

The distribution of the transverse residual stress, σ_y , along the length of the weld is shown by curve 1 in Fig. 6.2(c). Tensile stresses of relatively low magnitude are produced

[†] See Fig. 12.4 for more details.

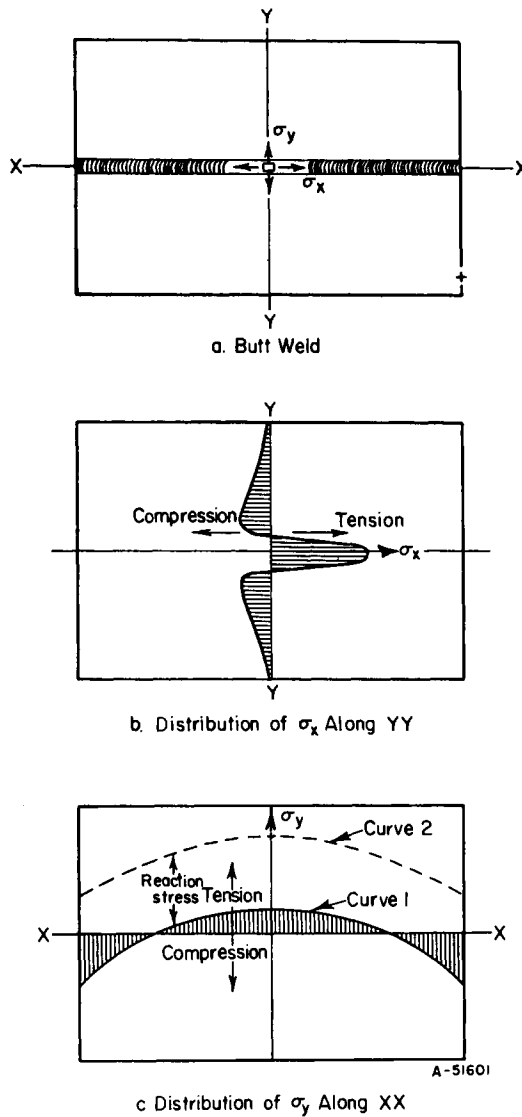


FIG. 6.2. Typical distributions of residual stresses in butt weld.

in the middle part of the joint and compressive stresses at the ends of the joint.

If the lateral contraction of the joint is restrained by an external constraint such as a series of springs, the distribution of σ_y is as shown by curve 2 in Fig. 6.2(c). Tensile stresses approximately uniform along the weld are added as the reaction stress. An external constraint, however, has little influence on the distribution of σ_x residual stresses.

Figures 6.3 and 6.4 show how reaction stresses build up during the multi-pass welding of a butt joint.⁽⁶⁰¹⁾ Figure 6.3 shows the test set-up. The test plates were 20 mm ($\frac{3}{4}$ in.) thick and were welded with E6016 electrodes 4 mm ($\frac{5}{32}$ in.) and 5 mm ($\frac{3}{16}$ in.) in diameter. Experiments were conducted using different amounts of root gap. Figure 6.4(a) shows how reaction load and reaction stresses built up in the base plate. The reaction stresses

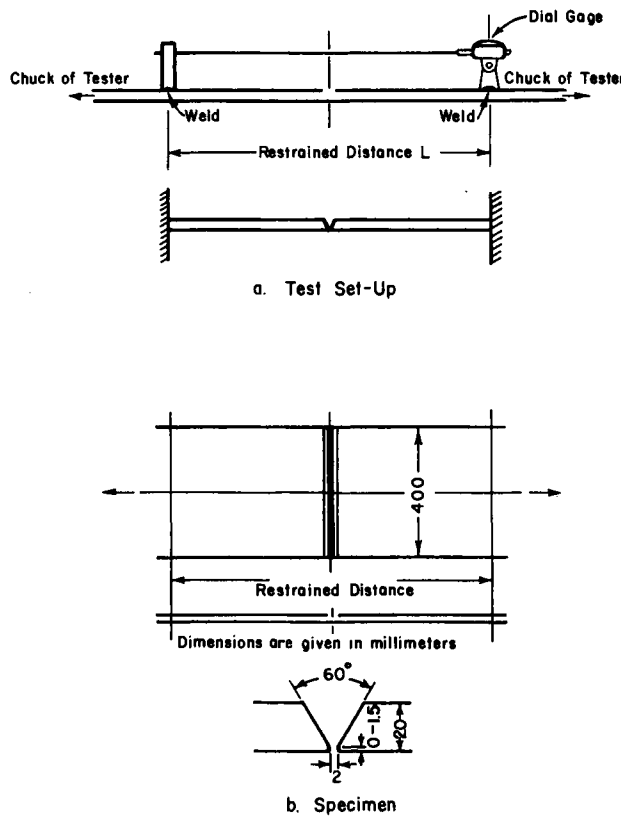


FIG. 6.3. Test set-up used for the study of reaction stresses by Yoshida *et al.*⁽⁶⁰¹⁾ Dimensions are given in millimeters.

increased as more welds were made (see Fig. 6.4(b)). As more weld passes were made, and as the cross-sectional area increased, the reaction stress in the weld cross-section did not increase as much as the reaction stresses in the base plate.

6.3 Analysis of Residual Stresses in Restrained Butt Welds

Kihara *et al.* did an analytical and empirical study of residual stresses in restrained butt welds.⁽⁶⁰²⁻⁶⁰⁴⁾

6.3.1 Elastic and plastic strains in areas near the weld

As stated above, residual stresses are result of incompatible strains produced in regions near a weld. Using the Gunnert strain indicator, shown in Fig. 4.2, Masubuchi^(314, 323) investigated the distribution of elastic and plastic strains in areas near a weld. The specimen was a slit-type weldment in carbon steel (see Fig. 6.5(a)). A double-vee slit 258 mm (10 in.) long was machined in a plate $19 \times 800 \times 1200$ mm ($\frac{3}{4} \times 31 \times 47$ in.) and was welded using covered electrodes. Figure 6.5(a) indicates the locations of the strain-measuring points. At each of the measuring points, strain-measuring depressions (see Fig. 6.5(b)) were prepared and the distances between the depressions measured.

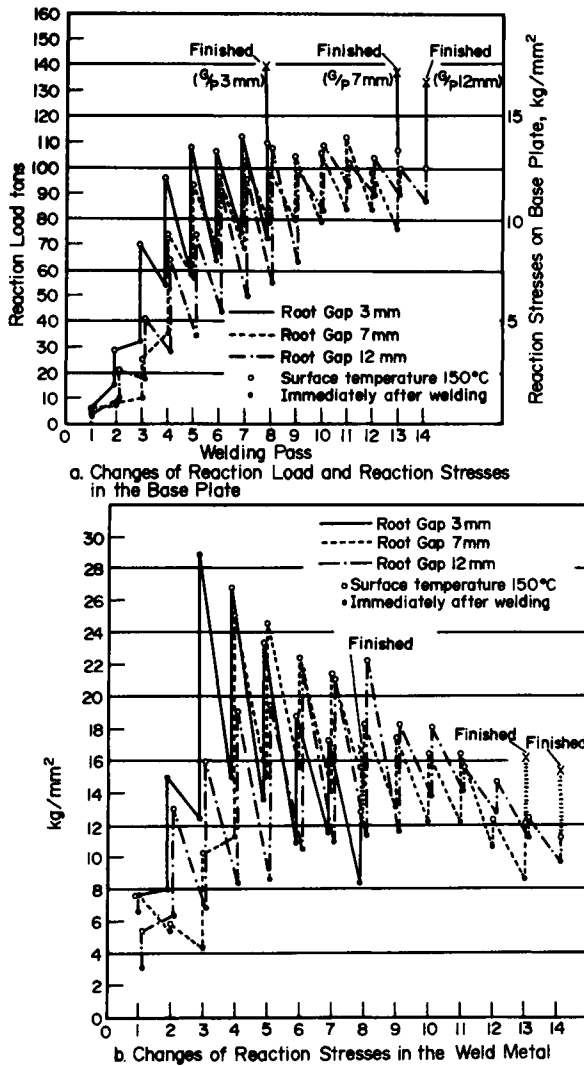


FIG. 6.4. Increase of reaction stresses during multipass welding by Yoshida *et al.*⁽⁶⁰¹⁾

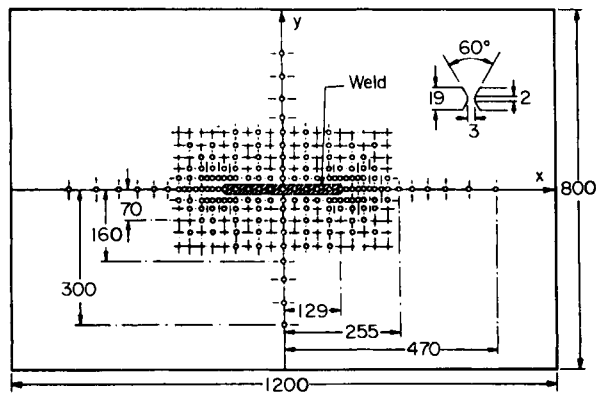
After the specimen was welded, the distances between the depressions were again measured and the strains produced by welding may be both elastic and plastic, particularly in areas near the weld, the elastic part of the strain was also measured by the relaxation method, using the Gunnert core drill, and residual stresses were determined.

The strains were measured in the following three directions:

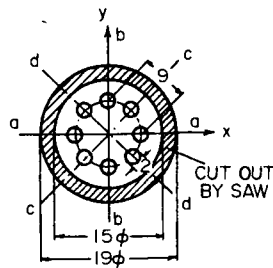
1. Along the weld line: ϵ_a , in Fig. 6.5(b).
2. Transverse to the weld: ϵ_b
3. Forty-five-degree incline to the weld line: ϵ_c or ϵ_d .

Figure 6.6 shows the distribution of the strains.

In order to determine the size of the plastic zone, the values of the octahedral shearing stresses were calculated from the measured values of ϵ_a , ϵ_b , and ϵ_c or ϵ_d . The results are



a. General View of Specimen and Locations of Residual Stress Measuring Points



b. Gage Marks for the Gunnert Method

FIG. 6.5. Slit-type specimen used by Masubuchi.^(314, 322)

shown in Fig. 6.7 which present the values of I as given by the following equations:

$$I = \frac{3}{\sqrt{2}} \tau'_{oct} = [\sigma'_x - \sigma'_x \sigma'_y + \sigma'_y + 3\tau'_{xy}]^{1/2} \quad (6.2)$$

where

$$\begin{aligned} \sigma'_x &= \frac{E}{1 - \nu^2} (\epsilon_x + \nu \epsilon_y), \\ \sigma'_y &= \frac{E}{1 - \nu^2} (\epsilon_y + \nu \epsilon_x), \\ \tau'_{xy} &= \frac{E}{2(1 + \nu)} \gamma_{xy}, \end{aligned} \quad (6.3)$$

E = Young's modulus,

ν = Poisson's ratio.

Equation (6.3) shows that the values of σ'_x , σ'_y , and τ'_{xy} indicate the apparent values of

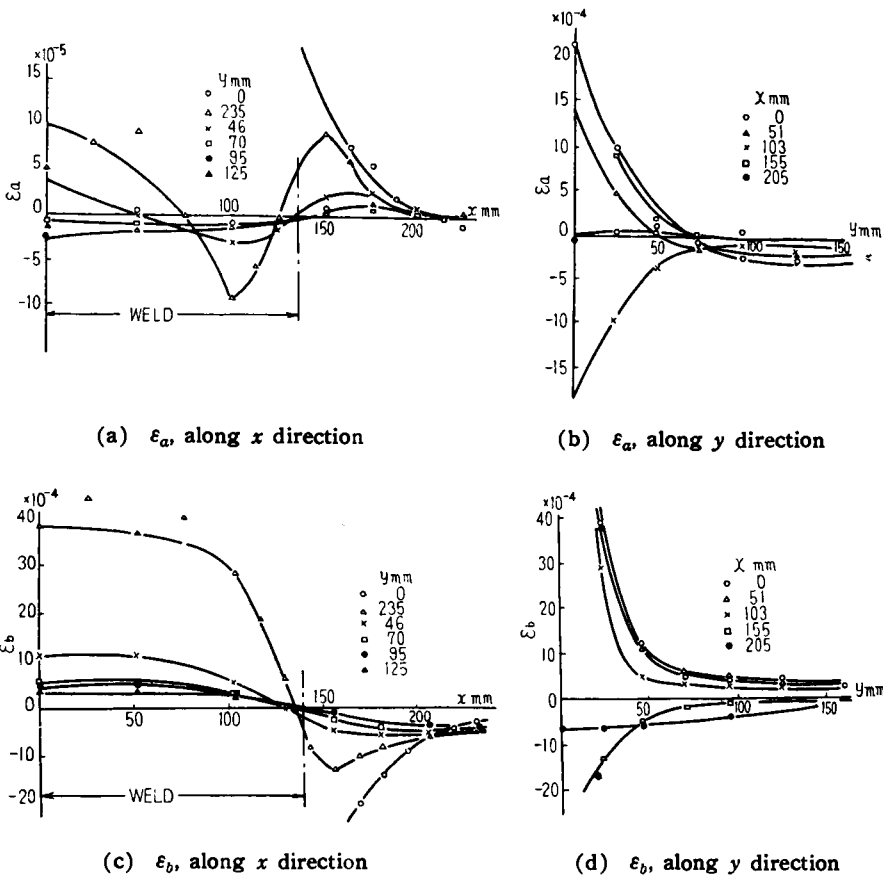


FIG. 6.6. Distributions of strain change produced during welding of the slit-type specimen.

Direction along the weld line: ... ϵ_a
 Transverse to the weld: ... ϵ_b
 Direction inclined 45° to the weld line: ... ϵ_c or ϵ_d

the components, assuming that the measured values of strain components $\epsilon_x, \epsilon_y,$ and γ_{xy} are elastic. The value τ'_{oct} is an invariant[†] that is usually designated on octahedral shearing stress in a plane stress field^(605, 606). According to von Mises, the yield condition in a plane-stress state can be shown as follows.[‡]

$$\tau'_{oct} = \frac{\sqrt{2}}{3} \sigma_{ys} \tag{6.4}$$

[†] A quantity which is not affected by the directions of axes.

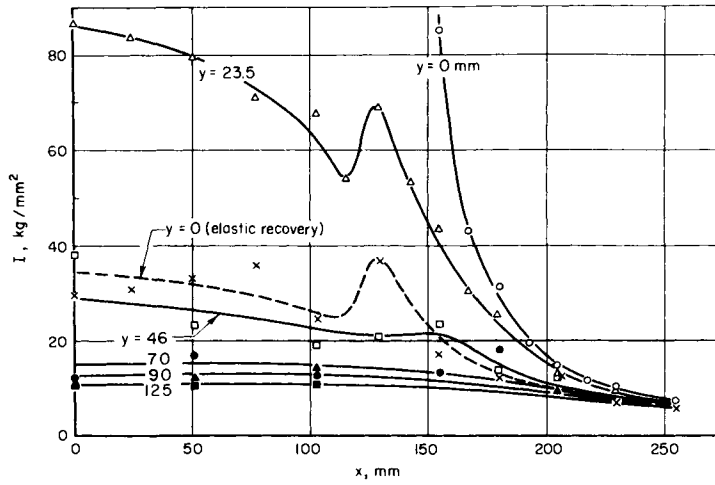
[‡] When a material is under three principal stresses, $\sigma_1, \sigma_2,$ and $\sigma_3,$ the condition of yielding is:

$$(\sigma_1 - \sigma_2)^2 + (\sigma_2 - \sigma_3)^2 + (\sigma_3 - \sigma_1)^2 = 2\sigma_{ys}^2$$

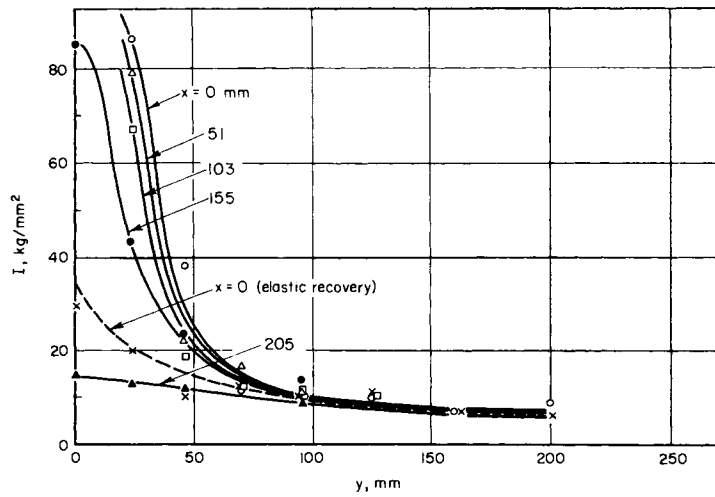
In a plane-stress condition, the stress normal to the plate $\sigma_3 = 0$. Then,

$$\begin{aligned} (\sigma_1 - \sigma_2)^2 + \sigma_2^2 + \sigma_1^2 &= 2\sigma_{ys}^2, \\ \sigma_1^2 - \sigma_1\sigma_2 + \sigma_2^2 &= \sigma_{ys}^2. \end{aligned}$$

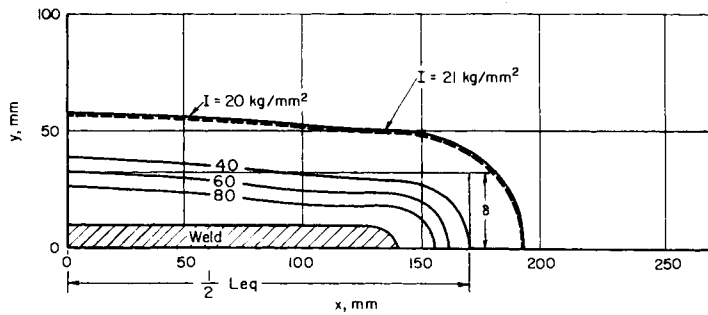
The above equation is for two principal stresses σ_1 and σ_2 (see Table 3.1). In the case of stress components $\sigma_x, \sigma_y, \tau_{xy},$ the effects of the shearing stress, $\tau_{xy},$ must be included. Thus eqn. (6.2) is obtained.



a. Distribution of I along x -direction



b. Distribution of I along y -direction



c. Equi- I curves

FIG. 6.7. Distribution of I as calculated from strain produced by welding. See eqn. (6.2).

or

$$I = \sigma_{ys}$$

where σ_{ys} = yield stress of the material.

Therefore I , an invariant indicating the residual-stress state, can be used to determine whether the material at a given position has undergone plastic strains or has deformed only elastically.

Masubuchi has theorized that when the value of I is larger than the value of σ_{ys} the region has undergone plastic strain.

Figure 6.7 shows that the value of I is generally large in regions near the weld. Curves of equal I value (equi- I curves) are also shown in Fig. 6.7(c). The half-breadth of the

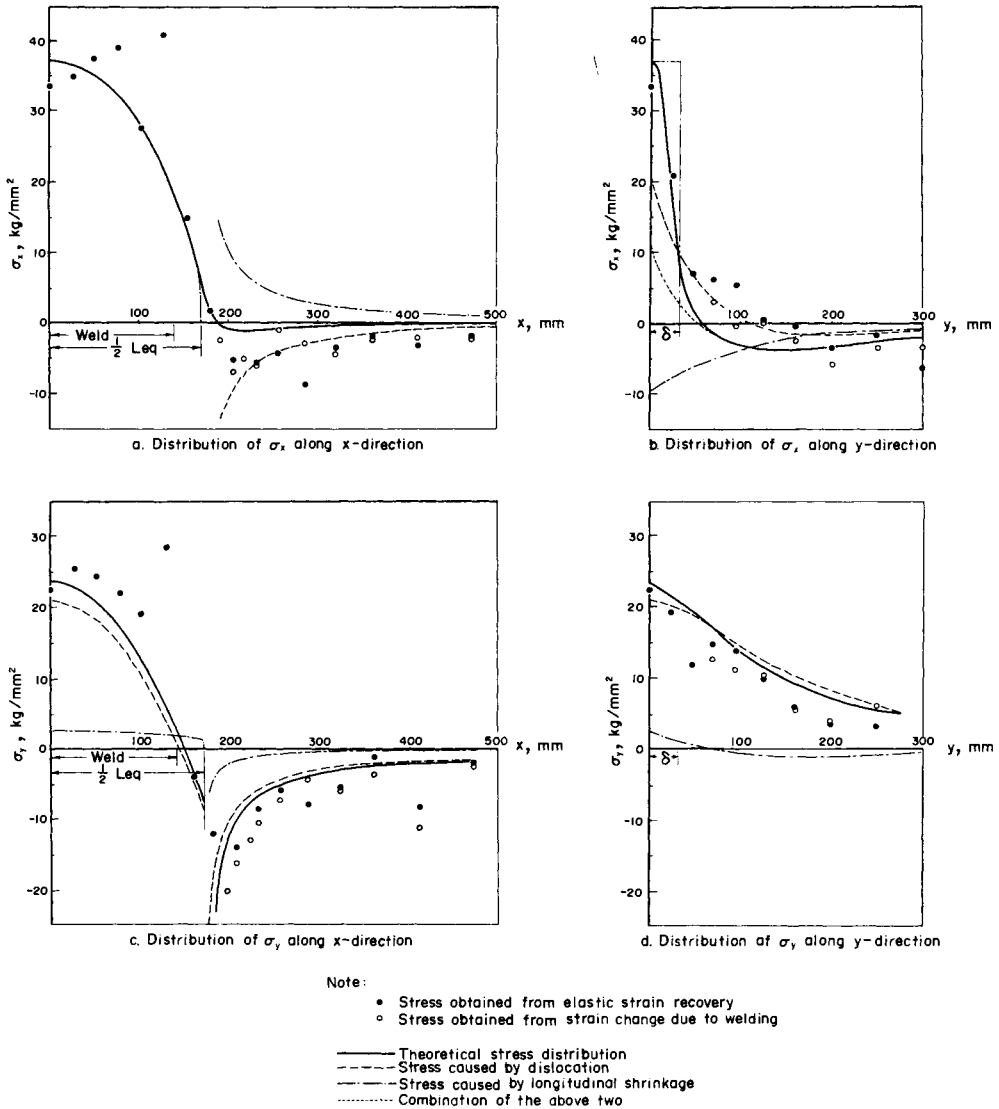


FIG. 6.8. Distributions of residual stresses.

plastic region that corresponds to the yield strength (21 kg/mm² or 30 ksi) was about 55 mm (2 $\frac{5}{32}$ in.) and the penetration of the plastic region beyond the end of the weld about 50 mm (2 in.).

After welding the strain energy release during cutting was measured along the *x*- and *y*- axes of the specimen. It was found that in regions far from the weld the value of the plastic strain release was approximately the same as that of the strain change due to the welding indicating that the strain changes were primarily elastic. In regions near the weld, however, the values of the elastic strain release were much less than those of the strain changes caused by welding. The broken lines in Fig. 6.7 show the values of *I* calculated from the elastic strain release. These values calculated on the welded metal were approximately 35 kg/mm² (50 ksi or 343 MN/m²), it can be concluded that the weld metal was in yield condition.

Figure 6.8 shows the distributions of residual stresses as follows:

Figure 6.8(a): Distribution of the longitudinal stress σ_x along the weld center line (*y* = 0).

Figure 6.8(b): Distribution of σ_x along the *y*-axis (*x* = 0).

Figure 6.8(c): Distribution of σ_y along the *x*-axis.

Figure 6.8(d): Distribution of σ_y along the *y*-axis.

In regard to the distribution along the weld line the transverse stress σ_y , it was found to be in tension in the weld zone, the highest value being at the center with decreasing values away from the center and toward the ends.

Longitudinal stress σ_x is highly tensile at the center of the weld and decreases near the ends. In the base plate, σ_x is compressive and approaches to zero much faster than σ_y . In regard to the distribution of σ_x along the *y*-axis, on the other hand, in the weld zone and its vicinity it is first highly tensile, changes rapidly to compressive, and then gradually approaches zero. From these characteristics, we can see that the longitudinal stress is caused mainly by the longitudinal contraction of the weld metal.

The distribution of transverse shrinkage across the weld, *u*, was also measured (see

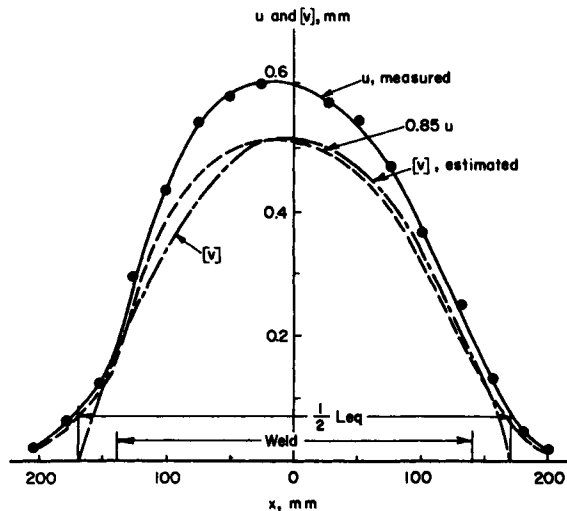


FIG. 6.9. Transverse shrinkage and estimated dislocation.

Fig. 6.9). The transverse shrinkage was great at the center of the weld and decreased near the both ends of the slit.[†]

6.3.2 Analytical determination of residual stresses

On the basis of data collected in previous investigations and the stress distributions as shown in Fig. 6.8, Masubuchi theorized that residual stresses in a constrained butt joint are caused by:

1. the elastic dislocation caused by transverse shrinkage, and
2. the incompatible strains produced in the region near the weld caused by longitudinal shrinkage of the weld metal and plastic deformation produced in the base plate.

It appears that residual stress transverse to the weld (transverse stress, σ_y) is determined mainly by the first factor, while residual stress parallel to the weld (longitudinal stress, σ_x) is determined mainly by the second factor.

It was found in previous experiments⁽⁶⁰²⁻⁶⁰⁴⁾ that in a constrained butt joint transverse shrinkage is mainly elastic except in a circular patch weld specimen with a high degree of constraint. After the completion of the welding, a slit was made by machining along the weld line, and the elastic recovery of shrinkage (or opening of the slit) was measured and compared with the transverse shrinkage produced during welding. In the slit-type specimen, the elastic recovery of shrinkage when the slit was made on the weld metal was about 80% of the value of transverse shrinkage. The value of elastic recovery increased up to about 85% of the value of transverse shrinkage when the slit was extended for 40 to 60 mm ($1\frac{5}{8}$ to $2\frac{3}{8}$ in.) beyond the end of the weld. The shapes of the curves of elastic recovery of shrinkage were quite similar to the shape of the transverse shrinkage curve. On the basis of these experimental results, it was decided to draw the curve of elastic-dislocation as 85% of the curve of transverse shrinkage (see Fig. 6.9).

Since the determination of distribution of incompatibility is very complicated, an approximate theory similar to the boundary-layer theory⁽³²⁴⁾ in aerodynamics has been developed for the residual stress caused by incompatible strains produced in the region near the weld. The welded joint is divided into two regions: the plastic region and the surrounding elastic region. The plastic region is assumed to occupy a slender rectangle of length L and width 2δ ($2\delta \ll L$), as shown in Fig. 6.10. The stress distribution in the elastic region can be calculated when the shearing stress τ_0 acting along the boundary of the plastic and elastic region can be determined. Regarding the stress distribution in the plastic region, the following simplified conditions are used based on the assumptions that the width of the plastic region is very small compared to its length and that the change of stress in the x -direction is much smaller than that in the y -direction:

1. Transverse stress σ_y is uniform in the y -direction.
2. The equilibrium condition between longitudinal stress and shearing stress is

$$\frac{d\bar{\sigma}_x}{dx} \cdot dx \cdot \delta + \tau_0 dx = 0 \quad (6.5)$$

[†] See Chapter 7 for more details of transverse shrinkage.

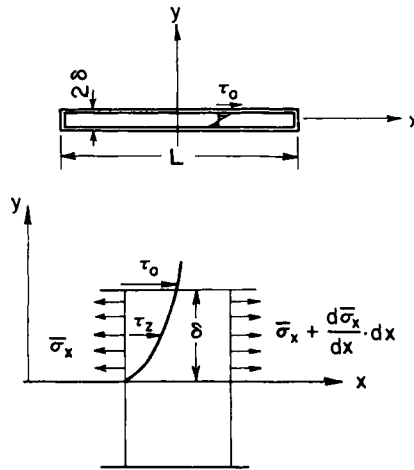


FIG. 6.10. Equilibrium of stress in plastic region.

or

$$\tau_0 = -\delta \frac{d\bar{\sigma}_x}{dx} \tag{6.6}$$

where $\bar{\sigma}_x$ = mean value of σ_x over the width of the plastic region. When the distribution of $\bar{\sigma}_x$ is known, the distribution of τ_0 is determined; thus, the stress distribution in the elastic region also can be determined.

The above analysis suggests that the distribution of residual stress in a butt weld can be calculated when the distribution of the following two are known experimentally:

1. Transverse shrinkage.
2. Longitudinal residual stress in the weld metal.

The distribution of dislocation $[v]$ is determined from transverse shrinkage (see Fig. 6.9).[†] The distribution of shearing stress τ_0 is determined from the longitudinal residual stress in the weld metal, assuming that experimental results obtained in the weld metal represent the stress values in the plastic region. Theoretical residual-stress distributions are shown in Fig. 6.8, where they are compared with experimental results. The theoretical stress distribution is obtained as the summation of two curves which correspond to the influence of transverse shrinkage and longitudinal shrinkage, respectively. A good correlation was obtained between the theoretical stress distribution and the experimental results. Figure 6.8 also shows that the term which corresponds to dislocation plays an important role in determining transverse residual stresses, while the term which corresponds to longitudinal shrinkage plays an important role in determining longitudinal residual stresses.

6.4 The Distribution of Residual Stress: Some Typical Cases

This section describes the typical distribution of residual stress in the following

[†] In estimating the distribution of dislocation the experimental results were modified in the following way: (1) to be symmetric in the direction of welding and (2) to decrease to zero at the end of the equivalent weld length.

weldments:

1. Plug welds.
2. Circular patch welds.
3. Welded shapes and columns
4. Welded pipes.

6.4.1 *Plug weld*

Watanabe and Satoh⁽⁶⁰⁷⁾ studied the residual stresses in a plug weld^(506,608) by depositing weld metals in a 20-mm (0.8-in.) diameter groove that had been made at the center of a low-carbon steel circular plate 6 mm (0.24 in.) thick and 200 mm (8 in.) in diameter (see Fig. 6.11). Total welding time was 10 seconds. An electrode 4 mm ($\frac{5}{32}$ in.) in diameter was used, and temperature changes that took place during welding were measured using a thermocouple. The residual stresses were measured using the Mesnager–Sachs boring-out technique: after welding, a small hole was drilled at the center of the specimen; the radius of this hole was then gradually increased by successive

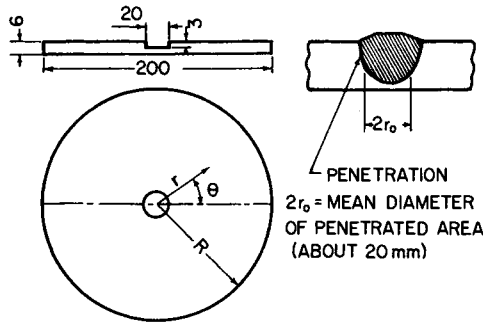


FIG. 6.11. Plug-welded specimen used by Watanabe and Satoh.⁽⁶⁰⁷⁾

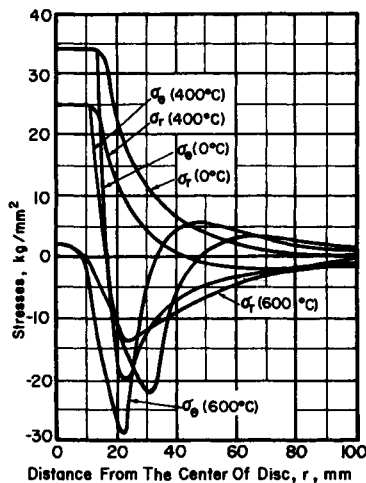


FIG. 6.12. Changes stresses during plug welding stress distributions at $\theta_{,=0} = 600, 400,$ and 0°C are shown.

drillings and the change of the diameter of the specimen measured by an optical comparator.

Figure 6.12 shows the calculated values of the thermal stresses during welding: the distribution of radial stress, σ_r , and circumferential stress, σ_θ , when the temperatures at the weld center, $\theta_{r=0}$, are 600° , 400° , and 0°C ($1,112^\circ$, 770° , and 32°F). The stress distribution at $\theta_{r=0} = 0^\circ\text{C}$ indicate the residual stress.

Figure 6.13 shows the distribution of residual stresses. In the weld and adjacent areas, tensile stresses as high as the yield stress of the material were produced in both radial and tangential directions. In areas away from the weld, radial stresses, σ_r , were tensile and tangential stresses, σ_θ , were compressive. Both stresses decreased as the distance from the weld, r , increased. The curves shown in Fig. 6.13 are the theoretical explanation of Fig. 6.12 (for $\theta_{r=0} = 0^\circ\text{C}$).

6.4.2 Circular patch weld

Patch welds are often used in repair jobs. Figure 6.14(a) shows a circular plate welded into a large plate with a circular hole. Since shrinkage of the inner plate is restrained by the surrounding outer plate, high residual stresses are produced and cracks often develop. Residual stresses in patch welds have been studied by several investigators including Bierett and Grüning,⁽⁶⁰⁹⁾ Harter *et al.*,⁽⁶¹⁰⁾ Kihara *et al.*,⁽⁶⁰⁴⁾ and Yoshida *et al.*⁽⁶¹¹⁾

Figure 6.14(b) shows the typical distribution of residual stresses in circular patch welds. Shown in the figure is the distribution of radial stress, σ_r , and tangential stress, σ_θ , along the diameter. High tensile residual stresses exist in the weld area. The maximum tangential stress, $\sigma_{\theta m}$, is higher than the maximum radial stress, $\sigma_{r m}$, or $\sigma_{\theta m} > \sigma_{r m}$. In the inner plate, both σ_r and σ_θ are tensile and approximately equal.

The residual stress distribution shown in Fig. 6.14(b) is illustrated schematically in Fig. 6.15. Residual stresses in a patch weld are produced primarily by two mechanisms:

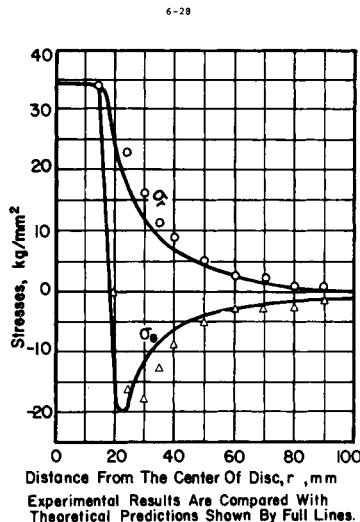


FIG. 6.13. Distributions of residual stresses in a plug weld experimental results are compared with theoretical predictions shown by full lines.

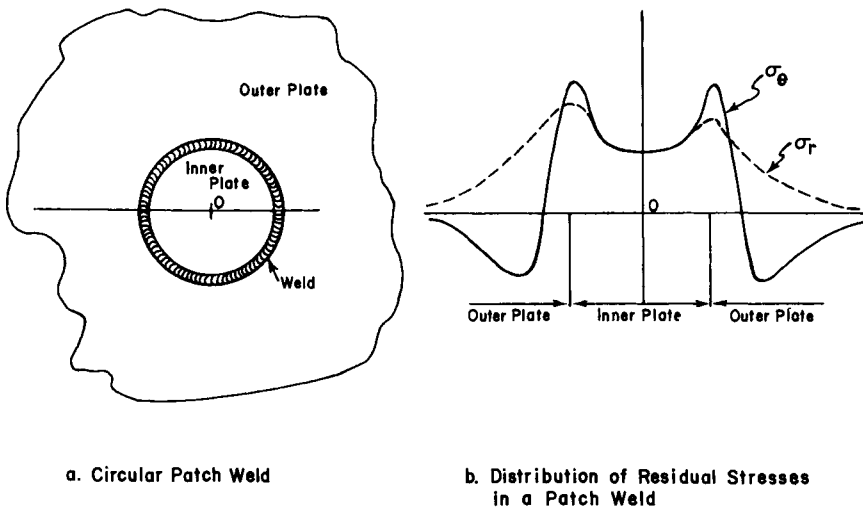


FIG. 6.14. Residual stresses in a circular patch weld.

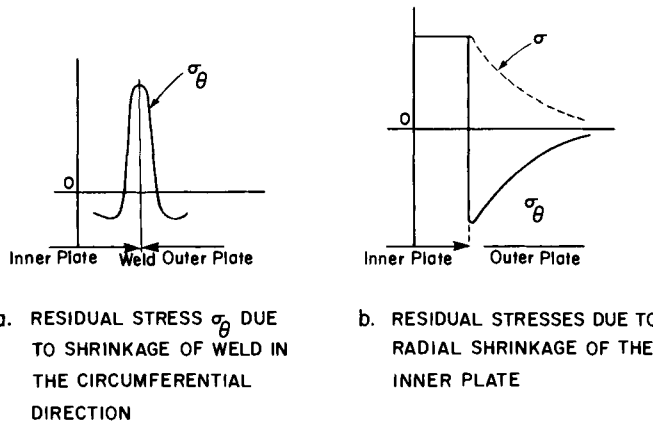


FIG. 6.15. Residual stresses produced in a circular patch weld due to circumferential and radial shrinkage.

1. Shrinkage of the weld metal in the direction parallel to the weld or in the circumferential direction.
2. Shrinkage of the weld metal in the direction perpendicular to the weld or in the radial direction.

Figure 6.15(a) shows a typical distributions of σ_θ due to shrinkage in the circumferential direction. Stresses as shown in Fig. 6.15(b) are produced when the shrinkage of the inner plate is restrained by the outer plate. Stress distributions as shown in Fig. 6.14(b) are produced by combining the stress distributions shown in Figs. 6.15(a) and (b).

Figure 6.16 shows how the patch diameter affects the residual stresses.⁽⁶¹¹⁾ The experiments involved in collecting this data were made on steel plates 9 mm ($\frac{3}{8}$ in.), 15 mm ($\frac{3}{4}$ in.), and 20 mm ($\frac{3}{4}$ in.) thick.

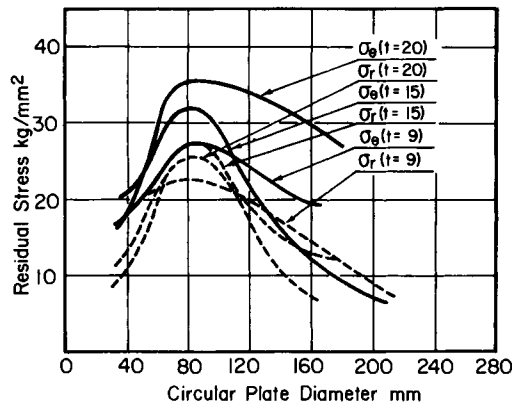
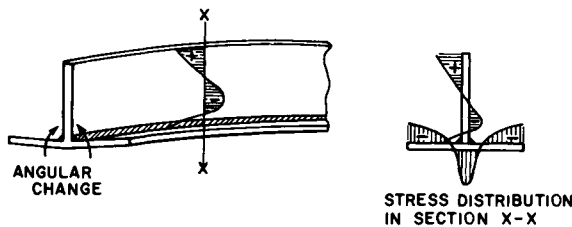


FIG. 6.16. Effect of patch diameter on residual stresses on the weld metal.⁽⁶¹¹⁾

6.4.3 Welded shapes and columns

Shapes and columns are often fabricated by welding. As already discussed in Section 5.5, it is now possible to simulate transient thermal stresses during welding and analytically determine residual stresses using the computer. Figure 6.17 shows the typical distribution of residual stress in built-up shapes.⁽⁶¹²⁻⁶¹⁵⁾

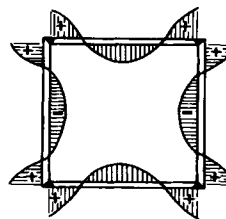
Figure 6.17(a) shows residual stresses and distortion produced in a welded T-shape.



a. RESIDUAL STRESSES AND DISTORTION OF A WELDED T-SHAPE



b. RESIDUAL STRESSES IN AN H-SHAPE



c. RESIDUAL STRESSES IN A BOX SHAPE

FIG. 6.17. Typical residual stresses in welded shapes.

High tensile residual stresses parallel to the axis are produced in areas near the weld in sections away from the end of the column. The figure on the right shows the distribution in Section X-X of residual stresses parallel to the axis. Stresses in the flange are tensile near the weld and compressive away from the weld. The tensile stresses near the upper edge of the web are due to the longitudinal bending distortion caused by longitudinal shrinkage. Angular distortion is also produced.

Figures 6.17(b) and (c) show the typical distribution of residual stress in an H-shape and a box shape, respectively. Shown in the figures are the residual stresses parallel to the axis. Residual stresses are tensile in areas near the welds and compressive in areas away from the welds.

Researchers at Lehigh University have conducted an extensive study of residual stresses in welded shapes.⁽⁶¹³⁻⁶¹⁵⁾ The results of their work on heavy welded shapes⁽⁶¹⁴⁾ are shown in Figs. 6.18 and 6.19. The shape designation 15H290 refers to an H-shaped beam with flange plates $14 \times 12\frac{1}{2}$ in. (356×318 mm) and a web plate $10 \times 1\frac{1}{2}$ in. (250×38 mm). The specimens were fabricated in A36 steel. The distribution of the longitudinal residual stresses are shown in Fig. 6.18. Figure 1.18(a) shows the results obtained on a shape fabricated using $1\frac{1}{2}$ -in. (12.5-mm) fillet welds, while Fig. 6.18(b) shows the results on a shape fabricated using $\frac{11}{16}$ -in. (12.5-mm) fillet welds. The residual stress distribution is given in an iso-stress diagram, that is, contour lines indicate constant stress.

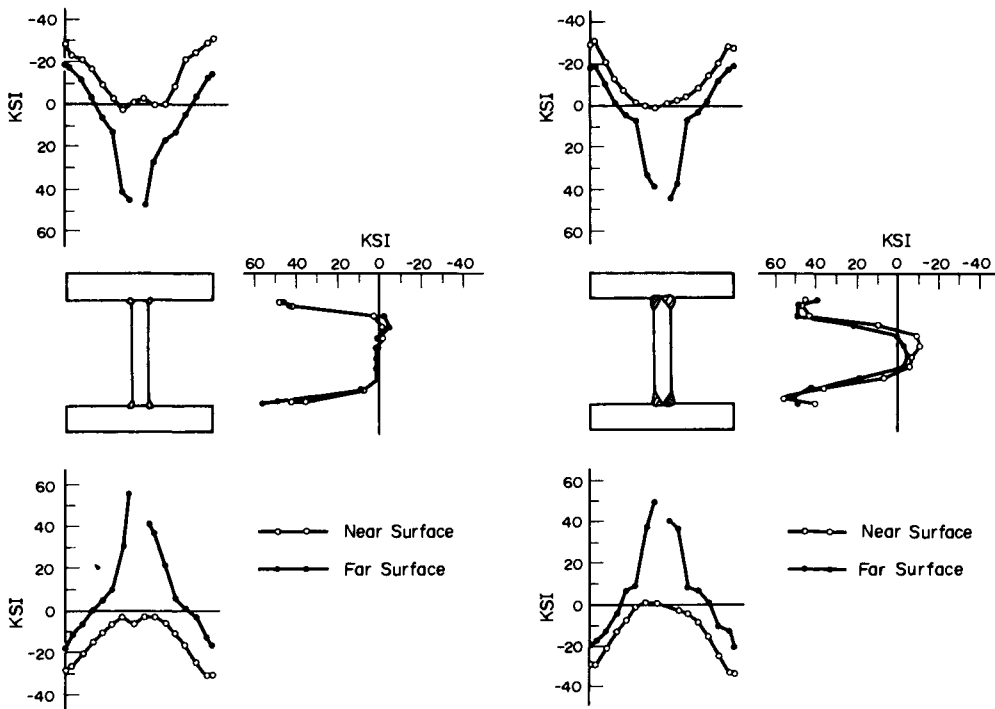


FIG. 6.18. Residual stresses in welded shapes 15H 290—Universal-mill plates, A 36 steel (Alpsten and Tall⁽⁶¹⁴⁾).

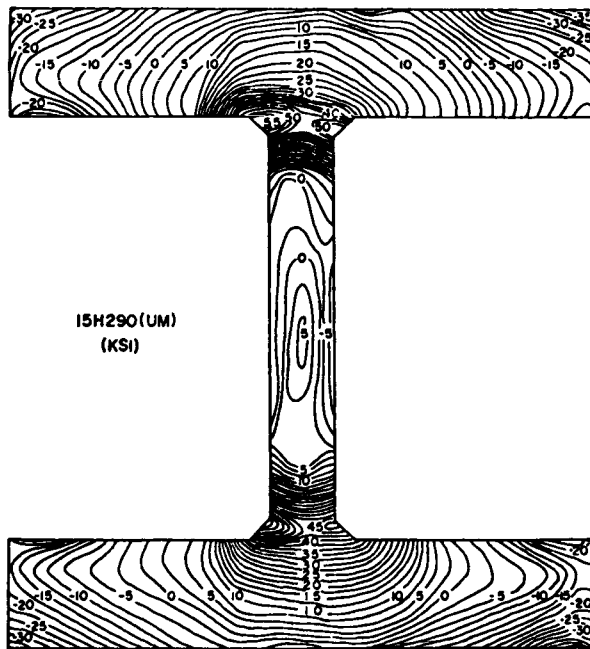


FIG. 6.19. Two-dimensional variation of residual stress in a welded shape 15H290—Universal-mill plates A 36 steel, $\frac{1}{2}$ in. (12.5 mm) fillet welds (Alpsten and Tall⁽⁶¹⁴⁾).

6.4.4 Welded pipes

The distribution of residual stress in a welded pipe is complex. In a girth-welded pipe, for example, shrinkage of the weld in the circumferential direction induces both shearing force, Q , and bending moments, M , to the pipe as shown in Fig. 6.20. The angular distortion caused by butt welding also induces bending moment. Distribution of residual stresses is affected by the following:

1. The diameter and wall thickness of the pipe.
2. The joint design (square butt, vee, X, etc.), and
3. The welding procedure and sequence (welded on outside only, welded on both sides, outside first, or welded on both sides, inside first).

Residual stresses in welded pipes have been studied by investigators including Watanabe *et al.*,⁽⁶¹⁶⁾ and Burdekin.⁽⁶¹⁷⁾ Figure 6.21 shows the results obtained by Burdekin. Two low-carbon steel pipes 30 in. (762 mm) long, 30 in. (762 mm) in diameter,

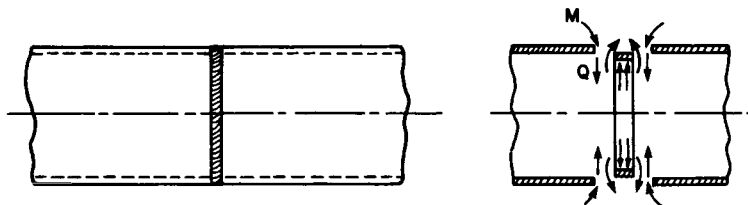


FIG. 6.20. Residual stresses in a welded pipe.

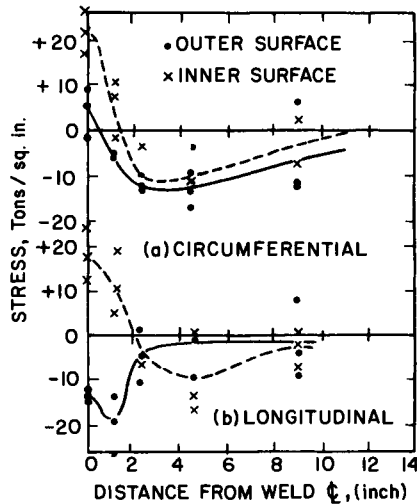


FIG. 6.21. Residual stresses in a girth-welded low-carbon steel pipe $\frac{7}{16}$ inch wall thickness 30 inch in diameter and 30 inches long (Burdekin⁽⁶¹⁷⁾)

and with a $\frac{7}{16}$ -in. (11 mm) wall thickness were girth welded. Residual stresses were then determined using the Gunnert technique.

6.5 Residual Stresses in Weldments in Various Materials

It has been firmly established that in welding low-carbon steel the maximum residual stress in the weld is as high as the yielded stress of the material (see Figs. 6.5, 6.6, etc.). Data is also available on residual stresses in weldments made in other metals.

6.5.1 General discussion on effects of material properties

As described in Section 5.6, experimental and analytical studies have been done at M.I.T. on transient thermal stresses and metal movement during welding. Various materials have been studied, including low-carbon steel, high-strength steels, stainless steel, aluminum alloys, titanium alloys, columbium, and tantalum. The experimental data and analytical predictions were in close agreement in all the materials studied except in the case of certain low-alloy, high-strength steels.

The magnitude and distribution of residual stresses in weldments were found to be affected by:

1. The temperature distribution in the weldment.
2. The thermal expansion characteristics of the material.
3. The mechanical properties of the material at elevated temperatures.

Table 6.1 compares some of the physical properties of steel, aluminum, and titanium.⁽⁵³⁵⁾ Figure 6.22 shows the values of the yield stress of several materials at elevated temperatures.⁽⁵²⁰⁾

The best way to predict the distribution of residual stresses in a weldment made in a given material is to go through a computer simulation. Figure 6.23 shows the residual

TABLE 6.1 Comparison of some physical properties of steel, aluminum, and titanium⁽²⁶⁾

Materials	Steel	Aluminium	Titanium
Density, $\sigma\text{lb/in}^3$	0.234	0.1	0.163
Young's modulus $E \times 10^6$ psi	30	10	17
Yield strength $\sigma_{ys} \times 10^3$ psi	35-150	30-50	40-150
Strength/weight $\sigma_{ys}/\rho \times 10^3$	123-150	300-500	250-920
Thermal conductivity, λ B.t.u./hr/ft ² /ft/°F	26.2	130	9
Coeff. linear thermal exp. $\alpha \times 10^{-6}/^\circ\text{F}$	6.8	13	4.7
Electrical resistivity, $10^{-6}\Omega\text{-cm}$	9.7	2.7	42
Melting point, °F	2800	1220	3040
Melting point of oxide, °F	FeO 2400	Al ₂ O ₃ 3700	

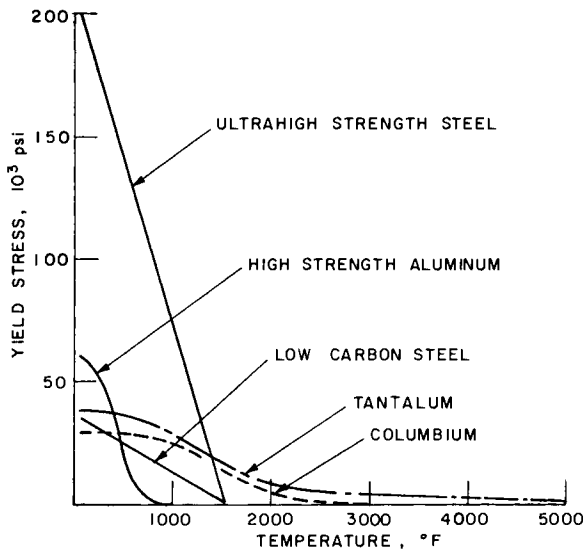


FIG. 6.22. Yield stresses of some structural materials at elevated temperatures.

stress distributions for low-carbon steel and ultrahigh-strength steel (300,000 psi yield strength).⁽⁵²⁰⁾ In both cases the maximum tensile stress at the weld center is as high as the yield stress. The tensile residual stress areas in ultrahigh-strength steel are narrow. This is primarily because only a narrow zone undergoes plastic deformation during welding. The maximum mechanical strain observed 1 in. from the weld line during welding decreases as the yield strength of steel increases (see Fig. 5.20).

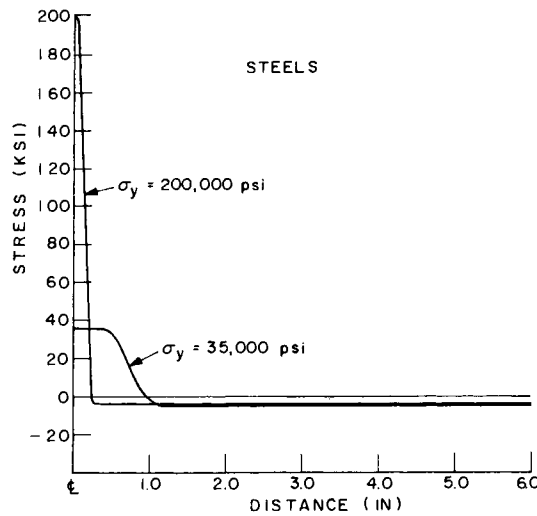


FIG. 6.23. Theoretical distributions of longitudinal residual stresses in weldments in low carbon steel and ultrahigh-strength steel.⁽⁵²⁰⁾

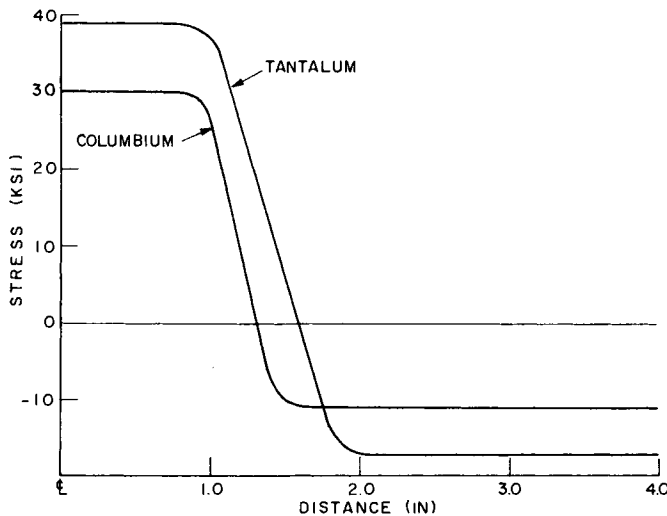


FIG. 6.24. Theoretical distributions of longitudinal residual stresses in weldments in columbium and tantalum.⁽⁵²⁰⁾

Figure 6.24 shows residual stress distributions for columbium and tantalum.⁽⁵²⁰⁾ The tensile residual stress zones are wide. Since both columbium and tantalum have a relatively low yield stress over a wide temperature range (see Fig. 6.22), the area of plastic deformation during welding is large. This suggests that residual stress and distortion can be problematic when welding refractory metals such as columbium and tantalum. This has been confirmed by researchers at the G. C. Marshall Space Flight Center, NASA; distortion is a problem when welding these metals.

Figure 5.31 shows the results of similar calculations done on welds in aluminum.

The maximum residual stress was as high as the yield stress in all the welding conditions under which these calculations were made.

6.5.2 High-strength steel

It has been found that in some high-strength steels the residual stress is considerably lower than the yield stress.

Experimental results. Masubuchi and Martin⁽⁴⁴²⁾ studied residual stresses in butt welds $\frac{5}{8}$ in. (16 mm) by 24 in. (610 mm) by 38 in. (965 mm) made in low-carbon steel and in SAE 4340 steel oil quenched and tempered at 500°F (260°C). The low-carbon steel butt joint was welded with E 6010 electrodes and the SAE 4340 steel butt joint was welded with E15016 electrodes. Electric resistance strain gages were mounted on both surfaces along the transverse line passing through the center of the weld line and along the longitudinal weld center line. One-inch-wide strips containing the strain gages were removed from the weld with a grinding machine, and the strain changes were measured.

Figure 6.25 shows the distribution of longitudinal residual stress along the transverse line. Residual stresses were tensile near the weld and compressive away from the weld. Figure 6.25(b) shows the distribution of longitudinal residual stress along the center line. Stresses were zero at the plate edge and increased gradually. As can be seen in the figure, the specimens were large enough to permit the production of a maximum amount of

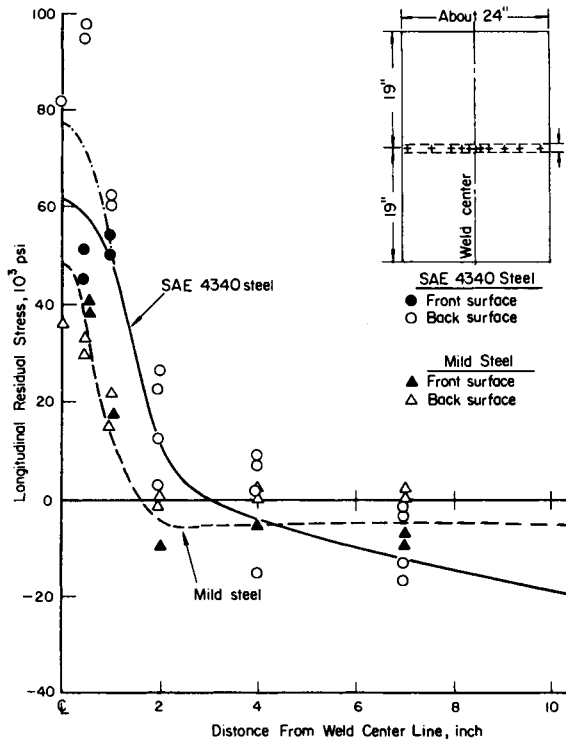


FIG. 6.25. (a) Distribution of longitudinal stresses along the transverse line passing the weld center.

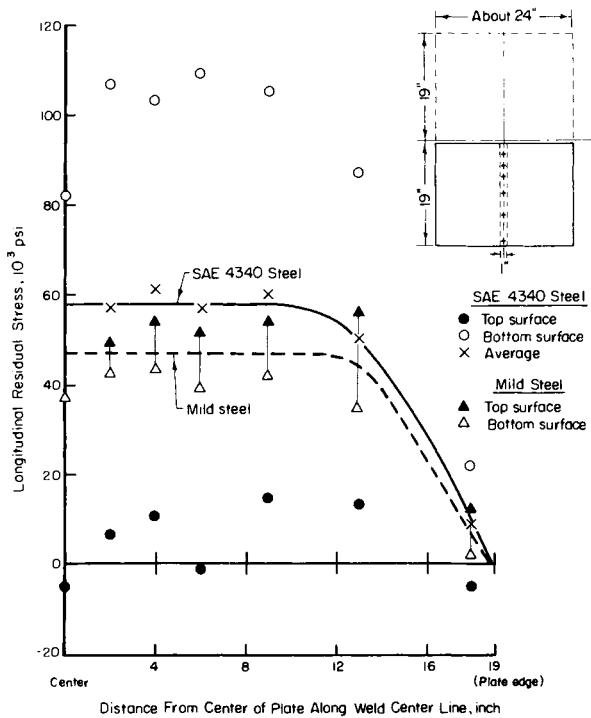


FIG. 6.25. (b) Distributions of longitudinal stresses along the weld center line.

FIG. 6.25. Residual stresses in 38-inch-long butt welds in low carbon steel and SAE 4340 steel oil quenched and tempered at 500°F (Masubuchi and Martin^(4,22)).

stress in the central area. The large differences in the stress values on the top and on the bottom surfaces of the SAE 4340 steel weldment indicate that it was bent in the longitudinal direction. The significant conclusion is that residual stresses in low-carbon steel and SAE 4340 steel weldments were similar despite the considerable difference in the yield strengths of the base metals and the weld metals used. The investigation produced the following data:

	Approximate yield stress (psi)
Low-carbon steel base metal	35,000–40,000
E6010 weld metal	60,000
SAE 4340 steel base metal (oil quenched and tempered at 500°F)	224,000
E15016 weld metal	150,000

The finding was confirmed on three low-carbon steel weldments and five SAE 4340 steel weldments that included butt welds and welded structural models.

Other investigations have also reported that the maximum residual stress in this kind of weld is considerably lower than the yield stress.^(618–621) Based upon experimental results obtained by Kihara *et al.*⁽⁶¹⁸⁾ and Yada *et al.*,⁽⁶¹⁹⁾ Yurioka⁽⁶²⁰⁾ has drawn

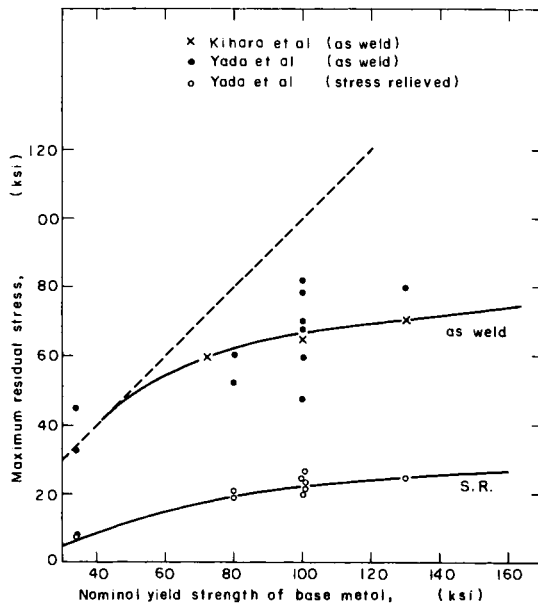
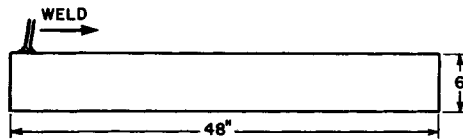


FIG. 6.26. Welding residual stresses in various high-strength steels.

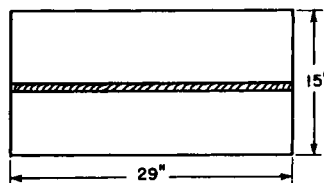
a curve (see Fig. 6.26) showing the relationship between the yield strength of the base metal and maximum residual stress.

Using the X-ray diffraction technique some investigators have reported compressive stresses near welds in certain high-strength steels.^{(622)†}

Hwang's analytical and experimental research. Hwang⁽⁵³⁵⁾ conducted analytical



a. WELD ALONG THE EDGE



b. BUTT WELD

Figure 6.27. Test specimens used by Hwang⁽⁵³⁵⁾

† Goldberg^(623, 624) also reported compressive stresses near the edge of a plate of high-strength steel (ST 52-3) that had been flame-cut.

TABLE 6.2 *Conditions of experiments by Hwang*

Material	Type of weld and (specimen size)	Process	Filler metal	Voltage	Ampere	Speed in./sec.
Low-carbon steel	Bead on edge (48 × 6 in.)	GMA	A 675	25	380	.322
Low-carbon steel	Bead on edge (48 × 6 in.)	GTA	None	12	295	.268
Q & T steel (A517)	Bead on edge (48 × 6 in.)	GMA	A 675	25	420	.333
Q & T steel (A517)	Bead on edge (48 × 6 in.)	GTA	None	12	295	.255
HY-80 steel	Butt weld (29 × 15 in.)	GMA	A 675	25	300	.483
Ti-6Al-2Cu-1Ta-1Mo	Bead on edge (56 × 7.5 in.)	GMA	6-2-1-0.8Ti	28	300	.358

Additional experiments were made on bead-on-edge welds in 308 stainless steel.

and experimental research on the thermal stress and metal movement that occurs during welding. Figure 6.27 shows the two types of specimen he used. Figure 6.27(a) shows the rectangular plate specimen most often used. A weld bead was laid along the longitudinal edge. Figure 6.27(b) shows the butt weld specimen used for HY-80 steel. Table 6.2 shows the specimen dimensions and the welding conditions. Measurements were made of (1) the heat flow, (2) the transient thermal strains, (3) the transient metal movement and, after welding was completed, (4) the residual stresses and distribution. Figures 6.28 through 6.32 show the distribution of residual stress as follows:

Figure 6.28: Low-carbon steel welded with gas metal-arc process.

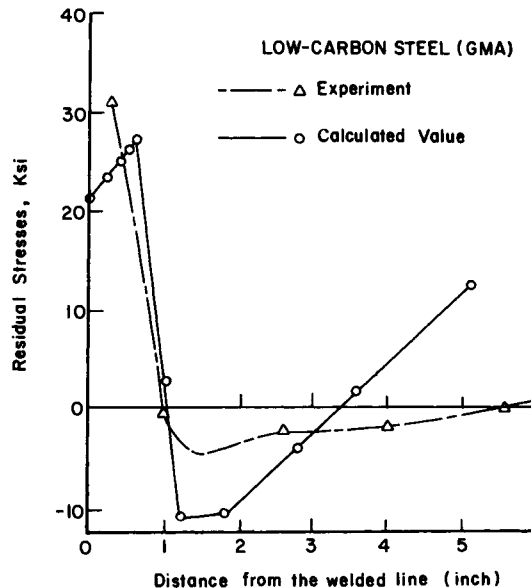


FIG. 6.28. Distribution of residual stresses in weldment of low-carbon steel (GMA).

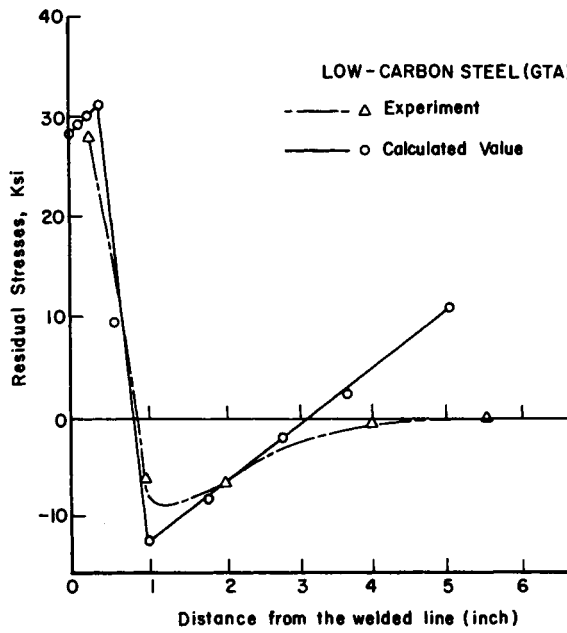


FIG. 6.29. Distribution of residual stresses in weldment of low-carbon steel (GTA).

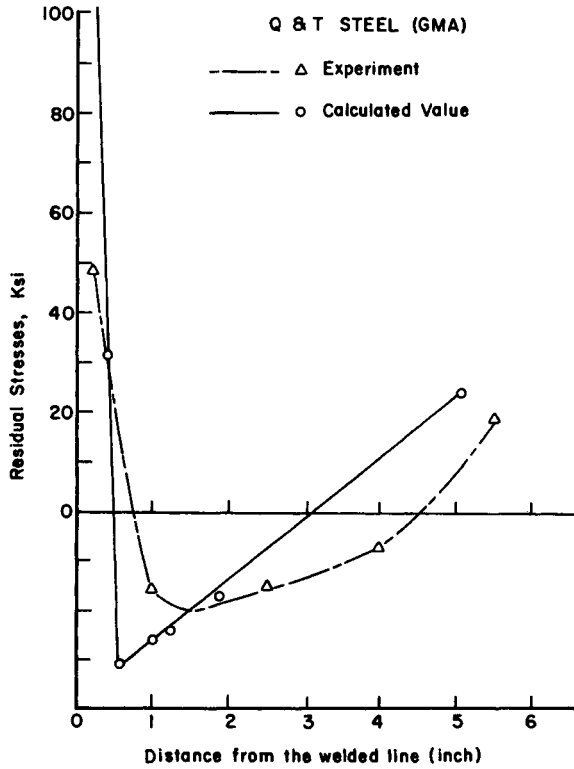


FIG. 6.30. Distribution of residual stresses in Q & T steel (GMA).

Figure 6.29: Low-carbon steel welded with gas tungsten-arc process.

Figure 6.30: Quenched and tempered steel (ASTM A 517) welded with gas metal-arc process.

Figure 6.31: Q&T steel welded with gas tungsten-arc process.

Figure 6.32: HY-80 steel butt joint welded with gas metal-arc process.

In the weldments in low-carbon steel, the experimental data and the analytical predictions agreed (see Figs. 6.28 and 6.29). But in the Q&T steel weldment and the HY-80 steel weldment the experimental values in regions close to the weld were significantly lower than those predicted analytically. The analytical prediction was made using the M.I.T. one-dimensional program described in Section 5.32, and the efforts of metallurgical transformation were not a part of the analysis.

Summary. The experimental analytical results obtained thus far can be summarized as follows:

1. Residual stresses determined by strain changes on low-alloy, high-strength steels are considerably lower than the yield stress of the material (Figs. 6.25, 6.26). Some investigators have even reported the existence of compressive stresses in certain areas adjacent to the weld.
2. During the measurement of transient thermal stresses in the welding of HY-130, a significant amount of strain relaxation was observed near the weld line immediately after the welding arc had passed.

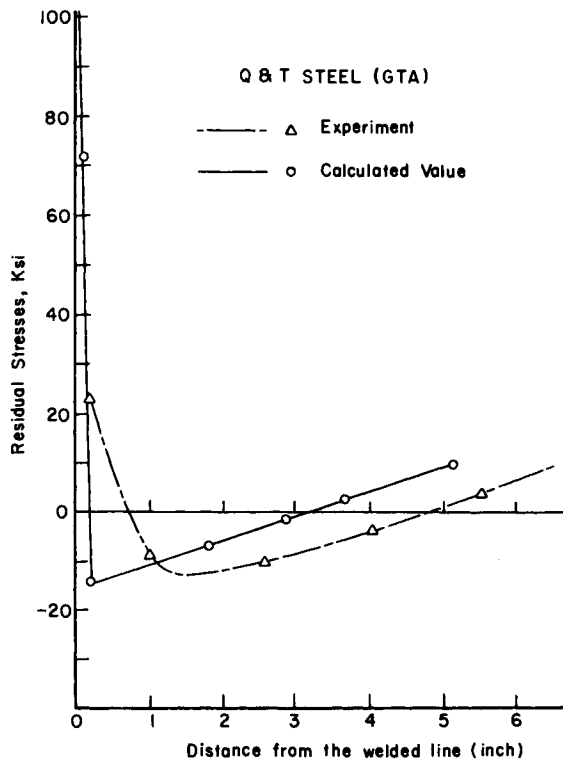


FIG. 6.31. Distribution of residual stresses in weldment of Q & T steel (GTA).

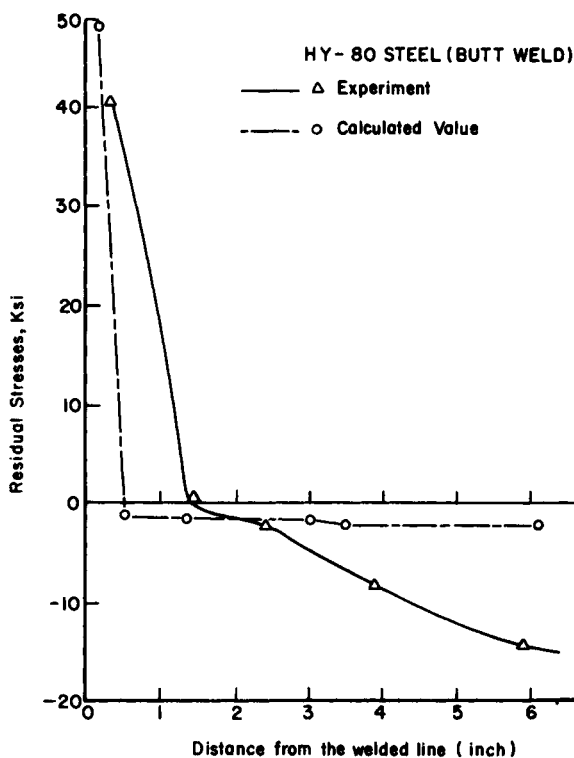


FIG. 6.32. Distribution of residual stresses in weldment of HY-80 steel (butt weld).

3. On the other hand, the analytical predictions showed high residual stresses concentrated in a narrow zone near the weld when these predictions did not take into account the effect of expansion due to phase change during cooling.

There are three possible longitudinal residual stress distributions for a butt weld made in high-strength steel (see Fig. 6.25).

Curve 0 shows the typical distribution of residual stresses low-carbon steel. The maximum stress value at the weld is as high as the yield stress of the material (an estimated 35 to 50 ksi).

Curves 1, 2, and 3 show the possible stress distributions in a high-strength steel such as HY 130 or 180.

If it is assumed that the maximum residual stress is as high as the yield stress, the distribution is as given by curve 1. In such a case the residual stress and distortion would cause severe problems in the fabrication of welded structures using high-strength steel.

In curve 2, the high tensile residual stresses are confined to small areas. In such a case the distortion would be significantly less, but cracking due to high tensile residual stresses would be a problem.

The stress distribution given by curve 3 is one that would cause few problems.

Neither experimental nor analytical data support curve 1. This possibility can be ruled out completely. Experimental results obtained using strain gages tend to support curve 3, while analytical results (neglecting the effect of phase transformation) tend to support curve 2.

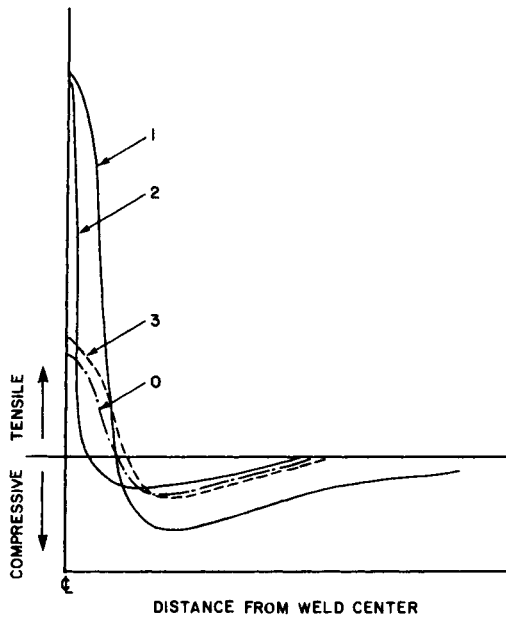


FIG. 6.33. Possible distributions of longitudinal residual stresses in a butt weld in high-strength steel.

On the basis of the experimental and analytical information obtained thus far, it is safe to assume that the residual stress distribution in an actual structure is a cross between curves 2 and 3. If one uses the X-ray diffraction technique to determine the residual stresses in weld metal and adjacent base-metal regions, he finds widely scattered results. Small regions have high-tensile stresses. Most regions have relatively low tensile stresses (50–80 ksi). Some areas even have compressive stresses.

6.5.3 Aluminum alloys

A considerable amount of information has been obtained on residual stresses in weldments made in aluminum alloys. Some of this is available in Chapter 5; Fig. 5.26 shows

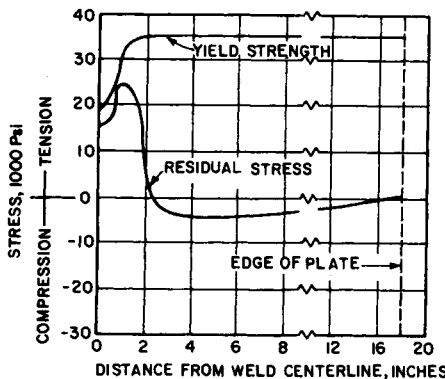


FIG. 6.34. Distribution of yield strength and residual stresses in a longitudinally welded 5456-H321 aluminum alloy plate 36 inches wide and $\frac{1}{2}$ inch thick (Hill⁽⁵³⁷⁾).

the residual stresses that result when a weld is made along the longitudinal edge of a rectangular plate in 5052-H32 aluminum alloy.

Hill⁽⁵³⁷⁾ investigated the residual stresses that occur when butt joints in 5456-H321 aluminum-alloy plates are welded with inert-gas-shielded arc welder using 5556 alloy consumable electrodes. Figure 6.34 shows a typical distribution of longitudinal residual stresses in a $\frac{1}{2} \times 36 \times 48$ -in. ($12.5 \times 914 \times 1219$ mm) panel that has been formed by welding two $\frac{1}{2} \times 18 \times 48$ -in. ($12.5 \times 457 \times 1219$ mm) plates. These tensile stresses are confined to the region in which the heat of welding has lowered the yield strength of the material.

6.5.4 Titanium alloys

Figure 6.35 shows the results obtained by Hwang⁽²⁶⁾ on a weldment in Ti-6Al-

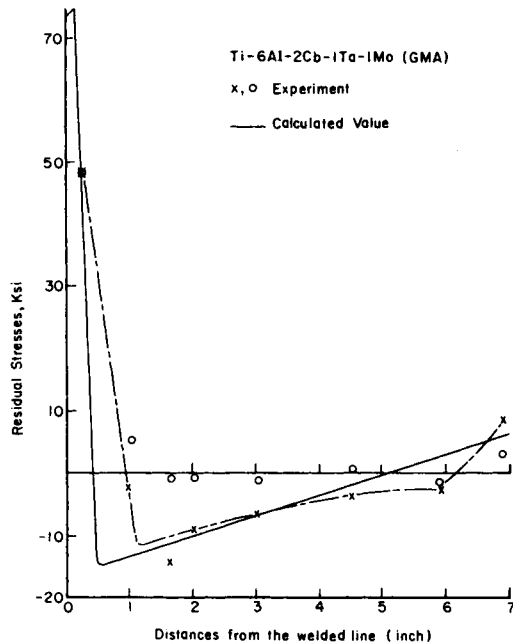


FIG. 6.35. Distribution of residual stresses in weldment of titanium alloy (GMA).

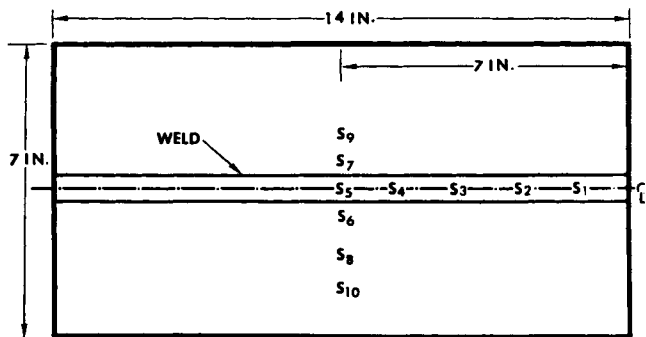


FIG. 6.36. Strain gage location on 6Al 4V weld panel.⁽⁶²⁵⁾

TABLE 6.3 Chemical composition and tensile properties for titanium alloys^(62s)

Material and condition	Filler metal diam, (in.)	Base metal thickness (in.)	Chemical composition, %										Plate tensile properties			
			Al	Sn	Va	Mo	Fe	Mn	C	N ¹	O ¹	H ¹	Ultimate strength (ksi)	Yield strength (ksi)	Elongation in. (%)	
Ti-5Al-2.5Sn annealed condition	0.060	—	5.56	2.72	—	—	0.031	0.000	0.007	0.009	0.070	0.006	122.0 ^(a)	112.5 ^(a)	16.0 ^(a)	
	—	0.200	5.40	2.50	—	—	0.420	0.010	0.020	0.008	0.140	0.006	—	—	—	
Ti-6Al-4V "A"	0.045	—	6.10	—	3.95	—	1.90	—	0.025	0.013	0.095	0.010	—	—	—	
	—	0.200	5.90	—	4.10	—	0.140	—	0.025	0.012	0.090	0.008	135.6 ^(b)	131.4 ^(b)	13.5 ^(b)	
Ti-8Al-Mo-IV duplex anneal	0.060	—	7.80	—	1.00	1.00	0.080	—	0.023	0.009	0.126	0.016	—	—	—	
	—	0.200	7.80	—	1.00	1.00	0.040	—	0.024	0.011	0.090	0.007	147.0 ^(c)	133.9 ^(c)	16.3 ^(c)	

^(a) Average of seven specimens.^(b) Average of two specimens.^(c) Average of nine specimens.

-2Cb-1Ta-1Mo welded by the gas metal-arc process (see Figure 6.27 and Table 6.2). The experimental results agreed with the analytical predictions.

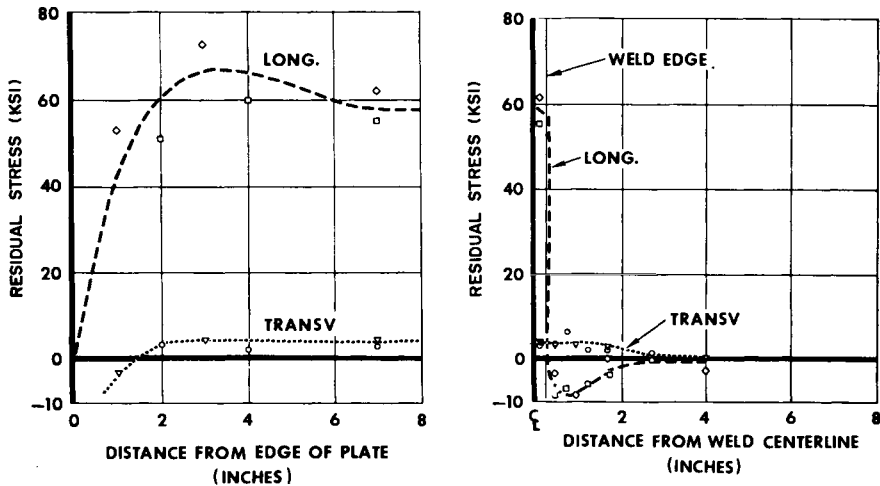
Robelotto *et al.*⁽⁶²⁵⁾ investigated the residual stresses that form when butt welds are made in titanium alloy plates 0.2 in. thick. Table 6.3 gives the chemical composition and the tensile properties of the titanium alloys investigated, Ti-5Al-2.5Sn, Ti-6Al-4V, and Ti-8Al-1Mo-IV. The butt welds shown in Fig. 6.36 were welded using the gas tungsten-arc process. Table 6.4 gives welding parameters used.

TABLE 6.4 Welding parameters for 5Al-2Sn, 6Al-4V, and 8Al-1Mo-IV Titanium alloys 0.200 in. thick⁽⁶²⁵⁾

	Weld passes	
	1	2
Current, amp	205	205
Voltage, V	12.5	12.5
Electrode holder travel speed, ipm	6	6
Filler metal feed, ipm ^(a)	7	7
Ti-6Al-4V filler metal diameter, in. ^(a)	0.045	0.045
Holddown material	Cu	Cu
Holddown spacing, in.	13/32	13/32
Backing material	Cu	Cu
Backing groove width, in.	3/8	3/8
Tungsten diameter, in. ^(b)	3/32	3/32
Gas cup size (Airco number)	8	8
Electrode holder helium-gas flow, cfh	60	60
Trailer shield argon flow, cfh	20	20
Backing helium gas flow, cfh	20	20

^(a) Filler metal feed for the Ti-8Al-1Mo-IV and Ti-5Al-2.5Sn test panels was 5 jpm and base metal filler metal diameter is 0.060 in. for each alloy.

^(b) Tungsten configuration: blunt.



(a) Along the weld center line (b) Perpendicular to the weld

FIG. 6.37. Residual stresses in as-welded 6Al-4V titanium⁽⁶²⁵⁾

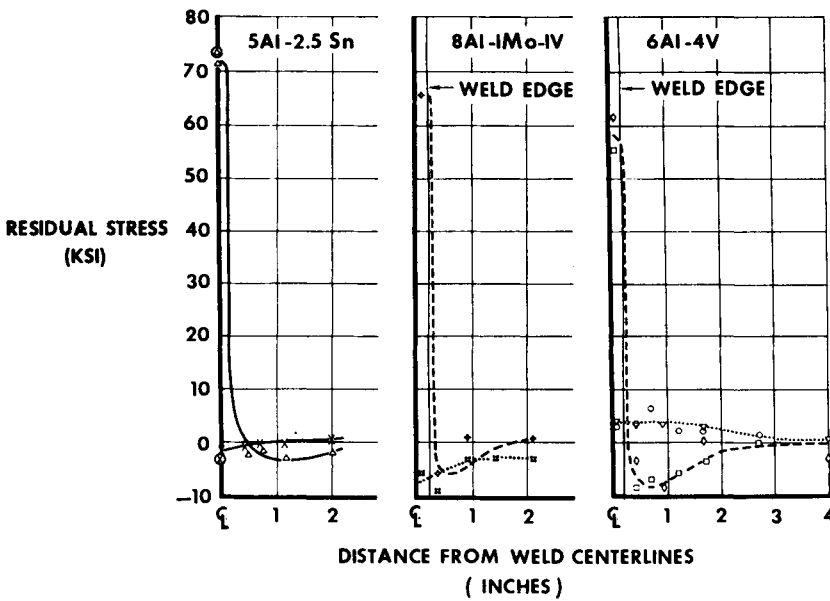


FIG. 6.38. Residual stresses in as-welded titanium alloys—perpendicular to weld.⁽⁶²⁵⁾

Figure 6.37 shows the residual stresses in a weldment made in Ti-6Al-4V. Figure 6.37(a) shows the longitudinal and transverse stress distributions along the weld center line, and Fig. 6.37(b) shows the stress distributions along the line perpendicular to the weld.

Figure 6.38 shows the stress distributions along the perpendicular line in welds made in the three alloys studied.

6.6 Effect of Specimen Size on Residual Stresses

When measuring residual stresses in a weldment, it is important that the welded specimen be large enough to contain residual stresses as high as those that exist in actual structures.

6.6.1 Effect of specimen length

DeGarmo *et al.*⁽⁶²⁶⁾ investigated the effect of weld length on residual stress in unrestrained butt welds made in low-carbon steel. Two series of weldments were prepared using the submerged arc process and the shielded metal-arc process (manual arc welding) as shown in Fig. 6.39. In each series the only variable was the length of the weldment:

	Weld length (in.)
Submerged arc process	3, 4, 5, 8, 12, 18, 24, 36
Shielded metal-arc process	5, 7, 10, 18, 48

The width of each specimen was sufficient to assure that full restraint could be applied.

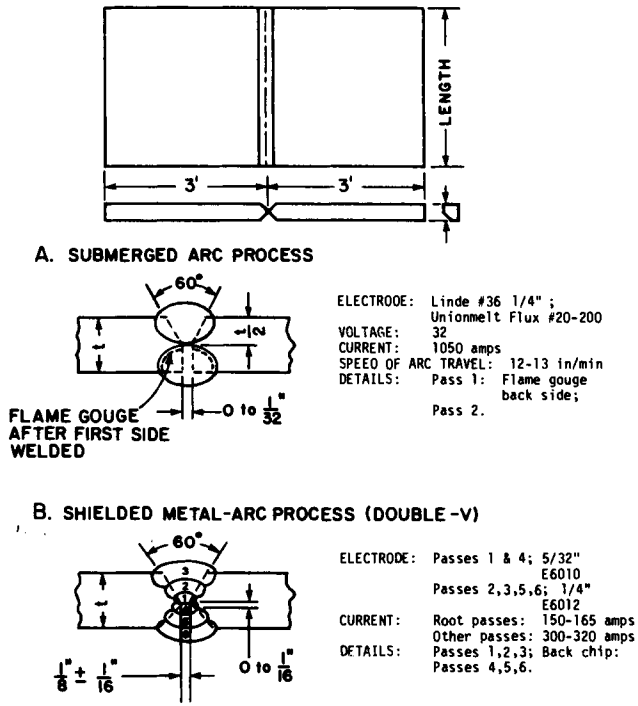


FIG. 6.39. Specimens used by DeGarmo *et al.* For studying the effect of weld length on residual stresses.

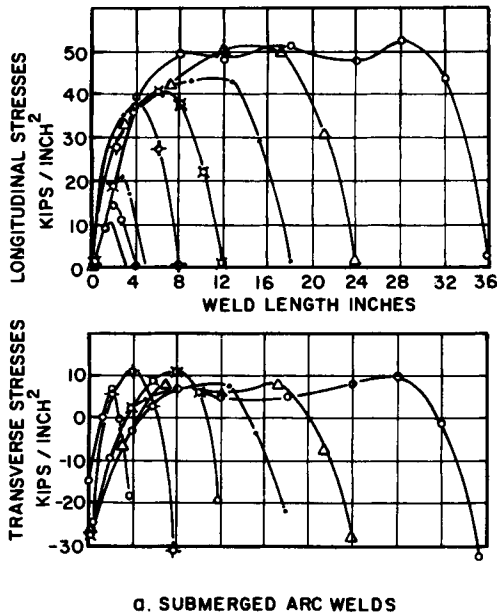


FIG. 6.40.(a) Distributions of residual stresses in butt welds of different lengths (DeGarmo *et al.*^(6.26)).

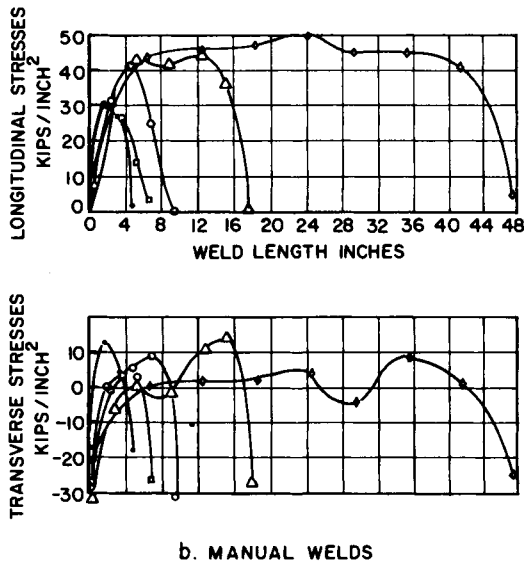


FIG. 6.40.(b) Distributions of residual stresses in butt welds of different lengths (DeGarmo *et al.*⁽⁶²⁶⁾).

Figures 6.40(a) and (b) show the distributions of residual stress in weldments made by the submerged arc process and the shielded metal-arc process, respectively. Shown are distributions of longitudinal and transverse stresses along the weld.

The longitudinal residual stress value must be zero at both ends of the weld while high tensile stresses exist in the central region. The peak stress in the central region increases with increasing weld length. This effect is shown clearly in Fig. 6.41 in which the peak stress for each panel is plotted vs. the weld length. The figure indicates that welds longer than 18 in. (457 mm) are needed to produce high tensile stresses in the longitudinal direction. As shown in Figs. 6.40(a) and (b), in welds longer than 18 in. Longitudinal residual stresses in the central region became uniform.

The transverse residual stresses shown in Fig. 6.40 were tensile in the central areas

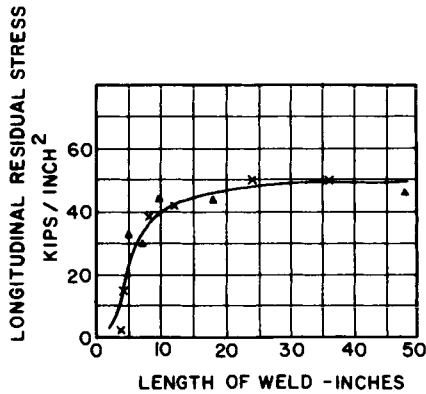


FIG. 6.41. Effect of length of weld on longitudinal residual stress (DeGarmo *et al.*⁽⁶²⁶⁾).

and compressive in the areas near the plate ends. The weld length had little effect on the maximum stress in either the central area or the areas near the plate ends.

6.6.2 Effect of specimen width

A simple way to analyze the effect of specimen width on stress distribution is to go through a computer simulation. The effect of specimen width is negligible as long as it is several times the width of the residual stress zone.

6.7 Residual Stresses in Heavy Weldments

When a weldment is made in a plate that is over 1 in. thickness, residual stresses in the thickness direction, σ_z , can become significant.

Figure 6.42 shows the distribution along the thickness direction of residual stresses in the weld metal of a butt joint, 1 in. (25 mm) thick, 20 in. (500 mm) by 20 in. (500 mm) in low-carbon steel. Shown in the figure are longitudinal stress, σ_x , transverse stress, σ_y , and the stress normal to the plate surface, σ_z . Welds made with covered electrodes, 0.1 to 0.2 in. diameter; welding operations were conducted from both sides alternately so that angular distortion could be minimized. The experiment was conducted by Gunnert using the Gunnert drilling technique, described in Section 4.2.7 (see Fig. 4.5).^(422, 423)

As shown in Fig. 6.42(a) and (b), longitudinal and transverse stresses were tensile in areas near both surfaces of the plate. Compressive stresses in the interior of the weld were apparently produced during the top and bottom welding passes.

Figure 6.42(c) shows the distribution of stresses normal to the plate surface, σ_z . σ_z must be zero at both surfaces. Though residual stresses were compressive in the case shown here, many investigators believe that σ_z in the interior of a thick weld can be tensile.

Other investigators have also reported experimental results on residual stresses in heavy weldments,^(538, 539, 627) but the information is still very limited.

The major difficulty seems to be a lack of adequate measuring techniques. As discussed in Section 4.8.1, in all of the stress measuring techniques in use today, including

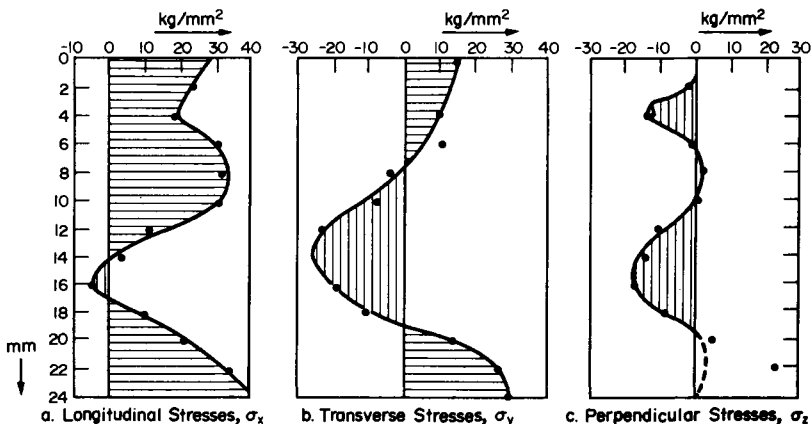


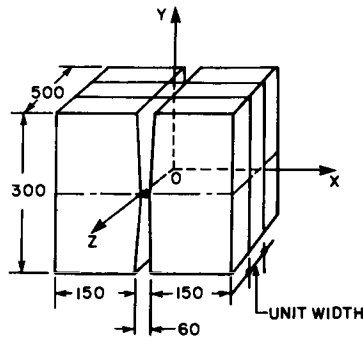
FIG. 6.42. Distributions along the thickness direction of residual stresses in the weld metal of a butt joint (Gunnert⁽⁴²²⁾).

the strain gage and X-ray diffraction techniques, the stresses are determined by measuring only the strains on the surface. There is no method, other than the as-yet undeveloped ultrasonic technique, that is capable of measuring the stress inside a body. When residual stress is measured in a heavy weldment, the surface on which the measurements are to be taken must be exposed through drilling or sectioning. Figure 4.5 shows the Gunnert drilling method and Fig. 4.6 shows the Rosenthal–Norton sectioning method.

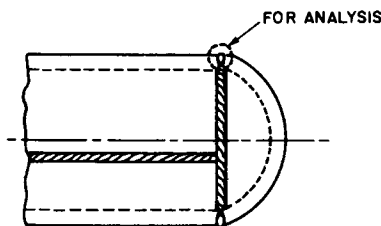
These methods are time-consuming and costly and provide stress measurements only at the drilled hole or along the sectioned block. But we need to know about the distribution of residual stresses throughout the entire weldment. We need to know how residual stresses may be changed or reduced by proper selection of welding procedures.

The development of analytical techniques may be one answer to our dilemma. The basic idea is explained in Fig. 4.28. The central question is: “How feasible is it to develop analytical models which can accurately analyze residual stresses in heavy weldments?” As described in Section 5.5.2, finite-element computer programs designated to analyze thermal stresses during the welding of heavy plates are currently being developed at M.I.T. (see Fig. 5.11). The following pages briefly describe the results obtained by Ueda *et al.*⁽⁵³⁸⁾

Study by Ueda et al.⁽⁵³⁸⁾ The weld joint as shown in Fig. 6.43(a) is idealized. This joint represents a joint between the cylindrical body and the hemispherical end plate, as shown in Fig. 6.43(b). The joint is biaxially symmetric with respect to the x - and y -axes (in the thickness direction). If welding passes are laid on both sides of the groove simul-



a. JOINT MODEL



b. WELD JOINT IN PRESSURE VESSEL

FIG. 6.43. Joint studied by Ueda *et al.*⁽⁵³⁸⁾

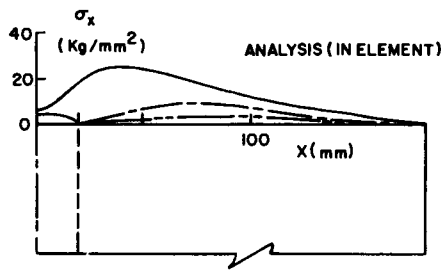
TABLE 6.5 Test conditions of the experiment reported in the paper by Ueda et al.^(5,38)

(a) Chemical compositions of base and weld metals (%)

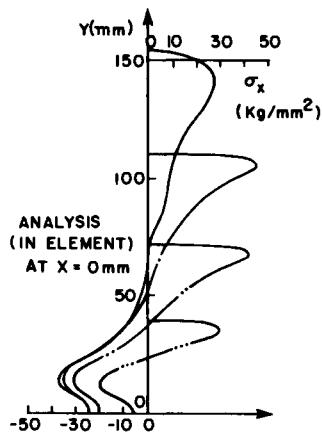
	C	Si	Mn	P	S	Cr	Mo
Base	0.09	0.29	0.46	0.04	0.013	2.38	1.03
Weld	0.07	0.42	0.78	0.012	0.012	2.28	1.06

(b) Welding conditions

Current	Voltage	Velocity	Heat-input	Preheating temperature
600 A	35 V	28 cm/min	45,000 J/cm	200°C



a. DISTRIBUTION ON THE SURFACE (Along the x-axis)



b. DISTRIBUTION ALONG THE Y-AXIS

FIG. 6.44. Transient stresses in the longitudinal directions.

taneously, the angular distortion can be prevented. The plate 300 mm (12 in.) thick was welded with 83 passes on each side of the groove.

The base metal used was ASTM A336 GF 22 and the wire used for welding was US 521 × G80. The chemical compositions are given in Table 6.5(a). Table 6.5(b) gives the welding conditions.

Figure 6.44(a) shows the transient longitudinal stresses (in the x-direction) on the specimen surface when it is heated to a peak temperature 200°C (392°F) during the intermediate processes of multilayer welding. Figure 6.44(b) shows the transient longitudinal stresses distributed in the thickness direction (y). The highest stress always appears just below the surface of the last layers.

Figure 6.45(a) shows longitudinal residual stresses on the surface, the highest stress being produced approximately 20 mm (0.8 in.) away from the toe of the final bead. Figure 6.45(b) shows longitudinal residual stresses induced along the y-axis.

As seen in Fig. 6.45, the highest longitudinal stress appears several layers below the bead surface where stress is positive but small. Judging from the residual stress distribution, delayed cracking would initiate below the finishing bead and propagate to the surface. The residual stresses obtained in the analysis were compared with those observed

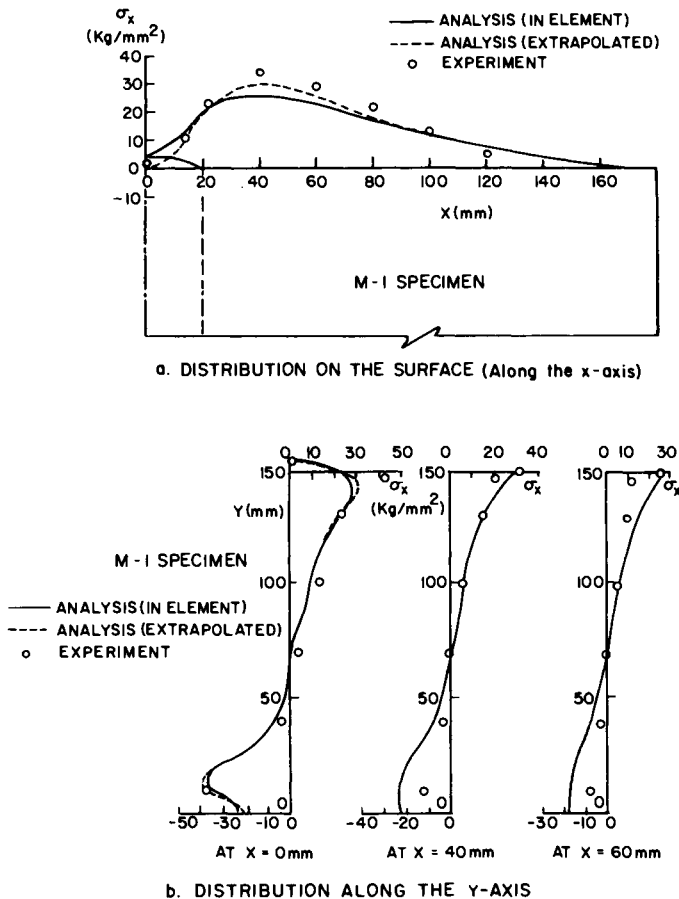


FIG. 6.45. Residual stresses in the longitudinal direction.

in the experiment in both Figs. 6.45(a) and (b), and the results were in close agreement. This would seem to indicate that the analysis is reliable enough to furnish information that cannot be obtained through experimentation.

6.8 Effects of Welding Sequence

When welding a long butt joint or a patch joint, various types of welding sequences are used in order to reduce residual stress and distortion. Figures 6.46(a), (b), (c), and (d) show backstep, block, built-up, and cascade sequences. The selection of a proper welding sequence is an important practical problem, especially when welding high restraint joints such as patch joints.

Investigators including Jonassen *et al.*⁽⁶²⁸⁾ Weck,⁽⁶²⁹⁾ Kihara *et al.*^(602, 603) and Watanabe and Satoh⁽⁴⁴²⁾ have studied how welding sequence affects residual stress build-up.

Kihara *et al.*^(602, 603) investigated how welding sequence affects residual stress and shrinkage in slit-type welds (see Fig. 6.5) and circular-patch welds. Welding sequences were classified as follows:

1. *Multilayer*. The first layer is completed along the entire weld length (there may be various ways of achieving this including straight forward, backstep, skip, etc.); then the second layer is welded and so on.
2. *Block welding*. A given length (or "block") of the joint is welded completely, then the next block is welded, and so on.

This experiment also investigated such fundamental problems as the effect of specimen constraint on residual stress when the degree of constraint is changed by changing the slit length.

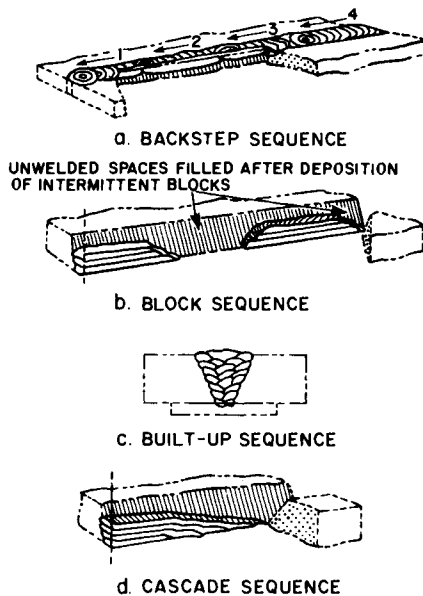


FIG. 6.46. Some welding sequences.

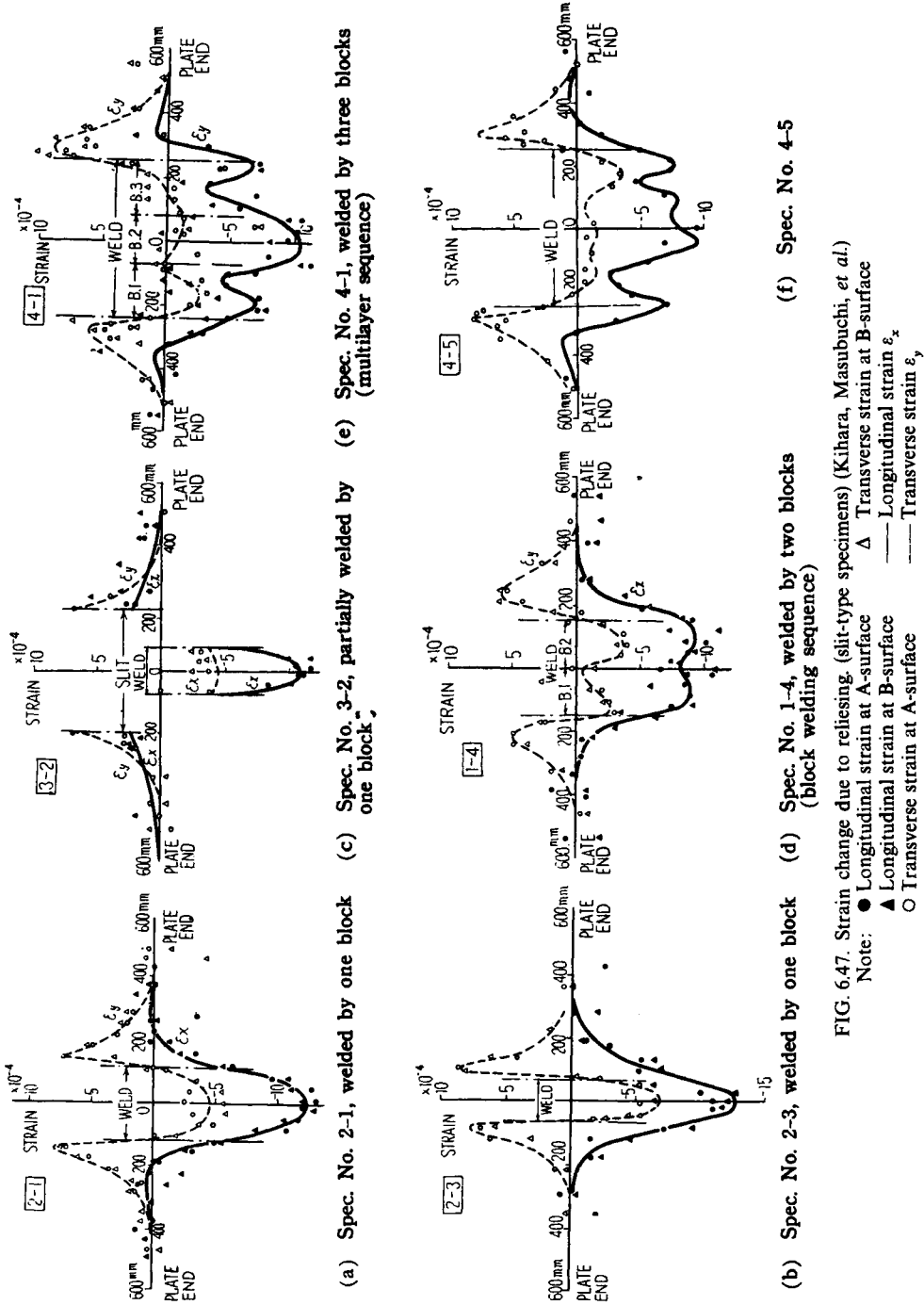
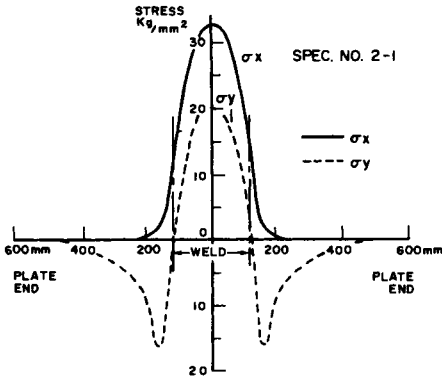
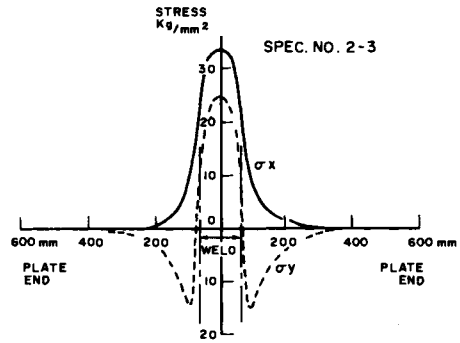


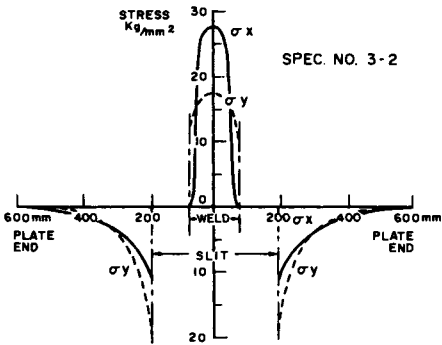
FIG. 6.47. Strain change due to relieving. (slit-type specimens) (Kihara, Masubuchi, et al.)



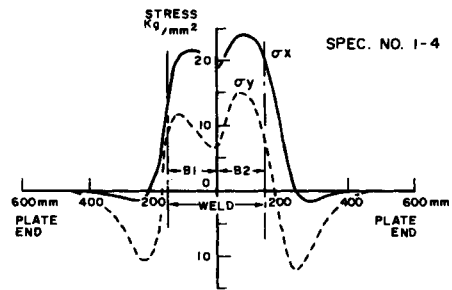
(a) Spec. No. 2-1, welded by one block



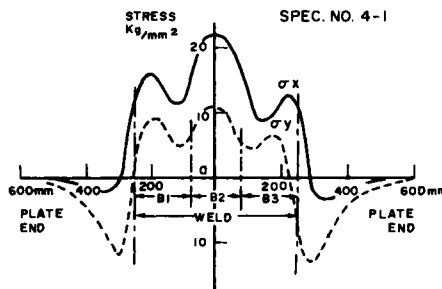
(b) Spec. No. 2-3, welded by one block



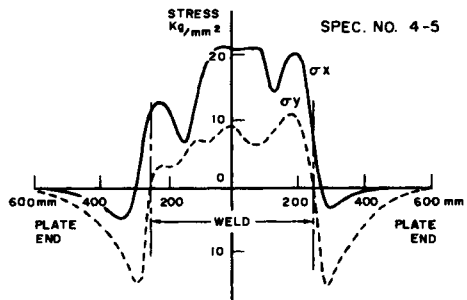
(c) Spec. No. 3-2, partially welded by one block



(d) Spec. No. 1-4, welded by two blocks (block sequence)



(e) Spec. No. 4-1, welded by three blocks (complete multilayer sequence)



(f) Spec. No. 4-5, welded by three blocks (multilayer sequence after adopting block sequence)

FIG. 6.48. Distributions of residual stress along weld line (split-type specimens) (Kihara, Masubuchi *et al.*).

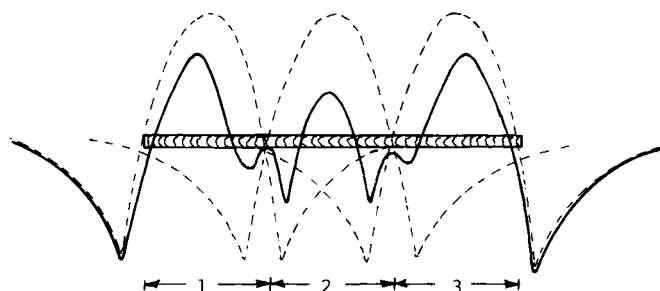


FIG. 6.49. Schematic explanation of complicated stress distribution on welded bead.

Detailed measurements of the residual stress were taken on the weld line of the specimens using an electrical resistance wire strain meter. The change of strain produced by cutting a 35-mm-wide (1.4 in.) strip from the specimen was measured. In some of the specimens Gunnert's extensometer was used. Both the strain changes due to cutting-out and the residual stress distribution obtained from them are shown in Figs. 6.47 and 6.48 respectively. The results using Gunnert's extensometer are shown in Fig. 6.49. From this data the following observations can be made:

The distribution of residual stress in those specimens welded with one block over the total slit length are shown in Figs. 6.48(a) and (b). They have a tendency analogous to the test results in Fig. 6.8. But in a specimen in which one bead was put on the mid-part of the slit, the residual stress distribution became as shown in Fig. 6.48(c). This varies from Figs. 6.48(a) and (b) in that Fig. 6.48 large compressive stress is produced in the longitudinal direction in the base metal. This is probably because residual stress in such a specimen is affected more by transverse shrinkage than by longitudinal shrinkage.

Figures 6.48(d), (e), and (f) show the results of tests made on specimens welded with two and three blocks. Both the longitudinal and transverse stress are tensile in the weld and compressive in the base metal; this is analogous to those results obtained when specimens were welded with one block, but the measured values on the weld line are so scattered that it is difficult to draw a smooth curve. The scattering can be seen in the specimen welded using the block method as well as the complete multi-layer method. Thus complicated distribution of residual stress is probably formed during welding by the superposition of the residual stress (see Figs. 6.48(a) or (b)) produced by the weld of each bead. Figure 6.49 shows the formation of this complicated stress distribution schematically. According to test results slit-type and circular-patch-welded specimens have an uneven residual stress distribution that is probably produced at each electrode exchange point. This seems to be one of the major reasons why we can draw no decisive conclusions about the relation between welding sequence and residual stress.

On the basis of experimental results obtained so far, one can summarize as follows:

1. As far as residual stresses along the weld are concerned, the effect of welding sequence was minor; high tensile longitudinal stresses were found in all welds tested.
2. Differences in welding sequence caused considerable differences in transverse shrinkage, in the amount of total strain energy produced in restrained joints, and in the amount of reaction stress in the inner plates of circular-patch welds. Block

welding sequences generally produced less shrinkage, less strain energy, and less reaction stress than multilayer sequences. Shrinkage is also discussed in Chapter 7.

References

- (601) YODHIDA, T., ONOUE, H., and KURIHARA, Y., "Study on reaction stress on groove welded joint (Report 1)", *Journal of the Japan Welding Society*, 32, No. 5, 434–442 (1963).
- (602) KIHARA, H. and MASUBUCHI, K., "Studies on the shrinkage and residual welding stress of constrained fundamental joint", *Reports of Transportation Technical Research Institute*, no. 7, 1954, no. 20, 1956.
- (603) KIHARA, H., MASUBUCHI, K., and MATSUYAMA, Y., *Effect of Welding Sequence on Transverse Shrinkage and Residual Stresses*, Report No. 24 of Transportation Technical Research Institute, Tokyo, 1957.
- (604) KIHARA, H., MASUBUCHI, K., and OGURA, Y., "Radial contraction and residual stresses in circular patch weld", Parts I and II, *Journal of the Society of Naval Architects of Japan*, **99**, 111–122, and **100**, 163–170 (1956).
- (605) HILL, R., *The Mathematical Theory of Plasticity*, Oxford University Press, London, 1950.
- (606) PRAGER, W. and HODGE, P. G., *Theory of Perfectly Plastic Solids*, John Wiley & Sons, Inc., 1951.
- (607) WATANABE, M. and SATOH, H., "Plastic study on residual stresses due to welding", *Technology Reports of the Osaka University*, **1** (13), 179–190 (Oct. 1951).
- (608) MASUBUCHI, K., "Calculation and measurement of residual stresses due to spot heating", *Welding in the World*, **1** (1), 18–27 (1963), and *Soud. Technical Communication*, **17** (3/4), 127–132 (Mar.–Apr. 1963).
- (609) BIERETT, G. and GRUNING, G., *Bulletin International Railway Congress Association*, **17**, 1185–1198 (1935).
- (610) HARTER, I., HODGE, J. C., and SCHOESSOW, G. J., "The value of electric arc welding in design", *Welding Journal*, **18** (9), 528–547 (1939).
- (611) YOSHIDA, T., ABE, T., and ONOUE, H., "Residual stresses in circular-patch welds", *Journal of the Society of Naval Architects of Japan*, **105** (1959).
- (612) DAWES, M. G., "Analysis of residual stresses in welded I beam connections", *British Welding Journal*, **12** (10), 507–516 (1965).
- (613) NAGARAJA RAO, N. R., ESATUAR, F. R., and TALL, L., "Residual stresses in welded shapes", *Welding Journal*, **43** (7), Research Supplement, 295s–306s (1964).
- (614) ALPSTEN, G. A. and TALL, L., "Residual stresses in heavy welded shapes", *Welding Journal*, **39** (3), Research Supplement, 93s–105s (1970).
- (615) BJORHOVDE, R., Brozzetti, J., Alpsten, G. A., and Tall, L., "Residual stresses in thick welded plates", *Welding Journal*, **51** (8), Research Supplement, 392s–405s (1972).
- (616) WATANABE, M., MINEHISA, S., and ONOUE, H., "Some experimental studies on the residual stresses of the welded pipes", *Journal of the Japan Welding Society*, **24** (), 84–89 (1955).
- (617) BURDEKIN, F. M., "Local stress relief of circumferential butt welds in cylinders", *British Welding Journal*, **10** (9), 483–490 (1963).
- (618) IKEDA, K. and KIHARA, H., "Brittle fracture strength of welded joints", *Welding Journal*, **49** (3), Research Supplement, 106s–114s (1970).
- (619) AKITA, Y. and YADA, T., "On brittle fracture initiation characteristics of welded structures", *Journal of the Society of Naval Architects of Japan*, **117**, 95–237–243 (1965).
- (620) YURIOKA, N., "Rational approach to the establishment of acceptance levels of heavy weldments", M.S. Thesis at M.I.T., May 1972.
- (621) ADAMS, C. M., Jr. and Corrigan, D. A., *Mechanical and Metallurgical Behaviour of Restrained Welds in Submarine Steels*, Final Report, Massachusetts Institute of Technology Welding Laboratory, Cambridge, Mass., Contract NOBS-92077, May 1966 (AD-634 747).
- (622) WAHLFRAT, H., *Schweisseigenspannungen*, HTM 31, 1976.
- (623) GOLDBERG, F., "The effect of residual stress and quality of the thermal cutting edges of the fatigue and static strength of steel", *Australian Welding Journal*, pp. 127–134 (Sept.–Oct. 1974).
- (624) GOLDBERG, F., Ruge, J., Schimoller, H., and Sabelstrom, W., "The relation between the residual stress, microstructure, and microhardness of gas and plasma cut surfaces", IIW Document No. I-537–74, 1974.
- (625) ROBELOTTO, R., LAMBASE, J. M., and TOY, A., "Residual stresses in welded titanium and their effects on mechanical behavior", *Welding Journal*, **47** (7), Research Supplement, 289s–298s (1968).
- (626) DEGRAMO, E. P., MERIAM, J. L., and JONASSEN, F., "The effect of weld length upon the residual stresses of unstrained butt welds", *Welding Journal*, **25** (8), Research Supplement, 485s–486s (1946).
- (627) UEDA, Y., FUKUDA, K., and ENDO, S., "A study on the accuracy of estimated residual stresses by the existing measuring methods", *Transactions of the Japan Welding Research Institute, Osaka Univ.* **4**, (2) 117–121 (1975).

- (628) JONASSEN, F., MERIAM, J. L., and DEGRAMO, E. P., "Effect of certain block and other special welding procedures on residual welding stresses", *Welding Journal*, **25** (9), Research Supplement, 492s-4962 (1946).
- (629) WECK, R. *Transverse Contractions and Residual Stresses in Butt Welded Mild Steel Plates*, Report No. R4, Admiralty Ship Welding Committee, Jan. 1947.
- (630) WATANABE, M. SATOH, K., KIMURA, K., and HOSHI, R., "Effect of welding methods and sequences on the residual stress distribution of welded joints", *Journal of the Japan Welding Society*, **24** (4), 146-153 (1955).

Distortion in Weldments

RESIDUAL stresses, discussed in Chapter 6, and distortion, discussed in this chapter, are closely related phenomena. During heating and cooling in the welding cycle, thermal strains occur in the weld metal and base-metal regions near the weld. The strains produced during heating are accompanied by plastic upsetting. The stresses resulting from these strains combine and react to produce internal forces that cause bending, buckling, and rotation. It is these displacements that are called distortion.

This chapter presents the present state of weld-distortion analysis. As in Chapter 6, discussions emphasize fundamentals: How do the various weld-distortion mechanisms work? What factors affect weld distortion and how do we analyze their effects?

The formulas, tables, and figures presented in this chapter have been collected from many sources. Different investigators often use different notations for the same or similar terms, resulting in a certain amount of confusion. Some of the data given in this chapter will therefore be in metric units and some in English units.

7.1 Fundamental Types of Distortion

Three fundamental dimensional changes that occur during the welding process cause distortion in fabricated structures:

1. Transverse shrinkage perpendicular to the weld line.
2. Longitudinal shrinkage parallel to the weld line.
3. Angular distortion (rotation around the weld line).

These dimensional changes are shown in Fig. 7.1 and are classified by their appearance as follows:

- (a) *Transverse shrinkage*. Shrinkage perpendicular to the weld line.
- (b) *Angular change* (transverse distortion). A non-uniform thermal distribution in the thickness direction causes distortion (angular change) close to the weld line.
- (c) *Rotational distortion*. Angular distortion in the plane of the plate due to thermal expansion.
- (d) *Longitudinal shrinkage*. Shrinkage in the direction of the weld line.
- (e) *Longitudinal bending distortion*. Distortion in a plane through the weld line and perpendicular to the plate.
- (f) *Buckling distortion*. Thermal compressive stresses cause instability when the plates are thin.

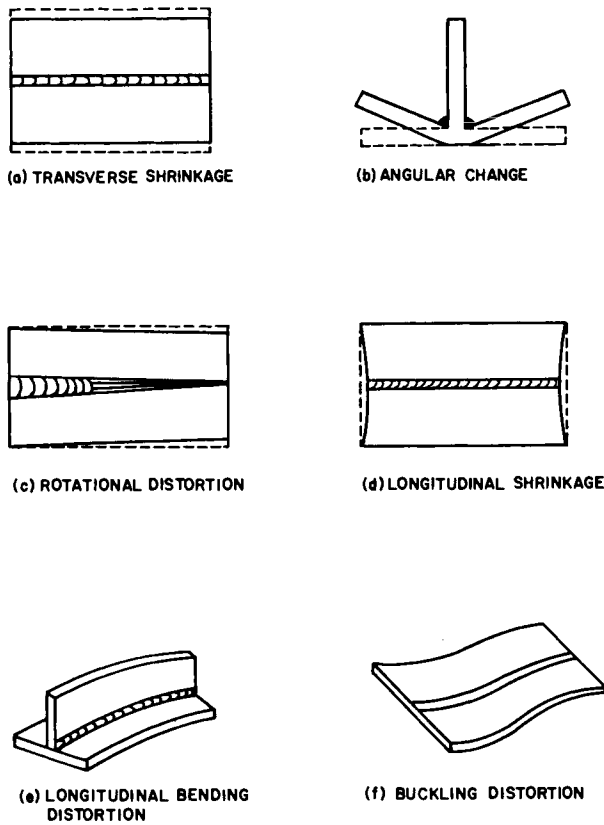


FIG. 7.1. Various types of weld distortion.

7.2 General Introduction to Weld Distortion

7.2.1 Three approaches to solving the distortion problem

There are three approaches to solving the problem of weld distortion (see Fig. 7.2):

1. The development of welding processes and fabrication procedures that minimize distortion.
2. The establishment of rational standards for acceptable distortion limits.
3. The development of proper techniques for removing distortion after it has occurred.

A proper combination of these approaches would be most effective in controlling weld distortion.

Minimizing distortion. The first approach is to minimize the distortion. It is much easier in the long run to build the structure without distortion than to reduce distortion later. If shrinkage and distortion of individual welds are reduced, the distortion resulting after fabrication of the entire complex welded structure is also reduced. A welding process that will reduce and that can be used in structure fabrication is needed. If there were a welding process available that would produce no shrinkage or distortion whatsoever, our problems would be solved.

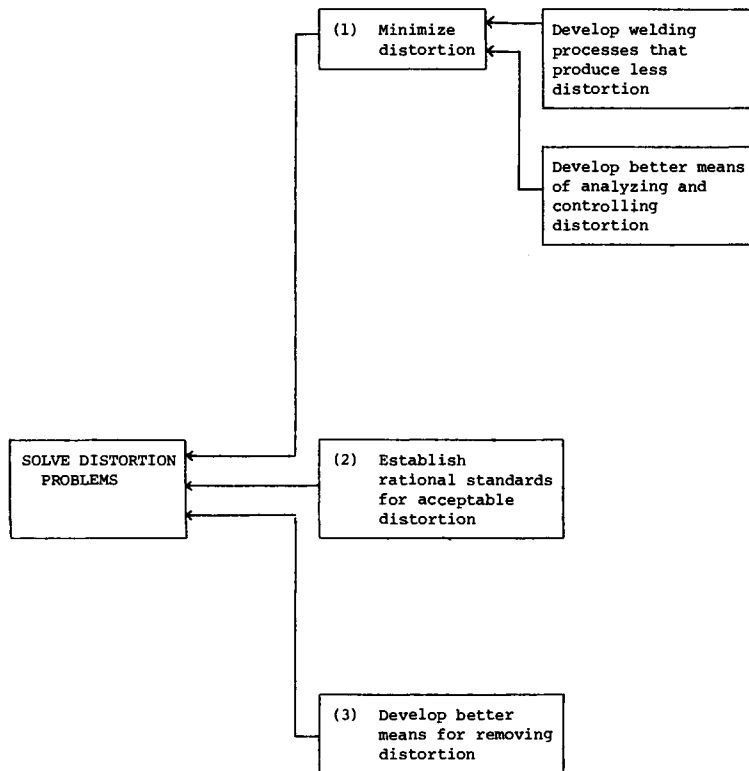


FIG. 7.2. Various approaches to solving distortion problems.

Presently, however, there is no process that completely eliminates distortion. Many factors within the welding procedure contribute to the distortion of a large, complex structure. These include the welding sequence, the degree of restraint, the welding conditions, the joint details, and the preheat and interpass temperatures. We must determine how these factors contribute to distortion before we can begin to analyze them systematically. These factors and the present state-of-the-art of their analysis is the subject of this chapter.

Rational standards for acceptable distortion. Because some distortion is inevitable, establishing standards that will define the acceptable distortion limits is an important technical problem. These standards should take into account:

1. The reliability of the structure.
2. The economic value of the structure.
3. The fabrication cost.

Such standards should be both rational and practical when they establish what distortion is acceptable and what distortion is not. They must insure the reliability of the structure, but must not require costly reworking unnecessary to the structure's reliability.

Removing distortion after it has occurred. Although post-weld straightening should be kept to a minimum, especially with heat-treated materials, distortion that exceeds the acceptable limits does occur. This distortion often occurs during fabrication, but can

also occur during service, by overload or collision, for example. When this happens, the distortion must be removed economically and with a minimum amount of damage to the structure.

Many techniques have been used in distortion-removal. The flame-heating of the plate at selected spots or along certain lines followed by cooling it with water is the most commonly used technique. Sometimes plates are hammered while they are being heated. This technique requires great intuitive skill on the part of the workman, however; very little scientific information, either analytical or experimental, is available on the material degradation and the mechanisms of distortion-removal that are operative when this treatment is used.

As stated above, this chapter is primarily concerned with analytical methods of predicting and controlling distortion, and presents background information and pertinent data upon which analytical systems can be built.

7.2.2 *Books and reviews available*

Several reviews and books have been written on distortion in weldments and welded structures.

Spraragen and his associates of the Welding Research Council prepared a series of comprehensive reviews on distortion and shrinkage that appeared in 1937, 1944, and 1950.⁽⁵⁰²⁻⁵⁰⁴⁾ Two reports from the Redstone Scientific Information Center, U.S. Army Missile Command, RSIC-410 [1965] and RSIC-820 [1968], contain information pertinent to distortion in welded structures.^(301,512) Welding Research Council Bulletins 149 and 174, published in 1970 and 1972, are the latest reviews about weld distortion.^(303,501)

In 1968 the Welding Institute (England) published a book entitled *Control of Distortion in Welded Fabrication*, a revision of a book originally published in 1957.^(701,702)

Four books on distortion and residual stresses have been published in Japan.^(505,507,703) One of these, published in English in 1959 by the Society of Naval Architects of Japan, systematically covers the studies done in Japan.^{(506)†} The book published in 1965 by Watanabe and Satoh also is quite comprehensive.⁽⁵⁰⁷⁾

In the Soviet Union several books have been written on distortion.^(508,509,705-707) One of these, written by Okerblom, has been translated into English.⁽⁵⁰⁸⁾

Battelle Memorial Institute issued an extensive handbook on weld distortion.⁽⁷⁰⁸⁾ It contains tables and figures on weld distortion and a bibliography containing 660 references published in various countries. The handbook, however, is not published.

7.2.3 *Methodologies for analyzing weldment distortion*

As already discussed in Sections 3.3 and 6.1, there are several ways to analyze residual stresses and distortion (see Figs. 3.13 and 6.1).

The orthodox method is analytical simulation. This approach makes it possible to study not only distortion after welding is completed, but also transient metal movement as well. This is its great advantage. It is important to follow the metal movement, because distortion during welding and distortion after welding is completed are quite different.

† Reference (704) includes many formulas on weld distortion.

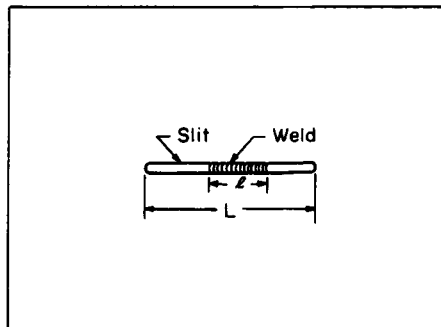
For example, Fig. 5.25 shows change of deflection during welding along the longitudinal edge of a rectangular plate. Distortion during welding is opposite to the distortion after welding is completed.

But analytical simulation is much too complex a method to be useful in very many situations. Computer programs are required to calculate the transient distortion, even in common, simple cases, such as a weld along the edge of a rectangular plate. The determination of the incompatible strains produced during welding in regions near the weld is the step that makes the analysis so complex.

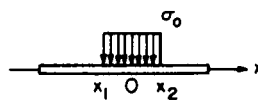
If one is concerned only with the distortion that remains after the welding is completed, analytical simulation is unnecessary; the distortion is treated as an elastic stress field containing incompatible strains. The mathematics involved in this are relatively simple, making this approach useful in analyzing actual practical joints. Several investigators, including Masubuchi,^(301, 303, 501, 512) have used this method to analyze weld distortion in various practical joints. Masubuchi^(314, 323) has proposed a study of weld distortion using an aerodynamic-theory approach (see Section 3.2.5).

The following section describes some of these analytical methods using examples from actual studies.

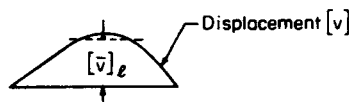
Analytical determination of the degree of restraint. Kihara and Masubuchi^(323, 603) developed a concept to analytically determine the degree of restraint in a slit weld joint (see Fig. 7.3). Welds similar to this type are frequently used in repair operations. In a slit weld, the transverse shrinkage is restrained by the bare metal surrounding the weld.



a. Slit-Type Specimen



b. Assumed Stress Distribution



c. Displacement Transverse

FIG. 7.3. Analysis of degree of restraint, k_s , of a slit-type weld.

In a slit joint, the degree of restraint, k_s , when welding is done between $x = x_1$ and x_2 (slit length L ; weld length $l = x_1$ to x_2), is defined by the following equation[†]

$$k_s = (\pi/2)(E/L)(l/L)(1/F), \quad (7.1)$$

where

$$F = \sum_{n=1}^{\infty} 1/n \left(\int_{\theta_1}^{\theta_2} \sin \theta \cdot \sin n\theta \cdot d\theta \right)^2,$$

$$x_1 = (L/2) \cos \theta_1,$$

$$x_2 = (L/2) \cos \theta_2.$$

Table 7.1 shows how eqn. (7.1) is derived.

TABLE 7.1 *Analytical determination of degree of restraint, k_s*

When normal stresses $\sigma_{y0}(x)$ are applied along both edges of a straight slit (length L) in an infinite plate, both edges move closer together. The relationship between the stress applied, σ_{y0} , and the closing of the slit, or dislocation, $[v]$ is as follows (see Table 3.5):

$$\sigma_{y0} = (E/4\pi) \int_{-L/2}^{L/2} \frac{1}{x-x'} (d[v]/dx)_x \cdot dx'. \quad (1)$$

The above equation is satisfied when $[v]$ and σ_{y0} are expressed as follows:

$$[v] = \sum_{n=1}^{\infty} A_n \sin n\theta, \quad \sigma_{y0} = (E/2L) \sum_{n=1}^{\infty} n A_n \frac{\sin n\theta}{\sin \theta}. \quad (2)$$

When uniform stress σ_0 is applied along the slit from $x = x_1$ to x_2 , or $\theta = \theta_1$ to θ_2

$$\sigma_{y0} = (E/2L) \sum_{n=1}^{\infty} n A_n \frac{\sin n\theta}{\sin \theta} = \begin{cases} \sigma_0, & \theta_1 \leq \theta \leq \theta_2 \\ 0, & 0 \leq \theta < \theta_1, \text{ and} \\ & \theta_2 < \theta \leq \pi \end{cases} \quad (3)$$

Coefficient A_n is determined as follows:

$$(E/2L)nA_n = (2/\pi)\sigma_0 \int_{\theta_1}^{\theta_2} \sin \theta \cdot \sin n\theta \cdot d\theta, \quad (4)$$

consequently, dislocation, $[v]$, is expressed:

$$[v] = (4L\sigma_0/\pi E) \sum_{n=1}^{\infty} (P_n/n) \sin n\theta \quad (5)$$

where

$$P_n = \int_{\theta_1}^{\theta_2} \sin \theta \cdot \sin n\theta \cdot d\theta.$$

The average value of $[v]$ from x_1 to x_2 , $[\bar{v}]_l$ is:

$$[\bar{v}]_l = \frac{1}{l} \int_{x_1}^{x_2} [v] dx = \frac{2}{\pi} \cdot \frac{L}{l} \cdot \frac{L}{E} \cdot \sigma_0 \cdot F \quad (6)$$

where

$$F = \sum_{n=1}^{\infty} P_n^2/n = \sum_{n=1}^{\infty} 1/n \left(\int_{\theta_1}^{\theta_2} \sin \theta \cdot \sin n\theta \cdot d\theta \right)^2.$$

Then

$$k_s = \frac{\sigma_0}{[\bar{v}]_l} = \frac{\pi}{2} \cdot \frac{E}{L} \cdot \frac{l}{L} \cdot \frac{1}{F}. \quad (7)$$

[†] Because K is used to express the stress intensity factor in the fracture mechanics theory, k_s is used in this chapter to express the degree of restraint. Read Chapter 14 (Section 14.5.2) for further details.

[‡] There was an error in the definition of F given in Reference (303). The definition given in Reference (323) is correct.

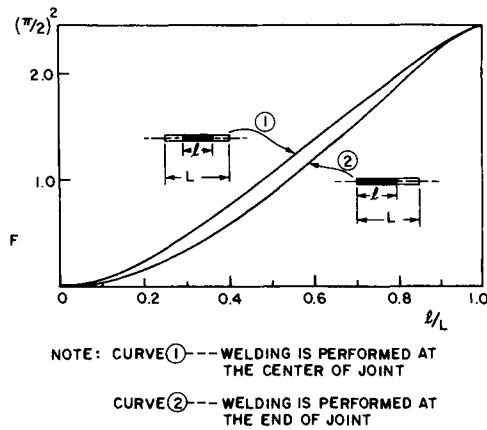


FIG. 7.4. Values of F as a function of l/L .
 l : weld length, L : slit (or joint) length.

Figure 7.4 shows the values of F as a function of l/L . Shown here are the values of F when the weld is located in the center of the slit (case 1) and when the weld is located at one end of the slit (case 2).

The physical meaning of k_s is as follows: When uniform stress σ_0 is applied along the part of the slit between $x = x_1$ and x_2 , the relationship between σ_0 and the mean value of dislocation over the portion of the slit where the load is applied, $[\bar{v}]_l$, is given by

$$\sigma_0 = k_s [\bar{v}]_l. \tag{7.2}$$

Masubuchi used the parameter k_s to study the effect of the degree of restraint on transverse shrinkage of a slit-type weld. Figure 7.5 shows a relationship between k_s values of

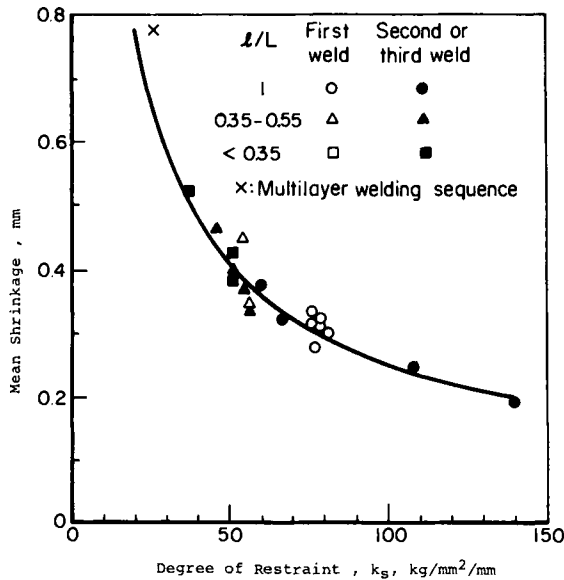


FIG. 7.5. Relationships between degree of restraint, k_s , and transverse shrinkage in a slit-type specimen.

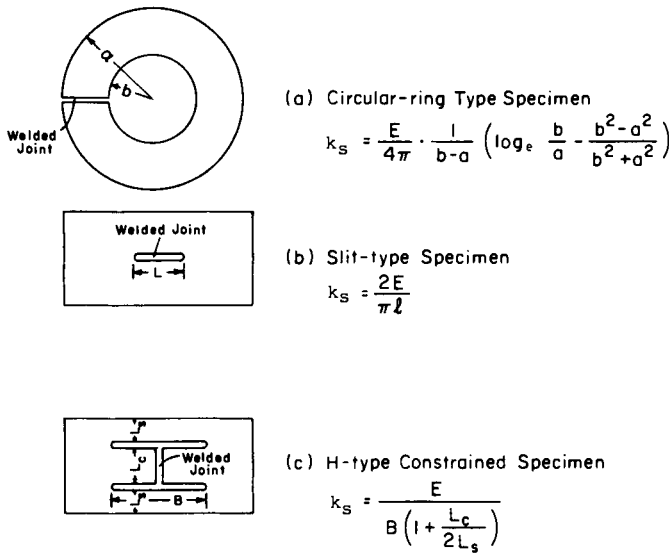


FIG. 7.6. Specimen types included in the analysis by Watanabe and Satoh.⁽⁷⁰⁹⁾

joints and values of transverse shrinkage determined experimentally. Experiments were conducted on joints with various slit lengths, L (3 to 4 in.) and weld lengths, l ($l/L = 0.3$ to 1.0). Results obtained with a block welding sequence and a multi-layer sequence are also plotted. The figure shows that transverse shrinkage decreases as the degree of restraint increases.

Kihara and Masubuchi⁽⁶⁰³⁾ analyzed the effect of the degree of restraint on the transverse shrinkage of a ring as shown in Fig. 7.6(a).⁽⁷⁰⁸⁾ Later, Watanabe and Satoh⁽⁷⁰⁹⁾ found that results obtained by different investigators using different types of specimens can be compared by using the degree of restraint. Figure 7.7 shows a relationship between

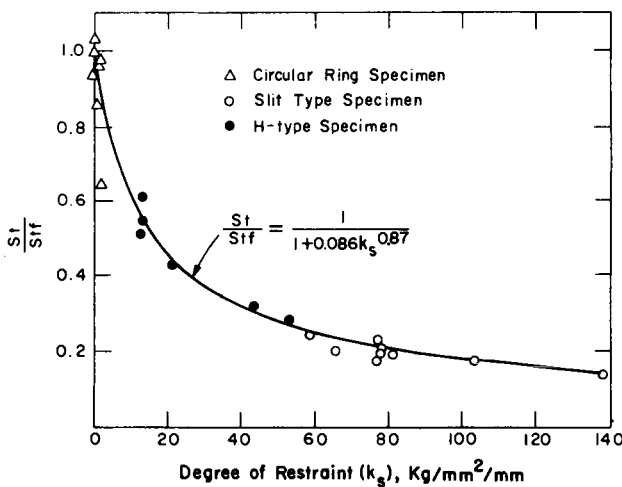


FIG. 7.7. Effect of external constraint on the transverse shrinkage of butt-welded joints (Watanabe and Satoh).⁽⁷⁰⁹⁾

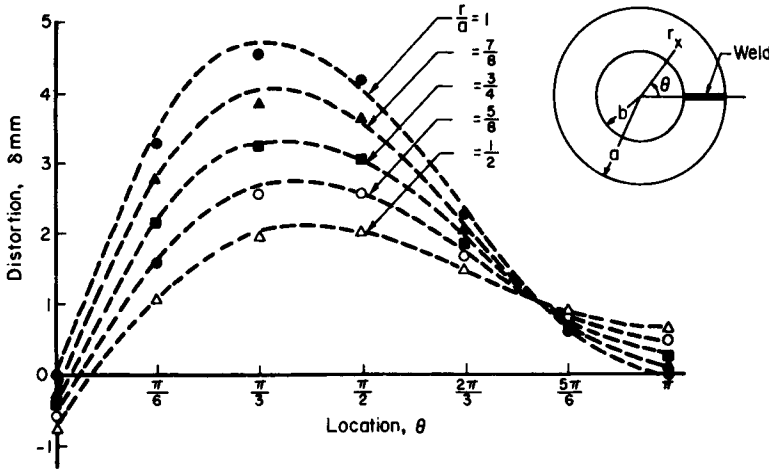


FIG. 7.8. Distortion of a ring-type specimen due to angular change at the weld.

Note: Points plotted in the figure are the distortions measured at various locations. Broken lines indicate the calculated distortion (angular change $\phi = 0.058$ radian).

the degree of restraint k_s and the ratio between the shrinkage of free welds, $s_{f,}$ and the shrinkage of restrained welds, S_r . Figure 7.6 also shows formulas used to calculate the degree of restraint of different specimens. Further discussions of the degree of restraint and its significance in weld cracking are presented in Chapter 14.

Analysis of distortion due to angular change. Kihara and Masubuchi⁽⁶⁰²⁾ analyzed distortion produced in a ring-type specimen by angular change due to butt welding. An example of distortion measured by a dial gage is shown in Fig. 7.8. A single-vee-type bevel was prepared in the ring-type specimen with a 24-in. (600 mm) outer diameter, 12-in (300 mm) inner diameter, and $\frac{3}{4}$ in. (19 mm) plate thickness. The results shown here were obtained after one side of the bevel was completely welded.

The distortion of a ring-type specimen due to angular change can be analyzed as a problem of ring-dislocation, as shown in Fig. 3.9. When the angular change at the weld is ϕ , the distortion, δ , of the ring is:

$$\frac{\delta}{a} = \frac{1 - \nu}{8\pi} \phi H(\rho, \theta) \tag{7.3}$$

where

$$H(\rho, \theta) = \rho \left[\left\{ 2 \frac{1 + \nu}{1 - \nu} \log \rho + \left(\frac{1 + \nu}{3 - \nu} \right) \frac{1 - \rho^2}{1 + \lambda^2} + \left(\frac{\lambda^2}{1 + \lambda^2} \right) \frac{1 - \rho^2}{\rho^2} \right\} \cos \theta + \frac{4(\pi - \theta)}{1 - \nu} \sin \theta \right]$$

$$\rho = \frac{r}{a},$$

$$\lambda = \frac{b}{a},$$

a = outer diameter of ring,

b = inner diameter of ring,

ν = Poisson's ratio of the material.

It is evident that the distortion of a circular ring can be calculated when the angular change at the weld (ϕ) is known. As shown in Fig. 7.8 an excellent correlation was obtained between the calculated and the measured distortion.

7.2.4 Development of weld-distortion analysis

Studies of weld distortion have been conducted since the 1930s. The results of these early studies have been summarized in a series of reviews by Spraragen and others.⁽⁵⁰²⁻⁵⁰⁴⁾ Most of the early studies were empirical.

Naka⁽⁷⁰³⁾ was the pioneer in the analytical study of shrinkage. In his work, most of which was carried out around 1940, he studied analytically and experimentally how a butt weld shrinks. Figure 7.6(b) shows the H-type constrained joint frequently used by Naka. To avoid mathematical complication, the analysis was kept one-dimensional, neglecting the change of shrinkage in the welding direction.

Okerblom⁽⁵⁰⁸⁾ also conducted extensive research on weld distortion.

During the 1950s several Japanese investigators, including Kihara, Watanabe, Masubuchi, and Satoh, carried out extensive study programs on residual stresses and distortion. Some of the results of these studies as they relate to residual stress are presented in Chapter 6. They concentrated on stress and distortion in practical joints. In order to analyze their experimental data, they frequently used an analysis based on the incompatibility concept. A number of empirical formulas on various types of distortion were developed, and one system of formulas developed by Watanabe and Satoh⁽⁷⁰⁹⁾ is presented here.

Most of the efforts during this period, however, concentrated on the distortion remaining after the welding is completed. Most of the experiments were on weldments in low-carbon steel made using covered electrodes.

In the 1970s and with the accessibility of modern computers, interest in analytical simulation has been renewed. The analysis of thermal stress was the focus of the first computer-simulation projects (see Chapter 5). Since then, the emphasis has been on transient metal movement.

7.2.5 Watanabe–Satoh's distortion formulas

Based on their extensive experimental and analytical studies, Watanabe and Satoh⁽⁷⁰⁹⁾ have developed formulas for various types of distortion (see Table 7.2 and Fig. 7.9). Table 7.2 includes formulas for

1. Transverse shrinkage in bead-on-plate and butt welds.
2. Angular changes in bead-on-plate, fillet, and butt welds.

The formulas cover the effects of various factors, including:

1. *Arc characteristics*: welding current I (amperes); arc voltage, v (volts); heat efficiency of the welding arc, n ; welding speed, v (cm/sec).
2. *Joint characteristics*: the cross-sectional area of the weld groove, A (cm²), and the weight of the deposited metal per unit weld length, W (g/cm).
3. *Electrode characteristics*: The melted weight of the wire per unit current and time (g/amp/sec); the deposition efficiency of the electrode, μ , and the electrode diameter, ϕ (mm).

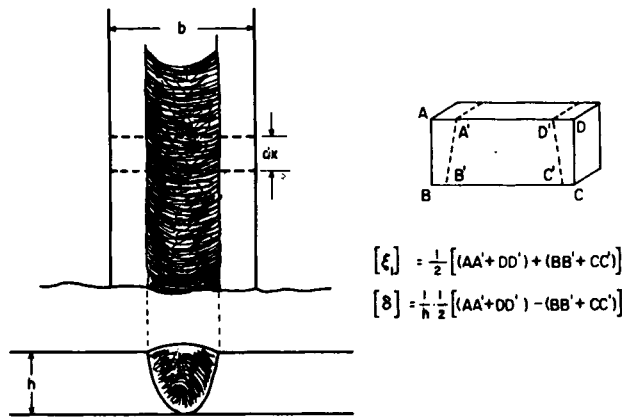


FIG. 7.9. Definition of inherent shrinkage.

In Watanabe and Satoh’s analysis, values called the “inherent shrinkage”, (ξ) , and the “inherent angular change”, (δ) , are used. It is assumed that the inherent strains that result in shrinkage distortion exist in a region of breadth, b , near the weld (see Fig. 7.9). When a small element, $bh \cdot dx$ ($h =$ plate thickness), is cut from the weld, the element will contract and bend; the original form $ABCD$ will change to $A'B'C'D'$. The components of the inherent distortion are as follows:

$$\begin{aligned} \{\xi\} &= 1/2 \{(AA' + DD') + (BB' + CC')\}, \\ \{\delta\} &= 1/h \cdot 1/2 \{(AA' + DD') - (BB' + CC')\}. \end{aligned} \tag{7.4}$$

7.3 Existing Allowable-Distortion Standards

The various industrial and military codes and specifications that cover welding fabrication provide standards for allowable distortion, most of which seem to be based upon experience obtained over years of working with steels, especially low-carbon steel. It appears that, with the exception of those used by the Navy, the same standards of allowable distortion that are used for structural steel are also used for aluminum. This section is an outline of the existing distortion standards.

7.3.1 Navy specification for ship hulls

Several U.S. Navy specifications contain allowances for shrinkage and unfairness in welded plating. These specifications include:

- NAVSHIPS 0900-0060-4010. “Fabrication, Welding and Inspection of Metal Boat and Craft Hulls”, 21 January 1971, Naval Ship Systems Command.
- NAVSHIPS 0900-000-1000. “Fabrication, Welding, and Inspection of Ship Hulls”, 1 October 1968, Naval Ship Systems Command.
- NAVSHIPS 0900-014-5010. “Fabrication, Welding, and Inspection of Non Combatant Ship Hulls”, December 1966, Naval Ship Engineering Center.

TABLE 7.2 Inherent shrinkage and inherent angular change in various welded joints⁽⁷⁰⁹⁾

Joints	Type of functions	Conventional formulas	Physical meaning of constants
Bead-on plate	Inherent shrinkage $\xi_1 \propto \left(\frac{Q}{h}\right)^2$	$\xi_1 = C \left(\frac{I}{h\sqrt{v}}\right)^2 \dots (1)$	$C \propto \left(\frac{\eta V}{\phi^{0.25}}\right)^2$
	Inherent angular change $\delta \propto (Qh^{-3/2})^{m+1} \exp(-nQh^{-3/2})$	$\delta = C_1 \left(\frac{I}{h\sqrt{vh}}\right)^{m+1} \times \exp\left\{-C_2 \left(\frac{I}{h\sqrt{vh}}\right)\right\} \dots (2)$	$C_1 \propto \left(\frac{\eta V}{\phi^{0.25}}\right)^{2.5}$ $C_2 \propto \frac{\eta V}{\phi^{2.25}}$ $m = 1.5$
Tee-fillet joint	Inherent angular change one pass: $\delta \propto (Qh^{-3/2})^{m+1} \exp(-nQh^{-3/2})$	$\delta = C_1 \left(\frac{I}{h\sqrt{vh}}\right)^{m+1} \times \exp\left\{-C_2 \left(\frac{I}{h\sqrt{vh}}\right)\right\} \dots (3)$	Ditto
	multi pass: $\delta \propto N(Qh^{-3/2})^{m+1} \exp(-nQh^{-3/2})$	$\delta = \frac{W}{w_0} \cdot C_1 \left(\frac{I}{h\sqrt{vh}}\right)^{m+1} \times \exp\left\{-C_2 \left(\frac{I}{h\sqrt{vh}}\right)\right\} \dots (4)$	
	$\delta \propto NQh^{-3/2}$ (when $h \geq 1$ cm)	$\delta = CWh^{-3/2}$ (when $h \geq 1$ cm) ... (5)	
Butt joint	Inherent shrinkage $\xi_1 - \xi_{10} \propto \left(\frac{Q}{h}\right)^2 N \log_e N$ where ξ_{10} is inherent shrinkage due to welding of first pass	$\xi_1 = C_1 \left(\frac{A}{h^2}\right) \log_e \left(\frac{W}{w_0}\right) + C_2 \left(\frac{A}{h^2}\right)^{1/2} \dots (6)$	$C_1 \propto \left(\frac{\eta V}{\mu a}\right) \left(\frac{\eta VI}{\phi^{0.5}}\right)$ $C_2 \propto \sqrt{\frac{\eta V}{\mu a}} \sqrt{\frac{\eta VI}{v}}$ $w_0 = \mu a l / v$
	Inherent angular change $\delta \propto \frac{Q^m N}{h^2} \left[2 \exp\left\{-nQh^{-3/2} \left(\frac{W}{W_A}\right)^{3/4}\right\} - \exp(-nQh^{-3/2}) \right]$	$\delta = C_1 \left(\frac{A}{h^2}\right) \left[2 \exp\left\{-C_2 h^{-3/2} \left(\frac{W}{W_A}\right)^{3/4}\right\} - \exp(-C_2 h^{-3/2}) \right] \dots (7)$	$C_1 \propto \frac{1}{w_0} \left(\frac{\eta VI}{\phi^{0.25} \sqrt{v}}\right)^{4/3}$ $C_2 \propto \frac{\eta VI}{\phi^{0.25} \sqrt{v}}$
Notations	I : (Welding current in A) v : (Welding speed in cm/s) W : (Weight of deposited metal per unit weld length in gr/cm = $7.8(A + A')$) A : (Sectional area of groove of butt joint in cm^2) A' : (Sectional area of groove due to back chipping in cm^2) w_0 : (Weight of deposited metal per unit weld length per welding of each pass in gr/cm)	h : (Thickness of plate in cm) W_A : (Weight of metal deposited in backing pass in gr/cm) V : (Arc voltage in V) η : (Heat efficiency of welding arc) μ : (Deposition efficiency of rod) a : (Melted weight of rod per unit current and unit time in gr/A. sec) ϕ : (Diameter of rod in mm)	

Examples of conventional formulas

Illumenite type 4 mm ϕ	$\xi_1 = 0.153 \times 10^{-6} \left(\frac{I}{h\sqrt{v}} \right)^2$ in cm
Unionmelt rod 4 mm ϕ	$\delta = 0.0240 \times 10^{-6} \left(\frac{I}{h\sqrt{v}} \right)^2$ in cm
Illumenite type 4 mm ϕ	$\delta = 0.131 \times 10^{-6} \left(\frac{I}{h\sqrt{vh}} \right)^{2.5} \exp \left(-10.0 \times 10^{-3} \frac{I}{h\sqrt{vh}} \right)$ in radian
" 6 mm ϕ	$\delta = 0.105 \times 10^{-6} \left(\frac{I}{h\sqrt{vh}} \right)^{2.5} \exp \left(-9.14 \times 10^{-3} \frac{I}{h\sqrt{vh}} \right)$ in radian
" 8 mm ϕ	$\delta = 0.0654 \times 10^{-6} \left(\frac{I}{h\sqrt{vh}} \right)^{2.5} \exp \left(-7.56 \times 10^{-3} \frac{I}{h\sqrt{vh}} \right)$ in radian
Unionmelt rod 4 mm ϕ	$\delta = 0.0448 \times 10^{-6} \left(\frac{I}{h\sqrt{vh}} \right)^{2.5} \exp \left(-5.92 \times 10^{-3} \frac{I}{h\sqrt{vh}} \right)$ in radian

Illumenite type 4 mm ϕ one pass

$$\delta = 0.0885 \times 10^{-6} \left(\frac{I}{h\sqrt{vh}} \right)^{2.5} \exp \left(-6.00 \times 10^{-3} \frac{I}{h\sqrt{vh}} \right) \text{ in radian}$$

Illumenite type 4 mm ϕ multi-pass

$$\delta = 10.5 \times 10^{-3} W h^{-3/2} \text{ in radian}$$

Illumenite type 3.2 mm ϕ	$\xi_1 = 0.0960 \left(\frac{A}{h^2} \right) \log_e \left(\frac{W}{w_0} \right) + 0.0416 \left(\frac{A}{h^2} \right)^{1/2}$ in cm
" 4 mm ϕ	$\xi_1 = 0.1021 \left(\frac{A}{h^2} \right) \log_e \left(\frac{W}{w_0} \right) + 0.0584 \left(\frac{A}{h^2} \right)^{1/2}$ in cm
" 5 mm ϕ	$\xi_1 = 0.1530 \left(\frac{A}{h^2} \right) \log_e \left(\frac{W}{w_0} \right) + 0.0745 \left(\frac{A}{h^2} \right)^{1/2}$ in cm
" 6 mm ϕ	$\xi_1 = 0.12249 \left(\frac{A}{h^2} \right) \log_e \left(\frac{W}{w_0} \right) + 0.0690 \left(\frac{A}{h^2} \right)^{1/2}$ in cm

Illumenite type 4 mm ϕ	$\delta = 0.221 \left(\frac{A}{h^2} \right) \left[2 \exp \left\{ -2.74 h^{-3/2} \left(\frac{W}{W_A} \right)^{3/4} \right\} - \exp \left\{ -2.74 h^{-3/2} \right\} \right]$
" 6 mm ϕ	$\delta = 0.221 \left(\frac{A}{h^2} \right) \left[2 \exp \left\{ -4.34 h^{-3/2} \left(\frac{W}{W_A} \right)^{3/4} \right\} - \exp \left\{ -4.34 h^{-3/2} \right\} \right]$
" 8 mm ϕ	$\delta = 0.164 \left(\frac{A}{h^2} \right) \left[\exp \left\{ -4.70 h^{-3/2} \left(\frac{W}{W_A} \right)^{3/4} \right\} - \exp \left\{ -4.70 h^{-3/2} \right\} \right]$

(Note)

In this table the magnitudes of C_1 and C_2 in eqns. (6) and (7) corresponding to the following welding conditions are shown.

Size of electrode (mm)	Current (A)	Welding Speed (cm/s).
3.2	120	0.3
4	150	0.3
5	210	0.3
6	260	0.3
8	340	0.3

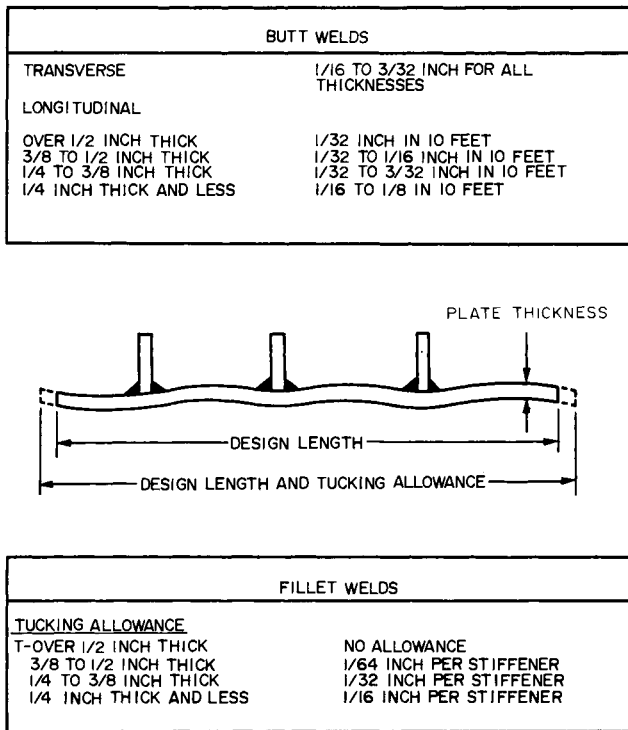


FIG. 7.10. Shrinkage allowances (For guidance only) for ship hulls for the Navy from NAVSHIPS 0900-060-4010).

Shrinkage allowances. General allowances for shrinkage for mild steel are given in Fig. 7.10. These values are for general guidance only and depend upon such factors as fixturing, joint restraint, welding process, sequence of welding, heat inputs, size of welds, etc.

Unfairness of welded plating. Figures 7.11 through 7.14 show the unfairness permitted in welded structures, as specified in NAVSHIPS 0900-060-4010. Figures 7.11 and 7.12 show the unfairness permitted in steel structures, while Figs. 7.13 and 7.14 show the unfairness permitted in aluminum structures.

The Navy unfairness standard was modified in 1968. Figure 7.15 had been used up to that time. Figure 7.15 comes from NAVSHIPS 0900-014-5010.

Unless otherwise specified, deviations from the molded form (surface ships) shall not exceed the following limits:

- ± 1/2 in. from the vertical longitudinal center plane,
- ± 1 in. in 100 ft of length,
- ± 1 in. of beam,
- ± 1/2 in. vertically from the base line.

The tolerances shown in Fig. 7.15 are given for three cases:

1. To be used on living quarters and longitudinal bulkhead plating; in other bulkheads an unfairness of 1 in. width will be permitted.
2. To be used on deck plating.
3. To be used on shell plating.

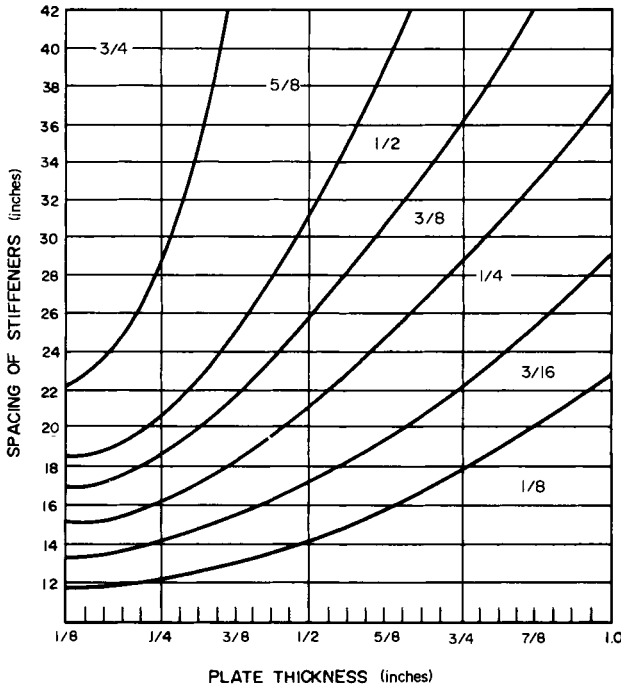


FIG. 7.11. Permissible unfairness in steel welded structures specified by the Navy (from NAVSHIPS 0900-060-4010).

APPLICABILITY OF TOLERANCES

a. Figures 7.11 and 7.13 are applicable in the following areas except where Figures 7.10 and 7.12 govern.

(1) Structural bulkheads forming a boundary of a living space (stateroom, office, berthing, messing, or lounge area) and passageways contiguous to such spaces.

(2) Decks within the hull and superstructure in way of the above living spaces.

(3) Decks exposed to the weather.

(4) Tank and main transverse bulkheads.

(5) Inner-bottom plate longitudinals

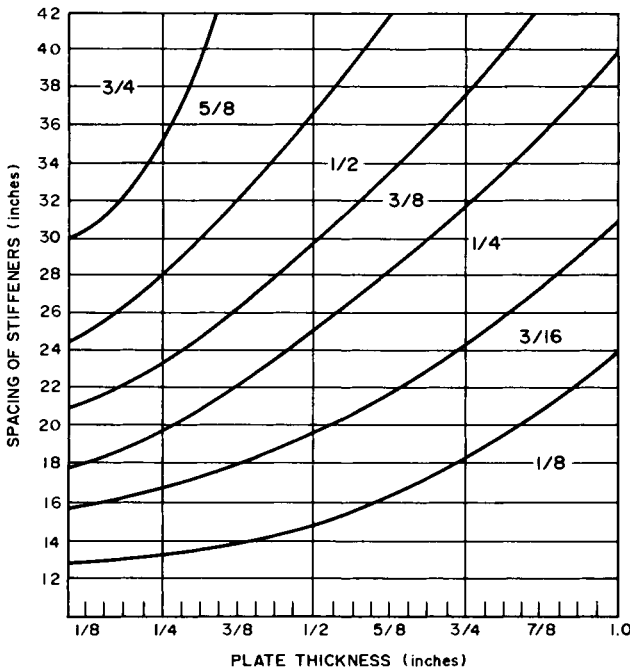


FIG. 7.12. Permissible unfairness in steel welded structures specified by the Navy (from NAVSHIPS 0900-060-4010).

b. Figures 7.12 and 7.14 are applicable as follows:

(1) Entire shell.

(2) Uppermost strength deck

(3) Longitudinal strength structure within the mid 3/5 length which includes inner-bottom tank top and the deck next below the uppermost strength deck if continuous above machinery spaces.

(4) In transversely framed boats, the permissible unfairness for structure noted in a(1), a(2), and a(3) above is reduced by 1/8 inch.

(5) Bulwarks and exterior superstructure bulkheads.

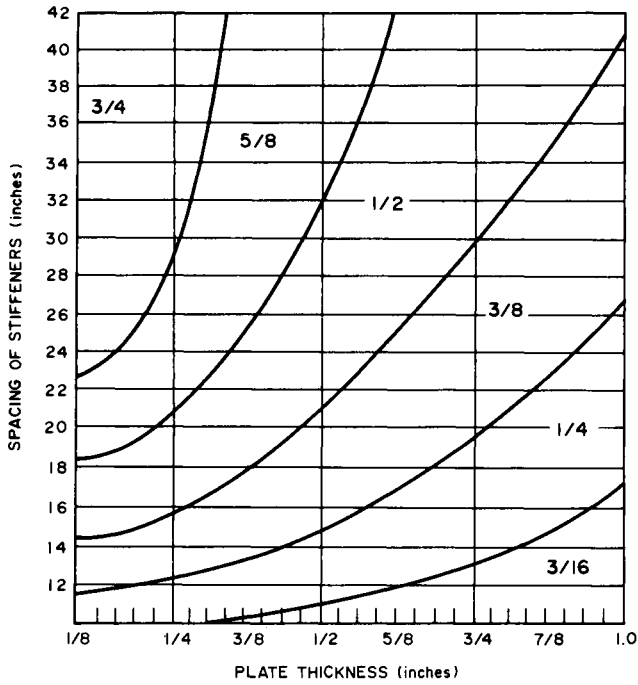


FIG. 7.13. Permissible unfairness in aluminum welded structures specified by the Navy (from NAVSHIPS 0900-060-4010).

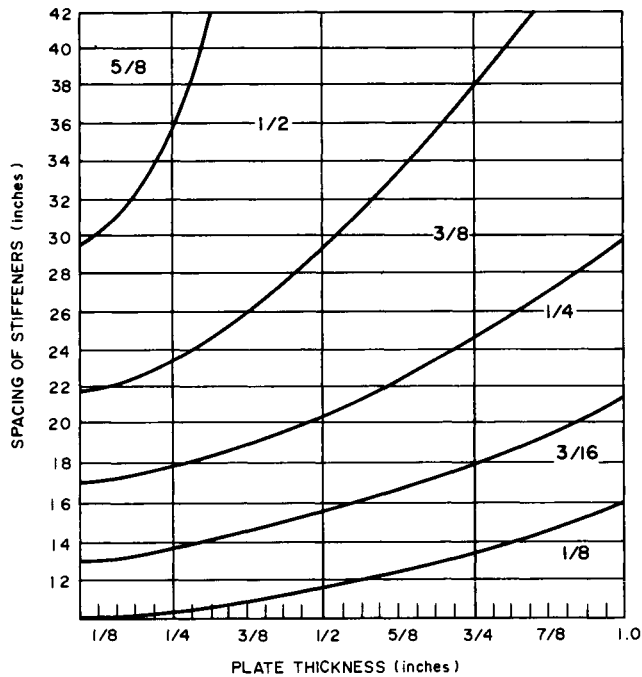
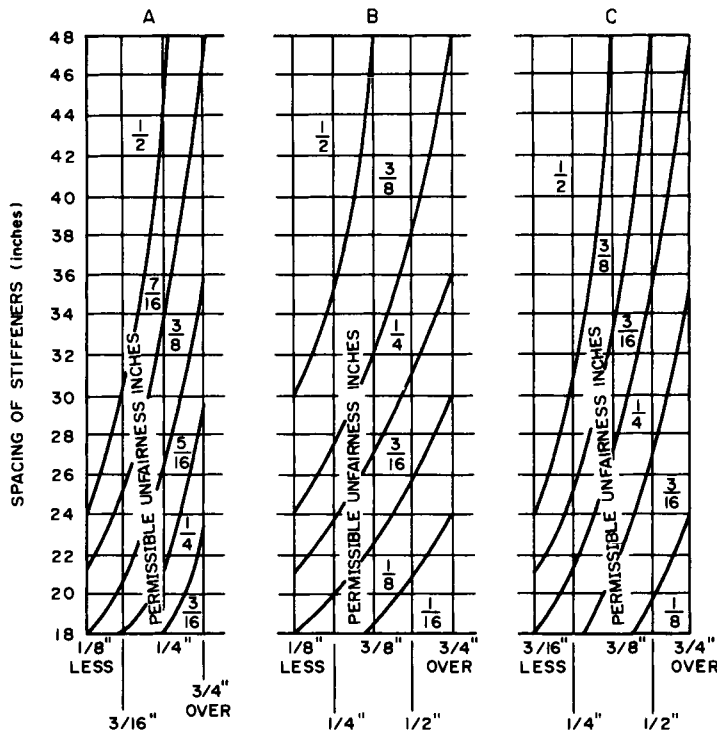


FIG. 7.14. Permissible unfairness in aluminum welded structures specified by the Navy (from NAVSHIPS 0900-060-4010).



- A TO BE USED ON LIVING QUARTERS AND LONGITUDINAL BULKHEAD PLATING IN OTHER BULKHEADS UNFAIRNESS OF 1" PER PANEL WIDTH WILL BE PERMITTED.
- B TO BE USED ON DECK PLATING.
- C TO BE USED ON SHELL PLATING.

(IN APPLYING THE ABOVE TOLERANCES, THE UNFAIRNESS OF THE PLATING SHALL BE MEASURED ACROSS THE MINOR DIMENSION OF THE PANEL)

FIG. 7.15. Tolerances for unfairness of welded structures, old specifications (from NAVSHIPS 0900-014-5010).

In each case, the tolerances are given as functions of the plate thickness and the stiffener spacing. If the plate thickness is $\frac{1}{4}$ in. and the stiffener spacing 24 in., for example, the values of the permissible unfairness would be:

- $\frac{5}{16}$ in. for case 1,
- $\frac{1}{4}$ in. for case 2,
- $\frac{3}{16}$ in. for case 3.

More recently, this Navy unfairness standard has been relaxed somewhat (see Section 7.7.4 and Fig. 7.47).

7.3.2 Allowable distortion in commercial ship hulls

The Research Committee on Steel Shipbuilding of the Society of Naval Architects of Japan has developed the Japanese Shipbuilding Quality Standard (JSQS).⁽⁷¹⁰⁾ The

TABLE 7.3 Dimensional tolerances specified by code for welding in building construction (AWS D1.0-69) and specifications for welded highway and railway bridges (AWS D2.0-69)

The dimensions of welded structural members shall be within the tolerances of the general specifications governing the work and also within the following special tolerances:

1. Deviation from straightness of welded columns:
Lengths of 45 ft and under:

$$\frac{1}{8} \text{ in.} \times \frac{\text{No. of ft of total length}}{10}$$

but not over $\frac{3}{8}$ in.
Lengths over 45 ft:

$$\frac{3}{8} \text{ in.} + \frac{1}{8} \text{ in.} \times \frac{\text{No. of ft total length} - 45}{10}$$

2. Deviation from straightness of welded beam or girders where there is no specified camber or sweep:

$$\frac{1}{8} \text{ in.} \times \frac{\text{No. of ft of total length}}{10}$$

3. Deviation from specified camber of welded beams or girders:

$$\pm 1/32 \text{ in.} \times \frac{\text{No. of ft of total length}}{10}$$

or $\pm \frac{1}{4}$ in., whichever is greater.

4. Lateral deviation between centerline of web and centerline of flange of built-up H or I members at contact surface:

$$\frac{1}{4} \text{ in. max.}$$

5. Deviation from flatness of girder webs in the length between stiffeners or in a length equal to depth of girder:

Intermediate stiffeners on both sides of web:

Web thickness not less than 1/150 of its depth
– 1/150 of total web depth
Web thickness less than 1/150 of its depth
– 1/120 of total web depth

Intermediate stiffeners on only one side of web:

Web thickness not less than 1/100 of its depth
– 1/150 of total web depth
Web thickness less than 1/100 of its depth
– 1/100 of total web depth

No intermediate stiffeners:

– 1/150 of total web depth

6. Combined warpage and tilt of flange of welded beams or girders shall be determined by measuring the offset at toe of flange from a line normal to the plane of the web through the intersection of the centerline of web with the outside surface of the flange plate. This offset shall not exceed 1/200 of total width of flange or $\frac{1}{8}$ in., whichever is greater.

7. Out of flatness of seats or bases:

To be set on grout: $-\frac{1}{8}$ in. max.

To be set on steel, hard masonry, canvas or lead:
– 1/100 in. max.

8. The maximum deviation from specified depth for welded built-up beams and girders, measured at the web centerline, shall be as follows:

For depths up to 36 in., incl.	$\pm \frac{1}{8}$ in.
For depths over 36 in. to 72 in., incl.	$\pm \frac{3}{16}$ in.
For depths over 72 in.	$+\frac{5}{16}$ in. $-\frac{3}{16}$ in.

JSQS includes dimensional tolerances for welded structures. The report of Committee III.3 “Fabrication Factors Affecting Structural Capability of Ships and Other Marine Structures” of the International Ship Structures Congress includes the results of a survey of dimensional tolerances.⁽⁷¹¹⁾

7.3.3 Buildings and highway and railway bridges

Table 7.3 gives the dimensional tolerances specified by the Code for Welding in Building Construction of the American Welding Society (AWS D1.0–69). The identical dimensional tolerances are included in the Specifications for Welded Highway and Railway Bridges of the AWS (AWS D2.0–69).

These codes and specification are to be used primarily for the design and construction of steel structures. The same dimensional tolerances appear to be used when aluminum alloys are used for buildings and highway bridges.

7.3.4 Pressure vessels

The ASME Boiler and Pressure Vessel Code is widely used in the design and fabrication of pressure vessels. Permissible out-of-roundness of cylindrical shells is given in Section VIII—Division 1, UG-80. Although the permissible out-of-roundness specifications given in the section were intended for steel vessels, they are commonly used in the design and fabrication of aluminum pressure vessels.

7.4 Transverse Shrinkage of Butt Welds

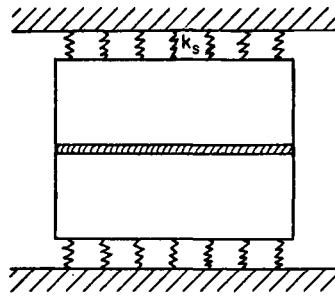
Figure 7.1(a) shows the typical transverse shrinkage in a simple butt weld. The shrinkage is shown to be uniform along the weld. But this is not usually the case in butt welds, especially when they are long. Actual structures usually exhibit a complex transverse shrinkage. The major factors that cause this non-uniform transverse shrinkage in butt welds are:

Rotational distortion. When welding is conducted progressively from one end of a joint to the other, the unwelded portion of the joint moves, causing a rotational distortion, as shown in Fig. 7.1(c).

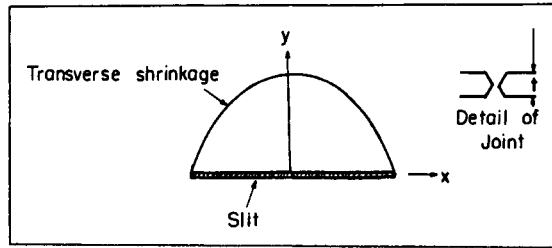
Restraint. The amount of transverse shrinkage that occurs in welds is affected by the degree of restraint applied to the weld joint. In Fig. 7.16 the external restraint is represented by a system of springs; the degree of restraint is expressed by the rigidity of the system of springs, k_s . The amount of shrinkage decreases as the degree of restraint, k_s , increases. In many joints, the degree of restraint is not uniform along the weld. For example, in a slit weld, as shown in Fig. 7.16, the degree of restraint varies along the length of the slit, being highest at the ends, causing the amount of transverse shrinkage to be great near the center of the joint and slight near the ends.

The rotational distortion is affected by the welding heat input and the location of tack welds. The welding sequence has a complex effect on the rotational distortion and the distribution of restraint along the weld.

The following discussion first presents formulas for the transverse shrinkage of butt



a. Definition of degree of restraint, k_s



b. Slit-Weld Specimen and Typical Distribution of Shrinkage

FIG. 7.16. Transverse shrinkage in a butt weld under restraint.

welds, and then examines rotational distortion and how restraint affects transverse shrinkage.

7.4.1 Formulas for the transverse shrinkage of butt welds^(303, 501)

Many investigators, including Capel,⁽⁷¹²⁾ Gilde,⁽⁷¹³⁾ Cline,⁽⁷¹⁴⁾ Campus,⁽⁷¹⁵⁾ Weck,⁽⁶²⁹⁾ Gyuot,⁽⁷¹⁶⁾ Spraragen and Ettinger,⁽⁵⁰⁴⁾ Malisius,⁽⁷¹⁷⁾ Watanabe and Satoh,⁽⁷⁰⁹⁾ and Naka,⁽⁷⁰³⁾ have proposed formulas for the estimation of transverse shrinkage of butt welds, which by and large are based on empirical information. Some of these formulas are contained in Welding Research Council (WRC) Bulletins 149⁽³⁰³⁾ and 174.⁽⁵⁰¹⁾

Malisius' formula.^(502, 717) On the basis of an analytical study, Malisius proposed the following formula:

$$S = \lambda_1 K \frac{Q}{S_1} + \lambda_2 b, \tag{7.5}$$

where S = axial shrinkage perpendicular to the weld, mm,

λ_1 = linear thermal expansion of the bar from T_0 to $\frac{T_1 - T_0}{2}$ ($= 0.004$)

T_0 = initial temperature of the bar,

T_1 = temperature above which the material is no longer elastic ($T_1 > T_0$),

λ_2 = linear thermal expansion of the weld from T_0 to T_1 ($= 0.0093$),

Q = cross-section of weld including reinforcement, mm^2 ,

S_1 = average thickness of bars, mm,

b = average breadth of weld, mm,

K = a constant depending on the thermal output of the welding process and the thermal conductivity,

$K = 43$ for arc welding, bare electrodes ($S = 1.0$ mm),

$K = 45$ to 55 for coated electrodes ($S = 1.4$ mm average),

$K = 64$ for atomic-hydrogen welding ($S = 1.4$ mm),

$K = 75$ for oxyacetylene welding ($S = 1.7$ mm).

For values of K , figures in the parentheses are shrinkage values in inches if $S_1 = b = 5$ mm (0.2 in.) $Q = 260$ mm^2 . The factor K is determined by experiment.

In extending the formula to butt welds in plates, Malisius applied the purely arbitrary factor 0.6 to K in order to account for the decrease in heat supply due to the moving electrode, and multiplied S by the factor 1.3 to account for the closing effect exerted by the section already welded on the still unwelded gap. The formula applied to butt welds is thus:

$$S = 1.3(0.6\lambda_1 K \cdot Q/S_1 + \lambda_2 b). \quad (7.6)$$

Spraragen-Ettinger's formula. Spraragen and Ettinger examined the shrinkage data obtained by several investigators and suggested the following formula:

$$S = 0.2A_w/t + 0.05d \quad (7.7)$$

where S = transverse shrinkage, in.,

A_w = cross-sectional area of weld, in.^2

t = thickness of plates, in.

d = free distance or root opening, in.

Watanabe-Satoh's formula. Watanabe and Satoh have proposed the formula shown in eqn. (6) of Table 7.2.

Capel's formulas. Capel⁽⁷¹²⁾ measured the transverse shrinkage of butt welds in aluminum, stainless steel, and carbon steel. Two plates, 20 in. (508 mm) long, 6 in. (152 mm) wide, and $\frac{1}{4}$ in. (6.4 mm) thick were welded. The edge preparation was a 60-degree V-groove, without a root gap. The aluminum plates were welded using the gas tungsten-arc process and the stainless steel and carbon steel plates using covered electrodes. Capel used a formula originally developed by Gilde⁽⁷¹³⁾ and proposed the following:

$$\begin{aligned} \Delta l (\text{aluminum}) &= \frac{20.4 \times W \times 10^3}{s \times u}, \\ \Delta l (\text{stainless steel}) &= \frac{22.7 \times W \times 10^3}{s \times u}, \\ \Delta l (\text{carbon steel}) &= \frac{17.4 \times W \times 10^3}{s \times u} \end{aligned} \quad (7.8)$$

where Δl = transverse shrinkage, mm,
 s = thickness of layer of weld metal, mm,
 u = welding speed, cm/min,
 $W = I \times V$ = electric power of welding arc,
 I = welding current, amperes,
 V = arc voltage, volts.

Table 7.4 gives the welding data used in Capel's experiments. Considerably higher heat inputs were used for welding aluminum. Consequently, actual values of shrinkage were considerably greater for aluminum welds than those for stainless steel and carbon steel, even though eqn. (7.8) gives the impression that shrinkage in an aluminum weld is only slightly greater than that in carbon steel. A comparison between the actual measurements and the calculated shrinkage is as follows:

		Δl_1 measured (mm)	Δl_2 calculated (mm)
Aluminum:	1st layer	2.2	2.5
	2nd layer	1.1	1.6
Stainless steel:	1st layer	0.8	0.8
	2nd layer	1.6	1.2
Carbon steel:	1st layer	0.4	0.5
	2nd layer	0.9	0.7

The total shrinkage after the two-layer welding was completed was 3.3 mm (0.13 in.) for aluminum, but only 1.3 mm (0.051 in.) for carbon steel.

Cline's data. Cline⁽⁷¹⁴⁾ studied the transverse shrinkage of butt welds in 2219-T87

TABLE 7.4 *Welding data used in Capel's experiments*

		Aluminum	Stainless steel	Carbon steel
First layer:				
$V \times I$ (watts)		4050	2320	2100
s (layer thickness, mm)		3.6	3.4	3.7
u (welding speed, cm min ⁻¹)		9	19	20
Final layer:				
$V \times I$		4050	2550	2100
s		5.6	2.6	2.3
u		9.2	18	22
Welding conditions:				
Aluminum	1st layer:	filler rod diameter 3 mm; electrode diameter $\frac{5}{32}$ in.; gas flow 8 l/min.		
	2nd layer:	filler rod diameter 4 mm; electrode diameter $\frac{5}{32}$ in.; gas flow 8 l/min.		
Stainless steel	1st layer:	electrode diameter 2.5 mm		
	2nd layer:	electrode diameter 3.25 mm		
Carbon steel	1st layer:	electrode diameter 2.5 mm		
	2nd layer:	electrode diameter 3.25 mm		

TABLE 7.5 Transverse weld shrinkage

Plate thickness (in.)	Welding speed (ipm)	Arc voltage (V)	Welding current (apm)	Energy input (joules/in)	Avg. trans. shrinkage (in.)
0.250	12	11.5	280	16,240	0.026
0.375	9	11.8	300	23,600	0.035
0.500	6	12.5	335	41,900	0.046

Note: Welds were made in flat position.

aluminum alloy. The plates were 36 in. (914 mm) long with thickness ranging from $\frac{1}{4}$ to $\frac{1}{2}$ in. (6.4 to 12.7 mm). Welding was done using the gas-tungsten arc process with DCSP single-pass techniques and helium as a shielding gas.

The average transverse weld shrinkage data obtained and welding process variables used are shown in Table 7.5. The shrinkage data was used to develop the following formula for calculating transverse shrinkage:

$$\Delta l = 0.1 (\sqrt{t} - 0.230) \quad (7.9)$$

where, Δl = transverse shrinkage, in.,
 t = plate thickness, in.

The average transverse weld shrinkage is plotted in Fig. 7.17 as a function of plate thickness.

He also found that:

1. Welding speed does not exert a significant influence on transverse shrinkage provided that the weld fusion zones are uniform in size.
2. The use of chill tooling does not significantly reduce transverse weld shrinkage in mechanized butt welds made in aluminum plate.

7.4.2 The mechanisms of transverse shrinkage in butt welds

The mechanisms of transverse shrinkage have been studied by several investigators including Naka⁽⁷⁰³⁾ and Matsui.⁽⁷¹⁸⁾ Iwamura⁽⁷¹⁹⁾ also conducted an analytical and experimental study of transverse-shrinkage mechanisms in butt welds in aluminum. The most important finding of these mathematical analyses was as follows: "The major portion of transverse shrinkage of a butt weld is due to contraction of the base plate. The base plate expands during welding. When the weld metal solidifies the expanded base metal must shrink, and this shrinkage accounts for the major part of transverse shrinkage. Shrinkage of the weld metal itself is only about 10 percent of the actual shrinkage."

Figure 7.18 is a schematic presentation that shows the changes of transverse shrinkage in a single-pass butt weld in a free joint after welding. Shortly after welding, the heat of the weld metal is transmitted into the base metal. This causes the base metal to expand, with a consequent contraction of the weld metal. During this period the points of sections A and A' do not move (Fig. 7.18(b)).

When the weld metal begins to resist the additional thermal deformation of the base

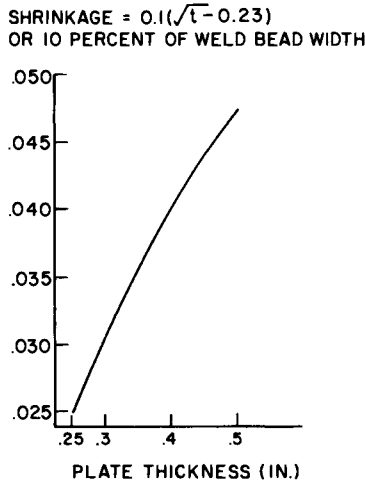


FIG. 7.17. Transverse weld shrinkage as a function of plate thickness in single pass mechanized DCSP gas tungsten-arc butt welds of 2219-T87 in thicknesses of .25-.50 in.^(7,12)

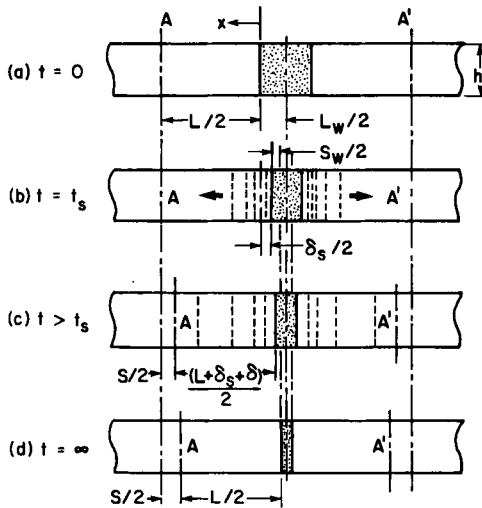


FIG. 7.18. Schematic presentation of a transverse shrinkage of a butt weld in a single pass.

metal, parts of sections A and A' begin to move in response. This starting time of the movement of A and A' is indicated by t_s .

The various thermal deformations of both the weld and base metals are defined as follows:

- δ_s : Thermal expansion of the base metal at $t = t_s$.
- δ : Additional thermal deformation of the base metal caused in $\overline{AA'}$ at $t > t_s$.
- S_w : Thermal contraction of the weld metal at $t > t_s$.

These deformations can be calculated by the following:

$$\delta_s = 2 \int_0^{L/2} [\alpha(T) \cdot T(t_s, x) - \alpha(T_0) \cdot T_0] dx, \quad (7.10)$$

$$\delta = 2 \int_0^{L/2} [\alpha(T) \cdot T(t, x) - \alpha(T) \cdot T(t_s, x)] dx, \quad (7.11)$$

$$S_w = [\alpha(T_M) \cdot T_M - \alpha(T_0) \cdot T_0] \cdot L_w \quad (7.12)$$

where $\alpha(T)$ = thermal expansion coefficient,

$T(t, x)$ = temperature,

T_M = melting temperature,

T_0 = initial and final (room) temperature.

Using these results, the transverse shrinkage can now be calculated from:

$$S = \begin{cases} 0 & \text{for } 0 \leq t \leq t_s, \\ -\delta + S_w & \text{for } t > t_s, \\ \delta_s + S_w & \text{for } t = \infty. \end{cases} \quad (7.13)$$

Thus we may conclude that the final transverse shrinkage depends on the thermal expansion of the base metal at $t = t_s$ and the thermal contraction of the weld metal.

In aluminum welds, studied by Iwamura,⁽⁷¹⁹⁾ for example, the following values are used:

Material: aluminum, 2219-T87.

Heat input: 16,100 joules/in. (630 joules/mm).

Plate thickness: 0.25 in. (6.4 mm).

Root Gap: 0.1 in. (2.5 mm).

Shrinkage: 0.026 in. (0.7 mm).

Using a constant thermal expansion coefficient, the thermal contraction of the weld metal can be estimated from eqn. (7.12):

$$S_w = 0.1 \times 17 \times 10^{-6} \times (1220 - 70) = 0.002 \text{ in.}$$

This means that S_w is less than 8% of the total shrinkage. Therefore, the thermal expansion of the base metal caused at $t = t_s$ is the most important factor in the final shrinkage of a single-pass butt weld in a free joint.

Effect of plate thickness. Matsui⁽⁷¹⁸⁾ studied analytically and experimentally how the plate thickness affects the transverse shrinkage in a butt weld. On the basis of mathematical analysis, the approximate transverse shrinkage can be expressed using an error function:

1. for a thin plate

$$S = (Q/c\rho h)\text{erf}(\beta_s), \quad (7.14)$$

2. for a thick plate

$$S = (Q/c\rho 2\pi\lambda t_s) \left\{ 1 + 2 \sum_{n=1}^{\infty} e^{-(nh)^2/4\lambda t_s} \right\} \text{erf}(\beta_s) \quad (7.15)$$

where $\beta_s = L/4\pi\lambda t_s$,
 Q = heat input,
 c = specific heat,
 ρ = density,
 λ = thermal diffusivity,
 h = plate thickness.

The following were assumed when the above formulas were derived:

1. Thermal expansion coefficient was constant.
2. The thermal radiation would be neglected.
3. The thermal contraction of the weld metal would be neglected.

Equation (7.14) indicates that the final shrinkage decreases with an increasing thickness.

Figure 7.19 shows the experimental results obtained by Matsui⁽⁷¹⁸⁾ on butt welds in low-carbon steel. The curves labeled T show the temperature changes, while the curves labeled S show the changes of transverse shrinkage. Most of the shrinkage occurs after the weldment has cooled down to a relatively low temperature. The figure shows that in a thicker plate transverse shrinkage starts earlier, but the final value of the shrinkage is smaller. The results confirm the predictions made by Matsui.

But it should be emphasized that this is true only if the same amount of heat input is always used, regardless of the joint thickness. Welding thicker plates may require more than one pass. Changes in the transverse shrinkage during multipass welding are discussed later.

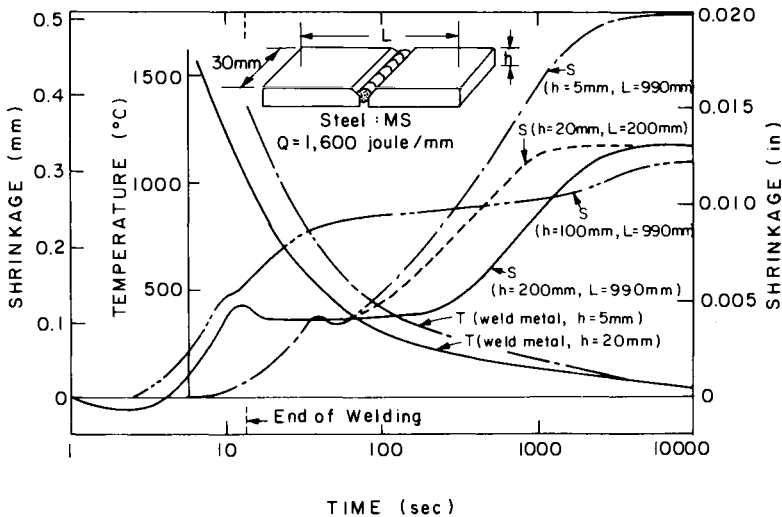


FIG. 7.19. Transverse shrinkage during welding and cooling for various plate thicknesses (h) and measuring distances (L) in free butt joints.

Note: The curves labeled T show the temperature changes, while the curves labeled S show the changes of transverse shrinkage.

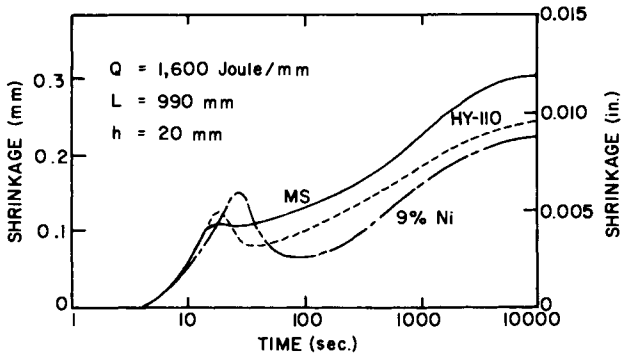
Effect of materials. The amount of transverse shrinkage is different for the various materials because the material properties related to eqns. (7.14) and (7.15) are different. For example, compared to steel, aluminum alloys, because of their higher heat conductivity and thermal expansion coefficients, shrink more. It is well known that transverse shrinkage in aluminum welds is greater than that in steel welds (see Capel's formulas, discussed earlier).

Phase transformation of ferrous materials also plays an important role. Matsui⁽⁷¹⁸⁾ has proposed that the expansion due to phase transformation should be subtracted from the estimated shrinkage in order to predict the real shrinkage (Fig. 7.20). As one can see from the figure, the actual shrinkage in 9% nickel steel was about 70% of the shrinkage estimated using eqn. (7.15).

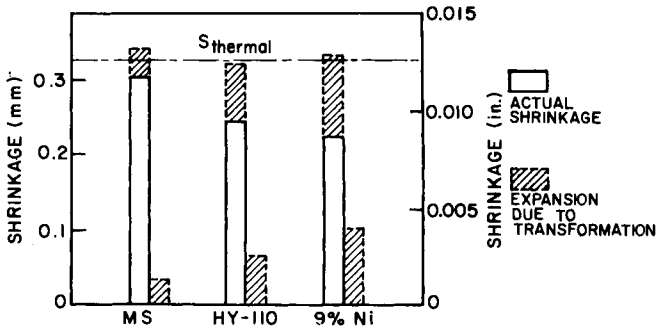
Effects of restraint and forced chilling. It is a well-known fact that transverse shrinkage decreases when a joint is restrained (see Fig. 7.7).

In a study at M.I.T., Iwamura⁽⁷¹⁹⁾ investigated how restraint and forced chilling affects the transverse shrinkage of butt welds in type 6061-T6 aluminum alloy. Details of the results are presented in his thesis, (see References (719) and (720)).

A series of eight experiments was performed measuring temperature, strain and transverse shrinkage changes during welding. 6061-T6 aluminum was used. The plates were 1/4 in. (6.4 mm) thick. The weld length was 4 in. (100 mm) for all specimens, in both



(a) TRANSVERSE SHRINKAGE DURING WELDING AND COOLING



(b) FINAL TRANSVERSE SHRINKAGE

FIG. 7.20. Effects of phase transformation on transverse shrinkage.

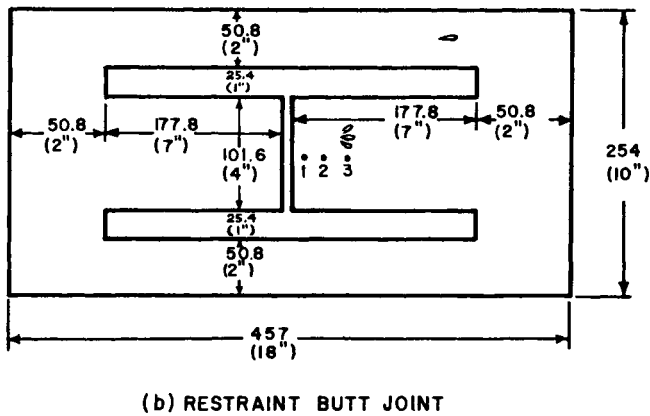
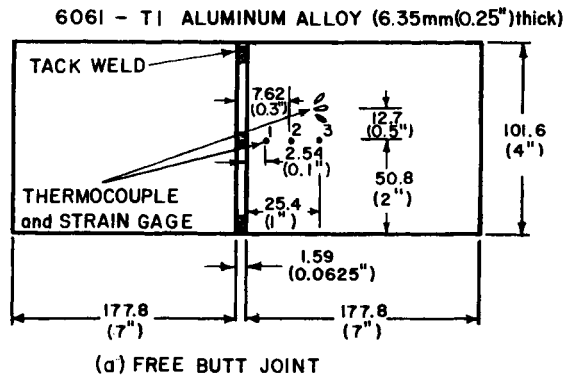


FIG. 7.21. Dimensions of specimens and locations of measuring temperature and strain.

the free butt joints and the restrained H-joints. Four specimens, two of each type, were chilled using dry ice. An effort was made to prevent angular change during welding. An automatic GMA welding machine was used with 200 amp, 25 V, 0.25 in./sec (6.4 mm/sec) and heat input of 20,000 joules/in. (790 joules/mm).

A description of the test specimen is shown in Fig. 7.21, where the locations of the strain gages and the thermocouples are indicated. Figure 7.22 provides information about the constraining and chilling equipment. Dry ice was used for chilling.

The mathematical analysis employed was basically the same as discussed earlier (see Figure 7.19 and eqns. (7.10) through (7.12)). The test designations were as follows:

Cooling	(Type of joint)	
	Free	Restrained
Cooled in the air	FN-1	RN-1, RN-3
Cooled in dry ice	FC-1	RC-1

Figures 7.23 and 7.24 show changes in temperature and shrinkage during and after welding in specimens without chilling and with chilling, respectively. Shown here are

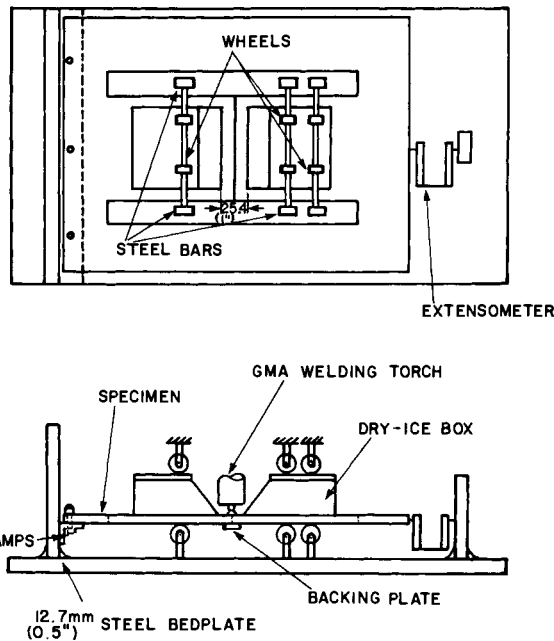


FIG. 7.22. Constraining and chilling equipment.

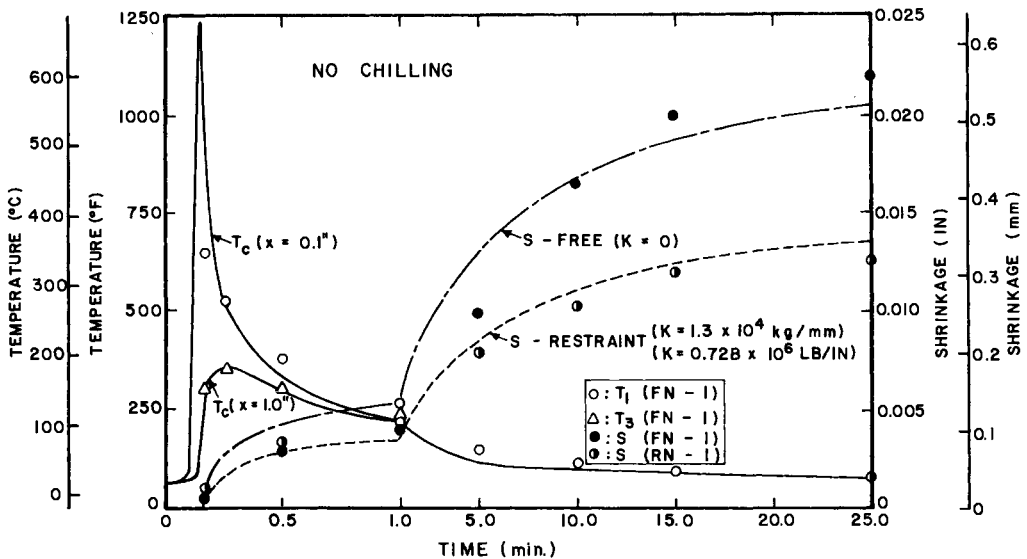


FIG. 7.23. Comparison of shrinkage and temperature in experiment and calculation.

the measured values and the calculated values of temperature and transverse shrinkage.

In general, the plate expanded after the start of welding and the expansion increased until the arc passed the center. Shrinkage occurred after the arc diminished. The amount of expansion was relatively small in comparison with the final amount of shrinkage. The increasing rate of shrinkage decreased as time passed. When chilling was used,

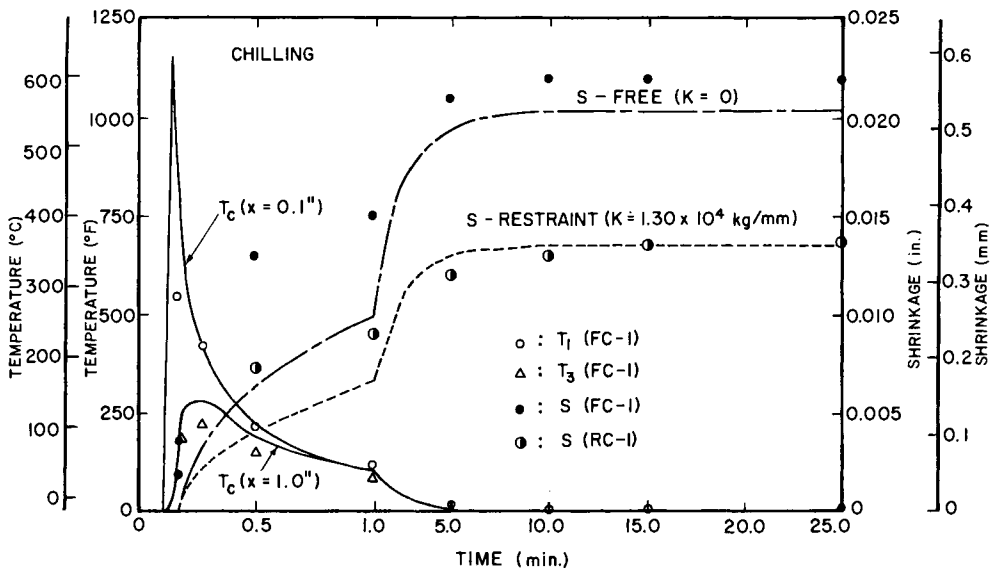


FIG. 7.24. Comparison of shrinkage and temperature in experiment and calculation.

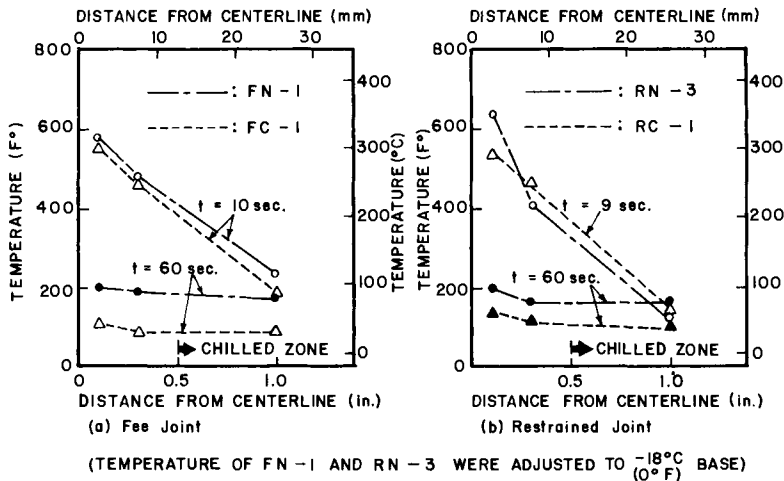


FIG. 7.25. Temperature distribution.

shrinkage occurred during welding. The final amount of shrinkage was almost the same in chilled and non-chilled specimens.

Figure 7.25 shows the temperature distribution in several joints. The chilling had little effect on the temperature distribution in the early stages of welding (the first 9 seconds, for example), but lowered the temperatures at a later stage (after 60 seconds, for example). The mathematical analysis indicates that the temperature distribution in the joint after the weld metal solidifies has a critical affect on transverse shrinkage (see eqns. (7.12)–(7.14)). In order that the chilling be effective, it is therefore important to alter the temperature distribution before the weld metal solidifies. But though it was

TABLE 7.6 Final amounts of shrinkage in experiments and calculations

Joint	Cooling	Experiment	Numerical calculation
Free	non-chilled	0.0189 (0.0218 ^(a))	0.0204
	chilled	0.0200 (0.0218 ^(a))	0.0204
	non-chilled	0.0110 (0.0126 ^(a))	0.0136
Restraint	non-chilled	0.0150 (0.0162 ^(a))	
	chilled	0.0132 (0.0138 ^(a))	0.0136

Shrinkage values are given in fraction of an inch.
^(a) Modified shrinkage by adding the expansion caused to the measured shrinkage

possible to alter the temperature distribution by chilling the metal at later stages, this was too late to effectively reduce transverse shrinkage.

Table 7.6 shows the final amounts of shrinkage in experiments and calculations obtained using the computer program. The final shrinkage in the free joints was about 0.02 in. (0.5 mm), in the restraint joints, about 0.014 in. (0.35 mm). Thus, restraint did reduce the amount of shrinkage by about 30%.

7.4.3 How welding procedures affect transverse shrinkage⁽³⁰³⁾

Kihara and Masubuchi have studied the transverse shrinkage that occurs during the multipass welding of constrained butt joints in carbon steel.⁽⁶⁰²⁾ Figure 7.26 shows schematically how the transverse shrinkage increases during multipass welding. Because the resistance against shrinkage increases as the weld gets larger, shrinkage was pro-

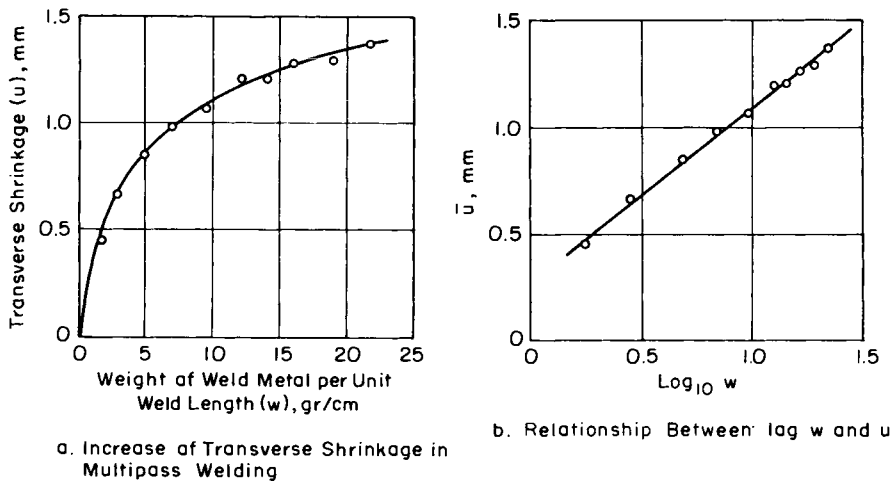


FIG. 7.26. Increase of transverse shrinkage during multipass welding of a butt joint (Kihara and Masubuchi).^(303,602)

w: Weight of weld metal per unit weld length (w), gr/cm.
 u: Transverse shrinkage (u), mm.

nounced during the early weld passes but diminished during later passes. It was found that a linear relationship existed between the transverse shrinkage, u , and the logarithm of the weight of the weld metal deposited, w , as shown in Fig. 7.26:

$$u = u_0 + b(\log w - \log w_0) \tag{7.16}$$

where u_0 and w_0 are the transverse shrinkage and the weight of the weld metal deposited, respectively, after the first pass is welded, and b is a coefficient.

Figure 7.27 shows that there are three methods for reducing transverse shrinkage:

1. If the total weight of the weld metal is decreased, as shown by arrow 1, the amount of shrinkage will change from B to C .
2. If the tangent b is decreased, as shown by arrow 2, the amount of shrinkage after the completion of the weld will change from B to D .
3. If the shrinkage after the first pass is moved from A to A' , as shown by arrow 3, the amount of shrinkage after the completion of the weld will change from B to E .

Using ring-type specimens (see Fig. 7.6), Kihara and Masubuchi studied how various factors including joint design, root opening, type and size of electrodes, degree of constraint, peening, and flame gouging affect transverse shrinkage (see Table 7.7). Among

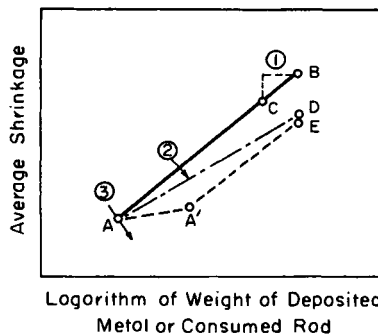


FIG. 7.27. Schematic diagram showing the methods to reduce transverse shrinkage of butt welds (Kihara and Masubuchi).^(303,602)

TABLE 7.7 Effects of various procedures on transverse shrinkage in butt welds^(303,602)

Procedures	Effects
Root opening	Shrinkage increases as root opening increases. See Fig. 7.28(a). Effect is large (Effects 1 and 2).
Joint design	A single-vee joint produces more shrinkage than a double-vee joint. Effect is large. (Effects 1 and 2).
Electrode diameter	Shrinkage decreases by using larger-sized electrodes. see Fig. 7.28(b). Effect is medium (Effect 3).
Degree of constraint	Shrinkage decreases as the degree of constraint increases. Effect is medium (Effect 2).
Electrode type	Effect is minor (Effect 2).
Peening	Shrinkage decreases by peening. Effect is minor (Effect 2).
Chipping and gouging	See Figs. 7.29(a) and 7.29(b).

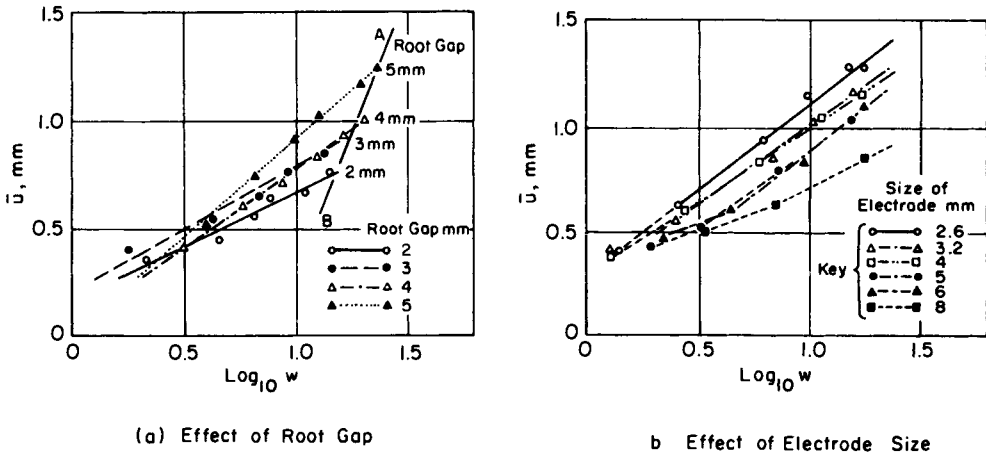


FIG. 7.28. Effect of root gap and electrode size on transverse shrinkage of butt welds. Note—specimens were ring-shaped, as shown in Fig. 7.6(a). Outer diameter = 600 mm, inner diameter = 300 mm, plate thickness = 19 mm, double-vee groove, w = weight of electrode deposited per unit weld length, gr/cm, \bar{u} = transverse shrinkage (mean value along the weld line), mm.

the various factors investigated, root gap and joint design had the greatest effect on transverse shrinkage.

Figure 7.28 shows how the root gap affects the transverse shrinkage. As the root gap increases, the shrinkage increases. As the root gap increases, the total amount of weld metal increases (Effect 1). The results show that Effect 2 also was significant. A single-vee joint produced more shrinkage than a double-vee joint. This was partly because the joint sectional area was larger (Effect 1), but Effect 2 also was significant.

Figure 7.28(b) shows how electrode size affects transverse shrinkage. Shrinkage decreases as the electrode size increases. As shown in Fig. 7.28, Effect 3 is most significant. This means that the use of large size electrodes will not reduce shrinkage unless they are used in the first pass. This was also confirmed experimentally.

Figure 7.29 shows the effect of chipping and rewelding (a simulated repair weld). Chipping the weld metal does not affect shrinkage; and rewelding increases shrinkage. Repeated chipping and rewelding reduces the slope (probably caused by strain hardening).

Figure 7.29 shows the effect of flame gouging and rewelding. Since heat is applied to the specimen during flame gouging, shrinkage increases during gouging as well as during rewelding.

7.4.4 Rotational distortion of butt welds

Kihara and Masubuchi⁽³⁰³⁾ found that rotational distortion (see Fig. 7.30) is affected by both heat input and welding speed. When $\frac{1}{2}$ -in. (12.7 mm) thick mild steel plates are welded using covered electrodes and a low welding speed, the unwelded portion of the joint tends to close (see Fig. 7.30(a)). When steel plates are welded using the submerged-arc process, the unwelded portion of the joint tends to open (see Fig. 7.30(b)). This means that the tack welds used must be large enough to withstand the stresses caused by the rotational distortion.

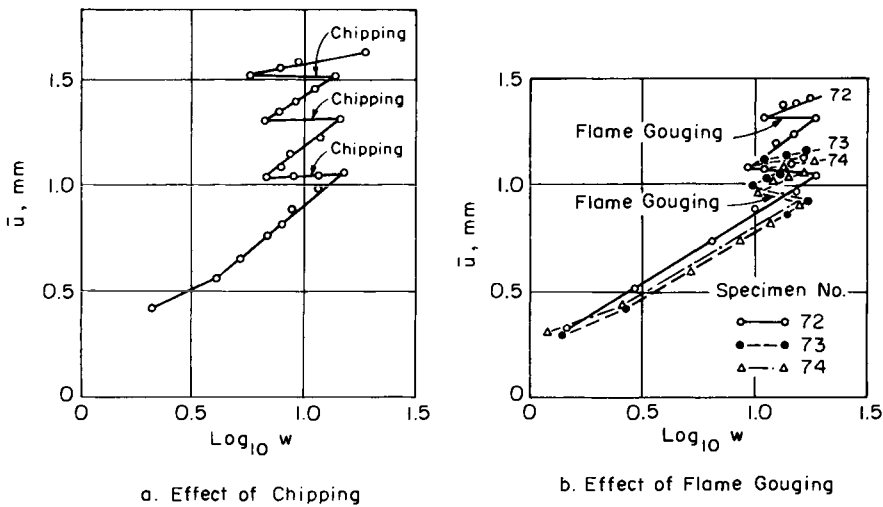


FIG. 7.29. Effects of chipping and flame gouging on transverse shrinkage of butt welds. See the note of FIG. 7.28

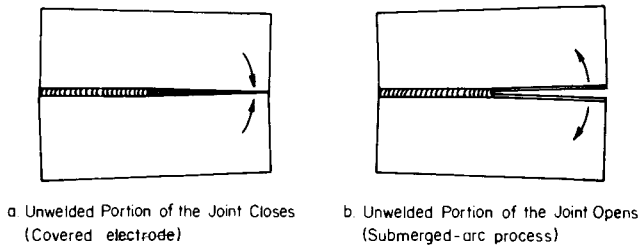


FIG. 7.30. Rotational distortion.

Rotational distortion causes two problems:

1. Rotational distortion is one component involved in the transverse shrinkage of a butt joint, especially in a long butt weld. When studying how the welding sequence affects the transverse shrinkage in a long butt weld, the effects of rotational distortion must be considered. The largest amount of rotational distortion occurs during the first pass, when the unwelded portions of the joint are relatively free.

2. The separating force produced by the rotational distortion can be large enough to fracture the tack welds and crack portions of the weld metal. Japanese shipbuilding companies have experienced cracking problems during the one-side submerged-arc welding of large steel panels.

During the 1950s Kihara and Masubuchi^(604,303,602) studied the rotational distortion that occurs during multi-pass welding. Because it was extremely difficult to analyze transient metal movement without an adequate computer technology, the study was primarily empirical.

Since 1970 several investigators have studied transient metal movement. Japanese investigators, including Fujita, Nomoto, and Ueda, have studied stresses in the weld metal during the submerged-arc welding of a long butt joint*. Bryan *et al.*⁽⁵³²⁾ of M.I.T.

* See Section 14.6.3.

studied transient rotational distortion that occurs during the gas metal arc welding of butt joints in 6061-T6 aluminum alloy plates $\frac{1}{4}$ in. (6.4 mm) thick.

The following pages discuss how rotational distortion changes during multi-pass welding of low-carbon steel based upon experimental results obtained by Kihara and Masubuchi.⁽⁶⁰²⁾ Figure 7.31 shows the distribution of transverse shrinkage during the multi-pass welding of a ring specimen (see Fig. 7.6(a)) with an outer diameter 1000 mm (40 in.), an inner diameter of 600 mm (24 in.), and a thickness of 19 mm ($\frac{3}{4}$ in.).

When welding was done from the inner circle (Specimen 21), the distribution of shrinkage after the welding of the first layer was as shown by line A_1 in Fig. 7.31(b); however, when welding was done in the opposite direction (Specimen 22), the distribution of shrinkage after the welding of the first layer was as shown by line B_1 . More shrinkage was produced in the region welded later. This is due to a tendency for rotational motion to occur in the direction that will close the unwelded plate edges.

The shrinkage-distribution changed as A_2, A_3, \dots , during multi-pass welding when welding was done from the inner circle to the outer one; however, the shrinkage distribution changed as B_2, B_3, \dots , when welding was done in the opposite direction. In the final stages of welding, more shrinkage was obtained in the outer circle than in the inner circle regardless of the welding direction. This is due to the difference in degree of constraint along the weld joint. The joint is more highly restrained in the region near the inner circle than in the region near the outer circle.

An analytical investigation was conducted of the above-mentioned phenomenon. Transverse shrinkage u was expressed in the following equation (see Fig. 7.31(a)):

$$u = \bar{u} \{1 + \alpha((r/\bar{r}) - 1)\} \tag{7.17}$$

where \bar{u} = mean shrinkage,

α = parameter to express the rotational component in shrinkage,

$\alpha = \tan \theta_1 / \tan \theta_0$,

r = radius,

\bar{r} = mean radius.

The parameter α was used in the analysis of experimental results. From the definition

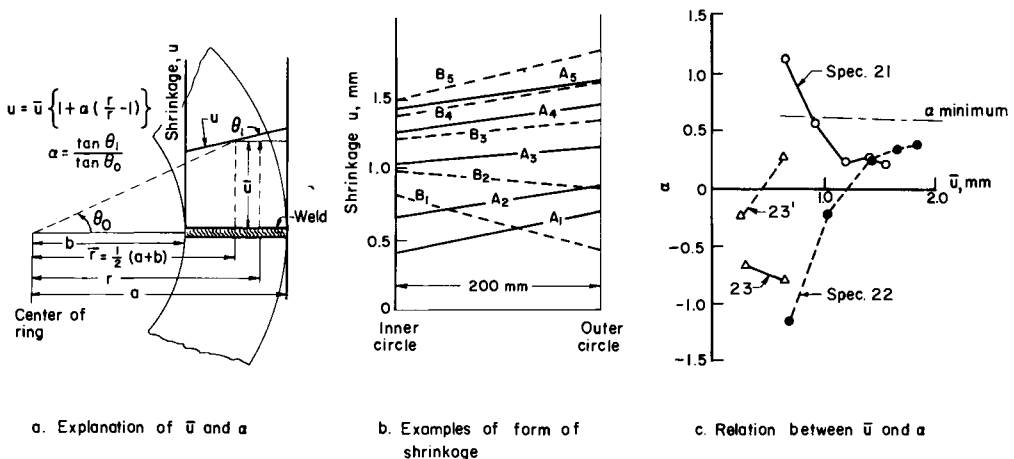


FIG. 7.31. Change of form of transverse shrinkage in multipass welding and influence of welding direction (ring-type specimen).

$\alpha = 0$ when the shrinkage is uniform along the weld line, $\alpha > 0$ when larger shrinkage is produced in the outer circle, and $\alpha < 0$ when larger shrinkage is produced in the inner circle. A theoretical study has shown that the amount of elastic-strain energy stored in a ring-form specimen becomes minimum when the value of α is about 0.65 in the type of specimen used in the experiment. Change of the value of α during multi-pass welding is shown in Fig. 7.31(c). The value of α after the welding of the first layer was quite different when different welding direction was used. However, the value of α approached a standard value during multi-pass welding regardless of the difference in welding direction. The fact that the experimental value of α is somewhat lower than the theoretically most stable value can be attributed to the uniform shrinkage of the metal during welding.

The phenomena observed when a joint was welded by submerged-arc welding were quite different. Specimens 23 and 23' were welded from the inner circle to the outer circle and in the opposite direction, respectively. As shown in Fig. 7.31(c), during welding of the first layer there was a tendency for the unwelded plate edges to open during welding. This was contrary to the closing motion obtained in manual-arc welding. When the second layer was welded, the opening tendency became greater.

Transient metal movement. Bryan *et al.*^(523,532) studied the transient rotational distortion that occurs during the gas metal arc welding of butt joints 23 in. (584 mm) long in 6061-T6 aluminum alloy plates, $\frac{1}{4}$ in. (6.4 mm) thick. Details of the results are given in References (523) and (532).

7.4.5 How welding sequence affects transverse shrinkage

In a long butt joint, several steps are involved in the welding. A variety of welding sequences may be used. These welding sequences are of two types:

The block-welding sequence. The joint is divided into several blocks; each block is welded separately, in turn.

The multilayer-welding sequence. Each layer is welded along the entire joint length before any of the next layer is begun. Both types have many variations.

Kihara *et al.*^(603,604) investigated how the welding sequence affects the magnitude and distribution of transverse shrinkage in slit-weld and patch-weld specimens. Figure 7.32 shows some of the experimental results obtained with slit-weld specimens ($19 \times 800 \times 1200$ mm). Specimens 1-1, 1-2, and 1-3 were welded using a block-welding sequence. The weld joint was about 500 mm (20 in.) long and was divided into three blocks. Welding of each block was done in eight layers. Each of the three specimens were block-welded in a different order:

	First	Second	Third
Specimen 1-1	Left block	Middle block	Right block
Specimen 1-2	Left block	Right block	Middle block
Specimen 1-3	Middle block	Right block	Left block

In Specimen 4-1, the joint was divided into three parts and welded using a multi-layer sequence from left to right.

Curves A_{11} , A_{12} , A_{14} , and A_{18} indicate the distribution of transverse shrinkage

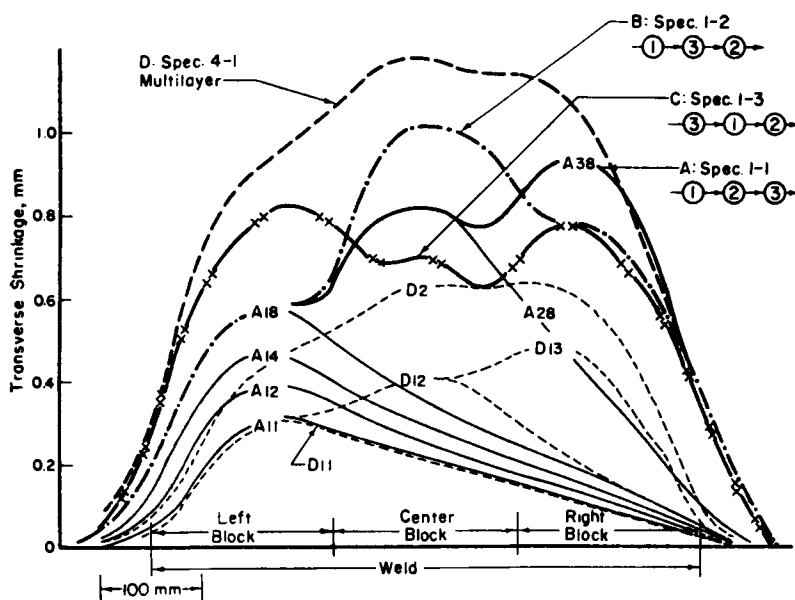


FIG. 7.32. Distribution of transverse shrinkage obtained in slit-type specimens with different welding sequences. Note: The slit-weld specimen is shown in Fig. 6.5.

after the completion of 1, 2, 4, and 8 layer in the first block Specimen 1-1. Curve A_{28} indicates the distribution of transverse shrinkage when the welding of the second block was completed, and curve A or (A_{38}) shows the distribution of transverse shrinkage after welding was completed. Curves B and C show the distribution of shrinkage after completion of welding on Specimens 1-2 and 1-3, respectively. Curves D_{11} , D_{12} , and D_{13} show the distribution of shrinkage after welding the first layer of the first, the second, and the third part of the joint of Specimen 4-1. Curve D_2 and D indicate the distribution of shrinkage after the welding of the second layer and when welding was completed, respectively. Quite uneven transverse-shrinkage distributions were obtained with block-welding sequences whereas the shrinkage distribution obtained with the multi-layer sequence was much more even, similar to that shown in Fig. 7.16 (obtained without an interruption of the welding).

An analytical investigation of the transverse-shrinkage distribution obtained in a slit-type specimen also was conducted. A parameter δ , defined by eqn. (5) of Table 3.6, was used in the analysis. From the definition, the shrinkage distribution which corresponds to $\delta = 0$ induces the minimum amount of strain energy in the plate at a given value of mean shrinkage. In Specimen 4-1, the value of δ was about 0.1 at the completion of the first layer (shrinkage curve, D_{13}) and it decreased as low as 0.02 at the final stage of welding. In Specimen 1-1, the value of δ was 0.52 when the welding of the first block was completed (shrinkage curve, A_{18}) and it decreased as low as 0.09 at the final stage of welding.

The shrinkage increase in a slit-type specimen was also investigated. A linear relationship was found between transverse shrinkage and the logarithm of weight of electrode consumed when a specimen was welded with a multi-layer welding sequence. When a specimen was welded using a block-welding sequence, however, the logarithmic rela-

tionship was valid only in the shrinkage and the electrode consumed obtained in each block. These results suggest that the mechanism of shrinkage obtained in the first layer when the separate plates are joined together is quite different from that obtained in the succeeding layers in which shrinkage occurs in the already joined plates.

Nearly the same results were obtained with circular-patch specimens welded using different welding sequences.⁽⁶⁰⁴⁾

7.4.6 *Metal movement and joint mismatch*

Gott *et al.*⁽⁷²¹⁾ studied metal movement and mismatching in aluminum welds. During girth welds engineers often experience mismatching such as that shown in Fig. 7.33. The following has been observed in production welding:

1. Any preweld mismatch (thickness direction misalignment) tends to increase during welding (under fixture conditions to be described) to the point where an apparent in-tolerance fit-up can become an out-of-tolerance weld.
2. The preweld gap closes appreciably during welding.

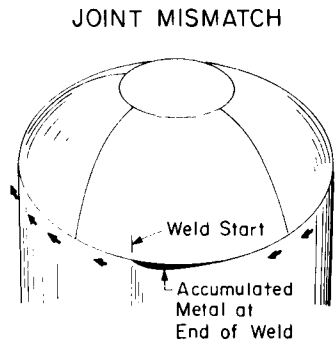


FIG. 7.33. Production girth weld with metal expansion causing mismatch at finish of dome to barrel weld.

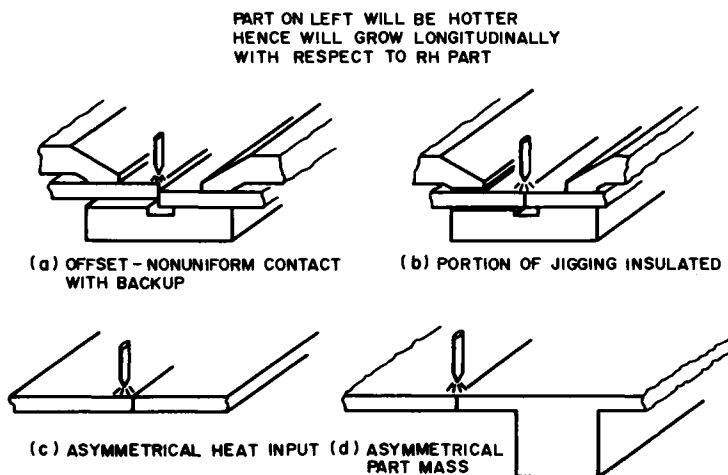


FIG. 7.34. Several causes of thermal unbalance.

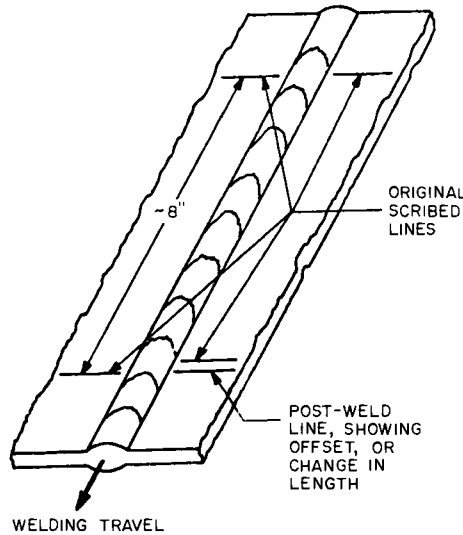


FIG. 7.35. System for showing relative growth of left-hand part.

3. The amount of welding-heat input needed for satisfactory penetration changes during welding in a manner that cannot be explained by straightforward heat-in and heat-out considerations.

4. Gross transverse weld shrinkage varies as a function of joint fit-up, in addition to showing the expected dependence on heat input. For example, a weld with an as-jigged, evenly distributed mismatch of 0.010 in. (0.25 mm) was found to be mismatched 0.25 in. (0.6 mm) after welding.

The heat-sink properties of the two sides of a joint to be welded are different from each other. This may be one important cause of joint mismatch. Several causes of heat unbalance are shown in Fig. 7.34. Mismatch was observed during the welding of a Saturn V dome-to-barrel girth joint. The cross-section of this weld is shown in Fig. 7.34.

Gott *et al.*⁽⁷²¹⁾ conducted experiments to demonstrate that thermal asymmetry could cause mismatch. Two panels were tack welded on one end to fix their initial alignment and marked with transverse scribe lines across both pieces. One piece was then insulated from contact with any heat sink (see Fig. 7.34). The panels were gas tungsten arc welded, starting at the tacked end. The growth of the insulated side is clearly indicated by the scribe lines (see Fig. 7.35). This growth was approximately 0.001 in./in. of weld.

Another set of panels was tack welded on either end to hold a pre-set mismatch by springing one piece to an arc; this mismatch ranged from zero at both ends to 0.058 in. (1.5 mm) in the center. The pieces were then welded in a fixture with the straight side in contact with the metal backing heat sink; the arced piece had no contact. Maximum mismatch of 0.058 in. (1.5 mm) in the center grew to 0.94 in. (24 mm) with similar increases at other points as shown in Fig. 7.36.

A third weld was performed on two pieces in symmetrical heat-sink conditions but with the electrode holder approximately $\frac{1}{16}$ in. (1.6 mm) side of center. A measured growth of more than 0.0005 in. (0.013 mm) of weld was noted in the part receiving more heat, measured in fashion similar to that in Fig. 7.35.

Based on these results it can be concluded that, if both parts are equally restrained, the growth of one part relative to the other can result in mismatch. This tendency has

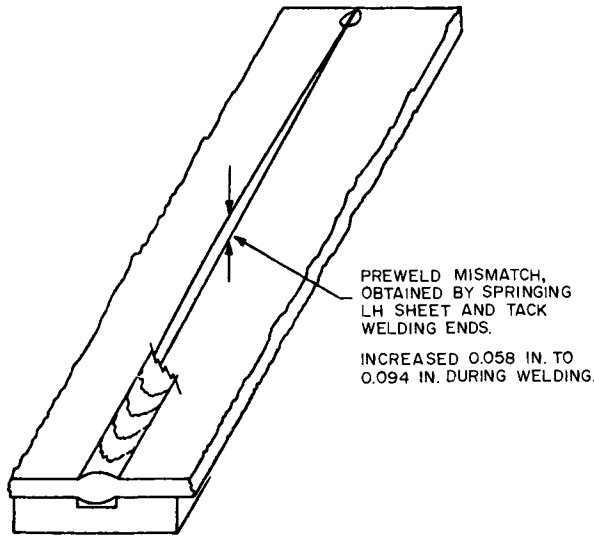


FIG. 7.36. Mismatch obtained by preweld bowing.

been observed in certain production-type girth welds as shown in Fig. 7.33. In this case it is evident that unbalanced heating resulted in a cumulative size difference and an unacceptable mismatch near the end of the weld.

Gott *et al.*⁽⁷²¹⁾ studied various subjects related to metal movement and joint mismatching including measurements of joint gap and residual stresses along girth welds. Some of his conclusions are as follows:

1. The longitudinal growth of the two parts being welded is often uneven.
2. The part that receives the greater amount of heat, or that sees the lesser heat sink, will grow longer, relative to its mate.
3. Jigging, part design, arc alignment, and thermal asymmetries are all capable of causing the length changes cited in # 2.

7.5 Transverse Shrinkage in Fillet Welds

A fillet weld undergoes less transverse shrinkage than a butt weld. Only a limited amount of study has been done on transverse shrinkage in fillet welds. Spraragen and Ettinger⁽⁵⁰⁴⁾ suggested the following simple formula:

1. For tee-joints with two continuous fillets:

$$\text{Shrinkage} = \frac{\text{leg of fillet}}{\text{thickness of plate}} \times 0.04 \text{ in.} \quad (7.18)$$

2. For intermittent welds—use correcting factor of proportional length of fillet to total length.
3. For fillets in lap joint (two fillet welds):

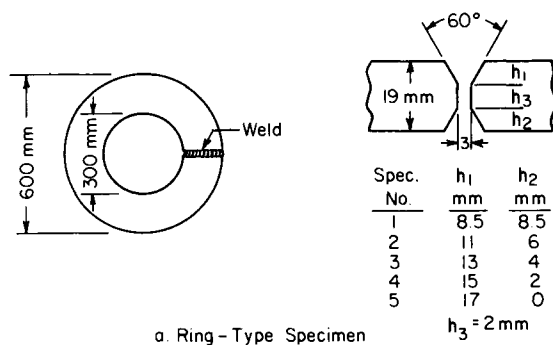
$$\text{Shrinkage} = \frac{\text{leg of fillet}}{\text{thickness of plate}} \times 0.06 \text{ in.} \quad (7.19)$$

Figure 7.10 shows the fillet-weld shrinkage allowed in the U.S. Navy specifications.

7.6 Angular Changes of Butt Welds

Angular change often occurs in a butt weld when the transverse shrinkage is not uniform in the thickness direction. A thorough investigation has been made of how various welding-procedure parameters, including the shape of the groove and the degree of restraint, affect the angular change in butt welds.

Figure 7.37 shows the experimental data obtained by Kihara and Masubuchi⁽⁶⁰²⁾ on the ring specimens discussed earlier. A radial groove was cut and then welded using covered electrodes $\frac{1}{4}$ in. (6.4 mm) in diameter. Five specimens with different types of grooves were tested. The grooves ranged from symmetrical double-vee to single-vee grooves. Welding was first completed on one side, then the specimen was turned over and the other side back chipped and welded. The angular change was measured after each welding pass. A mild increase of angular change was observed in the earliest stage of welding on the first side. The increase of angular change became greater in the intermediate stage, and then mild again in the final stage. The back chipping did not affect the angular change. Angular change in the reverse direction was produced during



a. Ring - Type Specimen

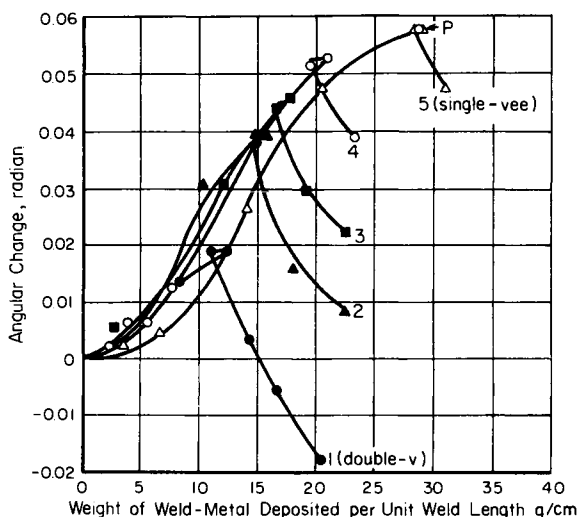


FIG. 7.37. Effect of shape of groove on angular change.

the welding of the second side. The angular change that remained after the welding was completed depended on the ratio of the weld metal deposited on the two sides of the plate (see Fig. 7.38). Since the angular change increased more rapidly during the welding of the second side, the minimum angular change was obtained in the specimen that had a

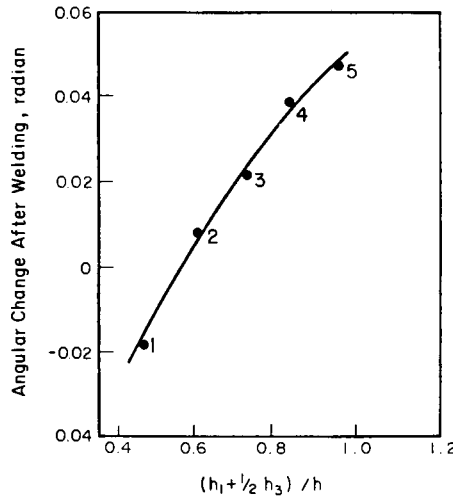


FIG. 7.38. Effect of groove shape on angular change in butt welds.⁽⁷⁰⁸⁾

Note: $h = h_1 + h_2 + h_3$

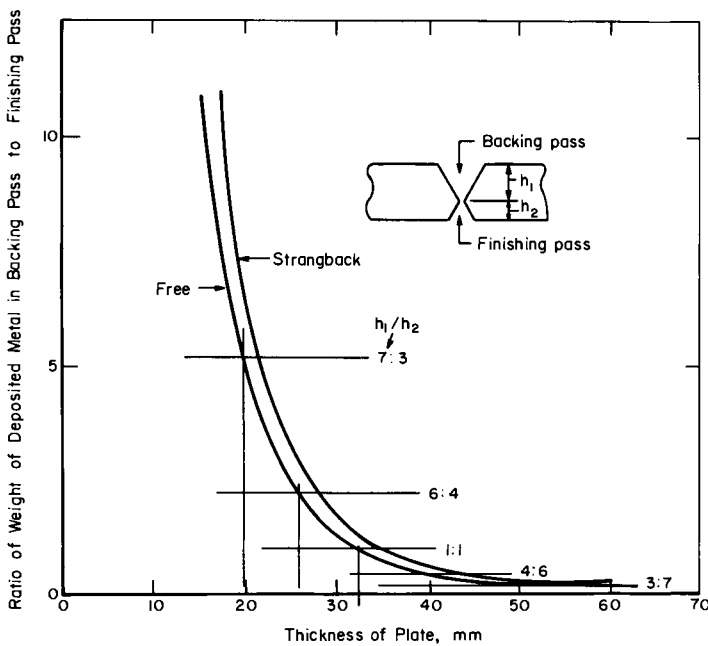


FIG. 7.39. The most suitable groove shape which gives zero angular distortion in butt welds.⁽⁷²²⁾

little larger groove in the first side. In the particular cases that Kihara and Masubuchi investigated, the angular change could be minimized (near zero) for a butt joint having a $(h_1 + \frac{1}{2} h_2)$ to h ratio of approximately 0.6.

An extensive program was conducted by the Shipbuilding Research Association of Japan⁽⁷²²⁾ on angular change in butt welds. Figure 7.39 shows the groove shape that most successfully minimized angular change in butt welds of various thicknesses. Curves are shown for situations with and without strongbacks.

Readers are reminded that the ordinate of Fig. 7.39 is expressed in terms of the ratio of the weight of the deposited metal in the backing to the finishing pass, w_1/w_2 , which can be expressed in terms of h_1 and h_2 as follows:

$$w_1/w_2 \propto (h_1/h_2)^2.$$

For example, when the plate thickness is 20 mm ($\frac{3}{4}$ in.), the ratio of h_1 and h_2 that gives the minimum distortion when the joint is free is 7 to 3. In terms of the weight of the deposited metal, the w_1/w_2 ratio is approximately 49 to 9, or a little over 5.

7.7 Angular Changes of Fillet Welds and the Resulting Out-of-plane Distortion

The panel structure, a flat plate with longitudinal and transverse stiffeners fillet welded to the bottom, is a typical structural component in ships, aerospace vehicles, and other structures (see Fig. 7.40). The major distortion problem in the fabrication of panel structures is that related to out-of-plane distortion caused by angular changes along the fillet welds.

Corrugation failures of bottom shell plating in some welded cargo vessels are believed to be caused when excessive initial distortion reduces the buckling strength of the plating (see Chapter 14).

When longitudinal and transverse stiffeners are fillet welded as shown in Fig. 7.40, the deflection of the panel, δ , changes in both the x -direction and y -direction. Because of the mathematical difficulties involved in two-dimensional analysis, most studies conducted thus far have been one-dimensional; that is, only the change of deflection, δ , in the x -direction is taken into consideration.

7.7.1 One-dimensional analysis

Figure 7.41 shows the typical out-of-plane distortion found in two types of simple

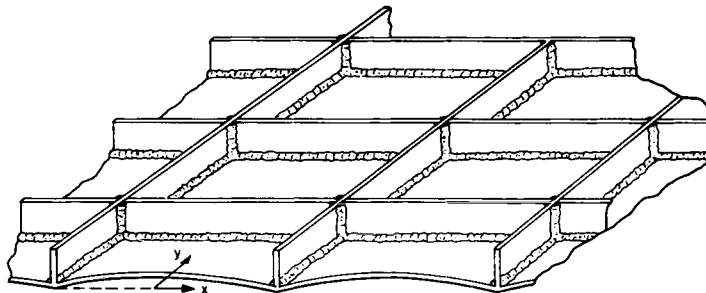


FIG. 7.40. Panel structure with longitudinal and transverse stiffeners.

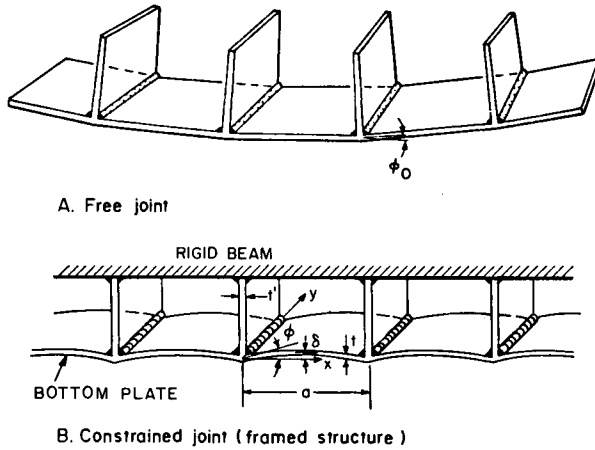


FIG. 7.41. Distortion due to fillet welds in two types of one-dimensional models.

fillet-welded structures. In both cases, the plates are narrow in the y -direction and the distortion is one-dimensional.

When a fillet joint is free from external constraint, the structure bends at each joint and forms a polygon (see Fig. 7.41(a)). But if the joint is constrained by some means, a different type of distortion is produced. For example, if the stiffeners are welded to a rigid beam (see Fig. 7.41(b)), the angular changes at the fillet welds will cause a wavy, or arc-form, distortion of the bottom plate.[†]

The investigation of steel weldments by Masubuchi *et al.* Masubuchi *et al.*⁽⁷²³⁾ found that the wavy distortion and resulting stresses could be analyzed as a rigid-frame stress problem. In the simplest case in which the sizes of all welds are the same, the distortion of all spans are equal and the distortion, δ , can be expressed as follows:

$$\delta/a = \left[\frac{1}{4} - \left(\frac{x}{a} - \frac{1}{2} \right)^2 \right] \cdot \phi \tag{7.20}$$

where ϕ = angular change at a fillet weld, radians,
 a = length of span[‡]

The maximum distortion at the panel center ($x = a/2$), δ_0 , is:

$$\delta_0 = \frac{1}{4} \cdot \phi \cdot a \tag{7.21}$$

The amount of angular change, ϕ , in a restrained structure is smaller than that in a free joint, ϕ_0 . The amount of ϕ also changes when the rigidity of the bottom plate, $D = Et^3/12(1 - \nu^2)$, and the length of the span, a , change.

Masubuchi *et al.*⁽⁷²³⁾ have found that the following relationship exists:[†]

$$\phi = \frac{\phi_0}{1 + (2D/a)(1/C)} \tag{7.22}$$

where C , the so-called “coefficient of rigidity for angular changes”, can be determined by welding conditions and plate thickness.

[†] Distortion of the specimen after the constraining member was removed was smaller than that obtained in a free joint; the constraint lessened the amount of angular change produced.

[‡] In a number of publications the span length is designated l .

Equation (7.22) was induced by using the minimum energy principle. As stated earlier, the amount of angular change ϕ in a constrained structure is smaller than that in a free joint, ϕ_0 . This indicates that a certain amount of energy is necessary to decrease the angular change from ϕ_0 to ϕ . If the necessary energy is represented by U_w , one may write:

$$U_w = \int_0^{\phi_0 - \phi} \frac{dU_w}{d(\phi_0 - \phi)} d(\phi_0 - \phi). \quad (7.23)$$

On the other hand, using the elastic beam theory, the strain energy stored in the constrained plate per unit width, U_p , can be expressed:

$$U_p = (D/a) \cdot \phi^2 \quad (7.24)$$

Since U_p increases and U_w decreases as the constrained angle increases, the condition for equilibrium of this system requires that the total energy $U_t = U_w + U_p$ should be at the minimum. Furthermore, for the simplification of the problem, the ratio of incremental welding energy change to angular change is assumed to be linear as follows:

$$dU_w/d(\phi_0 - \phi) = C(\phi_0 - \phi) \quad (7.25)$$

From eqns. (7.23) and (7.25) welding energy per unit width can be expressed:

$$U_w = (C/2)(\phi_0 - \phi)^2. \quad (7.26)$$

Accordingly, the condition of equilibrium is as follows:

$$\partial U_t / \partial \phi = -C(\phi_0 - \phi) + (2D/a)\phi = 0. \quad (7.27)$$

From this equation, eqn. (7.22) is obtained.

The investigation of steel weldments by Hirai-Nakamura. Hirai and Nakamura⁽⁷²⁴⁾ conducted an investigation to determine the values of ϕ_0 and C under various conditions. Figure 7.43 shows the values of ϕ_0 as a function of plate thickness, t (mm), and weight of electrode consumed per weld length, w (g/cm). In order to convert from w to the size of the fillet weld, D_f (mm), the following formula may be used (see Fig. 7.42).

$$w = (D_f^2/2) \times 10^{-2} \times (\rho/\eta_d). \quad (7.28)$$

where ρ = density of weld metal,
 η_d = deposition efficiency.

The fillet size, D_f , is commonly used in design work, while w is easy to determine in a welding experiment.

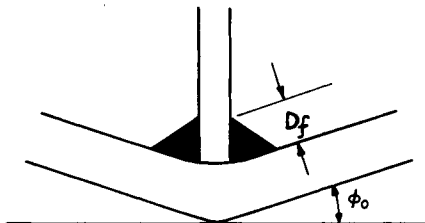


FIG. 7.42. Angular change of a free fillet weld.

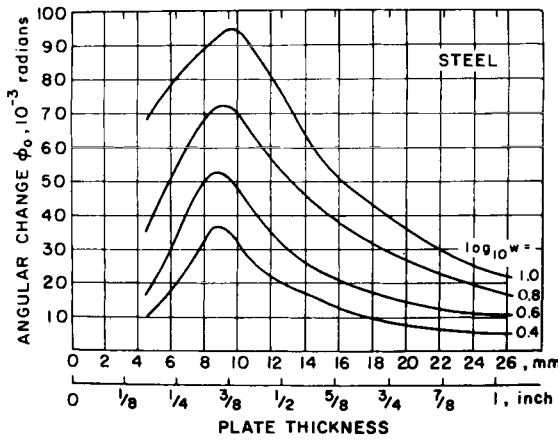


FIG. 7.43. Angular change of a free fillet weld, ϕ_0 , in steel.

The results shown in Fig. 7.43 were obtained using covered electrodes 5 mm (0.2 in.) in diameter. The maximum angular changes were obtained when the plate thickness was around 0.35 in (9 mm). When the plate was thinner than 9 mm (0.35 in.), the amount of angular change was reduced with the plate thickness. This is because the plate was heated more evenly in the thickness direction, thus reducing the bending moment. When the plate was thicker than 9 mm (0.35 in.), the amount of angular change was reduced as the plate thickness increased (because of the increase of rigidity).

Table 7.8 lists values of C for steel.[†] Hirai and Nakamura studied the effects of various welding parameters on the amount of angular change.

TABLE 7.8 Values of angular rigidity coefficient C for low-carbon steel

Amount of weld		C (kg · mm/mm)				
Fillet size D_f (mm)	Weight of consumed electrode per unit weld length	$\log_{10} w$	$t = 10$ mm	$t = 13$ mm	$t = 18$ mm	$t = 25.4$ mm
	w (g/cm)					
6.58	2.51	0.4	5400	19,900	76,100	170,100
7.38	3.16	0.5	4700	18,000	65,200	142,400
8.29	3.98	0.6	4100	16,300	56,100	130,200
9.30	5.01	0.7	3800	15,000	48,800	125,000
10.45	6.31	0.8	3500	13,600	43,000	116,800
12.20	7.95	0.9	3300	12,200	38,900	112,000
13.15	10.00	1.0	3100	11,000	36,100	108,200
14.80	12.60	1.1	3000	9,800	35,200	105,000
16.55	15.85	1.2	2950	8,800	34,800	102,000

$$^{(1)} w = (D_f^2/2) \times 10^{-2} \times 7.85/0.657 = 0.058 D_f^2.$$

[†] Hirai and Nakamura originally proposed the following formula to calculate values of C :

$$C = t^4 / (1 + (w/5)).$$

where t = plate thickness, mm,

w = weight of weld metal deposited per unit of weld length, g/cm.

After a thorough evaluation of the data on steel and aluminum, Tables 7.8 and 7.9 were prepared.⁽²¹¹⁾

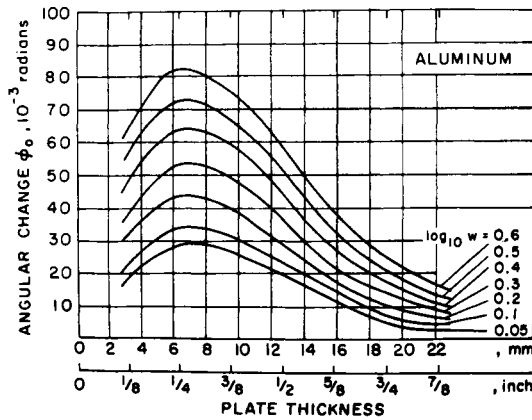


FIG. 7.44. Angular change of a free fillet weld, ϕ_0 , in aluminum.

The investigation of aluminum weldments by Taniguchi. A study was conducted at M.I.T. by Taniguchi^(725, 726) to experimentally determine the values of ϕ_0 and C for GMA welds in aluminum. The material used in the experiments was a strain-hardened, aluminum magnesium structural alloy, 5086-H32, that is widely used in marine and general structural applications; 5356 alloy was used as a filler metal.

Figure 7.44 shows the values of ϕ_0 . The maximum distortion occurred in plates that were approximately 7 mm ($\frac{1}{4}$ in.) thick. Table 7.9 lists the values of C .

Since aluminum is much lighter than steel, the w -value for an aluminum weld is much lower than that for a steel weldment of the same size. Figures 7.45(a) through (d) compare the distortion values at the midspan, δ_0 , in steel and aluminum structures.

7.7.2 Two-dimensional analysis

Limited studies have been made at M.I.T. of two-dimensional analysis of out-of-plane distortion of welded panel structures.^(727, 728) Shin⁽⁷²⁷⁾ analyzed two-dimensional distribution of distortion by expanding the minimum energy method described earlier (eqns. (7.23) through (7.27)). The finite-element method was used in the analysis. Brito⁽⁷²⁹⁾

TABLE 7.9 Values of angular rigidity coefficient for aluminum

Amount of weld		C(kg · mm/mm)							
Fillet size D_f (mm)	Wt. of consumed electrode per unit weld length w (g/cm)	$\log_{10} w$	Amount of weld						
			$t = 3.18$ mm	$t = 6.4$ mm	$t = 9.5$ mm	$t = 12.7$ mm	$t = 15.9$ mm	$t = 19.1$ mm	
8.969	1.122	0.05	57	782	14,390	22,800	31,000	78,400	
9.567	1.259	0.1	55	762	13,600	20,800	25,300	72,500	
10.660	1.585	0.2	52	725	7,900	17,000	18,000	31,800	
11.960	1.995	0.3	49	686	5,600	13,800	12,900	22,200	
13.420	2.512	0.4	46	645	4,300	11,000	9,200	17,000	
15.057	3.162	0.5	43	608	3,600	8,900	6,900	13,500	

⁽¹⁾ $w = (D_f^2/2) \times 10^{-2} \times 2.65/0.95 = 0.0139 D_f^2$.

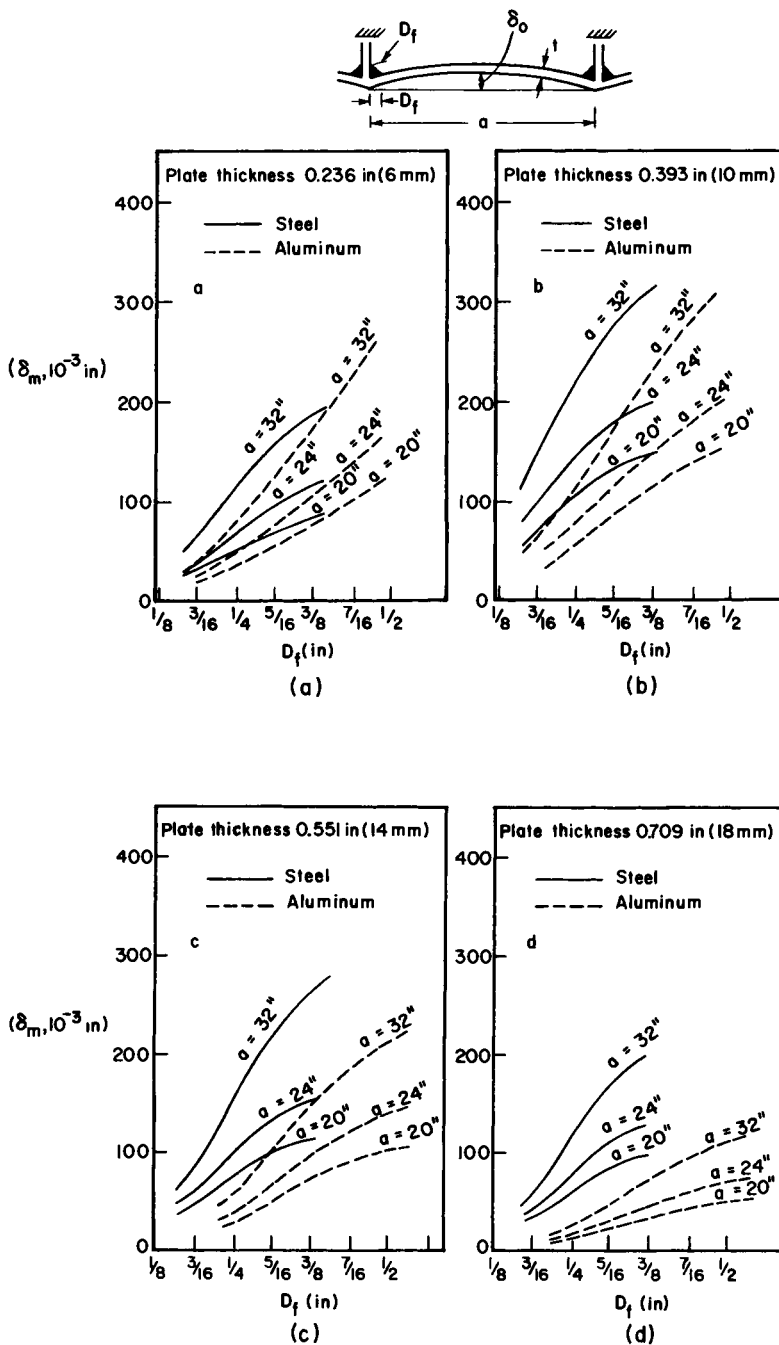


FIG. 7.45. Out-of-plane distortion, δ_o , as a function of plate thickness, T , span length, a , and the size of fillet weld D_f , for steel and aluminum.

conducted a series of experiments in the measurement of out-of-plane distortion of welded panel structures in 5052-H32 aluminum alloy. However, further discussions of these studies are not included here, because results obtained so far are not conclusive.

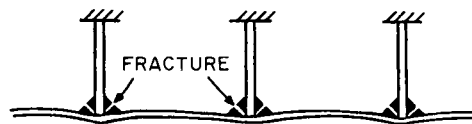
7.7.4 Analysis of allowable out-of-plane distortion

Background of the parametric study. Thus far discussions have been on how angular changes in fillet welds cause the out-of-plane distortion of a panel structure. Analyses have been carried out to determine the amount of this distortion, assuming it to be a function of a plate thickness, the floor space, and the weld size.

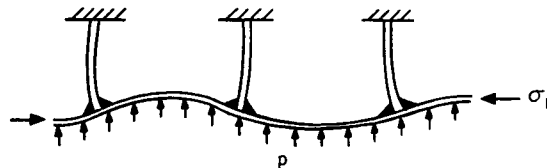
Out-of-plane distortion reduces the buckling strength of a panel. It is believed that the initial distortion and the residual stresses are the major reasons for the corrugation damage in the bottom plates of a number of transversely framed welded cargo ships. A number of studies have been made on how initial distortion affects the buckling strength of a panel structure (see Chapter 13).

However, these two kinds of studies, structural and welding, have rarely been integrated, probably because they are normally studied by different specialists, structural analysts, and welding engineers. Also, each subject is so complicated that an integrated study has to involve computations too complicated to be handled manually.

In practice, however, it is often necessary to combine the two analyses. For example, a simple way to reduce the amount of distortion shown in Fig. 7.41(b) is to reduce the size of the fillet welds. But if the fillet size is too small, the floors may be ripped from the plating during service, as shown in Fig. 7.46(a). On the other hand, if the fillet size is increased too much, distortion of the plate will become excessive and the plate may buckle during service, as shown in Fig. 7.46(b). In the case of the bottom plate of a ship, the plate is subjected to water pressure, p , and in-plane compressive stress, σ_b . Weld



A. DISTORTION MAY BE REDUCED BY REDUCING FILLET SIZES. BUT, FRAMES MAY BE RIPPED FROM PLATING DURING SERVICE



B. INCREASING FILLET SIZE CAUSES MORE DISTORTION WHICH MAY RESULT IN BUCKLING OF PLATING DURING SERVICE

FIG. 7.46. Out-of-plane distortion of a welded panel structure and possible failures during service.

distortion may be decreased by reducing the floor space, a , and/or plate thickness, t . But doing this will increase the hull weight.

In order to achieve the optimum design, it is important to analyze both weld distortion and its effects on the service behavior of the structure. A parametric study, including both analyses, can be important in the design and fabrication of certain critical structures, such as the bottom structures of high-performance, surface-effect ships made of aluminum.

Efforts have been made at M.I.T. and the University of São Paulo to integrate studies on weld distortion and the effects of initial deflection on the buckling strength of a panel structure.^(211, 730) Computers have been used extensively to handle the complex calculations required.

Details of the analysis are described in Chapter 13. The computer program developed consists of two parts. The first part calculates values of allowable initial distortion, δ_0 , for a given set of structural parameters, including plate thickness, frame spacing, aspect ratio of panel, and compressive in-plane stresses, while the second part calculates the amount of weld allowed to produce only distortion δ_0 . The formulas given in Section 7.7.1 are used in the distortion-analysis.

Comparison with Navy steel-structure specifications. As a part of the above study, we have compared the results of the parametric study with the allowable distortion specified by the U.S. Navy (see Figs. 7.11 through 7.15). An early effort was made by Goncalves and Taniguchi⁽⁷³¹⁾ at the University of São Paulo, Brazil, and the efforts were continued by researchers at M.I.T. and U.S.P.^(211, 730)

Figure 7.47 summarizes the results obtained under certain given conditions. Shown here are:

1. The values of permissible distortion for floor spacing of 800 mm (32.5 in.) for different plate thicknesses. The values are given for the following cases:

NAVSHIPS 0900-060-4010

- (a) For the entire shell, uppermost strength deck, longitudinal strength structure, etc. (see Fig. 7.11).
- (b) For other structures (see Fig. 7.14).

NAVSHIPS 0900-014-5010 (see Fig. 7.15)

- (a) For deck plating.
- (b) For shell plating.

The values of permissible unfairness set by these two specifications are different. For shell plating $\frac{1}{2}$ in. (12.7 mm) thick, for example, the permissible unfairness is $\frac{5}{8}$ in. (16 mm) in NAVSHIPS 0900-060-4010 and $\frac{1}{4}$ in. (6.4 mm) in NAVSHIPS 0900-014-5010.

2. The values of distortion likely to occur when steel plates are welded under normal conditions. The values were estimated by Goncalves and Taniguchi⁽⁷³¹⁾ who used formulas developed in Russia by Okerblom⁽⁵⁰⁸⁾ and in Japan by Masubuchi *et al.*⁽⁷²³⁾ The amount of weld metal was estimated to be $w = 10$ g/cm, where w is the weight of consumed electrodes per unit weld length.

3. The values of maximum initial unfairness determined by this parametric study. The calculations were made under the following conditions:

- (a) $\sigma_c = 6\text{kg/mm}^2$ and $w = 10.0$ g/cm,
- (b) $\sigma_c = 8\text{kg/mm}^2$ and $w = 9.5$ g/cm,
- (c) $\sigma_c = 10\text{kg/mm}^2$ and $w = 6.0$ g/cm.

In every case, the plate was 18 mm thick and $a/b = 0.5$.

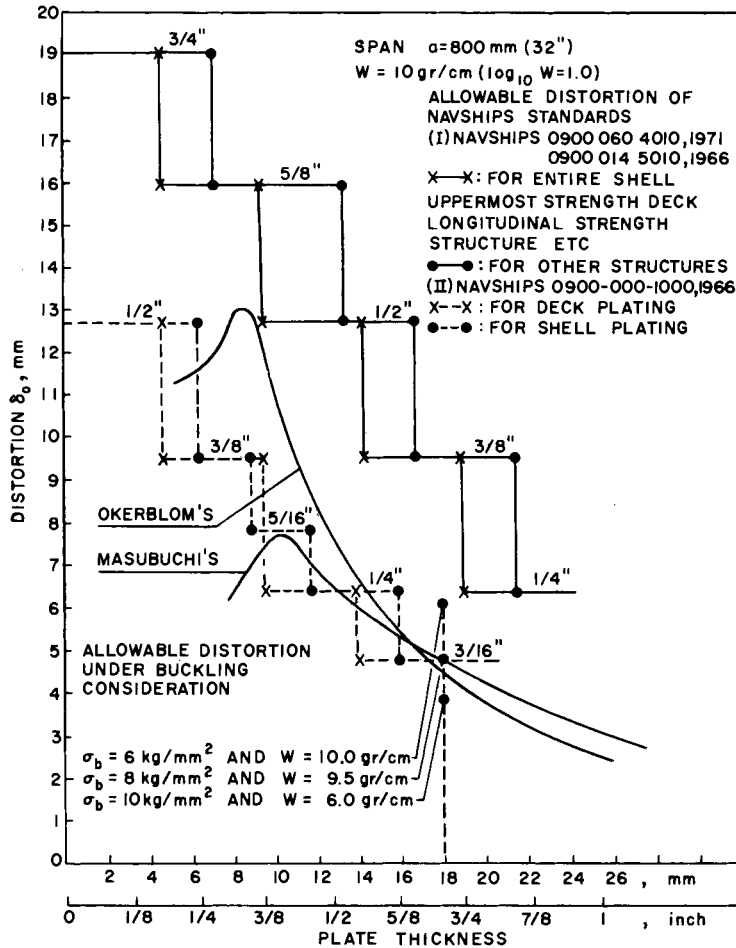


FIG. 7.47. Comparison among (1) possible distortion estimated from formulas by Masubuchi and Okerblom, (2) allowable distortion by navy specifications, and (3) allowable distortion under buckling consideration.

Logically, the above should be in the following order:

- (a) Values set by the buckling criterion should be the highest.
- (b) Values set by standards should be lower than a failure criterion so that a structure that meets the standard will not fail during service. However, the values set by the standards are higher than those likely to happen during welding.
- (c) Estimated distortion should be the lowest.

If the allowable distortion standards are too strict, fabricators will find it difficult to meet the standard. On the other hand, if they are too relaxed, the probability of buckling failure during service will increase.

The results shown in Fig. 7.47 indicate that the situation is delicate. Fabricators will find it difficult to meet the requirements given in NAVSHIPS 0900-014-5010. The requirements given in NAVSHIPS 0900-060-4010 should not be difficult to meet, but the structure may buckle during service (under the conditions in which the calculations were made).

The authors of Reference (211) did not mean to criticize Navy specifications on the basis of a simple analysis. Their major objective in the study was to demonstrate that it is technically possible to conduct a parametric study on weld distortion and its effects on service behavior. The results seem to indicate that a rather delicate situation now exists between the distortion that is likely to occur and the distortion that can be tolerated.

But it should be pointed out that this buckling analysis was done for transversely framed structures, while the Navy specifications are primarily for longitudinally framed structures. More study is needed on this subject.

Readers are also cautioned that Fig. 7.47 gives the impression that there will be less of a distortion problem if fabricating plates are thinner than $\frac{3}{8}$ in. (10 mm). The analysis given here is of the out-of-plane distortion that is caused by angular changes in the fillet welds. As the plate thickness is decreased, this distortion due to angular change is less, but the possibility of buckling distortion (discussed in Section 7.12) is greatly increased.

Comparison with Navy specifications for aluminum structures. A comparative study was also made of distortion in aluminum structures.⁽⁷²⁰⁾ Figures 7.48 and 7.49 show the

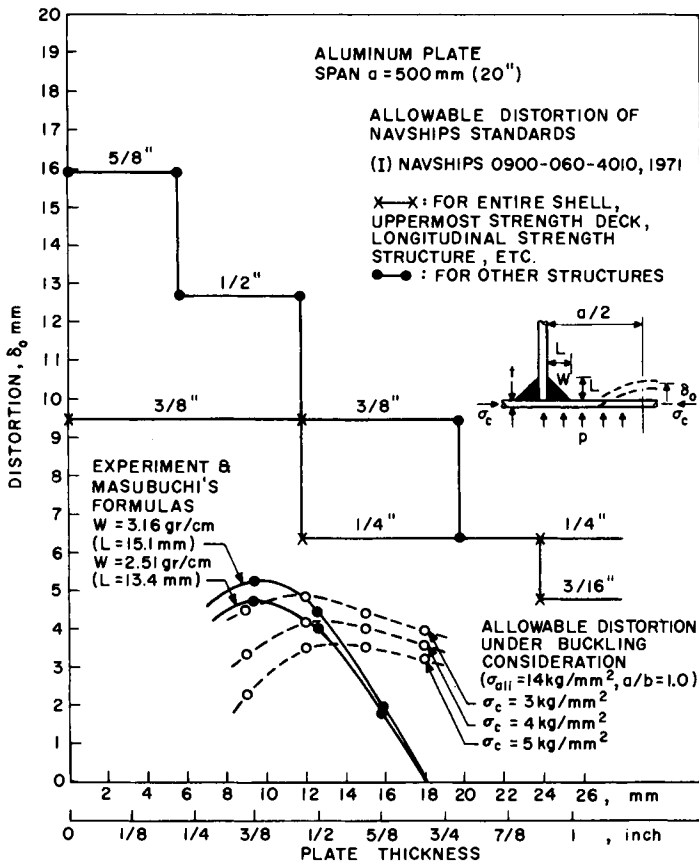


FIG. 7.48. Comparison among (1) possible distortion estimated from formulas by Masubuchi, (2) allowable distortion by Navy specifications and (3) allowable distortion under buckling consideration for an aluminum plate of 500 mm span.

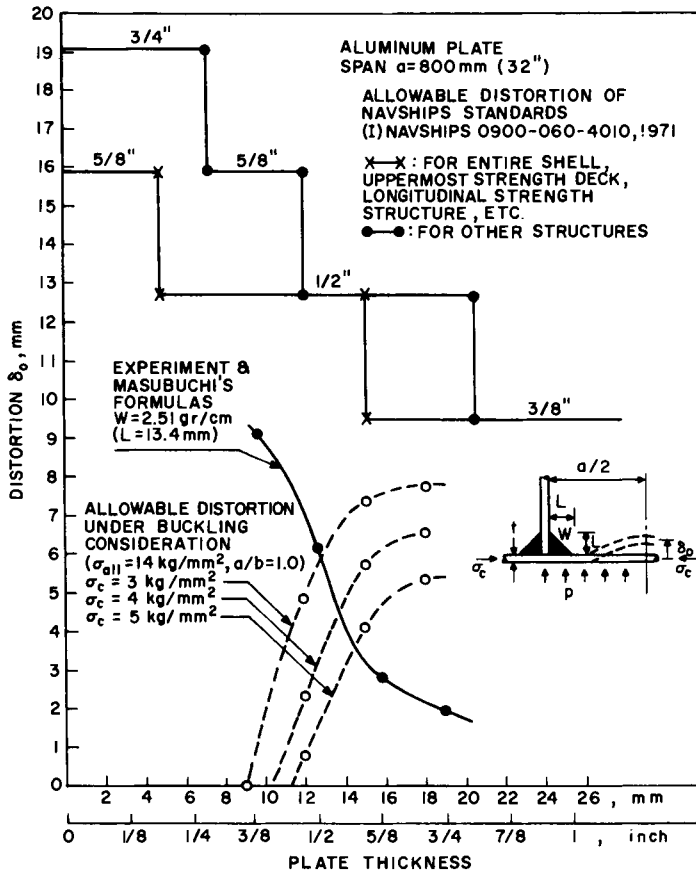


FIG. 7.49. Comparison among (1) possible distortion estimated from formulas by Masubuchi, (2) allowable distortion by Navy specification and (3) allowable distortion under buckling consideration for aluminum plates of 800 mm span.

results. A ship fabricator should have no difficulty meeting the current Navy specifications, but these specifications may be too relaxed as far as the prevention of buckling is concerned.

The amount of distortion appears to depend on the plate thickness. When the plate is over 14 mm ($\frac{9}{16}$ in) or 16 mm ($\frac{5}{8}$ in.) thick, the distortion is much less than the allowable distortion. When the plate is less than 12 mm ($\frac{1}{2}$ in.) or 10 mm ($\frac{3}{8}$ in.), however, the distortion problem becomes serious. Unfortunately the plates most widely used for light aluminum structures such as surface effect ships range from $\frac{1}{2}$ in. to $\frac{1}{4}$ in. (12.7 to 6.4 mm).

Figures 7.48 and 7.49 show that out-of-plane distortion can be reduced significantly by increasing the plate thickness, from $\frac{3}{8}$ in. (10 mm) to $\frac{1}{2}$ in., (12.7 mm) for example. But this significantly increases the weight of the structure. One way to solve the problem is to reduce the length of the span, from 800 mm (32 in.) to 500 mm (20 in.), for example. Figures 7.48 and 7.49 show that in fabricating structures, with plates $\frac{3}{8}$ in. (10 mm) thick, for example, weld distortion can be reduced and the amount of allowable distortion increased by reducing the span from 32 in. (813 mm) to 20 in. (508 mm).

The results verify that distortion analysis is extremely important in structural design.

An optimum design must take into account structural integrity, welding fabrication, structural weight as well as fabrication cost.

7.8 How Various Parameters Affect the Angular Distortion of Fillet Weld; Methods of Reducing Distortion

Section 7.7 discussed the angular changes that occur in fillet welds and how they cause out-of-plane distortion in panel structures that have been fabricated using ordinary welding procedures. This section discusses how various welding parameters affect those angular changes, and how the changes may be reduced. Two subjects are emphasized:

1. How welding conditions and other parameters affect the angular changes that occur in fillet welds.
2. How to use elastic prespringing to reduce angular changes.

7.8.1 How welding conditions and other parameters affect angular changes in fillet welds

Watanabe and Satoh⁽⁷⁰⁹⁾ studied how welding conditions and other parameters affect values of angular change in fillet welds. They proposed the following formula (see eqn. (4) of Table 7.2):[†]

$$\phi_0 = C_1(I/(h\sqrt{vh}))^{m+1} \exp\{-C_2(I/(h\sqrt{vh}))\} \quad (7.29)$$

where I = welding current, amperes,
 v = welding speed, cm/sec,
 h = plate thickness, cm.

C_1 , C_2 , and m are coefficients determined by the type of electrodes used. The values of C_1 , C_2 , and m for an ilmenite electrode are:

$$C_1 = 0.0885 \times 10^{-6}, \quad C_2 = 6.0 \times 10^{-3}, \quad m = 1.5.$$

Figure 7.50 shows the experimental data illustrating the relationship between the parameter x determined by I , v , and h and the value of angular change.

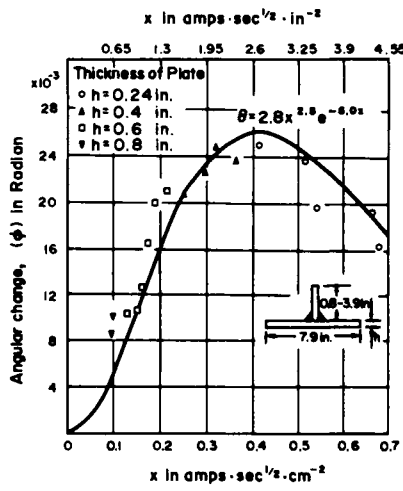
Effect of preheating. Watanabe and Satoh⁽⁷³²⁾ studied how preheating affects the angular distortion of fillet welds in low-carbon steel.⁽⁵⁰⁶⁾ The results are given in Fig. 7.51. Preheating reduced the angular distortion. Preheating the back of the plate proved more effective in reducing angular distortion than preheating the front.

7.8.2 Reduction of angular distortion by elastic prestraining

The angular distortion of a fillet weld can be reduced if an initial angular distortion is provided in the negative direction. There are basically two ways of doing this (see Fig. 7.52).

1. Plastic prebending (see Fig. 7.52(a)).
2. Elastic prestraining (see Fig. 7.52(b)).

[†] To express the angular change, ϕ_0 is used to maintain a notation consistent with that used in the preceding pages. Watanabe-Satoh used δ (as shown in eqn. (4) of Table 7.2).



Where $x = 10^{-3} \frac{I}{h\sqrt{v}}$
 I = Current, amp
 h = Thickness
 v = Welding speed
 e = Base of the common logarithm.

FIG. 7.50. Effect of welding conditions on the angular change of free tee-fillet welded joints. Electrodes used are of ilmenite type 4 mm in diameter.

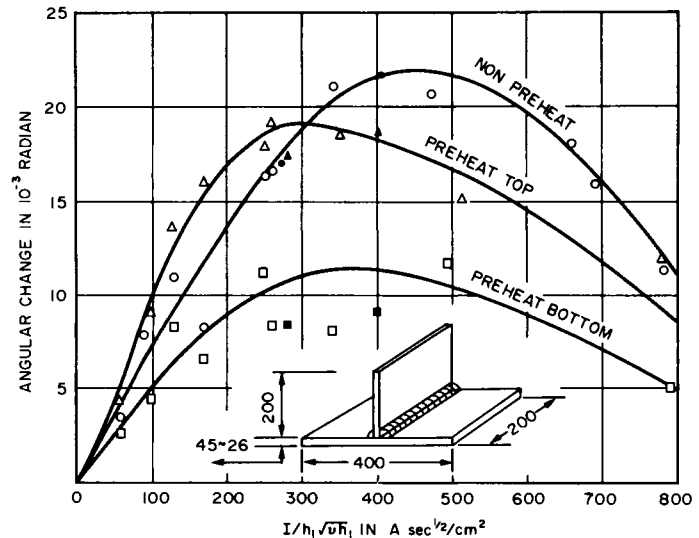


FIG. 7.51. Reduction of angular distortion of fillet welds by preheating (Watanabe-Sato^(506, 732)).

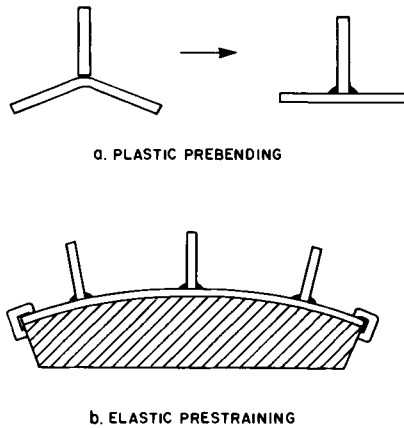


FIG. 7.52. Plastic prebending and elastic prestraining.

If an exact amount of plastic prebending could be used, a fillet weld with no angular distortion whatsoever would be the result.

In elastic pre-straining, a restraining jig is used. Often this is simply a bar of a certain size placed under the weld and the plate clamped in a jig. If the proper amount of prestraining is used, the fillet weld will have no angular distortion.

There are advantages and disadvantages with both methods. It is generally believed that in practice elastic prestraining is more reliable than plastic prebending. Since the weldment is clamped, the angular distortion is always much less than it would be if it were free. Even if an error is made in the amount of prestraining used, the angular distortion is always reduced. If plastic prebending is used, the amount of prebending used must be exact if a joint without distortion is to be produced. The amount of adequate prebending changes with the plate thickness, the welding conditions, and other parameters, and the bending-line must exactly match the weld line.

The following pages examine the use of elastic prestraining in the reduction of angular distortion in fillet welds and give some experimental results on the subject.

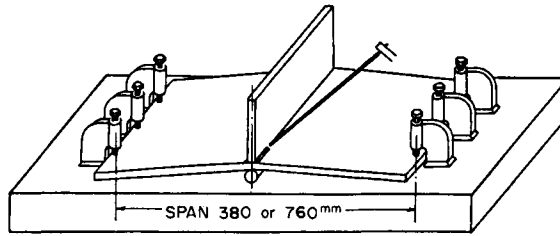
Data on steel weldments. Kumose *et al.*⁽⁷³³⁾ studied how effectively elastic prestraining could reduce the angular distortion of fillet welds in low-carbon steel. Figure 7.53(a) shows the experimental set-up. A round bar was placed under the bottom of a plate. The plate was then clamped to the bed. Figure 7.53(b) summarizes the results, including the relationship between the bottom plate thickness and the skin stress required to produce a zero angular distortion.

Skin stress, σ , is calculated as follows:

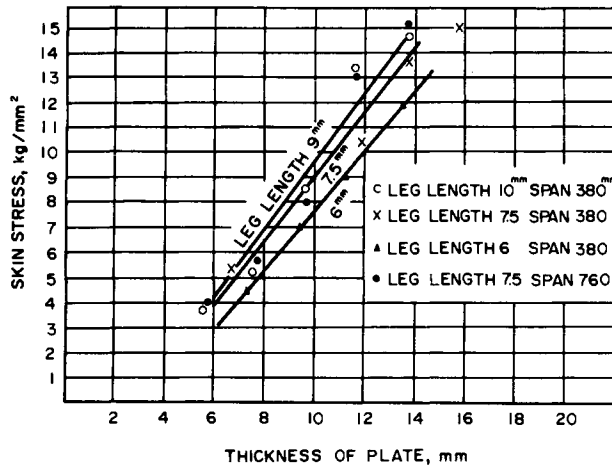
$$\sigma = [(6Dt)/L^2]E', \tag{7.30}$$

$$E' = E/(1 - \nu^2)$$

where D = diameter of the bar placed under the bottom of the plate,
 t = plate thickness,
 L = length of free span,
 E = Young's modulus,
 ν = Poisson's ratio.



A. Experimental set-up used



B. Relationship between plate thickness and skin stress required for obtaining zero angular change

FIG. 7.53. Effectiveness of elastic prestraining for reducing angular distortion of fillet welds (Kumose *et al.*).

E' instead of E is used to compute σ because the stress condition is in a plane-strain condition. When the weld length is short, E instead of E' should be used.

Data on aluminum weldments. Henry⁽⁷³⁴⁾ studied how effectively elastic prestraining could reduce the angular distortion of weldments in 5456 aluminum alloy. Using a uniform plate span and length, and relying on the GMA welding process, he investigated how angular distortion is affected by the degree of prestraining, the plate thickness, and the number of passes.

Figure 7.54 shows schematically the prestraining method used in the experiments. Note that the clamps only hold the bottom plate tips to the table and do not force them to be tangent. The round bar is placed under the plate along the longitudinal centerline (weld line) to induce a reverse curvature that will counteract the out-of-plane distortion caused by the welding.

All test specimens were 24 × 24 in. (610 × 610 mm). Thickness of .25 in., .375 in., and .50 in. (6.4, 10, and 12.7 mm) were used because they appear to be the most susceptible to welding distortion. The degree of prestraining (i.e. liner height) was calculated using a surface strain model and relied on the experimental strain-measurement data obtained from 5052-H32 aluminum alloy plates of the same thickness but of a different size

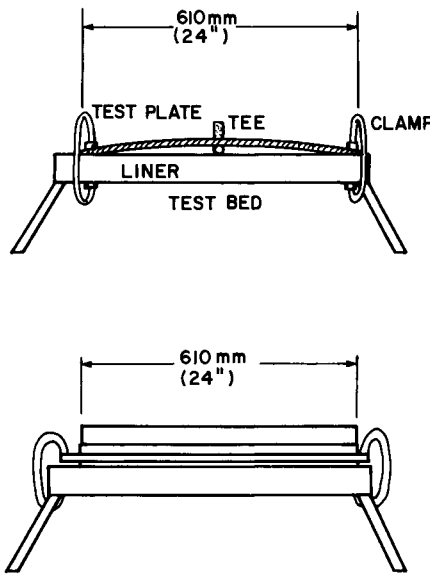
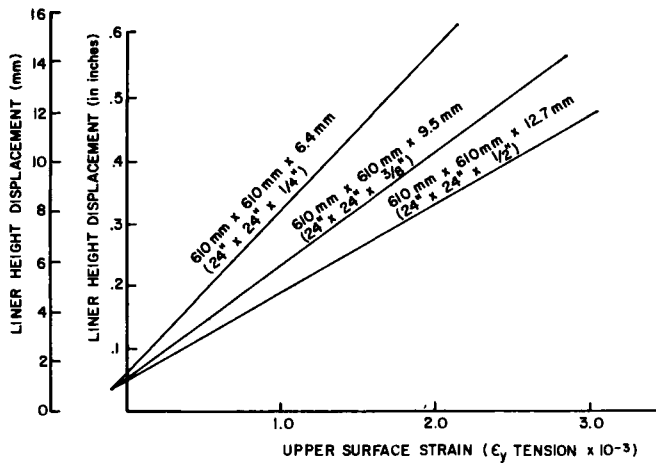


FIG. 7.54. Schematic pictorial of test setup.



7.55. Centerline Max. Strain (ϵ_y) Versus Liner Size For Several Plate Thicknesses From a Linear Extension Done From Data With 5052-H32 Al. Alloy

FIG. 7.55. Centerline max. strain (ϵ_y) versus liner size for several plate thicknesses from a linear extension done from data with 5052-H32 Al. alloy.

(18 in. span, 12 in. length). By assuming a linear approximation of liner height versus plate length, Fig. 7.55 was developed. This was done in the hope that these numbers would give a liner diameter for the minimum angular distortion.

Figure 7.56 plots the liner height versus the plate thickness for a tee height of 3 in. (76 mm). Based on the experimental results obtained, and on data on out-of-plane distortion generated by Taniguchi^(7.25) (see Section 7.7.1), Henry calculated the liner height that would give the least angular distortion.

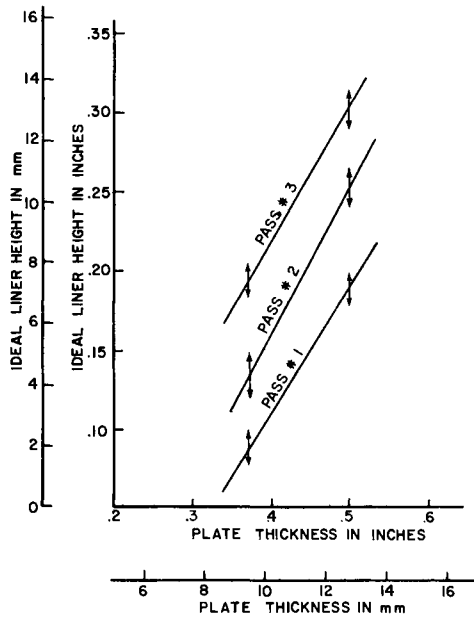
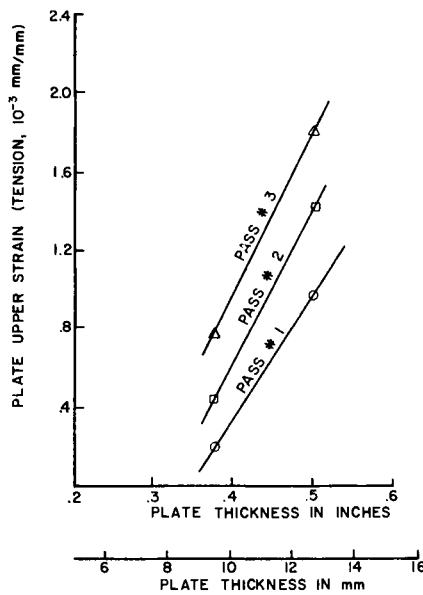


FIG. 7.56. Curves of ideal liner height versus plate thickness for a tee height of 76 mm (3 in.), 5456 Al. alloy plate size 610 × 610 mm (24 × 24 in.).



Max. Upper Strain (Tension) Versus Plate Thickness for 75 mm 3" Tees With 1, 2 and 3 Passes

FIG. 7.57. Max. upper strain (tension) versus plate thickness for 75 mm (3 in.) tees with 1, 2 and 3 passes.

By combining data given in Fig. 7.55 and 7.56, Fig. 7.57 was developed. Figure 7.57 shows the minimum-distortion values of plate upper surface strains. To use this curve, enter the plate thickness and the required number of passes (given in the material specifications) and find the required surface strain along the weld line. For example, suppose a job order involving a plate of 5456 aluminum alloy 10 ft long and $\frac{1}{2}$ in. (12.7 mm) thick with 3-in. (76 mm) tees at every foot specifies that the plate is to be GMA welded with three passes per fillet. Enter $t = \frac{1}{2}$ in. (12.7 mm) and number of passes per fillet = 3 in. (76 mm) to Fig. 7.57 and the required surface strain is given as 1.82×10^{-3} in./in.

7.9 Longitudinal Shrinkage of Butt Welds

The longitudinal shrinkage in a butt weld is approximately 1/1000th the weld length, much less than the transverse shrinkage. Only limited studies have been made of longitudinal shrinkage in a butt weld. King⁽⁷³⁵⁾ proposed the following formula:

$$\Delta L = \frac{0.12 \times I \times L}{100,000 \times t} \quad (7.31)$$

where I = welding current, amps,
 L = length of weld, in.,
 t = plate thickness, in.

For example, when $t = \frac{1}{4}$ in. (6.4 mm) and $I = 250$ amperes,

$$\Delta L/L = 1.2 \times 10^{-3}.$$

Figure 7.10 shows the allowances for the longitudinal shrinkage of butt welds provided in U.S. Navy specifications.

7.10 Longitudinal Shrinkage of Fillet Welds

Guyot⁽⁷¹⁶⁾ conducted an extensive study on the longitudinal shrinkage of fillet welds in carbon steel. He found that longitudinal shrinkage is primarily a function of the total cross-section of the joints involved. Restraint is more effective when the plates are thicker and wider. He therefore called the total cross-section of the welded plates in the transverse section the "resisting cross-section".

Figure 7.58 shows the results obtained by Guyot. In order to maintain symmetry in the transverse section and thereby keep longitudinal deflection to a minimum, he used cross-shaped assemblies as shown in the figure. Shrinkage values are expressed as a function of the resisting cross-sectional area, A_p , and the cross-sectional area of the weld metal, A_w . When the ratio A_p to A_w is less than 20, the following formula may be used:

$$\delta = \frac{A_w}{A_p} \times 25 \quad (7.32)$$

where δ = longitudinal shrinkage (mm) per 1 m of weld.

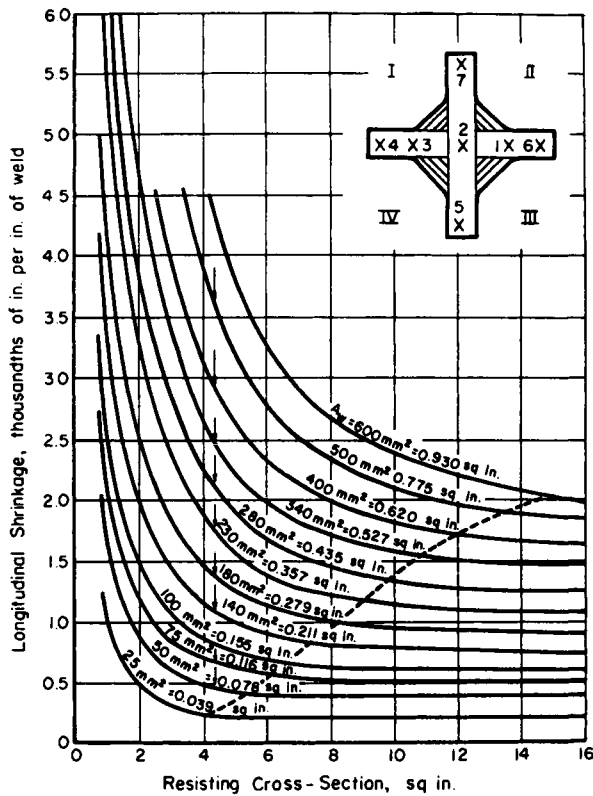


FIG. 7.58. Variation of longitudinal shrinkage as a function of the resisting cross-section area, A_p , and transverse cross-section area, A_w (Guyot).⁽⁷¹⁶⁾

Note: Experiments were made on cross-shaped assemblies as shown in the upper-right portion of the figure.

7.11 Longitudinal Bending Distortion

When the weld line does not coincide with the neutral axis of a weld structure, the longitudinal shrinkage of the weld metal induces bending moments, resulting in longitudinal distortion of the structure. This type of distortion is of special importance when fabricating T-bars and I-beams.

In the 1950s Sasayama *et al.*⁽⁷³⁶⁾ obtained experimental results on longitudinal bending distortion in steel weldments. A simple analysis similar to the beam theory was developed to analyze experimental data.

Recently a study was done at M.I.T. on the longitudinal bending distortion of aluminum weldments. A computer simulation of transient metal movement and distortion has also been attempted. On the basis of these recent developments it is now possible to use computer simulations to solve various practical problems related to bending distortion as induced by longitudinal shrinkage.

7.11.1 Investigation of steel weldments by Sasayama *et al.*

Sasayama *et al.*⁽⁷³⁶⁾ investigated longitudinal distortion of steel as caused in the fillet

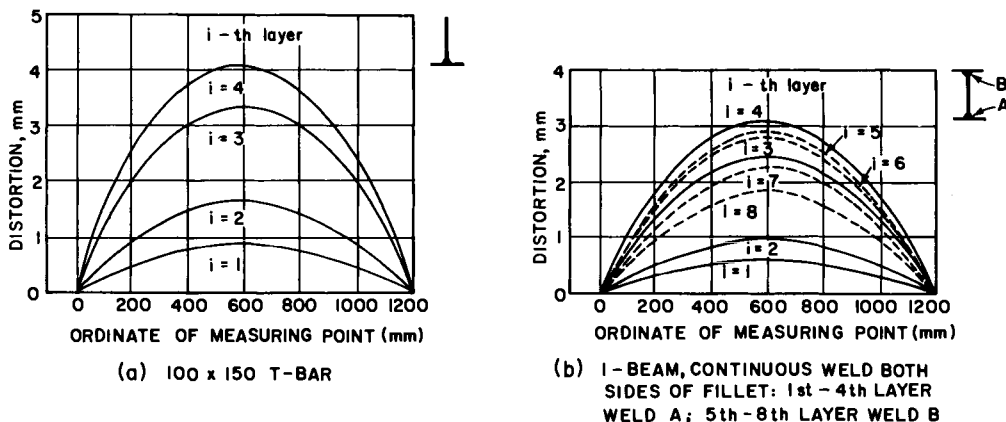


FIG. 7.59. Longitudinal deflection of steel due to fillet welding.

welding of various T-bars and I-beams in low-carbon steel (see Fig. 7.59 for experimental results). In a T-bar, the deformation gradually increases as the welding progresses (Fig. 7.59(a)).

In an I-beam the phenomena are somewhat different (see Fig. 7.59(b)); the deformation increases with the welding of the underside fillet, and decreases with the welding of the upper side. The deformation due to the welding of this second fillet is generally smaller than that of the first, causing some residual deformation to remain, even when the weight of the deposit metal of both fillet welds is equal and the geometry of the joint is symmetric. This occurs because the effective resisting area of the joint differs between the two; the upper flange does not effectively constrain the deformation during the welding of the underside of the fillet, since the upper flange is only tack welded to the web plate, but both flanges effectively constrain the welding of the upper side fillet, since the lower flange has already been welded to the web.

In analyzing their experimental results, Sasayama *et al.* developed a theory similar to the bending-beam theory. In the case of the bending distortion of a long, slender beam, longitudinal residual stress (σ_x) and the curvature of longitudinal distortion

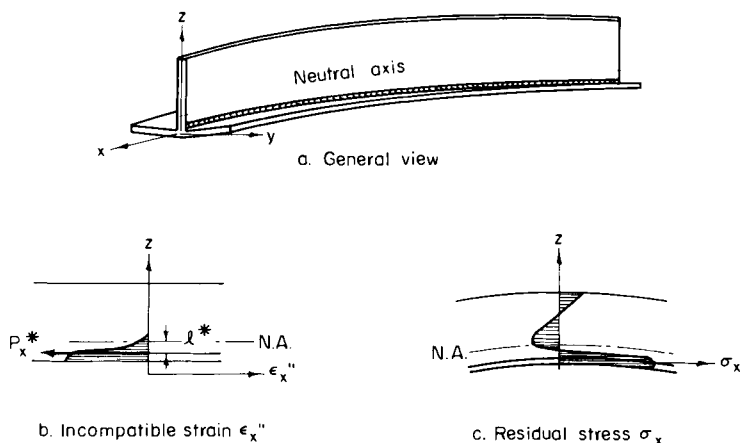


FIG. 7.60. Analysis of longitudinal distortion in a fillet-welded joint (Sasayama *et al.*⁽⁷³⁶⁾).

(1/R) are given by the following equation (see Fig. 7.60):

$$\left. \begin{aligned} \sigma_x &= -E\varepsilon_x'' + \frac{M_y^*}{I_y} z + \frac{P_x^*}{A} \\ 1/R &= M_y^*/EI_y = P_x^* l^*/EI_y \end{aligned} \right\} \quad (7.33)$$

where ε_x'' = incompatible strain,
 A = sectional area of the joint,
 I_y = moment of inertia of the joint around the neutral axis,
 P_x^* = apparent shrinkage force, $P_x^* = \iint E\varepsilon_x'' dydz$,
 M_y^* = apparent shrinkage moment, $M_y^* = \iint E\varepsilon_x'' z dydz = P_x^* l^*$,
 l^* = distance between the neutral axis and the acting axis of apparent shrinkage force.

Equation (7.33) shows that it is necessary to know the distribution of incompatible strain (ε_x'') in order to know the distribution of residual stress (σ_x) but the information about moment (M_y^*) is sufficient only for determining the amount of distortion (1/R). Moment (M_y^*) can be determined when the magnitude of the apparent shrinkage force (P_x^*) and the location of its acting axis are known. Through experiments, it was found that the acting axis of P_x^* is located somewhere in the weld metal. It is believed that the apparent shrinkage force (P_x^*) causes residual stress and distortion. More information can be obtained when the P_x^* value rather than the distortion value itself is used in the analysis of experimental results. For example, it makes it possible to separate the various factors that affect the magnitude of distortion into those caused by changes in geometry (A , I_y , or l^*) and those caused by changes in the value of P_x^* itself.

The increase of longitudinal distortion (apparent shrinkage force P_x^*) during multipass

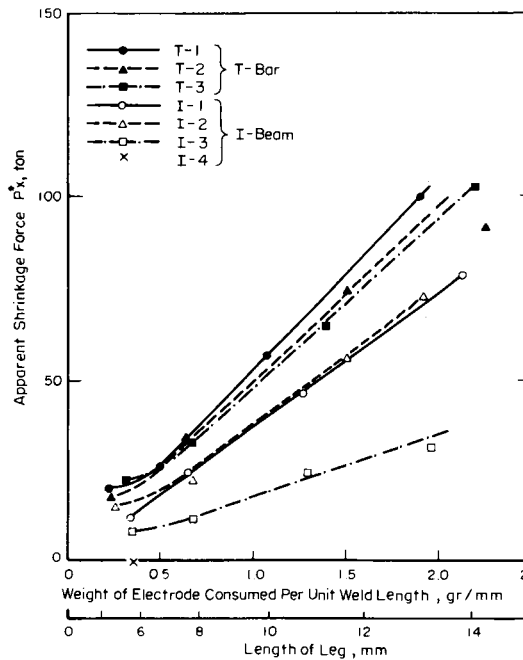


FIG. 7.61. Increase of longitudinal distortion during multipass welding (Sasayama *et al.*⁽⁷³⁶⁾).

welding is as shown in Fig. 7.61. All of the plate specimens were in mild steel 1200 mm (4 ft) long and 12 to 13 mm ($\frac{1}{2}$ in.) thick. The P_x^* values increased proportionally with the weight of the electrode consumed per weld length, except for the first layer. The large amount of distortion obtained in the first layer was due to the lack of resisting-area during that stage of welding; the flange plate was not yet attached firmly to the web plate.

Practically no distortion was produced during the intermittent welding (Specimen I-4). This was probably due to the fact that longitudinal residual stress does not reach a high value in a short intermittent weld.[†]

7.11.2 Investigations of aluminum weldments at M.I.T.

During the last few years, a series of experimental and analytical investigations have been conducted at M.I.T.[†] Yamamoto's⁽⁵³³⁾ series of experiments tried to analyze the longitudinal distortion mechanism in a built-up beam, to provide experimental data for the development of a computer program on longitudinal distortion, and to investigate a method of reducing longitudinal distortion. Experiments were performed in the following phases:

1. Simple rectangular plates were welded or heated along one edge by automatic GMA or GTA (no filler wire) welding processes. Some of the results are presented in Chapter 6.
2. T-section beams with the same web depth as the plates of the previous phase were welded by automatic GMA welding process under the same supporting condition used in the above phase.
3. A clamped T-section beam was welded by the automatic GMA welding process.

Strain-hardened and non-heat treatable aluminum–magnesium structural alloy 5052-H32 was used in the experiments. Filler wires 4043 and 2319 were used, the selection being based on ease of welding and material at hand.

Specimens $\frac{1}{2}$ in. (12.7 mm) thick and 4 ft (1220 mm) long were used so that one-dimensional characteristics could be measured. Welding conditions were changed during the various passes so that a good penetration and a minimum weld length for adequate joint strength could be obtained.

Figure 7.62 shows a typical test specimen and provides dimensions as well as strain gage and thermocouple locations. Yamamoto's Fig. 7.63 compares the longitudinal distortion values in steel and aluminum welds. Yamamoto obtained the results on aluminum welds and Sasayama *et al.* obtained those on steel welds. It is interesting to note that aluminum weld distortion is less than steel weld distortion. Because the thermal conductivity of aluminum is much higher than that of steel, the temperature gradient in an aluminum weld is considerably less than that in a steel weld.

Study of transient metal movement. As a part of the investigation Yamamoto studied the transient metal movement that occurs when the longitudinal edge of a rectangular plate is welded. The experimental data consisting of temperature changes, strain changes

[†] Further discussions are given in Chapter 16.

[†] Ujiie *et al.*⁽⁷³⁷⁾ of Mitsubishi Heavy Industries investigated distortion in aluminum structures and proposed a twin-GWA double-fillet welding technique that would reduce longitudinal distortion. The method seems to be effective if T-bars thicker than 20 mm (0.787 in.) are used.

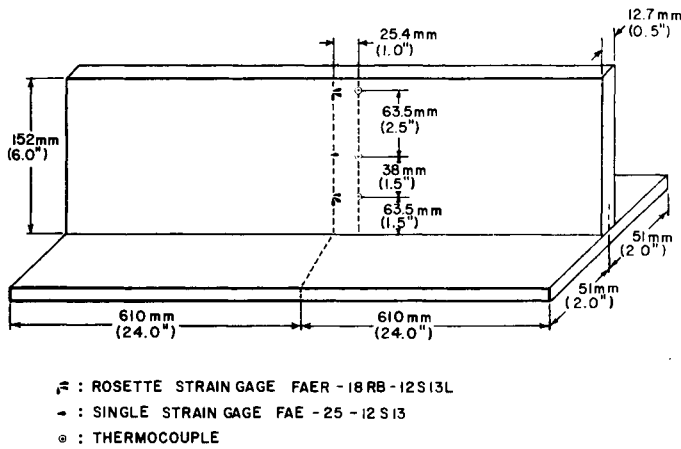


FIG. 7.62. Arrangement of the strain gage and thermocouple for T-section beam.

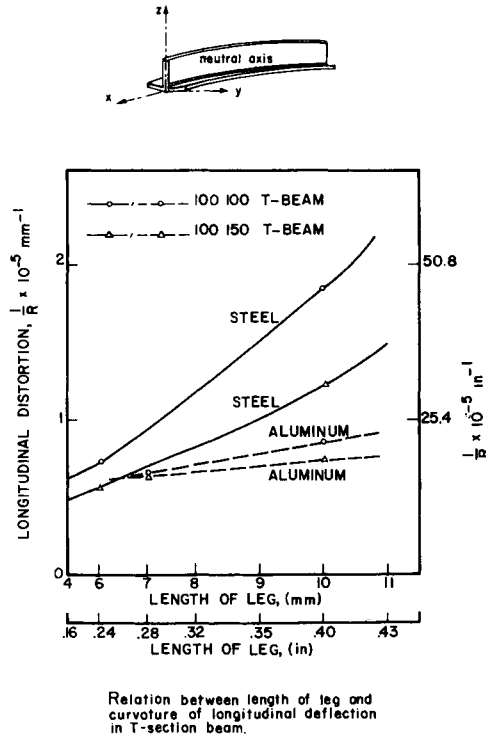


FIG. 7.63. Relation between length of leg and curvature of longitudinal deflection in T-section beam.

and deflection changes were compared with analytical predictions. The results are discussed in Chapter 5 (see Figs. 5.21 through 5.26).

Nishida's computer analysis. Nishida⁽⁵²⁷⁾ has developed a computer program capable of analyzing the transient distortion that occurs in built-up beams (see Section 5.5.3).

7.12 Buckling Distortion

When thin plates are welded, residual compressive stresses occur in areas away from the weld and cause buckling (see Fig. 7.64). Buckling distortion occurs when the specimen length exceeds the critical length for a given thickness in a given size specimen. In studying weld distortion in thin-plated structures, it is important to first determine whether the distortion is being produced by buckling or by bending. Buckling distortion differs from bending distortion in that:

1. There is more than one stable deformed shape.
2. The amount of deformation in buckling distortion is much greater.

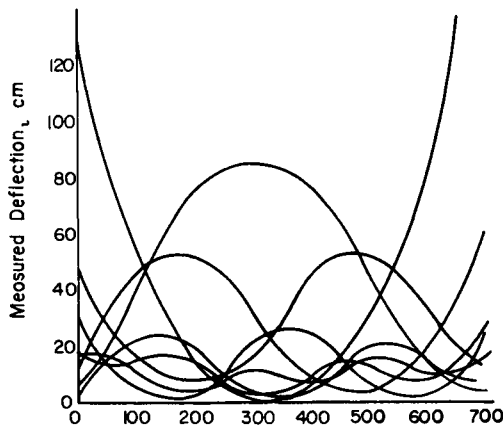
Since the amount of buckling distortion is large, the best way to avoid it is to properly select such structural parameters as plate thickness, stiffener spacing, and welding parameters.

7.12.1 Investigations by Masubuchi and others

The buckling distortion of welded plates caused by residual stresses has been studied by Masubuchi,⁽⁷³⁸⁾ Mura,⁽⁷³⁹⁾ and Watanabe and Satoh.⁽⁷⁴⁰⁾ Masubuchi⁽⁷³⁸⁾ investigated the buckling distortion that occurred in long steel strips ($2.3 \times B \times 7.200$ mm ($B = 100 \sim 400$ mm)) after weld beads had been laid along the center line of the strip using the submerged-arc process. Figure 7.64(b) shows eight different stable deformation patterns found along the weld center line in one specimen.



a. Buckling Distortion



b. Eight Stable Distortion Observed in One Specimen

FIG. 7.64. Buckling distortion of a bead-welded plate. Distortions along the weld line are shown.

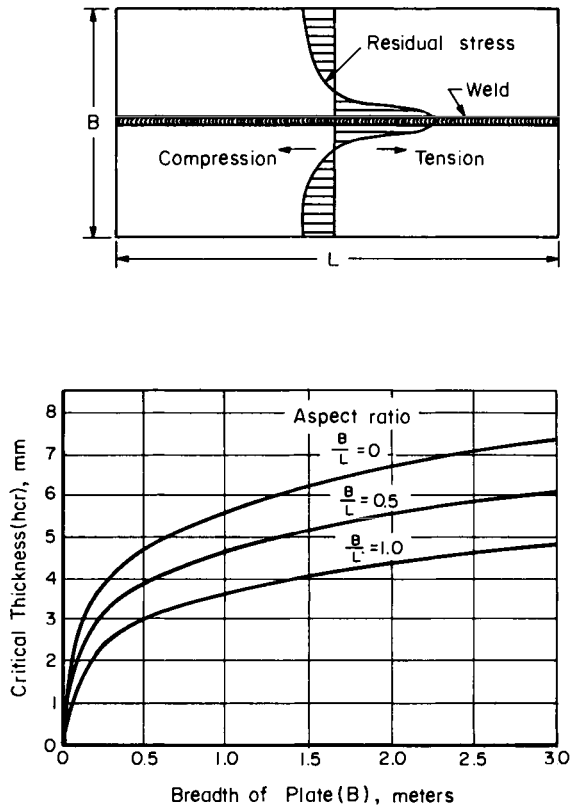


FIG. 7.65. Critical thickness for buckling distortion of a butt weld.⁽⁷⁴⁰⁾

Figure 7.65 shows the results obtained by Watanabe and Satoh.⁽⁷⁴⁰⁾ Shown are the calculated values of the critical thickness for various sizes of butt-welded plates. For example, when two panels 1 m (40 in) wide and 2 m (80 in) long are butt welded ($B = 2$ m, $B/L = 1$), the plate is going to buckle after welding if the thickness is less than 4.5 mm (0.18 in.). In a study of electron-beam welding conducted at Battelle, buckling distortion occurred in thin sheets of beryllium, aluminum, and stainless steel when they were electron beam welded.⁽⁷⁴¹⁾ The analysis developed by Watanabe and Satoh was used successfully in determining the critical thicknesses of these metals.

7.12.2 Recent investigation at Kawasaki

Engineers at Kawasaki Heavy Industries have conducted an extensive experimental and analytical investigation of out-of-plane distortion during the welding fabrication of thin panel structures.^(742, 743)

Experimental study. Figure 7.66 shows how distortion at the center of the panel increases during and after welding. As the welding heat input increases, the structure starts to deform sooner and the final distortion increases.

Figures 7.67 through 7.72 summarize the experimental results. Experiments were conducted under the following test conditions:

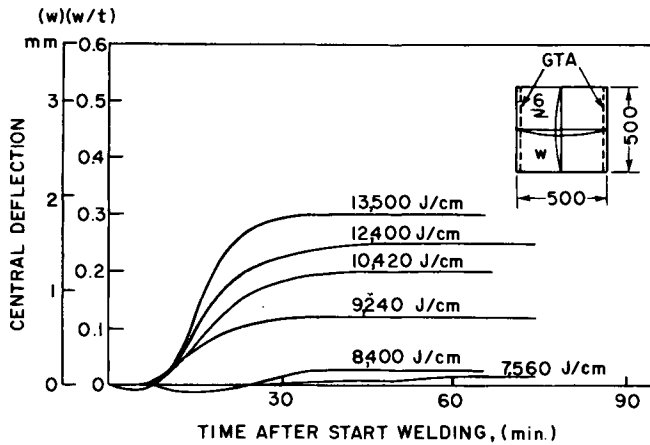


FIG. 7.66. Formation of out-of-plane distortion during welding fabrication of stiffened panel structures (Terai et al.).⁽⁷⁴³⁾ Welding was done between a low-carbon steel plate 6 mm ($\frac{1}{4}$ in.) thick and frames.

Material: low-carbon steel.

Plate thickness (t): 4.5 mm (0.18 in.) to 10 mm (0.4 in.).

Panel dimension (b): 500 mm (20 in.) and 1000 mm (40 in.).

Heat input: 7560 joules/cm (19,200 joules/in) and 13,500 joules/cm (34,300 joules/in.).

Welding process: gas tungsten arc and shielded metal arc.

Figure 7.67 shows the relationship between deflection, w/t , and heat input per unit thickness, Q/t (joules/cm²), for panels of 500 mm by 500 mm. The heat input–deflection relationship is similar to the load–deflection relationship in a buckling experiment. When the plate was 10 mm (0.4 in.) thick, buckling distortion was not consistently

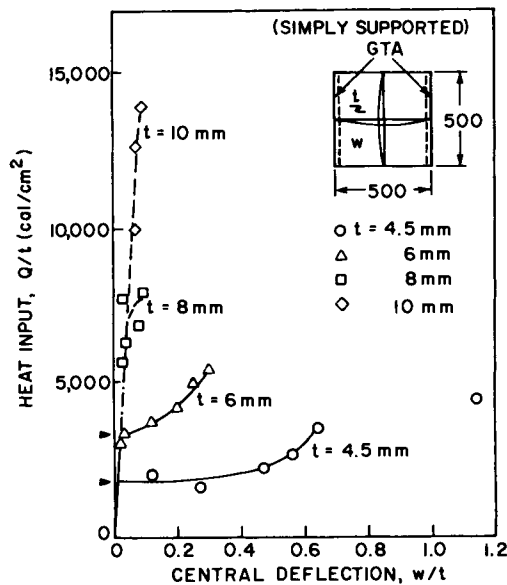


FIG. 7.67. Relationship between deflection and heat input for panels 500 × 500 mm.

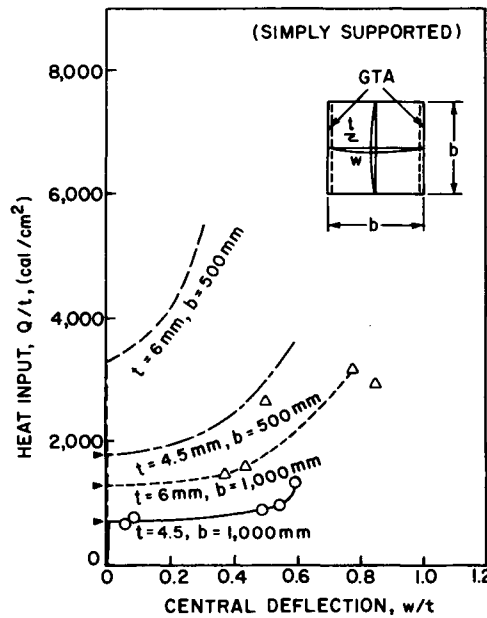


FIG. 7.68. Relationship between deflection and heat input for panels 500 × 500 mm and 1000 × 1000 mm.

present until the heat-input had reached 13,500 joules/cm². When the plate was 8 mm (0.3 in.) thick, the buckling appeared at a heat-input of approximately 8000 joules/cm². When the plate was 6 mm (0.24 in.) thick, the buckling appeared when the heat input had reached approximately 3500 joules/cm². And when the plate was 4.5 mm (0.18 in.) thick the critical buckling heat input was less than 2000 joules/cm². It is interesting to note that the experimental results clearly indicate the existence of a critical buckling heat-input for a given test condition.

Figure 7.68 shows that the critical buckling heat-input decreases as plate thickness decreases and the free span increases.

Figures 7.69 and 7.70 show the relationships between w/t and Q/t^3 , cal/cm⁴. The results indicate that for a given panel size the critical values of Q/t^3 are not affected by plate thickness.

Figure 7.71 shows the relationship between w/t and Qb/t^3 . The results indicate that buckling occurs when the value of Qb/t^3 exceeds about 3.5×10^5 cal/cm³.

Figure 7.72 shows the results obtained on panels welded using the shielded metal arc process. Results shown in Figs. 7.67 and 7.72 indicate that the critical heat-input for buckling is little affected by the difference in welding processes.

Analytical study. The buckling distortion of a welded panel has also been the subject of an analytical study. The critical buckling stresses under various boundary conditions were the first values calculated. Tables 7.10 and 7.11 show the following results:

TABLE 7.10: Buckling of a simply supported rectangular plate under uniform compressive stresses in one direction.

TABLE 7.11: Buckling of a rectangular plate under uniform compressive stresses in one direction when all sides are elastically built in.

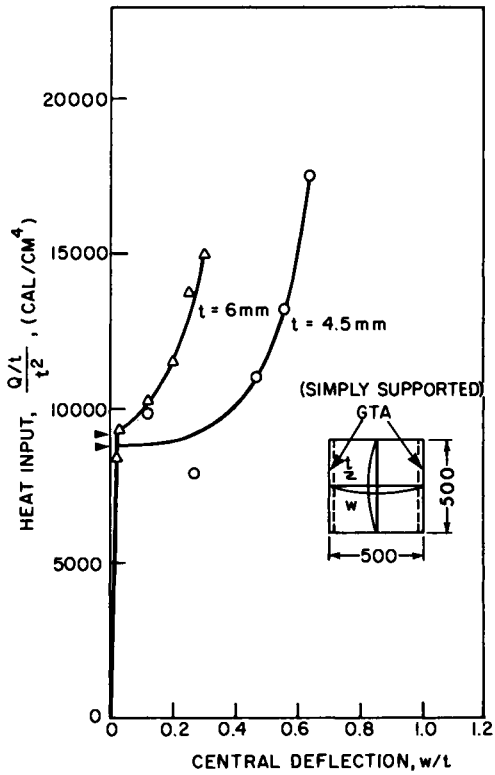


FIG. 7.69. Relationship between deflection and heat input expressed in Q/t^3 for panels 500×500 mm.

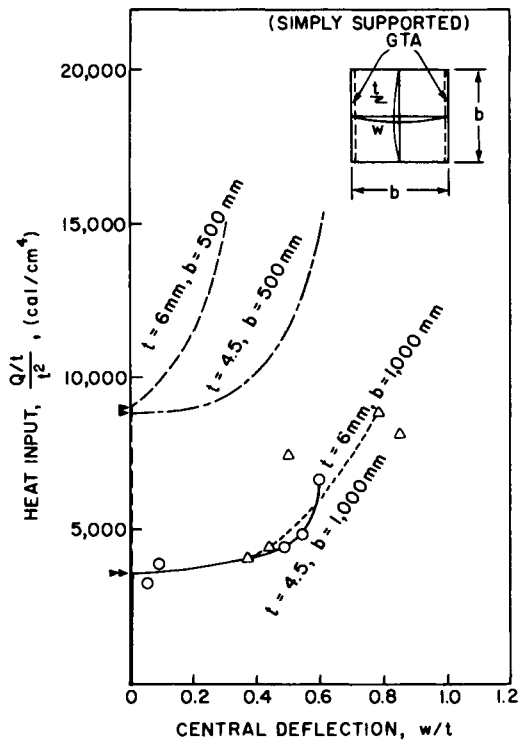


FIG. 7.70. Relationship between deflection and heat input expressed in Q/t^3 for panels 500×500 mm and 1000×1000 mm.

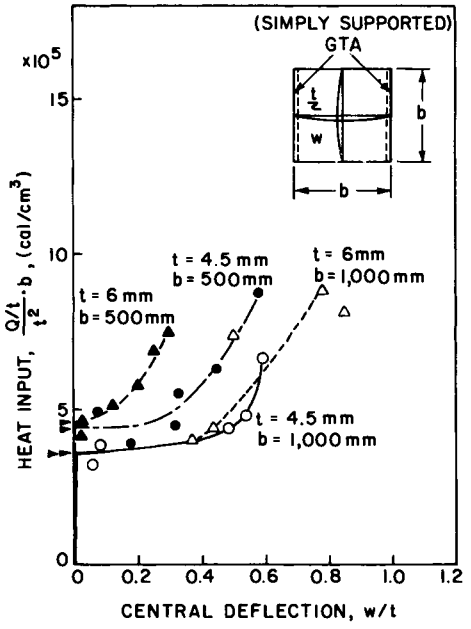


FIG. 7.71. Relationship between deflection and Qb/t^3 .

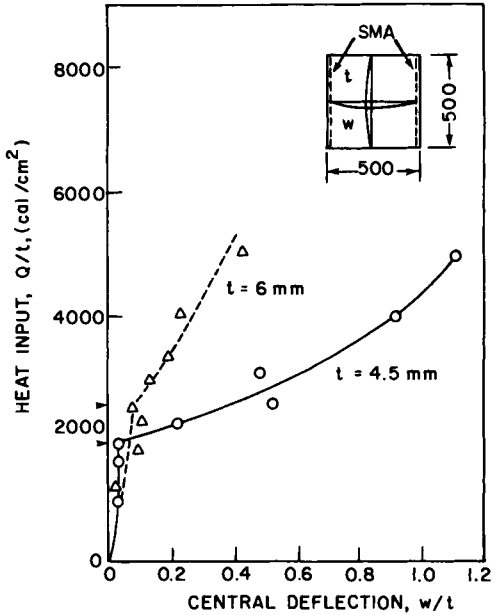


FIG. 7.72. Relationship between deflection and heat input for panels 500 × 500 mm welded by shielded metal arc processes.

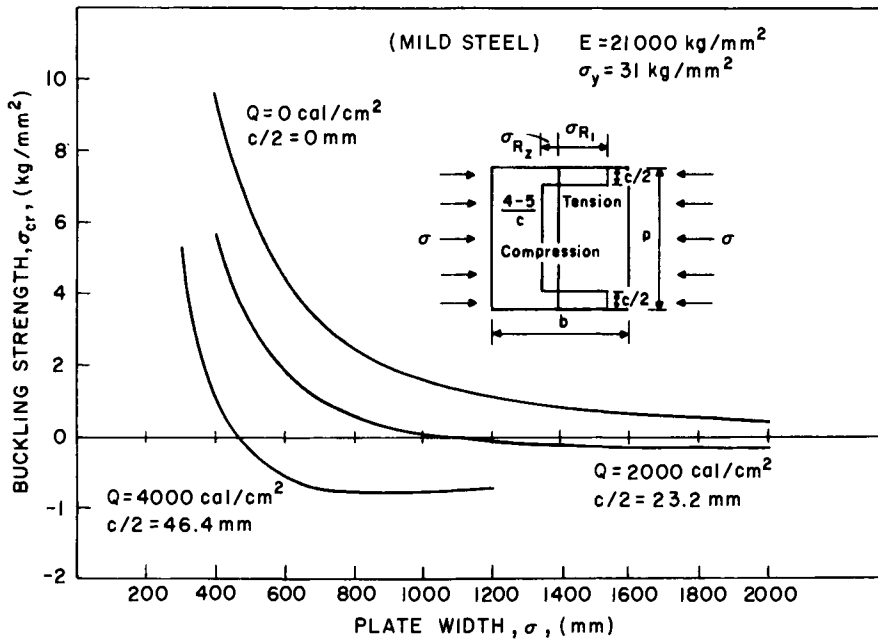


FIG. 7.73. Relationships between plate width and buckling strength (Terai et al.).⁽⁷⁴³⁾

TABLE 7.10. The buckling of a simply supported rectangular plate under a uniform compressive stress in one direction

1. Buckling of simply supported rectangular plate uniformly compressed in one direction
 If the wave of deflection surface is represented by the expression

$$w = am \sin(m\pi x/a) \sin(n\pi y/b).$$

Then

$$\sigma = [E\pi^2/12(1 - \nu^2)] [t/b]^2 [m(b/a) + (1/m)(a/b)]^2.$$

2. Buckling of simply supported rectangular plate with residual stress uniformly compressed in one direction
 If the wave of deflection surface is represented by the expression

$$w = a_{mn} \sin(m\pi x/a) \sin(n\pi y/b).$$

(i) When both sides $y = 0$ and $y = b$ are welded

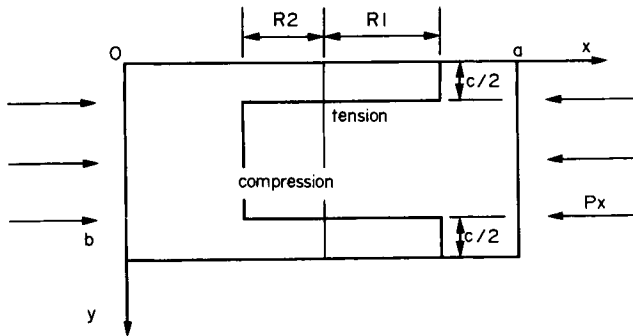


TABLE 7.10 (cont.)

Then the critical compressive stress will be

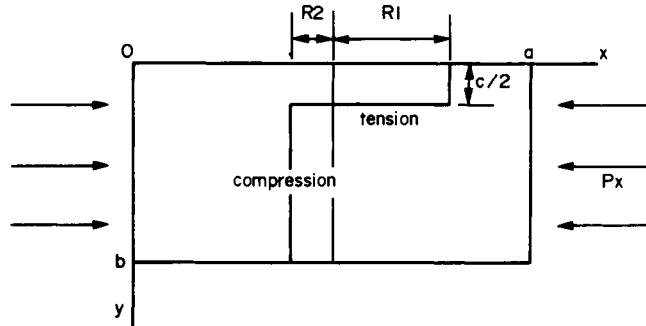
$$\sigma = [E\pi^2/12(1 - \nu^2)] [t/b]^2 [m(b/a) + (1/m)(a/b)]^2 - [(\sin(\pi(b - c)/b))/(\pi c/b)] \sigma_{R2}.$$

Here, $R2/t = \sigma_{R2}$.

$$\sigma = [E\pi^2/12(1 - \nu^2)] [t/b]^2 [m(b/a) + (1/m)(a/b)]^2 + [(\sin(\pi c/b))/(\pi(b - c)/b)] \sigma_{R1}.$$

Here, $R1/t = \sigma_{R1}$.

(ii) When one side $y = 0$ is welded



Then the critical compressive stress will be

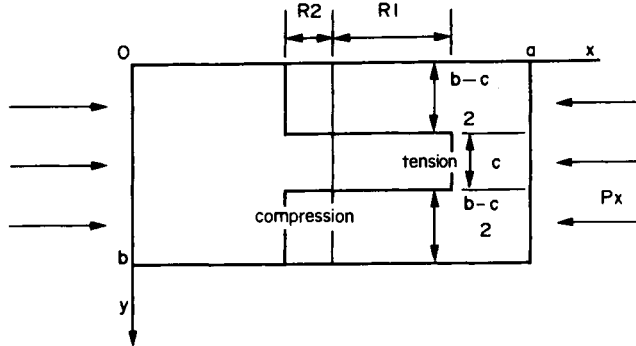
$$\sigma = [E\pi^2/12(1 - \nu^2)] [t/b]^2 [m(b/a) + (1/m)(a/b)]^2 - [(\sin(\pi c/b))/(\pi c/b)] \sigma_{R2}.$$

Here, $R2/t = \sigma_{R2}$.

$$\sigma = [E\pi^2/12(1 - \nu^2)] [t/b]^2 [m(b/a) + (1/m)(a/b)]^2 + [(\sin(\pi c/b))/(\pi(2b - c)/b)] \sigma_{R1}.$$

Here, $R1/t = \sigma_{R1}$.

(iii) When the center of the plate $y = 1/2b$ is welded



Then the critical compressive stress will be

$$\sigma = [E\pi^2/12(1 - \nu^2)] [t/b]^2 [m(b/a) + (1/m)(a/b)]^2 + [(\sin(\pi c/b))/(\pi c/b)] \sigma_{R2}.$$

... Here, $R2/t = \sigma_{R2}$.

$$\sigma = [E\pi^2/12(1 - \nu^2)] [t/b]^2 [m(b/a) + (1/m)(a/b)]^2 - [(\sin(\pi c/b))/(\pi(b - c)/b)] \sigma_{R1}.$$

Here, $R1/t = \sigma_{R1}$.

TABLE 7.11. Buckling of a rectangular plate due to uniform compressive stresses in one direction when all sides are elastically built in

1. Buckling of a rectangular plate uniformly compressive in one direction when all sides are elastically built in
If the wave of deflection surface is represented by the expression

$$w = a_{mn} [1 - \cos(2m\pi x/a)] [1 - \cos(2n\pi y/b)].$$

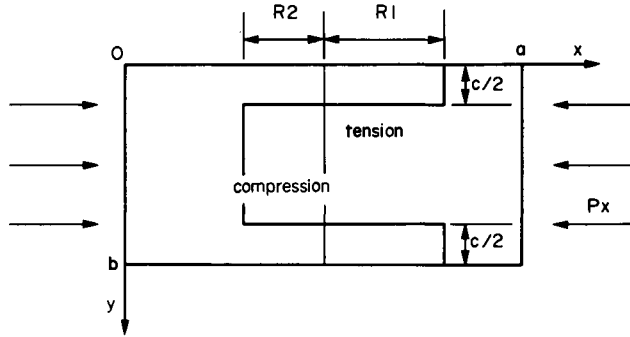
Then the critical compressive stress will be

$$\sigma = [E\pi^2/144(1 - \nu^2)] [t/b]^2 [48m^2(b/a)^2 + 48(1/m^2)(a/b)^2 + 32].$$

2. Buckling of rectangular plate with residual stress uniformly compressive in one direction when all sides are elastically built in

$$w = a_{mn} [1 - \cos(2m\pi x/a)] [1 - \cos(2n\pi y/b)].$$

- (i) When both sides $y = 0$ and $y = b$ are welded



Then the critical compressive stress will be

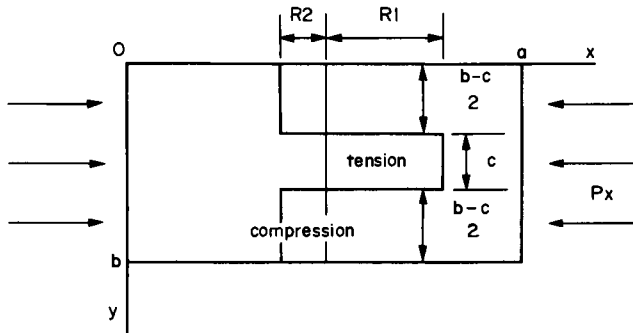
$$\sigma = [E\pi^2/144(1 - \nu^2)] [t/b]^2 [48m^2(b/a)^2 + 48(1/m^2)(a/b)^2 + 32] - [(4b/3\pi c) \sin(\pi c/b) - (b/6\pi c) \sin(2\pi c/b)] \sigma_{R2}.$$

Here, $R2/t = \sigma_{R2}$.

$$\sigma = [E\pi^2/144(1 - \nu^2)] [t/b]^2 [48m^2(b/a)^2 + 48(1/m^2)(a/b)^2 + 32] + [\{4b/3\pi(b - c)\} \sin(\pi c/b) - \{b/6\pi(b - c)\} \sin(2\pi c/b)] \sigma_{R1}.$$

Here, $R1/t = \sigma_{R1}$.

- (ii) When the center of the plate $y = 1/2b$ is welded



Then the critical compressive stress will be

$$\sigma = [E\pi^2/144(1 - \nu^2)] [t/b]^2 [48m^2(b/a)^2 + 48(1/m^2)(a/b)^2 + 32] + [(4b/3\pi c) \sin(\pi c/b) + (b/6\pi c) \sin(2\pi c/b)] \sigma_{R2}.$$

Here, $R2/t = \sigma_{R2}$.

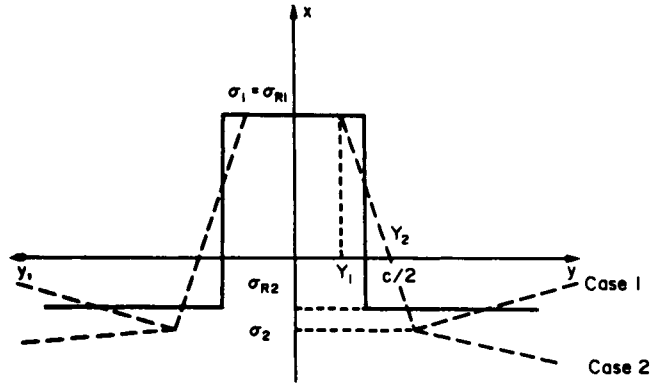
$$\sigma = [E\pi^2/144(1 - \nu^2)] [t/b]^2 [48m^2(b/a)^2 + 48(1/m^2)(a/b)^2 + 32] - [\{4b/3\pi(b - c)\} \sin(\pi c/b) - \{b/6\pi(b - c)\} \sin(2\pi c/b)] \sigma_{R1}.$$

Here, $R1/t = \sigma_{R1}$.

TABLE 7.12 Assumed residual stress distributions used for the analysis of buckling of a rectangular plate by residual stresses only

Residual stress distribution in the case of a bead-on-plate weld is represented by the following expression (Satoh *et al.*):

CASE 1	$b/2 = 10^{-2}Q/t$	$\sigma_1 = 1.0 \sim 1.1\sigma_y$ $Y_1 = 0.6 \times 10^{-3}Q/t$	$\sigma_2 = -0.25\sigma_y$ $Y_2 = 2.0 \times 10^{-3}Q/t$
CASE 2	$b/t = 0.33 \times 10^{-2}Q/t$	$\sigma_1 = 0.9 \sim 1.1\sigma_y$ $Y_1 = 0.18b/2$	$\sigma_2 = -0.1\sigma_y$ $Y_2 = 0.40b/2$



Modifying this welding residual stress distribution to rectangular distribution, the $c/2$ value is

CASE 1 $c/2 = 1.16 \times 10^{-3}Q/t$.

CASE 2 $c/2 = 0.14b$.

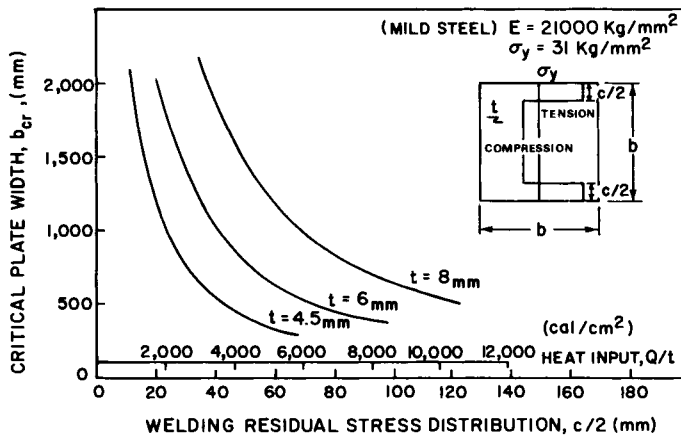


FIG. 7.74. How the width of residual stress tension zone C and the welding heat input (cal/cm²) affect the critical buckling stress.

Then the buckling stresses of a rectangular plate caused by residual stresses only were calculated. Table 7.12 shows the assumed residual stress distributions. Figures 7.73 through 7.76 show the results. Figure 7.73 shows the relationship between plate width and buckling strength. Figures 7.74 and 7.75 show how the width of the residual stress tension zone, C , and the welding heat input (cal/cm^2) affects the critical buckling stress. These figures are useful in determining whether a given panel structure buckles when it is welded under given conditions.

The buckling of a panel during welding may be avoided by the application of tensile stresses. Figure 7.76 shows the relationship between the width of the residual stress tension zone, C , and the prestretching stress necessary to prevent buckling distortion. This subject is presented in more detail in Section 7.13.4.

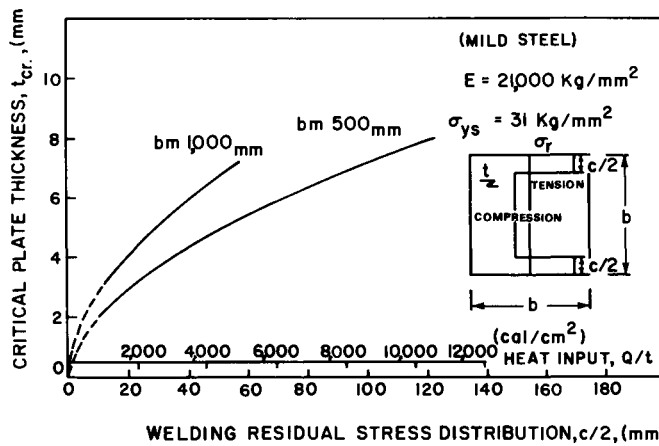


FIG. 7.75. How the width of residual stress tension zone C and the welding heat input (cal/cm^2) affect the critical buckling stress.

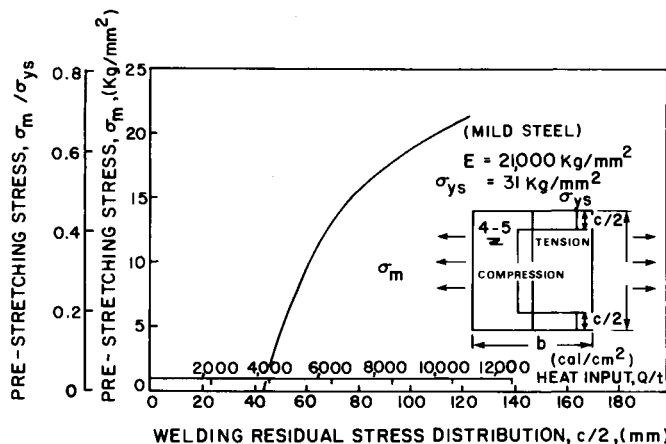


FIG. 7.76. How the width of residual stress tension zone C affects the amount of prestretching stress necessary to prevent buckling.

7.12.3 An investigation by Pattee

Pattee⁽⁷⁴⁴⁾ at M.I.T. conducted an analytical and experimental investigation of buckling distortion in aluminum welds.

Experiments were made to determine the buckling behaviour (during and after welding) of variously dimensioned aluminum plates with a number of different boundary conditions. Material used was the 5052-H32 aluminum alloy.

As stated earlier, the best way to cope with buckling distortion is to avoid it. Any plate has a critical buckling load. To avoid failure, the welding stresses must remain below this level. This can be achieved by welding less, using less heat, or removing the heat.

One way to weld less is to use intermittent welding; by halving the amount of welding, the critical load is approximately doubled. Another way is to decrease the weld-bead size, which results in smaller heat requirements during welding and hence in lower stress levels. A third way to reduce the stress levels is to remove the welding heat from the plate using chill bars, water-cooled backing plates, etc.

One can see from the above that, within normal operating ranges, lower heat-inputs significantly reduce the stress levels. Increasing the transverse moment of inertia in a structure will increase its resistance to buckling. This can be achieved by using a thicker

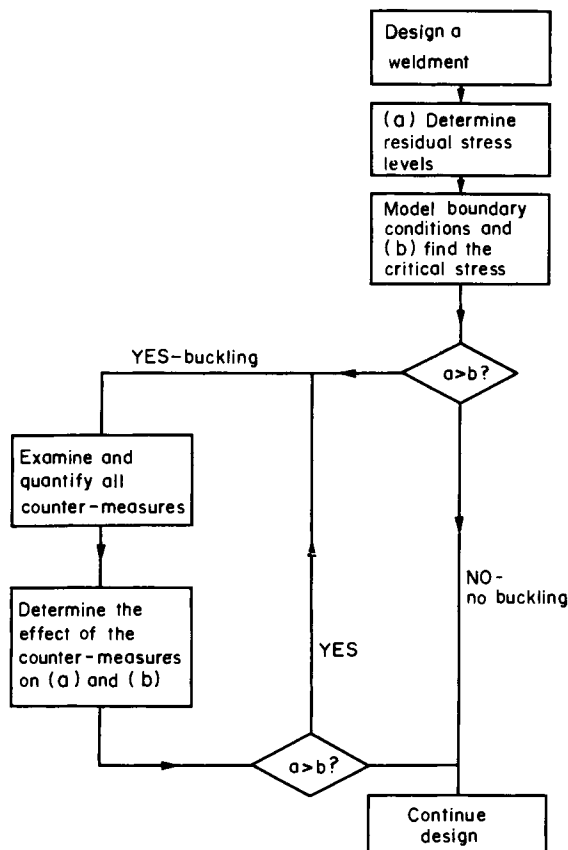


FIG. 7.77. Flow chart of the "system".

plate or by decreasing the stiffener plating. Neither are always reliable, since both require more welding and more material and increase the weight and the cost.

Based on these observations and on the analytical and experimental investigations he conducted, Pattee proposed a systematic approach to the buckling problem. A flow chart of the system is shown in Fig. 7.77. Its components include the following:

1. Derivations that described the buckling that occurs when thin plates are welded under commonly encountered boundary conditions.
2. Flexible computer programs that calculate either the critical loads or the critical dimensions.
3. A welding simulation program that predicts residual stress (such as M.I.T.'s 1-D or 2-D programs discussed above).
4. Calculations that determine the effect of any corrective measure. Examples produced using this system can be found in Reference (744).

7.13 Methods of Distortion-reduction in Weldments

Previous parts of this chapter have dealt with the mechanisms of various types of distortion as well as with the analytical prediction of distortions. This section presents several methods of reducing distortion in weldments, and includes the following subjects:

1. A review of commonly used distortion-reduction methods.
2. How external restraints affect residual stress and distortion.
3. Distortion-reduction through thermal-pattern control.
4. The reduction of out-of-plane distortion through stretching and heating.
5. The reduction of the longitudinal distortion of built-up beams through differential heating.

7.13.1 *A review of commonly used distortion-reduction methods*

In the following pages the common methods of reducing weld distortion are reviewed. References are made to information presented earlier if it has to do with reducing weld distortion.

Weldment dimension. The length, the width, and the thickness of a weldment all influence the amount of distortion.

The plate thickness greatly influences the angular distortion in a fillet weld (see Figs. 7.43, 7.44, 7.45, 7.47, 7.48, 7.49, and 7.50). Since the angular change of a fillet weld is caused by temperature differences between the top and bottom surfaces of the plate, at a certain plate thickness (about $\frac{3}{8}$ in. for steel and $\frac{1}{4}$ in. for aluminum—see Figs. 7.43 and 7.44 respectively) the angular change is maximum. When the thickness is greater than this, the angular change is less because of the rigidity of the plate. When the thickness is less than this, the angular change is less because the temperature differential between the top and bottom surfaces is less.

But this does not mean that when engineers fabricate thin-plated structures they will have fewer distortion problems. Buckling becomes more of a problem (see Section 7.12), and since buckling distortion, if present, is always serious, the best way to deal with it is to avoid it through the careful selection of structural parameters (plate thickness and

stiffener spacing, for example) and welding parameters. Figures 7.65 and 7.73 to 7.76 are useful in determining the critical buckling-distortion thickness in butt welds. Figure 7.77 is a flow chart of the computer-aided system for determining buckling probability in certain simple weldments.

When fabricating a T-bar or an I-beam, a process that involves a long, slender weldment, bending distortion caused by longitudinal weld shrinkage may become significant (see Section 7.11).

Joint design. Distortion is affected by joint design. As a general rule, distortion can be reduced by keeping the amount of weld metal used at a minimum. Figure 7.39 shows the groove shape that gives a zero angular distortion in butt welds.

Welding processes and welding conditions. Since residual stresses and distortion are the result of uneven heating during welding, it is generally true that the less total heat a process uses in joining, the less distortion will be produced. Weldments produced using narrow-gap welding, electron beam welding, and laser welding all exhibit less distortion than those produced using arc welding. A weld made using a low heat input generally exhibits less distortion than a weld made using a high heat input.

But we must also recognize that the influence of the temperature distribution and the heat input on various types of distortion is complex. For example, the transverse shrinkage of a butt weld is greatly affected by the temperature distribution in the base plates when the weld metal solidifies (see Fig. 7.18). The best way to reduce transverse shrinkage in butt welds, therefore, is to reduce the heat-spread before the weld metal solidifies.

The angular change of a fillet weld is greatly influenced by the temperature difference between the top and bottom surfaces. Figure 7.50 shows how welding conditions and other parameters affect angular change.

The longitudinal shrinkage of the weld zone induces bending distortion (see Section 7.11). Equation (7.33) shows that the bending distortion can be reduced (1) by placing the weld near the neutral axis of the weldment and (2) by reducing the amount of weld metal.

Multipass welding. A large percentage of the transverse shrinkage that takes place in butt welds occurs during the first and the second passes (see Fig. 7.26). Much work has been done on the question of how various procedure parameters affect transverse shrinkage (Table 7.7). One important finding has been that the use of larger diameter electrodes will result in less shrinkage (see Fig. 7.28).

Figures 7.37 through 7.39 suggest that a butt weld without angular distortion can be obtained through a proper selection of joint design and welding sequence.

Constraints. The use of external constraints to reduce distortion is a common practice in the fabrication of welded structures. Through the selection of appropriate strong-backs, jigs, clamps, and rollers, investigators have found that induced distortions can be reduced. Figure 7.7 shows how the transverse shrinkage of a butt weld decreases as the degree of constraint increases.

Equation (7.22) shows how the angular distortion of a fillet weld decreases as the degree of constraint increases. Figures 7.53 and 7.57 show how the angular change of fillet welds can be reduced through the use of elastic prestraining in steel and aluminum structures respectively.

Welding sequence. Investigators have found that welding sequence affects transverse distortion. Block-welding sequences were generally found to cause less shrinkage than multi-layer sequences (see Fig. 7.32).

Use of intermittent welding. Longitudinal bending distortion can be significantly reduced when intermittent fillet welds are used as shown in Fig. 7.61. But angular distortion is not significantly reduced when intermittent fillet welds are used, according to Hirai and Nakamura.⁽⁷²⁴⁾

Peening. When metal that has shrunk during welding is stretched by peening, some of the distortion is removed (see Table 7.7 and Chapter 14).

7.13.2 How external restraints affect residual stress and distortion

Engineers involved in welding fabrication want to know how to reduce distortion without increasing residual stresses. It is commonly believed that when a weld is made under restraint, distortion will decrease and residual stresses increase.

Recently M.I.T. researchers studied how an additional restraint would affect the residual stresses and distortion. Their idea was to weld a structural member under external restraint and then to release the restraint later, a process similar to elastic prespringing (see Fig. 7.52(b)). If a weld is made under restraint, the distortion will be reduced but the residual stresses will probably remain high; if the restraint is then released, some of the residual stresses will be reduced. Although releasing the restraint may increase the distortion, this distortion will only be elastic and thus small.

This additional-restraint welding technique should produce a weldment with little distortion, and the residual stresses will be no greater than those in weldments made without additional restraints.

Beauchamp⁽⁷⁴⁵⁾ studied how distortion and strains change during the welding fabrication of simple panels. Figures 7.78 and 7.79 show the two model configurations for the stiffened panels made of 5052-432 aluminum alloy plate. The strain-gage and thermocouple locations are also shown in the figures. After the stiffeners were welded, the models were joined by a butt weld, giving the configuration shown in Fig. 7.80. The dimensions of the models are shown in Figs. 7.78 and 7.79. Plate thicknesses of $\frac{1}{4}$, $\frac{3}{16}$, and $\frac{1}{8}$ in. (6.4, 4.8, and 3.2 mm) were used. GMA welding and 5556 aluminum alloy filler-wire were used. Elastic prestraining was used in all fillet weldings. After the fillet welds had cooled to room temperature, the plates were unclamped and residual stresses measured. Only transverse strains and stresses were measured. Because the experimental results

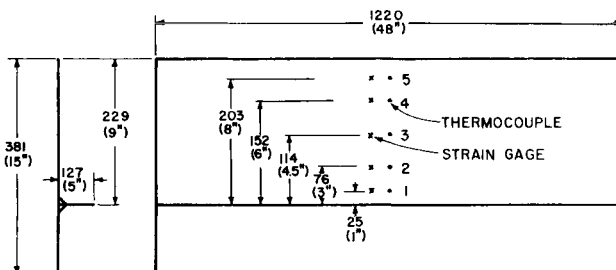


FIG. 7.78. Dimensions of model B.

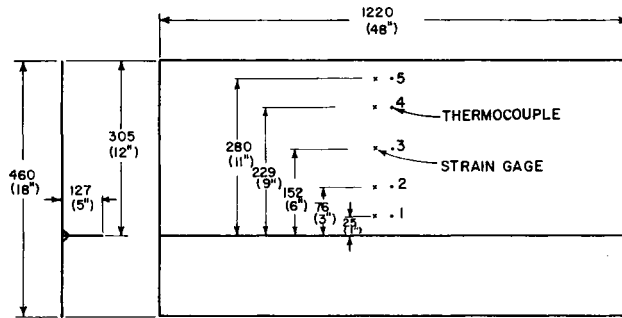


FIG. 7.79. Dimensions of model A.

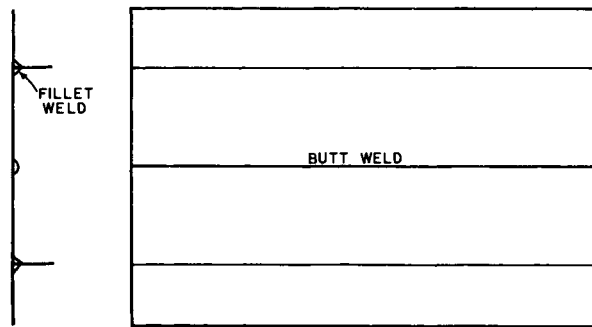


FIG. 7.80. Completed panel configuration.

are complex and occasionally confusing, they are not presented here in detail.[†] The general tendencies observed are as follows.

Stresses were introduced through elastic prestraining. The strains increased during welding. But when the clamps were released after the weldment had cooled to room temperature, much of the strain was released. Specimens welded under elastic prestraining showed little distortion, but the specimen welded under no prestrain showed a considerable amount of distortion.

Although these results are not yet conclusive, they suggest that this method will produce fabricated weldments with less distortion. Because of reaction stresses, residual stresses present after the welding is completed and before the weldment is released can be quite high. When the restraint is removed, most of the reaction stresses are released. The residual stresses present after the restraint is removed are about the same as those that exist in a weldment made under no restraint.

7.13.3 Distortion-reduction through thermal-pattern alteration

Distortion can be reduced by properly altering the thermal pattern in a weldment. This can be achieved by forced cooling and preheating.

Harvey research on rapid chilling. A study was conducted at the Harvey Engineering Laboratories^(7,46) for the Marshall Space Flight Center, NASA, to investigate the

[†] Some of these results are given in Reference (720).

feasibility of reducing warpage and residual stresses in aluminum weldments by controlling the thermal pattern during welding.⁽⁷⁴⁷⁾ The concept involves the use of cryogenic liquids and auxiliary heat sources to produce a contraction and expansion of the metal in the vicinity of the weld in such a manner as to counterbalance the expansion and contraction caused by welding.

In an analytical study, heat-extracting liquid CO₂ was used to produce an elastic deformation equivalent to the thermal expansion and contraction and the weld shrinkage (liquid-to-solid) that occurs during welding. The calculations were based on parameters observed during the performance of a previous study that used liquid CO₂ to chill weld panels $12 \times 48 \times \frac{5}{16}$ in. ($305 \times 1220 \times 8$ mm) in 2014-T6 aluminum alloy.

The mathematical results indicated that the thermal stresses would be counterbalanced if the portion of the plate heated by the arc would be contained within a 2-in. (51 mm) diameter circle surrounded by an area of approximately 45 in.² (290 m²) cooled to -100°F (-73°C). To accomplish this it was estimated that approximately 0.8 lb of liquid CO₂ per inch of weld (143 g/cm) would be needed.

On the basis of the analytical results obtained, the jet system was modified as indicated in Fig. 7.81. This jet system is designed to chill the front side of the weld and uses a fine wire brush as a sliding shield to keep CO₂ out of the arc. The actual design of the new jet system and shielding device includes provision for adjusting the thermal pattern as required to accomplish the objectives of the program. The system was also redesigned in order to improve its stability during operation and to insure its ability to reproduce the required chilling parameters.

Warpage and residual stress controls were experimentally developed as follows:

1. Procurement and preparation of materials.
2. Set-up of welding equipment with instrumentation.
3. Development of chilling systems and techniques.
4. Development of techniques for temperature and residual stress measurement.
5. Development of basic data on thermal stresses.
6. Development of thermal patterns for warpage and residual stress control.

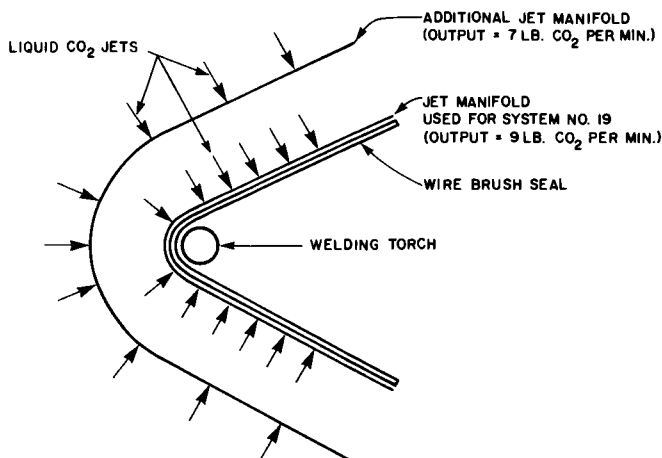


FIG. 7.81. Modified jet system number 19 used at Harvey Engineering.

Four ways of altering the thermal pattern during welding were developed, all employing jet-sprayed liquid CO₂ with or without the application of auxiliary heat. The basic systems included the following:

1. A V-shaped cryogenic jet system for cooling the front side of the weld.
2. A trailing cryogenic jet system for cooling the front side of the weld.
3. A circular cryogenic jet system for cooling the back side of the weld.
4. A trailing cryogenic jet system with auxiliary heating for the front side of the weld.

Experiments were conducted on welded $12 \times 48 \times \frac{5}{16}$ -in. ($305 \times 1220 \times 8$ mm) 2014-T6 aluminum alloy panels. It was possible to produce unwarped panels with any of the thermal-pattern alternation systems. Residual stresses could be reduced by using cryogenic cooling. But result-repeatability was very low except in the system using both chilling and heating.

Although the elastic-plastic strain relationship during welding is influenced by a great many dependent variables, the results of the work performed under the study prove that distortion and residual stress can be controlled by balancing the thermal stresses. Using a combination of theoretical and empirical methods, the optimum thermal pattern for a specific weldment can be determined; the computer program developed at M.I.T. (described in Chapter 5) can speed this process.

Iwamura's study on forced cooling. As discussed earlier (Section 7.4.2), Iwamura⁽⁷¹⁹⁾ studied how forced cooling affects the transverse shrinkage in aluminum butt welds. In order to significantly reduce transverse shrinkage, the weld must be quenched so that the temperature distribution in the base plate can be altered significantly when the weld metal solidifies. Chilling at a later time has little effect on transverse shrinkage (see Section 7.4.2 for further information).

Preheating. Because distortion is caused by uneven heating during welding, properly executed preheating can be a powerful distortion-reduction tool. It does this by either reducing the unevenness of the heating or by intentionally creating exact amounts of uneven shrinkage at precise locations on the parts to be welded.

Figure 7.51 shows how angular distortion in a fillet weld can be reduced by preheating. More information on distortion reduction through preheating is given in Sections 7.13.4 and 7.13.5.

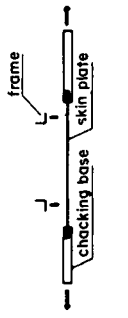
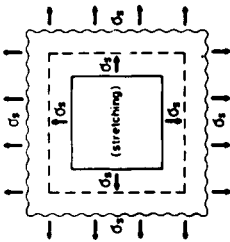
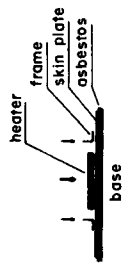
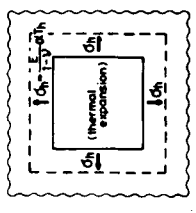
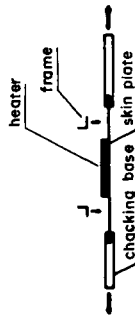
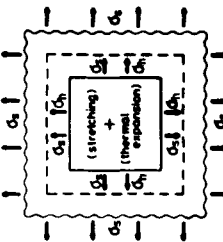
7.13.4 Reduction of out-of-plane distortion by stretching and heating

Engineers at Kawasaki Heavy Industries have developed several methods of reducing out-of-plane distortion during the fabrication of thin-plate panel structures.^(742, 743) The methods are so successful that they are called the Kawasaki "Perfect Panel Production" methods. They include the following (see Table 7.13):

1. SS method: straightening by stretching.
2. SH method: straightening by heating.
3. SSH method: straightening by stretching and heating.

In the SS method, the panel is stretched mechanically while it is being welded to a frame. When the stretching load is released after welding, the plate shrinks and little out-of-plane distortion results. Obviously tensile residual stresses remain in the plate

TABLE 7.13. Basic Concept of the Kawasaki perfect panel production method

<p>1) SS method straightening by stretching</p>			$\sigma_r = \sigma_s - \sigma'_r$ <p>here, $\sigma'_r = f(\sigma_m^s, \sigma_m^a, \dots)$</p>
<p>2) SH method straightening by heating</p>			$\sigma_r = \frac{E}{1-\nu} \alpha T_h - \sigma'_r$
<p>3) SSH method straightening by stretching and heating</p>			$\sigma_r = (\sigma_s \cdot \frac{E}{1-\nu} - \alpha T_h) - \sigma'_r$

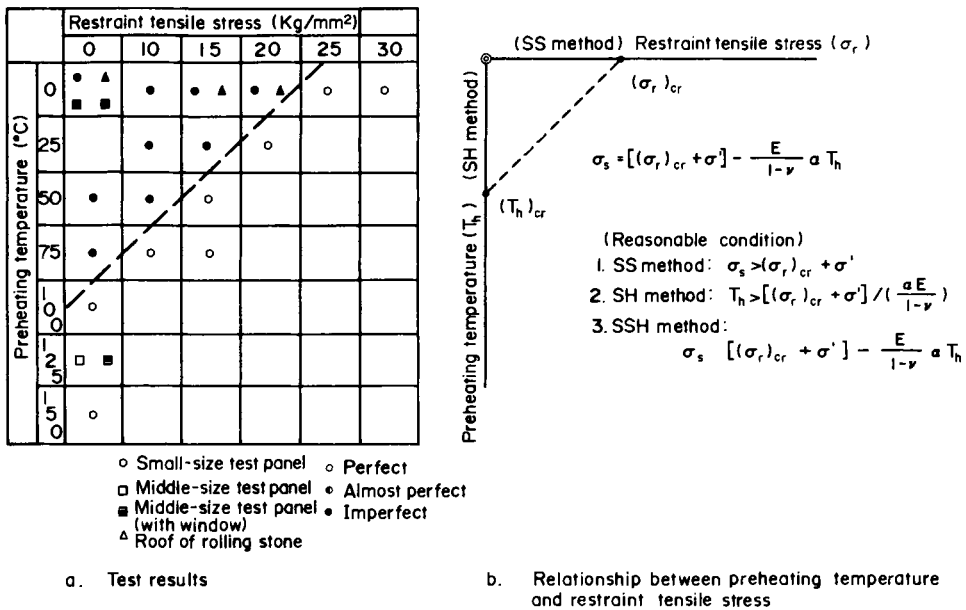


FIG. 7.82. Conditions for producing distortion-free panels using the SS, SH, and SSH methods.

and compressive residual stresses in the frame. This process is effective when a thin sheet is welded to a rigid-framed structure, such as the upper body of a railway car.

In the SH method, the panel is heated to a predetermined temperature before being welded to the frame. In other words, the plate is prestretched by preheating. Since the frame is not preheated, the plate shrinks more after welding, reducing the out-of-plane distortion of the plate.

In the SSH method, both mechanical stretching and preheating are used.

Figure 7.82 summarizes test results on various panel structures. As the value of prestretching stress increases the amount of preheating necessary to reduce distortion decreases. On the basis of the experimental results, the following formula has been developed (see Fig. 7.82(b)):

$$\sigma_s = [(\sigma_r)_{cr} + \sigma'] - [E/(1 - \nu^2)] \alpha T \tag{7.34}$$

- where
- σ_s = prestretching stress,
 - σ' = compressive residual stress in the plate caused by welding,
 - $(\sigma_r)_{cr}$ = critical compressive stress in the frame below which no out-of-plane deformation occurs,
 - α = coefficient of linear thermal expansion,
 - T = preheating temperature of the plate.

These methods are successfully used at Kawasaki Heavy Industries for fabricating railway car bodies and ship superstructures. Figure 7.83 shows how out-of-plane distortion can be reduced using the SSH method on a 7 mm ($\frac{1}{4}$ in.) low-carbon steel plate panel. The distortion is measured under the following three conditions:

1. No preheating and no stretching.
2. Preheating to 80°C (180°F) and stretching.
3. Preheating to 120°C (248°F) and stretching.

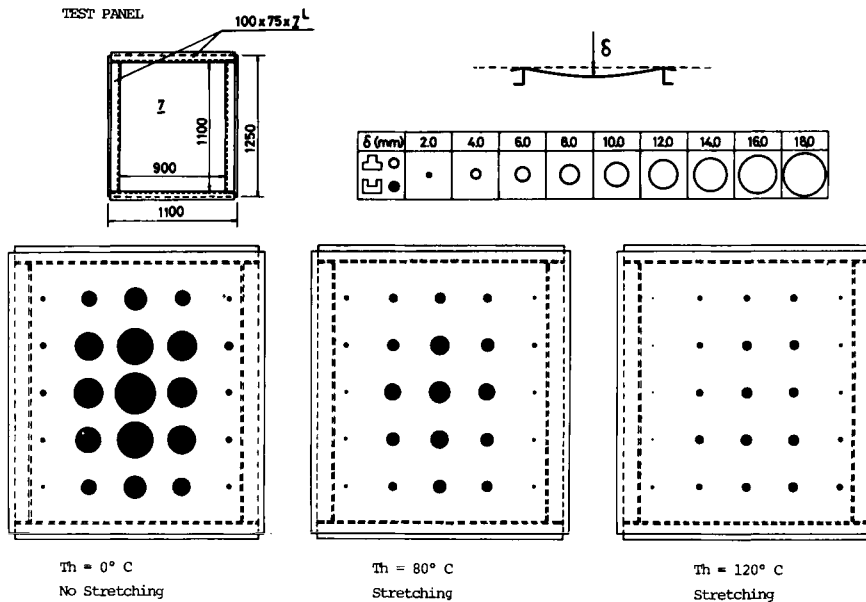


FIG. 7.83. How the SSH method reduces distortion in welded low-carbon steel plate panel structures 7 mm ($\frac{1}{4}$ in.) thick (Terai *et al.*)⁽⁷⁴³⁾

The circles shown in the figure indicate the amount of out-of-plane distortion, δ . The diameter of the circle indicates the magnitude of distortion. When the distortion is positive (when the plate is bent downward) the circles are black. When it is negative (when the plate is bent upward) the circles are white. The circles are larger in the central regions of the panel where the distortion is great. The figures clearly show that distortion can be reduced using the SH method.

7.13.5 Reduction of the longitudinal distortion of built-up beams by differential heating

The term “differential heating”, as coined by Masubuchi, refers to a distortion-reduction technique that intentionally creates temperature differences between the parts to be welded. The preheated part cools and contracts more than the part that is not preheated. The thermal stress generated can partially cancel out the residual bending stresses that would have resulted if the parts had been at the same temperature when joined. The result is distortion reduction.

Researchers at M.I.T. have studied how the longitudinal distortion of built-up beams can be reduced by differential heating.† Serotta⁽⁵³⁴⁾ conducted a series of experiments to investigate how differential heating reduces the longitudinal distortion of T-shaped built-up beams. As a material he chose 5052-H32 aluminum alloy, a strain-hardened and non-heat-treatable alloy, to permit ready comparison with results obtained by Yamamoto.⁽⁵³³⁾ The dimensions and the general arrangement of the experimental

† A limited study has also been done on the use of differential heating in the reduction of out-of-plane distortion in panel structures.⁽⁷²⁹⁾

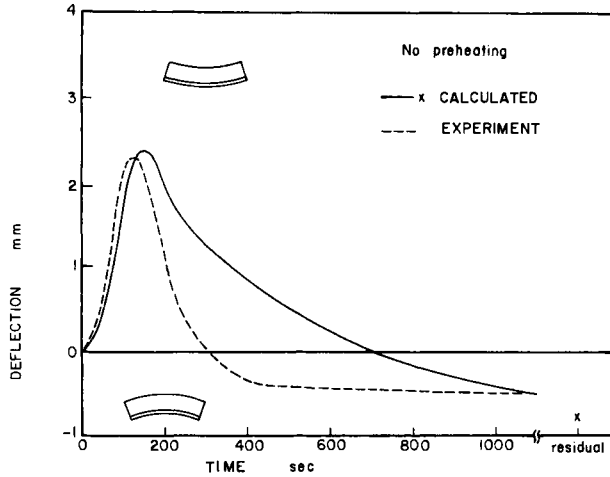


FIG. 7.84. Changes of deflection during welding fabrication of a tee-beam (no preheating).

equipment were also the same as the one used by Yamamoto⁽⁵³³⁾ (see Fig. 7.62). The aluminum plates, both the web and the flange, were 0.5 in. (12.7 mm) thick.

Nishida⁽⁵²⁷⁾ analyzed the experimental data generated by Serotta⁽⁵³⁴⁾ using the one-dimensional computer program discussed in Section 5.5.3. Results of the calculation are compared with the experimentally obtained values in Figs. 7.84 and 7.85.

Figure 7.86 shows how the post-welding deflection changes with the preheated temperature of the web. The discrepancies between the experimental data and the analytical results appear when the web is heated to a relatively high temperature. It is believed that the experimental data for high preheating temperatures is not accurate, since the temperature differential is reduced by conduction. Figure 7.86 shows that zero deflection can be achieved by heating the web to around 120°F (49°C).

When welding is done in two passes, the best technique is to produce a slightly positive

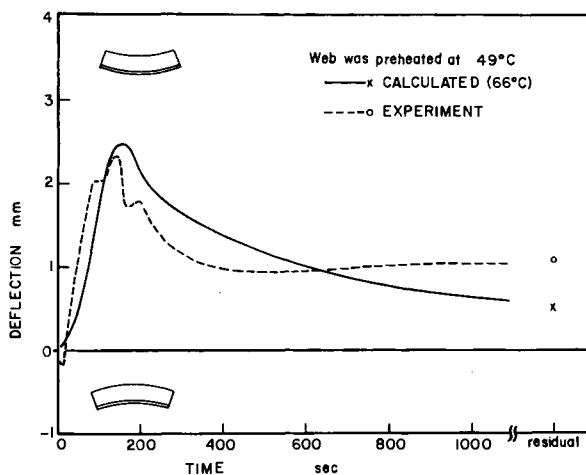


FIG. 7.85. Changes of deflection during welding fabrication of a tee-beam (the web plate was preheated to 120°F (49°C)).

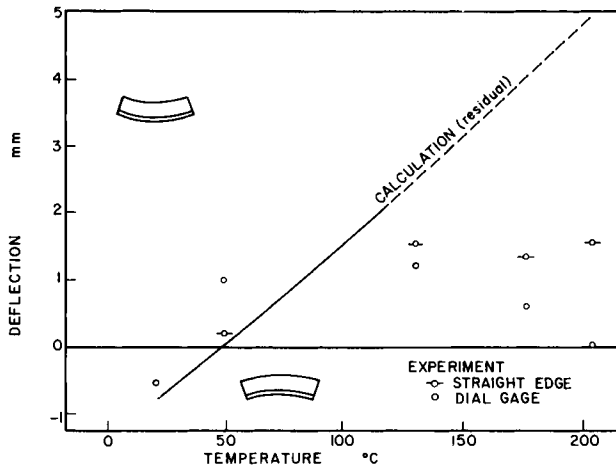


FIG. 7.86. Calculated final center deflection vs. preheating temperature of the web.

distortion after the first welding pass by using a higher preheating temperature, 170°F (77°C) for example, so that the distortion after the second pass will be close to zero.

The computer program developed by Nishida can be used to determine the optimum welding and preheating conditions for joining T-beams of various sizes.

7.14 Methods of Removing Distortion

Even though there are many distortion-reduction methods in regular use, distortion often exceeds tolerable levels. Distortion is also produced during service (from collision, for example). It becomes necessary to utilize methods of removing distortion.

7.14.1 Straightening by flame heating

The most common distortion-removal technique is to flame-heat the plate at selected spots or along certain lines and then to water-cool it. Sometimes plates are heated and hammered, a technique that requires great intuitive skill on the part of the workmen, since little scientific information, either analytical or experimental, is available on the distortion-removal mechanisms operative when this treatment is used. Although several papers have been written on flame-heating, they are primarily of an empirical nature.⁽⁷⁴⁸⁻⁷⁵³⁾ Scientific data on flame-straightening is still scarce.

Figure 7.87 illustrates the following methods of flame straightening:[†]

1. Line heating.
2. Pine-needle heating.
3. Heating in cross directions.
4. Spot heating.
5. Triangular heating.
6. Red-hot heating.

Line heating. In line heating, heat from the torch is applied along a line or a set of

[†] The terms used here may not be the same as those frequently used by workers in U.S. companies.

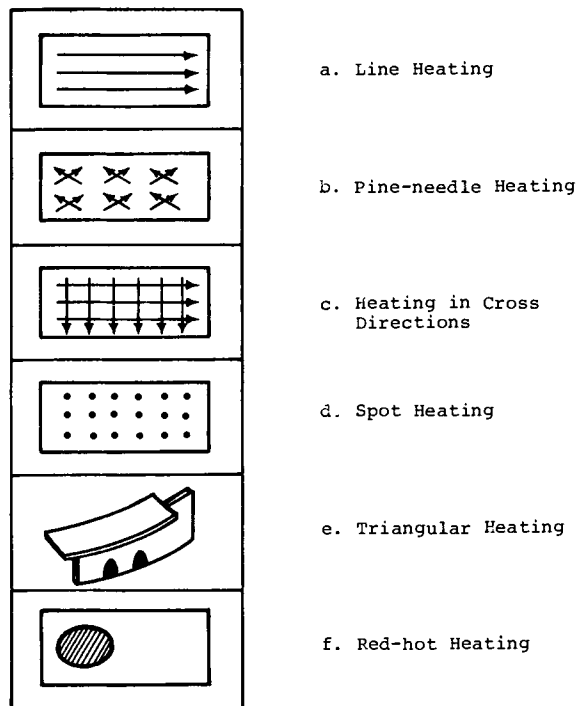


FIG. 7.87. Methods of flame-straightening.

parallel lines (see Fig. 7.87). This method is frequently used for removing the angular distortion produced by the fillet welds attaching a plate to its stiffeners. Line heating can also be used as a method for bending plates. Several investigators^(530, 754, 755) have studied line-heating shrinkage and distortion mechanism.

Figure 7.88 shows some line-heating data.⁽⁷⁵⁷⁾ Figure 7.88(a) shows the relationship between the travelling speed of the torch and the angular distortion of steel plates of various thicknesses. Figure 7.88(b) shows the relationship between the travel speed and the transverse shrinkage of the plate.

Pine-needle heating. In pine-needle heating, heat is applied along two short lines crossing each other, as shown in Fig. 7.87(b). This method is half-way between line heating and spot heating. Since the shrinkage and the angular distortion occur in two directions, this method produces a uniform distortion-removal effect.

Checkerboard heating. In checkerboard heating, heat is applied along a system of two lines crossing each other, as shown in Fig. 7.87(c). This method is often used to remove severe distortion. One must be careful not to overheat the metal.

Spot heating. In spot heating, heat is applied on a number of spots, as shown in Fig. 7.87(d). Spot heating is widely used for distortion-removal, especially in thin-plated structures.

Triangular heating. In triangular heating, heat is applied on a triangular-shaped area, as shown in Fig. 7.87(e). This method is useful for the removal of bending-distortion in frames.

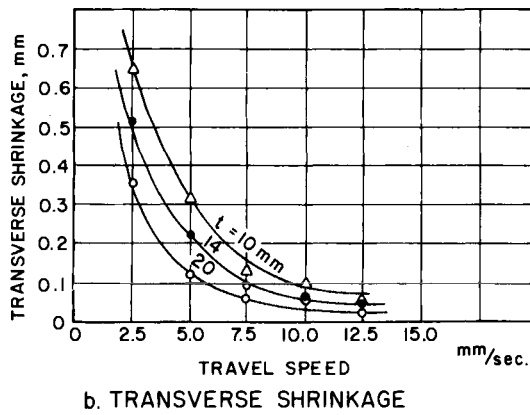
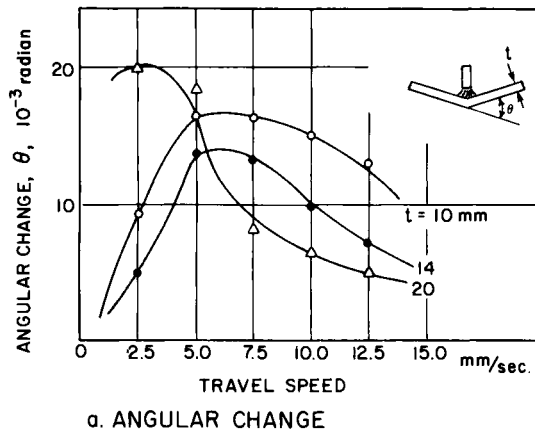


FIG. 7.88. Effects of travel speed of flame on angular change and transverse shrinkage of steel plates 10 to 20 mm ($\frac{3}{8}$ to $\frac{3}{4}$ in.) thick (Torch # 40).

Red-hot heating. When severe distortion occurs in a localized area, it may be necessary to heat the area to a high temperature and beat it with a hammer. This method can cause metallurgical changes, however.

7.14.2 Other techniques for removing distortion.

During the last several years attempts have been made to develop new distortion-removal techniques.⁽⁷²⁸⁾ The following pages discuss

1. The vibratory stress-relieving technique.
2. The electromagnetic-hammer technique.

Vibratory stress relieving.⁽⁷²⁸⁾ This technique reduces residual stress and distortion by means of vibrating the weldments.⁽⁷⁵⁶⁻⁷⁶⁰⁾ The equipment consists of a variable-speed vibrator, which is clamped to the workpiece, and an electronic amplifier. By varying the speed of the vibrator motor, the frequency can be varied until a resonant frequency has been reached for the workpiece. The piece is then allowed to vibrate for a

period which varies in length roughly in relation to the weight of the workpiece. Usually it ranges from 10 to 30 minutes.

The vibratory technique is much more economical than thermal stress-relieving techniques. It involves little in the way of expensive equipment (no furnace is needed) and achieves its objective in a relatively short time.

But there is almost a complete lack of scientific information on how it works. It is believed that the vibratory energy introduced in the workpiece realigns the lattice structure to relieve stress and stabilize the part without distortion. But there has been little published information regarding optimum conditions of vibratory stress relieving or its effectiveness in reducing residual stress and distortion.

The Battelle Memorial Institute, Columbus Laboratories, conducted a study supported by a group of industrial companies to evaluate the usefulness of vibratory stress conditioning.⁽⁷⁶⁰⁾

Electromagnetic hammer.⁽⁷²⁸⁾ The electromagnetic hammer, so called because it can be used in place of a hammer, consists of five essential parts: a power source, energy-storing capacitors, switches, transmission lines, and a magnetic coil. The use of electromagnetic forces to drive machinery has been common for many years, but the direct application of electromagnetic forces to metal working is a recent innovation.

The material to be straightened must be considered a part of a total magnet-forming system; its characteristics can significantly change the amount of deformation resulting from a given amount of stored energy. The conductivity of the material determines the effectiveness of energy conversion to magnetic forces. If the conductivity of the material is low, energy will be lost due to heat-generation in the workpiece. Because of this, a more conductive material such as aluminum will be deformed more at the same energy level than will a low-conductivity material like stainless steel.

Electromagnetic hammers have been used to remove the distortion in welded tanks and bulkheads in the Saturn V rocket.⁽⁷⁶¹⁾ In principle, such equipment could be used in other aluminum structures. A prototype developed by NASA was used at Avondale Shipyard, inc., in New Orleans, Louisiana, to evaluate its possible use in the shipbuilding industry.⁽⁷²⁸⁾

References

- (701) The Welding Institute, *Control of Distortion in Welded Fabrication*, London, 1968.
- (702) Institute of Welding, *Control of Welding Distortion*, London, 1957.
- (703) NAKA, T., *Shrinkage and Cracking in Welds*, Tokyo, Komine Publishing Co., 1950 (in Japanese).
- (704) KIHARA, H., editor, *Welding Data Book*, Japan Welding Engineering Association, 1954, and a new edition by Sampo Publishing Co., Tokyo, 1964.
- (705) NIKOLAEV, G. A., *Stresses and Strains in Welding (Napriazheniia i Deformatsii pri Svarke)*, Mashgiz, (in Russian).
- (706) GRIGOREV, A. A., and SIDORENKOV, A. P., *Local Welding Deformations in Sheet Metal Structures and Methods of Reducing Them (Mestnye Svarochnye Deformatsii ton Kolistovykh Konstruktsii i Mero-priiatii po ikh Umenysheniui Sudpromgiz)*, Leningrad, 1957 (in Russian).
- (707) TALYKOV, G. B., *Approximate Theory of Deformation and Stresses in Welding*, Izd-vo Leningrad, Iniv-ta, 1957 (in Russian).
- (708) Weld Distortion Handbook, Battelle Memorial Institute, Columbus, Ohio, 1969 (not published).
- (709) WATANABE, M. and SATOH, K., "Effect of welding conditions on the shrinkage and distortion in welded structures", *Welding Journal*, 40 (8), Research Supplement, 377s-384s (1961).
- (710) The Society of Naval Architects of Japan, *Japanese Shipbuilding Quality Standards (Hull Part)*, Tokyo, 1975.

- (711) Sixth International Ship Structures Congress (Boston), *Fabrication Factors Affecting Structural Capability of Ships and Other Marine Structures*, (Report of Committee III. 3), 1976.
- (712) CAPEL, L., "Aluminum welding practice", *British Welding Journal*, **8** (5), (1961) 245-248 (1961).
- (713) GILDE, W., "Contribution to the calculation of transverse shrinkage", (*Beitrag zur Berechnung der Querschrumpfung*), *Schweisstechnik*, **7** (1) 10-11 (1957) (in German).
- (714) CLINE, C. L., "Weld shrinkage and control of distortion in aluminum butt welds", *Welding Journal*, **44** (11), 523s-528s (1965).
- (715) CAMPUS, F., "Transverse shrinkage of welds", *Welding Journal*, **26** (8), 485s-488s (1947).
- (716) GUYOT, F., "A note on the shrinkage and distortion of welded joints", *Welding Journal*, **26** (9), 519s-529 (1947).
- (717) MALISIUS, R., *Electroschweissen*, **7**, 1-7 (1936) (in German).
- (718) MATSUI, S., "Investigation of shrinkage, restraint stresses and cracking in arc welding", Ph.D. Thesis at Osaka University, 1964 (in Japanese).
- (719) IWAMURA, Y., "Reduction of transverse shrinkage in aluminum butt welds", M.S. Thesis, M.I.T., May 1974.
- (720) PAPAZOGLU, V. J. and MASUBUCHI, K. *Development of Analytical and Empirical Systems for Parametric studies on Design and Fabrication of Welded Structures*, Final Report prepared from the Massachusetts Institute of Technology to the Office of Naval Research under contract N00014-75-C-0469, NR 031-773 (M.I.T. OSP 82558), 30 Nov. 1977.
- (721) GOTT, G., CLOVER, F. R., and RUDY, J. F., "Metal movement and mismatch in aluminum welds", *The Welding Journal*, **47** (8), Research Supplement, 337s-354 (1968).
- (722) *Researches on Welding Procedures of Thick Steel Plates Used in the Construction of Large Size Ships*, Report of Shipbuilding Research Association of Japan, 26 (Sept. 1959 (in Japanese)).
- (723) MASUBUCHI, K., OGURA, Y., ISHIHARA, Y., and HOSHINO, J., "Studies on the mechanisms of the origin and methods of reducing the deformation of shell plating in welding ships", *International Shipbuilding Progress*, **3** (19), 123-133 (1956).
- (724) HIRAI, S. and NAKAMURA, I., "Research on angular change in fillet welds", *Ishikawajima Review*, 59-68 (Apr. 1955) (in Japanese).
- (725) TANIGUCHI, C., "Out-of-plane distortion caused by fillet welds in aluminum", M.S. (Ocean Engineering) Thesis, M.I.T., Aug. 1972.
- (726) MASUBUCHI, K. and TANIGUCHI, C., "Distortion and residual stresses in welded aluminum structures", paper presented at the Third Inter-American Conference on Materials Technology, Rio de Janeiro, Aug. 1972.
- (727) SHIN, D. B., "Finite element analysis of out-of-plane distortion of panel structures", M.S. Thesis, M.I.T., May 1972.
- (728) DUFFY, D. K., "Distortion removal in structural weldments", M.S. Thesis, M.I.T., May 1970.
- (729) BRITO, V. M., "Reduction of distortion in welded aluminum frame structures", M.S. Thesis, M.I.T., May 1976.
- (730) MASUBUCHI, K., KITAMURA, K., and TANIGUCHI, C., *Buckling as a Limiting Criteria to Control Initial Distortion of Welded Structural Panels*, Escola Politécnica da Universidade de São Paulo, Brazil, 1975.
- (731) GONCALVES, E., and TANIGUCHI, C., *Comparative Analysis of Methods for Predicting Weld Distortion in Panel Structures*, Escola Politécnica da Universidade de São Paulo, Brazil, Dec. 1974.
- (732) WATANABE, M., SATOH, K., MORII, H., and ICHIKAWA, I., "Distortion in web plate of welded built-up girders due to welding of stiffeners and methods for decreasing it", *Journal of the Japan Welding Society*, **26**, 591-596 (1957).
- (733) KUMOSE, T., YOSHIDA, T., ABE, T., and ONOUE, H., "Prediction of angular distortion caused by one-pass fillet welding", *The Welding Journal*, **33**, 945-956 (1954).
- (734) HENRY, R. W., "Reduction of out-of-plane distortion in fillet welded high strength aluminum", M.S. Thesis, M.I.T., May 1974.
- (735) KING, C.W.R., *Transactions of the Institute of Engineers and Shipbuilders in Scotland*, **87**, 238-255 (1944).
- (736) SASAYAMA, T., MASUBUCHI, K., and MORIGUCHI, S., "Longitudinal deformation of a long beam due to fillet welding", *Welding Journal*, **34**, 581s-582s (1955).
- (737) UJIE, A., et al., *Automatic Welding of 5083 Aluminum Alloy*, The Committee of Light Metals for Shipbuilding Industry, Report 14, 1970-1972 (in Japanese).
- (738) MASUBUCHI, K., "Buckling-type deformation of thin plate due to welding", *Proceedings of Third National Congress for Applied Mechanics of Japan*, 1954, pp. 107-111.
- (739) MURA, T., "On the buckling deformations of thin plates due to welding", *Proceedings of the Third Japan National Congress for Applied Mechanics*, 1955, pp. 103-106.
- (740) WATANABE M. and SATOH, K., "Fundamental studies on buckling of thin steel plate due to bead-welding", *Journal of the Japan Welding Society*, **27** (6), 313-320 (1958) (in Japanese).
- (741) HAUSER, D., MISHLER, H. W., MONROE, R. E., and MARTIN, D. C., *Electron-beam Welding of Beryllium*, Technical Report AFML-TR-66-215 for Contract AF 33(615)-2671 (July 1966), Battelle Memorial Institute.

- (742) TERAI, K. *et al.*, "Study on prevention of welding deformation in thin-skin plate structures", *Kawasaki Technical Review*, no. 61, 61–66 (Aug. 1978).
- (743) TERAI, K. *et al.*, unpublished document.
- (744) PATTEE, F. M., "Buckling distortion of thin aluminum plates during welding", M.S. Thesis, M.I.T., Sept. 1975.
- (745) BEAUCHAMP, D. G., "Distortion in welded aluminum structures", M.S. Thesis, M.I.T., May 1976.
- (746) COLE, D. Q., *Development of Techniques for Controlling Warpage and Residual Stresses in Welded Structures*, Final Report under Contract NAS8–21174 from Harvey Engineering Laboratories, July 1968.
- (747) MASUBUCHI, K., *Integration of NASA-sponsored Studies on Aluminum Welding*, RSIC 670, Redstone Scientific Information Center, Redstone Arsenal, Alabama, 1967.
- (748) STITT, J. R., "Distortion can be designed out of welded structures", *Steel*, **134** 120–122 (8 Mar. 1954).
- (749) SCITT, J. R., "Distortion control during welding of large structures", SAE Paper from the Society of Automotive Engineers, Inc., New York, to the Society of Automotive Engineers and the American Society of Mechanical Engineers, Air Transport and Space Meeting, New York, N.Y., 27–30 April 1964, Paper 844B (1964), 8 pages (A64–20799).
- (750) YOSHIDA, T., Matsunaga, W., and Terai, K., "Application test of flame straightening", *Journal of the Japan Welding Society*, **24**, 24–31 (1955) (in Japanese).
- (751) TSALMAN, L. B., "Straightening welded fabrications by heating with the oxyacetylene torch", *Welding Production*, **5** (3) (1959), 29–31 (in Russian).
- (752) FAIERMAN, A. I., and Rezanov, A. N., "Methods of preventing welding distortions analyzed for the economic point of view", *Welding Production*, **7** (9), 17–20 (1961) (in Russian).
- (753) Fifth Conf. Soud. Contr. Mét. I., September 1965, Timisoara, "Prevention of distortion and straightening of weldments", (*Verformungsvorbeugung und Richten geschweisster Bauteile*), I. Avram and R. Grabovsky, pp. 673–694.
- (754) HASHIMOTO, T. and FUJISHIRO, Y., "An experiment of line heating designed with the table orthogonal array L (2³¹)", *Journal of the Society of Naval Architects of Japan*, **104** 201–225 (1959).
- (755) SATOH, K., MATSUI, S., TERAI, K., and IWAMURA, Y., "Water-cooling effect on angular distortion caused by process of line heating in steel plates", *Journal of the Society of Naval Architects of Japan*, **126**, 446–458 (1969).
- (756) "Stress relieve big weldments in minutes with vibration", *Machinery*, **74**, 100–103 (3 May 1968).
- (757) "New twist to the distortion problem", *Welding Engineer*, **47**, 48 (Apr. 1968).
- (758) WOZNEY, G. P., and CRAWMER, G. R., "An investigation of vibrational stress relief in steel", *The Welding Journal*, **47** (9), Research Supplement (1968).
- (759) WEIS, S. BAKER., and DAS GUPTA, R. D., "Vibrational residual stress relief in a plain carbon steel weldment", *Welding Journal*, **55** (2), Research Supplement, 47s-51s (1967).
- (760) CHEEVER, D. L. and ROWLANDS, E. W., "Vibrational conditioning of casting and weldments: an exploratory study", *Control of Distortion and Residual Stress in Weldment*, pp. 22–45, American Society for Metals (Nov. 1977).
- (761) *The Electromagnetic Hammer*, G. C. Marshall Space flight Center, NASA, SP-5034, Dec. 1965.

CHAPTER 8

The Strength of Welded Structures: Fundamentals

THIS short chapter is an introduction to the later chapters which discuss various subjects related to the strength of welded structures.

8.1 Strength of “Idealistic” and “Realistic” Structures

Besides the basic issues of structural and material strength, when one considers the strength of a structure that is welded, several additional factors are involved, the most important of which are residual stress and distortion. A weldment, which often contains several kinds of defects, is composed of three zones: the weld metal, the heat-affected base metal, and the unaffected base metal; each zone has a different metallurgical structure, and within the heat-affected zone itself are subzones containing different metallurgical structures.

In the usual analysis of the tensile strength, the fatigue strength, the buckling strength, etc., of a material, idealistic conditions of material and structure are usually assumed. The material is designated homogeneous and often assumed to be isotropic. It has no discontinuities, no initial stress, and is in a perfect shape. Flat plates are assumed to be perfectly flat.

There is nothing wrong with such idealizations in that through them we can do a basic, simple and useful analysis of several important problems related to the subject at hand. When considering the service behavior of a welded structure, however, some of these idealizations are no longer acceptable. A welded structure, more than any other kind of assemblage, is not adequately described by idealized simplifications, as shown in Table 8.1.

The following chapters will therefore be a study of the strength of not idealistic but realistic structures, a departure from the usual strength of materials analysis which only

TABLE 8.1 *Idealistic vs. realistic welded structures*

Idealistic structure	Realistic welded structure
Homogeneous	Composed of different zones, including weld metal, HAZ, and base metal
No discontinuities	Contains various types of defects, including cracks, pores, etc.
No initial stress	Initial stress
In a perfect shape	Initial distortion

attempts the former. Since there are many books about the strength of materials, including those analyzing brittle fractures, fatigue, buckling, stress corrosion cracking, this book will emphasize those topics that are unique to welded structures, and will discuss in depth the effects of residual stresses, distortion, and weld defects. The basic principles presented in this book can be applied to other types of structures, including those that are cast or forged.

8.2 Changes in Residual Stress in Weldments Subjected to Tensile Loading⁽⁵⁰¹⁾

Figure 8.1 shows a simple case of a longitudinal butt weld under uniform tensile loading. Wilson and Hao⁽³⁰⁴⁾ have made a detailed study of this kind of stress change in steel welds.

Curve 0 shows the lateral distribution of longitudinal residual stress in the as-welded condition. High tensile stresses exist in regions near the weld, while compressive stresses exist in regions away from the weld.

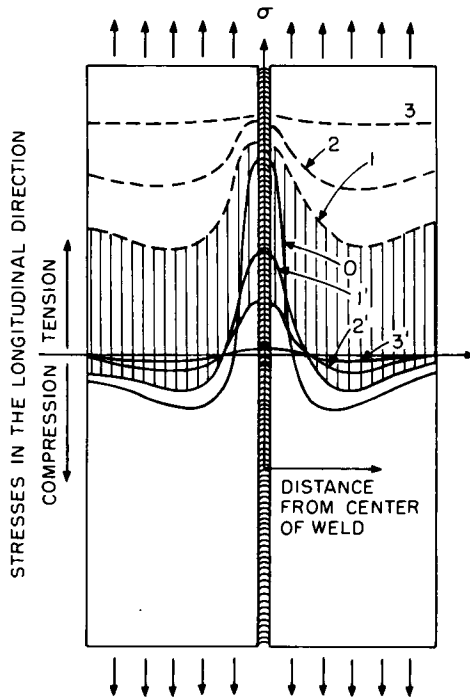


FIG. 8.1. Schematic distributions of stresses in a butt weld when uniform tensile loads are applied and of residual stresses after the loads are released.

Legend:

- Curve 0: Residual stresses in the as-welded condition.
- Curve 1: Stress distribution at $\sigma = \sigma_1$.
- Curve 2: Stress distribution at $\sigma = \sigma_2$.
- Curve 3: Stress distribution at $\sigma = \sigma_3$.
- Curve 1': Distribution of residual stresses after $\sigma = \sigma_1$ is applied and then released.
- Curve 2': Distribution of residual stresses after $\sigma = \sigma_2$ is applied and then released.
- Curve 3': Distribution of residual stresses after $\sigma = \sigma_3$ is applied and then released.

Curve 1 shows the stress distribution when a uniform tensile stress $\sigma = \sigma_1$ is applied. Yield stress is reached near the weld, and most of the stress increase occurs in areas away from the weld. Curve 2 shows the stress distribution when the applied tensile stress is increased to σ_2 . As the applied stress is increased, the stress distribution across the weld evens out, that is, the effect of welding residual stress on the stress distribution decreases.

When the level of applied stress reaches a certain point, yielding takes place across the entire cross-section. The stress distribution at this point of general yielding is shown by curve 3. Beyond this point, the effect of residual stress on the stress distribution vanishes.

Curve 1' shows the residual stress that remains when the tensile stress $\sigma = \sigma_1$ is released. curve 2' shows the residual stress distribution that remains when the tensile stress $\sigma = \sigma_2$ is released.

The residual-stress distribution after this kind of cyclic loading is more even than the original residual-stress distribution (curve 0). As the level of loading increases, the residual-stress distribution after the cycle becomes more even, that is, the effect of welding residual stress on the stress distribution decreases.

From the above discussion we can now state the basic facts concerning the effect of residual stress:

1. Residual stress significantly affects only those phenomena that occur under a low applied stress, such as brittle fracture and stress corrosion cracking.
2. As the level of applied stress increases, the effect of residual stress decreases.
3. The effect of residual stress on the performance of a welded structure is negligible when the applied stress has been increased beyond the yielding point.
4. The residual stress tends to decrease as the structure is subjected to repeated loading.

8.3 Local Stress Concentration Caused by Out-of-plane Distortion

Figure 8.2 shows a simple butt weld under transverse tensile loading. Because of the out-of-plane distortion, δ , the tensile loading causes a bending moment that produces high tensile stresses in regions near points B. Under certain conditions, the high stresses may cause cracks in regions near points B.

As the level of tensile applied stress, σ , increases and the joint is more stretched, δ decreases; stress concentrations in areas near points B decrease when tensile plastic deformation occurs in the area.

Out-of-plane distortion can cause serious problems if a crack occurs near points B and propagates out into other regions. Out-of-plane distortion can also affect brittle fracture; this will be discussed in Chapter 10. The effect of out-of-plane distortion on fracture strength becomes negligible after plastic deformation has occurred in areas near points B.

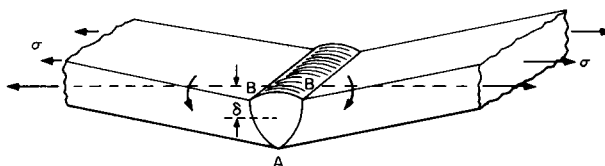


FIG. 8.2. Local stress concentration caused by out-of-plane distortion.

8.4 Instability of Columns Under Compressive Loading

Figure 8.3 shows columns under compressive loading. Even if a column has no initial distortion, it becomes unstable when the load exceeds a certain limit, as shown in Fig. 8.3(a). This phenomenon is known as buckling. In the case of a column with hinged ends, the critical stress, σ_{cr} , is expressed by:

$$\sigma_{cr} = \frac{P_{cr}}{A} = \frac{\pi^2 E}{(l/k_z)^2} \tag{8.1}$$

- where P_{cr} = critical load,
- A = cross-sectional area of the column,
- E = Young's modulus,
- I_z = moment of inertia of the column with respect to the z -axis,
- l = length of the column,
- $k_z = I/A$ = radius of gyration of the column.

It can be seen that for a given material the value of the critical stress will depend on the ratio, l/k_z , which is designated the slenderness ratio. In Figure 8.4, curve 1 represents schematically the relationship between the σ_{cr} and the l/k_z of a material.

As the values of the slenderness ratio, l/k_z , increase, the critical stress decreases. Since the value of Young's modulus for aluminum is about one-third of that for steel, the buckling stress of an aluminum column is only about one-third that of a steel column having the same slenderness ratio.

As the slenderness ratio decreases, the buckling stress increases. However, as the critical stress approaches the yield stress of the material (line 2) the experimental data for steel and aluminum begin to deviate from the Euler curve, which assumes that the material is perfectly elastic.

The analysis of buckling under plastic condition requires complex mathematical derivations. A commonly used technique is to assume that stresses and strains in the

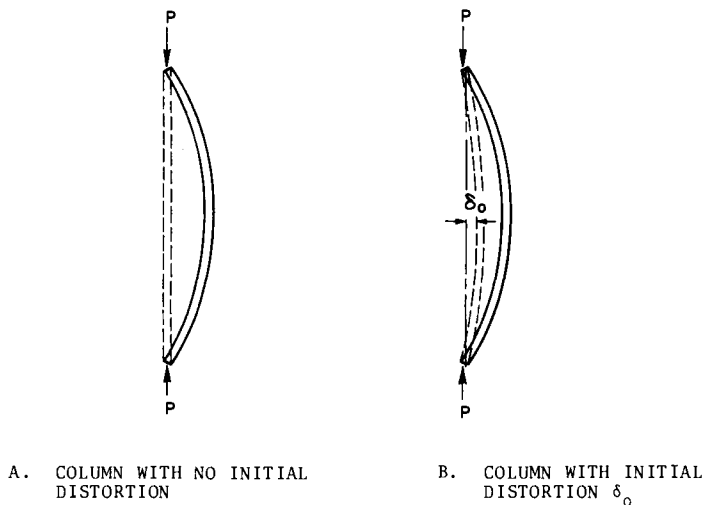


FIG. 8.3. Buckling of a column under compressive loading.

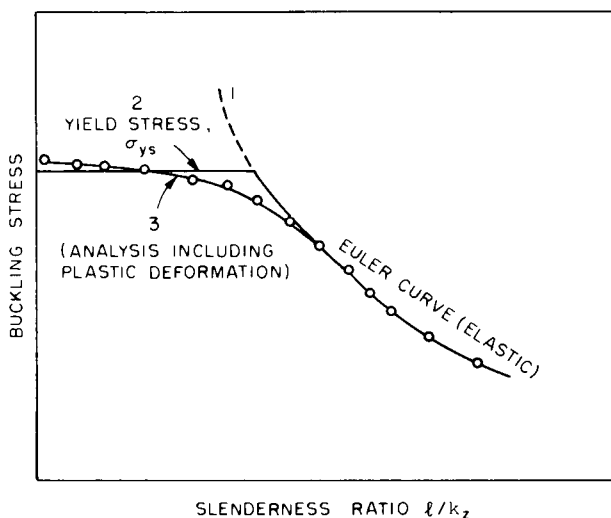


FIG. 8.4. Schematic relationships between slenderness ratio and buckling stresses of columns made with engineering materials.

axial direction of the bar, σ_{\pm} and ϵ_{\pm} , respectively, are given by the following equations:

$$\begin{aligned} \text{Elastic range:} & \quad d\sigma_{\pm} = E d\epsilon_{\pm}, \\ \text{Plastic range} & \quad d\sigma_{\pm} = E_t d\epsilon_{\pm}, \end{aligned} \tag{8.2}$$

where suffix \pm implies convex or concave sides of the column. $E_t (E_t \leq E)$ is often called the tangent modulus in the plastic range. The material is called “perfect plastic”, if $E_t = 0$ (see Fig. 8.5).

Theories have been developed to analyze the ultimate buckling stresses of columns with small slenderness ratios, as shown schematically by curve 3. The values of the ultimate buckling stress relative to yield stress (line 2) depend primarily on the plastic property of the material as indicated by E_t .

The analysis of buckling strength is a more complex task than our discussion thus far may have implied; the buckling strength of a welded column is significantly affected and made lower than indicated by curve 3 when initial distortion or unfavorable residual stresses are present.

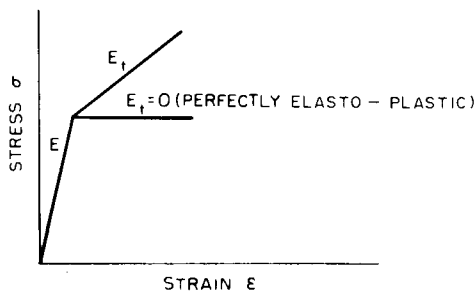


FIG. 8.5. Simplified stress-strain diagram in elastic and plastic ranges.

8.4.1 The effects of initial distortion on buckling

It has long been recognized that initial distortion can significantly reduce buckling strength. Figure 8.6, from Timoshenko's book,⁽⁸⁰¹⁾ shows in general terms the effect of initial distortion on the buckling strength of a steel column with a yield strength of 36,000 psi (25.2 kg/mm² or 248 MN/m²). Shown here are values of σ_{cr} for three different values of the ratio δ_0/l , where δ_0 is the amount of initial distortion as shown in Fig. 8.3(b).

More detailed analyses of the effect of initial distortion with emphasis on buckling in the plastic range have been conducted by Shanley,⁽⁸⁰²⁾ Beedle,⁽⁸⁰³⁾ Osgood,⁽⁸⁰⁴⁾ and Yamamoto.⁽⁸⁰⁵⁾

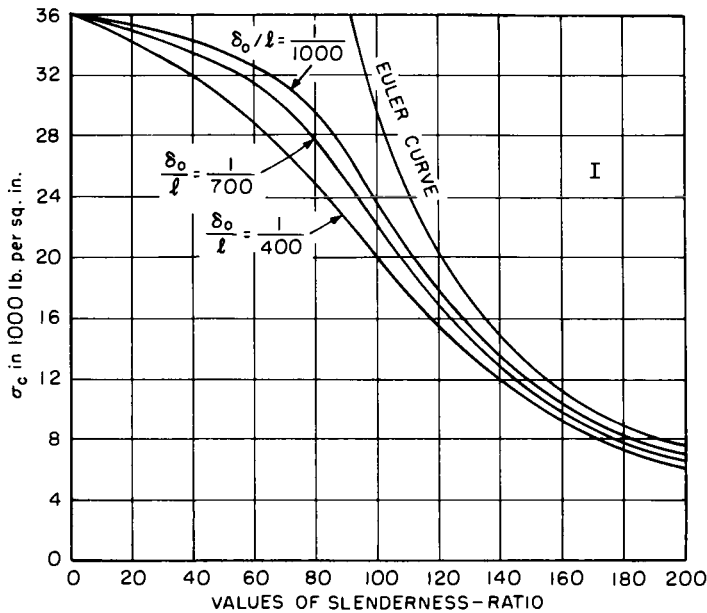


FIG. 8.6. Effect initial distortion, δ_0 , on buckling stress, σ_{cr} , of a hinged steel column under compressive loading.⁽⁸⁰¹⁾

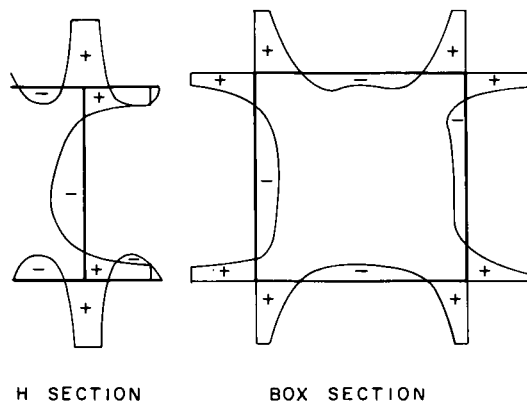


FIG. 8.7. Typical distributions of longitudinal residual stresses in an H-section and a box section fabricated by welding.

8.4.2 The effects of residual stress on buckling

As shown in Fig. 8.7, compressive residual stresses in the direction parallel to the weld line exist in base-metal regions away from the weld. Figures 8.7(a) and (b) show typical distributions of residual stresses in a welded H-beam and a box girder, respectively. These compressive residual stresses reduce, under certain conditions, the buckling strength of welded beams and columns.

Figure 8.8 shows the load-deflection diagram of a welded H-column under compressive loading.⁽⁸⁰⁶⁾ To simplify the analysis, it is assumed that the material is perfectly plastic. If the column had no residual stresses, the load-deflection relationship would be as

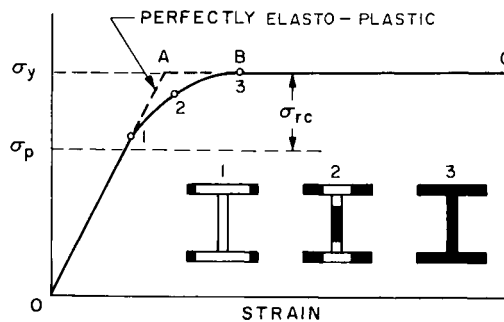


FIG. 8.8. Effect of residual stresses on the load-deflection diagram of a welded H-column under compressive loading.

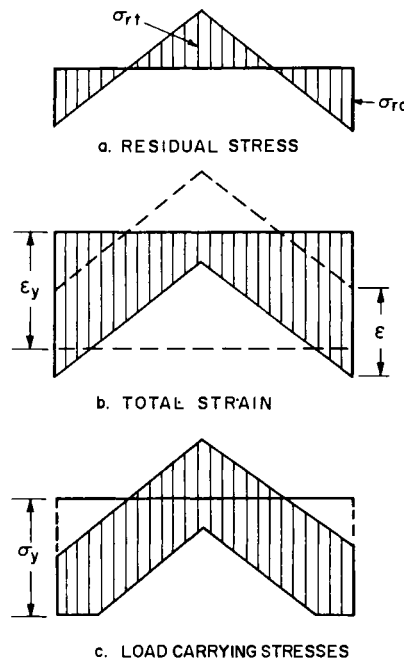


FIG. 8.9. Distributions of stresses and strains in the flange plate of an H-section under compressive loading.

shown by OABC. However, the load-deflection relationship of a welded column which has residual stresses is as shown by 0123C. This phenomenon is explained by Figures 8.9(a), (b) and (c), which show simplified distributions of stresses in the flange plate.

Figure 8.9(a) shows the distribution of residual stresses. If a uniform strain in the amount of ϵ is applied, the total strain is as shown in Fig. 8.9(b). If strains in areas near the outer edges exceed the elastic limit causing plastic deformation in those areas, the stress distribution is as shown in Fig. 8.9(c).

This is illustrated in case 1 of Fig. 8.8. Plastic deformation (shown in black) occurs in the outer edges of the flange plate. The load under that condition corresponds to the shaded area in Fig. 8.9(c), which is slightly less than the load required to produce the same strain in a column without residual stresses. This condition is shown by point 1 in Fig. 8.8.

As the load increases, the plastic zone extends as shown in black in cases 2 and 3 of Fig. 8.8, which correspond to points 2 and 3, respectively. When the load is increased beyond point 3, the effects of residual stress disappear and the cross-section is uniformly stressed to the yield point.

All this serves to illustrate how residual stresses decrease the proportional limit of a built-up column. Even though a column is fabricated with a material that is perfectly plastic, the built-up column containing residual stresses behaves non-elastically under the load exceeding σ_p . The amount of σ_p can be determined as follows:

$$\sigma_p = \sigma_{ys} - \sigma_{rc} \quad (8.3)$$

where σ_{ys} = yield stress,

σ_{rc} = maximum compressive residual stress, as shown in Fig. 8.9(a).

References

- (801) TIMOSHENKO, S., *Strength of Materials*, Third Edition, D. Van Nostrand Comp. 1955.
- (802) SHANLEY, F. R., "Inelastic column theory", *Journal of Aeronautical Science*, (1947).
- (803) YANG, C. H., BEEDLE, L. S., and JOHNSTON, B. G., "Residual stresses and the yield strength of steel beams", *Welding Journal*, 31 (4), Research Supplement, 205s-229s (1952).
- (804) OSGOOD, W. R., "The effect of residual stresses on column strength", *Proceedings of First U.S. National Congress of Applied Mechanics*, June 1951.
- (805) YAMAMOTO, Y., "Initial deflection and plastic buckling", *Journal of the Society of Naval Architects of Japan*, 97, 57-68 (1950)
- (806) ITO, F., "Residual stress and compressive strength of welded steel columns", *Journal of Japan Welding Society*, 36 (4), 386-394 (1967).

CHAPTER 9

Fracture Toughness

SINCE numerous publications on brittle fractures and the fracture toughness of various engineering materials are available elsewhere, this chapter covers only those subjects relevant to brittle fractures in welded structures. Some texts on brittle fracture are listed at the end of this chapter as References (901) through (910). Many of the discussions presented in this chapter come from Reference (102) by Masubuchi. Topics related to brittle fracture are covered in Chapters 9 and 10.

9.1 Elementary Concepts of Fracture⁽¹⁰²⁾

Fracture is the separation of a body into two or more parts. The nature of a fracture differs with the material involved, the nature of the applied stress, the geometrical features of the sample, and the conditions of temperature and strain rate.⁽⁹¹¹⁾

9.1.1 *Transgranular and intergranular fractures*

Fractures in polycrystalline materials may be classified into transgranular and intergranular types depending upon the crack path.⁽⁹⁰²⁾ The transgranular fracture traverses the grains of a polycrystalline aggregate, as shown in Fig. 9.1 (a) In the intergranular fracture, separation takes place between grain boundaries or along grain boundaries, as shown in Fig. 9.1(b).

Grain boundary separation is characteristic of the behavior of materials at elevated temperatures. Creep fractures, which occur under prolonged loading at an elevated temperature, occur, at least initially, along grain boundaries. Intergranular hot cracks occur in the weld metal during solidification and in the heat-affected base metal near the fusion zone where incipient melting occurs along grain boundaries. Intergranular cracks also occur in steel at room temperature under the simultaneous action of stress and certain environments. This phenomenon, called stress corrosion cracking, is covered in Chapter 12.

Other fractures which include brittle and ductile fractures (covered in this chapter) and fatigue fractures (covered in Chapter 11) are transgranular.

9.1.2 *Cleavage and shear fractures*

Two modes of fracture, both transgranular, are of importance in the present discussion: the cleavage mode and the shear mode.

The crystallographic nature of these failures can best be described with reference to the crystal structures of iron.⁽⁹⁰²⁾ Figure 9.2 shows the unit cell of the body-centered cubic (BCC) lattice, consisting of an atom located at each corner of the cube and another

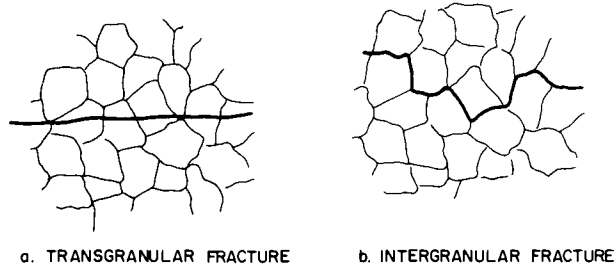


FIG. 9.1. Transgranular and intergranular fracture.

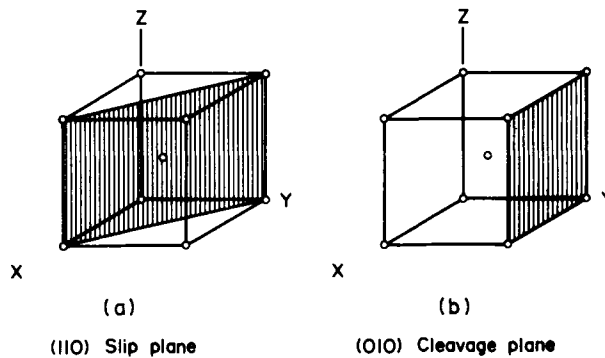


FIG. 9.2. Body centered cubic iron showing slip and cleavage planes.

at its center. Slip, or plastic flow, takes place by the shearing of certain crystallographic planes over one another. Slip translation always occurs in the direction having the minimum interatomic distance and usually on the planes having the greatest atomic density.

The three known slip planes in iron (all having common slip directions) are the cube diagonals (see plane (110) in Fig. 9.2(a)). Shear fractures are promoted by the action of shear stresses, somewhat the same as when one half of a deck of cards sliding over the other half separates the deck into two stacks.

The cleavage mode of fracture, on the other hand, is caused by normal tensile stresses and is typified by the fracture of mica when sheets are peeled apart. This type occurs in iron on a different set of crystallographic planes, of which plane (010) is shown in Fig. 9.2(b).

Table 9.1 shows cleavage and shear planes for various structures and materials. The three most common crystal structures in metals and alloys are:

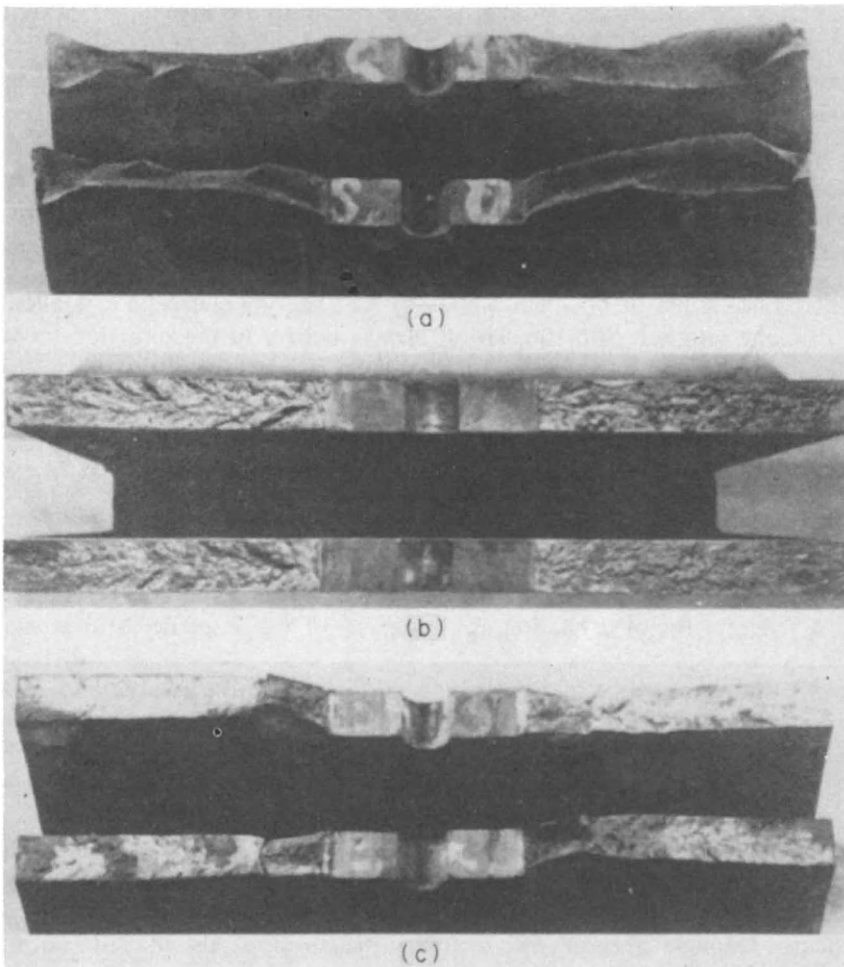
- Body-centered cubic (BCC)
- Face-centered cubic (FCC)
- Hexagonal close packed (HCP)

All metals except those with an FCC structure have cleavage planes; therefore, they show a ductile-to-brittle transition which is covered in this chapter. Aluminum alloys and austenitic stainless steels are two ordinary structural metals which do not fracture in a cleavage mode. These metals are commonly used for cryogenic applications.

Macroscopic fracture appearance. The two basic types of separation produce fractures

TABLE 9.1 *Cleavage and shear planes for various structures and materials*⁽⁹⁰⁵⁾

Crystal structure	Example	Cleavage plane	Primary shear planes
BCC	Li, Na, K, Fe, most steels, V, Cr, Mn, Cb, Mo, W, Ta, Ti(B)	{100}	{112}, {110}
FCC	Cu, Ag, Au, Al, Ni, brass, 300 series stainless steels	None	{111}
HCP	Be, Mg, Zn, Sn, Ti (α), U, Cd, graphite	{0001}	{1122}, {1010}, {0001}
Diamond	diamond, Si, Ge	{111}	{111}
Rock salt	NaCl, LiF, MgO, AgCl	{100}	{110}
Zinc blend	ZnS, BeO	{110}	{111}
Fluorite	CaF ₂ , UO ₂ , ThO ₂	{111}	{100}, {110}

FIG. 9.3. Photographs of fractured steel specimens showing the fracture appearance for the following modes of fracture: (a) shear, (b) cleavage, (c) mixed shear and cleavage.⁽⁹⁰²⁾

that differ radically in macroscopic appearance. Figure 9.3 presents photographs of fractured steel specimens showing the fracture appearance for (a) shear, (b) cleavage, and (c) mixed shear and cleavage. Occasionally, different parts of the same specimen fail in different ways, resulting in a fracture with a mixed appearance.

The part failing by shear appears gray and silky, while the part failing by cleavage appears bright and granular.

Microscopic observations of fracture surface. Cleavage and shear produce fracture surfaces which are distinctively different under the electron microscope. Figure 9.4 is a cleavage fracture surface of a low carbon steel broken by impact at 78°K.⁽⁹¹²⁾ A cleavage fracture surface is characterized by what is called the “river pattern”. It is believed that the river pattern is caused by a transgranular cleavage fracture propagating on more than one level.^(905, 912)

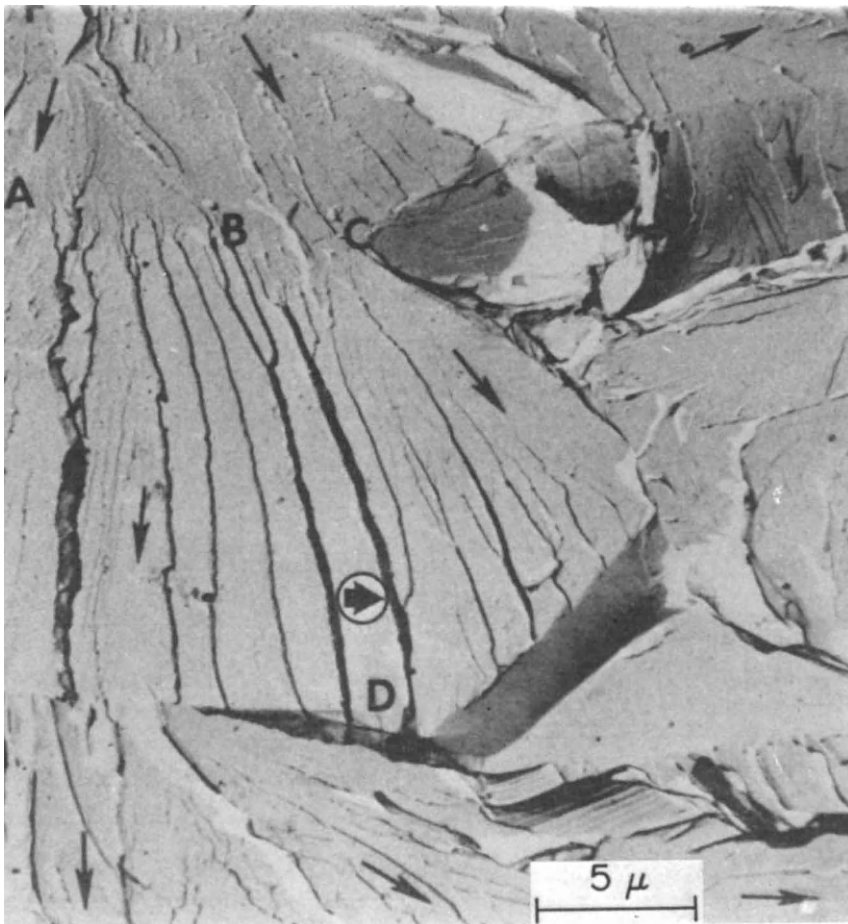


FIG. 9.4. Cleavage fracture surface of a low-carbon steel broken by impact at 78°K.⁽⁹¹²⁾ ABC is a grain boundary; BD is a typical river marking. The long arrows indicate local crack-propagation directions and the circled arrow indicates a cleavage step. Direct carbon replica. 5500X reduced in reproduction.

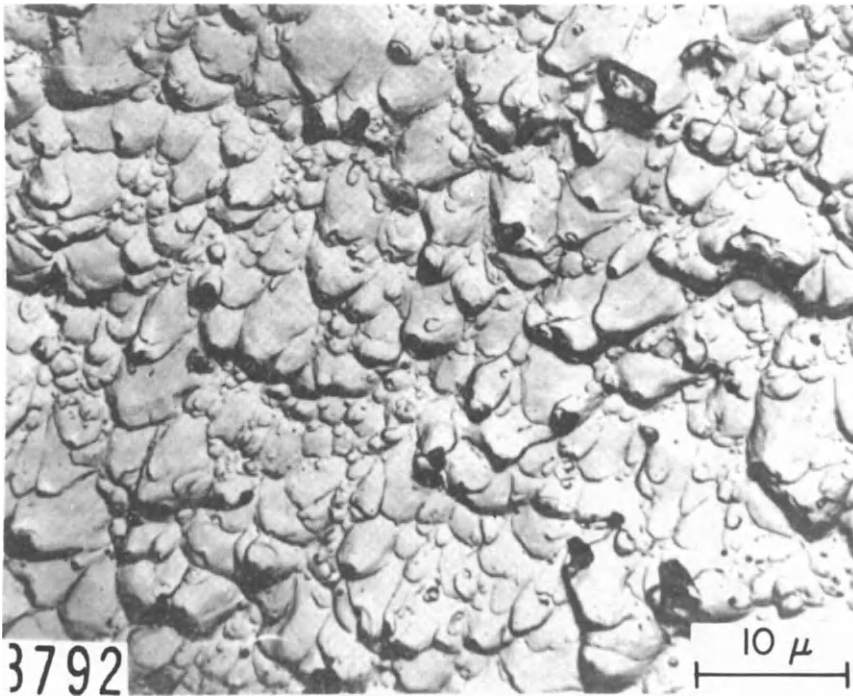


FIG. 9.5. Typical shear rupture dimples on surface of a shear lip in a steel specimen 3000X reduced in reproduction.^(9,12)

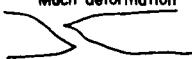
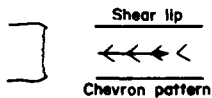

	Macroscopic	Microscopic about 50 X	Electron-microscopic about 5000 X
Ductile fracture	Much deformation 	Transgranular	Dimples
Brittle fracture	 Shear lip Chevron pattern	Transgranular	River pattern
Fatigue fracture	Very smooth  Striations	Transgranular	Striations
Stress corrosion cracking		Intergranular	
Creep fracture		Intergranular	
Hot tearing		Intergranular	

FIG. 9.6. Comparison of macroscopic and microscopic characteristics of various types of fracture.

Figure 9.5 shows the surface of a shear fracture in 4340 steel. The “equiaxed dimples” on the fracture surface are characteristic of a shear fracture.^(91,2)

9.1.3 *The different types of fractures compared*

Lest the above discussion sound too basic to have any bearing on practical problem-solving, it needs to be emphasized that when a fracture occurs one of the first things that must be done is determine its cause and origin.

Figure 9.6 compares the macroscopic and microscopic characteristics of six different types of fractures. This discussion will emphasize the first three: ductile fractures, brittle fractures, and fatigue fractures.

The first column summarizes the macroscopic characteristics of these fractures and they are discussed in Chapters 9 and 11 (see Figs. 9.3, 9.12, and 11.1).

Ductile, brittle, and fatigue fractures are transgranular, while stress corrosion cracking, creep fractures, and hot tearing are intergranular. Thus, one can conclude that intergranular fractures occur only at elevated temperatures or, in the case of stress corrosion cracking, in the presence of severe environments.

Under an electron microscope, ductile fractures exhibit the characteristic dimples (Fig. 9.5), brittle fractures the characteristic river markings (Fig. 9.4), and fatigue fractures the characteristic striations (Fig. 11.14), as discussed in Chapter 11.

9.2 **Brittle Fractures of Welded Structures**⁽¹⁰²⁾

The brittle fracture of structural steel has plagued engineers since about 1850, when steel first became available in quantities large enough for structural use.^(90,2) Brittle fracture does not occur only in welded construction, but also in riveted construction. Serious failures are more likely to occur in welded structures than in riveted structures, however, because:

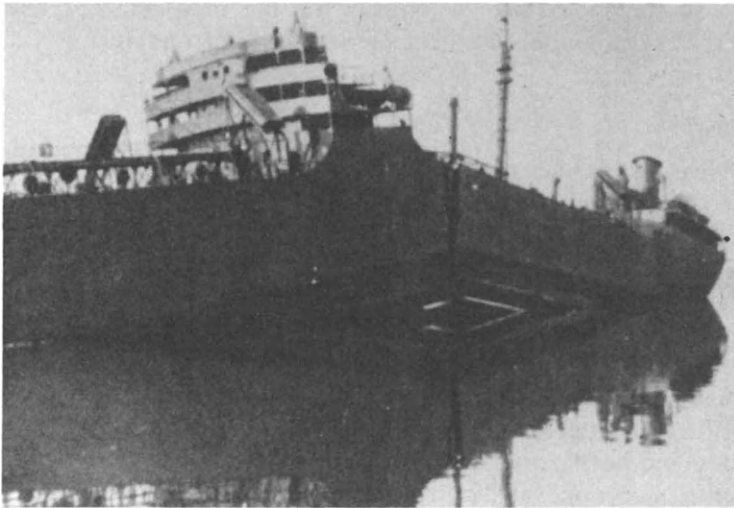
1. A welded structure does not have riveted joints which can interrupt the progress of brittle crack.
2. Welds may have various defects including cracks, slag inclusions, etc.
3. High tensile residual stresses in carbon steels and low-alloy high-strength steels may cause catastrophic brittle failures.

Parker’s book, entitled “Brittle Behavior of Engineering Structures”, cites a number of brittle fractures that have occurred in various structures including ships, bridges, storage tanks, pipelines, etc.^(90,2) The most extensive and widely known failures are those of cargo ships and tankers built in the United States during World War II.

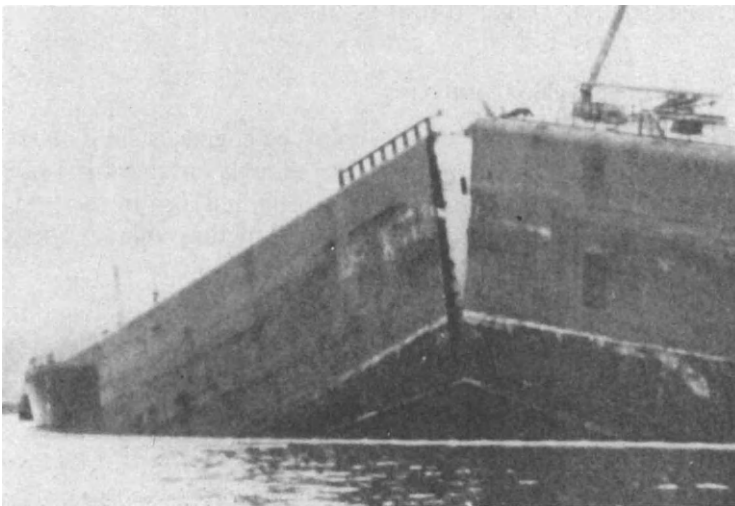
9.2.1 *Brittle fractures of welded ships*

To meet the urgent demand for a large number of ships needed for the war, the United States entered for the first time in history the large-scale production of welded ships. At that time, the technique of welding steel plates had been well established, but not enough was known about the design and fabrication of large welded structures and little about their fracture characteristics.

Ship failures began to occur in the winter of 1942–43. Figure 9.7(a) is a photograph of a



(a) T-2 Tanker Schenectady fractured in 1943



(b) Integrated Tug/Barge M. R. Ingram fractured in 1972

FIG. 9.7. Examples of Ships Completely Broken in Two⁽⁹¹⁵⁾

T-2 tanker, *Schenectady*, which fractured on 16 January 1943, at her fitting-out pier in Portland, Oregon. The failure occurred without warning. The sea was calm, the weather mild, her computed deck stress was only 9900 psi (7.0 kg/mm^2 or 68.3 MN/m^2).

The fracture extended across the deck just aft of the bridge and about midship; the break extended down both sides and around the bilges, but did not cross the bottom plating.⁽⁹⁰²⁾ The fracture transversed all girders and plating, thus almost completely severing the ship.

In April 1943 the Secretary of the Navy established the Board to Investigate the

Design and Method of Construction of Welded Steel Merchant Vessels. The Board issued a very comprehensive report in 1946.⁽⁹¹³⁾

Among approximately 5000 merchant ships built in the United States during World War II, about 1000 ships experienced a total of approximately 1300 structural failures of varying magnitudes before April 1946. Most of the ships were less than 3 years old.⁽⁹¹³⁾ Serious failures, such as the complete fracture of deck and bottom plating, occurred in about 250 ships. These numbers do not include casualties resulting from war damage or from external causes such as grounding or collision. About twenty ships either broke in two or had to be abandoned due to other kinds of massive structural failure. The details relating to these failures are presented in several readily available reports and books.

It was concluded from these early investigations that the fractures were a result of the brittle behavior of the steel and the presence of notches in the structure, either geometric notches or defects in welds.⁽⁹¹³⁾ Conventional factors of safety, based on the ultimate tensile properties of the steel as usually measured, which had heretofore proved satisfactory, did not seem to account for this type of failure.

Recommendations made as a result of these early investigations were mainly directed toward minimizing all forms of notch effects and toward improving the toughness of the steel. In 1948 the American Bureau of Shipping Specifications included notch-toughness requirements for hull steels by specifying the various grades and steel-making procedures. At the same time welding techniques and standards to minimize defects in welds were upgraded.

As a result of these improvements in design, materials, and fabrication, the number and extent of brittle fractures that have occurred in post-war welded or partially welded ships have decreased dramatically, though they have not disappeared completely. Between 1951 and 1953 two relatively new welded cargo ships and a welded tanker broke in two. In the winter of 1954 a longitudinally framed welded tanker in which an improved design, weld quality, and steel had been used also broke in two.⁽⁹¹⁴⁾

In January of 1972 the large integrated tug/barge *M. V. Martha R. Ingram* broke in two and sank in Port Jefferson Harbor, Long Island, New York (see photo in Fig. 9.7(b)).⁽⁹¹⁵⁾ The 620-ft (189 m) ship, which had cruised unscathed through two hurricanes, was only 9 months old when the fracture occurred.

9.2.2 Brittle fractures of structures other than ships

Brittle fractures in large structures made of medium carbon structural steel are not uncommon. Shank^(916, 917) conducted an extensive survey of brittle fractures in structures other than ships. His report, published in 1954, covers sixty-four structural failures in both riveted and welded structures, including tanks, bridges, pressure vessels, power shovels, gas transmission lines, a smoke stack, and a penstock.

In October 1886 a failure occurred during the hydrostatic testing of a riveted standpipe 250 ft (76 m) high in Long Island, New York. A vertical crack about 20 ft (6 m) long appeared at the bottom and the tower immediately collapsed. In January 1919 a riveted molasses tank in Boston, Massachusetts, fractured killing twelve persons and injuring forty others.^(902, 917)

In March of 1938 the Vierendeel truss bridge over the Albert Canal in Hasselt, Belgium, a welded structure only about a year old broke into three pieces and fell into the canal. In January of 1940 two other welded bridges over the Albert Canal suffered structural

damages although they did not collapse.⁽⁹⁰²⁾ In January 1951 the Duplessis Bridge in Quebec, Canada, suddenly collapsed and fell into the river. King's Bridge in Melbourne fractured in July (winter in Australia) 1962 when the bridge was only 1 year old. One span collapsed as a result of cracks that had developed in a welded girder made of BS968 grade (high-tensile) steel.⁽⁹¹⁸⁾ Failures have also occurred in storage tanks, pressure vessels, and transcontinental natural-gas transmission lines. Many of these failures occurred during pressure testing, and often were due to defective welding.⁽⁹⁰²⁾

Failures have occurred in high-strength steel members in military ships, aircraft, and rockets. Figure 9.8 shows the fractured pieces of a 260-in. (6.6-m) diameter rocket motor case which failed in April of 1965 during a hydrotest.⁽⁹¹⁹⁾

The pressure at the moment of failure was 542 psi (38 kg/m²), only about 56% of the proof pressure. The motor case was constructed of 250 grade maraging steel plate joined mostly by submerged-arc welding.

During an investigation of the failure, a defect that had not been detected by non-destructive testing techniques prior to aging was discovered. Non-destructive testing had not been conducted between aging and the hydrotest. The defect had indeed caused the failure and was in the heat-affected zone of a longitudinal submerged-arc weld on the cylindrical section of the motor case. The area where the defect was located had been repaired by a manual gas-tungsten arc (GTA) weld. The defect was submerged within the vessel wall and was oriented longitudinally. It was approximately 1.4 in. (36 mm) long and 0.10 inch (2.5 mm) wide. Four other undetected defects of significant size were also discovered, all of which were also located beneath manual GTA weld repairs. One of these defects was in the same longitudinal weld as the defect causing the motor case failure and was a secondary origin of the fracture. The others were discovered during reinspection of all welds by non-destructive testing techniques after hydroburst.

Figure 9.9 shows in detail the immediate vicinity of the primary and secondary origins. The inset sketches show the shapes and dimensions of the two origins. Figures 9.10 and 9.11 show the fracture surfaces near the two origins.

9.2.3 *Characteristics of brittle fractures*

Brittle fractures in welded structures of various types have the following characteristics:

1. *Fracture appearance.* The surface of a brittle fracture is a plane that is approximately perpendicular to the plate surface and is granular in appearance. The thickness near the fracture surface has been reduced very little, ordinarily less than 3%.

The same material does not prove to be brittle when tensile tests are conducted on ordinary specimens (round bars and flat plates with no notch). Steel plates generally fracture in the shear mode only after a considerable amount of plastic deformation has taken place.

A brittle fracture surface ordinarily contains chevron markings (see Fig. 9.12), which point back to the origin of the flaw responsible for fracture initiation. In the investigation of an actual failure, chevron markings provide important information about fracture initiation and propagation.

The illustration on the right in Fig. 9.12 shows a cross-section of a plate near the fracture surface. A considerable amount of deformation usually takes place in the areas near the surfaces of the plate, and are designated shear lips.

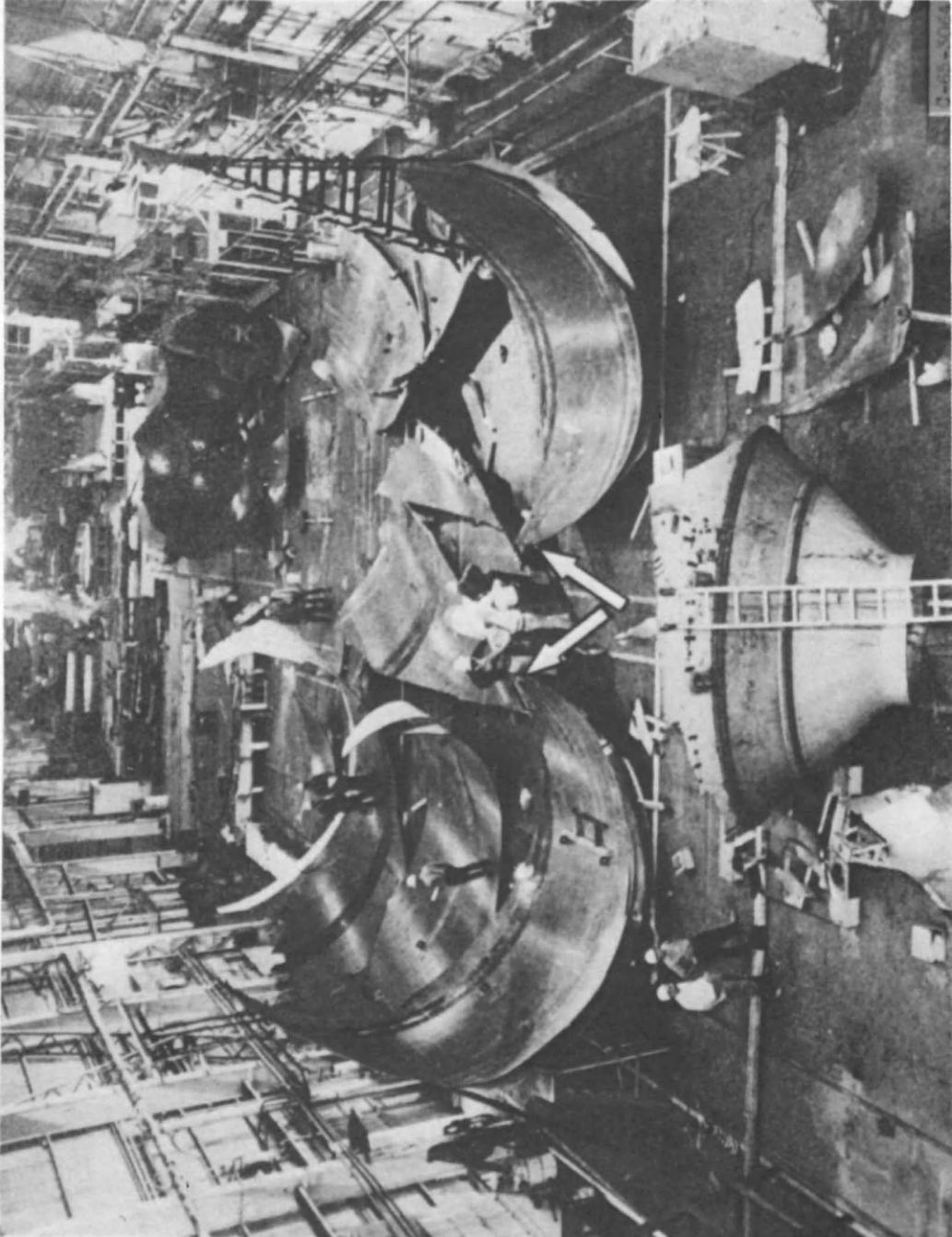


FIG. 9.8. Failed motor case with pieces laid out in approximately the proper relation to each other. View is looking forward with aft head in foreground. Origin of fracture is indicated by arrows.

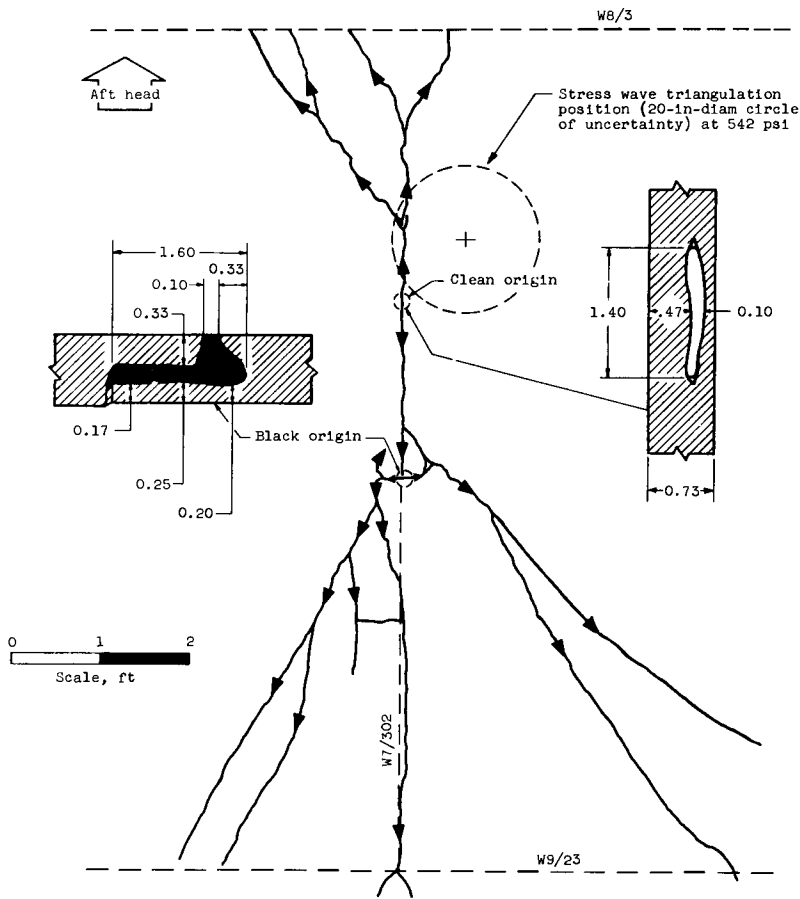


FIG. 9.9. Details in immediate vicinity of primary and secondary origins. Inset sketches show shapes and dimensions of the two origins.

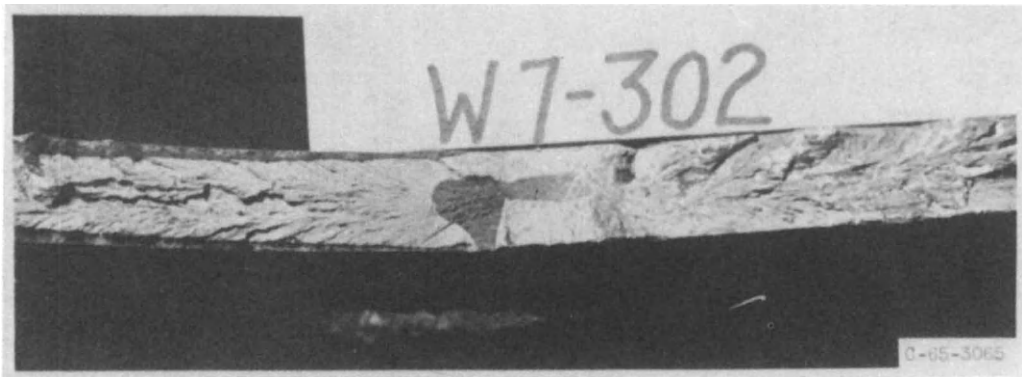


FIG. 9.10. Typical chevron markings on fracture surface showing directions of fracture propagation away from black origin.

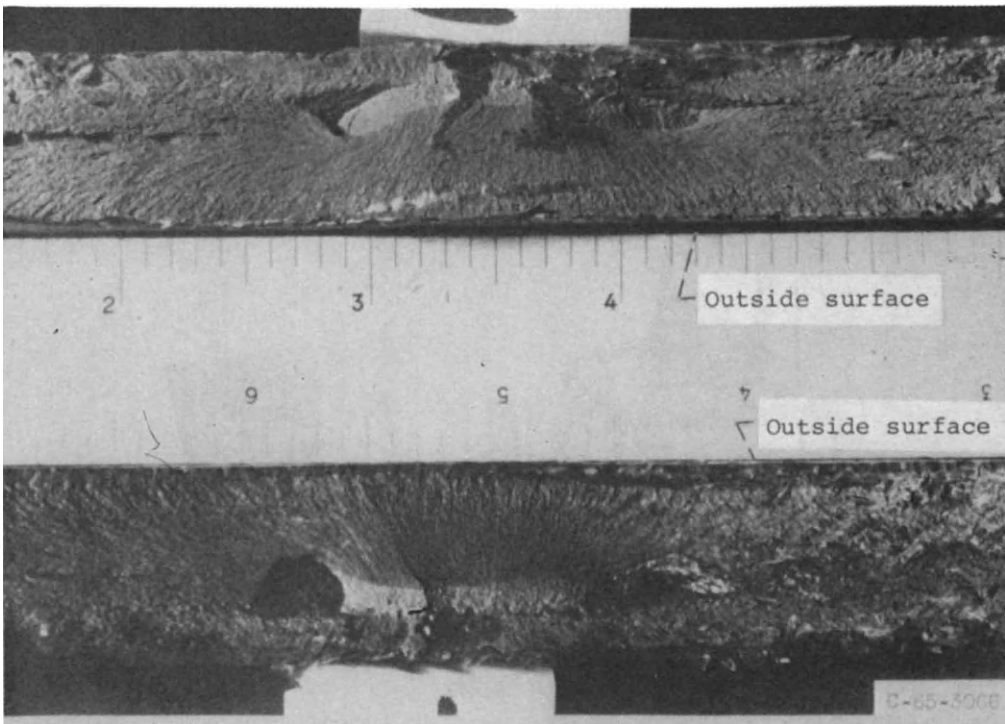


FIG. 9.11. Mating surfaces near the fracture origin on W7/302 weld.

2. *Temperature.* Most brittle failures occur during cold winters. In the case of brittle failures in ships during World War II temperatures involved were as high as 70°F (21°C) though the probability of such failures at that temperature is small accordingly to the analysis by Acker.⁽⁹⁰²⁾

3. *Stress at failures.* According to the statistics about brittle failures of ships during World War II, more failures occurred in heavy seas than in moderate and calm seas, though a number of failures occurred when the average stress in the structure was well below the yield stress of the material. The *Schenectady*, a T-2 tanker, fractured completely when the calculated stress at the deck was only 9900 psi (7.0 kg/mm² or 68.3 MN/m²).⁽⁹⁰²⁾ It is a characteristic of brittle fracture that a catastrophic fracture can occur without any general yielding and under a low average stress.

4. *Origins of failures.* According to a statistical investigation of failures of American ships built during World War II, about 50% of the failures originated from structural

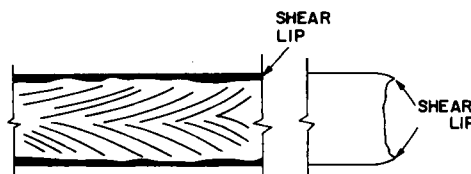


FIG. 9.12. Brittle fracture surface.

discontinuities, including square hatch corners, cutouts in shear strakes, ends of bilge keels, etc.^(9,20) About 40% of the failures started from weld defects including weld cracks, under-cuts, and lack of fusion. The remaining 10% of the failures originated from metallurgical defects such as the weld heat-affected zones and notches in flame-cut plate

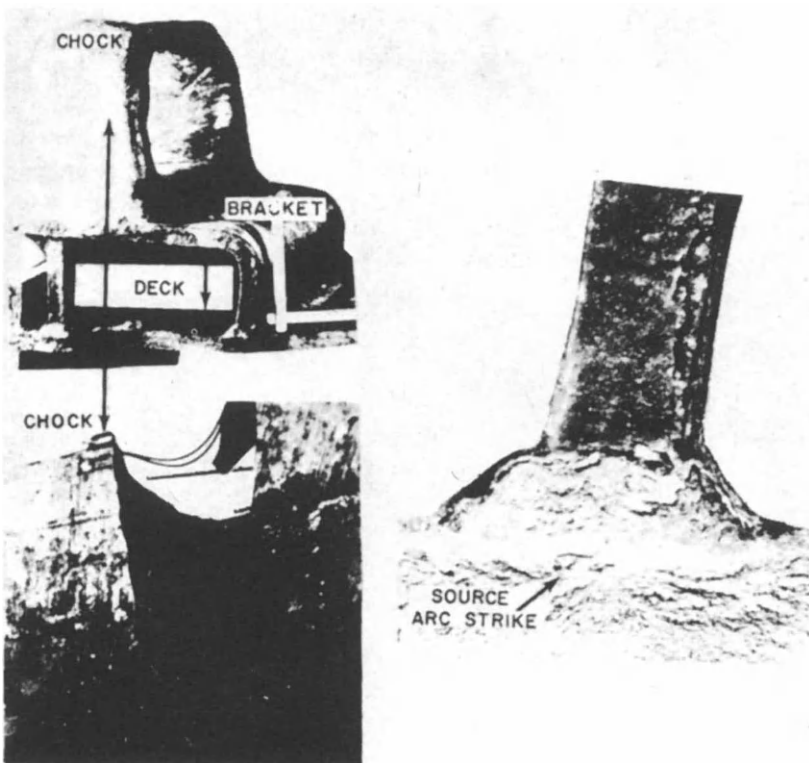


FIG. 9.13. Typical ship fracture which originated from an arc strike located in a region of high weld residual stress.^(1,12) The ship was the U.S.S. *Ponagansett* which fractured completely at dockside in Boston Harbor at a temperature of 35°F (2°C).

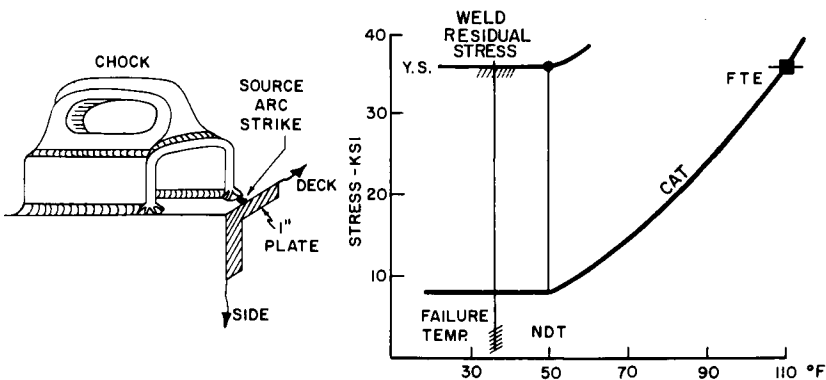


FIG. 9.14. Analysis of fracture initiation conditions of the U.S.S. *Ponagansett*^(1,12)

edges. In other words, all failures originated from notches that were causing severe stress concentrations.

A number of serious failures started from unimportant, incidental welds such as tack welds and arc strikes made on a major strength member. For example, a tanker, *Ponagansett*, broke in two in Boston Harbor in December 1947.⁽¹¹²⁾ The fracture initiated from a tack weld between a small clip and the deck plate (see Fig. 9.13). The Nil Ductility Transition (NDT) temperature of the material was 50°F (10°C), while temperature at the failure was 35°F (2°C) (see Fig. 9.14).

5. *Fracture propagation.* In most cases the fracture propagates in the base plate. Fractures seldom propagate in the weld metal or along the heat-affected zone in carbon steel structures.

Fractures in the deck or bottom plates of ships ordinarily propagate in the transverse direction because the major stresses in the hull of a ship are longitudinal.

A brittle fracture in a long pipe propagates in a rather unique manner, in most cases travelling down the longitudinal axis of the pipe in a fairly regular sinusoidal pattern with the wavelength of 3 ft (1 m) or so (see Fig. 9.15).⁽⁹⁰²⁾

Brittle fractures usually propagate at high speed. In fracture tests done on pipelines, propagation speeds of around 3000 ft (1000 m) per second have been observed.⁽¹⁰²⁾ Table 9.2 shows some brittle fracture velocity measurements in steel.^(921, 922) The observed crack speed, V , is compared with the speed of longitudinal sound waves in

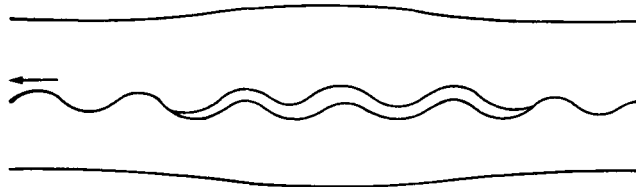


FIG. 9.15. Sinusoidal pattern of cleavage fracture of pipeline.

TABLE 9.2 Brittle fracture velocity measurements in steel^(921, 922)

Steel	Specimen identification	Test temp. (°C)	Mean applied stress (kg/mm ²)	Crack speed V (m/sec)	$V/C_0^{(c)}$
HT50 ^(a)	D	-40	20	1960	0.32
	B	-40	15	1600	0.26
	J	-30	20	1680	0.27
	C	-30	15	1440	0.23
	K	-20	15	1400	0.23
	E	-50	20	1800	0.29
MS ^(b)	1	-36	20	1300	0.21
	2	-43	25	1500	0.25
	4	-31	15	1050	0.17
	5	-42	15	1260	0.20
	6	-20	15	800	0.13

^(a) HT50: High-strength steel with 50 kg/mm² ultimate tensile strength.

^(b) MS: Mild steel.

^(c) $C_0 = \sqrt{\frac{E}{\rho}} = 5020$ m/sec.

the medium, C_0 :

$$C_0 = \sqrt{\frac{E}{\rho}}$$

where

$$E = \text{Young's modulus,}$$

$$\rho = \text{density}$$

In the case of steel, $C_0 = 5020$ m/sec (16,500 ft/sec). The observed values of V/C_0 range from 0.13 to 0.32. It has been known that the theoretical upper limit of V/C_0 is 0.38.

9.3 Evaluation of Notch Toughness

To avoid brittle fractures in a welded structure, the material used must have adequate notch toughness.

9.3.1 Notch sensitivity and transition temperature⁽¹⁰²⁾

Low carbon steel exhibits good ductility when an ordinary tensile specimen is tested. When the steel contains a sharp notch and the temperature is low, however, a crack may initiate from the notch, causing brittle fracture of the plate. Such a phenomenon is called "notch brittleness".

The temperature at which the mode of fracture changes from shear to cleavage is called the "transition temperature". The transition temperature is often used as a parameter to express the "notch sensitivity", or the sensitivity of a material to notch brittleness. The term "notch toughness", which indicates the resistance of a material against notch brittleness, also is often used as an antonym of notch sensitivity. The following sentences show how these terms are used:

"In order to avoid brittle fracture of a structure, it is necessary:

- (a) 'That the transition temperature of the material used is lower than the lowest anticipated service temperature of the structure.'
- (b) 'That the material does not show notch brittleness under the service temperature.'
- (c) 'That the material is not notch sensitive.'
- (d) 'That a material with good notch toughness is used.'

Although the transition temperature is widely used as a measure of the notch sensitivity of a material, it is not a definite and fixed temperature for each material. In most cases, the brittle-to-ductile transition takes place over a range.

Furthermore, the transition temperature of a material depends upon a number of factors including the size and shape of the specimen used, the type of loading (tensile, bending, etc.), and the loading speed (static or dynamic).

A material may exhibit a sharp transition over a narrow temperature range in one test, and a gradual transition over a wide temperature range in another. The actual transition temperature of a material may differ from test to test. Even when the same test is used, the transition temperature may differ depending upon the criteria used (absorbed energy, mode of fracture, etc.).

Tremendous efforts have been made in the last 30 years by a number of investigators all over the world to find a simple test that is suitable for evaluating a material's resistance to brittle fracture in a welded structure. Although many tests have been proposed, no test has as yet been selected by a majority of the investigators as the most appropriate. Consequently, when stating the transition temperature of a material, it is very important to describe the test method and the criterion used.

Among the many tests for notch toughness that have been proposed, the Charpy impact tests have been the most widely used, especially in commercial applications. The U.S. Navy uses extensively the drop-weight test and the drop-weight tear test (recently renamed the dynamic tear test). Both were developed at the Naval Research Laboratory.

9.3.2 Charpy impact tests^(102,923)

The details of the Charpy impact-testing procedures have been specified by the American Society for Testing Materials. The test uses a notched bar 10 mm square and 55 mm long (0.394 in. square and 2.105 in. long). ASTM specification E23-60 covers three types of notches: (1) V-notch, a 45 vee-shaped notch 2 mm (0.079 in.) deep, (2) keyhole notch, and (3) U-notch, 5 mm (0.197 in.) deep. Figure 9.16 shows the V-notch and the keyhole notch Charpy specimens and the method of supporting and striking the specimen.

A V-notch is smoothly machined with a special milling cutter, a carbide-tip cutter, of a specially prepared grinding wheel. It is important to prepare the root of the notch in an exact shape in order to avoid scattering of experimental data.

The Charpy impact tests, especially with the V-notch specimen, are widely used in the United States, Western European countries, and Japan. In Russia and other Eastern

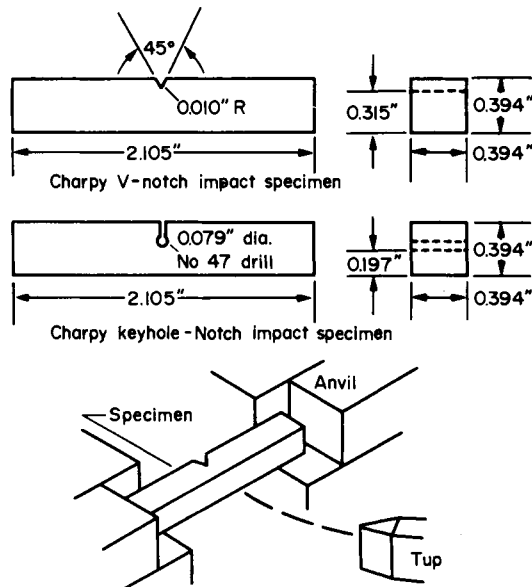


FIG. 9.16. Charpy impact test.

European countries, the Mesnager specimen is used. This is essentially a Charpy-type specimen with a 2-mm (0.079-in.) deep U-notch. Because of the difference in the notch shapes used in the V-notch Charpy and the Mesnager specimens, direct comparisons of data obtained in the Western world and those obtained in the Eastern world are difficult.

Figure 9.17 shows three common ways of preparing Charpy V-notch specimens from a plate. In Case 1, the specimen axis is parallel to the rolling direction of the plate and the notch is in the thickness direction. In Case 2, the specimen axis is perpendicular to the rolling direction and the notch is in the thickness direction. In Case 3, the notch is parallel to the plate surface.

Specimens may be taken from the midthick part of the plate as shown in Figure 9.17, or they may be taken in areas close to the plate surface. Case 1 is the most commonly used for evaluating notch toughness of steel.

To obtain a Charpy curve, specimens are tested over a range in temperature. In conducting tests at other than room temperature, specimens are usually placed in a liquid bath to attain the desired temperature and then placed in an impact testing machine and struck with a pendulum. The energy absorbed by the specimen in fracturing is measured, and the percentage of the fracture area that is cleavage or shear can be determined.

Figure 9.18 shows an example of test results on low carbon steel (carbon 0.23%, manganese 0.46%, silicon 0.05%). Shown here are:

1. Absorbed energy, in foot-lb.[†]
2. Lateral contraction at the notch root, percent.
3. Percentage of fracture surface area in fibrous appearance.

There are several criteria that have been used to interpret the results and determine the transition temperature:

1. The temperature at which the amount of energy absorption decreases to one-half (or some other fraction) of the maximum amount at high temperature. TrE in Fig. 9.18.
2. The temperature at which lateral contraction at the notch root rapidly decreases

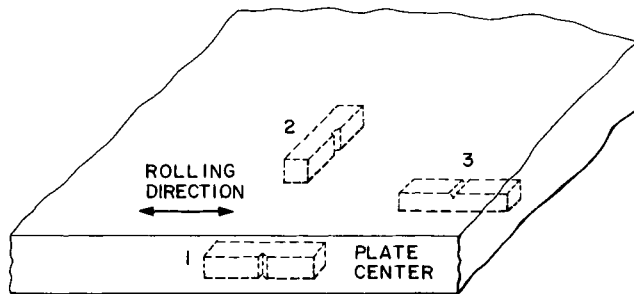


FIG. 9.17. Methods for preparing Charpy V-notch specimens from a plate.

[†] The Charpy V-notch absorbed energy is given by ft-lb or kg-m. The specific absorbed energy per square centimeter of sectional area (0.8 cm^2), kg-m/cm^2 , also is often used.

$$1 \text{ ft-lb} = 0.138 \text{ kg-m} = 0.174 \text{ kg-m/cm}^2.$$

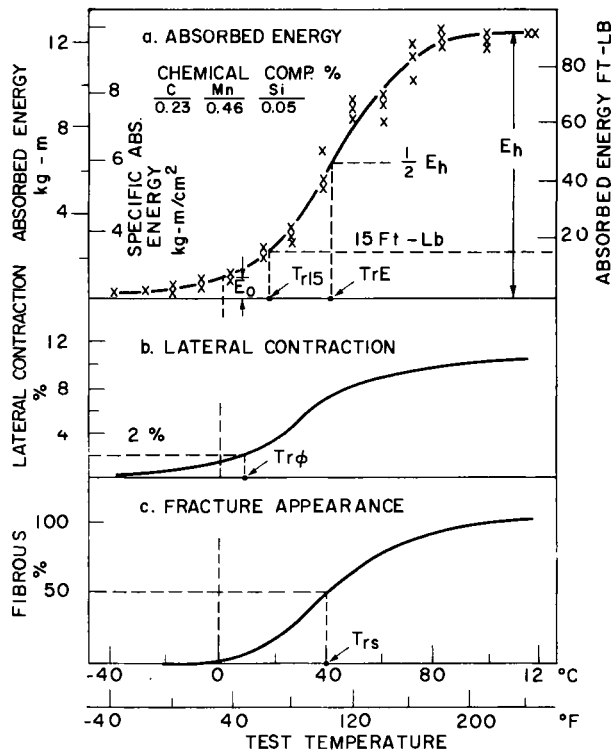


FIG. 9.18. Example of Charpy V-notch impact test data.

or the temperature which corresponds to a given amount (2%, for example) of the lateral contraction. $Tr\phi$ in Fig. 9.18.

3. The temperature which corresponds to a 50% fibrous fracture appearance. Tr_s in Fig. 9.18.
4. The temperature which corresponds to a given energy level (15 ft-lb, for example). Tr_{15} in Fig. 9.18.

The value of absorbed energy at a given temperature (32°F, for example) is also often used as a parameter to express the notch toughness of the material.

9.3.2 Use of Charpy impact test data for evaluating notch toughness of steel

The best criterion to evaluate the adequacy of a material for use in a welded structure is still a matter of controversy among investigators. Many studies have been conducted to determine the correlations between the service behaviors of welded structures and the results of laboratory tests which include Charpy V-notch impact tests.

NBS study on ship failures. In an extensive study carried out at the National Bureau of Standards on fractures in ships used during World War II, a correlation was obtained between Charpy V-notch impact test data and the characteristics of ship failure.^(920, 924) Figure 9.19 shows the data spread of Charpy impact fracture tests of ship steel. The

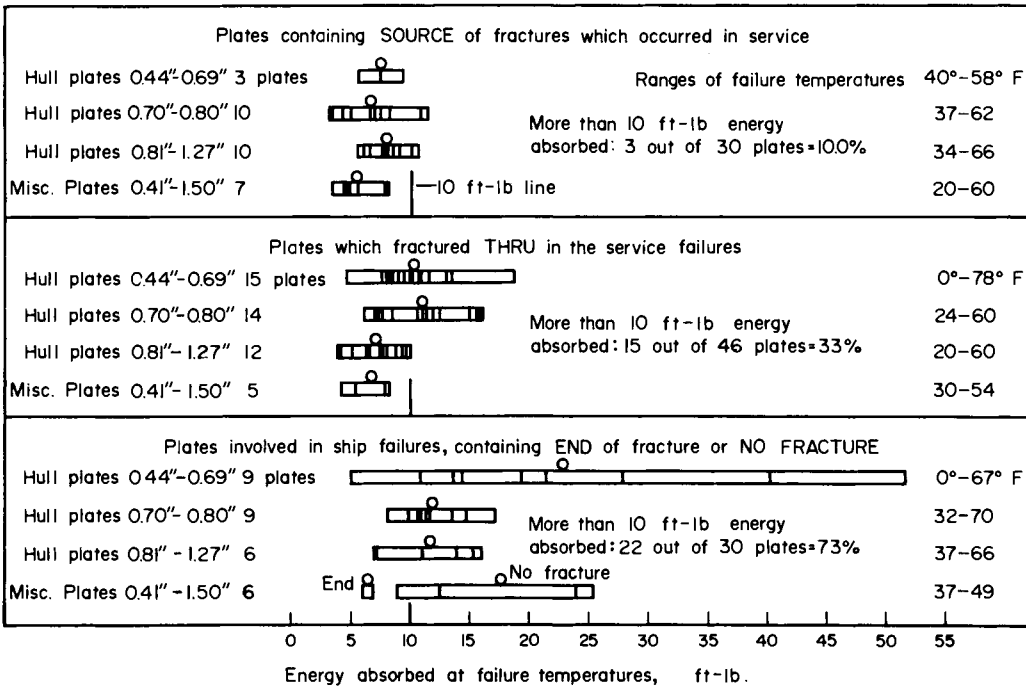


FIG. 9.19. Relation of energy absorbed by Charpy V-notch specimens at the temperature of the ship failures to the nature of the fracture in the ship plates.⁽⁹²⁰⁾ Vertical lines in the bars indicate values for individual plates. Circles above bars indicate average value for each group of plates.

Charpy V-notch impact tests show that plates in which fractures originated (source plates) were generally more sensitive than plates in which fractures did not originate (through and end plates). The correlation showed:

1. Only 10% of the fracture source plates absorbed more than 10 ft-lb (1.4 kg-m) at the failure temperature.
2. Thirty-three percent of the fracture through plates absorbed more than 10 ft-lb (1.4 kg-m) at the failure temperature.
3. Seventy-three percent of the fracture end plates absorbed more than 10 ft-lb (1.4 kg-m) at the failure temperature.

No relation was found between service performance and the tensile properties of the steel.

Based upon the above findings, Williams^(920, 924) proposed that the 15 ft-lb (2 kg-m) transition temperature (Tr_{15} in Fig. 9.18) be used to evaluate the adequacy of carbon steel for welded ships.

Study at Lloyd's.⁽⁹²⁵⁾ In 1958 Hodgson and Boyd⁽⁹¹⁴⁾ of Lloyd's Register of Shipping analyzed numerous brittle failures in several kinds of ships. On the basis of their detailed investigation, they proposed a 35-ft-lb (4.8 kg-m) Charpy V-notch (CVN) impact criterion coupled with a 30% fibrous-fracture appearance at 32°F (0°C) for steels used in welded ship hulls. In Fig. 9.20 their criterion is placed alongside the results of numerous ship failures. Their definition of success, failure, or borderline plates is as follows:

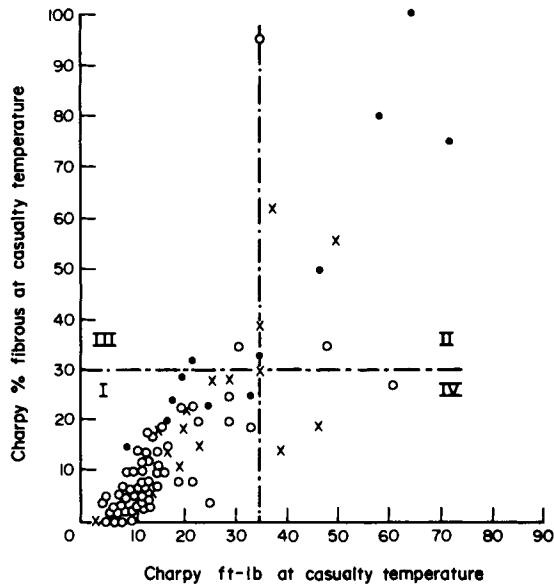


FIG. 9.20. Comparison of Boyd's (Lloyd's) 35 ft/lb and 30% fibrous-fracture-appearance criteria with test results from actual ship failure.^(9,14)

Legend: ○ Plates from hulls that failed in service.
 × Plates from hulls with borderline performance.
 ● Plates from hulls with successful performance.

1. "Success" plates are those which fractured in a ductile manner, or those in which a brittle fracture originating outside the plate was arrested.
2. "Failure" plates are those which were completely traversed by a brittle fracture.
3. "Borderline" plates are those which cannot be classified in either of the above groups.

The results of their analysis showed that only two plates which met both the 35 ft-lb (4.8 kg-m) and 30% fibrous-fracture-appearance criterion, Quadrant II, Fig. 9.20, could be classified as failure plates. Thus their criterion appeared to be very satisfactory and was proposed to Lloyd's. The 35-ft-lb (4.8 kg-m) requirement was accepted (for ABS Grade D steels), but the 30% fibrous requirement was not, although the percent of fibrous fracture is recorded for information.

The 30% fibrous-fracture requirement (which insures the presence of some shear) does have significance in that it implies that the material is performing at a temperature somewhat above that at which it is normally 100% brittle. In this regard, it is consistent with the requirement of the proposed criterion that NDT be 32°F (18°C) below the minimum service temperature. Because fibrous-fracture appearance is difficult to judge accurately, particularly with higher-strength steels, such requirements have never been widely accepted. Thus specifying that NDT be 32°F (18°C) below the service temperature is an indirect means of insuring some level of fibrous fracture and appears to be a more feasible criterion.

NRL studies. Pellini and associates conducted a series of critical studies on the usefulness of the Charpy V-notch impact test.^(1,12)

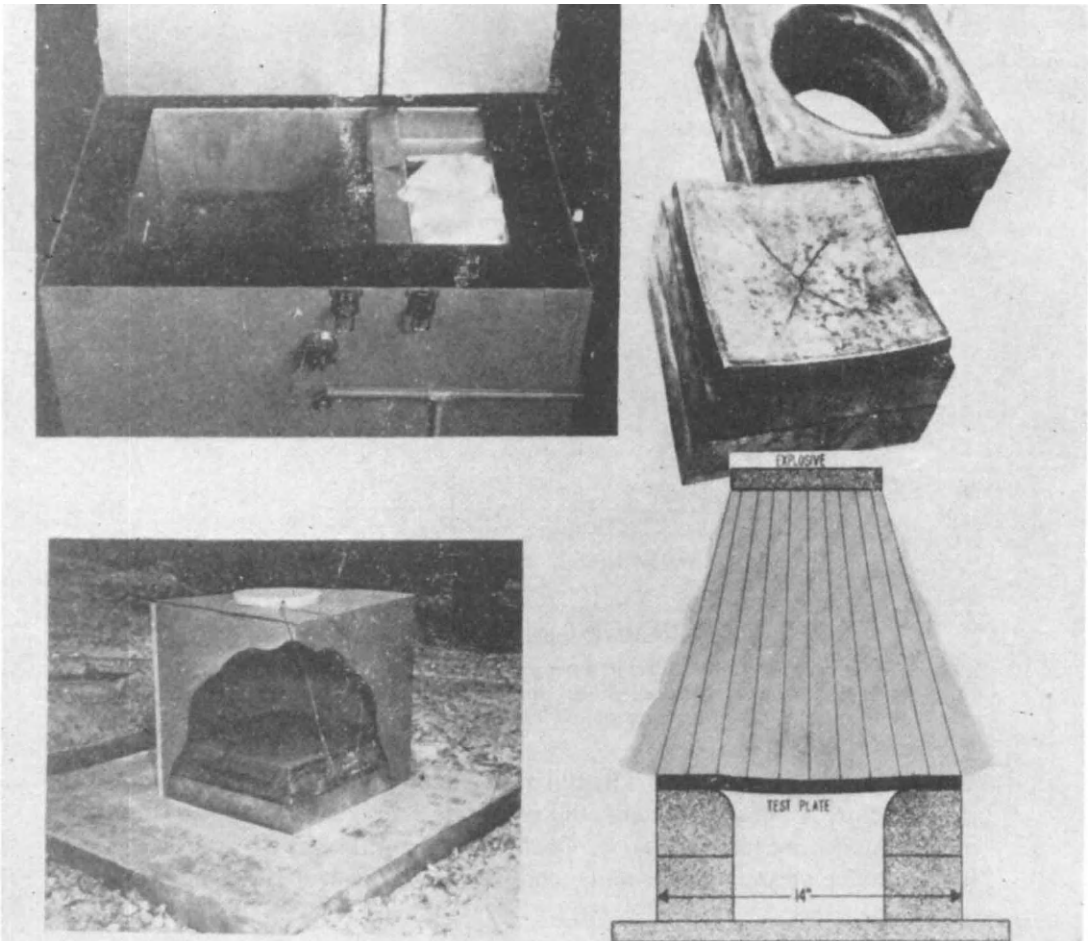


FIG. 9.21. Explosion-crack-starter test setup.

The explosion crack starter test was used as a method to simulate the service performance of steels. The test was developed to determine the fracture-propagation characteristics of steel when fracture initiation is forced. A plate was prepared for testing by depositing a short bead of brittle, hard-surfacing weld metal which was then notched to half the thickness of the deposit by means of a disk abrasive wheel. The test was performed by bulging 14 × 14-in. (356 × 356-mm) plate over a die, as shown in Fig. 9.21.

The explosive charge, standard 4-lb (1.8 kg) pentolite, was used at a high standoff of 24 in (610 mm) for $\frac{3}{4}$ - and 1-in. (19- and 25-mm) plate. The series of tests, conducted over a range of temperature, indicated that, with increasing temperature, fractures change from (1) “flat breaks”, indicating little or no deformation prior to fracture, to (2) “bulge breaks”, featuring forced initiation but easy propagation through the elastically loaded edge section, to (3) breaks limited to the plastic load region at the center, and finally to (4) ductile tears.

Figure 9.22 illustrates a typical correlation between fracture performance in the

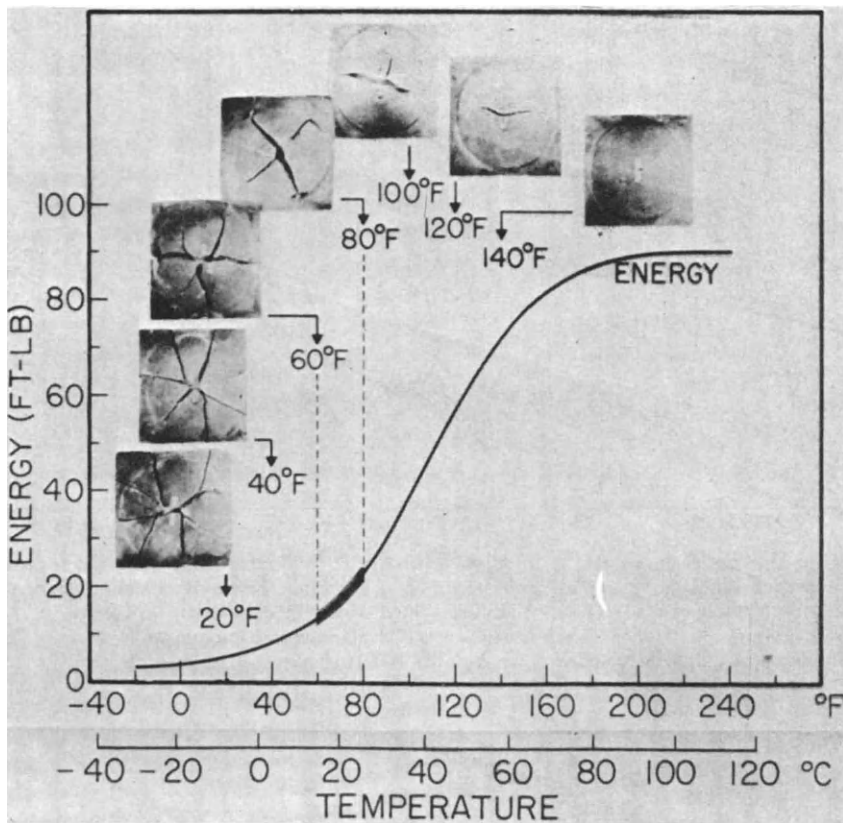


FIG. 9.22. Typical correlation of explosion crack starter test performance with Charpy V-notch transition curves for ship fracture steels. Flat break (NDT) fractures are obtained at temperatures below the 10 ft-lb transition temperature. Arrest characteristics are developed in the range indicated by the solid band which spans the 10 to 20 ft-lb transition temperature range. Full ductility is attained on approach to shelf temperatures.

explosion crack starter test and the Charpy V-notch transition curve taken from fractured ships. The transition from ductile fracture to brittle fracture (or flat break) occurred at temperatures which corresponded to 10 to 20-ft-lb of (1.4 to 2.8 kg-m) of absorbed energy in the Charpy V-notch test. The results indicate the adequacy of the Charpy V-notch 15-ft-lb transition temperature for evaluating notch toughness of low carbon steels.

Pellini and associates expanded their studies to cover several different steels including improved carbon steels, high-strength quenched-and-tempered steels, and intermediate strength low-alloy bainitic steels.⁽¹¹²⁾ The results are summarized in Fig. 9.23. It was found that NDT temperatures corresponded to Charpy impact test temperatures at energy values much higher than 15 ft-lb (2 kg-m). Also, the corresponding energy values varied greatly, depending upon steel types.

On the basis of the above findings, Pellini and associates at the Naval Research Laboratory have developed the drop-weight test and the drop-weight tear test (recently renamed the dynamic tear test).

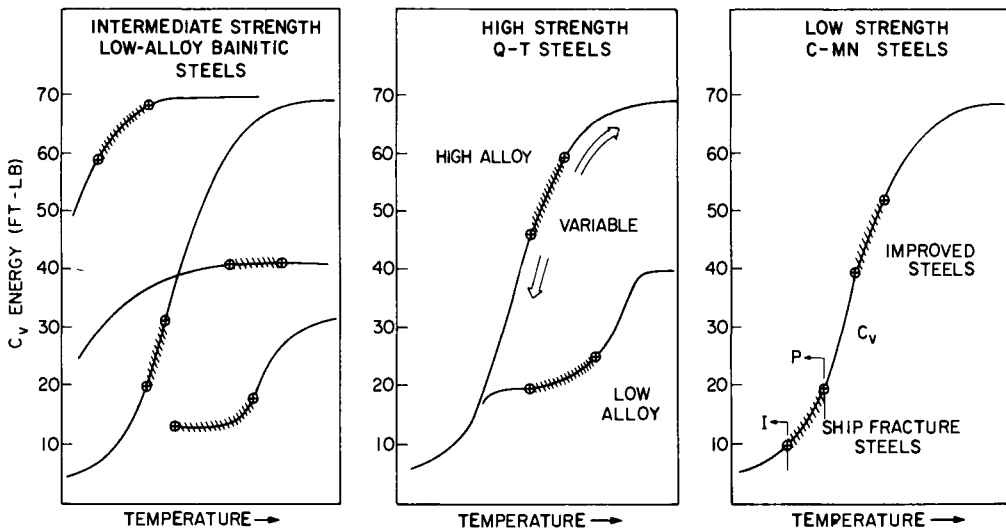


FIG. 9.23. Complications in the interpretation of Charpy V-notch impact test transition temperature range curves for different steels.⁽¹¹²⁾ The relative positions of the initiation to arrest correlation bands (NDT to FTE) are shifted widely in comparison to the toe region position of the Charpy V-notch curve which was typical of the ship fracture steels. The correlations for improved ship steels (C-Mn steels) are displaced to higher relative position of the Charpy V-notch curve. More complex relationships are indicated for steels of over 50 ksi (35 kg/mm²) yield strength.

9.3.4 Drop-weight test⁽⁹²⁶⁻⁹²⁸⁾

The drop-weight test was developed at the Naval Research Laboratory in 1952 and has been used extensively to investigate the requisite conditions for initiation of brittle fractures in structural steels. Drop-weight test facilities have been established at several naval installations, research institutions, and industrial organizations in this country and abroad. The method is used for specification purposes by industrial organizations and is referenced in several ASTM specifications and the ASME Boiler and Pressure Vessel Code. ASTM E208-69 provides the standard method for conducting drop-weight tests to determine nil-ductility transition (DNT) temperature of ferritic steels.⁽⁹²⁶⁻⁹²⁸⁾ The type of specimen and the method of test are shown in Fig. 9.24. The test procedure consists of dropping a weight on a rectangular flat-plate specimen containing a crack starter of a notched, brittle, hard-surfacing weld bead. This procedure is employed over a range of specimen temperatures. The specimen support is provided with a stop such that the maximum angle of bend of the specimen is 5 degrees. The crack starter weld develops a cleavage crack when the bend deformation reaches 3 degrees, which corresponds to incipient yielding. The additional 2 degrees of bend (dynamic bend) allowed by the stop provides a test of the ability of a metal to develop deformation in the presence of an extremely sharp notch.

Interpretation of test results. The major purpose of the test is to determine the nil-ductility transition (NDT) temperature, which is defined as the maximum temperature where a standard drop-weight specimen breaks when tested according to the provisions of this method.

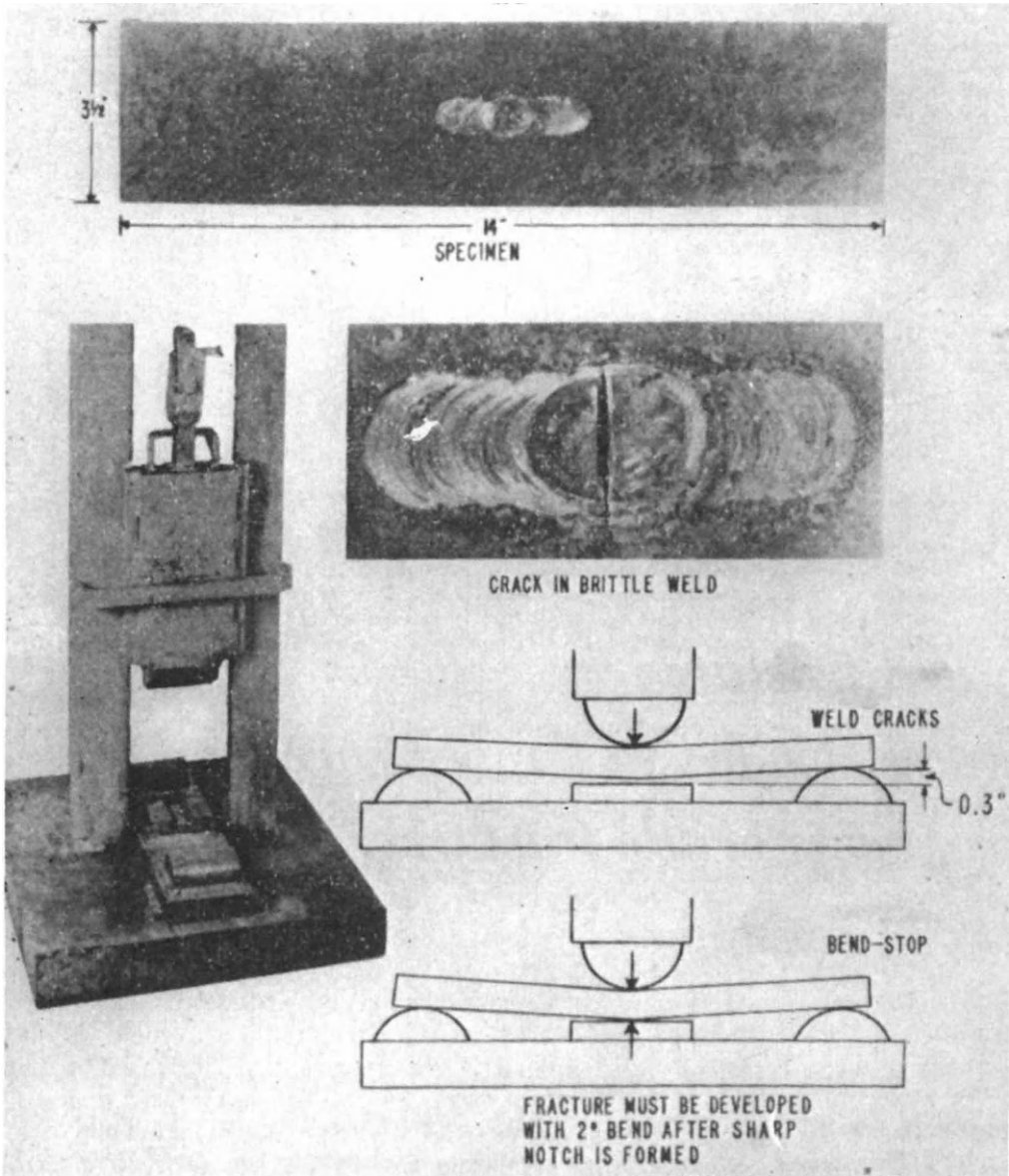


FIG. 9.24. NRL drop weight test.^(102, 923, 927)

The NDT temperature can be related to the fracture analysis diagram (FAD), as shown in Fig. 9.25, proposed by Pellini.^(927, 928) The FAD provides a generalized definition of the flaw size, relative stress, temperature relationships by a " Δt " or "temperature increment" reference to the NDT temperature. In order to locate the generalized diagram in a specific position on the temperature scale a single parameter needs to be determined. The NDT temperature of a material can be determined by the drop-weight test or the dynamic tear test.

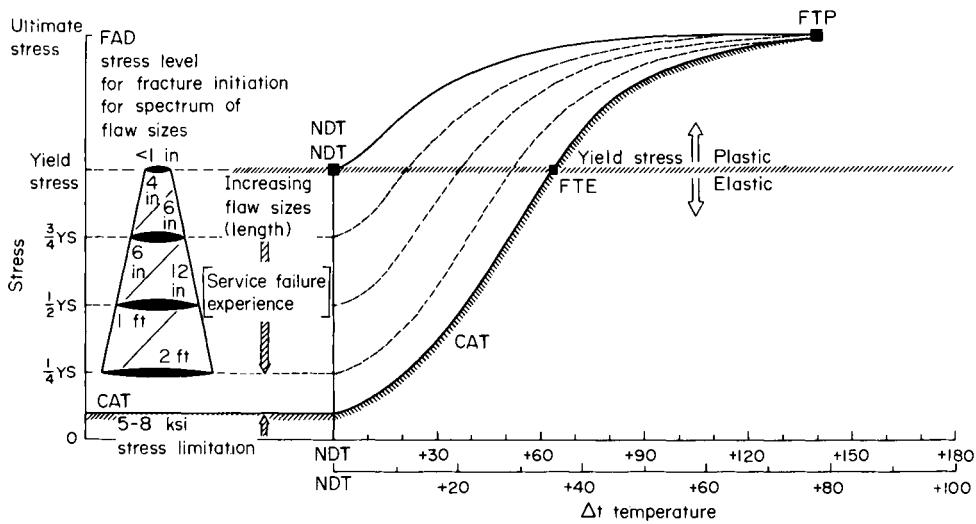


FIG. 9.25. Fracture analysis diagram (FAD). Note that the stress level for plastic (over yield) fracture is not indexed because of the lack of analytical procedures for its definition. Ultimate stress signifies only that maximum load and strain tolerance is attained at FTP for the specific flaw size cited. It obviously does not indicate the equivalent of the tensile test specimen maximum load of maximum strain limits.^(102, 927, 928)

The following important terms are used in the FAD:

CAT: Robertson Crack Arrest Temperature transition curve;

FTE: Fracture Transition Elastic, or the highest possible temperature for unstable fracture propagation through elastic stress fields;

FTP: Fracture Transition Plastic, or the temperature point of fully ductile tearing.

9.3.5 Dynamic Tear test^(112, 929)

The Dynamic Tear (DT) test was developed at the Naval Research Laboratory starting in 1960. It has used pendulum machines with direct readout of the energy required to fracture the specimen, and specimens of improved design with respect to crack-started conditions were evolved. To reflect these improvements, the name of the method was changed extensively in the study of the fracture resistance of ferrous and non-ferrous structural metals. The initial DT specimens were tested in a "Drop-weight Tear Test" (DWTT). Subsequently, to the "Dynamic Tear test" in 1967. DT test facilities have been established at several research laboratories and at the production plants of the world's major metal-producing companies. Military standard MIL-STD-1601 describes the method for the $\frac{5}{8}$ -in. (16 mm) dynamic tear testing of metallic materials⁽⁹²⁹⁾

Figure 9.26 illustrates the feature of $\frac{5}{8}$ -in. and 1-in. (16 mm and 25 mm) thick DT specimens. The original standard version involves a deep sharp crack introduced by the use of an electron beam weld which is embrittled metallurgically by alloying. For example, a titanium wire added to the site of the weld results in a brittle Fe-Ti alloy. The narrow weld is fractured easily in loading and thus provides a reproducible sharp crack. It has now been established that equivalent results may be obtained by the use of a deep

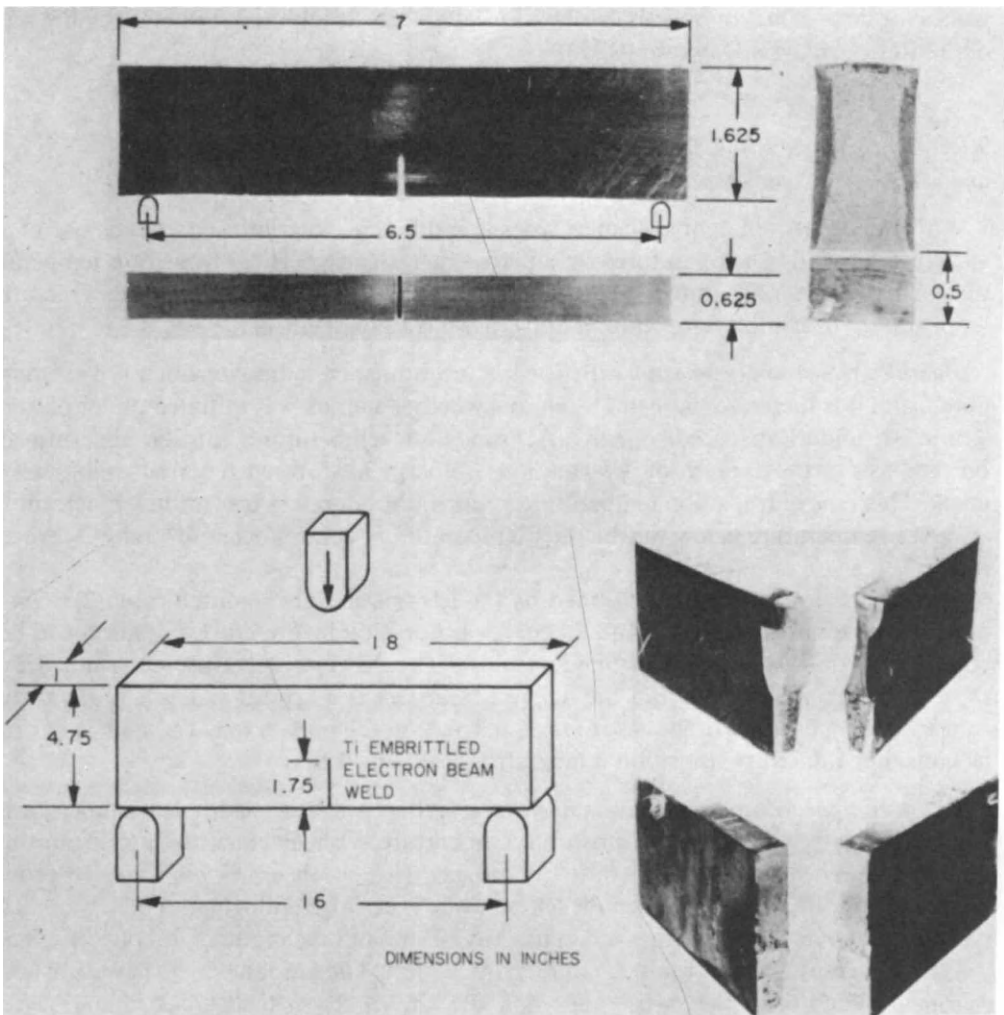


FIG. 9.26. Features of $\frac{5}{8}$ -in. and 1-in. DT Test Specimens.^(1,12) The $\frac{5}{8}$ -in. DT specimen (top) features a machine slit, with a knife-edge-sharpened notch tip. The 1 in. DT specimen (bottom) features the brittle electron beam weld, which is also used for the $\frac{5}{8}$ -in. DT, as desired. The broken halves of the 1-in. DT specimens illustrate brittle and ductile type fractures.

sharp crack produced by fatigue or by slitting, and then sharpening a deep notch by a pressed knife edge. DT specimens featuring a deep flaw produced by any of these methods are tested over a range of temperature. The testing machine is either a pendulum type or a drop-weight type of capacity more than sufficient to break the specimen in one blow.

In engineering applications, such as the determination of a fracture-safe design, analysis diagrams can be used to interpret the relationships between DT energy and flaw-size, stress-level relations for unstable fracture. For structural steels with a temperature-induced transition in the service temperature range, the toe region of the DT energy curve can be indexed to the Fracture Analysis Diagram (FAD), as shown in Fig. 9.25.

The shelf region of DT energy versus temperature relationships and DT energy

values for non-transition metals can be translated into structural parameters by the use of the Ratio Analysis Diagram (RAD).

9.3.6 *Ductility transition, fracture appearance transition, and crack arrest temperature*

With the use of different specimen types and different criteria has come the use of a variety of transition temperatures by different investigators. These transition temperatures can be classified into three groups: ductility transition temperature, fracture (appearance) transition temperature, and crack-arrest temperature.

Ductility transition temperature. Brittle fractures must be initiated from a pre-existing notch, and it is therefore important to know whether a crack was initiated under plastic strain or under absorbed energy. A transition temperature can be determined on the basis of the amount of deformation or energy absorption required to initiate a crack. This type of transition temperature is called the “ductility transition temperature, T_d ”. At a temperature below the ductility temperature, fractures occur in a pure cleavage mode.

Transition temperatures determined by (1) deformation at the notch root, (2) deformation at the maximum load, and (3) energy absorption before crack initiation can be considered “ductility transition temperatures”. The NDT temperature determined by the NRL drop-weight test, and the dynamic tear test is a typical example of ductility transition temperature. In the case of the Charpy V-notch impact test, $Tr\phi$ and $Tr15$ can be considered ductility transition temperatures (see Fig. 9.18).

Fracture appearance transition temperature. When a test is made at a temperature somewhat above the ductility transition temperature, a shear crack initiates from the notch root. When the test temperature is sufficiently high, the crack continues to grow in the shear mode. However, when the temperature is not high enough, the crack becomes unstable when its length reaches a certain critical size and the mode of fracture changes to cleavage resulting in a rapid fracture propagation. The amount of energy absorbed during the growth of the shear crack and the size of the critical crack change with temperature. Transition temperatures determined by these criteria are designated “fracture appearance transition temperatures” (T_f) because, in this transition temperature range, the fracture appearance changes significantly. For any given material, T_f is always higher than T_d .

Transition temperatures are considered Tr_f , determined by the percentage of fibrous appearance, the energy absorption after the maximum load, or by other parameters which indicate the amount of shear fracture. In the case of the Charpy V-notch test, for example, the TrE and Trs shown in Fig. 9.18 are fracture appearance transition temperatures.

Crack-arrest temperature. The crack-arrest temperature can be determined by the Robertson test, the ESSO test, and the double-tension test, all of which are designed to study the fracture propagation characteristics of a material, and will be described later in this chapter. Figure 9.27, a typical result, shows the relationship between the test temperature and the critical stress necessary for fracture propagation. When the temperature is below a certain point, brittle fractures can propagate under fairly low stress.

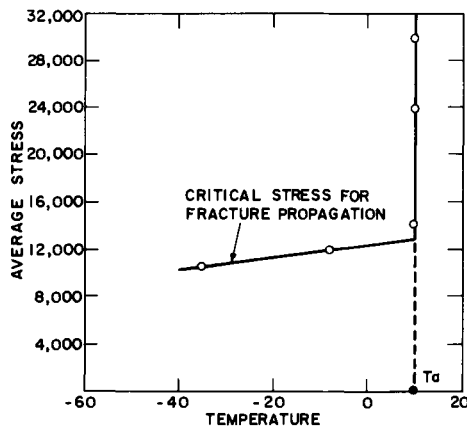


FIG. 9.27. Crack arrest temperature.

However, when the temperature is above a certain point, brittle cracks are arrested even under fairly high stress. This limiting temperature is called the “crack-arresting (transition) temperature” (T_a).

9.4 Various Tests for Evaluating Notch Toughness

The notch toughness of steel has been tested in various ways and by many investigators. Table 9.3 lists the typical tests used in the evaluation of notch toughness, and

TABLE 9.3 *Various tests for evaluating notch toughness of steel and brittle-fracture characteristics of welds*

This table does not include those tests which are aimed at determining the critical stress intensity factor, K_{Ic} . Fracture toughness tests are shown in Figs. 10.8 and 10.9.

-
- A. *Impact tests with small specimens*
 1. Standard Charpy impact tests and modified tests
 2. NRL Drop-weight test
 3. NRL DT test
 - B. *Static tests with small specimens*
 - B-1 Static fracture tests on notched specimens
 4. Tipper test
 5. Navy tear test
 6. Van der Veen test
 - B-2 Bend tests on welded specimens
 7. Lehigh test and Kinzel test
 8. Kommerell test
 - C. *Fracture tests of weldments by dynamic loading*
 9. Crack-starter explosion test
 10. Explosion bulge test
 - D. *Tensile tests of wide-plate specimens*
 - D-1 Fracture propagation tests
 11. Robertson test
 12. ESSO (or SOD) test
 13. Double-tension test
 - D-2 Welded-and-notched wide-plate tensile tests
 14. Wells-Kihara test
-

classifies them into four groups:

1. Impact tests with small specimens.
2. Static tests with small specimens.
3. Fracture tests of weldments using dynamic loading.
4. Wide-plate tension tests.

Some of the laboratory tests concentrate on the initiation of cleavage cracks and others on the stopping of a propagating cleavage crack, but almost all of the tests involve the introduction of a notch and the observation of brittle behavior as the test temperature is lowered. Since each of these tests emphasizes a different feature of the brittle-fracture process, it is not surprising that they rate the ability of a material to resist cleavage fracture in different ways. The tests almost always define a transition temperature below which cleavage fracture occurs under the test conditions.

The following pages briefly review various tests proposed and used by many investigators. Details of these tests can be found in references given.

9.4.1 *Impact tests with small specimens*

Impact tests using small specimens have been developed primarily to evaluate the notch toughness of a base plate. Since the standard Charpy impact tests, the NRL drop-weight test, and the NRL drop-weight tear test (or dynamic tear test) have been covered previously, the following pages will discuss tests other than these three.

Charpy tests are sometimes modified, either through (1) the employment of different test procedure or (2) the use of slightly different specimens.

The “double-blow” or “low-blow” technique, proposed and used by Orner and Hartbower,⁽⁹³⁰⁾ evaluates separately the energy required to initiate a crack and that required to propagate the crack. A low-energy pendulum blow is applied twice; the first blow to initiate a crack, the second to propagate it. The low-blow transition temperature is believed to be the maximum temperature at which an initiating crack can become self-propagating in a thick plate (where the energy required to produce shear lips is small compared with the elastic energy available for crack propagation).

Several investigators have proposed using specimens with pressed notches instead of machined vee notches.⁽⁹³¹⁾ Pressed notches are made using vee-shaped tools made of hard material.

Subsized specimens are often used to evaluate notch toughness in plates thinner than $\frac{3}{8}$ in. (10 mm), and specimens larger than the standard size have been used for the evaluation of heavy plates. But when specimens of non-standard size are used the interpretation of the results becomes problematic. For example, transition temperatures are lowered when specimens are subsized because of a decrease in the triaxiality of the stresses near the root of the notch. And such shifts are not the same for all regions of the curve.

9.4.2 *Static tests with small specimens*⁽¹⁰²⁾

Static tests using small specimens include:

(A) Static fracture tests on notched specimens

1. Notched-specimen tension tests, such as the Tipper tests.⁽⁹³²⁾

2. Tear tests, such as the Navy tear test.⁽⁹³³⁾
 3. Notched-specimen bend tests, such as the Van der Veen test,^(934, 935)
- (B) Bend tests on welded specimens
4. Longitudinal-bead-on-weld notched-bend tests, such as the Lehigh test⁽⁹³⁶⁾ and the Kinzel test.⁽⁹³⁷⁾
 5. Longitudinal-bead-on-weld bend tests, such as the Kommerell test,^(938,939)

Tests in Group (A) have been developed primarily for evaluating the notch toughness of unwelded base plates. Tests in Group (B) have been developed for evaluating the fracture characteristics of weldments or the effects of welding on the base plate, i.e. the weldability of steel.⁽²⁴⁰⁾

Figure 9.28 shows schematically specimens used for the Tipper test, the Navy tear test, and the Van der Veen test. Baker and Tipper⁽⁹³²⁾ at Cambridge University developed the side-notch tension specimen shown in Fig. 9.28(a). A specimen of full thickness is tested over a range of temperatures. The transition temperature is determined from the reduction in thickness at the middle point of the fractured surface between the notches or from the fracture appearance.

The Navy tear test, developed by Kahan and Imbemo⁽⁹³³⁾ at the New York Naval Shipyard, is shown in Fig. 9.28(b). The test specimen is flame cut from a plate of full thickness and is machined on the edge opposite the notch. Static asymmetric tensile loading is applied to the specimen using pins inserted in the pinholes. A transition temperature is determined from the following:

1. The energy needed to propagate fracture (the amount of energy absorbed by a specimen after maximum load until fracture).
2. The fracture appearance (the percentage of fibrous fracture).

Figure 9.28(c) shows the static bend test developed by Van der Veen.^(934, 935)

Figure 9.29 shows bend tests on welded specimens.

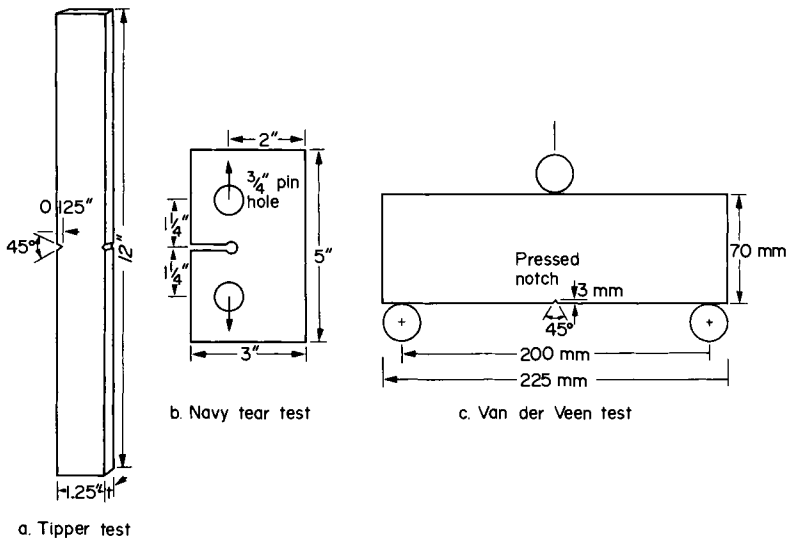


FIG. 9.28. Static fracture tests on notched specimens.

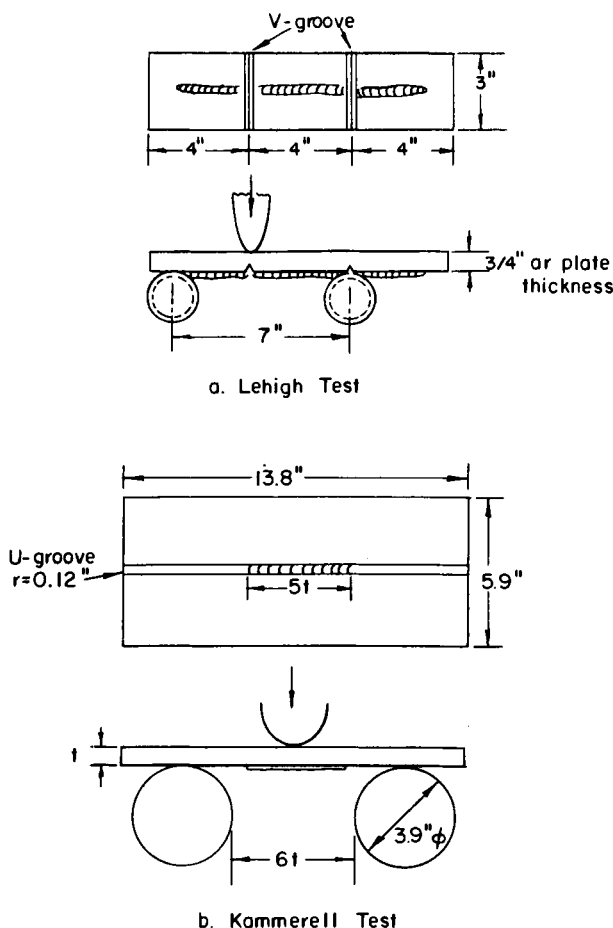


FIG. 9.29. Bend tests on welded specimens. Dimensions of the Kommerell test change depending upon the plate thickness. Dimensions shown in this figure are for plates less than 1 in. (25 mm) thick.

Longitudinal-bead-on-weld notch-bend tests were developed by Stout *et al.*^(240, 936) at Lehigh University and Kinzel *et al.*⁽⁹³⁷⁾ In both tests, a bending load is placed on a transverse notch cut across the weld metal laid on the specimen having a transverse notch cut across the metal laid on the specimen (see Fig. 9.29(a)). The basic philosophy of these tests is as follows. Since weld metal, heat-affected base metal, and unaffected base metal are exposed at the root of the notch, fractures can originate in the most sensitive structure; thus, the cleavage-fracture sensitivity of a welded joint can be evaluated. In the Lehigh test, duplicate test results may be obtained from a single specimen, since two notches are used.

Investigators at Lehigh used various criteria, including bend angle of maximum load, total energy absorbed, lateral contraction, appearance, and mode of fracture, for the evaluation of test results.^(240, 936)

The Kommerell-type longitudinal-bead-weld bend specimen was developed in Germany after a number of failures had occurred in welded bridges.⁽⁹³⁸⁾ A single-pass weld bead is made along a test plate, as shown in Fig. 9.29(b), the test plate is bent with

the weld on the tension side, whereupon small cracks appear in the weld metal or in the heat-affected zone. As bending proceeds, these cracks extend into the base plate. Brittle steel is unable to slow the progress of the cracks, and the specimen breaks suddenly while the bending angle is still small; ductile steel, on the other hand, stops the advance of the cracks, and the specimen breaks only after considerable deformation.

The bead-bend test of Austrian Standard M3052 is a modification of the Kommerell test.⁽⁹³⁹⁾ Dimensions of the specimen and required bend angles at room temperature are specified for different plate thicknesses.

9.4.3 Fracture tests of weldments by dynamic loading

Explosives and projectiles have been utilized as simple forms of dynamic loading in fracturing full-size weldments. The following tests have been proposed and used:

1. The crack-starter explosion test developed by Pellini and associates.^(940, 941)
2. The explosion bulge test developed by Hartbower and Pellini.^(942, 943)
3. The explosion tests of welded tubes conducted by Folkland⁽⁹⁴⁴⁾ Hauttmann,⁽⁹⁴⁵⁾ and Kihara *et al.*^(946, 947)

Explosion crack starter test. The explosion crack starter test was developed by Pellini *et al.*⁽⁹⁴⁰⁾ at the Naval Research Laboratory as a method of determining the fracture-propagation characteristics of steel when the fracture initiation is forced (see Fig. 9.21).

Explosion bulge test. The explosion bulge test was developed by Hartbower and Pellini^(942, 943) at the Naval Research Laboratory. Two plates, usually 10 × 20 in. (250 × 500 mm), are butt welded to form a square which is placed over a circular die and explosion-loaded by successive shots until it fails or develops a full-hemispherical bulge. The temperature of the test is controlled by equalization between the successive shots. The source point of the fracture is observed. The amount of deformation at fracture is determined by measurements of plate thickness and is expressed as percent reduction of plate thickness. The "bulge transition temperature" is defined as the temperature range in which the percent reduction of thickness decreases from 10 to 1%. These were primarily performance tests of welded joints.

9.4.4 Tensile tests of wide-plate specimens

The primary objective of the tensile testing of wide-plate specimens is to reproduce in the laboratory brittle failures as they occur in actual structures. The tests that have been used or proposed may be classified as follows:

1. Fracture propagation tests.
2. Tests on welded-and-notched wide plates.

The tests in the first group measure the fracture propagation characteristics of steel plate. These tests include the Robertson test, ESSO (or SOD) test, and the double tension test.

The tests in the second group have been used to study brittle fracture characteristics of welded plates.

Fracture propagation tests. Robertson,^(948, 949) at the Naval Construction Research Establishment, Scotland, developed the specimen type shown in Fig. 9.30. A cleavage

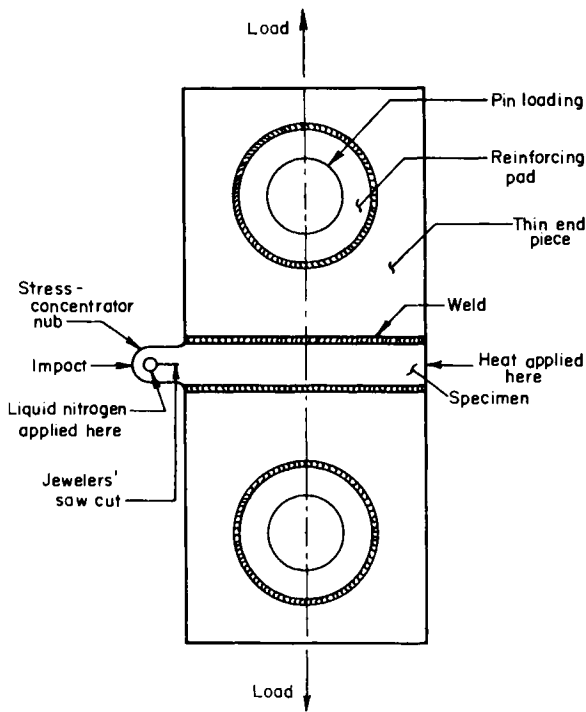


FIG. 9.30. Robertson test specimen.

crack is started at a notch on one edge of the plate by a bullet driven against a special nub. The amount of energy available from the explosion is large enough to start the crack but insufficient to make it propagate more than a very short distance. The uniform tensile load tends to keep the crack growing. The specimen contains a temperature gradient in the width direction, with the notched side being cooler. The crack travels across the specimen until it reaches a zone where the temperature is high enough to permit the material to flow sufficiently to stop the crack. The temperature above which a crack does not propagate can thus be determined at each stress level. A typical test result is shown in Fig. 9.27. The crack-propagation characteristics are expressed in terms of arresting temperature and critical stress.

Feely *et al.*⁽⁹⁵⁰⁾ at the Standard Oil Development Company studied fracture propagation characteristics of steels by using the test called the SOD or ESSO test. The specimen configuration was similar to the Robertson test; however, in the SOD test, the specimen was uniformly cooled to the desired temperature, and a selected load was applied.

In the SOD test, a brittle crack is initiated by applying an impact load at the notch while the specimen is under a certain preselected tensile stress. If the material is brittle and the stress is high enough, the specimen fractures completely in a cleavage manner. If failure does not occur, the tensile load is increased and the plate subjected to impact at successively high stress levels until it does. Thus, the critical stress for cleavage-fracture propagation at given temperature is obtained. Tests are then conducted at various temperatures to determine the arresting temperature. The results appear in a form very similar to those shown in Fig. 9.27. Yoshiki and Kanazawa^(951, 952) at the University of Tokyo developed the double-tension test in an attempt to eliminate the influence of

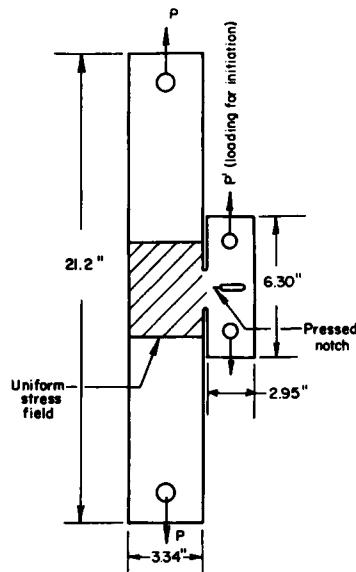


FIG. 9.31. Double-tension test specimen.

impact loading (used in the Robertson and the ESSO test) on test results. A double-tension test specimen, shown in Fig. 9.31, is composed of two parts: the crack initiation part and the main part. These two parts are connected by a narrow passage and loaded independently under static tension by two sets of testing apparatus. A cleavage crack is initiated in the crack-initiation part and is driven into the main part through the passage. The critical stress at a specific temperature is determined as the lowest stress in the main part at which complete fracture of the specimen occurs.

Welded-and-notched wide-plate tensile tests. Brittle fractures usually occur at stress levels well below the yield stress of the material. In many cases, fractures occur without any repeated or impact loading, and frequently start from a weld-joint flaw. Low-stress fractures do not occur in most laboratory tests, however. Even when a specimen contains sharp notches and fractures with low energy absorption that result in a brittle-fracture appearance, the fracture stress level is as high as the yield stress level. In fracture-propagation tests the fracture usually propagates at low stress; however, such expedients as the impact loading in the Robertson and SOD tests or the high-tensile stress applied on the auxiliary part of a specimen in the double-tension test are necessary to initiate a brittle crack.

Extensive research on the low-applied-stress fracture of weldments has been conducted, and it has been found that a low-applied-stress fracture can be obtained experimentally from a notch located in an area containing high residual tensile stress. Since this subject is rather important to the understanding of the brittle fracture of actual welded structures, it will be discussed further in Sections 9.5 and 10.4.

9.4.5. Use of various fracture toughness tests

Reasons for different tests. Many different tests for fracture resistance are necessary

because there are many characteristics to evaluate. No single test is capable of providing all the information needed.

When evaluating the fracture toughness of a base plate, the plate involved may be too thin for preparation as a proper specimen, or the fracture performance of an entire weldment or entire welded structure may be the concern.

The fracture initiation characteristics or the fracture propagation characteristics may be the concern.

The size and cost of the specimen can be an important factor in selecting the appropriate test. Sometimes a cheap and simple test, even though not an accurate simulation of an actual failure, will suffice. At other times a test that will accurately simulate actual failures is needed, however elaborate the facilities and procedural requirements.

A fracture test of a specimen large enough to simulate an actual welded structure will require a large testing machine. For example, a butt weld about 10 in. wide and 18 in. long is needed to simulate residual stresses as high as those existing in a large welded structure made of 1-in. thick plate.[†] The cross-section of the specimen is 10 in.²; if the fracture stress is 50,000 psi, 500,000 lbs are needed to fracture the specimen.

Tensile tests are preferred when the tests need to simulate fractures in actual structures and when a theoretical analysis of the test data is needed. However, a tensile test requires a testing machine of large capacity.

Bend tests and tear tests are often used to test fractures in relatively large specimens and can be carried out using a testing machine with a limited capacity. In these tests, however, the crack must propagate through several zones containing varying stresses, and this makes it difficult to analyze the experimental results.

Explosives and projectiles are often used as a simple means of dynamic loading and fracturing a full-size weldment, as discussed earlier. But explosives must generally be placed at some distance from the specimen in explosion tests (see Fig. 9.21) and this for the following reasons:

1. To provide a relatively even impact loading over a large area.
2. To provide an impact loading without an excessively high speed.

If explosives are placed directly against the specimen surface the results may not resemble closely enough an ordinary brittle fracture.

As mentioned above the speed of brittle fracture propagation in an actual structure is about 20 to 30% of the speed of a sound wave in the metal and the theoretical limiting speed is $0.38 C_0$ (see Table 9.2). Consequently, we are able to assume that the mode of fracture may change if the loading speed is greater than the limiting speed of a brittle fracture.

Use of different tests. Table 9.4 shows how different tests may be used for different purposes. This table has been prepared for an imaginary situation in which the structural reliability of a new welded structure is being evaluated. Suppose that the structure is being built with an entirely new material that must be evaluated from scratch. What kind of R & D program is appropriate; what test should be used?

(a) The first objective is to develop an adequate base plate. Initial screening tests are made on a number of experimental metals with varying chemical compositions and heat

[†] The effect of specimen size on residual welding stresses is discussed in Chapter 6.

TABLE 9.4 *Uses of various fracture tests*

-
1. Base plate development program
 - (a) Initial screening of experimental melts—Charpy
 - (b) Detailed study of selected melts—DWT or DT test
 2. Weld metal development program
 - (c) Initial screening of weld metal—weld metal Charpy
 - (d) Detailed study of selected weld metal—DT test
 - (e) Heat-affected zone study—DT test
 3. Weldment toughness study
 - (f) Initial study—Lehigh (Kinzel), Kommerell
 - (g) Detailed study of weldment performance—explosion bulge
 4. Study of fracture characteristics of actual structures
 - (h) Base metal fracture propagation study—Robertson SOD
 - (i) Welded joints—Wells-Kihara
 5. Establishment of standard (quality control in production and procurement)
 - (j) Correlation between study 4 and $\rightarrow \begin{cases} \text{Charpy} \\ \text{DT} \end{cases}$
 6. Prototype test
 - (k) Actual structure—under static and repeated loading
-

treatments. At this stage, simple tests using small specimens such as the Charpy V-notch test are used.

(b) During the initial screening several promising materials are selected for further evaluation in order to collect fracture toughness data under realistic conditions. Fracture tests, for example, are conducted using full-thickness specimens and the drop-weight test or the dynamic tear test are suitable for this.

(c) After several base plates have been developed, the weld metals suitable for the base plates are developed. Initial screening tests are made of a number of test welds and Charpy test specimens taken from them.

(d) After screening, a detailed evaluation is made of the promising materials. The drop-weight test may be suitable for this purpose.

(e) Tests are also made of the fracture toughness of the heat-affected zone. The drop-weight test may again prove suitable. Charpy V-notch specimens may be taken from various locations near the weld. Though the heat-affected zone consists of many regions having many different metallurgical characteristics, it is also very narrow, making the evaluation of fracture toughness of the heat-affected zone a complex task.

(f) After the evaluation of the weld metal and HAZ, the fracture performance of an entire weldment composed of the weld metal, HAZ, and the base plate is evaluated. At this stage, one would also want to study the effects of the welding procedure variables including the welding current, the arc travel speed, the preheat temperature, etc. Tests using relatively small specimens such as the Lehigh test and the Kinzel test may be used. One may want to evaluate fracture toughness of a weldment without an artificial notch having a predetermined depth. Failures of actual structures often initiate from weld defects and hard spots, and the Kommerell test may be used to evaluate the initiation and propagation of fractures in a weldment without an artificial notch.

(g) The performance of a reasonably large weldment is then evaluated, and the explosion bulge test may be used for this purpose.

(h) After completing these basic studies the fracture characteristics of the actual structure are evaluated as accurately as possible. This may be done using the Robertson or the SOD tests.

(i) Then the fracture characteristics of the welded joints are evaluated, using, perhaps, the Wells–Kihara test.

(j) After these large-scale tests are completed, quality-control standards in production and procurement must be established. If the service conditions of the structure are not severe and the materials to be used are similar to those on the market, the ordinary Charpy V-notch test may be used for quality control. But if the service conditions are severe, it may be necessary to use a reliable test such as the drop-weight test for the dynamic tear test.

In order to use small specimens when establishing standards, it is necessary to obtain correlations between the data on small specimens and the data on large-scale specimens.

(k) Before an actual structure is put into production, a prototype will probably be made and a series of tests conducted on this prototype. The tests may involve the simulation of actual service conditions.

In the testing of prototype structures, at least two kinds of tests should be conducted:

1. Tests to study the normal fracture behavior.
2. Tests to determine the lowest fracture stress.

Though the first kind of test is routine at present, the second is not. As mentioned above, many ships built during World War II fractured at stresses well below the yield stress of their structural material, and investigators including Wells, Kihara, and Masubuchi have attempted an experimental demonstration of weldment fractures that occur under a low applied stress. This subject will be discussed in detail in Section 9.5.

Among the over 5000 ships built during World War II only about twenty ships fractured completely, although cracks developed in over 1000 ships. If we built a prototype structure using the brittle material used in World War II ships and conducted fracture tests, the probability of a complete, catastrophic failure in that prototype structure would be 20/5000 or 0.4%. The probability of some cracks developing would be about 20%. In other words, the probability of the prototype structure performing perfectly without developing a single crack would be 80%. Yet once large-scale production starts, failures do happen in some structures and, from the point of view of the captain of a fractured vessel, the score is 100% failure.

Consequently, it is most important to determine what adverse conditions the structure will face during production and service. Only then will it be possible to establish the necessary measures to prevent the adverse conditions from occurring.

9.4.6 *Correlation of results obtained by various tests*

The correlation of notch-toughness data collected by means of various tests has been the concern of many investigators. The book by Hall *et al.*⁽⁹⁰⁴⁾ covers the correlation of transition-temperature data obtained by various tests.

As mentioned above, transition temperatures obtained by different tests can be classified into three types: ductility transition temperature T_d , fracture appearance transition temperature T_f , and crack-arrest temperature T_a . In general, there is a fairly close correlation between transition temperatures of the same type.

For example, Fig. 9.32 shows a correlation between fracture appearance transition temperatures determined with the standard Charpy (machined) V-notch specimens, vTrs, and those determined with Charpy pressed V-notch specimens, pTrs.⁽⁹⁰⁴⁾ A close correlation exists between those values which are similar.

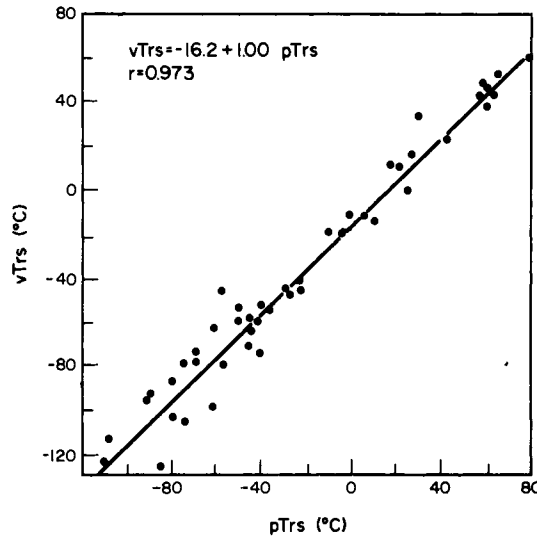


FIG. 9.32. Correlation between fracture appearance transition temperature determined with Standard Charpy (machined) V-notch specimens and Charpy pressed V-notch specimens. The figure has been prepared from data given in Reference (904).

Correlations are usually poor when different type transition temperatures are compared; for example, between T_d as determined by one test and T_f as determined by another.

9.5 Low Applied-stress Fracture of Welded Structures

In order to assist the reader to better understand the material presented in this section, the following information, given elsewhere, is presented in summary form:

1. Brittle fractures in welded structures often originate from small defects (see Fig. 9.13); the overall stress is often very low (only 10,000 psi (7.0 kg/mm² or 69 MN/m²) or so, which is only about one-third the yield strength of the material used).
2. Based upon the fracture mechanics theory, which will be discussed in Chapter 10, unstable fractures occur when stresses are applied to a structure containing a crack longer than a given value. However, the critical crack of low-carbon steel at the yield stress is several inches long.

Then why does a welded structure fail at a stress level of only one-third the yield strength and from a very small crack? A number of investigators, especially during the late 1940s to 1950s, tried to experimentally demonstrate the low applied-stress fracture of steel weldments.

9.5.1 Background information

Brittle fracture strength of notched tensile specimens. During the late 1940s and early 1950s a number of investigators studied the fracture characteristics of a series of notched specimens subjected to tensile loading. By conducting fracture tests under a range of

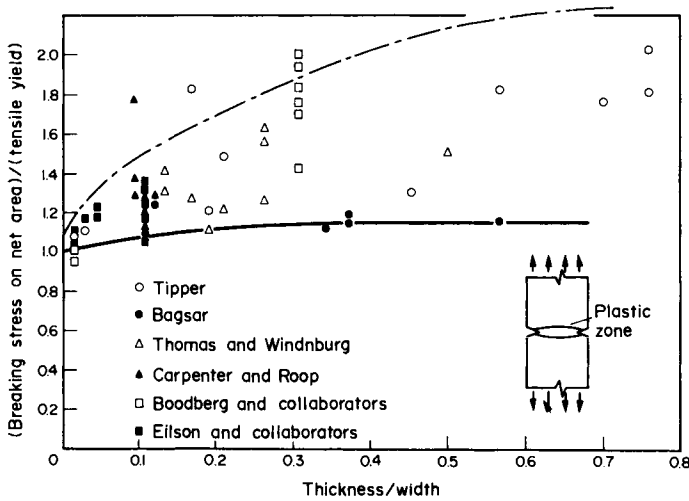


FIG. 9.33. Brittle fracture strength in notched tensile specimen (Wells).⁽⁹⁵³⁾

temperatures, they found that the mode of fracture changes from ductile to brittle when the test temperature is below a certain value, i.e. the transition temperature. They were delighted to be able to demonstrate brittle fractures in a laboratory.

Their delight was short lived. They soon discovered that the fracture stress of a specimen in low-carbon steel was always higher than the yield stress. Figure 9.33, prepared by Wells,⁽⁹⁵³⁾ shows the results obtained by several investigators.⁽⁹⁵⁴⁾ Fractures always occurred after general yielding of the specimen took place.

Greene's experiment with bend tests on welded plates. In 1949 Greene⁽⁹⁵⁵⁾ reported the results of bend tests on welded plates while he was studying the effects of stress-relieving treatments on the fracture characteristics of welded plates, as shown in Fig. 9.34.

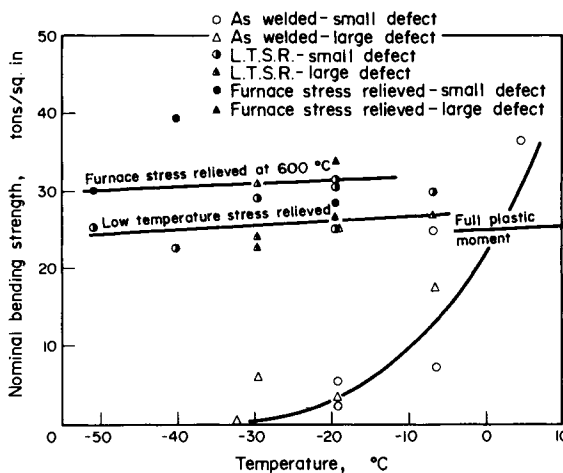


FIG. 9.34. Nominal bending strength plotted against temperature for Greene's experiments on wide plates with notched, central longitudinal welds.⁽⁹⁵⁵⁾

He found that as-welded specimens tested at low temperatures fractured at a stress level well below the full plastic moment.

Robertson's experiment on fracture propagation. In 1951 Robertson reported that a brittle fracture, once initiated, propagates at a stress well below the yield strength.^(948,949) He used the specimen shown in Fig. 9.30. A typical test result is as shown in Fig. 9.27.

9.5.2 Early studies on low-applied-stress fracture using welded-and-notched wide plates

Experiments by Wells. Wells⁽⁹⁵³⁾ knew that a stress as high as the yield stress is needed to initiate a crack in structural steel, but that a crack can propagate at a low stress once it is initiated. He hypothesized that when a sharp notch is located in the region near the weld where residual stress is as high as the yield strength, a brittle fracture may initiate and propagate under a low applied stress.

Wells tested the tensile strength of a series of welded specimens, each containing a sharp transverse notch, as shown in Fig. 9.35(a). Among the eleven specimens tested, one (No. H) fractured completely at an applied stress well below the yield stress (see Fig. 9.35(c)). Specimen F, tested at 15°C, fractured at the yield stress level. On three

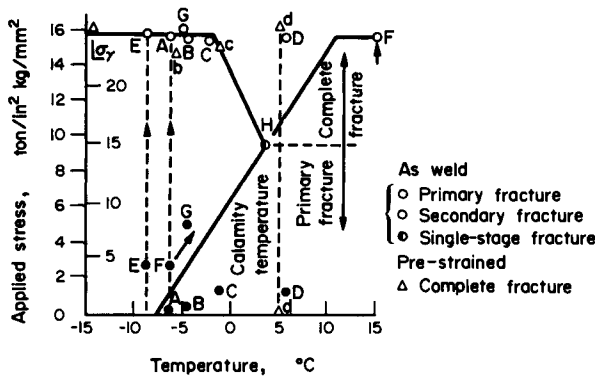
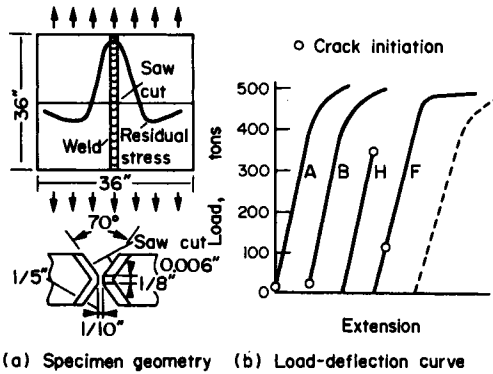


FIG. 9.35. The effect of residual stress on the brittle fracture initiation.

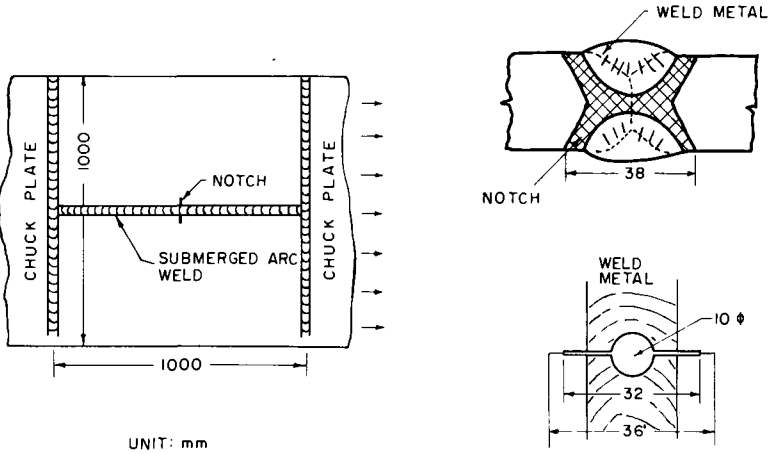
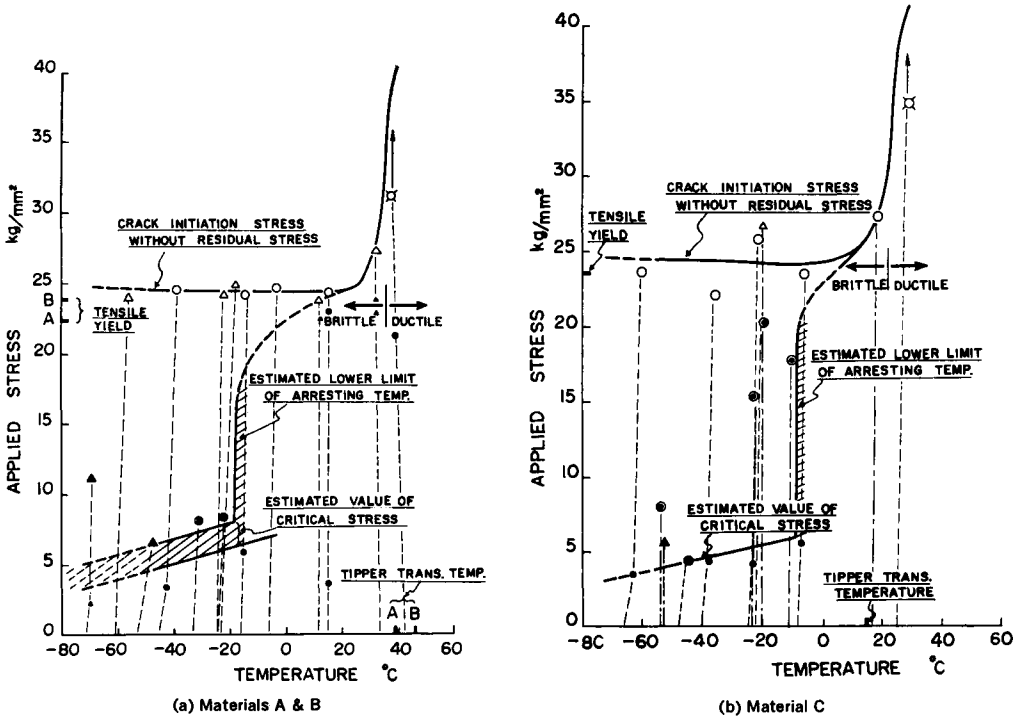


FIG. 9.36. Welded-and-notched wide-plate tensile test specimen used by Kihara and Masubuchi.⁽⁹⁵⁶⁾



- stress at partial fracture (●) and complete fracture of specimen without crack after welding (○)
- ▲— stress at partial fracture (▲) and complete fracture of specimen which contains spontaneous crack after welding (△)
- , △ single-stage fracture (including multiple-stage fracture prior to general yielding)
- × fracture in ductile manner

FIG. 9.37. Fracture strength of welded-and-notched wide plates.

Note: Data connected by broken lines in Fig. (b) belong to the preliminary test.

specimens tested at low temperatures, partial fracture occurred at very low applied stress, and complete fracture occurred after general yielding. Wells decided that catastrophic failure occurs at a certain temperature and named it the "calamity temperature".

Experiments by Kihara and Masubuchi. Kihara and Masubuchi,⁽⁹⁵⁶⁾ though interested in the results obtained by Wells, felt that catastrophic fractures could occur in a broad temperature range.[†]

They used specimens similar to those used by Wells (see Fig. 9.36). Figure 9.37 shows their results. Single-stage fractures at low applied-stresses indeed occurred in a number of specimens tested at low temperatures. Table 9.5 shows properties of steels used for the experiment. Figure 9.38 shows the general tendencies indicated by their experimental results, including the effects of a sharp notch and of residual stress on the fracture strength of a welded carbon-steel specimen.

When the specimen contains no sharp notch, fracture occurs at the ultimate strength of the material at the test temperature, as shown by curve *PQR*. When a specimen contains a notch (but no residual stress), fracture occurs at the stress levels shown by curve *PQST*. When the temperature is higher than the fracture transition temperature, T_f , a shear fracture occurs at high stress. When the temperature is below T_f , the fracture appearance changes, indicating cleavage, and the stress at the fracture decreases to

TABLE 9.5 Properties of steel used by Kihara and Masubuchi⁽⁹⁵⁶⁾

Chemical composition									
Steel designation	Chemical composition, % (check analysis)					Kind of steel	Character of steel-making		
	C	Si	Mn	P	S		Roll finish temperature (°C)	Ferrite grain size	Austenite grain size
B	0.28	Trace	0.50	0.023	0.034	Rimmed	1140	6 – 6.5	1.5
C	0.21	0.04	0.42	0.016	0.020	Semikilled	1030	6.5	2.5

Mechanical properties and notch toughness							
Steel designation	Mechanical properties			Notch toughness			
	Yield strength, (kg/mm ²)	Ultimate strength (kg/mm ²)	Elongation, % (GL = 50 mm)	V-Charpy test			Tipper test shear transition temperature (°C)
				Energy absorbed at 0°C (kg-m/cm ²)	15 ft-lb transition temperature (°C)	Shear transition temperature (°C)	
A	22.4	46.2	33	1.0	22	50	39
B	23.9	46.3	36	1.1	24	55	46
C	23.5	41.1	34	1.5	8	32	15

^(a) Steels A and B are made from the same charge.

[†] Kihara *et al.*⁽⁹⁵⁷⁾ also conducted fracture tests of welded spherical containers with notches similar to that shown in Fig. 9.36. Catastrophic failures were also obtained.

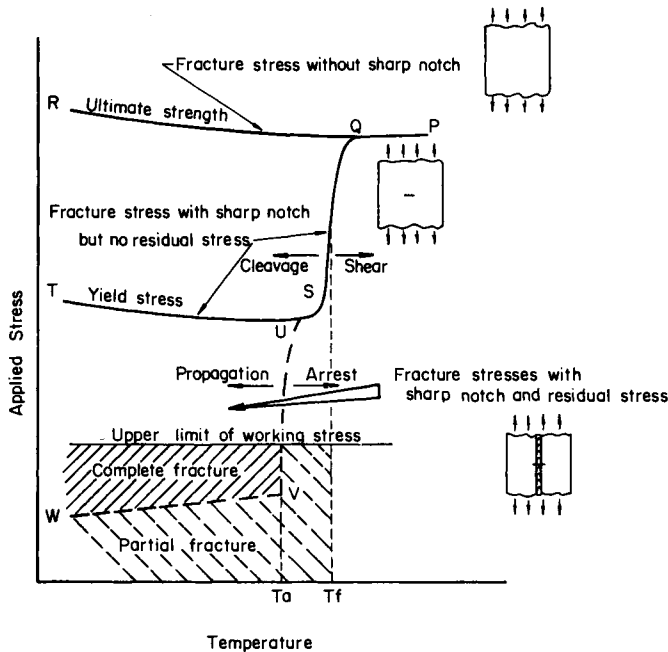


FIG. 9.38. Effects of sharp notch and residual stress on fracture strength (Kihara and Masubuchi).⁽⁹⁵⁶⁾

near the yield stress. When a notch is located in an area containing high residual tensile stresses, several types of fracture can occur:

1. At temperatures higher than T_f , the fracture stress is not affected by residual stress and is the ultimate strength (curve PQ).
2. At room temperatures lower than T_f but higher than the crack-arresting temperature, T_a , a low stress may initiate a crack, but the crack will be arrested.
3. At temperatures lower than T_a , one of two phenomena can occur, depending upon the stress level at fracture initiation:
 - (a) If the stress is below the critical stress, VW, the crack will be arrested after running a short distance. Complete fracture will occur at the yield stress (ST).
 - (b) If the stress is higher than VW, complete fracture will occur.

9.5.3 Further studies on low applied-stress fracture

Further studies on low applied-stress fracture have been conducted by a number of investigators. Since it is easier to discuss this subject after discussing the general theories of brittle fracture, the subject will be presented in more detail in Chapter 10.

9.6 Effects of Chemical Composition and Manufacturing Processes^(102, 902, 958)

The properties of a given type of steel are affected by its chemical composition as well as the manufacturing process variables involved such as grain size, roll finishing

temperature, and amount of cold working and prestraining. This section covers the effects of these factors on:

1. Tensile properties.
2. Notch toughness.
3. Weldability.

TABLE 9.6 *Typical formulae to determine effects of chemical composition on mechanical properties and notch toughness*

1. *Mechanical properties*

(a) Frazier–Boulger–Lorig's formulae^{(a)(959)}

$$\sigma_{yu}, \text{ psi} = (23,000 \pm 1500) + 29,200 \times \%C + 7200 \times \%Mn$$

$$\sigma_{uts}, \text{ psi} = (30,800 \pm 2200) + 104,000 \times \%C + 13,000 \times \%Mn$$

$$\text{Elongation, \%} = (38.2 \pm 2.4) - 32.6 \times \%C - 3.2 \times \%Mn$$

(b) Kihara–Suzuki–Tamura's formulae^{(b)(222)}

$$\sigma_y, \text{ psi} = (53,400 \times \%Cy + 23,900) \pm 5700$$

$$\sigma_{uts}, \text{ psi} = (87,000 \times \%Ct + 34,500) \pm 5000$$

$$\text{Elongation, \%} = (55.9 - 51.2 \times \%Ce) \pm 6400$$

2. *Transition temperature*

(a) Williams–Ellinger's formula^{(c)(920)}

$$T_{r15}, ^\circ\text{F} = (70 \pm 30) + 300 \times \%C + 1000 \times \%P - 100 \times \%Mn$$

$$+ 300 \times \%Si - 5(\text{ASTM Ferrite Grain Size Number})$$

^(a) Results were obtained for carbon steel. σ_{yu} = upper yield strength, σ_{uts} = ultimate tensile strength.

^(b) Results were obtained for Mn–Si high-strength steels. Values of Cy, Ct, and Ce are given in Table 9.7.

^(c) Formula based on experimental results on fractured ship plates.

TABLE 9.7 *Formulae for carbon equivalent for mechanical properties, notch toughness, and weldability*

1. *Mechanical properties*

(a) Kihara–Suzuki–Tamura's formula^{(a)(222)}

$$\text{Cy (Y.P.)\%} = C + \frac{1}{5}\text{Mn} + \frac{1}{7}\text{Si} + \frac{1}{7}\text{Cu} + \frac{1}{20}\text{Ni} + \text{Zero} \times \text{Cr} + \frac{1}{2}\text{Mo} + 1.1\text{V}$$

$$\text{Ct (T.S.)\%} = C + \frac{1}{5}\text{Mn} + \frac{1}{7}\text{Si} + \frac{1}{7}\text{Cu} + \frac{1}{20}\text{Ni} + \frac{1}{5}\text{Cr} + \frac{1}{2}\text{Mo} + \frac{1}{2}\text{V}$$

$$\text{Ce (Elongation)\%} = C + \frac{1}{9}\text{Mn} + \frac{1}{12}\text{Si} + \frac{1}{10}\text{Cu} + \frac{1}{20}\text{Ni} + \frac{1}{4}\text{Cr} + \frac{2}{5}\text{Mo} + \frac{2}{3}\text{V}$$

2. *Notch toughness*

(a) Kihara–Suzuki–Tamura's formula^{(b)(222)}

$$\text{Ce}_q = C - (1/2.6)\text{Mn} + 3.9\text{P} - (1/3.7)\text{Ni} + 1.3\text{Mo} + \text{Zero}(\text{Si} + \text{S} + \text{Cu} + \text{Cr})$$

3. *Weldability*

(a) Formula in *Welding Handbook* (for cold cracking)⁽⁹⁶⁷⁾

$$\text{Ce}_q = C + \frac{1}{6}\text{Mn} + \frac{1}{10}\text{Cr} - \frac{1}{50}\text{Mo} - \frac{1}{10}\text{V} + \frac{1}{40}\text{Cu} + \frac{1}{20}\text{Ni}$$

(b) Formula based on Sims–Banta's work (for cold cracking)⁽⁹⁰²⁾

$$\text{Ce}_q = C + \frac{1}{6}\text{Mn} + \frac{1}{24}\text{Si} + \frac{1}{29}\text{Mo} + \frac{1}{14}\text{V} + \text{Zero Cr}$$

(c) Kihara–Suzuki–Tamura's formula (for maximum hardness)^(c)

$$\text{Ce}_q = C + \frac{1}{6}\text{Mn} + \frac{1}{24}\text{Si} + \frac{1}{15}\text{Ni} - \frac{1}{5}\text{Cr} + \frac{1}{4}\text{Mo}$$

^(a) Results obtained for Mn–Si high-strength steels.

^(b) The formula was obtained by Kihara, Suzuki, and Tamura by analyzing results obtained by Rinebolt and Harris.⁽⁹⁵⁸⁾

^(c) The formula was obtained to express the effects of alloying elements on the maximum hardness of the weld heat-affected zone.

The discussion in this section will be about carbon steels and low-alloy high-strength steels that are used in the as-rolled condition, a relatively simple subject. This section does not cover quenched and tempered steels or maraging steels.[†]

9.6.1 Effects of chemical composition^(102, 902)

The effects of chemical composition on mechanical properties, notch toughness, and weldability of steel have been studied by many investigators. Further discussions on the effects of chemical composition on weldability of steels are given in Chapter 14.

Tables 9.6 and 9.7 summarize some of the formulae for determining the effects of the chemical composition on mechanical properties, notch toughness, and weldability. Included in Table 9.6 are formulae for determining the yield strength, the ultimate tensile strength, the elongation, and the 15 ft-lb. transition temperature. Included in Table 9.7 are the formulae for the carbon equivalent, a parameter which expresses the effect of a given alloying element on an equivalent amount of carbon. Table 9.8 has been prepared to show schematically the effects of major elements on the tensile strength, elongation, notch toughness, and susceptibilities to hot cracking and cold cracking. Also shown are major effects of the elements listed. Arrows are used to explain the effects. Arrows pointed upward indicate that the effects are favorable:

- Increase tensile strength.
- Increase elongation.
- Improve notch toughness.
- Reduce susceptibility to cracking.

TABLE 9.8 Effects of chemical compositions on properties of steel

Elements	Major function	σ_{UTS}	Elongation	Notch toughness	Weldability	
					Hot cracking	Cold cracking
C	Most important element Increase strength, hardenability	High ↑ 1	More ↓ 1	Ductile ↓ 1 Brittle	Crack ↓	Crack ↓
Mn	Increase hardenability	↑ 0.2 of C	↓ 0.1C	↑ 0.4C	↑ From Mn	↓ 0.15C
Si	Deoxidizer	↑ 0.15C	↓ 0.8C	—	↓ 0.4C	
P	Impurity			↓ 4C	↓ 0.3C	
S	Impurity			—	↓ 3C	
Al	Deoxidizer			↑	—	
Cr	Increase oxidation resistance, corrosion resistance	↑ 0.1C	↓ 0.25C	—	—	↓ 0.1C
Ni	Increase toughness Increase corrosion resistance	↑ 0.05C	↓ 0.05C	↑ 0.3C	—	↓ 0.05C
Mo	Strong carbide former Increase hardenability	↑ 0.5C		↓ 1.3C	—	↑ 0.02C

[†] Some discussions on chemical compositions on Q and T steels and maraging steels are given in Chapter 1.

The number given near an arrow indicates the significance of the effect of an element compared with the effect of carbon. For example, 1% increase in manganese results in an increase in the tensile strength to an extent comparable to an increase of 0.2 carbon. The concept of carbon equivalent is widely used (refer to Chapter 14).

Figure 9.39 shows the effects of several alloying elements on the Charpy V-notch 15 ft-lb transition temperatures. The figure was prepared by Kihara *et al.*⁽²²²⁾ and was based upon the experimental results obtained by Reinbolt and Harris⁽⁹⁵⁸⁾

In using the formulae given in Tables 9.6 and 9.7, it is important not to extrapolate the formulae beyond the stage of the alloy contents investigated in the experiments on which the formulae were based. Figure 9.39 may be used as a guide for the practical limits of the various alloying elements contained in structural steels.

Carbon.⁽¹⁰²⁾ Carbon is the most important alloying element. Carbon added to steel causes an increase in strength (yield and ultimate). As carbon is added, a greater proportion of carbide is apparent in the structure as observed under a microscope. However, the addition of carbon causes many undesirable effects including reduction in elongation, a reduction in notch toughness, and a reduction in weldability (an increase in the hardness of the heat-affected zone and an increase in susceptibility to both hot and cold cracking). Because of these adverse effects the carbon content of a weldable steel is normally below 0.25%. Many weldable high-strength steels restrain the amount of carbon content despite the fact that carbon increases the strength significantly.

Manganese.⁽¹⁰²⁾ Manganese is added to steel because it is a fairly good deoxidizer and it improves notch toughness (lowers transition temperature). An increase in manganese up to around 1.2% results in an improvement in notch toughness, but an addition of manganese over about 1.6% causes a rapid deterioration in notch toughness.

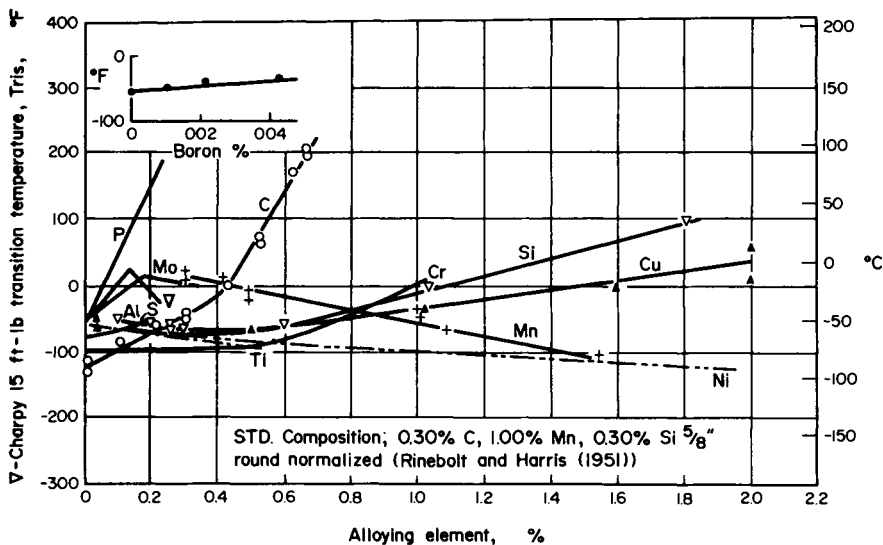


FIG. 9.39. Effect of various alloying elements on V-Charpy 15 ft-lb transition temperatures, summarized by Kihara *et al.*, from the data by Reinbolt and Harris.^(222,958)

Manganese also is known to retard the hot cracking of weld metal and in the heat-affected zone near the fusion line by reacting with the sulfur which causes the hot cracking.

Silicon.⁽¹⁰²⁾ Evaluation of the effect of silicon is complicated by the fact that silicon acts as both a deoxidizer and an alloying element. Consequently, the influence of silicon on the notch toughness will depend upon the concentration of other deoxidizing elements such as manganese and aluminum.

For example, in the experimental study conducted by Reinbolt and Harris (see Fig. 9.39 for summary of results), silicon up to 0.6% had little effect on notch toughness, but an addition of silicon over 0.6% caused an increase in the transition temperature.

Phosphorus.⁽¹⁰²⁾ An increase in phosphorus causes a drastic increase in the transition temperature (or a loss in the notch toughness) at a rate that equals that of carbon. Phosphorus is also known to cause hot cracking.

Sulfur⁽¹⁰²⁾ Sulfur in the form of sulfide inclusions often produces laminations in rolled steel plates. Laminations, whether of sulfide or oxide type, are oblate-shaped inclusions that have little strength when put under stress in the thickness direction. Laminated plates tend to act like several thin plates stacked together to form its thickness. When the notch toughness of a laminated plate is tested, the results tend to scatter, making an accurate analysis difficult. When laminations are not present, the effect of sulfur on notch toughness is minor. Sulfur is known to cause hot cracking, since FeS has a low melting point.

Aluminum.⁽¹⁰²⁾ Aluminum modifies the embrittling effect of oxygen; it alters the structure of sulfide inclusions, and it tends to combine with nitrogen. Aluminum is frequently used as a deoxidizer during steel-making. Aluminum tends to improve notch toughness.

Nickel.⁽¹⁰²⁾ Nickel improves notch toughness, especially in low-alloy steels. Many high-strength steels including HY-80, HY-130, and HY-180 contain larger amounts of nickel as the strength level increases.

Nitrogen and oxygen.⁽¹⁰²⁾ The effects of nitrogen and oxygen on notch toughness are complex because they react with both the steel and the other elements present, but they have been known to have a detrimental effect on notch toughness.

9.6.2 *Effects of manufacturing processes*^(102,902,923)

Effects of mill practices.⁽¹⁰²⁾ The deoxidation practice, the rolling operation, and the sizing operation affect notch toughness, and therefore are items of major concern.

Effects of deoxidation.⁽¹⁰²⁾ Steels can be classified into rimmed, semi-killed, and killed steels, depending upon the degree of deoxidation the steel receives during steel-making. Killing or deoxidation is ordinarily achieved by adding silicon or a combination of silicon and aluminum.

In killed steel the deoxidation is sufficiently complete, so that during freezing there is essentially no evolution of carbon monoxide gas. This minimizes segregation during solidification, so that the rolled skelp will be more uniform in composition and properties.

The absence of gas evolution also causes “piping”, or shrinkage voids, so a larger amount of steel must be cropped and discarded from the top of the ingot. Killed steels can be made with various carbon, manganese, or alloy contents and are generally more expensive than semi-killed or rimmed steels.

Semi-killed steels are only partially deoxidized and, as a result, are not as sound as killed steels. They have a higher level of segregation than killed steels, and the center and surface may differ noticeably in composition.

Effect of finishing temperature.⁽¹⁰²⁾ The hot mechanical-working range for mild steel, in practice, extends from approximately 1600 to 2100°F. During the hot rolling of the plate, the temperature at which mechanical working is finished has an influence on mechanical properties and notch toughness.

It is generally agreed that a high finishing temperature results in a coarse-grain structure, a slight reduction in strength, and a lower notch toughness. With a low finishing temperature, a finer grain size and higher toughness level is more likely to be obtained.

It is also well known that the yield and tensile strengths are increased by decreasing the grain size. Thus, as low a finishing temperature as is practical is desired from the standpoint of high yield and tensile strength and also for good notch toughness.

Effect of cold work and prestraining.⁽¹⁰²⁾ Cold working or prestraining increases yield strength and transition temperature. A rule of the thumb frequently used is that a permanent strain of 1% will raise the transition temperature 15 to 20°F.⁽⁹²³⁾

Gensamer *et al.*⁽⁹⁶⁰⁾ found that cold work when combined with aging is more effective in raising the transition temperature than cold work or aging alone. Figure 9.40 shows the typical results of their investigation. The figure shows that when an as-rolled semi-killed steel is subjected to various amounts of tensile strain, e.g. $\epsilon = 0\%$ to 10% and aged for 1 month, the transition temperature is raised considerably.

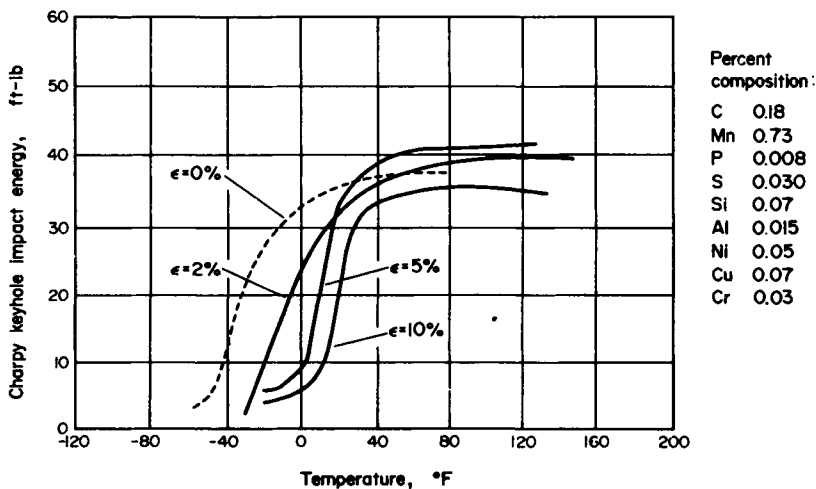


FIG. 9.40. Effect of cold work and aging on Charpy properties.^(923,960)

9.7 Notch Toughness Requirements and Fracture Control

Although a number of tests have been proposed and used for evaluating fracture toughness of materials, most specifications still employ the Charpy V-notch (CVN) impact value as the criterion for specifying notch toughness of structural steels. The drop-weight test and the dynamic tear tests are also used by the Navy and other specification societies.

Tables 1.2, 1.3 and 1.7 in Chapter 1 show the notch toughness values specified for various steels, including the American Bureau of Shipping system which classifies ship steels of ordinary strength into six grades—A, B, D, E, DS, and CS, as shown in Table 1.2. Among the six grades only two grades—D and E—have notch-toughness requirements. Similar requirements have been adopted for steels used in bridges, pressure vessels, and various other structures.

Figure 9.41 shows the Charpy V-notch impact requirements adopted by the seven major ship-classification societies⁽⁹²⁵⁾ (unified requirements). They have been grouped and surrounded in perimetric fashion to show general trends, particularly those concerning the toughness requirements for higher-strength steels: the RI, the NV, and the ABS have all lowered both the testing temperature and the impact energy requirements for higher strength steels.[†]

Lloyd's Register and Bureau Veritas have kept the same testing temperatures for higher-strength steels that were adopted for the Unified Requirements. Bureau Veritas maintains the same impact energy requirements, while Lloyd's makes the requirements proportional with the yield strength.

Pellini's study on fracture-control guideline. Pellini has developed a generalized

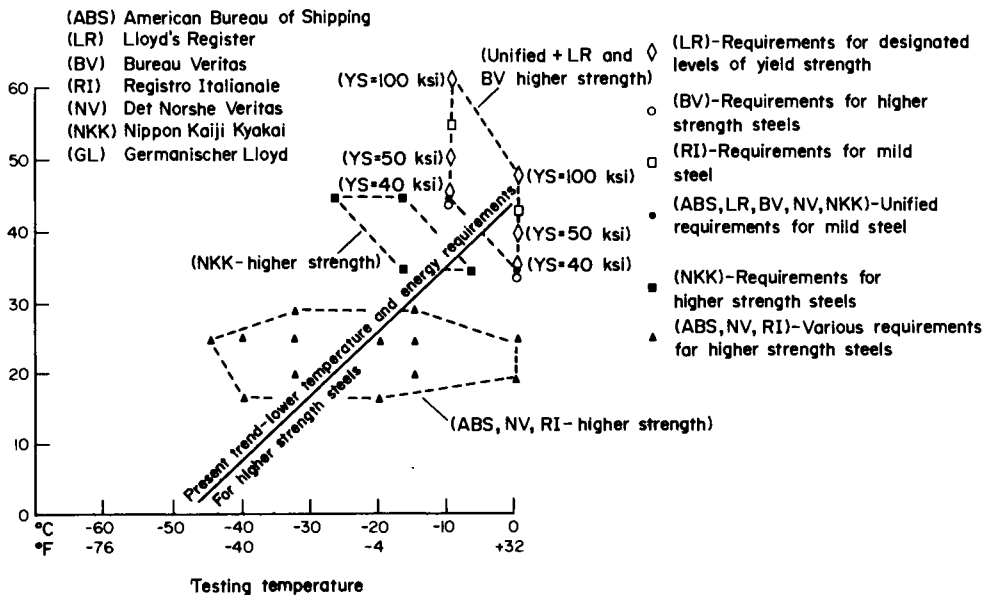


FIG. 9.41. CVN impact requirements of world unified ship.

[†] Pellini and associates found that the NDT temperatures for high-strength steels correspond to the Charpy impact test temperatures at energy values considerably higher than 15 ft-lb, as shown in Fig. 9.23.

fracture analysis diagram (FAD), as shown in Fig. 9.25. The NDT temperature can be determined by either the drop-weight test or the dynamic tear test. The FAD is widely used by the Navy.

Rolfe's study on fracture-control guidelines. Rolfe *et al.*⁽⁹²⁵⁾ in 1974 reported the results of his study on fracture-control guidelines for welded ship steel hulls. Attempts were made to use the fracture mechanics theory in developing practical fracture-control guidelines.⁽⁹⁰⁹⁾

9.8 Notch Toughness of Weld Metals

In order to avoid brittle fracture of welded structures, it is important that both the base plate and weld metal have adequate notch toughness. It is not difficult to obtain weld metal with notch toughness equivalent to ordinary carbon steel. However, it becomes a serious consideration when welding high-strength, quenched-and-tempered steels. These steels have both high yield strength and excellent notch toughness that is difficult to match in the weld metal.

The Welding Research Council Bulletin No. 111, prepared by Masubuchi, Monroe, and Martin,⁽⁹⁶¹⁾ presents results of a literature survey on the notch toughness of weld metals and the heat-affected zones. The survey was conducted in 1964. The base metals discussed include low-carbon steel and low-alloy, high-strength steels with up to 120,000 psi (84 kg/mm² or 827 MN/m²) yield strength. Welding processes considered include (1) shielded metal-arc welding, (2) submerged-arc welding, (3) gas metal-arc welding, and (4) electroslag and electrogas welding. The report covers the following subjects:

1. General trends of notch toughness of weld metals deposited with various welding processes as evaluated by the V-notch Charpy impact test.
2. Effects of various factors on notch toughness including:
 - (a) Chemical composition and microstructure.
 - (b) Factors related to welding procedures including heat input, multilayer welding techniques, welding position, preheating and post-weld heat treatments.
3. Notch toughness of the heat-affected zone evaluated by the Charpy impact test.
4. Evaluation of weld metal toughness with various tests other than the Charpy V-notch.

The following pages cover primarily the first subject as discussed in the *WRC Bulletin No. 111*. Some data have been upgraded to reflect the technical advances that have been made since the original survey in 1964.

It should be noted that data presented here are to show general trends in notch-toughness values of weld metals made with certain welding processes. Even when using the same welding process, notch-toughness values of weld metals may vary depending upon chemical composition of filler wire, welding conditions, and other parameters.

9.8.1 Requirements of various specifications for notch toughness of weld metals⁽¹⁰²⁾

Table 9.9 summarizes the requirements of various specifications for weld metal notch toughness in butt joints. Also, shown for comparison are the notch-toughness

TABLE 9.9 *Notch toughness requirements of various specifications*^(102, 961)

Base metal or weld metal	Specifications and classes	Charpy V-notch		
		Minimum energy absorption (ft-lb)	Temperature (°F)	
<i>International specification for ship steel</i>				
Base metal	Grade D*	35	32	
	Grade E	45	14	
<i>U.S. Navy HY-80 steel</i>				
	Thickness 2 inches or less*	60	- 120	
	Thickness over 2 inches*	30	- 120	
<i>AWS-ASTM (1964)</i>				
Covered-electrode-deposited metal	E6012, E6013, E6020, E7014, E7024	Not required		
	E7028*	20	- 0	
	E6010*, E6011, E6027, E7015, E7016, E7018	20	- 20	
	E8016-C3*, E8018-C3	20	- 40	
	E9015-D1, E9018-D1, E10015-D2, E10016-D2,, E10018-D2	20 ^(a)	- 60	
	E9018-M*, E10018-M, E11018-M, E12018-M	20	- 60	
	E8016-C1*, E8018-C1	20 ^(a)	- 75	
	E8016-C2*, E8018-C2	20	- 100	
<i>International specification for ship steel</i>				
	Joining Grade A steel*	35	68	
	Joining Grades B, C, D steels*	35	32	
	Joining Grade E steel*	45	14	
<i>IIW Commission II</i>				
Tensile strength of weld metal	61,000 to 67,000 psi	Quality I*, flat position	35	63
		Quality I*, vertical position	29	68
		Quality II*, flat position	46	68
		Quality II*, vertical position	40	68
		Quality III*, flat position	57	68
		Quality III*, vertical position	52	68
Tensile strength of weld metal	74,000 to 88,000 psi	Quality II, flat position	46	68
		Quality I, vertical position	40	68
		Quality III*, flat position	57	68
		Quality III*, vertical position	52	68
<i>IIW Commission XII</i>				
Submerged-arc-deposited metal	Minimum tensile strength of weld metal 60,000 psi	42C*	20	32
		42D*	20	- 4
	Minimum tensile strength of weld metal 71,000 psi	50C	20	32
		50D	20	- 4

^(a) Stress-relieved condition.

* Notch-toughness values are shown in Fig. 9.42.

requirements for some steel plates. Minimum values of Charpy V-notch absorbed energy at certain temperatures are specified. Figure 9.42 shows notch toughness requirements for entries marked in Table 9.9 with asterisks. No specification covers the notch toughness of weld metals in fillet joints.

Base metal. At an international conference held in London in 1959, ship-classification societies of the major shipbuilding countries approved an international specification

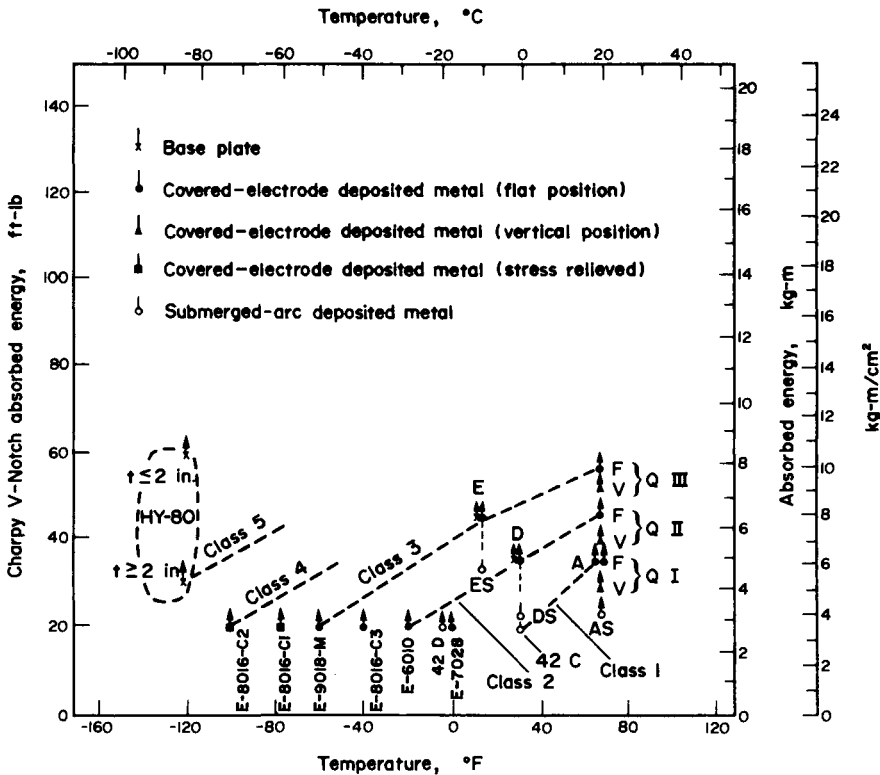


FIG. 9.42. Notch toughness required by various specifications.^(102,961)

1. International specification for ship steel: A, D, E (AS, DS, ES are 70% of A, D, and E, respectively; submerged-arc welding).
2. AWS: E-7028, E6010, E-8016-C3, E-9018-M, E-8016-C1, E-8016-C2.
3. IIW, Commission II: QI, QII, QIII for flat and vertical positions.
4. IIW, Commission XII: 42C, 42D (submerged-arc welding).

for ship steels.⁽⁹⁶²⁾ In this specification, steels are classified into five grades, A, B, C, D, and E.† Charpy V-notch values of 35 ft-lb at 32°F (4.8 kg-m at 0°C) for Grade D and 45 ft-lb at 14°F (6.2 kg-m at -10°C) for Grade E are specified. These requirements are represented in Figure 9.42 by points designated D and E.

Many specifications cover the notch toughness of high-strength structural steels. The U.S. Navy Specification MIL-S-16216 covers notch-toughness requirements for HY-80 steel, which is a low-carbon nickel-chromium-molybdenum steel. The minimum requirements for Charpy V-notch impact test values of steels in the quenched and tempered condition are 60 ft-lb (8.3 kg-m) for plates 2 in. (50 mm) thick or less and 30 ft-lb (4.1 kg-m) for plates over 2 in. (50 mm) thick.

Covered-electrode-deposited metals. Table 9.9 shows requirements of various specifications for the notch toughness of weld metals deposited with covered electrodes:

1. The AWS-ASTM specification for mild-steel covered electrodes (AWS A5 1-65 T and ASTM A-233-64) and for low-alloy-steel covered electrodes (AWS A5-64T and

† See Table 1.2 for ABS grade steels.

ASTM A316-64 T). Table 9.9 shows the notch-toughness requirements for weld metals made with various types of electrodes, E7028, E6010, E6011, etc.

2. Notch-toughness values which have been proposed for weld metals made with covered electrodes used for joining Grades A through E steels of the international specification for ship steels.
3. Notch-toughness values which have been recommended by Sub-Commission C, "Testing and Measuring of Weld Metal", of Commission II of the International Institute of Welding.⁽⁹⁶³⁾ Notch-toughness values have been recommended depending on (1) the tensile strength of the weld metal, (2) the quality of the weld (QI, QII, QIII), and (3) the welding position (flat or vertical).

Submerged-arc-deposited metals. Sub-Commission E, "Study of Weld Metal Deposited by All Processes", of Commission XII of IIW has proposed notch-toughness requirements for submerged-arc-deposited metals in carbon steel.⁽⁹⁶⁴⁾ Values shown in Table 9.9 are recommended, depending on (1) the minimum tensile strength of 60,000 psi (42 kg/mm² or 414 MN/m²) or 71,000 psi (50 kg/mm²) and (2) the class of weld (C or D).

Theoretically, requirements for the notch toughness of weld metal should be the same for all welding processes. However, several ship-classification societies currently accept submerged-arc-deposited weld metals with notch toughness lower than those of covered-electrode-deposited weld metals. Apparently, this is because of the difficulty in obtaining submerged-arc-deposited metals which meet the requirements for covered-electrode-deposited metals. For example, a ship classification society requires the following values for submerged-arc-deposited metals:

1. 25 ft-lb at 68°F (3.5 kg-m at 20°C) for joining Grade A steel.
2. 25 ft-lb at 32°F (35 kg-m at 0°C) for joining Grade E steel.
3. 35 ft-lb at 14°F (4.8 kg-m at -10°C) for joining Grade E steel.

These values are shown in Figure 9.42 by points designated AS, DS, and ES, respectively. These values are about 70% of the values required for covered-electrode weld deposits used in joining steels of corresponding grades.

Comparison of various specifications. To facilitate discussions in later pages of this textbook, the notch-toughness requirements of various specifications are divided arbitrarily into the following five classes, with Class 1 being the least severe and Class 5 the most severe:

- Class 1: QI, flat position; 42°C (35 ft-lb at 68°F; 20 ft-lb at 32°F).
- Class 2: QII, flat; Grade D; E6010 (46 ft-lb at 68°F; 35 ft-lb at 32°F; 20 ft-lb at -20°F).
- Class 3: QIII, flat; Grade E; E9018-M (57 ft-lb at 68°F; 45 ft-lb at 14°F; 20 ft-lb at -60°F).
- Class 4: E8016-C2 (20 ft-lb at -100°F).
- Class 5: HY-80 steel base metal over 2 in. (50 mm) thick (30 ft-lb at -120°F).

Basis for toughness requirements. It is still debatable (1) whether the Charpy V-notch impact test is an adequate test for evaluating notch toughness and (2) what notch-toughness level is really needed even for base metals. Nevertheless, attempts have been made to establish realistic requirements for the notch toughness of the base metal by:

1. Analysis of notch-toughness data obtained with specimens taken from fractured ships.

2. Comparison of notch-toughness data obtained with Charpy specimens and the fracture behavior of large-size specimens

However, almost no information has been obtained which can be used to establish realistic requirements for weld-metal and heat-affected-zone notch toughness. Most current specifications are apparently based on the principle that the notch toughness required for the base metal should also be required for the weld metal deposited by a welding process used to join the steel. This basic principle, however, is not always obeyed. For example:

1. The notch-toughness requirement for weld metals deposited with MIL-11018 electrodes, which have been used extensively for the fabrication of submarine hulls from HY-80 steel, is considerably less severe than that for HY-80 base metal. The requirement is 20 ft-lb at -60°F (2.8 Kg-m at -51°C) for the weld metal and 60 or 30 ft-lb at -120°F (8.3 or 4.1 kg-m at -84°C) for the base metal.
2. Some ship-classification societies allow lower notch toughness for submerged-arc-deposited metals than for covered-electrode-deposited metal.

The low toughness requirements have been set in some cases because weld metals with higher notch toughness are not available at the present time, not because notch toughness is less important in the weld metal than in the base metal.

9.8.1 Notch toughness of covered-electrode-deposited metals

There are abundant data on the notch toughness of weld metals deposited with different types of electrodes from various manufacturers. The following pages discuss the general trends observed in the notch toughness of weld metals deposited by a variety of electrodes types.

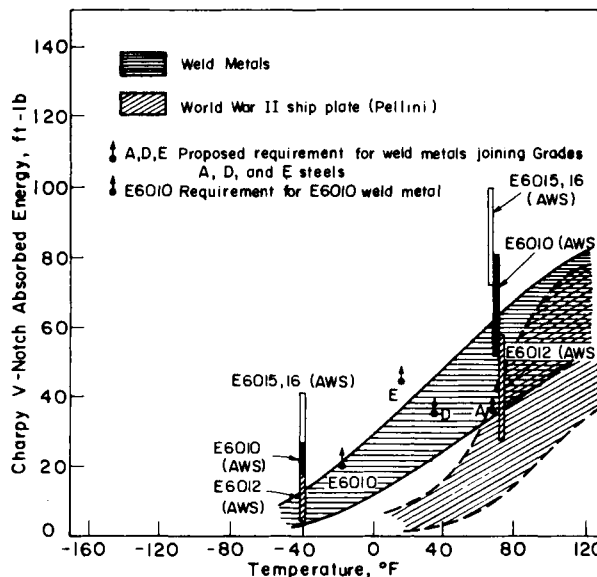


FIG. 9.43. Notch-toughness data of weld metals of mild-steel electrodes.

Mild steel electrodes E60XX. Figure 9.43 contains V-notch Charpy transition data for various weld metals:

1. A “band” which shows variation of transition curves for weld metals deposited with mild-steel electrodes. The band was obtained from data reported by Pellini⁽⁹⁶⁵⁾ on E6010 electrodes and by Watkinson⁽⁹⁶⁶⁾ on three types of British electrodes. A band for the notch toughness of ship steels used in World War II production is shown also.
2. Ranges of notch-toughness values expected in the as-deposited condition at 70°F and –40°F (21°C and –40°C) given in the *AWS Welding Handbook* for weld metal deposited by E6010, E6012, E6015, and E6016 electrodes⁽⁹⁶⁷⁾

Also shown in Figure 9.43 are some notch-toughness requirements. Figure 9.43 shows the general trends in the notch toughness of weld metals deposited with mild-steel-covered electrodes:

1. E6010 electrodes: The band for Pellini’s data for American E6010 electrodes and Watkinson’s data for British mild-steel electrodes is higher at all temperatures than the average band for ship steels for World War II production, indicating superior notch toughness. Data given in the latest *AWS Welding Handbook* and the recent toughness requirement for the E6010 electrode indicate that modern E6010 electrodes provide weld metals with better notch toughness than provided by the older electrodes used by Pellini and Watkinson.
2. Low-hydrogen electrodes: Modern E6015 and E6016 electrodes provide weld metals with notch toughness which almost can meet the Grade E requirement.
3. E6012 electrodes: E6012 electrodes do not meet even the Grade A requirement. E6012 and E6013 electrodes are not approved for use in joining main structural members because of the low notch toughness of their weld metals.

It is interesting to note that notch toughness of weld metals made by various types of low-carbon steel-covered electrodes is better than that of ordinary base plates. The major reason is that the carbon content (0.1% or lower) of the weld metal is lower than that of the base metal (about 0.2%).

Low-hydrogen, low-alloy electrodes. Figure 9.44 shows a band for notch toughness data of weld metals obtained with modern low-hydrogen, low-alloy electrodes, E9018, E10016 and 18, and E11016 and 18. These data were obtained by Sagan-Campbell⁽⁹⁶⁸⁾ and Smith.⁽⁹⁶⁹⁾

Also shown in Fig. 9.44 are some notch-toughness requirements as shown in Fig. 9.42. The figure shows that the notch toughness of weld metals deposited with modern low-hydrogen, low-alloy electrodes is much superior to that required of Grades D and E steels. However, no electrodes specification requires weld metals that meet the notch toughness requirements for HY-80 steel base metal. It should be noted that we are comparing HY-80 base plate of which excellent notch toughness has been obtained by a special heat treatment (quench and temper) to the weld metal in the as-welded condition.

9.8.2 Notch toughness of submerged-arc deposited metals

Heavy mild-steel ship plates. It has been known for some time that the notch toughness of two-pass submerged-arc-deposited metals decreases as the plate thickness increases.

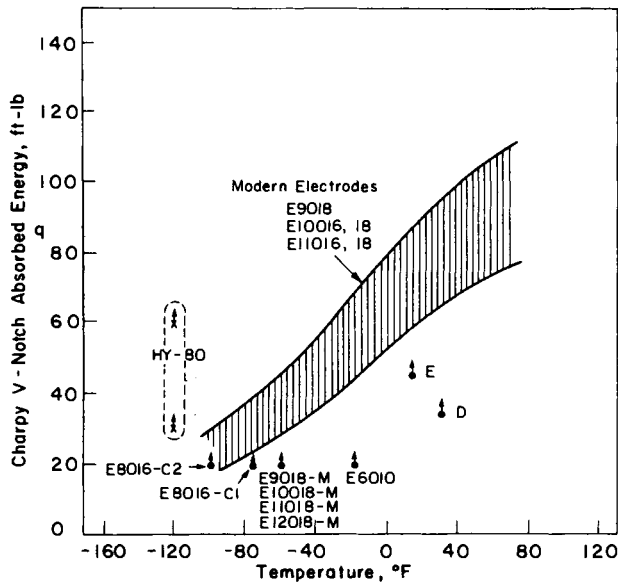


FIG. 9.44. Notch-toughness of weld metals of low-hydrogen high-strength steel electrodes.

In the fabrication of pressure vessels, which require high-quality welds of very heavy plates, multilayer procedures are used commonly. In the fabrication of merchant-ship hulls, there has been strong interest in reducing the number of passes, primarily for economic reasons.

Figure 9.45 was produced in the original survey made in 1964 based upon published data available at that time. The notch toughness of the multilayer-weld metal was excellent for mild steel, passing Grade D requirements. However, the notch toughness of the two-pass weld metal was poor; the weld did not meet Grade A requirements.

Since then considerable efforts have been made to improve notch toughness of weld metals made by the one-side submerged-arc process.[†] Figure 9.46 has been prepared to reflect recent developments.^(133,970) Included here are:

1. Notch toughness of weld metals made in two-passes (one-pass each side) on low-carbon steel plates in two thickness: 25 mm (1 in.) and 35 mm (1.4 in.) Improved bonded-type flux was used.
2. Ranges of notch-toughness values at 0, -20, and -40°C (32, -4, and -40°F) of weld metals made by the FCB (flux-copper backing) process.

High-strength notch tough steel. Many research programs have been and are being conducted for developing submerged-arc welding processes which provide weld metals with high strength and good notch toughness.

A research program was conducted for the Bureau of Ships at Battelle Memorial Institute^(971,972) for developing fluxes and filler wires for submerged-arc welding of HY-80 steel. Figure 9.45 shows the Charpy V-notch transition curves of (a) the weld metal which had the best notch toughness and (b) a weld metal made with conventional wire and flux. The welds were made in $\frac{1}{2}$ -in. (12.7 mm) thick HY-80 steel plate by the

[†] Refer to Section 1.7.3.

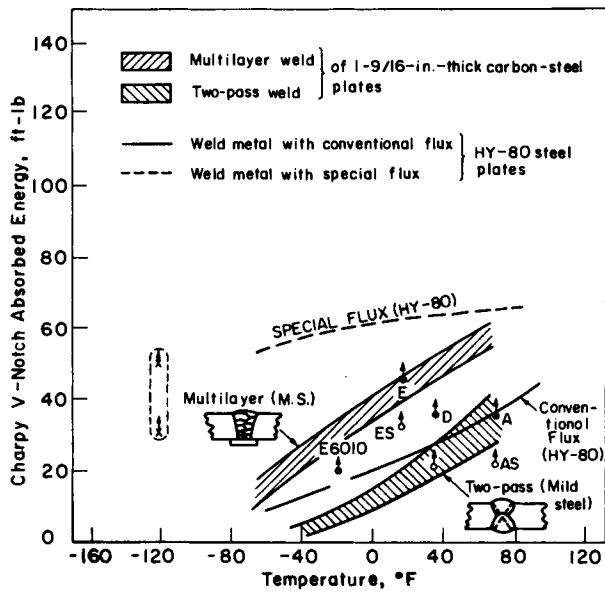


FIG. 9.45. Notch-toughness of submerged-arc deposited metals in mild steel and high-strength steels.

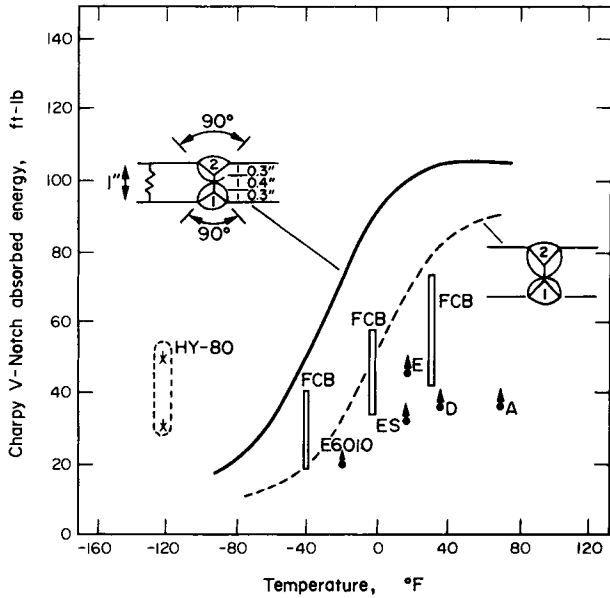


FIG. 9.46. Notch toughness submerged-arc deposited metals (improved recent data).

multilayer technique with heat inputs of 45,000 joules per inch (17,700 joules/cm) of weld bead. The improvement of the experimental weld metal was over 90,000 psi. (63 kg/mm² or 620 MN/m²).

The oxygen content of the experimental weld metal was less than one-half that of the conventional weld metal. Microscopic investigations revealed that the experimental

weld metal was significantly cleaner (with fewer inclusions) than the conventional weld metal. The investigators believed that the improvement in notch toughness was a result of the lower oxygen content and fewer inclusions in the experimental weld metal.

9.8.3 Notch toughness of gas metal-arc-deposited metals

Figure 9.47 shows two sets of data as follows:[†]

1. Notch toughness data obtained by Sekiguchi *et al.*⁽⁹⁷³⁾ on weld metals using low-carbon steel wires shielded by 100% CO₂ gas. The base plate was low-carbon steel.
2. Notch toughness of weld metals made with the Battelle Narrow-gap process using A-632 filler wire and shielding gas mixtures of CO₂ and argon (100, 20, and 0% argon).⁽⁹⁷⁴⁾ The base plate was HY-80 steel. The chemical composition (in percent) of the filler wire was:

C	Si	Mn	Ni	Cr	Mo	V	Zr	Al
0.04	0.57	1.36	1.22	0.13	0.45	0.15	0.005	0.013

The figure shows that the notch toughness of weld metal deposited with CO₂ shielding is fairly good but not excellent. The notch toughness of weld metals improves as the percentage of argon increases.

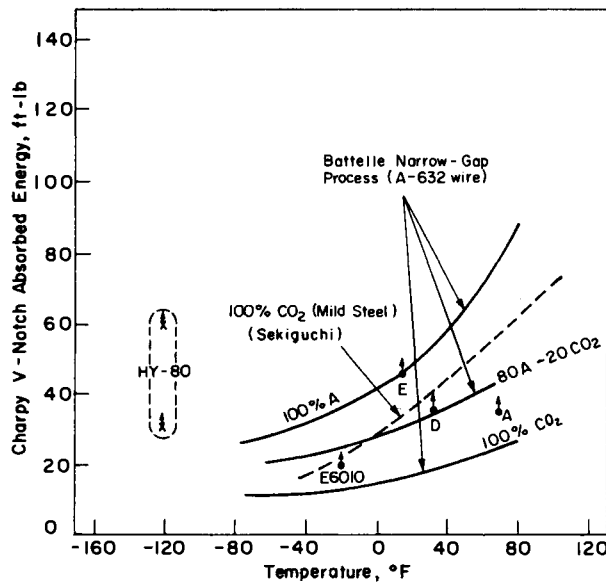


FIG. 9.47. Notch-toughness of gas metal-arc deposited weld metals.

[†] Although no special effort has been made to survey notch-toughness values of weld metals made with GMA process today, the author feels that notch-toughness values have been improved to some extent since the survey was made in 1964.

9.8.4 Notch toughness of electroslag- and electrogas-deposited metals

Notch-toughness data for electroslag- and electrogas-deposited metals appear in a number of articles. Direct comparisons of test data are different, since most Russian investigators used 2-mm-deep U-notch Mesnagar specimens, while Charpy V-notch or keyhole specimens were used by American, Western European, and Japanese investigators.[†]

Figure 9.48 was prepared in the original survey. The notch toughness of electroslag-deposited weld metal in the as-welded condition was very poor, although it could be improved by stress relieving and normalizing treatments.

Figure 9.49 has been prepared to include data obtained recently in Japan:

1. A notch-toughness curve of electroslag-deposited metals presented in a paper by Hasegawa.⁽⁹⁷⁵⁾ The base plate was a high-strength steel with 75,000 psi (52.7 kg/mm² or 517 MN/m²) yield strength.
2. Ranges of notch-toughness values at 0°C (32°F) of electroslag-deposited metals.^(131, 976) Base plates include low-carbon steel and high-strength steel with 74,000 psi (52 kg/mm² or 510 MN/m²) yield strength.

Notch-toughness values shown in Fig. 9.49 are significantly better than those shown in Figure 9.48.

9.8.5 Summary of notch toughness of weld metals up to 120,000 psi yield strength

As a summary, Figure 9.50 illustrates the general trends in the notch toughness of

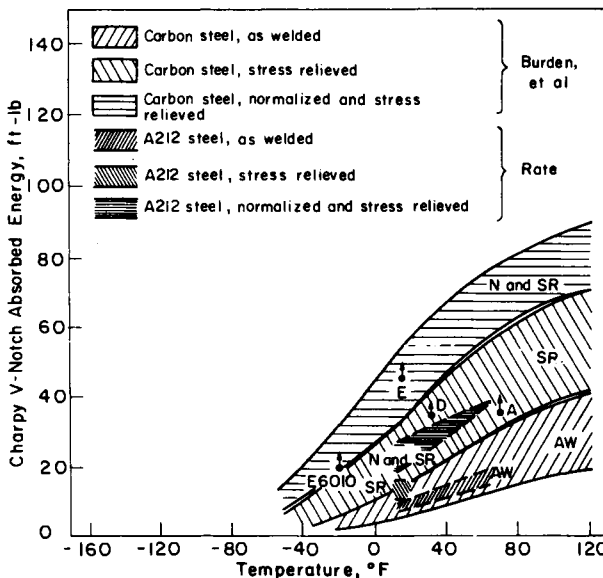


FIG. 9.48. Improvement through heat treatment of notch-toughness of electroslag-deposited metals.

[†] See Section 9.3.2.

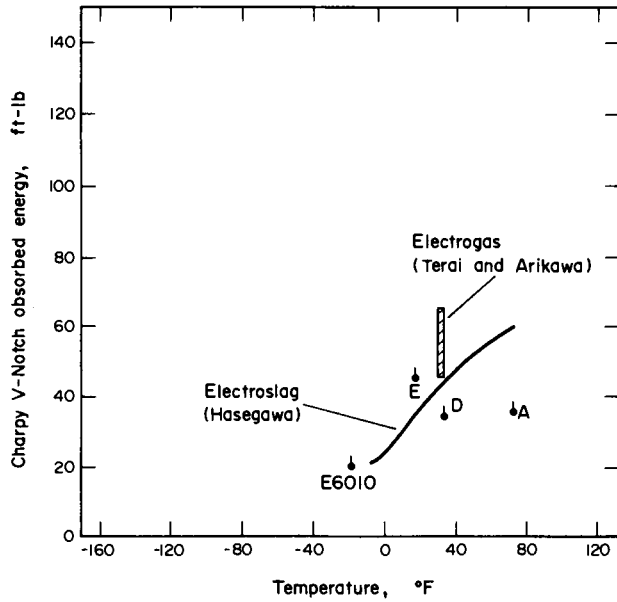


FIG. 9.49. Notch toughness of electroslag- and electrogas-deposited metals (improved recent data).

Notch-toughness level		Low ← Notch-toughness → High							
Class		0	1	2	3	4	5		
Typical V-notch Charpy value	ft-lb	Not specified	35	35	20	45	20	30	
	Temp, °F		68°F	32°F	-20°F	14°F	-60°F	-100°F	-120°F
Example			A	D	E6010	E	E9018 M	E8016-C2	HY-80 base plate
Shielded metal-arc welding									
E6012, E6013									
E6010, E6011									
E9018-M, E11018-M									
E8016-C2, E8018-C2									
Submerged arc welding									
Conventional 2 pass									
Conventional multilayer									
Special technique									
Gas metal-arc									
CO ₂ , CO ₂ -O ₂									
Argon, argon-CO ₂									
Electroslag, Electrogas									
As welded									
Normalized									

Note: The areas enclosed by dotted lines indicate that there is some uncertainty whether welds will meet the requirements.

FIG. 9.50. General trends in the notch-toughness of weld metals deposited by various welding processes (improved recent data included).

weld metals deposited by various welding processes. Figure 9.50 incorporates improved recent data.[†]

Here, notch-toughness level is classified arbitrarily in five classes, Class 0 being the lowest notch toughness and Class 5 being the highest notch toughness. Notch toughness is not specified for Class 0. The typical notch toughness value for Class 1 is 35 ft-lb V-notch impact of 68°F; this corresponds to the requirement for weld metals made with covered electrodes for joining Grade A steel. The requirements for Class 2 correspond to requirements for Grade D and E6010. The requirements for Class 3 correspond to Grade E and E9018-M. Values for Classes 4 and 5 correspond to E8016-C2 and HY-80 base plate, respectively.

This figure is prepared to provide general guidance for selecting welding processes when the weld needs to meet a certain notch-toughness level.

Weld metals which meet the Class 1 requirement can be obtained with all welding processes listed except when using E6012 and E6013 electrodes.

To meet the Class 2 requirement, welding procedures should be selected as follows:

1. Shielded metal-arc welding: E6010 electrodes can be used.
2. Submerged-arc welding: multilayer procedure with conventional wire and flux may be used. For two-pass welding, special wire and flux and wire also may be needed.
3. Gas metal-arc welding: argon and argon-CO₂ (with high argon content) shielded processes must be used.

Weld metals which meet the Class 4 requirement can be deposited by a limited number of processes, as follows:

1. Shielded metal-arc welding: low-hydrogen nickel-steel electrodes E8016-C2 and E8018-C2 will deposit weld metals which meet the Class 4 requirements in the stress-relieved condition.
2. Gas metal-arc welding: argon and argon-CO₂ (with high argon content)—shielded processes appear to be satisfactory.
3. Submerged-arc welding: with the use of special techniques, submerged-arc welding may be satisfactory.

No welding process can be guaranteed to deposit weld metals as tough as HY-80 steel base metal. The most promising welding process in this respect is the inert-gas metal-arc process. The inert-gas tungsten-arc process also deposits weld metals with a high notch toughness; however, the low deposition rates involved make this process unattractive for the fabrication of commercial structures.

9.8.6 *Notch toughness of weld metals over 120,000 psi yield strength*

Trends of notch toughness of both base plate and weld metals with yield strength over 120,000 psi (84.4 kg/mm² or 827 MN/m²) are already presented in Section 1.4.3 (see Figs. 1.9 through 1.11). Notch toughness of both base metal and weld metal decreases as yield strength increases. High-quality welding processes such as gas metal-arc welding

[†] Figure 9.50 is different from a similar figure presented in earlier publications, namely references (102), (961), and (977).

using argon shielding and gas tungsten arc must be used to join high-quality, high-strength steels.

References

- (901) LIEBOWITZ, H., editor, *Fracture*, vol. I through VI, Academic Press, New York, 1968–71.
- (902) PARKER, E. R., *Brittle Behavior of Engineering Structures*, John Wiley & Sons, Inc., New York, 1957.
- (903) BIGGS, W. D., *The Brittle Fracture of Steel*, Pitman Publishing Corporation, New York, 1960.
- (904) HALL, W. J., KIHARA, H., SOETE, W., and WELLS, A. A., *Brittle Fracture of Welded Plates*, Prentice-Hall, Inc., 1967.
- (905) TETELMAN, A. S. and MCEVILLY, A. J., Jr., *Fracture of Structural Materials*, John Wiley & Sons, Inc., New York, 1967.
- (906) AVERBACH, B. L., FELBECK, D. K., HAHN, G. T., and THOMAS, D. A., editors, *Fracture* [Proceedings of an international conference on the Atomic Mechanism of Fracture, held in Swampscott, Massachusetts, April 12–16, 1959], The Technology Press of M.I.T. and John Wiley & Sons, Inc., New York, 1959.
- (907) LOW, J. R., Jr., “The fracture of metals”, *Progress in Materials Science*, Pergamon Press, **12** (1), 1–96 (1963).
- (908) BROEK, D., *Elementary Engineering Fracture Mechanics*, Noordhoff International Publishing, Leyden, The Netherlands, 1974.
- (909) ROLFE, S. T., and BARSOM, J. M., *Fracture and Fracture Control in Structures. Applications of Fracture Mechanics*, Prentice-Hall, Inc., Englewood Cliffs, New Jersey, 1977.
- (910) PELLINI, W. S., *Principles of Structural Integrity Technology*, Office of Naval Research, Arlington, VA., 1976.
- (911) HAYDEN, H. W., MOFFAT, W. G., and WULFF, J., *The Structure and Properties of Materials*, vol III, Mechanical Behavior, John Wiley & Sons, Inc., New York, 1955.
- (912) *Fracture Toughness Testing and Its Applications*, ASTM Special Technical Publication No. 381, American Society for Testing and Materials, 1965.
- (913) *Final Report of a Board of Investigation to Inquire into the Design and Methods of Construction of Welded Steel Merchant Vessels*, Washington, D.C., Government Printing Office, 1947.
- (914) HODGSON, J. and BOYD, G. M., “Brittle fracture in welded ships”, *Quarterly Transactions of the Institution of Naval Architects*, **100** (3), 141–181 (July 1958).
- (915) CHAZEL, E. A., JR., GOLDBERG, J. E., NACHTSHEIM, J. J., RUMKE, R. W., and Stavovy, A. B., “Third decade of research under the Ship Structure Committee”, a paper presented at the Ship Structure Symposium, Washington, D.C., 6–8 Oct. 1975.
- (916) SHANK, M. E., “A critical survey of brittle failure in carbon-steel structures other than ships”, *Welding Research Council Bulletin*, No. 17, 1954.
- (917) SHANK, M. E., editor, *Control of Steel Construction to Avoid Brittle Fracture*, Welding Research Council, 1957.
- (918) “Fractured girders of the King’s Bridge, Melbourne”, *Engineering*, **217**, 520–522 (20 Mar. 1964).
- (919) SRAWLEY, J. E. and ESAGAR, J. B., “Investigation of Hydrotest Failure of Thiokol Chemical Corporation 260-inch-diameter SL-1 Motor Case”, NASA Technical Memorandum, NASA TM X-1194, Lewis Research Center, NASA (Jan. 1966).
- (920) WILLIAMS, M. L. and ELLINGER, G. A., “Investigations of structural failures of welded ships”, *Welding Journal*, **32** (10), Research Supplement, 498s–527s (1953).
- (921) BLUHM, J. Z., “Fracture arrest”, pp. 1–63 of vol. V of *Fracture*, edited by Liebouritz, L., Academic Press, New York, 1969.
- (922) YOSHIKI, M., ITAGAKI, H., and KANAZAWA, T., *Proceedings of the Second SESA International Congress on Experimental Mechanics, and Experimental Mech.*, pp. 458–462 (Sept. 1966).
- (923) MCCLURE, G. M., EIBER, R. J., HAHN, G. T., BOULGER, F. W., and MASUBUCHI, K., *Research in the Properties of Line Pipe*, American Gas Association, Catalogue No. 401PR (May 1962).
- (924) WILLIAMS, M. L., “Correlation of metallurgical properties and service performance of steel plates from fractured ships”, *Welding Journal*, **37**, Research Supplement, 445s–454s (Oct. 1958).
- (925) ROLFE, S. T., RHEA, D. M., and KUZMANOVIC, B. O., *Fracture Control Guidelines for Welded Ship Hulls*, SSC-244, Ship Structure Committee, 1974.
- (926) *ASTM E208–69 Standard Method for Conducting Drop-Weight Test to Determine Dil-Ductility Transition Temperature of Ferritic Steels*, American Society for Testing and Materials, 1969.
- (927) PELLINI, W. S. and PUZAK, P. P., *Fracture Analysis Diagram Procedures for the Fracture-Safe Engineering Design of Steel Structures*, NRL Report 5920, 15 Mar. 1963, also *Welding Research Council Bulletin*, Series No. 88, May 1963.
- (928) PELLINI, W. S., and PUZAK, P. P., *Practical Considerations in Applying Laboratory fracture test criteria*

- to the Fracture-safe design of pressure vessels, NRL Report 6030, 5 Nov., 1963; also *Transactions, American Society Mechanical Engineers, Series A, Journal of Engineering for Power*, pp. 429–443 (Oct. 1964).
- (929) Military Standard MIL-STD-1601 (SHIPS), *Method for 5/8 inch Dynamic Tear Testing of Metallic Materials*, May 1973.
- (930) ORNER, G. M. and HARTBOWER, C. E., "The low blow transition temperature", *ASTM Proceedings*, **58**, 623–634 (1958).
- (931) KOSHIGA, F., "On the pressed-notch Charpy test", *Journal of the Society of Naval Architects of Japan*, **104** (1959).
- (932) BAKER, J. F. and TIPPER, C. F., "The value of the notch tensile test", *Proceedings of the Institution of Mechanical Engineers*, **170**, 65–75 (1956).
- (933) KAHN, N. A. and IMBEMBO, E. A., "A method of evaluating transition from shear to cleavage failure in ship plate and its correlation with large-scale plate tests", *Welding Journal*, **27** (4), Research Supplement.
- (934) DE GEAFF, J. E. and VAN DER VEEN, J. H., "The notched slow-bend test as a brittle fracture test", *Journal of Iron and Steel Institute*, **173**, 19–30 (1953).
- (935) VAN DER VEEN, J. H., *Influence of Steel-making Variables on Notch Toughness*, Ship Structure Committee Report, Serial No. SSC-128 (June 1960).
- (936) STOUT, R. D., MCGEADY, L. J., SUND, C. P., LIBSCH, J. F., and DOAN, G. E., "Effect of welding of ductility and notch sensitivity of some ship steel", *Welding Journal*, **26**, (6), Research Supplement, 335s-357s (1947).
- (937) KINZEL, A. B., "Ductility of steel for welded structures", *The Welding Journal* **27** (5), Research Supplement, 217s-234s (1948); and *Transactions of ASM*, **40**, 27–82 (1948).
- (938) KOMMERELL, O., *Stahlbau-Technik*, **2**, 51–52 (1938).
- (939) MELHARDT, H., "New Austrian welding standards", *The Welding Journal*, **31** (7), 592–595 (1952).
- (940) PUZAK, P. P., Eschbacher, E. W., and Pellini, W. S., "Initiation and propagation of brittle fracture in structural steels", *The Welding Journal*, **31** (12), Research Supplement, 561s-581s (1952).
- (941) PUZAK, P. P., SCHUSTER, M. E., and PELLINI, W. S., "Crack-starter tests of ship fracture and project steels", *The Welding Journal*, **33** (10), Research Supplement, 481s-495s (1954), and Puzak, P. P., and Pellini, W. S., "Evaluation of significance of Charpy tests for quenched and tempered steels", *ibid.*, **35** (6), Research Supplement (1956).
- (942) HARTBOWER, C. E., and PELLINI, W. S., "Explosion bulge test of the deformation of weldments", *Welding Journal*, **30** (6), Research Supplement, 307s–318s (1951).
- (943) HARTBOWER, C. E., "Mechanics of the explosion bulge tests", *Welding Journal*, **32** (7), Research Supplement, 333s–341s (1953).
- (944) FOLKHARD, E., "Le comportement de tuyaux pour conduites forcées, soudés à l'arc, lors déssais par éclatement", *Revue de la Soudre: Lastijdschrift* (Brussels), **12** (1), 15–27 (1956).
- (945) HAUTTMANN, H., "Erprobung Trennbruchsicherer Baustahle in Berstversuchen", *Schweisstechnik* (Austria), **13** (2), 13–19 (1959).
- (946) KIHARA, H., ICHIKAWA, S., MASUBUCHI, K., OGURA, Y., IIDA, K., YOSHIDA, T., and Oba, H., "Explosion tests on arc-welded tubes with and without stress annealing", *Journal of the Society of Naval Architects of Japan*, **100**, 179–187 (1965).
- (947) KIHARA, H., ICHIKAWA, S., MASUBUCHI, K., IIDA, K., YOSHIDA, T., OBA, H., and Ogura, Y., "Explosion tests on arc welded tubes with various welding procedures", *Journal of the Society of Naval Architects of Japan*, **104**, 119–129 (1958).
- (948) ROBERTSON, T. S., "Propagation of brittle fracture in steel", *Journal of the Iron and Steel Institute*, **175**, 361–374 (Dec. 1953).
- (949) ROBERTSON, T. S., "Brittle fracture of mild steel", *Engineering*, **172**, 444 (Oct. 1951).
- (950) FEELY, F. J., JR., HRKTO, D., KLEPPE, S. R., and NORTHRUP, M. S., "Report on brittle fracture studies", *Welding Journal*, **33** (2), Research Supplement, 99s–111s (1954).
- (951) YOSHIKI, M., KANAZAWA, T., and ITAGAKI, H., "Double tension test with Flat temperature gradient", *Proceedings Third Japan Congress on Testing Materials—Metallic Materials*, pp. 103–106 (1960).
- (952) YOSHIKI, M. and KANAZAWA, T., *Studies on the Brittle Fracture Problems in Japan*, vol. 13 of the 60th Anniversary series, published by the Society of Naval Architects of Japan, 1967.
- (953) WELLS, A. A., "The mechanisms of notch brittle fracture", *Welding Research*, **7** (1955), 34r–56r.
- (954) KIHARA, H., *Researches on Brittle Fracture Initiation of Welded Steel Structures in Japan*, 1972.
- (955) GREENE, T. W., "Evaluation of effect of residual stresses", *Welding Journal*, **28** (5), 193s–204s (1949).
- (956) KIHARA, H. and MASUBUCHI, K., "Effect of residual stress on brittle fracture", *Welding Journal*, **38** (4), Research Supplement, 159s–168s (1959).
- (957) KIHARA, H., MASUBUCHI, K., and ISHII, H., "Brittle fracture strength of welded spherical container", *Welding Journal*, **38** (11), Research Supplement, 451s-456s (1959).
- (958) REINBOLT, J. A. and HARRIS, W. J., JR., "Effect of alloying elements on notch toughness of pearlitic steels", *Transactions of the ASM*, **43**, 1175–1214 (1951).

- (959) FRAZIER, R. H., BOULGER, F. W., and LORIG, C. H., *An Investigation of the Influence of Deoxidation and Chemical Composition on Notched-Bar Properties of Semi-Killed Ship Steel*, Ship Structures Committee Report SSC-53 (Nov. 1952).
- (960) GENSAMER, M., KLIER, E. P., PRATER, T. A., WAGNER, F. C., MACK, J. D., and FISHER, J. L., *Correlation of Laboratory Tests with Full Scale Ship Plate Fracture Test*, Ship Structures Committee Progress Report SSC-9 (1947).
- (961) MASUBUCHI, K., MONROE, R. E., and MARTIN, D. C., "Interpretive report on weld-metal toughness", *Welding Research Council Bulletin*, No. 111 (Jan. 1966).
- (962) KAKU, S., "Unified requirements for hull structural steels and some problems on their welding procedures", *Journal of the Japan Welding Society*, **33** (4), 11-16 (1964).
- (963) "Method of testing and approval of electrodes for welding mild and low alloy high tensile steel", *Welding in the World*, **1** (1), 2-17 (1963).
- (964) "Tentative methods for testing weld metal deposited by submerged-arc welding (mild steel)", *Welding in the World*, **1** (1), 28-37 (1963).
- (965) PELLINI, W. S., "Notch ductility of mild-steel weld metal", *British Welding Journal*, **6** (4), 162-174 (1959).
- (966) WATKINSON, F., "Notch ductility of mild steel weld metal", *British Welding Journal*, **6** (4), 162-174 (1959).
- (967) *Welding Handbook*, Sections 1 through 5, American Welding Society, New York.
- (968) SAGAN, S. S. and CAMPBELL, H. C., "Factors which affect low-alloy weld-metal notch-toughness", *Welding Research Council Bulletin*, Series No. 59, April 1960.
- (969) SMITH, D. C., "Development, properties and usability of low hydrogen electrodes", *The Welding Journal*, **38**, (9), Research Supplement, 377s-392s (1959).
- (970) TERAI, K., Private communication.
- (971) LEWIS, W. J., FAULKNER, G. E., MARTIN, D. C., and RIEPPEL, P. J. "Submerged-arc welding of HY-80 steel", *Welding Journal*, **40** (8), Research Supplement, 337s-345s (1961).
- (972) LEWIS, W. J., FAULKNER, G. E., and RIEPPEL, P. J., "Flux and filler wire developments for submerged-arc welding of HY-80 steel", *Welding Journal*, **40** (8), Research Supplement, 337s-345s (1961).
- (973) SEKIGUCHI, H., MASUMOTO, I., TAMAOKI, K., and ASAI, Y. "Impact properties of weld metals deposited with the CO₂-O gas shielded arc welding process—Part I", *Journal of the Japan Welding Society*, **32** (9), 732 (1963), abstract of a paper presented at the National Fall Meeting, 1963.
- (974) NELSON, J. W., RANDALL, M. D., and MARTIN, D. C., *Development of Methods of Making Narrow Welds in Thick Steel Plates by Automatic Arc Welding Processes*, Final Report to Bureau of Ships, Department of the Navy, on Contract NObs-86424, Battelle Memorial Institute, Mar. 1964.
- (975) HASEGAWA, M., *Automatic Welding as Applied to Japanese Shipbuilding*, Osaka Transformer Company, Ltd., April 1968.
- (976) TERAI, K., and ARIKAWA, M., *Recent Developments in One-side Automatic Welding*, published in English by the Sampo, Inc., Kanda Sakuma-cho, Chiyoda-ku, Tokyo, 1968.
- (977) MASUBUCHI, K., "Welding problems in shipbuilding", *Marine Technology*, **6** (1), 66-75 (Jan. 1969).

Theoretical and Experimental Studies of the Brittle Fracture of Welded Structures

10.1 Theories of Brittle Fracture

10.1.1 *The strength of an ideal solid and actual structures*⁽¹⁰²⁾

An ideal elastic solid is one that exhibits a total elastic response to all loads up to the point of actual atomic separation. Such a property is only theoretically possible, and that only in a crystalline solid containing no defects, but the ideal elastic solid has proven its usefulness as a working concept and has been a part of much of the thinking that has been done about the fracture of solids.

The usual means of calculating the theoretical strength of an ideal elastic solid presupposes that all the energy of separation is used in the creation of two new surfaces; and that the only energy used in this way is surface energy. The theoretical strength, σ_{th} , is as follows:

$$\sigma_{th} = \sqrt{\frac{ES}{a}} \quad (10.1)$$

where E = Young's modulus,
 S = surface energy per unit area,
 a = lattice parameter of crystal.

In the case of steel, for example, in which $a = 3 \times 10^{-8}$ cm, $E = 2 \times 10^6$ kg/cm², $S = 10^{-3}$ kg cm/cm², σ_{th} is approximately 2×10^5 kg/cm² (2000 kg/mm², or 3×10^6 psi), which is about $E/10$.

The strength of a real material is far less than this theoretical strength, σ_{th} , as shown in Fig. 10.1. Most modern commercial high-strength steels have an ultimate strength of approximately 3×10^5 psi (210 kg/mm² or 690 MN/m²). For ordinary low carbon steel, the ultimate tensile strength is about 6×10^4 psi (42 kg/mm² or 414 MN/m²) and the yield strength 3.5×10^4 psi (24.6 kg/mm² or 241 MN/m²).

The average stress at brittle fracture is far below the above figures. The average stress at the deck of the tanker 'Schenectady' when it fractured was only about 10^4 psi, 1/300th of the theoretical strength.

Real materials contain atomic irregularities, microscopic and even macroscopic cracks, and metallic and non-metallic inclusions, and these account for the great difference between the theoretical strength and the actual strength.

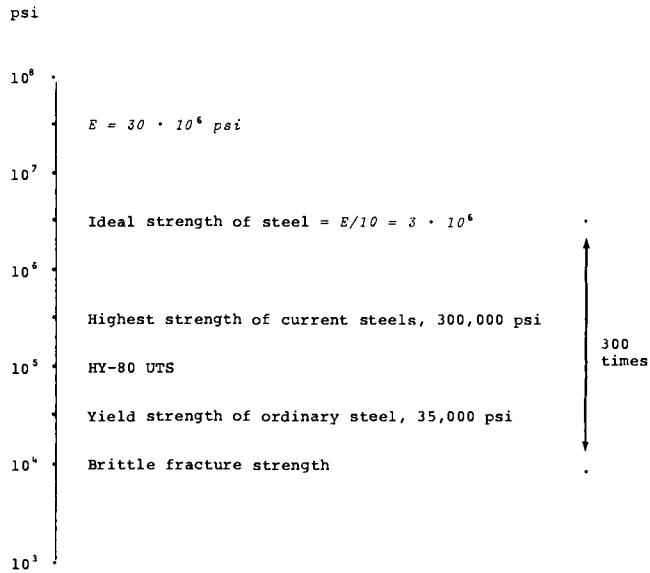


FIG. 10.1. Strength of an ideal solid and real materials.

Structure-sensitive properties. Material properties can be classified as either structure-sensitive or structure-insensitive.⁽¹⁰⁰¹⁾

	Structure-insensitive	Structure-sensitive
Mechanical	Density, elastic moduli	Fracture strength, plasticity
Thermal	Thermal expansion, melting point, thermal conductivity, specific heat	
Electrical	Resistivity (metallic)	Resistivity (semiconductor and at very low temperatures)

The structure-insensitive properties are well-defined properties of a phase of the material, but the structure-sensitive properties are dependent on not only the composition and crystal structure of the material but also the structural details which, in turn, depend upon the previous history of the sample. Properties such as notch toughness, yield strength, and ultimate tensile strength are structure-sensitive and can be altered significantly by varying the alloying elements and the heat-treatment conditions. Properties such as density and modulus of elasticity are structure-insensitive and are little affected by the imperfect condition of a material.

10.1.2 The Griffith theory and its modification⁽¹⁰²⁾

In the 1920s Griffith⁽¹⁰⁰²⁾ tried to explain the observed strength of real brittle solids (the elastic behavior up to fracture) by proposing the existence of an array of pre-existing flaws in these materials. His model is the basis of many modern fracture theories, especially the fracture mechanics theory.

Griffith calculated the strain energy release (per unit plate thickness) resulting from a crack of length $l = 2c$ in a thin plate under normal stress, σ , as follows:

$$\text{strain energy release} = -\pi c^2 \sigma^2 / E \quad (10.2)$$

where $E =$ Young's modulus.

The sign is negative because this is the energy which will be released in the propagation of the flaw. The surface energy associated with the crack is given by:

$$\text{surface energy} = 4cS \quad (10.3)$$

where S is the surface energy per unit area.

The size of the equilibrium crack can be calculated if the condition of net change in the potential energy is assumed to be zero:

$$\frac{d}{dc}(4cS - \pi c^2 \sigma^2 / E) = 0 \quad (10.4)$$

or

$$c = \frac{2SE}{\pi \sigma^2}. \quad (10.5)$$

The critical stress (fracture stress) for a crack of size $2c$ is given by

$$\sigma_c = \left(\frac{2SE}{\pi c} \right)^{1/2}. \quad (10.6)$$

As the crack extends or as c increases, the stress necessary to propagate it decreases.

The theory predicts strengths reasonably well for bodies which behave in a brittle fashion, such as glass and ceramic materials.

Orowan's modification. In the 1950s Orowan and associates tried to apply the Griffith theory to explain the brittle fracture of steel. It was found that when steel fractures the plastic flow adjacent to the fracture surface absorbs energy at the rate of at least ten times the surface energy level. Felbeck and Orowan⁽¹⁰⁰³⁾ accordingly proposed that the "S" term in eqns. (10.5) and (10.6) be replaced by "p", a term which includes both the surface energy and the energy of plastic deformation:

$$c = \frac{2pE}{\pi \sigma^2}, \quad (10.7)$$

$$\sigma_c = \left(\frac{2pE}{\pi c} \right)^{1/2}. \quad (10.8)$$

10.1.3 Development of theories of brittle fracture

Figure 10.2 shows schematically how different theories have been developed and used.

Following the work of Griffith and Orowan, Irwin^(1004, 1005) and associates developed what is now called the fracture mechanics theory. The fracture mechanics theory is the one most widely used today in the study of fractures. As will be discussed later in this chapter, the linear fracture mechanics theory, which is based on an elastic analysis, works reasonably well in describing the fracture of such brittle materials as the high-

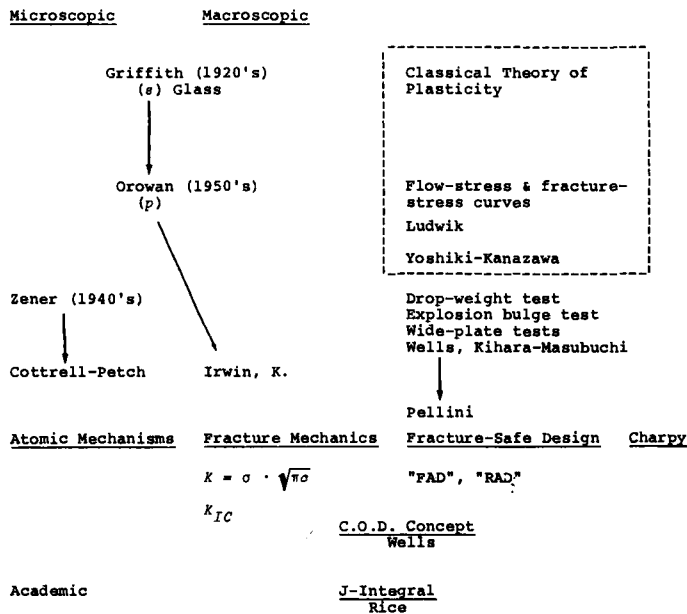


FIG. 10.2. Development of theories of brittle fracture.

strength steels having a yield strength of over 180 ksi (126.5 kg/mm² or 1.240 Mn/m²) that are used in aerospace applications. Fundamentals of the fracture mechanics theory will be discussed in Section 10.2.

Theories also have been developed by a number of investigators including Zener,⁽¹⁰⁰⁶⁾ Cottrell,⁽¹⁰⁰⁷⁾ and Petch⁽¹⁰⁰⁸⁾ for use in the study of microscopic and atomic mechanisms of fracture.^(906, 907) These theories are used primarily by academic investigators engaged in the basic study of fracture.

Several investigators have attempted to explain fracture using either the classical theory of plasticity or stress-strain diagrams.⁽¹⁰⁰⁹⁾ In the 1940s, for example Zener⁽¹⁰⁰⁶⁾ tried to explain the ductile-to-brittle transition using the flow-stress curve and the fracture-stress curve. Later Yoshiki and Kanazawa⁽⁹⁵²⁾ extended the work by studying the notch toughness of structural steels. However, because the empirical nature of this approach militates against its giving a complete explanation of the mechanisms of fracture, little work has been done along these lines recently.

The practical application of the theory of fractures is problematic. A simple theory, such as the linear fracture mechanics theory, can be used in describing the fracture of a brittle material in which the fracture occurs with a minimal amount of plastic deformation near the crack. But the theory has to become more complex if it is used to analyze the fracture of a more ductile material.

It is ironic that this simple-to-understand fracture mechanics theory can only be used to analyze those brittle materials which the designer would seek to avoid. Few practicing engineers want to design structures which fail during service. Better the use of a ductile material that will provide good service, a material that cannot be analyzed by the linear fracture theory.

The designer is usually not interested in analyzing how the structure may fail. His

major concern is to select materials wisely so that the structure which he is designing will not fail.

To meet this practical demand, attempts have been made to generate data and develop guidelines for the prevention of brittle fractures in welded structures. Experimental data have been developed using various fracture tests including drop-weight, explosion-bulge, and wide-plate tests. Pellini, working for the Naval Research Laboratory, has developed the fracture-safe design concept (refer to Section 9.7). This concept has been used by the Navy for the material selection and construction of naval vessels, especially submarines.

Charpy V-notch impact values are still widely used in the selection of commercial steels. This approach, however, is hardly theoretical.

Attempts have been made to extend the fracture mechanics theory to cover fractures with some amount of plastic deformation at the crack tip. The crack-opening displacement (COD) concept has been developed by Wells⁽¹⁰¹⁰⁾ and other investigators in the United Kingdom and has been used in that country to evaluate the fracture toughness of high-strength structural steels.⁽¹⁰¹¹⁾ In the United States, Rice⁽¹⁰¹²⁾ has developed a concept based upon the J-integral, a path-independent integral which expresses the energy-release rate. The theory, however, is highly mathematical.

10.2 Fracture Mechanics Theory

A number of books have been written on the fracture mechanics theory.^(901,905,908) The following pages present those fundamentals of the theory needed to understand the rest of this chapter. The material presented in this chapter is limited to the linear theory, because theoretical analyses of the fracture of welded structures have almost exclusively used this simple, linear form of the fracture mechanics theory.

10.2.1 Fundamentals of fracture mechanics theory

Since some of the technical terms and symbols used in the fracture mechanics theory are unique, they are listed in Table 10.1.

Modes of cracking. A crack in a solid can be categorized according to its mode, as illustrated in Fig. 10.3.⁽⁹⁰⁸⁾ Normal stresses give rise to the “opening mode” (Mode I) in which the displacements of the crack surfaces are perpendicular to the plane of the crack. In-plane shear stress causes the “sliding mode” (Mode II). The displacement of the crack

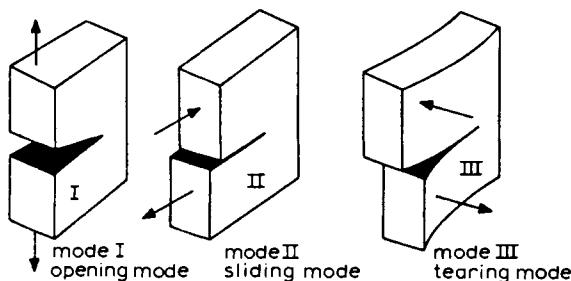


FIG. 10.3. The three modes of cracking.

TABLE 10.1 Some technical terms used in the fracture mechanics theory

c = Half crack length
 E = Young's modulus
 $\mathcal{G} = \frac{\delta U}{\delta l}, \mathcal{G}_I$ = Strain-energy release rate with crack extension per unit length of crack border, or, crack-extension force; subscript I refers to opening mode of crack extension; without subscript, mode is unspecified
 $\mathcal{G}_c, \mathcal{G}_{Ic}$ = Critical value of \mathcal{G} or \mathcal{G}_I at point of instability of crack extension, taken to be measure of fracture toughness of material
 $K = \sqrt{\mathcal{G} E} = \alpha \sigma \sqrt{\pi c}, K_I$ = Stress-intensity factor of elastic stress field in vicinity of crack front; subscript I refers to opening mode of crack extension; without subscript, mode is unspecified
 K_c, K_{Ic} = Critical value of K or K_I at point of instability of crack extension, taken to be an alternative measure of crack toughness of material
 L = Effective length of fracture-toughness specimen
 W = Width of plate specimen or depth of rectangular section beam specimen
 ν = Poisson's ratio
 σ, σ_c = Gross stress applied to specimen in tension, that is, applied load divided by WB in case of plate specimen, or $\pi D^2/4$ in case of notched round bar; subscript c refers to the point of instability of crack extension
 σ_{net} = Average net-section stress for a symmetrical plate specimen in tension
 σ_{YS} = Uniaxial tensile yield strength

surfaces is in the plane of the crack and perpendicular to the leading edge of the crack. The “tearing mode” (Mode III) is caused by out-of-plane shear stress. Crack surface displacements are in the plane of the crack and parallel to the leading edge of the crack. In the usual cracking situation, all three modes are present. Since Mode I is technically the most important, the discussions in this chapter are limited to Mode I.

Stress intensity factor. Consider a very simple case of a through-the-thickness Mode I crack of length $l = 2c$ in an infinite plate, as shown in Fig. 10.4. The plate is subjected to a uniform tensile stress, σ , at infinity. The stress components, σ_x, σ_y , and τ_{xy} , at a point,

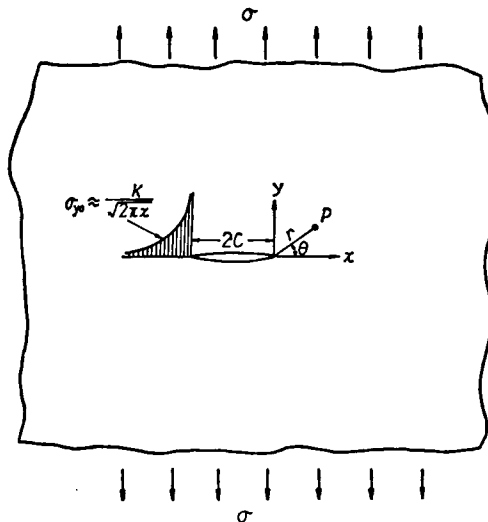


FIG. 10.4. Infinite plate containing a sharp crack of length $2c$ under uniform tensile stress σ .

$P(r, \theta)$, near the crack tip are expressed approximately by the following equations:

$$\begin{aligned} \sigma_y &\approx \frac{K}{\sqrt{2\pi r}} \cos \frac{\theta}{2} \left[1 + \sin \frac{\theta}{2} \sin \frac{3\theta}{2} \right] \\ \sigma_x &\approx \frac{K}{\sqrt{2\pi r}} \cos \frac{\theta}{2} \left[1 - \sin \frac{\theta}{2} \sin \frac{3\theta}{2} \right] \\ \tau_{xy} &= \frac{K}{\sqrt{2\pi r}} \sin \frac{\theta}{2} \cos \frac{\theta}{2} \cos \frac{3\theta}{2} \end{aligned} \tag{10.9}$$

where K is designated the “stress intensity factor”, expressed as follows:

$$K = \sigma \sqrt{\pi c}, \tag{10.10}$$

Along the x -axis, ($\theta = 0$), the stress components are:

$$\begin{aligned} \sigma_x = \sigma_y &= \frac{K}{\sqrt{2\pi r}} \\ \tau_{xy} &= 0. \end{aligned} \tag{10.11}$$

When a crack exists in a practical specimen with finite dimensions, the expression of the stress intensity factor, K , becomes more complex than that of eqn. (10.10), and can be expressed as follows:

$$K = \alpha \sigma \sqrt{\pi c}. \tag{10.12}$$

The expression of the correction factor, α , varies depending upon the geometry of the specimen and the location of the crack, or cracks.

A simple example would be the through-the-thickness crack of length $l = 2c$ existing in the central section of the specimen with width W and thickness t , shown in Fig. 10.5(a). After the specimen is subjected to a uniform tensile load P , the gross stress, σ , becomes:

$$\sigma = \frac{P}{Wt}. \tag{10.13}$$

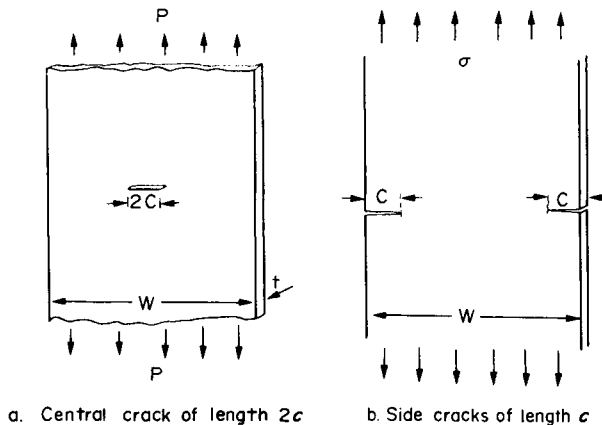


FIG. 10.5. Tensile tests of specimens containing cracks.

The net stress at the cross-section containing the crack, σ_{net} , is:

$$\sigma_{\text{net}} = \frac{P}{(W - 2c)t} \tag{10.14}$$

The stress intensity factor, K , is approximately:

$$K = \sigma \sqrt{\pi c} \sqrt{\left(\frac{W}{\pi c}\right) \tan\left(\frac{\pi c}{W}\right)}$$

or

$$\alpha = \sqrt{\frac{W}{\pi c} \tan\left(\frac{\pi c}{W}\right)} \tag{10.15}$$

The above expression is valid only when the value of σ is less than 80% of the yield stress of the material.

Corresponding values of α and $2c/W$ are given in Table 10.2. The value of α is only 1.02 when the length of the crack is about 20% of the width. This means that the simplest expression given by eqn. (10.10) may be used even when specimen is of a finite size as long as the crack is not very long as compared to the width of the specimen.

Figure 10.5(b) shows a specimen containing two side cracks of length c . When the gross tensile stress, σ , is applied to the specimen, K is expressed:

$$K = \sigma \sqrt{\pi c} \sqrt{\left(\frac{W}{\pi c}\right) \left[\tan\left(\frac{\pi c}{W}\right) + 0.1 \sin\left(\frac{2\pi c}{W}\right) \right]} \tag{10.16}$$

Strain energy release rate. Once K -value is determined, the rate of the elastic strain energy release due to crack extension, $\mathcal{G} = \delta U / \delta l$, is expressed:

$$\frac{\delta U}{\delta l} = \mathcal{G} = \frac{K^2}{E} \tag{10.17}$$

or from eqn. (10.12):

$$\mathcal{G} = \frac{\alpha^2 \pi}{E} \sigma^2 c. \tag{10.18}$$

The strain-energy-release rate is proportional to the crack length and the square of stress.

TABLE 10.2 Values of correction factor α for different values of $2c/W$

$\frac{2c}{W}$	$\alpha = \sqrt{\left(\frac{W}{\pi c}\right) \tan\left(\frac{\pi c}{W}\right)}$
0.074	1.00
0.207	1.02
0.337	1.05
0.466	1.11
0.592	1.20

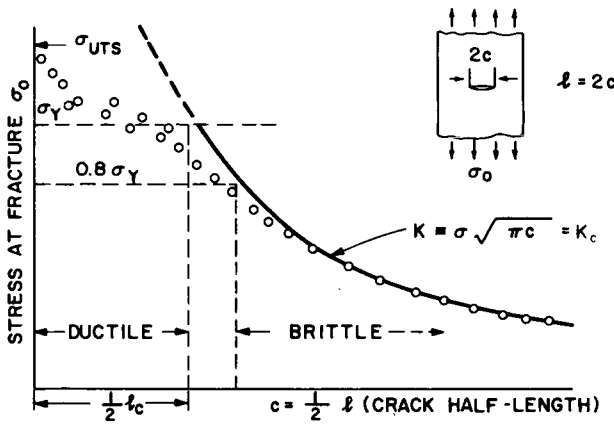


FIG. 10.6. Effect of crack length on fracture strength.

Critical stress intensity factor. Figure 10.6 shows the typical results when a series of fracture tests are conducted using specimens made of high-strength material and cracks of different lengths.⁽¹⁰¹³⁾ If the length of the initial crack is long enough, and if the fracture occurs before general yielding, the relationship between the initial crack length, $2c$, and the average fracture stress, σ , can be expressed by:

$$K = \sigma \sqrt{\pi c} = \text{const.} \tag{10.19}$$

Consequently, fracture occurs when the K value reaches a certain critical value K_c for that material. K_c is designated the “critical stress intensity factor”, or, more often, simply the “fracture toughness”.

When the fracture stress increases and exceeds approximately 80% of the yield stress, the experimental fracture stresses deviate from the $K = \text{constant}$ curve, and fracture occurs in a ductile manner. As illustrated in Fig. 10.6, the fracture mechanics theory should be used only when fracture occurs before general yielding.

Fracture toughness, K_c , has the following physical meanings:

1. Relative to the locally elevated stress field at the leading edge of a crack K_c represents the intensity of local tensile stress necessary for unstable crack propagation.
2. For a crack of length $2c$ in a large sheet, the K_c -value permits estimation of the membrane tensile stress σ necessary for unstable crack propagation through the relationship:

$$\sigma = \frac{K_c}{\sqrt{\pi c}} \tag{10.20}$$

3. Relative to the modified Griffith theory, the strain-energy-release rate G_c for unstable crack propagation may be directly expressed in terms of K_c by the relationship:

$$K_c^2 = E G_c \tag{10.21}$$

When further tests are conducted with specimens of different thicknesses, the K_c changes as shown schematically in Fig. 10.7. As the thickness increases, the K required to produce failure decreases and approaches a lower limit which is the critical stress

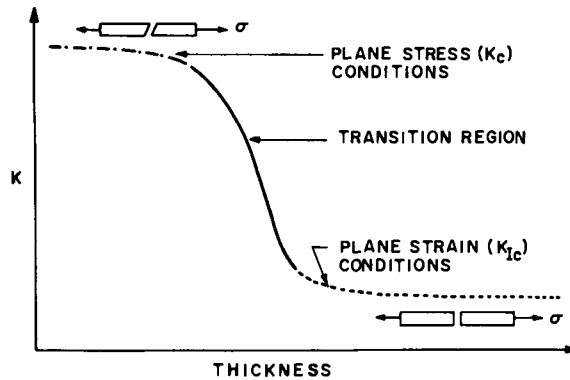


FIG. 10.7. Behavior of stress intensity required to produce failure as a function of material thickness.

intensity under plane-strain condition, K_{Ic} . From the engineering viewpoint, plane-strain fracture toughness, K_{Ic} , is considered a material constant.

10.2.2 Fracture toughness tests

The ASTM Committee on Fracture Testing of High-strength Sheet Materials⁽¹⁰¹⁴⁾ has described techniques of determining the fracture toughness of high-strength sheet materials. Their interest has been limited to materials, both ferrous and non-ferrous, having a strength-to-density ratio of more than 700,000 in.[†]

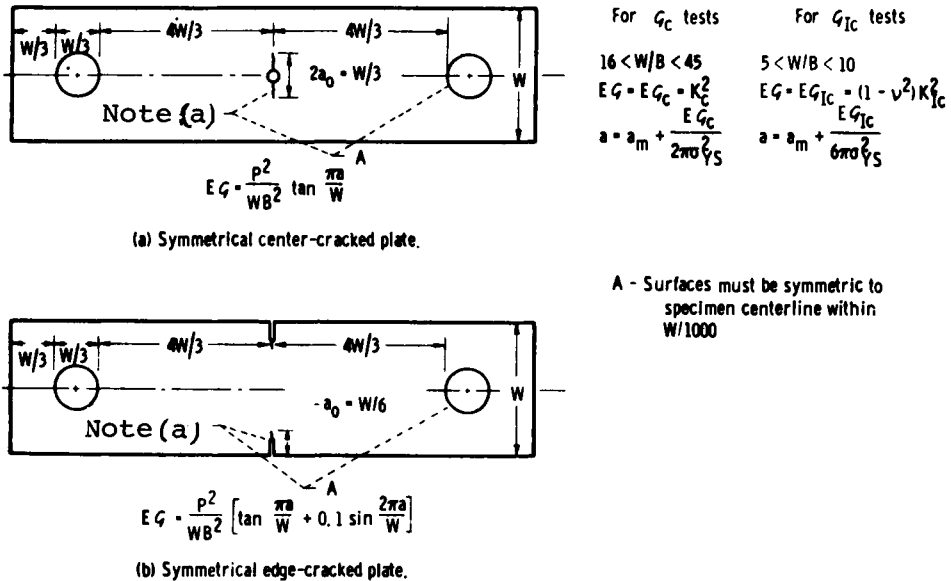


FIG. 10.8. Practical fracture toughness specimen types. Specimens for general use. (The factor $(1 - \nu^2)$ is an approximation.)⁽⁹¹²⁾ Note (a): see fig. 10.10 for details of the notch preparation.

[†] $\frac{lb/in^2}{lb/in^3} = in.$

Figure 10.8 shows practical fracture toughness specimen types for general use, while Fig. 10.9 shows specimens used in determining K_{Ic} .^(9,12) Figure 10.10 shows details of fatigue crack starter notches for center-cracked and edge-notched flat specimens.

Also shown in Figs. 10.8 and 10.9 are formulae for determining K_c and K_{Ic} .

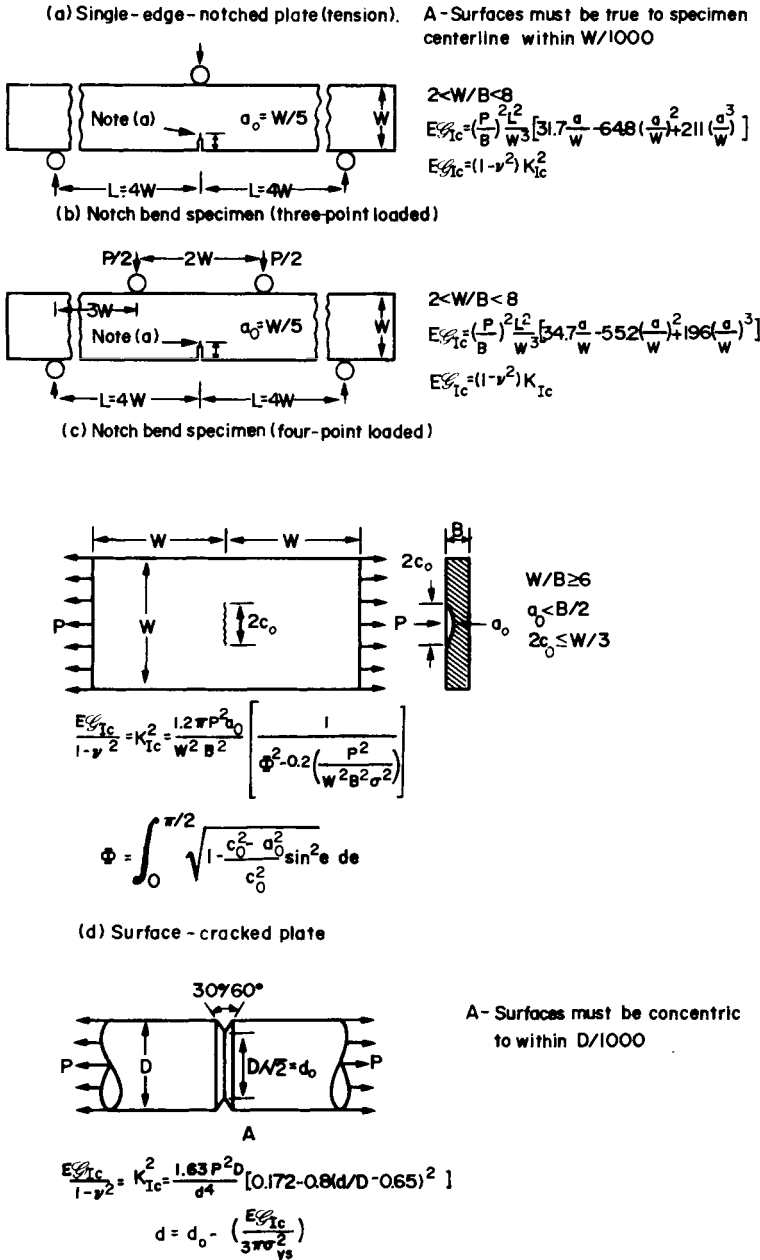


FIG. 10.9. Practical fracture toughness specimen types. Plane-strain tests. (For all specimens, $a = a_0 + E/6\pi\sigma_{ys}^2$, and the factor $(1 - \nu^2)$ is an approximation.)^(9,12) Note (a): See Fig. 10.10 for details of the notch preparation.

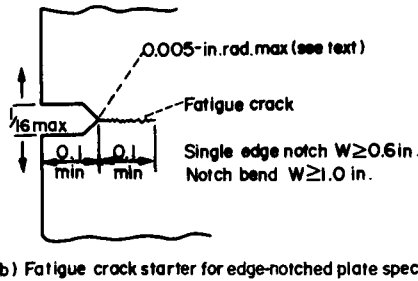
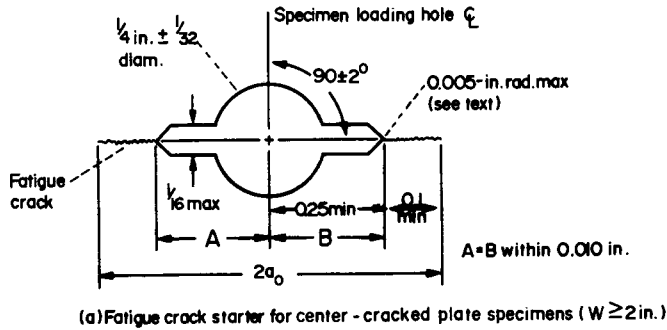


FIG. 10.10. Fatigue-crack starter notches for center-cracked and edge-notched plate specimens.

10.2.3 Analysis of crack opening displacement and plastic zone size at the crack tip

The discussion presented here is based upon the work by Wells.⁽¹⁰¹⁰⁾

Crack opening displacement. When an infinite plate containing a sharp crack of length $l = 2c$ is under uniform tensile stress σ , the stress components in areas near the crack are expressed by eqns. (10.9), see Fig. 10.4 and 10.11(a). Irwin⁽¹⁰¹⁵⁾ has shown that the precise expression for the normal stress, σ_y , along the x -axis is:

$$\sigma_y = \sigma \frac{x}{\sqrt{x^2 - c^2}}, \quad x > c. \tag{10.22}$$

By taking r as the distance from the crack tip:

$$x = c + r = c(1 + p) \tag{10.23}$$

where $p = \frac{r}{c}$.

When $p \ll 1$,

$$\frac{x}{\sqrt{x^2 - c^2}} = \frac{c(1 + p)}{c\sqrt{1 + 2p + p^2 - 1}} = \frac{1 + p}{\sqrt{2p + p^2}} \rightarrow \frac{1}{\sqrt{2p}}$$

Then the stress σ can be approximately expressed as:

$$\sigma_y = \sigma \frac{1}{\sqrt{2p}} = \sigma \sqrt{\frac{c}{2r}} = \frac{K}{\sqrt{2\pi r}} = \sqrt{\frac{EG}{2\pi r}}. \tag{10.24}$$

In a similar way, the precise expression for the normal displacement, η , within the slit:

$$\eta = \frac{2\sigma}{E} \sqrt{c^2 - x^2}, \quad x < c \tag{10.25}$$

may be expressed as:

$$\eta = \frac{2\sigma}{E} \sqrt{2cr} = 2 \sqrt{\frac{2Gr}{\pi E}}$$

where r is now measured in the opposite direction, or $x = c - r$. Then the crack opening displacement (COD) is:

$$\text{COD} = 2\eta = 4 \sqrt{\frac{2Gr}{\pi E}}. \tag{10.26}$$

The above analysis assumes that the material is perfectly elastic.

Crack tip plastic zone. When the applied load is increased, plastic deformation takes place in small areas near the crack tip,^(908, 1010) the shaded area in Fig. 10.11(b).

As a first approximation, it is assumed that the distribution of normal stress σ_y along the x -axis is as shown by curve ABC . Within the yielded zone, σ_y does not exceed the yield stress of the material σ_{YS} . The stress distribution in the elastic zone, BC , may be assumed to be the same as the elastic stress distribution for an imaginary, extended crack of length $2c_1$, which is expressed by curve $A'BC$.

The value of c_1 can be determined from the condition that the total loads for curve ABC and curve $A'BC$ must be the same, or:

$$2r_y \sigma_{YS} = \int_0^{r_y} \sigma_y d_y. \tag{10.27}$$

The integration in the right-hand side is the elastic stress distribution, eqn. (10.22),

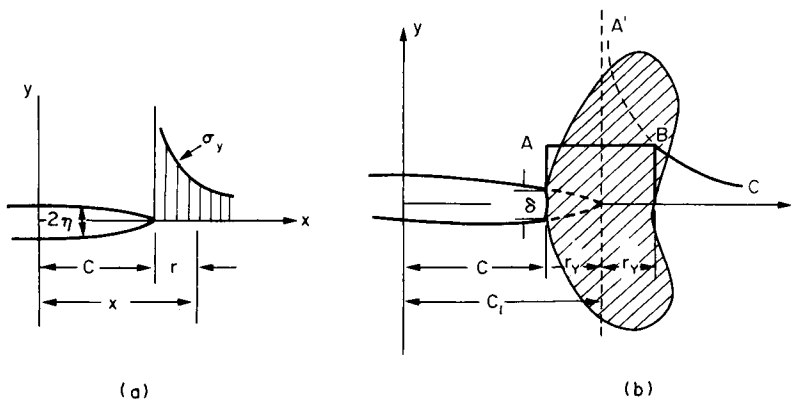


FIG. 10.11. Analysis of crack opening displacement and plastic zone size at the crack tip. (a) Crack opening in an elastic field. (b) Crack opening with plastic deformation near the crack tip.

of the imaginary crack of length $2c_1$:

$$c_1 = c + r_Y. \quad (10.28)$$

Then,

$$\int_0^{r_Y} \sigma \sqrt{\frac{c_1}{2r}} dr = \sigma \sqrt{\frac{c_1}{2}} \left[\int_0^{r_Y} \frac{dr}{\sqrt{r}} \right] = \sigma \sqrt{\frac{c_1}{2}} 2\sqrt{r_Y}. \quad (10.29)$$

Then eqn. (10.27) can be expressed:

$$2r_Y \sigma_{YS} = \sigma \sqrt{2c_1 r_Y}, \quad (10.30)$$

$$r_Y = \left(\frac{\sigma}{\sigma_{YS}} \right)^2 \frac{c_1}{2} = \left(\frac{\sigma}{\sigma_{YS}} \right)^2 \frac{1}{2} (c + r_Y), \quad (10.31)$$

$$\frac{r_Y}{c + r_Y} = \frac{1}{2} \left(\frac{\sigma}{\sigma_{YS}} \right)^2, \quad (10.32)$$

$$\frac{c}{r_Y} = 2 \left(\frac{\sigma_{YS}}{\sigma} \right)^2 - 1. \quad (10.33)$$

This approximate solution is assumed to be valid for stress levels up to $\sigma/\sigma_Y < 0.8$.

For example, when $\sigma = 0.5 \sigma_{YS}$

$$\frac{c}{r_Y} = (8) - 1 = 7 \quad \text{or} \quad r_Y = \frac{1}{7}c. \quad (10.34)$$

From eqn. (10.31),

$$r_Y = \left(\frac{K_1}{\sigma_{YS}} \right)^2 \frac{1}{2\pi} \quad (10.35)$$

where $K_1 = \sigma \sqrt{\pi c_1}$ for a crack of length $2c_1$.

Or,

$$R = 2r_Y = \left(\frac{K_1}{\sigma_{YS}} \right)^2 \frac{1}{\pi}. \quad (10.36)$$

The above equation is assumed to be valid up to $\sigma/\sigma_{YS} < 0.8$. Equation (10.36) can provide a rough estimate of the plastic zone size at the crack tip.

It can be assumed that the crack-tip-opening displacement (CTOD), δ , is the same as the elastic crack opening for an imaginary crack of length $2c_1$, or $\delta = 2\eta$ for $r = -r_Y$ of eqn. (10.25):

$$\text{CTOD} = \delta = \frac{4\sigma}{E} \sqrt{2c_1 r_Y}. \quad (10.37)$$

From eqn. (10.31),

$$\begin{aligned} \delta &= \frac{4\sigma}{E} \sqrt{2c_1} \frac{\sigma}{\sigma_{YS}} \sqrt{\frac{c_1}{2}} \\ &= \frac{4\sigma^2}{E\sigma_{YS}} c_1 \\ &= \frac{4G_1}{\pi\sigma_{YS}} \end{aligned} \quad (10.38)$$

where G_1 is due to the crack extension of a crack of length $2c_1$, or

$$G_1 = \frac{\pi}{4} \sigma_{YS} \delta. \tag{10.39}$$

10.3 Values of Fracture Toughness and Critical Crack Length of Various Materials

10.3.1 Fracture toughness values

Many experimental programs have been carried out to determine the fracture-toughness values of various materials. The results have appeared in several publications.^(903,905,908) Table 10.3, from one such publication, shows the typical values of K_{Ic} for various high-strength sheet materials.^(102,1016)

Figure 10.12 shows how the K_{Ic} values of different steels decrease as the yield strength increases.⁽¹⁰¹⁷⁾ For steels with a yield strength of over 180 ksi (126.5 kg/mm² or 1,240 MN/m²) the K_{Ic} value is usually low enough that the linear fracture mechanics approach can be used. However, when the yield strength falls below 180 ksi, the K_{Ic} value increases drastically, and the fracture mechanics approach cannot be used.

10.3.2 Critical crack length and microflaws

It is generally believed that the critical crack length of steel decreases as the tensile strength increases.

Martin experiment. The Martin Company (Baltimore)^(1018,1019) conducted burst tests on welded cylinders fabricated of a hot-work die steel, Vascojet 1000 (0.40C, 0.35Mn,

TABLE 10.3 Typical values of K_{Ic} for various materials^(102,1016)

Material	Yield strength (1000 psi)	K_{Ic} -value (1000 psi/ $\sqrt{\text{in.}}$)					
AISI 4340 steel (air melt)							
Tempered at 350° F	208.3	192					
Tempered at 425° F	203.9	204					
Tempered at 500° F	197.9	174					
Tempered at 700° F	181.6	204.5					
AMS 6434 (vacuum melt)							
Longitudinal	190	205					
Transverse	190	195.5					
Ti-6Al-4V							
Longitudinal	159	114					
Transverse	164	113					
Chemical composition (%) of AISI 4340 and AMS 6434 steels:							
	C	Mn	Si	Ni	Cr	Mo	V
AISI 4340	0.40	0.70	0.30	1.75	0.80	0.25	—
AMS 6434	0.33	0.70	0.30	1.75	0.80	0.35	0.20

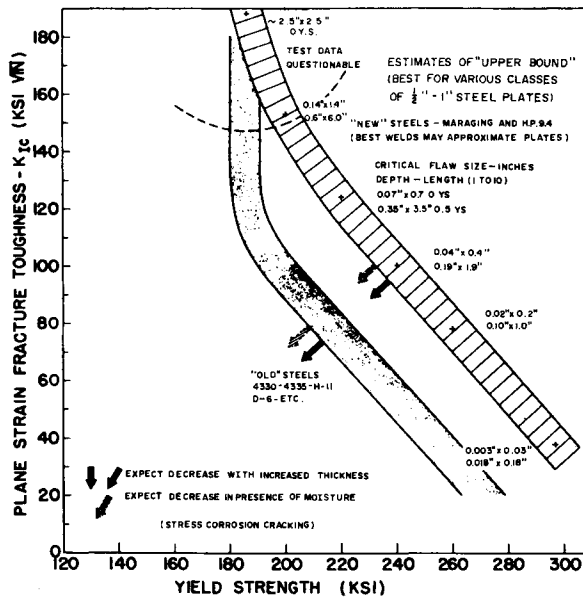


FIG. 10.12. Upper bound, best value, limits of plane strain fracture toughness (K_{Ic}) for $\frac{1}{2}$ to 1-in. plates of high-strength steels, as reported by various qualified laboratories.⁽¹⁰¹⁷⁾

0.90Si, 5.00Cr, 1.30Mo, 0.50V). After fabrication, the cylinders were austenitized, quenched, and then tempered at various temperatures to change the ultimate strength of the base plate. The relationship between the tensile strength of the base metal and the calculated hoop stress of the cylinders at actual bursting pressure is shown in Fig. 10.13.

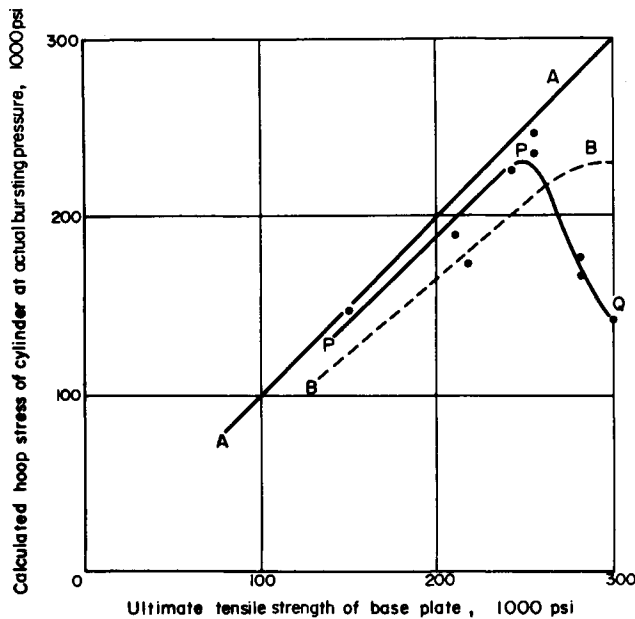


FIG. 10.13. Relationship between ultimate tensile strength of base plate and calculated hoop stress at fracture of welded cylinders in ultrahigh strength steels.

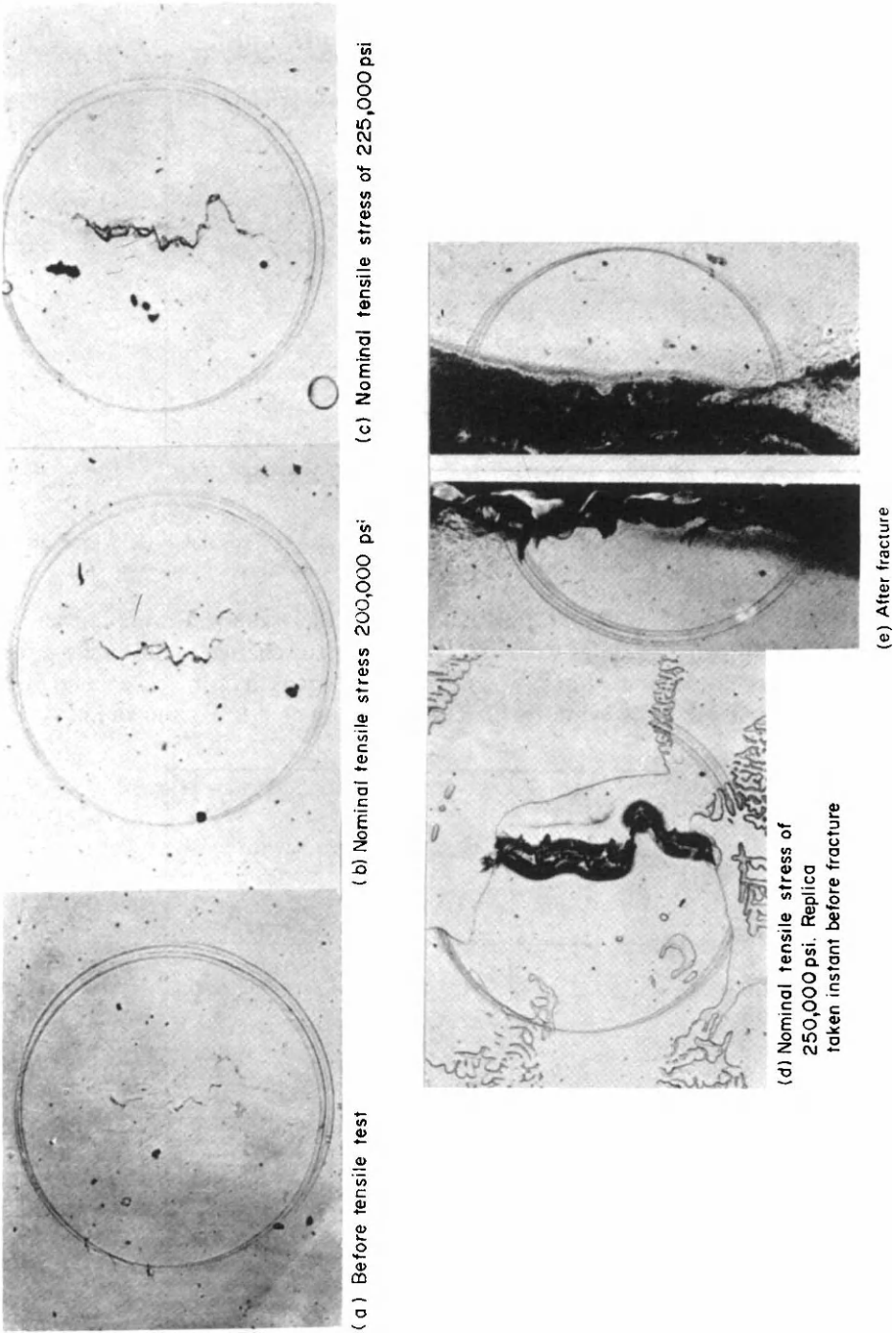


FIG. 10.14. Replicas of specimen surfaces taken during fracture testing.

When the ultimate strength of the base plate was less than 260,000 psi (182.8 kg/mm² or 1.792 MN/m²) the calculated hoop stress increased as the strength of the base metal increased, as shown by curve *PP*. The strength of the cylinders exceeded the yield strength of the base plate (curve *BB*) and came close to the ultimate strength of the base metal exceeding 260,000 psi; however, the strength of the cylinder decreased greatly, as shown by curve *PQ*. Fractures occurred at stresses well below the yield strength of the base plate.

When the ultimate strength was below 260,000 psi the critical crack length was longer than the lengths of the microflaws that existed in the cylinders. When the ultimate strength was over 260,000 psi, the critical crack length was shorter than the lengths of the microflaws.

Battelle experiment on ultrahigh-strength steel. Randall *et al.*⁽¹⁰²⁰⁾ investigated the influence of microcracks in the fracture of ultrahigh-strength steels (basically modifications of the AISI 4340 composition). The critical crack length of the materials was about 0.1 in. (2.5 mm). In fracture tests of longitudinal welded specimens 0.1 in. (2.5 mm) thick, it was observed through the use of a replica technique that fractures did occur from microcracks. Figures 10.14(a) through 10.14(e) are $\times 75$ photographs of a series of replicas from an area of the specimen surface at varying stress levels. The encircled areas contain microcracks in the weld metal. The weld was made using the electron-beam process. An enlargement of the cracks as the stress increases is apparent. The specimen failed at a nominal stress of 250,000 psi (176 kg/mm² or 1724 MN/m²), considerably below the expected 290,000 psi (204 kg/mm² or 2000 MN/m²) failure stress, the fracture having been initiated from the 0.01 in. (0.25-mm) long microcrack.

Battelle experiment on mild steel. The effect of the initial crack length on the fracture stress of mild steel was investigated at the Battelle Memorial Institute for the Ship Structure Committee.^(1021, 1022) The test apparatus was a 9-ft diameter sphere made of

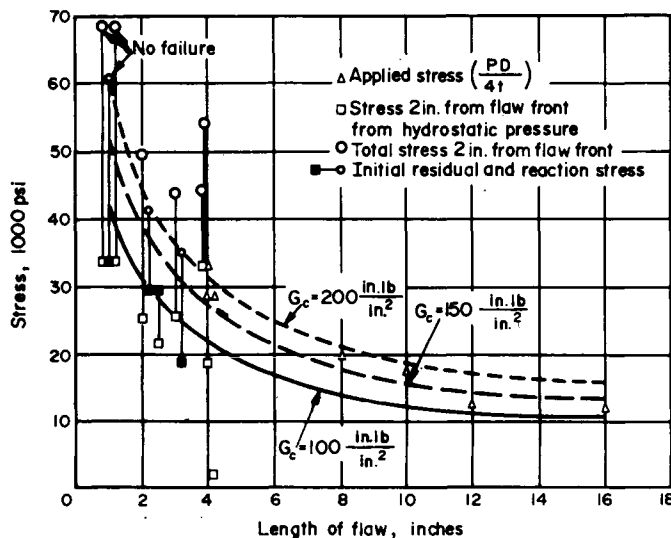


FIG. 10.15. Relationship of average stress for initiation of brittle fracture with length of initial flaw.⁽¹⁰²²⁾

$\frac{3}{4}$ in. (19 mm) high-yield-strength low-alloy steel with good notch toughness. The test plate was a $\frac{3}{4}$ in. (19 mm) thick by 23-in. (584 mm) diameter circular curved disk, which was welded into the wall to the sphere.

The load was applied by hydraulic pressure. Figure 10.15 shows the relationship between the length of the flaw and the normal stress at fracture. The applied fracture stress decreased as the flaw or crack length increased. This relationship can be explained by the fracture mechanics theory (see Fig. 10.6). The magnitude of G_c for the material used was estimated to be about 150 in.-lb/in² (2.7 kg-mm/mm²). The critical crack length at the yield-strength level (30,700 psi) was 3.1 in. (79 mm). Fractures did not initiate from 1-in. (25.4-mm) flaws.

10.4 Catastrophic Failures of Welded Structures from Subcritical Cracks.

From the material presented earlier in this chapter it can be stated that brittle fractures have the following characteristics:

1. A crack will grow under stress if its size exceeds the critical size as determined by the material properties and the given stress.
2. The critical crack length of steel decreases as the yield strength increases.

However, there is evidence that fractures have occurred in actual structures from flaws smaller than critical size (see Fig. 9.13). Fractures in welded ships originate in flaws of various kinds, most of which are of a length shorter than the critical crack length estimated from fracture tests. For example, in an experiment on ultrahigh-strength steel weldments conducted by Randall *et al.*,⁽¹⁰²⁰⁾ a fracture originated in a microcrack that was much shorter in length than the critical crack length of the material (0.1 in.). Additional factors cause a subcritical crack to grow to critical size. Boyd⁽¹⁰²³⁾ has discussed the effects of these additional factors on the initiation of brittle fracture. Various mechanical and metallurgical factors may affect the initiation of brittle fractures. They do this in three ways:

1. Supply additional energy (especially through residual stress).
2. Cause local embrittlement of the material.
3. Cause fatigue, stress-corrosion cracking, and other mechanisms.

10.4.1 *The Kihara-Masubuchi study of low applied-stress fractures in welded structures*

Using a welded-and-notched wide plate specimen, as shown in Fig. 9.36, Kihara and Masubuchi^(956,1024) demonstrated experimentally how low applied-stress fractures originate in subcritical cracks. The experimental results showed that when a crack is located in areas where high tensile residual stresses exist the crack can grow even though the level of applied stress is low. They explained the experimental results on the basis of fracture mechanics.

Figure 10.16 shows schematically the mechanisms of the low applied-stress fracture of weldments.^(1016,1024) Shown here are the relationships between the crack length, $l = 2c$, and the rate of release of strain energy, \mathcal{G} , for both specimens with residual stresses and specimens without.

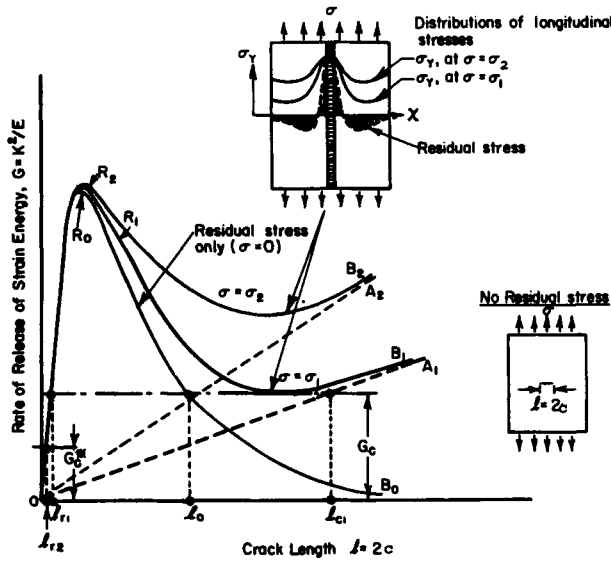


FIG. 10.16. Schematic diagram showing mechanisms of low-applied-stress fracture of weldments.

When a crack of length $l = 2c$ exists in the center of a large plate containing no residual stress, the relationship between l and \mathcal{G} is (see eqns. (10.10) and (10.17)):

$$\mathcal{G} = \frac{\pi}{E} \sigma^2 c = \frac{\pi}{E} \sigma^2 \frac{l}{2} \tag{10.40}$$

The \mathcal{G} -value increases proportionally with the crack length as shown in broken lines OA and OA_2 . As stress σ increases, the \mathcal{G} -value increases rapidly in proportion to the square of σ . When σ is low, a relatively long crack must exist to cause an unstable fracture. When the critical \mathcal{G} -value of the material is \mathcal{G}_c , the critical crack length is l_{c1} under the applied stress of σ_1 . From eqn. (10.40), one can expect that the \mathcal{G} -value will be significantly higher if cracks exist in an area containing high tensile residual stresses. Curves OR_0B_0, OR_1B_1 and OR_2B_2 show schematically \mathcal{G} - l relationships under residual stresses only, $\sigma = \sigma_1$ and $\sigma = \sigma_2$, respectively. It is important to note that the \mathcal{G} -value exceeds \mathcal{G}_c when the crack is longer than l_{r1} which is much shorter than l_{c1} . This explains why an unstable, catastrophic failure can originate in a crack much shorter than the critical size, l_{c1} , if the crack is located in an area containing high tensile residual stresses.

A crack may even occur when all the stress is residual. In such cases, however, the crack will be stopped at the end of length l_0 .

Experimental and analytical studies have been made to determine the exact shapes of curves OR_0B_0, OR_1B_1 , and OR_2B_2 . The results are given in Section 10.5.

The chain reaction of unfortunate events. In order for a small defect in a structure subjected to stresses much lower than the yield stress to grow sufficiently to cause the catastrophic brittle fracture of a large welded structure (the complete fracture of a ship, for example), a particular chain reaction of unfortunate events must take place, as Fig. 10.16 indicates. In the case of the weldment in that figure,

1. If the defect is located in an area with no residual stress or only a low residual stress, a crack will not grow from the defect.
2. If the defect is located in an area with a high residual stress, a crack may grow from the defect; but it will not propagate as an unstable fracture unless there are enough other stresses in large sections of the structure.

This explains why only a small percentage of the welded ships built during World War II suffered complete fracture.

Understanding low applied-stress fracture is of critical importance when designing a fracture-test prototype structure. The prototype must make it possible to examine the many factors that contribute to low applied-stress fracture and must make it possible to examine the way such fractures affect the service performance. This subject was examined in some detail in Section 9.5.

10.4.2 *Further investigations of the low applied-stress fracture of weldments*

The work done on low applied-stress fractures by Wells, Kihara, and Masubuchi has been continued by a number of investigators. It has been found that a low-applied-stress fracture can be obtained experimentally from a notch located in an area containing high residual tensile stress. A book published in 1967 by Hall, Kihara, Soete, and Wells⁽⁹⁰⁴⁾ summarizes the results of studies conducted in the United States (primarily at the University of Illinois), Japan, Belgium, and Great Britain. A report published in 1972 by Kihara summarizes the results obtained in Japan.⁽⁹⁵⁴⁾

1. *Effects of mechanical and thermal stress relieving.* Brittle fracture characteristics change when residual stress is removed. There are two ways to reduce or remove residual stress: the mechanical preloading method and the metallurgical thermal-stress-relieving method.

When an external load is applied to a weldment, residual stresses are redistributed due to local plastic deformation (see Fig. 8.1), and when the load is removed, the residual stresses are significantly reduced. This is called mechanical stress relieving. Figure 10.17 shows the results obtained by Kihara *et al.*⁽¹⁰²⁶⁾ They used welded-and-notched wide-plate specimens in carbon steel, as shown in Fig. 9.36. In a series of tests, they applied external loads at 20°C (68°F), which was above the critical temperature for crack initiation, T_c , to different stress levels: 5, 10, 15, 20, and 23 kg/mm² (7.1, 14.2, 21.3, 28.4, and 32.7 ksi). They then reduced the load. After these mechanical stress-relieving treatments, they cooled the specimens and applied tensile loads again at temperatures below -30°C (-22°F). As shown in Fig. 10.17(a), fractures occurred after the preloaded stresses were exceeded.

In another series of tests, stresses were relieved by heating the specimens in a furnace for 1 hour at 320, 420, 520, and 620°C (608, 788, 968, and 1148°F). Results of fracture tests conducted on these specimens are shown in Fig. 10.17(b). The fracture stresses were higher when the welds were heat treated at higher temperatures, indicating that the higher the temperature, the more residual stresses were relieved. These experiments all show that the fracture stress of welded structures can be increased by relieving residual stresses.

The results shown in Fig. 10.17(a) are very important from a practical standpoint. Proof tests are often used as acceptance tests of pressure vessels, pipelines, etc. In these

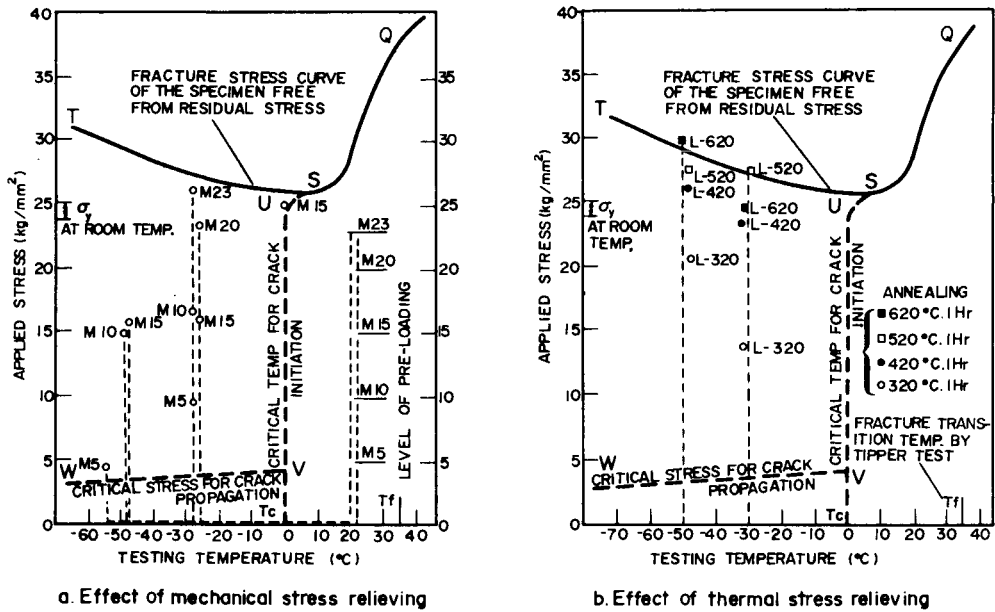


FIG. 10.17. Effects of stress-relieving treatments on brittle-fracture characteristics of welded-and-notched wide-plate specimens.⁽¹⁰²⁶⁾ (Refer to Fig. 10.16 for the explanations of curves QST and UVW.)

tests, welded structures are loaded to a stress level considerably higher than that expected during service. According to the results shown in Fig. 10.17, the proof test itself will relieve residual stresses and thus favorably affect the service behavior of the welded structure.[†]

2. *Effect of notch length and location.* According to the fracture mechanics theory, the fracture strength of a notched plate with no residual stresses should decrease as the crack length increases (see Fig. 10.6). In an actual weldment, however, the effect of the crack length becomes complicated by other factors, including residual stress (which greatly affects brittle fracture), and the different mechanical and metallurgical characteristics of the base plate, the heat-affected zone, and the weld metal. All of these exist in a narrow range, and when a crack is introduced in the weldment, their effect is complicated.

Figure 10.18⁽¹⁰²⁷⁾ shows the effect of the crack length in terms of fracture stress. Materials used in the tests are semi-killed steels. Yield strength and tensile strength of A-1 are 24.4 kg/mm² (34.7 ksi or 239 MN/m²) and 27.0 kg/mm² (38.4 ksi or 265 MN/m²), and those of A-2 are 43.9 kg/mm² (62.4 ksi or 430 MN/m²) and 48 kg/mm² (68.3 ksi or 471 MN/m²), respectively. As shown in the figure, the fracture stress takes a minimum value when the crack length is 36 mm (1.4 in.). In this particular case, the effects of both residual stress and embrittlement of the material are very severe. Thus, the crack length or the position of the crack tip in the weldment has a large effect on brittle fracture initiation.

3. *The effect of structural discontinuities.* In welded structures, structural disconti-

[†] The pros and cons of proof testing are discussed further in Chapter 16.

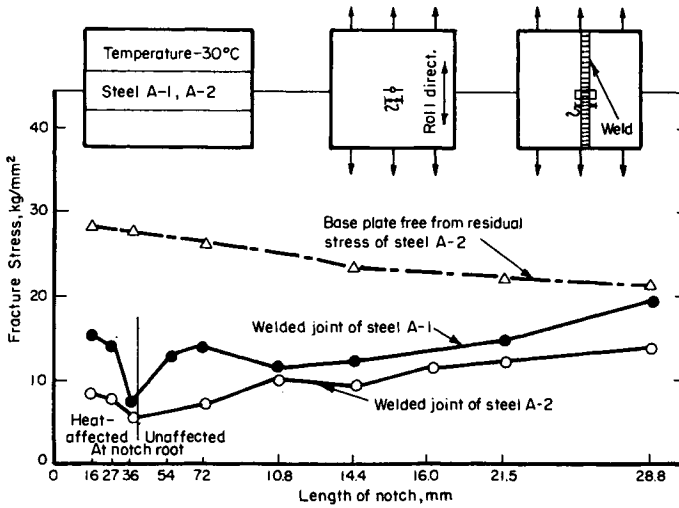


FIG. 10.18. Effect of notch length on brittle-fracture strength of welded joint and base plate.

Note: Notch radius 0.1 mm.

nities are often unavoidable because of the structural complexities involved. When a structural discontinuity exists, stress concentration occurs near it. Thus, if a crack is introduced at that region, the crack may grow even if the level of applied stress is moderate.

Kihara, Iida, and Narita⁽¹⁰²⁸⁾ studied this subject using the structural model specimen

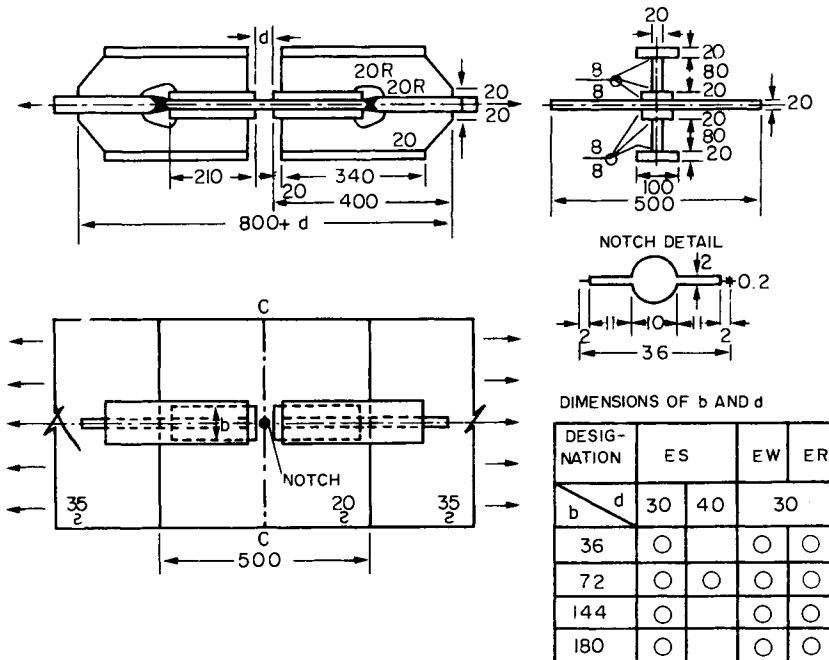


FIG. 10.19a. Details of structural specimens.

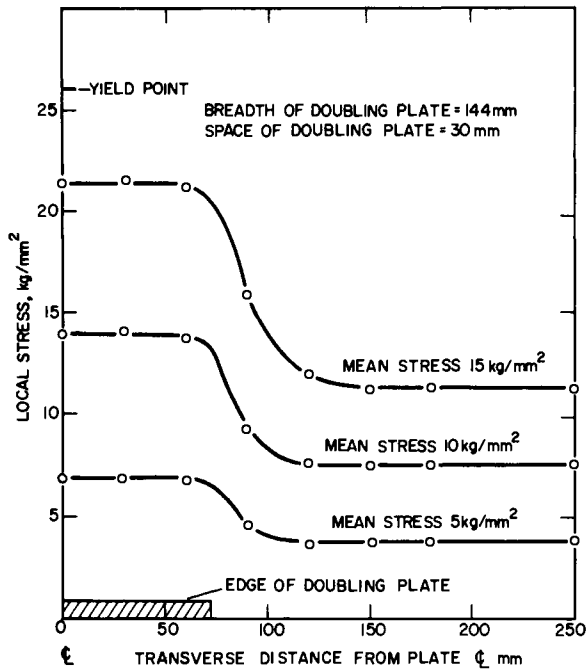


FIG. 10.19b. Transverse distributions of longitudinal stresses in ES-144-30 specimen (without a notch at the center of the main plate).

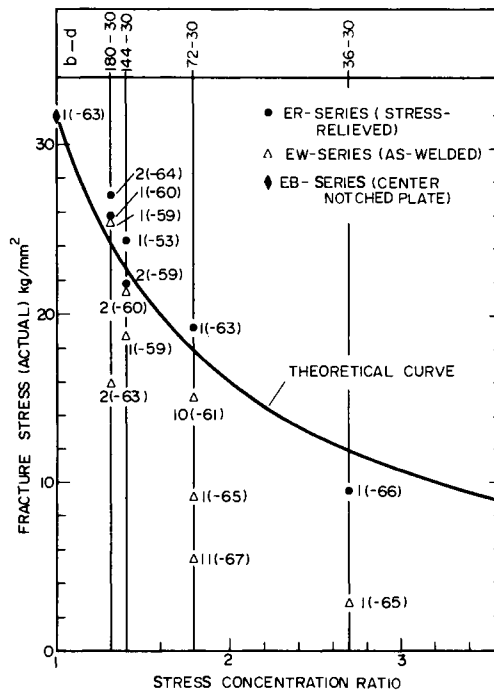


FIG. 10.20. Relation between brittle fracture stress and stress concentration ratio.

shown in Fig. 10.19(a). In this specimen, there is a doubling plate and a stiffener plate on both sides that are not continuous at the middle of the specimen. A notch is machined in the center of a non-continuous part. The notations for the specimen series indicated in the figure (ES, ER, and EW) represent the unnotched specimen, the stress relieved structural specimen, and the as-welded structural specimen, respectively. The test measures the stress concentration in the structural specimen. Figure 10.19(b) is an example of one such test, showing a stress concentration ratio of about 1.4. The stress concentration ratio is defined as:

$$\text{Stress concentration ratio} = \frac{\text{Local stress}}{\text{Mean stress}}$$

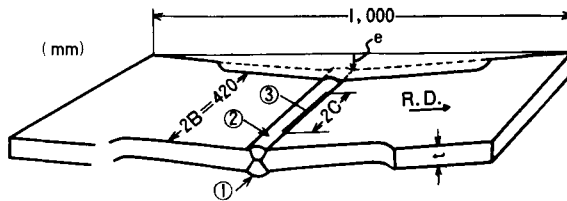


FIG. 10.21. Specimen configuration and geometry.

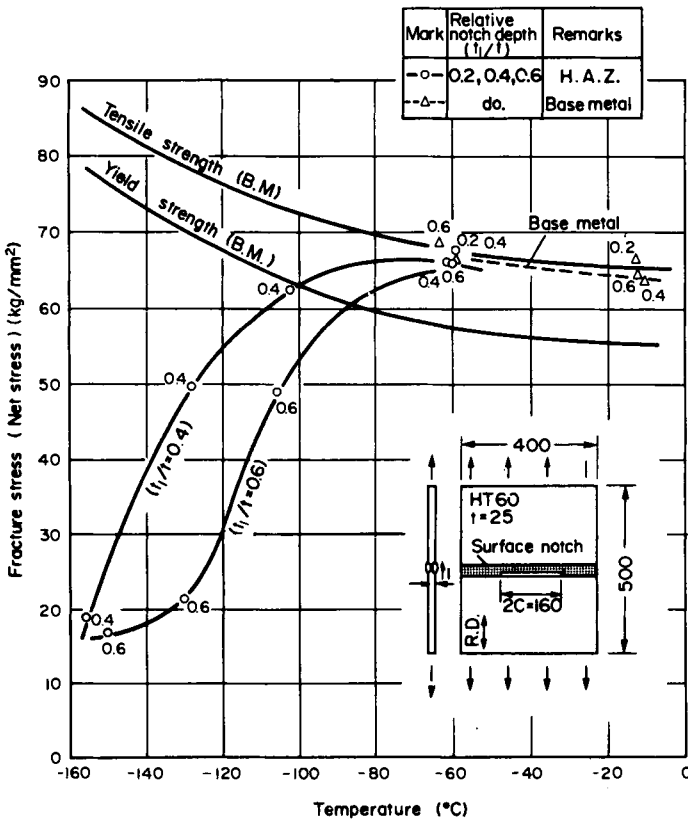


FIG. 10.22. Effect of notch depth on fracture stress in notched wide plate specimen.

Using these tests, the intensity of the stress concentration near the notch in Fig. 10.20 can be measured. The stress concentration ratio is a function of the dimensions of b and d in Fig. 10.19(a). The ratio increases as b is increased and/or d decreased. The experiment on the notched structural specimen was conducted at about -60°C (-76°F), the results of which are shown in Fig. 10.20. In stress-relieved specimens, the fracture stress decreased as the stress concentration ratio increased. When residual stress was added to the stress concentrated part, the fracture stress was lowered even more, as can be seen when comparing the fracture-stress data of the ER and EW test series.

Consequently, in order to prevent brittle fracture initiation in a welded structure, structural discontinuities must be avoided.

4. *The effect of angular distortion.* Distortion often occurs during welding fabrication. For example, the angular distortion shown in Fig. 10.21 was created by thermal, plastic distortion during the welding of a butt joint. If a crack or other defect such as an undercut are introduced at the toe of the weld metal, or along the heat-affected zone, low applied-stress brittle fracture may result. Figure 10.21 is a schematic representation of a toe crack in which stress concentrations at the root of the bead, bending stress caused by the angular distortion, tensile stress under the application of the load and residual stress all played a part. Such brittle fractures are more likely to occur as the angular

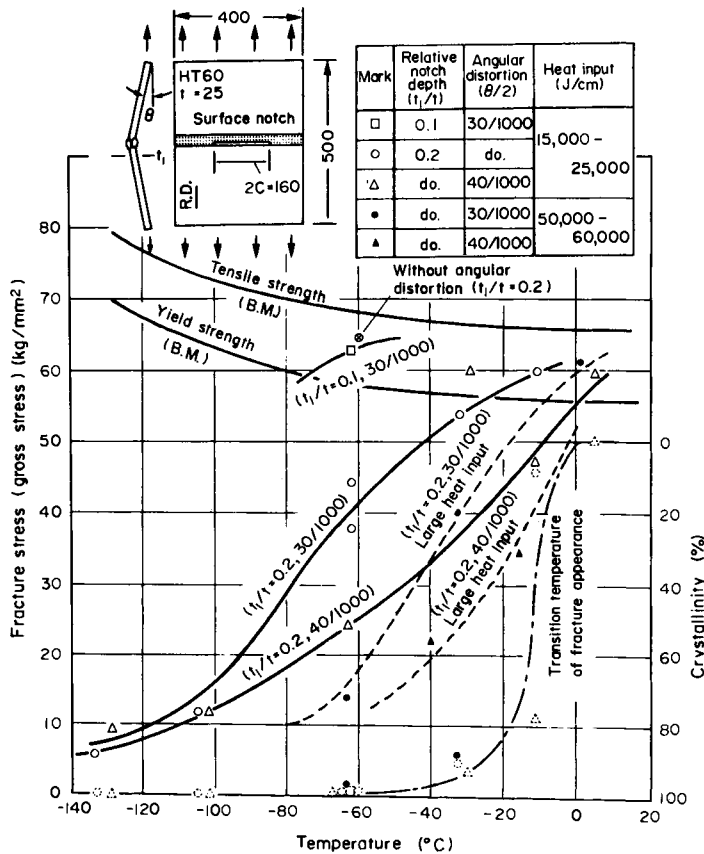


FIG. 10.23. Effect of angular distortion on fracture stress in notched wide specimen.

distortion increases. Displacement e or angle θ in Fig. 10.21 is generally used as a parameter representing the degree of angular distortion.

The first task is to determine the fracture strength of the specimen without angular distortion. Figure 10.22 shows the test results of a transversely welded notched plate (heat input: 15,000–25,000 J/cm) of quenched and tempered steel with an ultimate tensile strength of 60 kg/mm² (85.3 ksi or 588 MN/m²) HT-60, by Kihara *et al.*⁽¹⁰²⁹⁾ Here the parameter is the notch depth. As the depth of the notch is increased, the fracture stress is lowered and the transition temperature is shifted to the higher side.

Figure 10.23 shows the results of testing specimens made of the same material, but having an angular distortion. A comparison of Fig. 10.23 and 10.22 shows that the angular distortion greatly lowered the fracture stress even though the notch depths in Fig. 10.23 were smaller than those in Fig. 10.22. Though Fig. 10.23 also presents the effect of heat input, this subject will not be pursued any further at this time.

Figure 10.24 shows the effects of residual stress on the fracture strength of cross-welded specimens. Cross-welded specimens are employed in order to produce high tensile residual stresses normal to the notch plane. A comparison of Figs. 10.24 and 10.23 shows that residual stress greatly affects brittle fracture initiation. As shown above, angular distortion affects the brittle fracture of a welded structure, and it is therefore important to make every effort to avoid it during welding.

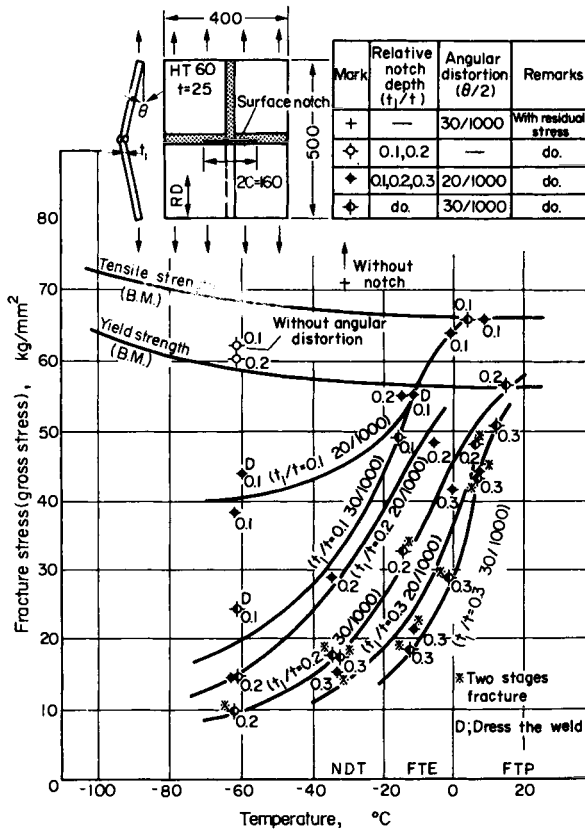


FIG. 10.24. Effect of residual stress on fracture strength of cross-welded specimens.

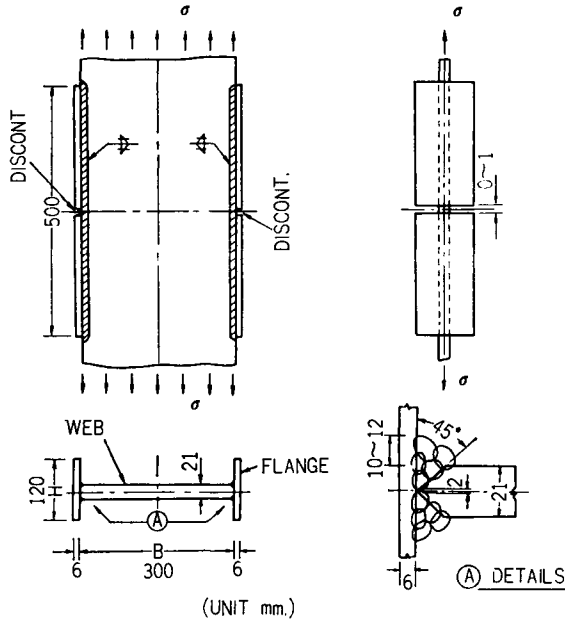


FIG. 10.25. Specimen configuration and geometry.

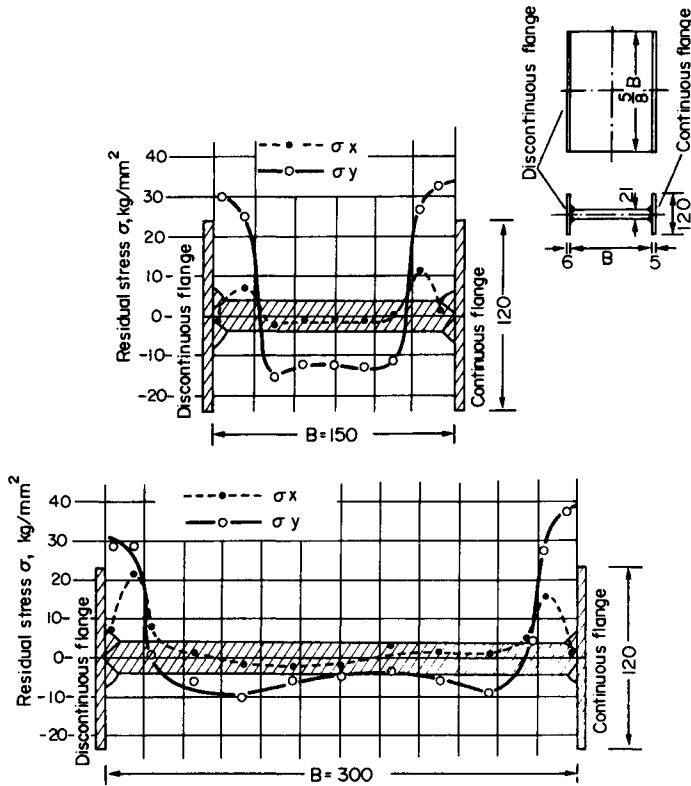


FIG. 10.26. Distributions of residual stress.

5. *Fracture tests of the I-shaped model.* Akita *et al.*⁽¹⁰³⁰⁾ studied the fracture characteristics of the I-shaped model shown in Fig. 10.25 which simulates the typical members of a ship structure. Discontinuity was introduced by using unconnected flange plates. There were no artificially made cracks to initiate brittle fracture. The magnitude of residual stresses along the center line of the specimen was changed by varying the width of the web plate.

Figure 10.26 shows the results of measuring residual stress, and provides data on specimens having two different web depths, 150 mm and 300 mm (6 and 12 in.). The maximum tensile residual stresses were the same in both cases, that is, about 30 kg/mm² (42.7 ksi or 294 MN/m²). But compressive residual stresses in the middle were different; the narrower the web, the higher the absolute value of compressive stress.

Figure 10.27 shows the test results. In this series of tests, the flange width is constant and the only varying parameter is the web width, that is, the distribution of residual stress. The figure suggests that web width affects brittle fracture initiation. From the point of view of linear fracture mechanics, it is possible that fracture stress may depend completely on the local stress near the crack; there may be no difference in the fracture

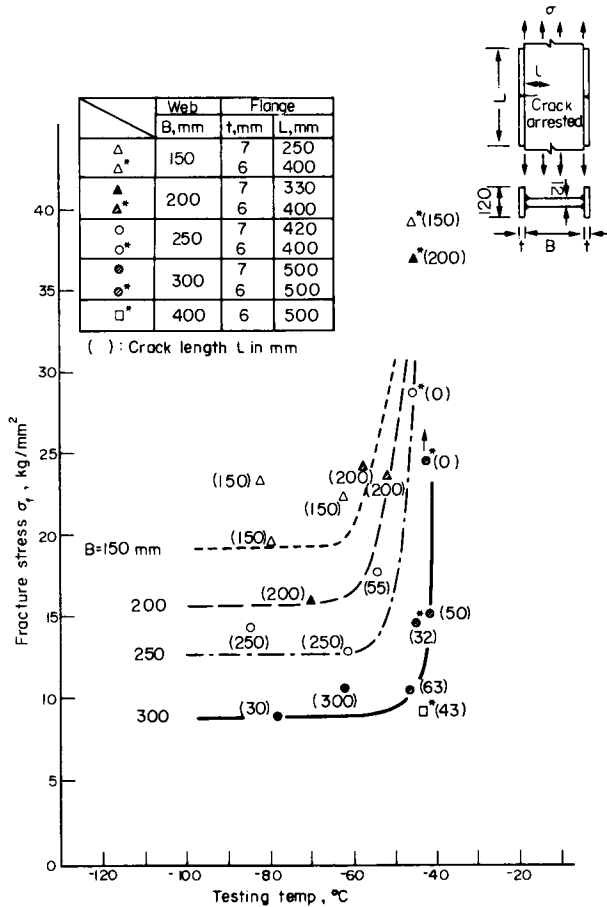


FIG. 10.27. Effect of flange width on fracture stress.

stresses of specimens with different web widths because the same magnitude of tensile stress is present in both specimens. But the test results show that the fracture stress is dependent not only on the stress near a crack but also on the pattern of its distribution. This implies that the effects of plasticity are involved.

10.5 Analytical Studies of the Brittle Fracture of Weldments

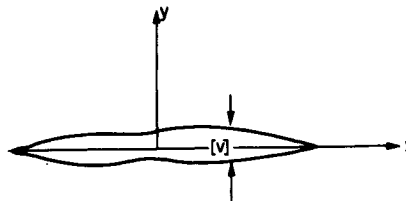
The results of experimentation on the brittle fracture of weldments have been analyzed from the point of view of the fracture mechanics theory.

10.5.1 The analysis of strain energy release in an arbitrary stress field

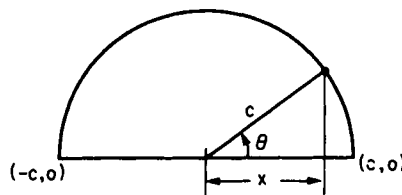
In order to analyze the effects of residual stress on the brittle fracture of weldments, it is first necessary to analyze the rate of the strain energy released when a crack occurs in a solid containing residual stress. Although there is more than one way to conduct the analysis, the following pages will describe only the analysis developed by Masubuchi.^(1024, 1031)

The analysis developed by Masubuchi has already been discussed at some length in Section 3.2. Table 3.6 shows the analytical relationship between residual stress before cracking, σ_{y0} , and dislocation (crack opening), $[v]$, when a straight crack of length $l = 2c$ occurs along the x -axis of the infinite plate (see Fig. 10.28). This relationship between σ_{y0} and $[v]$ is:

$$\sigma_{y0}(x) = \frac{E}{4\pi} \int_{-c}^c \frac{1}{x-x'} \left[\frac{d[v]}{dx} \right]_{x'} dx. \tag{10.41}$$



a. Crack opening or dislocation $[v]$



b. Coordinate system

FIG. 10.28. Dislocation $[v]$ produced by opening a straight crack in an arbitrary stress field.

The above equation can be satisfied, when σ_{y0} and $[v]$ are expressed as follows:

$$[v] = \sum_{n=1}^{\infty} A_n \sin n\theta \quad (10.42)$$

$$\sigma_{y0} = \frac{E}{4c} \sum_{n=1}^{\infty} n A_n \frac{\sin n\theta}{\sin \theta} \quad (10.43)$$

where

$$x = c \cos \theta$$

Both ends of the crack can be expressed by:

$$\begin{aligned} x = c & \quad \text{or} \quad \theta = 0, \\ x = -c & \quad \text{or} \quad \theta = \pi. \end{aligned}$$

When $\theta = 0$ and π , $\sin n\theta = 0$; or the crack opening is zero at both ends.

Often the distribution of residual stresses, σ_{y0} , is known. When this is the case, the value of coefficient A_n can be determined as follows:

$$A_n = \frac{4l}{\pi E n} \int_0^{\pi} \sigma_{y0} \sin n\theta \sin \theta d\theta. \quad (10.44)$$

The value of the elastic strain energy released due to the formation of the crack, U (per unit plate thickness), is:

$$\begin{aligned} U &= \int_{-c}^c \frac{1}{2} \sigma_{y0} [v] dx \\ &= \frac{1}{2} \int_0^{\pi} \left(\frac{E}{2l} \sum_{n=1}^{\infty} n A_n \frac{\sin n\theta}{\sin \theta} \right) \left(\sum_{m=1}^{\infty} A_m \sin m\theta \right) \frac{l}{2} \sin \theta d\theta \\ &= \frac{E}{8} \int_0^{\pi} \left(\sum_{n=1}^{\infty} n A_n \sin n\theta \right) \left(\sum_{m=1}^{\infty} A_m \sin m\theta \right) d\theta \\ &= \frac{E}{8} \frac{\pi}{2} \left(\sum_{n=1}^{\infty} n A_n^2 \right). \end{aligned} \quad (10.45)$$

The next step is to determine the rate of the strain-energy-release that takes place when the crack is extended. When the crack increases from l to $l + dl$, the value of the strain energy-release rate $[\partial U / \partial l]$ is shown by the following equation:

$$\left(\frac{\partial U}{\partial l} \right) = \frac{E \pi}{8} \frac{\partial}{\partial l} \left(\sum_{n=1}^{\infty} n A_n^2 \right). \quad (10.46)$$

In performing the above differentiation, note that the value of dislocation $[v]$, and therefore the values of coefficient A_n , change as the crack length changes. This relation is shown schematically in Fig. 10.29.

The result is shown in the following:

$$\begin{aligned} \left(\frac{\partial U}{\partial l} \right) &= \frac{E \pi}{8} \left(2A_1 \frac{\partial A_1}{\partial l} + 4A_2 \frac{\partial A_2}{\partial l} + \dots + 2nA_n \frac{\partial A_n}{\partial l} + \dots \right) \\ &= \frac{E}{8l} \pi \left(\sum_{n=1}^{\infty} n A_n \right)^2. \end{aligned} \quad (10.47)$$

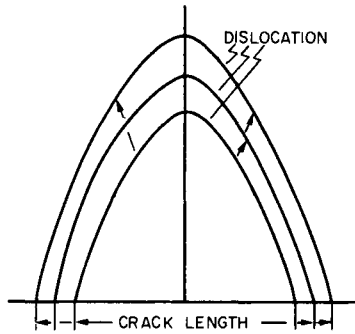


FIG. 10.29. Change of dislocation due to the increase in crack length (schematic figure).

Therefore, the value of dislocation $[v]$, strain energy U and strain-energy-release rate $(\partial U/\partial l)$ can be calculated if the stress distribution prior to cracking is known.

This analysis is not restricted to the analysis of cracking in a residual stress field. It can also be used to analyze cracking in a solid containing stresses in an arbitrary distribution.

Comparison to cracking under uniform stresses. The analysis of the strain-energy release that takes place when a crack occurs in a solid under uniform tensile stresses is the simplest application of the above analysis. When the stress that existed before cracking is uniform:

$$\sigma_{y0} = \sigma_0. \tag{10.48}$$

This means, in eqn. (10.43),

$$\sigma_{y0} = \sigma_0 = \frac{E}{4c} A_1 \tag{10.49}$$

or

$$A_1 = \frac{4c}{E} \sigma_0$$

and

$$A_2 = A_3 = A_4 = \dots = A_n = \dots = 0. \tag{10.50}$$

Then, crack opening $[v]$ is:

$$[v] = \frac{4c}{E} \sigma_0 \sin \theta = \frac{4c}{E} \sigma_0 \sqrt{1 - \left(\frac{x}{c}\right)^2} \tag{10.51}$$

or

$$\frac{[v]}{4c} = \left(\frac{\sigma_0}{E}\right) \sqrt{1 - \left(\frac{x}{c}\right)^2}. \tag{10.52}$$

From eqn. (10.45), the value of elastic energy released, U , is:

$$\begin{aligned} U &= \frac{E \pi}{8} \frac{A_1^2}{2} \\ &= \frac{E \pi}{8} \frac{1}{2} \left(\frac{4c}{E} \sigma_0\right)^2 \\ &= \frac{\pi c^2}{E} \sigma_0^2. \end{aligned} \tag{10.53}$$

The result is the same as that of eqn. (10.2) The strain-energy-release rate, $\partial U/\partial l = G$ is:

$$\begin{aligned}\frac{\partial U}{\partial l} &= \frac{E}{8l} \pi \left(\frac{4c}{E} \sigma_0 \right)^2 \\ &= \frac{\pi}{E} c \sigma_0^2.\end{aligned}\quad (10.54)$$

This result is the same as that of eqn. (10.40).

10.5.2 Determination of strain-energy-release rate in weldments

Figure 10.16 is a schematic diagram showing the mechanisms involved in the low applied-stress fracture of weldments. Studies have been made to determine quantitatively the rate of strain energy release.

Studies by Wells and Masubuchi. Masubuchi⁽¹⁰³¹⁾ analyzed the changes that take place in the G -values when a transverse crack in a butt weld grows due to the action of residual stress. This is the same as the exact determination of curve OR_0B_0 in Fig. 10.16. Masubuchi used the experimental data obtained by Wells⁽¹⁰³²⁾ for the numerical analysis. The analytical method used has been described in Section 10.5.1.

The results are shown in Fig. 10.30, 10.31, and 10.32. Figure 10.30 shows the distribution of longitudinal stresses in a butt weld.[†] The solid line shows the measured stress distribution determined by Wells, while the broken line shows the estimated distribution by Masubuchi.

Figure 10.31 shows the elastic slot opening caused by longitudinal residual stresses. The slot opening increases as the length of the slot increases. The slot-opening distribu-

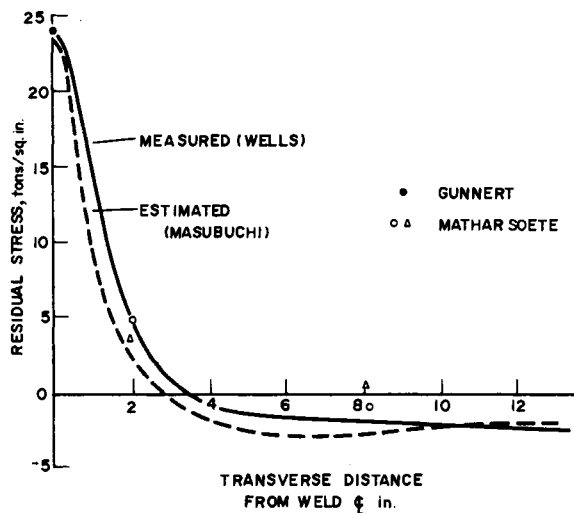


FIG. 10.30. Distribution of residual stress (longitudinal stress due to welding).

[†] The specimen geometry is shown in Fig. 9.35(a).

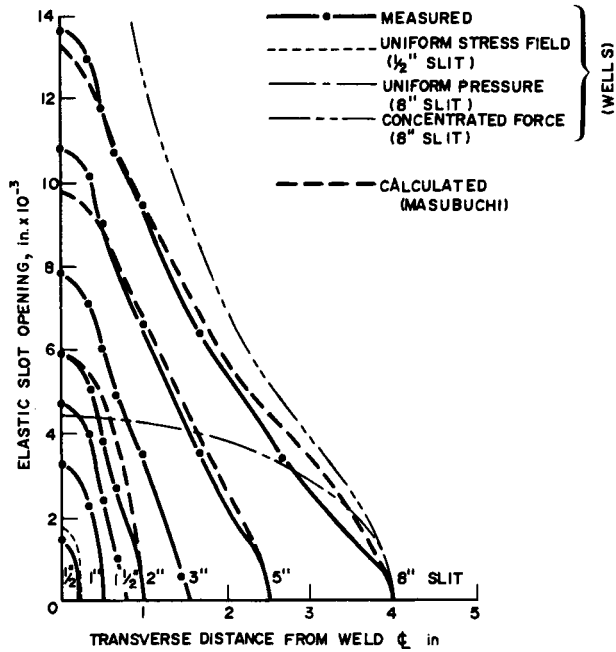


FIG. 10.31. Elastic slot openings arising from longitudinal residual stress.

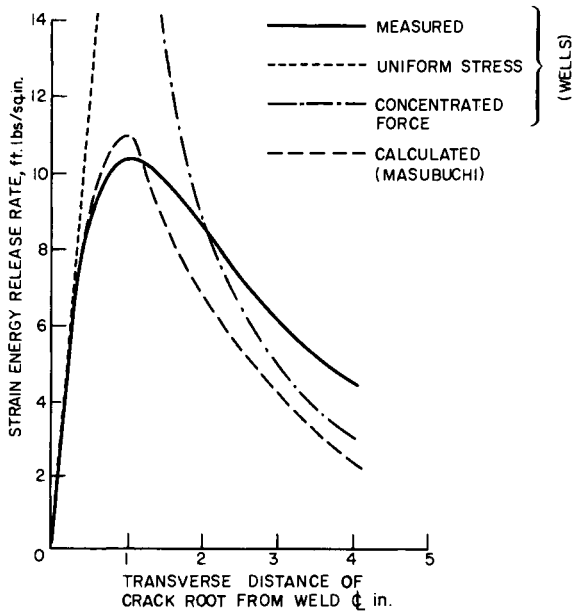


FIG. 10.32. Strain energy release rate for spontaneous fracture caused by longitudinal residual stress.

tions measured by Wells⁽¹⁰³²⁾ coincided with those calculated by Masubuchi.⁽¹⁰³¹⁾ The figure also shows some of the calculations by Wells. When the slot was short ($\frac{1}{2}$ in.), the measured distribution was similar to the calculated slot distribution for the uniform stress. When the slot was 8 in. (203 mm) long, the measured slot opening was less than the calculated distribution of the concentrated force in the center of the slot and was much larger than the calculated distribution of the uniform pressure.

Figure 10.32 shows the relationship between the crack length and the rate of release of residual stress energy.

Further study by Kihara *et al.* Kihara *et al.*⁽¹⁰³³⁾ conducted a rather comprehensive study on the strain-energy-release rate of weldments and the effects of mechanical stress-relieving. The specimen geometry was similar to that shown in Fig. 9.36. There was one as-welded specimen, and two specimens assigned to each of 5 degrees of prestraining, ranging from 5 kg/mm² (7.1 ksi or 49 MN/m²) to 25 kg/mm² (35.6 ksi or 245 MN/m²). Transverse distributions of the residual stresses in the longitudinal direction (parallel to the weld line), and the elastic opening of the central slit extending symmetrically in the transverse direction were measured. Examples of these measurements are shown in Figs. 10.33 and 10.34.

Figure 10.35 shows the measured rate of strain-energy release in the as-welded and the mechanically stress-relieved condition.

Figure 10.36 shows the measured rate of strain energy release in the as-welded specimen under various loading conditions. This figure shows actual values of \mathcal{G} in the schematic diagram (Fig. 10.16).

Utilizing the results shown in Fig. 10.36, a study was made to determine analytically the fracture stress of mechanically stress-relieved specimens. The results are shown

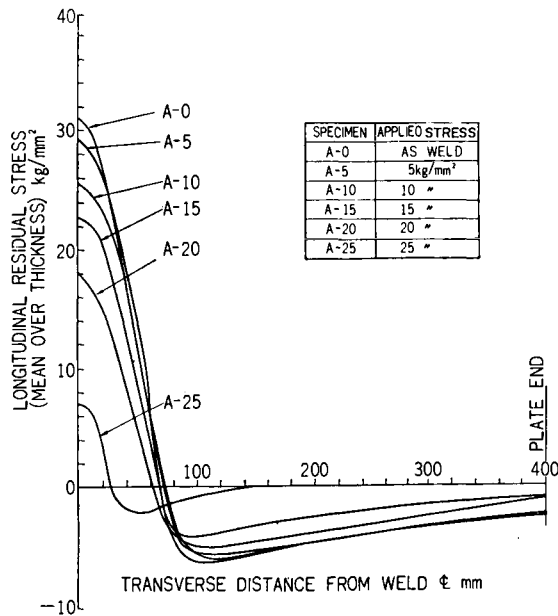


FIG. 10.33. Transverse distributions of longitudinal residual stress in as-welded and mechanically stress-relieved specimens (half of plane with longitudinal weld on center line).

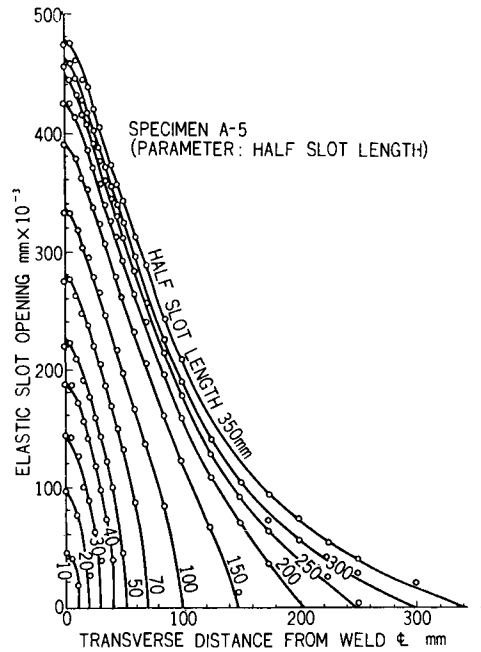


FIG. 10.34. Distributions of elastic slot opening in mechanically stress-relieved specimen loaded up to 5 kg/mm^2 (half of plane with longitudinal weld on center line).

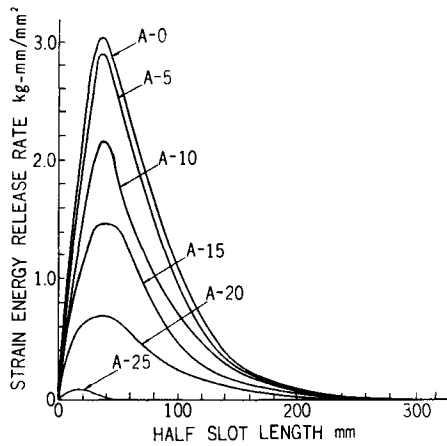


FIG. 10.35. Measured strain energy release rate in as-welded and mechanically stress-relieved specimens.

in Fig. 10.37. According to the analysis, the fracture stress of a mechanically stress-relieved specimen should be slightly higher than the preapplied stress. The calculated values of the fracture stress agreed closely with the experimental data, shown in Fig. 10.17.

10.5.3 Calculation of the stress-intensity factor in a residual-stress field

The stress-intensity factor of a crack in a residual-stress field can be calculated using

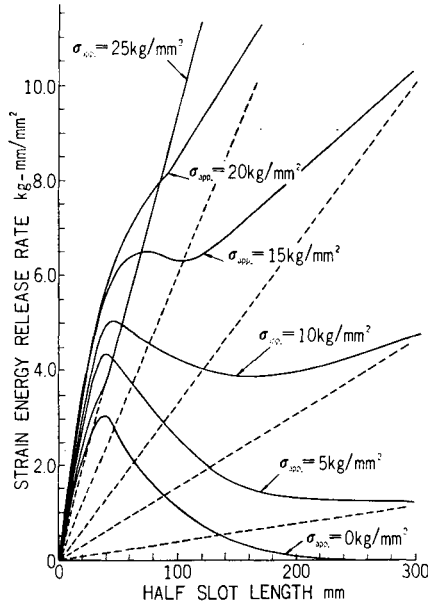


FIG. 10.36. Strain energy release rate in as-welded specimen under various loading conditions.

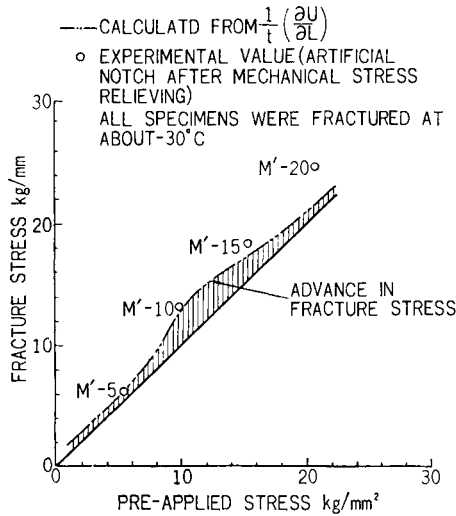


FIG. 10.37. Relation between fracture stress and pre-applied stress.

the analysis described in Section 10.5.1. However, it can also be determined from eqn. (10.10) by utilizing the principle of superposition.

Shown in Fig. 3.12 in Chapter 3 are three different cases as follows:

Figure 3.12(a): A plate with a crack under uniform stress, σ .

Figure 3.12(b): A plate with no crack under uniform stress, σ .

Figure 3.12(c): Uniform stress σ applied along both edges of the crack.

Since there is no stress concentration in Fig. 3.12(b), the stress intensity factor in

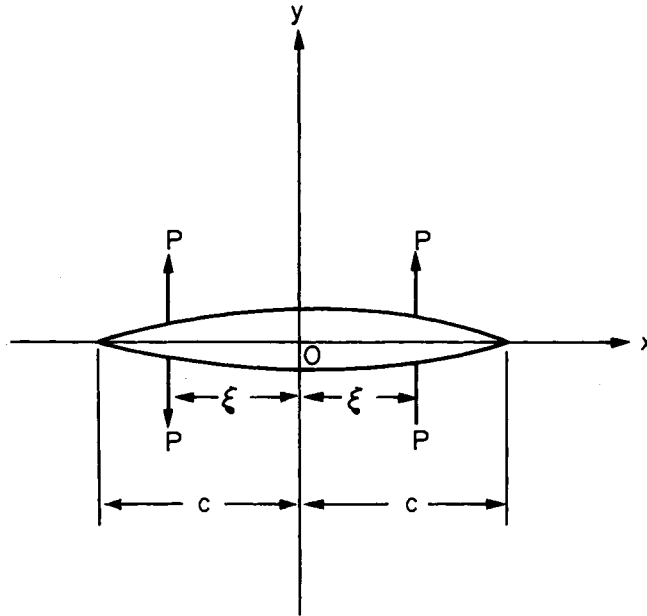


FIG. 10.38. Crack in an infinite plate subjected to symmetrical splitting forces P .

Fig. 3.12(a) is the same as that in Fig. 3.12(c). The problem can thus be reduced to that of a crack opened by internal pressure, the magnitude of which equals the applied stress. When the applied load has an arbitrary distribution, the internal pressure is a function of the position.

In a residual-stress problem, residual stress can be considered an arbitrarily distributed applied stress. The stress intensity factor of a cracked plate subjected to an arbitrarily distributed internal pressure symmetrical to the y -axis must be calculated. Assume that a pair of symmetrical splitting forces p are applied as shown in Fig. 10.38. K in this case is:

$$K = \frac{p}{\sqrt{\pi c}} \left(\sqrt{\frac{c + \xi}{c - \xi}} + \sqrt{\frac{c - \xi}{c + \xi}} \right). \tag{10.55}$$

If p is a function of ξ , the expression is changed to

$$K = \frac{1}{\sqrt{\pi c}} \int_0^l p(\xi) \left(\sqrt{\frac{c + \xi}{c - \xi}} + \sqrt{\frac{c - \xi}{c + \xi}} \right) d\xi \tag{10.56}$$

where l is the width of the region being acted on by the internal pressure. If one sets $p(x)$ equal to the residual stress $\sigma_y(x)$ at an arbitrary location ξ and integrates over the range of the crack length, then K is calculated as a function of c . Furthermore, when applied stress $q(x)$ is added to the residual stress, $p(x)$ is replaced by $q(x) + \sigma_y(x)$.

By using eqn. (10.56), it is possible to determine the K -value when the crack is located in an area containing residual stresses and the amount of external stress is known.[†]

[†] This analysis, however, does not take into consideration changes in the residual stress due to localized plastic deformation caused by external loading.

Example. Shown here is the calculation of K for the following conditions:

crack length = $2c$,

residual stress distribution:† $\sigma_y = \sigma_0 \left[1 - \left(\frac{x}{f} \right)^2 \right]$,

applies stress: σ (uniform),

$$\begin{aligned} K &= \frac{1}{\sqrt{\pi c}} \int_0^c \left\{ \sigma + \sigma_0 \left[1 - \left(\frac{x}{f} \right)^2 \right] \right\} \left[\sqrt{\frac{c+x}{c-x}} + \sqrt{\frac{c-x}{c+x}} \right] dx \\ &= \frac{1}{\sqrt{\pi c}} \int_0^c \left[(\sigma + \sigma_0) - \sigma_0 \left(\frac{x}{f} \right)^2 \right] \frac{2c}{\sqrt{c^2 - x^2}} dx, \end{aligned} \quad (10.57)$$

$x = c \cos \theta$, $dx = -c \sin \theta d\theta$;

$$\begin{aligned} K &= \frac{1}{\sqrt{\pi c}} \int_{\pi/2}^0 \left\{ (\sigma + \sigma_0) - \sigma_0 \left(\frac{c}{f} \right)^2 \cos^2 \theta \right\} \frac{2c}{c \sin \theta} (-c \sin \theta) d\theta \\ &= \frac{2c}{\sqrt{\pi c}} \int_0^{\pi/2} \left\{ (\sigma + \sigma_0) - \sigma_0 \left(\frac{c}{f} \right)^2 \cos^2 \theta \right\} d\theta \\ &= \sqrt{\pi c} \left\{ 1 + \frac{\sigma_0}{\sigma} \left[1 - \frac{1}{2} \left(\frac{c}{f} \right)^2 \right] \right\}. \end{aligned} \quad (10.58)$$

This example, though rather academic, shows that such a calculation is possible. The practical application of this approach will be given in Section 10.5.4 and 10.5.5.

10.5.4 Analytical studies of the effect of angular distortion on the brittle fracture of weldments

Ito and Tanaka⁽¹⁰³⁴⁾ conducted an analytical study to explain the experimental results shown in Figs. 10.22, 10.23, and 10.24. The geometry of the specimen used is shown in Fig. 10.21. Because the specimen is welded transversely, there is no high residual stress perpendicular to the crack surface. Embrittlement does not need to be considered since the notch is located at the same position in every specimen. The author will therefore discuss the brittle fracture characteristics of the bond between the base metal and the deposited metal. Since an exact analysis of the stress-intensity factor for this particular case has not yet been completed, this analysis will be approximate. When a plate of width $2B$ exhibits a through-thickness crack of length $2c$, the stress intensity factor under uniform tensile stress σ is expressed as follows:

$$K = f \left(\frac{c}{B} \right) \sigma \sqrt{\pi c} \quad (10.59)$$

where

c = half-length crack,
 B = half width of specimen,

$$f \left(\frac{c}{B} \right) = \sqrt{\frac{2B}{\pi c} \tan \frac{\pi c}{2B}}.$$

† This equation is often used to calculate the approximate distribution of residual stresses in areas extremely close to the weld. See Fig. 12.8 for further information.

The stress intensity factor at the deepest point of the surface crack can be approximated using the following:

$$\begin{aligned}
 K_p &= K \frac{t_1}{t} \\
 &= f\left(\frac{c}{B}\right) \sigma \sqrt{\pi c} \frac{t_1}{t}
 \end{aligned}
 \tag{10.60}$$

where t = plate thickness,
 t_1 = crack depth.

On the other hand, the stress intensity factor of the bending stress caused by angular distortion, K_B , can be approximated by using the following calculations.

When there is a side-crack of depth t_1 in a specimen of width t , the stress intensity factor is expressed as follows (Gross *et al.*).⁽¹⁰³⁵⁾

$$K'_B = Y_B \sigma_B \sqrt{t_1} \tag{10.61}$$

where σ_B = bending skin stress = $\frac{M t}{I 2} = \frac{6e}{t} \sigma$,

M = bending moment,

Y_B = correction factor

$$= 1.99 - 2.47\left(\frac{t_1}{t}\right) + 12.97\left(\frac{t_1}{t}\right)^2 - 23.17\left(\frac{t_1}{t}\right)^3 + 24.80\left(\frac{t_1}{t}\right)^4.
 \tag{10.62}$$

The stress-intensity factor of the same specimen under a uniform stress σ is

$$K_p = f\left(\frac{t_1}{t}\right) \sigma \sqrt{\pi t_1}. \tag{10.63}$$

Suppose

$$K_B = \frac{K'_B}{K'_p} K_p \tag{10.64}$$

then

$$K_B = 6 \frac{f(c/B)}{f(t_1/t)} Y_B \frac{e t_1}{t} \sigma \sqrt{c}. \tag{10.65}$$

Consequently, the stress intensity factor of the specimen is expressed:

$$\begin{aligned}
 K_I &= K_p + K_B \\
 &= f\left(\frac{c}{B}\right) \frac{t_1}{t} \sigma \sqrt{\pi c} + 6 \frac{f(c/B)}{f(t_1/t)} Y_B \frac{e t_1}{t} \sigma \sqrt{c}.
 \end{aligned}
 \tag{10.66}$$

Figures 10.39, 10.40, and 10.41 show the effects of notch length, notch depth and angular distortion on brittle fracture initiation. Figure 10.42 shows K_{Ic} vs. temperature of those test results where eqn. (10.66) is used in calculating K_{Ic} . From this figure we can see that K_{Ic} depends only on the temperature.

The validity of eqn. (10.66) is thus confirmed. In other words, the fracture stress of an actual welded joint can be predicted using eqn. (10.66).

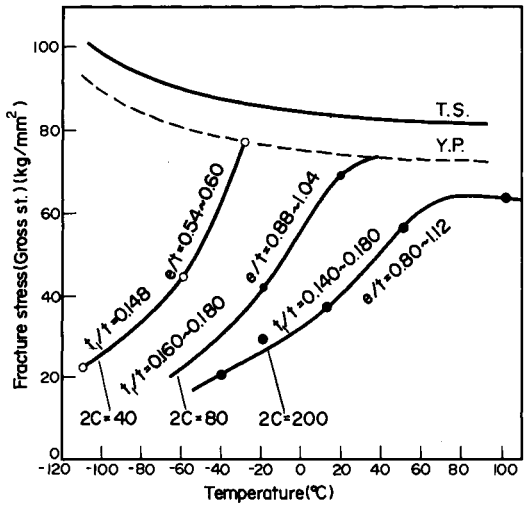


FIG. 10.39. Effect of surface notch length on the fracture stress transition characteristics of weld bonds (as-welded).

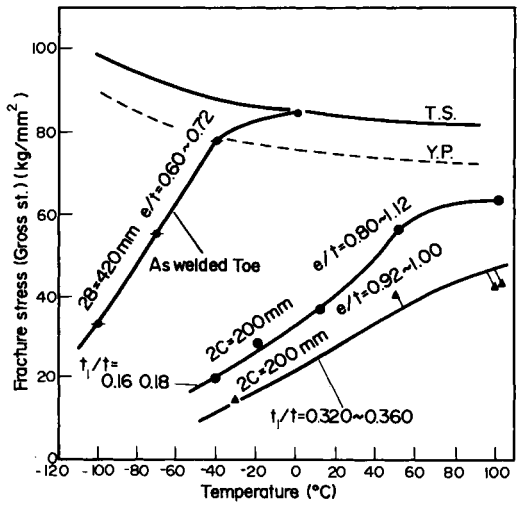


FIG. 10.40. Effect of notch depth on the fracture stress transition characteristics of weld bond (as-welded).

There are many assumptions in the above calculation. Though it is desirable to calculate a stress-intensity factor on an exact basis, approximate methods are useful in practical engineering.

10.5.5 The analysis of brittle fractures in an I-shaped structural model

The results of the brittle fracture experiments on the I-shaped model have been analyzed.^(1030, 1034)

Assumption. An accurate analysis of brittle fracture in an I-shaped model must be

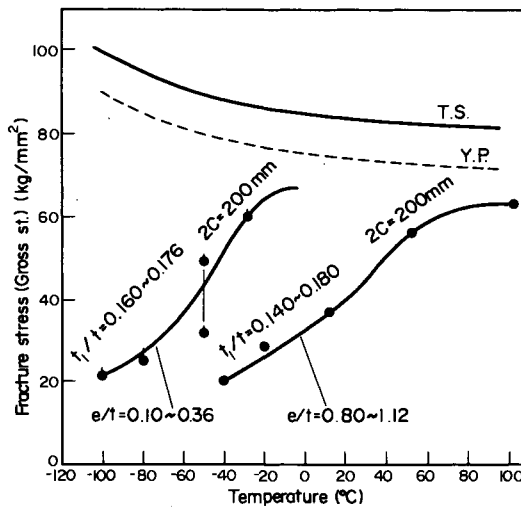


FIG. 10.41. Effect of angular distortion on the fracture stress transition characteristics of weld bonds (as-welded).

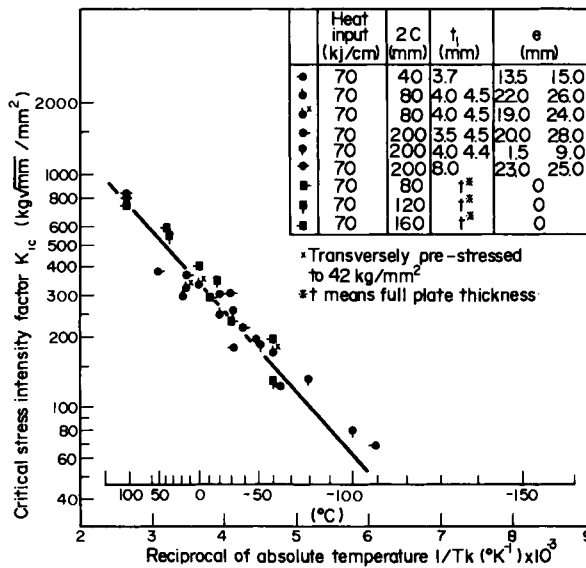


FIG. 10.42. Relation between reciprocal of absolute temperature and critical stress intensity factor.

three-dimensional. But a two-dimensional analysis was attempted in order to provide an approximation. Figure 10.43 shows the procedure. The pair of flanges is treated as a notch-effects case. On the basis of test results, the notch length, f , is assumed to be as follows:

$$f = f' \frac{t'}{t} \tag{10.67}$$

where $f =$ equivalent notch length,
 $f' =$ width of flange,
 $t =$ plate thickness of web,
 $t' =$ plate thickness of flange.

This relationship has been confirmed as valid within a given range of flange widths.

To simplify the calculation, the residual stress distribution is assumed to be rectangular, as shown in Fig. 10.44. Consequently, after the welded part has yielded due to applied

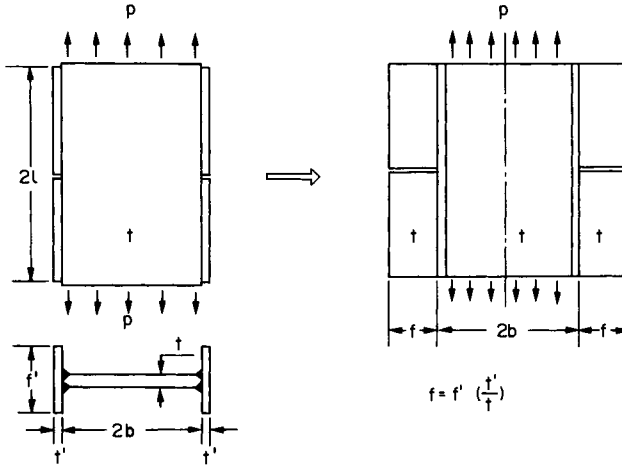


FIG. 10.43. Equivalent two-dimensional model of longitudinally welded "I"-shaped specimen.

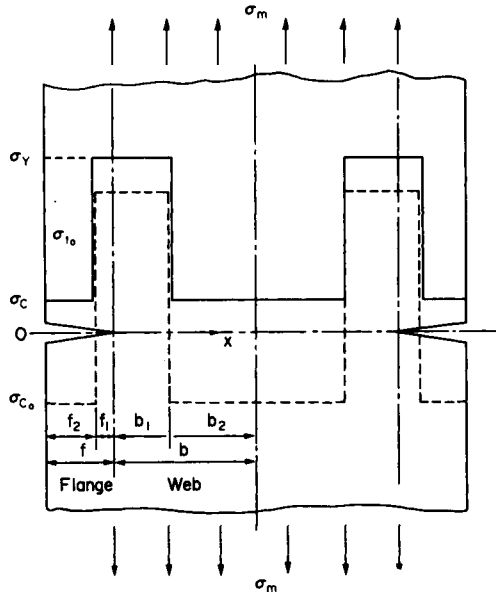


FIG. 10.44. Assumption of residual stress distribution.

stress σ_m , the stress distribution of the specimen can be written as follows:

$$\frac{\sigma_t}{\sigma_y} = 1,$$

$$\frac{\sigma_c}{\sigma_y} = \frac{\sigma_m}{\sigma_y} \left(\frac{b+f}{b_2+f_2} \right) - \left(\frac{b_1+f_1}{b_2+f_2} \right) \tag{10.68}$$

where σ_t = the stress over the range of tensile residual stress before loading,
 σ_c = the stress over the range of compressive residual stress before loading.

If a crack is introduced into the stress field mentioned above, the size of the plastic zone may no longer be negligible, and a correction may be needed. As Wells⁽¹⁰¹⁰⁾ has shown (see Fig. 10.11), the stress distribution outside the plastic zone will coincide with the measured stress distribution if the real crack length f is corrected to the imaginary crack length c , that is,

$$c = f + r_2 \tag{10.69}$$

where r_2 = plastic zone correction length. r_2 is determined as shown in Fig. 10.45 by the following expressions:

$$\int_{-r_2}^{r_1} \sigma_Y dr = \int_0^{r_1} \sigma_y dr,$$

$$(\sigma_y)_{r=r_1} = \sigma_Y \tag{10.70}$$

where σ_y = elastic stress distribution outside the imaginary crack, c .

If the stress distribution near the crack tip can be expressed as eqn. (10.71), and if the point splitting force P can be applied at x as shown in Fig. 10.46(a), then the stress distributions corresponding to Figs. 10.46(b) and 10.46(c) respectively can be expressed as

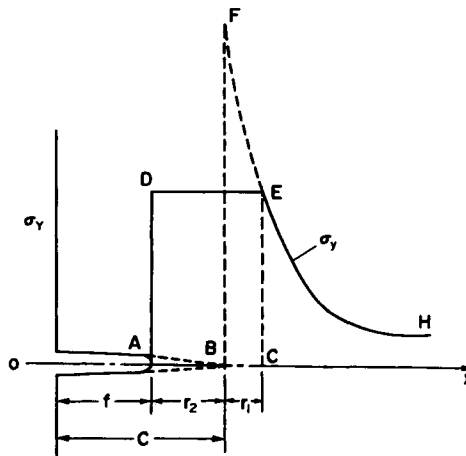


FIG. 10.45. Yielded-zone-size correction to elastic stress distribution at the tip of a crack.

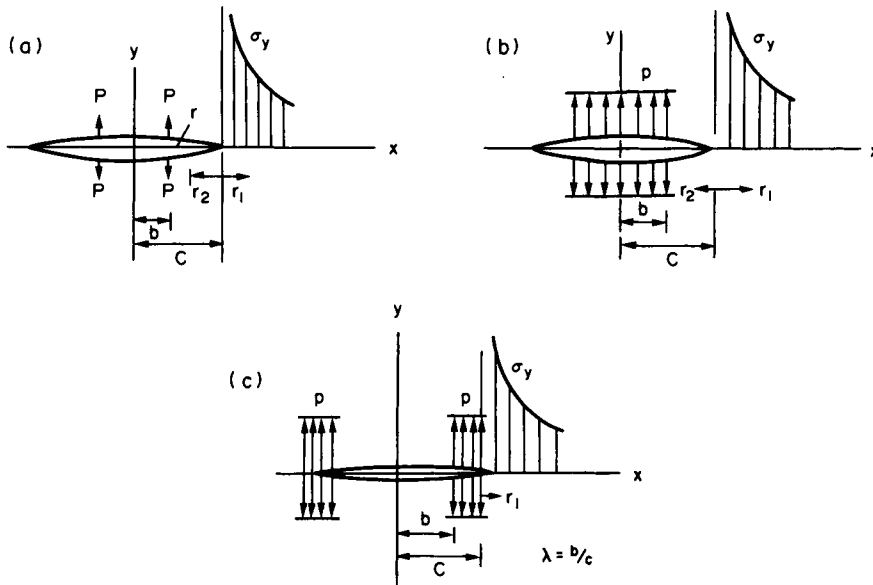


FIG. 10.46. Elastic stress distribution at the tip of a crack subjected to partially distributed internal pressure.

eqns. (10.72) and (10.73).

$$\sigma_y^{(y=0)} = \frac{P}{\pi} \frac{1}{\sqrt{2c} \sqrt{r_1}} \sqrt{\frac{c+b}{c-b}} \quad (10.71)$$

$$\sigma_y^{(y=0)} = \frac{P\sqrt{c}}{\sqrt{2r_1}} \left(\frac{2}{\pi} \sin^{-1} \lambda \right) \quad (10.72)$$

$$\sigma_y^{(y=0)} = \frac{P\sqrt{c}}{\sqrt{2r_1}} \left(1 - \frac{2}{\pi} \sin^{-1} \lambda \right) \quad (10.73)$$

where $\lambda = b/c$.

Calculation of the stress intensity factor. Using three different cases, the relationship between the imaginary crack length c and the range of the tensile residual stress distribution will now be examined.

(Case I)

$$c \leq f + b_1 \text{ and } \sigma_{y_2}^{(x=f+b_1)} \leq \sigma_y \quad (\text{cf. Fig. 10.47(a)}).$$

From eqn. (10.70):

$$\frac{(c-f)^2}{2(b_1+f-c) \cdot c} = \left[1 - \left(1 - \frac{\sigma_c}{\sigma_y} \right) \frac{2}{\pi} \sin^{-1} \frac{f_2}{c} \right]^2 \quad (10.74)$$

where σ_c/σ_y is equal to expression (10.72), consequently

$$K_{(x=c)} = \lim_{r_1 \rightarrow 0} \sqrt{2\pi r} \sigma_y = \sqrt{\pi f} \sigma_y \left[\sqrt{\frac{c}{f}} \left\{ 1 - \left(1 - \frac{\sigma_c}{\sigma_y} \right) \frac{2}{\pi} \sin^{-1} \frac{f_2}{c} \right\} \right] \quad (10.75)$$

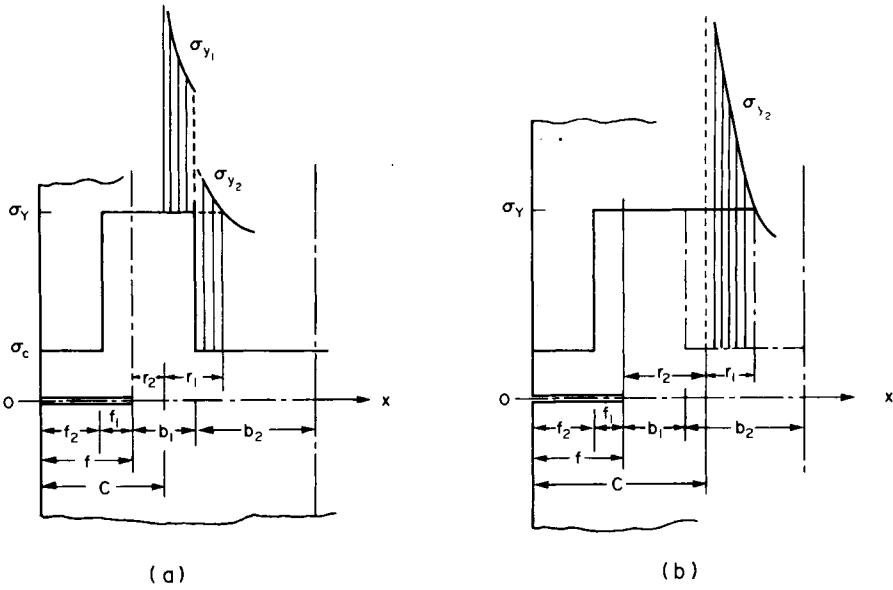


FIG. 10.47. Relation between imaginary crack length and residual stress distribution extent.

(Case II)

$$c \leq f + b_1 \text{ and } \sigma_{y_2}^{(x=f+b_1)} \geq \sigma_Y \text{ (cf. Fig. 10.47(a)).}$$

Similarly, the following expressions are deduced:

$$\frac{c-f}{1-\frac{\sigma_c}{\sigma_Y}} - (f+b_1-c) = \frac{1}{2}c \left[\frac{1}{1-\frac{\sigma_c}{\sigma_Y}} - \frac{2}{\pi} \sin^{-1} \frac{f_2}{c} \right]^2, \quad (10.76)$$

$$K_{(x=c)} = \sqrt{\pi f} \sigma_Y \left[\sqrt{\frac{c}{f}} \left\{ 1 - \left(1 - \frac{\sigma_c}{\sigma_Y} \right) \cdot \frac{2}{\pi} \sin^{-1} \frac{f_2}{c} \right\} \right]. \quad (10.77)$$

(Case III)

$$c > f + b_1 \text{ (cf. Fig. 10.47(b)),}$$

$$\frac{c-f}{1-\frac{\sigma_c}{\sigma_Y}} = \frac{c}{2} \left[\frac{1}{1-\frac{\sigma_c}{\sigma_Y}} - \left[1 + \frac{2}{\pi} \left(\sin^{-1} \frac{f_2}{c} - \sin^{-1} \frac{f_1}{c} \right) \right] \right]^2, \quad (10.78)$$

$$K_{(x=c)} = \sqrt{\pi f} \sigma_Y \left[\sqrt{\frac{c}{f}} \left[1 - \left[1 - \frac{\sigma_c}{\sigma_Y} \right] \left[1 + \frac{2}{\pi} \left(\sin^{-1} \frac{f_2}{c} - \sin^{-1} \frac{f+b_1}{c} \right) \right] \right] \right]. \quad (10.79)$$

Comparison between experimental results and calculations. Figure 10.48 shows the results of calculations in which residual stresses and specimen sizes are determined from actual data. On the other hand, the fracture toughness of material K_c is experi-

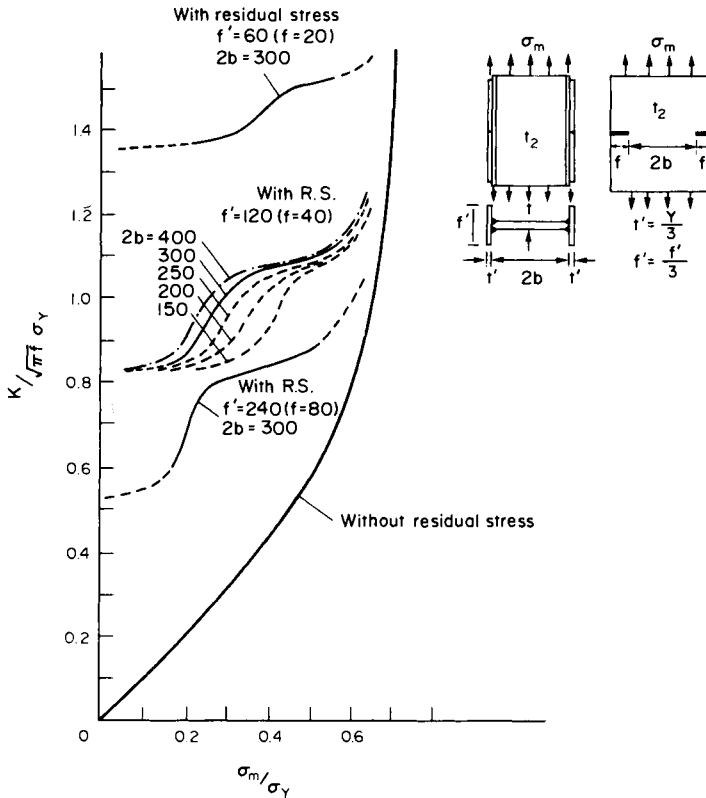


FIG. 10.48. Calculated values of stress intensity factor according to various specimen sizes.

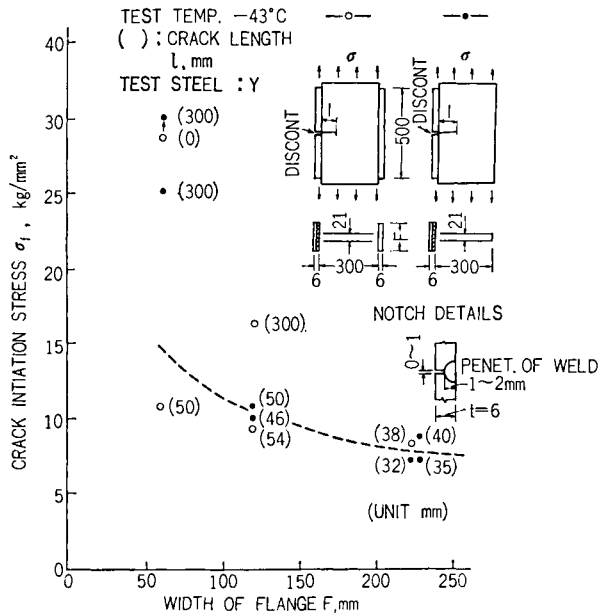


FIG. 10.49. Comparison between measured and predicted fracture stresses of longitudinally welded "I"-shaped specimens.

mentally determined as follows:

$$K_c = K_o \exp \left[-\frac{k}{T} \right] \quad (10.80)$$

where K_o , k = material constants,

$$K_o \text{ is determined from } \frac{K_c}{\sqrt{\pi f \sigma_y}} = 1.06 \text{ when}$$

$$T = 230^\circ \text{K} (-43^\circ \text{C}), f' = 120 \text{ mm}, \sigma_y = 35 \text{ kg/mm}^2,$$

$$k = 300^\circ \text{K},$$

T = absolute test temperature.

Fracture stress can be predicted from the above K_c data and the calculated K . Figure 10.49 compares the measured fracture stress with the predicted fracture stress. In spite of its many assumptions, the calculated curve compares well with the measured fracture stresses and, if accurate calculations were substituted for these assumptions, the difference between predicted and measured values would be even less.

References

- (1001) CHALMERS, B., *Physical Metallurgy*, John Wiley & Sons, Inc., 1959.
- (1002) GRIFFITH, A. A., "The phenomena of rupture and flow in solids", *Phil Trans. Roy. Soc.* **221**, 163–198 (1921), and "The theory of rupture", *Proceedings of the First International Congress of Applied Mechanics*, pp. 55–63 (1924).
- (1003) FELBECK, D. K., and OROWAN, E., "Experiments on brittle fracture of steel plates", *Welding Journal*, **34** (11), 370s–375s (1955).
- (1004) IRWIN, G. R., "Fracture", *Encyclopedia of Physics*, vol. VI, *Elasticity and Plasticity*, Springer-Verlag, Berlin, 1958, pp. 551–590.
- (1005) IRWIN, G. R., and PARIS, P. C., "Fundamental aspects of crack growth and fracture", pp. 1–46, vol. III of *Fracture*, edited by Liebowitz, H., Academic Press, New York, 1917.
- (1006) ZENER, C., *Fracturing of Metals*, American Society for Metals, Cleveland, 1948, p. 3.
- (1007) COTTRELL, A. H., "Theoretical aspects of fracture", *Fracture*, John Wiley & Sons, Inc., 1959, pp. 20–44.
- (1008) PETCH, N. J., "The ductile-cleavage transition in alpha-iron", *Fracture*, John Wiley & Sons, Inc., New York, 1959, pp. 54–64.
- (1009) OTANI, M., "Theory of brittle fracture", *Journal of the Japan Welding Society*, **32** (11), 3–11 (1963).
- (1010) WELLS, A. A., "Application of fracture mechanics at and beyond general yielding", *British Welding Journal*, pp. 563–570 (Nov. 1963).
- (1011) *Method for Crack Opening Displacement (COD) Testing*, DD19: 1972, British Standards Institution.
- (1012) RICE, J. R., "Mathematical analysis in the mechanics of fracture", vol. II of *Fracture*, edited by Liebowitz, H., Academic Press, New York, pp. 191–311 1968.
- (1013) *Workshop in Fracture Mechanics*, Text, 16–28 August 1964 in Denver, Colorado, arranged by Universal Technology Corporation, Dayton, Ohio.
- (1014) "Fracture testing of high strength sheet materials: a report of a Special ASTM Committee", *ASTM Bulletin*, No. 243, 29–40 (June 1960); No. 244, 18–28 (Feb. 1960); and *Materials Research and Standards*, **1** (11), 877–885 (Nov. 1961).
- (1015) IRWIN, G. R., "Analysis of stresses and strains near the end of a crack traversing a plate", *Journal of Applied Mechanics*, ASME, **24**, 361 (1975).
- (1016) KAMMER, P. A., Masubuchi, K., and Monroe, R. E., *Cracking in High-Strength Steel Weldments—A Critical Review*, DMIC Report 197, Defense Metals Information Center, Battelle Memorial Institute, Columbus, Ohio, Feb. 1964.
- (1017) PELLINI, W. S., Goode, R. J., Puzak, P. P., Lange, E. A., and Huber, R. W., *Review of Concepts and Status of Procedures for Fracture-Safe Design of Complex Welded Structures Involving Metals of Low to Ultra-high Strength Levels*, NRL Report 6300, U.S. Naval Research Laboratory, June 1965.
- (1018) *Effect of Heat-treatment Variations on the Bursting Strength of Thin-walled Pressure Vessels Fabricated from Vasojet 1000 Steel*, Report No. ER 10121–5, The Martin Company.
- (1019) MISHLER, H. W., MONROE, R. E., and RIEPPEL, P. J., *Welding of High-strength Steels for Aircraft and Missile Applications*, DMIC Report 118, 12 Oct. 1959.

- (1020) RANDALL, M. D., MONROE., and RIEPPEL, P. J., "Causes of microcracking and microporosity in ultra high-strength steel weld metal", *Welding Journal*, **41** (5), 193s-206s (1962).
- (1021) MARTIN, D. C., RYAN, R. S., and RIEPPEL, P. J., "Evaluation of weld-joint flaws as reinitiating points of brittle fracture", *Welding Journal*, **36** (5), 244s-251s (1957).
- (1022) SOPHER, R. P., LOWE, A. L., MARTIN, D. C., and RIEPPEL, P. J., "Evaluation of weld-joint flows as initiating points of brittle fracture, Part II", *Welding Journal*, **38** (11), 441s-450s (1959).
- (1023) BOYD, G. M., "The conditions for unstable rupturing of a wide plate", *Transactions of the Institute of Naval Architects*, **99** (3), 349-366 (July 1957).
- (1024) KIHARA, H. and MASUBUCHI, K., *Effect of Residual Stress on Brittle Fracture—Studies on Brittle Fracture of Welded Structures at Low Stress Levels*, Report No. 30 of the Transportation Technical Research Institute, Toyko, 1958.
- (1025) MYLONAS, C., "Prestrain size and residual stresses in static brittle-fracture initiation", *Welding Journal*, **38** (10), Research Supplement, 414a-424s (1959).
- (1026) KIHARA, H., MASUBUCHI, K., IIDA, K., and OBA, H., *Effect of Stress Relieving on Brittle Fracture Strength of Welded Steel Plate*, IIW, X-218-59 (1959).
- (1027) KIHARA, H., and OBA, H., "Effect of notch shape on brittle fracture of welded steel plate", *Journal of the Society of Naval Architects of Japan*, **108** (1960).
- (1028) KIHARA, H., IIDA, K., and NARITA, K., "Effect of stress concentration due to structural discontinuities on initiation of brittle fracture in low stress levels", *Journal of the Society of Naval Architects of Japan*, **112** (1962).
- (1029) KIHARA, H. KANAZAWA, T., OBA, H., SUSEI, S., MINAKATA, S., and YAMAMOTO, S., "Effect of notch size, angular distortion and residual stress on brittle fracture initiation of welded joints for high strength steels (The 1st Report)", *Journal of the Society of Naval Architects of Japan*, 125 (1969).
- (1030) AKITA, Y., MAEDA, T., and YADA, T., "On the brittle fracture initiation characteristics of welded structures (2nd Report)", *Journal of the Society of Naval Architects of Japan*, 118 (1965).
- (1031) MASUBUCHI, K., *Dislocation and Strain Energy Release During Crack Propagation in Residual Stress Fields*, Report of the Transactions of the Tech. Research Institute, Japan, No. 29 (1958).
- (1032) WELLS, A. A., "The brittle fracture strength of welded steel plate", *Quarterly Transactions of the Institution of Naval Architects*, **48** (3), 296-326 (July 1956).
- (1033) KIHARA, H., MASUBUCHI, K., KUSUDA, T., and IIDA, K., "Initiation and propagation of brittle fractures in residual stress fields", Document X-219-59, Commission X of the International Institute of Welding, 1959.
- (1034) ITO, T. and TANAKA, K., "Initiation of brittle fracture from a surface notch on HY-80 steel weld", *Proceedings of the First International Symposium on the Prevention of Cracking in Welded Structures based on the Prevention of Cracking in Welded Structures based on Recent Theoretical and Practical Knowledge held in Tokyo* (1971).
- (1035) GROSS, B., SRAWLEY, J. E., *Stress-Intensity Factors for Single-Edge Notch Specimens in Bending or Combined Bending and Tension by boundary Collection of a stress Function*, NASA TN D-3092 (1965).

The Fatigue Fracture of Weldments as it Relates to Residual Stress

THIS chapter discusses the fatigue fracture of weldments as it relates to residual stress. Although the question of how residual stresses affect the fatigue strength of a welded structure is even now, after many years of research, not fully understood, and although the experts still disagree some comments on this subject can still be made.⁽¹¹⁰¹⁾

Some people blame residual stresses whenever the cause of a failure in a welded structure cannot be explained in some other way. Others believe residual stress effects are wiped out after the structure is subjected to repeated loading and therefore do not affect the fatigue strength. It is the author's opinion that under certain conditions the residual stresses do affect the fatigue strength of a welded structure, though in many other cases the residual stresses present have only negligible effects on the fatigue strength.

Discussions in this chapter are short, because only limited studies have been made of the analysis of effects of residual stresses on the fatigue strength of welded structures. Major difficulties come from the following two reasons:

1. Residual stresses change by the application of repeated loading
2. Stress distributions around a crack change as the crack grows due to repeated loading.

In this chapter brief discussions on basics of fatigue fracture are presented first. To those who need further information references (905), (1101), and (1102) are recommended. Much of the information presented here comes from references (102). Then discussions are given on:

Fatigue strength of weldments.

Effect of residual stresses.

Some methods of improving the fatigue strength of weldments.

Until recently almost all information on fatigue fracture was developed based upon data generated by fatigue testing. Most of the information generated so far is of an empirical nature. Recently there have been significant developments in the application of fracture mechanics theories to fatigue fracture. It is hoped that this new analytical approach can be further extended to solve some practical problems related to the fatigue fracture of welded structures.

11.1 Introduction to Fatigue Fracture⁽¹⁰²⁾

When a material is subjected to repeated loading, fracture takes place after a certain

number of cycles. The lower the applied stress, the larger the number of cycles before fracture takes place.

As far as fatigue fractures of engineering structures are concerned, the following two types of fractures are important:

1. High-cycle, low-stress fatigue.
2. Low cycle, high-stress fatigue.

In high-cycle fatigue, the endurance limit of a material after several million cycles or more is usually the consideration. In low-cycle fatigue, on the other hand, fracture after repeated loading of less than 10^5 cycles is usually considered. For example, when the frequency of loading is 100 cycles per minute, then after:

1 hour:	6,000 cycles
1 day :	144,000 cycles
10 days:	1.44×10^6 cycles

11.1.1 *Fatigue failures of structures*

High-cycle fatigue is a problem in those portions of a structure subjected to fast, repeated loads, such as areas close to propellers, rotating machinery, and areas under constant vibrations. In such areas several million stress cycles can be achieved in a relatively short period of time. For example, in the design of modern aircraft the fail-safe design concept has been developed and applied.^(905,1103)

There are many structural components in which low-cycle fatigue, rather than high-cycle fatigue, is usually the problem. For example, cracks frequently found in the hull structure of a ship are caused by low-cycle fatigue.⁽¹¹⁰⁴⁻¹¹⁰⁹⁾ Reference (102) discusses fatigue fractures in ship structures.

When structural members are exposed to water and other corrosive environments, corrosion fatigue often becomes a serious problem.⁽¹⁰²⁾

11.1.2 *Characteristics of fatigue fracture*⁽¹⁰²⁾

A fatigue fracture goes through the following three stages:

1. The initiation of the crack.
2. The slow growth of the crack.
3. The onset of the unstable fracture.

During the early stages, a fatigue fracture exhibits several characteristics that enable the engineer to distinguish it from other types of fracture.

Initiation of fatigue crack. In most cases, fatigue cracks originate at the surface. The surface must be smooth if the fatigue strength is to be high. We will elaborate on this later.

But brittle fractures, on the other hand, can initiate at subsurface defects where the triaxiality of stress is great.

Growth of a fatigue crack. A small crack initiated grows slowly as stress cycles are

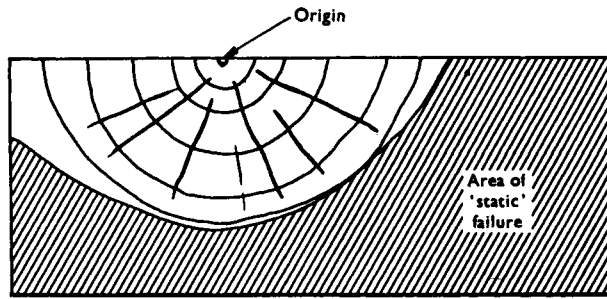


FIG. 11.1. Diagrammatic representation of a typical fatigue fracture surface.^(102,1101)

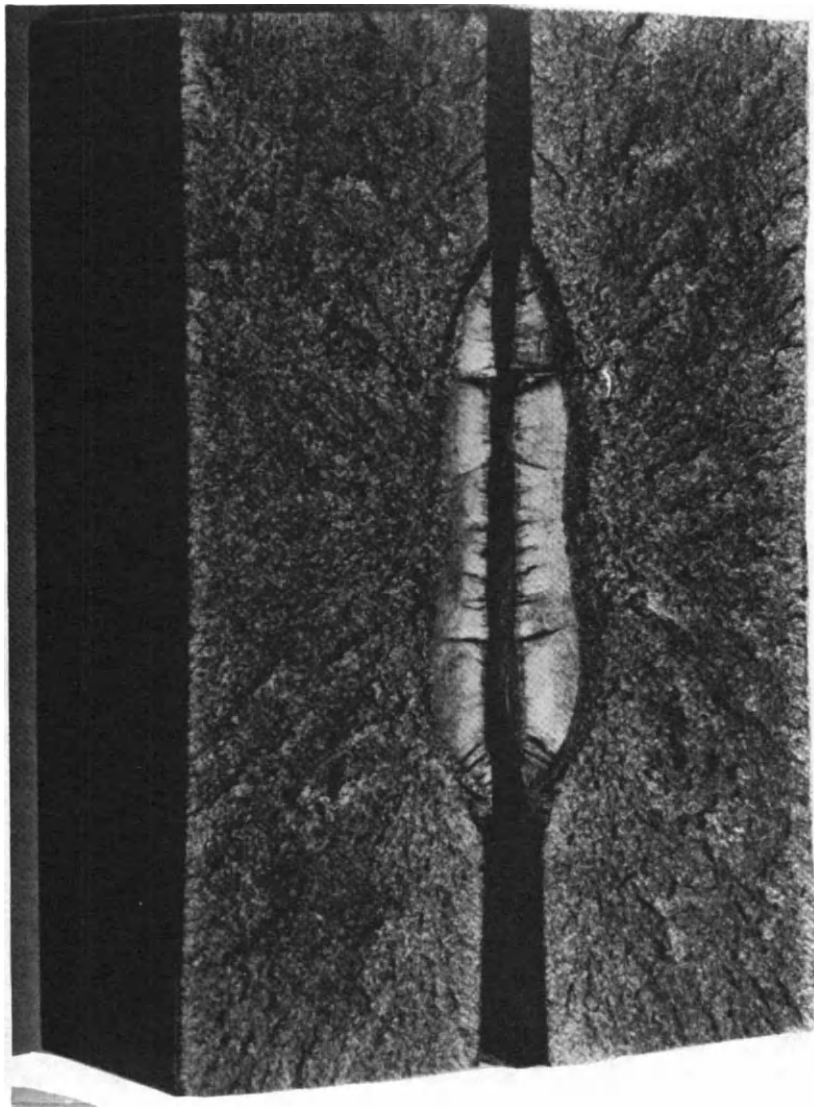


FIG. 11.2. Fracture surface of a specimen in which fatigue cracking was followed by brittle fracture.⁽¹¹⁰¹⁾

repeated. A fatigue crack is transgranular; propagating within grains rather than along grain boundaries.

Onset of unstable fracture. As the crack progresses, the stress on the residual cross-section increases so that there is a corresponding increase in the rate of crack propagation. Ultimately, a stage is reached when the remaining area is unable to support the applied load and final rupture occurs. The fracture surface of the final rupture area may be either crystalline or fibrous depending upon whether the fracture is brittle or ductile.

Fracture appearance. The above characteristics of fatigue fracture can be observed on fracture surfaces.

Figure 11.1 is a diagrammatic representation of a typical fatigue fracture surface.⁽¹⁰²⁾ The region surrounding the origin of a fatigue fracture has a smooth, silky appearance that extends to the limit of the fatigue fracture proper.

In the immediate vicinity of the crack's origin the surface may appear extremely

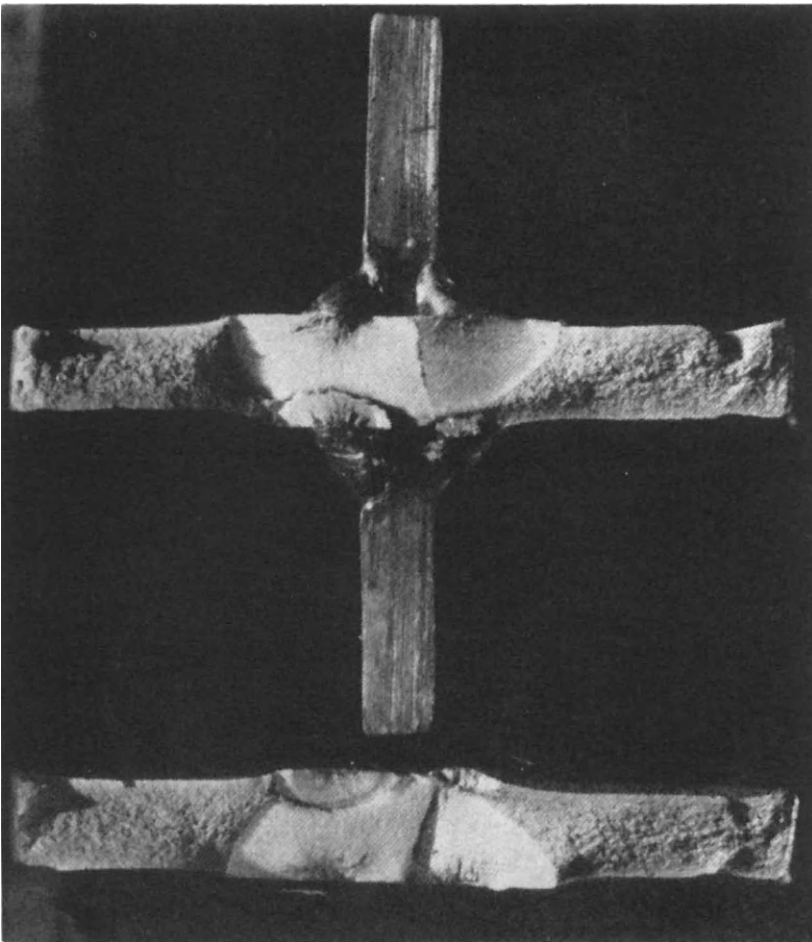


FIG. 11.3. Fracture surface of a specimen in which fatigue cracking was followed by a ductile fracture.⁽¹¹⁰¹⁾

smooth, a feature that is probably accentuated by a rubbing of the surface as the crack propagates. There is often a tendency for this smooth region to grow slightly, but progressively, rougher in texture as the distance from the origin increases. Careful examination of this smooth part frequently reveals the existence of concentric rings or beach markings around the fracture nucleus and radial lines emanating from it. The beach markings or striations are more evident under an electron-microscope as discussed in a later part of this chapter.

Figure 11.2 and 11.3 show typical specimens in which the initial cracking was due to fatigue, but in which the final fractures were brittle and ductile, respectively.⁽¹⁰²⁾

11.2 High-cycle Fatigue

This section is primarily concerned with high-cycle fatigue. However, the general discussion of fatigue including the definitions of stress cycle, $S-N$ curve, and fatigue-crack-growth mechanisms can also be applied to low-cycle fatigue.

11.2.1 Fatigue testing-stress cycles

Most of our knowledge about the fatigue behaviour of materials has come from laboratory tests on relatively simple specimens.

There are four basic parameters that can be used in defining the stress cycles to which fatigue specimens are subjected. They are:⁽¹⁰¹⁾

The minimum stress in cycle: S_{\min} .

The maximum stress in cycle: S_{\max} .

The mean stress: $S_m = \frac{1}{2}(S_{\min} + S_{\max})$.

The stress range: $S_r = S_{\max} - S_{\min}$.

The stress cycle is fully defined when any two of the above four quantities are given.

Figure 11.4 shows typical stress cycles used in fatigue tests. In the cycle shown in Fig. 11.4(a), the stress is varied from zero to tension (“pulsating tension” cycle). This type of cycle is most commonly used for the fatigue testing of plates and welded joints. A fairly large amount of data also exists for the case shown in Fig. 11.4(b), where $S_{\min} = -S_{\max}$ (“alternating” cycle).

In the cycle shown in Fig. 11.4(c), both the maximum and minimum stresses are tensile. The particular case in which $S_{\min} = 0.5S_{\max}$ is often called a “half tensile” cycle. Other cycles involving unequal tensile and compressive stresses, or wholly compressive stresses, also may be used.

The $S-N$ curve and fatigue strength. In order to determine the fatigue strength of a particular material under a given load condition, it is necessary to test several similar specimens. Each of these specimens is subjected to a given cyclic stress and the number of loading cycles required to produce failure in each specimen is recorded. The relationship between the applied stress, S , and the number of cycles to failure, N , is thus obtained.

Figure 11.5 shows the $S-N$ curve which represents the relationship between maximum stress and cycles to failure.⁽¹⁰²⁾

Figure 11.6 shows the relationship between the logarithms of both stress and the number of cycles, $\log S - \log N$.⁽¹⁰²⁾ Because $\log S - \log N$ relationships for many materials are approximately linear, most fatigue data are presented on the basis of $\log-\log$ relationships.

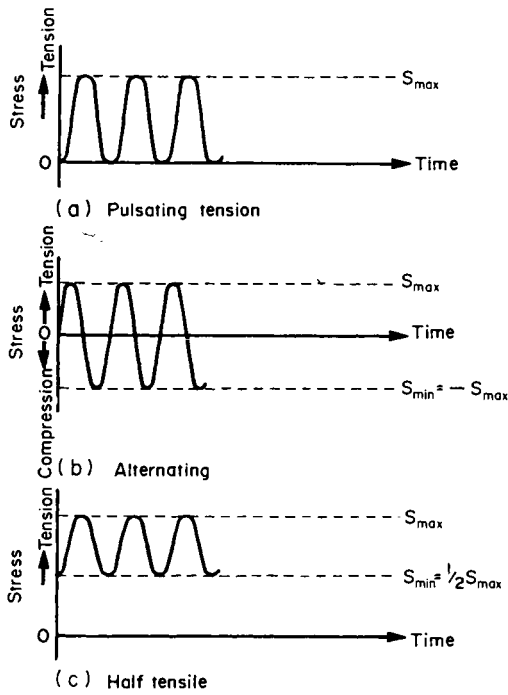


FIG. 11.4. Typical stress cycles used in fatigue tests.⁽¹¹⁰¹⁾

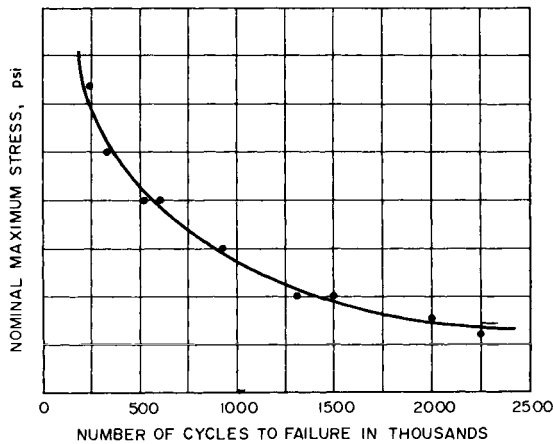


FIG. 11.5. Representation of relationship between maximum stress and cycles to failure (Wohler or S-N curve).⁽¹¹⁰²⁾

For plain ferrous metal specimens it has been found that the curve is almost parallel to the N -axis after about 2 to 5 million cycles, indicating that if the stress were slightly less, the specimen would have an infinite life. This limiting stress is called the endurance limit of the material. Most other materials do not exhibit an endurance limit, although the $S-N$ curve becomes substantially horizontal as N increases.

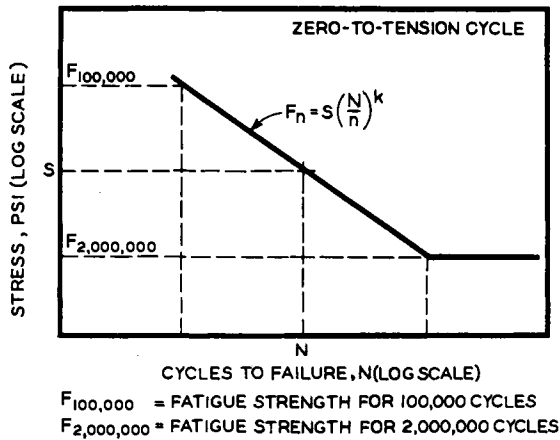


FIG. 11.6. S-N curve presented on a log-log scale.⁽¹¹⁰²⁾

The sloping line of Fig. 11.6 can be expressed by the relationship

$$F_n = S(N/n)^K \tag{11.1}$$

where F_n = the fatigue strength computed for failure at n cycles,
 S = the stress which produced failure in N cycles,

K = the slope of the best-fit straight line representing the data.⁽¹¹⁰²⁾

In such a relationship, the fatigue strength can be computed over the range covered by the sloping line for any selected number of cycles of the same type of stress cycle, if the slope of the line and one point on the line are known.⁽¹¹⁰²⁾

Only one type of stress cycle is represented on each S-N curve. Therefore, in order to understand the general fatigue behavior of a material or joint, it is necessary to have one S-N curve for each type of stress cycle.

The data for the various S-N curves can be summarized in a Goodman diagram. Figure 11.7 is a Goodman diagram for an as-rolled flat plate. It provides a composite

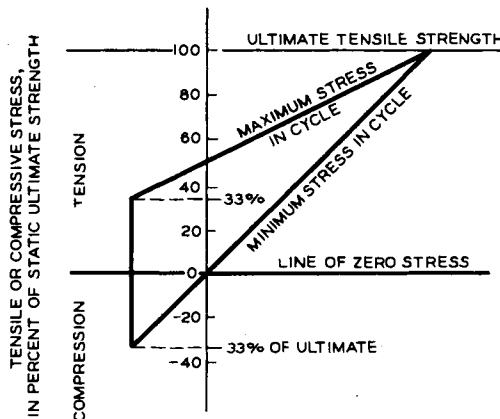


FIG. 11.7. Goodman diagram—a composite representation of the effects of various types of stress cycles on fatigue life.⁽¹¹⁰²⁾

representation of the effects of various types of stress cycles, including those ranging from static tension, through zero-to-tension, to complete reversal.

The range of stress is shown by the vertical distance between the two heavy sloping lines. For example, at the extreme left side of the diagram, the stress range is a complete reversal from a compressive stress to a numerically equal tensile stress. At the extreme right side of the diagram, the maximum stress line intersects the minimum stress line at the level of the ultimate tensile strength, and the range of stress is zero. At an intermediate point, the minimum stress line intersects the line of zero stress; the maximum stress represents the fatigue strength under a pulsating load (0 to tension). Unless a finite life is stated as the basis for the Goodman diagram, it usually pertains to the fatigue limit.⁽¹¹⁰²⁾ There are several modifications of the Goodman diagram.

11.2.2 How material strength, stress concentration, and environment effect the endurance limit

Materials.⁽¹⁰²⁾ Figure 11.8 shows the relationship between the endurance limit and the ultimate tensile strength of various steels.⁽¹¹⁰²⁾ As Fig. 11.8 illustrates, the fatigue strength of materials increases as the strength of the material itself increases at a ratio of about 50%. This relationship is true, however, only when the specimen is polished and the surface is very smooth. If the material is severely notched, the endurance limit will

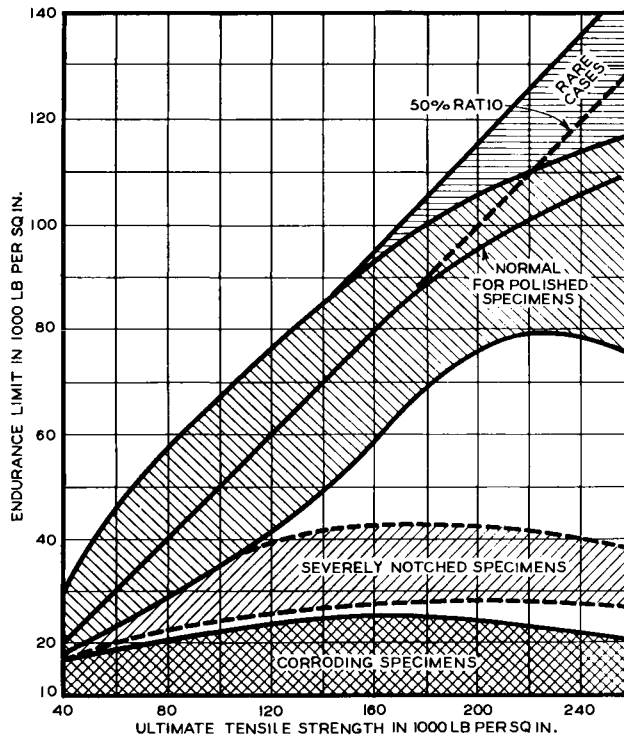


FIG. 11.8. Relationship between the endurance limit and ultimate tensile strength of various steels.⁽¹¹⁰²⁾

be reduced drastically. The change is even greater when a corroding specimen is involved. These latter effects—a reduction in the endurance limit due to a severely notched surface or a corroding material—are most severe when the material is a high-strength steel.⁽¹¹⁰²⁾

Stress Concentration.⁽¹⁰²⁾ The most deleterious factor affecting the fatigue life of metals is the localized concentration of stress by geometric discontinuities including cracks, notches, fillets, holes, surface imperfections, etc. The shape and size of a discontinuity determine how much stress will be concentrated at the point. Cracks concentrate the highest amount of stress, and generous fillets with a smooth, polished surface concentrate the lowest.⁽¹¹⁰²⁾

A surface notch affects the endurance limit of a material much more than a notch in the interior of the same material.

In most materials, the notch sensitivity tends to increase with increasing strength. When sharp notches are present, therefore, it is not unusual to find little or no fatigue strength advantage in using high-strength materials.

The presence of weld defects, especially those on or near the surface, reduces fatigue strength. This subject is discussed in detail in Chapter 15.

Corrosion. As shown in Fig. 11.8 when a material is subjected to a corrosive environment its fatigue strength is lowered. “Corrosion fatigue” is one of the most serious factors in the lowering of fatigue strength.

Many structures in the sea fail because the sea water accelerates the fatigue process. A common solution is to design with a low-strength alloy at a low working stress, say below 5000 psi, making the marine structure big and bulky. Within recent years, with the demand for higher performance, attempts have been made to use higher strength materials, but it has been found that the effect of the marine environment more than cancels out the useful increase in strength. The material’s reaction with the environment accelerates the rate of crack propagation across the component. In fact, the advances made with AISI 4340 steels and other high-strength materials in aerospace structures are often lost when these materials are submerged in sea water.

Figure 11.9 shows how notch and sea water affect the flexural fatigue strengths of

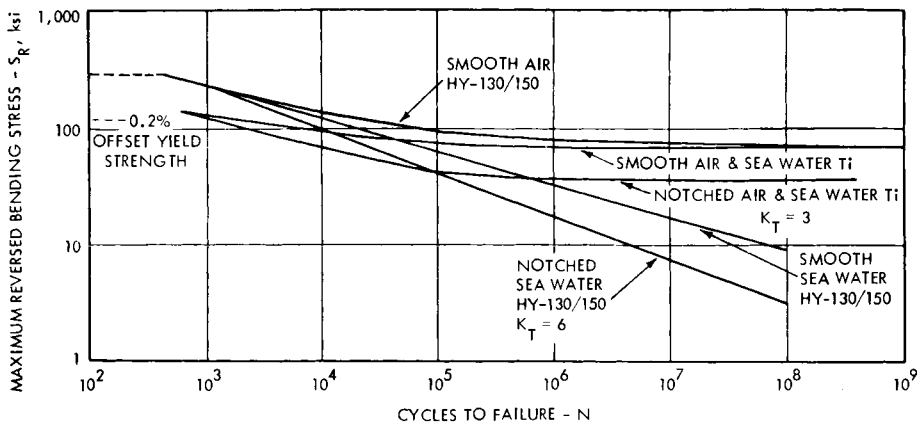


FIG. 11.9. Flexural fatigue curves for HY-130/150 steel and special grade Ti-6Al-4V.⁽¹²²⁾

Note: K_T is theoretical stress concentration factor.

HY-130/150 steel and special grade Ti-6Al-4V.⁽¹²²⁾ The figure shows the fatigue strength of HY-130/150 to be more severely damaged by notch and sea water than that of Ti-6Al-4V.

11.3 Low-cycle Fatigue

11.3.1 Characteristics of low-cycle fatigue⁽¹¹¹⁰⁻¹¹¹³⁾

During loading and unloading cycles, many metals exhibit low-cycle fatigue failure involving plastic deformation. Under such conditions, true stresses cannot be calculated using elastic theory, and plastic theory is not developed enough to handle such problems. The control and analysis of low-cycle fatigue, therefore, is easier if determined on the basis of strain rather than stress.

Cyclic stress and strain. Figure 11.10 illustrates the stress-strain relationships likely to develop under cyclic loading conditions. The relationship shown in Fig. 11-10(a) occurs when the applied force or moment is completely reversed within the elastic region; σ_t is the total stress range and ϵ_t is the total strain range. Figure 11.10(b) shows the relationship that develops when the reversed loading involves the plastic region. The stress-strain relationship is no longer linear and follows the hysteresis loop *BCDEB* during each cycle. σ_t is the total stress range but in this instance may be nominal or true. ϵ_t , the total strain range, involves two parts: (1) the elastic strain range ϵ_e and (2) the plastic strain range, ϵ_p , where $\epsilon_t = \epsilon_p + \epsilon_e$.

11.3.2 S-N relationships

High-cycle fatigue results are usually presented in the form of *S-N* diagrams, such as Fig. 11.5. Since the cyclic stresses needed for failure in the high-cycle region are well within the elastic region (see Fig. 11.10(a)) it is not important whether we use stress or strain as the independent variable.

With low-cycle fatigue, however, this is not the case. Most of the evidence collected over the last 10 years indicates that the strain becomes the dominant factor with decreasing fatigue life.⁽¹¹¹⁰⁾

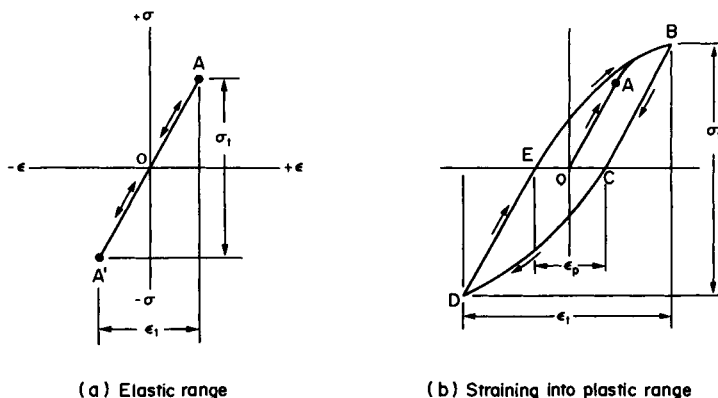


FIG. 11.10. Stress-strain relationships under cyclic loading.⁽¹¹¹⁰⁾

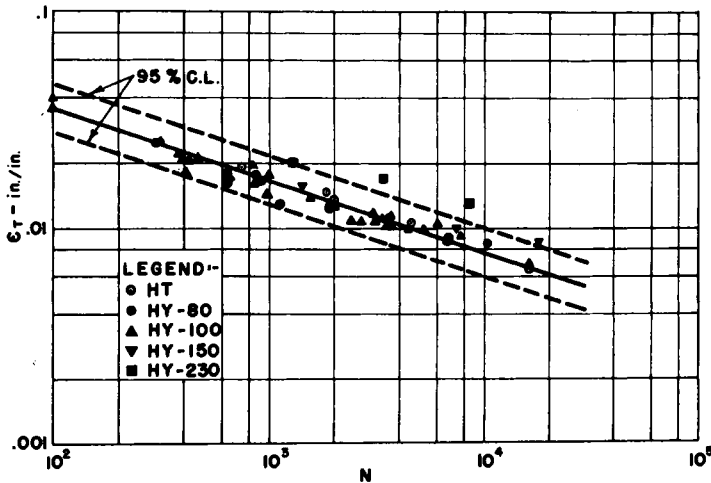


FIG. 11.11. Total strain range vs. cycles to failure for steels in air.⁽¹¹¹⁰⁾

Figure 11.11 shows the low-cycle fatigue results obtained for unnotched (smooth) specimens by the U.S. Navy Marine Engineering Laboratory. The yield strength of the steels ranges from 41,000 to 230,000 psi (28.8 kg/mm² or 237 MN/m² to 161.7 kg/mm² or 1586 MN/m²); total strain range versus cycles to failure is plotted. The similarity of behavior irrespective of yield strength is important to note. Perhaps even more significant is the fact that the behavior appears to be independent of the material as illustrated in Fig. 11.12. It seems that when strain is the controlling factor in low-cycle fatigue, the strength or type of material used makes little difference. Recent tests on pressure vessels tend to support this view for steels with yield strength from 30,000 to 90,000 psi.⁽¹¹¹⁰⁾ However, the high-cycle fatigue strength of materials varying in strength level are markedly different as shown in Fig. 11.8. Consequently the relationships shown seem to

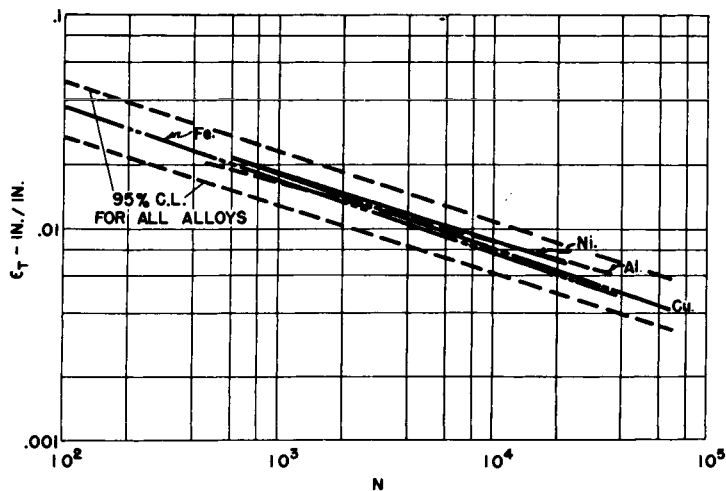


FIG. 11.12. Total strain range vs. cycles to failure for alloys in air.⁽¹¹¹⁰⁾

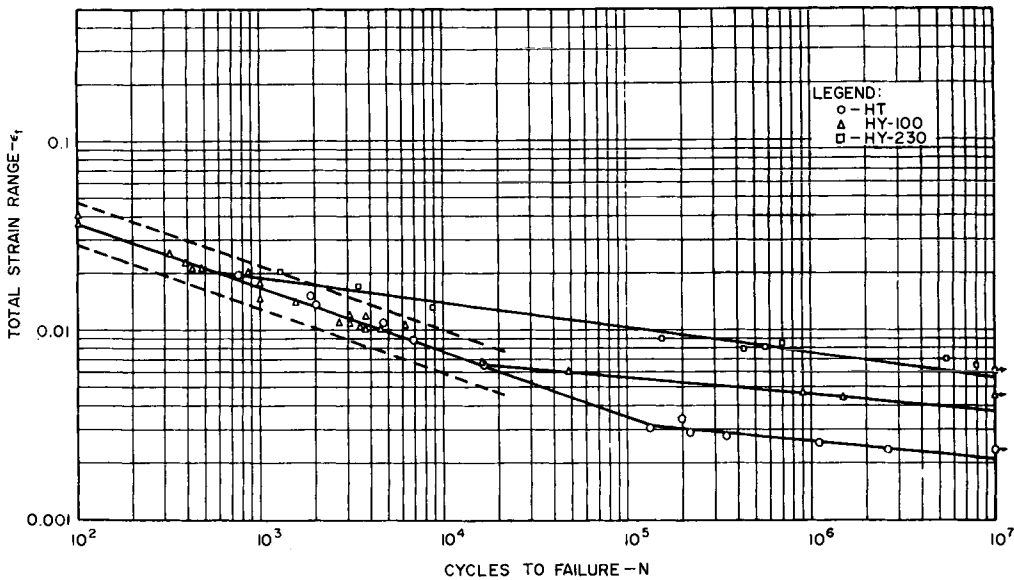


FIG. 11.13. Fatigue relationships for steels (completely reversed strain).^(122, 1110)

be valid only in the restricted range of 100 to 10,000 cycles. Divergence from the relationship is apparent for the HY-230 steel shown in Fig. 11.13.

In Fig. 11.13 three steels with markedly different yield strengths are shown. Above 1000 cycles, the advantages of using high-yield strength materials are apparent. However, for a given cycle life greater than 1000, the relationship shows that the high-yield strength materials can suffer low-cycle fatigue failure while apparently being cycled elastically. This actually has happened in tests of HY-230 steel and certain aluminum alloys.

11.4 Studies on Fatigue Crack Growth

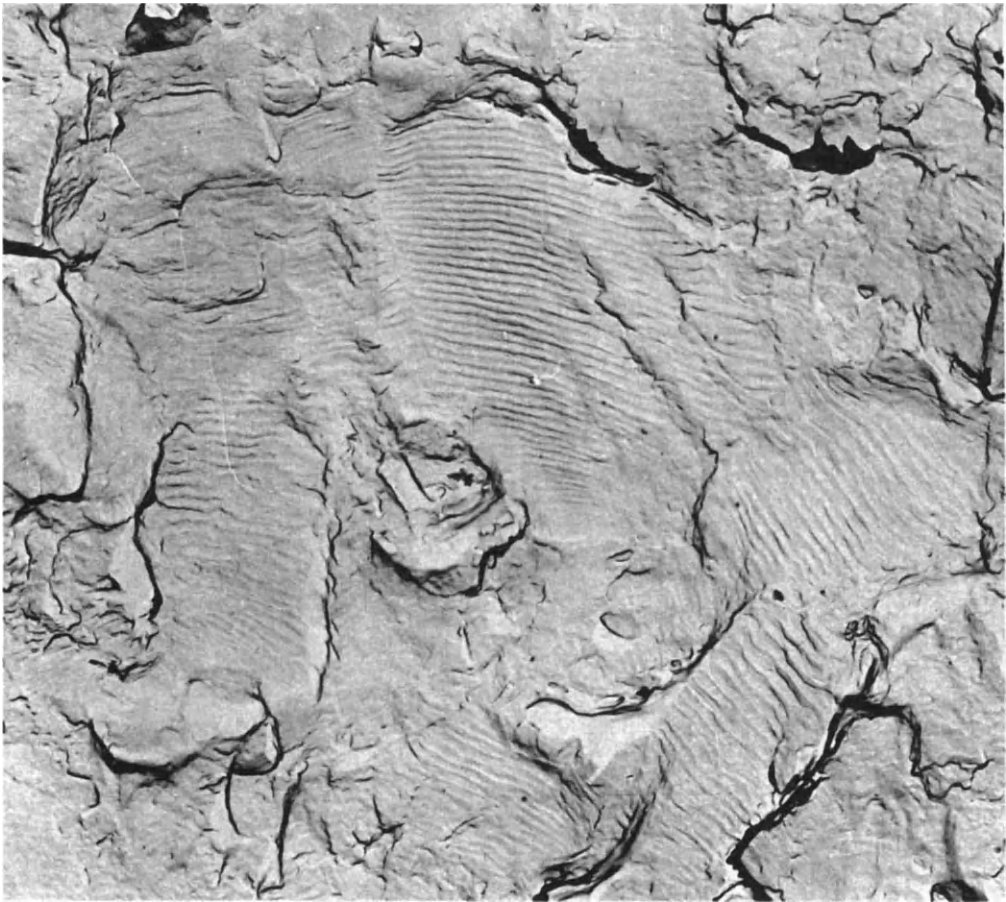
In recent years many studies have been made of fatigue crack growth. The use of electron-microscope fractography, the observation under an electron microscope of fracture surfaces (in most cases plastic replicas of fracture surfaces), is a research technique that has become increasingly common. It has been established that a fatigue fracture surface is characterized by patterns called "striations", as shown in Fig. 11.14 for Ti-8Al-1Mo-1V alloy. It is believed that a striation is formed during each loading cycle.

Figure 11.15 shows that a reasonable agreement exists between:

1. The crack growth rate dl/dn determined macroscopically from the number of cycles N and the length of crack l observed on a specimen subjected to repeated loading.
2. The striation spacings μ observed microscopically on the fracture surface.⁽¹¹⁰³⁾

The results shown here were obtained with a specimen in 2024-T3 aluminum alloy.

A number of investigators have applied the fracture mechanics theory (introduced in



6000X

FIG. 11.14. Electron microscopic fractograph of a Ti-8Al-1Mo-1V alloy (from an unpublished work at Battelle).⁽¹⁰²⁾

Note: The generally horizontal parallel lines are fatigue striations which indicate the location of the crack tip on successive stress cycles. An inclusion which influenced the growth of the fatigue crack is visible near the center of the field view. Net mean stress, 25,000 psi; net maximum stress, 43,500 psi, and crack length, about 0.1 inch.

Chapter 10) to fatigue fracture.^(905.1103) For example, the relationship between the crack-growth rate and the stress-intensity factor has been obtained. Figure 11.16 shows data on 7075-T6 aluminum-alloy.

Information was obtained by periodically measuring the length of a crack artificially initiated from a sharp saw cut. After knowing the crack length, $2a$, and the maximum stress, σ_g , the stress intensity factor for Case (a) was computed using[†]

$$K_{\max} = \alpha \sigma_g \sqrt{\pi a} \quad (11.2)$$

[†] Equations (11.2) and (11.3) are the same as eqns. (10.12) and (10.15), respectively, except the crack length is expressed as $2a$ instead of $2c$.

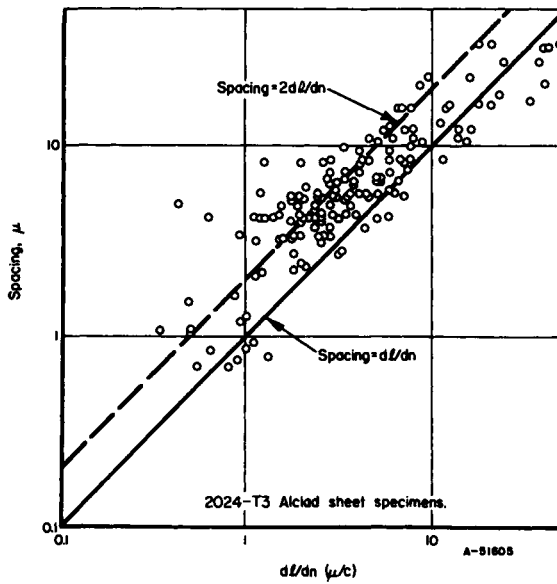


FIG. 11.15. Crack-growth-striation spacing versus crack-growth rates in 2024-T3 aluminum alloy.⁽¹¹⁰³⁾

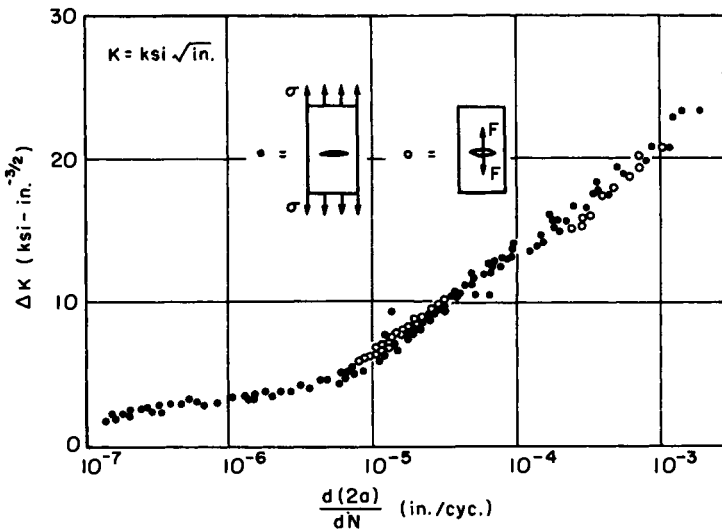


FIG. 11.16. Data on fatigue crack growth in 7075-T6 aluminum alloy.⁽¹¹⁰³⁾

where α is the correction factor for a finite panel of width $w = 2b$

$$\alpha = \sqrt{\frac{w}{\pi a} \tan \frac{\pi a}{w}} \tag{11.3}$$

Other equations must be used for computing the K -values for other cases.

Each crack growth rate measurement, $\Delta 2a/\Delta N$, was obtained by dividing the difference in the crack length reading, $\Delta 2a$, by the cyclic number change, ΔN .

Figure 11.17 shows similar bending results in medium strength steels for both centrally cracked panels and notched beams.⁽¹¹⁰³⁾

Figures 11.16 and 11.17 show that the crack growth rate depends upon the stress-intensity factor. As a fatigue crack grows, ΔK and $d(2a)/dN$ increase. Diagrams of ΔK vs. $d(2a)/dN$ show the relative crack-growth resistance of various materials. The ability to correlate data from one configuration to another makes it possible to correlate

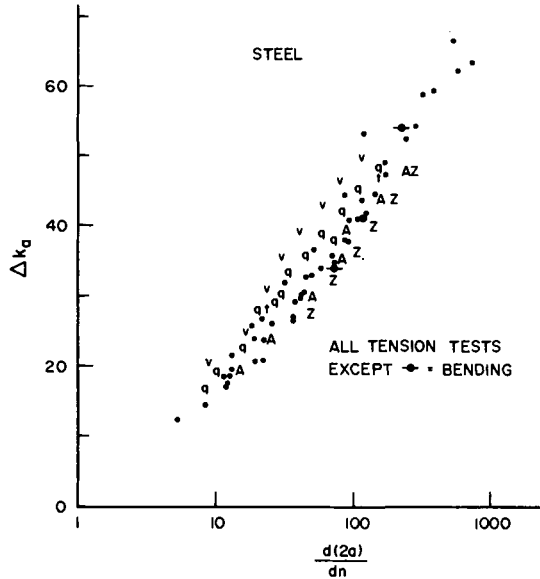


FIG. 11.17. Data on fatigue crack growth in carbon steel.⁽¹¹⁰³⁾

TABLE 11.1. Formulas on fatigue crack growth proposed by different investigators⁽⁶²⁰⁾

		Reference
Yang	$da/dn = f(K)$	(1114)
McClintock	$da/dn = \frac{7.5}{16} \frac{(\Delta K)^4}{\epsilon_f E^2 \sigma_y^2 \rho^2}$	(1115)
Krafft	$da/dn = \frac{Af(\Delta K/K_{max})}{E^3 K_{IC}^2 n_w} K_{max}^4$	(1116)
McEvily	$da/dn = A \frac{(\Delta K)^4}{\left(\frac{\sigma_y + \sigma_{UTS}}{2}\right) E \sigma_{UTS}^2 \epsilon_f}$	(1117)
Pearson	$da/dn = \frac{3.43 \times 10^7}{E} (K)^{3.6}$	(1118)
Forman	$da/dn = \frac{A}{(1 - \sigma_{min}/\sigma_{max}) K_c - \Delta K} (\Delta K)^n$	(1119)
Throop-Miller	$da/dn = \frac{A'}{E \cdot \sigma_y \cdot K_{IC}} (K_{max})^m$	(1120)
	$m = 3.5 \quad \text{S.D. of } m = 0.65$	

data from simple laboratory test configurations to more complex structural situations.^(905, 1107)

The application of fracture mechanics theories to fatigue crack growth has received a considerable amount of attention on the part of a number of investigators. For example, Table 11.1 shows the relationships between da/dn and K or ΔK as proposed by several different investigators. Much experimental data on fatigue crack growth has been generated recently.

11.5 Fatigue Strength of Welded Joints

Table 11.2 lists the fatigue strengths of several different welded joints in ordering structural steels.⁽¹¹²¹⁾ The data shown includes the fatigue strength at 100,000 cycles and 2,000,000 cycles for pulsating (0 to tension) and alternating (reversed) stresses. Figure 11.18 shows some of the welded specimens referred to in Table 11.2.

Specimens with transverse butt welds and with the reinforcements machined or ground off show fatigue strengths almost as high as those for plain unwelded plates. Therefore, when a joint with a high fatigue strength is needed, it is important to remove the butt weld reinforcement. Further discussion on this subject is given in Chapter 15 (Section 15.5.3).

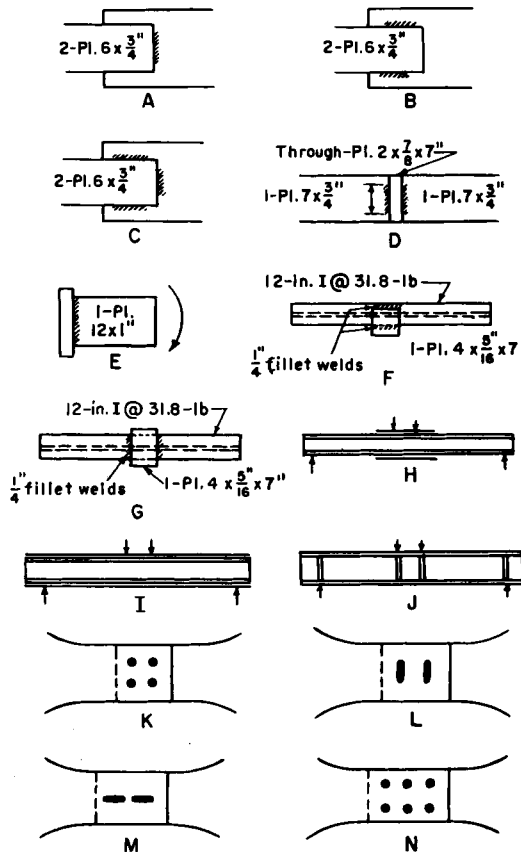


FIG. 11.18. Some of the welded specimens referred to in Table 11.2.

TABLE 11.2 Fatigue strengths of various types of welded joints in ASTM-A7 structural steel⁽¹¹²¹⁾

Type of joint	0 to tension		Reversed	
	F100,000	F2,000,000	F100,000	F2,000,000
Fatigue strengths of flat-plate specimens with and without butt welds, as-welded and with reinforcement removed flush				
Plain plate (A-7 steel) ^(a)	47.8	31.7	26.8	17.5
Transverse butt-welded joint (single-Vee)—as-welded	34.9	23.2	22.4	14.9
Transverse butt-welded joint (a) single-Vee—(b) single-U—reinforcement off	37.5(a)	28.7(a)	27.4(b)	16.0(b)
Longitudinal butt-welded joint (single-Vee)—as-welded	39.6	26.0	—	—
Longitudinal butt-welded joint (a) single-Vee, (b) double-Vee—reinforcement off.	47.1(a)	30.5(a)	21.0(b)	15.6(b)
Fatigue strengths of fillet welds of various arrangements in specimens designed for failure in the welds				
(a) Fillet-welded lap joints— $\frac{5}{16}$ -in. transverse welds. Failure in welds	30.3	18.5 +	16.2	11.3
(b) Fillet-welded lap joints— $\frac{5}{16}$ -in. longitudinal welds. Failure in welds	27.2	19.7	15.2	10.7
(c) Fillet-welded lap joints— $\frac{5}{16}$ -in. transverse and longitudinal welds. Failure in welds	28.3	20.5	13.1	8.9
(d) Tee joints— $\frac{5}{16}$ -in. fillet welds. Failure in welds.	19.1	9.6	13.3	6.2
(e) Moment connectors— $\frac{5}{16}$ -in. vertical fillet welds. Failure in welds	46.8	26.5	26.6	17.3
Fatigue strengths of rolled beams with lateral connection plates attached to the tension flanges				
(f) Beams with welded attachments. Longitudinal welds	24.4	13.6	—	—
(g) Beams with welded attachments. Transverse welds	19.2	12.2	—	—
Fatigue strengths of welded beams and girders				
(h) Rolled beams, 12-in., 31.8-lb I, with continuously welded, partial-length cover plates, $4 \times \frac{9}{16}$ -in., and $\frac{3}{8}$ -in. transverse fillet welds across square ends of cover plates	22.8	12.0	—	—
(i) Rolled beams, 12-in., 31.8-lb I, with continuously welded, full-length cover plates $4 \times \frac{9}{16}$ -in. top plate and $6 \times \frac{3}{8}$ -in. bottom plate, $\frac{3}{16}$ -in. fillet welds	41.1	22.8	—	—
(j) Built-up girders with continuous web-to-flange fillet welds and with middle stiffeners welded only to compression flange and upper half of web	46.7	17.6	—	—
Fatigue strengths of plug- and slot-welded joints (stresses given are those in welds)				
(k) Plug welds—weld failure	23.1	12.6	11.3	6.5
(l) Slot welds—transverse (balanced design for weld and plate failure)	20.0	10.2	10.0	5.3
(m) Slot welds—longitudinal (balanced design for weld and plate failure)	27.9	11.1	16.1	6.1

(cont.)

TABLE 11.2 (cont.)

Type of joint	0 to tension		Reversed	
	F100,000	F2,000,000	F100,000	F2,000,000
Fatigue strength of plug-welded lap joint designed to fail in plate material (stresses given are those in plate material)				
(n) Plug-welded lap joint—plate failure	26.3 24.1	10.1 11.7	14.2 14.1	5.3 6.6

⁽ⁿ⁾ Test specimens consisted of plates approximately 5×7 inches.

NOTE: Recent fatigue tests in Belgium of larger built-up girders subjected to ratios of minimum to maximum stress similar to those encountered in highway bridge have revealed no detrimental effect of welding ends of stiffeners to tension flanges. These tests involved one million cycles of loading. The University of Illinois tests showed a very substantial detrimental effect of welding the load-bearing stiffeners to the tension areas of the rolled beams, for approximately 2 million cycles of loading, zero to maximum tension.

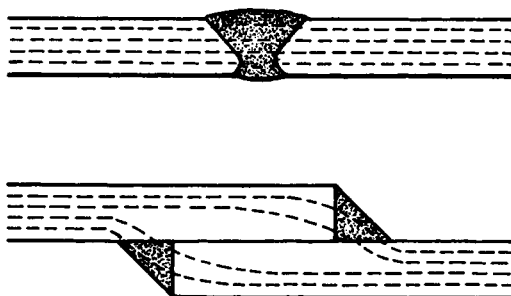


FIG. 11.19. Lines of stress flow in a butt weld and lap welds.

Lap welds have a fatigue strength considerably lower than that of butt welds. This is because lap welds disturb the flow of stresses more than do butt welds, as shown in Fig. 11.19.

The data in Table 11.2 suggest several general rules for improving the fatigue strength of a welded structure:

1. Use butt joints rather than lap joints.
2. Avoid intermittent fillet welds.
3. Avoid the use of joints that are inconsistent in their ability to deform locally.
4. Do not specify excessively large fillet welds.
5. Avoid joints at points where fatigue conditions are severe.

11.6 Effects of Residual Stresses on Fatigue Fracture

When compressive residual stresses exist in regions near the surface of a plate, the fatigue strength may be increased. An example of this is a drive shaft that has been induction hardened with a scanning coil covering all of the deep grooves. Fatigue problems with drive shafts have been reduced drastically by using this technique. LaBelle^(11,22) conducted a series of fatigue tests on actual shafts that had been processed to introduce compressive stresses at the stress raisers.

“The original shaft, made of AISI 5046 steel, was hardened and tempered to Bhn 226 to 269. . . rolling the fillets increased the shaft’s endurance limit from 40,000 to about 55,000 psi (28.1 kg/mm² or 276 MN/m² to about 38.7 kg/mm² 379 MN/m²), induction hardening raised it to nearly 80,000 psi (56.2 kg/mm² or 552 MN/m²), and nitriding to a depth of 0.0101 in. (0.25 mm) elevated it to 118,000 psi, three times the load carrying capacity of the original shaft. Although the nitrided shaft was made of a different steel (VCM, containing 0.35 C, 1.00 Cr, 1.00 Mo, 0.65 Ni), it was hardened and tempered to about the same hardness as the production shaft⁽¹¹²²⁾ and would have been expected to behave similarly. This large increase in endurance was brought about by nitriding the metal to a depth of only 0.010 in. (0.25 mm).

How residual stresses actually affect the fatigue strength of a welded structure is still a matter of debate. Though some investigators have reported that the fatigue strength increased when specimens had compressive residual stresses, especially on the specimen surfaces, others believe that the residual stress has only a negligible effect on the fatigue strength of weldments. Ross,⁽¹¹²³⁾ for example, has suggested that in a good weld residual stresses can be ignored.⁽¹¹²³⁾ Hebrant⁽¹¹²⁴⁾ has suggested that geometry affects fatigue behavior much more than residual stresses. But others⁽¹¹²⁵⁾ feel that there is significant evidence that residual stresses affect the fatigue strength.

In the textbook entitled *Fatigue of Welded Structures*, Munse⁽¹¹⁰²⁾ summarizes as follows:

“On the basis of the available data it is believed that the effects of residual stresses may differ from one instance to another, depending upon the materials and geometry of the members, the state of stress, the magnitude of applied stress, the type of stress cycle and perhaps other factors. Many of the investigations designed to evaluate the effects of residual stress have included tests of members that have been subjected to various stress-relief heat treatments. The changes in fatigue behavior resulting from these heat treatments, in some cases, have been negligible, while in other investigations, the various stress-relief treatments have produced an increase in fatigue strength of as much as twenty percent. Since it is impossible to carry out a heat treatment for stress relief without altering the metallurgical and mechanical properties of weldment, the question always arises as to whether benefits are derived from the reduction of residual stresses or from the improved properties in other respects.”

Our knowledge of the relationship between residual stress and fatigue strength is confused because:

1. The fatigue strength depends greatly on the condition of the surface. The effect of residual stress is secondary and is overshadowed by such major factors as weld geometry and surface irregularities.
2. Residual stresses change during repeated loading, as will be discussed later in this chapter.
3. A fatigue crack may initiate in a region containing tensile residual stresses. The rate of crack growth may be increased due to the existence of tensile residual stresses. However, when the crack grows and enters regions containing compressive residual stresses, the rate of crack growth may be reduced. As a result, the total effect of the residual stresses present on the overall crack growth may be insignificant.
4. When residual stresses are altered by a heat treatment or peening, the metallurgical and mechanical properties of the metal are also changed.

Section 8.2 briefly discusses how residual stresses in a weldment change when an external load is applied. Figure 8.1 shows a simple case of a longitudinal butt weld under

uniform tensile loading. Curve 0 shows the lateral distribution of longitudinal residual stress in the as-welded condition. When a uniform stress $\sigma = \sigma_1$ is applied, the stresses increase to those values shown by curve 1. When the load is released, residual stresses change to those shown by curve 1'. Curve 2' shows the distribution of residual-stresses that remain when the tensile stress $\sigma = \sigma_2$, ($\sigma_2 > \sigma_1$) is released.

What is important here is that the residual-stress distribution after this kind of cyclic loading is more even than the original residual-stress distribution (curve 0). As the level of loading increases, the residual stress distribution after each cycle becomes more even, that is, the effect of welding residual stress on the stress distribution decreases.

The above is concerned with the amount of residual-stress reduction that takes place during one cycle of loading and unloading. The stress changes during a number of cycles of repeated loading are more complex, especially if a fatigue crack is formed, causing a stress concentration near the crack tip.

In most of the experimental programs conducted thus far, fatigue tests have been made on specimens under as-welded and stress-relieved conditions, and data were evaluated on the basis of the $S-N$ curve. It has been very difficult to separate the effects of the various factors described above. So far little information has been obtained on:

1. How residual stresses affect the growth of a fatigue crack.
2. How residual stresses are redistributed during repeated loading.

With the recent development of the use of the fracture-mechanics theory to predict fatigue crack growth, it is hoped that more exact information can be obtained on how residual stresses affect the fatigue strength of weldments.

Despite the fact that how residual stresses affect fatigue strength is still a question being debated by scientists, several attempts have been made to use the alternation of residual stress as a means of improving the fatigue strength of a weldment. These are discussed next.

11.7 Some Methods of Improving the Fatigue Strength of Weldments

The fatigue strength of weldments can be improved in a number of ways. Some general rules for achieving this are discussed earlier in relation to Table 11.2. Textbooks by Gurney⁽¹¹⁰¹⁾ and Munse⁽¹¹⁰²⁾ discuss the subject in detail. The following pages discuss the use of a preferable distribution of residual stresses to improve the fatigue strength of weldments. It is possible to improve fatigue strength by creating residual compressive stresses at locations where fatigue cracks are likely to initiate (perhaps near notches). The following pages discuss how prior overloading, peening, local compression, and spot heating can affect the fatigue strength of some welded specimens. The information is taken primarily from the book by Gurney.⁽¹¹⁰¹⁾

11.7.1 *Prior overloading*⁽¹¹⁰¹⁾

If a specimen containing a stress concentration is loaded until yielding occurs at the notch, and the load is then removed, residual stresses will be left in the specimen. The sign of residual stress adjacent to a notch is opposite to that of the overload. In order to create compressive residual stresses adjacent to a notch it is necessary to apply a tensile overload.

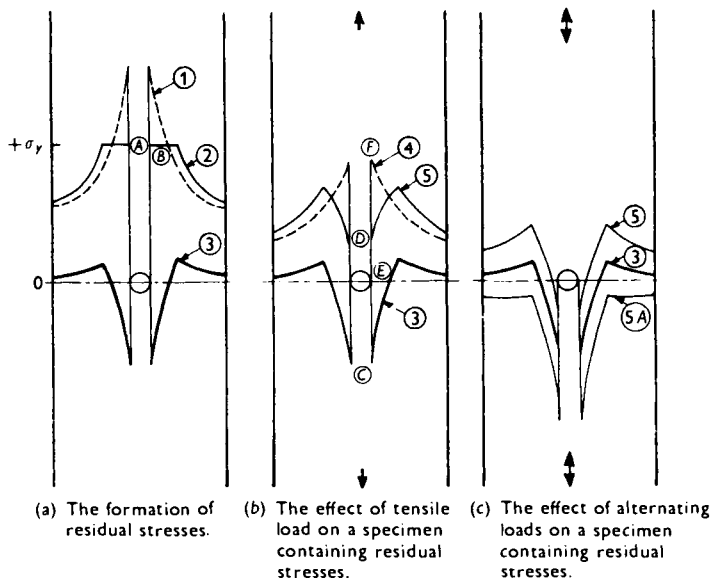


FIG. 11.20. The formation of residual stresses by prior overloading and the effect of subsequent external loading (Gurney).⁽¹¹⁰¹⁾

The way in which residual stresses are formed is illustrated qualitatively in Fig. 11.20. Suppose that, ignoring yielding, the elastic stress distribution can be represented by curve 1. But the actual stress distribution will be shown by curve 2 since yielding takes place in regions near the notch. When the load is removed, the whole specimen will unload elastically to leave the residual-stress distribution represented by curve 3, this being the result of subtracting curve 1 from curve 2.

The behavior of such a specimen during subsequent fatigue testing under a lower tensile load is shown in Fig. 11.20(b). If the elastic stress distribution due to the load by itself can be expressed by curve 4, the final distribution is given by adding these stresses to the residual stress (curve 3) and is of the form shown by curve 5. During a fatigue test, the stress will pulsate between curves 3 and 5.

If the specimen is subjected to an alternating load of the same range as shown in Fig. 11.20(c), the stress changes will be between curves 5 and 5A. Stresses in regions near the notch remain compressive during the fatigue testing.

Several investigators⁽¹¹²⁸⁾ have reported that fatigue strength increased when they applied tensile prior loading. Figure 11.21 shows the results obtained by Harrison, who studied how the fatigue strength of fillet-welded steel specimens could be increased by prior tensile overloading. He found that the S -log N curves for specimens preloaded at various levels of overload stress were approximately parallel to each other. If we assume they are straight lines, the equation of the "as-welded" S -log N curve can be written

$$S + K_1 \log N = A_1 \tag{11.4}$$

and for the preloaded S -log N curve:

$$S + K_2 \log N = A_2. \tag{11.5}$$

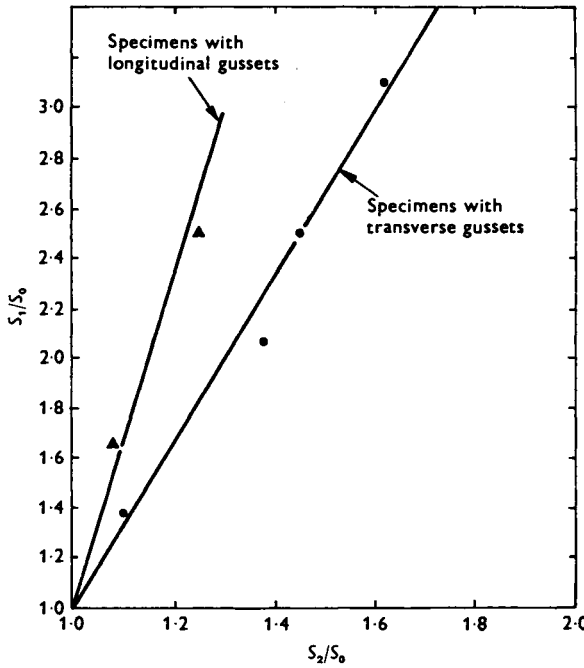


FIG. 11.21. The effect of prior overloading on the fatigue strength of steel specimens with non-load-carrying fillet welds under pulsating tension loading (Gurney).⁽¹¹⁰¹⁾

Since K_1 , K_2 , and A_1 are constant for a given type of specimen, and A_2 depends on the preload stress (S_1), it follows that

$$\frac{S_1}{S_0} \left(\frac{1}{K_2} - \frac{1}{K_1} \right) = \frac{S_2}{S_0} \left(\frac{1}{K_2} \right) - \frac{1}{K_1}, \tag{11.6}$$

where S_0 and S_2 are respectively the as-welded and preloaded fatigue strengths. Hence a linear relationship should exist between S_1/S_0 and S_2/S_0 passing through the point given by $S_1 = S_2 = S_0$. This was approximately confirmed by Harrison's results, which are shown in Fig. 11.21.

11.7.2 Peening

Peening is a cold-working process that consists of battering the surface of the component (usually either with a high-velocity stream of metal particles or with a tool operated by a pneumatic hammer), with the object of inducing compressive residual stresses in the surface layer.

Nacher⁽¹¹²⁹⁾ studied how peening affects the fatigue strength of butt and fillet welds. Gurney⁽¹¹⁰¹⁾ prepared Table 11.3, which summarizes the fatigue strengths of non-load-carrying fillet welds recorded by several investigators. The results show that peening increases the fatigue strength of transverse and longitudinal welds. Peening with a pneumatic hammer fitted with a solid tool (the method that produces the most severe deformation) gives a substantially greater improvement than either shot peening or

TABLE 11.3 Comparison of fatigue strength (tons/in.²) at 2×10^6 cycles for steel specimens with non-load-carrying fillet welds after peening by various methods (Gurney)^(1,101)

Peening method	Transverse welds						Longitudinal welds					
	Investigation	Fatigue strength		Increase (%)	Investigation	Increase (%)	Investigation	Fatigue strength		Increase (%)		
		As-welded	Peened					As-welded	Peened			
Shot peening	Braithwaite ^(1,130)	0-6.5	0-9.0	39	Braithwaite ^(1,130)		0-7.5	0-8.75	17			
	Gurney ^(1,131)	0-7.0	0-9.5	36	Gurney ^(1,131)		0-5.5	0-6.75	22			
Multiple-wire air hammer	Nacher ^(1,129)	0-12.7	0-15.3	20	Nacher ^(1,129)		0-8.2	0-9.9	20			
		± 9.5	± 10.8	14			0-7.1	0-10.8	52			
Solid tool air hammer	Harrison ^(1,132)	0-6.75	0-12.5	85	Gurney ^(1,133)		0-5.75	0-11	91			

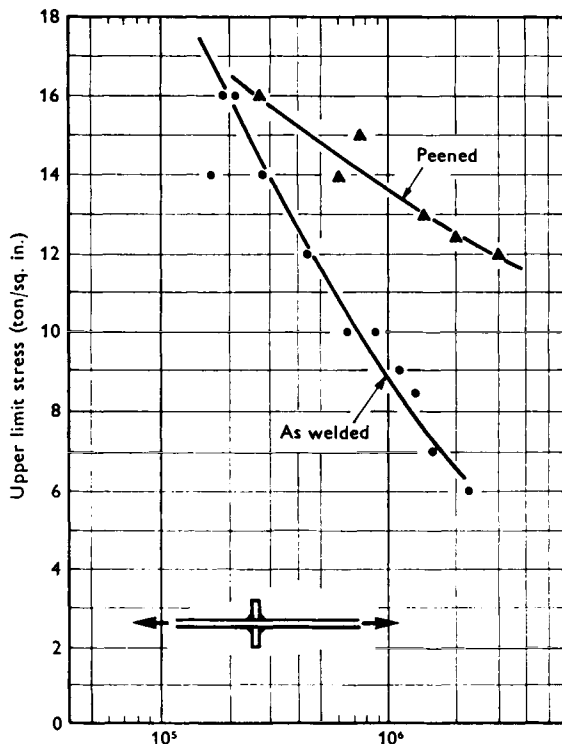


FIG. 11.22. The effect of hammer peening on the fatigue strength of mild steel with non-load-carrying transverse fillet welds (Gurney).⁽¹¹⁰¹⁾

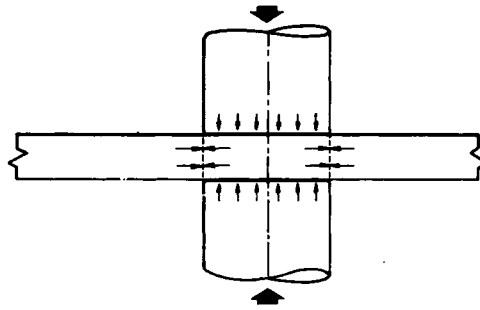
peening with a multiple-wire hammer. There is insufficient evidence to determine which is the more beneficial of these latter two processes.

Gurney⁽¹¹⁰¹⁾ stated that peening would increase the strength in a way similar to that found in non-load-carrying fillet-welded joints, at least for failures initiating at the weld toe.

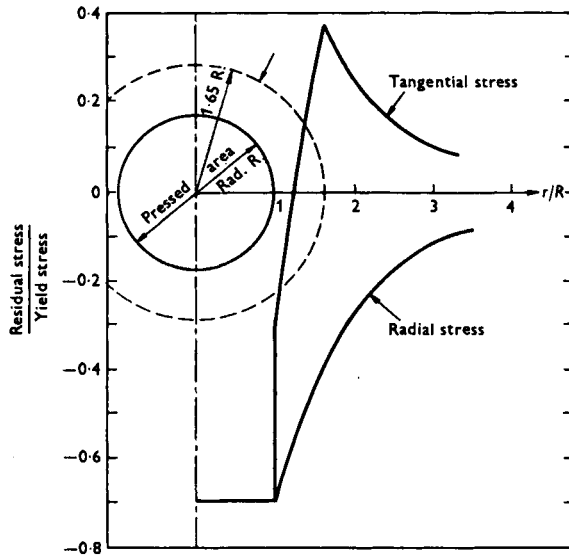
Figure 11.22 shows examples of the test data in Table 11.3. In his work on transverse fillet-welded specimens Harrison⁽¹¹³²⁾ tested a few specimens that had been peened and subsequently stress relieved. These gave a fatigue strength at 2×10^6 cycles of about $8\frac{1}{4}$ tons/in. (13.0 kg/mm^2 or 127 MN/m^2) which represents a 20% increase in strength as compared with the 85% increase due to the peening without subsequent stress relief shown in Fig. 11.22. The fact that the $S-N$ curves that he obtained for as-welded and peened specimens tend to coincide near the yield stress of the material can be interpreted as evidence that the increase in the fatigue strength is largely the result of beneficial residual stresses.

11.7.3 Local compression and spot heating

Residual stresses can be produced using local compression and spot heating. Figure 11.23(a) shows the principle of local compression. When the dies are put under a compression load, the material between the dies expands in the lateral direction causing residual stresses as shown in Fig. 11.23(b).



a. The Principle of Local Compression Treatment



b. Theoretical Residual Stress Distribution Due to Local Compression Treatment

FIG. 11.23. Local compression technique (Gurney)⁽¹¹⁰¹⁾

In spot heating, the structure is heated locally, usually with a gas torch, so as to produce local yielding resulting in compressive thermal stresses. When the locally heated metal cools it shrinks, causing residual stresses as shown in Fig. 11.24. This residual stress distribution is very similar to that caused by spot welding (see Fig. 6.12). The stress distributions shown in Figs. 11.23 and 11.24 are reversed.

These residual stresses can be used for improving the fatigue strength of a weldment. The basic principle is to produce compressive residual stresses in those local areas, especially near notches, where fatigue cracks are likely to initiate. Several investigators, including Puchner^(1134, 1135) and Gurney and Trepka,^(1136, 1137) have conducted ex-

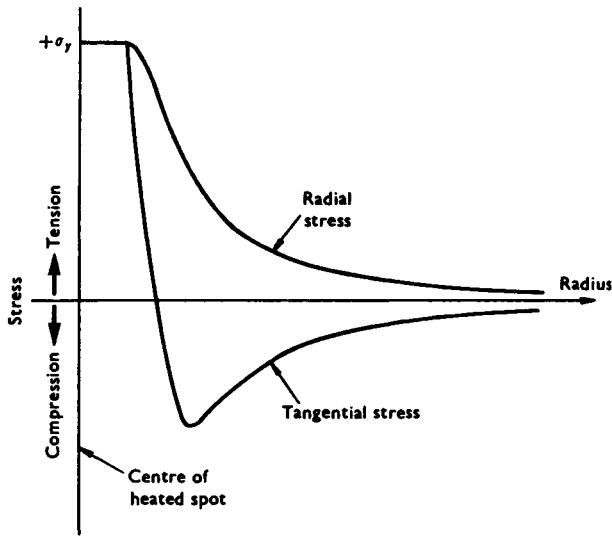


FIG. 11.24. Qualitative residual stress distribution due to spot heating.

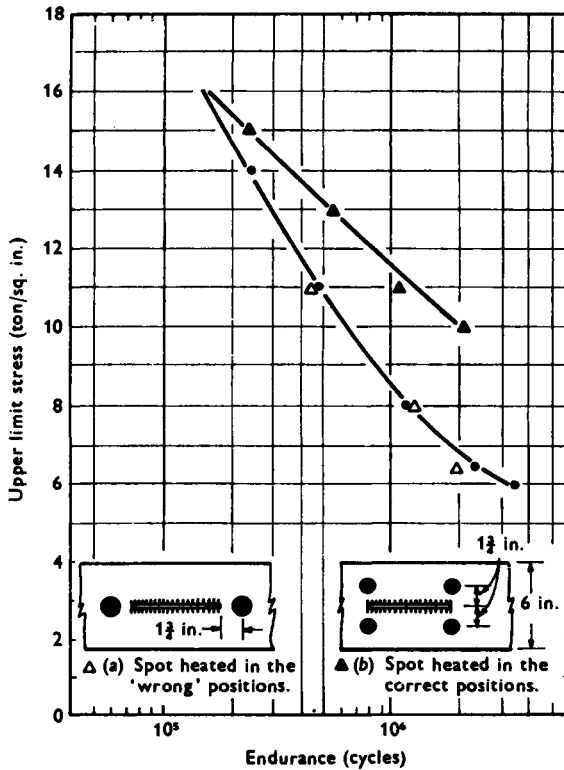


FIG. 11.25. Results of fatigue tests carried out to demonstrate that the increase in strength resulting from spot heating is due to the influence of residual stress (Gurney).⁽¹¹⁰¹⁾

tensive studies on this subject.⁽¹¹⁰¹⁾ As an example, Fig. 11.25 shows experimental results on spot heating. Several locations near the ends of a vertical plate fillet welded to a plate were spot heated.

By spot heating in the positions indicated in Fig. 11.25(b) compressive residual stresses were induced at the notches at the ends of the weld and a 53% increase in strength was obtained. But when spot heating was done at the center line of the specimen (Fig. 11.25(a)), even though the distance from the notch was the same and the same metallurgical effect produced, the residual stresses were tensile, and the fatigue strength measured was the same as for an untreated specimen.[†] This indicates that the strength increase is due to residual stresses.

11.7.4 Comparison of improvement techniques

Figures 11.26 and 11.27 compare how various improvement techniques affect the fatigue strength of transverse and longitudinal fillet welds, respectively. The mild steel

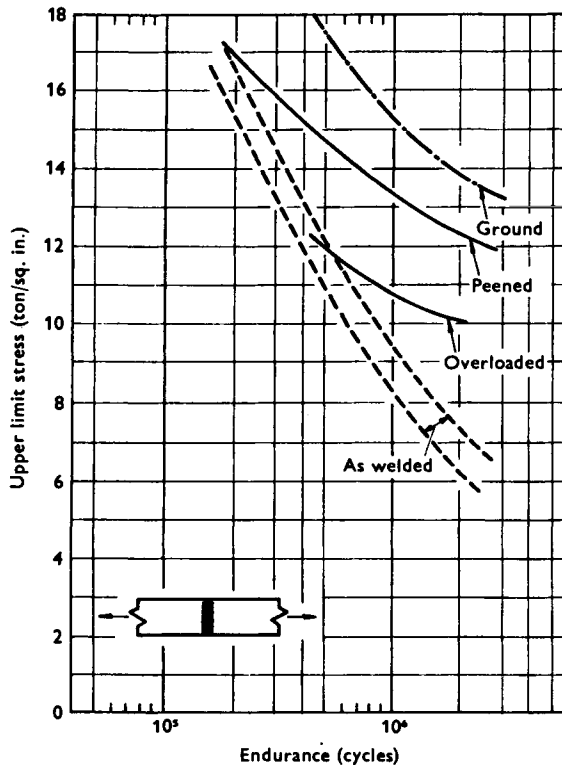


FIG. 11.26. Comparison of improvement methods for mild steel specimens with transverse non-load-carrying fillet welds (Gurney).⁽¹¹⁰¹⁾

[†] In the practical application of these techniques, sometimes they work and at other times they do not, as shown in Fig. 11.25. The designer or fabricator must know under what conditions the techniques work and must know how to control the practical procedures. Using fracture-mechanics theories, Nakamura⁽¹¹³⁸⁾ analyzed how residual stresses affect fatigue-crack growth. His results, because they have not been verified by experiments, are not presented here.

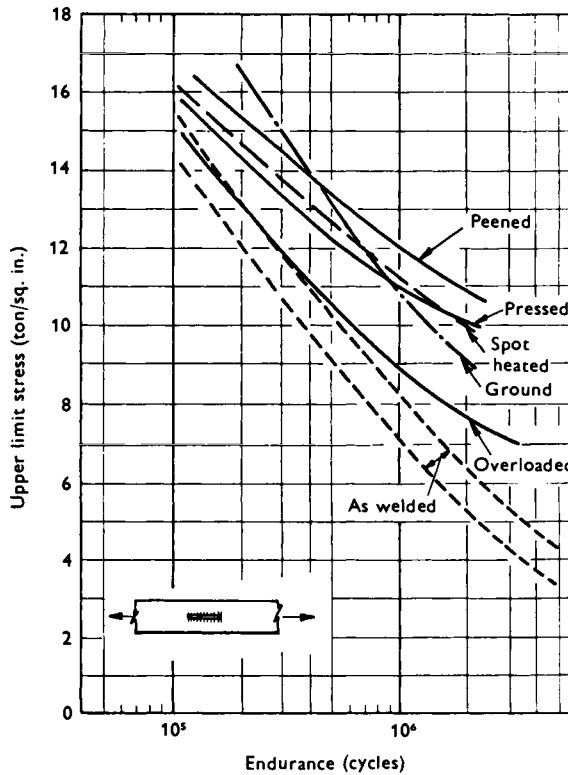


FIG. 11.27. Comparison of improvement methods for mild steel specimens with longitudinal non-load-carrying fillet welds (Gurney).⁽¹¹⁶¹⁾

specimens were tested at the British Welding Research Association. After being subjected to prior overloading the specimens were stressed at 15 tons/in.² before fatigue testing. The main conclusions were drawn as follows:

1. The fatigue strength can be significantly improved using these techniques, especially when the applied stresses and the number of cycles are high.
2. If the stress is high and the endurance is relatively short, grinding is likely to prove more satisfactory than any other techniques.

References

- (1101) GURNEY, T. R., *Fatigue of Welded Structures*, Cambridge University Press, 1968
- (1102) MUNSE, W. H., *Fatigue of Welded Steel Structures*, Welding Research Council, 1964.
- (1103) PARIS, P. C., "Fatigue crack growth", the Text Used for Workshop in Fracture Mechanics, 16-28 August 1964, held at Denver Research Institute, sponsored by Universal Technology Corporation, Dayton, Ohio.
- (1104) MASUDA, Y., "Low-cycle fatigue strength of ship structure", *Journal of the Japan Welding Society*, **5**, 473-479 (1968).
- (1105) NIBBERING, W., *Fatigue of Ship Structures*, Report of the Netherlands' Research Center T.N.O. No. 55, 1963.
- (1106) VASTA, J., "Fatigue structural models", NRL Report 6167, *Status and Projection of Developments in Hull Structural Materials for Deep Ocean Vehicles and Fixed Bottom Installations*, U.S. Naval Research Laboratory, pp. 212-221, Nov. 1966.

- (1107) VEDELER, G., "To what extent do brittle fracture and fatigue interest shipbuilders today?" Houdremont Lecture at the Annual Assembly of the International Institute of Welding, Oslo, Norway, 1962.
- (1108) VEDELER, G., "One learns from bitter experience", *International Shipbuilding Progress*, **5** (42), 67-77 (1958).
- (1109) YAMAGUCHI, H., "Fatigue failure in ship structures", *Journal of the Japan Welding Society*, **37** (10), 1041-1046 (1968).
- (1110) GROSS, M. R., "Low-cycle fatigue of materials", NRL Report 6167, *Status and Projection of Developments in Hull Structural Materials for Deep Ocean Vehicles and Fixed Bottom Installations*, U.S. Naval Research Laboratory, pp. 196-221, Nov. 1964.
- (1111) COFFIN, L. F., Jr., "Low-cycle fatigue: a review", *Applied Materials Research*, **1** (3), 129-141 (Oct. 1962).
- (1112) YAO, J. T. P. and MUNSE, W. H., "Low-cycle fatigue of metal—literature review", *Welding Journal*, **41** (4), Research Supplement, 182s-192s (1962).
- (1113) MANSON, S. S., "Interpretive report on cumulative fatigue damage in the low-cycle range", *Welding Journal*, **43** (8), Research Supplement, 344s-352s (1964).
- (1114) YANG, C. T., "A study of the law of crack propagation", *Journal of Basic Engineering*, **89**, 487 (1967).
- (1115) MCCINTOCK, F. A., "On the Plasticity of the growth of fatigue cracks", *Fracture of Solids*, John Wiley, New York, 1963, p. 65.
- (1116) KRAFFT, J. M., "A comparison of cyclic fatigue crack propagation with single cycle crack toughness and plastic flow", Presented to Committee E24, American Society for Testing and Materials, 1964.
- (1117) MCEVILY, A. I., *Proceedings of the 1st International Conference on Fracture*, vol. II, Japanese Society for Strength and Fracture of Materials, Sendai, Japan, 1965.
- (1118) PEARSON, S., "Fatigue crack propagation in metals", *Nature*, **211**, 1017 (1966).
- (1119) FORMAN, R. G., Kearney, V. E., and Engle, R. M., "Numerical analysis of crack propagation in cyclic-loaded structures", *Journal of Basic Engineering*, **89**, 459 (1967).
- (1120) THROOP, J. F. and MILLER, G. A., "Optimum fatigue crack resistance", *Achievement of High Fatigue Resistance in Metals and Alloys*, ASTM STP 467, American Society for Testing and Materials, 1970, p. 154.
- (1121) *Welding Handbook*, Sixth Edition, Section 1, American Welding Society, 1968.
- (1122) LABELLE, J. E., "Practical aspects of fatigue", *Metal Progress*, **87** (5), 68-73 (May 1965).
- (1123) ROSS, M., "Experiments for the determination of the influence of residual stresses on the fatigue strength of structures", *Welding Research BWRA*, **4**(5), 83r-93r (Oct. 1950).
- (1124) HEBRANT, F., LOUIS, H., SOETE, W., and VINCKIER, A., "The relaxation of residual welding stresses by static and fatigue loading", *Welding Research Abroad*, pp. 58-63 (Sept. 1957).
- (1125) DUGDALE, D. S., "Effect of residual stress on fatigue strength", *Welding Journal*, **38** (1), Research Supplement, 45s to 48s (1959).
- (1126) FORREST, G., "Some experiments on the effects of residual stresses on the fatigue of aluminum alloys", *Journal of the Institute of Metals*, **72** (1), 1-17 (1946).
- (1127) HEYWOOD, R. B., *The Effect of High Loads on Fatigue*, Colloquium on Fatigue, Inst. Union Theoretical and Applied Mechanics, Stockholm, 1955.
- (1128) HARRISON, J. D., "Further fatigue tests on fillet welded specimens subjected to prior overloading", *British Welding Journal*, **12** (5), 225-258 (1965).
- (1129) NACHER, A., "Influence of local heating and of surface peening on fatigue behavior of welded joints and details", I.I.W. Document XIII-255-61 (1961).
- (1130) BRAITHWAITE, A. B. M., "Fatigue tests on Bailey bridge transoms", *British Welding Journal*, **11** (12), 641-644 (1964).
- (1131) GURNEY, T. R., "Exploratory fatigue tests on plastic coated specimens", *British Welding Journal*, **10** (10), 530-533 (1963).
- (1132) HARRISON, J. D., "Further techniques for improving the fatigue strength of welded joints", *British Welding Journal*, **13** (11), 642-647 (1966).
- (1133) GURNEY, T. R., *The Effect of Peening and Grinding on the Fatigue Strength of Fillet Welded Joints in Two Steels*, BWRA Report E/12A/67, 1967.
- (1134) PUCHER, O., "Welded gusset plate connection under pulsating load, their fatigue strength and its increase due to local heating", *Schweissstechnik (Berlin)*, **6** (4), 109-114 (1956).
- (1135) PUCHNER, O., "Increase of the fatigue limit of plates and beams with welded on gusset plates by local heating", *Soudure de Techniques Connexes*, **14**, 27-32 (1960) and IIW Document XIII-179-59 (1959).
- (1136) GURNEY, T. R. and TREPKA, L. N., "Exploratory tests to determine the influence of local heating on the fatigue behavior of welded mild steel specimens", *British Welding Journal*, **6**, (10), 491-497 (1959).
- (1137) GURNEY, T. R., "The influence of residual stresses on the fatigue strength of plates with fillet welded attachments", *British Welding Journal*, **7** (6), 415-431 (1960).
- (1138) NAKAMURA, Y., "Study for improving fatigue strength by using compressive residual stress", unpublished work at the Department of Ocean Engineering, M.I.T., July 1973.

The Role of Residual Stress in Stress Corrosion Cracking and Hydrogen Embrittlement

WELDED structures are often exposed to environments which cause material embrittlement. Various technical terms are used to describe embrittlement caused by different environments as follows:^(102,905)

1. Stress corrosion cracking which occurs in materials under static or slowly increasing load in the presence of certain corrosive environments.⁽⁹⁰⁵⁾
2. Hydrogen embrittlement which occurs in certain materials containing hydrogen.⁽⁹⁰⁵⁾
3. Liquid metal embrittlement which occurs in materials under static or slowly increasing load, in the presence of particular liquids.⁽⁹⁰⁵⁾ For example, certain aluminum alloys become brittle when they are wetted by mercury and certain steels become brittle when they are exposed to liquid lithium.⁽¹²⁰¹⁾
4. Neutron irradiation embrittlement which occurs in certain materials after exposure to neutron irradiation. The nature of the embrittlement varies from one class of materials to another.⁽⁹⁰⁵⁾

There are a number of books which discuss the above subjects.^(201,905,1202,1203) When the material is severely embrittled, fracture may even occur by residual stresses alone. This chapter first presents brief discussions on stress corrosion cracking and hydrogen embrittlement. Then discussions are given on the role of residual stresses in stress corrosion cracking and hydrogen embrittlement of weldments. No further discussions are given on liquid metal embrittlement and neutron irradiation embrittlement which are much less common. The analyses presented in Section 12.4 should be applicable in the study of effects of residual stresses in weldments embrittlement by the existence of certain liquid metals or neutron irradiation.

12.1 Stress Corrosion Cracking⁽¹⁰²⁾

Stress corrosion cracking differs from other types of metal attacks in that it is a form of localized failure that is more severe. This is due to the combined action of stress and corrosion, an effect greater than would be expected from the sum of the individual effects of stress and corrosion acting alone. Stress corrosion cracking is the brittle fracture of a material that is otherwise ductile. The surface direction of the cracks is perpendicular to the direction of the load.⁽¹²⁰³⁾ Stress corrosion cracking should not be confused with other types of localized attack, such as pitting, galvanic attack, intergranular corrosion, impingement, or cavitation.

TABLE 12.1 *Materials and environment which cause stress corrosion cracking*^(102, 1203)

Material	Environment
Aluminum	Air, sea water, sodium chloride solutions
Copper-base alloys	Ammonia, steam
Steel	Alkalies, nitrates, hydrogen cyanide, hydrogen sulfate, anhydrous liquid ammonia, sodium chloride solutions, marine atmosphere
Stainless steels	Caustic, chloride solutions
PH stainless steels	Chloride solutions, marine atmosphere
Magnesium-base alloys	Chloride-chromate mixture, moisture
Nickel (commercial purity)	Aqueous or fused caustic at elevated temperature
Monel, Inconel	HF vapors
Titanium alloys	Red fuming nitric acid, HCl, dry molten chloride salts, salt water

Alloys. Pure metals, it is generally believed, do not crack as a result of stress corrosion. However, alloys prepared from pure metal can crack. In recent studies, cracking resistance has been improved through the use of extremely pure metals in the alloy. Some alloys in a particular base-metal system are more resistant to cracking than others. Such metals include aluminum, copper, and magnesium-base alloys. In these cases, cracking resistance improves as the alloy content is reduced and the composition approaches that of a pure metal.⁽¹²⁰³⁾

Environment. The corrosivity of a chemical medium cannot be used as an indication of how much it will promote corrosion cracking. Many rather corrosive solutions do not cause cracking. In fact, the environments that are most conducive to stress-corrosion cracking in some of the more common metals and alloys are shown in Table 12.1.

12.2 Hydrogen Embrittlement

Hydrogen embrittlement is one of the most common and serious types of time-dependent fracture.⁽⁹⁰⁵⁾ In laboratory testing, the presence of hydrogen results in a decrease in the ductility of unnotched tensile specimens and hence a decrease in the tensile strength of notched specimens. In service, failure can occur without warning minutes to years after a static load has been applied to a structure containing hydrogen.

The most spectacular and expensive failures have occurred in the petroleum industry, particularly in sour gas wells (containing H₂S) producing natural gas. Numerous failures of cadmium-plated, high-strength steel parts (hydrogen being introduced during electroplating) have plagued the aircraft industry.

Besides steels, which have a body centered cubic (BCC) crystal structure, titanium and zirconium and their alloys also are susceptible to hydrogen embrittlement. The hydrogen can be introduced into these materials during processing, cleaning (acid pickling), and electroplating operations.

There are two characteristics of hydrogen embrittlement. First, it is not a form of stress corrosion cracking. In fact, fracture often occurs when the metal serves, or has served, as a cathode during electroplating or in a cathodic "protection" operation. Second, embrittlement results from hydrogen contents that are greater than the equilibrium solubility limit (about 10⁻³ ppm by weight in iron and 20–30 ppm in Ti and Zr at

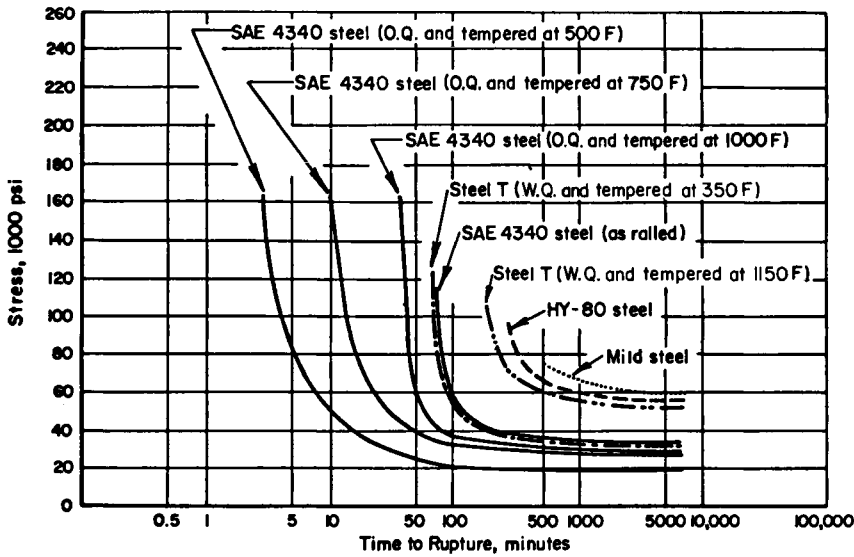


FIG. 12.1. Hydrogen-induced delayed-fracture characteristics of various steels (Masubuchi and Martin).⁽⁴⁴²⁾

Note: Curves are estimated from results obtained by Simcoe, *et al.*⁽¹²⁰⁴⁾ The commercial high-strength structural steel is identified above as Steel T. Table 12.2 contains approximate tensile strengths of these steels.

room temperature at one atmosphere hydrogen pressure). The excess hydrogen that causes embrittlement can be as low as 1 ppm in high-strength steel, and 35 ppm in Ti and Zr.

Figure 12.1 shows the hydrogen-induced delayed-fracture characteristics of various steels.⁽⁴⁴²⁾ Curves in the figure were estimated by Martin and Masubuchi⁽⁴⁴²⁾ from experimental results conducted by Simcoe and others⁽¹²⁰⁴⁾ on SAE 4340 steel quenched and tempered at high-strength levels.

Figure 12.1 shows steels general tendency to become more susceptible to hydrogen cracking as the strength level increases. For example, SAE 4340 steel oil quenched and tempered at 500° F (260° C) has the tensile strength of about 260,000 psi (183 kg/mm² or 1792 MN/m²). If hydrogen is charged to this steel while it is being subjected to a tensile stress of 80,000 psi (56.2 kg/mm² or 276 MN/m²) it takes about 15 minutes before it fractures. When the steel subjected to stress and hydrogen is at a lower strength level it takes a longer time before it fractures. For example, when HY-80 steel is subjected to a tensile stress of 80,000 psi (56.2 kg/mm² or 55 MN/m²) it takes about 400 minutes before it fractures.

12.3 Role of Residual Stresses in the Stress Corrosion Cracking and the Hydrogen-induced Cracking of Weldments

As stated in Section 8.2, residual stress significantly affects those phenomena that occur under a low applied stress. Since stress corrosion cracking and hydrogen-induced cracking of a weldment can occur without any external loading, residual stresses significantly affect stress corrosion cracking and hydrogen-induced cracking.

Stress corrosion cracks can occur in weldments in various materials and in different environments. Stress corrosion cracks due to H_2S have been found in a number of welded petroleum products storage tanks made of high-strength steels.⁽⁹⁰⁵⁾ McKinsey⁽⁴⁴³⁾ found a system of transverse cracks in a steel butt weld located in a boiling concentrated nitrate solution. Toy and Phillips⁽¹²⁰⁵⁾ reported the stress corrosion cracking of maraging steel weldments in air and pentaborane. Stress corrosion cracks also occur during the heat treatment of titanium weldments in the presence of chlorinated hydrocarbons, often found in cleaning agents.⁽¹²⁰⁶⁾

It is well known that hydrogen causes delayed cracking in steel weldments, especially in those made in high-strength steel. Hydrogen-induced cracking also occurs in titanium welds.

Some investigators have even used stress corrosion cracks and hydrogen-induced cracking to study the residual stresses in weldments, as described in Section 4.5. Radeker⁽⁴⁴⁴⁾ studied the use of stress corrosion cracking as a method to prove the existence of residual stresses in a steel weldment.

A study was made at Battelle Memorial Institute of the hydrogen-induced cracking and stress corrosion cracking of steel weldments.⁽⁴⁴²⁾ The primary objective of the study was to determine whether a hydrogen-cracking technique could be used to determine residual-stress distributions in weldments, especially complex weldments. In addition to experiments, analytical studies were done of the relationship between residual stresses and crack patterns. The analytical technique that was developed should prove useful in the study of various types of weld cracking.

The Battelle technique has been described briefly in an earlier part of this text (Section 4.5.1). The following pages present additional information on the experimental results. The results of the analytical study are presented in Section 12.5.

Experimental hydrogen-induced cracking tests were done on forty-five weldments in mild steel, HY-80 steel, a commercial high-strength structural steel, and SAE 4340 steel. Table 12.2 summarizes the experimental results, which can be stated as follows:

1. Mild steel was immune to hydrogen embrittlement. Of the six specimens that were charged with hydrogen up to 379 hours, only very small cracks were observed and then only in two specimens. No cracks were observed in the other four specimens which had been hydrogen charged up to $126\frac{1}{2}$ hours.
2. As the strength level of the steel increased, the weldments became more susceptible to hydrogen embrittlement.
3. Weldments made in SAE 4340 steel quenched and tempered at a very high strength level were very susceptible to hydrogen embrittlement. Extensive cracks were obtained in all specimens except the one that had been mechanically stress relieved. Cracks were found after only a few hours of hydrogen charging.
4. Cracks were also found in weldments exposed to a boiling aqueous solution consisting of 60% $Ca(NO_3)_2$ and 4% NH_4NO_3 .

Figures 4.16, 4.17, and 4.18 show crack patterns obtained in some specimens.

Figure 4.16 is a typical crack pattern in a simple butt weld. A system of transverse cracks has been obtained. The transverse cracks have apparently been caused by the high-tensile residual stresses that are present in the vicinity of the weld. The lengths of the cracks are uniform in the central portion of the weld but gradually decrease in length in regions several inches from the edge of the plate and no cracks are found near the

TABLE 12.2 *Summary of results of hydrogen-induced-cracking tests on welded specimens made from various materials*

Base plate and heat treatment	Approx. tensile strength (psi)	Number of specimens tested	Plate thickness (in.)	Hydrogen charging period (hr)	Summary of test results
1. Mild steel	75,000	6	$\frac{1}{2}$ to 2	Up to 379	Very small cracks in the heat-affected zone of two specimens, but no cracks in four other specimens hydrogen charged up to 126 $\frac{1}{2}$ hr
2. HY-80 (quenched and tempered)	100,000	4	$\frac{1}{2}$ to 2	Up to 216	Small cracks in two specimens, but no cracks in two other specimens
3. Commercial high-strength structural steel water quenched and tempered at 1150° F	120,000	1	$\frac{3}{4}$	4 $\frac{1}{2}$	No cracking
4. Commercial high-strength structural steel water quenched and tempered at 350° F	150,000	5	$\frac{1}{2}$, $\frac{3}{4}$	Up to 24	Several cracks were found in three specimens
5. SAE 4340 steel (as rolled)	150,000	1	$\frac{3}{4}$	14	No cracking
6. SAE 4340 steel (oil quenched and tempered at 1100° F)	175,000	1	$\frac{1}{2}$ ^(a)	6 $\frac{3}{4}$	Several transverse cracks
7. SAE 4340 steel (oil quenched and tempered at 750° F)	220,000	1	$\frac{1}{2}$ ^(a)	6	Fairly systematic cracks
8. SAE 4340 steel (oil quenched and tempered at 600° F)	240,000	1	$\frac{3}{4}$	1	Systematic cracks
9. SAE 4340 steel (oil quenched and tempered at 500° F)	260,000	25	$\frac{1}{4}$ to $\frac{3}{4}$	Up to 16	Extensive cracks in all specimens except one which had been mechanically stress relieved; cracks were found after hydrogen charging for a few hours or less

^(a) Ground from $\frac{5}{8}$ to $\frac{1}{2}$ in. thick.

plate edge. The results indicate that longitudinal residual stresses are less significant in regions near the plate edge.

Tests have also been made on various complex weldments. Systematic crack patterns that can be related to residual stress distributions have been obtained in specimens made in SAE 4330 steel oil quenched and tempered at 500° F (260° C). Figure 4.17 shows the crack pattern obtained on a specimen that simulated a panel structure composed of longitudinal and transverse frames fillet welded to a bottom plate.

12.4 Analysis of Crack Pattern

Masubuchi and Martin⁽⁴⁴²⁾ have developed a mathematical analysis based upon the fracture mechanics theory to determine the relationship between the residual stress distribution and the crack pattern.

12.4.1 General theory of crack pattern

A study has been made to develop a general crack-pattern theory produced in a solid containing residual stress by modifying the Griffith–Irwin fracture mechanics theory. However, there is a basic difference between subjects discussed in this crack-pattern theory and ordinary fracture-mechanics theory. In the crack-pattern theory, the major concern is to determine the crack pattern that is stable. In fracture-mechanics theory, on the other hand, the major concern is to determine what conditions produce unstable fractures. Another important problem in the crack-pattern theory is that it is essential to assume that residual stresses are not uniformly distributed in the solid. The crack may be curved, and there may be more than one crack.

When a crack occurs in a solid containing residual stresses, new surfaces appear and the residual stresses that existed in regions near the crack are partially released. If the decrease in residual stress–strain energy due to the strain release is greater than the energy required to produce the new surfaces, a crack will form since the total energy of the solid decreases due to the occurrence of the crack.

The increase of surface energy depends on the properties of the material and is considered proportional to the surface area of the crack. When a crack of length l (between A and B in Fig. 12.2) occurs in a plate of uniform thickness, the increase of surface energy per unit plate thickness, W_s , is given by:

$$\begin{aligned}
 W_s &= 2\rho l \\
 &= 2\rho \int_A^B ds
 \end{aligned}
 \tag{12.1}$$

where W_s = energy required to produce the new surface,
 ρ = amount of energy required to produce a surface of unit area
 $ds = \sqrt{dx^2 + dy^2}$ = line element.

The major characteristics of the residual stress changes that take place during the formation of the crack are:

1. Since residual stresses are released due to cracking, the stress changes are consi-

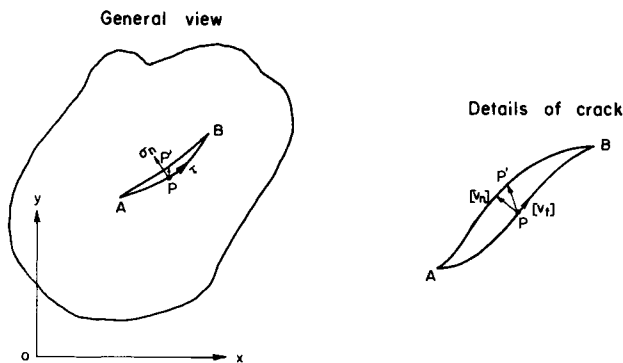


FIG. 12.2. Occurrence of a crack in a body containing residual stress.

dered elastic even when the pre-existing residual stresses are caused by plastic deformation†

2. If the crack surface remains free from stress after cracking, the normal and shearing stresses that were acting along the crack will be fully released.

Consequently, the decrease in elastic-strain energy of residual stresses per unit thickness due to the occurrence of the crack, W_e , can be determined from knowing (1) the residual stresses that were acting along the crack before cracking and (2) the relative displacement of both sides of the crack or the crack opening, as follows.

$$W_e = \int_A^B \frac{1}{2} \{ \sigma_n [v_n] + \tau [v_t] \} ds \quad (12.2)$$

where W_e = decrease in elastic strain energy,
 σ_n, τ = normal and shearing residual stresses, respectively, that were acting along the crack,
 $[v_n], [v_t]$ = relative displacements of both sides of the crack in the normal and tangential directions, respectively.

The decrease in the total energy of the system, U , is:

$$U = W_e - W_s. \quad (12.3)$$

Since the stress changes due to cracking are considered elastic, the relationship between the residual stress along the crack, (σ_n, τ) , and the crack opening, $([v_n], [v_t])$, can be determined analytically as a problem of the theory of elasticity. Masubuchi and Martin⁽¹²⁰⁷⁾ have conducted an analysis of stress changes due to crack formation. Consequently, the decrease in total energy, U , can be calculated when the path of the crack and the residual stresses that were acting along the crack are known.

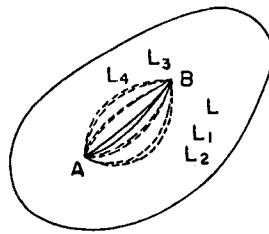
The stability of a crack is now considered. First of all, the value of U must be positive if a crack is to form. However, there may be many different crack paths between two points, A and B , as shown by L_1, L_2, \dots , in Fig. 12.3(a), that can satisfy this condition. Different values of the energy decrease U_1, U_2, \dots will be produced by these different crack paths. One crack path may result in a larger value of U than another crack path does. The crack path that produces the largest decrease in total energy is likely to be the preferred path between A and B . The crack also will extend as long as U is increased by the increase in crack length $[(\partial U / \partial l) > 0]$. The crack will stop when $\partial U / \partial l = 0$. The above-mentioned conditions are shown schematically in Fig. 12.3(b). Relationships between the length of crack and energy decrease, U , are shown for different crack paths. The crack path (including crack length) that corresponds to point X is more stable than other paths.

The discussion thus far has been about a crack between A and B . The analysis can be extended to a group of cracks. The crack pattern that produces the maximum value of U is the one that is most likely to occur. Further analyses have been made of the following simple crack patterns:

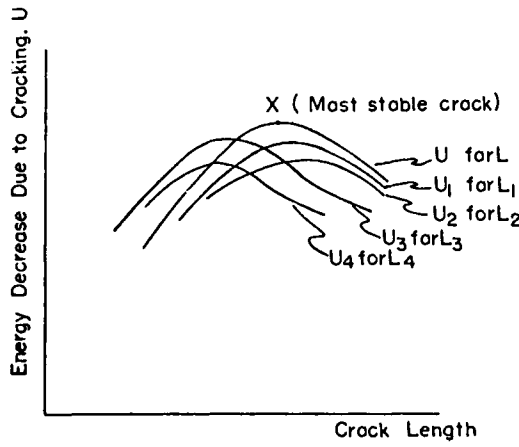
1. Transverse cracks as shown in Fig. 4.16.
2. Circular and radial cracks in radially symmetric stress fields.

The following pages describe the analysis of transverse cracks in welds.

† Even when a material is in the plastic state, the strain change during unloading is elastic.



a. Different Crack Paths



A-51957

b. Changes of Energy Decrease Due to Cracking, U, for Cracks Which Have Different Paths and Different Lengths

FIG. 12.3. Determination of the most stable crack.

12.4.2 Analysis of transverse cracks in welds

It was found in the experimental investigation that typical hydrogen-induced cracks are short, transverse, and adjacent to the weld, as shown in Fig. 4.16. It was also found that the properties of the material affected that crack pattern. When the material was embrittled severely by hydrogen charging, extensive cracks formed. When the material was embrittled less the cracks were less predominant or shorter and more widely spaced. When the material was tough beyond a certain limit, no cracks were produced during or after hydrogen charging.

The typical transverse cracks observed in most weldments were short, parallel, of about equal length, and spaced at about equal intervals. The results indicate that the distribution of longitudinal residual stresses has the following characteristics:

1. High tensile stresses exist in narrow regions on both sides of the weld.
2. The distribution of residual stresses along the weld is uniform except in regions near the end of the weld.

These characteristics have been proven in actual residual stress measurements (see Figs. 6.25 and 6.26).

On the basis of the experimental findings, analyses have been made for cracks in an

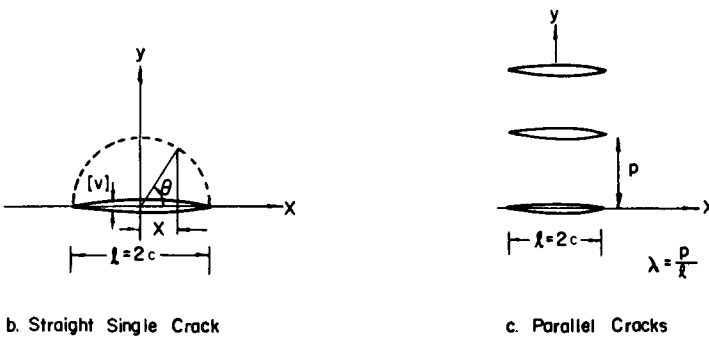
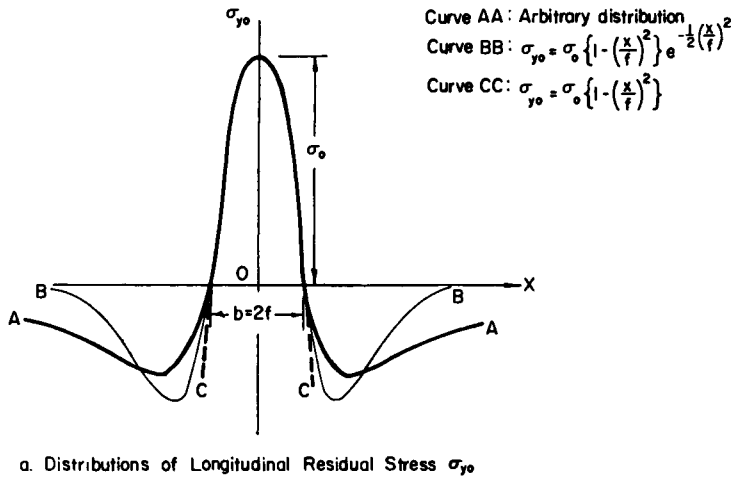


FIG. 12.4. Residual stresses $\sigma_{y0} = f(x)$ and transverse cracks.

infinite plate caused by the residual stresses as shown by curve AA in Fig. 12.4(a). It is assumed that residual stresses in the y-direction $\sigma_{y0} = f(x)$ vary along the x-direction but are uniform in the y-direction. Two types of transverse cracks were analyzed:

1. A straight single crack, as shown in Fig. 12.4(b).
2. Parallel cracks with equal length and equal spacing, as shown in Fig. 12.4(c).

A straight, single crack can be analyzed as described in Section 10.5.1. The analysis of parallel cracks is described in the following pages.

Analysis of parallel cracks. First, the residual stresses that exist along the crack before cracking are expressed by a modified series as follows:

$$\sigma_{y0} = f(x) = \frac{E}{2l} \sum_{n=1}^{\infty} n B_n \frac{\sin n\theta}{\sin \theta} \tag{12.4}$$

where E = Young's modulus,

$l = 2c$ = crack length,

θ = parameter which expresses the position x , $\cos \theta = x/c$.

$$B_n = \text{coefficient} = \frac{4l}{\pi E} \frac{1}{n} \int_0^{\pi} \sigma_{y0} \sin n\theta \sin \theta \, d\theta. \tag{12.5}$$

For a given stress distribution, σ_{y0} , and crack length, l , a series of coefficients B_1, B_2, B_3, \dots can be determined by conducting the integrations given in eqn. (12.5) from $\theta = 0(x = c)$ to $\theta = \pi(x = -c)$.

The opening of the crack in the y -direction, $[v]$, also can be expressed in a Fourier series as follows:

$$[v] = \sum_{n=1}^{\infty} A_n \sin n\theta. \tag{12.6}$$

Equation (12.6) satisfies the condition that the crack must be closed at both ends of the crack; i.e. $[v] = 0$ at $x = \pm c$ or $\theta = 0$ and π .

Equations (12.4) and (12.6) are essentially the same as eqns. (10.43) and (10.42), respectively. In the case of a single crack:

$$A_n = B_n. \tag{12.7}$$

Then eqns. (12.4) and (12.6) become identical with eqns. (10.43) and (10.42), respectively, or the analysis described in Section 10.6.1 can be used.

In the case of a system of parallel cracks, as shown in Fig. 12.4(c), the following relationship exists between coefficients B_n and A_n :

$$A_n = \sum_{j=1}^{\infty} \gamma_{nj} B_j \tag{12.8}$$

where γ_{nj} is an inverse matrix of matrix β_{nj} :

$$\beta_{nj} = \alpha_{nj} + \delta_{nj}, \tag{12.9}$$

$$\alpha_{nj} = \left(\frac{2}{\pi}\right)^2 \left(\frac{j}{n}\right) \int_0^{\pi} \sin \theta \sin n\theta \, d\theta \int_0^{\pi} \cos j\theta' (\cos \theta' - \cos \theta). \tag{12.10}$$

$$\left[\sum_{m=1}^{\infty} \frac{(\cos \theta' - \cos \theta)^2 + 3m^2 \lambda^2}{\{(\cos \theta' - \cos \theta)^2 + m^2 \lambda^2\}^2} \right] d\theta',$$

$$\lambda = \frac{p}{l},$$

$$\delta_{nj} = \begin{cases} 1 & (n = j), \\ 0 & (n \neq j). \end{cases}$$

In order to determine values of A_1, A_2, A_3, \dots for given values of B_1, B_2, B_3, \dots values of α_{nj} and γ_{nj} must be known. Numerical computations of α_{nj} and γ_{nj} have been done for several combinations of the crack interval-to-crack length ratio, $\lambda = p/l$.

The strain energy released by each of the parallel cracks, W_{e1} , is given by:

$$W_{e1} = \frac{E}{8} \cdot \frac{\pi}{2} \left(\sum_{n=1}^{\infty} \sum_{j=1}^{\infty} n \gamma_{nj} B_n B_j \right). \tag{12.11}$$

The decrease in total energy caused by the occurrence of each crack, U_1 , is given by:

$$U_1 = W_{e1} - 2\rho l. \tag{12.12}$$

The energy decrease per unit length in the y -direction, \bar{U} , is given by:

$$\bar{U} = \frac{1}{p} U_1. \quad (12.13)$$

The combination of l and p that gives the maximum value of \bar{U} determines the crack pattern.

Numerical analyses. Numerical analyses have been made of stress distributions mathematically expressed by the two following equations:

(1) Modified parabolic stress distribution

$$\sigma_{y0} = \sigma_0 \left\{ 1 - \left(\frac{x}{f} \right)^2 \right\} e^{-(1/2)(x/f)^2} \quad (12.14)$$

(2) Parabolic stress distribution

$$\sigma_{y0} = \sigma_0 \left\{ 1 - \left(\frac{x}{f} \right)^2 \right\} \quad (12.15)$$

where σ_0 = maximum stress at the weld center,
 $b = 2f$ = width of the tension zone of residual stress.

The stress distribution given by eqn. (12.14) is shown by curve BB in Fig. 12.4(a), which represents the residual-distortion in a weld with reasonable accuracy.[†] Curve CC in Fig. 12.4(a) shows the stress distribution given by eqn. (12.15); the parabolic stress distribution was used in an analysis of short transverse cracks, and the modified parabolic-stress distribution was used in an analysis of a crack that extended into the region where residual stresses were originally compressive.

A dimensionless parameter, μ , the “relative toughness of a weldment (against transverse cracking)”, has been introduced to characterize the hydrogen-induced cracking tendency of a weldment. The parameter is determined by the residual-stress distribution and the properties of the material as follows:

$$\mu = \left(\frac{K_c}{K_w} \right)^2 \quad (12.16)$$

where K_c = critical stress intensity factor of the material, see eqn. (10.20),

$$K_w = \sigma_0 \sqrt{\pi f},$$

σ_0 = maximum longitudinal residual stress at the weld center,

$b = 2f$ = width of the tension zone of longitudinal residual stresses.

K_w is a parameter determined by the residual-stress distribution Masubuchi and Martin designated K_w the “effective stress intensity factor of the weldment”. When the material has a greater fracture toughness, the value of μ increases; therefore μ may be called the “relative toughness of the weldment”.

[†] The stress distribution given by eqn. (12.14) satisfies the following equilibrium conditions required for residual stresses:

$$\int_{-\infty}^{\infty} \sigma_{y0} dx = 0, \quad \int_{-\infty}^{\infty} \sigma_{y0} x dx = 0.$$

TABLE 12.3 Summary of results of residual-stress measurements

Specimen code number	Type of steel	Joint type (specimen size)	Maximum stress in or near the weld, σ_0 (approximately) (psi)	Width of residual-stress tension zone b (in.)	$K_w = \sqrt{\frac{\pi}{2}} \sigma_0 \sqrt{b}$
OM1	Mild steel	Butt joint ^(a) $\frac{1}{2} \times 12 \times 16$ in.	60,000	4	151,000
TM1		Butt joint ^(b) $\frac{5}{8} \times 24 \times 38$ in.	50,000	3	109,000
3CM		Complex welded structure (bottom plate: $\frac{7}{16} \times 16 \times 24$ in.)	45,000 ^(e)	3 ^(e)	98,000
R1	SAE 4340	Butt joint ^(a) $\frac{1}{2} \times 12 \times 16$ in.	51,000	3	111,000
S1		Butt joint ^(c) $\frac{3}{4} \times 12 \times 16$ in.	52,000	3	113,000
S2		Butt joint ^(d) $\frac{3}{4} \times 18 \times 32$ in.	45,000 ^(f)	3	98,000
T41		Butt joint ^(b) $\frac{5}{8} \times 24 \times 38$ in.	61,000	6	188,000
3C41		Complex welded structure (bottom plate: $\frac{7}{16} \times 16 \times 24$ in.)	75,000 ^(e)	2.5 ^(e)	149,000

Notes: ^(a) The specimens were ground for $\frac{5}{8}$ in to $\frac{1}{2}$ in. thick.
^(b) Weld reinforcements were ground to form flash specimen surfaces.
^(c) Weld reinforcement was not ground.
^(d) Weld reinforcements were ground partially.
^(e) Values for the transverse section through the center of the longitudinal frame.
^(f) Estimated value.

The following results have been obtained:

1. A series of cracks result when the μ -value of a weldment is smaller than approximately 0.02.
2. No crack results when the μ -value is larger than about 0.3. The critical value of μ is 0.29 for the parabolic stress distribution and 0.25 for the modified parabolic stress distribution.
3. The length of the stable serial cracks is approximately the same as the width of the tension zone.
4. When a weldment is extremely brittle, with a μ -value of approximately 0.01, one or a few cracks of a series of cracks can easily penetrate into the region where residual stresses were originally compressive.

The results indicate that there are limitations on the properties of the material to be used in the hydrogen-induced-cracking test. The μ -value of a weldment before hydrogen charging must be larger than approximately 0.3, otherwise cracking may occur without hydrogen charging. The μ -value of the weldment, however, must decrease to about 0.02 during hydrogen charging in order for systematic cracks to occur. After the hydrogen cracks begin to form, it is best not to charge for too long a time, since cracks may grow beyond the stable crack length.

Analysis of experimental results. Masubuchi and Martin⁽⁴⁴²⁾ analyzed the experimental results.

First, the values of K_c before and after hydrogen charging were determined. On the basis of existing data, the K_c value of the SAE 4340 steel, oil-quenched and tempered at 500°F (260°C) without hydrogen embrittlement, was estimated to be approximately 175,000 psi√in. (620 kg√mm/mm²).^(442, 1014) In a separate experiment the K_c value of the material after hydrogen charging was found to be 16,800 psi√in. (59 kg√mm/mm²).

Table 12.3 summarizes the results of residual-stress measurements.[†] The K_w values of SAE 4340 steel welds $\frac{1}{2}$ to $\frac{5}{8}$ in. (12 to 16 mm) thick were about 100,000 to 200,000 psi√in. (354 to 709 kg√mm/mm²). Then, μ values of the weldments were determined as follows:

$$\mu = \left(\frac{K_c}{K_w} \right)^2$$

K_w , psi√in.	As-welded ($K_c = 175,000$ psi√in.)	Hydrogen-embrittled ($K_c = 16,800$ psi√in.)
100,000	3.1	0.028
150,000	1.4	0.013
200,000	0.77	0.007

The μ -values were larger than 0.3 in the as-welded condition and about 0.02 or lower in the hydrogen-induced-cracking technique. The results show that the hydrogen cracking technique should work effectively on weldments made in SAE 4340 steel oil quenched and tempered at 500°F (260°C).

References

- (1201) ROSTOKER, W., MCCAUGHEY, J. M., and MARKUS, H., *Embrittlement by Liquid Metals*, Reinhold Publishing Co., New York, 1960.
- (1202) BROWN, B. F., and BIRNBAUM, L. S., "Corrosion control for structural metals in the marine environment", NRL Report 6167, *Status and Projections of Developments in Hull Structural Materials for Deep Ocean Vehicles and Fixed Bottom Installations*, U.S. Navy Research Laboratory, Nov. 1964.
- (1203) BERRY, W. E., *Stress-corrosion Cracking—A Nontechnical Introduction to the Problem*, Battelle Memorial Institute, Defense Metals Information Center DMIC Report 144, 6 Jan. 1961.
- (1204) SIMCOE, C. R., Slaughter, E. R., and Elsea, A. R., "The hydrogen-induced delayed brittle fracture of high strength steels", unpublished manuscript.
- (1205) TOY, S. M. and PHILLIPS, A., "Stress corrosion characteristics of maraging steel weldments in air and pentaborane", *Welding Journal*, 49 (11), Research Supplement, 947s–504s (1970).
- (1206) "Stress-corrosion cracking of Ti–5Al–2.5 Sn", DMIC Memorandum 60, Defense Metals Information Center, Battelle Memorial Institute, Columbus, Ohio, Aug. 1960.
- (1207) MASUBUCHI K. and MARTIN, D. C., "An analytical study of cracks in weldments", *Kozokogaku Kenkyu* (Structural Engineering Research), Tokyo University Press, 1968, pp. 279–300.

[†] The residual stress distributions of mild steel and SAE 4340 steel specimens shown in Fig. 6.25 are those of specimens TMI and T41, respectively, of Table 12.3.

Effects of Distortion and Residual Stresses on Buckling Strength of Welded Structures

FAILURES due to instability, or buckling, sometimes occur in metal structures composed of slender bars and/or thin plates when they are subjected to compressive axial loading, bending, and/or torsional loading. It is known that residual compressive stresses decrease the buckling strength of a metal structure. Initial distortions caused by residual stresses also decrease the buckling strength. Presented in Section 8.4 are preliminary discussions on effects of initial distortion and residual stresses on buckling. The following pages discuss briefly:

1. Columns under compressive loading.
2. Plates and plate structures under compressive loading.
3. Corrugation damage of welded ships and allowable distortion of ship bottom plating.
4. Spherical and cylindrical shells subjected to external pressure.

Numerous studies have been made on the general subject of effects of initial distortion and residual stresses on buckling; however, only a small portion of these studies is concerned specifically with the effects of distortion and residual stresses on the buckling strength of welded structures.

This chapter discusses effects of distortion and residual stresses on buckling strengths of welded structures. We face a problem, however. The analysis of buckling strength of a structure, especially beyond yielding, is very complex by itself. The inclusion of effects of initial distortion and residual stresses on plastic buckling of a welded structure requires very extensive mathematical analyses. To avoid too lengthy analyses, this chapter provides a summary of pertinent experimental and analytical studies with limited analytical derivations. The WRC Bulletin 174 written by Masubuchi⁽⁵⁰¹⁾ is frequently used as a reference.

For those who need more detailed information on the general subject of buckling, references (1301)–(1303) are recommended. References (1304) through (1308) contain detailed information on buckling strength of welded structures.

Many publications discuss effects of initial distortion and residual stresses, not necessarily caused by welding, on buckling. They are also listed as references. References (1309) through (1322) cover columns and bars, references (1323) through (1339) cover plates and plate structures, and references (1340) through (1368) cover cylindrical and spherical shells.

13.1 Columns under Compressive Loading⁽⁵⁰¹⁾

Instability of built-up columns has been studied by a number of investigators analytically, as well as experimentally. As shown in Fig. 8.8, compressive residual stresses decrease, under certain conditions, the proportional limit of a fabricated column.

The effects of residual stresses on buckling strength of straight columns, mostly made of steel, have been studied by Osgood,^(804,1304) Tall *et al.*,⁽¹³⁶⁹⁾ Horne⁽¹³⁷⁰⁾ Kihara and Fujita,⁽¹³⁷¹⁾ and other investigators.⁽¹³⁷²⁾ It has been found that residual stresses can significantly reduce the buckling strength of columns.

If the column also has initial distortion, its buckling strength will be reduced further. Fujita⁽¹³⁷³⁾ conducted a mathematical analysis of the buckling strength of a column having both residual stresses and initial distortion.

The following pages discuss buckling strength of welded straight columns (no distortion) in steel and aluminum. Discussions on welded columns in heat-treated aluminum alloy are complicated, because we must consider the effects of partial annealing of the material in the vicinity of the weld, as well as residual stresses.

13.1.1 Welded steel columns

Figure 13.1 shows buckling strengths of steel I-beams built up by welding under compressive axial loading. It shows the relationship between the slenderness ratio of specimen, L/r (L is the specimen length and r is the radius of gyration), and the ratio of the critical stress to the yield strength of the material. Curves PQR and ST show distributions in the flange and web plate, respectively, of residual stresses in the longitudinal direction of an as-welded column. Welded joints between the web and flange plates caused residual tensile stresses in areas near the weld and compressive stresses in outer areas of the flanges and in the web plate. Curve AB shows the buckling strengths of as-welded columns, while curve CDE shows the buckling strengths of stress-relieved

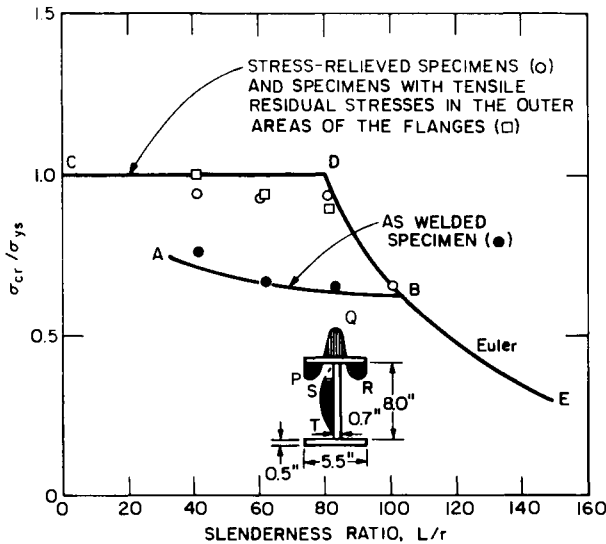


FIG. 13.1. Effects of residual stresses on buckling strength of columns (Kihara and Fujita).⁽¹³⁷¹⁾

specimens and specimens with tensile residual stresses in the outer areas of the flange. Curves *AB* and *CDE* are obtained by theoretical analysis; *DE* is the so-called Euler curve[†] and *AB* is obtained by considering the effect of residual stress on buckling strength. Buckling occurred in the weak axis of the columns. As-welded specimens had considerably lower critical buckling strength than did the other type of specimens indicating that an unfavorable residual stress distribution can cause a substantial decrease in the buckling strength. A good agreement was obtained between the experimental data and the theoretical values, as shown in Fig. 13.1.

13.1.2 Welded aluminum columns

Brungraber and Clark⁽¹³⁷⁴⁾ studied buckling strength of welded columns in aluminum alloys types 5456-H321, 5154-H34, and 6061-T6.

The mechanical properties in the vicinity of a weld vary from a minimum at or near the weld center to unaffected parent metal properties at some distances away from the weld. As an example, Fig. 13.2 shows a typical distribution of yield strength in the vicinity of a weld.

Figure 13.3 shows buckling strength of longitudinally welded columns of 6061-T6. Column strengths are given for different values of A_r/A , where A_r is the sum of the reduced strength areas and A is the total cross-sectional area of the column. The column strength decreases as A_r/A increases. For the case $A_r/A = 0.29$, the figure shows columns strengths neglecting residual stresses and including residual stresses. In the particular case shown here, the effect of residual stresses was minor. Residual stresses even caused some increase in buckling strength for the effective slenderness ratio of about 60. The effective

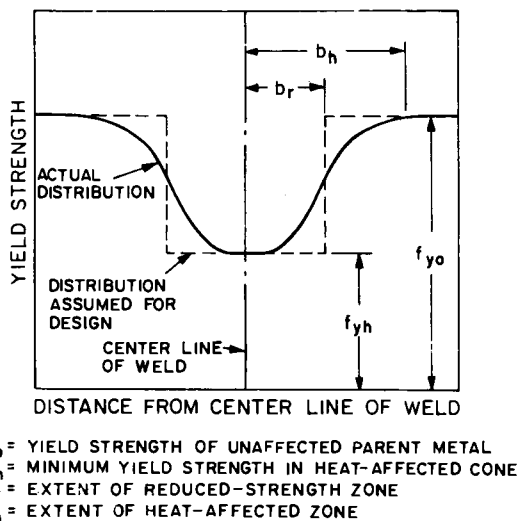


FIG. 13.2. Typical distribution of yield strength values in the vicinity of weld in aluminum.

[†] See eqn. (8.1).

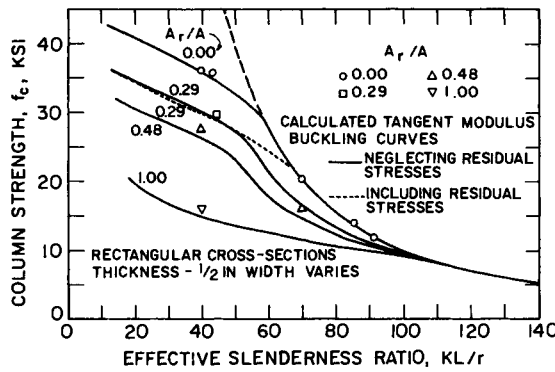


FIG. 13.3. Buckling strength of longitudinally welded columns of 6061-T6 aluminum.

slenderness ratio ($K \cdot L/r$) is defined as follows:

$$\frac{KL}{r} = \pi \sqrt{\frac{E_h I_r / I + E_0 (I - I_r) / I}{\sigma_c}} \tag{13.1}$$

where I_r = sum of the moment of inertia of the reduced strength area,
 $I - I_r$ = moment of inertia of the rest of the cross-section,
 E_h = tangent modulus of the reduced strength area,
 E_0 = tangent modulus of the unaffected base metal,
 σ_c = average stress corresponding to the buckling load.

Brungraber and Clark also studied buckling strengths of transversely welded columns.

13.2 Plates and Plate Structures Under Compressive Loading

13.2.1 Elastic instability of plates with residual stresses

Yoshiki, Fugita, and Kawai⁽¹³⁷⁵⁾ studied the elastic buckling of a simply supported rectangular plate welded along the center line, as shown in Fig. 13.4. As a result of analytical and experimental studies, they found that such residual stresses may even result in a slight increase, under certain conditions, in the buckling load of the plate.

The equilibrium equation of elastic buckling of plates with residual stresses may be given from the small deflection theory of plates as follows:⁽¹³⁰⁶⁾

$$D \Delta \Delta w + (N_x + n_x) \frac{\partial^2 w}{\partial x^2} + 2(N_{xy} + n_{xy}) \frac{\partial^2 w}{\partial x \partial y} + (N_y + n_y) \frac{\partial^2 w}{\partial y^2} = 0 \tag{13.2}$$

where $N_x/h, N_{xy}/h, N_y/h$ are components of stresses in the plate induced by applied loads, and $n_x/h, n_{xy}/h, n_y/h$ are components of residual stresses.

Assuming that a given rectangular plate is simply supported along the edges, the buckled plate deflection can be expressed by the following double Fourier sine series:

$$w(x, y) = \sum_{m=1}^{\infty} \sum_{n=1}^{\infty} \alpha_{mn} \phi_{mn}(x, y) \tag{13.3}$$

where

$$\phi_{mn}(x, y) = \frac{2}{\sqrt{ab}} \sin \frac{m\pi}{a} \left(x + \frac{a}{2} \right) \sin \frac{n\pi}{b} \left(y + \frac{b}{2} \right).$$

Substituting eqn. (13.3) into eqn (13.2) and utilizing the orthogonality condition of $\phi_{mn}(x, y)$ the following simultaneous equations for unknown constants α_{mn} can be obtained:

$$\lambda_{mn}^2 a_{mn} = \sum_{m=1}^{\infty} \sum_{n=1}^{\infty} a_{rs} \left[\left(\frac{r\pi}{a} \right)^2 (A_{rsmn} + L_{rsmn}) + 2 \left(\frac{r\pi}{a} \right) \left(\frac{s\pi}{b} \right) (B_{rsmn} + M_{rsmn}) + \left(\frac{s\pi}{b} \right)^2 (C_{rsmn} + N_{rsmn}) \right] \quad (13.4)$$

where
$$\lambda_{mn}^2 = D \left[\left(\frac{m\pi}{a} \right)^2 + \left(\frac{n\pi}{b} \right)^2 \right],$$

$$\left. \begin{aligned} A_{rsmn} &= \int_{-a/2}^{a/2} \int_{-b/2}^{b/2} N_x(\xi, \eta) \varphi_{rs}(\xi, \eta) \varphi_{mn}(\xi, \eta) d\xi d\eta, \\ B_{rsmn} &= - \int_{-a/2}^{a/2} \int_{-b/2}^{b/2} N_{xy}(\xi, \eta) \left(\frac{a}{r\pi} \right) \left(\frac{b}{s\pi} \right) \frac{\partial^2 \varphi_{rs}(\xi, \eta)}{\partial \xi \partial \eta} \varphi_{mn}(\xi, \eta) d\xi d\eta, \\ C_{rsmn} &= \int_{-a/2}^{a/2} \int_{-b/2}^{b/2} N_y(\xi, \eta) \varphi_{rs}(\xi, \eta) \varphi_{mn}(\xi, \eta) d\xi d\eta; \end{aligned} \right\} \quad (13.5)$$

$$\left. \begin{aligned} L_{rsmn} &= \int_{-a/2}^{a/2} \int_{-b/2}^{b/2} n_x(\xi, \eta) \varphi_{rs}(\xi, \eta) \varphi_{mn}(\xi, \eta) d\xi d\eta, \\ M_{rsmn} &= - \int_{-a/2}^{a/2} \int_{-b/2}^{b/2} n_{xy}(\xi, \eta) \left(\frac{a}{r\pi} \right) \left(\frac{b}{s\pi} \right) \frac{\partial^2 \varphi_{rs}(\xi, \eta)}{\partial \xi \partial \eta} \varphi_{mn}(\xi, \eta) d\xi d\eta, \\ N_{rsmn} &= \int_{-a/2}^{a/2} \int_{-b/2}^{b/2} n_y(\xi, \eta) \varphi_{rs}(\xi, \eta) \varphi_{mn}(\xi, \eta) d\xi d\eta, \end{aligned} \right\} \quad (13.6)$$

Eliminating α_{mn} from eqn. (13.4), the characteristic equation for determination of the plate-buckling load can be obtained. Assuming the distribution of residual stresses as shown in Fig. 13.4 and uniaxial compression, i.e. $N_x = N, N_{xy} = N_y = 0$, the following first approximate characteristic equation is obtained:

$$\begin{aligned} N_{cr} &= D \left(\frac{\pi}{a} \right)^2 \left(1 + \frac{a^2}{b^2} \right)^2 + T_x \frac{\sin \frac{2\pi\delta}{b}}{2\pi\delta} \left\{ \frac{1}{2} + \frac{c}{a} + \frac{c}{a-2c} \cdot \frac{1}{\pi^2} \left(1 + \cos \frac{2\pi c}{a} \right) \right\} \\ &+ \frac{6T_y}{\pi^2} \left(\frac{a}{b} \right)^2 \left\{ \frac{1}{2} + \frac{d}{b} + \frac{d}{b-2d} \cdot \frac{1}{\pi^2} \left(1 + \cos \frac{2\pi d}{b} \right) \right\}. \end{aligned} \quad (13.7)$$

where the compressive stress is taken positive.

The second and third terms on the right-hand side of eqn. (13.7) represent the influence of residual stresses η_x and η_y , and they are generally positive, resulting in slight increase of the buckling load of the plate.

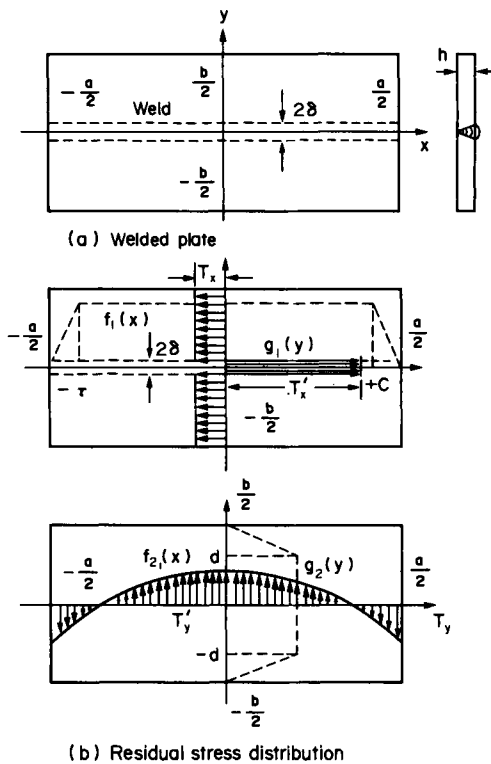


FIG. 13.4. Assumed distribution of residual stresses in a butt-welded rectangular plate.

Using four square plates of 6 mm (0.24 in.) thick and 500 mm (20 in.) long, two of which were welded along the center line, and the other two were not welded, the compression test was carried out. From the test results, it was revealed that two welded plates were buckled at 35.5 t, while the other two plates at 34.5 t. Theoretical production of the increase of the buckling load by residual stress was 1.8 t, from eqn. (13.7), which is the first approximate solution of the problem.

13.2.2 Plastic buckling of welded plates

Fujita and Yoshida⁽¹³⁷⁶⁾ further expanded the study of compressive strength of welded plates to cover plastic buckling, using the deformation theory of plasticity. Figure 13.5 shows the three types of specimens used in the experiments:

- V-type specimens with no residual stress,
- E-type specimens with welds along the edges,
- C-type specimens with a weld along the centerline.

Specimens were 1200 mm (47 in.) long, 600 mm (23 in.) wide, and 8 to 14 mm (0.3 to 0.55 in.) thick, and they were made in steel. Figure 13.5 also shows two stress-strain diagrams used in the analysis. Efforts were made to reduce initial distortion due to welding to a minimum; therefore, the initial distortion at the center of the panel was only about 1 to 2% of the plate thickness. Buckling tests were conducted with the plates being simply supported.

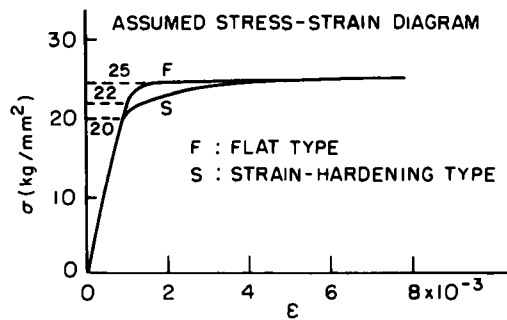
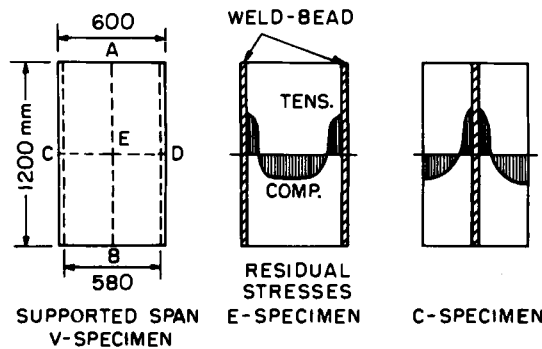


FIG. 13.5. Test specimens and assumed stress-strain diagram.

In the analysis of the buckling strength, simple distributions as shown in Figs. 13.6(a) and (b) were used to express the distributions of residual stresses in test specimens. It was also assumed that residual stresses are uniform in the welding direction.

Figure 13.6 summarizes results obtained on welded specimens. Shown here are experimental results and calculated values of the critical buckling strength. Calculations were made using the two stress-strain diagrams. Details of the mathematical analysis are given in reference (1306).

Figure 13.7 is prepared from data shown in Figs. 13.6(a) and (b) to illustrate how residual stresses affect the buckling strength. Shown here is the reduction of critical load due to residual stresses. For E-type specimens, which have compressive residual stresses in the central regions of the panel, the reduction of buckling strength due to residual stresses increases as the ratio of breadth to thickness, b/t , increases.

The effects of residual stresses on C-type specimens are rather complicated. When the b/t ratio is large ($b/t > 70$) and the plate buckles elastically, the buckling load even increases. When the b/t ratio is between 50 and 70, residual stresses reduce the buckling strength, but the effect of residual stresses decreases as the b/t ratio further decreases.

13.2.3 Buckling strength of panel structures

Many investigators have studied buckling strength of panel structures.⁽¹³⁷²⁻¹³⁷⁹⁾ By summarizing data obtained by several investigators, Faulkner^(1380, 1381) has prepared

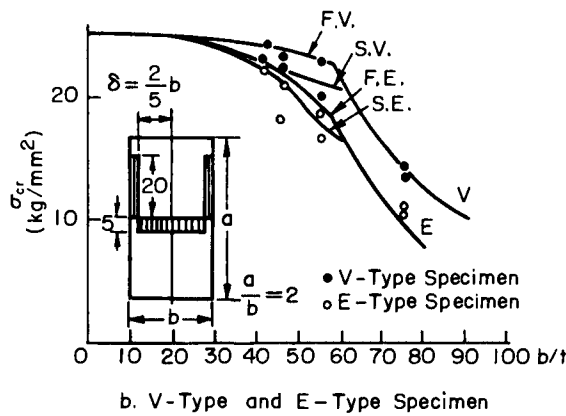
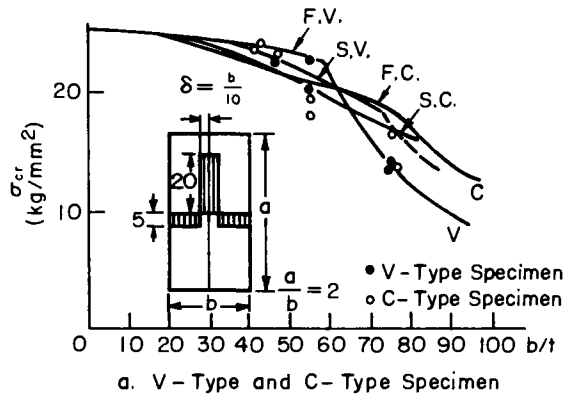


FIG. 13.6. Buckling strength of welded plate specimens.

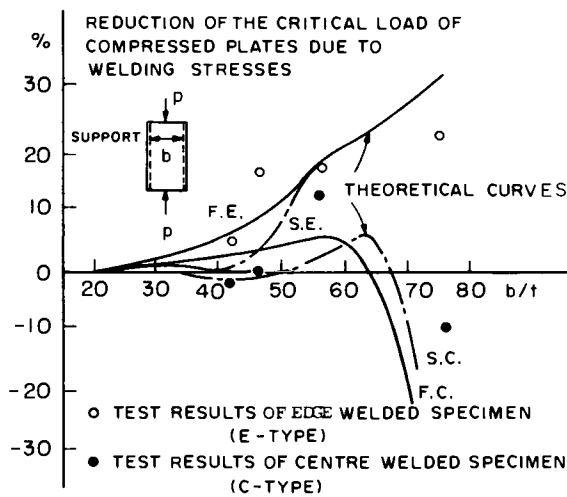


FIG. 13.7. Reduction of critical load of compressed plates due to welding residual stresses.

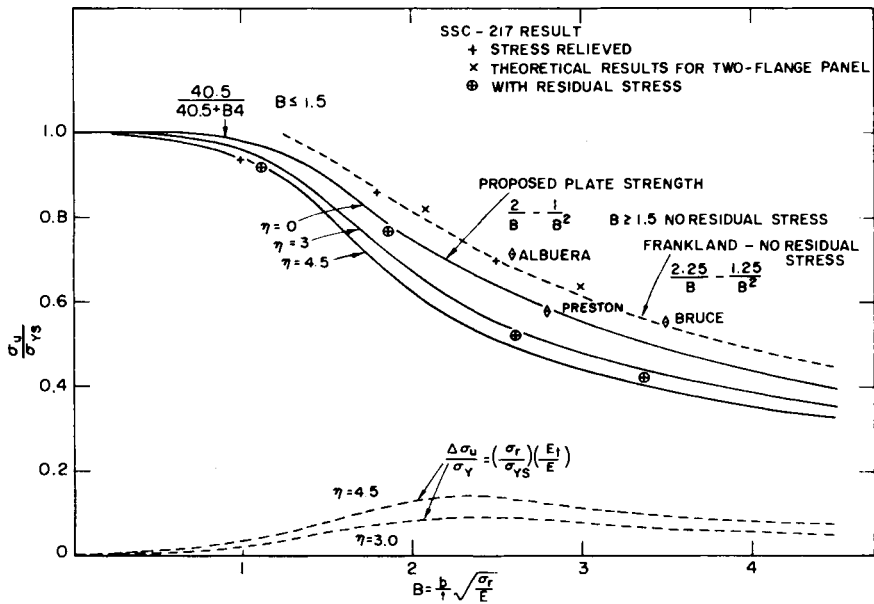


FIG. 13.8. Buckling strength of stiffened panels.

Fig. 13.8 showing effects of residual stresses on the buckling strength of panel structures.⁽¹³⁰⁸⁾

In the analysis, Faulkner used estimated residual stress distributions as shown in Fig. 13.9. It is assumed that:

1. Tensile residual stresses in areas near the weld are as high as the yield stress, σ_{ys} , and they extend into the area with the width of ηt , where t is plate thickness, in both sides of the weld.
2. Compressive residual stresses in areas away from the weld are constant and σ_r .

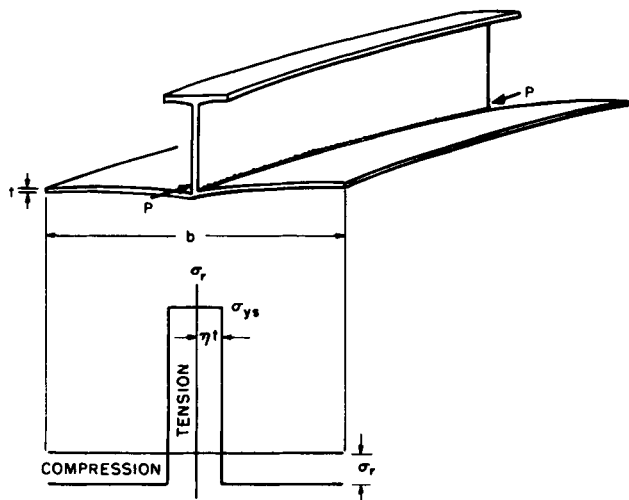


FIG. 13.9. Panel and assumed residual stress distribution.

Then,

$$(b - 2\eta t)\sigma_r = 2\eta t \sigma_{ys}, \tag{13.8}$$

$$\sigma_r = \frac{2\eta}{b/t - 2\eta} \sigma_{ys}. \tag{13.9}$$

Curves in Fig. 13.8 show values of σ_u/σ_{ys} , where σ_u is the buckling strength, for $\eta = 0$ (no residual stress), $\eta = 3$, and $\eta = 4.5$. Also shown here are values of $\Delta\sigma_u/\sigma_{ys}$, where $\Delta\sigma_u$ is reduction in buckling strength due to residual stresses; E_t is tangent modulus.

Figure 13.8 can be used by designers in estimating the buckling strength of welded panels.

13.3 Corrugation Damage of Welded Ships and Allowable Distortion of Ship Bottom Plating

13.3.1 Corrugation damage of welded ships and studies on buckling strength of ship bottom plating

The corrugation damage of bottom shell plating occurred in some ships having transverse framed bottoms of welded construction. The first examples of this damage were noticed in 1946, as discussed in a paper by Murray.⁽¹³⁸²⁾ Corrugation damages also occurred in some welded ships built in Japan. For example, a report from the Nippon Kaiji Kyokai⁽¹³⁸³⁾ discusses corrugation damages which occurred in twenty-two ships built from 1951 to 1953.

Figure 13.10 shows an example of the corrugation damage. In general terms, the

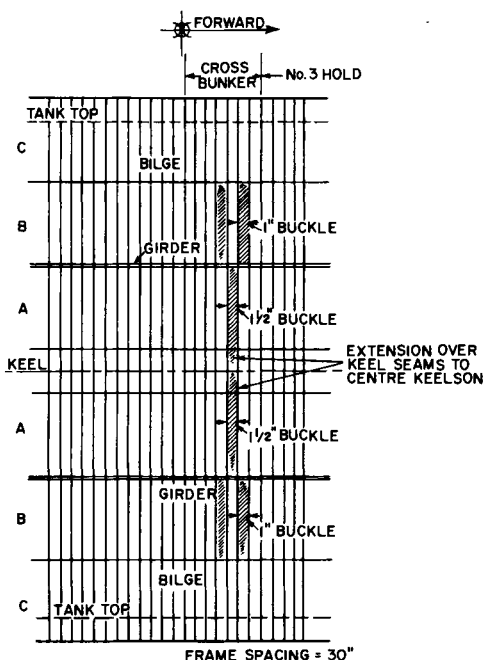


FIG. 13.10. Corrugation damage of ship bottom plating (Murray).⁽¹³⁸²⁾

corrugations noted in these ships were distributed throughout the midship half-length and were generally in an upwards direction between the floors. The depth of indentations at the maximum point was about $1\frac{1}{2}$ in. (38 mm),⁽¹³⁸²⁾ however, in some extreme cases the maximum indentation was over 3 in (76 mm).⁽¹³⁸³⁾

The corrugation damages occurred most frequently in all-welded, transversely framed ships, especially those with floor plates fillet-welded to the bottom plate.

Mechanisms of the corrugation damage have been studied by several investigators including Murray,⁽¹³⁸²⁾ Akita and Yoshimoto.^(1384, 1385) It has been found that the initial distortion and residual stresses produced in the bottom plate due to fillet welds between floor plates and the bottom plate are major reasons for the corrugation damage.

Figure 13.11 shows a typical distortion of the bottom plate. This type of distortion is often called “hungry horse”, since the outside appearance of the ship hull resembles that of a body of a hungry horse. The initial distortion and residual stresses decrease the buckling strength of the bottom plate which is subjected to water pressure, p , and axial compressive stress, σ_b . The compressive stresses are produced in the bottom structure when the ship is on the crest of a long wave or under the hogging condition.

Extensive research has been done on:

1. fabrication procedures for reducing the initial distortions and residual stresses;
2. the effects of the initial distortions and residual stresses on the buckling strength of the bottom structure.

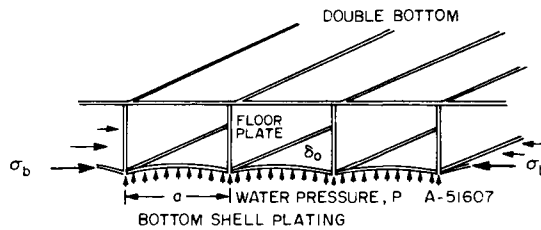


FIG. 13.11. Bottom shell plating of a transversely framed, welded cargo ship.

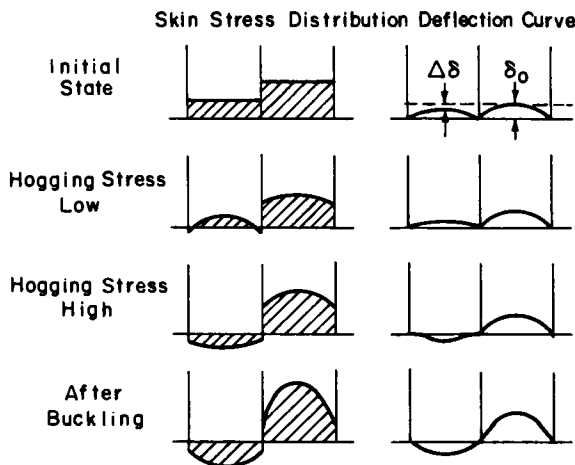


FIG. 13.12. Change in skin stress distribution and deflection curve of bottom shell.

Figure 13.12 illustrates how stresses and plate deformation change when compressive stresses are applied to a structure with irregular distortion. It has been recognized that the structure with irregular distortion is easier to buckle than the structure with regular distortion.⁽¹³⁸⁵⁾ When compressive stresses are applied to a structure with irregular distortion, the following phenomena happen:

1. While the external compressive stresses are low, distortions in all spans increase.
2. As the external compressive stresses increase, the span with small distortion tends to buckle outward, while the span with large distortion tends to bend further inward. This results in an S-shaped buckling.

Yoshiki *et al.*⁽¹³⁸⁶⁾ conducted an extensive experimental and analytical study on the buckling strength of ship-bottom plating. On the basis of the buckling strength, proposals have been made of the maximum distortion allowable in the ship-bottom plate, as shown in Fig. 13.13.

Shown here are values of δ_0/a as a function of the panel aspect ratio, $\alpha = a/b$ and

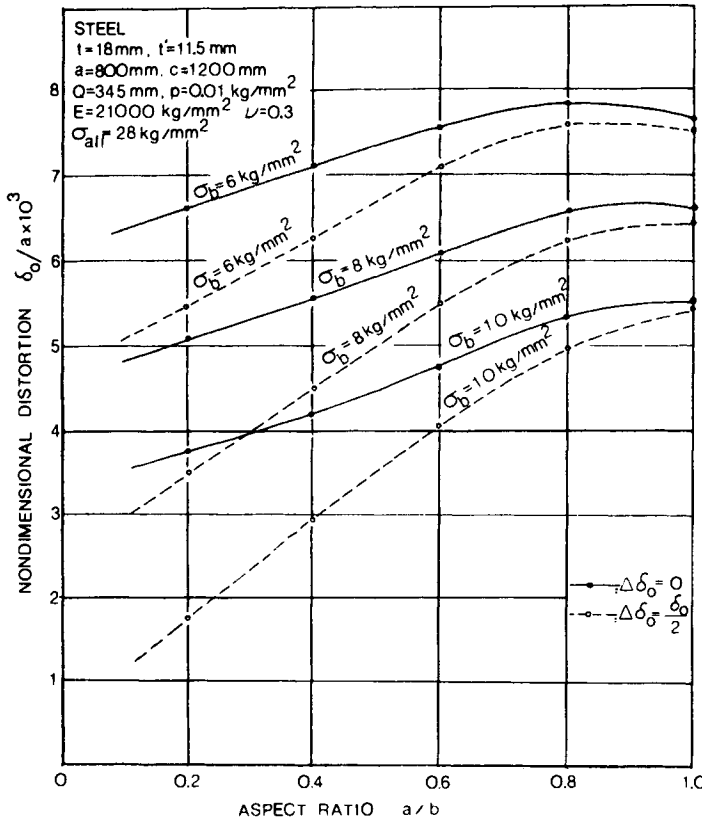


FIG. 13.13. Relationship among allowable initial distortion, δ_0/a , aspect ratio of panel, $\alpha = a/b$, and in-plane compressive stress, σ_b . ($\Delta \delta =$ difference between distortion δ_i and δ_{i+1} .)

Note: Shown here are calculations by Masubuchi *et al.*⁽²¹¹⁾ based upon the original research by Yoshiki *et al.*⁽¹³⁸⁶⁾

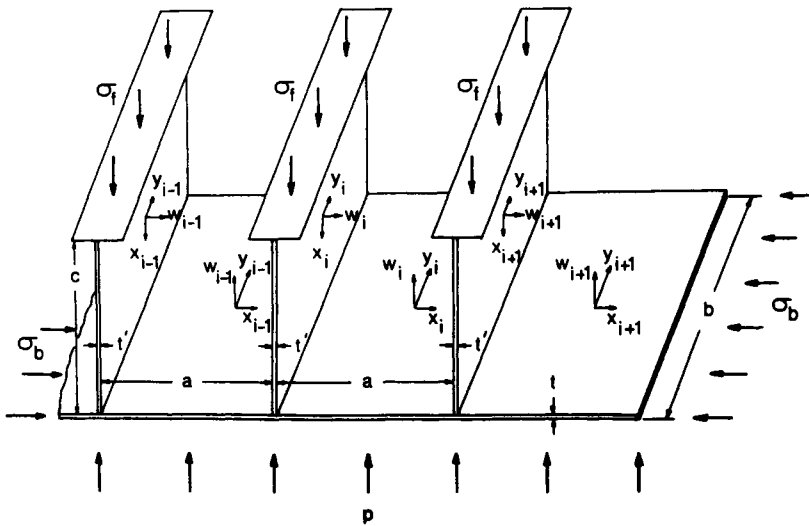


FIG. 13.14. Symbols used in buckling analysis.

compressive stresses, σ_b , where (see Fig. 13-14):

- δ_0 = allowable deflection at panel center,
- a = spacing of transverse frames,
- b = spacing of longitudinal girders,
- σ_b = compressive stresses applied to the bottom plate.

The allowable initial distortion was determined from the condition of yielding at the most stressed fiber. The yield stress of the material was assumed to be 40,000 psi (28 kg/mm²). The allowable initial distortion decreases (1) as the external compressive stress, σ_b , increases, and (2) as the value of α decreases by increasing a or by decreasing b .

Figure 13.13 shows the allowable initial distortion under the following two conditions:

1. Initial distortion is regular, or the amount of distortion is the same for every span, as shown in Fig. 13.12 ($\Delta\delta = 0$).
2. Initial distortion is irregular, or the amount of distortion varies, say $\Delta\delta = 1/2\delta_0$, as shown in Fig. 13.12.

13.3.2 Parametric study of out-of-plane distortion and its effect on buckling strength of welded panel structures

Many distortion problems are created in the design stage. Or, stated differently, distortion problems are often caused by design engineering and welding engineers are forced to solve them. At the same time, many distortion problems which may occur in later stages of fabrication could be prevented through a proper parametric study at the design stage.

Investigators at M.I.T. and the University of São Paulo, Brazil, have conducted a parametric study of out-of-plane distortion and its effect on buckling strength of welded panel structures by combining the analysis of weld distortion (discussed in Chapter 7.7) and the analysis of buckling (see Fig. 13.13).

Figure 13.15 shows a simplified flow chart of the computer program developed in this

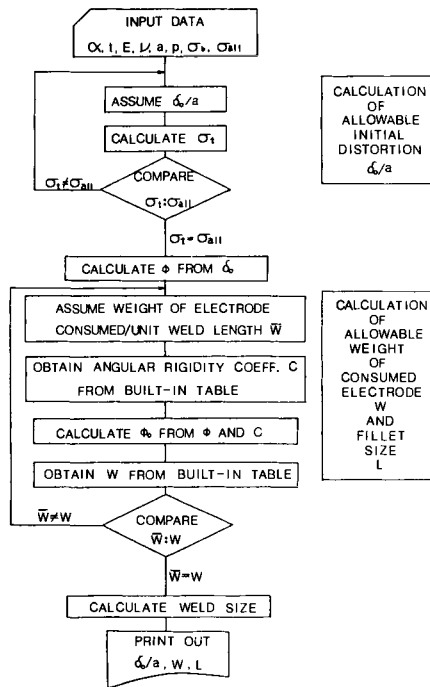


FIG. 13.15. Simplified flow chart of the computer program for parametric study of out-of-plane distortion and its effect on buckling strength of welded panel structures.

study. The first part of the program is to calculate values of allowable initial distortion, δ_0 , for a given set of structural parameters, including plate thickness, frame spacing, aspect ratio of panel, and compressive in-plane stresses, while the second part is to calculate the amount of weld needed to produce the distortion δ_0 .

Table 13.1 gives some details of mathematical derivations.

Computations were first made on low-carbon steel structures under the following conditions:

Plate thickness, $t = 12, 18, 24$ mm (0.5, 0.7 and 0.9 in.).

Spacing of transverse frames, $a = 0.5, 0.7, 1.0, 1.25, 1.5$ m (20, 27.5, 40, 50 and 60 in.).

Aspect ratio of panel, $\alpha = a/b = 0.5, 1.0, 1.5$.

In-plane compressive stress panel is subjected to, $\sigma_b = 6, 8, 10$ kg/mm² (8.5, 11.4 and 14.2 ksi or 59, 78, and 98 MN/m²),

while the following values were kept unchanged:

Allowable stress in plate, $\sigma_{all} = 28$ kg/mm² (40 ksi or 275 MN/m²).

Lateral pressure due to water, $P = 0.01$ kg/mm² (14.3 psi or 0.1 MN/m²). The allowable stress $\sigma_{all} = 28$ kg/mm² corresponds to the yield stress of steel. The lateral pressure of 0.01 kg/mm² corresponds to the water head of approximately 10 m (33 ft).

As described in Table 13.1, the allowable distortion is determined from the condition of yielding at the most stressed fiber. The total stress is calculated as a summation of:

Initial stress associated with weld distortion.

TABLE 13.1 Details of the parametric analysis of out-of-plane distortion and its effect on buckling strength of welded panel structures

The analysis of the buckling strength of a welded panel described here was originally developed by Yoshiki *et al.*⁽¹³⁸⁶⁾ However, descriptions given in this table come from the work by Masubuchi⁽²¹¹⁾ to provide better conformity with other parts of the textbook. Further details are given in reference⁽²¹¹⁾.

As shown in Fig. 13.14, a part of a ship structure is assumed to be longitudinally continuous shell plates supported by floor plates at constant intervals. The edge of the floor plates is assumed to be in a clamped condition, and the shell panels have small initial deflections produced by edge residual moments due to fillet welding.

The initial bending moment due to fillet welding is assumed to be uniformly distributed along the edge of the panels. Using the theory of thin elastic plates⁽¹³⁰²⁾, the initial deflection caused by residual moments $M_{\alpha x, i}$ and $M_{\alpha y, i}$ is obtained by:

$$w_{\alpha i}(x_i, y_i)/a = \frac{4a}{\pi^3 D_i} M_{\alpha x, i} \left\{ \sum_{n=1,3}^{\infty} (-1)^{(n-1)/2} \frac{1}{n} \phi_n(\alpha, x_i) \cos \frac{n\pi y_i}{b} + \tau_i \sum_{m=1,3}^{\infty} (-1)^{(m-1)/2} \frac{1}{m} \psi_m(\alpha, y_i) \cos \frac{m\pi x_i}{a} \right\} \quad (1)$$

where

$$\phi_n(\alpha, x) = \frac{\pi}{2n\alpha \cosh \frac{n\pi\alpha}{2}} \left(\frac{1}{2} \tanh \frac{n\pi\alpha}{2} \cosh \frac{n\pi x}{a} - \frac{x}{a} \sinh \frac{n\pi x}{a} \right),$$

$$\psi_m(\alpha, y) = \frac{\pi}{2m\alpha \cosh \frac{m\pi\alpha}{2}} \left(\frac{1}{2} \tanh \frac{m\pi\alpha}{2} \cosh \frac{m\pi y}{ab} - \frac{y}{b} \sinh \frac{m\pi y}{ab} \right),$$

$\alpha = a/b, D_i =$ flexural rigidity of plates,

$\tau_i = M_{\alpha x, i}/M_{\alpha y, i}$.

This deflection is obtained for each panel. The additional distortion, w_i , due to external loading is determined as the solution of the integral equation:

$$w_i(x_i, y_i) = w_i^*(x_i, y_i) + \int_{-a/2}^{b/2} \int_{-b/2}^{b/2} \left\{ p - \sigma_b t \frac{\partial^2 (w_i - w_{0i})}{\partial \xi_i^2} \right\} G(\xi_i, \eta_i, x_i, y_i) d\xi_i d\eta_i. \quad (2)$$

where $G(\xi_i, \eta_i, x_i, y_i)$ is Green's function of rectangular plate with simply supported edges and $w_i^*(x_i, y_i)$ is distortion of the panel produced by unknown bending moments along the continuous support to satisfy the continuity condition of the edge of the panels.

The maximum stress in shell panels occurs at the center of the panel and consists of three parts, as follows:

1. From the initial distortion, $\sigma_{\alpha x}$ and $\sigma_{\alpha y}$.
2. From the additional bending distortion due to external loading of lateral pressure, and in-plane force, σ_x and σ_y .
3. The compressive stress in the longitudinal direction, σ_b .

The total effective skin stress, $\bar{\sigma}_i$, is shown in:

$$\bar{\sigma}_i = \sqrt{\sigma_{ix}^2 - \sigma_{ix}\sigma_{iy} + \sigma_{iy}^2}$$

where

$$\sigma_{ix} = \sigma_{\alpha x} + \sigma_x + \sigma_b, \sigma_{iy} = \sigma_{\alpha y} + \sigma_y. \quad (3)$$

The allowable initial distortion may be determined from the condition of yielding at the most stressed fiber, $\bar{\sigma}_i = \sigma$ yield.

Bending stresses produced by (i) bending moment caused by application of in-plane stress, σ_b , to a plate with initial distortion, and (ii) water pressure, P .

Compressive stress produced by in-plane stress, σ_b .

Figure 13.16 shows values of (i) allowable initial deflection, $(\delta_0/a) \times 10^3$, and (ii) weight of weld metal per unit weld length, w (g/cm), and fillet size L (mm) for different values of floor spacing, a , and in-plane compressive stresses subjected to the panel, σ_b . The computations are made for plate thickness, $t = 12$ mm ($\frac{1}{2}$ in.); aspect ratio, $a/b = 1.5$;

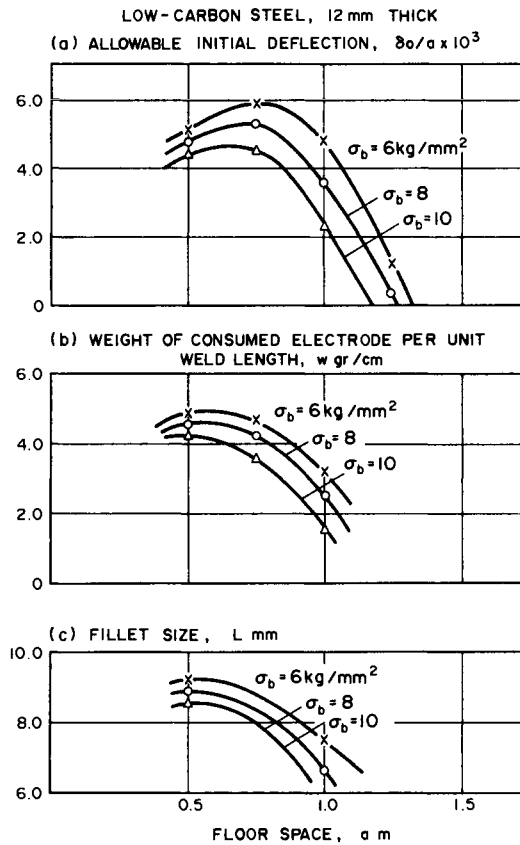


FIG. 13.16. Values of allowable initial deflection and weld size for various values of floor space and in-plane compressive stress, σ_b , for low-carbon steel plate 12 mm thick ($a/b = 1.5$, $p = 0.01 \text{ kg/mm}^2$, $\sigma_{all} = 28 \text{ kg/mm}^2$).

lateral pressure, $P = 0.01 \text{ kg/mm}^2$; and the allowable stress in the plate, $\sigma_{all} = 28 \text{ kg/mm}^2$ (40 ksi or 275 MN/m²). Figure 13.17 shows similar results for plate thickness of 18 mm (0.7 in.).

For example, when floor spacing is 750 mm and the compressive in-plane stress is 6 kg/mm^2 (8.5 ksi or 59 MN/m²), the maximum allowable initial deflection for a 12-mm ($\frac{1}{2}$ in.) thick plate is:

$$(\delta_0/a) \times 10^3 = 5.9$$

Therefore

$$\delta_0 = 5.9 \times 750 \times 10^{-3} = 4.425 \text{ mm (0.174 in.)}$$

To produce the initial distortion of 4.425 mm at the panel center, one needs 4.7 g/cm of weld or a weld size of 8.7 mm (0.34 in.). Stated differently, if the weld size is less than 8.7 mm, the initial deflection is less than 4.425 mm and, therefore, the plate will not buckle under the compressive stress of 6 kg/mm^2 .

As the in-plane stress, σ_b , increases, the allowable initial deflection decreases.

Figures 13.18 through 13.20 show similar results on aluminum structures. The

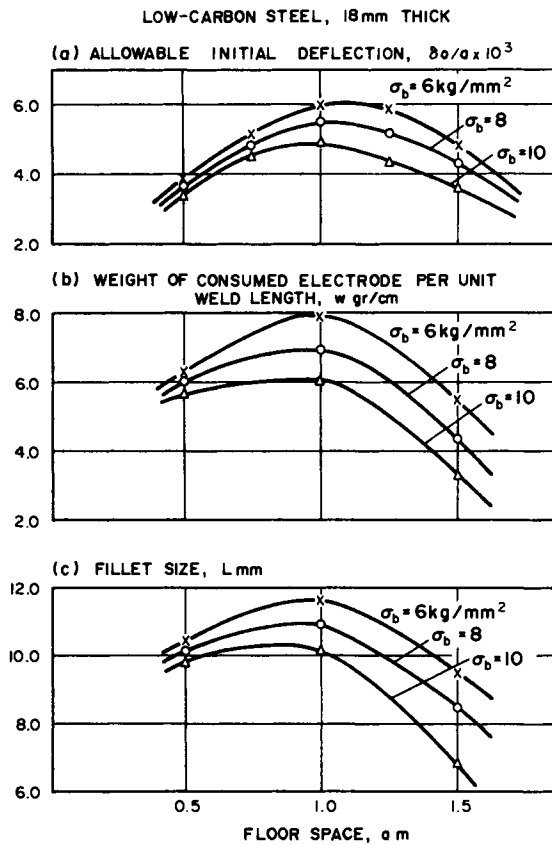


FIG. 13.17. Values of allowable initial deflection and weld size for various values of floor space and in-plane compressive stress, σ_b , for low-carbon steel plate 18 mm thick ($a/b = 1.5$, $p = 0.01$ kg/mm², $\sigma_{all} = 28$ kg/mm²).

computations are made for:

Plate thickness, $t = 9, 12$ and 15 mm (0.35, 0.5, and 0.6 in.).

Aspect ratio, $a/b = 1.0$.

Lateral pressure, $p = 0.005$ kg/mm² (7 psi or 4.8×10^4 N/M²) (corresponds to the water head of approximately 5 m or 16 ft).

Allowable in-plane stress, $\sigma_{all} = 14$ kg/mm² (20 ksi or 137 MN/m²).

Comparison with the Navy specifications. As a way to examine the validity of the parametric study, efforts have been made to compare the results of the parametric study with the allowable distortion established by the U.S. Navy. The results are presented in Section 7.7.4 (see Figs. 7.47, 7.48, and 7.49). It must be mentioned, however, that the parametric study was done for transversely framed structures, while the Navy specifications are primarily for longitudinally framed structures. More study is needed, especially on the parametric study for longitudinally framed structures.

13.4 Spherical and Cylindrical Shells Subjected to External Pressure

Spherical and cylindrical shells are widely used for pressure hulls of submersibles

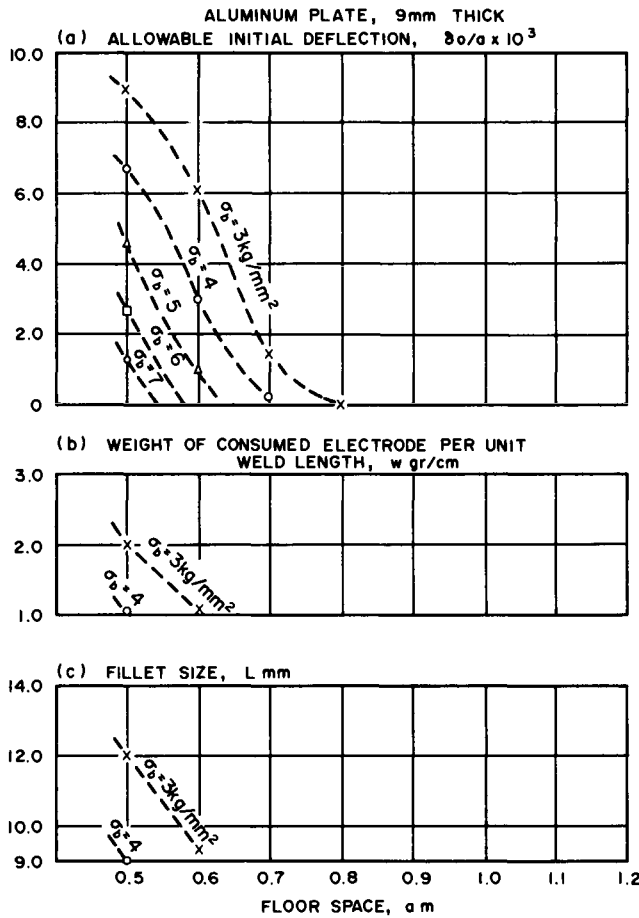


FIG. 13.18. Values of allowable initial deflection and weld size for various values of floor space and in-plane compressive stress, σ_b , for aluminum plate 9 mm thick ($a/b = 1.0$, $p = 0.5 \text{ kg/cm}^2$, $\sigma_{all} = 14 \text{ kg/mm}^2$).

and submarines. It has been well known that initial distortion and residual stresses reduce buckling strength of spherical and cylindrical shells subjected to external pressure. A number of papers have been written on this subject.⁽¹³⁸⁷⁻¹³⁹¹⁾ Discussions in the following pages come primarily from a report by Krenzke *et al.*^{(1391)†}

13.4.1 Spherical shells

The classical elastic buckling pressure, p_1 , of a spherical shell was first developed by Zoelly in 1915, and may be expressed as:^(1301, 1391)

$$p_1 = \frac{2E(h/R)^2}{\sqrt{3(1-v^2)}} = 1.21 E(h/R)^2 \quad \text{for } \nu = 0.3 \tag{3.10}$$

† The report covers discussions on prolate spheroidal shells which are not included in this book.

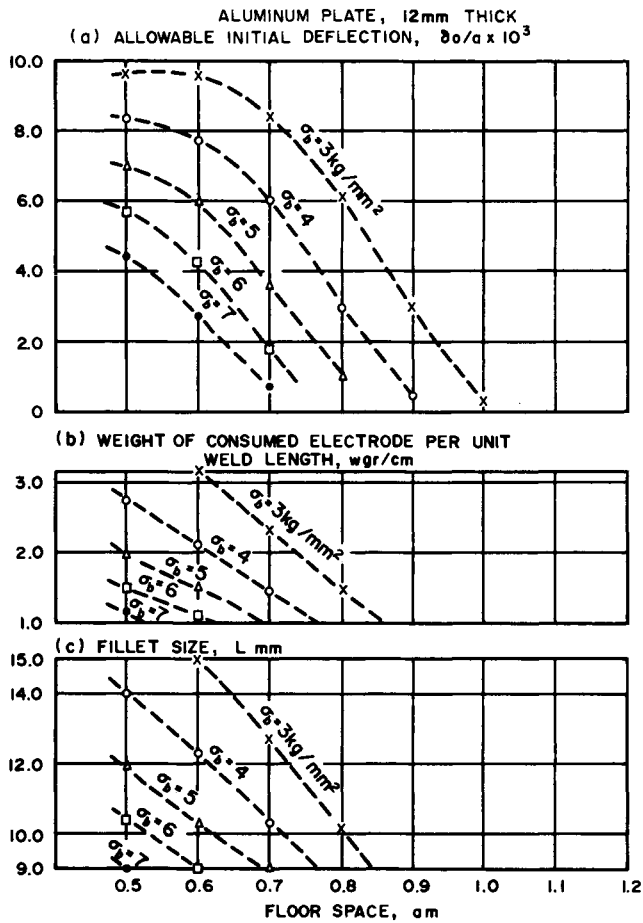


FIG. 13.19. Values of allowable initial deflection and weld size for various values of floor space and in-plane compressive stress, σ_x , for aluminum plate 12 mm thick ($a/b = 1.0$, $p = 0.5 \text{ kg/cm}^2$, $\sigma_{all} = 14 \text{ kg/mm}^2$).

where E = Young's modulus,
 ν = Poisson's ratio
 h = thickness,
 R = radius to the midsurface of the shell.

Experimental elastic collapse pressures are frequently as low as one-fourth or less of the pressure obtained from this classical theory. Recent tests have demonstrated that this large discrepancy is a result of the failure of the models to meet the idealized geometry and material assumptions of theory. The strength of those shells which fail in the inelastic region is also affected by these factors. Specific factors which decrease the strength of spherical shells include the presence of initial departures from sphericity, variations in thickness, non-isotropic material properties, adverse boundary effects and penetrations, mismatch, residual stresses, dynamic disturbances, and local loadings. Various theoretical attempts to quantitatively predict the effects of these factors have been relatively unsuccessful.

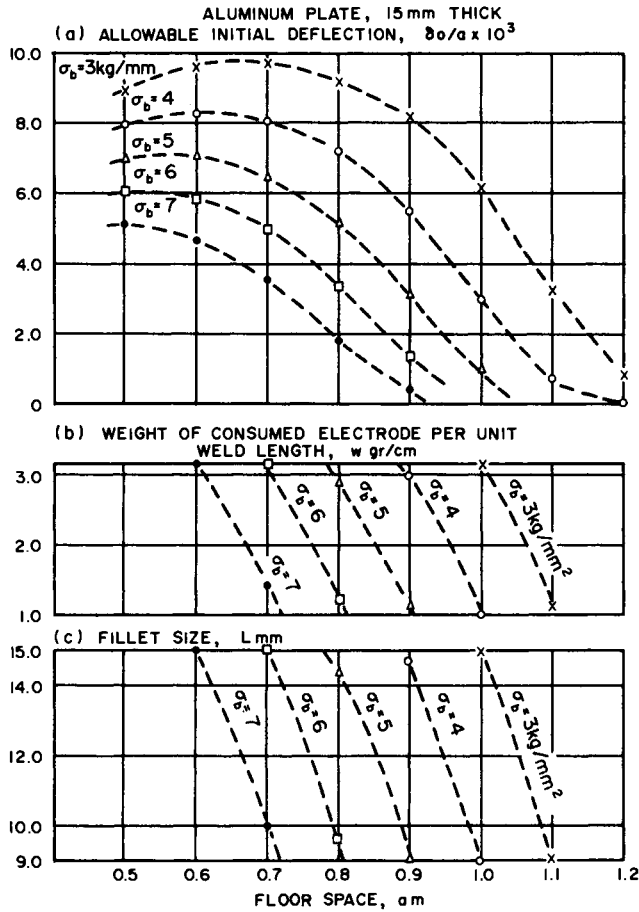


FIG. 13.20. Values of allowable initial deflection and weld size for various values of floor space and in-plane compressive stress, σ_x , for aluminum plate 15 mm thick ($a/b = 1.0$, $p = 0.5 \text{ kg/cm}^2$, $\sigma_{ult} = 14 \text{ kg/mm}^2$).

The lack of agreement between theory and experiment prompted the initiation of an extensive research program at the David Taylor Naval Ship Research and Development Center to develop reliable criteria for predicting the collapse strength of spherical shells.

As a result of the research, Krenzke *et al*, proposed that the collapse strength of both near-perfect shells and shells with initial imperfections may be predicted by the use of the following equations.⁽¹³⁹²⁾

$$P_3'' = 0.84kE \left(\frac{h_a}{R_{10}} \right)^2 \quad \text{for } \nu = 0.3, \tag{13.11}$$

$$P_E'' = 0.84k\sqrt{E_s E_t} \left(\frac{h_a}{R_{10}} \right)^2 \quad \text{for } \nu = 0.3 \tag{13.12}$$

$$\sigma'_{avg} = \frac{p(R_{10})^2}{2h_a R_1} \tag{13.13}$$

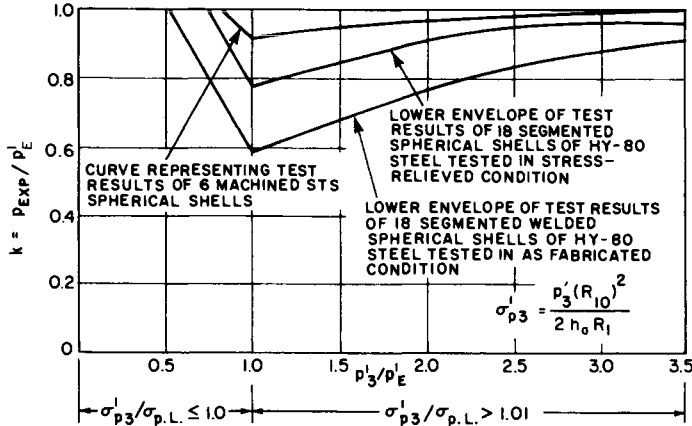


FIG. 13.21. Summary of model basin data on unstiffened spherical shells.

Note: $\sigma_{p,L}$ = proportional limit of material.

- where h_a = the average thickness over a critical arc length,
- k = an empirical coefficient based on test results and presented graphically in Fig. 13.21,
- R_{10} = the local radius to the outside surface of the shell over a critical arc length,
- E_s = the secant modulus,
- E_t = the tangent modulus,
- R_1 = the local radius to the midsurface of the shell over a critical arc length.

Equation (13.11) is utilized for the elastic buckling case; eqn. (13.12) for the inelastic stress region. Equation (13.13) is used to calculate the stress in the shell and is needed to solve eqn. (13.12). The primes in eqns. (13.11) through (13.13) indicate that the local geometry is used to calculate pressures and stresses.

For stress-relieved shells, the k -value used in eqns. (13.11) and (13.12) is described by the lower envelope of test results of the stress-relieved HY-80 steel shells presented in Fig. 13.21.

Similarly, the lower envelope of test results of the HY-80 steel shells tested in the “as-fabricated” condition (Fig. 13.21) was used to determine the k -value for spherical shells with residual fabrication stresses.

13.4.2 Cylindrical shells

For the determination of metallic ring-stiffened cylinder geometries, the following criteria were established:

1. *Axisymmetric shell failure.* The inelastic axisymmetric shell buckle strength for those shells which had a ratio of elastic to inelastic collapse pressure of less than 6 was calculated by the equation:

$$p_{ML} = p_{OL} + 0.2(p_{EL}/p_{OL} - 1.0)(p_L - p_{OL}) \tag{13.14}$$

- where p_L is Lurchick’s inelastic axisymmetric shell buckle pressure,⁽¹³⁹³⁾
- p_{EL} is Lurchick’s elastic axisymmetric shell buckle pressure,⁽¹³⁹³⁾
- and p_{OL} is Lurchick’s inelastic axisymmetric shell-buckle pressure modified by using midlay outside stresses rather than membrane stresses.

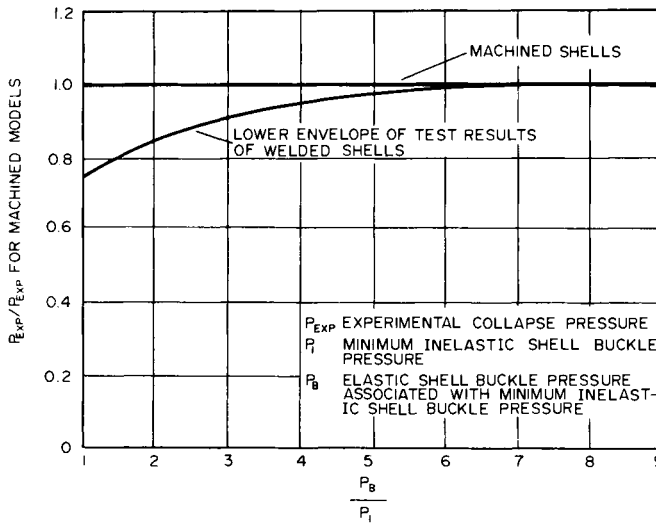


FIG. 13.22. A comparison of model basin data on machined ring-stiffened cylinders with welded cylinders.⁽¹³⁹²⁾

Lunchick’s inelastic shell buckle theory was used without modification for those shells having a ratio of elastic to inelastic strength greater than 6. The effects of residual stresses on the collapse strength were estimated from Fig. 13.22 by calculating the ratio of elastic to inelastic pressures and determining the collapse pressure reductions factor from the lower envelope of test results for welded shells.

2. *Asymmetric shell failure.* Both elastic and inelastic shell failures were calculated according to the theories of Reynolds.⁽¹³⁹⁴⁾ The effects of residual stresses were estimated using Fig. 13.22 in the manner described above.

3. *General instability failure.* The elastic and inelastic general instability pressures were calculated⁽¹³⁹⁵⁾ using the equation:

$$p_{st} = (E_s E_t)^{1/2} \frac{h}{R} \frac{\lambda^4}{(n^2 + \lambda^2/2 - 1)(n^2 + \lambda^2)^2} + \frac{E_t I_e}{L_f R_0 R_{cg}^2} (n^2 - 1) \tag{13.15}$$

where h is the shell thickness,

- I_e is the moment of inertia about the centroid of a section comprising one frame plus an effective length of shell,
- L_b is the bulkhead spacing,
- L_f is the typical frame spacing,
- n is the number of circumferential waves,
- R is the radius to the midsurface of the shell,
- R_0 is the outside radius of the shell,
- R_{cg} is the radius to the neutral axis of the frame, effective shell combination,

and
$$\lambda = \frac{\pi R}{L_b}.$$

The effects of residual stresses and imperfections on the general instability mode of

welded cylinders were assumed to be the same as those for the shell failure mode as shown in Fig. 13.22. Due to the uncertainties in this area, failure in the general instability mode was set at 1.05 times the design collapse pressure. The deep frames were designed to provide a ratio of elastic stability pressure in the overall mode to design collapse pressure of 1.5. The contribution of hemispherical end closures in resisting general instability failure was neglected. Strength of the deep frames was determined by the equation:

$$p_{DF} = \frac{3 EI_{DF}}{L_b R_o R_{DF}^2} \quad (13.16)$$

where I_{DF} is the moment of inertia about the centroid of a section comprising one deep frame and an effective length of shell, and R_{DF} is the radius to the neutral axis of such a section.

4. *Shell stresses at the frame.* The maximum stresses in the shell at the frame and in the flange of typical bay geometry as calculated by the analysis of Salerno and Pulos⁽¹³⁹⁶⁾ were not allowed to exceed 75% of the yield strength of the material at operating depth in order to:

- (a) Permit a reasonable chance of keeping the maximum stresses in the areas of structural details below the yield point of the material at operating depth and thus to account for, in a very general way, low-cycle fatigue, creep, stress corrosion, etc.
- (b) Ensure a reasonable stress level in the frame flange prior to collapse for those shells with initial out-of-roundness.

5. *Frame web buckling stress.* The elastic buckling stress in the frame webs was calculated⁽¹³⁹⁷⁾ according to:

$$\sigma_w = \frac{\pi^2 E}{2.73} (t/d)^2 \quad \text{for } \nu = 0.3 \quad (13.17)$$

where d is the web depth and t is the web width. This stress was set at a minimum of 3 times the yield strength of the material.

References

- (1301) TIMOSHENKO, S. and GERE, J. M., *Theory of Elastic Stability*, McGraw-Hill Book Co., Inc., New York, 1961.
- (1302) TIMOSHENKO, S. and WINOWSKY-KREIGER, S., *Theory of Plates and Shells*, McGraw-Hill Book Co., Inc., New York, 1959.
- (1303) BLEICH, H., *Buckling Strength of Metal Structures*, McGraw-Hill Book Co., Inc., New York, 1952.
- (1304) OSGOOD, W. R., *Residual Stresses in Metals and Metal Construction*, published by Reinhold Publishing Corporation, New York, 1954.
- (1305) JOHNSTON, B. G., *Guide to Design Criteria for Metal Compression Members*, Column Research Council, published by John Wiley & Sons, Inc., New York, 1966.
- (1306) YOSHIKI, M., YAMAMOTO, Y., ANDO, N., and KAWAI, T., *Studies on the Buckling Strength of Ship Structures*, Vol. 12 of the 60th Anniversary Series of the Society of Naval Architects of Japan, Tokyo, 1966.
- (1307) HELLER, S. R., Director, Graduate Course on *Analysis and Design of Cylindrical Shells under Pressure*, sponsored by the Institute of Ocean Science and Engineering, The Catholic University of America, Washington, D.C. 20017, 14–18 June 1971.
- (1308) EVANS, J. H., Editor, *Ship Structural Design Concepts*, Cornell Maritime Press, Inc., Cambridge, Maryland, 1975.

- (1309) SINGH, M. P. and ANG, A. H. S., "Columns with random imperfections and associated bracing requirements", *Journal of Structural Mechanics*, **4** (2), 161–180 (1976).
- (1310) NETHERCOT, D. A., "Buckling of welded hybrid steel I-beams", *ASCE Journal of the Structural Division*, **102** (3), 461–474 (Mar. 1976).
- (1311) ROORDA, J., "Random nature of column failure", *Journal of Structural Mechanics*, **3** (2), 239–257 (1974–1975).
- (1312) BALLIC, G., PETRINI, V., and UBANO, C., "Loading effects in beam columns", *Meccanica*, **9** (4), 265–273 (Dec. 1974).
- (1313) YOUNG, B. W. and ROBINSON, K. W., "Buckling of axially loaded welded steel columns", *Structural Engineering*, **63** (5), 203–207 (May 1975).
- (1314) SKALOUD, M. and NAPRSTEK, J., "Theoretical investigation into the limiting state of thin-walled steel columns", *Acta Technica CSAV*, **20**, (1), 45–72 (1975).
- (1315) GILBERT, R. B. and CALLADINE, C. R., "Interaction between the effects of local and overall imperfections on the buckling of elastic columns", *Journal of the Mechanics and Physics of Solids*, **22** (6), 519–540 (Dec. 1974).
- (1316) CALLADINE, C. R., "Inelastic buckling of columns: the effect of imperfections", *International Journal of Mechanical Science*, **15** (7), 593–604 (July 1973).
- (1317) CULVER, C., AGGRAWAL, V., and OSSENBRUGGEN, P., "Buckling of steel columns at elevated temperatures", *ASCE Journal of the Structural Division*, **99**, No. ST4, Paper No. 9682, pp. 715–726 (Apr. 1973).
- (1318) CULVER, C. G., "Steel column buckling under thermal gradients", *ASCE Journal of the Structural Division*, **98**, No. ST8, Paper No. 9150, pp. 1853–1865 (Aug. 1972).
- (1319) AOKI, T. and FUKUMOTO, Y., "Scatter in buckling strength of steel columns effect of residual stress distributions", *Proceedings of the Japanese Society of Civil Engineering*, No. 201, pp. 31–41 (May 1972) (in Japanese).
- (1320) BEER, H. and SCHULZ, G., "Theoretical basis of European buckling curves", *Const. Metal*, no. 3, pp. 37–57 (Sept. 1970) (in Japanese).
- (1321) CHUNG, B. T. and LE, G. C., "Buckling strength of columns based on random parameters", *ASCE Journal of the Structural Division*, **97**, No. ST7, paper No. 8259, pp. 1927–45 (July 1971).
- (1322) NISHINO, F., TALL, L., and OKUMURA, T., "Residual stress and torsional buckling strength of H and cruciform columns", *Japan Society Civil Engineers, Trans.*, no. 160, pp. 75–87 (Dec. 1968).
- (1323) HORNE, M. R., MONTAGUE, P., and Narayanan, R., "Influence on strength of compression panels of stiffener section, spacing and welded connection", *Proceedings of the Institute of Civil Engineering*, (London), **63** (2), 1–20 (Mar. 1977).
- (1324) MAEDA, Y. and HIKASA, T., "Analysis of buckling at stiffened plates with residual stresses", *Technological Report Osaka University*, **26**, (1276–1307), 299–309 (1976).
- (1325) TULK, J. D. and WALKER, A. C., "Model studies of the elastic buckling of a stiffened plate", *Journal Strain Analysis and Engine Design*, **11** (3), 137–143 (July 1976).
- (1326) INGRARSSON, L., "Cold-forming residual stresses, effect on buckling", *Int. Spec. Conf. on Cold-formed Steel Struct. 3rd Proc.: Res. and Dev. in Cold Formed Steel Des. and Constr.*, St. Louis, Mo., 24–25 Nov. 1975, vol. 1, pp. 85–119, publ. by Uni. of Moscow, Dept. of Div. Eng., Rolla, 1975.
- (1327) CRISFIELD, M. A., "Full-range analysis of steel plates and stiffened plating under uniaxial compression", *Proceedings of the Institute of Civil Engineering*, (London), **59**, pt. 2, pp. 595–624 (Dec. 1975).
- (1328) NEALE, K. W., "Effect of imperfections on the plastic buckling of rectangular plates", *Journal of Applied Mechanics, Transactions, ASME*, vol. 42, Ser. E no. 1, pp. 115–120 (Mar. 1975).
- (1329) PRAWEL, S. P., MORRELL, M. L., and LEE, G. C., "Bending and buckling strength of tapered structural members", *Welding Journal*, **53** (2), 75s–84s (Feb. 1974).
- (1330) TVERGAARD, V., "Imperfection—sensitivity of a wide integrally stiffened panel under compression", *International Journal of Solids Structures*, **9** (1), 177–192 (Jan. 1973).
- (1331) RUSHTON, K. R., "Buckling of laterally loaded plates having initial curvature", *International Journal of Mechanical Science*, **14**, (10), 667–680 (Oct. 1972).
- (1332) MANSOUR, A., "Post-buckling behavior of stiffened plates with small initial curvature under combined loads", *International Shipbuilding Progress*, **18**, (202), 217–240 (June 1971).
- (1333) DAWSON, R. G. and WALKER, A. C., "Post-buckling of geometrically imperfect plates", *ASEC Journal of the Structural Division*, **98**, no. ST1, Paper 8630, pp. 75–94 (Jan. 1972).
- (1334) SHERBOURNE, A. N. and KOROL, R. M., "Ultimate strength of plate in uniaxial compression", *ASCE, Nat. Struct. Eng. meeting*, Baltimore, MD., 19–23 April 1971. Prepr. 1386, 20 pp.
- (1335) SHERMAN, D., "Residual stresses and tubular compression members", *ASCE Journal of the Structural Division*, **97**, no. ST3, Paper 8001, pp. 891–904 (Mar. 1971).
- (1336) STEUP, H., "Effect of the initial deformations and the residual stresses on the buckling of plates in the post-critical range", *International Association for Bridge and Structural Engineering*, **29**, pt. 1, pp. 73–93 (1969) (in German).
- (1337) FUKUMOTO, Y. and ITO, Y., "Flange local buckling strength of plate girders", *Japan Society of Civil Engineers, Trans.*, no. 160, pp. 27–38 (Dec. 1968) (in Japanese).

- (1338) MOXHAM, K. E., *Theoretical Prediction of the Strength of Welded Steel Plates in Compression*, University of Cambridge, Eng. Dept., Technical Report Bulletin TR. 2, 1971.
- (1339) MOXHAM, K. E., *Buckling Tests on Individual Welded Steel Plates in Compression*, University of Cambridge, Eng. Dept. Technical Rep. Bulletin TR. 3, 1971.
- (1340) SHEINMAN, I. and SEMITSES, G. J., "Buckling analysis of geometrically imperfect stiffened cylinders under axial compression", *AIAA Journal*, **15**, (3), 374–382 (Mar. 1977).
- (1341) ALLAN, T., "Local buckling behavior of certain shell forms", IASS (Int. Ass. of Shell and Space Struct.), *World Congress on Space Enclosures (WCOSE-76)*, Montreal, Que., July 4–9, 1976, published by Concordia University, Bldg. Res. Ctr., Montreal, Que., 1976, vol. 1, pp. 365–375.
- (1342) HANSEN, J. S., "Influence of general imperfections in axially loaded cylindrical shells", *International Journal of Solids and Structures*, **11** (11), 1223–1233 (Nov. 1975).
- (1343) TALASIDIS, D., "Application of statistical methods in analysis of stability of imperfection-sensitive shells", *Konstruktion und Ingenieurbau*, Ber., no. 25–26, pp. 151–163 (1976) (in German).
- (1344) ARBOCZ, J. and Sechler, E. E., "On the buckling of stiffened imperfect cylindrical shells", *AIAA Journal*, **14**, 1611–1617 (Nov. 1976).
- (1345) GRISTCHAK, V. Z., "Asymptotic Formula for the buckling stress of axially compressed circular cylindrical shells with more or less localized shortwave imperfections", *Tech. Hogesch. Delft, Afd. Werktuigbouwkd.* (Rep.), WTHD, no. 88 (Sept. 1976).
- (1346) BOROS, I. E., "Effect of shape imperfections on the buckling of stiffened cylinders", Toronto Univ. Inst. Aersp. Stud UTIAS, Tech. Note, No. 200, May 1975.
- (1347) BAULD, N. R., JR., "Imperfection sensitivity of axially compressed stringer reinforced cylindrical sandwich panels", *International Journal of Solids Structures*, **10** (8), 883–902 (Aug. 1974).
- (1348) KEENER, J. P., "Buckling imperfection sensitivity of columns and spherical caps", *Quarterly of Applied Mathematics*, **32** (2), 173–188 (July 1974).
- (1349) AMAZIGO, J. C., "Asymptotic analysis of the buckling of externally pressurized cylinders with random imperfections", *Quarterly of Applied Mathematics*, **31**, (4), 429–442 (Jan. 1974).
- (1350) BHATIA, P. and BABCOCK, C. D., "Axial buckling of cylindrical shells with prismatic imperfections", *Journal of Applied Mechanics, Trans. ASME*, **41**, Ser. E, no. 3, 731–736 (Sept. 1974).
- (1351) PALASSOPOULOS, G. V., "On the buckling of axially compressed thin cylindrical shells", *Journal of Structural Mechanics*, **2** (3), 177–193 (1972).
- (1352) BRAUNS, Y. A. and RIKARDS, R. B., "Investigation of the initial imperfections and buckling modes of glass-reinforced plastic shells under hydrostatic pressure", *Polymer Mechanics*, **7** (6), 940–945 (Nov.–Dec. 1971).
- (1353) BALL, R. E. and RYAN, B. A., "Computer analysis of buckling of imperfect shells", *ASCE Journal of the Structural Division*, **99**, no. ST10, Paper 10072, pp. 2097–2108 (Oct. 1973).
- (1354) SINGER, J., "Buckling of integrally stiffened cylindrical shells—a review of experiment and theory", Contrib. to the *Theory of Aircraft Structures*, pp. 325–357. Publ. for Delft Univ. Press, Neth., 1972. Distributed by Int. Scholarly Book Serv., Inc., Portland, Oregon.
- (1355) BUDIANSKY, B. and HUTCHINSON, J. W., "Buckling of circular cylindrical shells under axial compression", Contrib. to the *Theory of Aircraft Structures*, pp. 239–259, *ibid*.
- (1356) TERNDRUP, P. P., "Buckling of unstiffened and ring stiffened cylindrical shells under axial compression", *International Journal of Solids Structure*, **9** (5), 671–691 (May 1973).
- (1357) KAO, R., "Note on buckling of spherical caps with initial asymmetric imperfections", *Journal of Applied Mechanics, Transactions of the ASME*, **39**, Ser. no. 3, pp. 842–844 (Sept. 1972).
- (1358) ROORDA, J., "Buckling of shells: an old idea with a new twist", *ASCE Journal of the Engineering and Mechanics Division*, **98**, No. EM3, Paper 8951, pp. 531–538 (June 1972).
- (1359) AMAZIGO, J. C. and BUDIANSKY, B., "Asymptotic formulas for the buckling stresses of axially compressed cylinders with localized on random axisymmetric imperfections", *Journal of Applied Mechanics, Trans. ASME*, **39**, Ser. E, no. 1, pp. 179–184 (Mar. 1972).
- (1360) HUTCHINSON, J. W., "On the postbuckling behavior of imperfection-sensitive structures in the plastic range", *ASME Paper 71-APM-FF*, 1971.
- (1361) AMAZIGO, J. C. and FRANSEY, W. B., "Buckling under external pressure of cylindrical shells with dimple shaped initial imperfections", *International Journal of Solids Structure*, **7** (8), 883–900 (Aug. 1971).
- (1362) STEPHENS, W. B., "Imperfection sensitivity of axially compressed stringer reinforced cylindrical panels under internal pressure", *AIAA Journal*, **9** (9), 1713–1719 (Sept. 1971).
- (1363) TENNYSON, R. C., MUGGERIDGE, D. B., and CASWELL, R. D., "New design criteria for predicting buckling of cylindrical shells under axial compression", *Journal of Spacecraft Rockets*, **8** (10), 1962–1967 (Oct. 1971).
- (1364) TENNYSON, R. C., MUGGERIDGE, D. B., and CASWELL, R. D., "Buckling of circular cylindrical shells having axisymmetric imperfection distributions", *AIAA Journal*, **9**, (5), 924–930 (May 1971).
- (1365) COHEN, G. A., "Computer analysis of imperfection sensitivity of ring-stiffened orthotropic shells of revolution", *AIAA Journal*, **9** (6), 1032–1039 (June 1971).

- (1366) KOO, R. and PERRONE, N., "Asymmetric buckling of spherical caps with asymmetrical imperfections", *Journal of Applied Mechanics, Trans. ASME*, **38**, Ser. E, no. 1, 172-178 (Mar. 1971).
- (1367) TURULA, P. and CHU, K. H., "Buckling of open cylindrical shells with imperfections", *ASCE Journal of Engineering and Mechanics Division*, **96**, N. EM6, Paper 7733, pp. 1125-1142 (Dec. 1970).
- (1368) ARBOCZ, J. and BABCOCK, C. D., JR., "Effect of general imperfections on the buckling of cylindrical shells", *ASME*, Paper 69-APM-6 for meeting 16-18 June 1969.
- (1369) TALL, L., HUBER, A. W., and BEEDLE, L. S., "Residual stress and the instability of axially loaded columns", a paper presented to a colloquium on the Influence of residual Stresses on Stability of Welded Structures and Structural Members, held at the 1960 Annual Meeting of Commission X of the IIW.
- (1370) HORNE, M. R., "The Effect of residual stresses on the behavior of continuous structures", a paper presented to a colloquium on the Influence of Residual Stresses on Stability of Welded Structures and Structural Members, held at the 1960 Annual Meeting of Commission X of the IIW.
- (1371) KIHARA, H. and FUJITA, Y., "The influence of residual stresses on the instability problems", a paper presented to a colloquium on the Influence of Residual Stresses on Stability of Welded Structures and Structural Members, held at the 1960 Annual Meeting of Commission X of the International Institute of Welding.
- (1372) "The effect of residual stresses on instability phenomena in metallic structures", *Welding Research Abroad*, **10** (10), 63-67 (1964).
- (1373) FUJITA, Y., "Ultimate strength of columns with residual stresses", *Journal of the Society of Naval Architects of Japan*, **102** (1958), and **107** (1960).
- (1374) BRUNGRABER, R. J. and CLARK, J. W., "Strength of welded aluminum columns", *Journal of the Structural Division*, Proceedings of the American Society of Civil Engineers, pp. 33-57 (Aug. 1960).
- (1375) YOSHIKI, M., FUJITA, Y., and KAWAI, T., "Influence of residual stresses on the buckling of plates", *Journal of the Society of Naval Architects of Japan*, **107** (1960).
- (1376) FUJITA, Y. and YOSHIDA, K., "Plastic design in steel structures (4th Report), Influence of residual stresses on the plate instability", *Journal of the Society of Naval Architects of Japan*, **115** (1964).
- (1377) NISHINO, F., UEDA, Y., and TALL, L., "Experimental investigation of the buckling of plates with residual stresses", *Test Methods for Compression Members*, ASTM, STP 419, 12, 1967.
- (1378) DWIGHT, J. B., CHIN, T. K., and RATCLIFFE, A. T., *Local Buckling of Thin Walled Columns, Effect of Locked-in Welding Stresses*, CIRIA, Res. Report No. 12, Part 1, May 1968.
- (1379) BECKER, H., GOLDMAN, J., and PAZERYCKI, J., *Compressive Strength of Ship Hull Girders, Part 1: Unstiffened Plates*, Ship Structure Committee Report SSC-217, 1970.
- (1380) FAULKNER, D., "Compression strength of welded ship panels", M.I.T. Department of Ocean Engineering Report 71-S (to be published; see also RINA, 1972).
- (1381) FAULKNER, D., "Welding stresses in ship panels", unpublished manuscript.
- (1382) MURRAY, J. M., "Corrugation of bottom shell plating", *Transactions of the Institute of Naval Architects*, London, 1954, vol. 94, pp. 229-250.
- (1383) *Report of Ship's Hull Failures Investigation Committee*, Nippon Kaiji Kyokai. (Japanese Ship Classification Society), 1954.
- (1384) *Investigation on the Corrugation Failure of Bottom Plating of Ships*, Report No. 19 of the Shipbuilding Research Association of Japan, Tokyo, June 1967.
- (1385) AKITA, Y., and YOSHIMOTO, K., "Effect of bottom unfairness on bottom plate buckling", *Journal of the Society of Naval Architects of Japan*, **95** (1954).
- (1386) YOSHIKI, M., KANAZAWA, T., and ANDO, N., "A study on the strength of ship's bottom platings", *Proceedings of the Second Congress of Theoretical and Applied Mechanics, New Delhi*, 15-16 Oct. 1956.
- (1387) GALLETLY, G. D., and BART, R., "Effects of boundary conditions and initial out-of roundness on the strength of thin-walled cylinders subject to external hydrostatic pressure", *Journal of Applied Mechanics*, **23**, 351-358 (1956).
- (1388) NASH, W. A., "Effect of large deflections and initial imperfections on the buckling of cylindrical shells subjected to hydrostatic pressure", *Journal of Aeronautical Sciences*, **22** 264-269 (1955).
- (1389) DONNELL, L. H., "Effect of imperfections on buckling of thin cylinders under external pressure", *Journal of Applied Mechanics*, **23**, 569-575 (1956).
- (1390) CICALA, P., "The effect of initial deformations on the behavior of a cylindrical shell under axial compression", *Quarterly of Applied Mathematics*, **9**, 273-293 (1951).
- (1391) KRENZKE, M. et al, *Potential Hull Structures for Rescue and Search Vehicles of the Deep-Submergence Systems Project*, David Taylor Model Basin, Washington, D.C., Mar. 1965, available through the Defense Documentation Center AD 614 632.
- (1392) KRENZKE, M. A. and KIERNAN, T. J., *The Effect of Initial Imperfections on the Collapse Strength of Deep Spherical Shells*, David Taylor Model Basin Report 1757 (Feb. 1965).
- (1393) LUNCHICK, M. E., *Plastic Axisymmetric Buckling of Ring-stiffened Cylindrical Shells Fabricated from Strain-hardening Materials and Subjected to External Hydrostatic Pressure*, David Taylor Model Basin Report 1393 (Jan. 1961).

- (1394) REYNOLDS, T. E., *Inelastic Lobar Buckling of Cylindrical Shells under External Hydrostatic Pressure*, David Taylor Model Basin Report 1392 (Aug. 1960).
- (1395) KRENZKE, M.A. and KIERNAN, T. J., *Structural Development of a Titanium Oceanographic Vehicle for Operating Depths of 15,000 to 20,000 Feet*, David Taylor Model Basin Report 1677 (Sept. 1963).
- (1396) SALERNO, J. L. and PULOS, J. G., *Stress Distribution in a Circular Cylindrical Shell Under Hydrostatic Pressure Supported by Equally Spaced Circular Ring Frames*, Polytechnic Institute of Brooklyn Aeronautical Laboratory Report 171-A (June 1951).
- (1397) SEELY, F. and SMITH, V., *Advanced Mechanics of Materials*, Second Edition, John Wiley & Sons, Inc., New York, 1955.

Weld Cracking and Joint Restraint

A LARGE amount of research, primarily experimental and metallurgical, has been conducted to investigate cracks in weldments. Weld cracking occurs for one or both of the following reasons:

1. The material is brittle.
2. High tensile stresses (transient or permanent) are present.

Metallurgical studies tend to concentrate on material brittleness caused by welding, while mechanical studies tend to concentrate on the stresses produced during welding. There have been several books and reviews on metallurgical aspects of weld cracking. ^(239, 240, 1016, 1401) For example, DMIC Report 197 presents a critical review of various theories of weld cracking. ⁽¹⁰¹⁶⁾ However, only a few books have discussed extensively the mechanical aspects of welding cracking. ^(507, 703) An obvious reason is the difficulty in analytically determining stresses in a weldment, especially in the weld metal and the heat-affected zone. This chapter discusses primarily mechanical aspects of weld cracking.

Discussions in this chapter are concerned primarily with cracks in weldments in steel, especially high-strength steels. Some of the fundamental aspects should also be applicable to weld cracks in other materials.

14.1 Classification of Weld Cracks

Cracks in a weldment may occur during or immediately after welding, and they may also occur long after welding is completed and even during service. The two general classifications by which all weldment cracks can be described are (1) appearance and location, and (2) conditions of formation. Classification by appearance can be broken down into visual, X-ray, and microscopic appearance. Visual appearance can further be subdivided into classification by location, orientation, and size.

14.1.1. Classification of weld cracks by appearance and location

Three different types of cracks occur in the weld metal (see Fig. 14.1); ^(1121, 1402)

Transverse weld metal cracks. These cracks are perpendicular to the axis of the weld and in some cases have been observed to extend beyond the weld metal into the base metal.

Longitudinal weld metal cracks. These cracks are predominantly within the weld metal and are usually confined to the center of the weld. Such cracks may occur as the

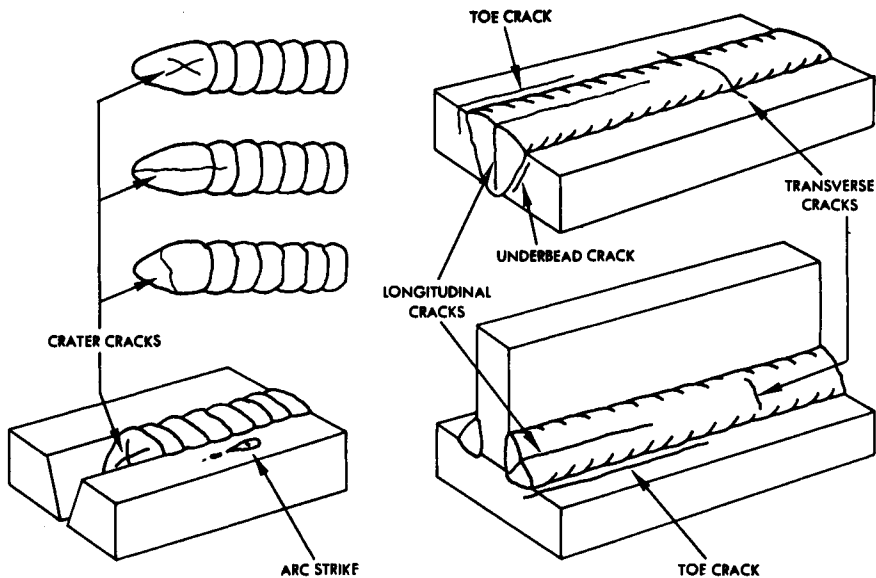


FIG. 14.1. Cracks in welded joints.⁽¹¹²¹⁾

Note: The underbead crack, limited mainly to steel, is a base metal crack usually associated with hydrogen. Toe cracks in steel can be of similar origin. In other metals (including stainless steel) cracks at the toe are often termed edge-of-weld cracks, attributable to hot cracking in or near the fusion line. Arc strikes are from accidental touching of the electrode to the work and may have small cracks. Crater cracks are shrinkage cracks from stopping the arc suddenly.

extension of crater cracks formed at the end of the weld. They may also occur as the extension through successive layers of a crack that existed in the first layer deposited. If a crack is formed in the first layer and is not removed or completely remelted when the subsequent layer is deposited, it tends to progress into the layer above and thence into the next adjacent layer and finally may appear at the surface.

Crater cracks. Whenever the welding operation is interrupted there is a tendency for the formation of cracks in the crater. These cracks are usually star-shaped and proceed only to the edge of the crater. However, they may be starting points for longitudinal weld cracks, particularly when they occur in the crater that is formed at the end of the weld.

Two types of base metal cracking can occur as a result of the welding operation:

Transverse base metal cracks. The type of cracking that is transverse to the direction of welding is usually associated with fillet welds on steels of high hardenability where the distance between the edge of the weld and the exposed edge of one plate is relatively small.

Longitudinal base metal cracks. These cracks are parallel to the weld and are in the base metal. They may be extensions of underbead cracks. For fillet welds, longitudinal base metal cracks may be divided into two types:

1. Toe cracks, which proceed from the toe of the fillet weld through the base metal, often starting from undercuts.

2. Root cracks, which proceed from the root of the fillet weld and progress through the base metal, being evident occasionally on the opposite side.

In the case of groove welds, cracks are more likely to occur in the heat-affected zone adjacent to the weld. Cracks may also occur at the edge of the weld in the zone of fusion between the weld metal and base metal. Usually this type of crack is associated with steels of high hardenability when weld metal and base metal are entirely different in composition, thereby promoting the formation of alloys of unpredictable properties in the zone of fusion.

14.1.2 *Classification of weld cracks by conditions of formation*

Cracks which form at temperatures near the bulk solidus temperature are called hot cracks. If a hot crack is open to the atmosphere, its surfaces are usually discolored by oxidation. Frequently, the surfaces at the tip of a hot crack will be smooth as a result of its formation while portions of the weldment were molten. Cold cracks are formed at much lower temperatures, generally below about 400°F (204°C). Their surfaces are bright and free of oxides right after formation. The term “delayed crack” is sometimes applied to cracks which form some time after the weldment has cooled to room temperature. Delayed cracks are a special type of cold crack.

14.2 Hot Cracking

Hot cracking occurs at temperatures near the melting point during or immediately after welding. Hot cracks occur in the weld metal and in the heat-affected zone immediately adjacent to the fusion zone. Hot cracks are inter-granular fractures.

Figure 14.2 shows hot cracking in a restrained fillet weld.⁽²³⁹⁾

14.2.1 *Mechanisms of hot cracking in the weld metal*

The phase diagram provides the interpretation of hot cracking and segregation. An alloy of 95% A, 5% B with a long freezing range (Fig. 14.3 [left]) commences to freeze at T_1 , depositing a crystal containing 1% B. Upon reaching temperature T_3 near the end of solidification, the alloy consists of crystals separated by thin films of liquid. In this condition the alloy is susceptible to hot cracking under the high shrinkage stresses generated by the contracting mass of metal during the long cooling period. Alloys with a short freezing range exhibit little tendency toward hot cracking during welding.

The first solid to be deposited by the 5% alloy in Fig. 14.3 (left) contains only 1% B. The last liquid to freeze contains 20% B. If no diffusion occurred, the solid weld metal will contain crystals varying widely in composition from center to outside. The variation in composition is called segregation. Segregation is slight in an alloy with short freezing range. A weld metal has a tree-like or dendritic form, because crystal growth is faster along certain crystal directions than along others. Welds are generally small in cross sections so that segregation and dendrites are on a small scale.

DMIC Report 197 prepared by Kammer *et al.*⁽¹⁰¹⁶⁾ has presented a generalized

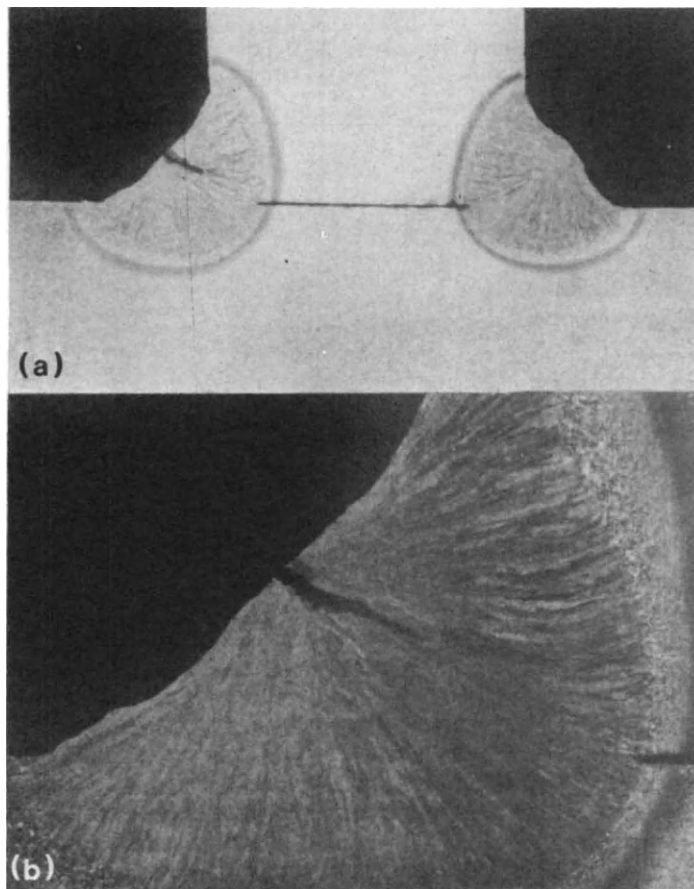


FIG. 14.2. (a) Hot crack in a restrained fillet weld. Bead on left of vertical member was deposited after the one on the right. Hot crack developed in the left bead because of the greater degree of restraint.⁽¹⁾ Specimen polished and lightly etched in nital to reveal weld metal and base metal heat-affected zones.^(2,39) (b) Enlarged view of left-hand fillet weld shown in (a). Note columnar growth of grains in weld metal structure.^(2,39)

theory of hot cracking.⁽¹⁰¹⁶⁾ This theory considers four stages during the solidification process:

1. *Primary dendrite formation.* The solid phases are dispersed in the liquid, with both phases capable of relative movement.
2. *Dendrite interlocking.* Both liquid and solid phases are continuous, but only the liquid is capable of relative movement. The liquid can move freely between the dendrites.
3. *Grain-boundary development.* The solid crystals are in an advanced stage of development and the movement of the liquid is restricted; relative movement of the two phases is impossible.
4. *Solidification.* The remaining liquid has solidified.

These stages are represented in Fig. 14.4. Stage 3 is the significant stage in cracking and is called the critical solidification range (CSR). Since the weld pool does not solidify

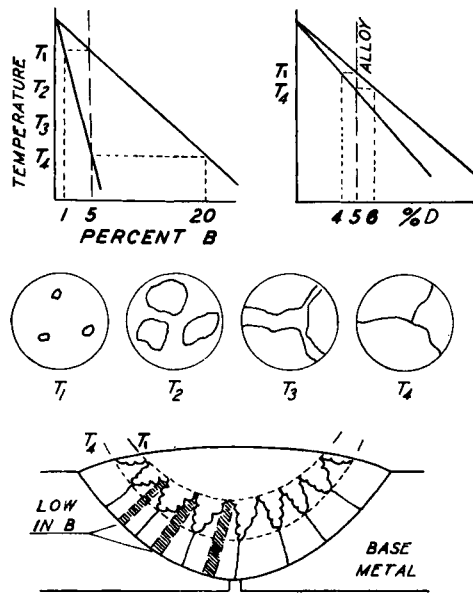
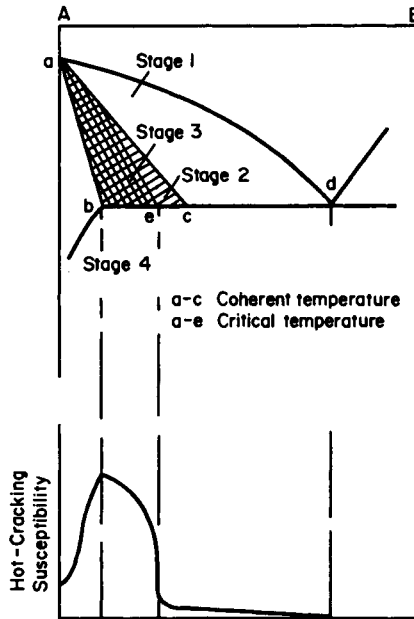


FIG. 14.3. Crystallization during freezing of an alloy (top), solidification of alloys with long (left), and short (right) freezing ranges (schematic) (center). The structure of the alloy at four temperatures during freezing (bottom)—dendritic solidification and segregation.



- Stage 1 - Dendrites freely dispersed in liquid. No cracking.
- Stage 2 - Interlocking of grains. "Liquid healing" possible if cracks form. "Accommodation" not important.
- Stage 3 - Critical solidification range. No "healing" of cracks possible if "accommodation" strain exceeded.
- Stage 4 - Solidification. No cracking.

FIG. 14.4. Effect of constitutional features on cracking susceptibility in binary systems.

according to equilibrium conditions, the liquidus and solidus can be depressed by undercooling and the solidus may be further depressed by the lack of diffusion. This increases the CSR and thus the likelihood of cracking.

The presence of a wide freezing range is not sufficient for cracking to occur. The alloy must pass through a stage in which the liquid is distributed in a form which allows high stresses to be built up between grains. The requirement is met by a liquid phase occupying almost all of the grain faces.

14.2.2 Hot cracking in the region of partial melting

In the base metal immediately outside the fusion zone is a region where the peak temperatures during welding fall between the solidus and liquidus temperatures and thus partial melting occurs. This region is also within the normally considered heat-affected zone.

Intergranular cracks have been observed in the heat-affected zones immediately outside the fusion zone of welds in some materials including quenched and tempered steels. It is believed that intergranular cracks (see Fig. 14.5) in HY-80 steel weldments are due to the partial melting of grain boundaries. These cracks are usually small, extending for only one to several grains. In many cases they even remain stable during service.

However, intergranular microcracks sometimes extend to macrocracks. Figure 14.6 shows how an intergranular crack changes to transgranular when it extends. In some cases a transgranular crack extends to a long crack. The transgranular macrocrack is cold cracking and it is believed to be due to hydrogen.

Freezing-cycle hot-tension test. To study the mechanisms of hot cracking, researchers at Battelle Memorial Institute used the freezing-cycle hot-tension test.[†] (Figure 14.7 shows the specimen used.) A 1-in. length in the center part of a specimen ($\frac{1}{2}$ in. in diameter, 6 in. long) is heated rapidly to a high temperature, and then is allowed to cool to a predetermined test temperature, after which the specimen is broken. A quartz sleeve is placed around the specimen to retain molten metal.

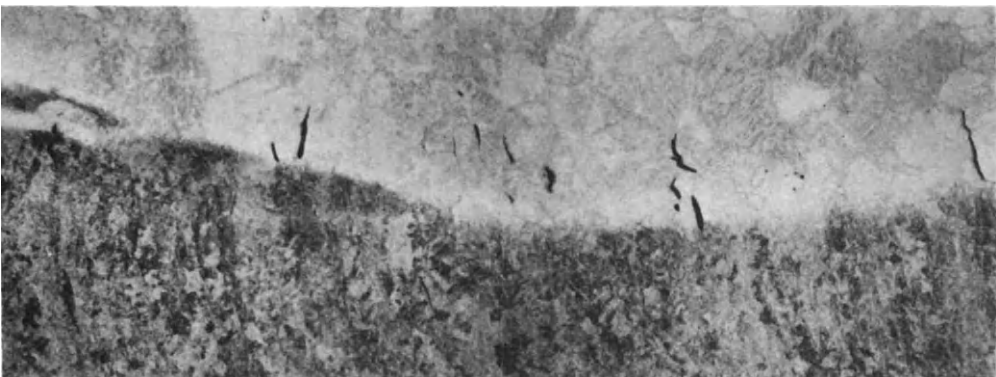


FIG. 14.5. Intergranular microcracks in the heat-affected zone of an HY-80 steel weldment.⁽¹⁴⁰⁴⁾
A double-tee joint $1\frac{1}{2}$ in. thick, welded with E11018 electrodes.

[†] Details of the test are presented in reference (1405).

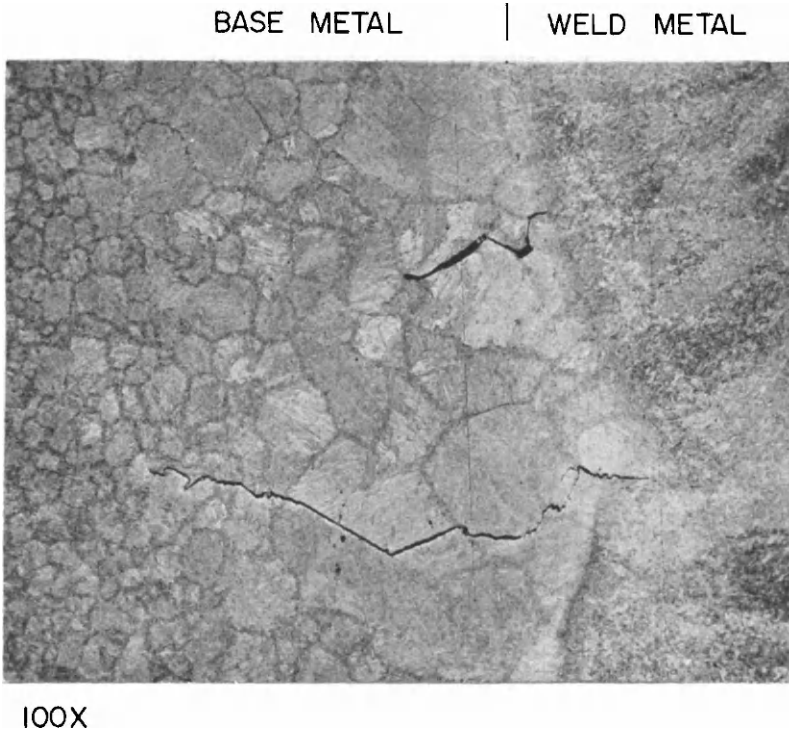


FIG. 14.6. Transgranular propagation of an intergranular microcrack in the heat-affected zone near the fusion zone of a heavy fillet weld in HY-80 steel.

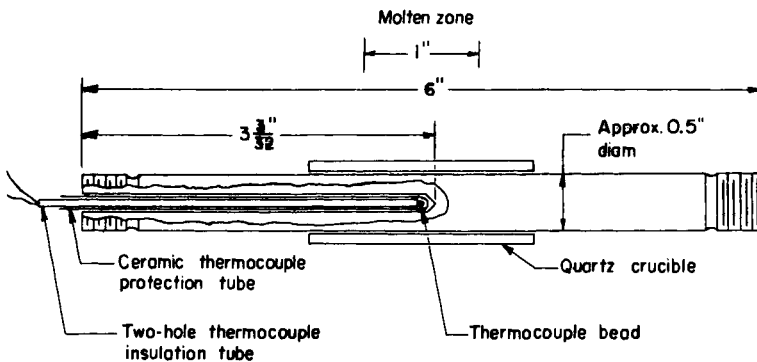
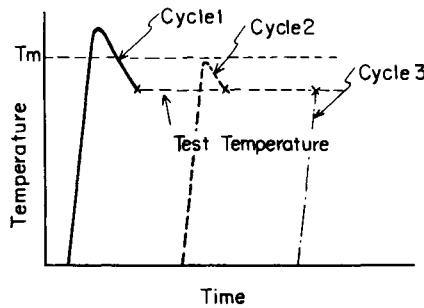


FIG. 14.7. Battelle freezing-cycle hot tension test specimen.

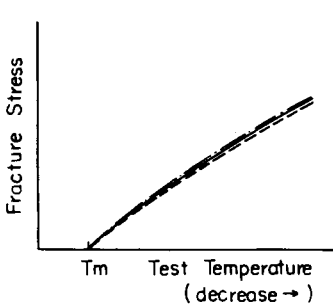
Specimens were fractured at high temperatures after they had been subjected to different thermal cycles which simulated the thermal histories encountered in various parts of a weldment (see Fig. 14.8).[†]

- Cycle 1: Specimens melted and then cooled to the test temperature and fractured.
- Cycle 2: Specimens heated to a temperature just below the solidus and then cooled to the test temperature and fractured.
- Cycle 3: Specimens heated directly to the test temperature and fractured.

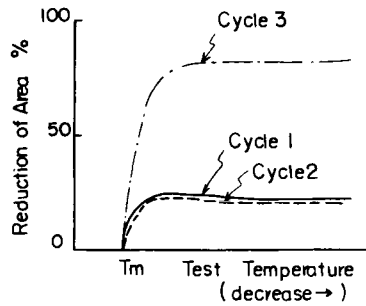
[†] The specimen was sometimes held at the maximum temperature for about 5 sec.



a. Test Thermal Cycles



b. Test Temperature vs. Fracture Stress Relationships



c. Test Temperature vs. Reduction-of-Area Relationships

FIG. 14.8. Schematic diagrams showing the effects of thermal cycles on the Battelle freezing-cycle hot-tension test results (T_m : melting temperature).

The cycles are shown schematically in Fig. 14.8(a). Cycles 1 and 2 simulate thermal cycles encountered during welding at portions in the weld metal and in the heat-affected zone, respectively. Cycle 3 is used for a control.

Figure 14.8(b) shows test temperature vs. fracture stress relationships while Fig. 14.8(c) shows test temperature vs. reduction-of-area relationships. Fracture stress increases as test temperature decreases. Effects of the thermal cycles on the test temperature vs. fracture stress relationships are not great. The relation between temperature and reduction-of-area changes significantly when the test thermal cycle is changed. For specimens heated directly to the test temperature, the reduction of area increases greatly as the test temperature is lowered from the solidus temperature. On the other hand, the reduction of area is very low for specimens subjected to cycles 1 and 2. This indicates that the ductility of the steel decreased greatly when the specimen was melted or heated to a temperature close to the solidus and fractured on cooling. The loss of ductility is believed to be caused by the formation of liquid films around grain boundaries.

Mechanisms of cracking. The results of the Battelle freezing-cycle hot-tension test indicate that the ductility of HY-80 steel decreases greatly when the specimen is heated to 2500°F (1371°C) or higher and fractured on cooling. Characteristics of stress and temperature conditions in the heat-affected zone are as follows:

1. The maximum temperature in the area adjacent to the fusion line is close to the solidus temperature, but gross melting does not occur in this area.
2. Tensile stresses are produced in the area during cooling. The amount of stress can be as high as the yield stress of the material at the temperature of the area. The amount of strain, however, is rather limited—maybe in the order of a few per cent elongation or less—since the heat-affected zone is surrounded by the base metal which is heated to a lower temperature.

Masubuchi and Martin^(1208, 1404) tried to explain the mechanisms of the heat-affected zone microcracking. Figure 14.9(a) is an idealized representation of the stress conditions in the heat-affected zone close to the fusion line. When the metal is heated rapidly to a temperature just below the solidus, liquation takes place along grain boundaries because of low-melting point segregations in the grain boundaries. During subsequent cooling, tensile stresses are produced by contraction, and strain concentration takes place in the grain boundaries. It has been hypothesized that if a system composed of grains of uniform size surrounded by a network of soft materials is at a uniform temperature gradient, and the residual stress gradient in the heat-affected zone is extreme, the changes of temperature and thermal stresses over several grains are not significant.

Since grains are surrounded by soft materials which have a low critical shear stress, sliding along grain boundaries can take place at a low applied stress. Because of the geometrical arrangement of the structure, the sliding is obstructed by hard grains. The stress concentration takes place in the soft material near the intersection of grains resulting in intergranular fractures, though the general deformation of the system is small. When two sliding planes, *AB* and *AC* in Fig. 14.9, meet at a triple point *A*, separation takes place along the third grain boundary *AD*.

Most theoretical research on the fracture of metals at high temperatures has been directed at the phenomena that occur in creep fracture. Zener⁽¹⁴⁰⁶⁾ first suggested that wedge-shaped microcracks were formed as a result of the intersection of two slip planes. The concept was further developed by several investigators, including Chen and Machlin, McLean⁽¹⁴⁰⁸⁾ and Gifkins.⁽¹⁴⁰⁹⁾

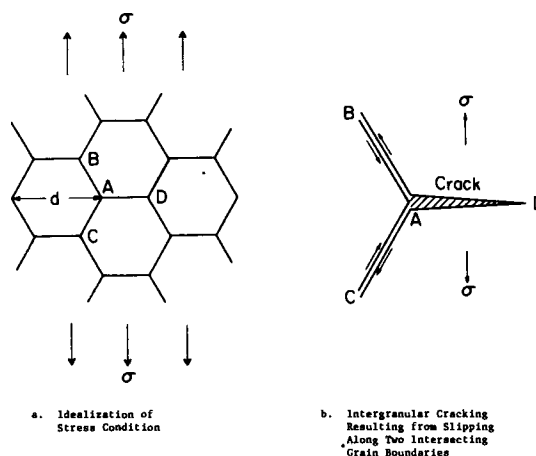


FIG. 14.9. Formation of intergranular cracking in the heat-affected zone adjacent to the fusion line.

Based upon these earlier studies, primarily of creep fracture, Masubuchi and Martin^(1404, 1405) suggested the following formula to express the critical stress for forming an intergranular microcrack in the weld heat-affected zone:

$$\sigma_{cr} = k \sqrt{\frac{\gamma E}{d}} \quad (14.1)$$

where k = a coefficient,
 γ = surface free energy of the grain-boundary material,
 E = Young's modulus of grains,
 d = grain diameter.

When liquation takes place along grain boundaries, γ decreases, resulting in intergranular cracking.

14.2.3 Effects of chemical compositions on hot cracking of steel weldments

In general, hot cracking can be eliminated by designing the composition of the weld metal or the base plate in accordance with the predictions of Borland's generalized theory of super-solidus cracking. Elements which result in formation of a liquid phase which covers almost all of the grain faces during freezing increase cracking susceptibility. Consequently, they should be eliminated from both the weld-metal and base-plate composition. In addition, elements which increase the length of the critical solidification range increase cracking susceptibility.

Where possible, these elements should also be eliminated or restricted in the composition. Unfortunately, it is not always possible to do this since some of the elements are needed for alloying. Table 14.1 lists the relative cracking potency factors for a number of elements. In general, the higher the number the more liable the element is to produce cracking in iron-binary alloys. It can be seen by these data that certain elements which

TABLE 14.1 Relative potency of elements in iron-binary systems⁽¹⁰¹⁶⁾

Relative potency, element	Per weight (%)
Si	1.75
P	121.1
Ti	13.8
As	40.2
Sn	16.8
Sb	(5.04)
Al	1.52
C	322.0
Cu	3.61
Mn	26.2
Co	0.30
Ni	2.93
Cb	28.8
Ta	13.0
B	917.0
S	925.0
Zr	15.2

are not normally intentionally added to steels are quite potent in producing hot cracking. An element such as sulfur (which is the most potent in this table) has to be limited to very low levels in high-strength steels to prevent both weld metal and heat-affected zone cracking. On the other hand, this table shows that carbon also has a high potency for producing hot cracking. Unfortunately, carbon cannot be eliminated from high-strength steels since it is the primary hardening and strengthening agent used in these steels.

In real alloys, the presence of a second element may significantly alter the expected effect of any given element. In steels, an example is the effect of manganese on sulfur. As the amount of manganese in the steel increases, the effectiveness of sulfur as a producer of hot cracks is reduced.

Inagaki⁽¹⁴¹⁰⁾ has suggested the following formula for evaluating hot cracking sensitivity (HCS) of a low-alloy high-strength steel:

$$[\text{HCS}] = \frac{C \left[\text{S} + \text{P} + \frac{\text{Si}}{25} + \frac{\text{Ni}}{100} \right] \times 10^3}{3\text{Mn} + \text{Cr} + \text{Mo} + \text{V}}. \quad (14.2)$$

Chemical compositions shown above are given in percent. When the [HCS] value is less than 4, the steel is believed to have good resistance against hot cracking.

According to Inagaki⁽¹⁴¹⁰⁾ the following simple formulas also may be used for preventing hot cracking in steel weldments:

$$\begin{aligned} \text{S} &< 0.035\% \\ \text{Ni} &< 1.0\% \\ \text{Mn} &> 0.80\% \\ \text{C} &< 0.15\% \\ \text{Mn/S} &> 35 \end{aligned}$$

14.3 Cold Cracking

Weldment cold cracking is generally defined as cracking which occurs below about 400°F (204°C). Cold cracks are generally transgranular. Cold cracks can be divided into two general types, short time and delayed. Short-time cracks are initiated during cooling to room temperature after welding or after a short time at room temperature. Delayed cracks are initiated after some time lapse at room temperature. Delay periods in terms of weeks and months have been reported. Weldment cold cracks can occur both in weld metal or in the heat-affected zone.

Fig. 14.10 shows toe cracks and underbead cracks which occurred in a bead-on-plate weld in SAE 4130 steel.⁽²⁴⁰⁾ Hydrogen is known to be responsible for cold cracking in steel weldments. Hydrogen embrittlement of steel is discussed in Chapter 12.

14.3.1 *Effects of chemical compositions on cold cracking of steel weldments*

Chemical composition is an extremely important factor in determining whether a steel is susceptible to cold cracking. The concept of “carbon equivalent” is widely used for evaluating the cold-cracking sensitivity of a steel plate, as discussed in Chapter 9 (see Tables 9.6 and 9.7). The relationship is valid for low-alloy steels which depend on

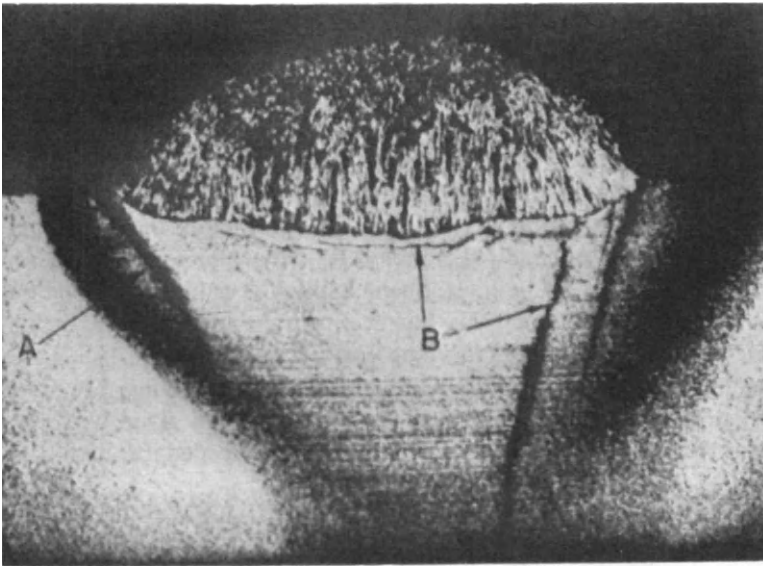


FIG. 14.10. Transverse section of bead weld in $\frac{1}{8}$ -in. SAE 4130 steel sheet, showing toe cracks (A) and underbead cracks (B). 15X. Etchant: Nital. From Reference (240).

martensitic transformation to attain high strength.

Carbon equivalent is a number which is used to express the composition of a steel in a very simple way. It is made up by adding to the percentage of carbon present in the steel, a factor for each important alloying element present. This factor is arrived at by dividing the percentage of the alloying element present by a number (usually a whole number) which experience has shown to be related to the influence of the alloying element on the characteristic being studied. A common formula for carbon equivalent (CE) is^(14.11)

$$CE = C + \frac{Mn}{6} + \frac{Ni}{20} + \frac{Cr}{10} + \frac{Cu}{40} - \frac{Mo}{50} - \frac{V}{10}. \quad (14.3)$$

When CE by the above formula exceeds 40, underbead cracking can occur. Cracking is also influenced by welding heat input and other factors, however.

Work on several types of steels has shown that susceptibility to hydrogen embrittlement is related to the hardness of the steel.⁽¹⁰⁹⁾ As the hardness increases, the amount of stress required to produce hydrogen cracking decreases. Since the carbon equivalent can be used as an approximate index of the ability to harden a steel, it is related to the hardness produced in the heat-affected zone of a weld. This is shown in Fig. 14.11. This figure shows the relationship between the hardness of the heat-affected zone of bead-on-plate weldments made from steels of various carbon equivalents. The welds were made at a single heat input (total energy per unit length of weld). This means that each heat-affected zone experienced the same thermal cycle during the welding operation regardless of the chemistry of the steel. Heat-affected-zone hardness increased almost linearly as the carbon equivalent increased. In Fig. 14.11, carbon equivalent (CE) is expressed by a simple formula as follows:

$$CE = C + \frac{Mn}{4} + \frac{Si}{4}. \quad (14.4)$$

Figure 14.11 also contains a curve for the underbead-crack sensitivity of this group of steels. The cracking index used was obtained from bead-on-plate tests made using a standard set of conditions. The test specimen is a rectangular piece of plate about 2 in wide (50 mm) wide and 4 in. long.[†] The test weld is about 1½ in. (32 mm) long. The weld specimens are sectioned longitudinally and the length of cracking measured on the longitudinal section. The length of cracking is then reported as a percentage of the total weld-bead length. This is the cracking index. Such cracking tests have become quite standard and, statistically, their reproducibility has been shown to be quite high. This test was originally developed to study the crack susceptibility of ship plate.

The data shown in Fig. 14.11 indicate that underbead cracking only occurs in structures above some critical hardness. This means that, for a given welding procedure, there is some critical carbon equivalent which must be exceeded if cracking is to occur.

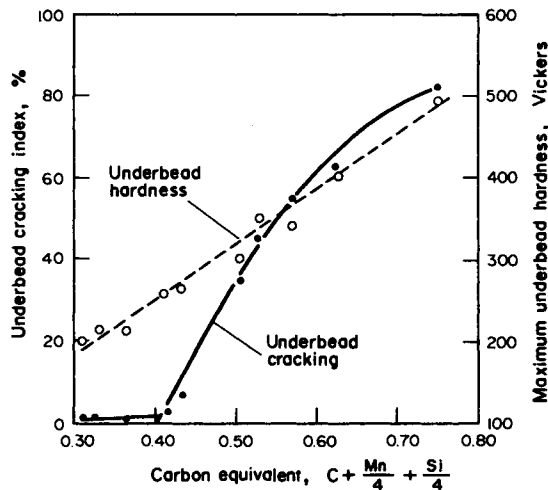


FIG. 14.11. Relation between underbead hardness, underbead cracking, and carbon equivalent.

14.3.2 *Methods of preventing cold cracking in steel weldments*

There are several methods for preventing cold cracking. They are:

1. the use of low-hydrogen processes,
2. preheating,
3. reduced joint restraint.

Reference (1412) discusses methods of reducing delayed cracks in ship welds.

Use of low-hydrogen processes. For welding high-strength steels which tend to be susceptible to cold cracking, it is important to use processes with low hydrogen. Fig. 14.12 shows the relationship between average underbead cracking and carbon equivalent for three different types of electrodes (see Table 1.18):

[†] The test specimen is very similar to that shown in Fig. 14.33.

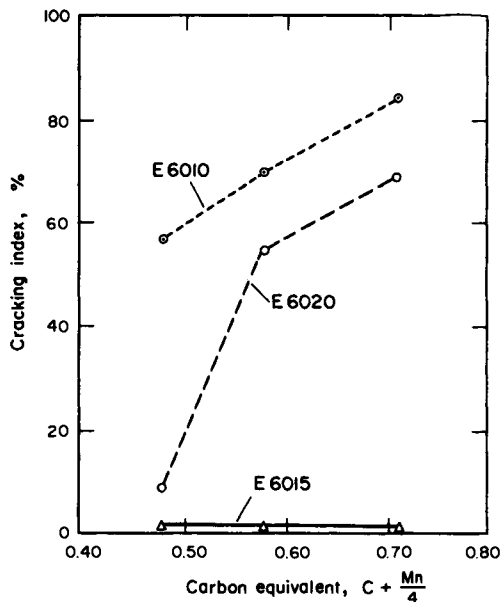


FIG. 14.12. Relation between carbon equivalent and underbead cracking for three types of electrodes which produce shield gases containing quite different amounts of hydrogen (E6010—highest to E6015—lowest).

E 6010 (high cellulose sodium),
 E 6020 (high iron oxide),
 E 6015 (low hydrogen sodium).

Welding conditions were such that the heat-affected zones of the test welds experienced the same thermal cycle during welding regardless of the electrode used. There is a wide difference in the amount of hydrogen in the shield gases produced by the three electrodes. For $\frac{3}{16}$ in. (4.8 mm) diameter electrodes, the E6010 shield gases contain about 50 to 60% hydrogen, E6020 about 30 to 40%, and E6015 about 5 to 10%.

Low-hydrogen electrodes are widely used for welding high-strength steels. Consequently, it is worthwhile to describe the need for care in the use of low-hydrogen electrodes. The term "low hydrogen" developed because these electrodes are produced to a maximum limit of moisture in the electrode coating. These electrodes are not as some people tend to think, "no-hydrogen" electrodes. The specified maximum moisture contents of low-hydrogen electrodes with different strength levels are

0.6% for E7015, E7016, E7018,
 0.4% for E80XX,
 0.2% for E100XX and E110XX.

Keeping a control on the moisture content in the electrode coating holds the hydrogen level to a minimum because water is a source of hydrogen when it dissociates in the arc. Hydrogen has been associated with both underbead cracks and toe cracks. Therefore, it is desirable to keep hydrogen at a low level.

For effective use, the low-hydrogen electrodes must be properly stored and kept dry. Fig. 14.13 shows the effect on moisture content of exposure to a humid atmosphere. If there is any doubt about the moisture level of the electrodes, they can be rebaked at

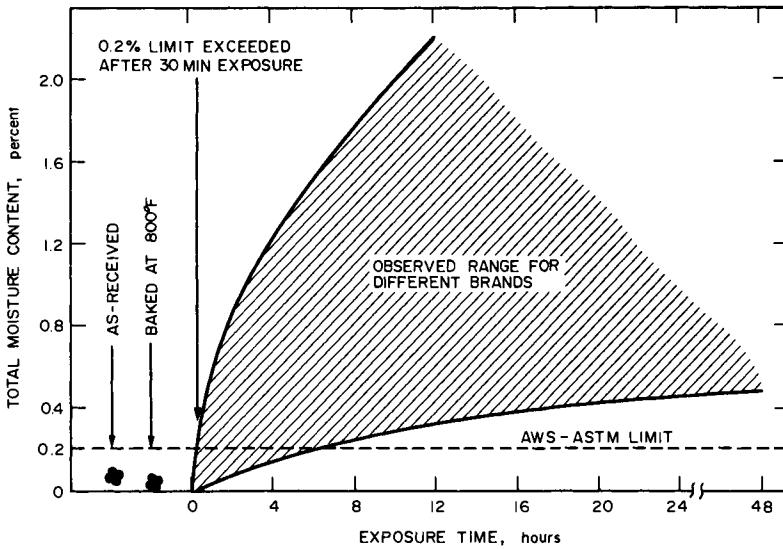


FIG. 14.13. Moisture pickup by E11018-G electrodes exposed to an atmosphere of 90% relative humidity at 75°F.⁽¹⁰⁹⁾

approximately 800°F (427° C) before use. Porosity at the start of a weld is one indicator that the electrode coating has picked up moisture. After baking the electrodes, make sure that they are placed in holding ovens until they are ready to be used. The welder is usually supplied with just the number of electrodes that he expects to use within a 4-hr period. Electrodes held out of the oven for a longer time are returned to be dried out. Reference (1412) states that, if the welder does not have a heated electrode container, the electrodes should be used within the following time limits:

E70XX	4 hr
E80XX	2 hr
E90XX	1 hr
E110XX	$\frac{1}{2}$ hr

Electrodes should be rebaked only once. Electrodes that would require a second rebaking should be discarded.⁽¹⁴¹²⁾

Preheating.⁽¹⁰⁹⁾ There are two reasons for the effect of preheating. Preheat reduces the maximum cooling rate which occurs in the heat-affected zone during welding. This reduction in cooling rate can lead to softer structures being produced in the heat-affected zone. The other effect of preheat is to maintain temperatures in the heat-affected zone above a critical temperature long enough to permit hydrogen to diffuse out of that zone during cooling. If this happens, there will be no hydrogen embrittlement in the heat-affected zone and, consequently, underbead cracking will not occur.

Figure 14.14 shows the effect of preheat and postheat on critical carbon equivalent for cracking. The data shown in this figure are taken from the standard underbead-cracking tests (see Fig. 14.33). It is obvious that, for a given chemical composition, the

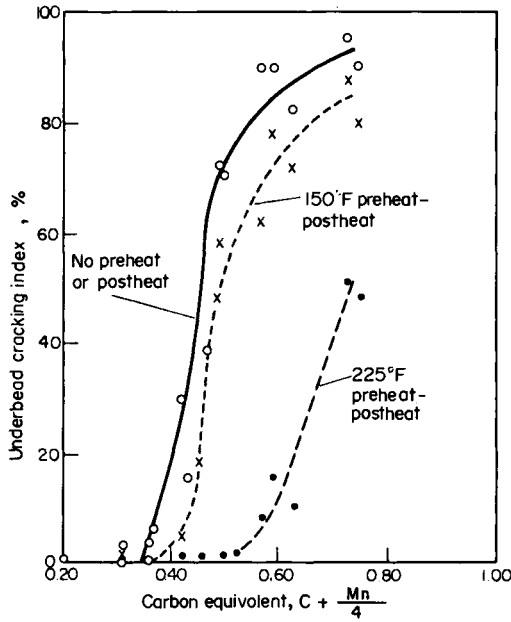


FIG. 14.14. Effect of preheat and postheat on critical carbon equivalent for bead-on-plate tests.

addition of a preheat drastically reduces the underbead-cracking tendency and increases the critical carbon equivalent.

The effectiveness of preheat for increasing the critical carbon equivalent level for underbead cracking has also been demonstrated in girth-weld tests made on pipe with a yield strength of 52 ksi (36.6 kg/mm² or 359 MN/m²). In Fig. 14.15, the relationship between underbead-cracking tendencies and pipe temperature is shown for three different carbon equivalents. The higher the carbon equivalent, the higher the preheat temperature has to be to eliminate cracking. These tests are an excellent simulation of an industrial

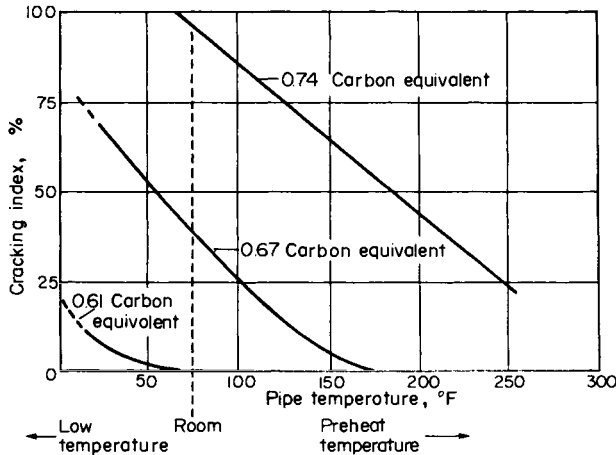


FIG. 14.15. Effect of pipe-temperature girth-joint cracking.

welding operation. The cracking index here is the percentage of 1-in. (25-mm) long specimens cut from a girth weld in a 30-in. (762-mm) diameter pipe that showed any evidence of cracking.

Joint restraint. The tendency for cold cracking increases as the joint restraint increases.

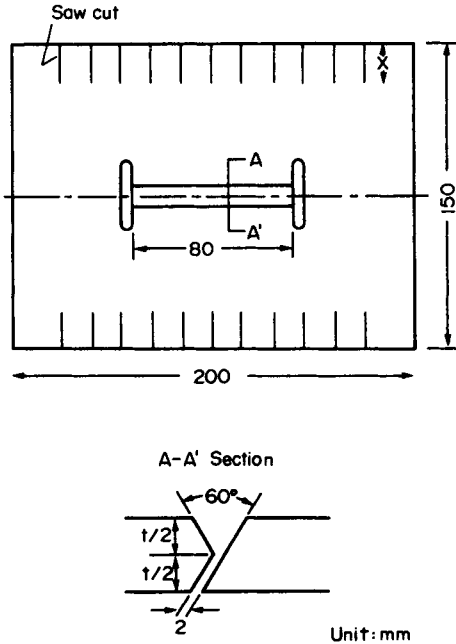


FIG. 14.16. Geometry of the saw-cut y-groove restraint cracking specimen used by Ito and Bessyo.⁽¹⁴¹³⁾

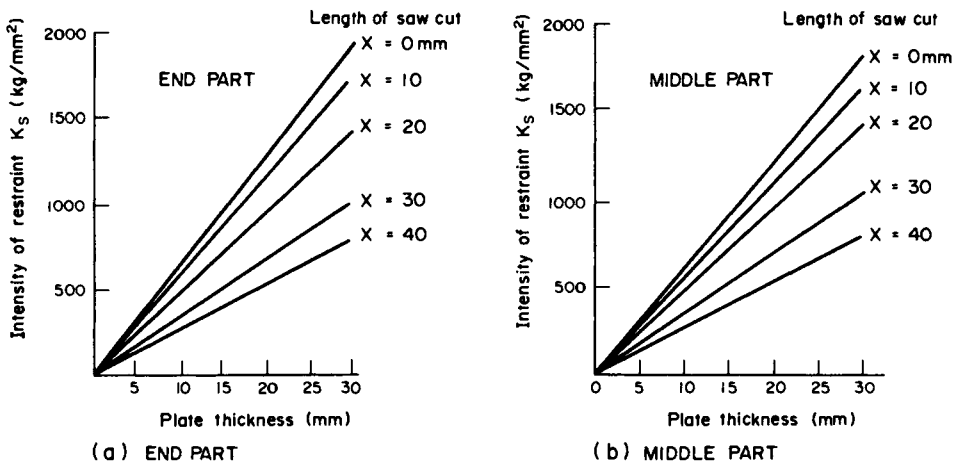
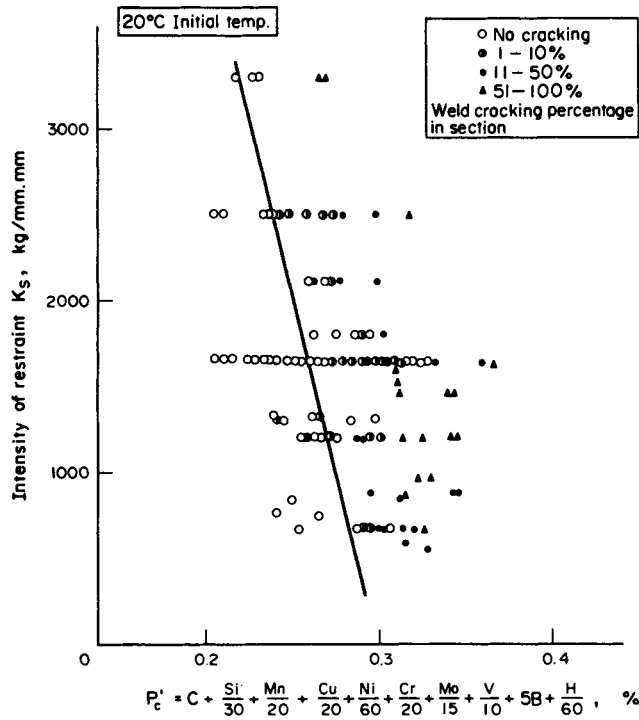
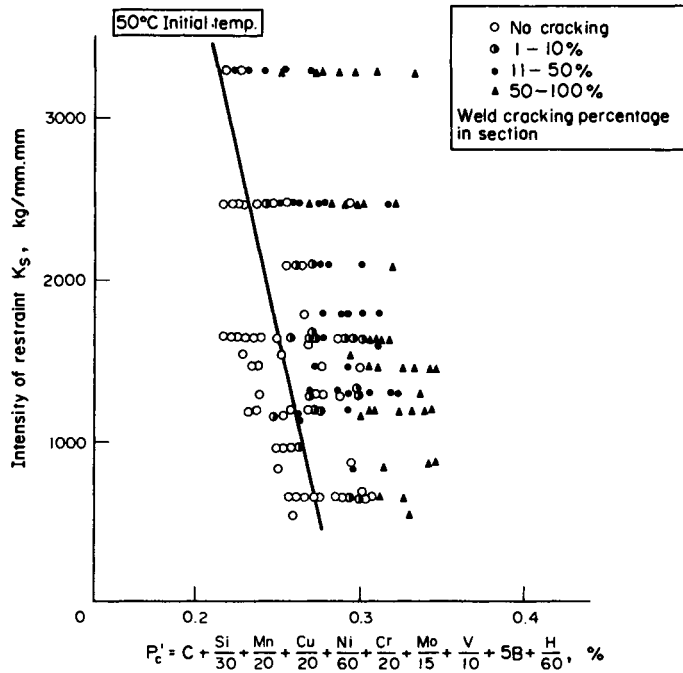


FIG. 14.17. Relationship between the intensity of restraint, plate thickness and the length of saw cut of the restraint specimen used by Ito and Bessyo.⁽¹⁴¹³⁾ The intensity of restraint was determined experimentally. The restraint intensity at the end of the joint is greater than that at the middle of the joint. The higher values at the end of the joint are used in the proceeding analyses.



(a) Initial temperature of 20°C



(b) Preheat at 50°C (122°F)

FIG. 14.18. Relationships between intensity of restraint K_S and cracking parameter P'_c .

The following pages describe results obtained by Ito and Bessyo.⁽¹⁴¹³⁾ Figure 14.16 shows the test specimen used. Figure 14.17 shows the relationships between plate thickness, the length of saw cuts, and the intensity of restraint K_s (kg/mm²).

Figures 14.18 (a) and (b) show test results obtained with initial temperatures of 20°C (68°F) and 50°C (122°F), respectively. Shown in these figures are the relationships between K_s and carbon equivalent P'_c ,

$$P'_c = C + \frac{\text{Si}}{30} + \frac{\text{Mn}}{20} + \frac{\text{Cu}}{20} + \frac{\text{Ni}}{60} + \frac{\text{Cr}}{20} + \frac{\text{Mo}}{15} + \frac{\text{V}}{10} + 5B + \frac{H}{60}, \quad (14.5)$$

where H = diffusible hydrogen (cm³) per 100g of the weld metal determined by a glycerine substitution method.[†]

Figures 14.18 (a) and (b) show that the critical joint restraint for causing cracking decreases as the carbon equivalent increases.

By summarizing experimental results Ito and Bessyo⁽¹⁴¹³⁾ have developed Fig. 14.19 which shows the relationships among:

- Carbon equivalent P'_c ,
- Intensity of restraint K_s (kg/mm²),
- and Cooling time from 300°C (572°F) to 100°C (212°F), (sec).

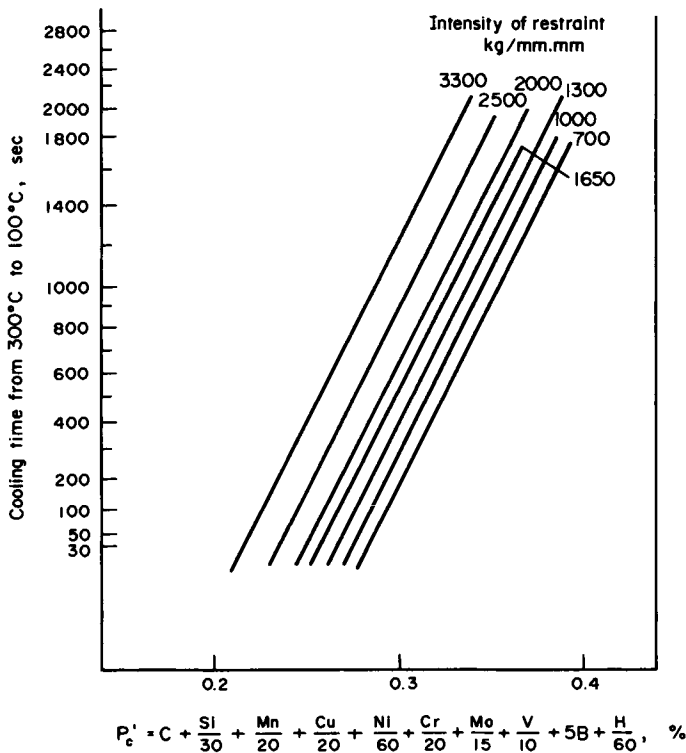


FIG. 14.19. Effect of restraint on the relationship between cracking parameter P'_c and cooling time from 300°C to 100°C.

[†] Immediately after welding a specimen was quenched in water at 20°C (68°F) and within 45 seconds it was placed in a collecting apparatus.

14.3.3 An analytical/empirical system for preventing cold cracking in steel weldments

A group of Japanese investigators conducted extensive research for developing a systematic method of preventing cold cracking in weldments in high-strength steels.^(1414, 1415) Figure 14.20 is a flow chart of the system.

From the chemical composition of the base metal, the carbon equivalent P_{CM} (%), is determined. By knowing the hydrogen content of the weld metal, H ($\text{cm}^3/100 \text{ g}$), and the intensity of restraint of a joint, K_s (kg/mm^2), one can determine the cracking sensitivity of the weldment P_w (%). From knowing P_w , one can determine the critical cooling time, $(t_c)_{cr}$, as shown in Fig. 14.21.

In order to weld the joint without cracking, one must select welding parameters, including welding conditions and preheating temperature, in such a way that the cooling time of the weld, $(t_c)_{ac}$, is longer than the critical cooling time. In other words, there is no cracking, when

$$(t_c)_{ac} \geq (t_c)_{cr},$$

but there is cracking, when

$$(t_c)_{ac} < (t_c)_{cr}.$$

1. When P_{CM} , H , and K_s are known. When chemical composition, H , and K_s are known, P_w can be determined as follows:

$$P_w(\%) = P_{CM} + \frac{H}{60} + \frac{K_s}{40,000}, \tag{14.6}$$

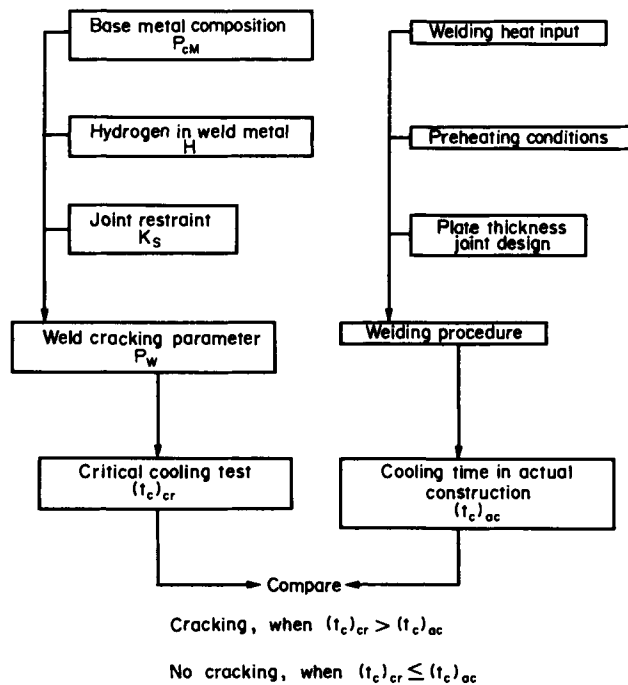


FIG. 14.20. Flow chart of basic procedure for preventing weld cracking in steel structures.

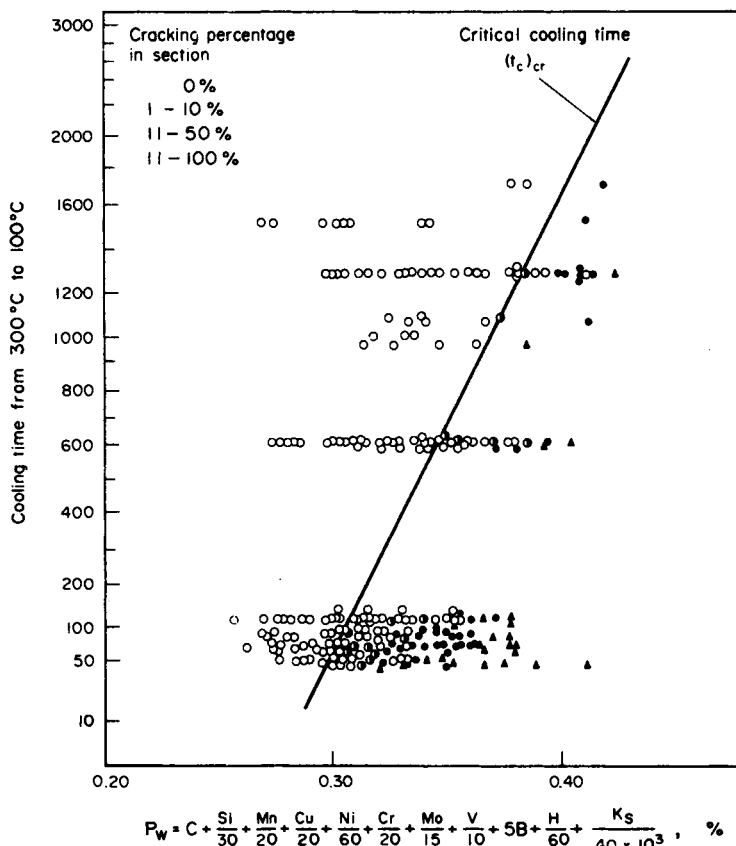


FIG. 14.21. Relationship between P_w and the cooling time from 300°C to 100°C.

$$P_{CM}(\%) = C + \frac{Si}{30} + \frac{Mn}{20} + \frac{Cu}{20} + \frac{Ni}{60} + \frac{Cr}{20} + \frac{Mo}{15} + \frac{V}{10} + 5B. \tag{14.7}$$

The above formulas are applicable within the following ranges:

- C = 0.07% ~ 0.22%, Si = 0 ~ 0.60%
- Mn = 0.40% ~ 1.40%, Cu = 0 ~ 0.50%
- Ni = 0 ~ 1.20%, Cr = 0 ~ 1.20%
- Mo = 0 ~ 0.70%, V = 0 ~ 0.12%
- Ti = 0 ~ 0.05%, Nb = 0 ~ 0.04%
- B = 0 ~ 0.005%

Plate thickness, $h = 19 \sim 50 \text{ mm } (\frac{3}{4} \sim 2 \text{ in.})$.

Hydrogen content of the weld metal, $H = 1.0 \sim 5.0 \text{ cm}^3/100 \text{ g.}$

Intensity of restraint, $K_s = 500 \sim 3300 \text{ kg/mm}^2$

Heat input, $J = 17,000 \sim 30,000 \text{ joules/cm } (43,000 \sim 76,000 \text{ joules/in.})$

The minimum preheating temperature can be determined using Figs. 14.22 (a) and (b). Table 14.2 shows example calculations of P_{CM} , P'_C , and P_w for certain values of

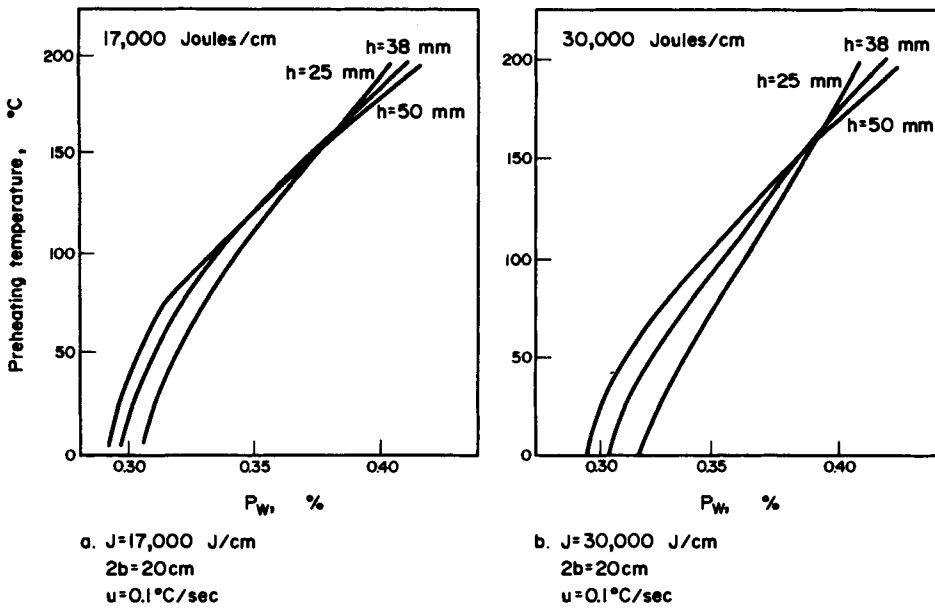


FIG. 14.22. Relationships between P_w and required preheating temperature (at 5 cm from the weld line).^(14,15)

TABLE 14.2 Example calculations of carbon equivalent values

	Ito and Bessyo ^(14,13)		Conventional equation (14.3)	
Chemical composition, %				
C = 0.12		0.120		0.120
Si = 0.32	1/30	0.011	—	—
Mn = 0.96	1/20	0.048	1/6	0.160
Cu = 0.25	1/20	0.013	1/40	0.006
Ni = 0.74	1/60	0.012	1/20	0.037
Cr = 1.02	1/20	0.051	1/10	0.102
Mo = 0.37	1/15	0.025	- 1/50	- 0.007
V = 0.03	1/10	0.003	- 1/10	- 0.003
B = 0.016	5	0.008		
		$P_{CM} = 0.291$		C.E. = 0.415
2. Diffusible hydrogen				
$H = 1.9 \text{ cm}^3/100 \text{ g}$	1/60	0.032		
		$P'_c = 0.323$		
3. Joint restraint				
$K_j = 1450 \text{ kg/mm}^2$	1/40,000	0.036		
		$P_w = 0.359$		

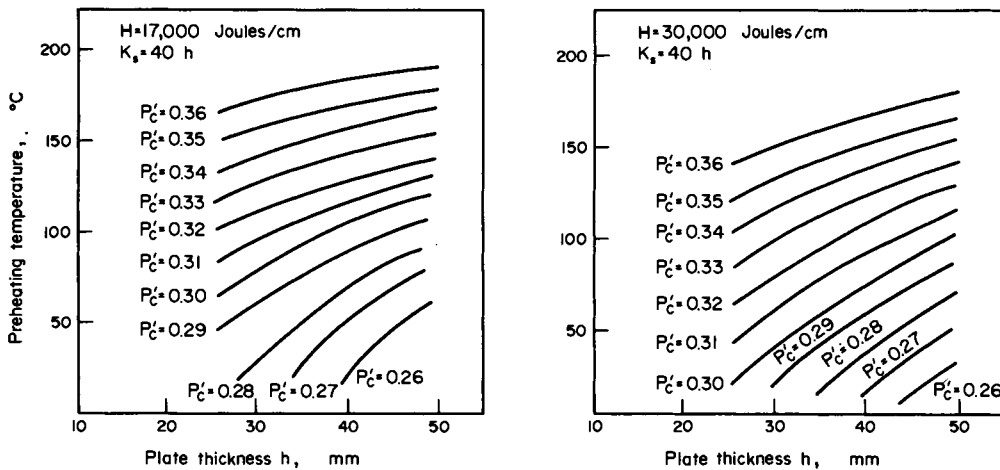
chemical composition, hydrogen content, and joint restraint. Also shown here is a computation of carbon equivalent by a conventional method using eqn. (14.3).

In the case shown here, $P_{CM} = 0.36\%$. If the plate thickness, h , is 25 mm, and the welding heat input is 17,000 joules/cm (43,200 joules/in.) the necessary preheating temperature is 120°C (248°F). If the heat input used is between 17,000 and 30,000 joules/cm (43,200 to 76,000 joule/in.) the necessary preheating temperature can be determined by a proper interpolation of values obtained in Figs 14.22 (a) (for 17,000 joules/cm) and 14.22 (b) (for 30,000 joules/cm).

2. When P_{CM} and H are known. Sometimes, the intensity of restraint K_s is unknown. In the case of the y-groove restrained cracking specimen shown in Fig. 14.16, $K_s = 70h$. In most applications, K_s is less than the above value. In Figs. 14.23 (a) and (b), it is assumed that $K_s = 40h$. Shown here are relationships between plate thickness, h , and preheating temperature for certain values of P'_c .

$$P'_c(\%) = P_{CM} + \frac{H}{60} \tag{14.8}$$

3. When P_{CM} is known. Sometimes the hydrogen content of the weld metal is unknown.



a. Heat input 17,000 Joules/cm

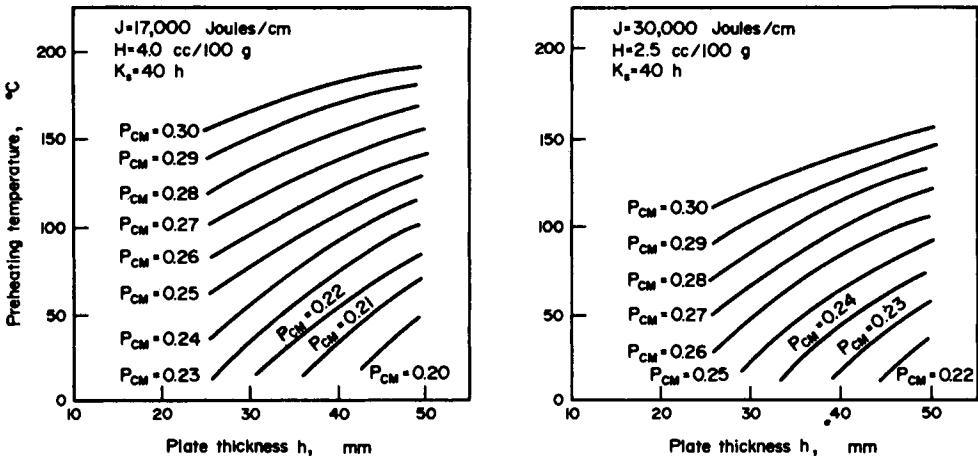
b. Heat input 30,000 Joules/cm

FIG. 14.23. Relationships among plate thickness, P'_c , and required preheating temperature.

TABLE 14.3 Standard values of diffusible hydrogen in weld metal

Electrode type	Cases using electrodes under normal control of drying and keeping	Cases using electrode under high moisture or improper keeping after drying	Cases using electrode with extremely low hydrogen
E7016	4.0 cm ³ /100 g	6.0 cm ³ /100 g	2.0 cm ³ /100 g
E9016	2.3	4.0	1.0
E11016	1.6	2.5	1.0

Note: Values shown are amounts of diffusible hydrogen (cm³) in 100 g of weld metal.



a. Assuming $J=17,000$ joules/cm, $H=4.0$ cc/100 g, $K_s=40$ h b. Assuming $J=30,000$ joules/cm, $H=2.5$ cc/100 g, $K_s=40$ h

FIG. 14.24. Relationship among plate thickness, h (mm), P_{CM} , and required initial temperature.

Table 14.3 shows standard values of hydrogen content in the weld metal. Figures 14.24 (a) and (b) show relationships between plate thickness, h , and preheating temperature under the following conditions:

Fig. 14.24 (a): $J = 17,000$ joules/cm,
 $H = 4.0$ cm³/100 g,
 $K_s = 40h$;

Fig. 14.24 (b): $J = 30,000$ joules/cm,
 $H = 2.5$ cm³/100 g,
 $K_s = 40h$.

4. Only the base-metal specification is known. In some applications, only the base-

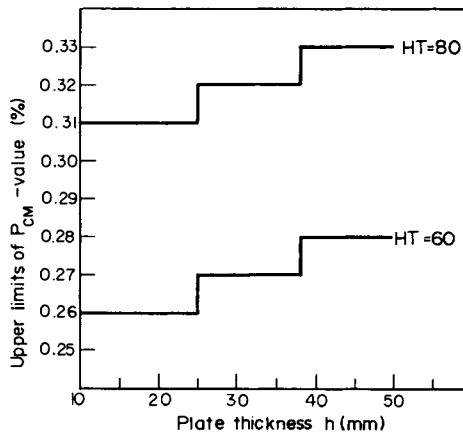


FIG. 14.25. Upper limits of P_{CM} -values for Japanese HT60 and HT80 steel.

Note: HT60 is similar to ASTM A572 steel; HT80 is similar to ASTM A514, A517 steels.

metal specification is known. Although it is difficult to determine the minimum preheating temperature for a variety of joints, some analysis could also be made.

Figure 14.25 shows upper limits of values of P_{CM} for two Japanese steels: HT60 and HT80, low-alloy high-strength steels with minimum ultimate tensile strength of 60 kg/mm (85.3 ksi) and 80 kg/mm² (114 ksi), respectively. From Table 14.3, one could assume that $H = 2.3 \text{ cm}^3/100 \text{ g}$. for HT60 steel and $H = 1.6 \text{ cm}^3/100 \text{ g}$ for HT80 steel, when low-hydrogen electrodes are used under a proper moisture control. Then the upper limits of values of P'_c are estimated as shown in Fig. 14.26.

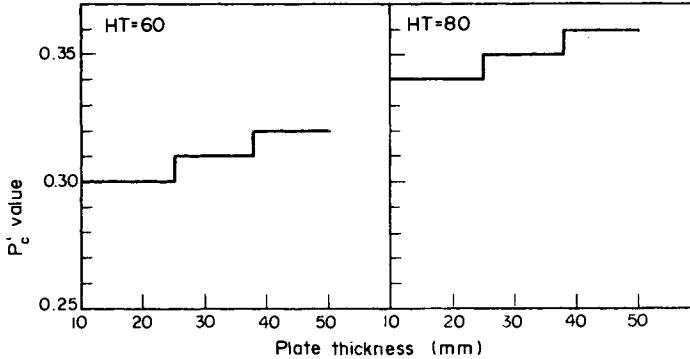


FIG. 14.26. Upper limits of P'_c -value for Japanese HT60 and HT80 steels—procedure 1 for determining required preheating temperature.

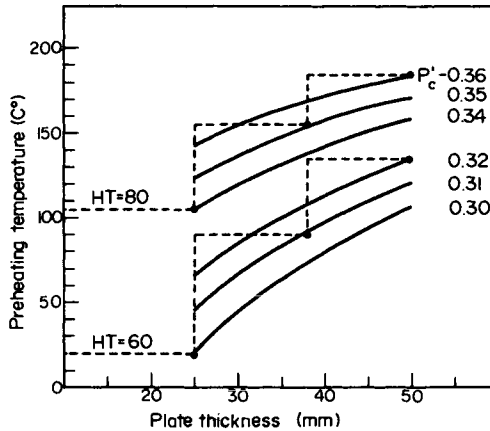


FIG. 14.27. Relationships between plate thickness and required preheating temperature—Procedure 2 for determining preheating temperature

TABLE 14.4 An example of standards of preheating temperatures for Japanese HT60 and HT80 steels

	Plate thickness, t		
	$t < 25 \text{ mm}$	$25 \text{ mm} \leq t < 38 \text{ mm}$	$38 \text{ mm} \leq t \leq 50 \text{ mm}$
HT60	20° C (68° F)	90° C (194° F)	135° C (274° F)
HT80	105° C (221° F)	155° C (311° F)	185° C (165° F)

25 mm = 1 in., 38 mm = 1.5 in., 50 mm = 2 in.

By assuming $K = 40h$, and the heat input is 30,000 joules/cm (76,000 joules/in.), one can obtain Fig. 14.27 by using Fig. 14.23 (b). From Fig. 14.27, one can prepare Table 14.4 as a standard for preheating.

14.4 Weld-Cracking Tests

A number of crack-sensitivity tests have been introduced and used by many investigators. The effects of various factors including base-metal composition, type of electrodes, and welding conditions on crack sensitivity have been studied in some detail.

A technique commonly employed in the study of weld cracking involves the use of crack-susceptibility tests. Over thirty different crack-susceptibility tests have been developed. Most of them were designed to simulate some particular application in which cracking was encountered. Therefore, caution should be used before applying the test when some other problem is being investigated. Others were designed as aids in research on the fundamentals of weldment cracking. Some of the desirable features of a cracking test are:

1. Ability to show a direct correlation with actual fabrication and service behavior.
2. Reproducibility of results with freedom from variation due to the human element.
3. Sensitivity to small changes in a test variable.
4. Ability to show the effects of several welding variables.
5. Economical preparation of the specimens and running of the test.
6. Applicability to all welding process.

Needless to say no test has been devised that possesses all of these features and it is not likely that one will ever be developed.

The most important step in selecting a suitable test is to decide what information is desired from the test. For example, if the test is to furnish information on a cracking problem encountered in a particular application, a test simulating the actual joint geometry and welding conditions should be selected. On the other hand, if the test is to furnish information on the basic causes of a particular type of cracking, a test that is relatively economical and simple to perform while allowing the effect of individual variables to be determined might be selected.

Further discussion are given on the following tests: †

1. Lehigh restraint test.
2. Houldcroft fishbone test.
3. Circular patch test.
4. Controlled thermal severity (CTS) test.
5. Cruciform test.
6. Longitudinal-weld underbead-cracking test.
7. Varestraint test.
8. Rigid restraint cracking (RRC) test and tensile restraint cracking (TRC) test.
9. Implant test.

These tests have been selected to show a variety of tests proposed and used by different investigators. Tests 1 through 6 have been used for some time; some of them were

† References (240) (1016), and (1416) cover many crack-sensitivity tests.

developed in the 1940s. Tests 7, 8, and 9 are recent developments. Details of test procedures are given in references cited.

14.4.1 *Lehigh restraint test*^(240, 1016, 1416, 1417)

This test (Fig. 14.28) is used to study, quantitatively, the degree of restraint necessary to produce weld-metal cracking. The degree of restraint is varied by changing the length of the slots along the edges of the plate. The restraint is expressed numerically by the width of the specimen between inner ends of the slots. The threshold degree of restraint is expressed as the width which was just sufficient to cause cracking. To provide sufficient restraint to cause cracking in thin plates, the length of the groove in the specimen is usually reduced from 5 to 3 in. (127 to 76 mm). The variables that can be studied include base metal, filler metal, preheat, post-heat, heat input, and the effects of multi-pass welding. Cracking is usually detected by examination of transverse sections of the weld. Although normally used for steels, the test could be applied to other materials.

14.4.2 *Houldcroft fishbone test*^(1016, 1418, 1419)

This test (Fig. 14.29) was originally developed to evaluate the cracking tendency of welds made in sheet material welded by the tungsten-arc process, with or without filler. The test can be used for a variety of materials and may be usable with fine-wire consumable-electrode welding. The test is based on the concept that if a weld is started on the left edge of a sheet which has the highest restraint, a crack can easily initiate and then propagate until the degree of restraint is insufficient to continue the crack. The restraint level in the test is controlled by the length of the slots along the edges of the specimen. The crack length is used as a measure of the crack sensitivity of the material. Usually six tests are made and the average crack length reported.

The welding jig used with the test is shown in Fig. 14.29. The carbon block is an essential feature of the test. It conducts heat poorly compared with the metal but conducts

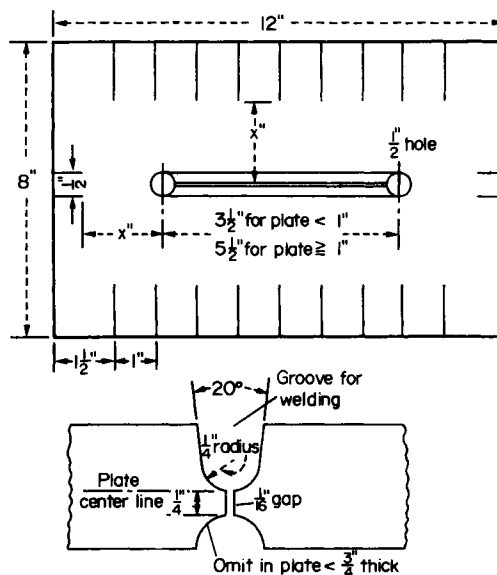


FIG. 14.28. Lehigh restraint test specimen.

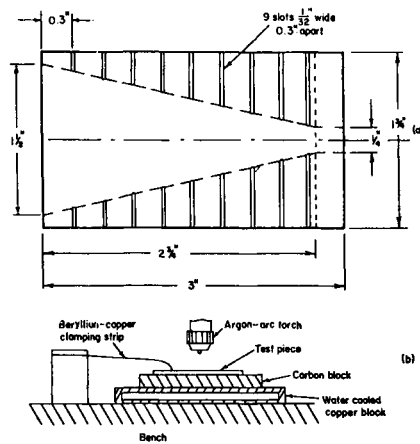


FIG. 14.29. Houldcroft fishbone specimen: (a) for $\frac{1}{16}$ -in. thick material (increased by 50% for $\frac{1}{8}$ -in. sheet); (b) section through test assembly.

the welding current efficiently, and also provides a convenient starting point for the arc. Fresh carbon blocks are used for each single test to insure that at the beginning of the test the block is at room temperature. The clamping strip holds the specimen in plate, but does not restrain the specimen.

14.4.3 *Circular patch test*^(1016, 1420, 1421)

The circular patch test (Fig. 14.30) essentially consists of welding a circular disk back into a square plate from which it was cut. However, a full penetration, circular, bead-on-plate weld has been used in evaluating sheet materials. Normally the test is used to investigate weld metal cracking, but it has been used to evaluate both hot and cold heat-affected zone cracking. The crack length is measured and expressed as a percentage of the total weld length. The test is suitable for use with all types of materials. Although the test is essentially a go-no-go test, it can be made semiquantitative by varying the patch diameter.

14.4.4 *Controlled thermal severity (C T S) test*^(1016, 1422)

The design (Fig. 14.31) of this test is based on the assumption that the extent of heat-affected zone cracking depends mainly on the cooling rate at about 572°F (300°C), as

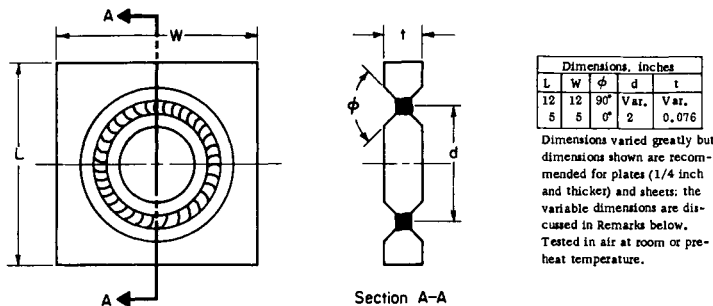


FIG. 14.30. Circular-patch test specimen.⁽¹⁴¹⁶⁾

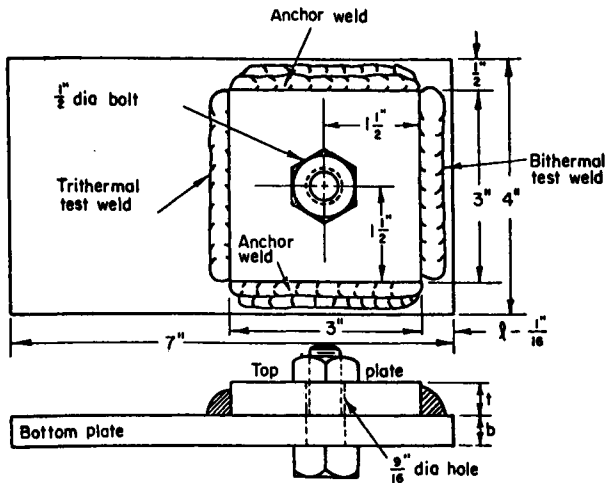


FIG. 14.31. Controlled-thermal-severity test specimen.

measured in the heat-affected zone adjacent to the fusion line. If a critical rate of cooling for a given electrode-steel combination is exceeded, cracking is supposed to occur irrespective of the external restraint applied. This test only evaluates the effects of cooling rate, not external restraint. The specimen consists of two plates, the square top plate and the rectangular bottom plate. The plates are clamped together with a bolt and two anchor welds. The two plate surfaces in contact are surface ground to obtain the best possible heat flow. After assembly the test specimen is allowed to cool to room temperature, and finally the bithermal weld is deposited, the specimen again allowed to cool, and finally the trithermal weld is made. Various thermal severities are obtained by using different thicknesses of plate. The thermal severity number, TSN, is calculated from the following equations:

$$\begin{aligned} \text{TSN} &= 4(t + b) \text{ for bithermal weld,} \\ \text{TSN} &= 4(t + 2b) \text{ for trithermal weld.} \end{aligned} \tag{14.9}$$

The severity of cracking is determined by measurements of crack length on metallographic sections.

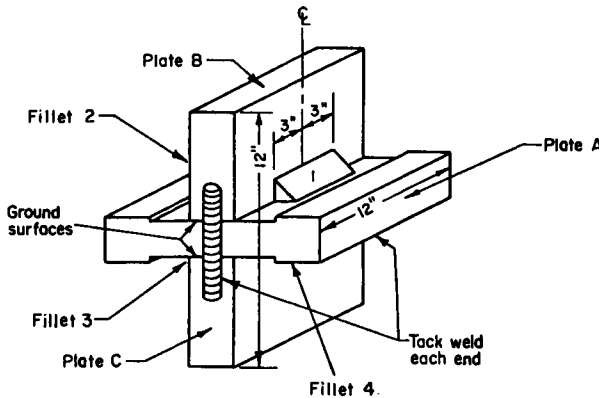


FIG. 14.32. Cruciform test specimen.

14.4.5 Cruciform test^(1016, 1423-1425)

The cruciform test (Fig. 14.32) is essentially a modification of the double-T-joint specimen which is used mainly for weld metal studies. However, the cruciform test is also used to differentiate between the cracking tendencies of various heats on armor steel. The test is designed to evaluate heat-affected zone cracking, but has been criticized on the ground that it was more sensitive to testing conditions than to differences in cracking susceptibility. The possibility of hydrogen diffusing from one fillet to another has also been pointed out. Before the fillet welds are deposited, the assembly is tack welded using a jig to obtain accurate fit-up. Each fillet is deposited, in the numbered sequence shown, at a constant, predetermined starting temperature. After welding the specimen is aged 48 hr at room temperature and stress relieved at 1150°F (788°C) for 2 hr. The specimen is then inspected for cracking, and sectioned for metallographic examination.

14.4.6 Longitudinal-weld underbead-cracking test^(1016, 1426-1428)

This test (Fig. 14.33) was developed to study underbead cracking of low-alloy and high-strength steels. The specimen consists of a block of steel, 2 in. (50 mm) wide by 3 in. (76 mm) long, and the full thickness of the plate being investigated. A bead, 1 1/4 in. (32 mm) long, is deposited on a specimen. The specimen is pre-cooled or preheated to one of several desired temperatures and during welding, and for 1 min afterwards, is immersed within 1/4 in. (6.4 mm) of its top surface in a liquid bath at a chosen temperature. It is then removed and held for 24 hr at room temperature and then is stress relieved at 1050°F (566°C) for 1 hr. The extent of cracking is determined by examining a longitudinal section through the weld by magnetic particle or metallographic techniques. The extent of cracking is expressed as a percentage of the total bead length. Although extent of cracking varies with individual specimens, an average of ten tests is reproducible within 10%; an average of five tests is reproducible within 20%. This test does not provide any variation on degree of restraint. Recent investigations indicate that this may be an important factor in underbead cracking, therefore the test may have lost some of its value.

14.4.7 Varestraint test.⁽¹⁴²⁹⁾

The Varestraint (Variable Restraint) test has been developed by Savage and Lundin⁽¹⁴²⁹⁾ for evaluating the hot-cracking tendency of a weldment. The test permits the evaluation of base metal weldability as well as determining the influence of the particular welding processes and associated welding variables on hot cracking.

The Varestraint testing procedure utilizes a small, laboratory scale specimen support-

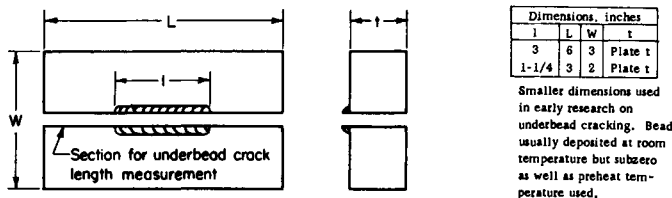


FIG. 14.33. Longitudinal-weld underbead-cracking test specimen.⁽¹⁴¹⁶⁾

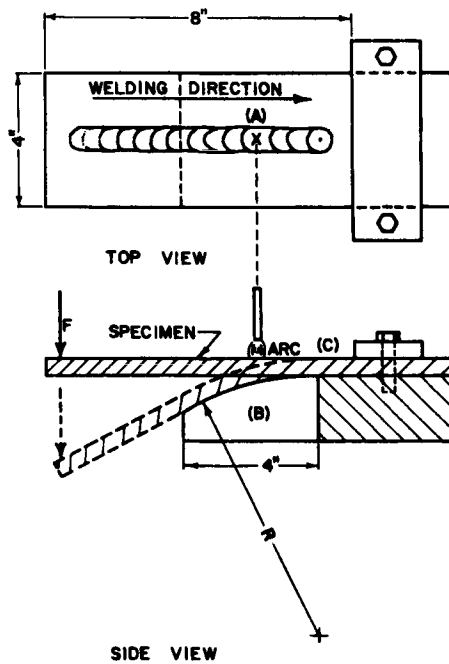


FIG. 14.34. Simplified sketch of the operation of the Vareststraint testing device.

ted as a cantilever beam, as shown schematically in Fig. 14.34. A weld is deposited from left to right, as indicated. As the arc passes the point marked *A* in Fig. 14.34, a massive, pneumatically actuated loading yoke bends the specimen downward suddenly to conform to the radius of curvature of top surface of the removable die block, *B*. Meanwhile, the arc travels steadily onward and is subsequently interrupted in the run-off area at *C*. Figure 14.35 is a schematic representation showing the typical relationship between the observed hot cracking and the location of the weld puddle at the instant of application of the augmented-strain.

Under normal conditions, weld metal hot cracking is produced only within a relatively narrow region directly behind the instantaneous position of the solid-liquid interface at the trailing edge of the weld puddle. Since the augmented-strain is automatically applied at a predetermined point in the arc travel, a fiduciary mark can be made on the specimen in advance of the test to identify the proper area for subsequent examination. Microfissuring in the weld heat-affected zone is normally observed only in the region of

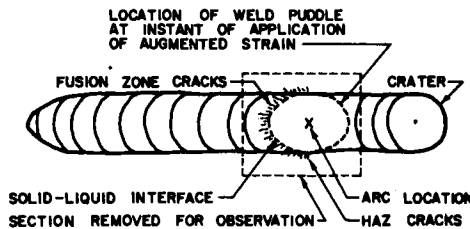


FIG. 14.35. Schematic representation of the section of the weld removed for metallographic observation. Top surface of weld showing location of arc, weld puddle, and solid-liquid interface at instant of straining.

the heat-affected zone at either side of the location of the weld puddle at the instant the augmented-strain is applied. Therefore, where metallographic examination is to be performed, a section corresponding to the dashed rectangular area in Fig. 14.35 is removed and subjected to suitable metallographic preparation.

Since the inherent restraint provided by the simple rectangular specimen is too low to cause cracking in the absence of augmented-strain, the minimum augmented-strain required to cause cracking with a given set of welding parameters provides one quantitative index of cracking sensitivity, called the *cracking threshold*. In addition, the variation of the cracking threshold produced by changes in welding process and welding parameters provides a quantitative method for comparing welding procedures.

14.4.8 Rigid-restraint cracking (RRC) test and tensile restraint cracking (TRC) test

The rigid restraint cracking (RRC) test and the tensile restraint cracking (TRC) tests have been developed by a group of Japanese investigators.⁽¹⁴³⁰⁻¹⁴³³⁾

Rigid restraint cracking test.⁽¹⁴³⁰⁻¹⁴³²⁾ Figure 14.36 shows schematically the rigid restraint cracking (RRC) test. When a certain length of a butt joint (called the restraining gage length, l) is kept constant by a proper clamping mechanism, reaction stresses in

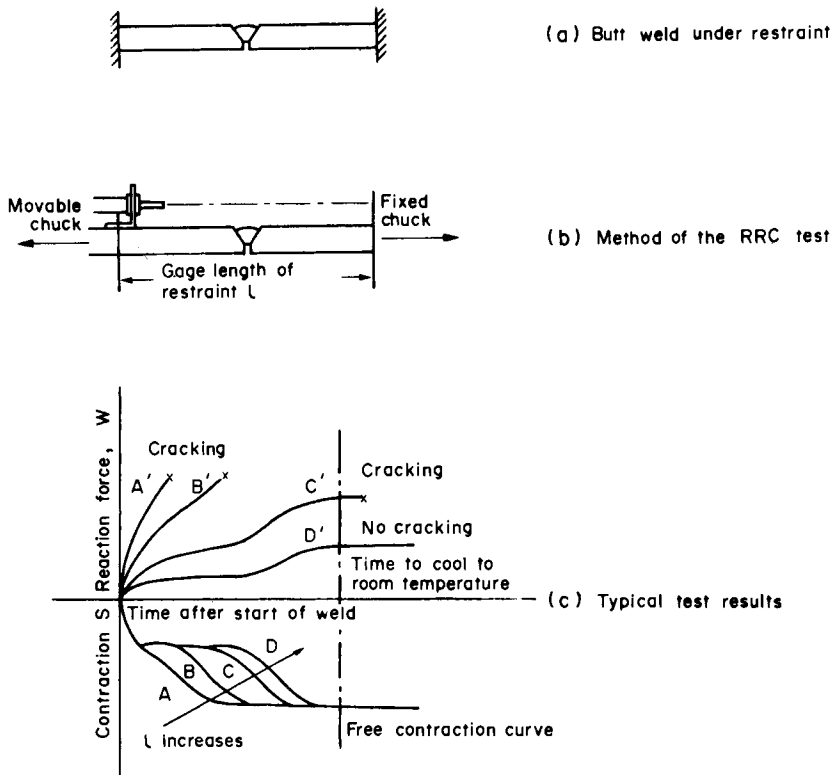


FIG. 14.36. Schematic diagram of the rigid restraint cracking (RRC) test.

the joint increase as the joint shrinks after welding. The value of reaction stress increases as l decreases, provided that other parameters such as heat input, plate thickness, etc., are the same.

When l is very small, reaction force in the weld metal increases to large values soon after welding is completed and the weld metal may crack, as shown by curves A' , B' in Fig. 14.36. When l is somewhat larger, the reaction force increases as shown by curve C' ; the weld may not crack immediately after welding but delayed cracking may occur when the base metal is high-strength steel. When l is sufficiently large, no cracking occurs as shown by curve D' .

Figure 14.37 shows how reaction force, W (ton), increases after welding a low-carbon steel joint 20 mm ($\frac{3}{4}$ in.) thick, 30 mm (1.2 in.) wide with the heat input of 16,000 joules/cm (40,600 joules/in.). Cracking occurred when $l = 200$ mm (8 in.), but no cracking occurred when $l = 300$ mm (12 in.).

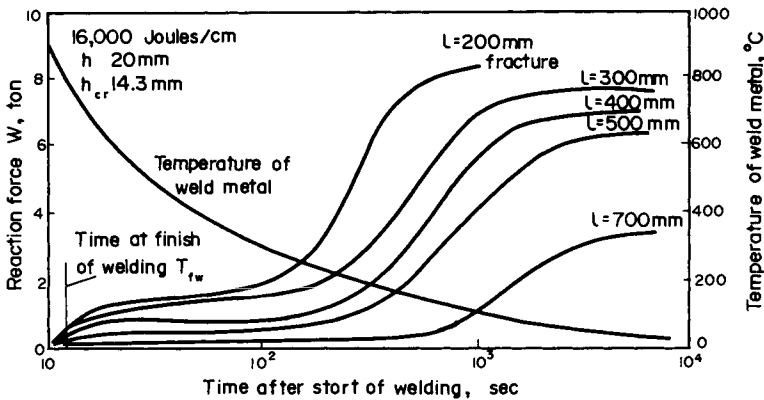


FIG. 14.37. Effect of restraining gage length l on reaction force.

Note: Low-carbon steel weldments, plate thickness $h = 20$ mm, $Q = 16,000$ joules/cm, breadth of specimen (weld length) = 30 mm.

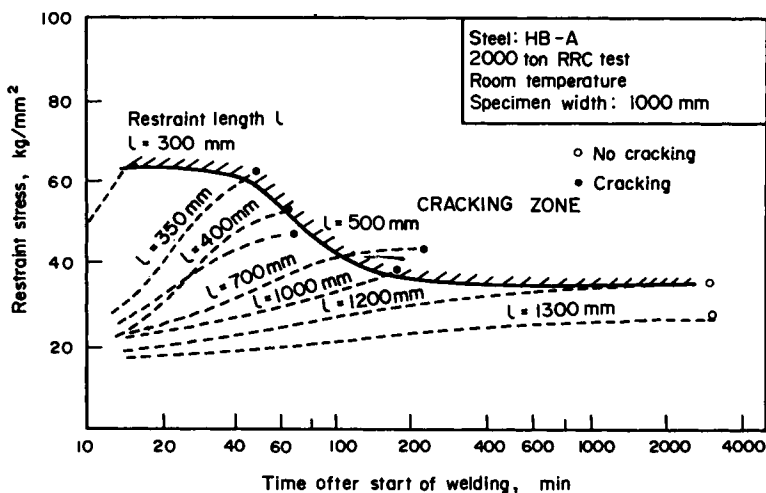


FIG. 14.38. Development of restraint stress during cooling and cracking in the RRC test.

In the RRC test, the intensity of restraint K_s (kg/mm^2) is:[†]

$$K_s = E \cdot \frac{h}{l} \tag{14.10}$$

where E = Young's modulus,
 h = thickness of the base plate,
 l = restraining gage length,

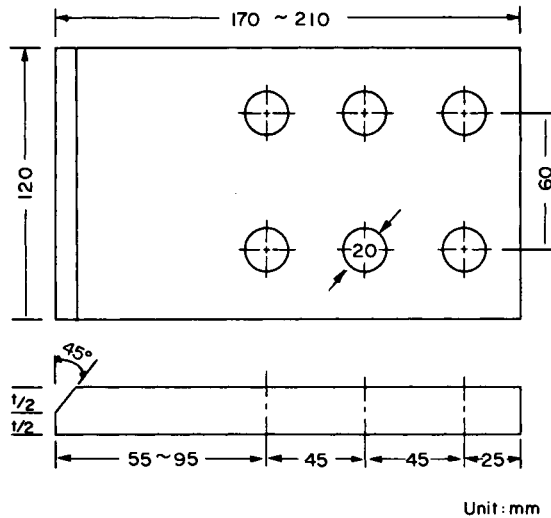
Figure 14.38 shows experimental results on HT80 steel. Shown here are reaction stresses in the weld metal. In the first pass weld of heavy plates, reaction stresses in the weld reach a very high value resulting in cracking. As the reaction stress decreases, it takes a longer time for cracking to occur. When the reaction stress is below a certain level, cracking does not occur even after a long period.

The results clearly indicate that cold cracking is a type of delayed fracture. Results shown in Fig. 14.38 are understandable on the basis of hydrogen-induced delayed-fracture characteristics as shown in Fig. 12.1.

Tensile restraint cracking test.^(1432, 1433) In the TRC test, tensile load is applied to a butt joint during welding or 3 to 4 min after welding is completed. Figure 14.39 shows the test specimen.

Figure 14.40 shows examples of loading curves and weld thermal cycles. Loading may be applied during welding or after welding is completed.

Figure 14.41 shows an example of test results. When a specimen is subjected to a certain stress, a crack initiates at a certain time and the crack grows with time. As the stress level decreases, the time necessary for crack initiation and that for fracture increase. When the stress is below a certain limit, a crack does not occur even after a long period.



Unit : mm

FIG. 14.39. TRC test specimen.

Note: Two specimens as shown in this figure are joined.

[†] See eqn. (14.13).

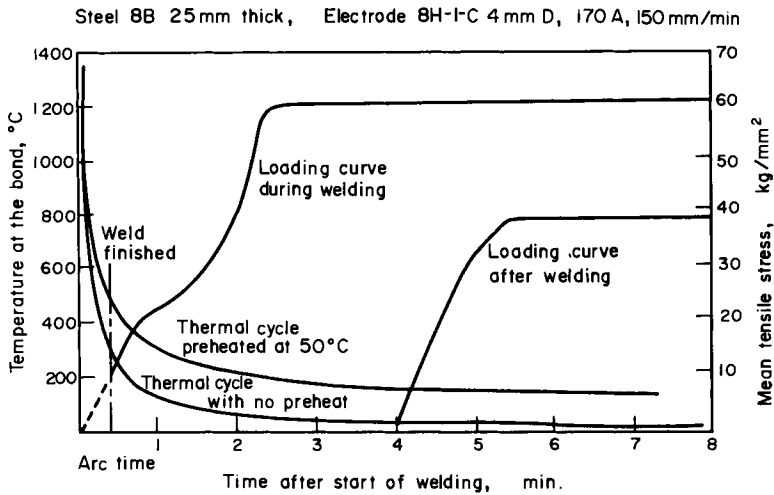


FIG. 14.40. Examples of loading curve and weld thermal cycle during the TRC test.⁽¹⁴³³⁾

- Note: (1) Steel 8B: quenched and tempered steel.
 C = 0.15, Si = 0.35, Mn = 1.06, P = 0.10, S = 0.008,
 Ni = 0.81, Cr = 0.43, Cu = 0.25, Mo = 0.40.
 Yield strength = 76.4 kg/mm² (109 ksi).
 Ultimate tensile strength = 87.9 kg/mm² (125 ksi).
- (2) Electrode 8H-I-C: E11018, 4 mm,
- (3) Welding conditions:
 Welding current = 170 amperes.
 Arc travel speed = 150 mm/min (6 in./min).

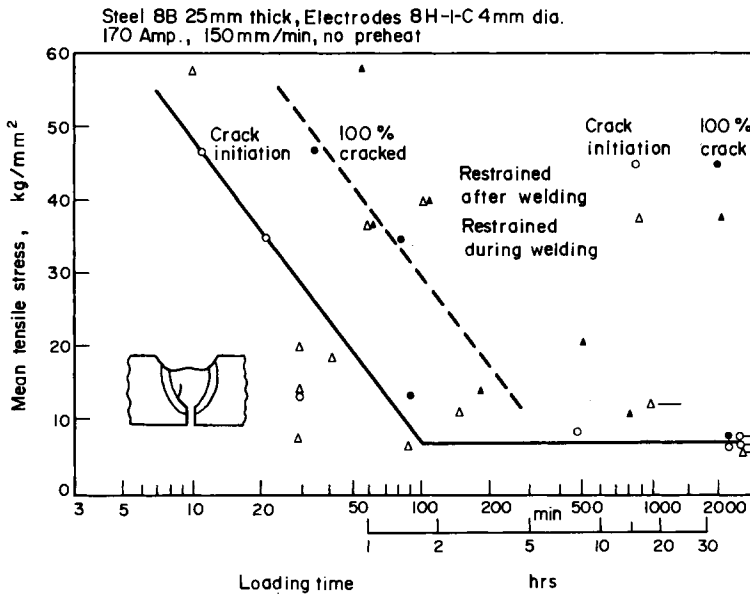


FIG. 14.41. Effect of tensile time in TRC test in weldments in steel 8B.⁽¹⁴³³⁾

14.4.9 Implant test⁽¹⁴³⁴⁻¹⁴³⁶⁾

The implant test has been developed by Granjon and others at the Institut de Soudure in France.^(1434, 1435)

By "implant" is meant a cylindrical sample of the material under study which fits easily into a hole specially drilled in a backing plate of the same, or another, material. If the thermal conductivity of the backing plate is identical with that of the implant, the latter undergoes the same thermal cycle as the plate when the weld bead is made. Consequently, all phenomena associated with the thermal cycle can be reproduced on this reduced, and therefore practical, sample—the "implant". The table in Fig. 14.42 lists the observations and determinations facilitated, or made possible, by the application of this method.

The basic consideration which justifies the implant method lies in the fact that at the same distance d from the weld junction of a weld bead on the plate (Fig. 14.43), the heat

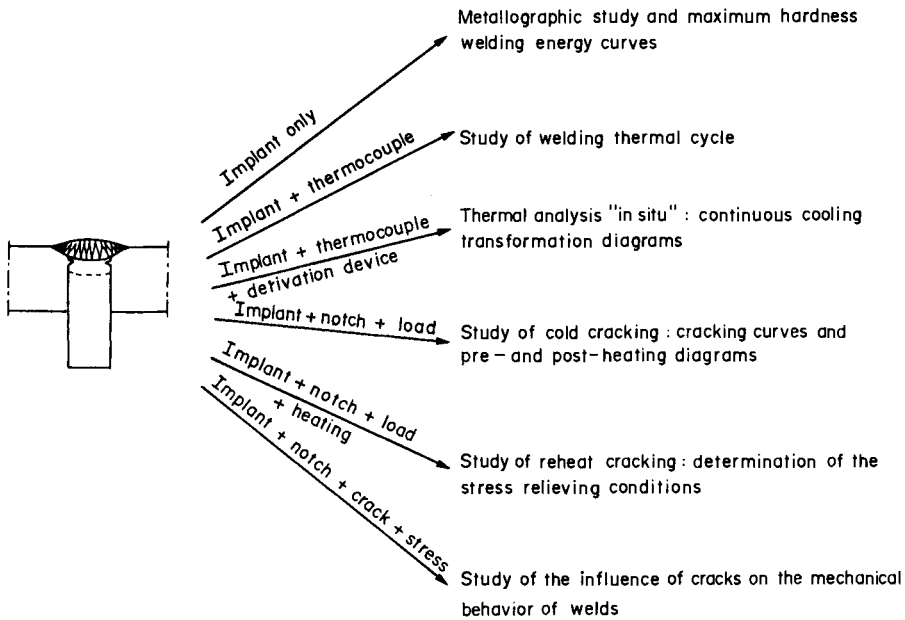


FIG. 14.42. Current applications of the implant method.

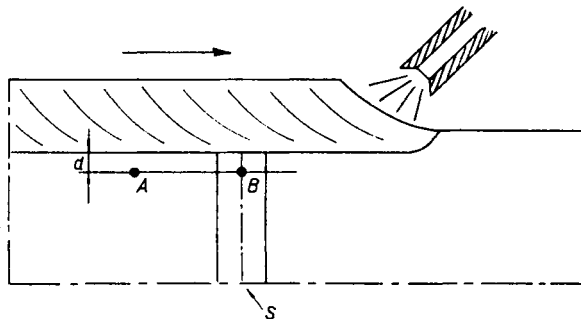


FIG. 14.43. Equivalence of heat cycles in plate and implant.

cycles at a point *B* of the implant and at a point *A* of the base plate are the same. In particular, the same results occur at points *A* and *B* if one measures, as a function of the welding energy, the cooling times of the welding cycles, e.g. between 800° and 500°C (1472° and 932°F).

When the implant test is used for studying cold cracking, a specimen with a vee-notch is usually employed, as shown in Fig. 14.44. After deposition of the weld bead, the specimen is subjected to a tensile load fixed at a given value. The cracking stress in relation to the cross-section at the bottom of the notch is used as a criterion to express the susceptibility to cracking.

Time of cracking or fracture. With the fixture used, the implant can be put under load shortly after welding, while it is still warm, or later. It can then be noted, as is shown in Tables 14.5 and 14.6, that the cracking and the fracture which appear rapidly when the

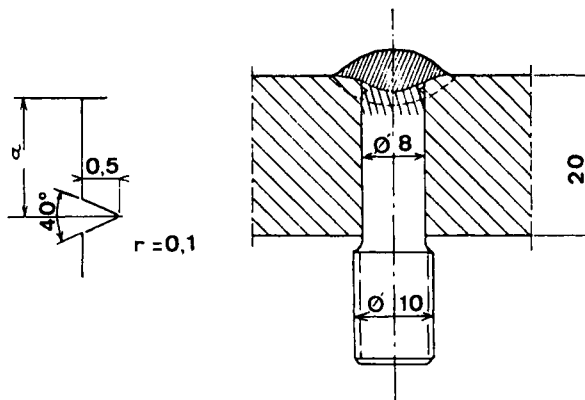


FIG. 14.44. Specimen for cold-cracking test.

TABLE 14.5 *Cracking or fracture time in terms of the time of application of the load t_c (c for time t_c). Steel A3 (C : Mn steel). Energy 15×10^3 J/cm. Thickness 20 min. Stress 24.4 hbar. Dry basic electrode⁽¹⁴³⁴⁾*

t_c	θ_c	Result
1 min 30 sec	100°	Fracture in 10 min
30 min	31°	Fracture in 48 min
1 hr	20°	Fracture in 54 min
3 hr	20°	Fracture in 1 hr 5 min
24 hr	20°	No cracking after 65 hr

Steel A3 (steel A52).
C = 0.25, Mn = 1.49, Si = 0.48, Al = 0.060.

TABLE 14.6 *Same experiment as in Table 14.5 with a steel (A4) susceptible to hardening. Stress 18 hbar⁽¹⁴³⁴⁾*

t_c	θ_c	Result
1 min 30 sec	100°	Fracture in 11 min
3hr	20°	Fracture in 11 min
50 hr	20°	Cracking (15%) after 64 hr
100 hr	20°	No cracking after 16 hr

loading takes place very soon after welding, can be greatly delayed or even avoided when the loading itself is postponed.

Cracking temperature: progress of the crack. It is also possible to switch off the load during a test to determine the moment and consequently the temperature at which the crack occurs and also the stress value as well as how it develops. Table 14.7, dealing with a C:Mn steel (A2) for which the cracking and fractures stresses under the welding conditions used are respectively 8 and 26 hbar (8.2 and 26.5 kg/mm² or 11.6 and 37.7 ksi), shows how a crack develops under a stress of 21.6 hbar (22 kg/mm² or 31.3 ksi) applied immediately after welding.[†] The crack seems to start very quickly (after 10 min) and at a temperature between 40° and 45°C (104° and 113°F). It develops further fairly slowly, which shows to what an extent tests of cold cracking must be prolonged. Similar results have been found for other steels showing that with immediate loading, the so-called cold cracking never really starts from dead cold, but at the end of cooling. Similarly, so-called delayed cracking starts in fact rapidly.

TABLE 14.7 Development of cracking in terms of time. 20-mm thick plate. Energy 10×10^3 J/cm. Steel As(0.18C:133Mn:0.48Si)⁽¹⁴³⁴⁾

t_c	t'	θ_r	Result
1 min 30 sec	6 min 30 sec	45°	No cracking
1 min 45 sec	10 min	40°	5% cracking
1 min 30 sec	30 min	28°	10% cracking
1 min 30 sec	1 hr	24°	20% cracking
1 min 30 sec	16 hr	20°	28% cracking

t_r = loading time

θ_r = temperature for t_r

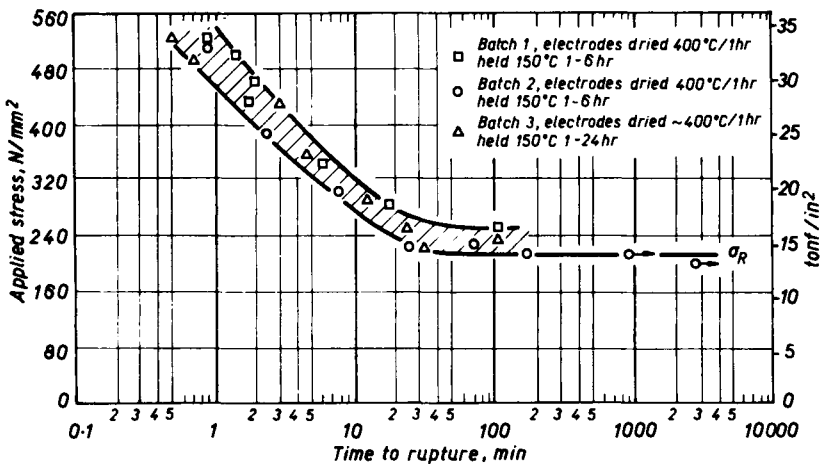


FIG. 14.45. Graph showing the reproducibility of the implant cracking test with separately dried batches of electrodes.⁽¹⁴³⁷⁾

[†] 1 hbar = 10 MN/m².

Reproducibility. It is believed that scattering of test results is reasonably small. Figure 14.45 shows test results reported by Hart and Watkinson.⁽¹⁴³⁷⁾ A series of tests were made to assess the reproducibility of the method, using 0.28 in. (7 mm) diameter specimens with 0.02 in. (0.5 mm) deep notches with radii in the range 0.0005–0.0002 in. (0.013–0.05 mm). These were welded with the same class E11018-M electrodes as in the first series, but dried at 400°C (204°C) for 1 hr, transferred to and held at 150°C (66°C) before use. Three batches of tests were made in this series. In two batches the tests were made on different days from electrodes dried and used in exactly the same manner. The third was made with electrodes dried at only approximately 400°C and used after holding at 150°C for between 1 and 24 hr. The small range of scatter in all these tests can be seen from Fig. 14.45.

14.4.10 *Recent trends and comparison of results obtained with different tests*

Although it is difficult to state recent trends of the use of weld cracking tests, without conducting an extensive survey, the author believes that current research efforts are directed toward developing methods for generating quantitative information on crack sensitivity. Recent efforts for developing Vareststraint, RRC, TRC, and implant tests indicate such trends. It is interesting to note that in these recent tests, stresses are applied to a welded specimen; while in older tests welds are made on a specimen or a series of specimens with predetermined restraint.[†]

The application of stresses has two advantages:

1. Stresses in a specimen can be varied in a range much larger than that which could be made available using restrained specimens.
2. By applying stress of a known value, one could easily determine the level of stress (and time) under which a crack initiates and propagates.

Efforts also have been made by various investigators to compare results obtained in different tests. The following pages show a few examples.

Study by Satoh and others.⁽¹⁴³²⁾ Satoh and others compared the RRC, the TRC, and the implant test. The RRC test is similar to the TRC test, but differs in the following manner. In the TRC test, a constant load is applied immediately or a few minutes after welding. In the RRC test, reaction stresses in the specimen increase by keeping the length of the specimen constant during welding and cooling. It has been found by experience that similar test results are obtained when the load is applied in the TRC test a few minutes after welding. Figure 14.46 shows that the relationships between critical reaction stress and fracture time determined by the RRC and the TRC tests are almost identical.

Figure 14.47 shows the correlation between the critical stresses determined by the RRC and the TRC tests and those determined by the implant test. The critical stresses for crack initiation determined by the implant test are almost equal to those determined by the RRC and TRC tests for each material and test condition. Table 14.8 shows the chemical compositions of the seven base plates tested. Two tests were made using a preheating of 50°C (122°F).

Study of Gordine.⁽¹⁴³⁸⁾ Gordine studied the weldability of some arctic grade line-pipe

[†] Further comments on restraint cracking tests are given in a later part of this chapter, see Fig. 14.52.

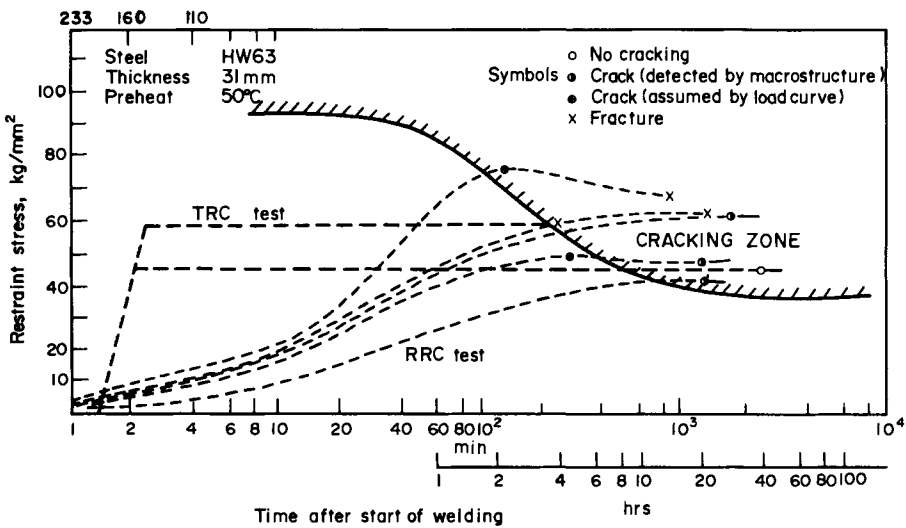


FIG. 14.46. Development of restraint stresses and cracking in RRC and TRC tests.⁽¹⁴³²⁾

Note: Welding conditions used:
 Welding current = 170 amperes.
 Arc voltage = 23 – 28 volts.
 Arc travel speed = 150 mm/min (6 in./min).

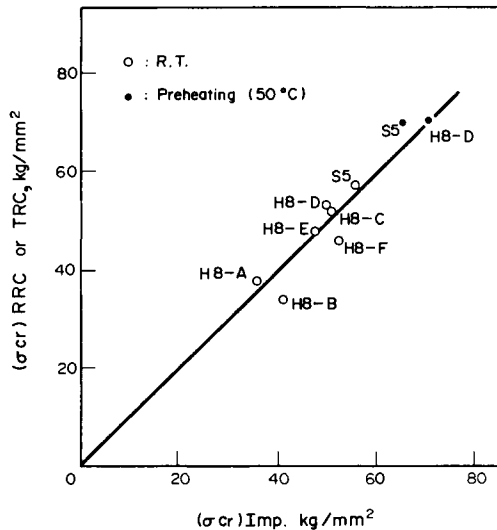


FIG. 14.47. Relation between σ_{cr} of implant test and that of RRC and TRC tests.⁽¹⁴³²⁾

steels using the controlled thermal severity (CTS) test and the implant test. Tests were made of ten different types of steels which may be separated into the following three categories (see Table 14.9).

1. Conventional X-65 line-pipe steel—steel F (included for comparative purposes).
2. Controlled rolled micro-alloy line-pipe steels—steels J, M, N, P, R, and Z.
3. Quenched and tempered steels—steels T and S.

TABLE 14.8 *Chemical compositions of steels tested by Satoh et al.⁽¹⁴³²⁾*

	Chemical composition (%)											P_{an}
	C	Si	Mn	Cu	Ni	Cr	Mo	V	P	S	C_{eq}	
H8-A	0.14	0.23	1.00	0.21	0.89	0.47	0.32	0.030	0.015	0.006	0.515	0.271
H8-B	0.14	0.28	0.94	0.24	0.03	0.82	0.35	0.043	0.023	0.005	0.564	0.277
H8-C	0.13	0.26	0.84	0.25	0.02	0.93	0.23	0.040	0.016	0.005	0.528	0.269
H8-D	0.13	0.35	0.95	0.26	0.99	0.53	0.49	0.040	0.008	0.005	0.560	0.282
H8-E	0.11	0.27	0.80	0.23	1.04	0.39	0.40	0.033	0.009	0.006	0.461	0.237
H8-F	0.15	0.29	0.86	0.17	0.91	0.47	0.40	0.030	0.010	0.008	0.524	0.279
S5	0.14	0.39	1.31	—	—	—	—	—	0.011	0.013	0.375	0.219

$$P_{an} = C + Si/30 + Mn/20 + Cu/20 + Ni/60 + Cr/20 + Mo/15 + V/10 + 5B.$$

$$C_{eq} = C + Si/24 + Mn/6 + Ni/40 + Cr/5 + Mo/4 + V/14.$$

Table 14.9 *Summary of implant test results in line-pipe steel (Gordine⁽¹⁴³⁸⁾)*

Steel	Carbon equivalent		Lower critical stress (ksi)	Maximum HAZ Vickers hardness
	Conventional ^(a)	Ito-Bessyo ^(b)		
A	.43	.19	82.0 (565 MPa)	303
F	.37	.23	61.2 (421 MPa)	442
J	.34	.19	87.0 (600 MPa)	326
M	.43	.18	87.0 (600 MPa)	274
N	.30	.14	86.6 (595 MPa)	294
P	.40	.21	59.2 (407 MPa)	422
R	.41	.21	47.0 (324 MPa)	360
S	.36	.19	71.0 (490 MPa)	360
T	.41	.18	76.0 (524 MPa)	391
Z	.47	.18	65.0 (448 MPa)	336

^(a) See eqn. (14.11).

^(b) See eqn. (14.7) for P_{CM} .

TABLE 14.10 *Controlled thermal severity test results for line-pipe steels (Gordine⁽¹⁴³⁸⁾)*

Steel	Thermal severity number	Max. HAZ Vickers hardness	Test temperature at which cracking first occurred	
A	5	318	< -36°C	(-32°F)
F	6	435	-16°C	(+3°F)
J	6	352	+21°C	(+70°F)
M	5	274	-27°C	(-16°F)
N	5	255	-36°C	(-32°F)
P	7	442	-17°C	(+2°F)
R	7	422	-17°C	(+2°F)
S	6	429	+21°C	(+70°F)
T	6	352	< 0°C	(+32°F)
Z	6	355	< 0°C	(+32°F)

The results of the CTS tests on the different line-pipe steels are summarized in Table 14.10. Data were obtained for eight of the ten steels in the program. Plate thicknesses used were determined by the wall thickness of the pipe and ranged from 0.375 to 0.720 in. (9.5 to 18.3 mm) with the corresponding thermal severity number varying from 5 to 7. Also shown in Table 14.10 are the maximum HAZ hardness values recorded. Selected test welds from the CTS tests were sectioned and polished, and hardness traverses were made across the weld and HAZ using a Vickers hardness tester with a 10-kg (22 lb) load. In most cases, the maximum HAZ hardness corresponded to the region of the HAZ through which the crack traversed.

In Fig. 14.48, typical stress/time curves obtained from the implant test are shown for three selected steels in the evaluation program. The data in Fig. 14.48 show the two extremes of behavior. Steel R exhibits a CS value of 47.0 ksi (324 MN/m²) whereas steel M has a much higher value of 87 ksi (600 MN/m²). Also shown for comparison is the stress/times curve for the conventional C-Mn X 65 steel, i.e. steel F.

A summary of the entire implant results for all ten steels is given in Table 14.9. The results show a wide range in CS values for the ten different materials. All steels tested, except for steels P and R, showed CS values higher than that of the conventional line-pipe steel, steel F.

As in the CTS tests, sections were taken through selected fractured implant test specimens and examined metallographically.

Of the two test methods used to determine the susceptibility to cold cracking, the implant test was found to give a more sensitive measure of cracking susceptibility, and more reliance was placed upon these results than those from the CTS test. The implant test confirmed that the majority of the steels tested had lower levels of susceptibility than the one conventional line-pipe steel that was also tested. Only steels P and R showed a

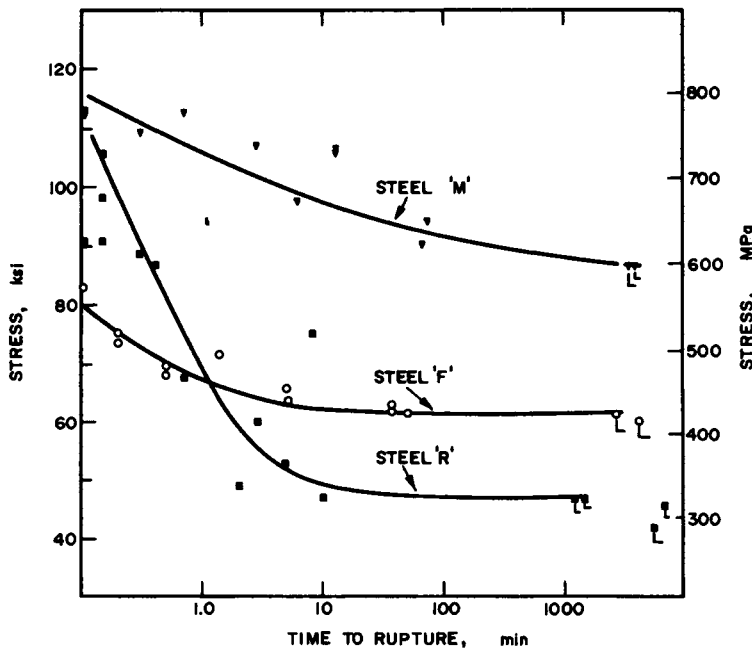


FIG. 14.48. Implant test results for steels M, F and R tested by Gordine.⁽¹⁴³⁸⁾

greater susceptibility to cold cracking than the conventional steel. The CTS results shown in Table 14.10 indicate little real difference between the cracking susceptibilities of the ten steels tested. Only steels A, M, and N showed a cracking tendency lower than the conventional line-pipe steel. They also showed much lower HAZ hardness levels. The remaining steels showed performances equal to or, in some cases, worse than the conventional steel.

Also shown in Table 14.9 are the carbon equivalents (CE) for the ten different steels. The carbon equivalent is commonly used as an indicator of the tendency of a steel to hardening in the HAZ and susceptibility to hydrogen-induced cracking. Most pipeline specifications impose upper limits upon the CE values of the line-pipe steels. The carbon equivalent formula used in most pipeline specifications is as follows:

$$CE = C + \frac{Mn}{6} + \frac{Cr + Mo + V}{5} + \frac{Ni + Cu}{15}. \quad (14.11)$$

Although this formula works very well for the conventional C/Mn line-pipe steels, it has been recognized by many workers that it is not as appropriate for the newer microalloy steels. The results in Table 14.9 confirm this very clearly. For example, steels A, M, and Z have high CE values as determined by the above formula and yet show quite low HAZ hardnesses and high resistances to HAZ cracking. Conversely, conventional line-pipe steel F has one of the lowest CE values and yet has high HAZ hardness and low tolerance to HAZ cold cracking.

Attempts have been made to modify the CE formula. One relationship that has been reported to work much better for the microalloy steels is the formula proposed by Ito and Bessyo.^(14.13)

The CE values obtained using this relationship are also listed in Table 14.9. In this case the correlation of CE value to HAZ hardness and cracking susceptibility is much better although still not perfect. Gordine concluded that it would appear that the Ito-Bessyo formula is, however, a better measure of the CE of the microalloy steels and is a more reasonable guide to the weldability of the steel.

14.5 Analytical and Experimental Determination of the Degree of Restraint of Weld-Cracking Test Specimens and Joints in Actual Structures

It has been well established that as the degree of restraint of a joint increases (1) reaction stresses in the joint increase, (2) distortion decreases, and (3) tendency for cracking increases. These effects have been discussed in various parts of this textbook as follows:

1. Chapter 3 discusses some basics of reaction stresses.
2. Chapter 4 (Section 4.7.4) discusses measurement of the degree of restraint of a welded joint.
3. Chapter 6 (Section 6.3) discusses residual stresses in restrained butt welds.
4. Chapter 7 discusses effects of restraint on distortion.
5. Earlier parts of Chapter 14 discuss effects of restraint on cracking.

What is needed here is to develop a methodology to determine, analytically and/or experimentally, the degree of restraint of a laboratory specimen and that of a joint in actual structures. Then one can utilize information obtained in a laboratory to

the welding fabrication of actual structures. The following pages discuss this subject with an emphasis on the prevention of weld cracking.

14.5.1 Historical development

Although many investigators in various countries have studied the effects of joint restraint on residual stresses, distortion, and cracking, a group of Japanese investigators since the late 1930s have made special efforts for conducting scientific research on this subject, as follows:

1. The development of ways of analytically expressing the degree of joint restraint in various types of joint configuration.
2. The generation of large amounts of experimental data describing how the degree of restraint affects distortion, residual stress, and cracking.

A number of investigators were involved in this work, and various notational systems were used.^(703, 1439-1442)† Kihara *et al.*⁽⁶⁰⁴⁾ used “K” to express the degree of restraint of a slit-type butt joint, as shown in Fig. 7.3.

Much of the work done in Japan from around 1940 to the early 1950s was carried out with little contact with the outside world, because of World War II; and some of these projects were significantly different from any done elsewhere. In the early 1950s, for example, when these Japanese investigators studied how the degree of restraint affects the transverse shrinkage in butt welds, they knew about the fracture mechanics theory being developed in the United States at that time, but had almost no personal contact with the United State investigators working in fracture mechanics. This is when the confusion began over the use of the notation “K”.

Although Japanese investigators for a number of years have used the notation “K” to mean “the degree of restraint in a welded joint”, that notation is more widely used (in the fracture mechanics theory) as the “stress intensity factor”. Having two different uses for *K* has caused some confusion. Recently attempts have been made within Commissions IX and X of the International Institute of Welding to develop a system of notations expressing the degree of restraint which are less confusing.^(320, 1443)

14.5.2 Analysis of reaction stress and weld cracking under restrained conditions

During the 1960s Satoh and Matsui^(1441, 1442) studied reaction stresses and weld cracking as they occurred under restrained conditions. The study concentrated its efforts on the weld metal cracking that occurs during the first pass in restrained butt joint.

Figure 14.49(a) is a butt joint under restraint. The hindered contraction between *A* and *A'* during cooling develops a reaction force, from which elongations of the base metal, λ_b , and the weld metal, λ_w , result. When both ends are fixed, the sum of λ_b and λ_w is equal to the free contractions *S* between *A* and *A'* at any given instant during cooling, or

$$\lambda_b + \lambda_w = S. \quad (14.12)$$

† Further details of the historical development are presented in reference (320).

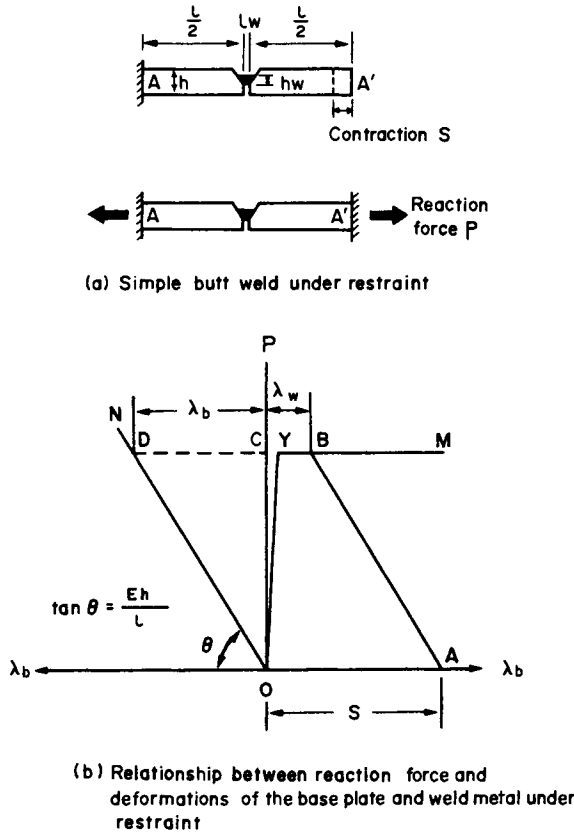


FIG. 14.49. Shrinkage of a butt weld under restraint.

When the plate thickness, h , is sufficiently greater than the depth of the weld throat, h_w , the behavior of the base metal can be regarded as elastic even when reaction stresses in the weld metal are high enough to cause cracking.

Figure 14.49(b) shows how the reaction force per unit weld length, P , increases with λ_w and λ_b . Line OYM represents the relationship between λ_w and P . Beyond point Y the weld metal deforms plastically and may eventually break. The straight line ON represents the relationship between λ_b and P . When $S = OA$ and when AB is parallel to ON , one may obtain $\lambda_b = \overline{CD}$, $\lambda_w = \overline{BC}$, and $P = \overline{OC}$. The gradient of the straight line ON is:

$$\tan \theta = \frac{Eh}{l} \equiv K_s \text{ (kg/mm}^2\text{)}. \tag{14.13}$$

K_s as defined here represents the reaction force per unit weld length necessary to produce average elastic strains of unit magnitude. Satoh and Matsui designated K_s "intensity of restraint". The reaction force P increases as K_s (or h/l) increases for a given value of S , and P increases as S increases for a given value of K_s .

Satoh and Matsui also used:

$$K_0 = \frac{K_s}{h} \text{ (kg/mm}^2\text{/mm)}. \tag{14.14}$$

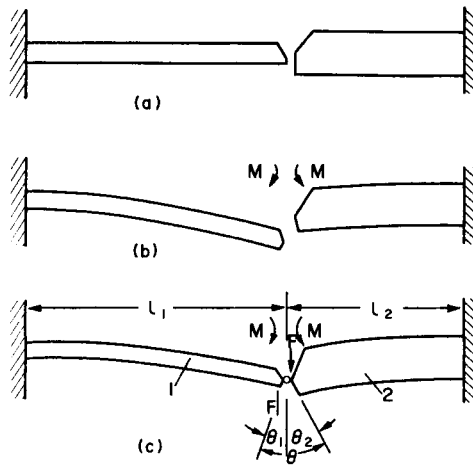


FIG. 14.50. Bending restraint of a butt joint with unsymmetric groove.

They called K_s the “coefficient of intensity of restraint”. K_0 defined in eqn. (14.14) is similar to k_s defined in eqn. (7.1).

Satoh *et al.*⁽¹⁴⁴⁵⁾ expanded the concept of restraint intensity to cover angular distortion, as shown in Fig. 14.50. The bending restraint intensity, K_B , is defined as:

$$K_B = M/\theta \tag{14.15}$$

where M = bending moment per unit weld length (kg mm/mm),
 θ = total angular distortion at the groove (radian).

The dimension of K_B is kg-mm/mm/rad = kg/rad.

Satoh *et al.*⁽¹⁴⁴⁵⁾ suggested the use of K_T to express the restraint intensity under tension. The definition is:

$$K_T = \frac{P}{\delta_x} \tag{14.16}$$

where P = force per unit weld length (kg/mm),
 δ_x = displacement in the direction perpendicular to the weld line (x-direction).

The dimension of K_T is kg/mm².

The restraint intensity of a short weld (a tack weld, for example) can be defined as:

$$K_T = \frac{P}{l\delta} \tag{14.17}$$

where P = total restraining force (kg),
 l = weld length (mm),
 δ = average displacement of a joint by the force P (mm).

The dimension of K_T is kg/mm².

In addition to the RRC and TRC tests for evaluating tendency for cracking under tension, the BRC (bending restraint weld cracking) test has been developed for evaluating the tendency for weld cracking under bending stresses.⁽¹⁴⁴⁵⁾

Units used to express the restraint intensity. Kihara, Masubuchi, and Matsuyama⁽⁶¹⁴⁾ used “ K ” ($\text{kg}/\text{mm}^2/\text{mm}$) to express the degree of restraint of a slit joint, as shown in Fig. 7.4, in studying effects of K on transverse shrinkage.

Satoh and Matsui^(1441, 1442) used “ K ” (kg/mm^2) to express the degree of restraint of a butt weld, as shown in Fig. 14.49.

This difference in units has added to the confusion with “ K ” ($\text{psi}\sqrt{\text{in}}$, $\text{kg}\sqrt{\text{mm}}/\text{mm}^2$) expressing the stress intensity factor in the fracture-mechanics theory.

In order to reduce confusion the following notations and technical terms are used throughout this textbook:

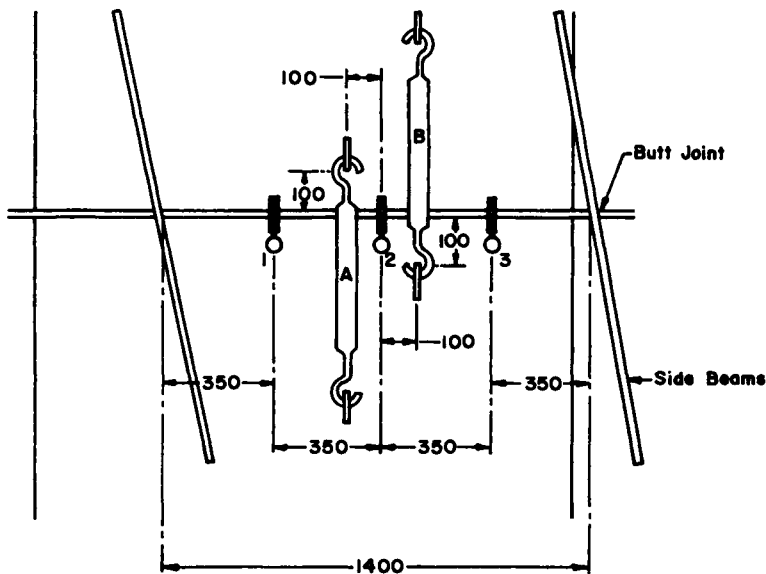
1. Use k_s ($\text{kg}/\text{mm}^2/\text{mm}$) to express “degree of restraint”.
2. Use K_s (kg/mm^2) to express “intensity of restraint”.

A further discussion on the comparison between k_s and K_s are given in reference (320).

14.5.3 Restraint intensity of practical joints

Efforts have been made to determine experimentally and analytically the degree of restraint of complex, practical joints.

Figure 14.51 shows how to determine experimentally the degree of restraint of a butt joint between deck assemblies of an actual cargo ship.^(1446, 1447) A and B are turnbuckles that are hooked to small steel pieces welded to the deck plate. Dial gages are numbered 1, 2, and 3. Changes in the gap between the deck plates are measured with dial gages while



A, B
1, 2, 3: dial gages
Unit, mm

FIG. 14.51. Measurement of the degree of restraint of a butt joint between deck assemblies of an actual cargo ship (Watanabe *et al.*)^(1446, 1447)

the plates are pulled together by the turnbuckles. The tightening force is determined by strain gages mounted on the turnbuckles. The restraint intensity of the joint is then calculated by eqn. (14.16).

With the use of modern computers it is possible to analytically determine the degree of restraint in a complex joint. In 1970 Masubuchi and Ich⁽¹⁴⁴⁸⁾ used a finite element method to calculate the degree of restraint in various butt joints including the Lehigh restraint specimens. Since then a number of investigations have extended the analysis to cover various complex joints, including joints between three-dimensional assemblies. Reference (1443) summarizes results obtained by various investigators on a variety of

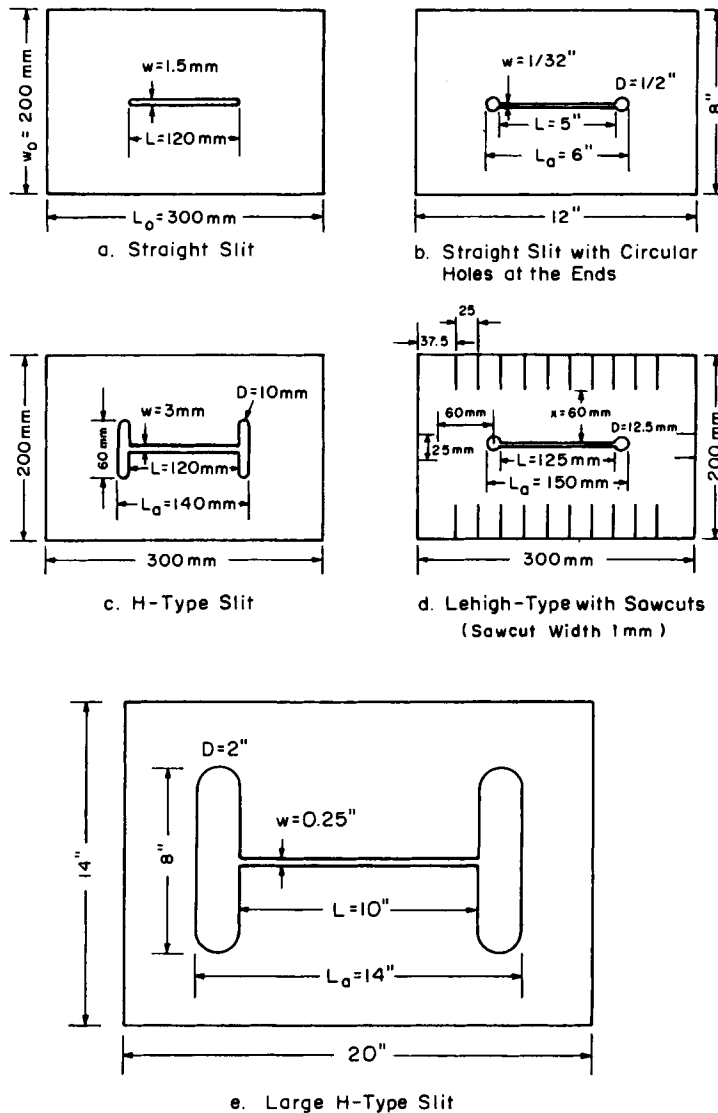


FIG. 14.52. Joint configurations analyzed by Masubuchi and Ich

joint configurations. Presented here are:

- Figure 14.52: Joint configurations analyzed by Masubuchi and Ich.⁽¹⁴⁴⁸⁾
- Table 14.11: Values of degree of restraint of joints studied by Masubuchi and Ich.
- Figure 14.53: Relationship between weld length to slit ratio, R , and non-dimensional degree of restraint for different cases studied by Masubuchi and Ich.
- Figure 14.54: Welded joints restrained by fillet welds.
- Figure 14.55: Measured values of restraint intensity of various butt joints in a spherical pressure vessel.
- Figure 14.56: Effects of plate thickness on measured values of restraint intensity.

1. *Restraint intensity of structural welds.* By summarizing relationships between plate thickness, h , and K_s for many structural welds, one can conclude that the upper limit of the restraint intensity, K_s , of practical joints is:

$$K_s = 40h. \tag{14.18}$$

TABLE 14.11 Values of degree of restraint of joints studied by Masubuchi and Ich

Slit length 1	$R = l/L$	10^3 psi/in	k_s kg/mm ² /mm	$\bar{k}_s = \frac{k_s}{(E/L)}$	Remarks
1. Rectangular plate with a straight slit (Fig. 14.52(a))					
$L = 120$ mm	$\left\{ \begin{array}{l} \frac{1}{3} \\ \frac{1}{2} \\ \frac{2}{3} \\ \frac{5}{6} \\ 1 \end{array} \right.$	4.60	127.36	0.724	
		3.55	98.21	0.559	
		3.05	84.49	0.481	
		2.86	79.30	0.451	
		2.94	81.53	0.464	
2. Straight slit with circular holes at the ends (Fig. 14.52(b))					
$L = 5$ in.	$\left\{ \begin{array}{l} 0.2 \\ 0.4 \\ 0.6 \\ 0.8 \\ 1.0 \end{array} \right.$	4.878	135.1	0.813	
		2.829	78.2	0.472	
		2.174	60.2	0.362	
		1.876	52.0	0.313	
		1.769	49.0	0.295	
3. H-slit (Fig. 14.52(c))					
$L = 120$ mm	$\left\{ \begin{array}{l} \frac{1}{3} \\ \frac{1}{2} \\ \frac{2}{3} \\ \frac{5}{6} \\ 1 \end{array} \right.$	3.13	86.78	0.493	
		2.30	63.78	0.363	
		1.89	52.35	0.298	
		1.65	45.83	0.258	
		1.46	40.45	0.230	
4. Leight-type specimen without sawcut					
$L = 125$ mm	1	1.74	48.17	0.285	k_s measured = 44 kg/mm ² /mm
5. Leight-type specimen with sawcut (Fig. 14.52(d))					
$L = 125$ mm	1	1.11	30.69	0.182	k_s measured = 27 kg/mm ² /mm
6a. Large H-slit specimen in steel (Fig. 14.52(e))					
$L = 10$ in	1	0.214	5.92	0.0714	
6b. Large H-slit specimen in aluminum (Fig. 14.52(e))					
$L = 10$ in.	1	0.0714	1.98	0.0714	

Note: 10^3 psi/in = 27.7 kg/mm²/mm.

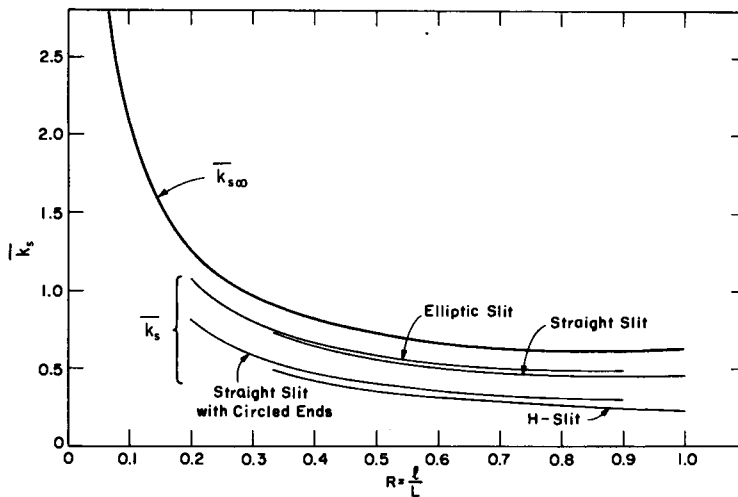


FIG. 14.53. Relationship between weld-length to slit-length ratio, R , and non-dimensional degrees of restraint for different cases being studied, $k_{s\infty}$ for an infinite plate and k_s for finite plates.

Joint Shapes	Analytical Expressions of K_s	Examples of Numerical Results
<p>(a) </p> <p>(b) </p>	$K_s = \frac{E\mu}{2a_1 \frac{B_{eq}}{x_0} \frac{\Delta}{x_0} + 1}$ <p>in which $\mu = D/E$</p> $\frac{B_{eq}}{x_0} = \frac{\nu}{(3+\nu) - E_1 \frac{-\Delta}{x_0} \exp \frac{\Delta}{x_0}}$ $\frac{1}{x_0} = \sqrt{\frac{\mu J_1}{(B_{eq} h_1)}} \quad J_1 = \left(1 + \frac{a_1}{a_2 \beta}\right) a_1$ $\beta = \frac{h_2}{h_1} \quad (a_1, a_2), a_1=1, a_2=2$ <p>where E : modulus of elasticity of material (kg/mm²) D : displacement coefficient of fillet weld (kg/mm.mm) ν : Poisson's ratio $E_1(-x)$: Logarithmic Integral $\left(\equiv -\int_x^{\infty} \frac{e^{-t}}{t} dt \right)$ a_1, a_2 : Numerical coefficient of effective width with respect to welding plate and restraining plate (=1 or 2) h_1, h_2 : Thickness of plate with respect to welding plate and restraining plate (mm)</p>	<p>Restraint Intensity of the Intersection of Butt and Fillet Joints</p> <p>Intensity of Restraint K_s (kg/mm.mm)</p> <p>$\mu = \frac{D}{E}$</p> <p>$\mu = \frac{L}{D}$</p>

FIG. 14.54. Values of intensity of restraint of butt joints restrained by fillet welds.

Note: Reference (1443) contains results on various types of joints.

Figure 14.55 those values of K_s measured on various joints in a spherical tank. Figure 14.56 (a) and (b) show relationships between h and K_s for various butt welds in ships and pressure vessels, respectively. Equation (14.18) is used in the study of the effect of joint restraint on cracking presented earlier in this Chapter (see Fig. 14.24).

2. *Effect of plate thickness.* As shown in eqn. (14.18), the value of K_s is proportional

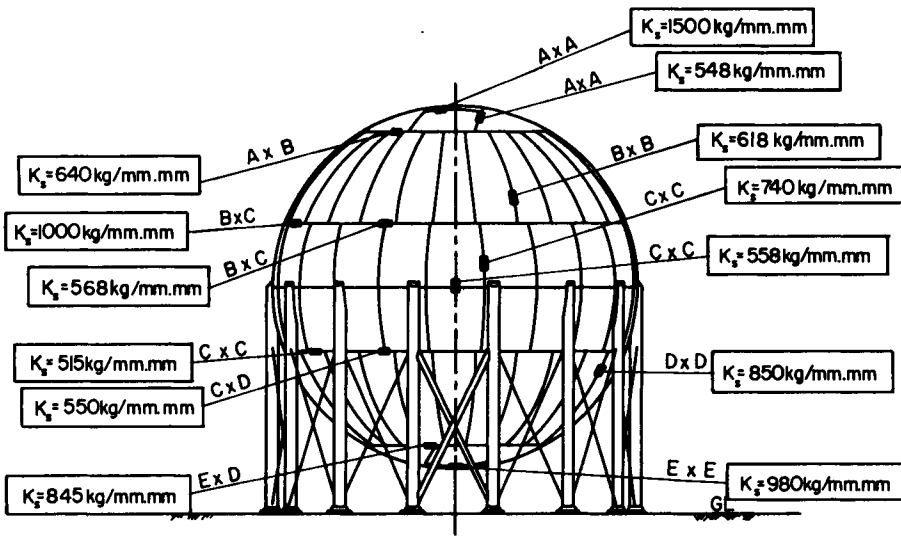


FIG. 14.55. Measured values of restraint intensity of various butt joints in a spherical pressure vessel.

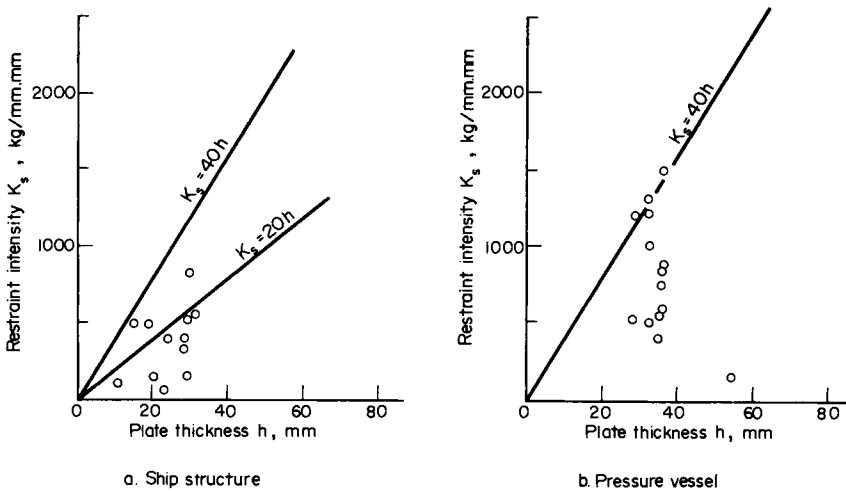


FIG. 14.56. Effects of plate thickness on measured values of restraint intensity.

Note: This figure shows results on ship structures and pressure vessels. Reference (1443) contains data on five different types of structures including ships, pressure vessels, bridges, buildings, and special cases such as tack welds, intersections of joints, etc.

to plate thickness. This is obvious from the definition of K_s as shown in eqn. (14.13). The value of the degree of restraint k_s is unaffected by plate thickness.

3. *Effects of joint length and weld length.* Both the joint length, L , and the weld length, l have significant effects on the degree of restraint. This can be understood from eqn. (7.1), the degree of restraint decreases as the joint length, L , increases. In Table 14.11 and

Fig. 14.53, a nondimensional parameter, \bar{k}_s , is used:

$$\bar{k}_s = \frac{k_s}{E/L} = \frac{k_s L}{E}. \quad (14.19)$$

\bar{k}_s may be called as the non-dimensional degree of restraint. \bar{k}_s is a useful parameter for studying the geometrical effects of different joints by eliminating effects of the joint length, L , and the modulus of elasticity of the material, E .

The degree of restraint increases as the weld length, l decreases, as shown in Fig. 7.5 and Fig. 14.53. The degree of restraint can become very high when making a short weld in a long joint.

4. *Effects of specimen size and saw cuts.* In the Lehigh restraint and other cracking tests, saw cuts are often used to change the degree of restraint, as shown in Figs. 14.28 and 14.52. The saw cuts reduce the degree of restraint to some extent; however, the extent is rather limited. Table 14.11 shows that the degree of restraint can be changed in the Lehigh test from 48 kg/mm²/mm (without saw cuts) to 31 kg/mm (with saw cuts).

As the specimen size increases the degree of restraint increases slightly. The size effect is shown in Fig. 14.53 which compares values of the degree of restraint of specimens with finite dimension to the degree of restraint of a straight slit in an infinite plate, k_{∞} , which is expressed by eqn. (7.1).

5. *Effectiveness of a crack stopping hole.* In repair welding of a crack, it is a common practice to drill a hole at the crack tip to prevent further extension of the crack. Figures 14.52 and 14.53 provide information on effects of a hole at the crack end on the restraint intensity. By comparing values of \bar{K} for (1) elliptical slit, (2) straight slit, and (3) straight slit with circled ends, one can find that \bar{k}_s -values for a slit with circled ends is only about two-thirds of a straight slit with the corresponding length.

However, an increase of the size of the stopping hole has little effect on further decreasing the restraint intensity. This can be understood from the small difference between the curve for straight slit with circled ends and that for a H-type slit (Fig. 14.52 (c)).

14.6 Further Advancement of Mechanical Analysis of Cracking Especially by Use of Fracture Mechanics Theories

Cracks in the weld metal and the base metal are types of fractures. Therefore, there is no reason to believe fracture-mechanics theories cannot be used to study weld cracking.

Looking back at the historical development of studies of fractures, fracture-mechanics theories have evolved as a means to quantitatively express the fracture resistance of a material.

Mechanical studies on weld cracking have been done by a number of investigators. The difficulty here is that stress changes during welding are extremely complex, especially in areas near the weld where cracks most frequently occur. Consequently studies conducted so far have been primarily empirical. Nevertheless, efforts have been made over the years to quantitatively express the sensitivity of a weld against cracking. Results of some of the major efforts are described in earlier parts of this chapter.

With the advancement of computer technology, it is now possible to handle complex mathematical computation with little time and cost. It is hoped that mechanical studies

on weld cracking will be advanced further, especially by applications of fracture mechanics theories.

14.6.1 *Similarities among theories of residual stress, joint restraint, and fracture mechanics*

In order to further advance studies on weld cracking by applying fracture-mechanics theories, it is important to recognize that theories of residual stress, joint restraint, and fracture mechanics are similar. This subject is discussed to some extent in Chapter 3, especially in Section 3.25.

When fracture occurs new surfaces appear. Therefore, fracture can be regarded as the creation of a macroscopic dislocation (see Fig. 3.8). Welding, on the other hand, can be regarded as the elimination of surfaces to be joined, or the elimination of a macroscopic dislocation. Consequently, the stress and strain changes that occur during fracturing are similar to those that occur during welding, except that the signs may be opposite.

Comparison between “ k_s ” and “ K ”. As an example of showing the similarities being discussed here, the following pages describe the degree of restraint of a slit weld “ k_s ” and the stress intensity factor “ K ”.

In a slit joint, the degree of restraint, k_s , when welding is done between $x = x_1$ and x_2 (slit length L ; weld length $l = x_1$ to x_2), is defined by eqn. (7.1), see Fig. 7.3. The physical meaning of k_s is as follows: When uniform stress σ_0 is applied along the part of the slit between x_1 and x_2 ,

$$k_s = \frac{\sigma_0}{[\bar{v}]_l} \quad (14.20)$$

where $[\bar{v}]_l$ is the mean value of dislocation over the portion of the slit where the load is applied.

Thus k_s represents the value of stress necessary to produce unit shrinkage. The unit commonly used is $\text{kg}/\text{mm}^2/\text{mm}$ or psi/in .

In the fracture-mechanics theory, the stress intensity factor, K , represents intensity of stress concentration near the tip of a crack. In a simple case of a through-the-thickness crack of length $l = 2c$ in an infinite plate subjected to uniform stress, σ , the stress intensity factor, K , is [see eqn. (10.10) and Fig. 10.4]:

$$K = \sigma \sqrt{\pi c}. \quad (14.21)$$

When a crack exists in a practical specimen with finite dimensions, the expression of the stress intensity factor, K , becomes more complex than eqn. (10.10) and can be expressed as follows:

$$K = \alpha \sigma \sqrt{\pi c}, \quad (14.22)$$

The commonly used unit of K is $\text{kg}/\text{mm}^2 \sqrt{\text{mm}}$ or $\text{psi} \sqrt{\text{in}}$.

Suppose that uniform tensile stress σ_0 is applied along the edges of a certain portion (from x_1 to x_2) of a straight slit extending from $-c$ to $+c$ in an infinite plate, as shown in Fig. 14.57(a). This stress state is very similar to that shown in Fig. 7.4(a), except that the signs of the force are opposite. In the case shown in Fig. 14.57(a), the slit

is opened by applying compressive stresses at the edges of the crack. In the case shown in Fig. 7.4 (b), the slit is closed by pulling the edges of the slit.[†]

The values of the stress intensity factor at both ends are

$$K_{\pm} = \frac{\sigma_0}{\pi} \sqrt{\pi c} \left\{ \sin^{-1} \frac{x_1}{c} + \sin^{-1} \frac{x_2}{c} \mp \left(\sqrt{1 - \left(\frac{x_1}{c}\right)^2} - \sqrt{1 - \left(\frac{x_2}{c}\right)^2} \right) \right\} \quad (14.23)$$

where K_+ = stress intensity factor at $x = +c$,
 K_- = stress intensity factor at $x = -c$.

Figure 14.57(b) is a simple case in which the uniform tensile stress, σ_0 , is applied along a portion of the edge, from $-x_1$ to $+x_1$. Then the stress intensity factor K is, by putting $x_2 = -x_1$ in eqn. (14.23),

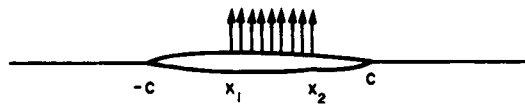
$$K = \frac{\sigma_0}{\pi} \sqrt{\pi c} \left(2 \sin^{-1} \frac{x_1}{c} \right). \quad (14.24)$$

If the load is applied along the entire length of the crack, i.e. $x_1 = c$,

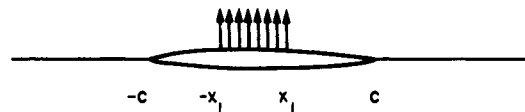
$$K = \sigma \sqrt{\pi c} \left(\frac{\text{kg}\sqrt{\text{mm}}}{\text{mm}^2} \text{ or } \text{psi}\sqrt{\text{in}} \right). \quad (14.25)$$

Equations (14.25) and (14.21) are identical. The degree of restraint in this simplest case is given as follows:

$$k_s = \frac{E}{\pi c} \quad (\text{kg/mm}^2/\text{mm} \text{ or } \text{psi/in}). \quad (14.26)$$



a. General case



b. Symmetric case

FIG. 14.57. Stress intensity factor for a slit subjected to uniform stress along a portion of the slit. Although stresses are applied on both sides of the slit, only the stresses applied on the upper side are shown in the figure.

[†] In the case shown in Fig. 7.4(b), stresses outside the slit are compressive causing compressive stress concentrations. From the standpoint of fracture mechanics K in this case may have to be negative.

14.6.2 *Applications of fracture mechanics theories to weld cracking*

So far applications of fracture mechanics theories of weld cracking have been rather limited.

Hot cracking. Most theoretical research on the fracture of metals at high temperatures has been directed at the phenomena that occur in creep fracture. Based upon earlier studies on creep fracture, Masubuchi and Martin suggested a formula to express the critical stress for forming an intergranular microcrack in the weld heat-affected zone. The formula is shown in eqn. (14.1).

Analysis of crack pattern in a residual stress field. Masubuchi and Martin^(1208, 1404) have developed an analysis for determining the crack pattern in a residual-stress field. This subject is discussed in Section 12.5. Although Masubuchi and Martin applied the theory to analyze crack patterns produced in weldments charged with hydrogen, this theory can be applied to a number of other cases involving cracking and spontaneous fractures in a weldment.

Masubuchi and Martin^(1208, 1404) have developed a dimensionless parameter, μ , “the relative toughness of a weldment (against transverse cracking)”, as shown by eqn. (12.16), to study the resistance of a weldment against transverse cracking. This parameter and similar parameters may be used to study the resistance of weldments against various types of cracks.

14.6.3 *Comments on restraint weld cracking tests*

Restraint weld-cracking tests, including the Lehigh test, the circular patch test, the controlled thermal severity (CTS) test, the cruciform test, etc., have been commonly used over the years to study weld cracking. These tests have their shortcomings, however.

First of all, the basic idea is that if these specimens are welded successfully without cracking using certain test materials (base plate, welding electrode, etc.) under certain test welding conditions, then these materials can be used successfully in actual construction. This assumes that the restraint intensity values that occur in actual construction are no greater than those of the restraint cracking specimen being tested. However, there is no guarantee that this assumption is true. In fact, Masubuchi and Ich⁽¹⁴⁴⁸⁾ found through mathematical analysis that the Lehigh restraint cracking test is very limited in terms of how much the degree of restraint can be varied.

Secondly, most of the cracking tests are go–no–go tests. It is very difficult to obtain quantitative data on a material’s resistance to cracking. More quantitative data can be obtained with newly developed tests such as the RRC, the TRC, and the implant tests.

On the basis of results obtained with the RRC, the TRC, and the implant tests, relationships between stress and time to cause cracking for different steels can be expressed by curves *A* and *B* of Fig. 14.58. Steel *A* is superior to steel *B* in terms of weldability.

If one uses a restraint cracking test which is capable of producing reaction stresses over a wide range, as shown by R1, the test is useful. In other words, one could evaluate the cracking tendencies of these steels and differentiate the two materials. However, if the cracking test being used is capable of producing reaction stresses only over a rather narrow range, as shown by R2 or R3, the usefulness of the test becomes very limited. If the range is R2, all specimens would pass; while if the range is R3, all specimens would

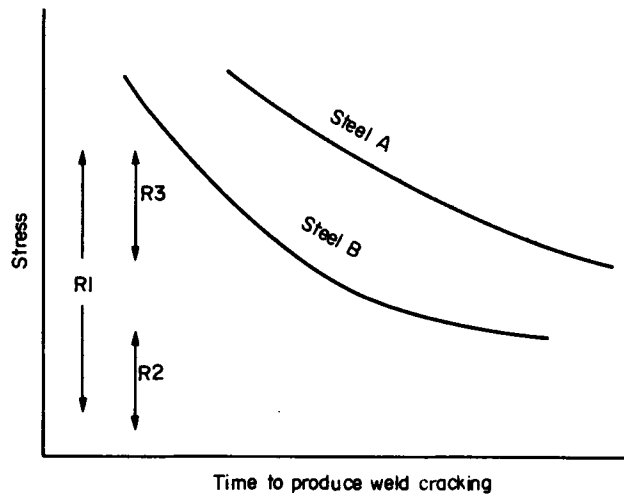


FIG. 14.58. Schematic relationship between stresses and time to produce cracking and ranges of stresses which can be produced by restraint cracking tests.

crack. Unfortunately, the ranges of the restraint intensity that most cracking tests can produce are rather limited.

The parameter P_w , developed by Ito and Bessyo and given by eqn. (14.6), shows the relative importance of restraint intensity K_s in carbon equivalent. An increase of K_s in the amount of 1000 kg/mm^2 ($1.4 \times 10^3 \text{ ksi}$ or $9.65 \times 10^3 \text{ MN/m}^2$) causes an increase of P_w of only 0.025. This means that the change of restraint intensity that can be made in a restraint weld-cracking test can produce only a minor change in carbon equivalent value. This explains why recently developed tests employ some additional stresses to produce cracking.

Another shortcoming is the “cracking ratio”, which is the ratio of the crack length to the entire weld length. On the basis of fracture mechanics, the “cracking ratio” may not be an adequate measure for evaluating how much a material resists cracking.

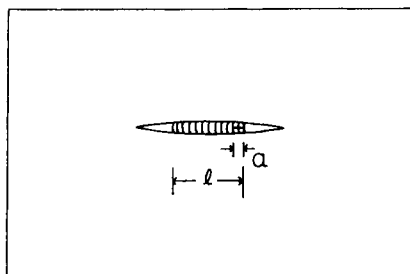
Suppose that a weld is made along a portion of a slit-type specimen, as shown in Figure 14.59(a), and a small crack of length a occurs at one end of the weld. The cracking ratio is a/l . As the crack length, a , increases, the stress intensity factor, K , at the crack tip increases sharply because

1. even when the stress level remains the same, K increases as the crack length increases, as shown in eqn. (14.21);
2. as the crack gets longer, the remaining weld length decreases and stresses applied to the remaining areas increase.

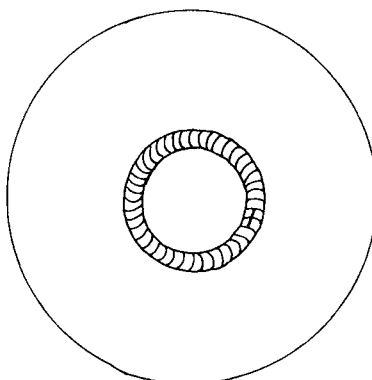
Consequently, as the crack lengthens it becomes more and more unstable. This analysis suggests that when a large number of restrained welded specimens are made, most of them will have either no cracking (or only short cracks) or almost 100% cracking; only a very few specimens will have cracks of intermediate length (50 to 75% cracking).[†]

In a circular patch weld (see Fig. 14.59 (b)) the situation may be different. As the short crack grows it may become more unstable since the K -value increases; however, as the

[†] As a crack extends K can be analyzed using the model shown in Fig. 14.57.



a. Small Crack of Length a Occurred at One End of the Weld Length l in a Slit-Type Specimen



b. Crack in Circular Path Weld

FIG. 14.59. Extension of a crack in a restrained weld specimen.

crack lengthens the K -value may not increase rapidly since most of the residual stresses will have been released.

It is hoped that the knowledge of restraint cracking can be expanded through the proper application of the fracture-mechanics theory.

14.6.4 *Applications of the transient thermal stress analysis to weld cracking*

With the recent development of computer technology and such techniques as the finite element method, the technology of analyzing transient thermal stresses and metal movement during welding has advanced significantly. Chapter 5 discusses some of the recent studies. It is expected that the analysis of transient phenomena during welding will be advanced further in the near future. The advancement in this field will undoubtedly have far-reaching effects in the mechanical analysis of weld cracking.

Some efforts along this line have already begun. Two research groups headed by Fujita⁽¹⁴⁵⁰⁾ and Satoh⁽¹⁴⁵¹⁾ have studied the transient thermal stresses and cracking that occur during the one-side-submerged arc welding of large butt joints. When large steel plates, for example 60 ft (18.5 m) long, 10 ft (3 m) wide, and 1 in. (25 mm) thick, are welded by the one-side-submerged arc process, cracks often occur at the end of the long butt weld. Analytical and experimental studies have been made (1) to determine

mechanisms of cracking and (2) to develop methods for preventing the cracking from occurring.

References

- (1401) PFLUGER, A. R. and LEWIS, R. E., editors, *Weld Imperfections*, Addison-Wesley Publishing Co., Reading, Massachusetts, 1968.
- (1402) MASUBUCHI, K., Class Note at M.I.T.
- (1403) BORLAND, J. C., "Suggested explanation of hot cracking in mild and low alloy steel welds", *British Welding Journal*, **8** (11), 526-540 (1961).
- (1404) MASUBUCHI, K. and MARTIN, D. C., "Mechanisms of cracking in HY-80 steel weldments", *Welding Journal*, **41** (8), Research Supplement, 375s-384s (1962).
- (1405) MISHLER, H. W., MONROE, R. E., and RIPPEL, P. J., "Studies on hot cracking in high-strength weld metals", *Welding Journal*, **40** (1), Research Supplement, 1s-7s (1961).
- (1406) ZENER, C., "The micro-mechanism of fracture", *Fracturing of Metals*, American Society for Metals, Cleveland, Ohio, pp. 3-31 (1948).
- (1407) CHEN, C. W., and MACHIN, E. S., "On the mechanism of intercrystalline cracking, *Acta Metallurgica*, **4** 655-656 (Nov. 1956).
- (1408) MCLEAN, D., "A note on the metallography of cracking during creep", *Journal of the Institute of Metals*, **85** 468-472 (1956-57).
- (1409) GIFKINS, R. C., "Mechanisms of intergranular fracture at elevated temperatures", *Fracture-Proceedings of the Swampscott Conference on Atomic Mechanisms of Fracture*, The Technology Press of MIT and John Wiley & Sons, Inc., 1959, pp. 579-627.
- (1410) INAGAKI, M., "Welding physical metallurgy", *Journal of the Japan Welding Society*, **34**, (11 and 12), 1128-1130 and 1213-1220 (1965).
- (1411) PHILLIPS, A. L., editor, *Fundamentals of Welding Metallurgy*, American Welding Society, New York, 1960. Same as *Welding Handbook*, Fifth Edition, Section I.
- (1412) MISHLER, H. W., *Preventing delayed cracks in ship welds—Part I and Part II*, SSC-262, Final Report on Project SR-210 *Delayed Cracking Phenomena*, Ship Structure Committee, 1976.
- (1413) ITO, Y., and BESSYO, K., "Cracking parameter of high strength steels related to heat affected zone cracking, Reports 1 and 2", *Journal of the Japan Welding Society*, **37** (9), 983-991 (1968); **38** (10), 1134-1144 (1969).
- (1414) SATOH, K., MATSUI, S., HORIKAWA, H., BESSYO, K., and OKUMURA, T., "JSSC guidance report on determination of safe preheating conditions without welded cracks in steel structures", I.I.W. Document IX-834-73, 1973.
- (1415) "Guidance report on determination of safe preheating conditions without weld cracks in steel structures", *Report of the Study Group on Weld Cracking of the Japanese Society of Steel Construction*, JSSC, vol. 8, no. 80, 22-50 (1972) (in Japanese).
- (1416) RANDALL, M. D., MONROE, R. E., and RIEPPEL, P. J., *Methods Evaluating Welded Joints*, DMIC Report 165, Dec. 1961, Defense Metals Information Center, Battelle Memorial Institute, Columbus, Ohio.
- (1417) STOUT, R. D., MCGEADY, L. J., and DOAN, D. E., "Quantitative measurement of the cracking tendency in welds", *Welding Journal*, **25**, 522s-531s (1946).
- (1418) HOULDCRAFT, P. T., "A simple cracking test for use with argon arc welding", *British Welding Journal*, **2** (10), 471-475 (1955).
- (1419) WILKINSON, F. J., COTTRELL, C. I. M., and Hoxley, H. V., "Calculating hot cracking resistance of high tensile alloy steels", *British Welding Journal*, **5** (12), 557-562 (1958).
- (1420) BORLAND, J. C. and Robertson, J. H., "Examination of the patch test for assessing hot cracking tendencies of weld metal", *British Welding Journal*, **9** (8), 494-499 (1962).
- (1421) HACKETT, J. E. and SEABORN, L. O., "Evaluation of the circular patch weld test", *Welding Journal*, **31** (8), 387s-392s (1952).
- (1422) COTTRELL, C. I. M., "Controlled thermal severity test, cracking test simulates practical welded joints", *Welding Journal*, **33** (6), 257s-272s (1953).
- (1423) POTEAT, L. E. and WARNER, W. L., "The cruciform test for plate cracking susceptibility", *Welding Journal*, **30** (2), 70s-76s (1960).
- (1424) WEISS, S., RAMSEY, J. N., and UDIN, H., "Evaluation of weld cracking tests on armor steel," *Welding Journal*, **35** (7), 348s-356s (1956).
- (1425) WINTERTON, K. and NOLAN, M. J., "Factors effecting severity of cruciform test for hardened zone cracking", *Welding Journal*, **39** (2), 77s-83s (1960).
- (1426) MALLETT, M. W., and RIEPPEL, P. J., "Arc atmospheres and underbead cracking", *Welding Journal*, **25** (11), 748s-759s (1946).

- (1427) SIMS, C. E., and BANTA, H. M., "Development of weldable high-strength steels", *Welding Journal*, **28** (4), 178s–192s (1949).
- (1428) VOLDRICH, C. B., "Cold cracking in the heat-affected zone", *Welding Journal*, **26** (3), Research Supplement, 152s–169s (1947).
- (1429) SAVAGE, W. F. and LUNDIN, C. D., "The Varestreint test", *Welding Journal*, **44** (10), Research Supplement, 433s–442s (1965).
- (1430) WATANABE, M., SATOH, K., and MATSUI, S., "Effect of restraint on root cracking of steel welds", *Journal of the Japan Welding Society*, **33**, (6), 446–457 (1964).
- (1431) SATOH, K. and MATSUI, S., "Development of reaction stress and weld cracking under restraint", *Journal of the Japan Welding Society*, **36**, (10), 1096–1109 (1967).
- (1432) SATOH, K., MATSUI, S., HORIKAWA, K., TAKAGI, O., TERAI, K., YAMADA, S., and OKUMA, Y., "Correlation of the implant test with the RRC and the TRC tests", *Transactions of the Japan Welding Society*, **6** (1), 31–41 (1975).
- (1433) SUZUKI, H., INAGAKI, M., and NAKAMURA, H., "Effect of restraining force on root cracking of high-strength steel welds in NR/M TRC test", *Journal of the Japan Welding Society*, **32** (1), 44–55 (1963) and *Transactions of National Research Institute for Metals*, Tokyo, vol. 6, no. 4 (1964).
- (1434) GRANJON, H., "The implants' method for studying the weldability of high strength steel", *Metal Construction and British Welding Journal*, **1** (11), 509–515 (1969).
- (1435) GRANJON, H., Debiez, S., and Gaillard, R., "Implant method at the Institute de Soudure", *Metal Construction and British Welding Journal*, **5**, (10), 384–389 (1973).
- (1436) MATSUI, S., and OHKUMA, Y., "Principle and use of implant test for studying weld cracking", *Journal of the Japan Welding Society*, **44**, (9), 716–727 (1975).
- (1437) HART, P. and WATKINSON, F., "Development and use of the implant cracking test", *Welding Journal*, **51** (7), Research Supplement, 349s–357s (1972).
- (1438) GORDINE, J., "The weldability of some artic-grade line-pipe steels", *Welding Journal*, **56** (7), Research Supplement, 201s–210s (1977).
- (1439) WATANABE, M., "On the fundamental theory of internal stresses", *Journal of the Japan Welding Society*, **17**, 281–291 (1948).
- (1440) WATANABE, M., "Thermal stresses and residual stresses of rectangular plate under one-dimensionally distributed temperature", *Journal of the Society of Naval Architects of Japan*, **86**, 173–184 (1954).
- (1441) SATOH, K. and MATSUI, S., "Reaction stress and weld cracking under hindered condition", *Technological Reports of the Osaka University, Faculty of Engineering*, Osaka University, Osaka, Japan, 1967.
- (1442) SATOH, K., "An analytical approach to the problem of restraint intensity in Slit weld", I.I.W. Document X-661–72, 1972.
- (1443) "Japanese studies on structural restraint severity in relation to weld cracking (Preliminary Report)", *Welding in the World*, **15** (7/8), 155–189 (1977).
- (1444) SATOH, K. and MATSUI, S., "Notation system of joint restraints", I.I.W. Document X-910–78, 1978.
- (1445) SATOH, K., MATSUI, S., NISHIMURA, I., IYAMA, H., CHIBA, N., HASEBE, S., and BESSYO, K., "Effect of intensity of bending restraint on weld cracking in multipass weld", I.I.W. Document IX-960–76, 1976.
- (1446) WATANABE, M., TAKAGI, O., SATOH, K., and ASO, F., "External constraint and shrinkage of butt-welded joints", *Journal of the Society of Naval Architects of Japan*, **104**, 153–162, (1958).
- (1447) WATANABE, M. and SATOH, K., "Evaluation of restraint intensity and reaction force for some weld cracking test specimens", *Journal of the Japan Welding Society*, **33** (7), 513–523 (1964).
- (1448) MASUBUCHI, K. and ICH, N. T., "Computer analysis of degree of constraint of practical butt joints", *Welding Journal*, **49** (4), Research Supplement, 166s–176s (1970).
- (1449) TADA, T., PARIS, P., IRWIN, G., *The Stress Analysis of Cracks Handbook*, DEL Research Corporation, Hellertown, Pa.
- (1450) FUJITA, Y. *et al.*, "Prevention of end cracking in one-sided automatic welding", *Journal of the Society of Naval Architects of Japan*, **133**, 267–275 (1973), and **135**, 379–391 (1974).
- (1451) SATOH, K. *et al.*, "Studies on deformations and cracking in one-sided welding", *Journal of the Society of Naval Architects of Japan*, **136**, 441–458 (1974).

Effects of Weld Defects on Service Behavior

SUBJECTS related to weld defects include:

1. Characterization of various types of weld defects.
2. Inspection of weld defects.
3. Studies of effects of weld defects on service behavior of welded structures.
4. Quality control of welding fabrication.

The subjects are too complex to be covered in just one chapter. In fact, another book would be needed to conduct a thorough discussion of all the subjects. Although this book covers subjects related to residual stresses, distortion, and their consequences, discussions on effects of weld defects are presented here because residual stresses and weld defects are closely related:

1. Weld defects most frequently occur in regions near the weld where high residual stresses exist; how much weld defects affect the service behavior of a welded structure is affected in turn by the nature and the magnitude of these residual stresses.
2. Residual stresses and distortion can be classified as imperfections, or as deviations from an ideal structure (see Chapter 8).

There are two reasons that weld defects (porosity, slag inclusions, incomplete penetration, and cracks) reduce the strength of welded joints. First, the presence of the defects decreases the sectional areas. Second, stress becomes concentrated around the defects. The extent to which weld defects affect structural strength depends upon the following factors:

1. *Nature and extent of defects.* Sharp cracks cause severe stress concentrations and thus affect the strength more than do porosity or slag inclusions, which cause only minor stress concentrations. The defects affect the strength more severely as the size and number of defects increase.
2. *Properties of the material.* The properties of a material are significant factors that determine how weld defects will affect the strength of a welded structure. If a material is ductile, the strength reduction will be proportional to the reduction of the cross-sectional area, as described later. In less ductile materials, the defects have a more serious effect. If the material is brittle, the absolute size of a defect will be important. If the defect exceeds the critical size, an unstable fracture can initiate at the defect.
3. *Type of loading.* When the structure is subjected to impact or repeated loading,

the defects will more seriously affect the strength than when the structure is subjected to static loading.

15.1 Weld Defects

Welds often contain various types of defects. The following pages briefly describe common weld defects. Descriptions as given in the *Welding Handbook*⁽¹¹²¹⁾ are often used in these pages.

1. *Porosity*. Figure 15.1 shows porosity. Porosity refers to the gas pockets or voids free of any solid material, frequently found in welds. Porosity is caused when gas is released as a weld metal cools and its solubility is reduced, and from gases formed by chemical reactions in the weld. Porosity may be scattered uniformly throughout the weld, isolated in small areas, or concentrated at the root. Though in many cases, porosity is spherical, in some it is worm-shaped, and elongated in the solidification direction of the weld metal. Porosity may be caused by excessive welding temperatures or incorrect manipulation.

2. *Slag inclusions*. Figure 15.2 shows slag inclusions. This term is used to describe the oxides and other non-metallic solids that become entrapped in the weld metal or between the weld metal and the base metal. They generally come from the electrode-covering material or from fluxes employed in the welding operations. In multilayer welding operations, failure to remove the slag between layers will result in slag inclusions in these zones.

3. *Tungsten inclusions*. In the gas tungsten-arc welding processes, the occasional touching of the electrode to the work or to the molten weld metal, particularly in the manual process, may transfer particles of the tungsten into the weld deposit. These tungsten inclusions generally are undesirable, and for critical work a limit on the size and numbers of these inclusions is specified.

4. *Incomplete fusion*. Incomplete fusion, or lack of fusion as it is frequently termed, is used to describe the failure to fuse together adjacent layers of weld metal or adjacent weld metal and base metal, as shown in Figs. 15.3 (a) and 15.3 (b). This failure to obtain fusion may occur at any point in the welding groove.

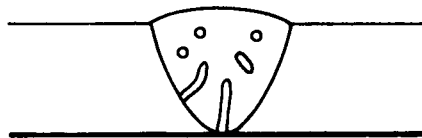
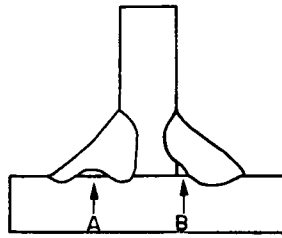


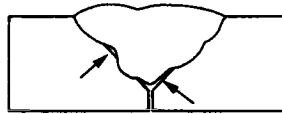
FIG. 15.1. Porosity



FIG. 15.2. Slag inclusions, between passes at A and at undercut at B.



a. Incomplete fusion in fillet welds.
B is often termed "bridging"



b. Incomplete fusion in a groove weld.

FIG. 15.3. Incomplete fusion.

Incomplete fusion may be caused by: failure to raise the temperature of the base metal (or previously deposited weld metal) to the melting point, or failure to remove slag, mill scale, oxides or other foreign material present on the surfaces to which the deposited metal must fuse.

5. *Inadequate joint penetration.* In this condition the joint penetration is less than that specified. Hence, partial joint penetration may or may not be a defect, depending on what is specified for that particular joint.

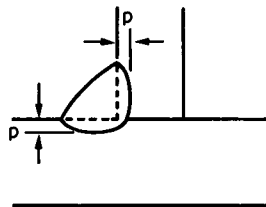
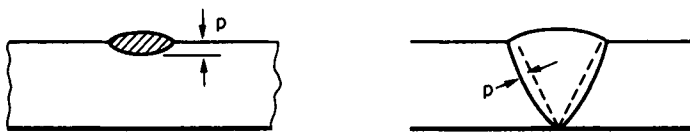


FIG. 15.4. Penetration, "P".

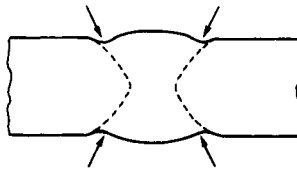
Often “inadequate joint penetration” is used (improperly) to describe what is defined as “incomplete fusion” in AWS A3.0–61 Definitions—Welding and Cutting. The AWS rationale is that “fusion” should be used when describing how completely the weld is bonded to or fused to the surface of the joint: “Penetration”, on the other hand, describes how far the weld extends into a joint, as shown in Fig. 15.4.

6. *Undercut*. This term is used to describe a groove melted into the base metal adjacent to the toe of a weld and left unfilled by the weld metal, as shown in Figs. 15.5 (a) and 15.5 (b). It also describes the melting away of the sidewall of a welding groove at the edge of a layer of bead, thus forming a sharp recess in the sidewall in the area to which the next layer or bead must fuse.

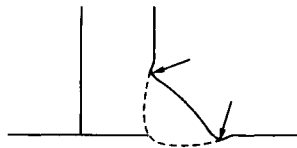
7. *Cracks*. Cracks result from ruptures of metals under stress. Although sometimes large, they are often very narrow separations in weld or adjacent base metal. Weld cracks are discussed in Chapter 14.

Cracks are one of the most harmful of welding defects and are prohibited by most specifications. However, small cracks, often called fissures or microfissures, may not reduce the service life. Specifications are reluctant to specify an allowable maximum crack size; rather, they tacitly admit that any cracks too small to be resolved by the required inspection procedure are permitted.

8. *Arc strikes*. Although arc strikes are not normally considered defects, fractures (brittle and fatigue) frequently initiate from arc strikes. Arc strikes are formed during the unintentional melting or heating of areas outside the intended weld deposit area. They usually are caused by the welding arc but can be produced beneath an improperly secured ground connection. The result is a small melted area that can produce undercut, hardening, or localized cracking, depending upon the base metal.



a. UNDERCUTTING IN A BUTT WELD



b. UNDERCUTTING IN A FILLET WELD

FIG. 15.5. Undercut.

15.2 Stress Concentration Caused by Weld Defects^(104, 1501)

Stress concentrations (local increases in stresses) occur when stresses are applied to a material that contains discontinuities such as pores, cracks, and inclusions. The shape of a defect and its orientation to the direction of loading significantly affect the stress concentrations around it. The problem of stress concentration caused by discontinuities has been studied by many investigators. Literature surveys on stress concentrations have been made by Sadowsky,⁽¹⁵⁰²⁾ Sternberg,^(1502, 1503) Neuber,⁽¹⁵⁰⁴⁾ Eshelby,⁽¹⁵⁰⁵⁾ Peterson,⁽¹⁵⁰⁶⁾ and Savin.⁽¹⁵⁰⁷⁾

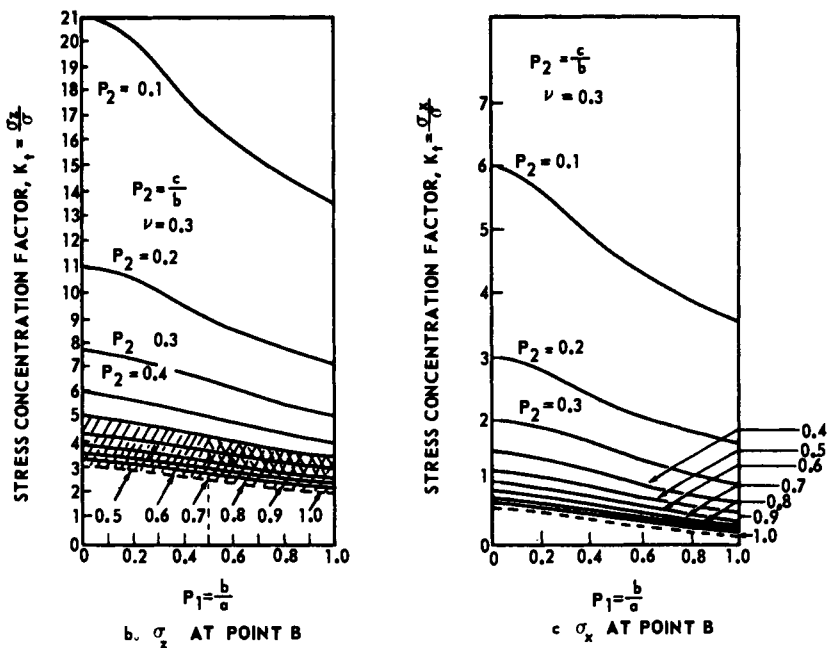
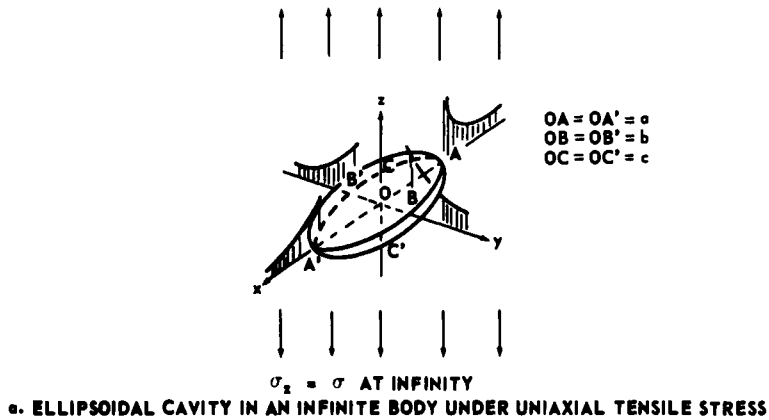


FIG. 15.6. Stress concentrations around an ellipsoidal cavity in an infinite body under uniaxial tensile stress.

15.2.1 Three-dimensional stress concentrations around a cavity

Figures 15.6 (a), (b) and (c) show the stress distributions around a general triaxial, ellipsoidal cavity in a homogeneous, isotropic, elastic body of infinite length that is under a uniform tensile stress, σ , at infinity. It is assumed that the stress at infinity is acting parallel to one of the major axes of the cavity (z -axis), as shown in Fig. 15.6 (a). The important stress concentrations occur along the “equator” $ABA'B'A$. The curves in Fig. 15.6 show how rapidly the tensile stresses drop to the average value, σ , within the material.

The severity of stress concentration is expressed frequently in terms of the stress-concentration factor, K_t , which is defined as the ratio of the stress at the point concerned and the stress at infinity, σ . Figures 15.6 (b) and (c) show values of σ_z/σ and σ_x/σ ($\sigma_y = 0$ at point B) as a function of the shape ratios $\rho_1 = b/a$ and $\rho_2 = c/b$.⁽¹⁵⁰²⁾ The value of Poisson’s ratio is assumed to be 0.3.

The curves for $\rho_2 = 1$ apply to a cavity in the shape of a prolate spheroid (cigar-shaped cavity). The limiting case of $\rho_1 = 0$, $\rho_2 = 1$ can be interpreted geometrically in two ways. If b is fixed and a approaches infinity, the shape of the cavity approaches that of a circular cylinder of infinite length; if a is fixed and b and c approach zero, the shape of the cavity approaches that of a line crack. The curves for $\rho_1 = 1$ apply to a cavity in the shape of an oblate spheroid (button-shaped cavity). The case of $\rho_1 = \rho_2 = 1$ applies to a spherical cavity. As shown in Figs. 15.6 (b) and (c), the stress concentrations are mild for cigar-shaped cavities, the value of σ_z/σ ranging between 2.05 (for a spherical cavity) and 3 (for a long cylindrical cavity). On the other hand, the stress concentrations occurring around a thin, button-shaped cavity having its surfaces perpendicular to the direction of loading will be high.

For all shapes, severe stress concentrations occur in σ_z , or “hoop stress” in the direction parallel to the applied stress. For all shapes other than the oblate spheroid, σ_z and σ_x at point B are larger, respectively, than σ_z and σ_y at the point A. The maximum stress concentration is found in σ_z at point B.

Porosity in the weld metals is spherical or worm-shaped, as shown in Fig. 15.1. Weld porosity with the shape of an oblate spheroid is rarely found; porosity seldom has sharp notches. Consequently, the stress concentrations around weld porosity are not severe. The values of the stress-concentration factors around porosity are shown in the hatched area in Fig. 15.6 (b) and (c)—either in the single-hatched areas ($\rho_2 > 0.5$) or more often in the double-hatched areas ($\rho_1 > 0.5$ and $\rho_2 > 0.5$).

A crack can cause a severe stress concentration if a load is applied in a direction perpendicular to the crack surface.

15.2.2 Stress concentration around inclusions

Stress concentrations around three-dimensional inclusions have been studied by investigators including Edwards,⁽¹⁵⁰⁸⁾ Miyamoto,⁽¹⁵⁰⁹⁾ and Eshelby.^(1505, 1510) Figure 15.7 shows how Young’s modulus of a spheroidal inclusion affects the stress concentrations around the inclusion. It is assumed that:

1. An infinite elastic body that contains an inclusion in the shape of a prolate spheroid (cigar-shaped inclusion) is subjected to a uniform tensile stress, σ , at infinity. Refer to Figure 15.6 (a), $\sigma_z = \sigma$ at infinity, $b = c$.

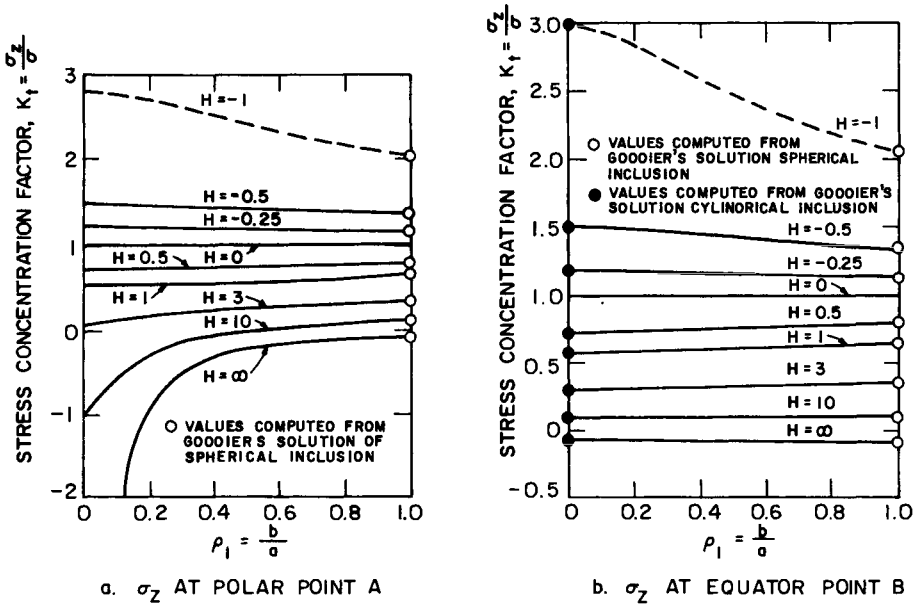


FIG. 15.7. Stress concentrations around spheroidal inclusions.⁽¹⁵⁰²⁾

2. The spheroidal core and the surrounding body are each composed of homogeneous isotropic material, but the elastic properties of the two materials can be different.
3. At the contact surface between the two media, coherence exists.

Figure 15.7 (a) and (b) show σ_z at points *A* and *B* (see Fig. 15.6 (a)) respectively, as a function of the shape ratio $\rho_1 = b/a$, for various values of a parameter, H , which indicates relative rigidity of the inclusion and surrounding medium as is shown on the following page.

$$H = \frac{E'}{E} - 1 \tag{15.1}$$

where E' and E are Young's moduli of the inclusion and of the surrounding media, respectively. Poisson's ratio is assumed to be 0.3 for both the inclusion and the surrounding media.

If $H = -1$, the problem reduces to that of a spheroidal cavity. If $H = 0$, the stress distribution is uniform since the elastic properties of the inclusion are identical with those of the surrounding media. The limit $H = \infty$ corresponds to an ideally rigid inclusion.

As shown in Figs. 15.7 (a) and (b), the tensile stress concentration decreases as H increases. A compressive stress concentration takes place at point *A* when H is greater than about 10.

Inclusions in weld metals have various shapes and contain various materials. Inclusions sometimes have sharp notches, as shown in Fig. 15.2. Materials contained in inclusions also vary greatly—from very hard materials such as tungsten to porous materials such as slag. Complete bonding between an inclusion and the surrounding media (as assumed in the preceding analysis) is obtained in some cases, but more frequently only a partial bonding is obtained. When an inclusion contains porous materials

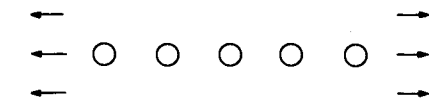
or when there is only a partial bond between the inclusion and the surrounding media, the stress concentrations around the inclusion are similar to those around a cavity.

15.2.3 *Stress concentrations around a number of holes*

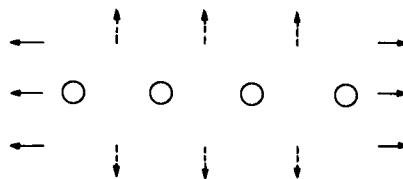
A weldment may contain more than one closely located defect as shown in Fig. 15.1 for porosity. Because of the mathematical complexity involved, studies of stress concentrations caused by more than one closely located defect were limited to two-dimensional cases. Today analyses of more complex cases can be made by use of the finite-element method.

For example, analytical solutions have been developed on stress concentrations for the following boundaries (refer to Fig. 15.8):

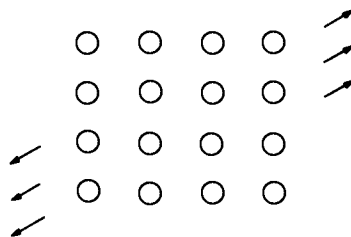
1. Infinite plate with a single row of holes under a uniaxial tensile stress parallel to the row of holes, as shown in Fig. 15.8 (a), by Peterson,⁽¹⁵⁰⁶⁾ Savin,⁽¹⁵⁰⁷⁾ Ishida,⁽¹⁵¹¹⁾ and Chen.⁽¹⁵¹²⁾
2. An infinite plate with a single row of holes under biaxial stresses, as shown in Fig. 15.8 (b), by Peterson.⁽¹⁵⁰⁶⁾
3. An infinite plate with infinite parallel rows of holes under uniaxial tensile stress, as shown in Fig. 15.8 (c), by Saito.⁽¹⁵¹³⁾
4. An infinite plate with two adjacent elliptical holes under biaxial tension.⁽¹⁵¹⁴⁾



(a) SINGLE ROW OF HOLES UNDER UNIAXIAL TENSILE STRESS PARALLEL TO THE ROW OF HOLES



(b) SINGLE ROW OF HOLES UNDER BIAXIAL STRESSES



(c) INFINITE PARALLEL ROWS OF HOLES

FIG. 15.8. Stress concentrations around multiple holes.

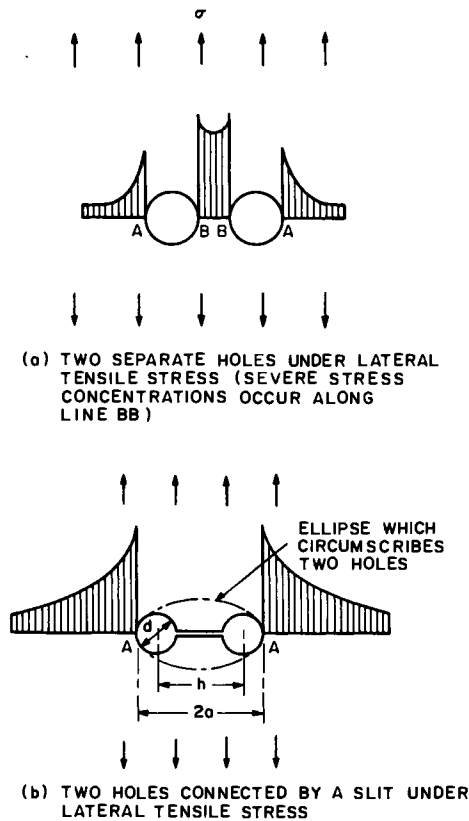


FIG. 15.9. Stress concentrations around two holes connected by a slit under lateral tension.

As an example of stress concentrations caused by multiple cavities, the following pages discuss stress concentrations due to two holes. When a plate that contains two holes located close to each other is under lateral tensile stress, severe stress concentrations occur in areas between the holes, as shown in Fig. 15.9 (a). Consequently, a crack may occur and connect the two holes, as shown in Fig. 15.9 (b). If the two holes are connected, severe stress concentrations occur outside the holes. Since the length of the discontinuity increases considerably when cracking occurs, the stress magnitudes and the areas of highly stressed regions increase greatly due to cracking.

Mori⁽¹⁵¹⁵⁾ made an analytical study of the stress distributions in an infinite plate that contained two holes connected by a slit under lateral tensile stress. Curves (1), (2A), and (2B) in Fig. 15.10 show the values of the stress-concentration factors for the following cases:

- Curve (1): Two holes connected by a straight slit under a lateral tensile stress, σ .
- Curve (2A) and (2B): Two separate holes under lateral tensile stress—curve (2A) for point *A* and curve (2B) for point *B*.

Curves (1), (2A), and (2B) show that as the distance between the two holes, h , increases, the stress-concentration factor for the separated holes decreases while the K_t value for the connected holes increases. In other words, the closer the two holes, the greater is

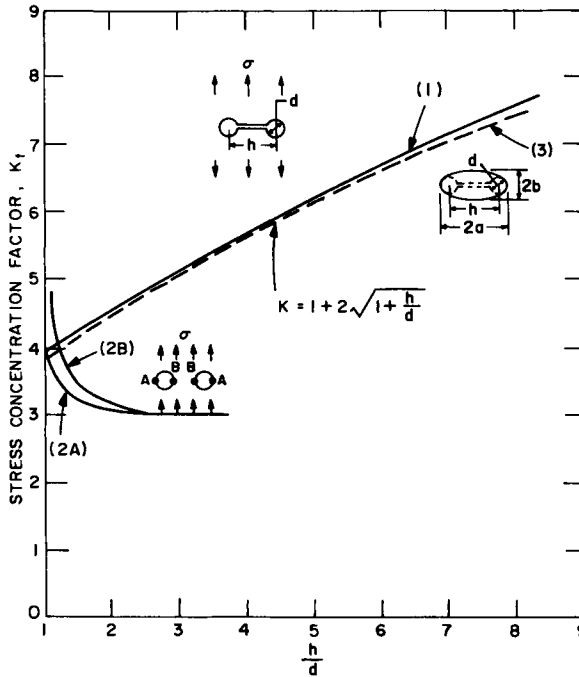


FIG. 15.10. Stress concentration for two holes connected by a slit under lateral tension.

the possibility of a crack occurring between the holes; but the less severe is the stress concentration after the holes are connected.

Curve (3) in Fig. 15.10 shows the values of the stress-concentration factor for an elliptical hole that circumscribes the two holes—the radius of the curvature of the ellipse at the point of contact is the same as the radius of the circles. The stress-concentration factor is given by:

$$K_t = 1 + 2 \sqrt{1 + \frac{h}{d}} \tag{15.2}$$

Values of K_t for curve (3) are close to those of curve (1). Equation (15.2) can thus be used for calculating the approximate values of the stress-concentration factor for two holes connected by a slit.

15.3 Effect of Defects on Ductile Fracture

When a material is ductile, fractures occur in the shear mode and propagate slowly. In such a case, the loss of strength due to defects is approximately proportional to the reduction of cross-sectional area.

15.3.1 Theoretical Considerations

Let us consider a case in which a flat plate (width, B , and thickness, t) containing a circular hole of diameter, d , is under a tensile load, P , as shown in Fig. 15.11. The average

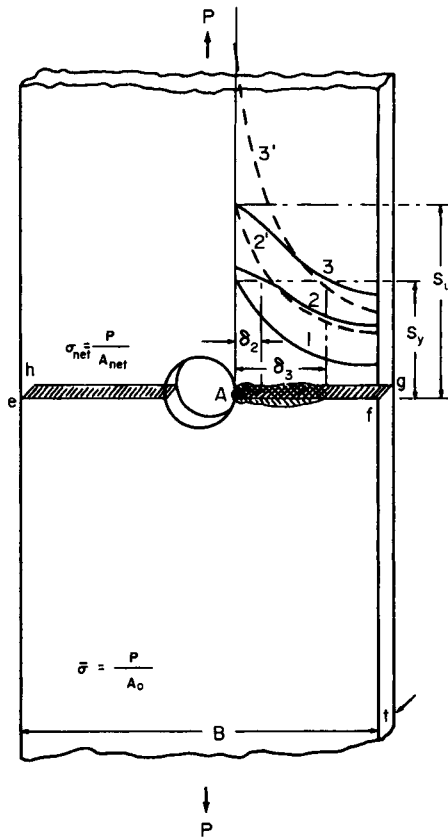


FIG. 15.11. Effect of defect on behavior of ductile material under tensile loading.

stress, $\bar{\sigma}$, and the net stress, σ_{net} , are defined as follows:

$$\bar{\sigma} = \frac{P}{A_0}, \quad \sigma_{net} = \frac{P}{A_{net}} = \frac{A_0}{A_{net}} \bar{\sigma} \tag{15.3}$$

where $A_0 = Bt$ is the original section area,
 $A_{net} = (B - d)t$ is the net section area,

When B/d is sufficiently large, the elastic stress-concentration factor, K_t , is close to 3. S_y and S_u are the yield strength and the ultimate tensile strength of the materials, respectively.

Curve (1) shows the distribution along line Af at the stress level $\bar{\sigma} = S_y/K_t$. The magnitude of stress at point A reaches the yield strength of the material. If the magnitude of applied stress exceeds S_y/K_t , plastic deformation takes place in the highly stressed regions as shown by the cross-hatched areas in Fig. 15.11, and finally fracture occurs.⁽¹⁵¹³⁾

It would be unrealistic to assume that fracture occurs at an average stress of S_u/K_t . When the average stress is S_u/K_t ; the stress distribution is as shown by curve 2, not as shown by curve 2' (elastic stress distribution).⁽¹⁵⁰⁷⁾ The stresses in the plastic region (depth, δ_2) are near the yield stress, S_y , and are considerably lower than S_u .

The stress distribution at fracture is as shown by curve 3, the average stress at fracture

being $\bar{\sigma}_f$. The maximum stress at point A , $K_t \bar{\sigma}_f$, is much higher than S_u . If the material is ductile (undergoes a large plastic deformation before fracture occurs), the plastic regions are extended and the stress concentrations around the defect are reduced.

However, since the section area along plane $efgh$ is less than the original section area, fracture usually occurs when the net stress approaches S_u . In other words, the average fracture stress $\bar{\sigma}_f$ is:

$$\bar{\sigma}_f = \frac{A_{\text{net}}}{A_0} S_u. \quad (15.4)$$

The average fracture stress of a specimen with a hole, $\bar{\sigma}_f$, is obviously lower than the average fracture stress of a specimen without a hole, or defect, S_u . The percentage loss in strength due to a hole is:

$$\begin{aligned} \frac{S_u - \bar{\sigma}_f}{S_u} &= 1 - \frac{\bar{\sigma}_f}{S_u} \\ &= 1 - \frac{A_{\text{net}}}{A_0} \\ &= \frac{A_0 - A_{\text{net}}}{A_0}. \end{aligned} \quad (15.5)$$

The loss of strength due to a hole or a defect is proportional to the reduction of the sectional area.

15.3.2 *Experimental studies*

A number of research programs have been carried out to determine experimentally how defects affect the strength of weldments in various metals. For example, Kihara *et al.*⁽¹⁵¹⁶⁾ summarized the experimental results obtained from a large number of specimens to show the general tendency of how weld defects affect the static tensile strength of welds in steel and aluminum. Welding Research Council Bulletin 152, prepared by Pense and Stout,⁽¹⁵¹⁷⁾ is an interpretive report on how weld defects influence the mechanical properties of aluminum alloy weldments. It includes material on how porosity and other defects influence the mechanical properties. Kedrov⁽¹⁵¹⁸⁾ has reported the results of experiments conducted in Russia.

Figure 15.12 summarizes the results obtained by Kihara *et al.*⁽¹⁵¹⁶⁾ on a large number of specimens. It shows how the size of a defect (expressed in terms of rate of defective area in percent) affects the static strength of butt-welded joints in low-carbon steel. The figure indicates that an appreciable decrease in the static strength occurs when the defective area accounts for 5% (or more) of the sectional area. A 10% loss of sectional area, for example, causes about a 10% loss of strength. Similar results also were obtained in aluminum welds.

An extensive study was made at the Martin Company⁽¹⁵¹⁹⁾ on how porosity affects the static strength of welds in high-strength aluminum alloys.^(104, 747) Welds were made in two materials (2219-T87 and 2014-T6), two thickness ($\frac{1}{4}$ and $\frac{3}{4}$ in.) (6.4 and 19 mm), and three welding positions (flat, horizontal, and vertical). The filler wire used was 2319 with the 2219-T87 material, and 4043 with the 2014-T6 material. Arc welding was GTA, D-C, straight polarity with helium shielding. Welds had to be intentionally

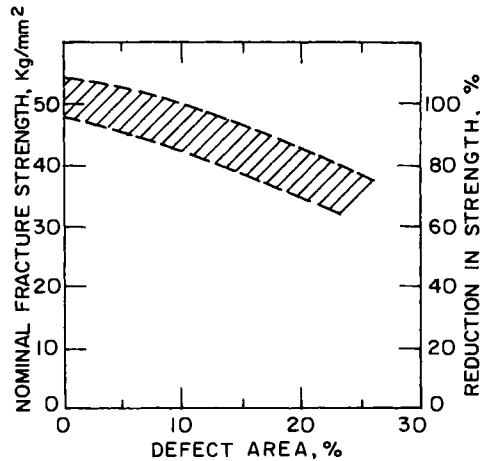


FIG. 15.12. Reduction in static tensile strength due to defects in weldments in low-carbon steel.⁽¹⁵¹⁶⁾

contaminated to produce porosity. This was done by metering additions of hydrogen and/or moisture to the shielding gas in the tungsten torch. However, large additions of hydrogen tended to form pores that were larger in number and finer than the typical porosity size-frequency distribution in production welding. In some instances the porosity was so fine that the X-rays would have been acceptable by most current standards; and yet the strengths of these welds were appreciably reduced.

Figure 15.13 shows how the porosity level affects the mechanical properties of transverse-weld specimens. The porosity level was chosen arbitrarily in five levels, 0 through 4, from water clear to very bad in radiographic inspections. Shown in the ordinate are the high, medium, and low values for each porosity level, and the "2 minimum" values of the following:

1. ultimate tensile strength,
2. yield strength,
3. Elongation for 0.4-, 1-, and 2-in. gage length.

Different curves are shown for data obtained with specimens with and without weld reinforcement.

Figure 15.13 shows that the ultimate strength decreased markedly as porosity increased.^(747, 1519) Elongation, especially with a short gage length, also was affected by the porosity level. The porosity level had the least effect on the yield strength.

Attempts were then made to determine the quantitative relationship between the porosity level and the ultimate strength. After specimens were fractured, fracture surfaces were examined to determine the loss of sectional area due to porosity. Results are shown in Fig. 15.14. In the first analysis, in which only pores larger than $\frac{1}{64}$ in. (0.4 mm) in diameter were counted, a drastic reduction in strength was observed. The results alarmed the investigators. In a later analysis, a more careful study was made to include all pores determined by a grid intercept method. Then a linear relation was observed between the loss of sectional area due to porosity and the reduction of strength.

An important finding obtained in the Martin study is the significance of small pores. If the reduction of strength due to a pore is determined by its cross-sectional area, a

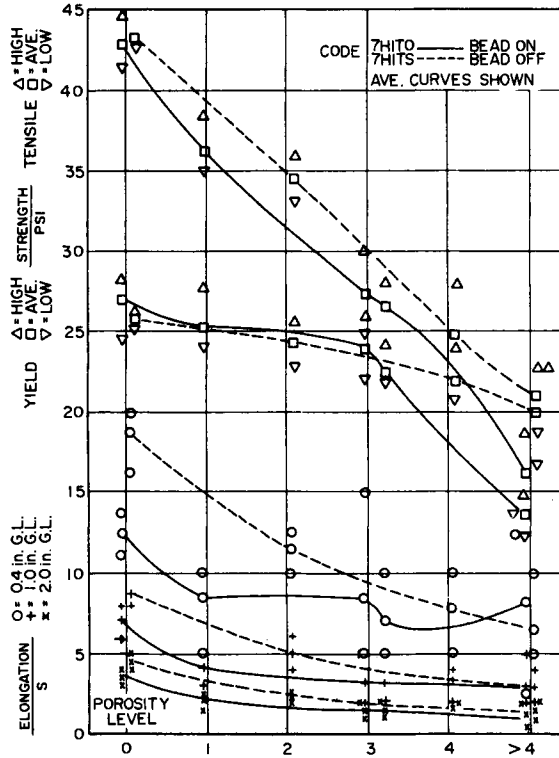


FIG. 15.13. Mechanical properties of 2219-T87, 1/4 in. aluminum alloy containing increasing levels of porosity, transverse horizontal position, D-C GTA weld 2319 filler metal.

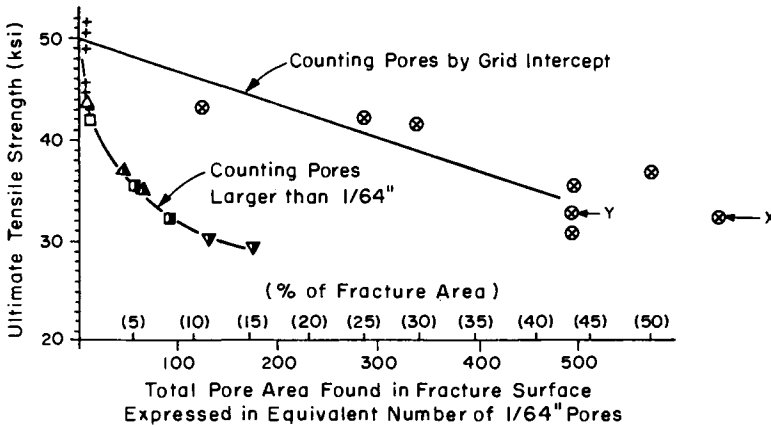


FIG. 15.14. Strength vs. pore area for 2014-T6, flat welds, 1/4 in. transverse test.

Note: Tested with reinforcement.

pore size which gives the least ratio of cross-sectional area to volume is to be desired. For a spherical void, the ratio of cross-sectional area to volume, α , is

$$\alpha = \frac{\pi R^2}{\frac{4}{3}\pi R^3} = \frac{3}{4} \frac{1}{R} \tag{15.6}$$

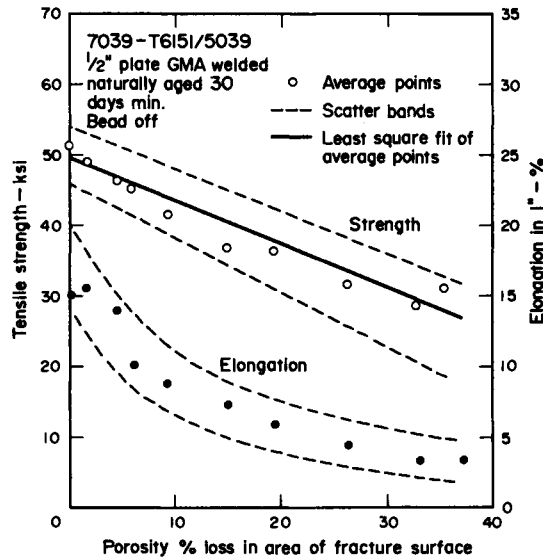


FIG. 15.15. Loss of tensile strength and percent elongation in 1-in. gage due to porosity in high-strength aluminum welds.⁽¹⁵²¹⁾

The value of α increases as R decreases. Thus, a given volume of contaminant gas in a freezing puddle can cause more damage in the form of small pores than large pores.

Figure 15.15 shows the results obtained by Shore⁽¹⁵²¹⁾ who studied porosity effects in $\frac{1}{2}$ in. (12.7 mm) thick 7039-T6151 alloy welded with 5039 filler wire by the GMA process. The tensile specimens had no weld reinforcement, and pores as small as $\frac{1}{250}$ in. (0.1 mm) in diameter were counted. The tensile strength of a weld decreased linearly with the increasing loss of sectional area. Shore observed about an 18% loss in strength for 10% porosity.

15.4 How Defects Affect Brittle Fracture

When a material becomes brittle, a fracture may initiate from a small defect to cause a catastrophic failure of the entire structure. The subject of brittle fracture is discussed in Chapters 9 and 10. The following pages summarize information pertinent to how weld defects affect brittle fracture.

15.4.1 Brittle failures of welded structures

Brittle failures have occurred in a number of steel structures, as discussed in Section 9.2. Although not limited to welded structures, the problem of brittle fracture is more serious in welded structures than in riveted structures, because:

1. A welded structure does not have riveted joints which can interrupt the progress of a brittle crack.
2. Welds can have various defects including cracks, slag inclusions, etc.
3. High tensile residual stresses in carbon steels and low-alloy high-strength steels are subject to catastrophic brittle failures.

The most extensive and widely known failures are those of cargo ships and tankers that were built in the U.S.A. during World War II (read Section 9.2.1).

A statistical investigation of failures of American ships built during the war has revealed that about 50% of the failures originated from structural discontinuities, including square hatch corners, cutouts in shear strakes, ends of bilge keels, etc. About 40% of failures started from weld defects including weld cracks, undercuts, and lack of fusion. The remaining 10% of the failures originated from metallurgical defects such as the weld heat-affected zones and notches in flame-cut plate edges. In other words, all failures originated from notches that created severe stress concentrations.

A number of serious failures started from unimportant, incidental welds such as tack welds and arc strikes made on a major strength member. For example, the tanker *Ponagansett* broke in two from a tack weld between a small clip and the deck plate, as shown in Fig. 9.13.

Figure 9.8 shows the fractured pieces of a 260-in. (6.6 m) diameter rocket motor case that failed in April of 1965 during a hydrotest. The failure originated from a defect that was not detected by non-destructive testing techniques prior to aging. Non-destructive testing was not conducted between the aging and the hydrotest.

15.4.2 How weld defects affect brittle fracture

Critical crack length. Suppose that a wide plate containing a crack of length $l = 2c$ is subjected to tensile loading, as shown in Fig. 10.6. If the fracture toughness of the material is K_c , an unstable fracture will occur when the stress exceeds the critical stress σ_c :

$$\sigma \geq \sigma_c \equiv \frac{K_c}{\sqrt{\pi c}}. \quad (15.7)$$

Stated differently, an unstable fracture will occur under stress σ if a crack longer than the critical value is present:

$$l \geq l_c = \frac{2}{\pi} \left(\frac{K_c}{\sigma} \right)^2. \quad (15.8)$$

The critical crack length at the yield stress is:

$$(l_c)_{\sigma=\sigma_{ys}} = \frac{2}{\pi} \left(\frac{K_c}{\sigma_{ys}} \right)^2. \quad (15.9)$$

It is well known that structures made of higher strength steels can generally only tolerate smaller defects. This happens because:

1. As the strength level of the material increases, the K_c value generally decreases, as shown in Fig. 10.12.
2. The very reason for using a higher strength material is to increase the operating stress, σ .

For example, if $K_c = 120 \text{ ksi}\sqrt{\text{in}}$ ($425 \text{ kg}\sqrt{\text{mm}/\text{mm}^2}$) and $\sigma_{ys} = 180 \text{ ksi}$ ($126.6 \text{ kg}/\text{mm}^2$ or $1241 \text{ MN}/\text{m}^2$) the critical crack length is (see Fig. 10.12):

$$l_c = \frac{2}{\pi} \left(\frac{120}{180} \right)^2 = 0.28 \text{ in. (7 mm)}$$

If K_c is $40 \text{ ksi}\sqrt{\text{in.}}$ ($142 \text{ kg}\sqrt{\text{mm}/\text{mm}^2}$) at $\sigma_{ys} = 240 \text{ ksi}$ (168.8 kg/mm^2 or 1655 MN/m^2) the critical crack length is:

$$l_c = \frac{2}{\pi} \left(\frac{40}{240} \right)^2 = 0.018 \text{ in. (0.45 mm).}$$

This indicates that when a structure is fabricated using a material with a very high strength level an unstable fracture may occur below yield since the structure is likely to contain flaws larger than the critical size. The results shown in Fig. 10.13 prove this statement. The results shown in Fig. 10.14 prove that the unstable fracture of a weldment made in very high-strength steel occurs from a small flaw.

On the other hand, the critical crack length of mild steel can be quite long. The results shown in Fig. 10.15 indicate that the critical crack length is about 3 in. (76 mm) at the yield-strength level of 30,700 psi (21.6 kg/mm^2 or 212 MN/m^2). Results obtained in other experiments also indicate that the critical crack length of low-carbon steel is on the order of several inches.

Figure 15.16 shows several general trends that indicate how the critical crack length at yield strength ($l_c)_{\sigma=\sigma_{ys}}$ decreases as the yield strength σ_{ys} increases.

Subcritical crack growth. The results presented in the preceding pages may give the reader the impression that a flaw longer than 3 to 4 in. (75 to 100 mm) must be present before an unstable brittle fracture can occur in structures made of low-carbon steel. However, catastrophic failures do occur from small flaws, as shown in Fig. 9.13. The question here is “How can the catastrophic failure of a welded structure in low-carbon steel occur from a flaw shorter than the critical size?” Subcritical crack growth is discussed in Section 10.5. Unstable fractures can initiate from a subcritical flaw when:

1. The flaw exists in areas of high residual tensile stress.
2. The flaw exists in areas of local embrittlement.
3. The flaw grows (by fatigue or stress corrosion cracking) until it reaches the critical size.

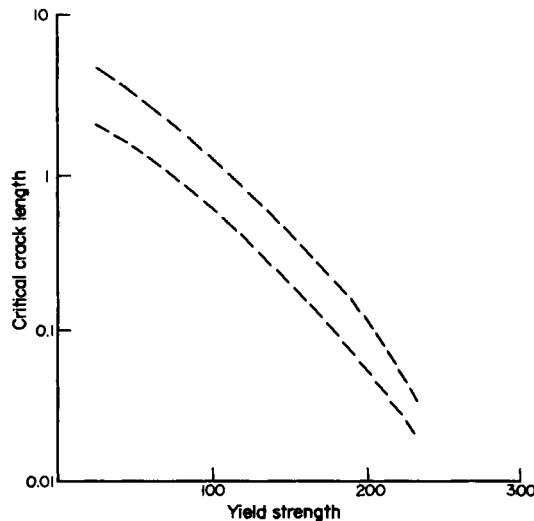


FIG. 15.16. General trend indicating effects of yield strength of steel σ_{ys} on critical crack length at the yield stress, $(l_c)_{\sigma=\sigma_{ys}}$

15.5 How Defects Affect Fatigue Fracture

A number of studies have been made on how weld defects affect the fatigue strength. Results have been summarized in several reports and books including those written by Kihara *et al.*,⁽¹⁵¹⁶⁾ Munse,⁽¹¹⁰²⁾ Pense and Stout,⁽¹⁵¹⁷⁾ Gurney,⁽¹¹⁰¹⁾ and Lundin.⁽¹⁵²²⁾ Studies of how defects affect the fatigue strength of weldments are being carried out in a number of laboratories around the world. Among the best known are the studies being carried out at the University of Illinois.

15.5.1 General trends

Figure 15.17 summarizes results obtained by Kihara *et al.*⁽¹⁵¹⁶⁾ on how defects affect the fatigue strength of butt welds in low-carbon steel. Compared to Fig. 15.12, which shows how porosity affects the static strength, the effects on fatigue are much greater. A 10% loss in sectional area due to porosity, for example, caused a 50% reduction in fatigue strength.

Figure 15.18 summarizes the results obtained at the Martin Company⁽¹⁵¹⁹⁾ on how porosity affects fatigue strength.^(104, 747) Shown here are relationships between reduction of sectional area due to porosity and cycles to failure of welded joints in 2219 and 2014 alloy plates $\frac{1}{4}$ in (6.4 mm) thick. The reinforcement was removed, and the specimens were cycled in axial tension (zero to a given value, or $R = 0$). Figure 15.18 shows cycles to failure under three stress levels: 10, 15, and 20 ksi. (7, 10.5, and 14 kg/mm² or 69, 103, 138 MN/m²).

The results shown in Fig. 15.18 can be interpreted in several ways. For example, 10% porosity causes:

1. Reduction in fatigue strength of the 10,000 cycle life from over 20 ksi (14 kg/mm² or 138 MN/m²) to around 12 ksi (8.5 kg/mm² or 83 MN/m²) (about one-half that of a sound weld).
2. Reduction in the number of cycles to failure under 20 ksi (14 kg/mm² or 138 MN/m²): from over 10^4 to around 10^3 (one-tenth that of a sound weld); under 10 ksi (7 kg/mm² or 69 MN/m²) from over 10^6 to around 5×10^4 (one-twentieth that of sound weld).

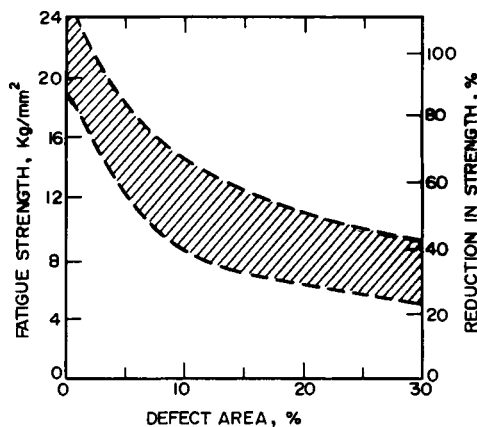


FIG. 15.17. Reduction in fatigue strength due to defects in mild-steel weldments.⁽¹⁵¹⁶⁾

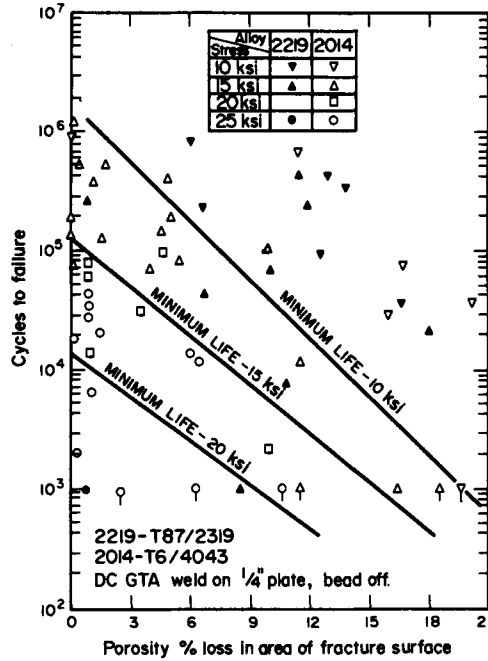


FIG. 15.18. Fatigue life vs. fracture pore count for 1/4 in. thick 2219 and 2014.^(1517,1519)

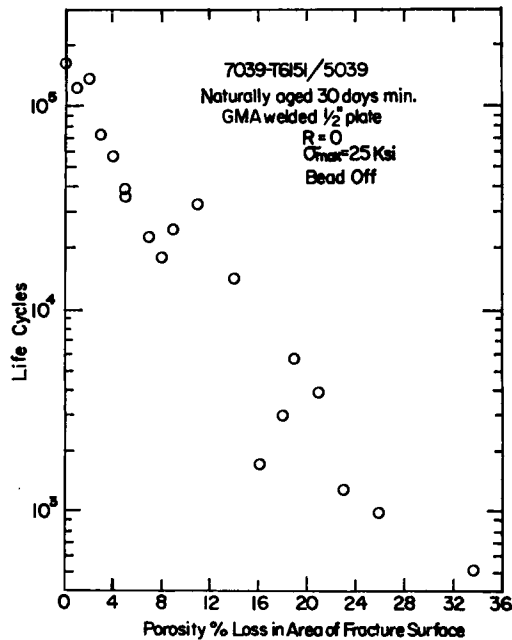


FIG. 15.19. Tension-tension fatigue life vs. porosity in 7039/5039.⁽¹⁵²¹⁾

Figure 15.19 shows similar results as obtained at the Ohio State University.⁽¹⁵²¹⁾ Welds were made in 7039-T6151 plates $\frac{1}{2}$ -in. (12.7 mm) thick using 5039 filler wire. The reinforcement was removed and the specimens were cycled to 25 ksi (17.6 kg/mm² or 172 MN/m²) (R = 0).

15.5.2 *Effects of defect location*

It is important to remember that fatigue fracture usually initiates from the surface. Figure 15.20 shows a crack initiated from a pronounced surface ripple at the start-stop position in a manual web-to-flange weld. As far as fatigue strength is concerned, defects on or near the surface are more damaging than those imbedded in the material.

Concerning how porosity location affects fatigue, the analysis of Lindh and Peshak⁽¹⁵²³⁾ of a titanium alloy serves as a guide. They show that scattered porosity will reduce the allowable stress range for 10⁶ cycles about 30% if it is deep-seated (radius/distance to surface < 0.02) and over 60% if close to the surface ($r/d > 0.5$). Figure 15.21 illustrates the behavior observed in a Ti-6Al-4V alloy. If the removal of the reinforcement notch exposes porosity to the surface, the benefit of removing the reinforcement notch may be diminished. How these conclusions are relevant to aluminum alloys has recently been demonstrated by Hersh⁽¹⁵²⁴⁾ who showed that fatigue failures in 0.1-in. (2.5-mm) thick 2219/2319 welds with the reinforcement removed invariably initiated at cracks, porosity, or lack of fusion exposed by the grinding.

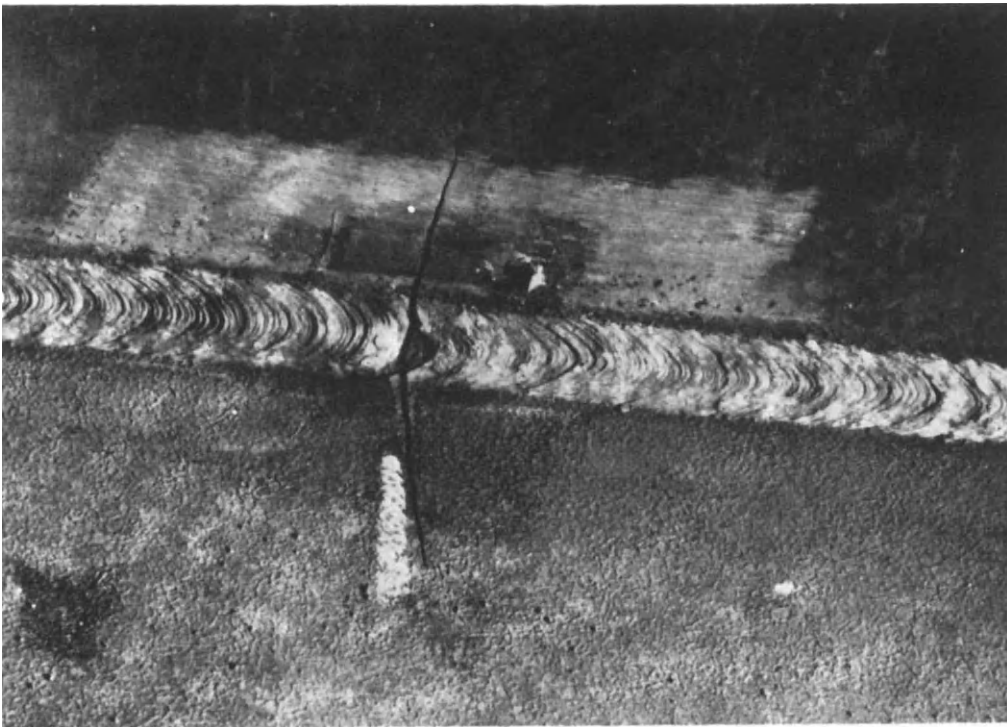


FIG. 15.20. Fatigue crack initiated from pronounced surface ripple at start-stop position in manual web to flange fillet weld.⁽¹¹⁰¹⁾

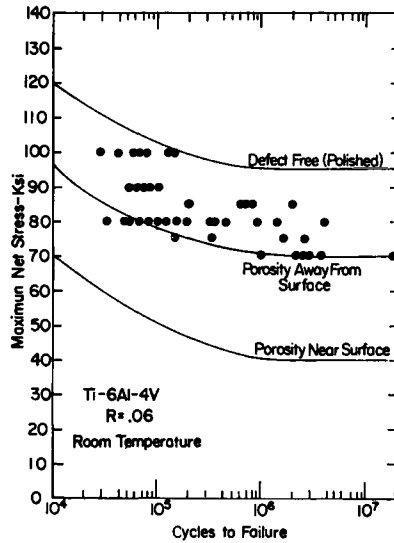


FIG. 15.21. Comparison of fatigue data for Ti-6Al-4V containing natural porosity defects with predicted results.⁽¹⁵²³⁾

15.5.3 Reinforcement and fatigue strength

The detrimental influence of reinforcement on fatigue strength has been well established. Dinsdale and Young⁽¹⁵²⁵⁾ found that the notch effect of the weld reinforcement could be expressed in terms of the angle subtended by the plate and the weld bead at its junction with the plate. The data of Fig. 15.22 indicates that the fatigue strength of NP 5/6 alloy is lowered progressively from 16 to 6.5 ksi (11.2 to 4.6 kg/mm² or 110 to 44.8 MN/m²) as the reinforcement angle becomes sharper (180 – 110°).

Mindlin⁽¹⁵²⁶⁾ tested $\frac{1}{4}$ and $\frac{3}{8}$ in. (6.4 and 10 mm) thicknesses of 5083-H113 welded

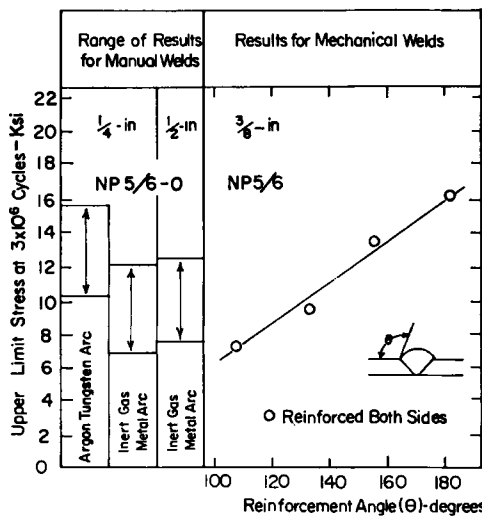


FIG. 15.22. Effects of reinforcement on fatigue strength.⁽¹⁵²⁵⁾

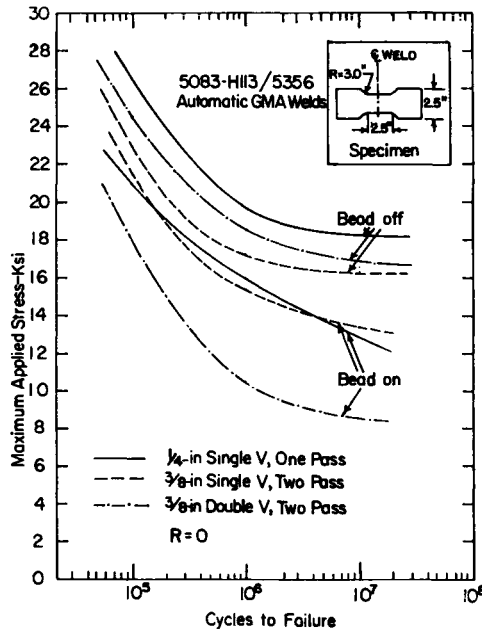


FIG. 15.23. Effects of welded bead on axial tension fatigue strength of transverse butt welds in 5083-H113 plate (5356 filler metal).⁽¹⁵²⁶⁾

with 5356 in tension fatigue ($R = 0$). Figure 15.23 summarizes the data for tests on welds with bead on and bead off. Not only was there an appreciable drop in the fatigue strength in the presence of single-V weld reinforcement, but the plates with double-V weld showed a large additional loss due to the notch effects of the double reinforcement.

Although reinforcement is detrimental to fatigue strength, it is a better practice to aim for a moderate overfill with a smooth blending into the plate surface than to run the risk of a severe notch from underfilling or perhaps undercutting. Removal of reinforcement may bring internal porosity or lack of fusion or bring the cracks closer to the surface.

Because they reduce the section and introduce a notch effect, whether they contain cracks or not, craters are more damaging than reinforcement and must be avoided in fatigue service.⁽¹⁵²⁷⁾

15.5.4 Analysis of fatigue crack growth

Attempts have been made to apply fracture mechanics to the study of the growth of fatigue cracks initiating from weld defects. The following pages describe the results obtained by Harrison⁽¹⁵²⁸⁾ on butt welds with a lack of sufficient penetration. Similar approaches can be taken to analyze how other types of defects affect the fatigue strength.

Figure 15.24 shows a defect and the nomenclature used for the analysis. On the basis of the fracture mechanics theory, the dependence of crack propagation rate on the range of K can be written as:

$$\frac{da}{dN} = f(\Delta K). \quad (15.10)$$

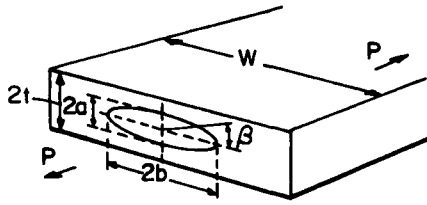


FIG. 15.24. Defect and nomenclature used.

- 2a = Defect width through thickness.
- 2b = Defect length.
- 2t = Material thickness at defect.
- W = Material width at defect.
- σ = Gross area stress = $P/2Wt$.
- $\Delta\sigma$ = The cyclic range of stress.
- K = Stress intensity factor.
- ΔK = Range of stress intensity factor.
- σ_u = Ultimate tensile stress of the material.
- ϕ = Complete elliptic integral =

$$\int_0^{\pi/2} \sqrt{1 - \left(\frac{b^2 - a^2}{b^2}\right) \sin^2 \theta} d\theta.$$

β = Angle defining a point on the circumference of the defect.

Paris and Erdogan⁽¹⁵²⁹⁾ suggest that

$$\frac{da}{dN} = B(\Delta K)^4 \tag{15.11}$$

gives the best agreement with all the available results, where B = constant.

For a crack in which b and t are both large with respect to a :

$$K = \sigma \sqrt{\pi a}. \tag{15.12}$$

However, in most cases of lack of penetration defects, t is not large with respect to a . In such a case:

$$K = \sigma(\pi a)^{1/2} \left(\frac{2t}{\pi a} \tan \frac{\pi a}{2t}\right)^{1/2}. \tag{15.13}$$

Substituting eqn. (15.13) in (15.11) we find that:

$$\frac{da}{dN} = B(\Delta\sigma)^4 \left(2t \tan \frac{\pi a}{2t}\right)^2. \tag{15.14}$$

It can be written:

$$\frac{da}{dN} = C \left(\frac{\Delta\sigma}{E}\right)^4 \left(2t \tan \frac{\pi a}{2t}\right)^2 \tag{15.15}$$

where C , a new constant = BE^4 , E being Young's modulus.

Integrating (15.15), the number of cycles required to propagate the crack size from $2a_1$ to $2a_2$ is given by:

$$2\pi C t \left(\frac{\Delta\sigma}{E}\right)^4 N = \cot\left(\frac{\pi a_1}{2t}\right) - \cot\left(\frac{\pi a_2}{2t}\right) - \frac{\pi}{2t}(a_2 - a_1). \tag{15.16}$$

If $2a_1 = 2a_i$, the initial defect size, and $2a_2 = 2a_{cr}$, the critical crack size at which failure occurs, then eqn. (15.16) gives N , the endurance to failure. In a real structure, $2a_{cr}$ might be taken to be the critical crack width for brittle fracture, if this mode of failure was likely, or it might be taken to be the material thickness in a pressure vessel since leakage would occur.

For the purpose of analyzing experimental results in small specimens, it will be sufficient to assume that a_{cr} is reached when the stress on the remaining net section is equal to the ultimate tensile strength of the material, σ_u :

$$a_{cr} = \frac{t(\sigma_u - \sigma)}{\sigma_u} \tag{15.17}$$

Equation (15.16) can be rewritten :

$$\left(\frac{\Delta\sigma}{EX^{1/4}} \right)^4 N = \frac{1}{\pi C} \tag{15.18}$$

where X is a parameter dependent solely on the geometries of the defect and specimen (or structure), and

$$X = \frac{1}{2t} \left[\cot\left(\frac{\pi a_i}{2t}\right) - \cot\left(\frac{\pi a_{cr}}{2t}\right) - \frac{\pi}{2t}(a_{cr} - a_i) \right] \tag{15.19}$$

If eqn. (15.18) is correct, we should be able to predict the life of the defective joint, knowing the constant amplitude service loading and the defect size and material thickness. To check the validity of eqn. (15.18), the results obtained by other investigators have been plotted in Fig. 15.25 in the form :

$$\log \frac{\Delta\sigma}{EX^{1/4}} \text{ against } \log N.$$

If eqn. (15.18) is correct, a straight-line relationship of slope = $-\frac{1}{4}$ should be obtained.

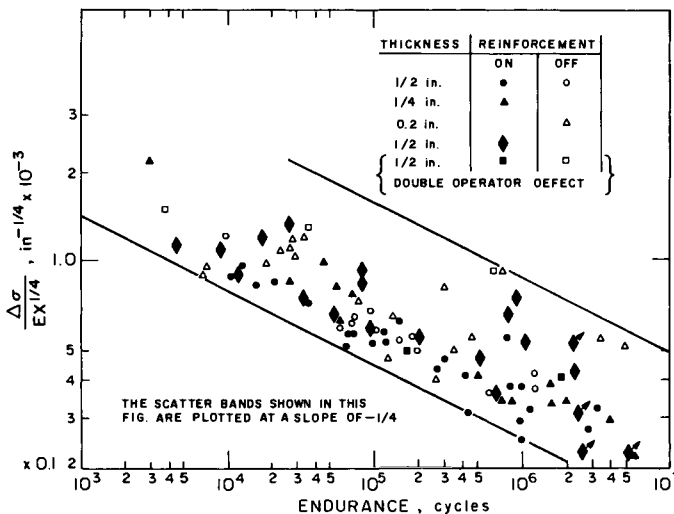


FIG. 15.25. Test results for aluminum welds.

The lines showing the extremities of the scatter band in this figure are drawn with this slope.

Although the scatter is considerable, it is not excessive in view of the number of results used, the variety of material thickness and defect size combinations, and the inevitable variations in initial root radii for this type of defect. It will also be seen that the upper edge of the scatter band is fixed by four high results and that if these were ignored the scatter band would be considerably narrower. It should be noted that the assumed slope of $-\frac{1}{4}$ agrees well with the results.

So far it has been assumed that the value of $2a$ (defect width) is small with respect to $2b$ (defect length), but this assumption is not always valid. Equation (15.18) can now be modified to take account of defect length and becomes:

$$\left(\frac{\Delta\sigma}{\phi_m EX^{1/4}}\right)^4 N = \frac{1}{\pi C} \tag{15.20}$$

Results obtained by several investigators are plotted on this basis in Fig. 15.26. The majority of the results plotted were obtained with a stress ratio

$$R = \frac{S_{\min}}{S_{\max}} = 0.$$

It has been shown by Gross⁽¹⁵³⁰⁾ that, for a given total strain range per cycle, the life in low-cycle fatigue is the same for a considerable variety of materials. Although we are dealing with high-cycle fatigue, the strain range which occurs at the crack tip will be considerable and there seems no reason why the independence of material properties should not be found. The parameter used has been K/E and not K and it is gratifying to find that when the scatter bands for aluminum alloys from Fig. 15.25 are superimposed on Fig. 15.26, which shows the results for steels, there is close agreement.

There are several ways in which the information from eqn. (15.18) can be presented. The one given here is that in which the maximum defect size is plotted against thickness for a variety of stresses and lives (Fig. 15.27 (a) and (b)). The curves plotted here are

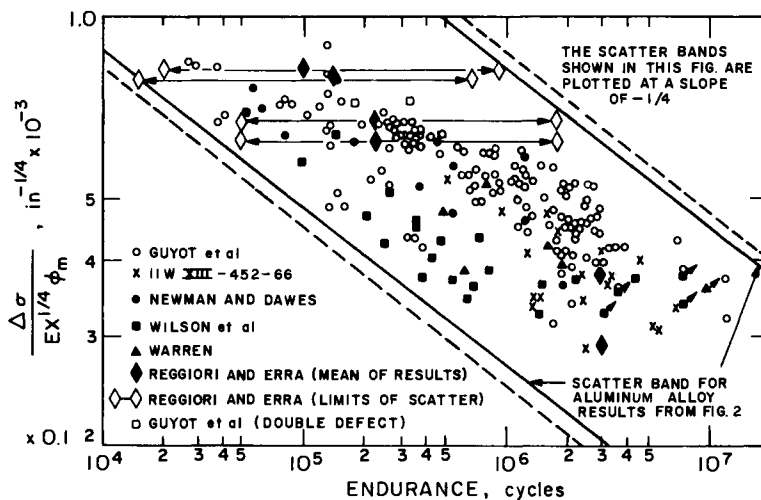


FIG. 15.26. Test results for steel welds.

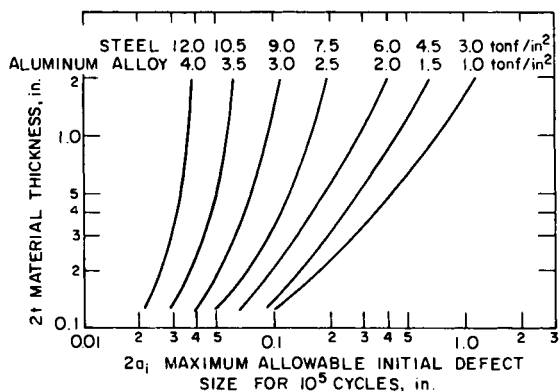


FIG. 15.27 a. Maximum allowable initial defect size for 10⁵ cycles.

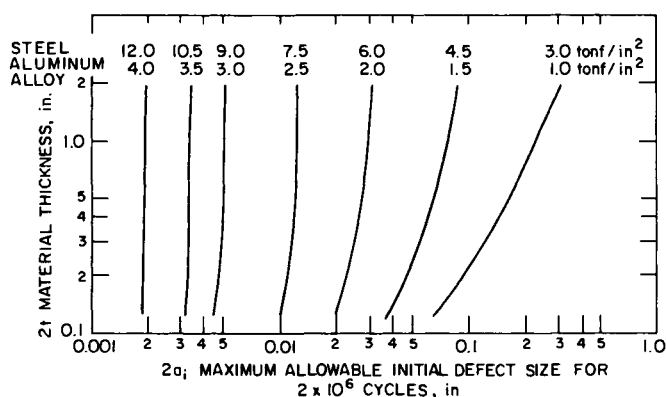


FIG. 15.27 b. Maximum allowable initial defect size for 2 x 10⁶ cycles.

based on the lower limit of the scatter band in Fig. 15.25. When making the calculations for these curves, a_{cr} was assumed to be equal to t .

15.6 Non-destructive Inspection of Welds

Various methods have been developed and used for the non-destructive inspection of weld defects. This section presents a brief discussion on non-destructive inspection methods commonly used for welds. Much of the information presented here comes from reference (1121). Further detailed information can be obtained from reference (1531).

15.6.1 Radiographic inspection

Radiographic inspection involves the use of radiation from specially constructed industrial X-ray machines, or the use of gamma rays from a radioactive substance. Short-wavelength radiations, such as X-rays or gamma rays, penetrate objects opaque to ordinary light. In general, the shorter the wavelength the greater the penetrating power. Should there be a cavity, such as a blowhole, in the weld interior, the beam of radiation will have less metal to pass through than if the metal were sound. Consequently, there

will be a variation in the absorption of the rays by the weld in the defective region, which variation, if measured or recorded on a film sensitive to the radiation, produces an image that will indicate the presence of the defect. The image is an X-ray shadow of the interior defect. Such a shadow picture is called a radiograph.

Sensitivity of radiographic films. It is generally assumed that radiographic methods will produce films having a sensitivity of 2%. Sensitivity in this context means the smallest percentage of weld-thickness difference that can be detected visually on a radiograph.

15.6.2 *Magnetic particle inspection*

Magnetic particle inspection is a non-destructive method of detecting the presence of cracks, seams, inclusions, segregations, porosities, lack of fusion, and similar discontinuities in magnetic materials (see Fig. 15.28). It is not applicable to non-magnetic materials. This method will detect surface discontinuities that are too fine to be seen with the naked eye, those that lie slightly below the surface and, when special equipment

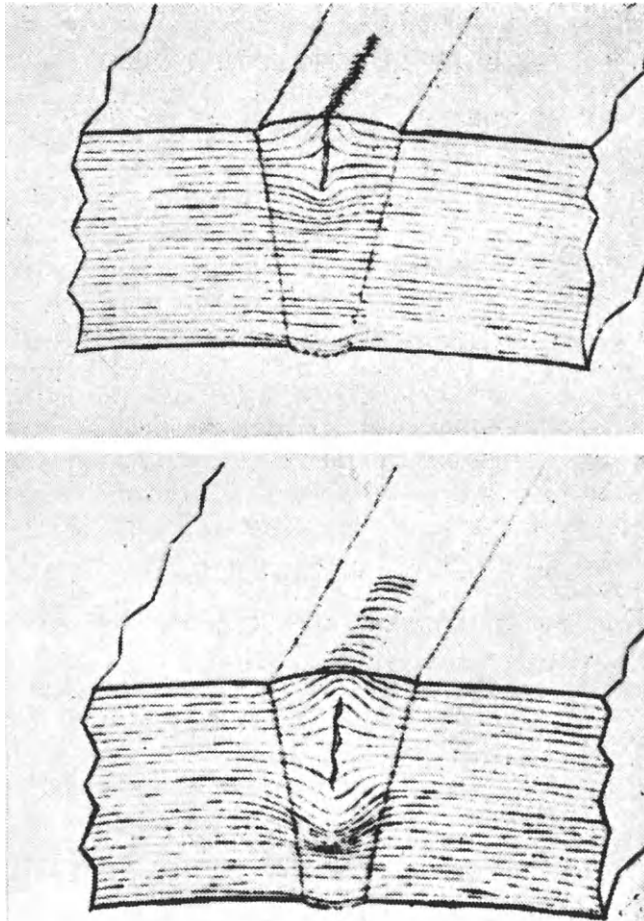


FIG. 15.28. The theory of magnetic particle inspection with its practical application.⁽¹¹²¹⁾

is used, more deeply seated discontinuities. Various forms and colors of magnetic particles are available. The type of surface and the type of defect will determine the material selected. There are two methods in applying magnetic particles: (1) dry method and (2) wet method.

In the dry method, finely divided, ferromagnetic particles in dry powder form, coated to afford greater particle mobility, are dusted uniformly over the work by means of a dusting bag, atomizer, or spray gun. The magnetic particles are available in gray, black, and red. The dry method is easier to use on rough surfaces and has maximum portability.

In the wet method, indicating particles smaller than those used in the dry method are suspended in a liquid bath of light petroleum distillate or water. Because of the small particle size, the wet method is more sensitive to fine surface defects; but for the detection of subsurface discontinuities, it is not as sensitive as the dry method.

The material, which is available in various colors, is flowed or sprayed over the surface to be inspected, or the part is immersed in the suspension. When the particles are coated with a dye that fluoresces brilliantly under ultraviolet (black) light, the sensitivity of the method is increased. Thus fluorescent inspection material indicates very small or fine discontinuities and permits rapid inspection of irregularity of dark surfaces.

The fluorescent magnetic particle method is applicable only to magnetic materials and should not be confused with fluorescent penetrant inspection, described later in this chapter.

15.6.3 *Ultrasonic inspection*

Ultrasonic inspection depends on the use of high-frequency sound waves to detect, locate, and help to measure discontinuities in a weldment. The successful application of the technique depends on several elements including: (1) adequate definition of the test problem, (2) knowledge of the principles of ultrasonic testing, (3) selection of the proper technique based on numbers (1) and (2), (4) evaluation of the test information, and (5) the skill of the personnel involved. Failure or deficiencies in any of the above elements may result in unsatisfactory results or an incorrect evaluation of weld quality.

The ultrasonic testing of welds depends on the use of a refined sonarlike technique. An electrical pulse is produced by the instrument, and a suitable transducer converts the electrical signal to mechanical vibrations, or sound. The sound waves used in weld inspection are usually in the frequency range between 1 MHz and 5 MHz.

The sound beam generated by the transducer is introduced into the part being tested through a liquid couplant. This thin film of liquid excludes air and permits the passage of the sound.

Discontinuities reflect part of the wave and this is picked up and appears as a pip (vertical indication) in the line on the screen of a cathode-ray tube. This is the principle of the ultrasonic reflectoscope. The instrument is designed to register the time required to reflect a wave from a discontinuity. The length of time is proportional to the distance travelled. Interruption of the sound wave is seen on the screen in the form of a horizontal displacement of the indication. This indication may be photographed if a permanent record is desired.

Testing techniques. The selection of straight-beam or angle-beam techniques is determined by the need to intercept a possible defect perpendicular to its plane or at a

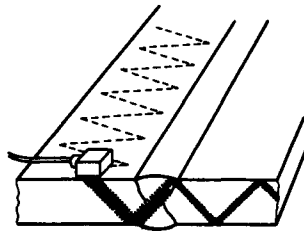
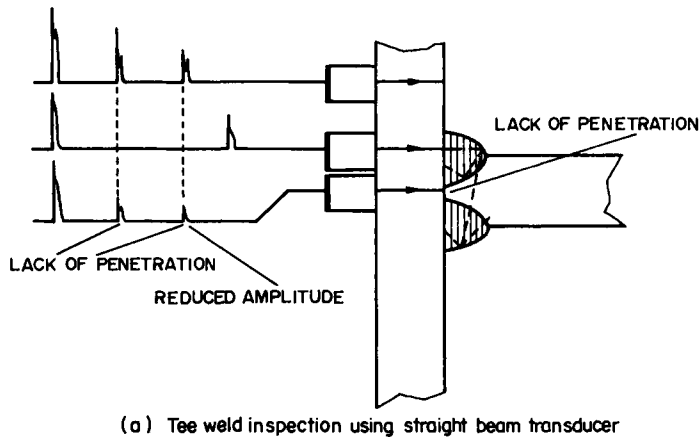


FIG. 15.29. Ultrasonic inspection of welds.

corner (Fig. 15.29a). If the defect cannot be accurately predicted, then multiple scans using various sound beam directions may be required to increase the probability of detecting such random defects.

The sound beam interrogates only a small portion of the entire volume of the weld at a given instant. In order to check the entire volume of the weld the transducer must be moved in some adequate scan pattern. It is usually oscillated so that the sound beam scans the weld in various directions (Fig. 15.29(b)).

15.6.4 Liquid-penetrant inspection

Penetrant inspection is a sensitive, non-destructive method of detecting and locating minute discontinuities that are open to the surface, such as cracks, pores, and leaks. It employs a penetrating liquid which is applied over the surface and enters the discontinuity. Subsequently, after the excess of penetrant has been cleaned from the surface, the penetrant which exudes or is drawn out of the crack is observed, indicating the presence and location of the discontinuity. It is particularly useful on non-magnetic materials, where magnetic particle inspection cannot be used. In the welding field, it is used extensively for exposing surface defects in aluminum, magnesium, and austenitic steel weldments, and for locating leaks in all types of welds.

Penetrant inspection is relatively inexpensive and rapid. The process is essentially simple and operators find no difficulty in learning to use it properly. Penetrant inspection is the most sensitive method for locating fine, short, and shallow cracks in non-magnetic materials. The magnetic particle method is equal in this respect on magnetic materials and is more reliable on cracks that may be filled with foreign material.

The two varieties of the penetrant method are fluorescent penetrants and visible dye (or color contrast) penetrants, differing in the manner in which the indications are revealed and viewed.

Fluorescent penetrant inspection. This method makes use of a highly fluorescent liquid with unusual penetrating qualities. It is applied to the surface of the part to be inspected and is drawn into extremely small surface openings by capillary action. After

TABLE 15.1 Uses and limitations of non-destructive testing methods

	Radiographic	Magnetic particle	Ultrasonic	Liquid penetrant
When to use	Detection of internal flaws and defects, weld flaw detection, cracks seams, porosity, holes and inclusions, checking assemblies, and determining thickness variations	Suitable for the detection of either surface or sub-surface flaws, cracks, porosity, non-metallic inclusions and weld defects	PULSE-ECHO METHOD used to find internal defects, cracks, lack of bond, laminations, inclusions, porosity, grain structure. RESONANCE METHOD used primarily for thickness gaging and laminar flaws	Used to locate open-to-the-surface porosity, laps, cold shuts, lack of weld bond, fatigue and grinding cracks
Where	Forgings, castings, tubing formed metal parts, welded vessels, field testing of welds, corrosion surveys and assemblies	Used on all types of <i>ferromagnetic</i> materials, tubing, piping of any size, shape, composition, or state of heat treatment. In-service testing for fatigue cracks	Used on all metals and hard non-metallic materials, sheet, tube, rod, forgings, castings, field and production testing, welds, silver-testing, welds, silver-brazed pipe joints	Used on all metals, glass, ceramics, castings, forgings, machine parts, cutting tools, and field inspection
Why	Detects variety of flaws provides a permanent film record. Gamma sources very portable, X-ray machines operable at various energy levels for different materials and thicknesses	Simple in principle, easy to perform, portable for field testing, fast for production testing. Method is positive and cost is economical	Fast and dependable, easy to operate, lends itself to automation, results of test immediately known, relatively portable, highly accurate and high sensitivity	Simple to apply. Accurate, fast, low initial cost, and per test cost, easy to interpret results, no elaborate setup required.
Limitation	Power source required for X-ray. Both produce radiation hazard. Well-trained technician needed to interpret radiographs	Test parts must be magnetic. Requires demagnetizing after test. Power source is required and parts must be clean before testing	Requires contact with part to be tested. Interpretation of defects requires considerable training. No permanent record reproduction of test results (without automatic recording devices.)	Limited to open-to-the-surface defects. Surface cleanliness required.

the penetrant has been applied to the surface, and sufficient penetration time has been allowed, the excess is removed from the surface, but not from the defects being sought. A developer is then applied which draws penetrant from the defect and produces fluorescent indications when observed under black light. The high contrast of the fluorescent makes it possible to detect minute indications easily.

Dye penetrant inspection. This method is essentially similar in materials and techniques to fluorescent penetrant inspection except that it makes use of visible dyes instead of fluorescent dyes in the penetrant. Also, the indications are observed under normal white light, a particularly useful property when portability is a factor that must be considered, or where the use of black light is impractical.

Dye penetrant inspection is a three-stage operation. The part is sprayed with a cleaner to remove all oil, grease, and foreign materials. It is then sprayed with the dye penetrant, which penetrates surface cracks and irregularities. The excess penetrant is removed. The part is then sprayed or brushed with the developer. This may be a chalky substance that dries on contact. The substance is stained by the dye, which rises by capillary action from flaws in the surface and marks them clearly in red.

15.6.5 *Comparison of various tests*

Table 15.1, prepared from a paper by Shanahan and Jenny,⁽¹⁵³²⁾ compares radiographic, magnetic particle ultrasonic and liquid-penetrant inspection methods. The table discusses when, and why these methods are to be used as a part of ship construction. It also discusses their limitations.

15.7 Evaluation of Reliability of Welded Structures

15.7.1 *Discussion of the present situation*

Extensive uses of welding for fabrication of large, critical structures started during World War II. In the early days most welded structures were put into use after very few non-destructive inspections other than visual inspections. Some welded structures experienced failures, many of which originated from weld defects (refer to Chapter 9 for brittle fracture). The need was recognized for developing reliable methods for non-destructive inspection of welds. Since then, much effort has been made in the world for developing and improving NDT methods. Today there are a number of NDT methods which can be used for inspecting welds, as discussed in the preceding part of this chapter. Significant efforts also have been made:

1. To develop better understanding of mechanisms of fractures which have led to the development of fracture-mechanics theories.
2. To improve fracture toughness of materials.

Due to a combined effect of these and other efforts, the reliability of welded structures has improved significantly over the years. One might expect that repair welds have been reduced considerably.

On the contrary, however, the total cost for fabricating critical structures such as pipelines, submarines, and nuclear pressure vessels has increased significantly over the

years. A significant portion of the cost increases (after adjusting the effect of inflation) comes from the inspection and repair procedures after welding.

Firstly, as the technology of non-destructive testing advances an increasing number of small defects can be detected. Many of these defects would have gone undetected in previous years. Once defects are detected, there is a tendency that end users of the structure and/or inspecting agencies demand that the defects be repaired. Consequently, the continuing development of NDT techniques means more repair work. If this idea is carried to its extreme, it means that as the testing equipment becomes more capable the number of repair welds will increase.

Secondly, society has been increasingly concerned with consequences of potential failures, such as oil spills of large tankers, possible explosions of cryogenic tankages containing liquefied natural gas, etc. Requirements for inspection and repair have become more and more stringent. If this current trend continues there will be a further significant increase in these costs.

The subject of quality control and inspection has an effect similar to that of a double-edged sword. If inspections are exercised properly during fabrications as a means of process control, the use of NDT methods can result in delivering more reliable structures with some added cost. On the other hand, if inspections are used for punitive actions by government agencies and for lawsuits by companies involved, increased uses of inspections can result in considerable delay in construction and a skyrocketing increase in cost. Although the direct cost required for inspection and repair may not be great, the financial loss due to the fact that structures are laid idle can be enormous.

How to find defect is a matter of applied physics—radiography, magnetism, ultrasonic waves, etc.—discussed in Section 15.6. How to evaluate effects of defects which have been detected on the service behavior of welded structures is a matter of applied mechanics—brittle fracture, fatigue, etc.—discussed in Sections 15.3 to 15.5. However, what to do with the structure which contains some defects involves many technical, financial, and legal considerations. For example:

1. Suppose that defects are found in a component of a critical structure (a space rocket, a submarine, etc.). Should we repair them now? The repair work will certainly delay the construction. There is no guarantee that the repair work can be done satisfactorily. The component may work satisfactorily without even repair, but some problems may develop at a later stage of construction. The cost for repair at later stages (for example, a pipeline after being laid under ground) can be extremely high.
2. Suppose that defects are found in completed welded structures. What should be done about the structures? The owner of the structure may decide to use the structure as it is risking possible failures which may or may not involve loss of human lives. The owner may decide to have the structure repaired and sue the fabricator to recover the financial loss. The owner may want to sell the structure for less demanding tasks. Before deciding what to do, the owner analyses pros and cons of various possible actions and their consequences. The analysis will cover technical and non-technical subjects.

The above discussions show the latitude of subjects to be considered in dealing with structures containing defects. The analyses obviously cover various subjects; technical, financial, legal, etc. Parties involved including the owner, the fabricator, the material

suppliers, the classification society, government agencies, and insurance companies, may have different opinions. Each party has a temptation to interpret the situation for their own advantage. A common way to solve the problem is to refer to rules and regulations. It is very important that rules and regulations covering the evaluation of weld defects be rational and fair.

Today a number of rules cover non-destructive testing of welded structures. For example, inspection of naval ship construction is governed by several specifications including:

1. NAVSHIPS 0900-060-4010: "Fabrication, Welding and Inspection of Metal Boat and Craft Hulls", January 1971.
2. NAVSHIPS 0900-000-100: "Fabrication, Welding and Inspection of Ship Hulls", October 1968.
3. NAVSHIPS 0900-014-5010: "Fabrication, Welding and Inspection of Non-Combatant Ship Hulls", December 1966.

United States merchant vessels are constructed in accordance with requirements by the U.S. Coast Guard and the American Bureau of Shipping. There are a number of government agencies and societies which issue specifications for construction of various structures including pressure vessels, bridges, building, etc.

In the case of the navy specifications, for example, qualification requirements include:

1. Welding procedures.
2. Welders and welding operators.
3. Welding equipment.
4. Non-destructive test equipment and personnel.
5. Non-destructive test procedures.

Acceptance standards. Acceptance standards have been established for the following inspection methods:

- (a) Visual.
- (b) Magnetic particle.
- (c) Liquid penetrant.
- (d) Radiographic.
- (e) Ultrasonic.

Details of the specifications are not presented here, since they are described in the above Navy specifications.

When one examines details of these specifications to see how they can be used for evaluating reliability of welded structures, he finds that these specifications are rather naive. For example, a typical statement by many requirements on cracking is as follows: "All welds shall be free of cracks." No mention is normally made of the minimum crack length which may be accepted.

In the light of modern scientific criteria, some of the ideas behind these standards are naive and primitive in the extreme. Dr. R. Weck,⁽¹⁵³³⁾ former Director General of the Welding Institute, wrote a paper entitled "A Rational Approach to Standards for Welding Construction". This paper criticizes in length how irrational current standards are.

The current acceptance standards do not incorporate, at least in an explicit manner, the scientific information on how weld defects affect the service behavior of welded

structures discussed in Sections 15.3.4 and 15.3.5. Some of the difficulties in incorporating this scientific information into the standards are:

1. Such defects as porosity and slag inclusions are easy to find by radiography and other methods, but these defects have only a minor effect on the behavior of welded structures.
2. Defects such as arc strikes and short cracks are difficult to locate, but these defects can seriously reduce the strength.

Consequently, current quality assurance relies on multiple procedures including control of material selection, structural design, welding procedures, etc., in addition to non-destructive testing.

A basic problem is mismatch among certain technologies involved and demands. Our ability to find defects has improved significantly during the last 30 years. The demand of our society on the reliability of welded structures has been increasingly stringent over the years. However, our ability to judge how a given defect affects the service performance has not yet been perfected. Above all, welding techniques are not 100% reliable, especially when welding is done manually. According to Wormeli,⁽¹⁵³⁴⁾ the average reject rate in linear inches of weld for the entire Alaska pipeline project from the North Slope to Valdez was less than 1%. One must recognize, however, that 1% repair of an 800-mile (1300 km)-long pipeline means weld repairs totalling 8 miles (13 km) long scattered along various portions of the pipeline. The total construction cost far exceeded the original estimate. In some cases, say some components of a nuclear reactor, we may be pushing the demand to a point which is almost impossible to meet.

Although there are no exact data, we could probably say that over 50% of all repair welds done in the world today are unnecessary and some repair welds even have damaged the structure to some extent. We must find some way to stop the trend of increased inspection and repair. It is the author's opinion that there are basically two ways to solve the problem:

1. To develop a rationale for accepting some defects which are not harmful.
2. To improve reliability of welding operations to reduce weld defects.

15.7.2 *Development of a rationale for accepting defects, a systems analysis*

As stated earlier, an analysis of decision-making for repairing or not repairing defects in welded structures involves technical as well as non-technical aspects. Only few analytical studies have been made on this subjects. Discussions in the following pages come from a study by Yurioka^(620,1535) at M.I.T.

Yurioka tried to develop an analytical system useful for design and fabrication of welded structures. Although construction of an actual structure involves complex procedures, Fig. 15.30 illustrates a simplified procedure. First, the initial design group determines an initial design which satisfies requirements by the customer. Then the structural design group prepares a detailed structural design which includes material selection. During this period, some iteration processes may take place between the initial design group and the structural design group and even the fabrication group to modify the initial design, and finally the design is completed.

Then, the production starts. The production stage includes a number of operations

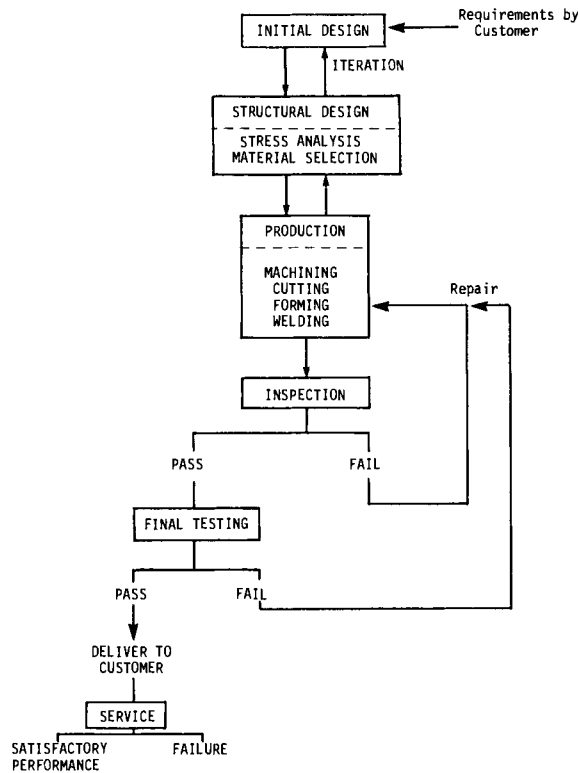


FIG. 15.30. Procedure for design and fabrication of welded structures.

including machining, cutting, forming, welding, etc. After welding is completed, the welds will be inspected, perhaps by the quality assurance group which is independent of the production group. A representative of the customer may be involved in the inspection. Welds which do not pass the inspection will be sent back to the production group for repair.

After the fabrication is completed, the structure will be subjected to the final testing, such as a pressure testing of a vessel. When the structure passes the final testing, it will be delivered to the customer.

During the M.I.T. study an attempt was made to develop a system which could assist a fabricator in making various decisions. Although the system developed so far does not deal with the decision-making for repair welding, it is presented in this paper as an example of a system analysis on welding fabrication.

The system that has been developed covers the following subjects:

1. *Material selection.* A designer must select a material most suitable for the particular application. It may be wiser to select a material with a slightly lower strength, but higher fracture toughness and better fabricability.

2. *Allowable flaw size and repair.* The inspection standard for acceptable flaws must be severe enough to obtain adequate reliability of the structure. However, if the standard is too severe, it will cause unnecessary repair jobs, which will result in delay in fabrication

and higher costs. One must not forget that the repair weld may not be defect-free and the repair may cause further degradation of the material.

3. *Stress relieving.* One must decide whether or not the structure be stress-relieved, how should it be done? As the stress-relieving temperature increases, more complete reduction of residual stresses can be achieved. However, a treatment at a certain temperature for a certain period may result in material degradation. The following pages present some results on the second subject: allowable flaw size and repair.

Analyses were made of fatigue crack growth of surface and embedded transverse cracks in a butt weld in a pressure hull of a deep submersible.[†] Figure 15.31 shows a surface crack in the weld metal. The major applied stress is the hoop stress σ_H . Analyses were conducted on weldments in several high-strength steels including HY-80, HY-100, HY-130, HP-9-4, and maraging steel.

To analyze the rate of crack growth a formula originally proposed by Kraft⁽¹⁵³⁶⁾ was used:

$$\frac{da}{dN} = A \left(\frac{K_{\max} - K_{\min}}{K_{\max}} \right)^4 K_{\max}^4 \tag{15.21}$$

When stress distribution normal to a crack is not uniform, a stress intensity factor at the right hand of a crack in an infinite plate is obtained in the form of the following equation:⁽¹⁵³⁷⁾

$$K_I = \frac{1}{\sqrt{\pi\alpha}} \int_{-\alpha}^{\alpha} \sigma(x) \left(\frac{\alpha + x}{\alpha - x} \right)^{1/2} dx. \tag{15.22}$$

For a weldment, $\sigma(x)$ should be the sum of the non-uniform weld residual stress, $\sigma_R(x)$, and the applied cyclic stress, σ_H , as shown in Fig. 15.31.

The distribution of longitudinal residual stress was assumed to be (see Fig. 12.4):

$$\sigma_R = \sigma_{R_0} \{ 1 - (x/f)^2 \} \exp(-1/2(x/f)^2) \tag{15.23}$$

where σ_{R_0} = the maximum longitudinal residual stress at the weld center,
 f = half width of the tension zone of residual stress.

Figure 6.26 was used to estimate the value of σ_{R_0} for welds in different materials.

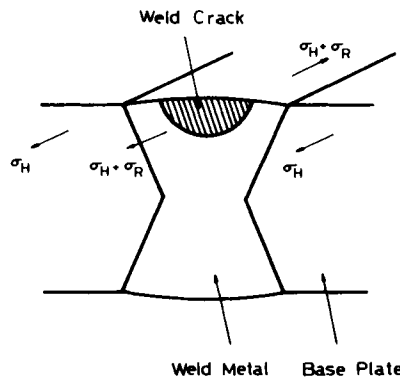


FIG. 15.31. A transverse crack in a butt weld subjected to residual stresses, $\sigma_R(x)$, and repeated hoop stress, σ_H .

[†] Refer to Fig. 1.4.

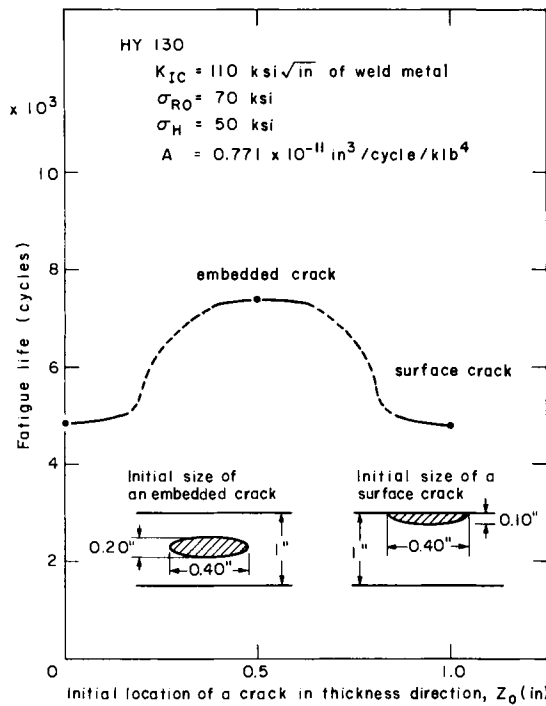


FIG. 15.32. Effects of size and location of an initial crack on the fatigue life (the number of cycles when the initial crack becomes a through-the-thickness crack) in butt welds in HY-130 steel.

Note: A is the coefficient of crack growth rate:

$$\frac{da}{dN} = A(\Delta K)^4.$$

Since the analyses were directed toward the safety of a pressure hull of a deep submersible, the structures were to fail when the cracks grew to become through-the-thickness cracks. Figure 15.32 shows effects of the size and location of an initial crack on the fatigue life (the number of cycles when the initial crack becomes a through-the-thickness) in butt welds in HY-130 steel. It was assumed that pulsating stresses of 0 to 50 ksi (35.2 kg/mm² or 345 MN/m²) are applied. The figure shows that a surface crack decreases the fatigue life more than an embedded crack.

In evaluating the extent of damage to a structure by a defect, Yurioka used the concept of utility. The utility can be defined as the value in use of a set of goods in terms of their quantity or of their attributes.⁽¹⁵³⁸⁾ It is more logical to make use of a utility function to compare the alternatives with respect to their quantity or attributes. Their general utility function may be of the form:

$$u(x) = u_0(1 - e^{-x/\gamma}). \tag{15.24}$$

The constant, γ , is related to how much diminishing marginal utility should be assessed by the analyst. If an infinitely large number is assessed to γ , the utility function becomes linear so that there is no diminishing marginal utility as shown in Fig. 15.33.

Since the designed stresses for pressure vessels are relatively high and the fatigue of

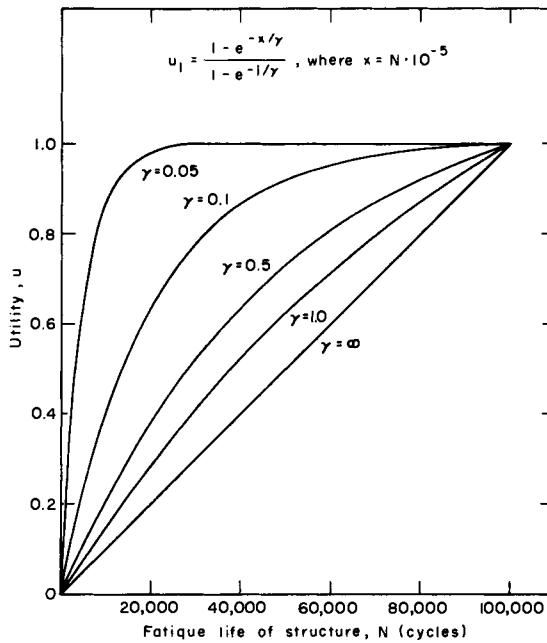


FIG. 15.33. Utility of a structure with respect to fatigue life.

pressure vessels is thus considered to be low-cycle–high-stress type, the maximum utility for pressure vessels may be given when a number of cycles of loading become 10^5 . Defining the maximum utility within the sequence range as a unit for convenience, the utility function for pressure vessels can be expressed by:

$$u(x) = u_0(1 - e^{-x/\gamma}) \tag{15.25}$$

where $u_0 = 1/(1 - e^{-1/\gamma})$,
 $x = N \times 10^{-5}$, N is fatigue life.

As the predicted fatigue life is probabilistically deviated following the log-normal distribution function, the expected utility for pressure vessels should be given as:

$$E[u(N)] = \int_0^\infty u(x') \cdot p(x) dN \tag{15.26}$$

where $x = N \times 10^{-5}$, and $x' = \log N$.

By introducing the concept of utility as a function of the fatigue life it becomes possible to express quantitatively the damage caused by an initial crack of a certain size. Figure 15.34 shows analytical results for butt welds in HY-130 steel subjected to the hoop stress of 50 ksi (35.2 kg/mm² or 345 MN/m²). The value of γ was estimated to be 0.05. In this study, (a, b) represents an initial elliptical crack with the half length of a inch along the minor axis and b inch along the major axis. Shown in the figure are curves of certain values of utility for different values of a and b . Curves are shown under two conditions: as welded and after repair weld. In the case of after repair, it was assumed that the K_{IC} value of the material would be decreased by 10 ksi $\sqrt{\text{in}}$ (35.4 kg $\sqrt{\text{mm}}$ /mm²). The possible effect of an increase of residual stresses due to repair welding was not included in the analysis.

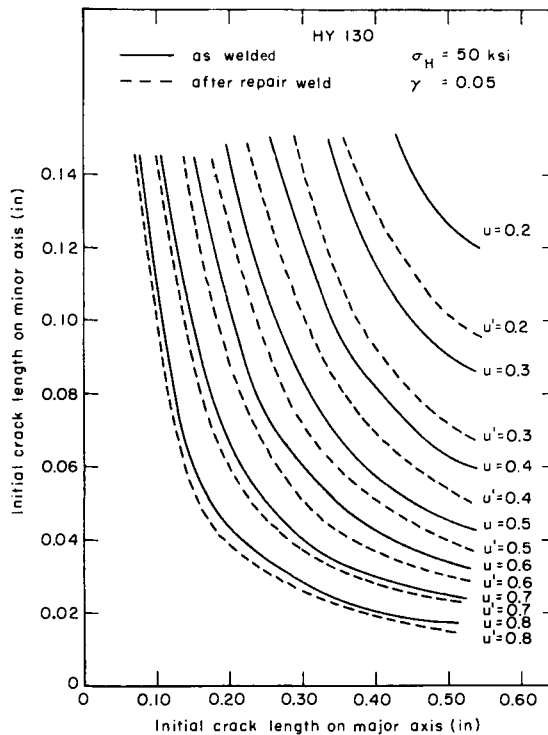


FIG. 15.34. Utility of pressure vessel with various initial crack size after welding or repair welding.

On the basis of the current welding technology it is likely that an initial crack of a size (0.10, 0.10) or (0.02, 0.35) would inevitably occur in the weld. Then it is extremely difficult to achieve the utility over 0.83, which is equivalent to mean fatigue life of 8700 cycles.

15.7.3 Improvement of reliability of welding operations

Although the development of a rationale for accepting defects which are not harmful can provide a partial solution to the problem, it is more important to improve the reliability of welding operations in order to reduce or prevent weld defects from happening. One of the very basic problems in welding today is that most welding operations are done manually and there is always room for human error. Although a number of automatic welding machines have been developed, most automatic welding machines available today do not have sensing and control devices during welding. It is hoped that with the use of modern electronics and computer technologies we could develop "smart" welding machines which have sensing and control capabilities in real time.⁽¹⁵³⁹⁾

References

- (1501) MASUBUCHI, K., unpublished manuscript.
- (1502) SADOWSKY, M. A. and STERNBERG, E., "Stress concentration around a triaxial ellipsoidal cavity", *Journal of Applied Mechanics*, **16** (2), 148-157 (June 1949).

- (1503) STERNBERG, E., "Three-dimensional stress concentration in the theory of elasticity", *Applied Mechanics Review*, **11** (1), 1–4 (1958).
- (1504) NEUBER, H., "Theory of Notch Stresses: Principles for Exact Calculation of Strength with Reference to Structural Form and Material," translated from a publication of Springer-Verlag, Berlin, Göttingen, Heidelberg, United States Atomic Energy Commission, Office of Technical Information, 1958.
- (1505) ESHELBY, J. D., "The elastic field outside an ellipsoidal inclusion", *Proceedings of the Royal Society, London, A* **252**, 561–569 (1959).
- (1506) PETERSON, R. E., "Analytical approach to the study of the effect of small cavities on fatigue strength", *Nondestructive Testing*, pp. 193, 194, 202 (1960).
- (1507) SAVIN, G. N., *Stress Concentration Around Holes*, Pergamon Press, New York, 1961.
- (1508) EDWARDS, R. H., "Stress concentrations around spheroidal inclusions and cavities", *Journal of Applied Mechanics*, **18** (1), 19–30 (Mar. 1951).
- (1509) MIYAMOTO, H., "Stress concentration around a spherical cavity in an infinite elastic body", *Transactions of the Japan Society of Mechanical Engineers*, **19** (87), 60– (1953).
- (1510) ESHELBY, J. D., "Elastic inclusions and inhomogeneities", *Progress in Solid Mechanics*, **2** North-Holland Publishing Company, Amsterdam, pp. 89–140 (1961).
- (1511) ISHIDA, M., "On some plane problems of an infinite plate containing an infinite row of circular holes", *Bulletin Japan Society of Mechanical Engineers*, **3** (10), 259–265 (May 1960).
- (1512) CHEN, L., "On the problem of stress concentrations in the presence of many holes", *Problems of Continuum Mechanics, Contributions in Honor of the Seventieth Birthday of Academician N. I. Mushkelishvili*, published by the Society of Industrial and Applied Mathematics, Philadelphia, Pennsylvania, 1961, pp. 69–73.
- (1513) SAITO, H., "Stress in a plate containing infinite parallel rows of holes", *Zeitschrift für angewandte Mathematik und Mechanik*, **37** (3/4), 111–115 (1957).
- (1514) JONES, N., and HOZOS, D., "A study of the stresses around elliptical holes in flat plates", Paper No. 70-DE-M, *Transactions of the ASME, Journal of Engineering for Industry* (1970).
- (1515) MORI, K., "On the tension of an infinite plate containing two circular holes connected by a slit", *Transactions of the Japan Society of Mechanical Engineers*, **30** (209), 96–103 (1964).
- (1516) KIHARA, H., TADA, Y., WATANABE, M., and ISHII, Y., *Nondestructive Testing of Welds and Their Strength*, 60th Anniversary Series, 7, The Society of Naval Architects of Japan, Tokyo, (1960).
- (1517) PENSE, A. W. and STOUT, R. D., *Influence of Weld Defects on the Mechanical Properties of Aluminum Alloy Weldments*, WRC Bulletin 152, Welding Research Council (July, 1970).
- (1518) KEDROV, A. L., "Influence of some technological defects in the production of welded joints on their strength", *Investigations of Welded Bridge Structures, Transactions of the All-Union Scientific-Research Institute of Transportation*, no. 24, 195–286 (1957).
- (1519) RUPERT, E. J. and RUDY, J. F., *Analytical and Statistical Study of the Effects of Porosity Level on Weld Joint Performance*, Technical Summary Report under Contract NAS 8–11335 from Martin Marietta Corporation, Martin Company to Marshall Space Flight Center, NASA (Mar. 1966).
- (1520) HASEMEYER, E. A., *Aluminum Welding for Space Vehicles and Welding in Outer Space*, a report prepared by Welding Development Branch Manufacturing Engineering Laboratory, G. C. Marshall Space Flight Center, NASA (Aug. 1970).
- (1521) SHORE, R. J., "Effects of porosity on high-strength aluminum 7039 welds", M.S. Thesis, Ohio State University, 1968.
- (1522) LUNDIN, C. D., *The Significance of Weld Discontinuities—A Review of Current Literature*, WRC Bulletin 222, Welding Research Council, New York (Dec. 1976).
- (1523) LINDH, D. V. and PESHAK, G. M., "The influence of weld defects on performance", *Welding Journal*, **48** (2), Research Supplement, 45s–46s (1969).
- (1524) HERSH, M. S., "Effect of discontinuities on fatigue properties of aluminum welds", *Welding Journal*, **48** (9), Research Supplement, 389s–394s (1969).
- (1525) DINSDALE, W. O. and YOUNG, J. G., "Significance of defects in aluminum alloy fusion welds", *British Welding Journal*, **9**, 482–493 (1962) and **11**, 229–243 (1964).
- (1526) MINDLIN, A., "Fatigue of Al–Mg alloys", *Welding Journal*, **42** (6), Research Supplement, 276s–281s (1963).
- (1527) NORDMARK, G. E., *Effects of Weld Terminations on the Fatigue Strength of Welds in 5456-H321 Plate*, ALCOA Research Laboratories, Report No. 12–63–48 (1963).
- (1528) HARRISON, J. D., "The analysis of fatigue test results for butt welds with lack of penetration defects using a fracture mechanics approach", *Welding in the World*, **8** (3), 168–181 (1970).
- (1529) PARIS, P. C. and ERDOGAN, F., "A critical analysis of crack propagation laws", ASME Winter Annual Meeting, Paper 62-WA-230 (Nov. 1962).
- (1530) GROSS, M. R., "Low-cycle fatigue of materials for submarine construction", *Naval Engineers Journal*, pp. 783–795 (Oct. 1963).
- (1531) MCMASTER, R. C. (editor) *Nondestructive Testing Handbook*, vols. I and II, Ronald Press, New York, 1959.

- (1532) SHANAHAN, W. F., and JENNY, D. E., "Quality assurance in naval shipyards", *Marine Technology*, **8** (1), 97-108 (Jan. 1971).
- (1533) WECK, R., "A rational approach to standards for welded construction", *British Welding Journal*, pp. 658-668 (Nov. 1966).
- (1534) WORMELI, J. C. "Alyeska—a welding milestone", *Welding Journal*, **56** (9), 31-38 (1977).
- (1535) MASUBUCHI, K. and YURIOKA, N., "A systems analysis of significance of weld defects", *Significance of Defects in Welded Structures*, Proceedings of the Japan-U.S. Seminar, 1973, Tokyo, University of Tokyo Press, 1974.
- (1536) KRAFT, J. M., "On prediction of fatigue crack propagation rate from fracture toughness and plastic flow properties", *Transactions of the American Society of Metals*, **58**, 691 (1965).
- (1537) PARIS, P. C., *Application of Mushelishvili's Method to the Analysis of Crack Tip Stress Intensity Factors for Plane Problems*, Fracture Mechanics Research for the Boeing Airplane Company, Institute of Research, Lehigh University, Bethlehem, Pennsylvania.
- (1538) DE NEUFVILLE, R. and STAFFORD, J. H., *System Analysis for Engineers and Managers*, McGraw-Hill, New York, 1971.
- (1539) A proposal entitled "Improvement of Reliability of Welding by In-Process Sensing and Control (Development of Smart Welding Machines for Girth Welding of Pipes)", M.I.T., Dec. 1978.

Further Discussion on Some Selected Subjects

IN the preceding chapters, the emphasis of discussion is placed on scientific information on subjects covered by presenting experimental data and analytical results. Many figures, tables, and formulas are included to present quantitative rather than qualitative discussions. Although they contain useful information, the author feels that an additional chapter is needed to assist practicing engineers to fully utilize the information presented in the previous chapters.

For example, if one is interested in using peening for reducing distortion, one should also consider possible adverse effects of peening on brittle fracture. The use of intermittent welding is an efficient way of reducing distortion, especially longitudinal distortion; however, it may result in a reduction in fatigue strength. Although information pertinent to these subjects is given in various parts of this textbook, this chapter attempts to draw these important considerations together for the convenience of the reader.

Thus, the major objective of this chapter is to discuss various subjects of design and fabrication considerations which practicing engineers are likely to face. However, this chapter is by no means intended to cover all important subjects related to design and fabrication; rather, it is limited to some selected subjects related to residual stresses, distortion and their consequences, which have been examined in previous chapters.

As shown in Fig. 1.1, problems which practicing engineers face are related not only to residual stresses and distortion but also to various other subjects including welding metallurgy, non-destructive testing, etc. These problems are dealt with in this chapter.

The format of this chapter is different from the previous ones. Discussions are kept as concise as possible with few experimental data and analytical formulas. Figures and tables given in previous chapters are cited as needed.

In preparing the chapter, efforts are made to avoid duplications with existing documents. For example, “dos” and “donts” of design and fabrication of welded structures are described in a number of documents, including:

1. specifications issued by a number of government agencies and classification societies, including the Army, Navy, Air Force, Coast Guard, AWS, ASME, etc.,^(246, 1601 – 1605)
2. handbooks such as the *Welding Handbook*,^(119, 967, 1121, 1606)
3. manuals such as the *Hull Welding Manual*.⁽¹⁶⁰⁷⁾

While these specifications, handbooks, and manuals describe what should be done in design and fabrication of various welded structures, they generally do not describe why a certain action must be taken.

This chapter discusses:

1. the reasons why certain procedures are taken, and what might happen if the procedures are not followed properly;
2. the consequences and implications, or pros and cons, of various procedures such as peening, preheating, etc.

Most discussions are directed toward steel structures, though the last part covers residual stresses and distortion in weldments in various materials.

The author does not intend to discuss many problems in this chapter. But rather he discusses how this book can be used in solving some practical problems in design and fabrication of welded structures. It is hoped that discussions given in this chapter will provide readers with some ideas of how the book can be used for solving other practical problems.

16.1 Welding Design

Regarding welding design, the following subjects are discussed:

1. Basic principles for preventing brittle fractures.
2. Basic principles for preventing fatigue fractures.
3. Effects of structural discontinuities.
4. Butt joints vs. lap joints.
5. Intermittent vs. continuous fillet welds.
6. Scallops and small radius cuts.
7. Plug welds or slot welds.
8. Control of distortion in the design stage.

16.1.1 Basic principles for preventing brittle fractures

There are basically three ways of preventing brittle fractures of welded structures:

1. *Materials.* Use materials with sufficient fracture toughness.
2. *Design.* Reduce stresses, especially stress concentrations due to structural discontinuities.
3. *Fabrication.* Eliminate sharp notches by careful fabrication.

Among the above three items, the use of ductile material is the most important. Stated differently, preventing brittle fractures by relying on good design and fabrication while using materials which do not have sufficient fracture toughness is impractical, if not impossible. This is discussed in Sections 9.5 and 10.4.

Figure 9.37 shows that extensive brittle fractures can occur at very low stresses when the material is brittle, or when the temperature is below the ductile-to-brittle transition temperature. The critical stress for fracture propagation for low-carbon steel is 5 to 7 kg/mm² (7 ~ 10 ksi or 49 ~ 67 MN/m²), which is only 20 to 30% of the yield stress. Even when the level of applied stress is below the critical stress, partial fractures can occur.

If one tries to prevent brittle fracture of a structure by reducing stresses, the design stress must be below the critical stress for fracture propagation. Considering the fact

that most practical structures such as ships, pressure vessels, and bridges have some structural discontinuities caused by hatches and other openings, attachments to other members, etc., it is impractical to reduce stresses near structural discontinuities below the critical stress. Even when the design stresses are reduced to very low values, partial fractures would still occur, especially in regions near the weld where high tensile residual stresses exist.

The other extreme approach is to use materials with extremely high fracture toughness with a hope that design and fabrication considerations could be neglected. However, the use of materials with excessive fracture toughness is uneconomical. Even though brittle fractures could be avoided, the structure would still be plagued by fatigue fractures which are extremely sensitive to notches.

The most practical approach is to take a combined, or a middle-of-the-road, approach, using materials with sufficient fracture toughness, combined with careful design and fabrication. The question here is what constitutes sufficient toughness and careful design and fabrication. This, of course, depends upon the types of structure, their costs, liabilities caused by failures, etc. Design criteria could be different for different structures such as bridges, pipelines, oil tankers, submarines, airplanes, and nuclear reactors for the following reasons:

1. *Material cost vs. total cost.* For some structures, such as submarines and space vehicles, the cost for structural materials is small compared to the total cost of the structure. In such cases, use of materials with superior toughness can be justified so long as it helps to achieve better performance or increased reliability. On the other hand, for some other structures, such as pipelines, the material cost is important in building a structure which is economically feasible.
2. *Fracture toughness vs. other material properties.* Fracture toughness is only one of the various material properties which must be satisfied for a material to be useful for the structure being considered. For example, materials to be used for supersonic airplanes must have a high strength-to-weight ratio. Consequently, a designer is forced to use ultra-high strength materials by sacrificing some fracture toughness.
3. *Liability of fractures.* Liability caused by fractures varies widely depending upon the structure. For example, liability caused by fracture of a nuclear reactor is extremely high. Even within the same structure, the seriousness of a fracture varies among the structural members being considered. For example, a fracture of a bottom plate of a ship is more serious than a fracture of one of the frames.
4. *Engineering cost.* The engineering cost that can be afforded for the analysis of fracture potential also varies widely depending upon the structure being considered. For example, a large amount of engineering cost can be justified for selecting materials for a pressure vessel of a nuclear reactor. However, a far less amount can be justified for selecting hull materials for an ordinary cargo ship.

Consequently, there is a wide range of margin of fracture toughness, as well as the engineering cost which can be spent for fracture analysis. Some examples are as follows:

- (a) For some aerospace applications, materials with high strength-to-weight ratio are widely used even though their fracture toughness may be somewhat low. To ensure the fracture safety of the structure, extensive analyses using fracture mechanics theories are made. Figures 10.8 and 10.9 show the specimens for determining fracture toughness values (K_c and K_{Ic}) of materials.

- (b) For a hull of a submarine, which must withstand severe impact loading, materials with extremely high fracture toughness, such as HY-80 steel, must be used even though they may be considerably expensive. The NRL drop-weight test and the dynamic tear test are commonly used for selecting the material. Since the material is very ductile under normal operating conditions, the linear fracture-mechanics theory is not applicable (see Fig. 10.12).
- (c) For ordinary cargo ships and bridges, materials with relatively small fracture toughness margin are used. Simple tests, such as the Charpy V-notch test, are commonly used for selecting materials. Extensive fracture analyses are seldom used for routine design.

16.1.2 *Basic principles for preventing fatigue fractures*

Although brittle fractures can be catastrophic, they seldom occur provided materials with reasonable fracture toughness are used. On the other hand, it is very difficult to prevent the occurrence of any fatigue fractures in complex structures, such as ships, bridges, etc. Fatigue fractures originate from various types of stress raisers and it is difficult to eliminate all the stress raisers in a complex structure. However, it is possible by proper design and inspection (1) to minimize the possibility of producing fatigue cracks and (2) to detect and repair them while they are still short.

As discussed in Chapter 11 (Section 11.2.2), the most deleterious factor affecting the fatigue strength is the localized concentration of stress by geometric discontinuities including cracks, notches, etc., especially those on or near the surface. Consequently, the best principle for preventing fatigue fractures in a complex structure is to eliminate as much as possible these "hard spots".

16.1.3 *Effects of structural discontinuities*

Structural discontinuity, as used here, means an abrupt change in the general contour of the structure rather than a sharp notch or crack. It is recognized that in the way of stress raisers the local stresses are increased well above the average stress level. For example, the stress intensity at the edge of a circular opening may be about three times the average stress (see Fig. 15.6).[†] Obviously, it is at these places of high stress concentration that sharp notches and defects are particularly dangerous; i.e. there is the chance of creating a notch within a stress raiser, thus superimposing notch effects.

According to a statistical investigation of structural failures of American ships built during World War II, about 50% of the failures originated from structural discontinuities, including square hatch corners, cutouts in shear strakes, ends of bilge keels, etc., as described in Section 9.2.3. Even experimental studies were made to prove that a fracture can happen from a notch located near a structural discontinuity (see Figs. 10.19 and 10.20).

Hence, it is important in designing to eliminate, where practicable, details such as butt welds, small insert plates, drain holes, and scallops in the vicinity of structural discontinuities. Also, special control over workmanship is recommended in these areas to avoid notch-like defects.

[†] The stress concentration near a circular opening of a two-dimensional plate is similar to that near a long cylindrical cavity of a three-dimensional body discussed in Fig. 15.6.

16.1.4 *Butt joints vs. lap joints*

Butt joints are widely used in welded structures, for the following reasons:

1. The joint efficiency is high. For a number of materials, joints with 100% efficiency can be achieved.
2. It is easy to obtain watertight and airtight joints.
3. The joint design is simple.
4. The joint surface is almost flush.

Butt joints are especially superior to lap and fillet joints in terms of fatigue strength, as discussed in Section 11.5 (see Table 11.2, Figs. 11.18 and 11.19).

Weld reinforcement. The term “reinforcement” was originated during the early days of welding development. At that time, the welds were not as strong as the base plate, and people did not trust welds. They thought that it might be a good idea to make the joint somewhat thicker than the base plate, and the excessive material was called “reinforcement”.

However, it has been well established that the weld reinforcement is harmful to fatigue strength (see Table 11.2 and Fig. 15.22). The fatigue strength can be increased by removing the reinforcement. However, one must be careful of the following:

1. Be careful not to produce notches during machining or grinding operations for removing the reinforcement.
2. Be careful not to reveal porosity and other internal defects by removing the reinforcement.

The important thing to remember is that the fatigue strength of a welded joint is very sensitive to any notches on the surface.

Double plate for providing additional strength. Often, it becomes necessary to increase the strength of a structure. For example, the strength of an old girder bridge needs to be increased, since it has to carry larger loads. A simple solution is to increase the moment of inertia by placing a double plate fillet welded on the flange of the old girder, as shown in Fig. 11.18(H). On the basis of the strength of materials, or more precisely the bending moment diagram, the most efficient way to increase the strength of the girder is to place a double plate outside the flange plate.

However, one must be careful not to reduce the fatigue strength of the girder by introducing a new structural discontinuity and possible notches. Example “H” of Table 11.2 and Fig. 11.18 shows how the presence of a double plate reduces the fatigue strength.

16.1.5 *Intermittent vs. continuous fillet welds*

Intermittent welds are often used for fillet joints. Pros and cons of intermittent fillet welds are as follows:

Longitudinal distortion. It has been found that intermittent welds are very effective in reducing longitudinal distortion. Figure 7.61 shows that practically no distortion was produced during the intermittent welding of a fillet joint. This can be explained by the difference in the distribution of longitudinal residual stresses which cause longitudinal bending distortion.

Figures 16.1 (a) and (b) show schematically the distribution of longitudinal residual stress, σ_x , in a continuous fillet weld and an intermittent fillet weld, respectively. These figures are constructed, based upon the experimental data shown in Figs. 6.40 and 6.41. There are two basic facts:

1. The longitudinal stress must be zero at both ends of each weld.
2. As shown in Fig. 6.41, a relatively long weld length is necessary to have high longitudinal residual stresses. When the weld length is about 3 inches or so, the amount of σ_x is very low.[†]

Angular distortion. The reduction in angular distortion, as shown in Fig. 7.1(b), due to the use of intermittent welding is not so drastic. Hirai and Nakamura⁽⁷²⁴⁾ conducted an experimental study and found that the difference in the angular distortion between a continuous and an intermittent weld is negligible when compared on the basis of the apparent weight of electrode consumed per weld length, w_a , as follows (see Fig. 16.1).

$$w_a = w \frac{l}{l + p} \tag{16.1}$$

where w = weight of electrode consumed per weld length, g/cm,
 l = length of each weld,
 p = pitch or the interval between intermittent welds.

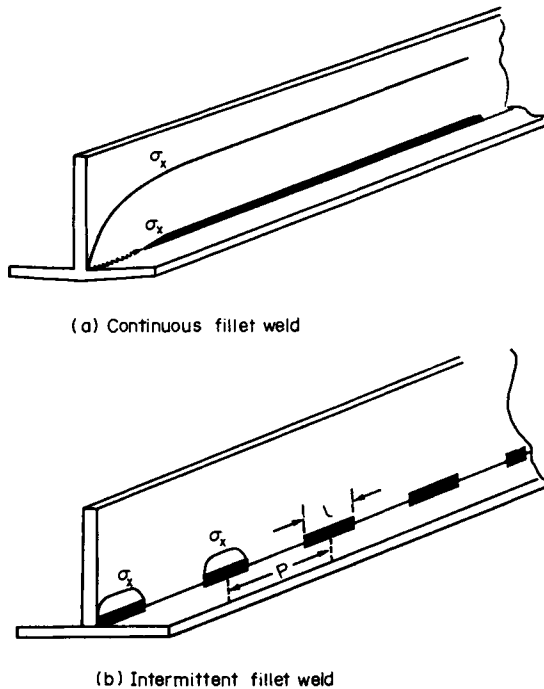


FIG. 16.1. Schematic diagrams showing distributions of longitudinal residual stress, σ_x , along the weld line of fillet welds.

[†] This can be explained by the fact that the longitudinal stress, σ_x is caused by the differential of plastic strains on the y and the z directions, $\partial \epsilon_x / \partial y$ and $\partial \epsilon_x / \partial z$ (see Fig. 6.10).

Equation (7.23) shows the relationship between w and fillet size D_f (see Fig. 7.4(b)). According to Hirai and Nakamura, Fig. 7.47 still can be used for estimating the angular change produced in an intermittent fillet-welded joint, provided that w_a , instead of w , is used. For example, when $l = 2$ inches and $p = 4$ inches:

$$w_a = w \frac{2}{6} = \frac{1}{3} w.$$

The value of w_a is considerably smaller than w . However, curves in Fig. 7.47 are shown for different values of $\log w$. Consequently, the reduction of angular change is about 50. The reduction in angular change is substantial; but it is not as drastic as in the case of longitudinal distortion.

Fatigue strength. It has been well established that the fatigue strength of an intermittent weld is significantly lower than that of a continuous weld. Fatigue fractures often occur from the end of an intermittent weld which acts as a stress raiser.

16.1.6 *Scallops and small radius cuts*

The *Hull Welding Manual* states that there have been occasions when serious cracks were found to have started at irregular edges of rounded cutouts or at jagged scallops. Had these cuts been smooth enough instead of jagged, the crack might not have developed. Several tankers suffered major bottom shell fractures which initiated at scallop areas.

The present trend is away from the widespread use of scallops, because improperly cut scallop is potentially dangerous. In some areas where scallops must be used, care must be taken to reduce the stress concentrations produced by the scallop, especially in the major strength members such as the shell and deck plates.

16.1.7 *Plug welds or slot welds*

Plug welds and slot welds should not be used except where absolutely necessary.⁽¹⁶⁰⁷⁾ To substantiate this comment, Table 11.2 shows that fatigue strengths of plug welds and slot welds are poor (K, L, M, N of Table 11.2).

16.1.8 *Control of distortion in the design stage*

Many distortion problems are created in the design stage. Or, stated differently, distortion problems are often caused by design engineers, and welding engineers are forced to solve them. Of course, many designers try to avoid distortion problems in the design stage, and they consult with welding engineers. Unfortunately, however, answers which welding engineers provide tend to be empirical and qualitative, while designers need analytical and quantitative answers which can be used for parametric studies in structural design. An important objective of this textbook is an analytical system on residual stresses, distortion, and their effects on the service behavior of welded structures. The information presented in various parts of this textbook should be useful for closing the gaps between designers and welding engineers. Discussed here are two examples of

the control of weld distortion by a proper selection of structural design parameters, such as plate thickness, the amount of weld, etc.

1. Control of out-of-plane distortion of a welded panel structure.
2. Control of buckling distortion.

Control of out-of-plane distortion. Chapter 7.7 discusses angular changes of fillet welds and the resulting out-of-plane distortion of welded panel structures (see Fig. 7.40). Analyses have been made to determine the amount of out-of-plane distortion as a function of the plate thickness, the spacing between stiffeners, and the weld size. Further analyses have been made to study the effects of out-of-plane distortion on the buckling strength of the panel structure. The results are compared with the Navy specifications on allowable distortion, as shown in Fig. 7.47 for steel and Figs. 7.48 and 7.49 for aluminum.

Similar analysis can be made to solve a number of distortion problems.

Control of buckling distortion. Buckling distortion is discussed in chapter 7. Buckling distortion occurs most commonly during welding fabrication of thin-plate structures. It occurs when

1. the plate is thin,
2. the unsupported span is long, and
3. the amount of weld is large.

A unique nature of buckling distortion is that the amount of distortion is much greater than that in other types of distortion, such as bending distortion. Consequently, the most effective way of controlling buckling distortion is to prevent it from occurring by a proper selection of structural and welding parameters.

Figures 7.66 through 7.73 show buckling distortion occurred during welding fabrica-

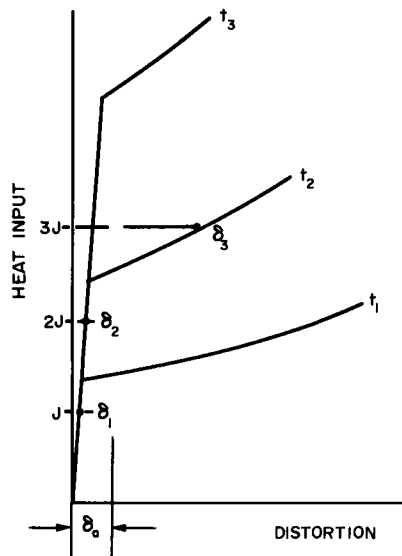


FIG. 16.2. Schematic diagram showing effects of heat input and plate thickness on out-of-plane distortion due to buckling.

tion of panel structures. Welds were made along longitudinal edges of a square panel. On the basis of information given in these figures, Fig. 16.2 is prepared to schematically explain the effects of welding heat input and plate thickness on out-of-plane distortion of a panel structure. Shown here are cases for three thicknesses $t_1 < t_2$, and $t_2 < t_3$. Let us assume that the plate thickness of the current design is t_2 and the heat input used is H (joules/in.). When welding is done in one pass, distortion would be δ_1 ; the amount of distortion is much less than the allowable distortion, δ_a . When welding is done in two passes, distortion would increase to δ_2 , but it is still less than δ_a . However, when welding is done in three passes, distortion would increase considerably to δ_3 , which is more than is acceptable.

When plate thickness is decreased to t_1 , buckling occurs in two passes. This means no repair weld is likely to be allowed.

The distortion problem would virtually disappear when the plate thickness is increased to t_3 . However, we must pay the penalty of additional weight.

A key in the analysis and control of buckling distortion is to determine the critical values of plate thickness, t , the length of unsupported span, a , and heat input, J . Chapter 7.12 presents analytical results for determining critical conditions for buckling distortion (Fig. 7.74 and Tables 7.10 through 7.12).

16.2 Welding Fabrication

Regarding welding fabrication, the following subjects are discussed:

1. Welding heat input limitations.
2. Effects of welding parameters on shrinkage and cracking potential.
3. Various methods of reducing distortion.
4. Influence of joint restraint on residual stresses and distortion.
5. Preheat and interpass temperature.
6. Post-weld thermal treatments.
7. Vibratory stress relieving.
8. Peening.
9. Mechanical stress relieving and prooftesting.
10. Residual stresses and distortion in weldments in various materials.

16.2.1 Welding heat input limitations

When welding conditions are changed in order to control residual stresses and distortion, metallurgical structures and mechanical properties of the heat-affected zone also change. In the fabrication of welded structures, especially in high-strength steels, one must always consider the effects of welding conditions on the metallurgical characteristics of a weldment. How to control welding heat input to obtain optimum heat-affected-zone structures for various materials is an important subject in welding metallurgy. Many publications are available on this subject.⁽²³⁹⁻²⁴⁵⁾ Some discussions on the effects of welding heat input on properties of welds are presented in Chapters 2 and 14.

As the cooling rate increases, hardness of the heat-affected zone increases, as shown in Fig. 2.14. Reducing heat input results in higher hardness of HAZ and an increased

tendency for cold cracking. Effects of heat input on cracking tendency are discussed in Chapter 14 (Section 14.3.3). Effects on heat input on notch toughness of HAZ are rather complex. Too rapid cooling causes the formation of brittle material, but too slow cooling also causes a reduction in notch toughness, as shown in Fig. 2.15. Loss of fracture toughness can be a significant problem for welding quenched and tempered high-strength steels of which excellent fracture toughness has been achieved by Q & T treatments. Some specifications specify the maximum heat input for welding Q & T steels (Section 2.4.3).

16.2.2 *Effects of welding parameters on residual stresses, distortion, and cracking potential*

Effects of welding parameters (welding current, arc travel speed, electrode diameter, etc.) on residual stresses, distortion, and reaction stresses during welding recharged joints are discussed in Chapters 5, 6, 7, and 14.

It is now possible to simulate by computer transient thermal stresses and metal movement during welding of simple weldments. This subject is discussed in Chapter 5, especially Section 5.9. It is hoped that the capability of computer simulation can be significantly expanded in the near future.

Chapters 6 and 7 present a number of figures, tables, and formulas describing the effects of welding parameters on residual stresses and distortion, respectively, in various types of welded joints. For example, Table 7.7 and Figs. 7.27–7.30 show the effects of welding procedures on transverse shrinkage of butt welds.

Chapter 14 discusses weld cracking and joint restraint. For example, Fig. 14.40 shows how reaction stresses are produced during the welding of a restrained butt weld. This result may be compared with that shown in Fig. 7.20. The mechanisms of transverse shrinkage on butt welds are discussed in Section 7.4.2.

The information presented in these chapters should be useful for studying the effects of welding parameters and welding procedure on residual stresses, distortion, and cracking potential. As an example, the effects of the diameter of electrodes on transverse shrinkage and reaction stresses are discussed.

Large vs. small diameter electrodes. Should we use large-diameter electrodes or small-diameter electrodes for reducing transverse shrinkage of a butt weld? The use of electrodes in a larger diameter means the use of higher welding current and a larger amount of weld metal per pass. This subject is discussed in Section 7.4.3 (see Table 7.7 and Fig. 7.28). By the use of electrodes of a larger diameter, the amount of transverse shrinkage after welding the first pass increases to some extent since the amount of deposited metal increases. However, this change is expressed by the change from A to A' in Fig. 7.28, which shows the relationship between the amount of weld metal, $\log w$, and shrinkage, U . When a comparison is made of the same amount of weld metal, transverse shrinkage is reduced by use of electrodes with a larger diameter. The use of electrodes with a large diameter will not reduce the transverse shrinkage of a butt weld unless they are used in the first pass, as shown in Fig. 7.28.

It has also been found that the use of electrodes of a larger diameter is beneficial in reducing reaction stresses in the first-pass weld metal. The first-pass weld metal is often under high reaction stresses, especially in welding a highly restrained joint, and cracking

often occurs (see Fig. 14.37). By using electrodes with a large diameter during the first pass, it is possible to reduce reaction stresses in the weld metal. The amount of shrinkage increases slightly by use of larger-diameter electrodes, but the amount of weld metal is increased significantly, resulting in lower reaction stresses.

16.2.3 *Various methods of reducing distortion*

Various methods of reducing distortion are discussed in Chapter 7. Basically, there are two ways for reducing distortion:

1. Provide additional restraint to the weldment concerned.
2. Modify the thermal pattern in the weldment.

Additional restraint. The use of additional restraint is an effective method of reducing distortion. Section 7.8.2 discusses reduction of angular distortion by elastic prestraining.

Modification of thermal pattern. Distortion can be reduced by properly modifying the thermal pattern of the weldment concerned. This subject is discussed in detail in Sections 7.14.3, 7.14.4, and 7.14.5. Methods covered are:

- Forced cooling,
- Preheating,
- Stretching and heating,
- Differential heating.

16.2.4 *Influence of joint restraint on residual stresses and distortion*

It is generally believed that distortion can be reduced by restraining a weld joint, but the restraint causes higher reaction stresses. The question here is what happens when the restraint is released after welding is completed. When a weld is made under restraint and the restraint is released later, it may be possible to fabricate a welded joint with less distortion than a weld made under no restraint, and residual stresses may be no higher than those in a free joint. Limited experiments were conducted at M.I.T. to examine this idea (see Section 7.13.2).

Although results are not yet conclusive, they suggest that a method involving an application of an external restraint during welding which will be released later is a good way for reducing distortion. This method may be applicable in fabricating aluminum structures which do not have high rigidity and with metals which tend to have good resistance against cracking which may occur when the structure is still under restraint.

16.2.5 *Preheat and interpass temperature*

Preheating involves raising the temperature of the base metal or a section of the base metal above the ambient temperature before welding. Interpass temperature is the temperature of the deposited weld metal before the next pass in a multi-pass welding is made.

Present specifications by the Navy, AWS, and others base their recommendations on functions of base-metal chemistry (steel designation, carbon equivalent, etc.), base-metal thickness, and welding processes (or electrode types). Table 16.1 shows minimum preheat

TABLE 16.1 Minimum preheat and interpass temperature specified by the AWS Specifications for Welded highway and Railway Bridges⁽¹⁶⁰⁴⁾

Thickness of thickest part at point of welding (in.)	Welding process				
	Shielded metal arc welding with other than low hydrogen electrodes	Shielded metal-arc welding with low hydrogen electrodes; submerged-arc welding; gas metal-arc welding; or flux cored arc welding	Shielded metal-arc welding with low hydrogen electrodes; submerged-arc welding; gas metal-arc welding; or flux cored arc welding	Shielded metal-arc welding with low hydrogen electrodes; submerged-arc welding with carbon or alloy steel wire, neutral flux; gas metal-arc welding; or flux cored arc welding	Submerged-arc welding with carbon steel wire, alloy flux
	ASTM A36; A53 Grade B; A375; A500; A501; A529; A570 Grades D and E	ASTM A36; A242 Weldable Grade; A375; A441; A529; A570 Grades D & E; A572 Grades 42, 45, and 50; A588	ASTM A572 Grades 55, 60 and 65	ASTM A514	ASTM A514
To $\frac{3}{4}$, incl.	None ^(b)	None ^(b)	70° F	50° F	50° F
Over $\frac{3}{4}$ to $1\frac{1}{2}$, incl.	150° F	70° F	150° F	152° F	200° F
Over $1\frac{1}{2}$ to $2\frac{1}{2}$, incl.	225° F	150° F	225° F	175° F	300° F
Over $2\frac{1}{2}$	300° F	225° F	300° F	225° F	400° F

^(a) Welding shall not be done when the ambient temperature is lower than 0° F. When the base metal is below the temperature listed for the welding process being used and the thickness of material being welded, it shall be preheated (except as otherwise provided) in such manner that the surface of the parts on which weld metal is being deposited are at or above the specified minimum temperature for a distance equal to the thickness of the part being welded, but not less than 3 in., both laterally and in advance of the welding. Preheat and interpass temperatures must be sufficient to prevent crack formation. Temperatures above the minimum shown may be required for highly restrained welds. For A514 steel the maximum preheat and interpass temperature shall not exceed 400° F for thicknesses up to $1\frac{1}{2}$ in., inclusive, and 450° F for greater thicknesses. Heat input when welding A514 steel shall not exceed the steel producer's recommendation.

^(b) When the base metal temperature is below 32° F, preheat the base metal to at least 70° F and maintain this minimum temperature during welding.

and interpass temperature specified by the AWS specifications for welded highway and railway bridges.⁽¹⁶⁰⁴⁾ U.S. Navy specifications (NAVSHIPS 0900-060-4010 and others) go into further details in specifying preheating and interpass temperatures for welding various ferrous and non-ferrous metals. For example, specified preheating and interpass temperatures for welding HY-80/100 are as follows:

Thickness	Preheat and interpass temperature (°F)	
	Minimum	Maximum
$1\frac{1}{8}$ in. and over	200	300
$> \frac{1}{2}$ in. to $< 1\frac{1}{8}$ in.	125	300
$\frac{1}{2}$ in. or less	60	300

However, current specifications do not consider the effects of welding heat input in determining preheating and interpass temperatures. Chapter 14 presents some experimental and analytical efforts along this line. Figure 14.27 shows recommended preheating temperatures for HT-60 and HT-80 steels based upon analytical/experimental research on weld cracking. Although no special effort has been made in preparing this textbook to compare recommended preheating temperatures given in Fig. 14.27 with current specifications by the U.S. Navy, AWS, and other organizations, further detailed analysis may reveal some correlations or contradictions among different specifications.

Minimum preheating and interpass temperatures are specified to avoid cracking by reducing cooling rate (refer to Section 14.3.2). Preheating also is a simple way to remove moisture from the surface of a weldment.

Maximum preheating and interpass temperatures are sometimes specified to avoid the occurrence of undesirable structures, especially in the heat-affected zone, due to excessively slow cooling.

16.2.6 *Post-weld thermal treatments*

Stress-relief heat treatment is defined as the uniform heating of a structure to a suitable temperature, holding at this temperature for a predetermined period of time, followed by uniform cooling. Heat treatments that involve changes in grain structure and dimensional changes may be injurious to a part; consequently, stress-relief heat treatment is usually performed below the critical range.

In its Boiler and Pressure Vessel Code, the American Society of Mechanical Engineers indicates the minimum temperatures and times at which post-weld heat treatment is to be performed for welded power boilers and unfired pressure vessels. These vary depending on the type or grade of steel involved. Maximum post-weld heat treatment temperatures obviously must be welded below the critical temperatures for the steels.

The effects of thermal stress relieving on brittle fracture is discussed in Section 10.4.2

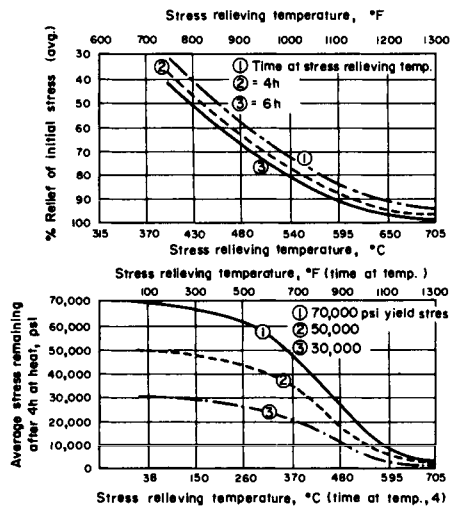


FIG. 16.3. Effect of temperature and time on stress relief.⁽¹⁶⁰⁶⁾

(see Fig. 10.17). Fracture stresses of welded-and-notched wide-plate specimens increased as the heat-treatment temperature increased.

The percentage relief of internal stresses is dependent on steel type, composition, or yield strength. The effects of varying time and temperature are shown in Fig. 16.3.⁽¹⁶⁰⁶⁾ The temperature reached during the stress-relief treatment has a far greater effect in relieving stresses than the length of time the specimen is held at that temperature. The closer the temperature is to the critical or recrystallization temperature, the more effective it is in the removal of residual stresses, provided proper heating and cooling cycles are employed.

During the thermal stress relieving of a large, complex weldment, it is often difficult to keep the temperature distribution of the weldment uniform. Uneven cooling from stress-relief treatment may even cause some residual stresses. With the development of computer-aided analyses of thermal stresses, it is possible to analyze detailed stress changes in a weldment during thermal stress relieving.⁽¹⁶⁰⁸⁾

When a thermal stress-relief treatment is employed to reduce residual stresses, other important properties must be taken into consideration. The microstructure and tensile and impact strength are among the properties affected by the stress-relief treatment. It is necessary, therefore, to select a temperature that will develop the desirable properties in the steel, while at the same time providing the maximum stress relief.

Controlled low-temperature stress relief. This process was originally developed to reduce residual stresses in weldments too large to be stress relieved in a furnace. The metal on either side of a welded joint is heated to a temperature of 350 to 400° F (175 to 205° C), while the weld itself is kept relatively cool. The progression of these heated bands of metal, parallel to the weld and adjacent to each side, results in a traveling zone of thermal expansion in the base metal and a reciprocal tensile stress in the weld. The theory of this procedure is that two zones of compression are expanded thermally, thereby increasing the tensile stress in the weld beyond the yield. When the metal contracts, the stress falls below the yield.

When the process is used correctly, a reduction in the longitudinal stress of butt welds is achieved in some measure.⁽⁴⁴³⁾ Many consider that longitudinal weld stresses are of primary importance since they attain values up to the yield strength in tension. Others question the validity of low-temperature stress relief, claiming that in restrained plates both longitudinal and transverse residual stresses approach the yield point of the material. Yet, reductions in transverse residual stresses ranging up to 60%, as well as a considerable reduction in the longitudinal stresses, are reported. This indicates that low-temperature stress relief is an inexpensive means of obtaining a substantial reduction of shrinkage stress in ductile materials.

In most materials, the low-temperature stress-relief treatment will not improve the metallurgical properties of the weld metal and heat-affected zones, and the treatment should not be regarded as a substitute for post-weld thermal treatment when such treatment is required to provide ductility and notch toughness. The process operates in the temperature range associated with possible strain aging, but available data indicate that the medium-strength ductile materials are not adversely affected.

16.2.7 Vibratory stress relieving

Vibratory stress relieving is a somewhat controversial subject and there is little

published research data on this topic.⁽⁷⁵⁶⁻⁷⁶⁰⁾ Moreover, opinions of this treatment vary greatly. Some believe it to be very effective; others consider it to have little effect. The following statements come from the *Welding Handbook*.⁽¹⁶⁰⁶⁾

Mechanical energy in the form of low-and high-frequency vibrations has been used to relieve residual stresses in weldments. The procedures used vary, but generally consist an oscillating or rotating wave generator which is mechanically coupled to the part to be stress relieved. The part may be vibrated at one of its natural (resonant) frequencies, although this approach may be difficult to use in a part of complex shape. For such a system to be effective, it must produce plastic yielding in the region to be stress relieved; however, the yielded region may be quite local and may already be at a residual stress level at or near the yield point prior to treatment. The yielded region may also be moved progressively along the part to achieve full coverage. It may not be possible or even necessary to eliminate all residual stresses by this method, but it may be possible to reduce the magnitude of peak stresses. If such a reduction is accomplished, a vibratory stress-relief system could provide a means of reducing distortion in parts machined after welding and could improve resistance to brittle fracture if it is triggered by high levels of residual stress. In some instances, plastic yielding is not achieved by vibratory stress relief due to the size or complexity of the part involved. Even in these cases, some improvement in distortion when machining after welding has been reported.

Unfortunately, vibratory stress-relief treatments do not change the metallurgical structure of welds or heat-affected zones to which they are applied, and thus no improvement or change in mechanical properties of the treated zone may be expected. In those instances where thermal stress-relief treatments are expected to alter the strength or toughness of the weldment by changes in microstructure, vibratory stress relief will not be a satisfactory substitute.

16.2.8 Peening

Peening is the mechanical working of metals by means of impact blows. Various specifications and codes allow the use of peening on intermediate weld layers for reducing distortion and residual stresses; however, they prohibit the use of peening on the first and the last layer. Peening of the first layer may conceal cracking, or it could actually pierce the weld. Peening the last layer is prohibited largely in the belief that cold working would reduce notch toughness of the weld metal, since there is no subsequent application of heat to anneal it.

Although peening has been used by the welding industry for a long time (over 40 years), scientific information on peening and its effects is still lacking. The following comments may be made on peening:

1. Peening can reduce distortion (see Table 7.7, for example). However, since the extent of distortion reduction by peening is rather limited, every pass needs to be peened to produce substantial reduction of distortion.
2. Peening may result in some reduction in residual stresses in welded joints. To be effective in reducing residual stresses, it is important to peen the last welding pass. (However, this is prohibited by specifications.)
3. Cold working by peening may cause reduction in notch toughness. Consequently, specifications do not allow peening of the last welding pass.

4. Peening may conceal cracking or may even extend existing cracks, if not executed carefully. This may be an important reason for prohibiting peening of the first pass.
5. Peening can increase fatigue strength by producing compressive residual stresses in regions near the surface of a structure (see Section 11.5).

However, one must be careful not to produce notches during peening operations. These notches may significantly reduce fatigue strength and wipe out favorable effects of compressive residual stresses.

16.2.9 Mechanical stress relieving and prooftesting

When tensile load is applied to a longitudinal weld and then released, residual stresses in the weldment are released, as shown in Fig. 8.1. This phenomenon is called mechanical stress relieving. The favorable effects of mechanical stress relieving on brittle fracture are discussed in Section 10.5.2. Figure 10.25 shows that, when a weldment is stress relieved at a temperature above the ductile-to-brittle transition temperature and then subjected to tensile loading at a temperature below the transition temperature, fracture occurs after the load exceeds the stress-relieving load. Prior overloading also increases fatigue strength, as discussed in Section 11.5.1.

Prooftesting is frequently performed on various welded structures. Practically all pressure vessels are given their final test by means of hydrostatic internal pressure. The stress level of prooftesting is often higher than design stresses. Although the primary purpose of the prooftesting is to examine the structural integrity of a final product, the prooftesting also accomplishes mechanical stress relieving.

Cylindrical and spherical pressure vessels can be proofstressed readily by hydrostatic loading. In cylindrical vessels, hydrostatic loading produces circumferential stress approximately double the longitudinal stress, so that relief of residual stress in circumferential welds will be only half the relief in longitudinal welds.

References

- (1601) NAVSHIPS 0900-060-04010, "Fabrication, Welding, and Inspection of Metal Boat and Craft Hulls", Naval Ship Systems Command, Department of the Navy, Washington, D.C. 20360 (Jan. 1971).
- (1602) NAVSHIPS 0900-014-5010, "Fabrication, Welding, and Inspection of Non-Combatant Ship Hulls", Naval Ships Engineering Center, Navy Department, Washington, D.C. (Dec. 1966).
- (1603) American Bureau of Shipping, *Rules for Building and Classing Steel Vessels*, Washington, D.C. (Dec. 1966).
- (1604) AWS D2.0-69, *Specifications for Welded Highway and Railway Bridges*, American Welding Society, 1969.
- (1605) AWS D1.0-69, *Code for Welding on Building Construction*, American Welding Society, 1969.
- (1606) *Welding Handbook*, Volume 1, Seventh Edition, American Welding Society, 1976.
- (1607) AWS D3.5-62, *Hull Welding Manual*, American Welding Society, 1962.
- (1608) FUJITA, Y., NOMOTO, T., and AOYAGI, A., "A study on stress relaxation due to heat treatment", I.I.W. Document X-697-73, Department of Naval Architecture, University of Tokyo, Japan.
- (1609) DUNEGAN, H. and HARRIS, D., "Acoustic emission—a new nondestructive testing tool", *Ultrasonics*, 7 (3), 160-166 (July 1909).
- (1610) KANAZAWA, T. and KOBAYASHI, A.S. (editors), *Significance of Defects on Welded Structures, Proceedings of the Japan—U.S. Seminar, 1973*, Tokyo, University of Tokyo Press, 1974.
- (1611) NICHOLS, R. W. (editor), *Acoustic Emission*, Applied Science Publishers, Ltd., London, 1976.

Index

- Adhesive bonding 47
- Airy's stress function 103
- Alpha stabilizers 36
- Aluminum and aluminum alloys 8, 12, 28–36
 - additions to steel 382
 - classifications 28
 - cutting and welding processes 33–36
 - distortion 281, 291, 298–9, 311
 - fatigue crack growth 461
 - heat treatments 29–30
 - high-strength 588
 - low-cycle fatigue 460
 - marine applications 30–31
 - mechanical characteristics 31–32
 - mechanical properties 30
 - metallurgy 28–30
 - optimum material trend line 33
 - properties 28–30, 178
 - residual stresses 210, 218–19
 - thermal stresses 161
 - weld defects 588
- Analytical simulation 238, 239
- Angular distortion 236, 243–6, 288, 313, 425–6, 438–40, 623
 - coefficient of rigidity for 278
 - of butt welds 275–7
 - of fillet welds 277, 288–94
- Angular rigidity coefficient 280, 281
- Arc characteristics 244
- Arc efficiency 62, 178, 181
- Arc strikes 580, 610
- Automatic welding processes 50–57

- Battelle program 151–2, 155
- Bead-bend test 367
- Bend tests 374
- Bending distortion, longitudinal 295–9
- Bending stresses 505, 563
- Beta stabilizers 36
- Biharmonic function 104
- Block welding 229, 232–3, 270, 314
- Bridges 253, 343–4
- Brittle coatings 140
 - drilling technique 122–3
- Brittle fracture 341–50, 374, 591–2
 - analytical studies 429–47
 - appearance 344
 - catastrophic failures 418
 - characteristics of 344–50, 418
 - effect of weld defects 591–3
 - origins of failures 347–8
 - prevention 619–21
 - propagation 349–50
 - ship structures 341–3, 347, 349, 353–7, 373, 400, 592, 621
 - stress at failures 347
 - structures other than ships 343–4
 - temperature effects 347
 - theories 400–4
- Buckling
 - distortion effects on 333
 - residual stress effects 334–5
 - under compressive loading 331
- Buckling distortion 300–12, 625–6
- Buckling strength 491–517
 - columns under compressive loading 492–4
 - panel structures 497–500, 503–7
 - plate structures under compressive loading 494–500
 - ship bottom plating 500–3
- Buckling stresses 331, 332
- Building construction 253
- Built-up beams, thermal stresses 164
- Bulge transition temperature 367
- Butt joints 622

- Capel's formulas 255–6
- Carbon additions 381
- Carbon equivalent 528–33, 536, 539, 560
- Cavities, stress concentrations 582
- Ceramics 12
- Charpy V-notch impact test 351–7, 362, 364, 372, 404
- Checkerboard heating 323
- Chemical composition 378, 380
- Chevron markings 344, 346
- Circular patch test 545
- Circular patch welds 203–4
- Cline's data 256
- Cold working 383
- Columbium 210
- Columns
 - compressive loading 331–5, 492–4
 - welded aluminum 493–4
 - welded steel 492–3
- Compatibility condition 103

- Composite materials 12
- Compressive loading
 - columns under 331–5, 492–4
 - plate structures under 494–500
- Compressive stresses 303, 505
- Computer programs 168, 172, 191, 239, 265, 284, 299
- Computer simulation 180–6, 191, 295
- Concrete 13
- Continuous cooling transformation (CCT) diagrams 81, 84
- Controlled thermal severity (CTS) test 545–6
- Cooling rate effects 81–84
- Corrosion 11
- Corrosion fatigue 457–8
- Corrugation damage of welded ships 500–3
- Cost aspects 620
- Crack arrest 2
- Crack-arrest temperature 362–3
- Crack growth 108
 - subcritical 593
- Crack growth rate 612, 613
- Crack length, critical 414–18, 592
- Crack opening 106
- Crack opening displacement 411–12
- Crack patterns 481–90
 - theory 483–4
- Crack-sensitivity tests 543
- Crack stability 484
- Crack stopping hole 569
- Crack susceptibility 554
- Crack-tip-opening displacement 413
- Crack tip plastic zone 412–14
- Cracking 518–76, 580, 610
 - circular 484
 - classification by appearance and location 518–20
 - classification by conditions of formation 520
 - classification of types 518–20
 - cold 528–43
 - delayed 528
 - effects of chemical compositions 528
 - prevention 530, 537–43
 - short time 528
 - crater 519
 - fracture mechanics theories 572
 - hot 520–8
 - effects of chemical compositions 527–8
 - in region of partial melting 523
 - mechanisms of 520, 525
 - sensitivity formula 528
 - theory 521, 572
 - hydrogen-induced 560
 - intergranular 526
 - longitudinal base metal 519
 - longitudinal weld metal 518–19
 - mechanical analysis 569–75
 - modes of 404–5
 - parallel 486
 - radial 484
 - reasons for occurrence 518
 - root 520
 - thermal stress analysis 574–5
 - toe 519
 - transverse base metal 519
 - transverse weld metal 518
 - under restraint 562–4
- Cracking index 534
- Cracking potential 627
- Cracking temperature 555
- Cracking tests 543–61, 572–4
 - recent trends and comparison of results 556–61
- Cracking threshold 549
- Cracks, transverse 484–90
- Critical crack length 414–18, 592
- Critical solidification range, 521, 527
- Critical stress 331, 402
- Critical stress intensity factor 408
- Cross-welded specimens 426
- Cruciform test 547
- Crystal structures 337
- Cylindrical shells
 - subjected to external pressure 507–8, 511–13
 - thermal stresses 162
- Deep Submergence Rescue Vehicle (DSRV) 6
- Deep Submergence Search Vehicle (DSSV) 6
- Deflection 179
- Deoxidation effects 382
- Design 619–26
- Differential heating 320–2
- Dimensional changes, determination of 109
- Dimensional effects 312
- Dislocation 88, 201
 - in circular ring 98
 - in multiply-connected region 96
 - stress problem caused by 105
 - stressed body 96
- Displacement fields 159
- Distortion 2–4, 36, 108–10, 145, 155, 163, 164, 174, 177, 184–6, 190, 229, 236–327, 627
 - acceptable limits 237
 - allowable standards 245–53
 - analysis methodologies 238–44
 - analysis studies 244
 - buckling 236
 - design control 624–5
 - due to angular change 243
 - effect on buckling 333
 - effect on buckling strength 491–517
 - fundamental types 236
 - general introduction 236–45
 - in aluminum structures 286
 - longitudinal 622
 - longitudinal bending 236
 - methods of reducing 628
 - minimizing 236
 - of ring-type specimen 243–4
 - of ship bottom plating 500–7
 - out-of-plane 277, 283–8, 330, 503–7, 625
 - problem and its solution 236
 - reduction methods 312–22
 - removal 237–8, 322–5
 - reviews 238

- rotational 236, 253
- transient 239
- Watanabe-Satoh's formulas 244-5
- Double plate effect on fatigue strength 622
- Double-tension test 368-9
- Drop-weight test 358-60
- Ductile fractures 341, 586-91
- Dye penetrant inspection 607
- Dynamic tear test 360-2

- Elastic strain 193, 194
- Elastic strain release 199
- Elastic theory 110
- Elasticity modulus. *See* Young's modulus
- Electrical-resistance welding 47
- Electrodes 20, 48
 - characteristics 244
 - coated 48, 78, 531, 532
 - continuously fed 51
 - covered 47, 193, 255, 267, 280, 387, 389
 - heat flow 85-86
 - large vs. small diameter 627-8
 - low-hydrogen 530, 531, 542
 - mild steel 390
 - moisture content 531
 - size of 267
 - tungsten 50
- Electrode gas welding process 54-57, 394
- Electromagnetic hammer 325
- Electron-beam welding 57, 301
- Electroslag welding 52-54, 394
- Endurance limit 456-8
- Engineering cost 620
- ESSO test 368
- Explosion bulge test 367
- Explosion crack starter test 356, 367
- Extensometers 115-17, 140, 232
- External pressure
 - cylindrical shells subjected to 507-8, 511-13
 - spherical shells subjected to 507-11

- Fabrication 626-33
- Fatigue
 - high-cycle 450, 453
 - high-stress 450
 - low cycle 450, 458-60, 614
 - low stress 450
- Fatigue crack growth 450, 460-4, 598-602
- Fatigue crack initiation 450
- Fatigue crack starter notches 410
- Fatigue fracture 341, 449-77
 - characteristics of 450-3
 - effect of residual stresses on 466-8
 - effect of weld defects 594-602
 - introduction to 449-53
 - prevention 621
- Fatigue life 614
- Fatigue strength 11, 453, 464-6, 624
 - and reinforcement 597-8
 - double plate effect on 622
 - methods of improving the 468-76
- Fatigue testing-stress cycles 453
- 'F'-cooling curve 84
- Ferrous alloys 6
- Fillet welds 622
- Finishing temperature 383
- Finite-element technique 158, 159, 166, 281
- Flame gauging 267
- Flame-heating 238
- Flame straightening 322-4
- Fluorescent penetrant inspection 606-7
- Fluxes 49
- Forced chilling 261-5, 317
- Fracture
 - brittle. *See* Brittle fracture
 - cleavage 336-41
 - control guide lines 384-5
 - ductile 341, 586-91
 - elementary concepts 336-41
 - fatigue. *See* Fatigue fracture
 - intergranular 336
 - low-applied-stress 373-8, 418-19
 - macroscopic appearance 337-9
 - microscopic observations 339
 - shear 336-41
 - transgranular 336
 - types of 341
- Fracture analysis diagram (FAD) 359-61, 385
- Fracture appearance transition temperature 362
- Fracture liability 620
- Fracture mechanics 104, 106-8, 240, 374, 464
 - theory 404-14, 421, 483, 569-75
 - weld cracking 572
- Fracture propagation 375
- Fracture propagation tests 367
- Fracture roughness 620
- Fracture strength 426
- Fracture stress 402
- Fracture tests 428-9
- Fracture toughness 336-99
 - aluminum 32-33
 - correlation of test results 373
 - definition and terminology 11, 408
 - dynamic loading tests 367
 - effects of chemical composition and manufacturing processes 378-83
 - evaluation tests 369-73
 - titanium alloys 43-44
 - static tests with small specimens 364-7
 - trends in 23
 - values of 414-18
- Fracture toughness tests 409-10
- Freezing-cycle hot-tension test 523, 525
- Fusion welding 47

- Gage length 138
- Gannert extensometer technique 115-17
- Gas metal-arc process 51-52, 174, 393
- Gas-shielded-arc welding 50-52
- Gas tungsten-arc welding 50, 51, 344
- Glass 12

- Glycerine substitution method 536
 Goodman diagram 455-6
 Goursat's stress functions 99-102
 Grid systems 140
 dividing technique 122
 Griffith theory 401-2
 Gunnert drilling method 144, 120-1
 Gunnert extensometer 232
 Gunnert strain indicator 141
- Hardness measurement techniques 113, 131-3
 Harmonic functions 104
 H-beam 334
 Heat-affected zone (HAZ) 28, 50, 52
 cooling rate 77-88
 determinations of thermal history 75-76
 effects of welding conditions 80
 heat input control 80-84
 loss of strength 36
 structure prediction 69
 thermal cycles 76
 thermal history 75-84
 Heat dissipation 61-62
 Heat flow
 in electrodes 85-86
 in weld metal 85-86
 in weldments 60-87, 109-10, 159-60
 analysis of 177-9
 basic considerations 62-67
 computer-aided analyses 68-69
 development of mathematical analyses 67-69
 dimensionless expressions 71-73
 effect of heat-source shape 65-66
 fundamental equation 64
 linear and non-linear theories 66-67
 mathematical analysis 62-69
 quasi-stationary state and non-stationary state 64-65
 simple solutions for analysis 69
 summary of past studies 68
 temperature changes at start and end of weld 75
 temperature distribution in non-stationary state 73-75
 temperature distribution in quasi-stationary state 69-71
 three-dimensional case, finite thickness 70-71
 three-dimensional case, semi-infinite plate 70
 two-dimensional case, finite breadth 71
 two-dimensional case, infinite plate 71
 Heat generated by welding arc 60-61
 Heat input 80-84, 181, 182, 184, 267, 302, 303, 311, 626-67
 Heat-treatment 16, 29-30, 630-2
 Heating, distortion caused by 317-20
 Heyn-Bauer machining technique 120
 Holes, stress concentration around 584-6
 Hooke's law 90, 102
 Hoop stress 582
 Houldcroft fishbone test 544
- Hydrodynamics 104
 Hydrogen content in weld metal 541
 Hydrogen cracking 113, 133, 489, 531, 560
 Hydrogen embrittlement 478-90
 I-beams 295, 296, 313
 Impact test. *See* Charpy V-notch
 Implant test 553-6
 Inclined plane 89
 Inclusions 578, 582-4, 610
 Incompatibility 103, 104, 110, 200
 Incomplete fusion 578-9
 Inherent shrinkage 246
 Intermittent welding 298, 311, 314, 622
 Internal pressure 437
 Interpass temperature 628-9
 Iron-binary alloys 527
 I-shaped structural model 428-9, 440-7
 Isothermal transformation (ITT) diagram 81
- J-integral 404
 Joining technology development 8-10
 Joint characteristics 244
 Joint design 313
 Joint efficiency 1
 Joint mismatch 272-4
 Joint penetration 579-80
 Joining processes 47
 Joint restraint 313, 314, 534-6, 628
 cracking under 562-4
 critical 536
 historical development 561-2
 reaction stress under 562-4
 theory 570-1
 see also Restraint degree; Restraint intensity
- Kommerell-type longitudinal-bead-weld bend specimen 366
- Lap joints 622
 Laser welding 57
 Lehigh restraint test 366, 544
 Linear net heat input 181, 184
 Linear net heat intensity 181, 184
 Liquid-solid phase joining 47
 Lloyd's Register of Shipping 354-5
 Load-deflection diagram 334, 335
 Local compression 472
 Longitudinal-weld underbead-cracking test 547
- Magnetic particle inspection 603-4
 Malisius' formula 254-5
 Manganese additions 381
 Manufacturing process variables 378, 382-3
 Material cost vs. total cost 620
 Materials development 4-8
 Materials selection 10-13
 Mathar-Soete drilling technique 117-19
 Mechanical properties 90-92

- Mesnager-Sachs boring-out technique 120
 Metal movement 151, 164, 173, 179, 180, 186,
 238, 270, 272-4, 298-9
 Microcracking 417, 526, 527
 Microfissuring 548
 Microflaws 414-17
 Miller index 126
 Minimum energy principle 279, 281
 M.I.T. one-dimensional programs 152-6
 Multilayer welding 228, 229, 270, 314
 Multipass welding 155-6, 172, 192, 194, 265,
 297-8, 313
- Narrow-gap welding process 52
 Naval Research Laboratory 355-8, 367
 Navy tear test 365
 Nickel additions 382
 Nitrogen effects 382
 Non-destructive testing 2, 602-9
 Notations x
 Notch-bend tests 366
 Notch effects 107, 343, 621
 Notch sensitivity 350-1
 Notch toughness 20, 343, 350-63
 evaluation 353-7, 363-73
 of specifications 385-9
 of weld metals 385-97
 of weld metals below 120,000 psi yield strength
 394-6
 of weld metals over 120,000 psi yield strength
 396-7
 requirements 384-5
 Notched tensile specimens 374
- One-dimensional analysis 277
 One-side submerged-arc welding 50
 Overloading 468-70, 476
 Oxygen effects 45, 382
- Peening 314, 470-2, 632-3
 Penetrant inspection 605-6
 Penetration defects 599
 Phase transformation 261
 Phosphorus effects 382
 Photoelastic coatings 140
 drilling technique 123-4
 Pine-needle heating 323
 Plane strain 409
 Plane strain analysis 161-2
 Plane stress 196
 Plane stress analysis 161-2
 Plastic buckling of welded plates 496-7
 Plastic deformation 110, 330, 335, 412, 420
 Plastic strain 193, 194, 198
 Plastic strain release 199
 Plastic zone 194, 335, 411
 Plate structures under compressive loading
 494-500
 Plug welds 202-3, 624
- Plywood 13
 Poisson's ratio 583
 Porosity 35, 46, 578, 582, 588-9, 610
 Prebending effects 288-94
 Preheating 288, 532, 533, 537-43, 628-9
 Pressure vessels 253, 459, 613-14, 633
 Prestraining 288-94, 315, 383
 Principle of virtual work 158-9
 Prooftesting 633
- Radiographic inspection 602-3
 Rapid chilling 315
 Ratio Analysis Diagram (RAD) 26-28, 362
 Reaction stresses 141, 192, 194, 233, 551, 562-4
 Red-hot heating 324
 References xi
 Reinforcement 622
 and fatigue strength 597-8
 Relative toughness of weldment 488
 Reliability evaluation 607-15
 Reliability improvement 615
 Repair welding 569
 Residual stresses 2-4, 88-111, 297, 420, 437
 analysis techniques 189-91
 analytical determination 200-1
 analytical simulation 189-91
 buckling stresses caused by 310
 compressive 428, 475, 499
 definition 92
 distribution 191, 192, 199, 201-8, 442
 effect of external restraints 314
 effect of material properties 208-22
 effect of specimen length 222-5
 effect of specimen size 222-5
 effect of specimen width 225
 effect of welding parameters 180-4, 627
 effect of welding sequence 229-33
 effect on buckling 334-5
 effect on buckling strength 491-517
 equilibrium condition of 92-94
 in heavy weldments 225-9
 in restrained butt welds 193-201
 longitudinal 191, 201, 224, 228, 612
 macroscopic and microscopic 92
 magnitude and distribution 189-234
 mathematical analysis 144-5
 measurement of 112-47
 characteristics of techniques 137
 classification of techniques 112-13
 cost and time factors 139
 field application 139-40
 hydrogen-induced cracking technique 113,
 133
 in heavy and complex weldments 144-5
 selection of techniques 136-40
 stress-corrosion cracking technique 113,
 133-6
 stress-relaxation techniques 112, 114-24
 stress-sensitive properties 113, 130-3
 X-ray diffraction 112, 125, 139
 occurrence of 94

- parameters affecting 108–10
- produced by mismatching 95–102
- produced by uneven distribution of non-elastic strains 102–4
- tensile 428, 475, 499
- terminology 92
- theory 570–1
- thickness-direction distribution 138
- transverse 191, 224
- under tensile loading 329–30
- vs. fracture mechanics theory 106
- vs. vortex theory 104–6
- see also* Fatigue fracture; Hydrogen embrittlement; Stress corrosion cracking
- Resisting cross-section 294
- Restraining jig 290
- Restraint degree 239–43, 253, 261–5, 561–71
- Restraint intensity 536, 540, 551, 562–9
 - effect of crack stopping hole 569
 - effect of joint length and weld length 568
 - effect of plate thickness 567–8
 - effect of specimen size and saw cuts 569
 - of structural welds 566–7
- Restraint weld cracking tests 572–4
- Rewelding 267
- Rigid-restraint cracking (RRC) test 549–51
- Rigidity modulus 90
- River pattern 339
- Robertson test 367, 372
- Rocket motor case 344
- Root gap effects 267
- Rosenthal-Norton sectioning technique 121–2, 144
- Rotational distortion 267–70

- Saturn V Space Vehicle 9
- Scallops 624
- Semi-automatic processes 49
- Shear modulus 90
- Shielded metal-arc welding 47–49
- Ship bottom plating
 - buckling strength 500–3
 - distortion of 500–7
- Ship plate, heavy mild-steel 390
- Ship structures
 - brittle fracture 341–3, 347, 349, 353–7, 373, 400, 592, 621
 - corrugation damage 500
- Shrinkage 36, 110, 117, 199–201, 204, 229, 233, 236
 - allowances 245, 248
 - analytical study 244
 - inherent 245
 - longitudinal 236
 - butt welds 294
 - fillet welds 294
 - reviews 238
 - transverse 236, 239, 241, 242, 244
 - butt welds 253–74
 - fillet welds 274
- SI units ix
- Silicon additions 382
- Slag inclusions 578, 610
- Slenderness ratio 331, 494
- Slip planes 337
- Slot welds 624
- S-N diagrams 453–6, 458
- SOD test 368, 372
- Soldering 8
- Solid-phase welding 47
- Solidification process 521
- Specifications 609
- Spherical shells subjected to external pressure 507–11
- Spot heating 323, 473–5
- Spraragen-Ettinger's formula 255
- Stäblein successive milling technique 119–20
- Steels 4–8, 12–28, 295–8, 357
 - carbon 134, 380
 - C-Mn 555, 559
 - die 414
 - ferritic 80
 - high strength 4, 12–21, 23–28, 52, 80, 133, 134, 166–73, 211–18, 380, 391, 530, 537, 612
 - HT 16
 - HT-60 542, 630
 - HT-80 542, 551, 630
 - HY-80 4, 11, 12, 21–23, 52, 81, 84, 165, 391, 511, 523, 525, 621
 - HY-100 6, 11, 12, 21, 81
 - HY-130 6, 11, 12, 165, 169, 614
 - HY-140 6
 - HY-180 12
 - HY-230 460
 - line-pipe 559, 561
 - low-alloy 80, 134, 380
 - low carbons 13–21, 48, 208, 209, 280, 288, 290, 302, 619
 - maraging 11, 12
 - medium-strength 463
 - microalloy 560, 561
 - mild 417
 - notch-tough 391
 - over 120,000 psi yield strength 23–28
 - QT 50 16
 - quenched and tempered 21, 52, 81
 - SAE-4330 482
 - ship 387
 - structural 13
 - ultrahigh-strength 173, 209, 417, 418
 - up to 80,000 psi yield strength 13–21
 - up to 120,000 psi yield strength 21
- Straightening by flame heating 322–4
- Strain 89–91, 110, 297, 314, 315
- Strain energy 104, 106, 108, 233, 402
- Strain energy release 199, 429–35
- Strain energy release rate 407, 418, 430, 432, 434
- Strain gages 114–15, 139, 140, 143–4, 164, 173, 176
- Strain hardening 156, 157
- Strain measurement 136, 140–4
- Strain rate 156, 158
- Strain-relaxation 92
- Strength of ideal solid and actual structures 400–1
- Strength of welded structures
 - fundamentals 328–35

- 'idealistic' 328-9
- 'realistic' 328-9
- Strength-to-weight ratio 10
- Stress 88-89, 91
- Stress analysis 3
- Stress changes in body 96
- Stress components, determination of 138
- Stress concentration 422, 424-5, 457, 468, 621
 - around cavity 582
 - around holes 584-6
 - around inclusions 582-4
 - around sharp notch 107
 - caused by out-of-plane distortion 330
 - due to weld defects 581-6
- Stress concentration ratio 424-5
- Stress corrosion cracking 11, 113, 133-6, 478-90
- Stress distribution 330, 443, 488, 612
- Stress functions 99-102
- Stress intensity 88
- Stress intensity factor 108, 240, 405-7, 435-40, 444-7, 461, 463, 488, 490, 570, 571, 612
- Stress-relaxation techniques 112, 114-24
- Stress relieving 324-5, 420, 424, 434, 435, 612, 630, 633
- Stress-strain diagram 332, 403
- Stress-strain relationship 90, 110
- Stress-temperature curve 94-96
- Stretching 317-20
- Striations 460
- Structural discontinuities 421-2, 621
- Structure-insensitive properties 401
- Structure-sensitive properties 401
- Submerged-arc welding 49-50, 300, 388, 390, 391
- Sulfur effects 382
- Surface effect ships (SES) 8
- Surface energy 402, 483

- Tantalum 210
- T-bars 295, 296, 313
- T-beams 320, 322
- Temperature vs. fracture stress relationship 525
- Temperature changes at start and end of weld 75
- Temperature distribution
 - in non-stationary state 73-75
 - in quasi-stationary state 69-71
- Tensile loading, residual stress under 329-30
- Tensile restraint cracking (TRC) test 549-51
- Tensile stresses 310, 330
- Tensile tests 367-70
- Thermal conductivity 62, 63, 66, 261
- Thermal diffusivity 63, 66
- Thermal expansion coefficients 261
- Thermal pattern 628
- Thermal-pattern alteration 315-17
- Thermal properties 66
- Thermal severity number (TSN) 546
- Thermal stresses 92, 109, 148-9
 - analysis 574
 - assessment of current status and future prospects 186-7
 - bead-on-plate welding 159
 - computer simulation 180-6
 - during welding along longitudinal edge of strip 173-80
 - effects of welding parameters 180-4
 - experimental studies on 164-80
 - high-strength steels 166-73
 - one-dimensional analysis 151-6, 165, 179
 - studies of 150
 - three-dimensional analysis 162-4
 - two-dimensional analysis 156-62, 166, 180
- Thick plate, thermal stresses 162-3
- Tipper test 365
- Titanium 12, 36
 - contamination 45
 - mechanical properties of welds 46
 - oxygen effects in 45
 - porosity 46
 - welding processes 44-46
- Titanium alloys 8, 12, 36-46, 219-22, 460
 - alloying elements 43
 - contamination 45
 - fracture toughness 43-44
 - impurity effects 42
 - in commercial production 41
 - mechanical properties 41-43
 - mechanical properties of welds 46
 - optimum material trend line (OMTL) 43
 - porosity 46
 - welding processes 44-46
- Transition temperature 350-1, 362-3, 367, 619
- Triangular heating 323
- T-section beams 298
- Tungsten inclusions 578
- Two-dimensional analysis 281-3

- Ultrasonic techniques 113, 130-1, 140, 604-5
- Undercut 580
- Unfairness of welded plating 248-51
- Units ix
- Utility function 613

- Van der Veer test 365
- Varestraint test 547-9
- Vertical automatic welding processes 52-57
- Vibratory stress relieving 324-5
- von Mises' yield criterion 157
- Vortex theory 104-6

- Watanabe-Satoh's formulas 244-5, 255
- Weld cracking. *See* Cracking
- Weld defects 2, 344, 577-617
 - common 578-80
 - development of rationale for accepting 610-15
 - effect on brittle fracture 591-3
 - effect on ductile fracture 586-91
 - effect on fatigue fracture 594-602
 - effect on structural strength 577
 - location effects 596
 - nature and extent of 577

642 *Index*

- stress concentration due to 581–6
- Weld location 155
- Weld metal 204
 - heat flow 85–86
 - notch toughness 385–97
- Weld metal zoning 27
- Weldability 561
- Weldability index 84
- Welded-and-notched wide plates 375, 418
- Welded pipes 207–8
- Welded shapes and columns 205–6
- Welded structures
 - advantages 1
 - problems with 2
- Welding arc, heat generated by 60–61
- Welding conditions 288, 313
- Welding processes 47–57, 313
- Welding sequence 314
- Welding speed 181, 182, 184, 185, 267
- Welding techniques, development 8–10
- Wells-Kihara test 372
- X-ray analysis 126
- X-ray diffraction 112, 125–30, 139, 140
- X-ray diffractometer 112, 128, 130
- X-ray film 112, 126–30
- X-ray machines 602
- Yield function 158
- Yield strength 4
- Young's modulus 90, 91, 331, 583, 599
- 'Z'-cooling curve 84